



BESSY - Annual Report

2006

Published by:
Berliner Elektronenspeicherring-Gesellschaft
für Synchrotronstrahlung m.b.H. (BESSY)

Albert-Einstein-Str.15
12489 Berlin
Tel. +49 30 6392 2999
Fax +49 30 6392 2990
info@bessy.de
www.bessy.de

Edited by:
Dr. Kai Godehusen



BESSY GmbH
Albert-Einstein-Straße 15
12489 Berlin . Germany
Fon +49-30 / 63 92 - 29 99
Fax +49-30 / 63 92 - 29 90

Geschäftsführung:
Prof. Dr. Dr. h.c. Wolfgang Eberhardt
Prof. Dr. Eberhard Jaeschke
Aufsichtsratsvorsitzender:
Prof. Dr. Dr. h.c. mult. Joachim Treusch

Sitz der Gesellschaft:
Berlin
Handelsregister:
Amtsgericht Charlottenburg
HRB 14 635

Bankverbindung:
Deutsche Bank AG
Berlin
Kto 417 300 101
BLZ 100 700 00



Dear BESSY-users and friends,

Diamonds, glass and STARS ...

This year's Highlights appear to be shiny and sparkling. But researchers took a closer look at diamonds and glass and found that glass although breakable in our everyday experience is well suited for locking up toxic wastes in a stable, durable way for long time. Whereas blue diamonds are not only of jewellers' interest, they appear to be superconductors behaving essentially like their metal superconducting cousins, such as niobium.

Niobium is the basis of all linear accelerator (linac) modules for free electron lasers (FEL). Our FEL project received excellent marks in spring by the Wissenschaftsrat and we are eager now to build and operate the recommended two-stage cascaded FEL to demonstrate the feasibility of HGHG principle in the STARS project, the other sparkling issue. We are confident to achieve the goal since the successful operation of the Femtoslicing Source is already the first step of a cascaded FEL. In addition, recent measurements at BESSY showed for the first time that the accelerator modules can be adopted for continuous wave operation in a superconducting linac, which is also a major ingredient of our FEL project.

Sadly our long time member of the scientific advisory board and supporter Neville Smith will not see the BESSY-FEL up and running. He deceased after a short suffering from cancer. We will miss his advice and his companionship.

BESSY attracts many people with all different kinds of scientific and social background and we are pleased that we welcomed some 6,500 visitors during the year. Among them were visitors during the "Lange Nacht der Wissenschaften", our Breakfast Physics during the summer holiday, delegates on a workshop on the use of Synchrotron Radiation in Arts and Archäometry and our new minister of Science and Education Dr. Annette Schavan. We participated in the initiative "Germany – Land of Ideas" showing ideas and innovation during the entire year and presented BESSY at fairs, at the event "Highlights der Physik" and at political events.

Free electron lasers have been in a one week focus during the FEL06 conference hosted by BESSY in collaboration with FZ Rossendorf in Berlin. Some 200 participants literally from all over the world discussed new developments and research opportunities during the four day conference.

The 25th users meeting in December has seen a record number of participants and poster contributions in BESSY history reflecting the growing interest in the use of synchrotron radiation and the tremendous variety of research topics.

In 2006 all together six prominent members of our user community and staff received calls for appointments as university professors based upon work carried out at BESSY. We would like to congratulate them and all our users for the exiting research they have been performing and we thank our staff members for their efforts and their never decreasing engagement.

Enjoy reading the Annual Report and the Highlights 2006.

Status of the BAM wavelength shifter used as a primary source standard

R. Klein, G. Brandt, L. Cibik, M. Gerlach, M. Krumrey, G. Ulm

Physikalisch-Technische Bundesanstalt, Abbestraße 2 – 12, 10587 Berlin, Germany

M. Scheer

BESSY GmbH, Albert-Einstein-Straße 15, 12489 Berlin, Germany

For the extension of source based radiometry to the hard X-ray range, the PTB is investigating the BAM wavelength-shifter (WLS) as a possible primary source of calculable synchrotron radiation [1]. For more than 20 years PTB has been using the calculable radiation of bending magnets from the BESSY I and BESSY II electron storage rings in the visible, UV, VUV and X-ray spectral range for radiometry [2], especially for the calibration of radiation sources [3] and energy-dispersive detectors [4]. The usable spectral range of bending magnet radiation is limited on the high energy side due to the exponentially decreasing flux for photon energies much higher than the characteristic energy. To increase the high energy limit, a source with higher characteristic energy is needed as is the case for a superconducting WLS. Due to the magnetic field gradients in a WLS, the determination of the magnetic induction at the radiation source point is more complicated as in the case of a bending magnet and requires special attention since the accuracy of the determination limits the obtainable accuracy in the calculation of the spectral radiant power.

The BAM 7 T - WLS had been explicitly specified for radiometric use. Unfortunately, due to a rearrangement of steerer components in the straight section of the WLS, the WLS can not be operated anymore in its specified mode with a symmetric electron trajectory. This leads to an inhomogeneous irradiation in the horizontal plane and an unbearable uncertainty in the determination of the location of the radiation source point in the WLS field map [1]. This problem can be circumvented by a operation of the WLS at a reduced field of 6 T in order to place the radiation source point in the center of the device as described in [1]. Although this special operation ensures a homogeneous illumination in the horizontal plane, it sacrifices some of the benefits of a higher characteristic energy of the WLS as compared to bending magnet radiation due to the decreased magnetic field value. In addition, a dedicated electron optic for the storage ring is required for this operation.

Another problem for radiometric use of the BAM WLS is the failure of the NMR probes used for the measurement of the magnetic induction at the source point. This problem is still unsolved and imposes a stringent limit on the accuracy in the determination of the magnetic induction at the radiation source point. The magnetic induction is currently determined at another WLS that is of the same design and set to the operation parameters of the BAM WLS. The relative uncertainty of this approach is estimated to be about $2.5 \cdot 10^{-3}$ which is more than one order of magnitude worse than the specified value and can only be regard as an interim solution.

Despite these limitations the characterization of the WLS have been continued using the BAMline [5] in the white light mode. The vertical distributions of the synchrotron radiation have been measured by a HPGe - detector and compared to calculations. A 4 mm Cu filter of known thickness in front of the detector was used to absorb the low energy

photons. Fig. 1 shows the measured vertical distribution of the photons in the energy range from 70 keV up to 90 keV (red dots). The calculation is illustrated by the solid line. The lower part of Fig. 1 shows the relative deviation between calculation and measurement within the experimental uncertainty marked by the error bars. The deviations remain within the limit given by the uncertainty in the determination of the parameters needed for the calculation (dotted line). Similar good agreement was found for other intervals of the photon energy.

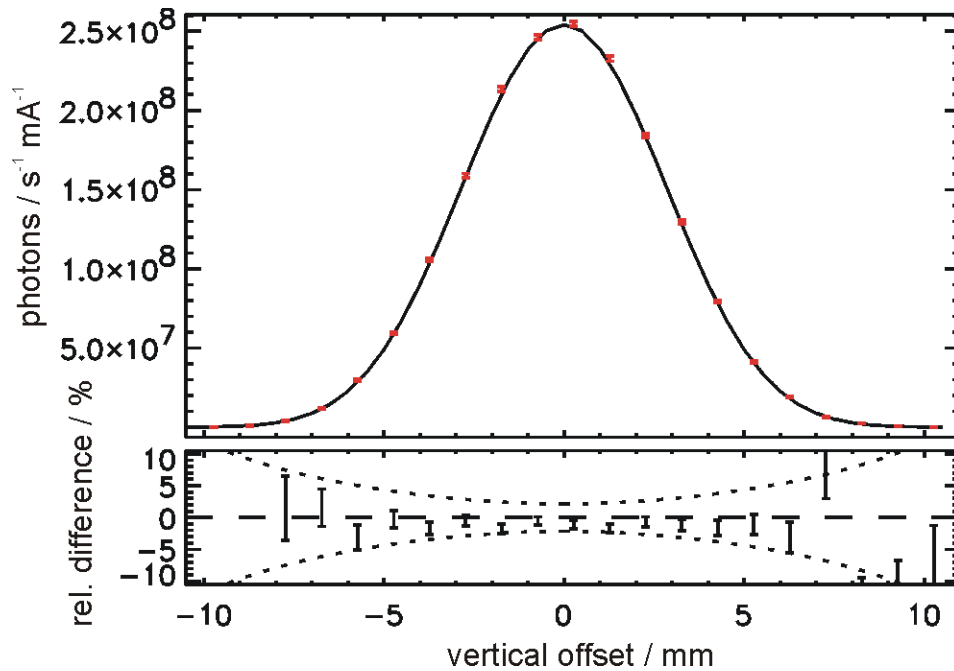


Fig. 1: Upper part: measured (red dots) and calculated (solid line) vertical distribution of the WLS within for photons in the range from 70 keV and 90 keV. Lower part: relative deviation between measurement and calculation (error bars). The dotted line shows the error limit given by the uncertainty in the determination of the parameters needed for the calculation.

In another experiment the synchrotron radiation spectrum of the WLS was measured in the orbital plane and compared to the calculation. For this experiment no Cu filter was used and the spectrum is dominated by photon energies around the characteristic energy. In this energy region, the influence of the poorly known magnetic induction at the source point is not as dominant as it would be the case for higher photon energies [1]. The experiment was performed with only five electrons stored in the storage ring. The measured spectrum is shown in Fig. 2 (black line). The green line shows the calculation by the Schwinger formula [6] taking into account only filter absorption (beamline window and detector entrance window) and air absorption. Taking additionally into account the detector properties as Ge - escape, incomplete charge collection and fluorescence from deadlayers [4], the red curve is calculated. A detection efficiency of unity is assumed for this photon energy range. The measured spectrum is well described by the calculation as shown in the lower part of Fig. 2. However, for detector calibrations at higher photon energies, where the detection efficiency is not unity anymore and has to be measured, the precise knowledge of the magnetic induction at the source point is essential as it affects the spectrum almost in the same way as a finite detector thickness.

The suitability of the BAM WLS as a primary radiometric source standard has been shown in principle. Nevertheless, the WLS in its current operation mode does by far not reach the specified performance. A replacement of the defect NMR samples is essential for the radiometric use of the device at higher photon energies.

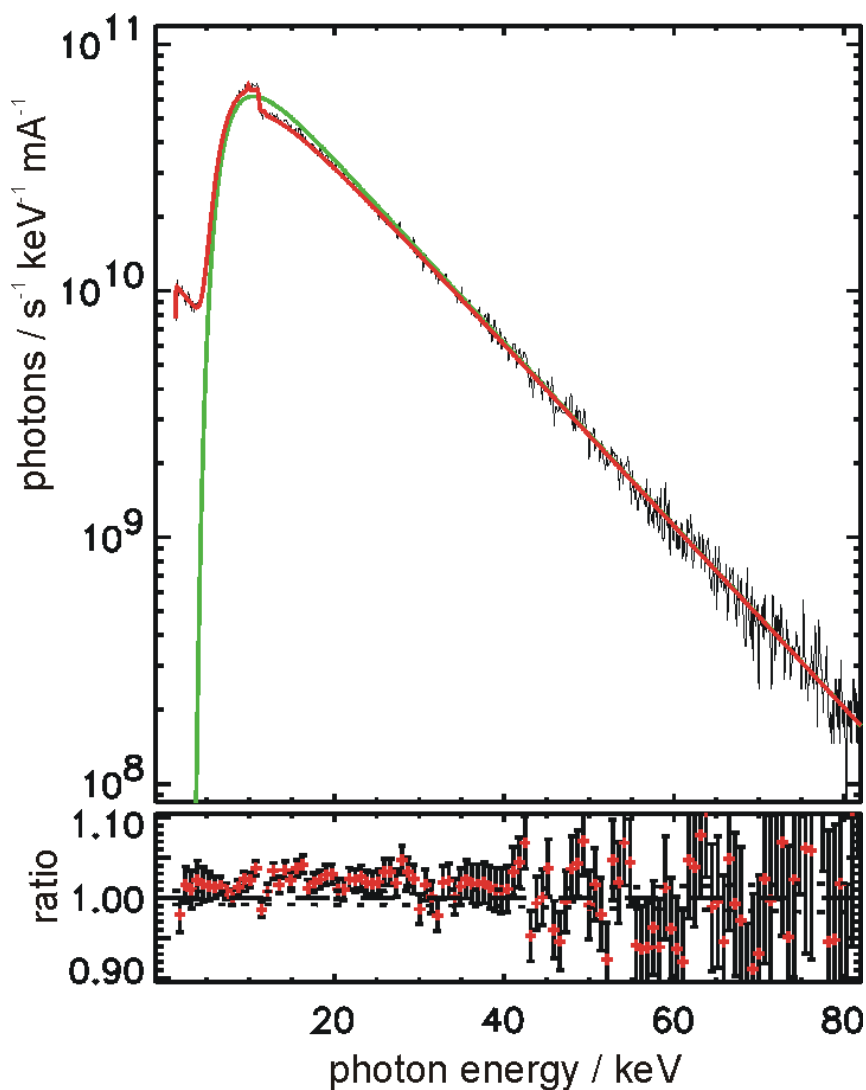


Fig. 2: Upper part: Measured spectrum of WLS radiation with five electrons stored (black line). The green line shows the corresponding Schwinger calculation, the red line a calculation taking the detector properties into account. Lower part: Ratio of the measured spectrum and the Schwinger calculation taking the detector properties into account.

- [1] R. Klein et al., BESSY Annual Report 2005
- [2] G. Ulm, Metrologia **40** (2003) S101 – S106
- [3] M. Richter et al., Nucl. Instr. And Methods A **467/468** (2001) 605 - 608
- [4] F. Scholze et al., Metrologia **38** (2001) 391 - 395
- [5] W. Görner et al., Nucl. Instr. and Meth. A **467-468**, (2001) 703 - 706
- [6] J. Schwinger, Phys. Rev. **75** (1949) 1912

Thin Transmission Photodiodes as Monitor Detectors in the X-ray Range

M. Krumrey, M. Gerlach and P. Müller

Physikalisch-Technische Bundesanstalt, Abbestr. 2-12, 10587 Berlin, Germany

Many synchrotron radiation experiments require a monitoring of the incident photon flux using a so-called I_O detector. The ratio of the photon flux in monochromatized radiation to the storage ring current is often not constant, and ionization chambers cannot easily be integrated especially in soft X-ray UHV beamlines. Instead, the photocurrent from a metal mesh, a thin foil or a mirror coating is sometimes used, but the resulting currents are relatively low and often unstable. Silicon photodiodes of appropriate thickness, operated in transmission geometry in air or in UHV, provide high and stable photocurrents as well as high transmittance. With known responsivity and transmittance of the diodes, the transmitted photon flux can be calculated. While the measurement of the transmittance only requires monochromatic radiation of high spectral purity, the determination of the responsivity with low uncertainty also requires a detector standard. In the PTB laboratory at BESSY II, a cryogenic electrical substitution radiometer is available as primary detector standard in the X-ray range. Responsivity and transmittance as well as the homogeneity of both quantities over the diode surface have been investigated for photodiodes from different European, Japanese and US manufacturers with thicknesses between about 5 μm and 20 μm [1].

All measurements were performed at the four-crystal monochromator beamline which is one of the detector calibration beamlines in the PTB laboratory at BESSY II [2]. At this beamline, monochromatized synchrotron radiation of very high spectral purity is available in the photon energy range from 1.75 keV to 10 keV [3]. The beam size ranges between 0.2 mm and 0.5 mm. The thin transmission diodes were mounted in a UHV reflectometer in order to investigate the homogeneity of their transmittance and their responsivity.

The transmittance was simply measured by inserting the diode in front of another Si photodiode. The responsivity of the transmission diodes was determined against the other Si photodiode serving here as transfer detector standard. This diode was previously calibrated with relative uncertainties below 1 % against a cryogenic electrical substitution radiometer, serving as primary detector standard [4]. The homogeneity was determined by raster scans over the entire surface. The energy dependence of the transmittance and the responsivity was measured in the center of the diode as well as on different positions on the surface, if inhomogeneities had been found in the raster scans.

TABLE 1. Investigated Transmission Photodiodes

Manufacturer	Country of origin	Effective area mm^2	Thickness		Measured transmittance at		Measured responsivity at	
			nominal μm	measured μm	4 keV %	10 keV %	4 keV mA/W	10 keV mA/W
Sintef	Norway	10 x 10	6	6.5	51.3	95.1	113.0	10.9
		10 x 10	12	11.8	29.0	91.1	159.2	19.4
		10 x 10	12	13.0	25.6	90.2	186.1	23.9
Micron Sem.	UK	2.5 x 2.5	20	20.0	12.9	85.8	221.4	35.4
IRD	US	6.5 \emptyset	5	4.7	61.3	96.5	78.1	8.6
Hamamatsu	Japan	10 x 10	5	5.5	56.4	95.8	110.0	10.1
		10 x 10	10	10.8	33.2	92.2	174.3	20.0
for comparison: Ion chamber, air at ambient pressure, two 50 μm Be windows			50000		53	95	12.3	0.8

The investigated transmission photodiodes are listed in Table 1. The measured thickness was obtained from the transmittance measurements in the center of the diode. Of course, the thinnest diodes have the highest transmittance, but their responsivity is lower. The optimum thickness depends

on the photon energy range and on the available and required photon flux. Ion chambers, which are much larger and more difficult to incorporate in UHV beamlines, deliver at least one order of magnitude lower photocurrents, even if operated at atmospheric pressure. At higher photon energies where many experiments are performed in air, the use of ion chambers is more convenient, but their responsivity decreases rapidly: at 30 keV, the responsivity of the 5 cm long ion chamber mentioned in Table 1 is only 0.02 mA/W while a 100 μm thick transmission diode with 97 % transmittance has a responsivity of 9 mA/W, which is more than two orders of magnitude higher.

The transmittance and responsivity of two different thin transmission diodes are shown in Fig. 1. The calculated transmittance for 5.5 μm and 13 μm Si (in the latter case including 0.3 μm Al for the contact layers) is also shown. Just below the Si K edge at 1.84 keV, the transmittance can again rise above 60 %. The responsivity mainly depends on the thickness of the diode, especially at high energies. At energies below about 3 keV, the thickness of the radiation entrance layer (silicon oxide or Al) influences the responsivity. It was shown almost two decades ago that Si p on n diodes with a thick oxide layer can degrade under irradiation due to charging effects in the oxide [5], while Si n on p diodes show much better radiation stability [6]. The same behavior is expected for thin diodes. As even the thinnest diodes will not be used in transmission below 1 keV, aluminum contact layers of up to 0.2 μm thickness are also acceptable.

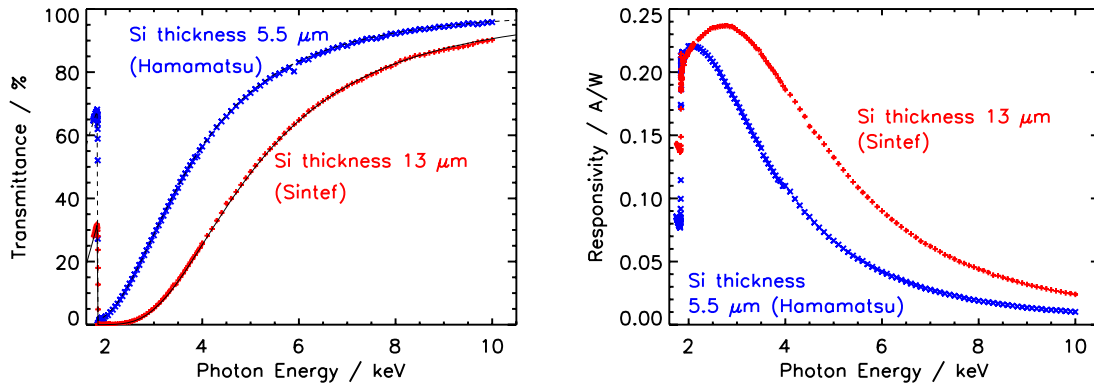


FIGURE 1. Measured and calculated transmittance (left) and responsivity (right) of two different transmission photodiodes. As expected, the thinner diode has a higher transmittance but a lower responsivity.

The homogeneity of transmittance and responsivity has been investigated for all diodes at two different photon energies, typically 10 keV and 4 keV. Some examples are shown in Fig. 2 and 3. Several diodes exhibit gradients in the detector thickness over the surface which can be observed in the transmittance and responsivity distribution. This affects the application only if the beam position changes during the experiment. Other diodes showed a homogeneous transmittance, but exhibit structures in the responsivity which can be related to crystal imperfection of this particular device. Further improvements of the homogeneity would be desirable.

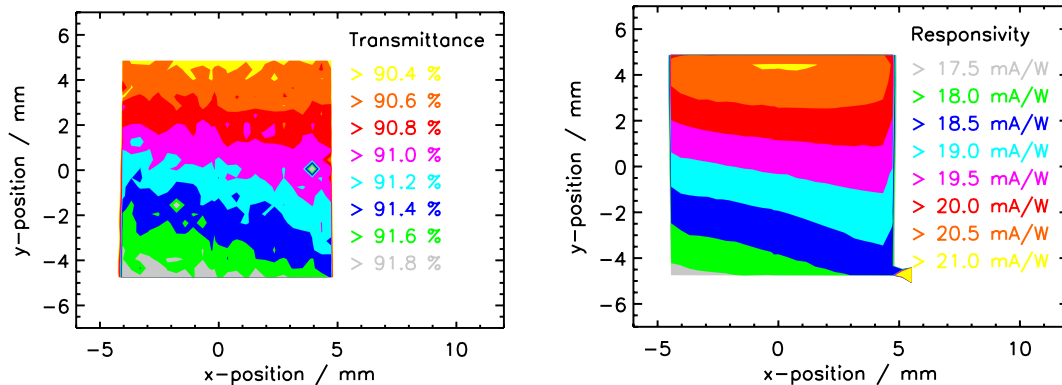


FIGURE 2. Homogeneity of an 11.8 μm thick diode (Sintef) at 10 keV. The gradient in transmittance and responsivity is related to a thickness variation between 11.0 μm and 12.4 μm .

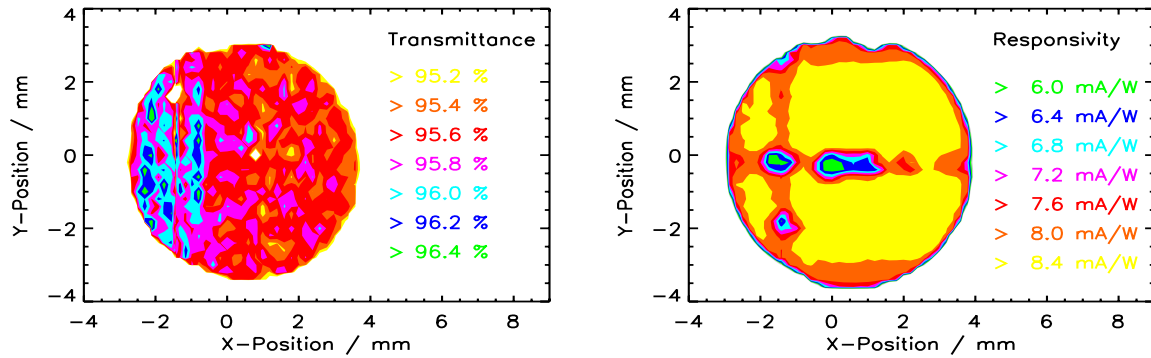


FIGURE 3. Homogeneity of a $4.7 \mu\text{m}$ thick diode (IRD) at 10 keV. While only a slight gradient is visible in the transmittance distribution (low thickness variation), the responsivity distribution seems to be affected by imperfections in the diode material.

CONCLUSION

Thin transmission photodiodes are well suited as monitor detectors for photon energies above about 4 keV. The appropriate thickness has to be selected depending on the photon energy range. The thinnest investigated diodes are only about $5 \mu\text{m}$ thick, but not all transmission diodes presented here are currently commercially available. The homogeneity should be further improved by the manufacturers, and the radiation hardness might be critical for diodes with thick oxide layer. For higher photon energies, large area transmission diodes with thicknesses between $100 \mu\text{m}$ and $500 \mu\text{m}$ are available and have been tested for photon energies up to 60 keV.

REFERENCES

1. M. Krumrey, M. Gerlach, M. Hoffmann and P. Müller, *AIP Conf. Proc.* **879**, 1145 – 1147 (2007)
2. A. Gottwald, U. Kroth, M. Krumrey, P. Müller, M. Richter, F. Scholze, and G. Ulm, *Metrologia* **43**, S125 – S129 (2006).
3. M. Krumrey and G. Ulm, *Nucl. Instr. and Meth. A* **467-468**, 1175 - 1178 (2001).
4. M. Krumrey, L. Büermann, M. Hoffmann, P. Müller, F. Scholze, and G. Ulm, *AIP Conf. Proc.* **705**, 861 – 865 (2004).
5. E. Tegeler and M. Krumrey, *Nucl. Instr. and Meth. A* **282**, 701 - 705 (1989).
6. F. Scholze, R. Klein, and T. Bock, *Appl. Opt.* **42**, 5621-5626 (2003).

A cryogenic electrical substitution radiometer for hard X-rays

M. Gerlach, M. Krumrey, L. Cibik, P. Müller and G. Ulm

Physikalisch-Technische Bundesanstalt, Abbestr. 2-12, 10587 Berlin, Germany

Cryogenic electrical substitution radiometers (ESR) are regarded as the highest-accuracy primary standard detectors from the visible to the soft X-ray region. They are well established in radiometry to determine radiant power with low uncertainties [1]. Operated at liquid helium temperature, an ESR is based on the equivalence of electrical heating power and radiant power. Its cavity absorber is thermally linked to a fixed temperature heat sink via a heat resistance, and it is equipped with a thermometer and a heater that allows the supply of electrical heating power (Fig. 1). The absorber temperature is kept constant by an active control. When radiation is provided, the electrical heating power required to keep the absorber at constant temperature undergoes a reduction equivalent to the incident radiant power so that the radiant power is obtained through the measurement of the electrical heating power.

Usually, the absorbers are made of copper. The reason for this is the excellent thermal conductivity of this material at low temperatures. Copper also has a moderate heat capacity, which ensures a short response time. However, at photon energies above 20 keV the use of already existing copper absorber 100 μm in thickness prevents the use of the ESR as primary detector standard due to increasing transmittance.

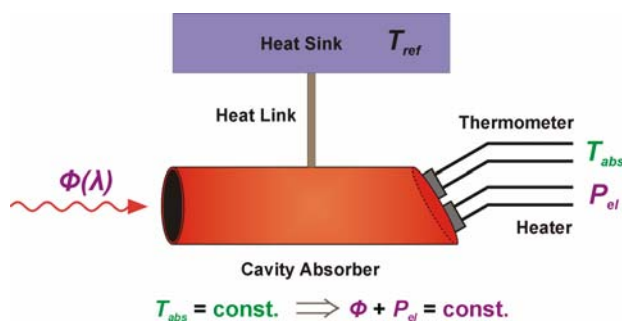


Fig. 1. Operating principle of an electrical substitution radiometer

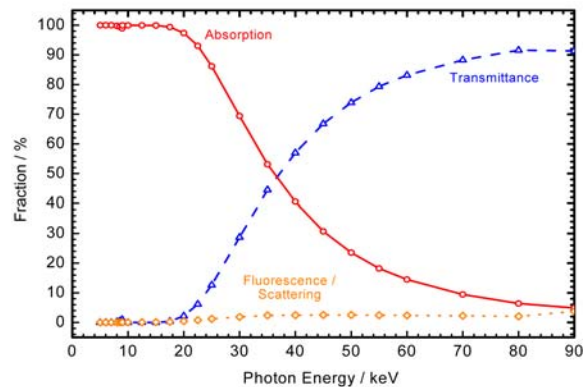


Fig. 2. Radiant properties of the already existing copper absorber of 100 μm thickness, simulated with Geant4

Using the Monte Carlo code Geant4 [2], the complete radiation interaction can be simulated. The simulated properties of the copper absorber having a thickness of 100 μm are shown in Fig. 2. To achieve absorption close to unity also for hard X-rays up to energies of 60 keV, the copper absorber would have to have a thickness of several millimeters. Therefore, other materials and geometries have been studied. The validity of the Monte Carlo simulations has been investigated in experiments with monochromatized synchrotron radiation.

Monte Carlo simulations using Geant4 and scattering experiments

While transmittance and energy absorption in matter can be calculated with various programs, the interaction of radiation in a complex structure like a cavity absorber can only be fully characterized with Monte Carlo techniques that also cover scattering processes as well as

fluorescence. The Monte Carlo code Geant4, in combination with its low energy extension and G4LECS [3], which also takes Doppler-broadening of scattered photons into account, was applied for the simulation of a new cavity absorber. To legitimate the usage of Geant4, scattering experiments were performed at the 7 T wavelength shifter at the BAMline [4], so that simulations could be compared directly to the experimental results, both normalized to the same number of incident photons. An energy-dispersive CdTe-detector (XR-100T-CdTe, Amptek Inc.) with a collimator was used for the experiments. This detector is very convenient for angle-dependent experiments because of its compact size and Peltier cooling, in contrast to the LN₂ cooling of conventional Ge detectors.

Firstly, response functions for monochromatic radiation were measured in the energy range from 2 keV up to 110 keV, which already showed good agreement with the simulations with Geant4 (Fig. 3), including the escape lines of Cd and Te and the Compton edge. The linewidth in the simulation is based on experimental data. To include also scattering effects and fluorescence, a copper foil of 1 mm thickness was exposed to monochromatic radiation of 50 keV. The detector was rotated around the foil and spectra were taken under different angles, horizontally and vertically to the plane of polarization.

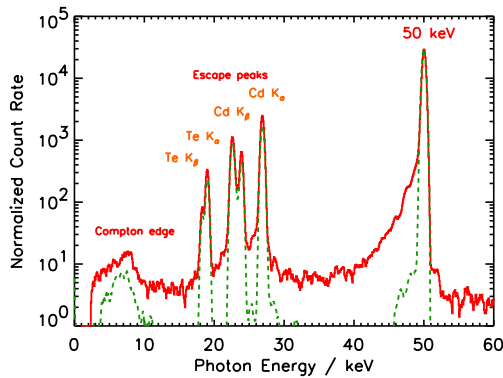


Fig. 3. Measured response function of a CdTe-detector for monochromatic radiation of 50 keV (solid line) and simulation with Geant4 (dashed)

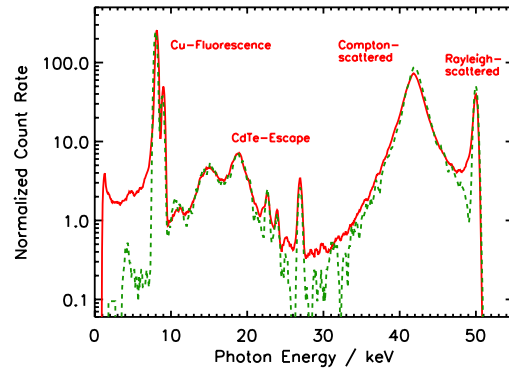


Fig. 4. Detected radiation from a Cu foil at an angle of 170° to the incident 50 keV beam, and simulation with Geant4 (dashed)

It was shown that not only the Rayleigh- and Compton-scattered photopeaks were reproduced by the simulations qualitatively as well as quantitatively, but also the escape lines, including their Compton-scattered contribution, and the fluorescence line of Cu which can be detected around 8 keV (Fig. 4). Even polarization effects were in very good agreement. The fluorescence does not vary with the polarization in the angular dependence in both simulation and experiment, while the scattered rate strongly depends on the polarization as shown in Fig. 5.

The new absorber for hard X-rays

For the new absorber, extensive simulations were performed for a large variety of materials including Cu and Au as well as Ag, Pt, W and Al. Also the geometry of the absorber was varied including different thickness of base and shell. As shown in Fig. 6, the use of a pure gold plate would cause significant losses due to Au-L fluorescence.

The simulations resulted in an absorber with a gold base 500 μm in thickness and a cylindrical shell made of copper 80 μm in thickness to reduce losses caused by fluorescence. It meets the absorption requirements, provides a tolerable heat capacity at liquid helium temperature and exhibits a sufficient thermal conductivity. To make it also applicable for

energies below 100 eV, where reflection starts to occur, the base was inclined by 30° as for conventional copper absorbers. The cavity absorber was manufactured by electroforming at PTB and was implemented into the existing ESR [5].

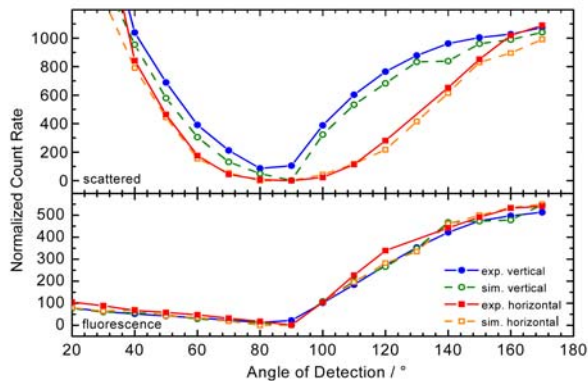


Fig. 5. Scattered contribution of radiation and fluorescence, recorded vertically and horizontally to the polarized beam

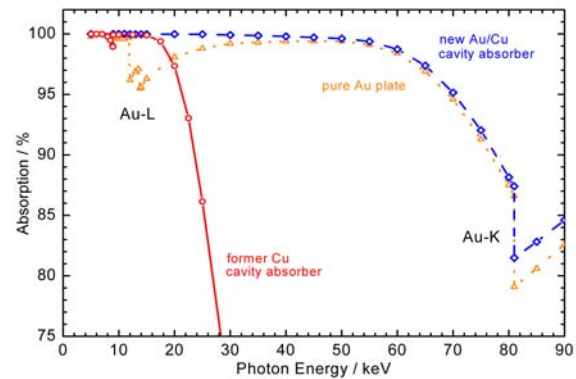


Fig. 6. Simulated absorption of the former copper absorber (solid line) compared to a pure gold-plate 500 μm in thickness (dotted) and the new absorber with gold base and copper shell (dashed).

Monochromatized synchrotron radiation of high spectral purity was then used to calibrate different silicon photodiodes against the ESR for photon energies from 60 eV up to 60 keV. The responsivity of these diodes was determined with relative uncertainties below 1 %. The ESR was also successfully employed in a comparison measurement with a free air ionization chamber, which resulted in a first time experimental determination of the mass energy-absorption coefficients of dry air in the energy range from 10 keV to 60 keV.

Conclusion

The Monte Carlo simulation code Geant4 was used to model a cavity absorber of an ESR. Scattering experiments were performed to verify the accuracy of Geant4. A new cavity absorber for hard X-rays was developed and manufactured at PTB. The ESR with its new absorber has been used successfully to calibrate silicon photodiodes within the energy range from 60 eV to 60 keV with relative uncertainties below 1 %. Mass energy-absorption coefficients of air were measured by comparison to a free air ionization chamber.

References

- [1] A. Gottwald et al., *Metrologia* **43**, S125 (2006)
- [2] S. Agostinelli et al., *Nucl. Instr. and Meth. A* **506**, 250 (2003)
- [3] R.M. Kippen, *New Astron. Rev.* **48**, 221 (2004)
- [4] W. Görner et al., *Nucl. Instr. and Meth. A* **467-468**, 703 (2001)
- [5] H. Rabus, V. Persch, and G. Ulm, *Appl. Opt.* **36**, 5421 (1997)

Detector Calibration and Spectrometer Characterization for Solar Observations

A. Gottwald, C. Buchholz, A. Fischer, A. Kampe, U. Kroth, C. Laubis,
H. Schoeppe, F. Scholze, M. Richter

Physikalisch-Technische Bundesanstalt, Abbestr. 2-12, 10587 Berlin

Characterization and calibration of space-based radiometric instruments in the spectral range from the vacuum-ultraviolet to x-rays already has some tradition in the PTB laboratory at BESSY [1]. In particular, the calibrations for the SUMER and CDS instruments for the very successful SOHO mission, which is still in service after about 12 years, founded the competence in the particular field of radiometric characterization of instruments for extraterrestrial and solar astronomy. This field has received much interest due to the grown knowledge of interaction between solar activities and Earth's atmosphere ("space weather"). Numerous missions are planned or already underway: In 2006 the EIS (Extreme ultraviolet Imaging Spectrometer) of the Solar-B satellite, and the EUNIS and MOSES spectrometers (sounding missile missions) were launched successfully, all three of them with radiometric traceability to BESSY as primary source standard.

In 2006, PTB characterized two new instruments in their final flight versions (figure 1): In cooperation with MPS (Max Planck Institute for Solar System Research, Katlenburg-Lindau) the LYRA (Large Yield Radiometer) instrument received its final calibration. It is scheduled for launch in 2007 with the ESA mini-satellite mission PROBA. For the second instrument, SOL-ACES, PTB is contracted to IPM (Fraunhofer Institute for Physical Measurement Techniques, Freiburg). SOL-ACES (Solar Auto-Calibrating Extreme UV Spectrometer) will be part of the European contribution to the International Space Station ISS. The traceability of these instruments is realized by means of detector-based radiometry, i. e., their spectral responsivity is determined using monochromatized synchrotron radiation and photodiode detectors traceable to cryogenic radiometers as primary detector standards.

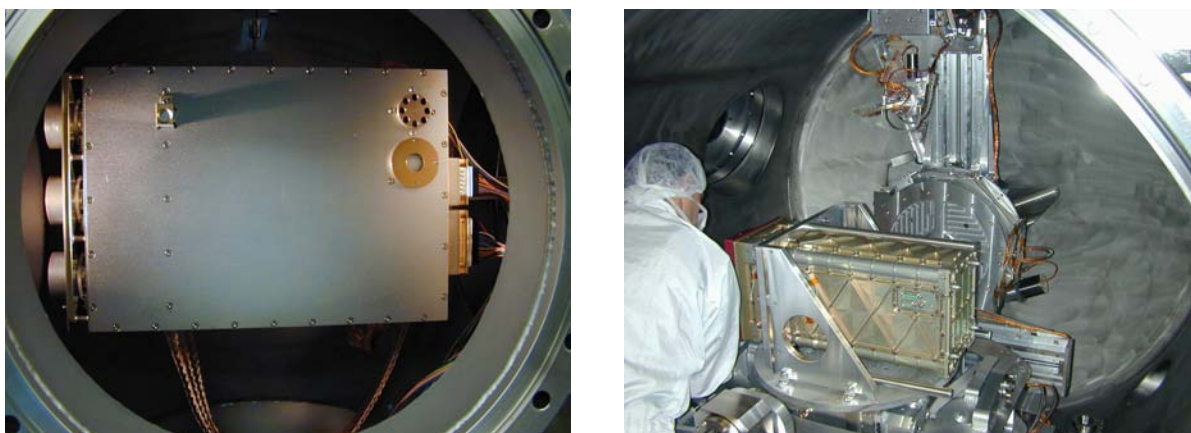


Figure 1.

Left: LYRA (MPS) in the VUV reflectometer. **Right:** SOL-ACES (IPM) in the EUV reflectometer.

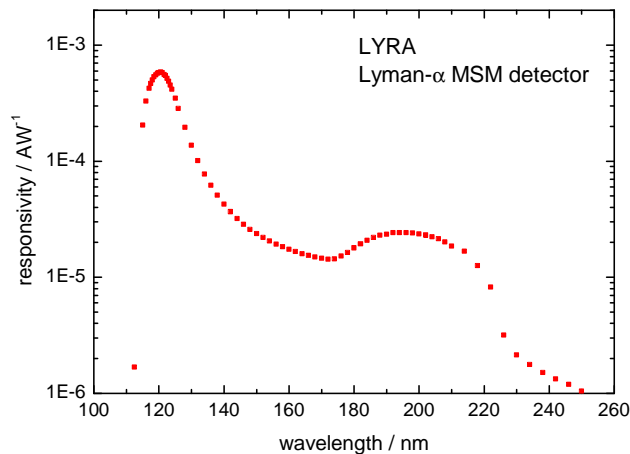


Figure 2. Calibration result of one of the Lyman-alpha channels of the LYRA instrument.

LYRA will monitor the solar emission in four passbands from 1 nm to 220 nm and applies newly developed solar-blind diamond-based photodetectors [2]. These detectors were intensively characterized with respect to their stability, linearity, etc., and each of the four detection channels was individually calibrated concerning its spectral responsivity. As an example, figure 2 gives the result for the Lyman-alpha channel (highest sensitivity around 121 nm). The MSM (metal-semiconductor-metal) detector used here is a photoconductor based on diamond and Ti/Pt/Au multilayer structures and shows a responsivity of 0.6 mA/W at 121 nm. This is orders of magnitude lower compared to AXUV semiconductor photodiodes which are typically used as standard detectors. However, the AXUV has to be used with strong filters to reject visible light so that the disadvantage of the low responsivity is reduced in comparison to the visible rejection ratio of the solar-blind device, indicated by the edge structure in the MSM detector response around 225 nm.

SOL-ACES is a system consisting of four grazing incidence spectrometers and two ionization chambers in combination with two filter wheels [3]. The spectrometers cover the wavelength range from 16 nm to 220 nm with a spectral resolution from 0.5 nm to 2.3 nm. These high-efficiency spectrometers will routinely be re-calibrated during the mission by two three-signal ionization chambers to be operated with 42 band pass filters. Re-measuring the filter transmissions with the spectrometers also allows a very accurate determination of the changing second order (optical) efficiencies of the spectrometers as well as the stray light contributions to the spectral recording in different wavelength ranges. The radiometric characterization of the system included comparison of the ionization chambers as standard detectors to standards traceable to the PTB cryogenic radiometers, measurement of the filter transmissions, and characterization of the spectrometers. The goal is to allow measurements of the solar irradiance with standard uncertainties of 3 % to 5 % in the spectral range covered by the instrument which would be a so far unrivalled accuracy for such measurements.

[1] M. Richter et al., *Adv. in Space Res.* **37** (2006) 265 – 272

[2] A. BenMoussa et al., *Diam. and Rel. Mat.* **15** (2006) 802 – 806

[3] G. Schmidtke et al., *Adv. in Space Res.* **37** (2006) 272 – 283

New Method for Polarization Dependent Reflectance Measurement

A. Gottwald, U. Kroth, W. Paustian, H. Schoeppe, R. Thornagel, M. Richter

Physikalisch-Technische Bundesanstalt, Abbestr. 2-12, 10587 Berlin

The characterization of optical materials, i. e. measurement of the reflectance, transmittance, and determination of optical constants from the ultraviolet (UV) down to the extreme-ultraviolet (EUV) spectral regions has attracted growing interest during the last decade. However, with decreasing wavelength the practical problems for precise measurements are of increasing challenge, mainly due to (air) absorption, contamination, and stability issues. In its laboratory at BESSY II, PTB has established the characterization of materials, filters, and mirrors from UV to x-ray spectral range using reflectometers. For the wavelength interval between 40 nm and 400 nm, a normal-incidence monochromator beamline delivers spectral dispersed radiation for this purpose [1]. In this dedicated VUV beamline, the radiation in the beamline focus shows elliptical polarization with a degree changing with wavelength, instead of the typically linear polarization in the storage ring plane. The main cause for this is the off-axis aperture needed to suppress the high portion of on-axis x-rays of the BESSY II storage ring, which would induce intolerable heat load to the first mirror. The initial polarization characteristics can be calculated using Schwinger's theory. It is adulterated by the grating (three different are in use which differ in line density and coating), mirror, filter and beamsplitter plate characteristics. As a consequence, the beamline up to now was not suited for direct determination of any polarization-dependent optical characteristics. These characteristics got more and more in focus of interest: One prominent example is the investigation of the optical anisotropy in CaF_2 at 157 nm [2] with its severe impact on the development of commercial photolithography at this wavelength.

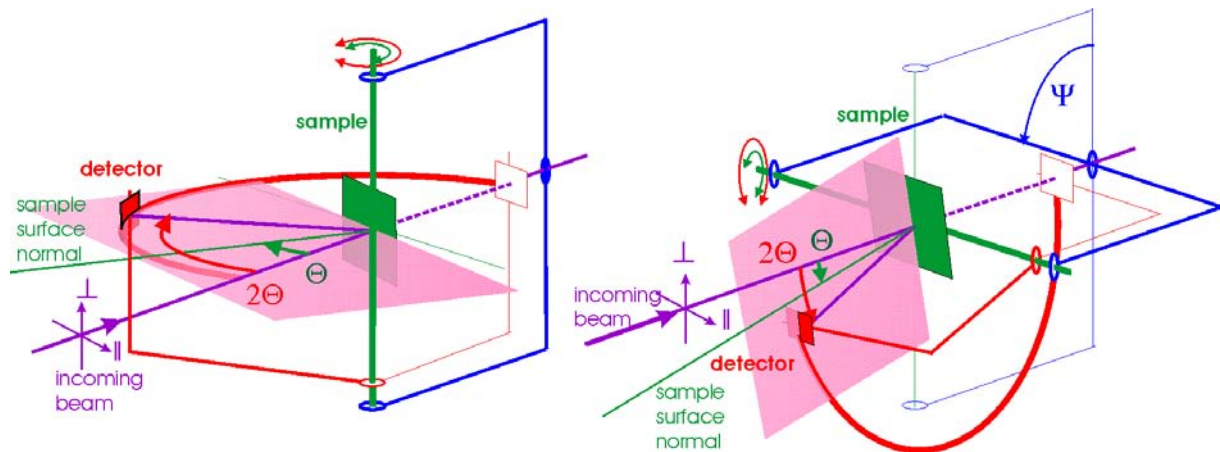


Figure 1. Scheme of the setup for polarization dependent reflectometry: Two measurements are needed in the shown different geometries, i. e. with a 90-degree turn around the beam axis. Left is the standard geometry used for measurements with negligible polarization effects.

For the determination of the polarization-dependent reflectivity (i. e. reflectance R and the polarisation P_R) of a sample, the (initially unknown) degree of polarization P_ϕ of the monochromatized radiation in the beamline must be taken into account. P_ϕ is defined by the intensities (radiant power) of the radiation with polarization (electrical field) vectors in and perpendicular to the storage ring plane, i. e. $P_\phi := (\Phi_{\parallel} - \Phi_{\perp}) / (\Phi_{\parallel} + \Phi_{\perp})$. P_R as well as the polarization dependence in the responsivity of a photodetector P_D are defined analogously, however, here with regard to the incidence plane of the radiation on the sample and detector, respectively. The idea behind the newly developed method is to use a second beamline with 100 % linear polarization in the storage ring plane ($P_\phi = 1$) to determine the detector polarization P_D , and then to determine P_ϕ for the VUV reflectometry beamline by means of this photodetector. To obtain a polarization responsivity, the detector is used with a tilt of 50° with respect to the incoming beam. Figure 2 shows the measured value for P_D (for a selected Si photodiode) and P_ϕ for the VUV reflectometry beamline in the wavelength region from 100 nm to 160 nm.

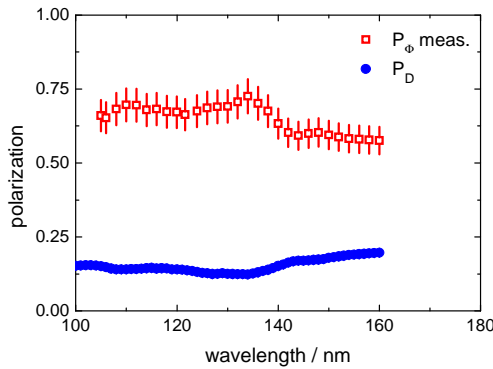


Figure 2. Polarization P_ϕ of the VUV reflectometry beamline radiation, and polarization sensitivity P_D of a silicon photodiode tilted by 50° .

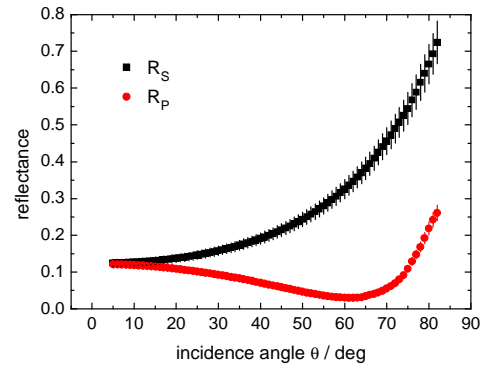


Figure 3. Example for a polarization dependent measurement of a thin layer mirror at 121 nm wavelength; shown is the angular dependence of the polarization-dependent reflectances R_s and R_p .

The polarization dependent reflectivity of a sample can then be determined by two perpendicular reflection measurements (see fig. 1), i. e. with a 90-degree turn of the apparatus around the beam axis ($\Psi=90^\circ$), which can be realized by the reflectometer [3]. From these measurements, R and P_R can be determined from which the s- and p-reflectance (R_s , R_p) of the sample can be calculated using the now known value P_ϕ for the beam polarisation. The uncertainty for P_R amounts up to 10 % and is mainly caused by the small values for the detector's polarization sensitivity.

We gratefully acknowledge the scientific co-operation for development of polarization optics in the VUV with the the Institut d'Optique Théorique et Appliquée (Orsay, France).

- [1] M. Richter et al., Nucl. Instr. and Meth. **467 – 468** (2001) 605
- [2] M. Letz et al., Phys. Rev. B **67** (2003) 233101
- [3] M. Krumrey et al., Proc. SPIE **1547** (1991) 136

Long-term reproducibility of PTB's EUV Reflectometry

Christian Laubis, Frank Scholze, Christian Buchholz, Andreas Fischer, Annett Kampe,
Sven Plöger, Frank Scholz, and Gerhard Ulm

Physikalisch-Technische Bundesanstalt, Abbestraße 2-12, 10587 Berlin, Germany

The Physikalisch-Technische Bundesanstalt (PTB) with its laboratory at the electron storage ring BESSY II¹ is the European centre of EUV radiometry and supports the national and European industry by carrying out high-accuracy at-wavelength measurements in the EUV spectral region², particularly to support the development of EUV lithography, which holds the key to the next generation of computer technology. PTB operates an EUV reflectometry facility, designed for at-wavelength metrology of full-size EUVL optics with a maximum weight of 50 kg³ and a diameter of up to 550 mm and a micro-reflectometry station for reflectometry with sub 10 μm spatial resolution⁴. An absolute uncertainty of 0.10 % is achieved for peak reflectance, with a reproducibility of 0.05 %. For the centre wavelength an uncertainty of 2 pm is achieved with a long-term reproducibility of 1.1 pm and a short-term repeatability below 0.06 pm. In response to the increasing demands⁵ of our customers, substantial improvements in the total measurement uncertainty and repeatability at PTB have been demonstrated⁴. This is illustrated below in Figure 1, where the wavelength of the Be K absorption edge, measured as a reference, is shown for the operation time of the EUV beamline starting from the commissioning in mid 2000. In the initial phase of operation we worked on a reliable definition of this reference wavelength and an optimization of the alignment procedures. From mid 2001, the stability improved substantially and further optimization of the procedures for beamline set-up checks during 2002 resulted in an operation with nearly no run-away at all in the wavelength calibration. We are aiming for a calibration interval of ± 1.9 pm, corresponding to 1.1 pm 1σ (ref. ²).

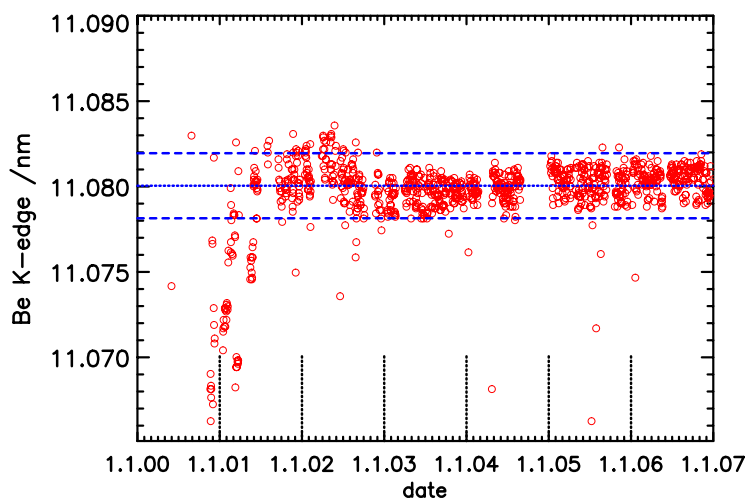


Figure 1 Wavelength of the Be K absorption edge measured as a wavelength reference during the operation of the EUV beamline starting from the commissioning in mid 2000. The dashed lines indicate the tolerance limits and the dotted line the reference value. A total number of 970 data points is shown in the figure.

Obviously, the wavelength calibration of the beamline is only one parameter among many others influencing the final result of a reflectance measurement for a multilayer mirror. Therefore we also measure a set of Mo/Si multilayer mirrors regularly to check for any other deviations that might influence our results. Figure 2 shows the centre wavelength at 50 % threshold for these multilayer mirrors measured over a period of 5 years. It must be noted, that

the time axes of Figure 1 and Figure 2 do not coincide. The initial drift in our wavelength calibration is not seen in Figure 2. What shows up indeed is a slight initial relaxation of the multilayer period by interlayer diffusion. The results confirm very well the reproducibility² of 1.1 pm 1 σ we claim for our wavelength measurements.

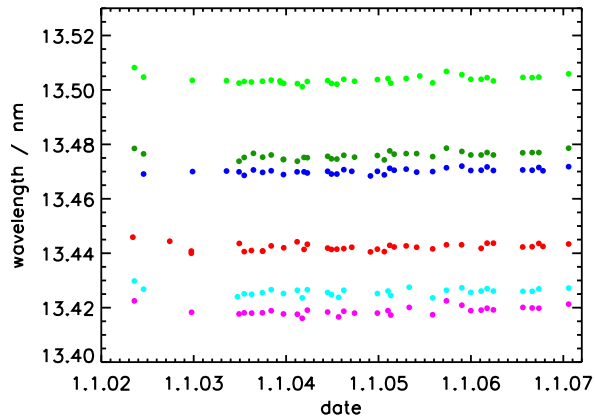


Figure 2 Centre wavelength at 50 % threshold for a set of Mo/Si multilayer mirrors routinely measured over a period of 5 years.

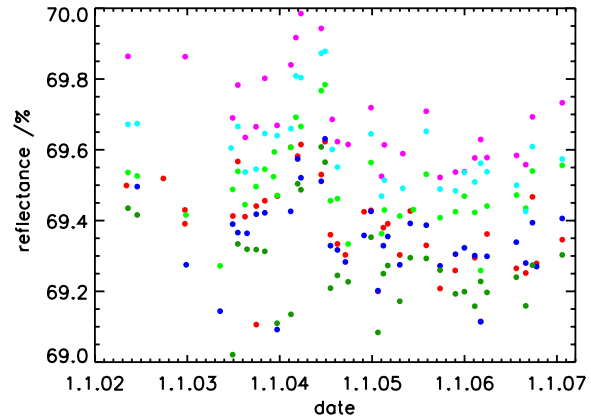


Figure 3 Peak reflectance for a set of Mo/Si multilayer mirrors routinely measured over a period of 5 years.

Figure 3 shows the peak reflectance for these multilayer mirrors. The reduced scatter of the data indicates the improvements we made during 2004 to achieve a tighter control of homogeneity of the photodiode detector used for the measurements. The results confirm the reproducibility² of 0.1 % 1 σ we claim for our reflectance measurements.

Acknowledgement

The authors gratefully acknowledge the BESSY staff for reliable operation of the storage ring as an essential prerequisite for high-accuracy measurements and the group of Stefan Braun, Fraunhofer IWS Dresden, for providing the mirrors.

References

- ¹ R. Klein, C. Laubis, R. Müller, F. Scholze, G. Ulm, "The EUV metrology program of PTB," *Microelectronic Engineering* **83**, 707-709 (2006)
- ² F. Scholze, J. Tümmeler, G. Ulm, "High-accuracy radiometry in the EUV range at the PTB soft X-ray radiometry beamline", *Metrologia* **40**, S224-S228 (2003)
- ³ J. Tümmeler, H. Blume, G. Brandt, J. Eden, B. Meyer, H. Scherr, F. Scholz, F. Scholze, G. Ulm, "Characterization of the PTB EUV reflectometry facility for large EUVL optical components", *Proc. SPIE* **5037**, 265-273 (2003)
- ⁴ F. Scholze, C. Laubis, C. Buchholz, A. Fischer, S. Plöger, F. Scholz, H. Wagner, and G. Ulm, "Status of EUV Reflectometry at PTB", *Proc. SPIE* **5751**, 749-758 (2005)
- ⁵ H. Meiling, V. Banine, P. Kuerz, N. Harned, "Progress in the ASML EUV program", *Proc. SPIE* **5374**, 31 - 42, (2004)

Measurement of the degree of linear polarization at the EUV reflectometer

Frank Scholze, Christian Laubis, Christian Buchholz, Andreas Fischer, Annett Kampe, Sven Plöger, Frank Scholz, and Gerhard Ulm

Physikalisch-Technische Bundesanstalt, Abbestraße 2-12, 10587 Berlin, Germany

The Physikalisch-Technische Bundesanstalt (PTB) with its laboratory at the electron storage ring BESSY II¹ is the European centre of EUV radiometry and supports the national and European industry by carrying out high-accuracy at-wavelength measurements in the EUV spectral region², particularly to support the development of EUV lithography, which holds the key to the next generation of computer technology³. PTB operates an EUV reflectometry facility, designed for at-wavelength metrology of full-size EUVL optics with a maximum weight of 50 kg⁴ and a diameter of up to 550 mm and a micro-reflectometry station for reflectometry with sub 10 μm spatial resolution. An absolute uncertainty of 0.10 % is achieved for peak reflectance, with a reproducibility of 0.05 %. For the centre wavelength an uncertainty of 2 pm is achieved with a long-term reproducibility of 1.1 pm and a short-term repeatability below 0.06 pm⁵. Measurements at PTB use linearly polarized radiation⁶, whereas EUV optics are operated with unpolarized sources and the status of polarization changes throughout the optical system. Therefore, to transfer these high-accuracy measurements to the EUV optical components under working conditions, it is essential to study the polarization dependence in detail. Taking advantage of all mechanical movements for detector and sample, measurements with arbitrary orientation of the electric field vector can be carried out up to an angle of incidence of 20°. At 20° angle of incidence, the influence of the degree of polarization causes the largest contribution to the measurement uncertainty. Therefore, we designed a polarimeter for linear polarization with a multilayer operated at the Brewster angle, to accurately measure the degree of linear polarization. For the polarimeter, we used a multilayer mirror with 10.2 nm period. The polarimeter is shown schematically in Fig. 1.

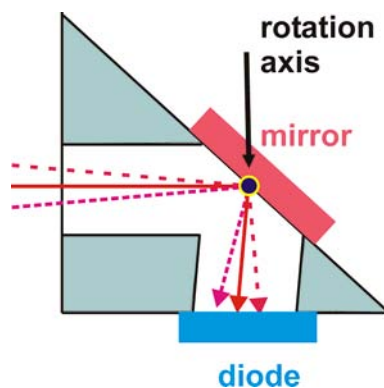


Fig. 1 EUV polarimeter: A Mo/Si multilayer mirror with 10.2 nm period is mounted in the rotation axis of a rotary feedthrough. An AXUV photodiode (not shown on the photo) is mounted close to the mirror at the area isolated with Kapton tape. The functional scheme is shown at the right. Due to the very close mounting of mirror and diode, an angular range of $\pm 5^\circ$ can be scanned.

A Mo/Si multilayer mirror with 10.2 nm period is mounted in the rotation axis of a rotary feedthrough. An AXUV photodiode is mounted close to the mirror. Due to the close mounting of mirror and diode, an angular range of $\pm 5^\circ$ can be scanned to adjust the angle of incidence to the Brewster angle without moving the diode. This is an essential prerequisite to achieve an

optimum suppression ratio. The slight variation of the angle of incidence at the diode does not influence the responsivity for the AXUV type of diode used here. Fig. 2 shows the measured peak reflectance as function of the azimuth ϕ for the angle of incidence adjusted to the Brewster angle ($R_p=0$). The minimum value is $R = R_s I_p/I$. With $R_s = 67.2 \%$, we get $I_p/I = 1.5 \%$ and thus a degree of linear polarization of 97 %, measured at the corresponding peak wavelength of 14.3 nm.

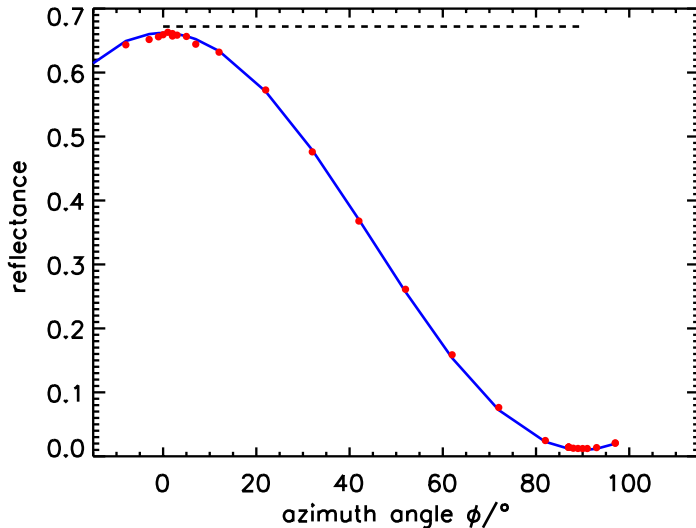


Fig. 2 Reflectance at the Brewster angle, 42.5° angle of incidence, as function of azimuth angle (\bullet). The line is a calculation for a degree of linear polarization of 97%, i.e. a contribution of 1.5% P-polarized light in the S-polarization orientation. The peak reflectance for S-polarization, indicated by the dashed line, is 67.2 %.

Fig. 3 shows measurements of the spectral reflectance of the polarimeter at the azimuth $\phi=90^\circ$. The angle of incidence was varied in the range $\pm 2.5^\circ$ around the Brewster angle. Due to the high degree of linear polarization, a significant contribution of P-polarized radiation is seen in the reflectance. The spectral reflectance R_p , however, is much narrower than R_s . It is therefore possible to decompose the overlapped R_s and R_p contributions. To obtain the pure R_p contribution, we subtracted the reflectance measured at $\phi=0^\circ$ scaled with the ratio $I_p/I = 1.5 \%$. Comparing the scaled R_s contributions in Fig. 3 with the measured reflectance, reveals a nearly constant offset in the side regions where R_p should be near zero. Therefore, we subtracted additionally a constant background of 0.08 % due to diffusely scattered radiation. Additionally shown are model calculations of R_s and R_p . Due to the significantly different bandwidth of R_s and R_p , an accurate determination of the degree of polarization is possible not only at the Brewster angle. Fig. 3 illustrates that a degree of 97 % linear polarization is valid for the complete spectral range covered by these measurements, at least from 13 nm to 15 nm. Already for 20° angle of incidence off normal, the influence of the degree of polarization causes the largest contribution to the measurement uncertainty. Typical values are $R_s = 70 \%$ and $R_p = 50 \%$, yielding a reduction of measured peak reflectance of 0.3 % for 97 % degree of linear polarization. This is a significant contribution compared to the uncertainty of 0.1 % for normal incidence⁵. It should also be noted, that a correction for the degree of polarization is non-trivial even if the degree of polarization is known. For larger angles of incidence, where the influence is significant, not only the peak reflectance but also the bandwidth of the spectral reflectance is polarization dependent (Fig. 3). Consequently, measurements in both polarization orientations would be needed for correction. As this is at least a time consuming effort, we estimated the influence of the not ideal polarization on the measurement and treated it as an uncertainty. If lower uncertainty is needed, it would be possible to correct for this effect.

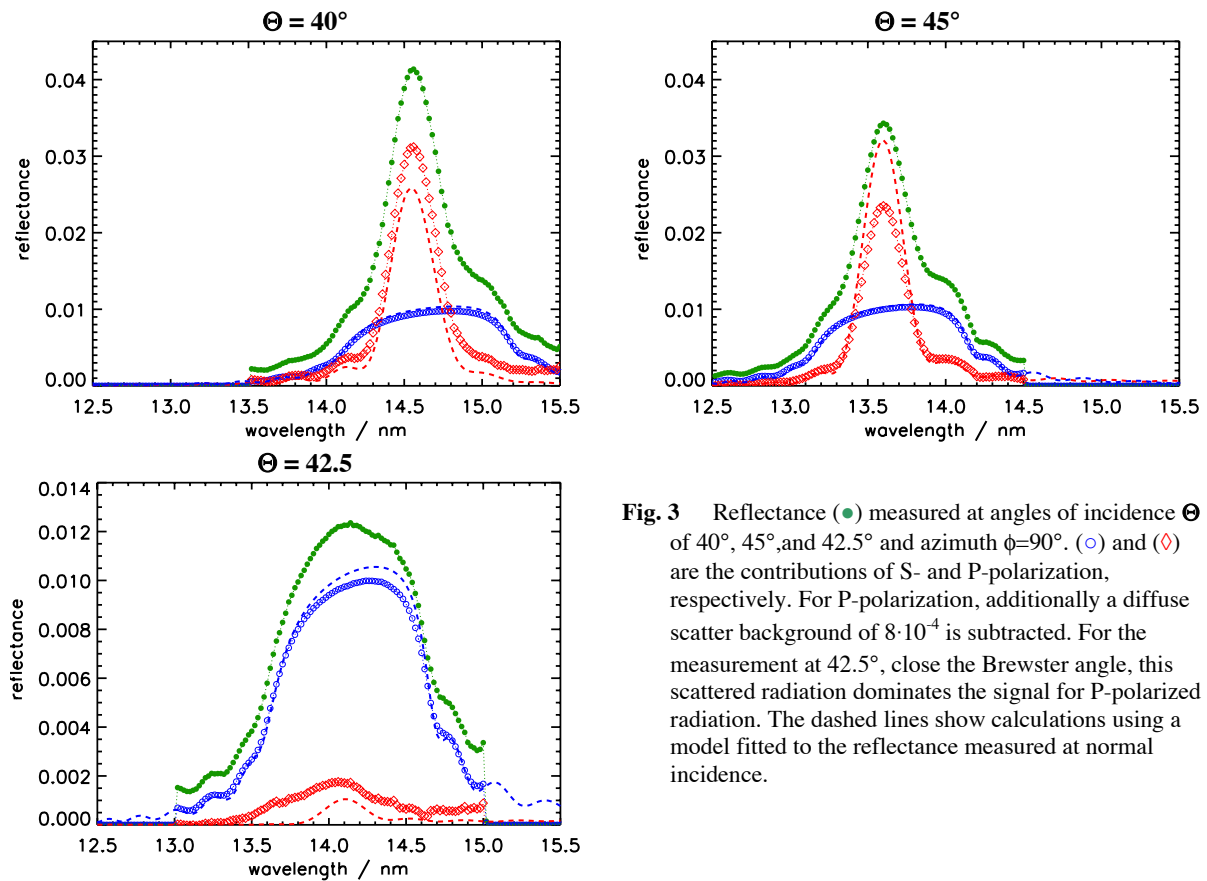


Fig. 3 Reflectance (●) measured at angles of incidence Θ of 40°, 45°, and 42.5° and azimuth $\phi=90^\circ$. (○) and (◇) are the contributions of S- and P-polarization, respectively. For P-polarization, additionally a diffuse scatter background of $8 \cdot 10^{-4}$ is subtracted. For the measurement at 42.5°, close the Brewster angle, this scattered radiation dominates the signal for P-polarized radiation. The dashed lines show calculations using a model fitted to the reflectance measured at normal incidence.

A compact and versatile polarimeter for the EUV spectral range with high suppression ratio was designed. We measured the degree of linear polarization in the EUV reflectometer to be 97% in the EUV spectral range.

References

- ¹ R. Klein, C. Laubis, R. Müller, F. Scholze, G. Ulm, "The EUV metrology program of PTB", *Microelectronic Engineering* **83**, 707-709 (2006)
- ² F. Scholze, C. Laubis, C. Buchholz, A. Fischer, S. Plöger, F. Scholz, H. Wagner, and G. Ulm, "Status of EUV Reflectometry at PTB", *Proc. SPIE* **5751**, 749-758 (2005)
- ³ H. Meiling, V. Banine, P. Kuerz, N. Harned, "Progress in the ASML EUV program", *Proc. SPIE* **5374**, 31 - 42 (2004)
- ⁴ J. Tümmler, G. Brandt, J. Eden, H. Scherr, F. Scholze, G. Ulm, "Characterization of the PTB EUV reflectometry facility for large EUVL optical components", *Proc. SPIE* **5037**, 265-273 (2003)
- ⁵ F. Scholze, J. Tümmler, G. Ulm, "High-accuracy radiometry in the EUV range at the PTB soft X-ray radiometry beamline", *Metrologia* **40**, S224-S228 (2003)
- ⁶ F. Scholze, C. Laubis, C. Buchholz, A. Fischer, S. Plöger, F. Scholz, and G. Ulm, "Polarization dependence of multilayer reflectance in the EUV spectral range", *Proc. SPIE* **6151**, 615137 (2006)

Polarization dependence of EUV multilayer reflectance

Frank Scholze, Christian Laubis, Christian Buchholz, Andreas Fischer, Annett Kampe, Sven Plöger, Frank Scholz, and Gerhard Ulm

Physikalisch-Technische Bundesanstalt, Abbestraße 2-12, 10587 Berlin, Germany

Reflectance measurements at PTB¹ use linearly polarized radiation with a degree of linear polarization² of 97 %. For many applications, EUV optics are operated with unpolarized sources and the status of polarization changes throughout the optical system. For a full understanding and specification of the optics it is therefore essential to know the polarization properties. This holds particularly for large solid angle collector mirrors in laser pulsed plasma EUV sources. A full experimental characterization of the optics would, however, require a high effort. For the design of optical elements it is therefore worth knowing whether widely used codes as the IMD software³ yield reliable results. Therefore, we measured the reflectance of a multilayer mirror with 10 nm period for different angles of incidence up to 45°. Taking advantage of all mechanical movements for detector and sample⁴, measurements with arbitrary polarization can be carried out up to an angle of incidence of 20°. For higher angles of incidence the polarimeter was used, see ². At normal incidence (1.5° off normal), the reflectance peak of this multilayer appears at 19 nm, Fig. 1. Many side-wiggles are observed in the wavelength region down to the Si L-edge. Towards longer wavelengths, the absorptance in the multilayer stack becomes too high and also in a calculation no interference structures appear. In part (a), the main peak is shown at a linear scale. Using the optical data for Mo as supplied with the IMD software yields some “edges” in the calculated reflectance (dashed line, Fig. 1 (a)). Looking at the optical data reveals discontinuities in this spectral region due to the matching of different data sets. For our final fit, these jumps were smoothed by an interpolation. Additionally shown in part (a) is the calculation using the same geometrical parameters as given in Table 1 but with the smoothed optical data for Mo. The uncertainty of the optical data prevents a simultaneous fit of several geometrical parameters using only the reflectance in the main peak region. The pronounced side wiggles, however, allowed a precise determination of the multilayer stack geometry as shown in part (b) of Fig. 1. Please note that all side-wiggles are well represented by the calculation. The fit over this wide spectral range was also much less influenced by modifications of the optical constants. The thickness of the MoSi₂ interlayers was set to typical values taken from literature⁵. We do not claim that the parameters from Table 1 are unique, but the experimental data are practically ideally represented by these parameters. Therefore, these parameters should be useful to predict the multilayer behavior for different angles of incidence.

layer	thickness /nm	roughness /nm	remarks
SiO ₂	1.687	0.2	oxidized top Si layer
Si	6.369	0.2	
MoSi ₂	0.5	0.5	35 periods d = 10.216 nm
Mo	2.828	0.6	
MoSi ₂	1.0	0.88	
Si	5.887	0.3	
Si	∞	0.3	substrate

Table 1 Compilation of the geometrical parameters used for the calculation of the multilayer reflectance.

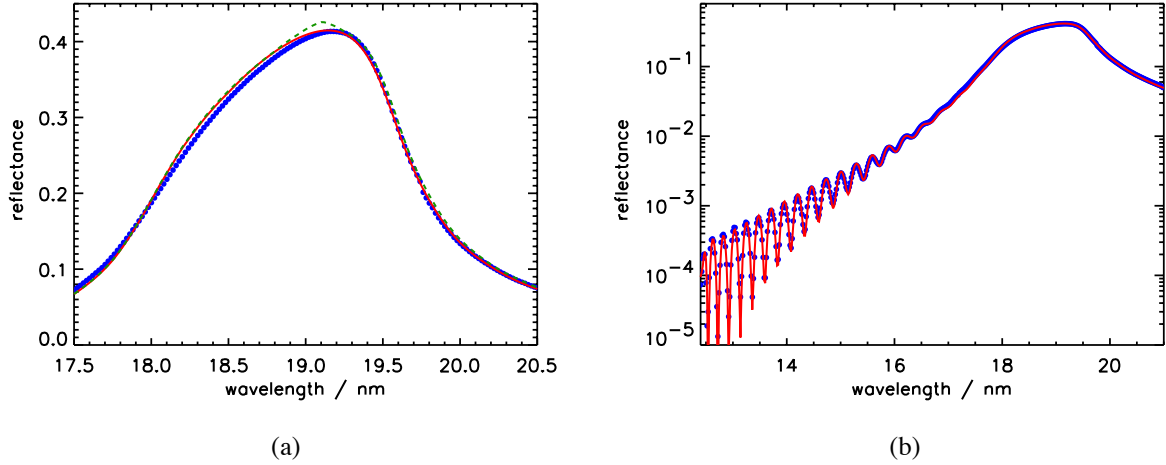


Fig. 1 Reflectance of a Mo/Si multilayer with 35 bi-layers and a period of 10.216 nm at an angle of incidence of 1.5° for S-polarization (\bullet). The solid red line is a calculation using IMD with the best fit parameters summarized in Table 1. Part (a) shows the main peak region at a linear scale. Here, a dashed line is shown additionally. It represents a calculation using the optical data for Mo as supplied with the IMD software. It has some discontinuities in this spectral region due to the matching of different data sets from literature. For our final fit (solid line), these jumps were smoothed by an interpolation. Part (b) shows the same data and calculation over the full spectral range at a log scale. Please note that all side-wiggles are well represented by the calculation.

Fig. 2 shows the peak reflectance for S- and P-polarized radiation as function of angle of incidence. The lines show calculations using a layer model fitted to the reflectance of the mirror measured at normal incidence (Fig. 1). The measured values follow the calculated trend. The calculated curves, however, show structures not apparent in the experiment. This is illustrated by simply interpolating the data with a 3rd order polynomial.

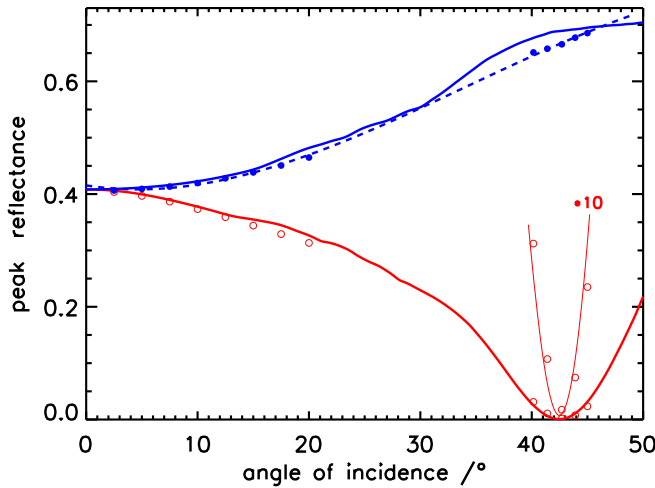


Fig. 2 Comparison of peak reflectance for S-polarized radiation (\bullet) and P-polarized radiation (\circ) as function of angle of incidence. The region around the Brewster angle is also shown on a 10 times expanded scale. The lines show calculations using a layer model fitted to the reflectance of the mirror measured at normal incidence (Fig. 1). The dashed line is a simple interpolation of the data for S-polarization using a 3rd order polynomial.

Fig. 3 shows the peak wavelength as a function of the angle of incidence. The peak wavelength λ is related to the double-layer thickness d of the coating by the Bragg equation, $\lambda = 2dn_\lambda \cos\Theta_{ML} = \lambda_0 \cos\Theta_{ML}$, with n_λ being the (average) index of refraction at wavelength λ and Θ_{ML} the propagation angle in the multilayer coating. This dependence, assuming constant n_λ and $\Theta_{ML} = \Theta$ would result in constant values in the presentation of Fig. 3. For angles up to 30° the values for S-polarization are indeed almost constant. For larger angles of incidence, calculated as well as measured values deviate from this dependence due to diffraction and changes in the optical constants. Again, the calculation shows structures not present in the measured data.

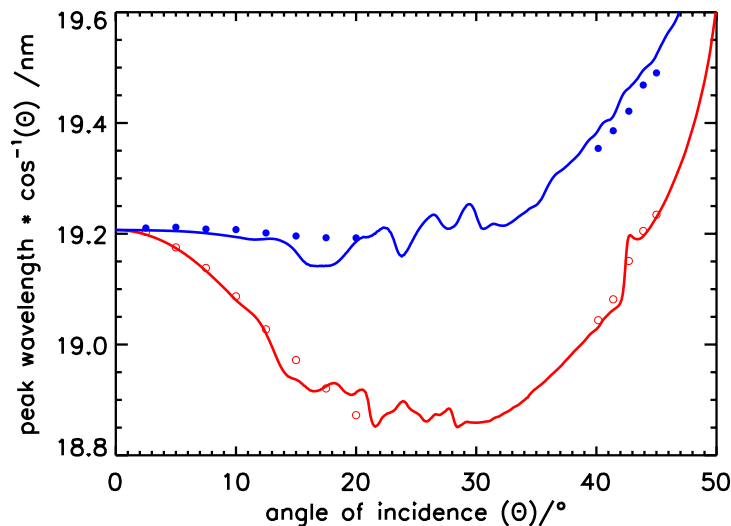


Fig. 3 Comparison of peak wavelength for S-polarized radiation (●) and P-polarized radiation (○). For a better readability, the data are normalized with the suspected \cos -dependence according to the Bragg-equation. The lines show calculations using a model fitted to the reflectance measured at normal incidence see Fig. 1.

Taking advantage of all possible movements of detector and sample in the EUV reflectometer, we demonstrated the ability to measure detailed polarization properties of EUV optics up to angles of incidence of 20° to the normal. The results shown here reveal significant differences between reflections in S- and P-polarization geometry already for rather small angles of incidence, such as 5° . The polarization dependencies obtained over a wide range of the angle of incidence were compared to calculations with the IMD-code based on a multilayer model fitted to the reflectance measured at near normal incidence. The comparison reveals that the IMD-code accurately predicts the general trends in wavelength, peak reflectance and bandwidth. For individual wavelengths, the accuracy of calculations with IMD presently obviously suffers from the optical data available. Measurements using the highly polarized radiation in the PTB's EUV reflectometer with variable orientation of the plane of reflection are a promising tool to improve the situation.

Acknowledgement

The authors thank Torsten Feigl and Sergiy Yulin from Fraunhofer IOF in Jena for providing the multilayer mirrors.

References

- ¹ R. Klein, C. Laubis, R. Müller, F. Scholze, G. Ulm, "The EUV metrology program of PTB," *Microelectronic Engineering* **83**, 707-709 (2006)
- ² F. Scholze, C. Laubis, C. Buchholz, A. Fischer, A. Kampe, S. Plöger, F. Scholz, and G. Ulm, "Measurement of the degree of linear polarization at the EUV reflectometer", this annual report
- ³ D.L. Windt, "IMD - Software for modeling the optical properties of multilayer films", *COMPUTERS IN PHYSICS* **12**, 360-370 (1998)
- ⁴ F. Scholze, C. Laubis, C. Buchholz, A. Fischer, S. Plöger, F. Scholz, and G. Ulm, "Polarization dependence of multilayer reflectance in the EUV spectral range", *Proc. SPIE* **6151**, 615137 (2006)
- ⁵ S. Yulin, T. Feigl, T. Kuhlmann, N. Kaiser, A. I. Fedorenko, V. V. Kondratenko, O. V. Poltseva, V. A. Sevryukova, A. Yu. Zolotaryov, and E. N. Zubarev, "Interlayer transition zones in Mo/Si superlattices", *J. Appl. Phys* **92**, 1216-1220 (2002)

CD characterization of EUV masks by EUV scatterometry and rigorous FEM-Simulation

Frank Scholze, Christian Laubis

Physikalisch-Technische Bundesanstalt, Braunschweig and Berlin, Germany

Jan Pomplun, Sven Burger, Frank Schmidt

Zuse Institute Berlin, Berlin, Germany

Uwe Dersch, Christian Holfeld

AMTC GmbH&CoKG, Dresden, Germany

Scatterometry, the analysis of light diffracted from a periodic structure, is a versatile metrology for characterizing periodic structures, regarding critical dimension (CD) and other profile properties. When exposing an EUV mask with EUV radiation of 13.5 nm, the radiation is reflected by the multilayer stack which is about 300 nm thick. For EUV radiation, all layers in the stack contribute to the reflection. Therefore, only EUV scatterometry¹ provides direct information on the mask performance comparable to an EUV lithography tool. With respect to the small feature dimensions on EUV masks, the short wavelength of EUV is also advantageous since it provides more diffraction orders as compared to UV. PTB's EUV reflectometer^{2,3} at the storage ring BESSY II allows mask surface scanning in Cartesian coordinates at 10 μm positioning reproducibility. The probed area (photon beam size) is about 1 mm square. We present measurements on prototype EUV masks and we demonstrate the use of EUV scatterometry to determine the CD and side-wall geometry of lines including technological imperfections like side-wall angles and corner rounding using rigorous calculations of EUV diffraction. Results of a scatterometry measurement are shown in Fig. 1. A structure of lines&spaces was illuminated at an angle of 6° to the normal and perpendicular to the orientation of the lines. The design CD of the structure was 140 nm and the design duty cycle 1:5 (dark:bright).

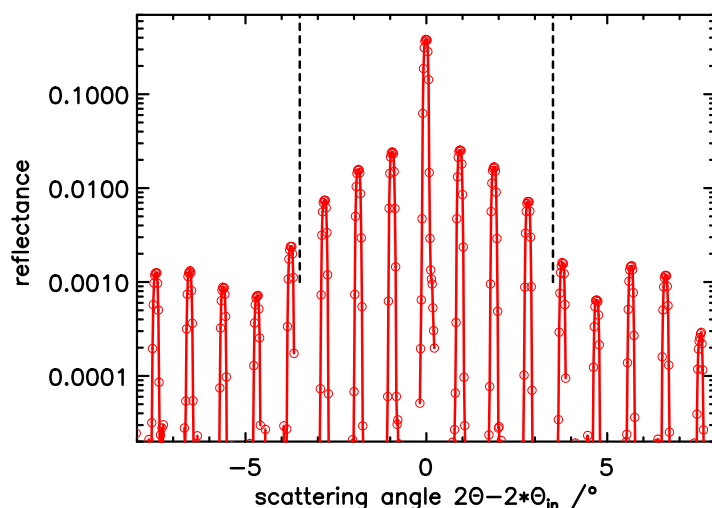


Fig. 1 Typical measurement of diffracted intensity as function of detector angle, $\lambda=13.65$ nm. The angle is shown as difference angle to the specular reflected beam.

For homogeneous regions, reflectometry at open multilayer (ML) or absorber areas can be used to obtain detailed information on layer thicknesses⁴. By comparison of the reflectance in ML and absorber areas, information can be obtained on the absorber thickness and the thinning of the capping layer due to oxidation in the open ML regions after buffer etch.

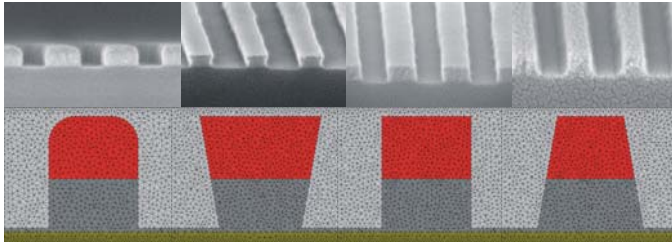


Fig. 2 SEM pictures of EUV mask patterns and corresponding triangulated geometries for FEM computation.

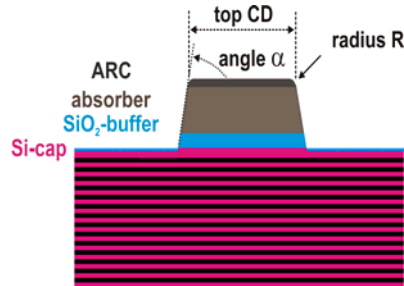


Fig. 3 Scheme of the geometrical parameters varied for simulation: Top CD, sidewall angle, height, and top corner radius.

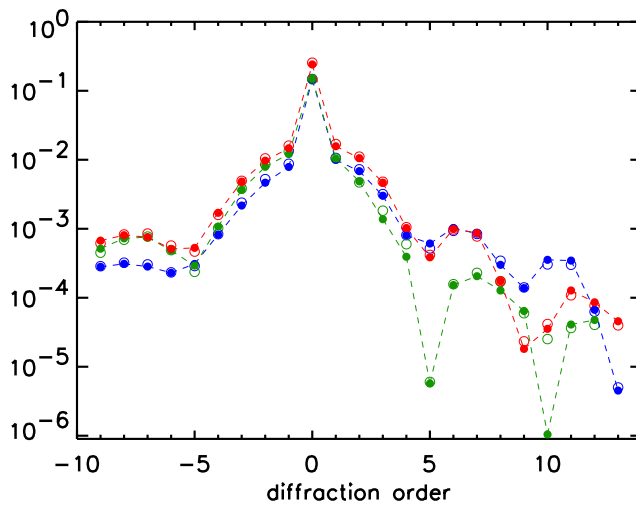


Fig. 4 Reflectance of -9th to 13th diffraction order at wavelengths of **13.4 nm**, **13.65 nm** and **13.9 nm**. Experimental values (○) and simulated values (●) agree for almost all points simultaneously. The lines connecting the simulated values and are only to guide the eye.

Fig. 2 shows SEM cross sections of lines on EUV masks together with the triangulation models used for the FEM calculations. Fig. 3 defines the geometrical parameters varied and Fig. 4 shows measured diffraction orders for 3 different wavelengths. The measured diffraction orders do not carry direct information about the absorber line profile. For the numerical simulations we use an adaptive finite element approach on irregular meshes and domain decomposition techniques for EUV mask simulations⁵. This gives us the opportunity to model geometrical structures accurately. The FEM method is especially suited for this application:

- Maxwell's equations are solved rigorously without approximations
- The flexibility of triangulations allows modelling of almost arbitrary structures
- With appropriate localized ansatz functions physical properties of the electric field like discontinuities and singular behaviour can be modelled very accurately
- The convergence of the FEM method to the exact solution is proven mathematically

In our work we used the FEM solver JCMharmony which has been successfully applied to various electromagnetic field computations like waveguide structures⁶, DUV phase masks⁷, and other nano-structured materials⁸. The geometrical parameters given in Table 1 are obtained by minimizing the difference between calculated and measured diffraction intensities with an optimization algorithm. The results individually calculated for all 3 wavelengths agree pretty well.

wavelength	top CD	sidewall angle	height (FEM)	height (reflectom)	corner radius
13.40 nm	147.5 nm	89.5°	76.4 nm		6 nm
13.65 nm	147.3 nm	90°	75.3 nm	74.9 nm	6 nm
13.90 nm	147.8 nm	90°	77.4 nm		6 nm

Table 1 Compilation of the geometrical parameters obtained by FEM simulation of the measured diffraction intensities.

We demonstrated that single wavelength EUV scatterometry in combination with FEM simulations is a viable method for an accurate and robust destruction free characterization of EUV masks. We compared experimental diffraction orders to FEM simulations. For the FEM simulations, the EUV mask is described with a finite number of geometrical parameters and then the best fitting values determined by minimizing the deviation of experimental data to simulated values. The FEM method is well suited for the simulation of EUV masks since it allows computation of nearly arbitrary geometries, is very accurate and very fast as a precondition for the solution of the given inverse problem. We considered the top critical dimension, the sidewall angle, the height of the absorber lines and the top corner radius as unknown parameters. The search for the best fitting geometry at three different wavelengths gave nearly the same values for the top critical dimension and the absorber sidewall angle proving both robustness and accuracy of the method. Using as many diffraction orders as possible, effectively improved the significance of the results. The absorber corner radius and total stack height have only minor influence on the diffraction pattern and could only be estimated using all available diffraction orders. The stack height, however, can be determined unambiguously by reflectometry at absorber fields.

The combination of reflectometry at dark and bright test fields and scatterometry at lines&spaces provides full information on layer thicknesses, top CD, and sidewall angles.

Acknowledgement

The investigation shown here is part of the “ABBILD” project, supported by the Bundesministerium für Bildung und Forschung.

References

- ¹ J. Perlich, F.-M. Kamm, J. Rau, F. Scholze, and G. Ulm "Characterization of extreme ultraviolet masks by extreme ultraviolet scatterometry," *J. Vac. Sci. Technol. B* **22**, 3059-3062 (2004)
- ² R. Klein, C. Laubis, R. Müller, F. Scholze, G. Ulm, "The EUV metrology program of PTB," *Microelectronic Engineering* **83**, 707-709 (2006)
- ³ C. Laubis, et al., "Characterization of large off-axis EUV mirrors with high accuracy reflectometry at PTB", *Proc. SPIE* **6151**, 61510I (2006)
- ⁴ F. Scholze, B. Bodermann, C. Laubis, G. Ulm, M. Wurm, U. Dersch and C. Holfeld, "CD characterization of EUV masks by EUV scatterometry", *BESSY annual report* **2005**, 17-19 (2005)
- ⁵ J. Pomplun, S. Burger, F. Schmidt, L. Zschiedrich, F. Scholze, C. Laubis, U. Dersch, "Rigorous FEM-Simulation of EUV-Masks: Influence of Shape and Material Parameters", *Proc. SPIE* **6349** 63493D (2006)
- ⁶ S. Burger, R. Klose, A. Schädle, F. Schmidt, and L. Zschiedrich, "FEM modelling of 3D photonic crystals and photonic crystal waveguides," *Proc. SPIE* **5728**, 164-173 (2005)
- ⁷ S. Burger, R. Köhle, L. Zschiedrich, W. Gao, F. Schmidt, R. März, C. Nölscher, "Benchmark of FEM, Waveguide and FDTD Algorithms for Rigorous Mask Simulation," *Proc. SPIE* **5992**, 378-389 (2005)
- ⁸ C. Enkrich, M. Wegener, S. Linden, S. Burger, L. Zschiedrich, F. Schmidt, C. Zhou, T. Koschny, C. M. Soukoulis, "Magnetic metamaterials at telecommunication and visible frequencies," *Phys. Rev. Lett.* **95**, 203901 (2005)

Coherent synchrotron radiation at the Metrology Light Source

Ralph Müller¹, Arne Hoehl¹, Roman Klein¹, Gerhard Ulm¹,
Ulrich Schade², Karsten Holldack², Godehard Wüstefeld²

¹*Physikalisch-Technische Bundesanstalt, Abbestraße 2-12, 10587 Berlin, Germany*
²*Berliner Elektronenspeicherring-Gesellschaft für Synchrotronstrahlung m.b.H., Albert-Einstein-Str. 15, 12489 Berlin, Germany*

The region of the electromagnetic spectrum from 0.1 THz to 20 THz (3 mm to 15 μm wavelength) is a frontier area for research in physics, chemistry, biology, materials science and medicine. Sources of high quality radiation in this area have been scarce [1]. In the MIR and FIR region with wavelengths between 2 μm and 300 μm , electron storage rings are excellent broadband sources of high brilliance and power, in comparison with standard thermal sources. For wavelengths above 300 μm the low net transmittance of the extracting optics of an IR beamline caused by diffraction due to the larger natural opening angle of the radiation and the finite sizes of the optical elements involved may limit the use of the synchrotron radiation. The frequency range between 0.1 THz to 1 THz bridges the gap between the microwaves and the FIR and has proven to be challenging to access and is therefore referred to as the “THz gap” [1]. Coherent synchrotron radiation (CSR) from storage rings could bridge the gap since it offers powerful broadband radiation in the frequency range below 1 THz [1].

CSR occurs when the electrons in a bunch emit synchrotron radiation in phase. CSR intensity is proportional to the square of the number of electrons per bunch in contrast to the linear dependence of the usual incoherent radiation. Since the number of electrons per bunch is typically very large ($\geq 10^6$), the potential intensity gain for a CSR source is huge. During the past few years, at BESSY II a new technique to generate stable, coherent THz radiation from the electron storage ring has been developed [2, 3]. The option to produce CSR is also envisaged for the Metrology Light Source of the PTB by tuning the quadrupoles in an appropriate way. The required control of higher-order terms of the momentum compaction factor α , with respect to momentum deviating electrons, will be performed by 3 families of sextupoles and one octupole family [4]. The emitted spectral range of the bunches compressed to 1 mm in length will be the same as for BESSY II. The expected radiant power of CSR at the MLS can be estimated by applying the BESSY II results (see Fig. 1). A scaling has to compare the charge per bunch limited by the bursting instability, the passing time of the bunch through the acceptance angle of the detector, and the different emission cone due to the characteristic energy of the dipole radiation. This yields, under the assumption of identical bunch lengths, a value of 12 % of the power compared to the BESSY II ring [4]. This, however, only applies to the stable emission process, not to the bursting case, which depends on the maximum stored current per bunch.

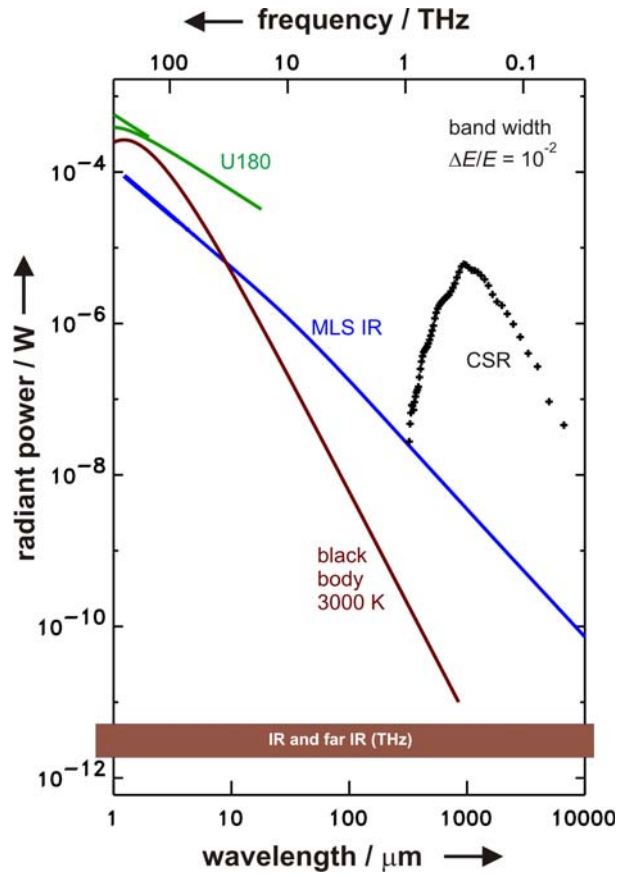


Figure 1. Expected radiant power for stable, coherent synchrotron radiation (CSR) (crosses) at the MLS compared with the incoherent radiation from a bending magnet, IR radiation from the undulator U180 and radiation from a black body of 3000 K and 10 mm^2 emitting area. The estimation is based on the measurement of CSR at the IRIS beamline at BESSY II.

Recent calculations have shown that the bunch length at the MLS operated in the low-alpha mode is smallest in the straight sections and largest in the section between the bending magnets [4]. This is illustrated in Fig. 2 which shows a simulation of the bunch length at the entrance and at the exit of the bending magnet following a straight section. Therefore, a higher intensity and a broader spectrum of the CSR are expected at the bending magnet ports that are located closest to a straight section, as is the case for the dedicated THz beamline [5]. The optical design of the MLS-THz beamline is comparable with the new THz beamline at BESSY II [6]. The plane extraction mirror will be placed at about 1550 mm and deflects the beam upwards to a combination of mirrors which focus the beam outside the radiation shielding wall to the experiment located at the roof of the bunker. A quartz window after the first mirror separates the UHV of the storage ring from the rest of the beamline. Construction of the the THz beamline should be finished in 2007. Operation will start in 2008.

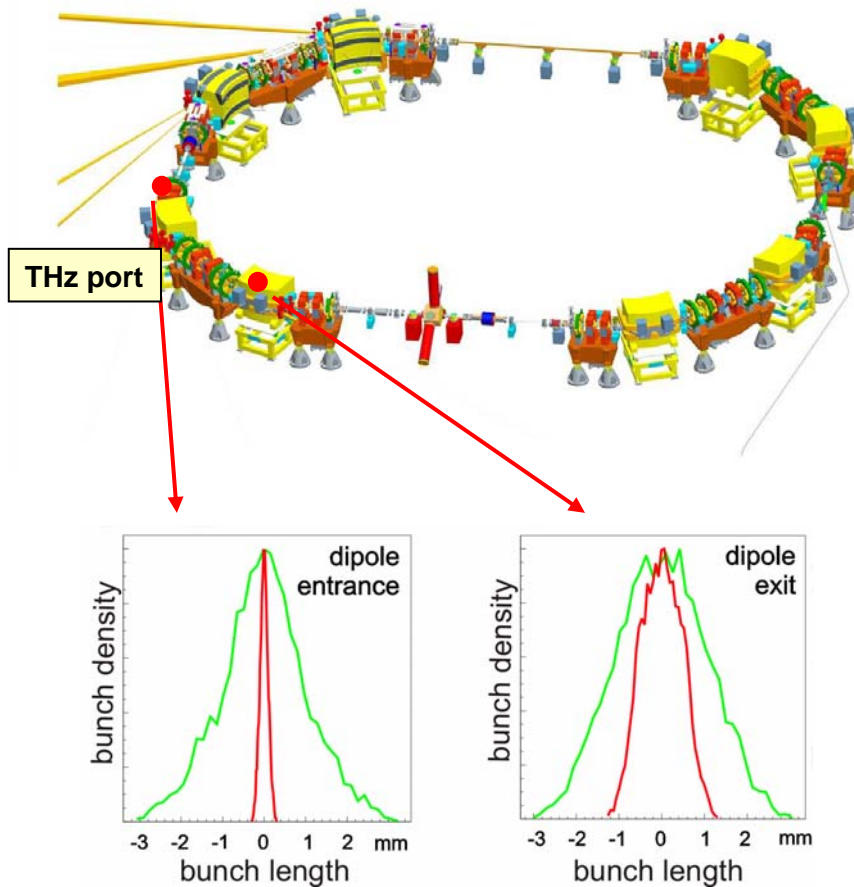


Figure 2. Design of the Metrology Light Source (upper picture). The lower picture shows plots of the simulated electron bunch length at the entrance (left) and exit side (right) of an MLS bending magnet following the straight section for 1 mm rms long bunches for normal operation (outer curve). For special operation, 10 times shorter bunches (inner curve) are only feasible at the entrance side of the bending magnet, where the exit port of the THz beamline is nearby.

- [1] see articles in the “Beam Dynamics Newsletter” of the International Committee for Future Accelerators, No. 35 (2004)
- [2] M. Abo-Bakr, J. Feikes, K. Holldack, G. Wüstefeld, H.-W. Hübers, *Phys. Rev. Lett.* **88**, 254801 (2002)
- [3] M. Abo-Bakr, J. Feikes, K. Holldack, P. Kuske, W. B. Peatman, U. Schade, G. Wüstefeld, H.-W. Hübers, *Phys. Rev. Lett.* **90**, 094801 (2003)
- [3] U. Schade et al., *Rev. Sci. Instrum.* **73**, 1568 (2001)
- [4] R. Klein, G. Ulm, P. Budz, K. Bürkman, J. Rahn, G. Wüstefeld, *Proc. of the EPAC 2006*, Edinburgh, United Kingdom, 3314 (2006)
- [5] R. Müller, A. Hoehl, R. Klein, U. Schade, G. Ulm, U. Schade, K. Holldack, G. Wüstefeld, *Infrared Physics & Technology* (2006), *Infrared Phys. Technol.* **49**, 161 (2006)
- [6] K. Holldack, S. Khan, R. Mitzner, T. Quast, G. Wüstefeld, *Proc. of the EPAC 2004*, Lucerne, Switzerland, 2284 (2004)

Reference-free investigation of an ancient Chinese ceramic by X-ray fluorescence analysis

M. Kolbe, B. Beckhoff

Physikalisch-Technische Bundesanstalt, Abbestraße 2-12, 10587 Berlin, Germany

O. Hahn

Bundesanstalt für Materialforschung und –prüfung, 12200 Berlin, Germany

A. G. Karydas, C. Zarkadas¹, D. Sokaras

Institute of Nuclear Physics, N.C.S.R. Demokritos, Aghia Paraskevi, 15310, Athens, Greece

M. Mantler

Technische Universität Wien, Wiedner Hauptstr. 8-10, 1040 Wien, Austria

Abstract. In a proficiency test of the International Atomic Energy Agency (IAEA) involving atomic and nuclear methods the Physikalisch-Technische Bundesanstalt (PTB) contributed to the investigation of an ancient Chinese ceramic employing reference-free X-ray fluorescence analysis (XRF). The respective XRF measurements were performed at BESSY II employing different excitation energies in the hard X-ray range. A fundamental parameter based XRF quantitation approach was used to evaluate the fluorescence spectra. Due to absolutely calibrated instrumentation of PTB all experimental values were obtained in a completely reference-free manner. The analytical results of the Chinese ceramic achieved by reference-free XRF are in line with target values given by the IAEA .

Introduction. The Reference Material Group of the Chemistry Unit of the IAEA's analytical laboratories conducted a proficiency test of applications of nuclear analytical techniques to investigate the authenticity of art objects. For this test an ancient Chinese ceramic has been provided to 36 laboratories around the world, of which 24 reported their results to the IAEA. The methods applied were mostly Instrumental Neutron Activation Analysis (INAA) and XRF but also Prompt Gamma-ray Activation Analysis (PGAA), Proton Induced Gamma-ray Emission (PIGE), Proton Induced X-ray Emission (PIXE), Inductively-Coupled-Plasma Mass-Spectrometry (ICP-MS), atomic absorption spectroscopy (AAS), and Inductively-Coupled-Plasma Optical-Emission-Spectrometry (ICP-OES). Our goal in taking part in this test was to prove the corresponding capabilities of absolutely reference-free quantification in XRF analysis [1]. In general, XRF table-top devices are to be pre-calibrated by means of appropriate calibration or standard reference materials prior to the analysis of an unknown sample. However, in the PTB laboratory at BESSY all relevant experimental parameter are well-known due to the absolute calibration of all detectors employed in an XRF experiment. Hereby, fundamental parameter based quantitation of XRF analysis without any reference samples is enabled.

Experimental. The ancient Chinese ceramic was provided as a fine powder by the IAEA. This sample was pressed at a pressure of about 200 - 300 kN to a pellet without adding any additional binding material. The measurements were performed in equipment for reference-free XRF analysis at PTB's four-crystal monochromator beamline that provides monochromatized X-ray radiation of high spectral purity in the energy range from 1.75 keV to 10.5 keV [2].

¹ Present affiliation: PANalytical B.V., 7600 AA Almelo, The Netherlands

The UHV chamber for XRF is equipped with calibrated diaphragms in fixed but changeable positions to define the geometry between the incident radiation, the sample surface, and the fluorescence radiation. Due to the calibration of the diaphragms the solid angle of detection is well known. Using calibrated photodiodes the flux of the incident radiation is determined. The fluorescence radiation is measured with an energy-dispersive Si(Li) detector that is calibrated with respect to its response function and efficiency. Hence all data necessary for a reference-free fundamental parameter based evaluation of the fluorescence analysis are provided due to this calibrated equipment. Three excitation energies were chosen according to a typical composition of ceramics. Thus the sample has been excited at 3.0 keV, 7.0 keV, and 9.7 keV. The spectra are shown in figure 1.

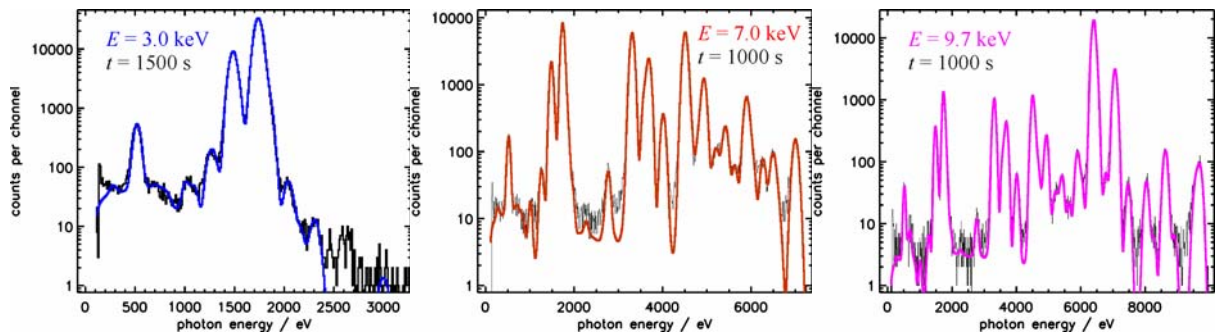


Fig. 1: XRF spectra of an ancient Chinese ceramic excited at different photon energies E . The colored lines show the fit of the line energies convoluted with the experimentally determined response function of the calibrated detector to retrieve the count rate for each fluorescence line.

Data evaluation. The count rates of relevant fluorescence lines were determined from the XRF spectra using the best fit based on the minimization of χ^2 employing experimentally based detector response functions. During the registration of the spectra the incident photon flux was monitored by means of a calibrated transmission photodiode [3]. Using these data in the fundamental parameter approach the weight fraction of each element has to be determined. Besides the primary excitation, secondary and tertiary excitation [4] by energetic higher fluorescence lines as well as by photoelectrons has to be included. The photoelectron secondary excitation effect has been investigated for typical main matrix constituents such as Mg, Al, and Si in an IKYDA project. The fluorescence intensity of the respective $K_{\alpha,\beta}$ fluorescence lines of one-elemental free-standing foils of about $2 \mu\text{m}$ thickness each has been evaluated in dependence on the excitation energy. The energy of photoelectrons induced scales with the one of the incident photons allowing for multiple secondary excitations with increasing energies. Hence the measured fluorescence line intensity increases with increasing incident photon energy. Figure 2 shows the effect for a $1.6 \mu\text{m}$ thick silicon foil. Here, the experimental deduced intensities were compared to the fundamental parameter approach without including any photoelectron secondary excitation. At 7 keV excitation energy the fluorescence line intensity is increased by about 4 % and at 9.7 keV the increase is about 5.5 %. Such data are also available for Mg and Al, whereas for other light elements

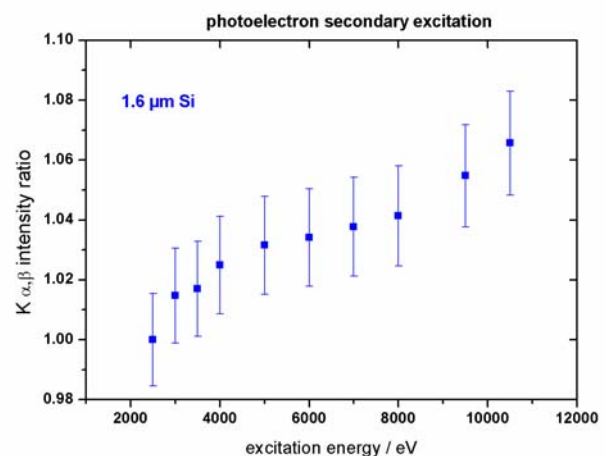


Fig. 2: Increase of element-specific fluorescence intensity of Si $K_{\alpha,\beta}$ by photoelectron secondary excitation.

the corresponding enhancement factor has to be approximately scaled with the atomic number based on the available data. Associating the main matrix components with 2 μm thick foils, the aforementioned secondary excitation data were included in the calculation of the matrix elements of the Chinese ceramic by increasing the fluorescence intensity of the respective elements by the given factor.

The elemental weight fractions determined were converted to the weight fractions of the respective oxides. Table 1 shows our results in the second column with the relative uncertainty compared to the given target value of the proficiency test of the IAEA. The instruments' contribution to the relative uncertainty is about 3 %, the results are considerably more affected by the tabulated fundamental atomic parameters of the elements, some of which only have estimated uncertainties. The deviations of the rare earth elements in the last three rows of the table are likewise due to problems with the spectra deconvolution of the minor peaks or due to problems with the fundamental parameters in the energy range of the respective L absorption edges.

	determined value ($\mu\text{g/g}$)	rel. uncertainty (%)	IAEA's target value ($\mu\text{g/g}$)
SiO ₂	676600	25	675000 \pm 7000
Al ₂ O ₃	246600	25	239000 \pm 4000
CaO	7252	20	6200 \pm 500
MgO	6367	25	7000 \pm 1200
K ₂ O	23120	15	23000 \pm 2000
TiO ₂	9023	15	9500 \pm 400
MnO	256	15	260 \pm 10
Fe ₂ O ₃	24560	20	27000 \pm 1000
Ni	24	20	25.7 \pm 7.4
Cu	22	20	26.9 \pm 9.5
Zn	54	20	58.5 \pm 6.6
Pm	249	30	
Nd	130	30	51.9 \pm 7.2
Sm	77	30	8.7 \pm 1.0

Table 1: compilation of results using all three excitation energies simultaneously

Conclusion. We have shown, that reference free X-ray fluorescence analysis provides within the frame of its current uncertainties the same results as the target value given by the evaluation of all reported data by the IAEA, except for rare earth elements.

Acknowledgement. Some of the authors (MK, BB, AK, CZ, DS) would like to thank for the support by the Greek State Scholarships Foundation IKY and the German Academic Exchange Service DAAD within the frame of their IKYDA program under the project number 314-ikyda-dr.

References

- [1] B. Beckhoff, M. Mantler, M. Bavdaz, G. Fraser, M. Kolbe, M. Krumrey, A. Owens, A. Peacock, D. Pullan, F. Scholze, G. Ulm, Evaluation of complete standardless quantitation for synchrotron radiation induced X-ray fluorescence analysis, BESSY Annual Report (2003) 31-34
- [2] M. Kolbe, B. Beckhoff, M. Krumrey, G. Ulm, Thickness determination for Cu and Ni nanolayers: Comparison of reference-free fundamental-parameter based X-ray fluorescence analysis and X-ray reflectometry, Spectrochimica Acta B 60 (2005), 505-510
- [3] M. Krumrey, M. Gerlach, M. Hoffmann, P. Müller, Thin Transmission Photodiodes as Monitor Detectors in the X-ray Range, AIP Conf. Proc. 879 (2007), 1145
- [4] M. Mantler, VXRF: A software package for teaching (and learning) XRF, Advances in X-ray Analysis 43 (2000), 429-434

Status of the Metrology Light Source

Guido Brandt, Rolf Fliegau, Arne Hoehl, Roman Klein, Ralph Müller, Gerhard Ulm
Physikalisch-Technische Bundesanstalt, Abbestraße 2-12, 10587 Berlin, Germany

Thomas Birke, Jörg Borninkhof, Klaus Bürkmann-Gehrlein, Reiner Daum, Olaf Dressler, Volker Dürr, Jörg Feikes, Holger Glass, Hans Georg Hoberg, Jörg Kolbe, Ralph Lange, Ingo Müller, Joachim Rahn, Günter Schindhelm, Tobias Schneegans, Thomas Schröter, Dirk Schüler, Godehard Wüstefeld
Berliner Elektronenspeicherring-Gesellschaft für Synchrotronstrahlung m.b.H., Albert-Einstein-Str. 15, 12489 Berlin, Germany

The Physikalisch-Technische Bundesanstalt (PTB), the German national metrology institute, is setting up a dedicated low-energy electron storage ring in close cooperation with the BESSY GmbH. The new storage ring, named Metrology Light Source (MLS), will be mainly dedicated to metrology and technological developments in the UV, VUV and EUV spectral range. The MLS can be operated with parameters optimized for special calibration tasks, which is rarely possible at a large multi-user facility. Here we report the status and the anticipated instrumentation and utilization of the MLS.

The MLS is being built adjacent to the BESSY II facility. The storage ring building is completed, and all major parts of the storage ring and the injection system have already been supplied [1, 2]: The 100 MeV racetrack microtron, the injection system with four Delta like slotted pipe kicker magnets and one air-cooled septum magnet, all magnets and girders, the 500 MHz RF cavity and the vacuum system. Each of the four quadrants of the storage ring was baked out in an external oven and then placed into the MLS bunker (see Fig. 1). The commissioning of the 100 MeV injection microtron started in January 2007. The vacuum system of the ring will be closed in March 2007 and the commissioning of the storage ring will begin in May 2007.

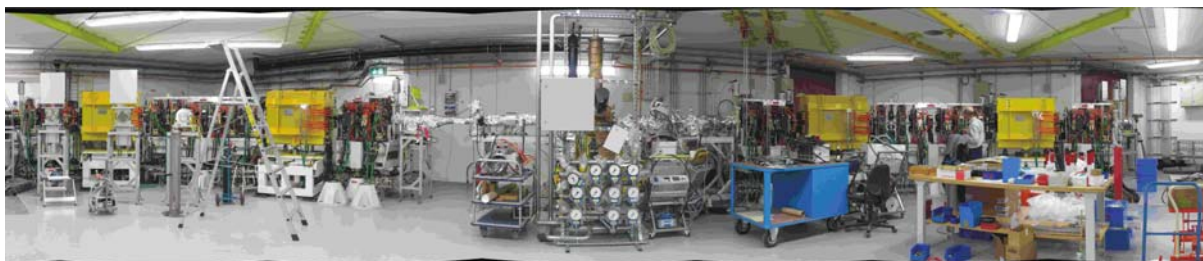


Figure 1. A 180° panorama view in the MLS Bunker. Status of 19th January 2007.

The MLS has been designed by the BESSY GmbH [3] to meet PTB's demands for a UV/VUV source with high stability and reproducibility, and to complement the spectral region covered by the BESSY II electron storage ring at the lower photon energy range [4, 5]. The electron energy can be chosen in the range from 200 MeV to 600 MeV, i.e. the characteristic photon energy can be tuned in the range from 11.6 eV up to 314 eV. This allows the high-energy end of the bending magnet spectrum to be adjusted in such a way that radiation which would lead to higher diffraction orders and stray light in a monochromator is suppressed. Furthermore, the tuning of the characteristic photon energy is very helpful to achieve an effective reduction of the heat load and the contamination of the optical components of the beamlines, which is necessary for stable measurement conditions.

The electron beam current can be adjusted in a range of more than 11 orders of magnitude, i.e. from a single electron (1 pA) up to 200 mA, in order to adjust the photon flux to the measurement task. The MLS has a circumference of 48 m and is designed as an asymmetric double-bend achromate with twofold symmetry. Each of the eight 45° bending magnets can be equipped with two front ends. The MLS has two long and two short straight sections. The long straight section can accommodate undulators of the BESSY II design which enables PTB to operate its U180 undulator in the MLS. Injection will be effected from a 100 MeV microtron, the energy is then ramped to the desired value. The anticipated lifetime at a maximum electron beam current of 200 mA is calculated to be in the

range from better than 1 h to about 10 h for operation at 200 MeV and 600 MeV electron energy, respectively.

Essential for PTB is the use of the storage ring as a primary source standard for the calibration of radiation sources and energy-dispersive detectors (source-based radiometry) [6]. The spectral photon flux of the synchrotron radiation from bending magnets can be precisely calculated from classical electrodynamics using the Schwinger equation, if all parameters entering the equation are known. At the MLS, PTB will install equipment to be able to measure of these parameters with high accuracy [5]. In Fig. 2, the expected photon flux available at the MLS and BESSY II is shown. In combination with monochromator beamlines as a source of monochromatic radiation of high spectral purity, the MLS will also be used for detector-based radiometry and reflectometry.

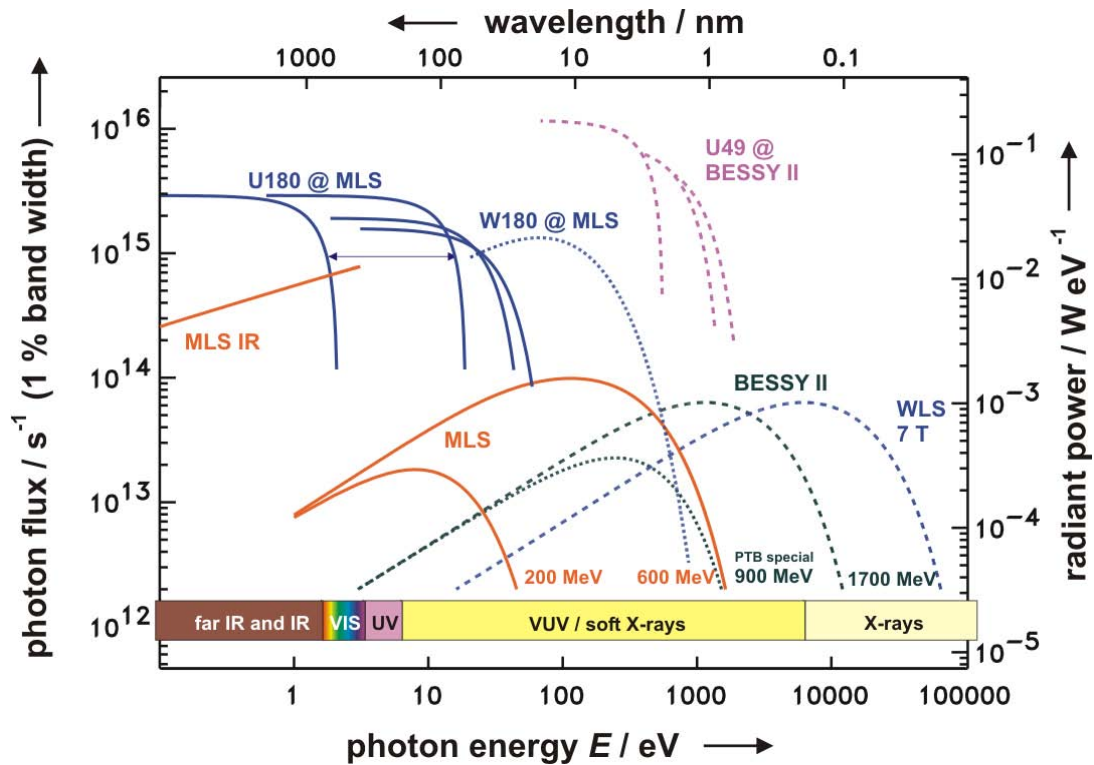


Figure 2. Calculated photon flux and radiant power available at the MLS for 200 MeV and 600 MeV electron energy emitted from a bending magnet and the PTB undulator U180 and the wiggler W180 (undulator U180 operated in the wiggler mode) as compared to bending magnet radiation of BESSY II for 1700 MeV and 900 MeV (a special PTB operation mode) and the PTB undulator U49.

At present, PTB is using BESSY II as a calculable radiation source (primary source standard) and is operating 10 experimental stations at four bending magnet beamlines and one insertion device beamline in its BESSY II laboratory [7]. The instrumentation there available is designed primarily for the coverage of the EUV, VUV and X-ray spectral range. At the MLS, the instrumentation will cover the spectral range from the FIR up to the VUV region and will therefore considerably expand and improve the measurement capabilities on the low-energy side as compared to the BESSY II instrumentation. The radiation from four bending magnets and from one undulator will be used. Seven stations will be set up on the experimental floor for the coverage of the UV up to the VUV spectral range, and on the top of the storage ring bunker roof, an FIR/THz and two IR stations [8] are planned. Another four bending magnets and an undulator straight-section are available for a future upgrade. Figure 3 illustrates the planned instrumentation at the MLS. A list of the beamlines and typical applications is given in table 1.

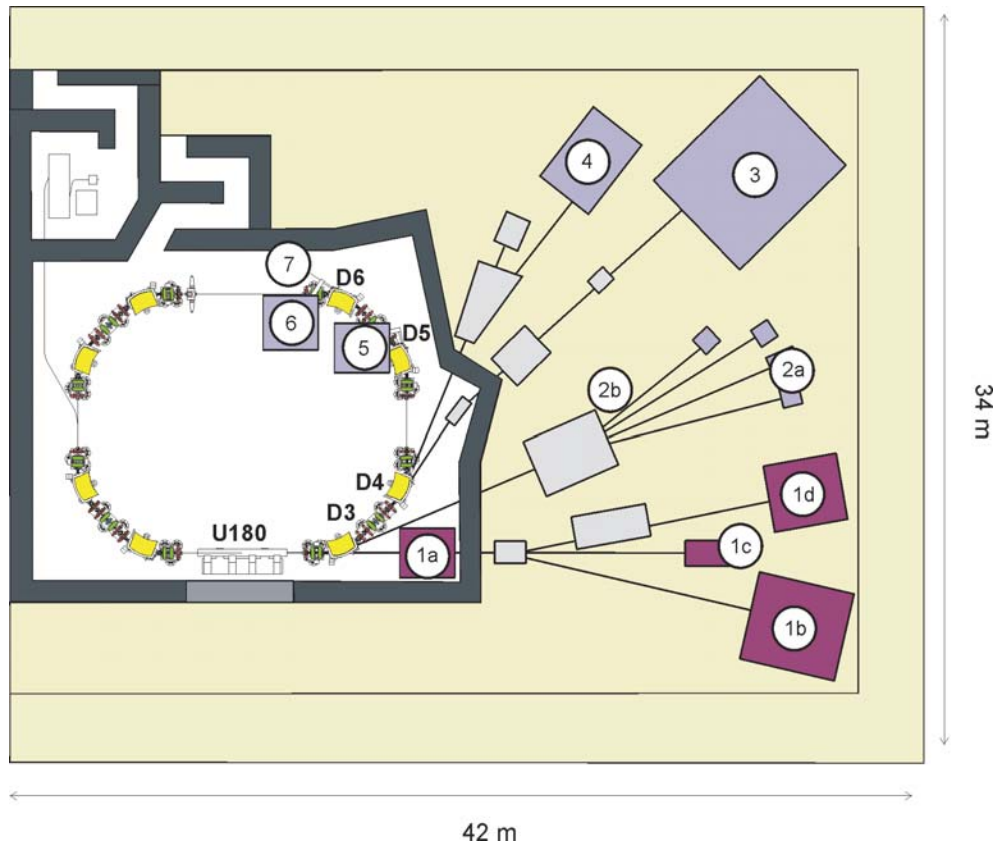


Figure 3. Planned beamlines and experimental stations at the MLS.

Table 1: List of Planned Beamlines and Typical Applications.

No. in Fig. 3	Beamline and Application	No. in Fig. 3	Beamline and Application
1a	IR undulator radiation 2 mm to 20 mm/ Compton-backscattering laser	3	EUV plane grating monochromator (reflectometry), 4 nm to 40 nm
1b	deflected undulator radiation (high-flux experiments)	4	UV/VUV monochromator (detector calibration, reflectometry), 40 nm to 400 nm
1c	direct undulator radiation / Compton-backscattering detector	5	FIR/THz beamline 0.6 μm to 8 mm
1d	UV/VUV monochromator for undulator radiation, 4 nm to 400 nm	6	IR beamline 0.6 μm to 8 mm
2a	direct bending magnet radiation (use of calculable photon flux)	7	diagnostics frontend
2b	UV/VUV monochromator 4 nm to 400 nm (source calibration)		

The radiation from a 180 mm–period-length undulator (U180) will be directed to a combined normal incidence (NI) and grazing incidence (GI) monochromator (station 1d). This combined set-up will cover a wide spectral range from 4 nm to 400 nm using a modified collimated grating monochromator (cPGM) design with an additional normal incidence mirror. For average radiant power, PTB's measurement capabilities at the MLS within the framework of detector-based UV and VUV radiometry will be extended to cover a dynamic range from fW to mW. This also provides the basis for developing and applying advanced (micro-) spectroscopy and metrology techniques for the quantitative but standard-free analysis of gases and surfaces.

Alternatively, the direct undulator radiation (station 1c) or the undispersed, deflected undulator radiation (station 1b) can be used. The undispersed, calculable radiation (see below) from a bending

magnet can be either used at a white light beamline (station 2a) or for the calibration of a combined NI and GI monochromator system (station 2b) that will be used thereafter for the calibration of radiation sources.

The development of EUV lithography (EUVL) at 13 nm is critically based on the availability of a suitable metrology. To fulfill the growing demands of the industry, we are planning a dedicated EUV beamline at the MLS (station 3).

Station 4 uses a NI-monochromator that will be transferred from the BESSY II radiometry laboratory after an upgrade, and will primarily be used for detector calibration and reflectometry in the UV and VUV spectral range from 40 nm to 400 nm.

Three beamlines dedicated to the use of IR synchrotron radiation are planned at the MLS [8]: The long period undulator U180 at station 1a provides radiation with high flux in the MIR spectral range, a THz beamline at station 5, optimized for the FIR/THz spectral range, and the MLS-IR beamline at station 6, optimized for the MIR to FIR. The front ends of all IR beamlines are on the roof of the bunker of the MLS.

Like BESSY II, the MLS will be operated as a primary source standard and PTB will therefore install equipment for the measurement of all parameters entering into the calculation of the emitted photon flux. E.g., at a diagnostics front-end (station 7), instrumentation for the measurement of small electron beam currents, down to a single stored electron, will be set up. The electron energy will be measured by Compton backscattering of laser photons at station 1c.

In summary the project Metrology Light Source is well under way. The MLS will take up user operation in 2008. The machine layout is optimized for the coverage of the THz/FIR and the UV, EUV and VUV spectral region and will mainly be used for radiometry and technology development in this spectral region. A special mode of operation will allow the production of coherent synchrotron radiation and thus the production of THz/FIR radiation with enhanced intensity. In a first stage, 10 experimental stations and a diagnostics front-end will be set up. However, the design of the storage rings allows a future upgrade by a similar number of additional stations.

- [1] K. Bürkmann et al., Proc. of the EPAC 2006, Edinburgh, United Kingdom, 3299 (2006)
- [2] P. Budz et al., Proc. of the EPAC 2006, Edinburgh, United Kingdom, 3296 (2006)
- [3] M. Abo-Bakr et al., MLS Design-Studie, BESSY mbH, July (2003)
- [4] G. Ulm et al., AIP Conf. Proc. **879**, 167 (2007)
- [5] R. Klein et al., Proc. of the EPAC 2006, Edinburgh, United Kingdom, 3314 (2006)
- [6] G. Ulm, Metrologia **40**, S101 (2003)
- [7] R. Klein et al., Synchrotron Radiation News **15**, no. 1, 23 (2002)
- [8] R. Müller et al., Infrared Phys. Technol. **49**, 161 (2006)

TXRF-NEXAFS study of nitrogen compounds in coastal Antarctic fine aerosol particles

J. Osán^a, S. Török^a, B. Beckhoff^b, G. Ulm^b, C. Abete^c and R. Fuoco^d

^aKFKI Atomic Energy Research Institute, P.O. Box 49, H-1525 Budapest, Hungary

^bPhysikalisch-Technische Bundesanstalt, Abbestr. 2-12, D-10587 Berlin, Germany

^cCNR-ICCOM, Via Risorgimento, 35, I-56126 Pisa, Italy

^dDepartment of Chemistry and Industrial Chemistry, University of Pisa, Via Risorgimento, 35, I-56126 Pisa, Italy

While compounds in the gas phase can be measured by high temporal and spatial resolution using optical and remote sensing methods it is crucial to have analytical methods that enable us to measure the aerosol samples collected in a short time whilst retaining the information on the size distribution of the particles. Although ion chromatography (IC) is a relatively simple analytical method for the determination of major ionic species in aerosols, its major disadvantages are the destructiveness and the relatively high detection limit that needs a relatively high sample volume for reliable analysis [1]. Total-reflection X-ray fluorescence (TXRF) spectrometry is sufficiently sensitive for a multielemental analysis of size-segregated aerosol samples of around 10^{-9} g [2]. Cascade impactors allow the collection of aerosols directly on the reflector surface. A near edge X-ray absorption fine structure (NEXAFS) investigation in conjunction with TXRF spectroscopy analysis of minute samples on wafer surfaces is a unique non-destructive method for the speciation of the atmospherically important low-Z elements (C, N and O) [3]. Due to the extremely high sensitivity of the technique, a nanoscopic amount of material is enough to carry out the measurement.

Coastal Antarctic aerosol particles were collected near the Italian base located at Terra Nova Bay (Ross Sea), on silicon wafers using a 7-stage May cascade impactor, from 14 to 19 February 2004. For comparative purposes, aerosol samples were also collected with the same instrument near the sea-shore in Alghero (Sardinia, Italy), from 6 to 11 June 2004. The May impactor has, at a 20 l/min sampling flow, aerodynamic cut-off diameters of 1, 0.5 and 0.25 μm for stages 5 to 7, respectively. The sampling duration varied between 1 to 10 (for stage 7), 5 to 50 (for stage 6) and 10 to 100 minutes (for stage 5), to obtain the best loading of particles in the impacted lines. The shorter collection times were applied in Alghero, while the lower concentration of aerosols in Antarctica required an order of magnitude longer sample collection duration.

The TXRF experiments were performed at the plane grating monochromator (PGM) beamline of Physikalisch-Technische Bundesanstalt (PTB), the German national institute for metrology, at the electron storage ring BESSY II using undulator radiation that provides a high photon flux of high spectral purity in the soft X-ray range. The K edge of nitrogen was examined on the wafer samples in the UHV irradiation chamber of PTB. The beam profile was $140 \times 40 \mu\text{m}^2$, which resulted in an illuminated area of $3.2 \text{ mm} \times 40 \mu\text{m}$ at an angle of incidence of 2.5° . For a typical energetic scan at the N-K edge, the incident photon energy was varied from 395 eV to 415 eV in steps of 125 meV. At each point of the scan a TXRF spectrum was recorded for 20 s and the detected N-K α count rate was deduced. To determine the molar ratio of ammonium and nitrate in the aerosol samples, $(\text{NH}_4)_2\text{SO}_4$ and NaNO_3 standards prepared on silicon wafers were measured in identical conditions. Using a linear combination of the TXRF-NEXAFS spectra recorded for the two standards, a semi-quantitative ammonium/nitrate ratio was obtained [1].

TXRF-NEXAFS spectra collected at the K edge of nitrogen provide information on the chemical environment of nitrogen in the samples. Figure 1 shows N K-edge TXRF-NEXAFS spectra of

fine aerosol samples (on May-impactor stages 7, 6 and 5) collected in Antarctica on 14 February 2004, and in Alghero on 11 June 2004. At Terra Nova Bay more than 90 % of nitrogen was present as ammonium in submicrometer aerosol particles (0.25–1 μm) and the ammonium contribution in the 1–2 μm size fraction decreased to 40–50 %. The ammonium to nitrate ratio showed a decreasing trend with increasing particle sizes in the range of 0.25–2 μm . These results are in accordance with the IC results reported elsewhere [4, 5]. According to Teinilä et al. [4], the dominant mode containing ammonium had a peak at ~ 0.3 μm aerodynamic diameter, and the nitrate-containing particle mode peaked at slightly below 2 μm . The ammonium-to-nitrate molar ratio was found on average to be 40%/60% in the supermicrometer modes. However, our results were obtained from a 2 m^3 sampled air volume, which is one order of magnitude smaller than for the IC results of Teinilä et al. [4] (30 m^3). At Alghero, more than 90 % of nitrogen was present as nitrate at stage 5 on 6 June 2004, which decreased to 70 % on 11 June 2004. The higher nitrate content was expected due to the characteristics of aerosols throughout Europe [6]. Since both sampling sites were on coastal areas, nitrate was mostly present as NaNO_3 , which was formed by heterogeneous reactions of sea salt aerosols with gaseous HNO_3 and other nitrous compounds [4]. The results obtained for Terra Nova Bay (Antarctica) show the applicability of the presented technique, supported by the fact that our observations on ammonium and nitrate species at the different size fractions fit in the trends expected from analyses of greater sample volumes [7].

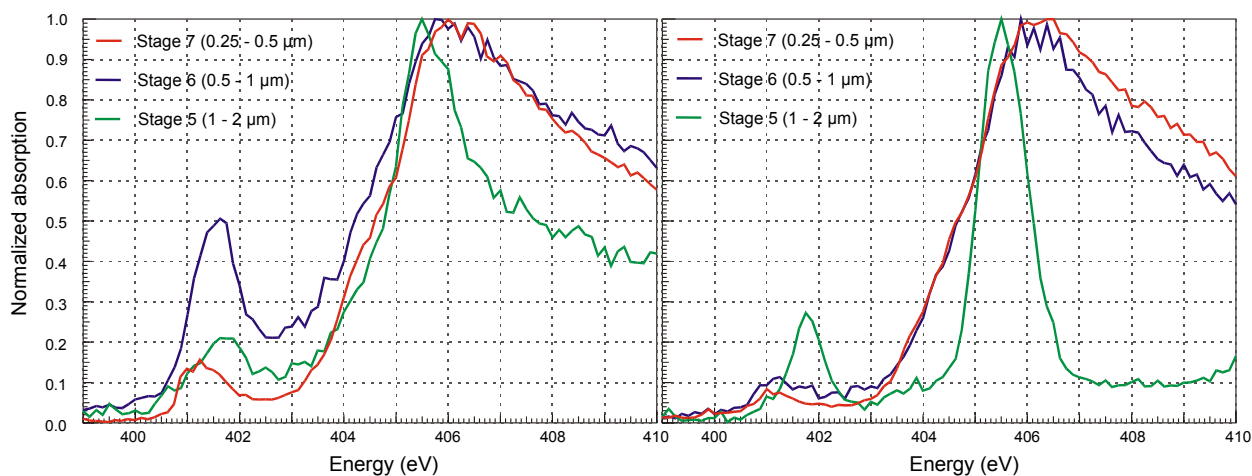


Fig. 1. N K-edge TXRF-NEXAFS spectra of fine aerosol samples collected in Antarctica (left) and in Alghero (right)

This work was partially financially supported by the Italian Research Programme in Antarctica (PNRA) and by the Hungarian Scientific Research Fund (OTKA) through project no. T049581.

References

- [1] Török S, Osán J, Beckhoff B, Ulm G. Powder Diffr. 19, 81–86 (2003)
- [2] Strelcić C, Wobraschek P, Kregsamer P, Pepponi G, Pianetta P, Pahlke S, Fabry L. Spectrochim. Acta B 56, 2085–2094 (2001)
- [3] Beckhoff B, Fliegau R, Ulm G, Weser J, Pepponi G, Strelcić C, Wobraschek P, Ehmann T, Fabry L, Pahlke S, Kanngießner B, Malzer W. Solid State Phenom. 92, 165–170 (2003)
- [4] Teinilä K, Kerminen VM, Hillamo R. J. Geophys. Res. Atmos. 105, 3893–3904 (2000)
- [5] Fattori I, Becagli S, Bellandi S, Castellano E, Innocenti M, Mannini A, Severi M, Vitalec V, Udisti R. J. Environ. Monit. 7, 1265–1274 (2005)
- [6] Kerminen VM, Hillamo R, Teinilä K, Pakkanen T, Allegrini I, Sparapani R. Atmos. Environ. 35, 5255–5265 (2001)
- [7] Osán J, Török S, Beckhoff B, Ulm G, Hwang H, Ro CU, Abete C, Fuoco R. Atmos. Environ. 40, 4691–4702 (2006)

A calibrated wavelength-dispersive spectrometer for the determination of atomic fundamental parameters with small relative uncertainties in the soft X-ray range

M. Müller¹⁾, R. Fliegau¹⁾, B. Beckhoff¹⁾, B. Kanngießer²⁾, and G. Ulm¹⁾

¹⁾Physikalisch-Technische Bundesanstalt, Abbestraße 2-12, 10587 Berlin, Germany

²⁾Technische Universität Berlin, Hardenbergstraße 36, 10623 Berlin, Germany

Abstract. A wavelength-dispersive grating spectrometer (WDS) that can be calibrated absolutely was built for various applications at the plane grating monochromator beamline for undulator radiation of the PTB at BESSY II. The device will be used to determine atomic fundamental parameters absolutely with small relative uncertainties. Well known fundamental parameters such as Coster-Kronig coefficients, transition probabilities of fluorescence and satellite lines as well as fluorescence yields are crucial for a reliable quantitative reference free X-ray fluorescence analysis (XRF). The chosen energy range from 270 eV to 1760 eV covers the K-fluorescence radiation of light elements from C to Si and the L-fluorescence radiation of transition metals. Initial experiments have been performed to characterize the new spectrometer and to evaluate thin free standing samples in the nanometer range.

Introduction. Quantitative reference free XRF gains an increasing importance among non-destructive analytical methods aiming at various fields of basic research and industrial applications (i.e. process control, quality management). The main advantage of this method is to directly compare measured XRF spectra with computed fluorescence radiation intensities instead of employing any pre-calibration curves based on reference samples. The physical interactions between radiation and atoms relevant in XRF are described by fundamental interaction coefficients (absorption and scattering), transition probabilities, and fluorescent yields. With these fundamental atomic parameters, the number of fluorescence photons emitted from a sample can be described as a function of sample properties (elemental composition and concentrations, thickness, layer structure, etc.), experimental setup, and the characteristics of the exciting radiation. Therewith the reliability of this method strongly depends on the relative uncertainties of the fundamental parameters employed. Especially in the soft X-ray range (below 2 keV) the relative uncertainties of these parameters are quite large (up to 40% [1]) or often not even known. Using calibrated instrumentation, especially an energy-dispersive Si(Li) detector, the absolute determination of fundamental parameters has proven as a good method to achieve small relative uncertainties (i.e. 7% [2]). The aim of the

present spectrometer is to get access to fundamental parameters which can not be obtained by a Si(Li) detector, due to its medium energy resolution (about 100 eV for Cu-L $_{\alpha}$ at 928 eV), such as Coster-Kronig coefficients, transition probabilities of fluorescence lines and fluorescence yields.

Spectrometer set-up. The design of the WDS provides very good mechanical stability, high energy resolution (about 1 eV for Cu-L $_{\alpha}$ at 928 eV) and good detection efficiency. The WDS consists of an entrance slit, a spherical reflection grating (1200 l/mm) and a CCD-detector (1024x1024 pixel, 13.5 μ m x 13.5 μ m pixel size). All three elements are arranged on a Rowland circle (radius 2490 mm), whereas the CCD-detector is moveable along the Rowland circle (see Fig.1). The mechanical stability and the CCD-detector ensure the long-time stability of the device in respect to both, its detection efficiency and its energy scale. For a reliable calibration this characteristics are indispensable.

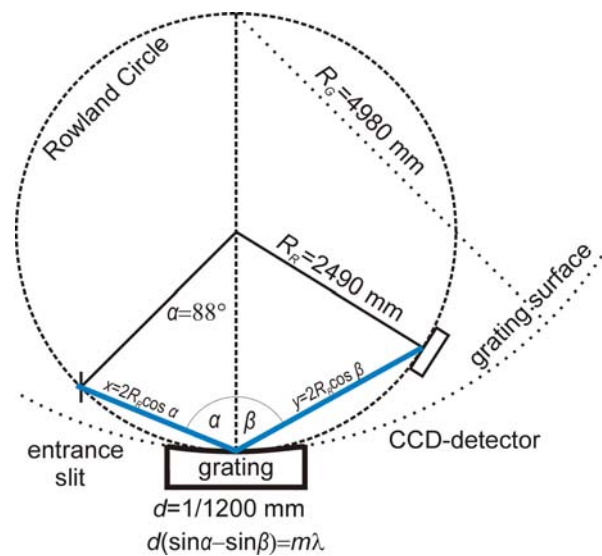


Fig.1: Sketch of the spectrometer geometry (blue line: path of the radiation)

Experimental arrangement.

Monochromatized undulator radiation provided by the plane grating monochromator beamline of PTB at BESSY II was employed in the current study. Fig. 2 shows schematically the experimental arrangement. The incident radiant power can be absolutely determined by using a calibrated photodiode placed behind the exit diaphragm. In the same arrangement, the absorption correction factors of thin samples can be experimentally determined by means of transmission measurements.

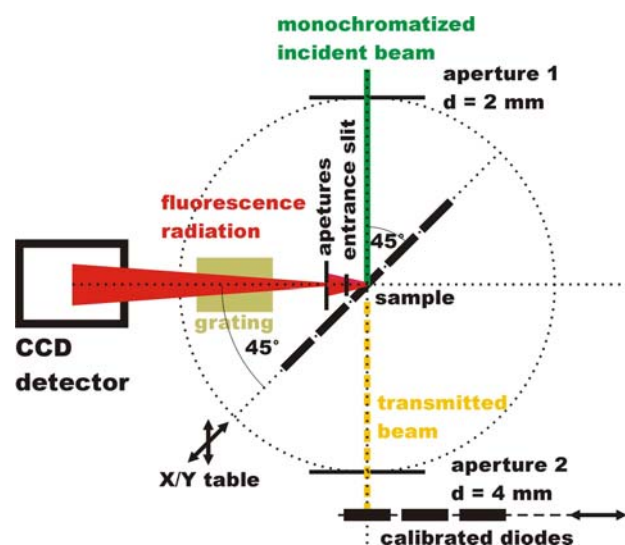


Fig.2: Experimental set-up

Calibration. The experimental set-up allows for replacing the spectrometer by a Si(Li) detector that is absolutely calibrated with respect to both its efficiency and its response behavior [3]. Therewith the product of the effective solid angle of collection and the detection efficiency of the WDS can be obtained for selected photon energies by comparison to the absolute XRF measurements previously performed with the assembly consisting of the Si(Li) detector and a calibrated diaphragm. For the determination of the response behavior of the WDS, the system was illuminated directly with monochromatized undulator radiation during PTB's special user shifts at BESSY. In order to correctly simulate the full illumination of the spectrometer during XRF experiments, the angle of incidence of the monochromatic radiation was scanned from the minimal to the maximal angle accepted by the WDS.

Initial results. As a first example for the determination of fundamental parameters employing the new spectrometer, the determination of the transition probability for the hole-transitions from the K shell of Mg was chosen. Fig. 3 shows the recorded spectrum of a 2 μm thin Mg foil, excited with monochromatic radiation of 1487 eV photon energy. The K_α fluorescence line has an intensive satellite line on its high energy side, caused by shake-off and shake-up processes. The photon energy of the satellite line is about 10 eV higher

than the photon energy of the diagram line and the intensity ratio is about 5%. Both lines originate from the same transition (KL), but differ in the state of the atom before relaxation. In the case that a photon of the satellite line will be emitted, the atom has an additional hole in the L shell before the transition. To determine the transition probability for the Mg KL and KM transitions, the count rates of the K_α line plus the satellite line and the K_β

line were obtained. Because of the self-absorption effect, these count rates were corrected by experimentally determined

absorption correction factors. The resulting transition probability for Mg is 98.4 % for the KL transition and 1.6 % for the KM transition. The relative uncertainty of these results is mainly caused by the background subtraction and the determination of the peak areas from the spectra. Due to the ongoing work on the response functions, the peak areas were determined without employing them explicitly. Therewith the relative uncertainties of the results are about 5%.

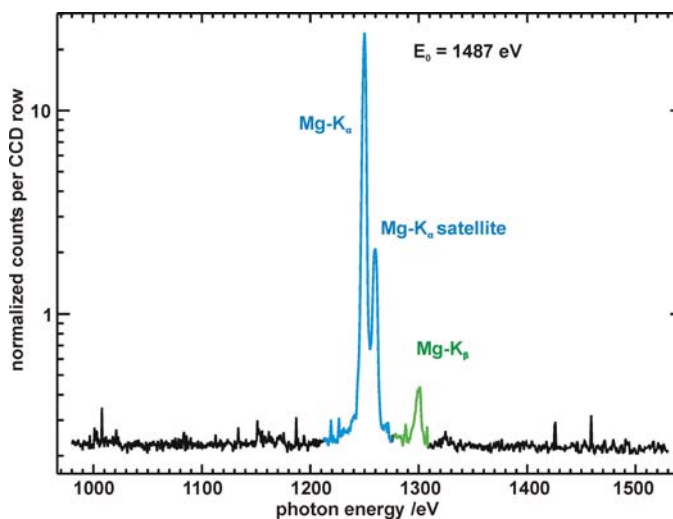


Fig.3: Spectrum of a thin Mg foil, recorded by the wavelength-dispersive spectrometer

Conclusion. The initial results shows that atomic fundamental parameters related to the soft X-ray range can be determined with small relative uncertainties, which still holds when a high energy resolution detector is needed for their determination. Once the calibration of the employed spectrometer is completed, selected fundamental parameters such as Coster-Kronig coefficients will be accessible with relative uncertainties of about 10%.

References.

- [1] M. Krause, C. Nestor, C. Sparks, and E. Ricci, Oak Ridge National Laboratory, Report No.: ORNL-5399 (1978)
- [2] M. Müller, B. Kanngießner, B. Beckhoff, and G. Ulm, *Phys. Rev. A* 74, 012702 (2006)
- [3] F. Scholze, B. Beckhoff, M. Kolbe, M. Krumrey, M. Müller, and G. Ulm, *Microchim. Acta* 115, 275 (2006)

Electrodeposition of Nickel- Iron using Pulse Plating

BARBARA ZITTERMANN, IVO RUDOLPH, DANIEL SCHONDELMAIER

Bessy GmbH, Application Center for Microtechniques (AZM), Albert- Einstein- Strasse 15, 12489

Berlin, Germany

eMail: zittermann@bessy.de, Tel.: +49 30 6392 4722, Fax: +49 30 6392 4682

Introduction

For many years now galvanic deposition has been playing a decisive role for industry. Especially since the LIGA technique is used for the production of micro components, there has been a steady increase of electroplating in the area of micro structure development. Above all the degree of HARMS (High Aspect Ratio Micro Structures) increases enormously and with it the requirements to the electrodeposition process. Especially the deformation of the produced micro parts which is caused by internal tension within the metals or alloys often entails the uselessness of the parts for further application (such as hot embossing or injection moulding). With a high aspect ratio, usually even small deformations are enough to disable the tool.

One possibility to decrease the tension within the metals or alloys is the use of pulse current during the deposition process instead of direct current which is normally used for electroplating. This technique called Pulse Plating induces depositions which are much more fine-grained and more homogenous than such which are produced by standard methods. Additionally their structures contain less impurity atoms, a fact that implicates the minimization of inner tension.

Impact of the pulse current

Unipolar pulse current

Unipolar pulse currents usually consist of a simple rectangular pulse (Fig. 1 a) or a rectangular pulse overlapping a direct current (Fig. 1 b).

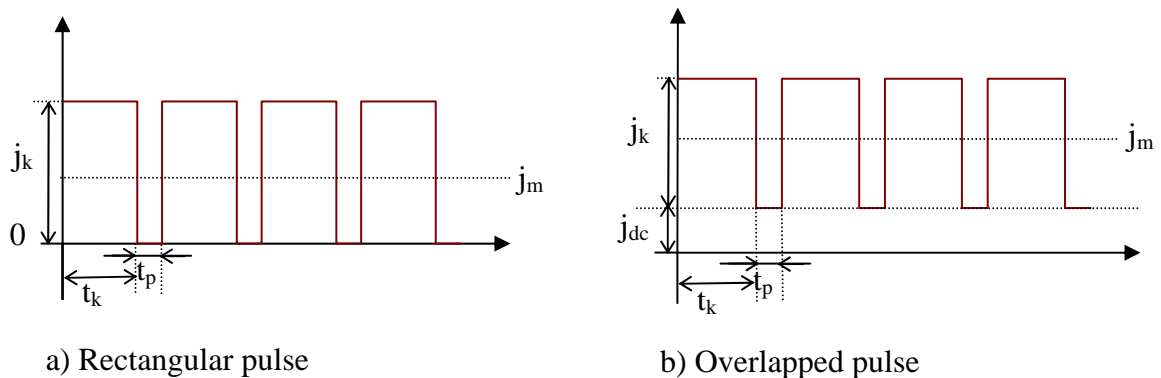


Fig. 1: Unipolar pulse current

The adjustable pulse parameters are: the cathodic current density j_k , the cathodic current time t_k , the time of current pause interval t_p and, if given, the direct current density j_{dc} . The average current density j_m , which can formally be compared to the current density used in direct current deposition, is established by equation (1).

$$j_m = j_k \frac{t_k}{t_k + t_p} (+j_{dc}) \quad (1)$$

It follows that in Pulse Plating the pulse parameters arise as independent and freely adjustable parameters, in addition to the parameters of direct current deposition, such as for example the composition and temperature of the used electrolyte, the pH-value and the shape and the dimensions of the substrate area .

In Pulse Plating as well as in direct current deposition, the mass transport mechanisms that provide subsequent delivery of metal cations to the cathode play a decisive role. But as opposed to direct current deposition, in Pulse Plating there exists a diffusion coating directly at the cathode which periodically increases and decreases along with pulse frequency. The thinner this pulsating diffusion coating is, the closer it follows the cathode's surface profile and the more homogeneous is the accessibility of the cathode's surface in all its places for the depositing metal.

If the pulse frequency is low, the pulsating diffusion coating cannot extend very far inside the electrolyte so convection is not relevant for the mass transport. The metal ions from inside the electrolyte therefore need to diffuse into the diffusion coating. This results in a second, outer diffusion coating comparable to that of the direct current deposition.

While the pulsating diffusion coating limits the current density of each current pulse, the outer, stationary diffusion coating restricts the applicable average current density. The high concentration gradient within the pulsating diffusion coating makes it possible for the current density of each pulse to adapt values which can be up to a thousand times higher than the possible maximum average current density. Therefore the velocity of the deposition during a current pulse is significantly higher than with a comparable direct current deposition. This influences the kinesis of simultaneous reactions, thus the relative velocity of concurring reactions, which is of decisive importance for the deposition of an alloy. In Pulse Plating of a binary alloy layer, for example, the deposition of one component can be advantaged compared to that of another, in relation to the frequency of the pulse pattern and the density of the pulse current. This makes it possible to vary the composition of depositional alloy layers by variation of pulse parameters.

During pulse pause intervals, the diffusion coatings acquire cations from inside the electrolyte. At the same time, undesirable reaction products are being repressed into the electrolyte. Therefore, within a average time, near the cathode results a higher concentration of metal ions and a lower concentration of impurity atoms than with direct current deposition. This decreases the possibility of including the reaction products within the deposition layer, so that the by Pulse Plating plated metals or alloys contain less impurity atoms, are purer and have less inner tension then depositions produced by direct current plating. At the same time, during pulse pause intervals diffusion leads to a decrease of impurities within the already deposited layer which makes them even more homogenous and causes further reduce of inner tensions. It is also possible that growth centres on the cathode are being blocked by adsorption of inhibiting additives, forcing the system to granulate new germs with every new pulse. Furthermore, the high excess voltages during the pulses lower the speed of surface diffusion which leads to a high degree of Ad-atoms and thus also advantages the accumulation of new germs. Therefore, layers deposited by Pulse Plating are extremely fine-grained and smooth.

Bipolar pulse current

With the bipolar method, in addition to the cathodic current pulses anodic current pulses are being programmed as shown in figure 2. The average current density can be calculated by the following formula:

$$i_m = \frac{i_k t_k - i_a t_a}{t_k + t_a + t_p} \quad (2)$$

In those current-time-progresses with anodic pulses, which are also known as reverse pulses, the layer to be deposited is periodically built up cathodically and partly reduced inbetween by the anodic current pulses.

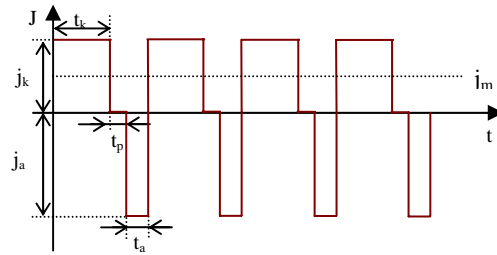


Fig. 2: Bipolar pulse current

The average current density has to be cathodic so metal can be deposited on the cathode during the whole process. Otherwise, the substrate would be reduced according to the rules of electrolysis.

The function of anodic current pulses is to optimize the ability of steering of the process. The streamlines of the electrical field which are bundled in certain areas of the cathode surface do not run differently during pole reversal so in those points where during cathodic pulse more metal is plated than in others, during reverse pulse more is dissolved. This makes it possible to repress the creation of dendrites. The growth of the deposition occurs altogether in a very homogenous way which minimizes the inner tensions of the layer to be plated. Therefore the method of Pulse Plating is adequate for HARMS if all parameters are optimally adjusted.

Furthermore, the pulsating diffusion coating acquires metal ions during the anodic pulse which preferably discharge and deposit during the following cathodic pulse. The probability that reaction products are included in the metal structure is thus even further reduced than by using unipolar current pulses.

Anodic current pulses should always be shorter but stronger than the cathodic pulses. Otherwise the reduction of metal in those places where too much has been accumulated before cannot occur without reducing the deposition on the whole surface, which would not have any of the desired effects but would only lengthen the time of the plating process.

Results

With many experimental series it could be shown that the Pulse Plating method can provide significant improvements for the deposition of nickel-iron alloy layers over the direct current method. Especially the bowing of the substrates and the related inner tension were investigated. They are reduced by more than half in a substrate deposited by Pulse Plating, compared with one deposited by direct current. The finer grains and better homogeneity of the pulse current layers are also clearly recognizable.

The optimum pulse pattern varies, depending on size and structure of the sample. But it could be shown that the use of Pulse Plating already remunerates before the optimum pattern is found. Even with arbitrary pulse patterns the depositions have better properties than with direct current plating.

The significant influence of the electrolyte composition on the layer properties has been demonstrated, and the necessity of keeping the concentration of its components constant has been proved. Measures to keep the concentration level have been introduced and partly already automatized.

The current flow at the cathode has been successfully checked, and precepts for the minimum duration of the current pulses and current pause intervals could be deduced.

Furthermore, the limit current density when plating on steel dummies and silicon wafer covered with plating base has been determined, which cognizance is necessary to program optimum current pulse patterns.

In further experimental series, the influence of the respective pulse parameters on the deposition characteristics were investigated more closely, and first tendencies have already been found as well as for samples with large surface areas as for substrates with micro structures.

All in all it was possible to launch the process of Pulse Plating successfully.

Integration of circuit paths in polymer micro-structures by hot embossing

Alexander Mai, Ivo Rudolph, Daniel Schondelmaier

Bessy GmbH, Anwenderzentrum für Mikrotechnik, Albert-Einstein-Straße 15, D 12489 Berlin

During the last years in the AZM there were several projects which dealt with the creating of micro structures in different polymers e.g. for bio or analysis applications. Here was recognized that such miniaturized laboratories also need corresponding circuit paths for readout the desired information.

Within the project at first it was necessary to establish a new process to structure a metallic plating base on a polymer surface and to create the desired circuit path - layout.

In a second step one has to optimize the process of structuring the polymer by micro hot embossing. Here one has to make sure that after the step no defects in terms of interruptions appear and that also the circuit paths show exactly the form of the used mould insert.

1 Structuring of a metallic layer on PMMA and PC surfaces

This process contains a UV-Lithography, the deposition and structuring of the plating base and the enhancement of the structured layout by electroplating. The UV-Lithography is less different from the standard process on a Si surface. But one has to attend the compatibility of the polymer compared to the corresponding solvents and the backing process which takes place in an oven and not on the hot plate.

The plating base has to fulfil two conditions. It must offer a good adhesion on the polymer and the structuring with the desired resolution must be possible. Therefore a plating base consisting of a Cr and an Au layer deposited by vacuum evaporation is chosen. The structuring of the plating base occurs by the lift off process. The ratio of Cr to Au of about 2:1 minimizes the required duration of the lift off process and thus the residence time of the polymer inside the solvent. Fig. one shows a structured Cr/Au plating base with an accomplished resolution of about two micro meters.

Last the structured layout will be enhanced by electroplating which is in this case an gold electrolyte. Before this step the substrates pass through an O₂ plasma to ensure a high degree of wetting during the electroplating.

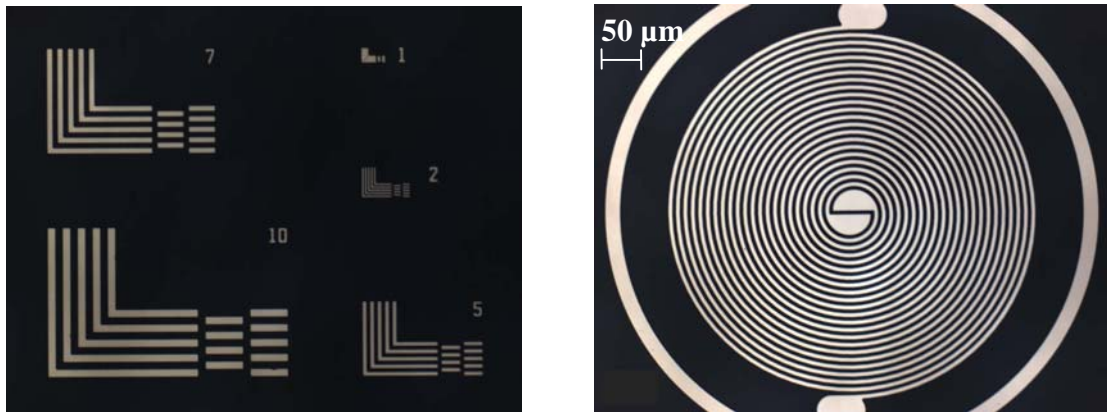


Figure 1: Cr/Au plating base with an accomplished resolution of about two micro meters

2 Realizing of micro structures in the polymer by micro hot embossing

To integrate the metallic circuit paths in polymer micro structures, hot embossing is used. Thereby a micro structured mould insert and the polymer substrate are heated above the glass transition temperature (T_G) of the polymer. After the force or distance controlled embossing process both are cooled down below T_G and are separated. The result one can see in Fig. 2.

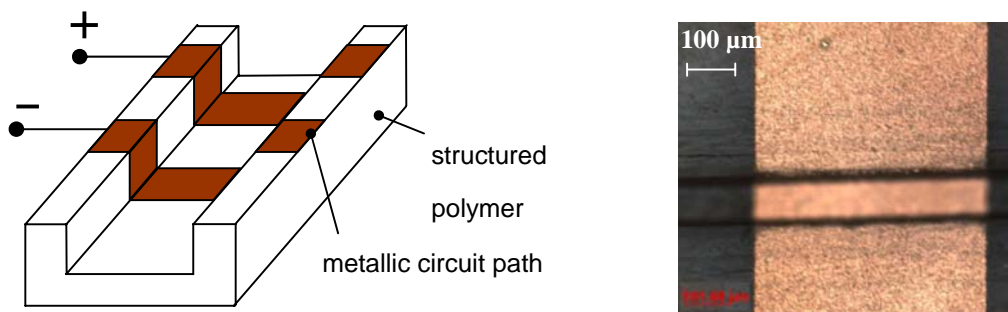


Figure 2: Structured polymer and metallic circuit path

In order that also after the embossing step the circuit paths act as this, during the process no interruptions of the paths may appear. For this purpose tests with different material thicknesses are carried out. The results shown in Fig. 3 correspond to a mould insert with a height of 25 μm and a PC substrate. Like one can see, a material thickness in the range of the height of the structure minimizes the number of interrupted circuit paths.

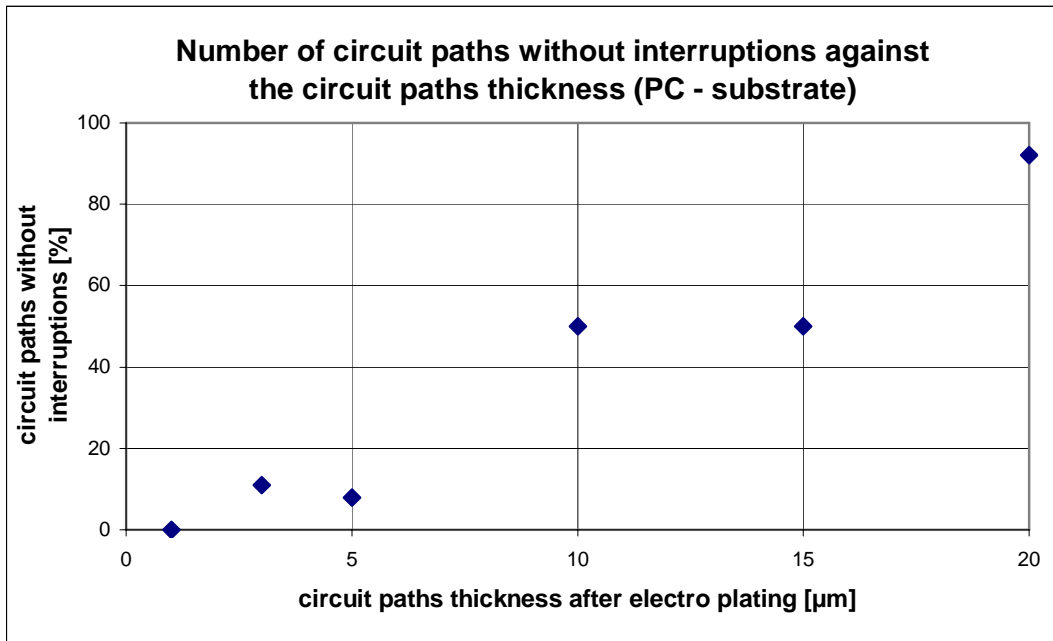


Figure 3: Number of circuit paths without interruptions after the structuring by hot embossing against circuit path thickness

3 Outstanding researches

To finish the project successfully it is still necessary to pass the following researches.

At first it's necessary to repeat the hot embossing tests with different polymers and different heights of the structured tool. Additionally the whole chip has to be capped with a second substrate so that it can be used as a miniaturized laboratory.

Fabrication of Nanofluidic Cells for Near Edge X-ray Absorption Fine Structure (NEXAFS) Analyses of Liquid Water

Christian Weniger^{1,3}, Philippe Wernet², Arne Schleunitz^{1,*}, Daniel Schondelmaier¹

¹BESSY GmbH - Application Center for Microengineering, Albert-Einstein-Str.15, 12489 Berlin, Germany

²BESSY GmbH - Experimental Group, Albert-Einstein-Str.15, 12489 Berlin, Germany

³Technisch-Fachhochschule-Berlin, Luxemburger Str. 10, 13353 Berlin, Germany

*Corresponding author: Arne Schleunitz, Phone: +49 30 6392-5615, Fax: +49 30 6392-4682,

E-mail: schleunitz@bessy.de

Introduction

Liquid water is probably the most important but also the least understood substance on earth. Structure and anomalous properties of water are both determined by a fluctuating network of hydrogen bonds connecting the constantly mobile molecules. It turns out that established experimental techniques for the investigation of the H-bonding network in water (neutron and x-ray diffraction and infra-red, IR, absorption and Raman spectroscopy) do not allow for unique assignments of local H-bonding configurations [1, 2]. X-ray absorption spectroscopy at the O K-edge and specifically the investigation of the near edge structure (NEXAFS) can yield unique information about the local H-bonding environment of the molecules in liquid water [3].

Transmission mode proved to be a reliable way of measuring the O K-edge absorption spectrum [4]. Due to the short penetration depth of soft x-rays in water, thin water films with thicknesses in the submicron range are needed for this. Furthermore, the water sample has to be held in vacuum in a closed holder due to the high vapor pressure of the liquid. Following the pioneering experiment by Yang and Kirz [5] our aim is to develop nanofluidic cells for NEXAFS investigations of liquid water.

Fabrication

The x-ray path length within the liquid should be limited to a few hundred nanometers to allow sufficiently high output signals for appropriate data interpretation. To create an ultrathin liquid film using nanoscaled geometries and provide it for vacuum measurements is technically very challenging, because the protective membranes isolating the liquid from the vacuum have to be both mechanically robust and transparent to x-rays. Yang et al. were the first realizing extended x-ray-absorption fine structure of liquid water using silicon nitride (Si_3N_4) membranes [5]. However, the achieved thickness of the water film defined by polymeric spacers made of polymethylmethacrylate (PMMA) did not go below one micrometer.

At the application center for microengineering at BESSY we are currently working on the fabrication of a nanofluidic cell which uses metallic spacers between to Si_3N_4 membranes to form a one-dimensional nanofluidic channel for liquid films which are only a few hundred nanometers thick. We use microstructuring techniques - which were developed initially by the semiconductor industry for the accurate patterning in the micro- and nanometer range – such as photolithography, chemical vapor deposition (CVD) and etch procedures. The assembled fluidic cell, which is sketched in figure 1, will be utilized for x-ray transmission measurements at BESSY for the investigation of water.

The fabrication starts with a double-side polished silicon substrate (Si-wafer) which is coated on both sides with a 100nm thick Si_3N_4 film that will serve on the one hand as the membrane and on the other hand as a mask material for a subsequent etching step. The entire process flow is illustrated in figure 2: The back side of the Si-wafer is lithographically structured by the deposition of a photosensitive resist, the exposure with UV-light through a mask and a development step that transfers the mask pattern into the resist. A subsequent dryetch step opens the Si_3N_4 membranes selectively (3-4). Another lithography

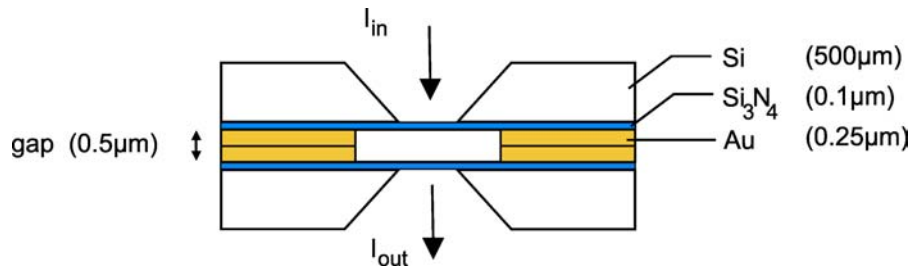


Figure 1: Schematic of the assembled fluidic cell which consists of two cell parts. Metallic spacer made of Au define an one dimensional nanofluidic channel with a net height of $500nm$. The liquid within the channel is isolated from the vacuum by two $100nm$ thick Si_3N_4 membranes. This way transmission measurements can be performed using the nanofluidic cell.

step is applied to the front side of the substrate (5). A $250nm$ thick Au layer is deposited by sputtering technique (6) which is then partly removed using a lift-off step (7). The remaining parts of the layer form the metallic spacers that in turn define the fluid height in the assembled cell and the nanofluidic channel (8). The silicon substrate is anisotropically etched from the back side through the opened nitride with heated Potassium Hydroxide (KOH). That way we generate $1mm^2$ large Si_3N_4 windows (9) of which one is shown in the picture in figure 3 that was taken with an optical microscope. To finish the fabrication and to seal the nanofluidic channel we mount two of the fabricated cell parts using a proper adhesive technology (10). However, first test runs showed that sporadic leakage and contamination of the liquid may occur. A better technique to merge the cell parts more reliably using a mechanical mount is under development.

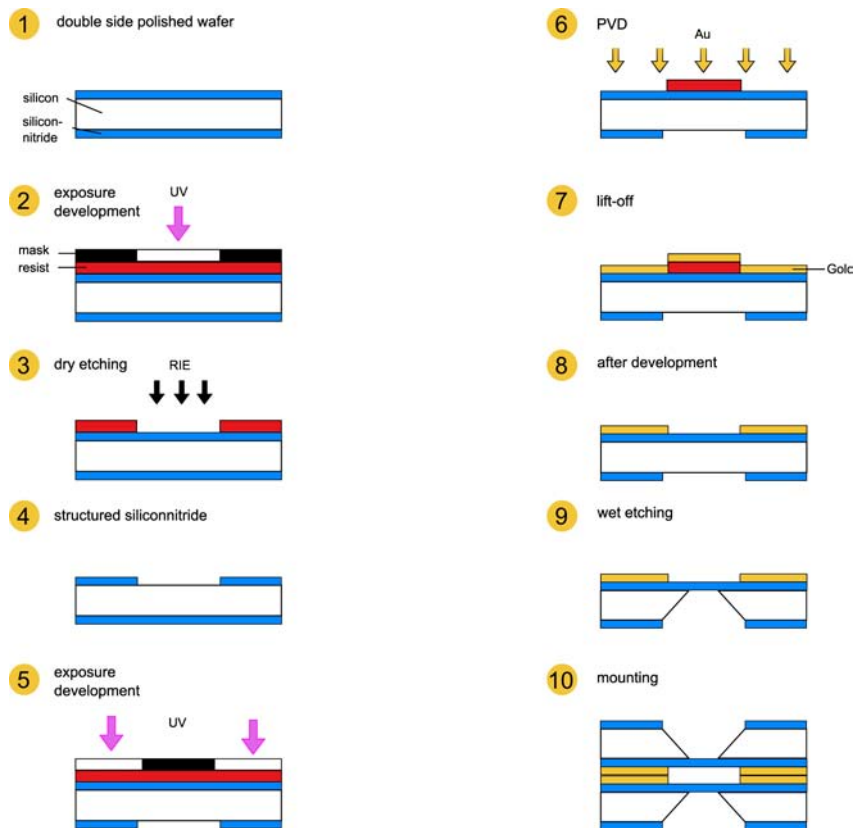


Figure 2: Process flow of the cell fabrication using different lithography, deposition and etch steps.

Preliminary Results

First x-ray transmission measurements at BESSY with the uncovered Si_3N_4 membrane revealed that no unfavorable contaminations remain after completing the fabrication procedure. The recorded transmission data were compared with several membrane thicknesses given by the literature and a good agreement was observed.

First rough characterizations of the assembled fluidic cell were done by FTIR measurements. The spectrum shown in figure 4 proves successful filling of the one dimensional nanofluidic channel with liquid water. The prominent O-H stretching band at around 3500cm^{-1} indicates a water film thickness in the sub-micron range. Furthermore, no contamination of the liquid was observed.

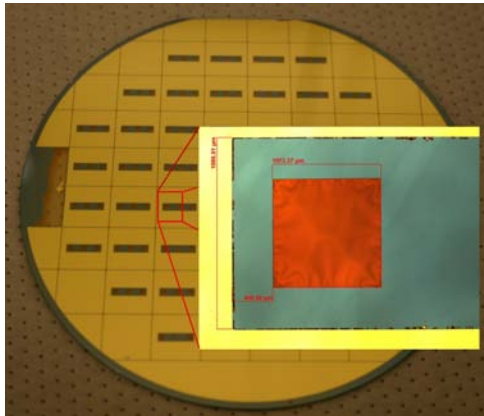


Figure 3: Front side of a processed wafer showing several cell parts. The outlines of the fluidic channel defined by the Au spacer can be seen as the horizontal bars. The detailed photo shows the uncovered Si_3N_4 membrane within the channel structure.

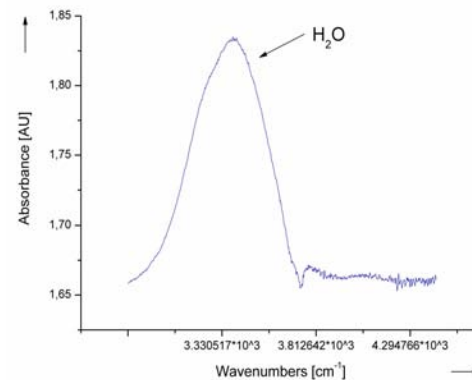


Figure 4: IR absorption spectrum of the assembled fluidic cell with liquid water in the region of the O-H stretch vibration.

References

- [1] SOPER, A. K.: The radial distribution functions of water and ice from 220 to 673 K and at pressures up to 400 MPa. In: *Chemical Physics* Vol. 258 (2000), p. 121–137
- [2] STENGER, J.; et al.: Ultrafast Vibrational Dephasing of Liquid Water. In: *Physical Review Letters* Vol. 87 (2001), p. 027401
- [3] WERNET, Ph.; et al.: The Structure of the First Coordination Shell in Liquid Water. In: *Science* Vol. 304 (2004), p. 995 – 999
- [4] NÄSLUND, L.A.; et al.: X-ray Absorption Spectroscopy Measurements of Liquid Water. In: *J. Phys. Chem. B* Vol. 109 (2005), p. 13835–13839
- [5] YANG, B. X.; KIRZ, J.: Extended x-ray-absorption fine structure of liquid water. In: *Physical Review B* Vol. 36 (1987), p. 1361–1364

Investigation of photonic band gap materials for visible wavelengths

J. Kouba, M. Kubalski, W. Eberhardt, B. Loechel

BESSY GmbH, Application Centre for Microengineering, Albert Einstein Str. 15, 12489 Berlin, Germany

Using an experimental setup based on transmission measurements utilizing white light broad band source, photonic band gaps in visible range could be successfully identified by at BESSY AZM fabricated 2-dimensional photonic crystals slabs based on LPCVD silicon nitride. Comparing the transmission measurements with theoretically calculated spectres, a good agreement could be found. By varying the geometry of the photonic crystals, the position of the band gap can span a large part of the visible spectra.

Photonic crystals are electromagnetic materials with spatially periodical dielectric properties. First proposed by Yablonovitch [1] and John [2], the spatial periodicity of photonic crystals leads to Bloch-Floquet theorem and to the existence of photonic bands, analogous to electron bands in crystalline solids. Further, for a certain spatial dielectric functions, the dispersion relation reveals photonic band gaps, frequency regions, where light propagation cannot take place. Photonic crystals are receiving lot of interest since they enable strong confinement and localization of light on sub wavelength, which is why they are believed to become the core components of future novel electro optical systems. Besides passive components such as waveguides, splitters or wavelength filters, active photonic devices such as single photon sources [3] or laser resonators [4] were presented recently. Many activities exist of the field of photonic crystals for infra red wavelengths. Comparatively less research work has been performed on the field of photonic crystals for visible wavelengths, where photonic crystals also have large potential as both passive and active photonic components.

Using an own, at BESSY AZM developed fabrication process described elsewhere [5], photonic crystal slabs based on LPCVD stoichiometric silicon nitride could be successfully prepared for the measurements. Figure 1 shows a characteristic example of a fabricated photonic crystal slab.

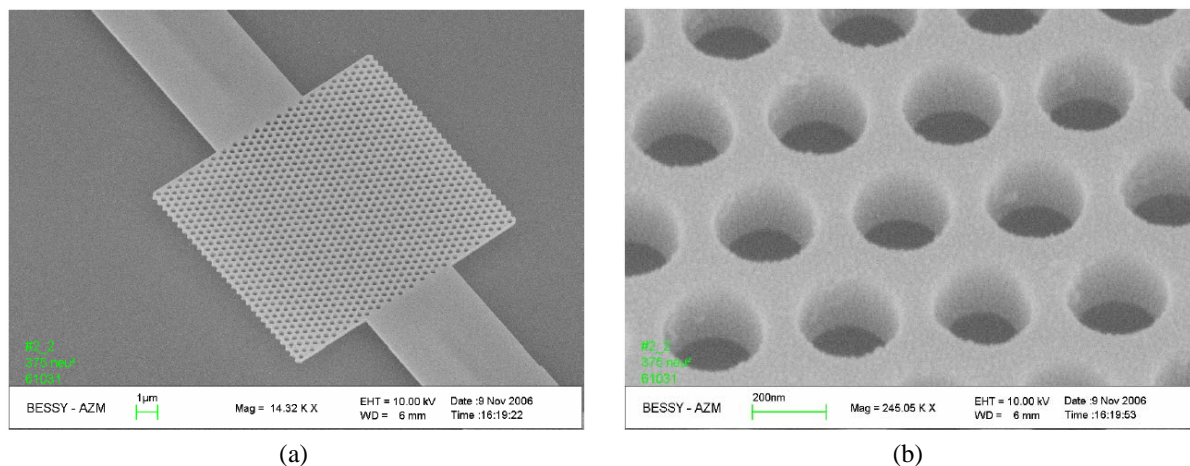


Figure 1 – Fabricated photonic crystal slab (a) with incoming and outgoing waveguides for the in-coupling and out-coupling of the light; close-up view (b) of the silicon nitride membrane illustrating its high quality

In order to realize the band gap in the visible wavelength range, the periodicity of the photonic crystal must be in the range of the half of the desired band gap wavelength, which illustrates the technological challenge of the fabrication task.

Using an FDTD algorithm, a simplified, 2-dimensional model consisting of 9 periods of holes in silicon nitride was investigated in order to predict the occurrence of photonic band gaps [6]. The results of the simulation are presented in Figure 2.

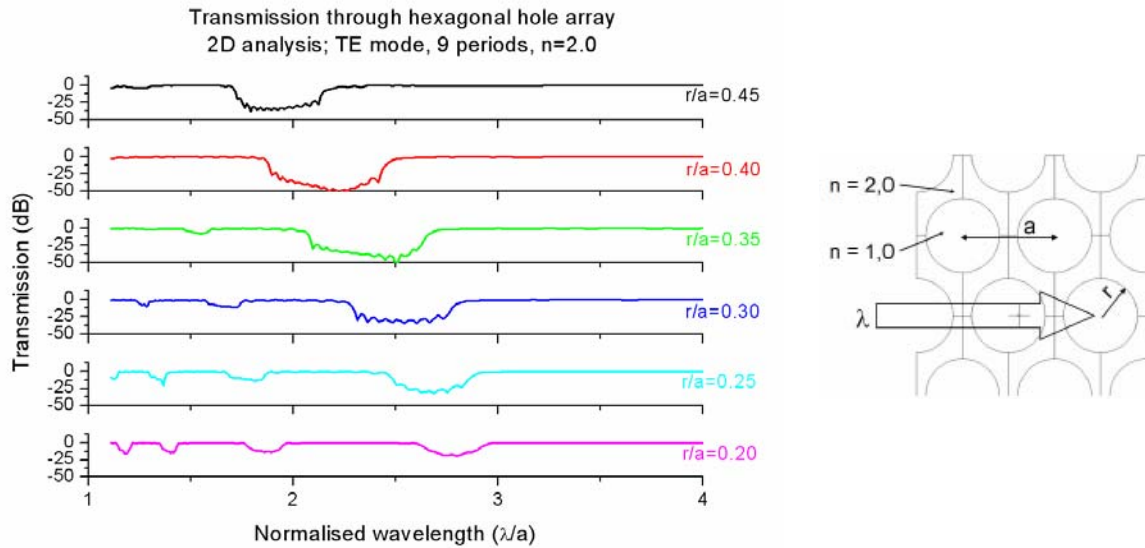


Figure 2 – Theoretical band gap calculation using a model described in [6]; the position and the shape of the band gap depends strongly on the geometrical parameters (a and r) of the photonic crystal and can thus be adjusted by varying the geometry of the photonic crystal

Using an experimental setup described elsewhere [6], the transmission spectra of the fabricated photonic crystals could be experimentally measured. Figure 3 shows two examples of successfully measured photonic band gaps.

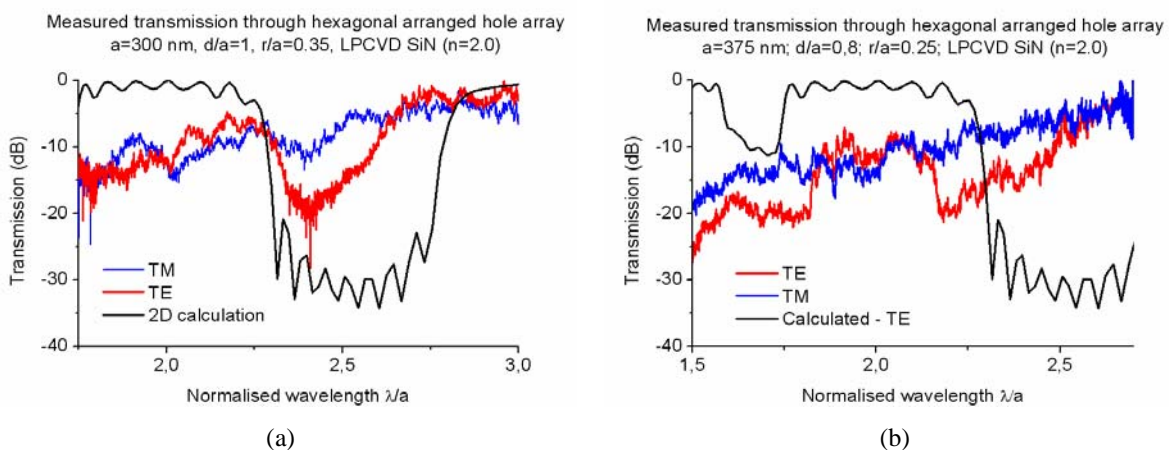


Figure 3 – Experimentally measured photonic band gaps between 650 – 750 nm; in both cases, photonic band gap opens for TE polarised light; in the left case (a), the position of the band gap matches perfectly the theoretical prediction; on the right side (b), two band gaps open as predicted

As can be seen in Figure 3, the position and the nature of the measured band gaps matches very well the theoretical prediction. The perfect match, however, can not be reached since the theoretical prediction uses strongly simplified model, not taking into account the 3-dimensional nature of the investigated photonic crystal. By this way, scattering of light out of plane is not taken into account. This scattering is responsible for the high losses as observed in the measurements (see Figure 3).

By varying the geometric parameters, the band gap can be shifted towards the desired wavelength as can be seen in Figure 4.

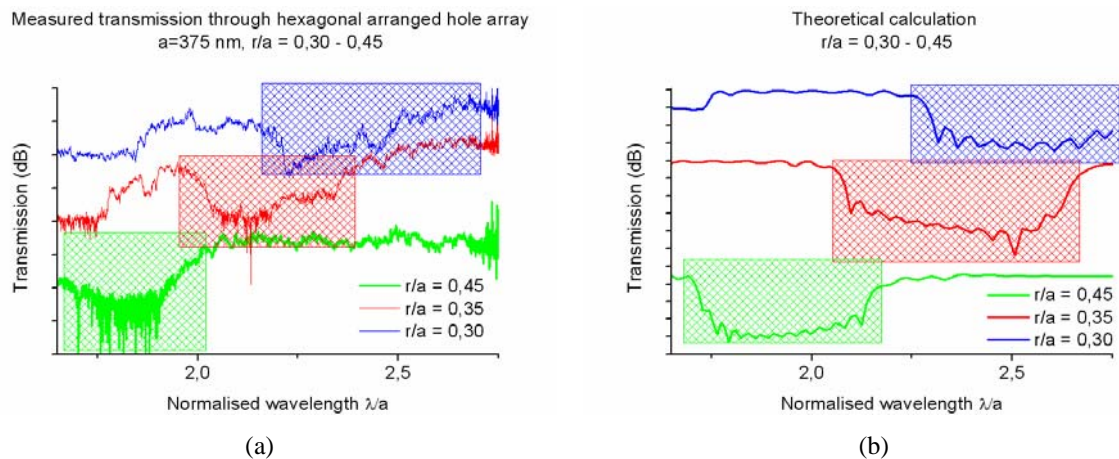


Figure 4 – By increasing the r/a ratio, the band gap can be shifted towards shorter wavelength (a) in accordance with the theoretical prediction (b)

As illustrated in Figure 4, at a fixed period of the photonic crystal of $a=375$ nm, wavelength range of approximately 650 – 1000 nm can be spawned by only varying the r/a ratio.

Concluding, photonic band materials for visible range could be successfully fabricated and experimentally characterised at BESSY AZM. The measured transmission characteristics match well the theoretical predictions. In the ongoing work, 3-dimensional simulations will be performed in order to achieve an even better match between the theory and the experiment. Also, some basic applications of photonic crystal shall be realized and experimentally characterised. Using the gathered experimental and theoretical knowledge, an optical sub-wavelength resonator should be build using photonic crystals.

The authors would like to acknowledge the financial support of the EU funding program ProFIT (Program for Support of Research, Innovations and Technology), Grant Number 10133408.

1. Yablonovitch, E., *Inhibited Spontaneous Emission in Solid-State Physics and Electronics*. 1987.
2. John, S., *Strong localization of photons in certain disordered dielectric superlattices*. Physical Review Letters, 1987. **58**(20): p. 2486–2489.
3. Painter, O., et al., *Two-Dimensional Photonic Band-Gap Defect Mode Laser*, in *Science*. 1999. p. 1819-1821.
4. Laurent, S., et al., *Indistinguishable single photons from a single-quantum dot in a two-dimensional photonic crystal cavity*, in *Applied Physics Letters*. 2005, AIP. p. 163107-3.
5. Kouba, J., W. Eberhardt, and B. Loechel. *Wavelength filter for visible wavelengths based on photonic crystal*. in *Photonics Europe*. 2006. Strasbourgh: SPIE.
6. Kouba, J., *Fabrication and Investigation of Silicon Nitride Photonic Crystals in Visible Wavelength Range*, in *BESSY GmbH*. to be published in 2007, Technische Universität Berlin: Berlin.

Lithographically fabricated ultra-hydrophobic surfaces for bio chip applications

O. Mertsch*, A. D. Walter, D. Schondelmaier and B. Loechel

BESSY GmbH, Application Center for Microtechniques (AZM), Albert- Einstein- Strasse 15, 12489 Berlin, Germany

*Corresponding author: Olaf Mertsch, Phone: +49 30 6392-4600, Fax: +49 30 6392-4682,
E-mail: mertsch@bessy.de

ABSTRACT

A new and efficient way for fabricating ultra-hydrophobic and ultra-porous surfaces for bio chip and MEMS applications and for the production of nano-membranes is presented. Basis of this method is a back-side UV-exposure with some substantial changes in the exposure conditions. Plant-like structures of resist have been generated with wetting contact angles of about 125° . Additionally added layers after lithographic patterning like thin metal oxide and self assembled mono layers (SAM) will increase the contact angle (ca) of more than 165° . Due to the lithographic fabrication method such surfaces can easily be integrated into micro fluidic channels via multi step exposures.

1 INTRODUCTION

Since the middle of last century the wettability of surfaces has become of great interest to many different research fields and technical applications. First of all a very special surface morphology which leads to the so called "Lotus Effect" is of great importance for self cleaning products like paintings, glass panels for applications in cars and buildings and furthermore for biological and medical systems [1]. In such special cases ultra-hydrophobic surfaces with contact angles of more than 150° allow very interesting new solutions for MEMS and μ -TAS applications.

The big advantage of this effect is the generation of micro drops and therewith the minimization of the probe volume and the surface contact between the fluid and the solid walls. Hence, nonspecific adsorption mainly in biotechnology applications can be reduced drastically [2]. Because of the increasing surface to volume ratio, forces based on molecule interactions like hydrophilic bonding, van der Waals forces and capillary forces became the dominating parameters for drop volumes below $10 \mu\text{L}$ [3].

The most important thing for the whole drop fluidic field is the availability of ultra-hydrophobic surfaces on which the fluidic samples form drops. That means contact angles above 150° and very low contact angle hysteresis are necessary for sufficient drop transportation [8]. Such surfaces can be fabricated by different technical approaches [6-8] but there are always problems because of sticking effects on different surfaces morphologies. Therefore, not every surface is capable for drop motion experiments.

This paper presents a new way for creating ultra-hydrophobic surfaces with the demanded properties by a very simple back-side lithographic exposure [see also 9,10]. Big advantage of this technique is the creation of nano-porous structures and side walls within one step so that hydrophobic surfaces can be produced by the resist only. Furthermore, different layer techniques are presented which cause even more ultra-hydrophobic surfaces with very low hysteresis.

2 RESULTS

The results from the back-side exposures are shown in Figure 2 and 3. Caused by the back-side exposure conditions and a transparent substrate which mainly works as a several hundred micrometer thick spacer between the mask and the resist (proximity exposure) the loss of structure accuracy is very high. The proximity effect is normally not appreciated in lithographic applications but here the key to ultra-hydrophobic structures

2.1 Structured SU 8

Figure 2 shows a variation of the exposure dose from 50 (picture 1) to 300 (picture 6) mJ/cm^2 through a mask with square structures of $12 \mu\text{m}$ width and a distance of $40 \mu\text{m}$ between the patterns. As one can see, the structures broadened when the dose is increased until they finally grow together. Result of this is an increasing contact area between the drop and SU 8, while the contact to the plating base is decreased. Simultaneously the contact angle

increases to values of nearly 125°. Figure 3 shows a pattern of 12 µm square structures with different distances ranging from 12 to 120 µm all exposed with a constant dose of 200 mJ/cm². The contact angles measured on such surfaces without an additional coating are given in table 1.

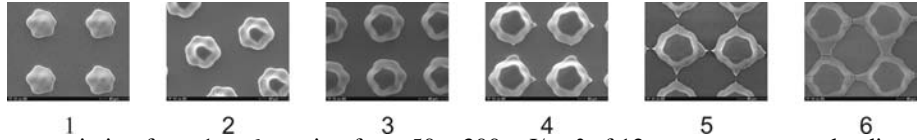


Figure 2: Dose variation from 1 to 6 ranging from 50 – 300 mJ/cm² of 12 µm structures and a distance of 40 µm.

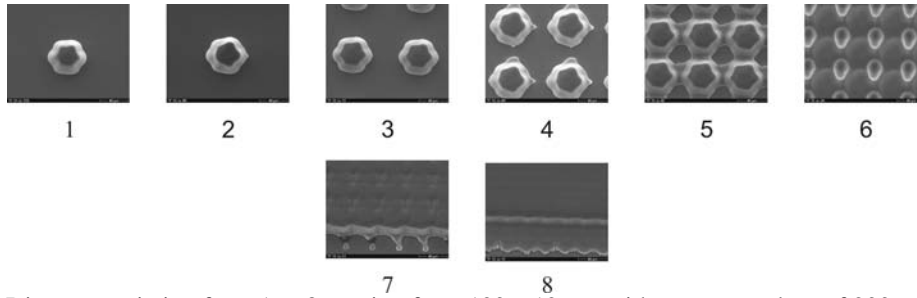


Figure 3: Distance variation from 1 to 8 ranging from 120 – 12 µm with a constant dose of 200 mJ/cm² and a structure width of 12 µm.

Assuming from the large hysteresis of all structures, the Wenzel-state is preferred by wetting those surfaces. There is an increasing contact angle for the structures when the spaces between them are decreasing. The peak of the non wetting behavior is reached with a structure distance of 60 µm (see figure 3.4 and 2.4). For shorter distances the wettability of the surface is mainly influenced by the Au (contact angle around 70°) and for bigger distances the contact angle is determined by the characteristics of the SU 8. But if the structures network becomes to dense the resist forms smooth planes like shown in figure 3.7 and 3.8 and the contact angle decreased to values of plane SU 8. To increase the non-wetting behavior, the SU 8 surfaces can easily be coated with thin metal films which serve as adhesion layer for different self assembled mono layers and cause further surface tension reduction.

Table 1: Overview of contact angles (ca) on structured SU 8 surfaces. The standard deviation of all contact angles (ca) is less than ± 3°.

structure width [µm]	structure distance [µm]	ca [°]	hys. [°]
12	120	88	64
12	96	91	77
12	72	86	70
12	60	125	100
12	42	103	86
12	30	86	47
12	21	83	41
12	12	85	39
SU 8 with flash exposure		88	44

Table 2: Overview of contact angles on structured SU 8 surfaces covered with two different metal thin films and self assembled mono layers. The standard deviation of all contact angles (ca) is less than ± 3°.

structure width [µm]	structure distance [µm]	ca [°]	hys. [°]	ca [°]	hys. [°]
		Au-ODT		TiO-Dyna	
12	120	122	29	165	11
12	96	162	17	163	16
12	72	163	29	162	16
12	60	162	33	162	19
12	42	146	45	163	26
12	30	123	22	160	35
12	21	113	12	159	60
12	12	114	13	161	47
Au-ODT		112	13		
TiO-DYNASYLAN®				150	60

2.2 Coating with SAM

In this part we used Octadecanethiol (ODT) together with a 50 nm Au-layer and 3,3,4,4,5,5,6,6,7,7,8,8-Tridecafluorooctyltriethoxysilan (DYNASYLAN®) together with an 800 nm TiO-layer. Structures shown in figure 3 were coated with these SAM-metal-films and the contact angle results are shown in table 2.

The wetting behavior of the SU 8 structures can be increased dramatically by both coating techniques, whereas the changing caused by the TiO film is more effective. The reason for this is, that DYNASYLAN® on a oxidized

titanium plane surfaces like on silicon or glass ($R_a \sim 90$ nm) is already ultra-hydrophobic with a contact angle around 150° . The following macro roughness produced by the SU 8 structures has not very big influence on the contact angle itself but the hysteresis can be reduced dramatically to values below 15° . These results explained that the drops on such surfaces are in the fakir-state and the penetration of the space between them is limited by the very porous side walls (figure 4). The same could be observed for the Au-ODT surfaces with hysteresis around 30° . Although these are very promising results for droplet transportation experiments, the hysteresis is still to high for that.

2.3 Reduced exposure dose

In this section we used the same mask as before but reduced the exposure dose below 50 mJ/cm². That means, we are working very close to the threshold dose for SU 8. Below these values one can hardly see a cross linking effect at all. For practical reasons the resist thickness was increased above the finally expected thickness of finished structures. With that exposure condition we can make sure that the propagated light will be totally absorbed inside the resist layer. The results of these exposure conditions are shown in figure 5 as example for a structured nano porous membrane.

The SU 8 structures can be modified in a way that the whole structures become very porous and show a very strong not wetting behavior. For surfaces like this coated with TiO-DYNASYLAN® thin films, we could achieve contact angles of $165^\circ \pm 2^\circ$ with a hysteresis of only 5° . Furthermore, with decreasing structure width on the mask one can achieve nearly flat surfaces with nano porous properties (figure 5). They easily can be integrated into fluidic structures by multi step exposures.

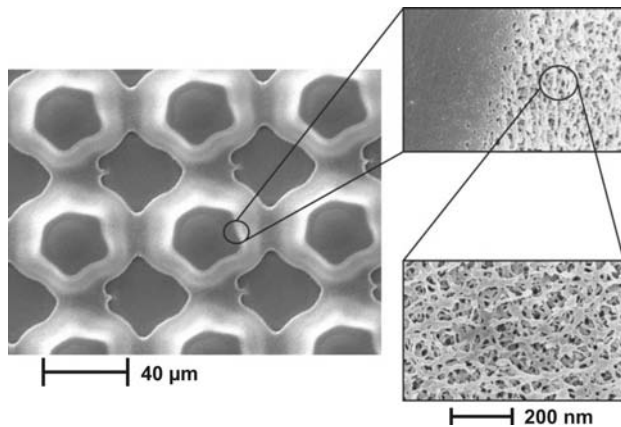


Figure 4: The detail view of one of the plant-like structures with porous side walls in the range of 200 nm.

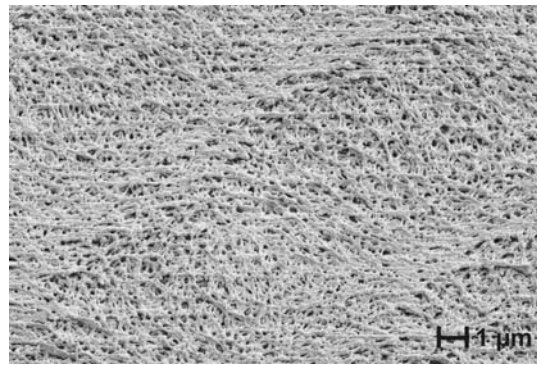


Figure 5: A nearly flat surface made by back-side exposure with nano holes below 1 µm.

3 OUTLOOK

The nano porous structures are going to be used in EWOD (electro wetting on dielectric) processes as dielectricum and as ultra-hydrophobic surfaces for providing the drop form of the fluids. Furthermore, there are projects in preparation for using the nano porous flat surfaces as nano membranes for gassing and mass transfer procedures in microfluidics.

REFERENCES

- [1] Cerman, Z., Stosch, A.K., Barthlott, W., *Biol. Unserer Zeit*, **2004**, 34, 290-296
- [2] Yoon, J.-Y., Garrell, R.L., *Anal. Chem.*, **2003**, 75, 5097-5102
- [3] Squires, T.M., Quake, S.R., *Reviews of modern physics*, **2005**, 77, 977-1026
- [4] Brochard, F., *Langmuir*, **1989**, 5, 432-438
- [5] Subramanian, R.S., Moumen, N., McLaughlin, J.B., *Langmuir*, **2005**, 21, 11844-11849
- [6] Chaudhury, M.K., Whitesides, G.M., *Science*, **1992**, 256, 1539-1541
- [7] Moumen, N., Subramanian, R.S., McLaughlin, J.B., *Langmuir*, **2006**, 22, 2682-2690
- [8] Petrie, R.J., Bailey, T., Gorman, C.B., Genzer, J., *Langmuir*, **2004**, 20, 9893-9896
- [9] Lü, C., Yin, X., Wang, M., *Sensors and Actuators A*, **2006**
- [10] Yoon, Y.-K., Park, J.-H., Allen, M.G., *Journal of Micro-Electromechanical Systems*, **2006**, 15, 1121-1130
- [11] Wenzel, R.N., *Industrial and Engineering Chemistry*, **1936**, 28, 988-994
- [12] Cassie, A.B.D., Baxter, S., *Trans. Faraday Soc.*, **1944**, 40, 546-551

Deep X-ray Lithography of SU-8 Photoresist: Influence of Process Parameters and Conditions on Microstructure Quality

Martin Bednarzik and Bernd Löchel

Application Center for Microengineering/Anwenderzentrum für Mikrotechnik

In collaboration with Microresist Technology GmbH in Berlin, the Center for Advanced Microstructures and Devices in Baton Rouge and the Micro Chem Corp. in Newton, the Application Center for Microengineering (AZM) started a test row for a systematic investigation of the influence of process parameters on the quality of micro structures made of SU-8. For the investigations Micro Chem Corp. supplied two types of SU-8 photoresist material with different content of PAG (Photo acid generator). Silicon wafers with a standard plating base of Titanium and Gold were used to carry out experiments at AZM. All exposures were done at the dipole beamline DIP06.1a. The wafers were spincoated and prebaked at MRT. For the investigations two levels of Residual Solvent Content were considered, which is easy to realize by a prebake on a programmable hotplate. The resist thickness was set to approximately 1000 μm . All the parameters and levels (factors) are shown in Table 1 below. To determine the influence of all factors on the micro structure quality respectively responses namely sidewall profile, top scum/skin, residue and collapse. DoE was used to analyze the results (Design of Experiments). The multiple correlation analysis was done at the Micro Chem Corp. using JMP software.

Trial/Wafer	PAG (%)	Solvent Cont. (%)	PEB Temp. (°C)	PEB Time (min)
1	1.25	3	60	60
2	5.0	3	60	20
3	1.25	6	60	20
4	5.0	6	60	60
5	1.25	3	90	20
6	5.0	3	90	60
7	1.25	6	90	60
8	5.0	6	90	20

Table 1: Number and conditions of factors for modelling

Experimental

For the Design of Experiments a 2^{K-1} Design with 8 trials was preferred. Different exposure doses on each wafer were applied. Figure 1 shows an X-ray mask supplied from the CAMD. The mask is divided into six equal fields. For the experiments six different doses were applied with two different top to bottom dose ratios, which lead to 48 experimental conditions. After exposure at the dipole beamline the resist has to be heated up by a so called Post Exposure Bake (PEB) on a hotplate. PEB must be performed to crosslink and to make the SU-8 stable. The mechanical properties of a fully crosslinked SU-8 photoresist are similar to those of epoxies.

In a last process step, the development, which was kept constant for all 8 wafers, unexposed SU-8 was washed away from the substrate. After Development the samples were rinsed with IPA and

dry blown with Nitrogen. For the investigations in the SEM/LEO all 8 wafers had to be covered in a sputtering system with a very thin gold layer. Afterwards each wafer was diced into 6 pieces according the applied dose and top to bottom ratio.

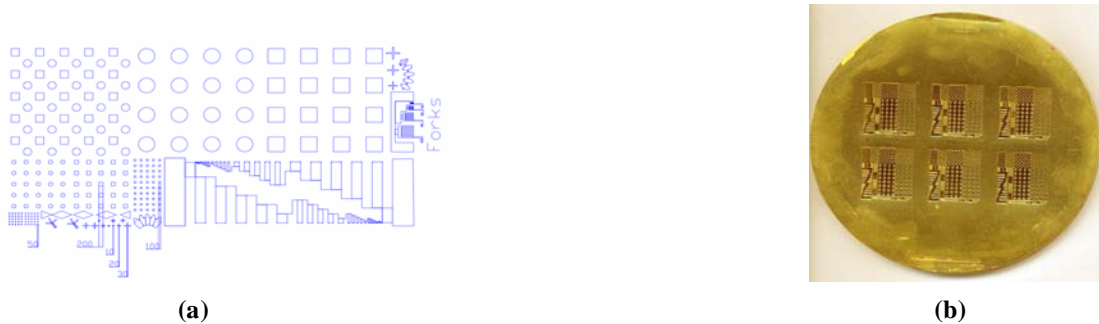


Figure 1: Test pattern forks and post used for investigations (a) and X-ray masks used for experiments (b)

Rating

With a rating scheme the quality of the structures was determined. Each exposed field from six per trial was investigated by SEM/LEO (qualitative rating). The scheme with the rating criteria is described in Table 2. Sidewall profile, top scum/skin and residue were rated by 1, 2, 3, 4 and 5. Table 2 below shows the best (1) and the worst case (5). For the determination of the quality of SU-8 resist structures much more pictures were taken into consideration.

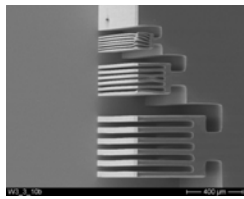
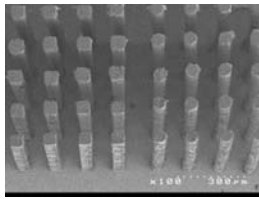
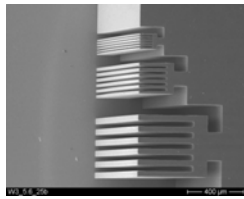
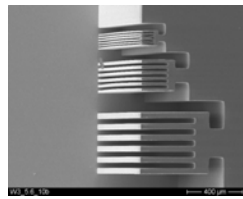
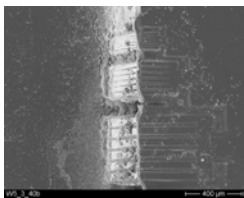
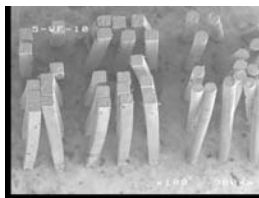
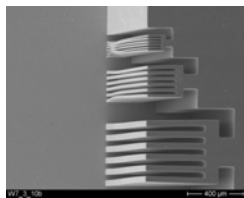
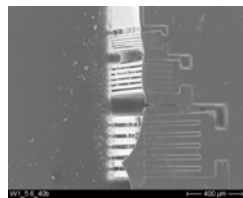
Rating	Residue	Structural collapse	Sidewall profile	Top-scum (skin)
1 - best				
5 - worst				

Table 2: SEM pictures of rated SU-8 micro structures

Conclusion

DOE was used to optimize PAG concentration, solvent content, PEB time and PEB temperature, bottom dose, and dose ratio. It is clear that the independent factor, solvent content, has a major influence on all four responses (top scum, residue, structure collapse and sidewall profile). No other factor had such an across-the-board affect on all responses. Top scum and residue fit polynomial models easily with correlation coefficients of, respectively 0.85 and 0.95. Both top

scum and residue were controlled not only by the independent factors, but also by more than one interaction. Most notably, the interaction between solvent content and bottom dose were significant in predicting top scum and residue. Table 3 below shows a brief summary of each independent factor and several interactions. A single * indicates a 90% confidence interval for significance, two ** indicates 95%, three *** indicates 99% and NS indicates not significant. Although the predictive model correlation for structure collapse and sidewall profile were low, two independent variables were found to be highly (99%) significant; namely solvent content and PEB temp. As shown in Figure 2 below, a high solvent content (of 6%) and a low PEB temperature (60°C) should produce the least structure collapse and the best sidewall profile.

	Top Scum	Residue	Structure Collapse	Sidewall Profile
Correlation Coefficient	0.85	0.95	0.5	0.69
PAG	**	*	*	NS
Solvent Content	***	***	***	***
PEB Temp	***	**	***	***
PEB Time	***	**	NS	NS
Bottom Dose	***	***	NS	**
Solvent Content x Bottom dose	***	***	*	NS
Solvent Content x PEB Temp	NS	**	**	**
PAG x Solvent Content	***	*	NS	**

Table 3: Summary for the Design of Experiments of ~1000 µm thick SU-8 Photoresist

Not all possible interactions were tested because the number of terms in the polynomial equation were limited by the number of trials (n) to n-1. For this reason, only interactions whose main effects showed significance were only included in the model. The predicted optimum process parameters can be determined with the polynomial model from multiple correlation analysis: PAG = 5 %, Solvent Content = 6 %, PEB Temp. = 60 °C, PEB Time = 40 min and Bottom Dose = 12 J/cm³ (see Table 4).

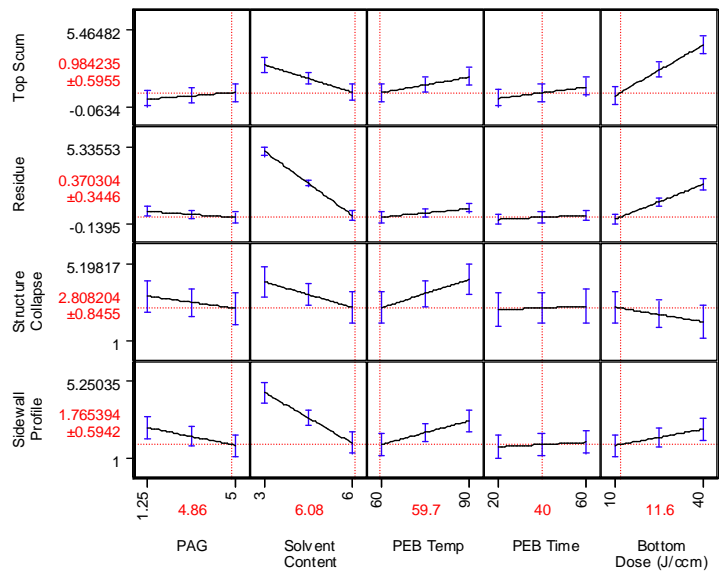


Table 4: Influence of all factors on responses for a 1000 µm SU-8 process using X-ray lithography

The authors would like to acknowledge the financial support of BMBF under contract number 16SV1747.

Fabrication of Polymeric Nanostructures using Nanoimprint Technique

Arne Schleunitz*, Josef Kouba, Daniel Schondelmaier, Bernd Loechel

BESSY GmbH, Application Center for Microengineering, Albert-Einstein-Str. 15, 12489 Berlin

*Corresponding author: Arne Schleunitz, Phone +49-30-6392-5615, Fax +49-30-6392-4682,
e-mail schleunitz@bessy.de

Introduction

Nanotechnology and the underlying nanosciences enables scientists and engineers to structure and manipulate matter at the molecular level. New “nanoengineered” products and materials will have an impact on a variety of industrial markets such as telecommunications, energy technology, biotechnology, etc. However, the economical success of nanotechnology and its ability to revolutionize commercial markets, as it did in science and research areas in the past decades, strongly depends on new fabrication techniques that are easily accessible for the industrial environment allowing to built nanostructures and nanodevices without demanding technical efforts. Thus, many international research activities are focused on alternative techniques to cost-intensive and limited-access fabrication methods with nanometer resolution.

Nanoimprint Technique

One approach to fabricate accurate nanostructures in the nanometer range is an imprinting technology which is derived from the industrial established hot embossing. It basically requires three components: a rigid stamp with suitable (nano-)feature sizes, an “imprintable” material and the equipment for pressing the stamp against the material with adequate control of the temperature, pressure and parallelism.

Chou et al. published in 1995 for the first time the possibility to transfer a nanoscaled structure from a stamp into a polymeric substrate using hot embossing [1]. He presented the “nanoimprint” technology, which is illustrated in figure 1, as a relatively straightforward method for the pattern transfer in the nanometer range. A stamp made of silicon (Si), silicon dioxide (SiO₂) or metal is imprinted under pressure into a polymer or resist which is heated up well above its glass transition temperature (T_g) so that the stamp structures can penetrate into the viscous polymer. The stamp remains for a certain amount of time in the polymer to ensure proper cavity filing and to improve the imprint results. Next, the system is actively cooled below T_g . During the cooling phase the stamp remains within the polymer to compensate deformation caused by shrinking of the material. After reaching a temperature slightly under T_g , the stamp is gently removed and finally the negative stamp pattern is transferred to the polymer. Depending on the application, one can remove the residual polymer in the compressed areas with an additional anisotropic etch step. That enables the subsequent pattern transfer into the substrate with another etch step that is not shown in figure 1.

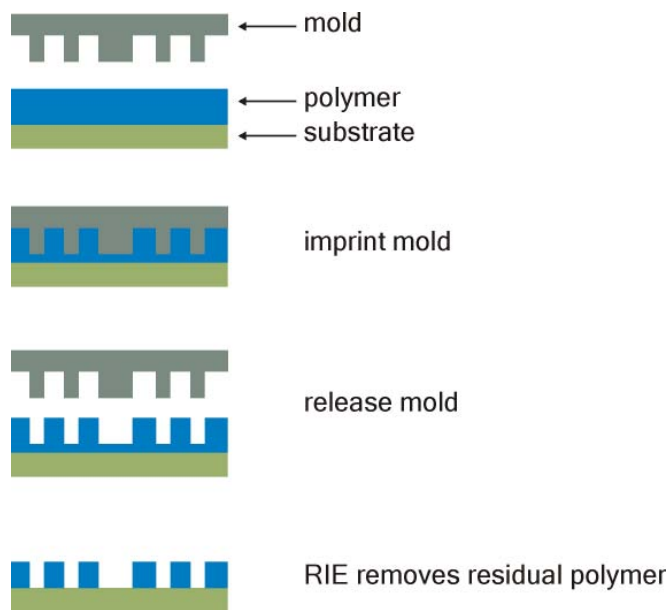


Figure 1: Schematic of the nanoimprint lithography process: A rigid mold with feature sizes in the nanometer range is pressed into a heated polymeric material. The mold is removed after actively cooling the system below the glass transition temperature of the polymer. An anisotropic etch step can remove the residual polymer in the compressed areas, if necessary.

The nanoimprint technique was developed as an alternative lithography method for nanopatterning of resists in the semiconductor industry below the physical limitations of resolution which are associated with optically

driven systems. However, the nanoimprint lithography (NIL) was not able to accomplish the initial expectations as a so called Next-Generation Lithography (NGL) and plays only a minor role in this area so far. Nevertheless, the nanoimprint has a high potential for a cost-effective fabrication technology of less demanding and inexpensive permanent nanostructures in polymeric micro-nano-systems. It allows patterning at different scales (from micron down to tens of nanometers) making it suitable for a number of application in optics, sensors and microfluidics [2].

Imprinted Polymeric Nanostructures

The application center for microengineering at BESSY recently established an entire process line that is related to the nanoimprint technique. This includes the fabrication of suitable molds and the imprint technique for polymeric nanostructures. We developed an adequate process to fabricate nanostructured stamps made of silicon using e-beam lithography and dry etch techniques. Furthermore, we are currently working on a fabrication technique for metallic molds [3]. Figure 2 shows SEM micrographs of exemplary nanostructured silicon molds.

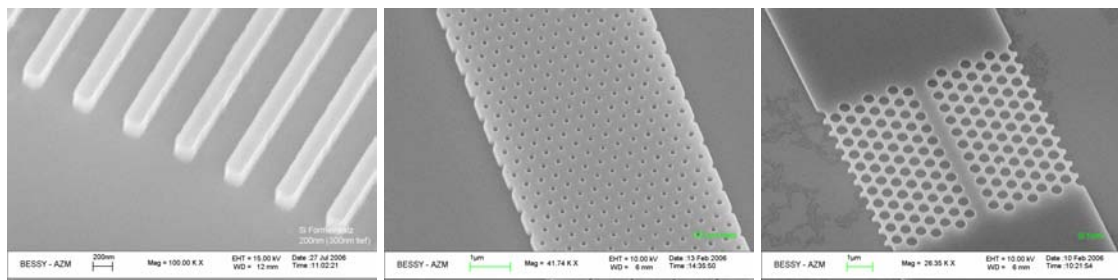


Figure 2: Nanostructured stamps made of silicon were successfully fabricated using e-beam lithography and dry etch technique. A wide variety of nanoscaled geometries is available and is not limited to lines and holes as shown here.

Some preliminary imprint tests were performed to demonstrate the ability to pattern different polymers in the sub 100nm range using the silicon stamps. We used a hot embossing machine from Jenoptik MT (HEX 03) to imprint nanostructure for applications in optics and microfluidics in polymethylmethacrylate (PMMA), polycarbonat (PC) and Teflon[®]. Figure 3 shows SEM micrographs of polymeric nanostructures that were fabricated by the nanoimprint technique at BESSY.

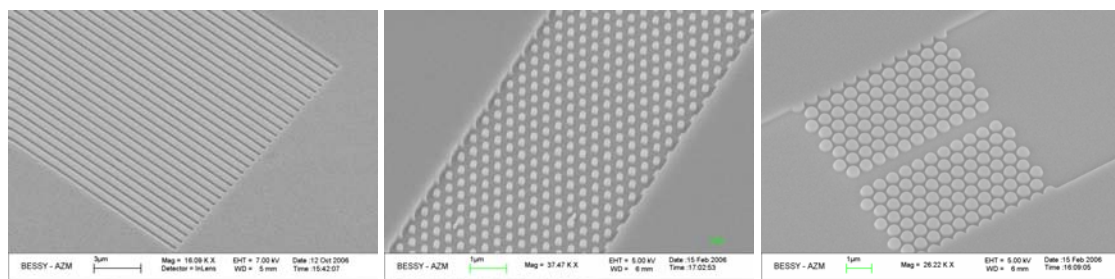


Figure 3: Polymeric nanostructures fabricated by imprinting a silicon stamp into Teflon[®] (left) and NIL resist (middle and right) for potential application in optics and microfluidics show feature size below 100nm.

References

- [1] S.Y. Chou, P.R. Krauss and P.J. Renstrom, *Appl. Phys. Lett.* **76**, 3114 (1995)
- [2] L.J. Guo, *J. Phys. D: Appl. Phys.* **37**, R123-R141 (2004)
- [3] J. Kouba, A. Mai, G. Ropers, M. Kubenz, W. Eberhardt, B. Loechel, *J. Phys. Conference Series* **34**, 897-903 (2006)

Vibrational Satellites in Spectra of Xe/C₂F₆ Mixtures

V.A. Alekseev

Institute of Physics, St.Petersburg State University, Peterhof, 198504 Russia

N. Schwentner

Institute für Experimental Physik, Freie Universität Berlin, Arnimallee 14, D-14195, Germany

Motivation.

Recently we reported¹ on vibrational satellites to transitions of dipole-forbidden states (*DFS*) which were observed for Xe atoms in mixtures with CF₄. These satellites appear in absorption and excitation spectra as spectrally narrow bands near Xe(*DFS*) + CF₄ $\nu_3 = 1$ asymptotic energies. Only the IR active ν_3 mode of the CF₄ molecule induces such satellites. New experiments were performed to search for similar satellites in mixtures of Xe with other molecular gases. Here we report on the vibrational satellites detected in Xe/C₂F₆ mixtures.

Experimental.

Synchrotron radiation was dispersed by the 10m normal incidence monochromator². After passing a cell filled with a mixture of Xe and C₂F₆ it was recorded by a GaAs photodiode and picoammeter (Keithley Instruments). Fluorescence was detected via a Mg₂F side-on window with use of a solar blind photomultiplier. The optical pathlength of SR radiation in the gas cell prior to the fluorescence observation zone was reduced with a special adapter. Fluorescence spectra of Xe/C₂F₆ mixtures contain the Xe 6s[3/2]₁ resonance band and an emission of Xe₂* dimers formed in the three body recombination process. Obviously collisions with C₂F₆ do not deactivate excited Xe atoms but transfer population down to lower-lying states.

Results and discussion.

Figure 1 shows Vac UV fluorescence excitation spectra of pure Xe and of mixtures with C₂F₆ and CF₄ near the 6d[3/2]₁ resonance. The band on the blue side of the resonance in mixture with C₂F₆ (trace 1) appears only when the cell contains both Xe and C₂F₆. The energy of this band closely matches the energy of the Xe 7p[1/2]₀ dipole-forbidden state increased by one quantum of the C₂F₆ ν_{10} mode (1251 cm⁻¹, ref.3). The spectrum of a mixture with CF₄ (trace 2) is shown for comparison. It displays a satellite of the same dipole-forbidden state of Xe due to excitation of one ν_3 -mode quantum (1281 cm⁻¹) of CF₄. This satellite is already known¹.

Unlike CF₄, the C₂F₆ molecules have several IR-active vibrations. The C₂F₆ ν_{10} (0 → 1) transition yields the strongest band in the IR-spectrum. Two other spectrally narrow bands of comparable intensity correspond to ν_5 and ν_6 modes.³ However, no satellites due to excitation of ν_5 and ν_6 modes were observed in the present experiments. It is likely that the symmetry of these vibrations is an essential factor. This interesting question requires further studies.

In experiments with Xe/CF₄ mixtures, satellites of several other 7p states as well as 6p' and 6d states of the Xe atom were observed in the spectral region near the strong 6d[3/2]₁ resonance. These bands are much weaker than the 7p[1/2]₀ satellite (Fig.1) and show up only at CF₄ pressures of few hundred mbar. Strong photoabsorption of C₂F₆ itself in this region hampers observation of satellites at such high pressures. We encountered the same problem in experiments with other molecular gases. Fortunately, collisions with C₂F₆ do not quench excited Xe atoms, but transfer population to the lower-lying states which made it possible to record the 7p[1/2]₀ satellite in the excitation spectra. Few more satellites were found at $\lambda > 120$ nm, where the C₂F₆ absorption is weaker. Like in Xe/CF₄ mixtures,⁴ a

spectrally broad satellite on the far blue wing of the Xe first resonance line was observed as well. These results will be discussed elsewhere.

Conclusion.

Spectroscopic studies of Xe mixtures with CF₄ and C₂F₆ show that a vibrational coupling between electronic states of transient species (collisional complexes) generates a large manifold of new absorption bands. The same mechanism can induce new emission bands in collisions of excited atoms with vibrationally excited molecules. This may be of applied interest. The experiments should be continued for other atomic gas/molecular gas mixtures, including those which are of interest for astrophysics and atmospheric spectroscopy. Essential requirements are a large strength of the vibrational transitions and a near energy resonance with electronic transitions in the atom. The symmetry of vibrations seems to be important as well, a fact which needs clarification. Similar effects may occur in collisions of two atoms. In particular, the resonance $ns \leftrightarrow np$ transitions in alkali atoms closely match the energies of some transitions between resonance and dipole-forbidden states of the Xe atom.

Acknowledgement.

We are grateful to the BESSY staff and especially to Dr. Reichardt. We thank Mrs M. Völzke and H. Kreft for their assistance in running experiments at BESSY. VA acknowledges financial support from the Deutsche Forschungsgemeinschaft via Sfb 450 and an individual grant.

References.

1. V.A. Alekseev, N. Schwentner, Chem. Phys. Lett. (2007) in print
2. G. Reichardt *et al.*, NIM A 467-468 (2001) 462-465
3. P.M. Chu, F.R. Guenther, G.C. Rhoderick, and W.J. Lafferty, "Quantitative Infrared Database" in *NIST Chemistry WebBook, NIST Standard Reference Database Number 69*, Eds. P.J. Linstrom and W.G. Mallard, June 2005, National Institute of Standards and Technology, Gaithersburg MD, 20899
4. V. A. Alekseev, N.K. Bibinov, I.P. Vinogradov, Opt. Spectrosc., 73 (1992) 154.

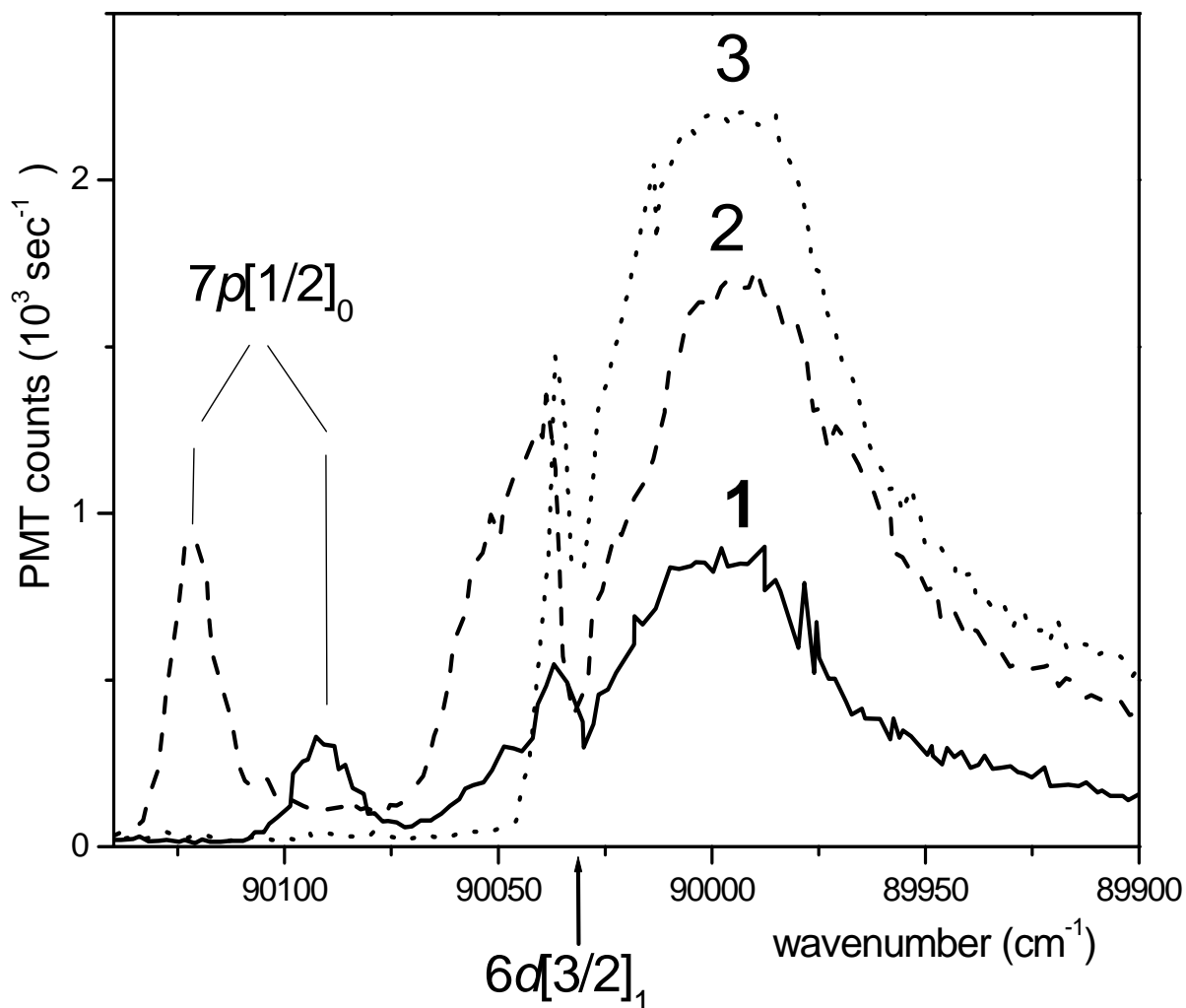


Figure 1.

Vac VU fluorescence excitation spectra around the Xe $6d[3/2]_1$ resonance transition: **1** – Xe(9.2 mbar)/ C_2F_6 (2 mbar), **2** – Xe(9.2 mbar)/ CF_4 (4.4 mbar), **3** – Xe(9.2 mbar). The two vertical sticks indicate the energies of the Xe $7p[1/2]_0$ state increased by $CF_4 \nu_3$ (1281 cm^{-1}) and $C_2F_6 \nu_{10}$ (1250 cm^{-1}) quanta. The dip around the resonance transition is due to the strong absorption of SR radiation near the entrance window. Fluorescence from this region is not seen by the side-on photomultiplier. The signal on the red side of the resonance transition is due to excitation of Xe_2 dimers. Because C_2F_6 strongly absorbs in this region, the spectrum **1** is much less intense than **2** and **3**.

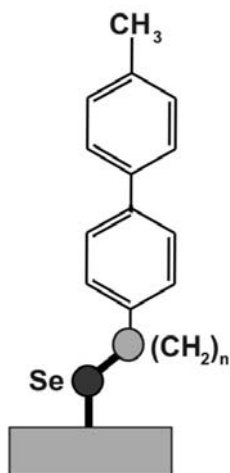
Effect of surface binding configuration in selenium-based aliphatic self-assembled monolayers

Andrey Shaporenko,¹ Jan Müller,² Tobias Weidner,¹ Andreas Terfort,² and Michael Zharnikov¹

¹Angewandte Physikalische Chemie, Universität Heidelberg, 69120 Heidelberg, Germany

²Anorganische und Angewandte Chemie, Universität Hamburg, 20146 Hamburg, Germany

During the last two decades self-assembled monolayers (SAMs), which are 2D polycrystalline films of semi-rigid molecules that are chemically anchored to a suitable substrate, have attracted considerable attention in the scientific community. One area of particular interest is their use for molecular electronics either as films or as single molecules. In this context, an important question is whether the frequently used thiolate chemistry for the attachment of molecules to metallic surfaces provides the best electronic contact for these systems. An obvious alternative is the use of the higher homologue selenium since it not only promises similar reactivity, but presumably offers a better electronic match for the metal surface. To make experimental results comparable, one must gain fundamental knowledge about the influence of this group on the overall orientation of the bound molecule. However, almost nothing is known about the structure-determining properties of selenium.



Scheme 1. Structure of the BPnSe molecules used in this study.

For the sulfur-based systems, it could be shown in the past that the spatial orientation of the binding orbitals of sulfur is a determining factor for the orientation of the alkyl chains in alkanethiolate (AT) SAMs. Analysis of the experimental data implied an sp^3 bonding configuration of the chemisorbed sulfur head group on Au(111) and sp bonding on Ag(111), associated with surface-S-C angles of $\sim 104^\circ$ and $\sim 180^\circ$, respectively. In this study, we show that the same is true for selenium. The systems used in this study are SAMs of 4,4'-biphenyl-substituted alkaneselenolates, $\text{CH}_3(\text{C}_6\text{H}_4)_2(\text{CH}_2)_n\text{Se}^-$ (BPnSe, $n = 2-6$) on gold and silver substrates (Scheme 1). In the BPnSe films, the intermolecular interaction between the SAM-constituents is predominately mediated by the biphenyl moieties. Under these circumstances, one can expect that the packing density and molecular orientation in the BPnSe SAMs do not depend on the length of the alkyl part. However, the exactly opposite behavior is observed. As follows from the quantitative evaluation of the X-ray photoemission data (Figure 1, left panel), the effective thickness of the BPnSe SAMs on both Au and Ag does not exhibit a continuous increase with increasing length of the aliphatic linkage, but shows a systematic zig-zag variation superimposed onto the general increase trend. This suggests that the packing density of the BPnSe SAMs depends on the length of the alkyl part of the BPnSe molecules in a specific, “odd-even” way. The “odd-even” variation of the packing density is accompanied by the corresponding variation in the inclination of the SAM constituents (Figure 1, right panel). The average tilt angle of the biphenyl moieties exhibits a systematic zig-zag variation with the varying n . The respective information could be derived from near-edge X-ray absorption fine structure (NEXAFS) experiments (Figure 2) or, more precisely, from the numerical analysis of the linear dichroism of the π_1^* absorption resonance (285.1 eV).

The “odd-even” changes in the packing density and inclination of the biphenyl moieties in the BPnSe SAMs correlate with each other. A smaller molecular inclination, as it, e.g., occurs for an odd n on Au, corresponds to a larger packing density, and vice versa, as it, e.g., takes place for an even n on Au. It can then be reasonably assumed that the zig-zag changes in the packing density of the biphenyl moieties result from the respective variation of molecular inclination, since strongly inclined molecules require more space than less inclined ones.

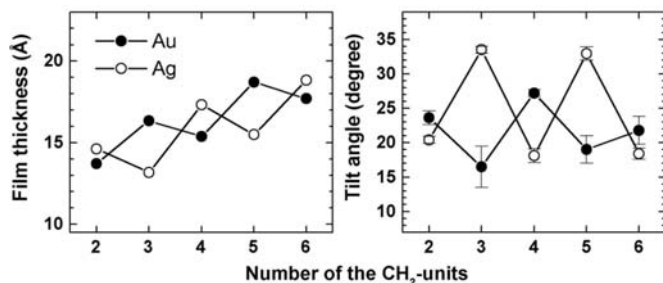


Fig. 1. Effective thicknesses of the BPnSe SAMs (left panel) and the average tilt angles (right panel) of the biphenyl moiety in these films as functions of the number n of the methylene units in the alkyl part.

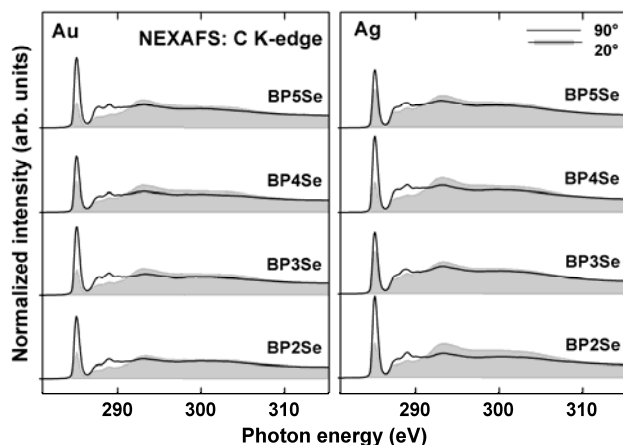


Fig. 2. Carbon K-edge NEXAFS spectra of the BPnSe SAMs on Au and Ag acquired at normal (90°) and grazing (20°) X-ray incidence.

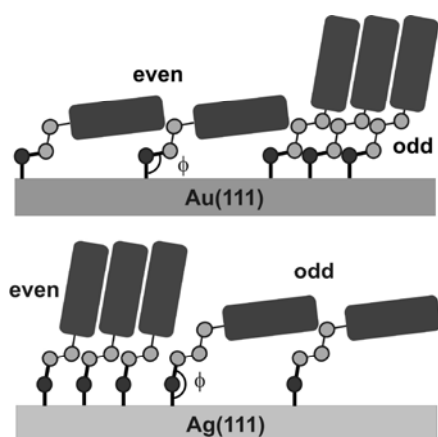


Figure 3. Schematic drawing of the orientation and packing of the BPnSe molecules in the respective SAMs on Au and Ag for an odd and an even number of the methylene units in the alkyl chain. There is a significant energy contribution related to the persistence of the preferable binding geometry of the anchor group.

The changes in molecular inclination of the biphenyl moieties can only be caused by the changes in the orientation of the adjacent $\text{CH}_2\text{-CH}_2$ segment of the alkaneselenolate anchor. The latter can, in turn, only be explained by dropping the “free joint” model for the substrate–selenium–carbon linkage. It should be exchanged for a model suggesting a predominant surface–Se–C angle, associated with a definite hybridization of the Se atom. Assuming an sp^3 bonding configuration of the chemisorbed Se headgroup on Au and sp bonding on Ag, analogous to the S headgroup in AT SAMs, one gets the predominant substrate–Se–C angles of $\sim 104^\circ$ and $\sim 180^\circ$, respectively. This yields a more tilted orientation for the last $\text{CH}_2\text{-CH}_2$ segment of this chain for an odd n on Au and an even n on Ag (see Figure 3), which allows for a more upright orientation of the adjacent biphenyl moieties and for a denser molecular packing. Similarly, for an even number of the CH_2 units in the BPnSe SAMs on Au or for an odd number of these entities for the films on Ag, a less tilted orientation of the last segment of the alkane chain is predicted, resulting in a larger tilt of the adjacent biphenyl moieties and, thus, in a reduced density.

The most interesting and important finding of this study is the fact that the bonding configuration of the Se headgroup is the deciding factor in the balance of structure-building interactions in the alkaneselenolate SAMs. Considering, that similar effects have been observed in biphenyl- and terphenyl-substituted AT SAMs as well, we can conclude on the generality of this phenomenon for different SAM systems. This work has been supported by DFG (ZH 63 9/2) and BMBF (05KS4VHA/4).

Ethylene epoxidation over copper-silver bimetallic catalyst : surface characterization under reaction conditions

S. Zafeiratos^{1*}, V.I. Bukhtiyarov², M. Hävecker¹, D. Teschner¹, E. Vass¹, P. Schnörch¹,
G. Weinberg¹, A. Knop-Gericke¹, R. Schlögl¹

¹*Fritz-Haber-Institut der MPG., Faradayweg 4-6, 14195 Berlin, (Germany)*

²*Borekov Institute of Catalysis, Lavrentieva Avenue 5, 630090, Novosibirsk, (Russia)*

*spiros@fhi-berlin.mpg.de

Introduction

The unique ability of silver to selectively catalyze the partial oxidation of ethylene to ethylene oxide has attracted scientific interest in this system for several decades. Although the selectivity of this reaction in industrial processes has exceeded 80 %, research is still continuing in the field since there is no thermodynamic limit for further increasing selectivity. Recently Barteau et al. found that copper-silver bimetallic catalysts offer improved selectivities compared to pure silver in the direct epoxidation of ethylene [1]. Due to the low adsorption enthalpy, ethylene epoxidation is impossible to study under UHV conditions. This limits the information regarding the chemical state of the surface and adsorbents under reaction conditions. Recent development of a photoelectron spectroscopy apparatus, which is able to operate in the mbar pressure range, allows monitoring of the chemical status of the surface under working catalytic conditions.

Experimental

In situ XPS and NEXAFS experiments were performed at beamline U49/2-PGM1 and PGM2 at BESSY II in Berlin. All spectra were recorded using two excitation energies in order to distinguish between surface and bulk located species. Copper-silver nanopowder (~100 nm, 2.5% Cu), was purchased from Sigma-Aldrich[®]. The catalyst was measured in a C₂H₄ to O₂ ratio of 1:2 and a total pressure of 0.5 mbar at 250° C. Production of ethylene oxide was measured using a Proton Transfer Reaction Mass Spectrometer (PTRMS) which allows differentiation between C₂H₄O and CO₂. Post reaction Scanning Electron Microscopy results showed that the nanostructure morphology of Cu-Ag is practically unaffected during reaction (fig. 1d).

Results and Discussion

In fig. 1a the PTRMS signal of C₂H₄O as a function of temperature and time is presented. The rapid increase and decrease of the signal upon heating at 250° C and cooling respectively,

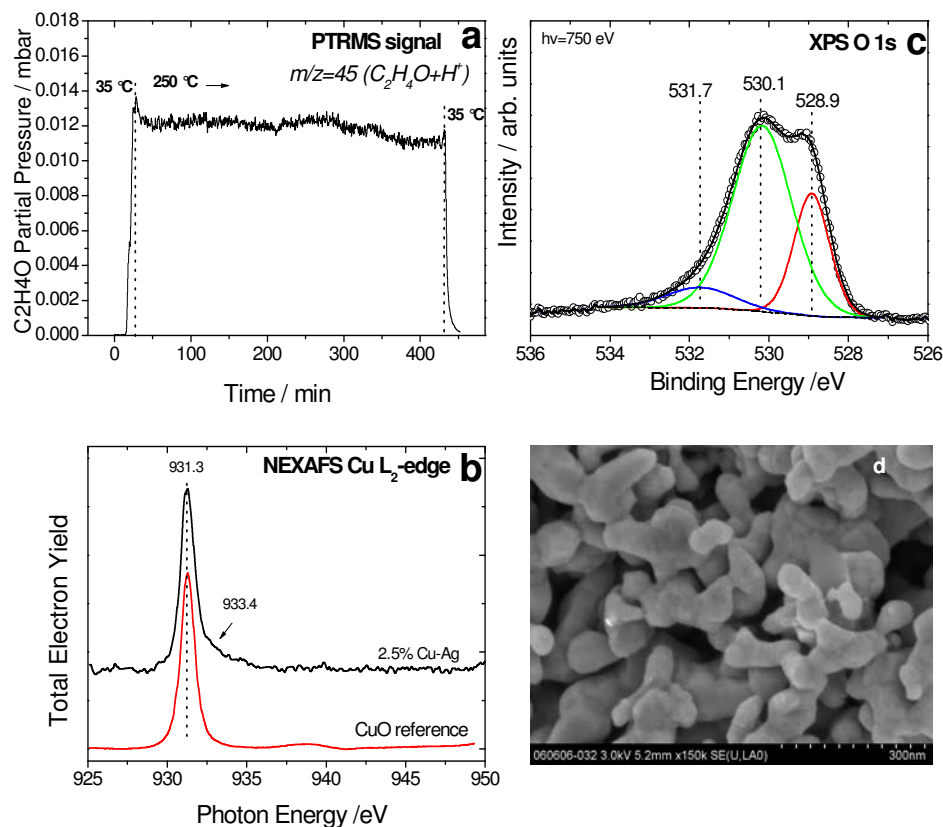


Figure 1. a) PTRMS signals from C₂H₄O with time and temperature b) in situ Cu L₂-edge NEXAFS c) in situ O 1s photoelectron spectra, d) Post-reaction SEM image of Cu-Ag catalyst.

highlights the catalytic activity and long term stability of the catalyst. In situ Total Electron Yield (TEY) NEXAFS spectra measured simultaneously with the PTRMS data shows that copper is mainly Cu²⁺. However, the small shoulder at 933.4 eV (marked with an arrow) indicates that copper at lower valences, most probably as Cu¹⁺, is also present. From in situ photoelectron spectroscopy results of Cu 2p_{3/2} transition (data not shown) the main peak is accompanied by a satellite feature ca. 9 eV at higher BEs characteristic of CuO [2]. Comparison with reference spectra recorded in H₂ atmosphere reveals an additional component at low BE site. This component is an indication of co-existence more than one Cu oxidation states in agreement with NEXAFS spectra.

In fig. 1c the O 1s spectrum recorded in-situ is shown. During reaction 3 oxygen components were used to fit the overall spectrum. Two broad components (~1.8 eV) at 530.1 eV and 531.7 eV (surface located) and a narrow (1.1 eV) at 528.9 eV (predominantly in the bulk). The peak at 530.1 eV was previously assigned both to: electrophilic oxygen linked with the epoxidation path of ethylene on silver foil [3], and to Cu₂O oxygen on Cu foils [4]. The distinction of the origin of this peak in our spectra is difficult; however the case of Cu₂O oxygen is less likely due to the minor contribution of Cu¹⁺ in the Cu 2p and NEXAFS spectra. Peaks at 528.9 and 531.7 eV are nicely correlated with oxygen in CuO and hydroxyl groups, respectively

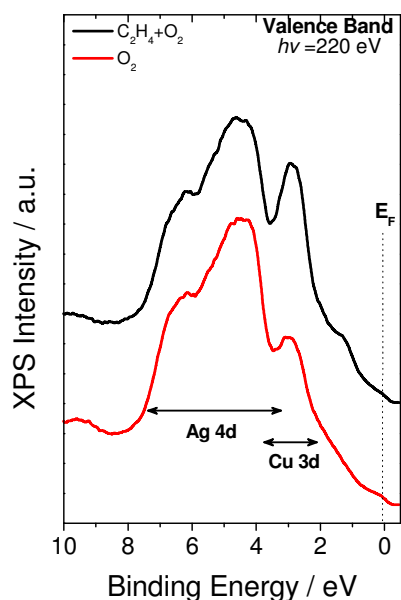


Figure 2. Valence band spectra of Ag-Cu catalyst recorded in situ at 250° under 0.5 mbar ($C_2H_4+O_2$) and O_2

[2]. The Ag $3d_{5/2}$ region (data not shown) is dominated by a metallic silver peak at 368.15 eV. Spectra subtraction using Ag $3d_{5/2}$ peak recorded in hydrogen atmosphere as a reference, revealed an additional Ag $3d_{5/2}$ component in the low BE site (367.7 eV). This peak is an indication of ionic silver which is probably formed during the reaction [3].

Valence band spectra recorded during ethylene oxidation and pure O_2 atmosphere (0.5 mbar, 250° C) are presented in Figure 2. The valence band region is mainly dominated by Ag 4d (4-8 eV) and Cu 3d (2-4 eV) intensities. After subtraction it was evident that extra features at 1.5 and 3.1 eV exist under reaction conditions. These extra features can be induced both,

from new Ag and Cu oxidized states, and/or changes of the Ag-Cu surface stoichiometry. Since core level spectra did not reveal additional oxidized species compared to O_2 atmosphere, enhanced Cu surface segregation during reaction is the most probable cause of these features. The most reliable model of Cu-Ag surface arrangement consists of silver nano-aggregates *partly* decorated with a thin layer of oxidized copper in +2 and +1 valence. This prevents silver agglomeration leading to the long term catalytic stability demonstrated in fig. 1a. It should be noted that experiments performed on monometallic silver nanoparticles showed that very fast particles agglomeration take place upon heating at 250° C which leading to the decrease of the catalytic activity.

Acknowledgment

BESSY staff is gratefully acknowledged for their support during the measurements.

References

1. J.T. Jankowiak, M.A. Barteau, J. Catal. 236 (2005) 366
2. J. Chijsen, L.H. Tjeng, J. Van Elp., Phys. Rev. B. 38 (1988) 11322
3. V.I. Bukhtiyarov, A.I. Nizovskii, H. Bluhm, et. al. J.Catal. 238 (2006) 260.
4. H. Bluhm, M. Hävecker, A. Knop-Gericke, et. al. J.Phys. Chem. B (2004), 108 14340.

Studies of Novel Catalysts for New Generation Fuel Cells by Synchrotron High-Resolution XPS

Adam Lewera^{1,2}, Ralf Hunger³, Paul S. Bagus⁴, Wolfram Jaegermann³, Andrzej Wieckowski¹

¹*Department of Chemistry, University of Illinois at Urbana-Champaign, Urbana, Illinois, USA*

²*Department of Chemistry, Warsaw University, Warsaw, Poland*

³*Institute of Materials Science, Darmstadt University of Technology, Darmstadt, Germany,*

⁴*Department of Chemistry, University of North Texas, Denton, Texas, USA*

(funding by BMBF contract 05 KS4RDA/0)

Using synchrotron XPS we have studied the electronic properties of nanosized Pt/Ru catalyst of different composition. Such system is known to be an effective material to react methanol to CO₂ in so-called Direct Methanol Fuel Cells (DMFC). Understanding electronic-level origin of fuel cell catalysis promises rapid progress in search for new catalytic materials for existing and incoming fuel cell technologies. Theoretical background was described by Mavrikakis, Hammer and Norskov [1] who correlated changes in heterogeneous catalytic activity directly to the position of a center of the catalyst d-band. More recently, different theoretical models have also been employed to help to understand the core-level electrons BE shifts in bimetallic catalysts. The present project concerns electronic effects in fuel cell anode catalysis and the overall strategy aiming at developing correlations between electron core- and valence-level observable and catalytic activity at selected solid/liquid interfaces. For the investigated Pt/Ru systems we have found clear evidence that the binding energy (BE) of Pt 4f electrons was shifted towards higher values (relative to pure Pt), and that the shift depends on the degree of Pt and Ru intermixing. We have also found a small but reproducible Ru 3d electrons BE shift that depends on the catalyst sample composition. Investigation of the valence band spectra has provided us with evidence that the d-band center of such material is shifted down in comparison to pure Pt and Ru, which is a strong support to Mavrikakis-Hammer-Norskov theory. Our data are unique and, collectively, they enhance the understanding of the origin of the activity of different fuel cell catalysts. Further, they form a link between predictions from the general theory of heterogeneous catalysis and the fuel cell reactivity. The work on other systems (in particular Ru/Se for oxygen reduction reaction) is in progress.

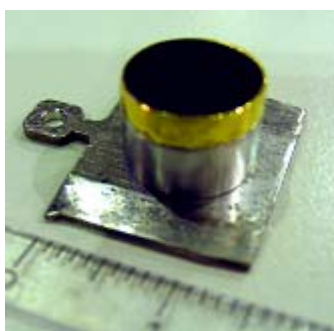


Fig. 1 Pt/Ru catalyst immobilized on a gold disk substrate for XPS experiment

To prepare the catalyst sample for synchrotron XPS experiment the known amount of nanoparticles were dispersed in controlled volume of miliQ water by sonication that yields a homogeneous suspension of the particles. A controlled volume of the suspension was applied to the surface of gold disk and dried (cf. Figure 1). A thin nanoparticle film obtained was electrochemically reduced in 0.5M H₂SO₄ in evolving hydrogen atmosphere (-100mV vs. RHE for 2h) prior to XPS experiment. Such treatment assures full reduction of Ru component [2]. In order to prevent the re-oxidation during the transfer to vacuum for the synchrotron XPS investigations, the electrochemical processing was conducted in a purpose-designed inert gas cell, which is directly attached to a vacuum load-lock. The experiments were conducted in the

SoLiAS experimental station of the TU Darmstadt, which is dedicated to the analysis of solid/liquid interfaces (SoLiAS = Solid/Liquid Interface Analysis) by means of synchrotron photoelectron spectroscopy [3]. SoLiAS is equipped with a Phoibos 150-MCD9 electron analyser, and was operated at the U49/2-PGM2 beamline of the CRG BTU Cottbus, Hahn-Meitner-Institut and TU Darmstadt. The XPS spectra were recorded in normal emission. The BE of each photoelectron peak was calibrated with respect to Fermi edge for every sample and every excitation energy.

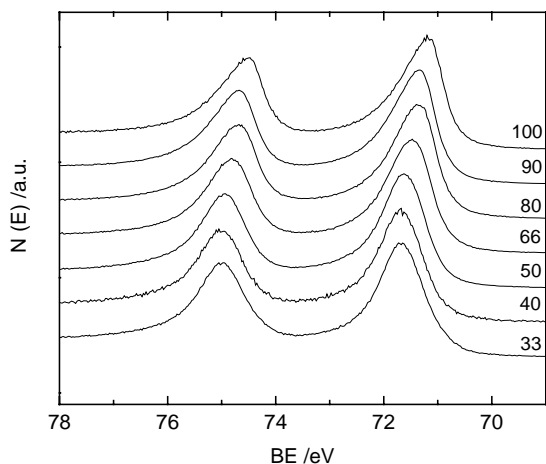


Figure 2: Pt 4f spectra (normalized to the same height) for Pt/Ru catalysts of different composition. Numbers at right denote the percent of Pt for each catalyst. Excitation energy 370 eV

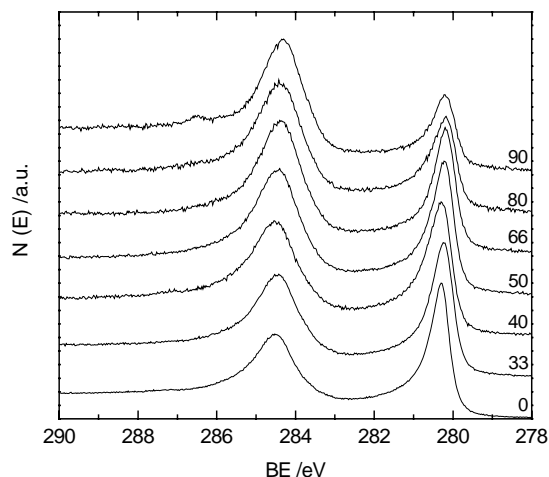


Figure 3: Ru 3d spectra (normalized to the same height) for Pt/Ru catalysts of different composition. Numbers at right denote the percent of Pt for each catalyst. Excitation energy 370 eV

The Pt 4f and Ru 3d core levels spectra were measured and are shown on Figures 2 and 3, respectively. We have found that the Pt Δ BE is ~ 0.5 eV toward lower BE from low to high Pt content (See Figure 2 and 4) and the Ru Δ BE has the same sign but a much smaller magnitude (See Figure 3 and 4). The same sign and the different magnitudes of the Δ BE's are assigned as arising from a lattice expansion in going from Ru with little or no Pt to dominantly Pt particles [4]. The apparent paradox of small Ru Δ BE while there is large Pt Δ BE is resolved and shown to be due to the different responses of the Pt and Ru BE's to the changes in the lattice constants, which is a new and unexpected result.

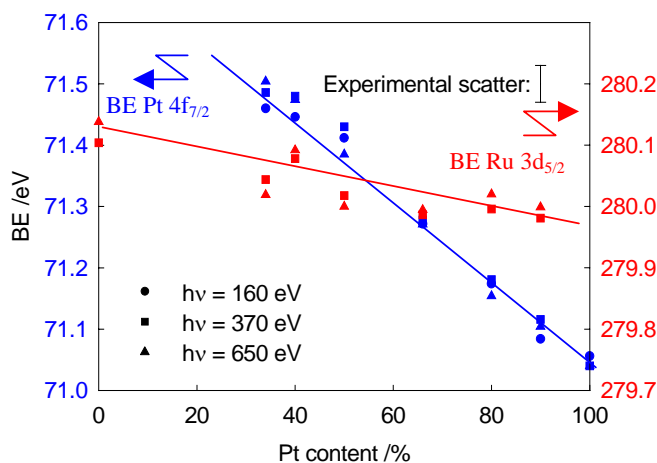


Figure 4. Pt 4f and Ru 3d BE shift as a function of catalyst's composition and excitation energy.

The electronic structure of the catalyst samples was investigated by measuring the valence band emissions (Fig. 5). The d-band center of gravity was calculated as $\Sigma N(\epsilon)\epsilon d\epsilon / \Sigma N(\epsilon) d\epsilon$, where $N(\epsilon)$ in general is DOS, and in our case registered XPS intensity. It shows clear downshift in the case of Pt/Ru catalysts as compared to pure Pt and Ru (Fig 6). This is a strong support for Hammer-Norskov-Mavrikakis theory, although the mechanism of chemical

reaction (methanol oxidation) is different on Pt/Ru catalyst (so called bifunctional mechanism) than on pure Pt and Ru. We speculate that downshift of d-band center weakens the CO binding to the catalysts surface (CO is a molecule which poison the catalyst), but further work is needed to clarify this issue.

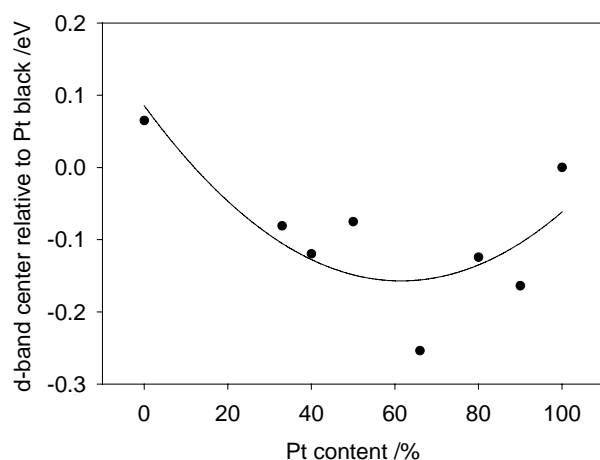


Figure 6. D-band center placement, relative to Pt black as a function of nanoparticles composition, $h\nu = 90\text{eV}$

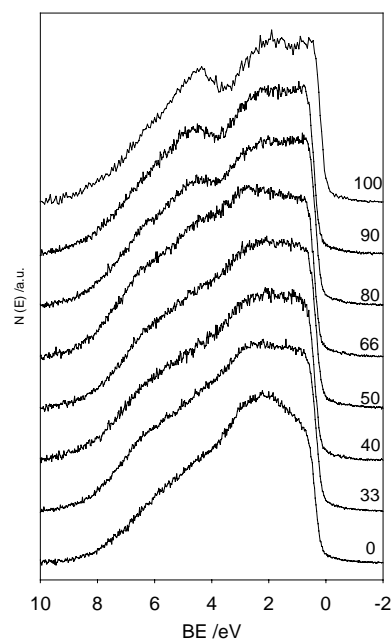


Figure 5. Valence band spectra of Pt/Ru nanoparticle catalyst after Shirley-type background correction. Numbers denote the percent of Pt for each sample. Excitation energy 650eV .

In addition we observed that the Pt $4f_{7/2}$ peak binding energy linearly correlates with the electrocatalytic activity (not shown), namely with the methanol oxidation current per Pt surface unit. The origin of this correlation is not well understood yet and more work is needed to explain such behavior, but solving this issue would significantly extend the understanding of origin of the fuel cells catalytic activity and the physical (electronic) factors influencing it, which is of great importance to scientific community as well as to fuel cells industry. The work on this subject is in progress.

Acknowledgements This work was supported by the USA National Science Foundation under grant NSF CHE03-49999, the Polish Science Foundation under grant 3T09A 054 26, and the German ministry for education and research, BMBF grant No. 04KSA RD/1 (SoLiAS). AL was partially supported by the Warsaw University under grant BW-172108. The support by Patrick Hoffmann and Dieter Schmeißer (BTU Cottbus) in running the beamline U49/2-PGM2 is greatly appreciated. We are indebted to Sascha Hümann and Peter Broekmann (Uni Bonn) for their valuable contributions to the design, manufacture, and operation of the electrochemical setup.

Literature:

- [1] M. Mavrikakis, B. Hammer, J. K. Nørskov *Phys. Rev. Lett.* **81** (1998) 2819
- [2] A. Lewera, W. P. Zhou, C. Vericat, J. H. Chung, R. Haasch, A. Wieckowski, P. S. Bagus *Electrochimica Acta* **51** (2006) 3950
- [3] T. Mayer, M.V. Lebedev, R. Hunger and W. Jaegermann, *Appl. Surf. Sci.* **252** (2005), p. 31-42.
- [4] A. Lewera, W. P. Zhou, R. Hunger, W. Jaegermann, A. Wieckowski, S. Yockel, P. S. Bagus, submitted *Chemical Physics Letters*.

Synthesis and Structure of an ultra-thin Aluminosilicate Film

D Stacchiola, S Kaya, J Weissenrieder, H Kühlenbeck, S Shaikhutdinov, H-J Freund
M Sierka, T Todorova, J Sauer

Fritz-Haber-Institut der Max-Planck-Gesellschaft, Faradayweg 4-6, Berlin D-14195
Humboldt-Universität zu Berlin, Institut für Chemie, Unter den Linden 6, Berlin D-10099
This work is supported by the Deutsche Forschungsgemeinschaft through SFB 546

Employing surface sensitive techniques for better understanding of the mechanisms of catalytic reactions on zeolites at a fundamental level is very challenging. Due to the insulating properties of silica and alumina, this “surface science” approach can be successful only when applied to thin films grown on conducting metal substrates as previously demonstrated for single component oxides. In this work, preparation of well-ordered, ultra-thin aluminosilicate films on a metal substrate is reported for the first time. The preparation of well-ordered thin silica films was reported only recently on a Mo(112) surface [1]. The film exhibited a $c(2 \times 2)$ LEED diffraction pattern with respect to Mo(112). Two models have been proposed in the literature for the structure of thin silica films: a model consisting of a layer of isolated $[\text{SiO}_4]$ clusters arranged in a $c(2 \times 2)$ structure on the Mo(112) surface with all oxygen atoms bonding to the Mo substrate, referred as a “isolated cluster” model [2], and a two-dimensional network of corner sharing $[\text{SiO}_4]$ tetrahedra, with one oxygen of each tetrahedron binding to the bridging site of protruding Mo atoms of the metal surface (see Fig. 1), referred to as the “2D-network” model [3].



Figure 1: Models of 1 monolayer silica films on Mo(112).

Photoelectron spectroscopy (PES) of the core levels, when applied to the oxide surfaces, is a very powerful tool for determining the oxidation state of the metal cations and average oxide stoichiometry. PES can resolve whether different oxygen and/or cations species are present in the oxide. In addition, analysis of angular resolved spectra may provide useful information on the depth distribution of the different species.

In all film preparations, the Si2p region showed only a single peak at ~ 103 eV, which can be straightforwardly assigned to the tetrahedrally coordinated Si^{4+} atoms. Regarding the oxygen states, at least two different O species were distinguished with binding energies (BE) of 530.3-531.2 and 532-532.5 eV, i.e. separated by ~ 1.5 eV after spectra deconvolution. The high BE values fall into the region reported for bulk silica.

In order to increase spectral resolution we have further employed synchrotron facilities at BESSY II, Berlin (beam-line UE52-PGM1). The O1s region of silica film is shown in Fig. 2, where two oxygen species at 532.5 eV and 531.2 eV are unequivocally resolved. When measured at grazing emission (80° with respect to the surface normal), the low BE signal is practically vanished, indicating that these species are located below the layer consisting of O species with the high BE. This finding fully agrees with the assignments of the 531.3 eV peak to the interface (Si-O-Mo) oxygen atoms and 532.5 eV peak to the topmost O layer within the Si-O-Si network. Since these two peaks are well separated, the integral intensity

ratio can be precisely measured and is found to be 3:2 at normal emission, as predicted for the 2D-network model based on the XPS measurements. Meanwhile, the cluster model should result in the ratio of 1:1. In addition, Fig. 2 shows the Mo3d region, where only one partially oxidized Mo species at 228.2 eV is observed beyond the metallic Mo at 228 eV. Again, consistent with the 2D-network model.

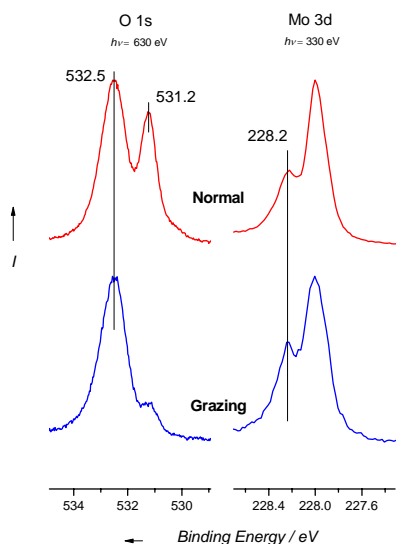


Figure 2: The O1s and Mo3d core regions in the photoelectron spectra for the “O-poor” film observed at normal (top) and grazing (bottom) emissions

Formation of ice films on electro-conducting single crystal substrates is used to grow thin, well-ordered ice films, which allow to employ various surface sensitive techniques for studying chemical reactions on ice. Adsorption of water on thin silica films was therefore also studied. Fig. 3 shows the O1s PES spectra of the silica film exposed to water at 90 K.

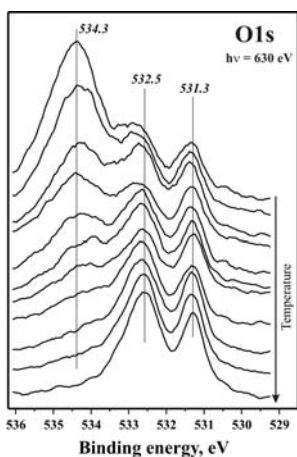


Figure 3: Consecutive PE-spectra of the silica film, exposed to 6 L of water at 90 K, on slow heating to 200 K. The states at 532.5 and 531.3 eV are assigned to the surface and interfacial O species in the silica film

Two O species at 532.5 and 531.3 eV observed on the clean film have been previously assigned to the O atoms in the top-most (O-Si-O) and interface (Si-O-Mo) layers, respectively. Note, that in order to minimize the photon-induced changes in the water overlayer, we slowly moved the sample while recording the consecutive spectra, which take only ~10 seconds each. Adsorption of 6 L of water results in a signal centered at 534.3 eV, which can be attributed to the intact water molecules. Upon slow heating, this signal gradually attenuates, finally resulting in the spectrum of the clean silica surface. Due to a relatively broad spectral feature of water, it is difficult to follow a crystallization process as observed by IRAS. However, no hydroxyl species (expected at ~533.5 eV) were detected upon heating to 200 K, which is consistent with non-dissociative adsorption of water observed independently by IRAS.

For the synthesis of aluminosilicate films, in order to facilitate intermixing of Al and Si in the film, we have used co-deposition of Al and Si onto the O/Mo(112) surface in an oxygen environment followed by annealing in vacuum.

Based on LEED, STM and DFT results, we proposed that the structure of aluminosilicate films grown on Mo(112) consist of a 2D network of corner-sharing $[\text{SiO}_4]$ tetrahedra with some Si^{4+} ions replaced by Al^{3+} , present in the film as $[\text{AlO}_3]$.

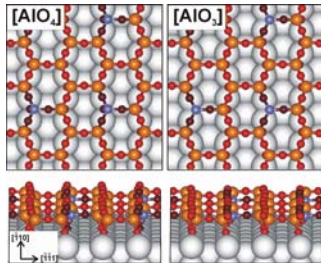


Figure 4: The top and perspective views of the $[\text{AlO}_4]$ and $[\text{AlO}_3]$ models of the aluminosilicate films grown on Mo(112).

Proof for the $[\text{AlO}_3]$ model comes from the analysis of the high-resolution PES using synchrotron radiation. The O1s region for the aluminosilicate films are shown in Fig. 5, together with the spectra for silica from Fig. 2 for comparison.

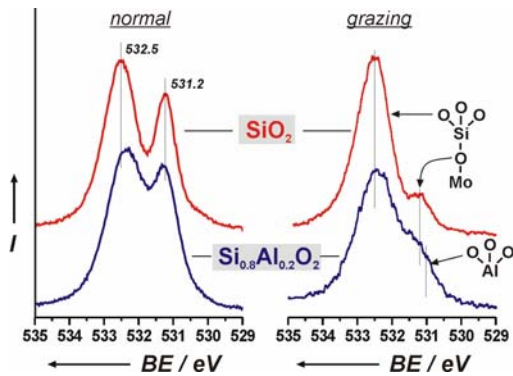


Figure 5: O1s region of the PES spectra of the silica (red) and aluminosilicate (blue, Al:Si ~ 1:5) films measured at normal and grazing emission.

The presence of ~20 mol. % of Al in the silica film broadens the spectra. This can be explained by the heterogeneity of the environments presented to O species (e.g., bonded both to Si and Al atoms). Our DFT calculations have revealed that the O atoms in Si-O-Al bonds exhibit the BE of ~531 eV, which therefore overlaps with the signal coming from interface oxygen atoms in Si-O-Mo bonds. As a result, the intensity of the low BE signal is notably increased when compared to a pure silica film. The fact, that the Al-bonded O species are within the top layer of the film, leads to a less attenuated signal at grazing emission. On the other hand, the Al-O-Mo species present in an $[\text{AlO}_4]$ model would manifest itself, according to our calculations, by a signal at ~530 eV, which is missing in the experimental spectra. Therefore, our PES results also favor the $[\text{AlO}_3]$ model.

References:

- [1] T. Schroeder, M. Adelt, B. Richter, M. Naschitzki, J. B. Giorgi, M. Bäumer, H.-J. Freund, *Surf. Rev. Lett.* **7**, 7 (2000).
- [2] MS Chen, AK Santra, DW Goodman, *Phys. Rev. B*, **69**, 155404 (2004)
- [3] J. Weissenrieder, S. Kaya, J.-L. Lu, H.-J. Gao, S. Shaikhutdinov, H.-J. Freund, M. M. Sierka, T. K. Todorova, J. Sauer *Phys. Rev. Lett.* **95** (2005) 076103

XMCD measurements of non-oxidised 2.5 nm FePt nanoparticles chemically prepared

Margeat Olivier,^a Amiens Catherine,^a Ciuculescu Diana,^a Bruno Chaudret,^a Kawwam Mohammad,^b Fauth Kai,^b Schütz Gisela,^b Spasova Marina,^c Farle Michael^c

a: LCC-CNRS, 205, route de Narbonne, 31077 Toulouse, France

b: Max-Planck-Institut für Metallforschung Heisenbergstr. 3, 70569 Stuttgart, Germany

c: Experimentalphysik, Universität Duisburg-Essen, Lotharstr. 1, 47048 Duisburg, Germany

Magnetic nanoparticles are of interest for both the fundamental studies of their magnetic properties and the many applications they offer, whatever they are soft or hard ferromagnets. Size and shape controls of magnetic nanoparticles have been achieved in our group through the decomposition of organometallic precursors in organic solvents, in the presence of organic capping ligands (mostly long chain amines and carboxylic acids). Thanks to the use of a new iron precursor, Fe[N(SiMe₃)₂]₂, iron nanoparticles¹ and iron-based alloys (FeNi², FePt, FeRh) are now under extensive investigations in our group. The aim of the beamtime was to measure directly the spin and orbital contributions to the magnetic moment of Fe atoms in ultrafine iron nanoparticles (NPs) embedded in a polymer matrix³ (diameter < 2 nm).*

Results obtained on 2.5nm FePt NPs:

The synthesis of these NPs consists in the simultaneous decomposition of two metallic precursors: an iron one (Fe[N(SiMe₃)₂]₂) and a platinum one (Pt(acac)₂). Decomposition occurs in mesitylene as solvent, at 200°C under 3 bar of dihydrogen as reducing agent (see Fig.1).

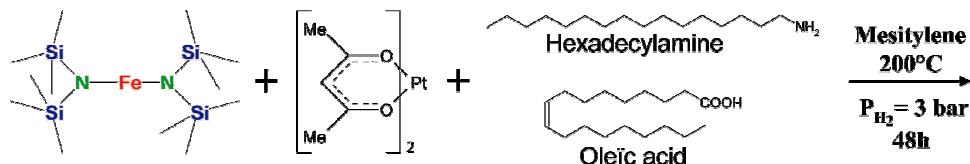


Fig.1: Reaction leading to the 2.5 nm FePt NPs

These NPs have been characterized by Transmission Electron Microscopy (TEM). Typical TEM images are displayed Fig.2, showing spherical NPs with a 2.5 nm mean size, well sprayed on the TEM grid. They present homogeneous sizes and shapes, and their composition has been studied by EDX in micro and nano-probe modes. A composition of the NPs close to Fe₅₀Pt₅₀ has been evidenced.

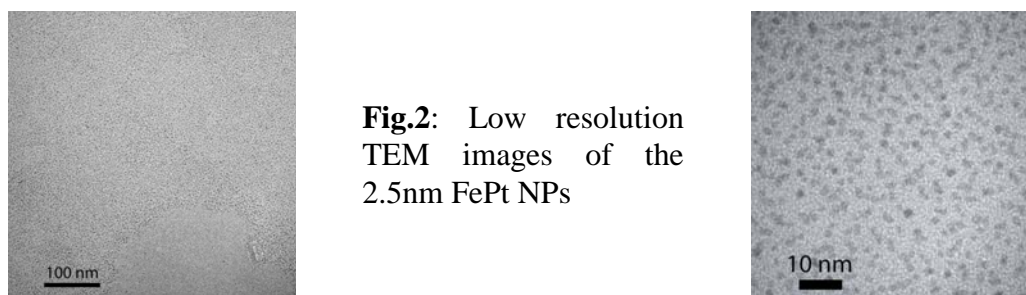


Fig.2: Low resolution TEM images of the 2.5nm FePt NPs

High-Resolution TEM investigations were also performed to study the structural aspects of these objects. A typical HRTEM image is displayed Fig.3 (left), evidencing the cristallinity of a single particle, and also the presence of stacking faults (here shown along the (111) plane). These stacking faults have been observed on all of the single particles studied. The Fast

Fourier Transform (FFT) of the signal is displayed Fig.3 (right) and confirms that the NPs possess the fcc bulk structure of the FePt alloy. Moreover the particles are chemically disordered as super-reflexions from a chemical ordering of Fe and Pt atoms within the particle are not visible.

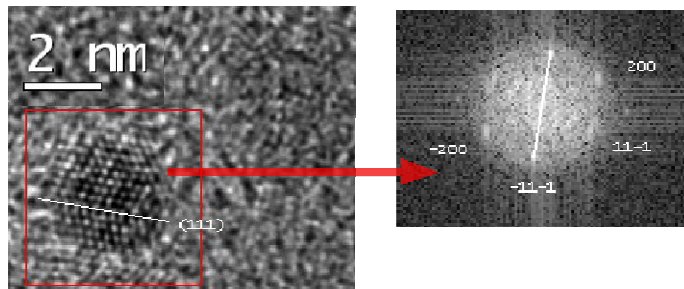
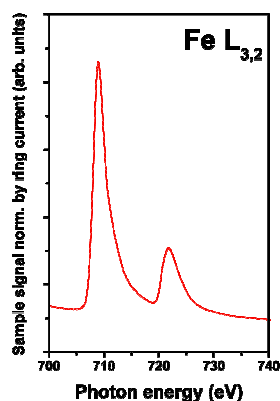


Fig.3: HRTEM image (left) of a single 2.5 nm FePt nanoparticle, and the corresponding Fast Fourier Transform (FFT) of the signal (right)

The study of the magnetic properties of these NPs was not possible to realize by SQUID, as the sample obtained after synthesis was too oily and thus could not be dried to study in a powder form. Moreover the signal was too weak when the NPs were deposited on a substrate. However such deposited NPs can give a signal large enough to be studied by XMCD. We thus have studied the magnetic properties with element sensitivity by XMCD at the $L_{2,3}$ edges of iron atoms to determine the magnetic properties of the FePt NPs and their spin and orbital contributions.



Experiments were carried out on line PM-3. The nanoparticles were deposited as dense layers on silicon substrate in a glovebox (starting from a colloidal solution of the NPs) and then transferred in the measurement chamber using a portable UHV container.

The XAS spectrum displayed Fig.4 shows typical absorptions characteristic of non-oxidized Fe atoms, as oxidation traces would result in clear doublets at both L_2 and L_3 edges.

Fig.4: X-ray Absorption Spectroscopy (XAS)

XMCD measurements consists then to apply a magnetic field, and to study the differences in the spectra under +1.5T and -1.5T. XMCD signals were recorded at various temperatures, to study the NPs both in their superparamagnetic regime and blocked regime. Fig.5 shows the results obtained at both Fe and Pt edges at 15K.

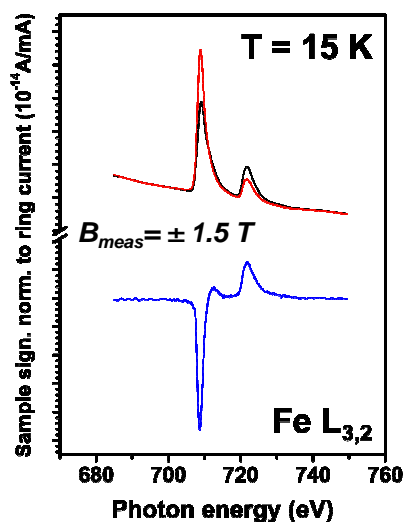
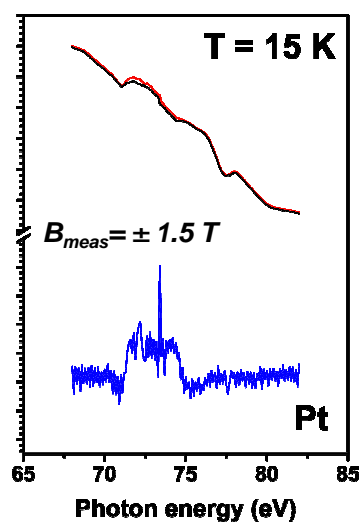


Fig.5: XAS (up) and XMCD (down) signals at the Fe (left) and Pt (right) edges



At the Pt-edge, it appears that the Pt atoms are magnetic and ferromagnetically coupled to the Fe atoms, which is a confirmation that Fe and Pt atoms are both present in each particle. Quantitative data from the analysis of the XMCD signals at the Fe-edge are still in progress, and will give us the exact values of μ_S and μ_L , and of the total magnetic moment per particle. Such values are rich as a fundamental interest, and will help us to determine whether the Fe and Pt atoms are creating a true alloy or are partially segregated within the particles.

More generally this work on Fe-based alloys is of high interest and is still the subject of extensive work, as other ones like FeRh NPs which will be studied during the next beamtime (first semester of 2007).

Acknowledgements:

We thank C.-H Fischer and I. Lauermann (both HMI) for access to the CISSY glove-box system, and the permission to adapt it for our transfer purposes. Thank also to A. Vollmer and M. Neeb (BESSY) for the vacuum transfer chamber. This project was supported by the EU contract number: RII 3 CT-2004-506008.

1. Dumestre, F.; Chaudret, B.; Amiens, C.; Renaud, P.; Fejes, P., Superlattices of iron nanocubes synthesized from Fe[N(SiMe₃)₂]₂. *Science* **2004**, 303, (5659), 821.
2. Margeat, O.; Ciuculescu, D.; Lecante, P.; Respaud, M.; Amiens, C.; Chaudret, B., NiFe Nanoparticles: a Soft Magnetic Material? *Small* **2007**, in press.
3. Margeat, O.; Dumestre, F.; Amiens, C.; Chaudret, B.; Lecante, P.; Respaud, M., Synthesis of iron nanoparticles: Size effects, shape control and organisation. *Progress in Solid State Chemistry* **2005**, 33, (2-4), 71.

*Experimental difficulties:

The extreme sensitivity to oxidation of the ultrafine iron nanoparticles (NPs) embedded in a polymer matrix, that were expected to be measured at first, has led us to employ important precautions for the introduction of the samples into the UHV measurement chamber. That's why an airless sample transfer system was used, consisting in a preparation of the samples in a glove-box from BESSY, followed by a transfer in a portable UHV container that could be connected to the main measurement chamber. Unfortunately the measurements showed an absorption spectrum characteristic for slightly oxidized iron atoms. The transfer system thus appeared to be not efficient enough for this kind of sensitive samples, as the precautions taken were not sufficient. For the next beamtimes, a technical solution has been found with a glove-box connected directly to the measurement chamber, allowing safe sample transfers.

Other samples were envisaged to face this eventuality of oxidation problems: FePt and FeRh NPs, which are interesting bimetallic compounds based on the same Fe precursor (Fe[N(SiMe₃)₂]₂) used for the synthesis of the ultrafine Fe NPs embedded in the polymer matrix. Their studies were of interest as they were the subject of the following beamtimes (occurring last October for FePt, and next march for FeRh). Iron alloyed NPs are known to be slightly less sensitive to oxidation than pure iron NPs. Unfortunately the FeRh NPs revealed to be also too sensitive to support this transfer without oxidizing and thus will be also studied later with the new transfer system. Case was different for the FePt NPs and that's why we present here the results concerning these chemically prepared FePt NPs.

In-situ XPS study on $(\text{MoV})_5\text{O}_{14}$ selective oxidation catalysts

P. Schnörch, E. M. Vass, S. Zaferiatos, D. Teschner, M. Hävecker,

A. Knop-Gericke, R. Schlögl

*Department of Inorganic Chemistry, Fritz-Haber Institute of the MPG, Faradayweg 4-6,
14195 Berlin, Germany*

Introduction

Catalytic reactions involving partial oxidation of simple hydrocarbons belong to the most important processes in the chemical industry [1]. Different molybdenum and vanadium oxides as mixed oxides are successfully applied in those reactions. Therefore, Mo based selective oxidation catalysis (propane and propylene to acrylic acid) is one of the main research area in our department. The surfaces of catalytic materials strongly depend on the gaseous environment and temperature. Therefore in-situ experiments under working conditions are necessary to identify the active phase of catalysts. In-situ spectroscopy techniques in the soft X-ray range like XAS and XPS were applied to learn about the electronic structure of the working catalyst surface. In this study we investigated two different catalytic formulations, Mo-V mixed oxides with and without W in the crystal lattice. These are good candidates for these reactions.

Experimental

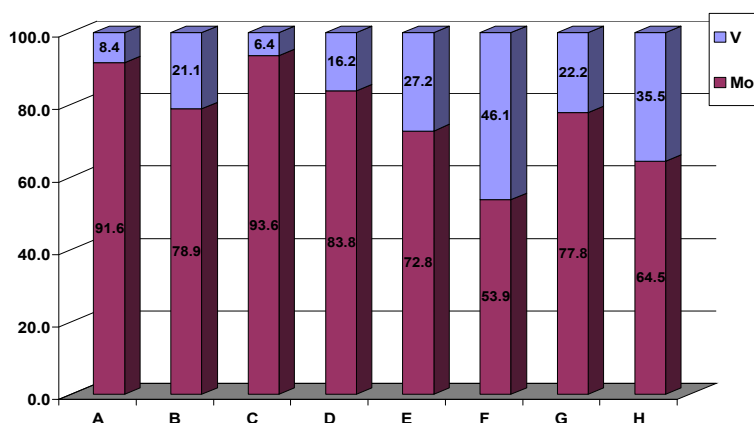
The experiments were performed at beamline U49/2-PGM2. The $(\text{Mo}_{0.68}\text{V}_{0.23}\text{W}_{0.09})_5\text{O}_{14}$ [(MoVW)Ox] and $(\text{Mo}_{0.91}\text{V}_{0.09})_5\text{O}_{14}$ [(MoV)Ox] catalysts were prepared by spray-drying technique from the mixed solution of ammonium heptamolybdate, ammonium metatungstate and vanadyl oxalate. The samples were investigated in a variety of reaction mixtures. At 0.5 mbar, propylene-oxygen ratio (1:2; 1:1) was varied; and water (0.1 mbar) was added to the mixtures. The catalytic reactions were measured at 350°C. Mo 3d, O 1s, V 2p, W 4f, C 1s and valence band spectra were recorded under reaction conditions at different excitation corresponding to different information depth. In addition in-situ XAS spectra were taken at OK-edge and VL-edges. Selected mass numbers were recorded by Proton transfer reaction mass spectrometer, simultaneously to the XPS and absorption spectra, which allowed us to measure the catalytic activity and correlate it to the spectroscopic information.

Results

Other than the total oxidation products CO_2 and water, both catalysts produced aldehydes such as acrolein, acetaldehyde, propanal, formaldehyde however no acids under these low-pressure conditions. On the other hand at higher pressure (1 bar) both catalysts are able to produce acrylic acid as well. The reason to this discrepancy might be a pressure barrier existing between atmosphere and mbar conditions. Further investigations are under progress to examine the reason of this pressure dependence on the reaction.

The catalytic activity was depending on the reaction conditions. In 2:1 oxygen propylene ratio both catalysts showed higher activity. (MoVW)Ox was more active and selective compare to the W-free sample independently from the O₂/propylene ratio.

The elemental composition of the samples measured with bulk sensitive excitation indicated good agreement with the theoretical composition and with the ICP experimental data. XP spectra recorded in surface sensitive mode however revealed vanadium enrichment in the surface near region of both samples (Fig1, Fig2).



A	2 O ₂ : 1 C ₃ H ₆ at RT in bulk sensitive mode
B	2 O ₂ : 1 C ₃ H ₆ at RT in surface sensitive mode
C	2 O ₂ : 1 C ₃ H ₆ at 350 C° in bulk sensitive mode
D	2 O ₂ : 1 C ₃ H ₆ at 350 C° in surface sensitive mode
E	2 O ₂ : 1 C ₃ H ₆ at 350 C° + H ₂ O in bulk sensitive mode
F	2 O ₂ : 1 C ₃ H ₆ at 350 C° + H ₂ O in surface sensitive mode
G	2 O ₂ : 1 C ₃ H ₆ at 350 C° off H ₂ O in bulk sensitive mode
H	2 O ₂ : 1 C ₃ H ₆ at 350 C° off H ₂ O in surface sensitive mode

Fig1. Molybdenum and Vanadium ratio in “bulk” (~18Å) and “surface” (~8 Å) sensitive mode

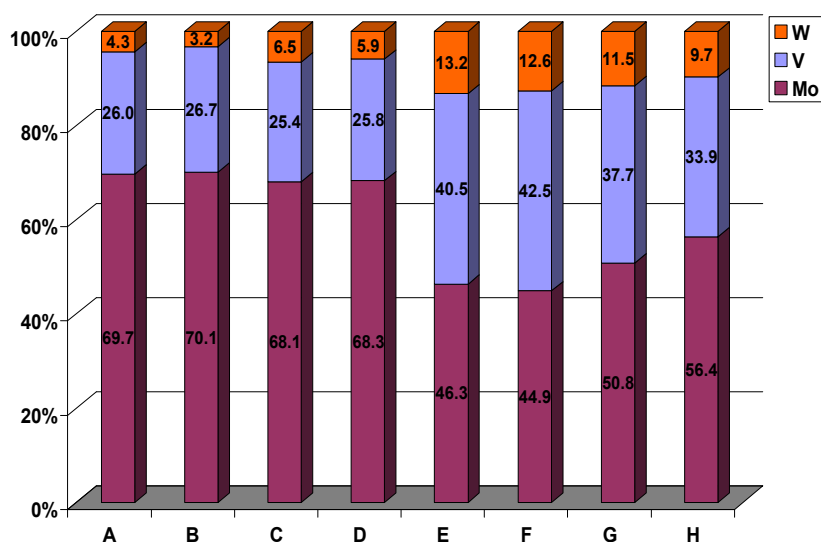


Fig2. Molybdenum, Vanadium and Tungsten ratio in “bulk” (~18Å) and “surface” (~8 Å) sensitive mode

For (MoVW)Ox the Mo3d state was not significantly altered in the different conditions; it was mainly Mo⁶⁺.

(MoV)Ox contained different Mo oxidation states at room temperature (Mo⁶⁺, Mo⁵⁺). During reaction the Mo⁵⁺ state disappeared. The loss of Mo⁵⁺ correlates with the removal of surface carbon.

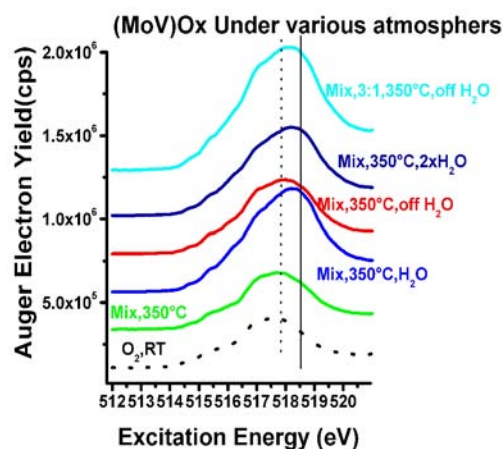


Fig3. (MoV)Ox Auger Electron Yield VL3 spectra

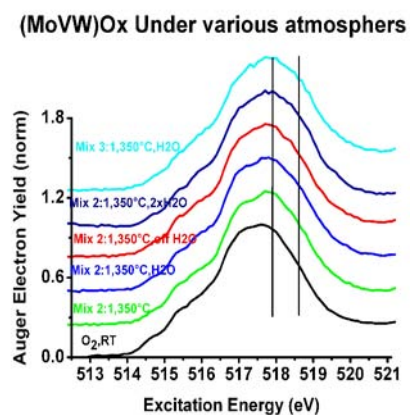


Fig4. (MoVW)Ox Auger Electron Yield VL3 spectra

Vanadium was in a mixed oxide state of V^{5+} and V^{4+} in both samples. The V2p core level indicated more oxidized vanadium under the reaction condition. The ratio of V^{5+}/V^{4+} was higher with W in the oxide lattice. The initial tungsten oxidation state was 6+ and it was not modified under the reaction. From Auger Electron Yield spectra vanadium was clearly more oxidized in the presence of water in the case of (MoV)Ox .

Conclusion

It can be concluded from the result that (MoVW)Ox has higher activity and selectivity than the tungsten free sample in propylene selective oxidation reaction. The W containing catalyst possesses greater structure stability and is therefore less sensitive to the presence of water to strongly modify the surface structure and composition.

Acknowledgement

The authors thank the Bessy staff for their continual support during the experiments.

References

- [1] J. Holmberg, R.K. Grasselli and A. Andersson, *Appl. Catal. A: General* **270** (2004), p. 121
- [2] S. Knobl, G. A. Zenkovets, G. N. Kryukova, O. Ovsitser, D. Niemeyer, R. Schlögl, G. Mestl, *Journal of Catalysis* **215** (2003) 177

The influence of steps on the adsorption of methane on platinum surfaces

C. Papp, B. Tränkenschuh, R. Streber, T. Fuhrmann, R. Denecke*, H.-P. Steinrück.
Lehrstuhl für Physikalische Chemie II, Universität Erlangen-Nürnberg, Egerlandstr. 3,
D-91058 Erlangen.

Methane, the simplest hydrocarbon and one of the most important natural resources, is used in many technologically relevant processes, like e.g., the Fischer-Tropsch synthesis. Due to the high hydrogen content of methane it is relevant as H₂ source for, e.g., fuel cells. Furthermore, methane also serves as model system for the activated adsorption of alkanes and their reaction behavior on surfaces. In order to study the influence of defects, such as steps, our substrates were two stepped platinum surfaces, namely the Pt(355) and the Pt(322) surface; both have 5 atom row wide terraces and (111) and (100) oriented steps, respectively. The results obtained are compared to results from the flat (111) surface of platinum [1]. Lately, a molecular beam study of the adsorption of methane on a Pt(533) surface showed an enhanced initial sticking coefficient for this system [2]. However, the study was performed at higher surface temperatures and thus also included the surface reaction of adsorbed species to carbon. We are able to separately analyze those two elementary steps, by investigating first and directly the adsorption at low temperatures and subsequently the reaction of the adsorbates on the surface.

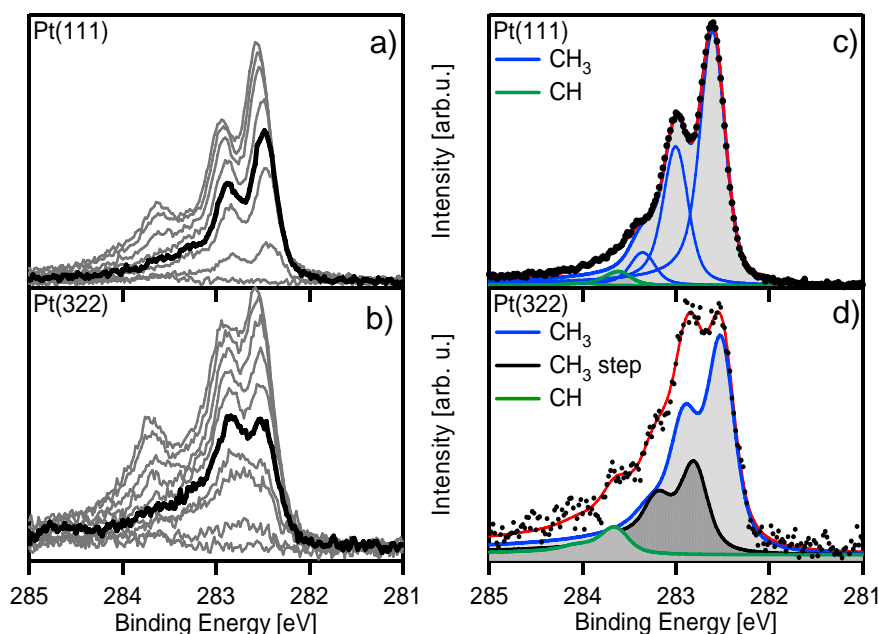


Fig. 1: Selected C 1s XP spectra of methane adsorption experiments on a) a Pt(111) ($E_{kin}=0.71$ eV) and b) a Pt(322) ($E_{kin}=0.54$ eV) surface at 120 K. The quantitative evaluation of the bold spectra from a) and b) for the respective surfaces is shown in (c) for Pt(111) and in d) for Pt(322).

We recorded C 1s spectra in-situ with an excitation energy of 380 eV at beam-line U49/2-PGM1. The data were collected in a time-dependent manner (step ~ 8 s), while adsorbing methane with a supersonic molecular beam on the two stepped and on a flat Pt(111) crystal. This allowed us to directly determine the relative initial sticking coefficient of methane. The apparatus used for these measurements is described in detail elsewhere [3].

In Fig.1 (a) and (b) selected XP spectra of adsorption experiments of methane on Pt(111) and Pt(322), respectively, are shown, yielding methyl (CH₃) species. These methyl species are found on the surface, independent of the kinetic energy, as explicitly shown for Pt(111) [1]. In the case of the stepped surface, the relative abundance of step and terrace adsorbed methyl is changing with exposure.

Especially in the intermediate exposure range (bold spectra), the differences in the XP spectra between the stepped and the flat surface are evident. The decomposition of the C 1s spectra taken after adsorption at a surface temperature of 120 K reveals separate features for the resulting methyl species adsorbed on steps and terraces [4], as shown for the (322) surface in Fig. 1. (d). Both contributions show vibrational fine structure, as observed previously on Pt(111) [1], see also Fig. 1 (c). The binding energy difference between the adiabatic peaks of step and terrace methyl is found to be 300 and 370 meV for Pt(322) and Pt(355) (data not shown), respectively, with the terrace contribution appearing at the same C 1s binding energy as on Pt(111) (see Ref. [4] for details).

For the Pt(322) crystal the total methyl coverage and the coverage of methyl adsorbed at step sites vs. the adsorption time are shown in Fig. 2 (a). The values for the total coverage for a certain adsorption time (i.e., exposure), which are increasing with increasing kinetic energy of the impinging molecules, are similar for all Pt surfaces studied, namely the (111), the (355) and the (322) surface shown here. In contrast to this similarity of the total coverage, the coverage at the step sites on the Pt(355) crystal is ~ 2 times higher as on the Pt(322) surface [4]. Interestingly, adsorbed CH_3 is found to preferentially migrate to the more attractive step sites, even at temperatures as low as 120 K, as found from the very steep increase in the coverage of this species compared to terrace methyl. A stronger bonding on step sites was also found for adsorption of CO on these two crystals [5].

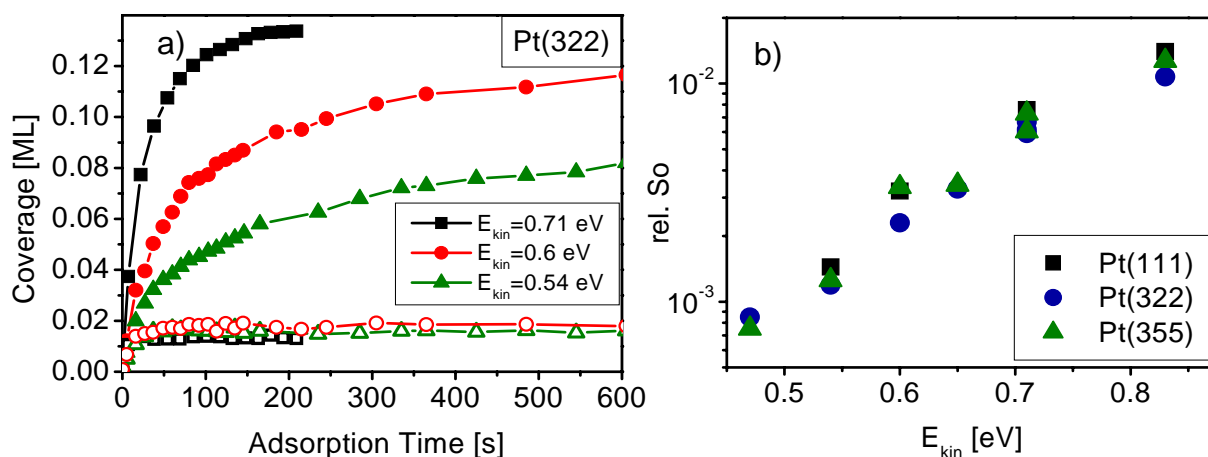


Fig. 2: a) Total methyl coverage (solid symbols) and coverage of methyl adsorbed on step sites (open symbols) resulting from uptake experiments with different kinetic energies; b) relative initial sticking coefficients (rel. So) as a function of kinetic energy.

From the initial increase of the total coverage curves of our time-dependent measurements we were able to determine the relative initial sticking coefficient of methyl on the three different surfaces. This dissociative sticking coefficient of methane at 120 K is increasing with increasing kinetic energy of the impinging methane molecules, showing the activated nature of the process, but is not significantly changing when going from flat to stepped platinum surfaces, as can be seen in Fig. 2 (b).

We also performed temperature-programmed XPS experiments, shown in Fig. 3 (a) and (b), by heating the sample with a fixed rate of 0.5 K/s while measuring every 10 K. These experiments show that stepped surfaces have a higher reactivity, recognizable by the ~ 40 K lower transition temperatures, for the dehydrogenation reaction of CH_3 to CH compared to the Pt(111) surface [1]. While this increased reactivity also extends to the terrace bound methyl molecules, the differently oriented steps exhibit yet a different reaction behaviour.

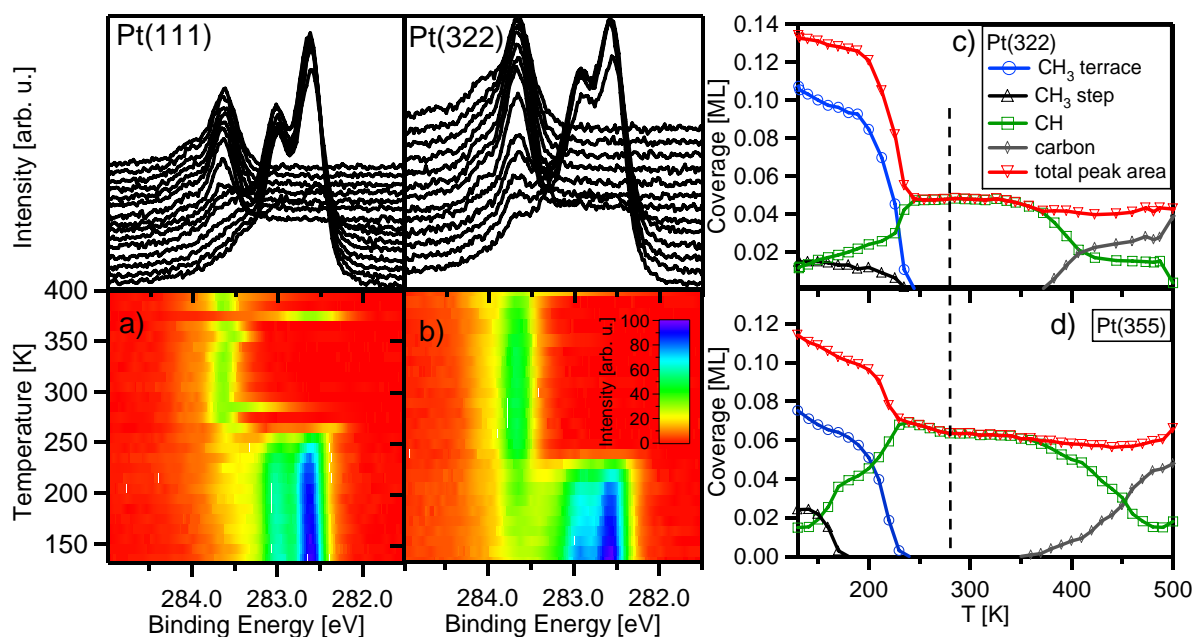


Fig. 3: Waterfall plots (top) and colour-coded density plots (bottom) of C 1s spectra obtained by TPXPS during heating of methyl layers on a) Pt(322) and b) Pt(355). The quantitative analysis of these TP-XPS experiments is shown in c) for Pt(322) and in d) for Pt(355). The dotted line describes the transition temperature on Pt(111).

A comparison of the quantitative analysis of data from both stepped surfaces is depicted in Fig. 3 (c) and (d). Using the same heating rates, different transition temperatures can be seen. On Pt(111), the first dehydrogenation step ($\text{CH}_3 \rightarrow \text{CH}$) is finished at 280 K (dashed line) and the second one ($\text{CH} \rightarrow \text{C}$) starts only at 430 K [1]. On Pt(322), the first step is finished at 240 K for both terrace and bridge CH_3 , while complete dehydrogenation starts at 370 K. For Pt(355), dehydrogenation from CH_3 to CH is finished again at 240 K for terrace species, but step species are completely dehydrogenated already at 180 K. The second reaction step starts at 360 K [4]. So both stepped surfaces are more reactive towards dehydrogenation, with Pt(355) being the most active one. Interestingly, the CH species only gives rise to one C 1s component, thus not enabling discrimination between terrace and step species. The observed different thermal reactivity of the stepped surfaces could also explain the recently reported observation of an enhanced initial sticking coefficient for a stepped Pt(533) surface, since those measurements have been performed at a surface temperature of 600 K, thus including the subsequent surface dehydrogenation steps [2].

This work has been supported by the DFG (Ste 620/4-3).

* New address: Wilhelm-Ostwald-Institut für Physikalische und Theoretische Chemie, Universität Leipzig, Linnéstr. 2, D-04103 Leipzig

[1] T. Fuhrmann et al., Chem. Phys. Lett. 390 (2004) 208; T. Fuhrmann et al., New J. Phys. 7 (2005) 107.

[2] A. T. Gee et al., J. Chem. Phys. 118 (2003) 3334.

[3] R. Denecke et al. Surf. Rev. Lett. 9 (2002) 797.

[4] C. Papp et al., J. Phys. Chem. C In press.

[5] B. Tränkenschuh et al., Surf. Sci. 601 (2007) 1108.

Preferential oxidation of CO over supported and alloy catalysts in H₂-rich gas for fuel cell applications

D. Teschner¹, E. Vass¹, S. Zafeiratos¹, P. Schnörch¹, M. Hävecker¹, A. Knop-Gericke¹,
H. Sauer¹, J. Kröhnert¹, F. Jentoft¹, R. Schlögl¹, G. Hutchings², O. Pozdnyakova-Tellinger³,
K. Lázár³, A. Wootsch³

¹*Fritz-Haber-Institut der Max-Planck-Gesellschaft, Faradayweg 4-6, D-14195 Berlin*

²*Cardiff University, POB. 912, CF10 3TB, Cardiff, United Kingdom*

³*Institute of Isotopes, CRC, HAS, POB 77, Budapest, H-1525, Hungary*

Scientific background:

Application of fuel cell powered systems in transportation recently receives increasing attention because of their theoretically high fuel efficiency and low environmental impact. Among the numerous types of fuel cells developed so far, one of the most promising is the Proton Exchange Membrane Fuel Cell (PEMFC) operated with hydrogen. However, depending on the type of anode, the CO concentration in the hydrogen feed must be kept under 1-100 ppm [1]. During the production of hydrogen by reforming a noticeable amount of CO (5-15%) is formed together with H₂, H₂O and CO₂. First a water gas shift (WGS) stage reduces the amount of CO to 0.5-1% [2]. This still high amount of CO can be removed by preferential oxidation (PROX) using mainly Pt, Cu(Ox) or Au nanoparticles supported on reducible oxides (CeO₂, Fe₂O₃) or using bimetallic catalysts like Pt_xSn. The difficulty to overcome is to selectively oxidize CO in a very high excess of hydrogen with as little water formation as possible. The interesting point on these materials is that they show high selectivity towards CO oxidation and optimal performance at or near the temperature on which the fuel cell operates, therefore providing the possibility of implementing the catalyst directly into the fuel cell and make system integration possible for mobile applications.

Experimental and aim of the work

Pt/CeO₂, Pd/CeO₂, CuO/CeO₂ samples were prepared by wet impregnation while Au/Fe₂O₃ and Pt₃Sn by precipitation. All catalysts (except Au/Fe₂O₃: only dried, or dried and calcined) were calcined and reduced. The samples were tested for their catalytic performance in the PROX reaction and were characterized by HRTEM, XRD, and ¹¹⁹Sn-Mössbauer spectroscopy. In situ investigations were conducted by DRIFTS and by XAS and high-pressure XPS at BESSY. Our objective was to correlate structure, surface electronic state and surface species with the catalytic performance for all these different materials and thus indicate mechanistic similarities/differences. Further aim was to elucidate whether one general reaction mechanism applies for all these materials.

Results

Mössbauer and XRD measurements suggested the formation of well-ordered Pt₃Sn alloy after high-temperature O₂/H₂ treatment of the Pt_x/Sn precipitate. On the other hand, the

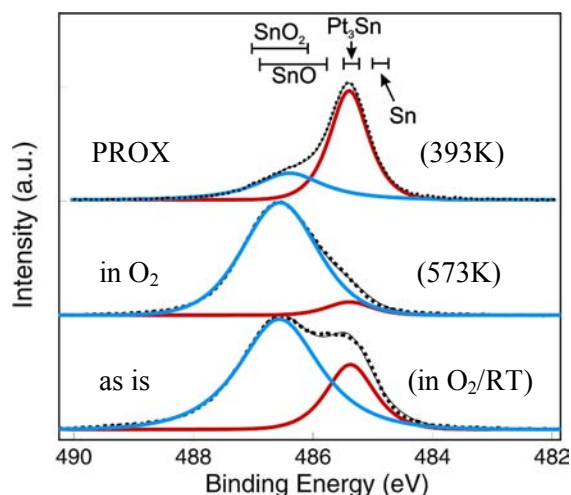


Figure 1: Sn 3d region of Pt₃Sn under different conditions; (pressure: 0.5-1 mbar)

surface of Pt_x/Sn during oxidation was dominated by SnO_x, which was not removed completely in the final reductive treatment (Figure 1). Even during the PROX reaction, high-pressure XPS (XPS) revealed the existence of a mixed Pt₃Sn/SnO_x surface with OH groups and adsorbed water on the oxide. The results indicate a bifunctional mechanism, the isolated carbonyls being converted by an oxidant from the tin-oxide phase.

Contrary to the Pt-Sn alloy, CO interacts very strongly with platinum on Pt/CeO₂ [3] giving rise to high carbonyl coverage throughout the parameter field (pCO, pO₂, T) studied. Likely no oxygen activation occurs on Pt, and no correlation of any IR-active species (inc. carbonyls) with the activity could be found. HRTEM [4] indicated an ordered oxygen vacancy

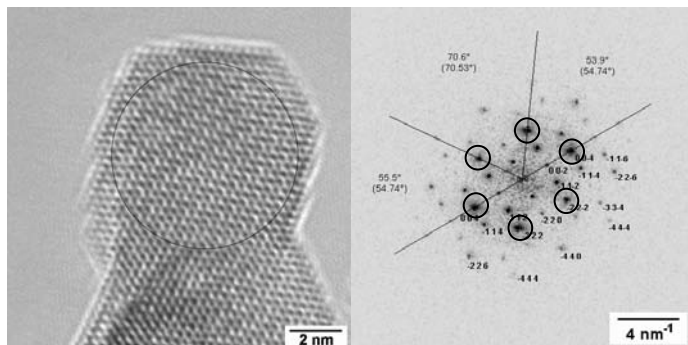


Figure 2: HRTEM image of Pt/Ceria after PROX reaction; the power spectrum indicates reflections not allowed for CeO₂ (these are the spots not marked with circles)

structure (CeO_{1.695}) after use in the PROX reaction (Fig. 2), while XPS revealed an only slightly reduced surface (mainly Ce⁴⁺) with the vacancy density depending on the CO/O₂ concentration of the feed. The CO oxidation activity seems to correlate with the abundance of oxygen vacancies. At higher

vacancy density water desorption is hindered, thus surface water blocks H_{ads} oxidation sites. All these results are in good accordance with the exceptionally low optimal operation temperature (~330–340 K).

Pd/CeO₂ performed poorly in the PROX reaction [5]; CO conversion was limited to ~10%. High-pressure XPS showed that ceria itself is in a similar state as in Pt/CeO₂, therefore the bad performance was related to palladium. The same XPS experiments clearly indicated that a Pd-hydride was responsible for the high hydrogen oxidation activity.

Copper remained mainly CuO in CuO/CeO₂ under PROX condition, but on the surface Cu₂O appeared. The surface reduction coincided with the onset of PROX activity, hence the

best performance was observed at ~400–430 K. Partial pressure dependent in-situ DRIFTS experiments indicated that, unlike on Pt/CeO₂, the CO oxidation activity correlated with the carbonyl coverage. XPS showed an almost entirely oxidized ceria surface; hence no H₂ activation and hydrogen spillover occurred on the copper-oxide particles.

HRTEM indicated metallic gold particles in the pre-calcined Au/Fe₂O₃ sample, and no

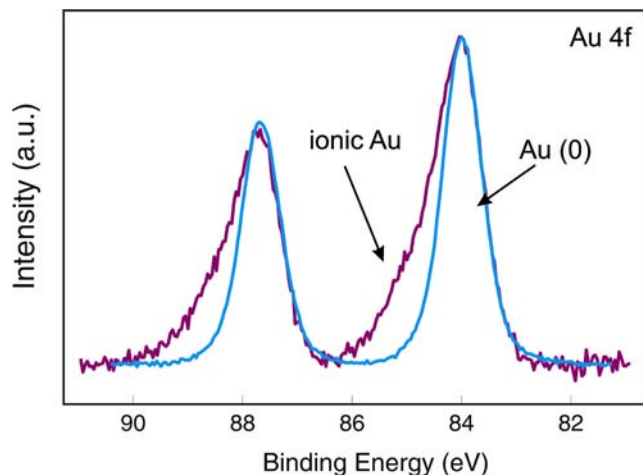


Figure 3: Au 4f region of Au/Fe₂O₃ during PROX reaction (~ 1 mbar); Good catalyst, pre-calcined at 823 K (blue); dried sample (magenta)

particles were found before calcination (in the dried state). XPS confirmed the presence of *only* metallic gold during PROX reaction with the pre-calcined material, however ionic gold was clearly observed with the dried sample. Small metallic gold particles on Fe₂O₃ are selective in the PROX process, while ionic

gold turned out to be very active in the undesired side-reaction of H₂ oxidation [6]. Therefore a calcination step is crucial to synthesize a selective gold sample, however too high temperature (873 K) induce sintering, which result in a completely inactive material.

Conclusion

There are several ways to reach (or at least come close) to targeted performance in PROX reaction: use materials with high intrinsic selectivity (small metallic Au particles); do not activate H₂ (CuO); avoid materials with high activity in H₂ oxidation (Pd, ionic gold); suppress desorption of the undesired side product (O vacancies in Pt/Ceria); separation of CO and O₂ activation. Therefore it is likely that no general mechanism can be formulated.

Acknowledgement

The authors thank the BESSY staff for their continual support during the measurements. The work was supported by the Athena Consortium.

References

- [1] A. J. Appleby, F. R. Foulkes, Fuel Cell Handbook, Van Nostrand Reinhold, New York, 1989.
- [2] J. N. Armor, Appl. Catal. 176 (1999) 159.
- [3] O. Pozdnyakova, D. Teschner, A. Wootsch, J. Kröhnert, B. Steinhauer, H. Sauer, L. Toth, F. C. Jentoft, A. Knop-Gericke, Z. Paál, R. Schlögl, J. Catal. 237 (2006) 1.
- [4] D. Teschner, A. Wootsch, O. Pozdnyakova, H. Sauer, A. Knop-Gericke, R. Schlögl, RKCL. 87 (2006) 235.
- [5] O. Pozdnyakova, D. Teschner, A. Wootsch, J. Kröhnert, B. Steinhauer, H. Sauer, L. Toth, F. C. Jentoft, A. Knop-Gericke, Z. Paál, R. Schlögl, J. Catal. 237 (2006) 17.
- [6] P. Landon, J. Ferguson, B. E. Solsona, T. Garcia, A. F. Carley, A. A. Herzing, Ch. J. Kiely, S. E. Golunskic, G. J. Hutchings, Chem. Commun. (2005) 3385.

In-situ time resolved study of the transformation of goethite to hematite at 250°C and 50bar

Murray, Joseph

We have investigated the kinetics of transformation of goethite to hematite under hydrothermal conditions ranging from 230°C to 250°C in sodium hydroxide liquor. Our results have shown that the rate of transformation is dependant on the temperature, available hematite surface area and the presence of anatase.

Experiments were conducted at 250, 240 and 230°C where the rate of transformation was seen to decrease with the decreasing temperature. The plot of extent of reaction versus time illustrates this in figure 1. The extent of the reaction was measured by the dissolution of goethite as it was the strongest peak signal available and its disappearance meant the completion of transformation. We observed that transformation does not occur in the absence of hematite seed within several hours, and the rate of the transformation rapidly decreases for temperatures below 240°C. The amount of available hematite surface area increases the rate of transformation and was examined by using a fixed ratio of goethite to hematite, but with hematite of different surface areas. The more surface area available, the more growth sites and hence the faster the reaction progressed.

The presence of anatase was found to inhibit transformation with no conversion taking place.

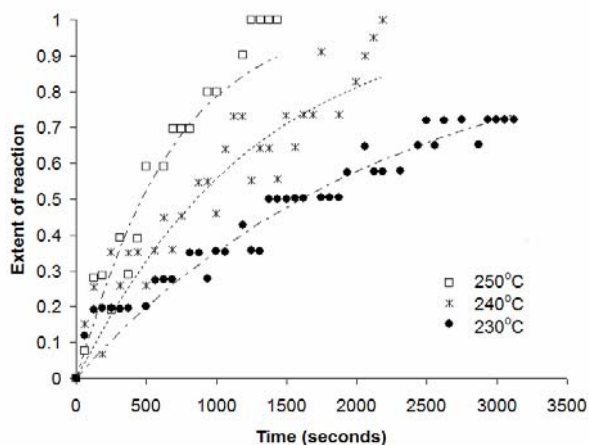


Figure 1: Extent of reaction (alpha) of the transformation of goethite to hematite at three different temperatures.

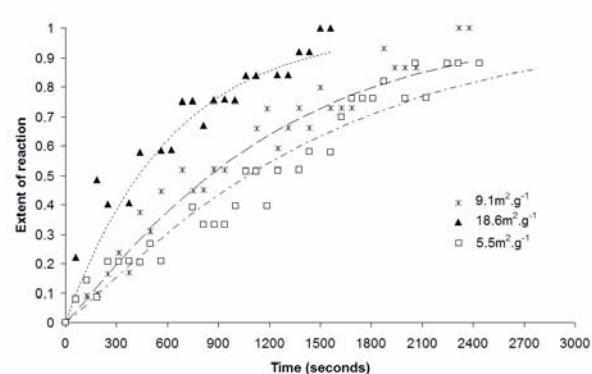


Figure 2: Variation of rate of reaction with hematite surface area.

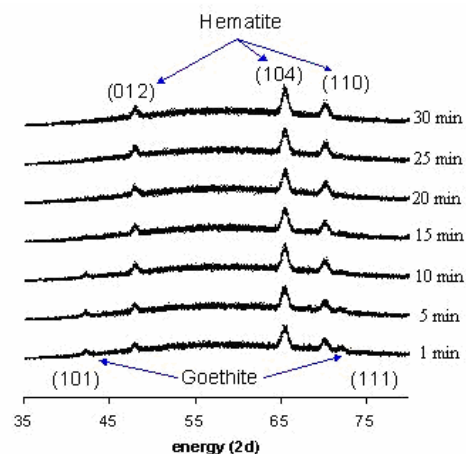


Figure 3: In situ time-resolved synchrotron diffraction patterns of the transformation of goethite to hematite. The (101) peak of goethite is seen to disappear with the appearance of (012) hematite.

In-situ time resolved study of the reaction of calcium hydroxide and anatase at 250°C

Croker, Denise

The reaction of lime and anatase in sodium aluminate solution was investigated.

X-Ray diffraction patterns were collected at 60-second intervals following the addition of calcium hydroxide (lime) and anatase to sodium aluminate solution at 250°C. Due to the large volume of data collected, the diffractograms are presented at ten-minute intervals in Figure 1. Initially only anatase is present, detected by the peak at 50keV (3.5Å). The intensity of this peak decreases for approx. twenty minutes and after this point a new peak appears at 54keV (3.27Å). This is a reflection indicative of kassite- $\text{Ca}(\text{TiO}_2)_2(\text{OH})_2$. Kassite persists and is joined by a perovskite (CaTiO_3) reflection at about 50minutes. The perovskite peak increases for the remainder of the experiment.

The peak area data for the anatase, kassite and perovskite reflections is presented in Figure 2.

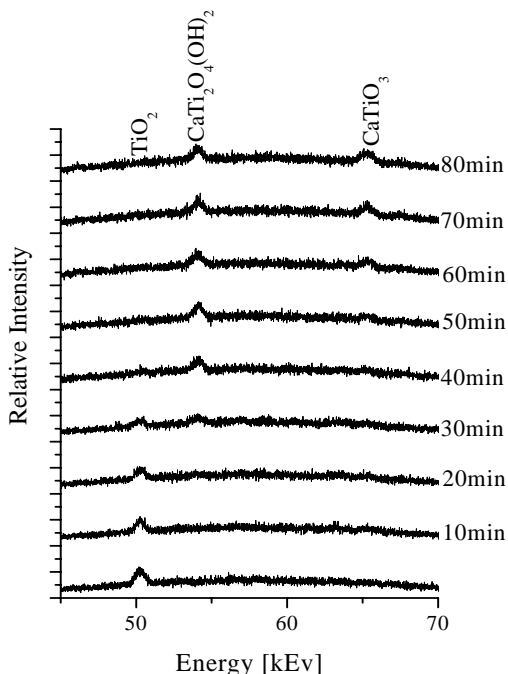


Figure 1: X-Ray diffraction patterns following the reaction of lime and anatase at ten-minute intervals in Bayer liquor at 250°C.

The area of the anatase peak decreases slowly at first and drops sharply once kassite precipitation starts (approx. 18 minutes). It takes just over forty minutes for the anatase peak area to decrease to zero, illustrating that all the anatase has been consumed. Up to this the area of the kassite peak increases steadily, reaching a maximum at approx. 42 minutes.

A small amount of perovskite appears to be present from the start of the experiment. At 40minutes, the area of this peak begins to increase rapidly. This occurs after the anatase peak has disappeared. The kassite peak itself begins to decrease inferring that the kassite is being consumed by perovskite formation.

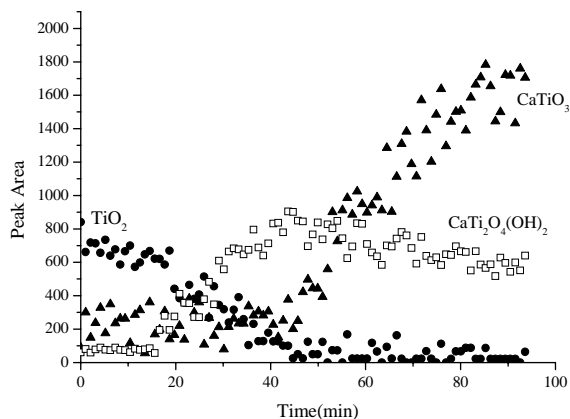


Figure 2: Peak areas of the anatase, perovskite and kassite reflections, obtained by integrating the area under the reflections in figure 2. Kassite precipitation is only significant after 18 minutes and reaches a maximum at about 40 minutes. Perovskite formation only becomes significant after this point.

The data suggests that kassite can act as an intermediate in the formation of perovskite but further investigation is necessary.

Dehydrogenation and Oxidative Dehydrogenation of *n*-Butane using Vanadium Based Catalysts: an in situ XPS study

E.M. Vass, D. Teschner, M. Hävecker, S. Zafeiratos, P. Schnörch,
A. Knop-Gericke, R. Schlögl

Fritz-Haber-Institut der Max-Planck-Gesellschaft, Faradayweg 4-6, D-14195 Berlin

Scientific Background and Aims

Catalytic dehydrogenation of light alkanes is a valuable reaction for the production of essential building blocks required for industrial applications. One reaction of particular interest is the dehydrogenation of *n*-butane to form butenes and butadiene, which are precursors for the manufacture of synthetic rubber. Currently many commercial processes for the dehydrogenation of light alkanes contain chromia or platinum supported on alumina. The process is endothermic, requiring high reaction temperatures and low pressures. Unfortunately at higher temperatures cracking can occur and formation of coke or carbonaceous deposits is enhanced, resulting in catalyst deactivation. Hence oxygen regeneration steps are required to remove carbon deposits from the catalyst surface. Research continues in this area as it is important to understand the nature of the active species and causes of deactivation in order to develop future catalysts.

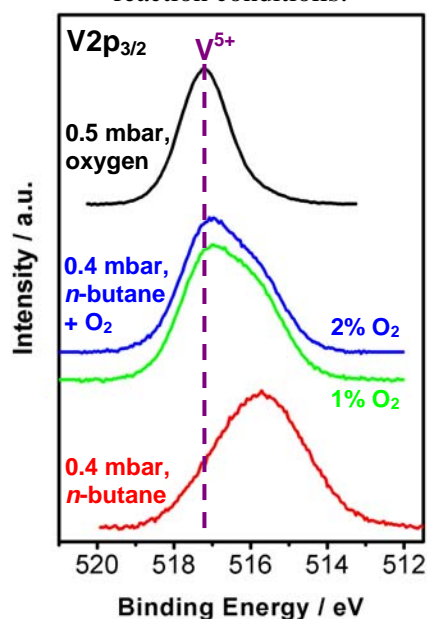
Vanadia-containing catalysts have been shown to be active as selective dehydrogenation or oxidative dehydrogenation catalysts [1, 2]. In the current study, we selected V_xO_y /alumina catalysts with a range of vanadium loadings and used surface sensitive techniques to develop links between surface structure and catalytic activity.

Results and Discussion

The surface electronic structure of V_xO_y /alumina catalysts (1-8 wt% V) was investigated using high pressure in situ XPS. Typically the catalyst surface was examined under either a dehydrogenation (0.4 mbar *n*-butane) or oxidative dehydrogenation (0.4 mbar 1-2 % oxygen in *n*-butane) atmosphere. The reaction products were monitored concurrently by proton transfer reaction mass spectrometry (PTRMS).

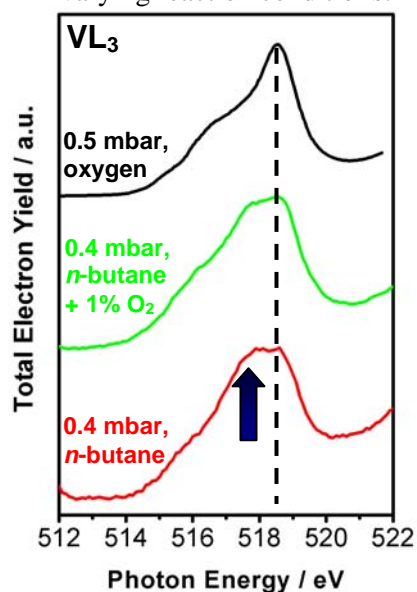
In and oxygen atmosphere, the XP spectrum (figure 1) shows that vanadium is in the +5 oxidation state. Raman spectroscopy [3] showed that the fresh

Figure 1. $V2p_{3/2}$ XPS of 3.5% V/alumina under varying reaction conditions.



3.5% V/alumina catalyst contains mainly polyvanadates. Dehydrogenation and oxidative

Figure 2. VL₃ NEXAFS of 3.5% V/alumina under varying reaction conditions.



dehydrogenation (ODH) of *n*-butane were investigated over the 3.5% V/alumina catalyst. For both reactions, the catalysts were found to be active and the major products formed were butene and butadiene. On addition of oxygen (1-2 %) to the feed, the product selectivity changed and formation of oxygenated side-products, such as furan and dihydrofuran, increased. The change of feed to include oxygen also caused a decrease in formation of benzene which has been associated with catalyst deactivation.

Vanadium XP (figure 1) and NEXAF (figure 2) spectra measured during the reactions confirm that addition of oxygen to the reaction mixture helps to maintain a V⁵⁺ species. In particular the V2p XPS (figure 1) shows marked differences in the oxidation state of the vanadium species under varying reaction conditions. Pure *n*-butane as the reactant shows an increase in reduction with an average oxidation state of vanadium less than 4. Ideally, the oxygen content of the feed could be optimised to reduce formation of oxygenated side products while maintaining a higher vanadium oxidation state.

Finally, the 1, 3.5 and 8 % V/alumina catalysts were examined ex situ after deactivation under ‘real’ dehydrogenation conditions (1 bar *n*-butane, 723 K). V2p XPS showed a main peak at 515.9 eV, indicating that mainly V³⁺ species were present. Hence the vanadium was greatly reduced during the deactivation process. The carbon K-edge absorption spectrum for the 3.5% V/alumina (figure 3a) and 8% V/alumina are similar, the predominant feature at 288.5 eV shows the presence of unsaturated hydrocarbons when compared with reference compounds (figure 3). Due to the absence of higher energy features, it is unlikely that the carbon species is solely graphite. The carbon NEXAFS of 1% V/alumina (not shown) was similar to that of a styrene reference [5].

Figure 3. C K-edge NEXAFS of post-reaction 3.5% V/alumina (a) and reference spectra of *n*-butane [4] (b), benzene [4] (c) and graphite (d).

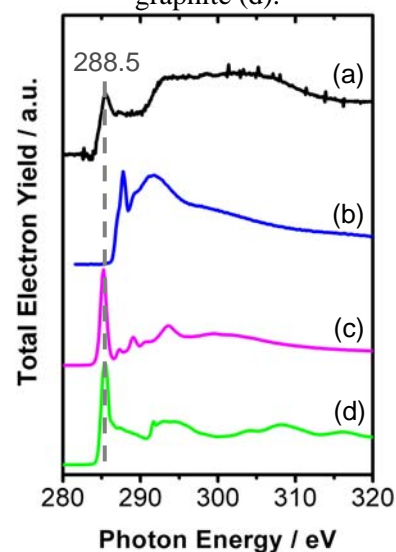
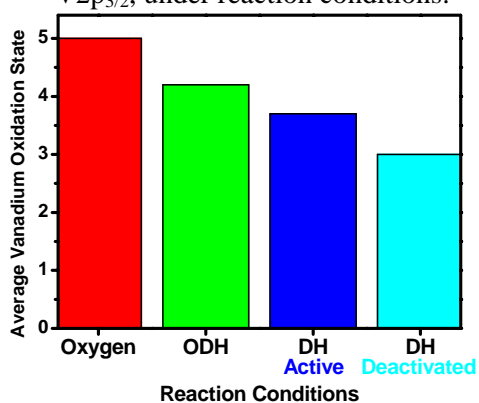


Figure 4. Average vanadium oxidation state, calculated by deconvolution of $V2p_{3/2}$, under reaction conditions.



This is in agreement with Raman spectroscopy studies [6] which suggest that polystyrene is an intermediate in the formation of carbon deposits during dehydrogenation over V_xO_y /alumina catalysts.

By combining the results of the in- and ex-situ experiments, a general trend relating vanadium oxidation state to catalytic activity under different reaction conditions can be observed (figure 4). Under dehydrogenation

conditions (*n*-butane, 723 K) the vanadium oxidation state decreases with time on stream. After this initial change carbon was deposited on the catalyst surface, causing deactivation of the catalyst. Hence, the investigations suggest that maintenance of a higher oxidation state of vanadium is a crucial step in preventing catalyst deactivation.

Conclusions

In the final analysis, high pressure in situ XPS and NEXAFS were shown to be useful analytical techniques for the investigation of V_xO_y /alumina surfaces under reaction conditions. The benefit of oxidative dehydrogenation was to maintain a higher oxidation state of vanadium; however more oxygenated side-products were produced. Links between the electronic structure of vanadium and catalytic activity were successfully established.

Acknowledgements

The authors would like to thank the staff of BESSY for their support during the measurements. The funding for this work was provided by the ATHENA Project, which is jointly funded by the EPSRC (UK) and Johnson Matthey Catalysts plc.

References

- [1] J.M. Lopez Nieto, P. Concepcion, A. Dejoz, H. Knozinger, F. Melo, M.I. Vazquez, *Journal of Catalysis*, **189** (2000), 147.
- [2] I.E. Wachs, B.M. Weckhuysen, *Applied Catalysis A: General*, **157** (1997), 67.
- [3] Z. Wu, H.-S. Kim, P.C. Stair, S.R. Rugmini, S.D. Jackson. *J. Phys. Chem. B* **109** (2005), 2793.
- [4] A.P. Hitchcock, D.C. Mancini, *Journal of Electron Spectroscopy and Related Phenomena*, **67** (1994), 1.
- [5] C. Kolczewski et al, *J. Chem. Phys.* **124** (2006), 034302.
- [6] S.D. Jackson, S. Rugmini, P.C. Stair, Z. Wu, *Chemical Engineering Journal*, **120** (2006), 127.

Protein adhesion on magnesium implants during in vivo and in vitro corrosion.

¹R. Dargel, ¹K. Bechstein, ²F. Witte, ¹C. Vogt

¹Institute for Inorganic Chemistry, University of Hannover, Callinstr. 9, 30167 Hannover, Germany,

²Department of Orthopaedic Surgery, Hannover Medical School, Anna-von-Borries-Str.1-7, 30625 Hannover, Germany

Introduction

Biodegradable magnesium alloys represent a novel class of temporary metal implants that corrode in vivo¹. The major aim in the development of biodegradable metal implants is to control the corrosion process in vivo, but as the environment of in vitro experiments still differ from in vivo conditions, predictions about the in vivo corrosion are difficult to make. However, it is crucial to understand the degradation process in vivo in order to assess potential health risks and implant functionality. It is well known that proteins affect the corrosion behaviour of metals, and that the presence of proteins can either inhibit or accelerate the corrosion process^{2,3}.

Of particular interest are the corrosion layer and its closest vicinity of only a few micrometers, as possible structural changes for example in the distribution of proteins, fatty acids and peptides will probably occur in this area and influence the in vivo corrosion process. In this study, we evaluated the feasibility of synchrotron-based infrared micro-spectroscopy (SR-FTIR) for spatially (laterally) high-resolved and sensitive analysis of organic structures on a micrometer scale. Embedded bone cross-sections of rabbit-bones after the implantation of degradable magnesium rods as well as in vitro corroded magnesium implants were investigated. Different magnesium alloys were used to show the more general approach of protein adsorption to different biodegradable magnesium implants.

Experimental setup

Synchrotron-radiation based infrared spectroscopy was performed in reflection mode on explanted bone-implant specimens and on specimens that were immersed in human serum under physiological conditions. The bones of adult New Zealand White rabbits with implants of magnesium alloy LAE442 were harvested 2 and 12 weeks after implantation. The in vitro measurements were performed on magnesium alloy WE43 after immersion in human fresh frozen plasma at 37°C and constant stirring for 24 and 56 hours. After immersion the samples were dried and measured with SY-FTIR.

In vivo and in vitro specimens were fixated, embedded and cut to prepare cross-sections. All animal experiments were performed in accordance with the animal welfare legislation of the county of lower saxony, Germany. The measurements of the in vivo samples were performed in reflection mode, with an aperture of 30 microns, a spectral resolution of 4 cm⁻¹ wavenumbers and a step size of 5 microns. The investigation of in vitro treated magnesium alloys were carried out with an aperture of 20 microns, a spectral resolution of 4 cm⁻¹ wavenumbers and a step size of 5 microns.

Results

Adhesive proteins were found in vivo on the surface of implanted magnesium samples adjacent to surface areas of direct bone contact at the 2 and 12 week time interval.

In the in vivo samples at a time interval of 12 weeks we found at least 4 areas with differing compositions (Fig. 1). EDX distribution-images basing on the intensities of the Calcium signal (Fig.1a) and of the Phosphorous signal (Fig. 1b) clearly indicate that area 2 consists of bone material while there are no bone signals in area 3. This agrees with the distribution images based on the IR-intensities of the phosphate bands (Fig.1d). The IR spectra shown in Fig.1e reveal the broad phosphate bands of the calcium apatite as well as Amide I (1655 cm⁻¹) and Amide II (1543 cm⁻¹) peaks, which originate from the proteins within the bone tissue. In the spectrum measured in area 1 far away from the bone tissue we observe these amide peaks at the same wavenumbers, which indicates that proteins have migrated out of organic tissue onto the corrosion layer. The absence of phosphate peaks proves the absence of bone tissue, which agrees with the EDX-measurements. Distribution images based on the peak intensity of

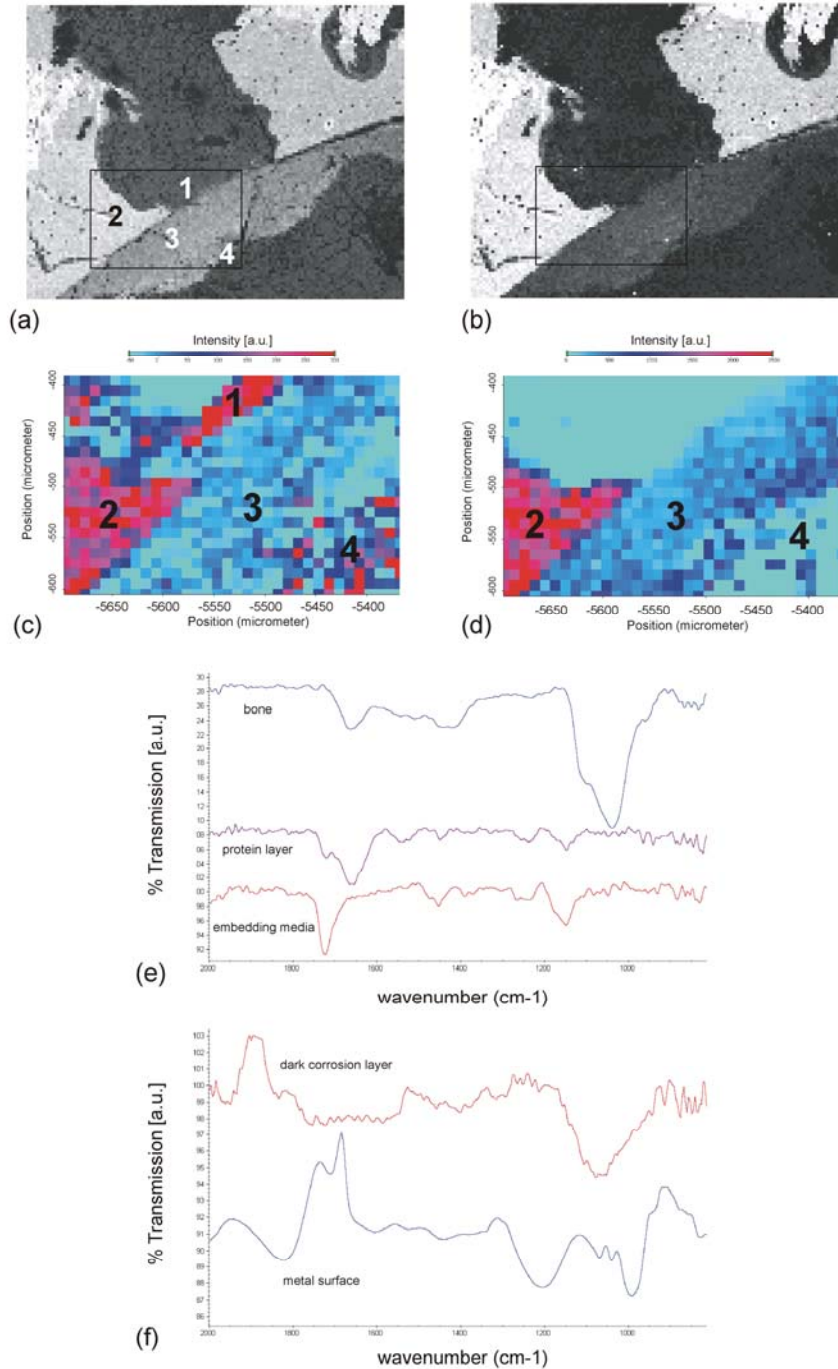


Figure 1: Magnesium alloy LAE442 (area 4) implanted for 12 weeks displaying local pure protein agglomeration (area 1) on the corrosion layer (area 3) by spatial distribution of amide I (c, e) and phosphorous bands (d, e) in SY-FTIR and no calcium (a) and no phosphorous content (b). Area 2 represents bone matrix.

the Amide I bands (Fig.3c) clearly show that proteins only occur within a thin layer of about 20 microns at the surface of the corrosion layer, while no protein signals can be found within the corrosion layer.

In vitro tests reveal that protein adhesion could also be determined on the corrosion layer of WE43 samples by SY-FTIR as early as 24 and 56 hours after immersion in human serum at 37°C and constant stirring (Fig. 2). Proteins adhere on the top of the corrosion layer. No

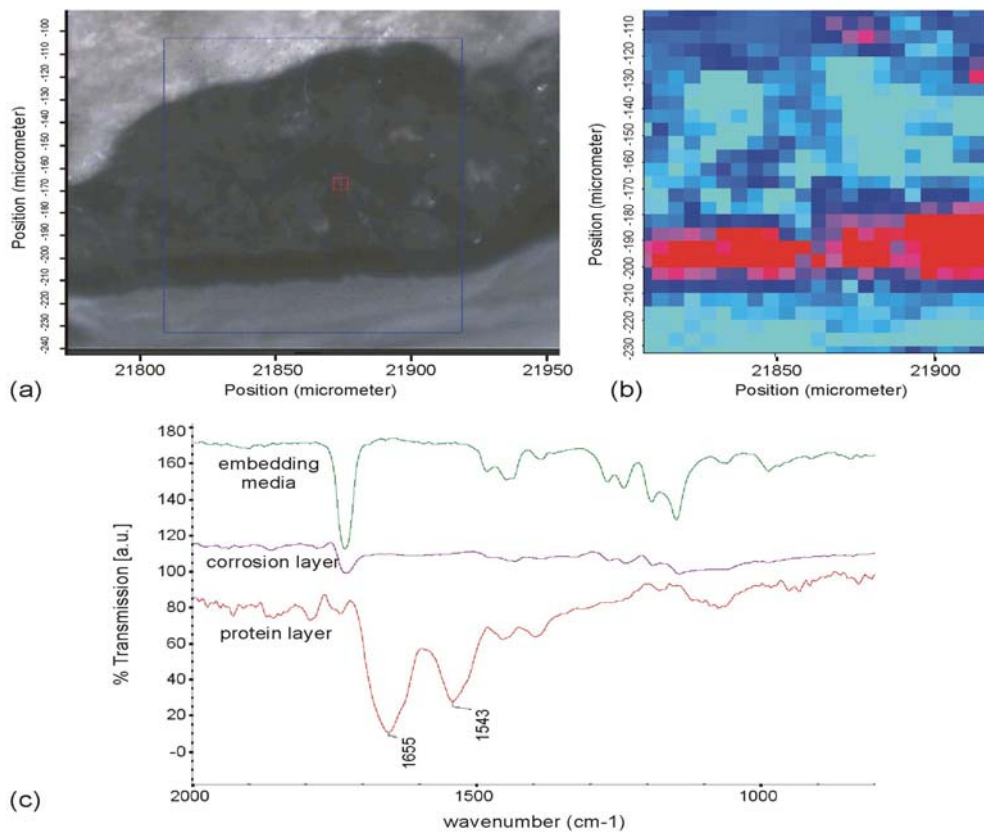


Figure 2: Image of the corroded in vitro magnesium alloy (a), displayed in high (red) intensities of amide I bands in a mapping (b). Typical IR spectra of corrosion layer, protein layer and embedding media display typical amide I and II bands only in the protein layer (c).

proteins or lipids were detected inside the corrosion layer. Thereby, the reflected IR signals from the uncorroded metal were distorted, preventing a sound signal analysis.

Discussion

The measurements indicate that SY-FTIR is an appropriate analytical technique to gain spatially high-resolved IR-spectra from cross-sections of bones and the surface of embedded sample materials. Furthermore, the received IR-spectra demonstrated the existence of at least three regions of different chemical compositions in the vicinity of the corroded magnesium alloys. We found that the proteins adhere on top of the corrosion layer independently of the magnesium alloy in vitro and in vivo forming an additional thin layer. This thin protein layer was not capable in preventing the growth of the corrosion layer into the bulk material. The proteins remained on surface of the corrosion layer were not observed inside the corrosion layer by SY-FTIR. These results implicit that proteins can interfere with the corrosion process just at the surface of implant, but this protein layer is not able to stop the corrosion process beneath it. We have shown that SY-FTIR in reflection mode is suitable for the investigation of the bone-implant interfaces of embedded magnesium implants.

References

- [1] Witte F, Kaese V, Haferkamp H, Switzer E, Meyer-Lindenberg A, Wirth CJ, Windhagen H. In vivo corrosion of four magnesium alloys and the associated bone response. *Biomaterials* 2005;26:3557-3563.
- [2] Sousa SR, Barbosa MA. Corrosion resistance of titanium CP in saline physiological solutions with calcium phosphate and proteins. *Clinical Materials* 1993;14:287-294.
- [3] Williams RL, Brown SA, Merritt K. Electrochemical studies on the influence of proteins on the corrosion of implant alloys. *Biomaterials* 1988;9:181-186.

Experimental and *ab initio* studies of the PbTe (001) surface

L.V.Yashina¹, R. Püttner², A.S.Zyubin³, S. Dedyulin¹, M.Poygin², V.S.Neudachina^{1,3},
V.I.Shtanov¹, S.Yu. Vasiliev¹

¹*Department of Chemistry, Moscow State University, Leninskie gory, 119992 Moscow, Russia*

²*Institut für Experimentalphysik, Freie Universität Berlin, Arnimallee 14, D-14195 Berlin-Dahlem, Germany*

³*Institute of Problems of Chemical Physics RAS, 142432 Chernogolovka, Moscow Region, Russia*

The surfaces of lead chalcogenides have been subjected to numerous theoretical and experimental investigations [1-2]. The studies are mainly motivated by the importance of these semiconductors for long-wavelength sensor devices, diode lasers, and the thermophotovoltaic energy converters production [3]. Notwithstanding the fact that the physics and chemistry of bulk lead chalcogenides are widely covered in literature, the structural and electronic properties of the PbTe (001) surface are still unclear. One of the important characteristics of the surface is the surface core-level shift (SCLS), i.e. the difference in terms of binding energies (BEs) of core-level electrons originating from surface and bulk-related atoms. Information on the SCLS may be helpful to understand the surface reactivity. SCLS was experimentally observed in S 2*p* spectrum for PbS surface (001) at LN₂ temperature [4,5]. In the present report, we describe the results of a X-ray photoelectron spectroscopy (XPS) study of SCLS at the (100) surface of PbTe.

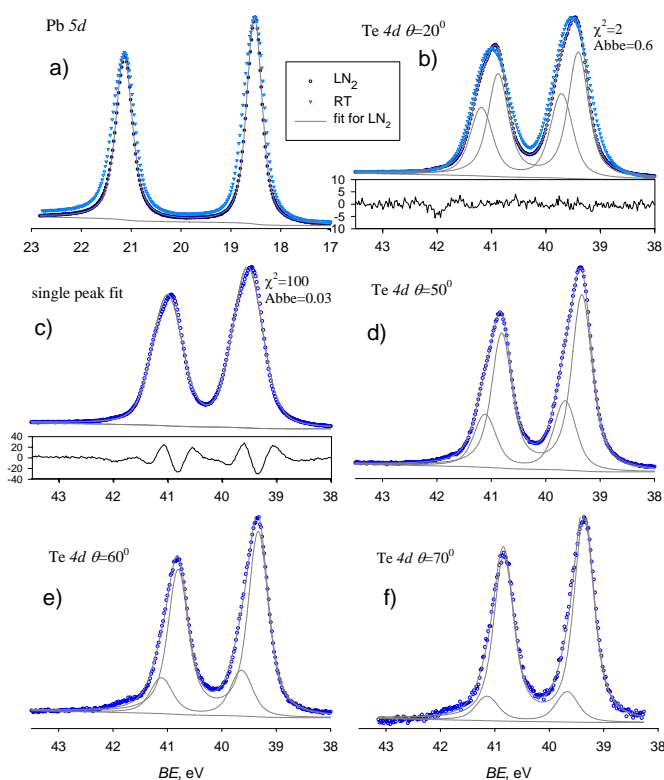


Fig.1. Spectra for PbTe (001) surface obtained at LN₂ and RT $h\nu=125$ eV: a) Pb 5*d*, b) Te 4*d* 2-doublet fit, c) same spectrum as in Fig.b, but with single doublet fit, d-f) the spectra obtained at different detection angles.

The photoemission experiments were performed at the Russian-German beamline. The spectra were taken with an experimental setup that consists of a preparation chamber equipped by an analysis chamber equipped with a CLAM 4 (Thermo VG Scientific) electron energy analyzer. Clean surfaces for the measurements were obtained by cleaving the PbTe single crystals along the (001) plane under a base pressure in the low 10^{-10} mbar range. The structural perfection of the cleaved surfaces was confirmed by sharp LEED pattern. The Pb 5*d* and Te 4*d* core-level spectra were recorded at different photon energies and detection angle, both at LN₂ temperature and at room temperature (RT). All spectra were fitted by the Gaussian – Lorentzian convolution functions with simultaneous optimization of the background.

The Pb 5*d* and Te 4*d* spectra are shown Fig. 1. The Pb 5*d* spectra for both, LN₂ temperature and RT are well described with 1 doublet; therefore we can conclude that the SCLS has to be very small for Pb atoms. A difference in the phonon broadening is observed for the spectra taken at LN₂ and room temperature. A one-doublet approximation for the Te 4*d* spectrum leads to systematic

deviation of the calculated profile from the experimental data, which is clearly illustrated by the residuum in Fig.1c and the statistical parameters, especially Abbe criterion. The best description for the Te 4d spectrum was obtained by fitting two doublets with a splitting of 0.30 ± 0.02 eV. It should be mentioned that at room temperature these two components are not resolvable due to phonon broadening.

In order to ascribe the observed doublets in the Te 4d spectra to the bulk and surface states, additional experiments have to be performed. One approach to this question is a variation of the photon energy or the detection angle since this leads to a variation of the surface sensibility and, hence, to a change in the relative intensities of the components. A second approach for the identification of the surface component is the comparison of the spectra recorded before and after a surface reaction (e.g. due to oxidation), which influences the uppermost layer only.

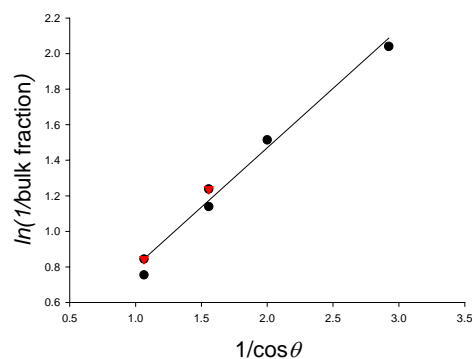


Fig. 2. Correlation between the intensity of bulk-related peak and detection angle θ .

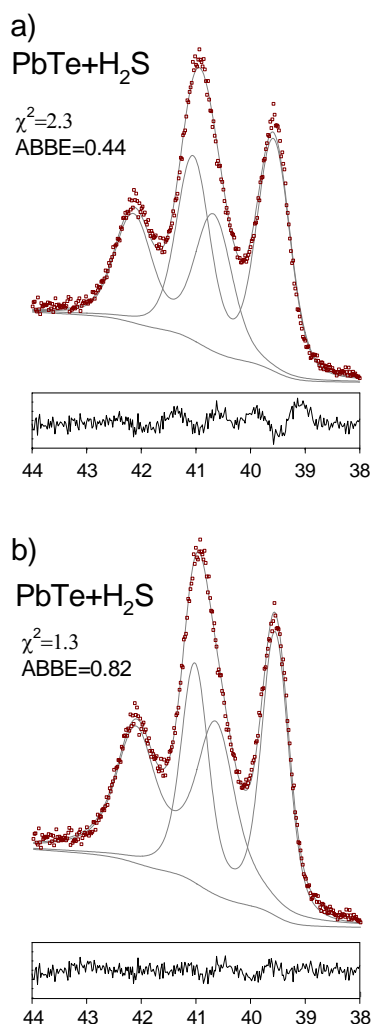


Fig. 3. Te 4d spectra with IML H₂S. Contrary to (a) a SCLS of the Te 4d level is taken into account in (b).

In our experiments, the variation of the photon energy was limited by the strong decrease of photoionisation cross-section and the photon flux provided by the monochromator at higher PEs. By changing the detection angle θ , we observed a good qualitative correlation between the experimental surface-to-bulk intensity ratio, I_s/I_b , and the Hill equation (see Figs 1d-f and 2):

$$I_s / I_b = \exp\left(\frac{d}{\lambda \cos \theta}\right) - 1$$

where d is the interatomic distance and λ the electron inelastic mean free path.

We also performed the modification of the clean PbTe (001) surface by means of O₂ and H₂S adsorption. Unfortunately, these reactions lead to several intermediate states, which overlap with the initially observed bulk-related peak. Therefore, an exact separation of the bulk component in order to reliably define the spectral parameters is hardly possible. The Te 4d spectra for the PbTe surface after H₂S exposure were treated within two approximations. In the first case (presented in Fig. 3a) the bulk component was treated with fixed parameters for the peak shape, which were obtained from describing the clean PbTe(001) surface with one doublet. In the second case the spectra were treated with the constrained parameters of the bulk-related component derived from fitting the Te 4d spectra of the clean surface with two components. The results are depicted in Fig. 3b. As it is clear from both the differential curves as well as the statistical χ^2 and Abbe criteria, the second option provides a distinctly better description of the experimental data.

In addition, we investigated the cleaved surface with SEM, AFM, and STM, and found that the density of nm-scale and atomic steps is relatively low. As shown in Fig.4 different step sizes including monoatomic steps are present at the surface, however, the fraction of atoms positioned at the step edges does not exceed several

percent of the total amount of surface atoms. Thus we can conclude that the surface imperfection can contribute to Te $4d$ spectrum, however, only with a relatively low intensity.

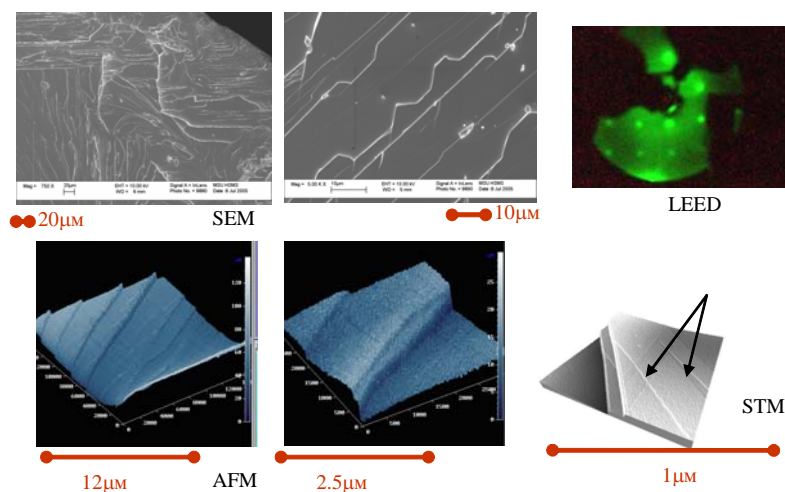


Fig. 4. SEM, AFM, STM images and LEED pattern of PbTe surface. Arrows show atomic steps

(LanL2DZP). The $(\text{PbTe})_{56}$ cluster modelling the (100) surface of PbTe surface is presented in Fig.5. We optimized the coordinates of the “central” 8 atoms. Four of them are located in the centre of the surface-modelling face, and the next four are those situated in the near-surface layer (right under the surface) and are thus directly bonded to the first four ones. We have calculated the core level shifts for the cluster after optimization in the initial state approximation, i.e. as a difference between electrostatic potentials in the centre of the atomic position of a core state of a separated non-excited neutral atom and of a non-excited atom at the surface or in the bulk of the cluster. The calculated SCLS comprises -0.33 eV for Te $4d$ and -0.08 eV for Pb $5d$. The calculated values are close to those observed in the experiment; therefore one may conclude that the SCLS is adequately described in the initial state approximation.

Based on the whole set of experimental data and calculation results, we assume that tellurium atoms are present in the spectra in at least 2 states. One of them is related to bulk, and the second one corresponds to the atoms located at the atomically flat surface. This can serve as a ponderable argument for the presence of SCLS at the (001) surface of pure PbTe.

The authors would like to thank BESSY staff for support.

- [1] A.A. Lazarides, C.B. Duke, A. Paton, A. Kahn, Phys. Rev. B. 52 (1995) 14895.
- [2] J. Ma, Yu Jia, Y. Song, E. Liang, L. Wu, F. Wang, X. Wang, X. Hu, Surf. Sci. 551 (2004) 91.
- [3] D.Khokhlov (Ed.). Lead Chalcogenides: Physics And Applications, Gordon&Breach, 2002.
- [4] J.A. Leiro, K. Laajalehto, M.S. Peltoniemi, M. Torhola, A. Szczerbakow, Surf. Interface Anal. 33 (2002) 964.
- [5] I.G.Batyrev, L.Kleinman, J.Leiro, Phys Rev B 70 (2004) 073310-1-3.

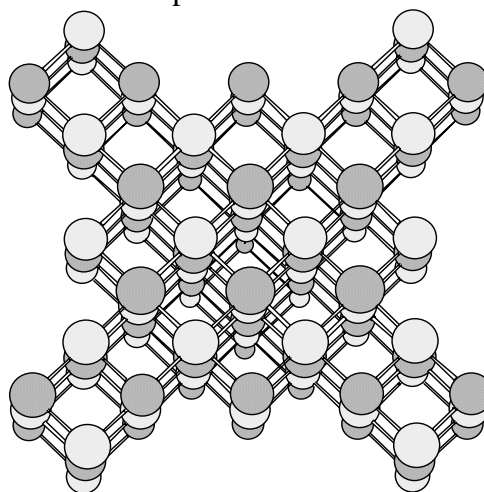


Fig. 5. $(\text{PbTe})_{56}$ cluster modelling PbTe (100) surface. Te atoms are light gray, Pb atoms are dark gray.

Structure of hydrophobically modified telechelic and semi-telechelic poly(2-isopropyl-2-oxazoline in concentrated aqueous solution.

Elena Maltseva¹, Françoise M. Winnik², Franziska Emmerling¹, and Andreas Thünemann¹

¹ Federal Institute for Materials Research and Testing, Richard-Willstaetter-Str. 11, 12489 Berlin, Germany

² Department of Chemistry and Faculty of Pharmacy, Université de Montréal, Pavillon J.-A.-Bombardier, 4075 Montréal, Canada

Water soluble associative polymers have received increasing interest due to their wide-ranging applications from medicine (as drug or gene delivery systems) to microelectronics or paper coatings and paintings (as rheology modifiers). These polymers are designed to undergo a second assembly step *via* non-covalent interactions, with a relatively small number of components, to form nanostructures, such as polymer micelles.

In the present work we reveal the structure of micelles formed by hydrophobically modified poly(2-isopropyl-2-oxazoline) (PIPOZ) in concentrated aqueous solution (10 wt %). Hydrophobic modification of PIPOZ ($M_w = 13\,000$ g/mol, PDI = 1.2) was achieved by introducing *n*-octadecyl groups either on one or on both ends of the polymer chains (semi-telechelic or telechelic PIPOZ, respectively). Both polymers form transparent viscous solutions in water at room temperature.

The SAXS patterns (Figure 1) of 10 wt % semi-telechelic and telechelic PIPOZ in water were measured at the Microfocuse Beamline of BESSY. The best fit of the SAXS data for both polymers was obtained taking into consideration cylindrical shape of the micelles. The SAXS pattern of telechelic PIPOZ is fitted with the core/shell model [1]. The core radius is equal to 1.1 nm while the radius of both core and shell is c.a. 6 nm, a length of the cylinders is ca. 20 nm. In the case of semi-telechelic PIPOZ the experimental curve is fitted with cylinders with length of ca. 40 nm and a radius of 1.3 nm. The later result can be explained by the low electron density contrast between solvent (water) and extended, very good solvated PIPOZ shell that makes the hydrophilic PIPOZ shell ‘invisible’ (contrast matching). Obviously, polymer chains in the telechelic PIPOZ contain less water than in the semi-telechelic PIPOZ.

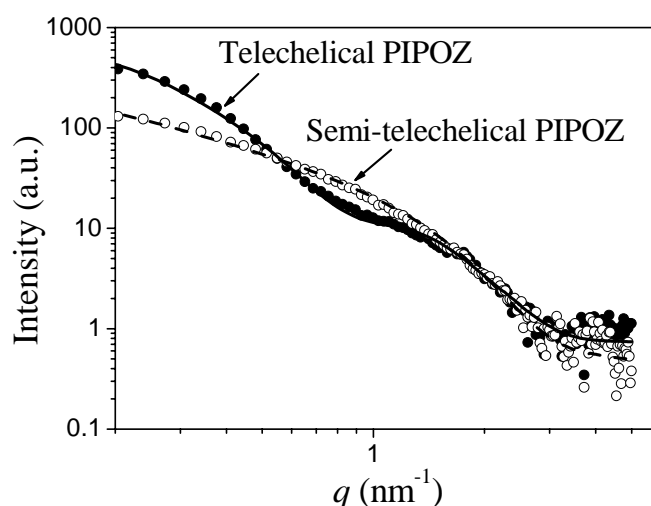


Figure 1. SAXS curves of concentrated telechelic (filled circles) and semi telechelic (open circles) hydrophobically modified PIPOZ. The best fit of the SAXS data for both polymers was obtained considering cylindrical shape of the micelles (solid and dashed lines respectively).

The core for both polymer micellar solutions should be formed by assembled *n*-octadecyl chains and its radius should be smaller than the length of *n*-octadecyl chain in *all-trans* conformation ($l_{\max} = 1.265 \text{ \AA} \cdot 17 + 1.5 \text{ \AA} = 23.0 \text{ \AA}$ [2]). Moreover, the ratios between

core and shell volumes of the model cylinder for telechelic PIPOZ ($V_{\text{core}} / V_{\text{shell}} = 0.05$) is comparable to the calculated ratios between volumes of alkyl chains and PIPOZ ($V_{\text{alkyl chains}} [2] / V_{\text{PIPOZ}} [3] = 0.062$). Since the size of hydrophobic core as well as volumes of core and shell are realistic it can be concluded that both telechelic and semi-telechelic PIPOZ form elongated (cylindrical) micelles (with alkyl chains in the hydrophobic core and PIPOZ chains as the hydrophilic shell) in highly concentrated aqueous solutions.

This work was supported by the Adolf-Martins-Fellowship program of Federal Institute for Materials Research and Testing

References:

- [1]. S. Förster, N. Hermsdorf, C. Böttcher and P. Lindner, *Macromolecules* 2002, **35**, 4096-4105.
- [2] H. Heerklotz et al. *JACS*. 2004, **126**, 16544-16552
- [3] D. W. Van Krewelen „Properties of Polymers“, Chapter 4, **Elsevier, Amsterdam**, 1990

Mechanism for H₂S detection with superionic low-temperature sensors

L.V. Yashina¹, R. Püttner², M. Poygin², V.S. Neudachina^{1,3}, V.I. Shtanov¹, A.B. Tarasov³, A.V. Levchenko³, T.B. Shatalova¹, Yu.A. Dobrovolsky³

¹*Department of Chemistry, Moscow State University, Leninskie gory, 119992 Moscow, Russia*

²*Institut für Experimentalphysik, Freie Universität Berlin, Arnimallee 14, D-14195 Berlin-Dahlem, Germany*

³*Institute of Problems of Chemical Physics RAS, 142432 Chernogolovka, Moscow Region, Russia*

Toxicity of hydrogen sulphide (H₂S), which is released into environment as a result of many natural and technological processes, draws enormous attention to the development of highly sensitive and selective sensors for its detection in gaseous and liquid media. Cheap portable sensors for H₂S detection are of high demand in oil&gas, mining, and waste disposal industries, as well as for different scientific applications. Recently a new electrochemical superionic low-temperature H₂S sensor has been developed. It exhibits ultimate combination of high sensitivity and selectivity. The sensor may be used at ambient conditions (temperature - 40 ÷ +60⁰ C, relative air humidity 10-95 %); its application does not require any additional thermo- or hydrostaticing [1]. Although the characteristics of the sensor thus obtained are well reproducible, the mechanism of sensor activity still remains unknown. In order to shed light onto the mechanism of H₂S detection, we have investigated the H₂S/O₂ adsorption at the surface of chalcogenide working electrodes to model the sensor detection-relaxation cycles. The experiments have been performed using synchrotron-induced core-level photoemission at BESSY.

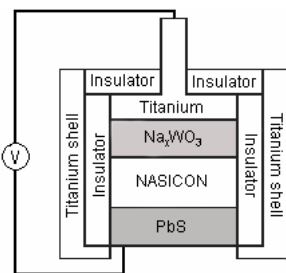


Fig. 1. Scheme of the sensor structure

surface.

The photoemission experiments have been performed at the Russian-German beamline (RGLB). The spectra were recorded using CLAM 4 (Thermo VG Scientific) electron energy analyzer. The Pb 5*d* spectra have been recorded at $h\nu = 125$ eV and analyzer pass energy (PE) of 2.5 eV, and the S 2*p* spectra were taken at $h\nu = 205$ eV and PE = 10 eV. Additionally, O 1*s* spectra have been recorded at $h\nu = 600$ eV and PE = 10 eV. Due to monochromator construction the absolute energy scale had uncertainty of ≈ 0.2 eV. Consecutive exposures to H₂S and O₂ were conducted in the preparation chamber.

The sensor electrochemical cells used for experiments consist of a working electrode (WE) – polycrystalline PbS, which has been grown from solution on the surface of polished and annealed pellet consisting of Na-conducting solid electrolyte NASICON (SE). The deposition was performed starting from the aqueous solutions of Na₂[Pb(OH)₄] and (NH₂)₂CS (thiourea). The film thickness and grain size have been controlled by adjusting temperature and growth duration. The opposite side of the pellet has been attached to the pressed reference electrode (RE) consisting of Na_{0.5}WO₃. The sensor design is illustrated in Fig. 1. Fig. 2 shows a typical microstructure of the WE

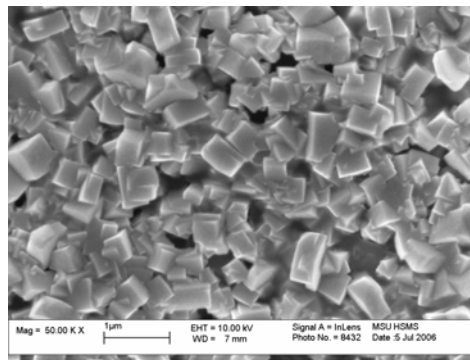


Fig. 2. Typical SEM image of PbS working electrode (50 K).

The H₂S exposure was conducted for 15 min at gas pressure of $8 \cdot 10^{-5}$ mbar. In order to model the sensor working conditions, consecutive O₂ exposure has been conducted for 30 min at $5 \cdot 10^{-4}$ mbar. Two H₂S/O₂ cycles have been performed.

For the data analysis, the spectra were fitted by the Gaussian – Lorentzian convolution

functions with simultaneous optimization of the background described by the equation

$$U(E) = a + s \cdot S(E) + t \cdot T(E),$$

where $S(E)$ is a Shirley background and $T(E)$ is a Tougaard background.

Initially the surface of the PbS working electrode is totally oxidized. Both, the Pb 5*d* and the S 2*p* spectra (the latter is illustrated in Fig. 3a) are dominated by a component at higher BEs corresponding to the formation of PbSO₄. The hardly distinguishable S 2*p*_{3/2} line corresponding to the bulk of PbS is located at BE = 160.6 ± 0.1 eV (component I); all chemical shifts have been calculated by taking component I as a reference. The components located at essentially higher BEs in S 2*p* spectra have the following chemical shifts (ChS): $+5.6 \pm 0.1$ eV (component IV), $+7.2 \pm 0.1$ eV (component V), and $+8.3 \pm 0.1$ eV (component VI). Taking the available data on different sulphur species on the surface of PbS into account [2, 3], one can attribute component IV to the formation of species containing sulphur in +4 oxidation state (supposedly SO₃²⁻). The nature of component VI remains unclear; since it has a BE almost 1 eV higher than for sulphur in SO₄²⁻, it may, however, be related to oligosulphates formation (S₂O₇²⁻, etc.). One can also suppose that it can be related to species like S₂O₈²⁻; however, high reactivity of these species, which are considered to be one of the strongest oxidizers, as well as their relative instability leads us to conclusion that their appearance at the surface is rather improbable. Thus, the WE surface before H₂S exposure consists sulphur atoms predominantly in +6 state (sulphate).

After the first H₂S exposure the relative intensity of the component corresponding to Pb-S bond increases essentially in the Pb 5*d* spectra, thus indicating the reduction of surface species. In the S 2*p* spectra (fig. 3, b) at least 2 additional states appear between those related to SO₄²⁻ and S²⁻ peaks appear. Component II and II have a chemical shift of

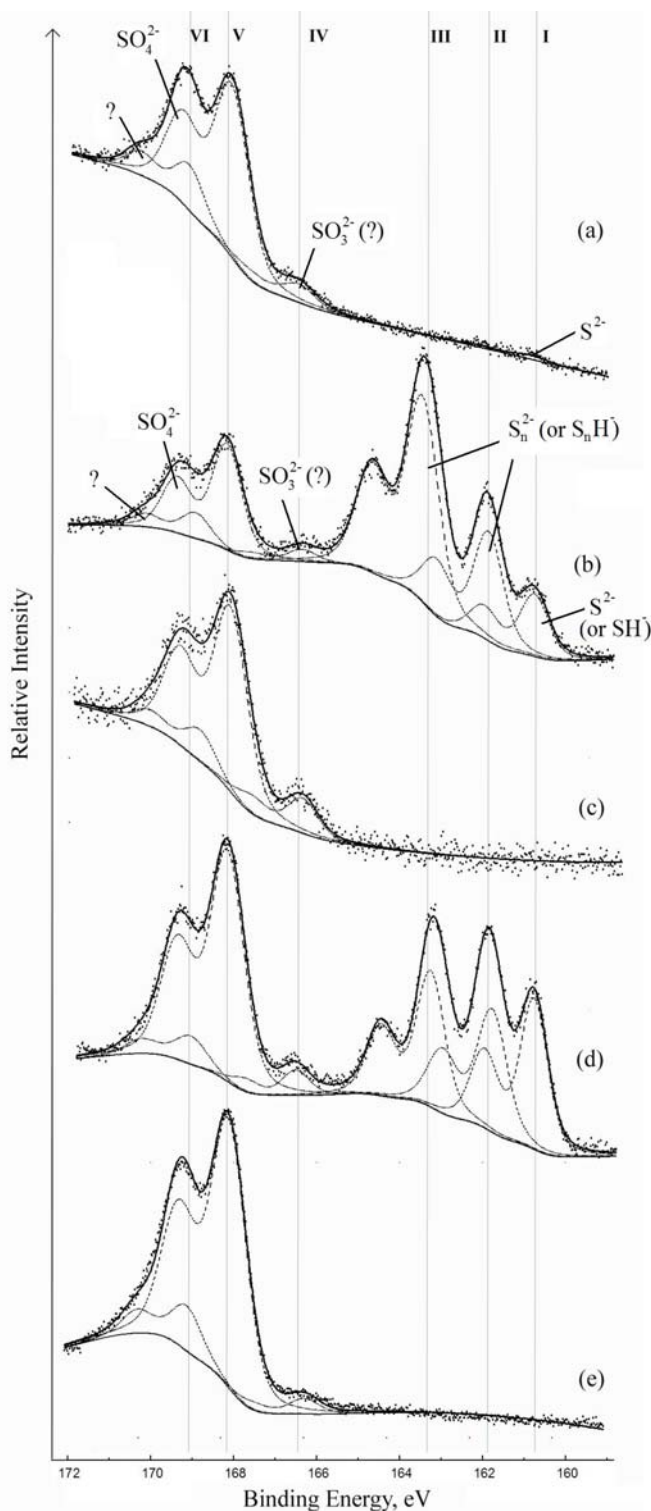


Fig. 3. S 2*p* spectra: (a) initial surface; (b) first H₂S exposure; (c) consecutive O₂ exposure – end of first cycle; (d) second H₂S exposure; (e) second consecutive O₂ exposure – end of second cycle.

+1.1±0.1 eV and +2.7±0.1 eV, respectively, towards higher BEs relative to component I. We refer these components to the formation of oligosulphides at the surface as a result of H₂S adsorption [2,3]. The structures S_n²⁻ or S_nH⁻ contain two types of sulphur atoms: those bonded to Pb and those bonded to S only; since their environment differs, a difference in binding energy should be observed. The quantity of S-S bonds increases with increase of *n*. Based on the analysis of the relative intensities we suggest that component II is related to a Pb-S bond and component III to S-S bonds in oligosulphides. From the intensity ratio of these components we conclude that the average formula of oligosulphide is PbS₄. After H₂S exposure, the fraction of component V (corresponding to SO₄²⁻) decreases substantially; this is accompanied by an increase of the intensity of component I. Therefore, we conclude that H₂S exposure leads to partial reduction of sulphur atoms giving a number of species which contain S atoms in lower oxidation states.

Consecutive exposure of the surface to oxygen leads to its oxidation (Fig. 3c). The obtained spectra have the same features as those before H₂S exposure; namely, Pb 5*d* spectra contain mostly the component corresponding to a PbSO₄ formation, and S 2*p* spectra with 3 components only (IV, V, VI; see fig. 3, c). Note that, although the relative intensity of these components in the spectra is slightly different from the one observed initially, their BE as well as other peak features is equal to that registered before the exposures. It is interesting to note that components IV and VI are present in all sulphur spectra; their relative intensity remains almost the same, notwithstanding the treatment of the working electrode. We suppose that these components refer to the irreversible formation of some sulphur species, which appear to be very stable at the surface. In general, the spectral changes indicate that after consecutive H₂S-O₂ exposure the surface of the working electrode fully recovers; the H₂S adsorption seems to be a reversible process.

In order to confirm the observed behaviour and to further investigate the sensor mechanism, we performed a second cycle of H₂S-O₂ exposures. As a result of spectra treatment we found out that the same components are present in both Pb 5*d* and S 2*p* spectra. In case of S 2*p*, after H₂S exposure the relative intensity of components differs from that observed after the first exposure, namely, the fraction of component II increases substantially (see fig. 3, d). We suppose that in this case the ratio of Pb-S and S-S bonds changes, i.e. the second cycle leads to decrease of *n*. The calculations involving relative intensity show that the average formula of oligosulphide is PbS₂ (corresponding to the shortening of the oligosulphide chains). Consecutive O₂ exposure returns the surface to the oxidized state, with the same components being observed at the surface as before the exposures (see fig. 3, e).

As a result of data analysis, we found that the surface of the PbS working electrode undergoes reversible reduction during H₂S detection. The surface is reduced by H₂S only partially; different oligosulphides are reversibly formed. Further oxygen exposure returns the surface to the initial (oxidized) state. The obtained data are of great importance for the understanding of electrochemical sensor activity mechanism, and should be considered in combination with other sets of data obtained both for surfaces of working electrodes, as well as WE/SE and SE/RE interfaces.

The authors would like to thank BESSY staff for support.

- [1] A. V. Levchenko, Yu. A. Dobrovolsky, T. S. Zyubina, N. G. Bukun, L. S. Leonova, V. S. Neudachina, E. V. Tikhonov, V. I. Shtanov. *Asian J. Phys.* 14 (2005) 17.
- [2] K. Laajalehto, I. Kartio, E. Suoninen, *Int. J. Mineral Processing*, 51 (1997) 163
- [3] P. Nowak, K. Laajalehto, *App. Surf. Sci.* 157 (2000) 101.

Anchoring of Metal Organic Frameworks (MOFs) on Functionalized Organic Surfaces

*O. Shekhah, H. Wang, M. Krizikalla, T. Strunskus and Ch. Wöll
Lehrstuhl für Physikalische Chemie I, Ruhr-Universität-Bochum
Universitätsstr. 150, 44780 Bochum*

Metal Organic Frameworks (**MOFs**) are a new promising class of nanoporous materials, which have found many applications, due to their almost unlimited variability in structure, properties and fascinating design [1-5]. A new dimension in MOFs application opens up when these MOF materials can be addressed on the nanoscale, by attaching them to surfaces in a well-defined way and then, for example, loading them with metal organic precursors. This opens up the possibility to fabricate metallic nanoparticles embedded in the well-defined nanopores of the MOFs exhibiting interesting electronic and catalytic properties [3-5].

In this work the specific anchoring of two different type of **MOFS**, namely (Metal Organic Radical Open Frameworks (**MOROFs**) and layer based metal organic frame works (**LBMOFs**)) to surfaces has been investigated. For the experiments described here, two different organic ligands have been used. MOROFs are fabricated by mixing tricarboxylic acid substituted perchlorotriphenyl-methyl radical (PTMTC) ligand with copper di-acetate yielding different types of MOROFs, which have strong intramolecular antiferromagnetic properties and act like a nanoporous molecular magnet. LBMOFs are fabricated by mixing the 1,3,5 tricarboxylic benzene (BTC) ligand with copper(II) acetate or Zinc(II) acetate yielding different MOF structures.

Near edge x-ray absorption fine structure (NEXAFS) measurements were performed at the HE-SGM beam line using partial electron yield detection. The C K-edge polarization dependence NEXAFS spectra of the mercapto hexadecanic acid (MHDA) SAM (Fig.1a), of the SAM modified with Cu(II) acetate (Fig.1b), and after the subsequent treatment with the MOROFs are shown in Fig. 1. An unambiguous proof of the presence of PTMMC ligand bound to the surface of the SAM, is provided by the observation of a resonance at 282.9 eV in the NEXAFS spectra (Fig. 1c). 282.9 eV is an unusually low energy for a NEXAFS resonance. The resonance at 282.9 eV is assigned to an excitation of C1s core electrons in the half filled highest occupied electronic state of the radical [6] and it directly demonstrates the presence of a carbon radical on the surface. The results indicate that only the acid form of PTMTC is anchored on the SAM whereas no deposit is obtained after treatment with the basic form (Fig.1d).

A sequential deposition of organic molecules employing metal-ions to form layers with defined thickness has been reported for mercaptohexadecanoic acids and for polyelectrolytes [7,8], but is here for the first time applied to the selective growth of MOF-structures on a functionalized substrate. Infrared reflection absorption spectroscopy and x-ray photoelectron spectroscopy (XPS) results have shown that there is indeed a layer-by-layer growth of the Zn-BTC MOFs with the increasing number

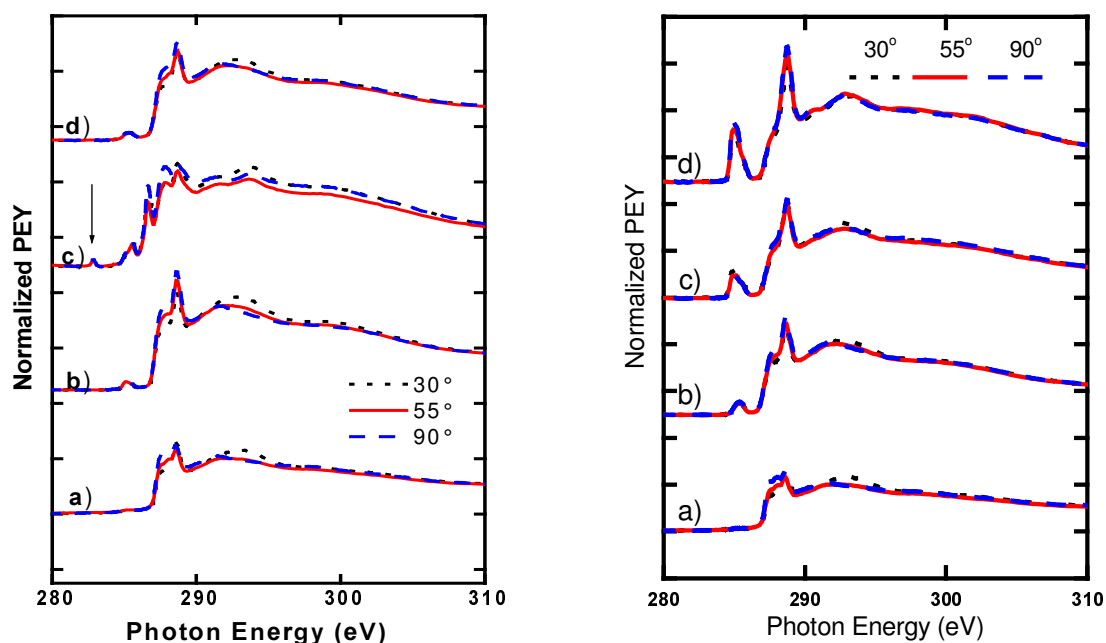


Fig.1. C-K edge NEXAFS spectra of a) MHDA, b) MHDA after immersion for 30 min in Cu-di-acetate, c) MHDA after immersion for 30 min in Cu-di-acetate then for 60 min in PTMMC (acid form), d) MHDA after immersion for 30 min in Cu-di-acetate then for 60 min in PTMMC (basic form).

a) MHDA, b) MHDA after immersion for 30 min in Zn-acetate, c) MHDA after immersion for 30 min in Zn-acetate then for 60 min in BTC (acid form), d) MHDA after immersion for 30 min in Zn-acetate then for 60 min in BTC (8 cycles).

of deposition cycles. The heights measured by atomic force microscopy (AFM) and the NEXAFS data (shown in fig.2) reveal an orientation of the BTC-units which is mainly perpendicular to the surface (average tilt angle 50° - 60°).

This layer-by-layer deposition of MOFs on organic surfaces not only makes it possible to coat surfaces with MOF-layers of defined thickness but, even more interestingly, opens up the possibility to synthesize completely new types of MOFs with compositions and structures not accessible by bulk synthesis routes, e.g. frame-works containing two different organic ligands arranged in an alternating fashion.

Support for travelling costs for the synchrotron measurements by the BMBF through grant 05 ES3XBA/5 is gratefully acknowledged.

References

1. O. M. Yaghi, C. E. Davis, G. Li, and H. Li, *J. Am. Chem. Soc.* **119** (1997) 2861.
2. O. M. Yaghi, H. Li, and T. L. Groy, *J. Am. Chem. Soc.* **118** (1996) 9096.
3. S. Hermes, F. Schröder, S. Amirjalayer, R. Schmid, and R. A. Fischer, *J. Mater. Chem.*, **16** (2006) 2464.
4. S. Hermes, F. Schröder, R. Schmid, L. Khodeir, M. Muhler, A. Tissler, R. W. Fischer, and R. A. Fischer, *Angew. Chem. Int. Ed.*, **44**(38) (2005) 6237.
5. S. Hermes, F. Schröder, R. Chelmoski, Ch. Wöll, and R. A. Fischer, *J. Am. Chem. Soc.* **127** (2005) 13744.
6. O. Shekhah, H. Wang, T. Strunskus, Ch. Wöll, submitted to *JACS* 2007.
7. A. Ulman, and S. D. Evans, *J. Am. Chem. Soc.*, **113** (1991) 5866.
8. G. Decher, *Science*, **277**(5330) (1997) 1232.

In situ X-ray photoelectron spectroscopy on supported powder and model Au/TiO₂ catalysts – influence of the material gap

Y. Denkwitz¹, S. Kielbassa¹, B. Schumacher¹, J. Bansmann¹, P. Schnörch², E. Vass²,
M. Hävecker², A. Knop-Gericke², R. Schlögl² and R.J. Behm¹

¹ Inst. of Surface Chemistry and Catalysis, Ulm University, D-89069 Ulm

² Dept. Inorganic Chemistry, Fritz-Haber-Institut der MPG, Faradayweg 4-6, D-14195 Berlin

supported by DFG within SPP 1091 (Be 1201/9-3) and SFB 569 via TP B2

Oxide supported Au catalysts with finely dispersed small Au nanoparticles have attracted considerable interest in recent decades because of their high activity for numerous reaction, e.g., the low-temperature CO oxidation. The question of oxygen activation and the role of ionic Au^{δ+} or Au⁰ species in the reaction mechanism are still controversially discussed [1-4]. To investigate the influence of the reaction atmosphere on the support and on the chemical /electronic state of the Au surface atoms in more detail, we performed a comparative *in-situ* high pressure XPS study on the interaction of different reactive gases, O₂, CO and CO/O₂ mixtures, with dispersed Au/TiO₂ catalysts and planar Au/TiO₂(110) model catalysts. These two catalyst systems differ by their density of surface defects. The dispersed catalysts consist of a highly defective support material, while the model catalysts, on the other hand, are supported on almost ideal surfaces of fully oxidized and atomically smooth TiO₂(110) substrates. The two catalysts used in this study have comparable Au particle sizes (~3 nm) and they were pre-conditioned in the same way prior to the exposure, with only metallic Au⁰ species being detectable after conditioning [5,6].

First, the Au/TiO₂(110) model catalyst was exposed to 0.3 mbar O₂ at increasing temperatures up to 400°C, in order to study the extent of surface oxidation of the Au particles. All Au 4f spectra (fig. 1, left panel) exhibit the same characteristics, almost symmetric peak shapes and a constant peak width (FWHM 0.8 eV), indicating that the spectra are dominated by a single Au species. A small shift of about 0.5 eV to higher BEs in the Au 4f signal, from RT to 400°C, remaining after calibration to a constant Ti 2p peak BE (459.2 eV), indicates that both temperature as well as the ambient atmosphere (vacuum or O₂ at 400°C) affect the

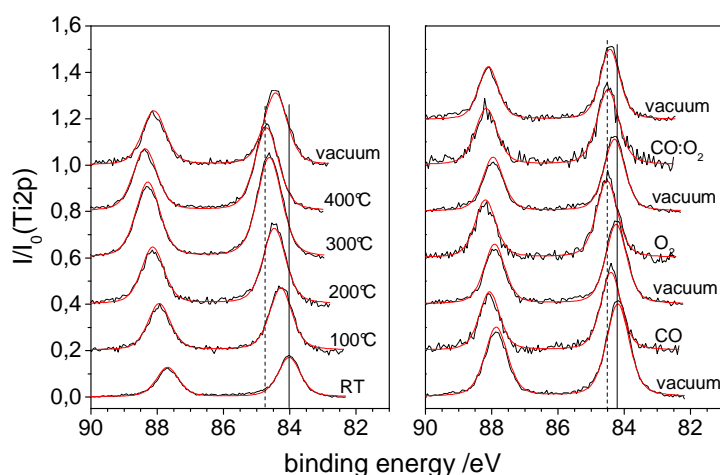


Fig. 1: Left panel: Sequence of Au 4f spectra recorded on a Au/TiO₂ model catalyst in vacuum at RT, in 0.3 mbar O₂ at temperatures up to 400°C and in vacuum at 400°C; right panel: Sequence of Au 4f spectra recorded at 80°C on a Au/TiO₂ model catalyst in vacuum, 0.3 mbar CO, vacuum, 0.3 mbar O₂, vacuum, 0.3 mbar O₂/CO (1:1) and vacuum.

electronic/chemical state of the Au particles. The origin of this shift is not yet clear, but based on the constant peak shape it can not be related to surface oxide formation, which should show up as a high BE shoulder on the Au 4f peak (larger FWHM and different peak shape). Additionally, during the whole experiment the O 1s/Ti 2p intensity ratio remains constant, indicating that oxygen adsorption on the well ordered TiO₂(110) support is insignificant. In the second part of this experiment (fig. 1, right panel), we stepwise approached the situation during the CO oxidation reaction by exposing the model catalyst first

to CO (0.3 mbar), then to O₂ (0.3 mbar), and finally to a 1:1 O₂/CO gas mixture (0.3 mbar total pressure) at 80°C, which represents a typical reaction temperature [7]. In between the measurements, the reaction cell was pumped off, and additional XPS measurements were performed under vacuum conditions to identify permanent changes of the model catalyst surface after the different stages of this sequence. Analogously to the data in the first sequence (O₂ exposure up to 400°C, cf. fig.1, left panel), the Au 4f peak shapes and FWHMs remain constant, indicating that also under these conditions significant surface oxidation can be ruled out.

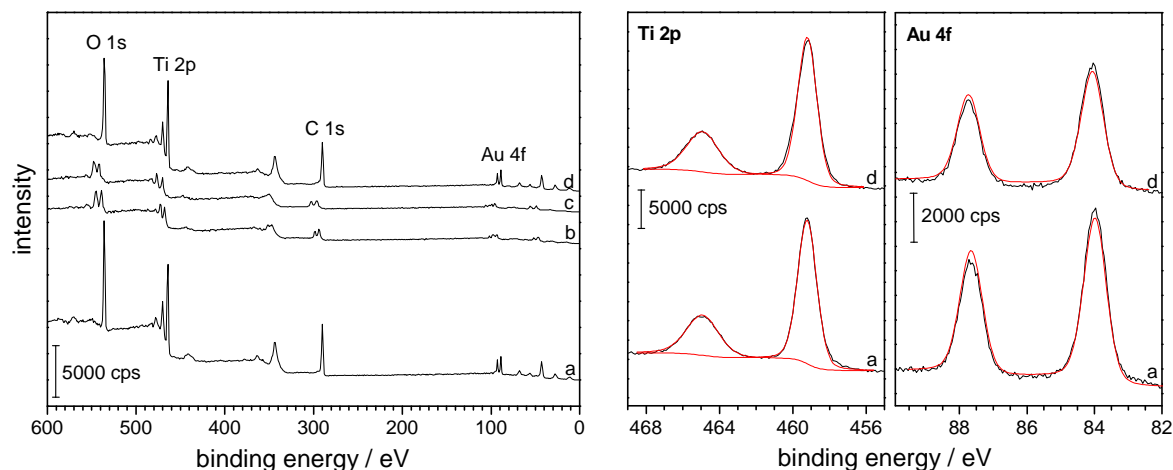


Fig. 2: XP spectra of the Au/TiO₂ powder catalyst at 80°C recorded (a) in vacuum after conditioning in O₂, (b and c) during O₂ exposure after 2 and 9 min, respectively, as well as (d) after O₂ exposure in vacuum. Left part: survey scans ($h\nu = 850$ eV), right part: Ti 2p ($h\nu = 619$ eV) and Au 4f ($h\nu = 234$ eV) peaks recorded at a higher resolution.

For the powder catalyst, exposure to 0.3 mbar O₂ leads to a shift in the BE of all peaks compared to the measurements under vacuum conditions due to sample charging (fig. 2). The energy shift is inhomogeneous and results in broadened peaks of each signal. The charging effects could be removed by quantitative comparison with a C 1s contamination peak, which is assumed to be constant in shape and BE under the present conditions. (It should be noted that for O₂ exposure at 400°C an additional charging was not observed.) The resulting Au 4f and Ti 2p spectra closely resemble those obtained before O₂ exposure, indicating that also on the dispersed catalyst significant Au oxidation can be ruled out. In addition, the O 1s/Ti 2p intensity ratio increases during O₂ exposure, indicative of oxygen adsorption. This increase in intensity ratio is reversible, i.e., the adsorbed oxygen can be pumped off again (fig. 2d); the oxygen must be weakly adsorbed, most likely in a molecular state.

In a series of experiments displayed in fig. 3, we investigated the effect of exposing a fresh Au/TiO₂ powder catalyst to a CO/O₂ mixture under reaction conditions (1:1 mixture, 80°C, 0.3 mbar total pressure). During exposure, a significant shift in the BEs occurred (fig. 3b-d), increasing with the reaction time. After subsequent evacuation, the energy shift is reduced but not completely removed. All signals are broadened again and show the typical features of inhomogeneous charging. Removal of the charging effects (see above) leads to Au 4f and Ti 2p peaks very similar to those obtained before exposure to the

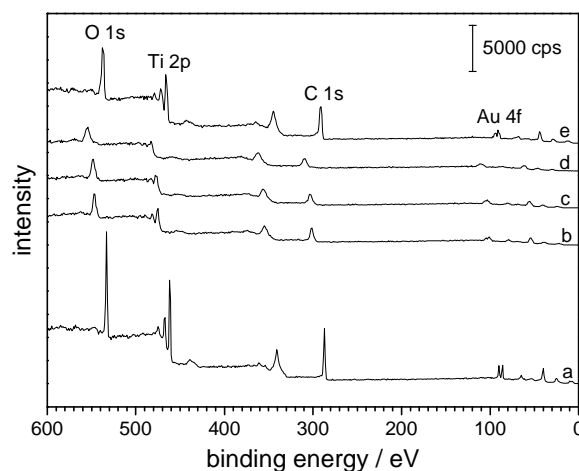


Fig. 3: XP survey spectra of the Au/TiO₂ powder catalyst recorded (a) in vacuum after heating in O₂, during CO oxidation at 80°C after (b) 4 min, (c) 9 min and (d) 45 min as well as (e) in vacuum.

reaction gas mixture (fig. 3a). Hence, the metallic character of the Au particles is maintained also under reaction conditions.

For both systems, the model catalyst as well as the dispersed catalyst, we found no detectable Au oxide formation upon exposure to O₂, CO or to a CO:O₂ (1:1) reaction mixture at 80°C. This result apparently contrasts recent findings in an *in-situ* high pressure XPS data on a dispersed Au/TiO₂ catalyst [4], where the authors reported an increasing intensity of a 0.9 eV up-shifted component, which they related to a final-state shifted signal (small Au particles). The discrepancy to our present results is almost certainly caused by the different morphology of the catalysts, due to the different pre-treatment. The unconditioned Au/TiO₂ catalyst (pre-treatment: drying in air at 50 - 80°C) contained a high content of very small (and possibly not completely reduced) Au clusters/particles, while the catalysts used in the present study were characterized by 3 nm diameter, metallic Au particles. Obviously, these larger particles are significantly more stable against oxide formation or adsorbate induced changes in the electronic structure of the Au particles.

Finally, the significant amount of adsorbed oxygen on the powder catalyst during O₂ exposure at 80°C may point to weakly bound, molecular oxygen species adsorbed on the support, most likely on defect sites, but more definite measurements are necessary for a clear assignment. In total, the experiments clearly demonstrate the potential of comparative *in-situ* studies on model systems and realistic catalysts of well defined structural characteristics and under comparable conditions.

Acknowledgements

We gratefully acknowledge F. Weigl, H.-G. Boyen and P. Ziemann (Ulm University) for preparing the Au nanoparticles for the model catalysts and BESSY staff for technical support.

Reference

- [1] J. Guzman, B. C. Gates, *J. Am. Chem. Soc.* **2004**, *126* 2672.
- [2] V. Schwartz, D. R. Mullins, W. Yan, B. Chen, S. Dai, S. H. Overbury, *J. Phys. Chem. B* **2004**, *108* 15782.
- [3] J. A. van Bokhoven, C. Louis, J. T. Miller, M. Tromp, O. V. Safonova, P. Glatzel, *Angew. Chem.* **2006**, *118* 4767.
- [4] E. A. Willneff, S. Braun, D. Rosenthal, H. Bluhm, M. Hävecker, E. Kleimenov, A. Knop-Gericke, S. L. M. Schröder, *J. Am. Chem. Soc.* **2006**, *128* 12052.
- [5] S. Kielbassa, A. Häbich, J. Schnaidt, J. Bansmann, F. Weigl, H.-G. Boyen, P. Ziemann, R.J. Behm, *Langmuir* **2006**, *22* 7873.
- [6] B. Schumacher, V. Plzak, M. Kinne, R. J. Behm, *Catal. Lett.* **2003**, *89* 109.
- [7] B. Schumacher, Y. Denkwitz, V. Plzak, M. Kinne, R. J. Behm, *J. Catal.* **2004**, *224* 449.

Formation of Kinetically Stable, Flat Lying Thiolate Monolayers

Mihaela G. Badin,¹ Asif Bashir,¹ Simone Krakert,² Thomas Strunskus,¹ Andreas Terfort,² and Christof Wöll¹

¹ Lehrstuhl für Physikalische Chemie I, Ruhr-Universität Bochum, D-44780 Bochum, Germany

² Institut für Anorganische und Angewandte Chemie, Universität Hamburg, D-20146 Hamburg, Germany

The adsorption of a dodecane thiol ($C_{12}SH$) on a gold surface is compared to the adsorption of the same molecule modified to a thioacetate ($C_{12}SAc$). This work addresses the question if and what kind of thiolate monolayers can be formed from thioacetates. In Fig.1 the results obtained by x-ray photoelectron spectroscopy for the C 1s, S 2p, and O 1s regions are shown. In the S 2p region only one sulfur species with a binding energy of 161.8 eV can be found for both adlayers, being consistent with the formation of a thiolate upon adsorption for both films [1]. In the C 1s region the line for $C_{12}SH$ is much more intense than that of $C_{12}SAc$, revealing that the adlayer of the thioacetate is considerably thinner. One also notes a considerable shift of about 0.4 eV to lower binding energy for the C 1s core level line of $C_{12}SAc$ compared to $C_{12}SH$. A similar shift has been observed before for thiol molecules

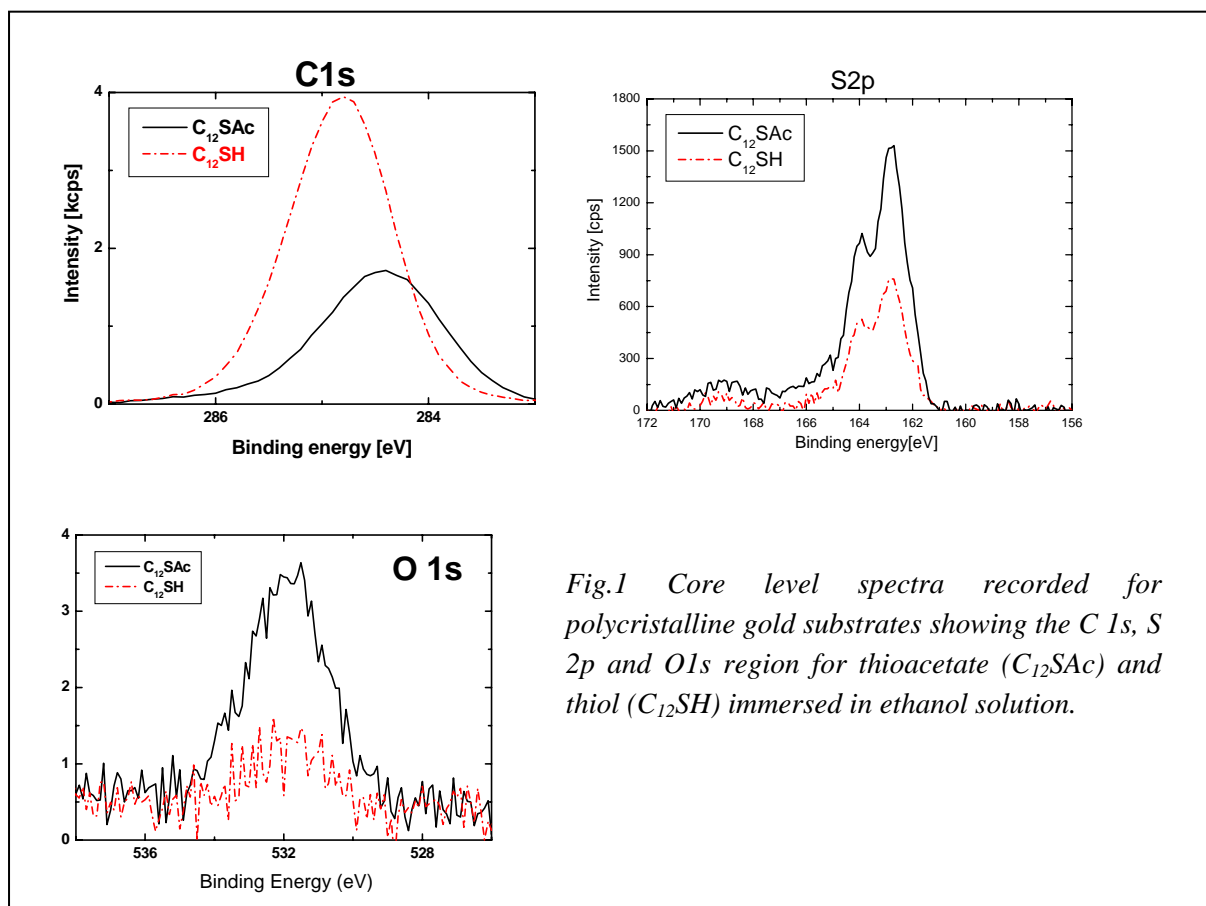


Fig.1 Core level spectra recorded for polycrystalline gold substrates showing the C 1s, S 2p and O 1s region for thioacetate ($C_{12}SAc$) and thiol ($C_{12}SH$) immersed in ethanol solution.

lying flat on metal surfaces [2] and is probably due to final state effects, i.e., by a better screening of the C 1s core holes by the metal electrons [3]. Therefore, the XPS results indicate flat lying molecules. Consistent with this are the observations in the O 1s regime. While in the monolayer generated from the thiol only trace amounts of oxygen can be found, the layers made from $C_{12}SAc$ contain about one oxygen atom for every three molecules. Since this cannot result from the adsorption of intact thioacetate molecules (for which a ratio of 1:1 would be expected), we believe that the oxygen atoms rather stem from the oxidation of the monolayer after formation during manipulation and transfer into

the XPS set-up. It has been reported in the past that the sulfur atoms of flat-lying thiolates are rather prone to oxidation by atmospheric oxygen [4].

To obtain more detailed information about the orientation of the thiolate molecules in the two kinds of monolayers, NEXAFS spectra were recorded (Fig.2). The spectra of the C₁₂SH SAM very closely resemble earlier NEXAFS results reported for alkanethiolate-based SAMs [5]. In the spectrum for the C₁₂SH the resonance denoted R* has been shown to result from an excitation into unoccupied orbitals with stronger R character [6, 7]. These signals show a pronounced variation of the resonance intensity with the angle of incidence. A quantitative analysis of this linear dichroism reveals a tilt angle of $\theta = (63 \pm 5)^\circ$. For the C₁₂SAc-based SAM, the NEXAFS spectra are quite different. While the R* resonance is much less pronounced, an additional π^* -resonance can be seen at energy of 285 eV. This resonance is attributed to a small amount of C=C double bonds, possibly generated by some beam damage. Since the spectra as well as their angle dependency are significantly different compared to the ones for the thiol-derived monolayers, the orientation of the alkyl chains in the adlayers obtained by immersion in C₁₂SAc must be considerably different. Note, that in previous work it has been found

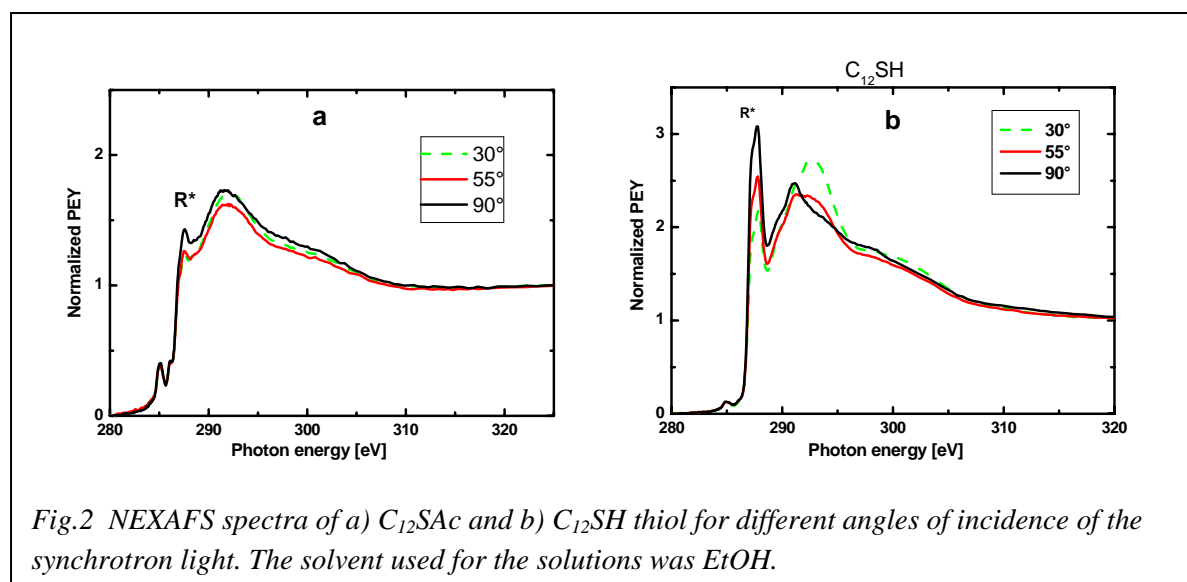


Fig.2 NEXAFS spectra of a) C₁₂SAc and b) C₁₂SH thiol for different angles of incidence of the synchrotron light. The solvent used for the solutions was EtOH.

that if alkane chains are in direct contact with a metals surface, the R* resonance is modified in a way similar to that seen in the figure 2 obtained here for the C₁₂SAc layers [8]. The NEXAFS results are consistent with a monolayer in which the axes of the hydrocarbon chains are parallel to the gold surface.

Support for travelling costs for the synchrotron measurements by the BMBF through grant 05 ES3XBA/5 is gratefully acknowledged.

References:

1. Ch. Zubrägel, C. Deuper, F. Schneider, M. Neumann, M. Grunze, A. Schertel and Ch. Wöll, Chem. Phys. Lett. **283** (1995) 308.
2. H.-J. Himmel, Ch. Wöll, R. Gerlach, G. Polanski, H.-G. Rubahn, Langmuir **13** (1997) 602.
3. G. Witte and Ch. Wöll, J. Chem. Phys. **103** (1995) 5860.
4. D. Käfer, G. Witte, P. Cyganik, A. Terfort, Ch. Wöll, J. Am. Chem. Soc. **128** (2006) 1723.
5. G. Hähner, Ch. Wöll, M. Buck, M. Grunze, Langmuir, **9(8)** (1993) 1955.
6. P.S. Bagus, K.Weiss, A. Schertel, Ch. Wöll, W. Braun, C. Hellwig and C. Jung, Chem. Phys. Lett. **248** (1996) 129.
7. K. Weiss, P.S. Bagus, and Ch. Wöll, J. Chem. Phys. **111(15)** (1999) 6834.
8. G. Witte, K. Weiss, P. Jakob, J. Braun; K. L. Kostov, Ch. Wöll, Phys. Rev. Lett. **80** (1998) 121.

Magnetic and structural investigation of Mn²⁺ doped ZnSe semiconductor nanoparticles

C. Graf,^{a,b} A. Hofmann,^{a,b} C. Boeglin,^c E. Rühl^{a,b}

^aPhysikalische und Theoretische Chemie, Institut für Chemie und Biochemie, Freie Universität Berlin,
Takustr. 3, 14195 Berlin

^bInstitut für Physikalische Chemie, Universität Würzburg, Am Hubland, 97074 Würzburg

^cInstitut de Physique et de Chimie des Matériaux de Strasbourg, 23, rue du Loess, BP43, 67034 Strasbourg, France

Diluted magnetic semiconductor nanoparticles represent a class of materials with unique optical, electronic, and magneto-optical properties because they combine the magnetic spin properties of the dopant with unique electronic properties of the nanoscopic semiconductor lattice. Especially, manganese doped materials show promising magnetic spin characteristics, that are based on Mn²⁺ as a paramagnetic center, where a group II cation is substituted in the lattice. Previous investigations on the location and the properties of Mn²⁺ in nanocrystals have been accomplished by different experimental approaches, such as electron paramagnetic resonance, photoluminescence, and magnetic circular dichroism [1]. However, none of these methods provides specific information on the important question, whether all Mn²⁺ is located in the bulk of the crystal lattice.

We have used for the first time X-ray magnetic circular dichroism (XMCD) experiments on diluted magnetic semiconductor nanocrystals in order to study the local electronic structure and magnetic properties of Mn²⁺ embedded in the lattice of ZnSe nanoparticles. These particles are prepared by a metallo-organic high temperature approach in an oxygen-free atmosphere [1]. In this synthesis, dimethyl manganese is used as a precursor, hence Mn is integrated as Mn²⁺ into the nanoparticles. The efficient elimination of those Mn²⁺ ions, which may physically be adsorbed on the surface of the nanocrystals was accomplished by immersing the samples into pyridine, leading to a ligand exchange on their surface. X ray diffraction measurements reveal, that the particles have a zincblende structure with a small amount of wurtzite structure occurring as stacking faults [2]. High resolution electron microscopy measurements and an analysis of the pair distribution function yield an average particle diameter of 2.8±0.2 nm [3]. An inductive coupled plasma analysis of the particles shows that they have an average content of about 0.3 to 0.8 manganese ions per nanocrystal [3]. The photoluminescence spectrum of the pyridine-treated ZnSe:Mn nanocrystals shows near 350 nm excitation the characteristic Mn²⁺-emission at 580 nm [3]. This emission is assigned to the internal Mn²⁺ ⁴T₁ → ⁶A₁-transition, which is known to be typical for Mn²⁺ ions occurring in the bulk of the crystal lattice [1]. However, it cannot be fully excluded from these results that also surface-bound Mn²⁺ shows are present [1]. This is because energy transfer could also occur if Mn²⁺ is either surface-bound or located in the surrounding matrix [1]. EPR measurements yield a hyperfine coupling constant, which is nearly identical to those of Mn²⁺ ions inside bulk ZnSe [3].

The particles are spin-coated on Cu substrates and exposed to air for at least one day before the XMCD experiments. Mn²⁺ at the surface of the nanocrystals should be quickly oxidized under these conditions [4], while the oxidation of Mn²⁺ in bulk crystal is expected to be considerably slower. The XMCD measurements are performed at the BESSY storage ring at the beam line UE56/2. The experiments are performed at T=5 K at magnetic field strengths ranging from 0.1 T to 6 T. Left or right circularly polarized X rays are absorbed by the samples, where Fig. 1(a) shows a typical pair spectra recorded at the MnL_{2,3} edges applying 6 T. The spectra are normalized to the incident photon flux. Low Mn²⁺ concentration and absorption from ZnSe explains that the experimental X-ray absorption is superposed to a substantial non-structured background, which is subtracted prior to data analysis. The difference between both curves shown in Fig. 1(a) yields the XMCD signal, as shown in Fig. 1(b). This results in a narrow feature at 641 eV, where the Mn L₃ edge is located. Such a narrow feature indicates that all Mn²⁺ is bound in the same local environment. Otherwise, chemical shifts would occur,

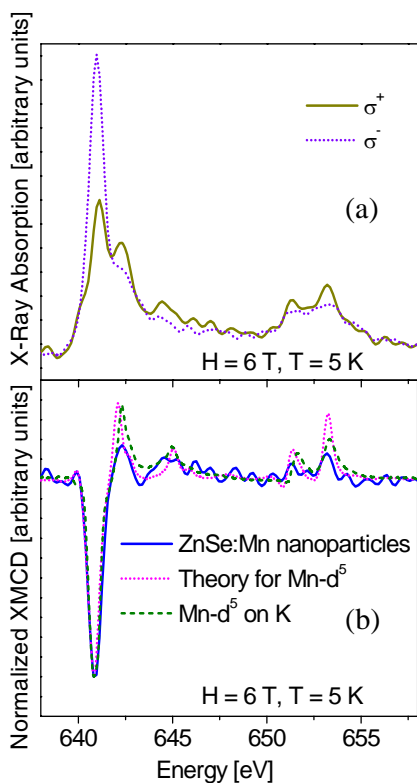


Fig. 1. (a): Left polarized (σ^- , solid line) and right polarized (σ^+ , dotted line) X ray absorption spectra of ZnSe:Mn at the Mn $L_{2,3}$ edges. (b): The X-ray magnetic circular dichroism spectrum (solid line) is derived from the absorption spectra. The experimental XMCD spectrum of single Mn- d^5 atoms on a potassium surface (dashed line) and a calculated XMCD spectrum of the fully spin-polarized d^5 atomic ground state ($2p^63d^5 \rightarrow 2p^53d^6$ -transitions) in the limit of zero crystal field and $T=5$ K (dotted line) are included for a comparison [5].

value of the integral of the peak occurring at 641 eV, which results from the Mn^{2+} embedded in ZnSe, is even at the highest applied magnetic field (6 T) about 50% lower than that derived from single Mn- d^5 atoms on a potassium surface performed at 6 T, as well as the theoretical value for a fully spin polarized d^5 atomic ground state [5]. This implies that the ZnSe environment effectively hinders the polarization of the Mn^{2+} ions. This may be due to lattice defects in the ZnSe:Mn nanocrystal, which are indeed observed in the XRD measurements [2].

This work was supported by the Deutsche Forschungsgemeinschaft (Projekt C8, Sonderforschungsbereich 410).

References:

- 1) D. J. Norris, N. Yao, F. T. Charnock, T. A. Kennedy, *Nano Lett.* **2001**, *1*, 3.
- 2) V.I. Korsunskiy, R.B. Neder, A. Hofmann, S. Dembski, C. Graf, E. Rühl, *submitted to J. Appl. Cryst.* **2006**.
- 3) A. Hofmann, C. Graf, C. Boeglin, E. Rühl, *submitted to ChemPhysChem* **2007**
- 4) Y. Yonamoto, T. Yokoyama, K. Amemiya, D. Matsumura, T. Ohta, *Phys. Rev. B* **2001**, *63*, 214406.
- 5) P. Gambardella, S. S. Dhesi, S. Gardonio, C. Grazioli, P. Ohresser, C. Carbone, *Phys. Rev. Lett.* **2002**, *88*, 047202.
- 6) B. Gilbert, B. H. Frazer, A. Belz, P. G. Conrad, K. H. Neilson, D. Haskel, J. C. Lang, G. Srajer, G. De Stasio, *J. Phys. Chem. A* **2003**, *107*, 2893.

which would lead to multiple features or substantial broadening. Further evidence for this assignment comes from a comparison, where the experimental XMCD spectrum of single Mn atoms in a d^5 state deposited on a potassium surface (pink dashed curve) as well as the calculated XMCD spectrum for the $2p^63d^5 \rightarrow 2p^53d^6$ transitions of a fully spin-polarized d^5 atomic ground state in the limit of zero crystal field at $T=5$ K (green dotted curve) are displayed in Fig. 1(b) [5]. It is known that transition metal impurities on alkali metal surfaces have atomic-like ground states with full spin and orbital moment values [5]. All spectra shown in Fig. 1(b) are normalized to the feature occurring at 641 eV. The shape of the Mn L_3 XMCD peak from Mn-doped nanoparticles fully agrees with the results from previous work. Somewhat reduced intensity in the fine structures of the Mn^{2+} -doped nanoparticle sample is most likely a result of a lower energy resolution and a reduced signal-to-noise level in the present work compared to earlier work on macroscopic surfaces [5]. This is remarkable, considering that oxidation to higher Mn-oxidation states as well as partial ferromagnetic or antiferromagnetic coupling between single manganese impurities leads to significant broadening of the multiplet features at the Mn $L_{2,3}$ edges [5]. A partial oxidation of Mn^{2+} to Mn^{3+} would lead to a significant broadening and change of the peak shape of the isotropic X ray absorption spectrum as well [6]. In the present case such a broadening was not observed. Hence, it is concluded from the present XMCD and isotropic X ray absorption results that exclusively isolated and non-oxidized Mn^{2+} ions are present in the bulk of ZnSe nanoparticles. This also implies that reactions of the metal ions with surface ligands can be excluded. The quantitative analysis of the XMCD spectra requires a normalization of the integrated isotropic X-ray absorption at the Mn L_3 edge, so that a comparison to related work can be made [5]. This analysis yields that the absolute

Elastic Light Scattering from Free Nanoparticles in the Soft X-Ray Regime

B. Langer^{1,2}, H. Bresch¹, B. Wassermann¹, C. Graf¹, R. Lewinski¹, R. Flesch¹,
B. Österreicher³, T. Leisner^{3,4}, U. Becker⁵, and E. Rühl¹

¹Physikalische und Theoretische Chemie, Institut für Chemie und Biochemie, Freie Universität Berlin, Takustr. 3, 14195 Berlin

²Max-Born-Institut für Nichtlineare Optik und Kurzzeitspektroskopie, Max-Born-Str. 2A, 12489 Berlin

³Fakultät für Mathematik und Naturwissenschaften, TU Ilmenau, Max-Planck-Ring 14, 98693 Ilmenau

⁴IMK, Forschungszentrum Karlsruhe, Postfach 3640, 76021 Karlsruhe

⁵Fritz-Haber-Institut der MPG, Faradayweg 4-6, 14195 Berlin

Nanosopic matter in the gas phase is of current interest since it represents the link between condensed matter and the gas phase. The aim of this work is to study size effects of structural and dynamic properties of nanoscopic matter in the gas phase by using angle-resolved elastic light scattering, which is also known as Mie scattering [1]. Mie scattering is well-known in the visible regime, where size-effects of microparticles, which are much larger than the wavelength of the incident radiation, are probed [1]. Related experiments on free nanoparticles require VUV radiations [2], or even shorter wavelengths. First results on the use of soft X-rays are reported in this work [3].

Structured nanoparticles are prepared by chemical syntheses [2,3]. The samples are dispersed in suitable solvents, such as ethanol. Subsequently, the dispersions are sprayed into the gas phase at ambient pressure by using an atomizer. The solvent is evaporated and the particles are size selected by a differential mobility analyzer (DMA). An aerodynamic lens system focuses the beam of nanoparticles to a diameter of $\sim 500 \mu\text{m}$ into the scattering center, which is located in a high vacuum chamber. There, the particle beam is crossed by monochromatic synchrotron radiation from BESSY (beamlines UE49/2-PGM and UE-52-SGM). Angle-resolved elastic light scattering is detected by a rotatable CsI-coated microchannel plate (MCP) photon detector. It is tuned in the polarization plane of the synchrotron radiation, covering the angle range between 3° and 140° . Two types of experiment are performed: (i) studies on the scattered light intensity at fixed photon energy and (ii) scans of the photon energy near a core-level absorption edge at fixed scattering angle.

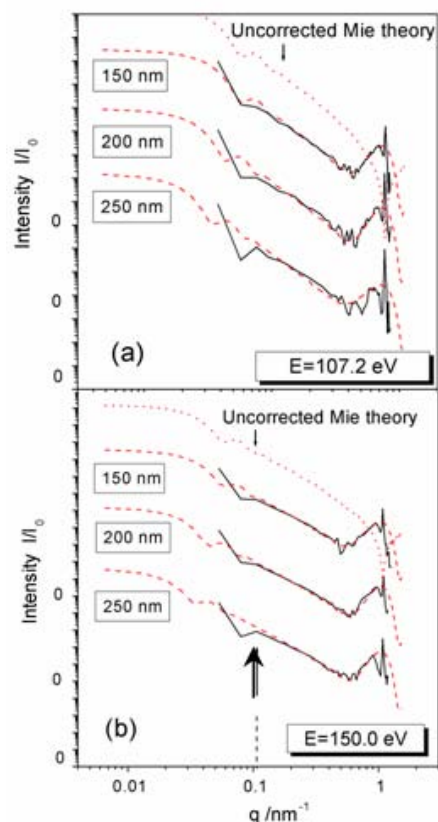


Fig. 1: Scattered light intensity from variable size SiO_2 nanoparticles. The dashed curves correspond to modeled results. The dotted curve is the result of Mie simulations. Further details: see text.

particles are size selected by a differential mobility analyzer (DMA). An aerodynamic lens system focuses the beam of nanoparticles to a diameter of $\sim 500 \mu\text{m}$ into the scattering center, which is located in a high vacuum chamber. There, the particle beam is crossed by monochromatic synchrotron radiation from BESSY (beamlines UE49/2-PGM and UE-52-SGM). Angle-resolved elastic light scattering is detected by a rotatable CsI-coated microchannel plate (MCP) photon detector. It is tuned in the polarization plane of the synchrotron radiation, covering the angle range between 3° and 140° . Two types of experiment are performed: (i) studies on the scattered light intensity at fixed photon energy and (ii) scans of the photon energy near a core-level absorption edge at fixed scattering angle.

The present experiments are carried out by using pre-made SiO_2 nanoparticles of ~ 150 , ~ 200 , and ~ 250 nm, as derived from electron microscopy. Fig. 1 shows the angle-resolved scattering patterns recorded at two photon energies, i.e. at the Si 2p-edge (107.2 eV) and in the Si 2p-continuum (150.0 eV),

where the scattering wave vector q is used. The full curves are the experimental results. These agree well with dashed curve, which are obtained from model simulations taking changes in reflectivity, which is due to a rough and graded surface, as well as diffuse and specular reflection into account. Note that a sharp maximum near $q=1$ is due to the particle beam hitting the detector. For a comparison, Fig. 1 also includes Mie simulations (dotted curve), where significant deviations from the experimental results are observed. These become evident for the distinct minimum occurring in the Mie simulations at $q\sim 1$, whereas this minimum occurs at smaller q -values in the experimental and model results. There is also a distinct step in the experimental spectra, which is observed near the angle of total internal reflection ($q\sim 0.1$, arrow in Fig. 1). The position of this feature is also shifted in the Mie simulations and the model results, indicating that there are limitations in both approaches in the low q -regime. Fig. 2 shows scans of the scattered light intensity near the Si 2p-edge, recorded at scattering angles, where the Mie model is applicable (see dashed curves in Fig. 2, using the optical constants from ref. [4]). The near-edge spectrum (NEXAFS) of SiO₂ is included in Fig. 2 for a comparison. The spectral features in experiment and model simulations agree well with each other in the Si 2p-regime, whereas below 90 eV significant discrepancies occur. It is important to note, that the particles occur in narrow size distributions, which are also considered by the Mie model. This yields for the three samples under study the following diameters: 147 nm ($\pm 7.1\%$), 192 nm $\pm 5.0\%$, and 240 nm $\pm 4.6\%$). Evidently, Mie scattering from single particles in the soft X-ray regime is suitable to determine accurately the particle size as well as size distributions, which are consistent with results from electron microscopy. This emphasizes the applicability of the present approach to characterize size-dependent structural and optical properties of free nanoscopic particles by using the nanoparticles beam approach in conjunction with tunable synchrotron radiation in the soft X-ray regime [3].

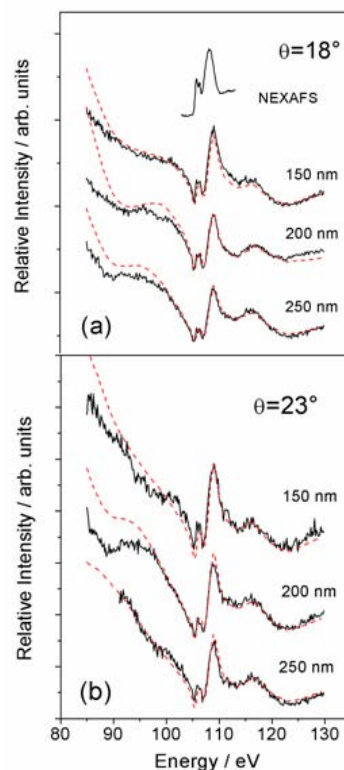


Fig. 2: Energy resolved scattered light intensity from size-selected SiO₂ nanoparticles at given scattering angles (full curves) in comparison with Mie simulations (dashed curves).

This project has been supported by the Bundesministerium für Bildung und Forschung (contract No. 05-KS4WW1/7) and the Fonds der Chemischen Industrie. We gratefully acknowledge the excellent beamline support by Kai Godehusen and Olaf Schwarzkopf.

References

- [1] P. A. Baron K. Willecke (Eds.) *Aerosol Measurement*, Wiley, New York (2001).
- [2] J..N Shu, K.R. Wilson, M. Ahmed, S.R. Leone, C. Graf, and E. Rühl, *J. Chem. Phys.* **124**, 034707 (2006).
- [3] H. Bresch, B. Wassermann, B. Langer, C. Graf, R. Flesch, U. Becker, B. Österreicher, T. Leisner, and E. Rühl, *Faraday Discuss.*, invited article, to be submitted for publication (2007).
- [4] E. Filatova, V. Lukjanov, R. Barchewitz, J.M. André, M. Idir, and Ph. Stemmler, *J. Phys., Condens. Matter* **11**, 3355 (1999).

Investigation of the Electronic Properties of Structured II-VI-Semiconductor Nanoparticles in Selected Environments

C. Graf^{a,b}, R. Lewinski^{a,b}, S. Dembski^b, B. Langer^a and E. Rühl^{a,b}

^a Institut für Chemie und Biochemie, Freie Universität Berlin, Takustr. 3, 14195 Berlin

^b Institut für Physikalische Chemie, Universität Würzburg, Am Hubland, 97074 Würzburg

Semiconductor nanoparticles (quantum dots, QD) have unique size-dependent optical and electronic properties. Especially, small nanoparticles have a large surface-to-bulk ratio. Therefore, it is expected that the particle surface dominates their physical and chemical behavior, so that the local environment near the surface strongly influences their properties. All previous investigations of QD using soft X rays have been carried out on samples deposited on a surface. Hence, an influence of the substrate on the electronic properties of the particles cannot be excluded. Further, as a result of the large surface-to-bulk ratio of nanoparticles a significant influence on their electronic properties by the substrate appears to be possible. The approach of confining simple model particles in an electrodynamic trap has been demonstrated to be suitable to investigate liquid and solid micro- and nanoparticles without any contact to a substrate.^[1] More recently, this method was successfully used for NEXAFS measurements on single silica colloids.^[1] Based on the results on preliminary studies, we used this approach for investigating the electronic structure of II-VI semiconductor nanoparticles in selected solid and liquid environments. CdSe/ZnS core shell nanoparticles (3.2 nm in diameter), stabilized with the hydrophilic ligand cysteamine are dispersed in a liquid non-volatile siloxane graft/block copolymer and injected with a piezo injector in an electrodynamic trap, where a single liquid microdroplet is stably stored under ultra high vacuum conditions. In this way, it is possible to investigate quantum dots by soft X ray spectroscopy in a liquid environment which is not influenced by any substrate. A direct measurement of the total electron yield (TEY) is not possible, because of the electric quadrupole field of the trap. Therefore, NEXAFS spectra are obtained from X ray excited optical luminescence (XEOL). For a comparison, CdSe/ZnS nanoparticles are investigated in a solid silica environment. Therefore, the QD are embedded in a controlled way in silica colloids (450 nm diameter).^[2] Firstly, the QD are coated by the amphiphilic polymer polyvinylpyrrolidone (PVP). Subsequently, they are attached to amino-functionalized silica colloids, so that the interparticle distance can be adjusted by the length of the polymer. Finally, the particles are coated by a silica layer of about

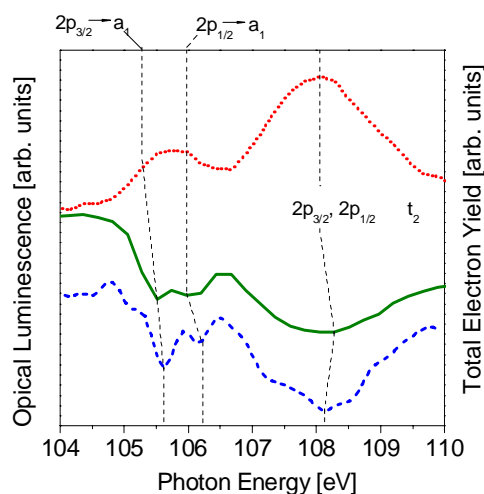


Fig. 1: XEOL spectra of a liquid siloxane block/graft copolymer droplet (blue dashed line) and TEY (red dotted line) and XEOL (green solid line) spectra of solid silica colloids (d = 160 nm) on a graphite coated Cu substrate in the regime of the Si 2p edge (104 - 110 eV).

15 nm thickness. These QD doped silica colloids are adsorbed on a Cu surface. Therefore, their X ray excitation spectra are recorded in the TEY- as well as the XEOL-approach, so that the results of both techniques can be directly compared to each other. Firstly, pure siloxane block graft polymer droplets are investigated. Therefore, XEOL spectra of the polymer droplets as well as TEY- and XEOL spectra of solid silica colloids (d = 160 nm) on a graphite coated Cu surface are recorded in the regime of the Si 2p edge (104 - 110 eV) (see Fig. 1). Both XEOL spectra are inverse to the TEY spectrum of the silica colloids. Such an inversion has been observed before, which is due to the competitive absorption of sites, that are responsible for the luminescence and those that are not involved. The efficiency of the luminescence channels has also to be taken into account (cf. ref. [3]). In the case of the silica colloids, the minima in the XEOL spectrum are nearly identical with the maxima of the TEY spectrum of the

same particles. Similar findings are reported for the TEY and EELS spectra of amorphous SiO₂.^[4a] This shows that the luminescence originates from the entire sample. The NEXAFS structures of the silica colloids are characteristic for Si that is bound in a tetrahedral oxygen environment^[4a] The XEOL spectrum of the siloxane block graft polymer droplets shows also the typical Si-O resonances, which are only slightly shifted compared to the solid colloids. Further, less pronounced minima are observed, which are typical for Si-C σ^* bond orbital resonances.^[4b] It could be shown that the NEXAFS structures of the polymer droplets remain unchanged after several hours of continuous irradiation with photon energies below 200 eV. The influence of the dispersion medium and functionalization on the properties of the outer ZnS shell is probed by XEOL spectra of CdSe/ZnS nanoparticles dispersed in the liquid polymer droplets and embedded in silica colloids. First results are obtained from studies in the S 2p regime (150 -180 eV) (not shown in this report). The CdSe core of the quantum dots is selectively excited in the Cd 3d regime (405 - 425 eV). In this energy regime it was not possible to measure XEOL spectra of QD that are trapped in microdroplets. This is because of low target density and rapid radiation damage. Therefore, it is only possible to measure XEOL- and TEY-spectra of silica colloids doped with CdSe/ZnS nanoparticles on a Cu substrate (see Fig. 2). These results are compared with those on CdSe NP in liquid droplet where the charging current of the trapped microdroplet is measured as a function of the photon energy. Such measurements require more than 1000 times lower synchrotron radiation intensity than the studies on liquid droplets, so that radiation damage of the sample is successfully minimized. Unlike the spectra shown in Fig. 1 the XEOL spectrum at the Cd 3d edge is not inverted. Thus, in the case of the CdSe core, which shows a high photoluminescence after excitation with visible light, there is also above the Cd 3d absorption edge the optical luminescence the most effective decay process. All spectra shown in Fig. 2 are similar to those reported for surface deposited CdSe nanoparticles.^[6] The broad features occurring at 410 – 412 eV and 415 – 420 eV correspond to the 3d_{3/2} and 3d_{5/2} fine structure components. The TEY spectrum of the silica colloids doped with CdSe/ZnS nanoparticles and the charging curve of the QD in the droplet show an excellent agreement. This result clearly indicates

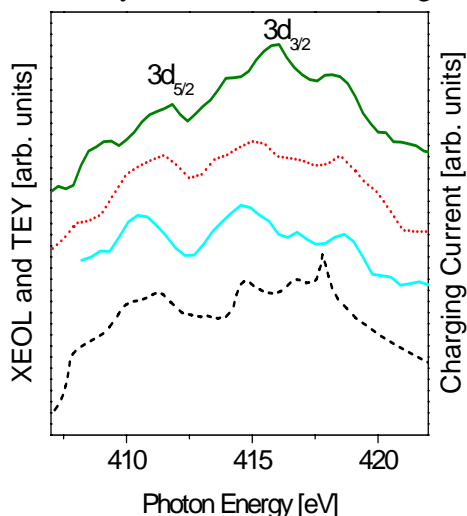


Fig. 2: XEOL (green solid line, top) and TEY spectra (red dotted line) of silica colloids ($d = 450$ nm) doped with CdSe/ZnS nanoparticles on a Cu substrate as well as charging current dQ/dt of CdSe/ZnS nanoparticles dispersed in a liquid siloxane block/graft copolymer droplet (cyan solid line) in the regime of the Cd 3d edge (405 - 425 eV). The NEXAFS spectrum of CdSe nanoparticles ($d = 3.2$ nm) on a silicon substrate (black dashed line) is shown for a comparison (as taken from ref. [6]).

that the inner core of the particles is not influenced by the embedding matrix, whereas results recorded at the S 2p-edge show that significant changes of the outer shell are observed in the near-edge spectra.

This work is supported by the DFG (SFB 410-TP 8) and the BMBF.

References

1. (a) M. A. Hamza, B. Berge, W. Mikosch, and E. Rühl, *Phys. Chem. Chem. Phys.* **6**, 3484 (2004), (b) M. Grimm, B. Langer, S. Schlemmer, T. Lischke, U. Becker, W. Widdra, D. Gerlich, R. Flesch, and E. Rühl, *Phys. Rev. Lett.* **96**, 066801 (2006).
2. C. Graf, S. Dembski, A. Hofmann, and E. Rühl, *Langmuir* **22**, 5604 (2006).
3. S. J. Naftel, Y. M. Yiu, T. K. Sham, and B. W. Yates, *J. Electron Spectrosc.* **119**, 215 (2001).
4. X. H. Sun, Y. H. Tang, P. Zhang, S. J. Naftel, R. Sammynaiken, T. K. Sham, H. Y. Peng, Y. F. Zhang, N. B. Wong, and S. T. Lee, *J. Appl. Phys.* **90**, 6379 (2001), (b) J. H. Kang, K. Cho, J. K. Kim, C. E. Park, S. J. Uhm, and B. B. Khatua, *J. Adhes. Sci. Technol.* **18**, 1815 (2004).
5. B. Gilbert, B. H. Frazer, H. Zhang, F. Huang, J. F. Banfield, D. Haskel, J. C. Lang, G. Srajer, and G. De Stasio, *Phys. Rev. B* **66**, 245205 (2002), (b) M. Han, Y. Luo, J. E. Moryl, R. M. Osgood, and J. G. Chen, *Surf. Sci* **415**, 251 (1998), (c) F. Jalilvand, *Chem. Soc. Rev.* **35**, 1256 (2006).
6. K. S. Hamad, R. Roth, J. Rockenberger, T. van Buuren, and A. P. Alivisatos, *Phys. Rev. Lett.* **83**, 3474 (1999).

Kinetics of palladium oxidation and methane oxidation on Pd(111) and (110)

Dmitry Zemlyanov¹, Harald Gabasch², Bernhard Klötzer², Axel Knop-Gericke³, Robert Schlögl³

¹Materials and Surface Science Institute, University of Limerick, Limerick, Ireland

²Intitut für Physikalische Chemie, Universität Innsbruck, A-6020, Innsbruck, Austria

³Fritz-Haber-Institut der Max-Planck-Gesellschaft, Faradayweg 4-6, D-14195 Berlin, Germany

The proposal was supported through Integrated Infrastructure Initiative I3 in FP6 R II 3 CT-2004-506008.

Palladium is considered as the best catalyst for the catalytic combustion/partial oxidation of methane and other small hydrocarbons, which is an environmentally benign process for power generation with low NO_x emissions and for removal of residual methane from the emission gases of methane-powered vehicles [1]. Investigation of the oxidation mechanism of palladium and the mechanism of oxide decomposition is critical for developing/improving Pd-based catalysts. Palladium oxidation is a complex process consisting of several steps, among them formation of different metastable surface oxide phases [2, 3].

In this project we aimed to study in detailed mechanism of palladium oxidation on Pd(111) and on Pd(110) surfaces, expecting difference in kinetics of the close-packed (111) surface and more open (110) surface.

The kinetics of palladium oxidation was studied by in situ XPS on Pd(111) and Pd(110) surface at 0.2-0.8 mbar O₂ at 275C - 425C. The characteristic O 1s and Pd 3d_{5/2} spectra are shown in Figure 1. Three peak detected in the Pd 3d_{5/2} spectrum are assigned to metallic palladium, Pd(B), to oxidation state, peaks Pd(Ox1) and Pd(Ox2).

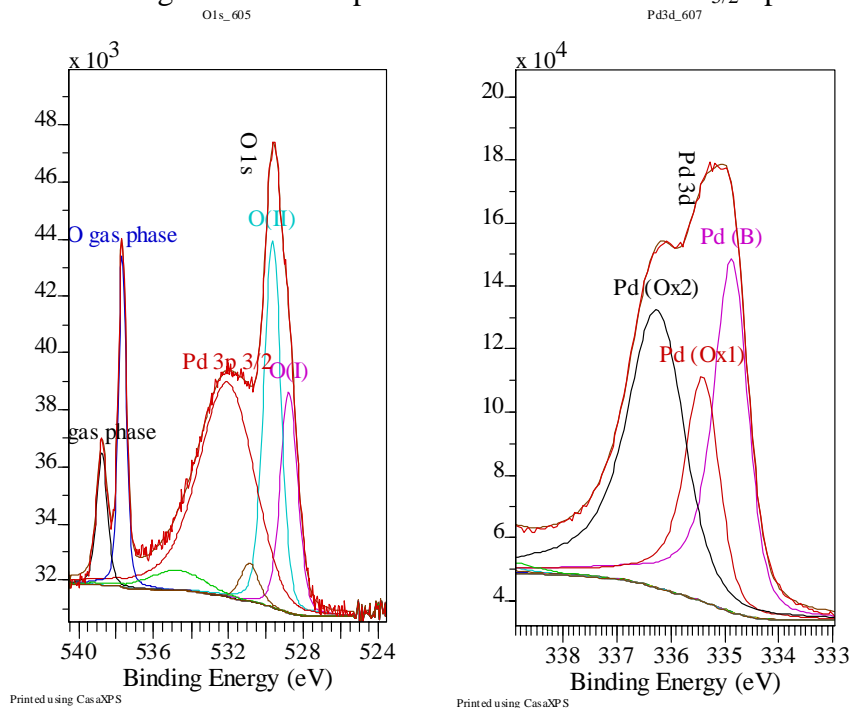


Figure 1. The characteristic O 1s and Pd 3d_{5/2} spectra obtained in-situ during Pd(111) oxidation.

the bulk PdOas shown in Figure 1.

Palladium oxidation can be monitored with the O(II) and Pd(Ox2) peaks as shown for Pd(111) in Figures 2. Palladium oxidation was found to be complex process, which consists of at least 3 stages. The first slow stage is formation of Pd “seeds”. The seed formation is competing with seed decomposition and the resultant rate is depending on oxygen pressure

and temperature. At high temperature, the seed decomposition is prevailing over seed formation and higher pressure is required to overcome this limitation (the right panel of Figure 2). The second stage is oxide particle growth. A 3D growth of PdO particles was observed during this stage. The PdO particles are supposed to grow from the PdO seeds. The reaction rate at this stage is likely not a function of pressure but temperature. Completed coverage of the surface by the PdO particles results in deceleration of the oxidation process. The third stage is slow oxidation of palladium due to mass-transport limitation. The low reaction rate at this stage is explained by slow diffusion of either oxygen through PdO or palladium atoms towards the surface.

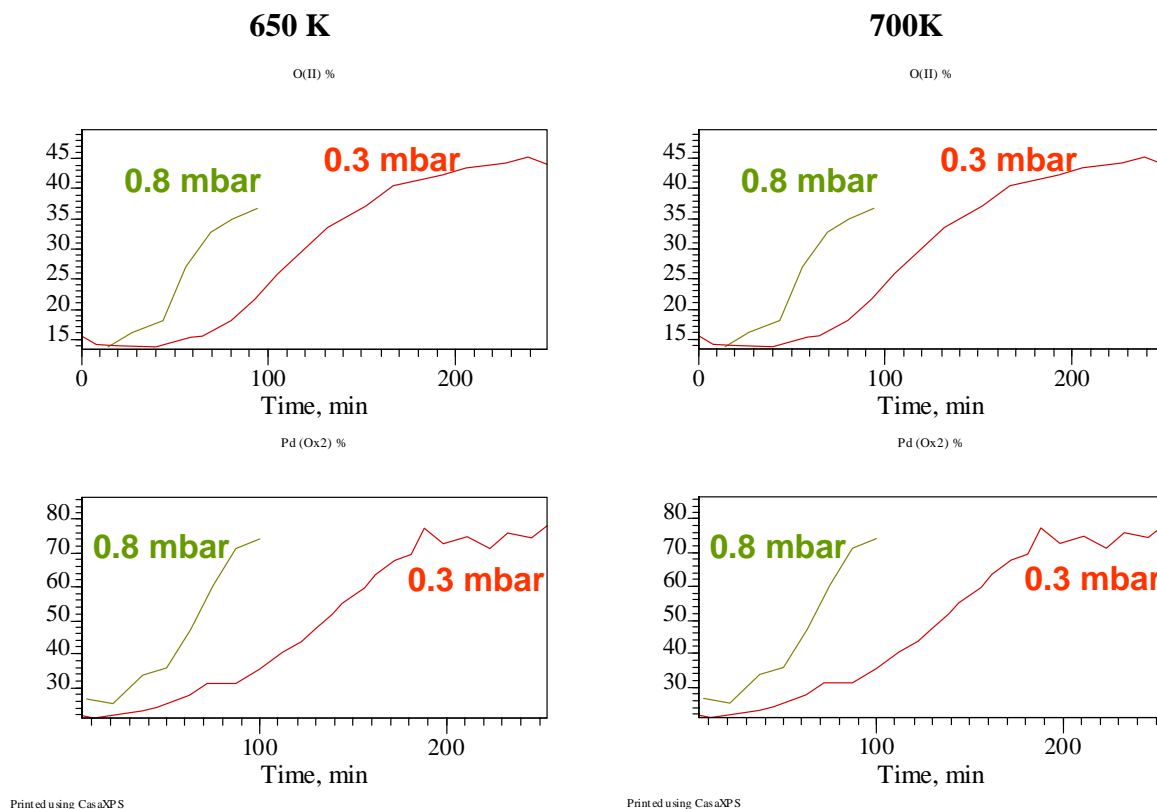


Figure 2. Relative intensity of the O(II) and Pd(Ox2) peaks observed on Pd(111) as a function of the exposure time depending on O₂ pressure and temperature. The left panel: the oxygen treatment was performed at 650K; the right panel: the oxygen treatment was performed at 700K.

Figure 3 represents relative intensity of the O(II) and Pd(Ox2) peaks observed on the Pd(110) surface during oxidation. The open Pd(110) surface oxidises faster and at lower temperature comparing with close-packed Pd(111). The obtained data allow us to draw the full model of palladium oxidation and explain kinetic peculiarities of the process.

The Pd seed are responsible for a catalytic activity maximum of methane combustion on Pd(111) and Pd(110). The activity reaches the maximum at maximum coverage of the PdO seeds. The deeper oxidation did not have such effect as the PdO seed coverage. In general, kinetics of total methane oxidation can be explained in the terms of palladium oxidation.

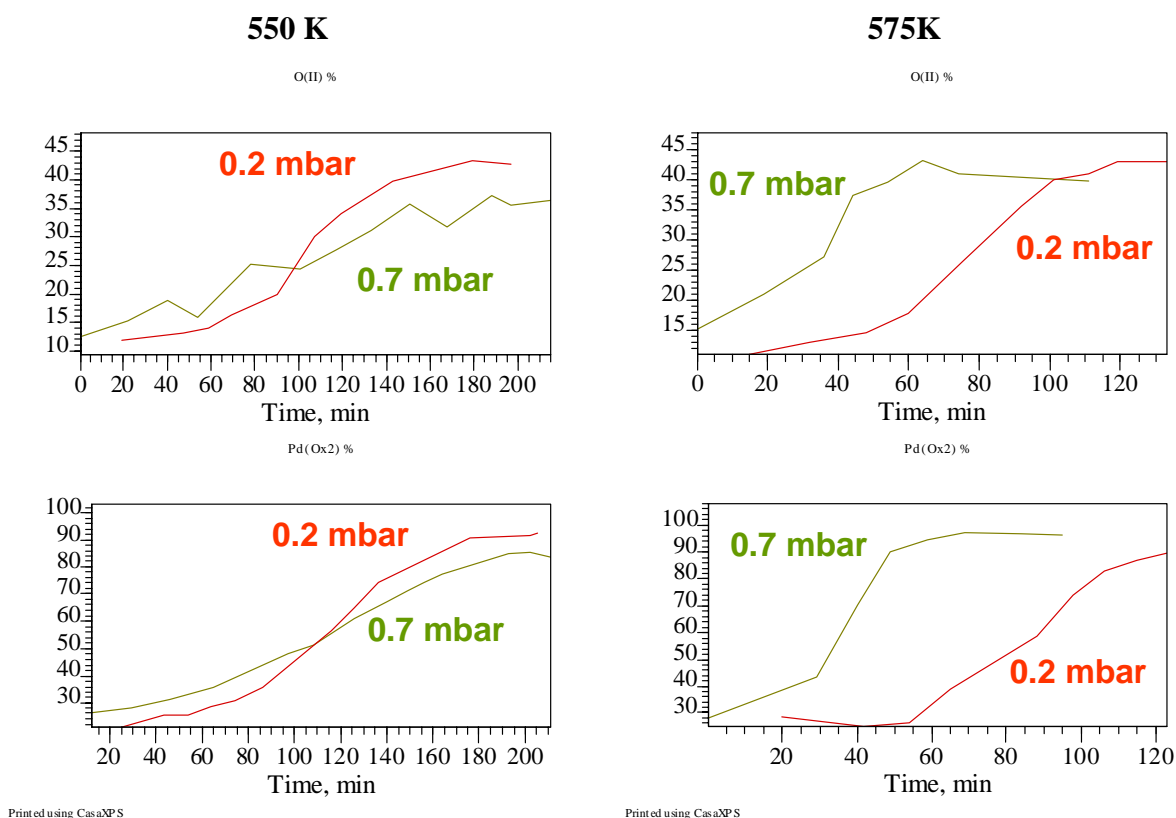


Figure 3. Relative intensity of the O(II) and Pd(Ox2) peaks observed on Pd(110) as a function of the exposure time depending on O₂ pressure and temperature. The left panel: the oxygen treatment was performed at 650K; the right panel: the oxygen treatment was performed at 700K.

References

- [1] G. Zhu, J. Han, D.Y. Zemlyanov and F.H. Ribeiro, *Journal of the American Chemical Society* 126 (2004) 9896.
- [2] H. Gabasch, W. Unterberger, K. Hayek, B. Kloetzer, E. Kleimenov, D. Teschner, S. Zafeiratos, M. Haevecker, A. Knop-Gericke, R. Schloegl, J. Han, F.H. Ribeiro, B. Aszalos-Kiss, T. Curtin and D. Zemlyanov, *Surface Science* 600 (2006) 2980.
- [3] D. Zemlyanov, B. Aszalos-Kiss, E. Kleimenov, D. Teschner, S. Zafeiratos, M. Haevecker, A. Knop-Gericke, R. Schloegl, H. Gabasch, W. Unterberger, K. Hayek and B. Kloetzer, *Surface Science* 600 (2006) 983.

Relating one-particle spectral function and dynamic spin susceptibility in superconducting $\text{Bi}_2\text{Sr}_2\text{CaCu}_2\text{O}_{8-\delta}$

D. S. Inosov,¹ S. V. Borisenko,¹ I. Eremin,^{2,3} A. A. Kordyuk,^{1,4} V. B. Zabolotnyy,¹ J. Geck,¹ A. Koitzsch,¹ J. Fink,¹ M. Knupfer,¹ B. Büchner,¹ H. Berger,⁵ and R. Follath⁶

¹*Institute for Solid State Research, IFW Dresden, P. O. Box 270116, D-01171 Dresden, Germany.*

²*Max Planck Institut für Physik komplexer Systeme, D-01187 Dresden, Germany.*

³*Institute für Mathematische und Theoretische Physik, TU-Braunschweig, 38106 Braunschweig, Germany.*

⁴*Institute of Metal Physics of National Academy of Sciences of Ukraine, 03142 Kyiv, Ukraine.*

⁵*Institut de Physique Appliquée, Ecole Polytechnique Fédérale de Lausanne, CH-1015 Lausanne, Switzerland.*

⁶*BESSY GmbH, Albert-Einstein-Strasse 15, 12489 Berlin, Germany.*

The puzzling magnetic resonance structure observed in superconducting cuprates is one of the most controversial topics in today's high- T_c superconductor physics. Existing theories waver between the itinerant magnetism and the local spins, as it appears that both approaches can qualitatively reproduce the main features of the magnetic spectra. It is a long standing question, which one of these two components (itinerant or localized) predominantly forms the integral intensity and the momentum-dependence of the magnetic resonances. One needs to be able to estimate their contribution quantitatively, carefully taking into account all the information about the electronic structure available from experiment.

To demonstrate such a possibility, we have fitted the experimental angle-resolved photoemission (ARPES) spectra of optimally doped $\text{Bi}_2\text{Sr}_2\text{CaCu}_2\text{O}_{8-\delta}$ (BSCCO) taken all over the Brillouin zone to create a parametric model of the renormalized single-particle Green's function (Fig. 1). Within the random phase approximation (RPA) we estimated the Lindhard function χ_0 and the dynamic spin susceptibility χ in the odd and even channels (Fig. 2) and compared the resulting spectrum calculated for optimally doped BSCCO with the available inelastic neutron scattering (INS) measurements.

The results are qualitatively similar to those obtained previously for the bare Green's function. The intensity of the resonance in the even channel is approximately two times lower than in the odd channel, which agrees with the experimental data. The absolute intensities of the resonances also fit the most recent experimental data perfectly well. As for the momentum dependence of χ , Fig. 2d shows the dispersions of incommensurate resonance peaks in both channels along the high-symmetry directions, calculated from the Green's function model with the self-energy derived from the ARPES data. We see the W-shaped dispersion similar to that seen by INS on $\text{YBa}_2\text{Cu}_3\text{O}_{6+\delta}$ (YBCO) and to the one calculated previously by RPA for the bare Green's function. At (π, π) both resonances are well below the onset of the particle-hole continuum at ~ 65 meV (dashed line), which also agrees with previous observations. At higher energies magnetic excitations are overdamped, so the upper branch of the "hourglass" near the resonance at (π, π) suggested by some INS measurements is too weak to be observed in the itinerant part of χ and is either not present in BSCCO or should originate from the localized spins.

In Fig. 2 we additionally show three constant-energy cuts of χ in the odd channel below the resonance, at the resonance energy, and above the resonance. As one can see, besides the main resonance at (π, π) the calculated χ reproduces an additional incommensurate resonance structure, qualitatively similar to that observed in INS experiments. Below the resonance the intensity is concentrated along the $(k, 0)$ and $(0, k)$ directions, while above the resonance it prevails along the diagonal directions $(k, \pm k)$.

The comparison of ARPES and INS data supports the idea that the magnetic response below T_c (or at least its major constituent) can be explained by the itinerant magnetism. Namely, the itinerant component of χ , at least near optimal doping, has enough intensity to account for the experimentally observed magnetic resonance both in the odd and even INS channels. The energy difference between the odd and even resonances seen in the experiments on both BSCCO and YBCO, cannot be explained purely by the difference in χ_0 between the two channels, but requires the out-of-plane exchange interaction to be additionally considered. In this latter case the experimental intensity ratio of the two resonances agrees very well with our RPA results. Also the calculated incommensurate resonance structure is similar to that observed in the INS experiment. Such quantitative comparison becomes possible only if the many-body effects and bi-layer splitting are accurately accounted for. A possible way to do that is to use the analytical expressions for the normal and anomalous Green's functions fitted to the ARPES data. We point out that such method is universal and can be applied also to other systems with electronic structure describable within the self-energy approach.

For details and further references see D. Inosov *et al.*, cond-mat/0612040.

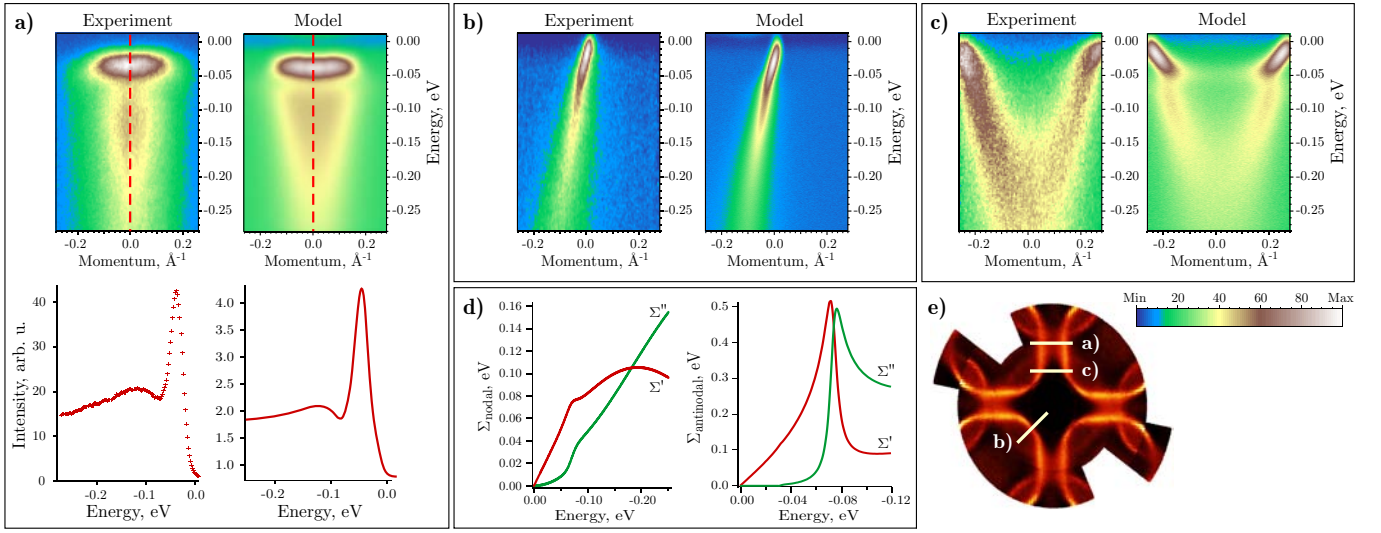


Fig. 1: Comparison of the model with experimental ARPES spectra of Bi-2212. **a)** Spectra at the $(\pi,0)$ point with the corresponding energy distribution curves (below) taken along the dashed lines. **b)** Nodal spectra along the (π,π) direction. **c)** Comparison of the experimental and model spectra taken at an intermediate position in k -space to check the validity of the interpolation of the self-energy between the nodal and antinodal directions. **d)** The Kramers-Kronig consistent real and imaginary parts of the nodal and antinodal self-energies. **e)** Positions of the cuts a)–c) in k -space.

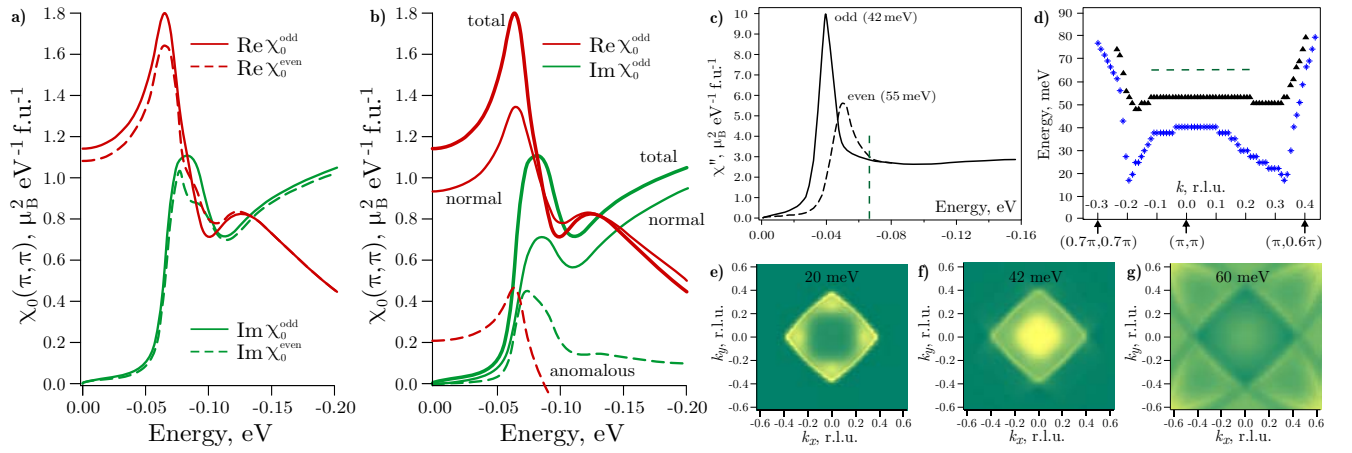


Fig. 2: **a)** Energy dependence of the real and imaginary parts of the Lindhard function χ_0 at the (π,π) point for the odd and even channels. **b)** Contributions of the normal (thin solid curves) and anomalous (dashed curves) components to the real and imaginary parts of χ_0^{odd} in the SC state. The sum of two components is shown as thicker curves. **c)** k -integrated susceptibility in the odd (solid curve) and even (dashed curve) channels. **d)** k -dependence of the resonance energies in odd ($*$) and even (\blacktriangle) channels along the high-symmetry directions $(0,0) - (\pi,\pi) - (\pi,0)$. The dashed lines mark the onset of the particle-hole continuum (position of the “step” in χ_0''). Second row: Constant energy cuts of χ'' in the odd channel below the resonance (**e**), at the resonance energy (**f**), and above the resonance (**g**). The center of each BZ image corresponds to the (π,π) point.

Investigation of the low energy electronic structure of YBCO

V. B. Zabolotnyy¹, S. V. Borisenko¹, A. A. Kordyuk^{1,2}, J. Geck¹, D. S. Inosov¹, A. Koitzsch¹,
J. Fink¹, M. Knupfer¹, B. Büchner¹, S.-L. Drechsler¹, R. Follath³, R. Weber³, V. Hinkov⁴,
B. Keimer⁴

¹Leibniz-Institute for Solid State and Material Research, D-01171 Dresden, Germany

²Institute of Metal Physics, 03142 Kyiv, Ukraine

³BESSY GmbH, Albert-Einstein-Strasse 15, 12489 Berlin, Germany

⁴Max-Planck-Institut für Festkörperforschung, 70569 Stuttgart, Germany

YBa₂Cu₃O_{7-δ} is the first superconductor to cross the boiling point of liquid nitrogen soon after the initial discovery of high temperature superconductivity [1] and, probably, one of the most widely investigated one. Despite this, the early photoemission studies did not turn out to be as successful as, for instance, those done for Bi-2212. According to LDA calculations, the bilayer-split plane derived bands and the quasi-one-dimensional band arising due to Cu-O chains are expected to be the most prominent features in the low energy electronic structure of YBCO-123. Although in some of the earliest ARPES studies [2-3] an evidence for the bilayer splitting, as well as for the chain band was reported, no clear indication for the bilayer splitting can be found in one of the most recent investigations performed with significantly improved momentum and energy resolution [4]. Contradicting attribution of the same spectral features to different bands [3-5] along with a presence of a strongly dispersing surface state and difficulties with clear observation of a superconducting gap [6] moved us still further away from complete understanding of the photoemission data for this compound. Recent observation of the resonance in the inelastic neutron scattering [7, 8] along with the above mentioned indications in early ARPES studies, renders this compound a propitious target for additional detailed ARPES investigation.

The data discussed in this report were collected at the beamline UE112-PGM1 with SES 100 electron energy analyzer and at the recently put into operation UE112-LowE PGMr beamline equipped with SES R4000 analyser. In Fig. 1 (a) we show an experimentally obtained FS map. The couples of square-like features centred at the S points correspond to the bonding (inner one) and the antibonding (outer one) band. It is also easy to recognize that the two weaker features, parallel to k_x axis, correspond to a quasi-one-dimensional chain band. Following the predictions of the LDA calculations [9] the dispersion of all three bands can easily be traced down to energies of about 200 meV, as can be seen from Fig. 1 (c).

Though the measurements were performed at temperatures much below T_C , neither

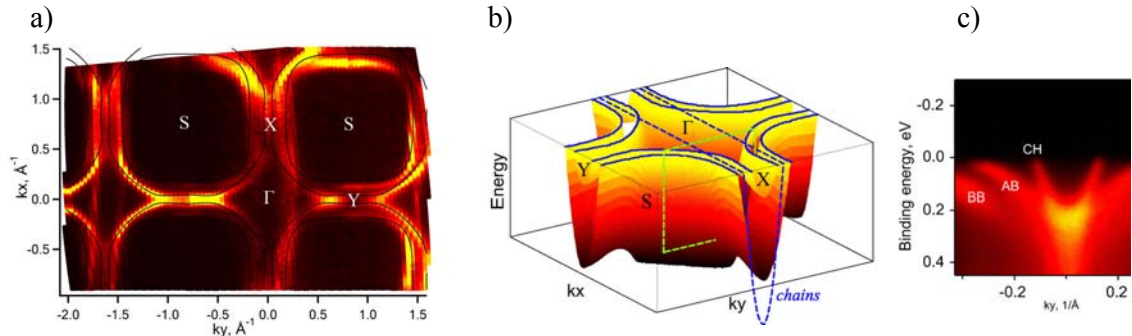


Fig. 1. (a) Fermi surface map YBa₂Cu₃O_{7-δ} measured using wide acceptance angle mode of SES R4000 analyzer, $h\nu = 100$ eV. Schematics of the low-energy bands (panel b) and the experimental spectrum of YBa₂Cu₃O_{6.85} (panel c) that clearly showing the presence of bilayer split bonding (BB), antibonding (AB) and chain (CH) bands. Green rectangle denotes the cut position in k -energy space of the reduced Brillouin zone.

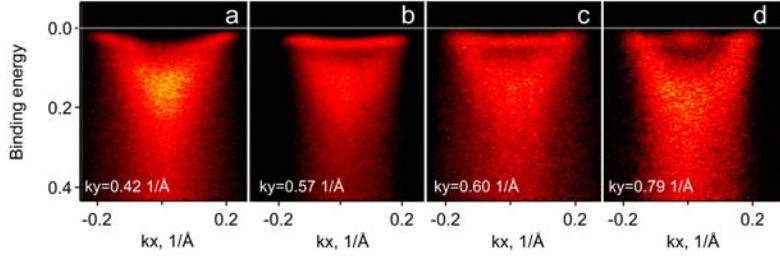


Fig. 2. Renormalization effects and opening of the superconducting gap in $\text{YBa}_2\text{Cu}_3\text{O}_{6.6}$, $T_C=61\text{K}$, $h\nu = 50\text{ eV}$

comes from the estimate of the doping level based on the FS area, which gives $x \approx 0.30$ instead of expected $x \approx 0.15$. Similar overdoping of the near-surface region probed in photoemission experiment was observed in our numerous subsequent measurements for the samples with the same stoichiometry, proving this to be a robust effect. Therefore the overdoping effect provides a natural explanation to the problems experienced with gap observation in ARPES and STM experiments and also dispels an apparent contradiction between the high T_C for the sample and the doping level of the near-surface crystal region, most likely, modified after cleavage. The ARPES technique can also provide information concerning the thickness of the overdoped region. Analyzing the spectra more thoroughly it was found that a single EDC measured in the vicinity of the X/Y point, in addition to the two peaks from overdoped bilayer split bands, always contains an extra peak (not shown here) at energies about 40–50 meV that practically disappears above T_C , similar to the one observed in [5].

By tuning the polarization and the excitation energy it is possible to partly suppress the photoemission from the overdoped component, so that the whole spectrum attains familiar superconducting features, like those normally observed in the Bi-2212 systems [10, 11]. In particular, in Fig. 2 (a) one can see the widely discussed kinks in the band dispersion at the energy of about 50 meV. When moving closer to the Y point (panel b), similar to Bi-2212, the renormalization becomes so strong that the spectral weight gets concentrated in one practically flat and non-dispersing feature. However, in the very vicinity of the Y point the overdoped component takes over again. In panel (d) one can notice the appearance of the anti-bonding band of the overdoped component as well as the increase of the spectral weight at the Fermi level, which becomes especially pronounced when comparing to image (b). The fact that it is possible to detect the superconducting component in ARPES experiments tells us that the thickness of the overdoped layer is of the order of photoelectron escape depth, i.e. 5–10 Å and is comparable to one lattice spacing along the c-axis.

References

- [1] J. G. Bendorz, K. A. Müller, *Z. Phys. B* 189, **64** (1986)
- [2] G. Mante et al. *Phys. Rev. B* 9500, **44**, (1991)
- [3] M. C. Schabel et al., *Phys. Rev. B* 6090, **57**, (1998)
- [4] M. C. Schabel et al., *Phys. Rev. B* 6107, **57** (1998)
- [5] D. H. Lu et al. *Phys. Rev. Lett.* 4370, **86** (2001)
- [6] J. G. Tobin et al., *Phys. Rev. B* 5563, **45** (1992)
- [7] H. F. Fong et al., *Phys. Rev. Lett.* 1939, **82** (1999)
- [8] P. Bourges et al., *Science* 1243, **288** (2000)
- [9] O. K. Andersen et al., *J. Phys. Chem. Solids* 1573, **56** (1995)
- [10] T. Kim et al., *Phys. Rev. Lett.* 167002, **90** (2003)
- [11] A. Kaminski et al., *Phys. Rev. Lett.* 1070, **86** (2001)

analysis of the leading edge gap positions nor the experimental band dispersion supported the existence of a superconducting gap larger than 10 meV, which is in contrast with T_C of about 90 K and nearly optimal doping of the sample. Explanation to this apparent controversy

EXAFS characterization of In implanted GaN

M. Katsikini¹, F. Pinakidou¹, E.C. Paloura¹, E. Wendler², W. Wesch² and A. Erko³

¹School of Physics, Aristotle University of Thessaloniki, Thessaloniki, 54124, Greece

²Institut für Festkörperphysik, Friedrich-Schiller Universität Jena, Germany

³BESSY mbH, Germany

InGaN/GaN heterostructures find applications in the fabrication of high efficiency light emitting diodes as well as in high – frequency, high – power microelectronic devices.¹ Ion implantation followed by annealing is a promising method for the growth of nanomaterials^{2,3}, as for example InGaN quantum dots which enhance the emission characteristics of InGaN – based laser diodes.⁴ Here, we apply EXAFS spectroscopy at Ga K edge, for the study of In implanted GaN samples. The samples are studied in the as-grown and as-implanted states as well as after rapid thermal annealing (RTA).

A 400nm – thick – GaN sample was grown on Al₂O₃ by Plasma Enhanced Molecular Beam Epitaxy⁵. The sample was diced and the individual pieces were implanted at 77 K with 700 keV In ions with fluence equal to $5 \times 10^{15} \text{cm}^{-2}$. The implanted samples were subjected to RTA at 800° and 900° C for 15 sec. In order to prevent nitrogen loss during the annealing, the implanted samples were sandwiched with unimplanted ones and the annealing was performed in N₂ atmosphere under pressure of 200 Torr. The Ga K EXAFS spectra were recorded at the KMC – II beamline. The fluorescence photons were detected using a Si photodiode. The spectra were normalized with the intensity of the impinging to the sample beam, I₀. In order to avoid polarisation effects, the angle of incidence was equal to the magic angle (55° to the sample surface). Rutherford backscattering shows that implantation leads to the formation of a ~200nm – thick surface amorphous layer. Since the information depth of the fluorescence photons, calculated following the procedure described by Troger *et al*⁶, is approximately equal to 6μm, the EXAFS spectra contain information of both the completely amorphous as well as the highly defective layer that lies underneath.

Prior to analysis the EXAFS spectra were subjected to subtraction of the atomic background and transformation from the energy space to the photoelectron wavenumber (k) space. The Fourier Transforms (FT) of the resulting $\chi(k)$ spectra are shown in Fig. 1. The amplitude of the FT corresponds to the radial distribution function around the absorbing atom and thus the first and the second peaks in the FT correspond to the 1st and 2nd nearest neighboring (nn) shells of the Ga atom, that consist of N and Ga atoms, respectively. The $\chi(k)$ spectra were fitted using the FEFFIT program with the photoelectron scattering theoretical paths that were constructed with FEFF8 code.⁷ A model of hexagonal GaN with $a=3.173\text{\AA}$,

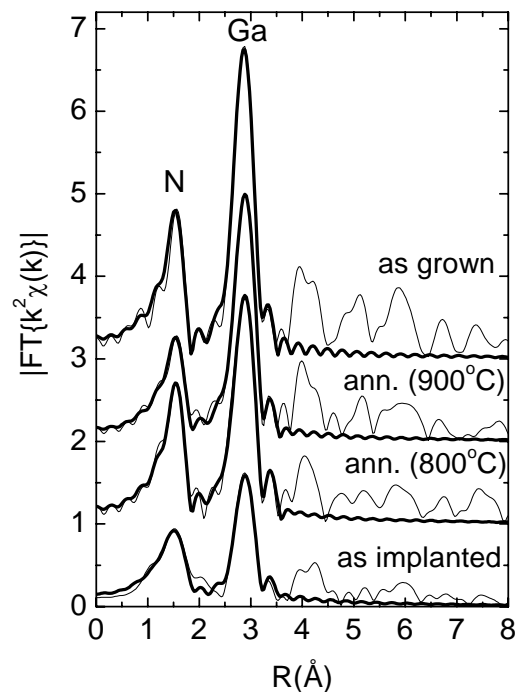


Figure 1: Amplitude of the Fourier transforms of the $k^2 \chi(k)$ spectra from the as – implanted and the annealed samples. The FTs are calculated in the k - range $[3.3, 14 \text{\AA}^{-1}]$. The experimental and the fitting curves are shown in thin and thick lines, respectively.

Table I: Fitting results of the Ga K edge EXAFS spectra. R are the nearest neighboring distances, N are the coordination numbers and σ^2 are the Debye Waller factors. The provided errors are the uncertainties in the determination of the parameter values calculated by the FEFFIT program.

Sample	$R_{\text{Ga-N}}(\text{\AA})$ ± 0.01	$R_{\text{Ga-Ga}}(\text{\AA})$ ± 0.005	$N_{\text{Ga-N}}$	$N_{\text{Ga-Ga}}$	$\sigma^2_{\text{Ga-N}}$ ($\times 10^{-3} \text{\AA}^2$)	$\sigma^2_{\text{Ga-Ga}}$ ($\times 10^{-3} \text{\AA}^2$)
as grown	1.94	3.178	4 (fixed)	12(fixed)	1.5 ± 0.7	5.2 ± 0.3
as implanted	1.95	3.187	3.5 ± 0.4	4.8 ± 0.6	6.7 ± 1.4	5.0 ± 0.7
annealed (800°C)	1.94	3.192	3.8 ± 0.6	11.4 ± 2.1	1.9 ± 1.4	6.6 ± 1.2
annealed (900°C)	1.94	3.193	3.1 ± 0.3	10.6 ± 0.8	2.8 ± 0.9	5.7 ± 0.4

$c = \sqrt{\frac{8}{3}}a$ and $u = \frac{3}{8}$ is used in order to have the maximum path degeneracy and reduce the number of the

paths used in the fitting. The fitting was performed in the 3 first nn shells (Ga-N, Ga-Ga and Ga-N), up to a distance of 3.8Å. The fitting results for the first two nn shells are listed in Table I.

The EXAFS analysis reveals a marginal increase of the Ga – Ga distance after implantation and annealing, probably due to the incorporation of the In atoms in the Ga sublattice and / or due to the formation of point and extended defects. Implantation also causes a decrease of the coordination number in the 1st and 2nd nn shells of Ga. A similar behavior was observed in GaN layers that were amorphized by 4.7MeV Au implantation.⁸ However, the undercoordination of Ga reported by Ridgway *et al* was more severe, most probably due to the higher mass and energy of the implanted ions. Although annealing at 800°C causes the recovery of the coordination numbers in both the 1st and 2nd nn shells, further increase of the annealing temperature to 900°C causes reduction of the coordination number $N_{\text{Ga-N}}$ in the 1st nn shell. This result could be attributed to loss of nitrogen which was previously reported.^{9,10}

In conclusion, implantation of 700 keV In ions into GaN with a fluence of $5 \times 10^{15} \text{cm}^{-2}$ causes the formation of a 200nm – thick surface amorphous layer while the underlying GaN layer is severely defected. Implantation causes decrease of the coordination number of the 1st and 2nd nn shells of Ga which are recovered after annealing at 800°C. Further increase of the annealing temperature to 900°C causes loss of nitrogen from the GaN samples.

¹ Group III-nitride Semiconductor Compounds: Physics and Applications, edited by B. Gil (Oxford, Clarendon, 1998).

² E. Borsela, M. A. Garcia, G. Mattei, C. Maurizio, P. Mazzoldi, E. Cattaruzza, F. Gonella, G. Battaglin, A. Quaranta and F. D'Acapito, *J. Appl. Phys.*, **90**, 4467 (2001).

³ A. B. Denison, Louisa J. Hope-Weeks, Robert W. Meulenberg, and L. J. Terminello, in Introduction to Nanoscale Science and Technology, edited by Massimiliano Di Ventra (Kluwer Academic Publishers, Boston, 2004), p.194-198.

⁴ R. A. Oliver, G. Andrew D. Briggs, M. J. Kappers, C. J. Humphreys, S. Yasin, J. H. Rice, J. D. Smith and R. A. Taylor, *Appl. Phys. Lett.*, **83**, 755 (2004).

⁵ T. D. Moustakas, T. Lei, and R. J. Molnar, *Physica B* **185**, 36 (1993).

⁶ L. Tröger, D. Arvanitis, K. Baberschke, H. Michaelis, U. Grimm, E. Zschech, *Phys. Rev. B*, **46**, 3283 (1992).

⁷ A. L. Ankudinov, B. Ravel, J. J. Rehr, and S. D. Conradson, *Phys. Rev. B* **58**, 7565 (1998).

⁸ M. C. Ridgway, S. E. Everett, C. J. Glover, S. M. Kluth, P. Kluth, B. Johannessen, Z. S. Hussain, D. J. Llewellyn, G. J. Foran and G. de M. Azevedo, *Nucl. Instrum. Methods Phys. Res. B*, **250**, 287 (2006).

⁹ K. N. Lee, X. A. Cao, C. R. Abernathy, S. J. Pearton, A. P. Zhang, F. Ren, R. Hickman, and J. M. Van Hove, *Solid State Electronics* **44**, 1203 (2000).

¹⁰ J. C. Zolper, D. J. Rieger, A. G. Baca, S. J. Pearton, J. W. Lee, and R. A. Stall, *Appl. Phys. Lett.* **69**, 538 (1996).

Mg K – edge study in Norwegian ilmenite using XANES.

M. Klepka, I.N. Demchenko, K. Lawniczak-Jablonska and D. Batchelor¹

Institute of Physics Polish Academy of Sciences, al. Lotnikow 32/46 PL-02668 Warsaw, Poland

¹ Bayerische Julius-Maximilians-Universität Würzburg, Sanderring 2 97070 Würzburg, Germany

Ilmenite is a natural mineral used by many companies all over the world as a source for white pigment production. TiO_2 (white pigment) is produced mainly by sulphate method, where reaction of titanium raw material with sulphuric acid is the first step of the process [1,2]. Knowledge about the ionic states of elements and phase content in ilmenites is fundamental to proper adjustment of the chemical reactions. The origin of the minerals influence the composition through the minority elements and thus have a large influence on efficiency, safety, kinetics of reaction and the quality of products. In this report we present the studies of ilmenite mined in Norway. The elemental composition evaluated using Single Particle Electron Probe Microanalysis (SP EPMA) showed as a minority element Mg at the level of 4 – 8 atomic % [3]. Our previous study on this mineral indicated the presence of three main phases: ilmenite (FeTiO_3), hematite (Fe_2O_3) and enstatite (MgSiO_3).

The amount of enstatite phase detected by X-ray Diffraction (XRD) did not fully account for the amount of Mg element found by SP EPMA. Therefore, one suspects that Mg atoms substitute Fe atoms in ilmenite creating MgTiO_3 phase which is very similar to FeTiO_3 and cannot be detected by XRD. The other possibility is formation of a small amount of MgO which is below the background of the diffraction pattern.

Knowing that the shape of XANES spectra is a fingerprint of the chemical state of elements we have studied the K – edge of Mg, in this ilmenite. The goal of the experiment was to get information about possible phases containing the Mg. As reference samples MgSiO_3 and MgTiO_3 pure compounds were chosen.

Measurements were performed at station UE 52 PGM at BESSY. Two kinds of detection mode were applied, fluorescence using Si(Li) detector and Partial Electron Yield (PEY) using channeltron. Samples were prepared by pressing powder into a conductive carbon type and measured at room temperature.

Fig. 1 – 3 shows Mg K-edge for Norwegian ilmenite and reference samples in both fluorescence and PEY mode.

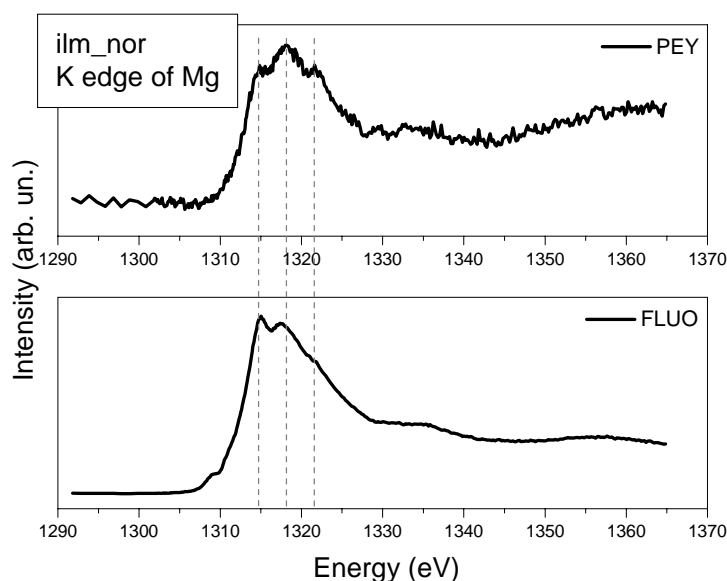


Fig. 1. The experimental XANES spectra of Mg K-edge for Norwegian ilmenite (top spectrum corresponds to PEY, bottom – fluorescence)

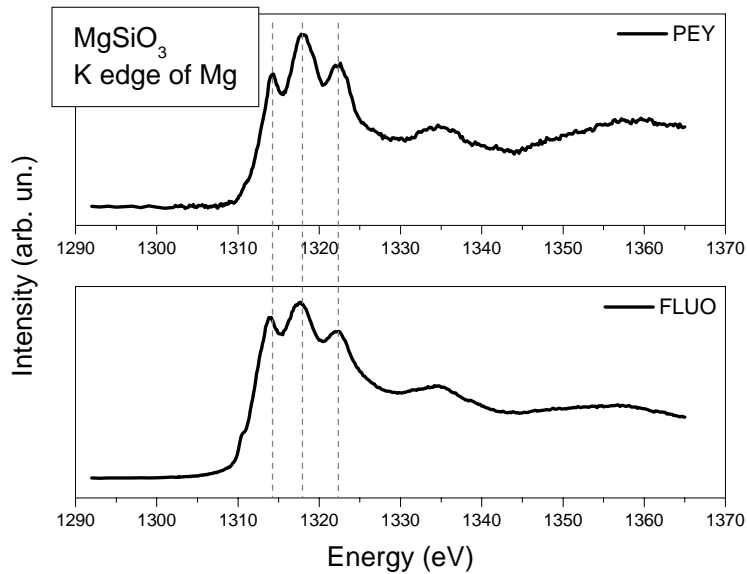


Fig. 2. The experimental XANES spectra of Mg K-edge for MgSiO_3 (top spectrum corresponds to PEY, bottom – fluorescence)

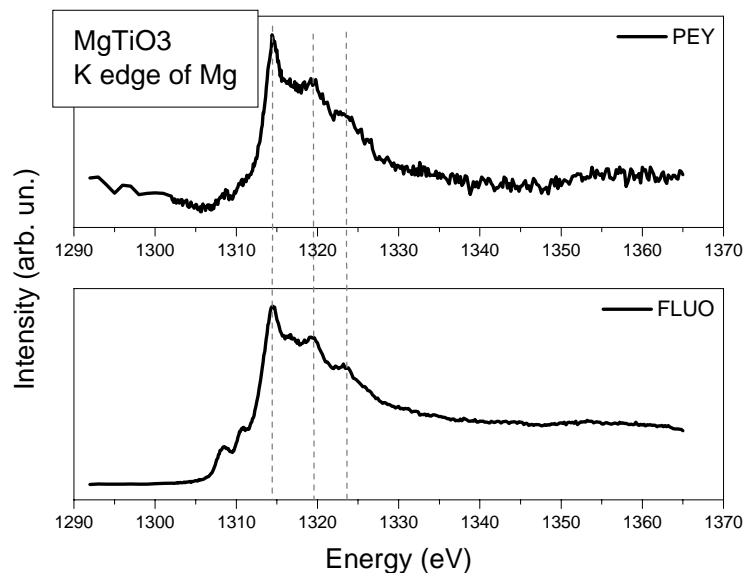


Fig. 3. The experimental XANES spectra of Mg K-edge for MgTiO_3 (top spectrum corresponds to PEY, down – fluorescence)

The observed difference in Fig. 1 between fluorescence and PEY spectra for ilmenite may be due to fact that the sample is non-homogenous, as was confirmed by SP EPMA measurements, and that Mg is bonded in different phases even in a single grain. The size of grains was evaluated by Scanning Electron Microscope to be circa $100 \mu\text{m}$. PEY is a surface sensitive technique and fluorescence gives information from the bulk of the grain. As can be seen in Fig. 2 and 3 fluorescence spectra for reference samples show a large degree of self absorption effect due to the high concentration of Mg. For further analysis the self absorption needed to be corrected for which was done with the Athena program using Fluo Algorithm [4]. Measured and corrected spectra are presented at Fig. 4 A and B.

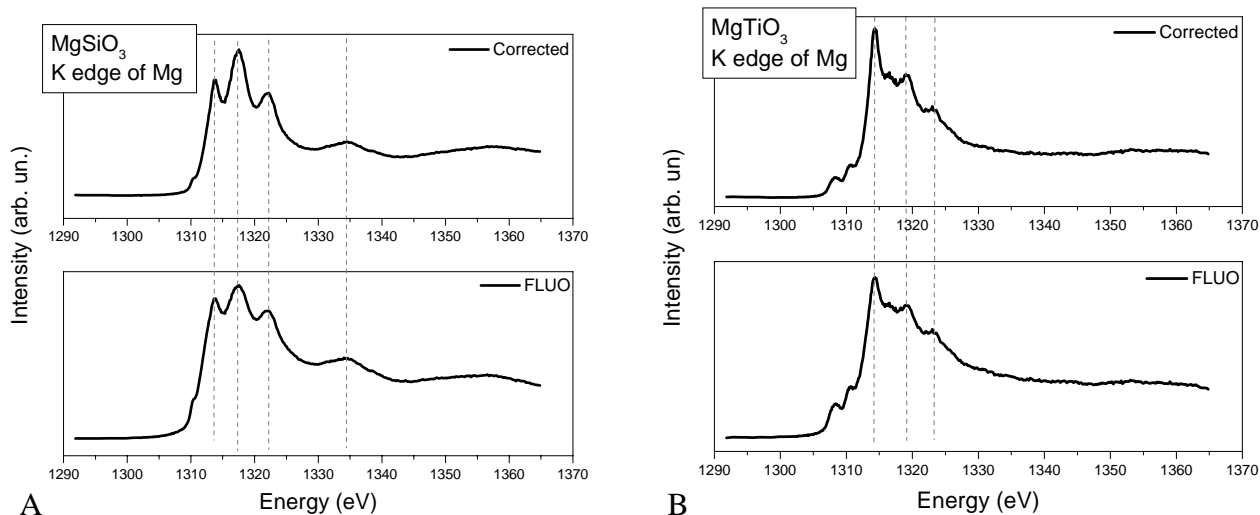


Fig. 4. The experimental XANES spectra of Mg K-edge for MgSiO_3 (A) and MgTiO_3 (B) (top – fluorescence after self absorption correction, bottom – fluorescence without correction)

The shape of Mg K edge for ilmenite indicates that MgSiO_3 and MgTiO_3 may be present. Preliminary fitting of the phase content using XANDA dactyloscope freeware program [5] results with $45,8\% \pm 1,1\%$ of Mg atoms bounded in MgSiO_3 and $54,2\% \pm 1,0\%$ in MgTiO_3 phases (Fig. 5).

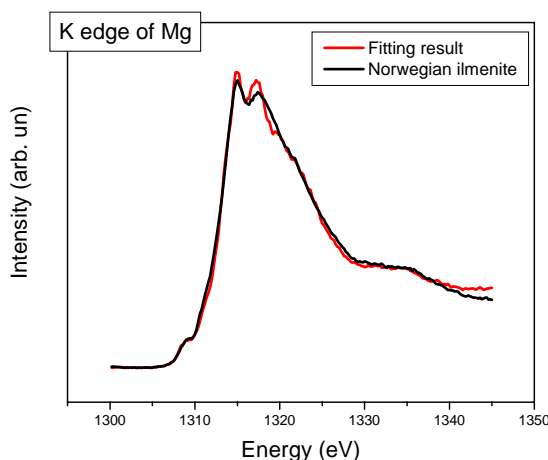


Figure 5. The experimental XANES spectra of Mg K-edge for Norwegian ilmenite compared with fitting result from XANDA program.

Future study will be devoted to ilmenites mined in India, China and Australia. The edges of other minority elements will also be studied.

This work was partially supported by the Contract R II 3.CT-2004-506008 of the European Commission.

References:

- [1] T. Chernet, Minerals Engineering, 12 (1999) 485
- [2] R.G. Teller, et al., J. Solid State Chem., 88(1990), 351 – 367
- [3] M. Klepka, et al, J. Alloys and Compounds, 401 (2005) 281 – 288
- [4] <http://www.aps.anl.gov/xfd/people/haskel/fluo.html>
- [5] <http://www.desy.de/~klmn/xanda.html>

X-ray absorption spectroscopy study of the effects of Si addition on the properties of hard nitride coatings

A. Gutiérrez ^a, J. L. Endrino ^b, S. Palacín ^a, F. Schäfers ^c, L. Soriano ^a

^a Dep. Física Aplicada, Universidad Autónoma de Madrid, 28049 Madrid, Spain

^b Lawrence Berkeley National Laboratory, 1 Cyclotron Rd. Building. 53, Berkeley, CA, 94720

^c BESSY GmbH, Albert-Einstein-Straße 15, 12489 Berlin, Germany

Nanostructured ceramic coatings are being intensively investigated because they open a wide field of new materials with improved mechanical and tribological properties. The final behaviour of such coatings depends on their composition and microstructure. Si addition in nitride compounds has shown to improve significantly their hardness. For instance, in the Ti-Si-N coating system, coating hardness ranging from 40 to 80 GPa has been reported in the composition range of 2-20 at.% Si. To explain this improvement, a detailed investigation on composition, structure, and atomic short-range order surrounding Ti and Si atoms is needed. X-ray absorption spectroscopy (XAS) is a very appropriate tool for this kind of studies since it is very sensitive to the local environment around a specific atomic element, giving information on the composition, structure, and short range symmetry

In this work, several TiSiN and AlCrSiN coating compounds with different Si content have been studied by XAS in order to investigate the effects of Si addition on the composition, structure and phase development of these coatings. AlCrSiN thin films have been obtained by cathodic arc evaporation, whereas TiSiN coatings have been grown by magnetron sputtering. Changes in the structure and chemistry of the Si-containing coatings as compared with those without Si can influence the mechanical properties, grain size and morphology, defect content, film porosity or phase content of this films. To get some insight on these changes, X-ray absorption spectra have been measured at the Si, Cr, and Ti K-edges in fluorescence yield mode. XAS measurements were carried out at the BESSY KMC1 line, using a standard chamber equipped with a solid state fluorescence detector.

Figure 1(a) shows XAS spectra at the Ti K-edge of TiSiN samples with different Si content. In this case, all spectra keep a similar lineshape to that of titanium nitride, independently of Si content. The pre-edge region, which is associated to transitions from Ti-1s states to Ti-3d states hybridized with Si-2p states, does not show significant changes with Si-addition. This suggests a weak interaction between Ti and Si. Fig. 1(b) shows XAS spectra at the Si K-edge of the same TiSiN samples, as well as a SiO₂ single crystal, as a reference sample for comparison. In all cases the spectral lineshape is typical of amorphous Si₃N₄ [1], with a main peak at 1845 eV, and a weaker structure at 1861 eV. The main peak of SiO₂ is located at 1847, so we can not exclude the presence of SiO₂ for very low Si content. Except for this small oxygen presence no significant changes in the lineshape is observed with silicon content. Hence, both Ti-K and Si-K XAS results suggest that the interaction between Ti and Si is weak and that amorphous Si₃N₄ aggregates are formed inside a TiN matrix.

Fig. 2(a) shows XAS spectra at the Cr K-edge of AlCrSiN with different Si content. Similarly to the TiSiN samples, the pre-edge region, at 5960 eV, is associated with transitions from Cr-1s states to Cr-3d states hybridized with 2p empty states of the ligand atoms. This hybridization allows 1s-3d transitions, which are otherwise dipole forbidden. The spectrum for the AlCrN sample shows only a tiny pre-edge peak at this position, very similar to that reported in previous works for Cr₂O₃ [2-4], suggesting that Cr in this compound is in the form of Cr³⁺. The intensity of this peak slightly increases for sample with a Si content of 5%. For samples with even higher Si content, the intensity increase is still more predominant. The increase of this feature could be explained in the case of oxide compounds in terms of a valence increase from +3 to +4, +5 or +6, or in terms of a reduction of crystalline domains down to the nanoscale [12]. The presence of high valence Cr would involve a shift to higher energies of the main absorption edge, which is not observed in our samples, so the presence of

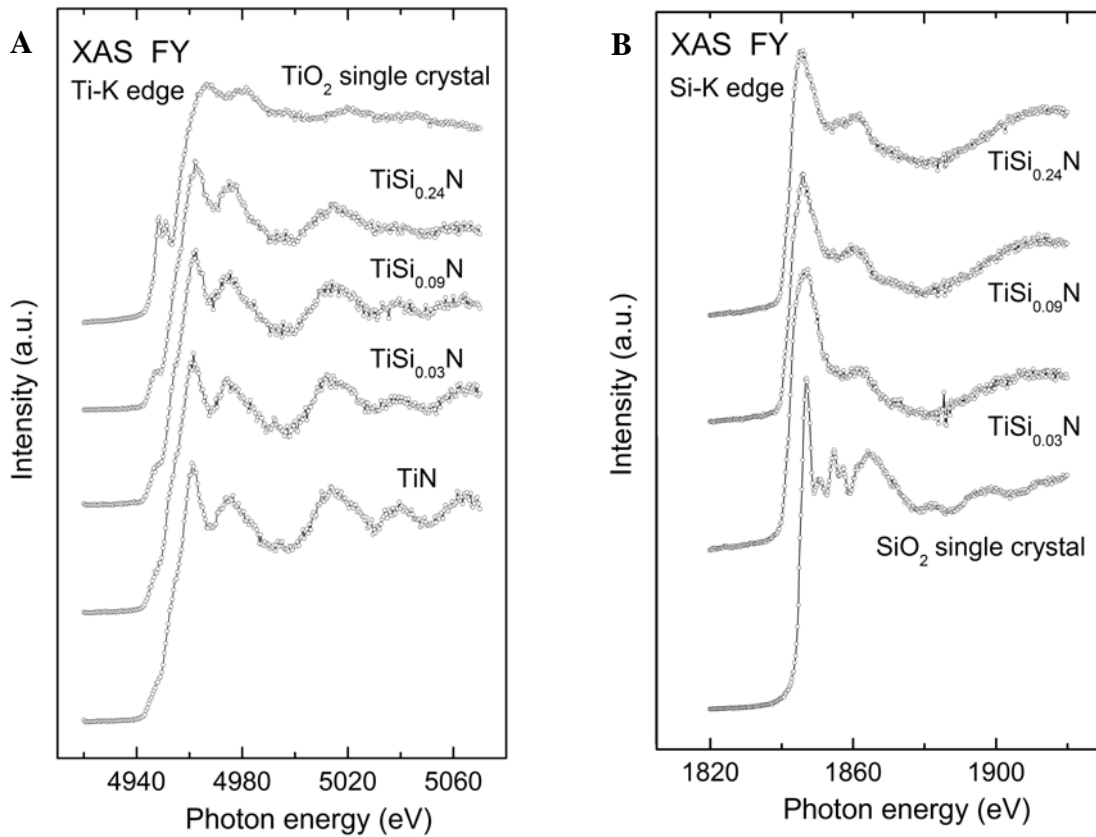


Figure 1: X-ray absorption spectra at the Ti-K edge (a), and at the Si-K edge (b) of several TiSiN samples with different Si content.

this kind of Cr compounds can be excluded. The only explanation for the observed intensity increase in samples must take into account a chemical interaction between Si and Cr, which would give rise to Cr-3d Si-2p hybridization. Consequently, the peak at 5960 eV can be assigned to transitions from Cr-1s states to Cr-3d states hybridized with Si-2p empty states. Additionally to this pre-edge intensity increase, the addition of Si produces a smoothing of the overall spectral lineshape, which is consistent with the amorphization of the microstructure, as observed by XRD [1]. Fig 2 (b) shows XAS spectra at the Si K-edge of AlCrSiN samples with different Si content, as well as a pure SiO₂ single crystal as a reference sample. We can exclude that Si incorporates to the lattice as an atomic solid solution, because the spectra do not resemble that of pure Si [1]. The spectrum for sample with 5 at. % Si (bottom), has a peak at 1847 eV, which is aligned with the main peak of the spectrum for SiO₂ single crystal. This indicates that at low Si content there is some oxygen contamination in the form of SiO₂. Additionally, the edge positions at 1842 eV, as well as the peak observed at 1850 eV, are evidences for the presence of crystalline Si-N compounds in this sample. The feature assigned to SiO₂ disappears for samples with higher Si content. The spectra for samples with 9 and 14 at. % of Si are very similar, with a main peak at 1844 eV. This energy position corresponds to the main peak observed for Si₃N₄, suggesting that Si is in the form of some nitride compound. However, the more complex spectral lineshape as compared to that of Si₃N₄, could be an evidence of the formation of some ternary Si-N-X compound.

In summary, the present comparative work reports evidence of both reduced and increased silicon solubility for samples prepared at a high deposition temperature. In the TiSiN system, we have observed features corresponding to a-Si₃N₄ in all of the deposited samples and there was not any significant change with silicon content. Both Ti-K and Si-K spectra suggests that there was a weak interaction between Ti and Si. On the other hand, for

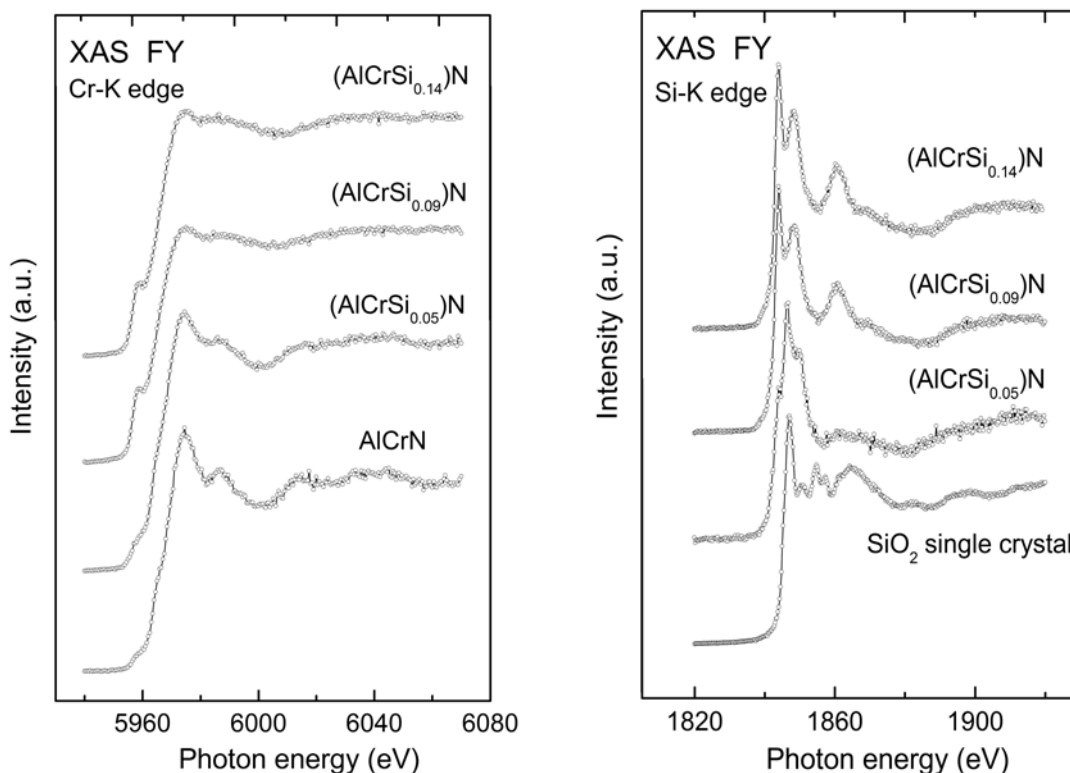


Figure 2 X-ray absorption spectra at the Cr-K edge (a), and at the Si-K edge (b) of several CrAlSiN samples with different Si content.

the quaternary AlCrSiN system, there was strong evidence of the formation of Si-N-X complex compounds, where X could account for Cr, Al, or both. Samples also showed the amorphization of the Cr-based crystal structure with increasing Si content.

Acknowledgements:

This work was supported by the EU Research Infrastructure Action under the FP6 *Structuring the European Research Area* Programme, through the contract R II 3-CT-2004-506008; and by the Spanish CICYT through the contract BFM2003-03277. A.G. thanks the Spanish *Ministerio de Educación y Ciencia* for financial support through the “*Ramón y Cajal*” Program. J. L. E. would like to acknowledge the financial support of the Air Force Office of Scientific Research under grant F49620-98-1-0499.

References:

1. J.L. Endrino, S. Palacín, M.H. Aguirre, A. Gutiérrez, F. Schäfers, *Acta Materialia*, *in print* (2007).
2. J. Berry, *Amer. Mineralogist* **89** (2004) 790.
3. A. Pantelouris, H. Modrow, M. Pantelouris, J. Hormes, and D. Reinen, *Chemical Physics* **13** (2004) 300.
4. S-J. Hwang, H-S. Park, J-H. Choy, *Solid State Ionics* **151** (2002) 275.

A STUDY OF EMPTY ELECTRONIC STATES IN HIGHLY ORIENTED POLY(VINYLDENE FLUORIDE) AND ITS CARBONIZED DERIVATIVES USING SYNCHROTRON RADIATION

S.S. Chebotaryov¹, L.A. Pesin¹, E.M. Baitinger¹, S.E. Evsyukov².

¹Chelyabinsk State Pedagogical University, 454080, Chelyabinsk, Russia

²instrAction GmbH, Donnersbergweg 1, D-67059 Ludwigshafen, Germany

In this paper we shall partially consider the results obtained at the Russian-German beamline of Berlin electronic storage ring in the single bunch mode (current 10-20 mA). A study of radiative modification of fluorine empty states on the surface of PVDF (Kynar, thickness 50 μm) under monochromatic SR ($h\nu=700$ eV) has been made. The vacuum level was $(5-7)\cdot 10^{-10}$ Torr. Before the measurements the sample and the chamber were kept at temperature about 130° C during 24 hours. Echelette grating having 1200 dashes/mm and $Cff=2,25$ was used to receive monochromatic synchrotron radiation. The aperture width was 200 μm . NEXAFS spectra were measured using secondary electron multiplier KEITHLEY@14. The energy resolution in the energy range 680-700 eV was 0.6 eV. All the measured spectra were normalized to the current in the storage ring.

Integral intensity of the spectra must be proportional to the fluorine surface content after some additional treatment [1]. This parameter has been calculated as an area of each spectrum in the 685-700 eV interval after linear background subtraction. Fig. 1 demonstrates a general tendency of the spectra intensity to decrease with photon dose elevation in accord with our preliminary degradation experiments [1] and model calculations [2].

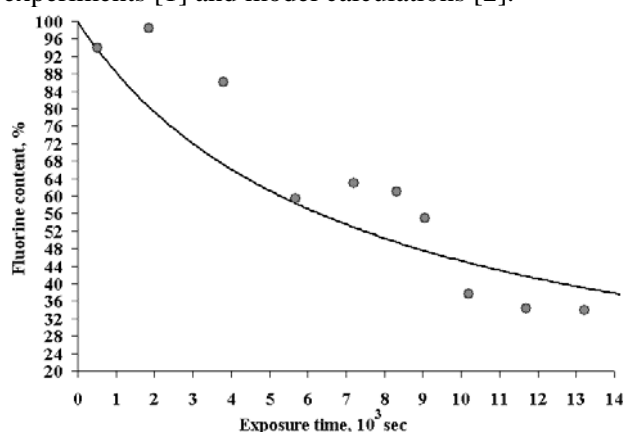


Fig.1. Integral intensity of fluorine NEXAFS in 685-700 eV range versus duration of SR exposure (circles) and a calculated curve (solid line).

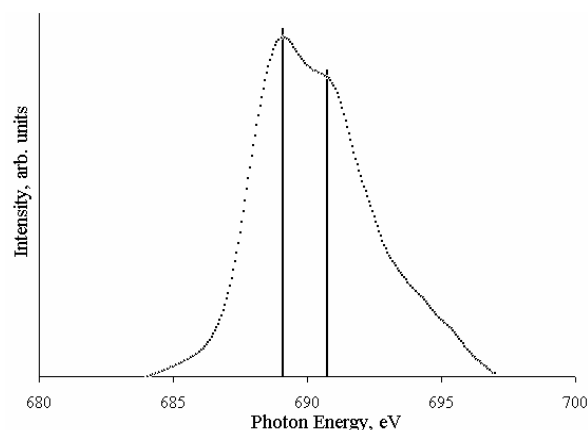


Fig. 2. Two dominant maxima (at ca. 689 and 691 eV) of the fluorine NEXAFS after the smoothing and subtraction of linear background of the spectrum.

NEXAFS spectra of fluorine show significant changes in their shape and intensity with elevation of radiation dose (or duration of SR exposure).

The changes in the spectra shape caused by SR concern mainly the relative intensity of two dominant maxima (Fig. 2). The first of them dominates in the spectrum of pristine polymer. With the increase of the radiation dose redistribution of intensity between these features occurs (Fig. 3).

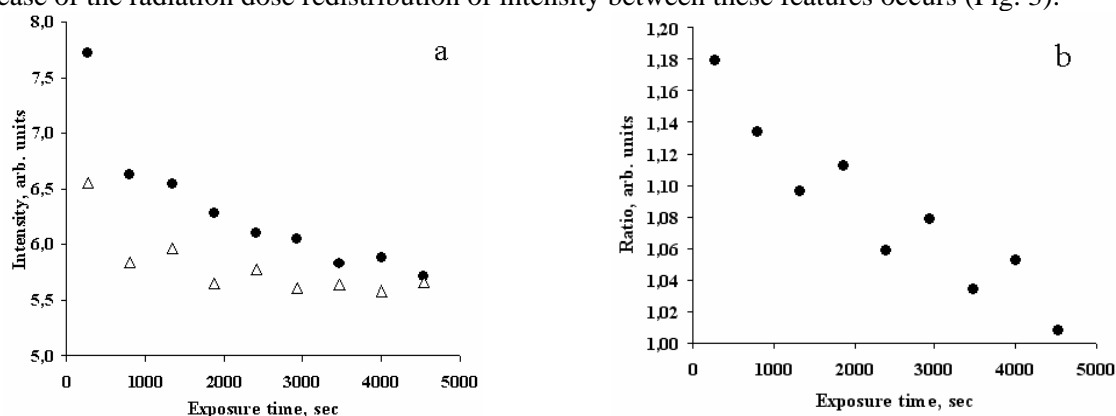


Fig. 3. Changes in the intensity of the first (●) and second (Δ) maxima (a) and its ratios (b) versus duration of SR exposure.

This effect has been simulated using the original software for imitation of tailing the features of empty DOS due to uncertainly relation. All the spectra were shifted down along the photon energy scale at 684 eV. According to [3] the tailing of an one-electron density of states can be described by

the following equation: $G(E) = \frac{1}{\pi} \int_{-\infty}^{\infty} dE' \frac{G_0(E') \cdot \text{Im}S(E)}{[E' - E + \text{Re}S(E)]^2 + [\text{Im}S(E)]^2}$, where $G(E)$ represents the

shape of the experimental spectrum without taking into account instrumental broadening and a background, $G_0(E)$ – is the one-electron density of states, E - energy of an electron in a band, E' – a current energy value. To get the minimal number of fitting parameters the one-electron density of states was simulated by δ -function. For each δ -function only intensity and a position at the energy scale have been varied. A complex function $S(E)$ describes the Lorenz broadening of the one-electron

bands: $S(E) = \gamma_0 \cdot E + i(\gamma_1 + \gamma_2 \cdot E + \gamma_3 E^2)$, it being restricted to a few initial terms of decomposition by energy in a Taylor sequence, Zero term in a real part does not influence on shape the of $G(E)$, γ_i – Coefficients, featuring the electronic correlations – (γ_0), decrease of a lifetime of carriers due to scattering caused by defects (γ_1), dependence of a lifetime on energy band states (γ_2 and γ_3).

The computer calculations shows that the variations of these coefficients make changes in the shape of function $G(E)$ in a different ways. The first of them change the width of energy state, and the larger value of energy the higher is an energy position of the corresponding feature in $G(E)$. The magnification of value of the coefficient γ_1 homogeneously tailing the fine structures of the $G(E)$ curve. The increase of values γ_2 and γ_3 leads to strong broadening of high-energy features of DOS.

The best fitting of experimental data for starting spectrum with model curves has been gained at following parameters, which did not vary in further treatment of NEXAFS data for carbonizing film.

γ_0, eV^{-1}	γ_1	γ_2, eV^{-1}	γ_3, eV^{-2}
0.25	0.02	0.15	0.015

Imitation of NEXAFS is shown in Fig. 4 for the starting spectrum.

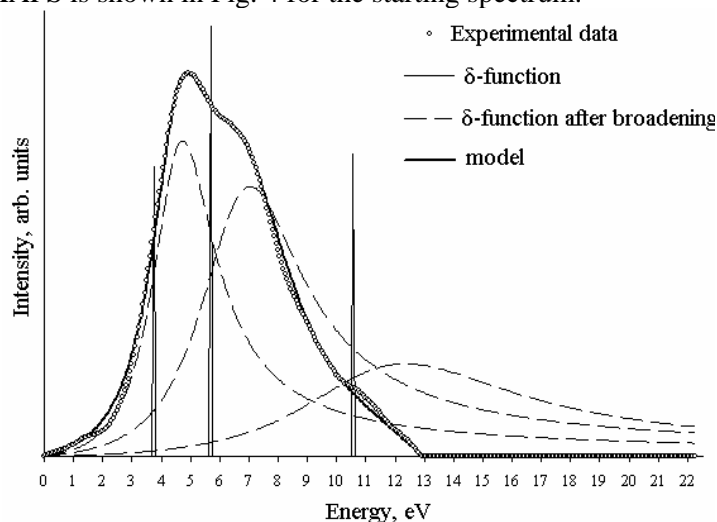


Fig. 4. NEXAFS and its model imitation for the starting spectrum.

After δ -functions broadening routine the obtained curves have been summarize and the background has been subtracted by Shirley method. As one can see from Fig. 4, the model spectrum satisfactorily reproduces the shape of experimental NEXAFS that allows to estimate the actual energy positions of the main features of fluorine empty DOS.

The Figs. 5 and 6 show the intensity of the model δ -functions variation.

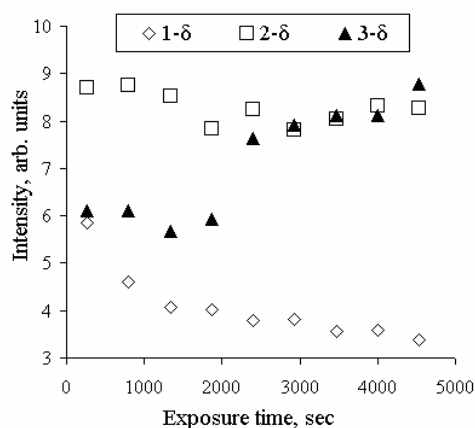


Fig. 5. Variation of intensity of the model δ -functions (first \diamond , second \square , third \blacktriangle) versus duration of SR exposure. .

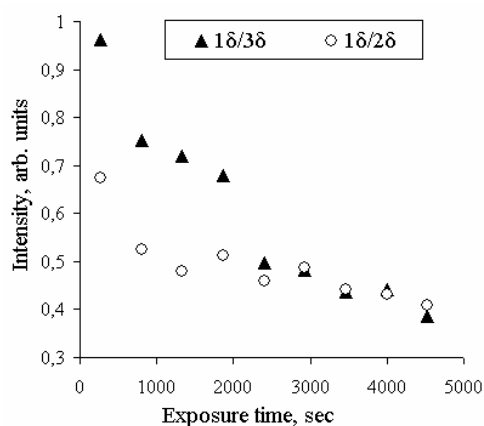


Fig. 6. Variation of relative intensity of the model δ -functions: first and second \circ , first and third \blacktriangle .

The energy positions of model δ -functions differs from positions of curves maximum after broadening:

First			Second			Third		
Position of δ	After broadening	difference	Position of δ	After broadening	difference	Position of δ	After broadening	difference
3.94	4.81	0.87	5.88	7.13	1.25	10.35	12.00	1.65

Evidently after broadening energy positions of curves maximum are higher than position of the appropriate δ -functions.

A preliminary interpretation of the results obtained is based on the suggestion of two-step process of dehydrohalogenation under synchrotron radiation. The reason of two-step process may be due to conformations of a polymeric chain making binding energy between each of two fluorine atoms and a carbon atom different in a monomeric fragment of PVDF $-\text{CH}_2-\text{CF}_2-$. The energy difference between empty states of two neighbouring fluorine atoms can be evaluated from the experimental data (2 eV). Probably, under the action of photons at first a proton eliminates transferring a part of the electron density to the bond C-F. Then the process runs at the expense of energy obtained due to dissipation of the synchrotron radiation and weakly bonded fluorine atoms eliminate.

In the nearest future NEXAFS spectra of carbon are necessary to reveal the detailed features of the processes of chemical and radiative carbonization of PVDF but it is possible only using multi bunch mode due to low intensity of radiation in the range 280-315 eV.

The authors are grateful to ATOFINA (France) for a granted sample of PVDF.

1. S.S. Chebotaryov, E.M. Baitinger, A.A. Volegov, I.G. Margamov, I.V. Gribov, N.A. Moskvina, V.L. Kuznetsov, S.E. Evsyukov, L.A. Pesin. *Radiative defluorination of poly(vinylidene fluoride) under soft X-ray radiation* // Radiation Physics and Chemistry. V 75. - P. 2024-2028. (2006).
2. Voinkova I.V., Ginchitskii N.N., Gribov I.V., Klebanov I.I., Kuznetsov V.L., Moskvina N.A., Pesin L.A., Evsyukov S.E., *A model of radiation-induced degradation of the poly(vinylidene fluoride) surface during XPS measurements*. Polym. Degrad. Stab., 89(3), - P. 471-477. (2005).
3. Yu.A. Babanov, V.E. Naish, O.B. Sokolov, V.K. Finashkin. *Electron-electron correlation in metals. II* //Fizika metallov i metallovedenie. 35(6). p. 1132-1146. (1973). (in Russian)

Magnetic order in rare earth manganites studied with resonant magnetic scattering

E. Dudzik, R. Feyerherm, O. Prokhnenko, N. Aliouane, D. Argyriou
Hahn-Meitner-Institut Berlin, Glienicker Str. 100, 14109 Berlin

The orthorhombic rare earth manganites are a group of materials that shows a complex interplay of magnetism and electric polarisation. They contain two different magnetic ions, manganese and a rare earth metal, whose spins show several stages of magnetic ordering [3]. Experiments were carried out for the rare earth metals Terbium and Dysprosium. At room temperature these manganites are paramagnetic. The first magnetic phase transition occurs around 40 K, where the Mn moments order in a sinusoidal spin density wave whose period changes with temperature. At a second transition the Mn order locks into a helicoidal spin density wave in the bc plane. The rare earth ions order magnetically at temperatures below 10 K.

Both DyMnO_3 and TbMnO_3 show a spontaneous electric polarization below the intermediate lock-in transition (see Fig. 1, above). In TbMnO_3 the electric polarisation sets in below 28 K, and after an initial rapid increase rises gradually towards lower temperatures. The DyMnO_3 polarisation on the other hand rises rapidly below the lock-in temperature at about 16 K, reaches a maximum value which is double the Tb polarisation, and then drops to TbMnO_3 levels at about 5 K. The Dy polarisation also shows a marked hysteresis at low temperatures.

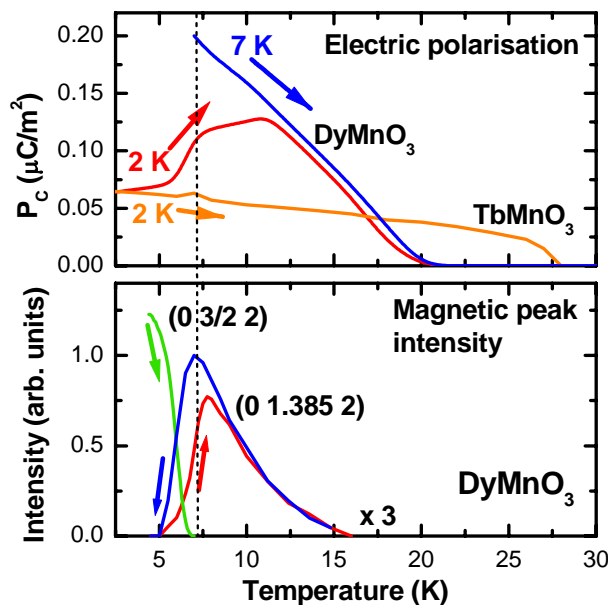


Fig. 1: Above: electric polarisation in TbMnO_3 and DyMnO_3 (after Goto et. al. [3]). Below: Magnetic diffraction peak intensities in DyMnO_3 .

The electric polarisation in TbMnO_3 has been explained theoretically [4] on the basis of neutron diffraction measurements. Below the lock-in the helicoidal ordering of the Mn moments with two components M_1 and M_2 in the a and b directions leads to a net moment $M = M_1 e_1 \cos Qx + M_2 e_2 \sin Qx$ at each ion. This order breaks both time reversal and spatial inversion symmetry and leads to a polarisation $\mathbf{P} \sim M_1 M_2 [\mathbf{e}_3 \times \mathbf{Q}]$ (see Fig. 2).

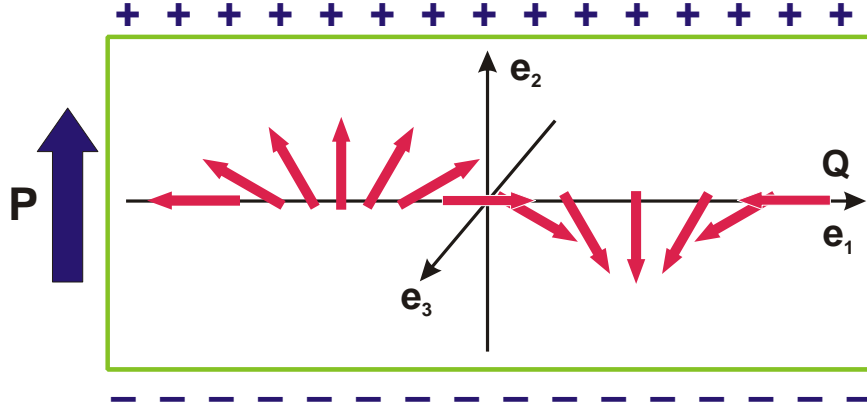


Fig. 2: Helicoidal magnetic order can induce an electric field in a crystal that is perpendicular to the magnetic propagation vector.

Our experiment was motivated by the question why the temperature dependence and the magnitude of the DyMnO_3 polarisation is so different from that of TbMnO_3 . Dy is practically opaque for neutrons, so x-ray resonant scattering was used to study the magnetism. The experiments were carried out at the new high-energy MAGS beamline operated by the Hahn-Meitner-Institute at BESSY. Samples were cooled in a closed-cycle cryostat mounted on a six-circle diffractometer. Measurements were done both at the Dy L_3 -edge at 7790 eV and non-resonant at 12398 eV.

X-ray resonant scattering clearly shows the three stages of magnetic ordering (see Fig. 3). Below the Neel temperature of 40 K, the Mn orders in a sinusoidal spin wave with a propagation vector $\tau_{\text{Mn}}=0.385 b^*$. Although the diffraction peaks from the Mn magnetic order could not be observed directly, we found second order diffraction peaks which are due to a structural distortion associated with the Mn order at positions $k \pm 2\tau_{\text{Mn}}$ (Fig. 3, red inset).

These peaks persist below the lock-in transition at 16 K. At the lock-in, a second set of diffraction peaks appear at positions $k \pm \tau_{\text{Mn}}$ (Fig. 3, orange inset), which are resonant at the Dy L_3 edge. Linear polarization analysis shows that these peaks are of magnetic origin. This shows that in the lock-in regime, where the spontaneous electric polarization appears, the Dy moments have ordered with the same periodicity as the Mn.

At temperatures below 4.35 K the Dy moments order independently of the Mn. This leads to the collapse of the magnetic diffraction peaks at $k \pm \tau_{\text{Mn}}$ and the appearance of magnetic peaks with a period of $\tau_{\text{Dy}} = 0.5 b^*$ (Fig. 4, blue inset). As in the case for the Mn, these magnetic diffraction peaks are found to be associated with a second order structural distortion. These peaks should appear at integer order positions, but instead are found at peak positions of $q = 0.905 b^*$. It appears that competition with the persisting Mn order shifts both the Dy and the Mn second order structural peaks slightly from their expected positions towards one another [5].

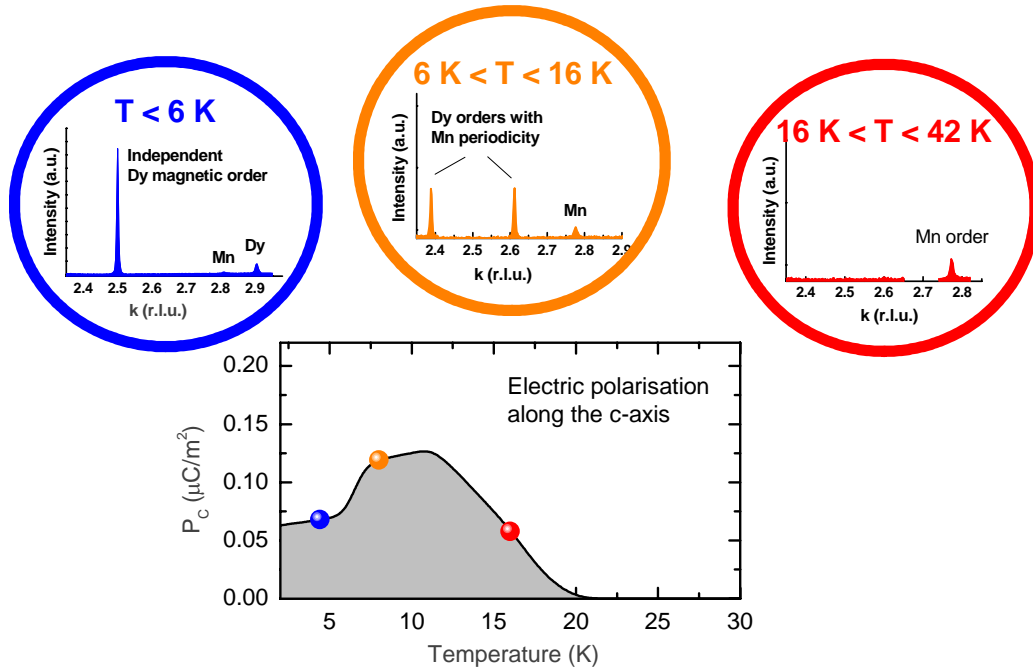


Fig. 3: Electric polarisation in DyMnO₃ shown with the x-ray diffraction data for high, intermediate and low temperatures (red, orange and blues insets, respectively).

The transition from the independent Dy magnetic order to the induced order above the Dy Neel temperature shows a strong hysteresis (see Fig.1 below). This hysteresis coincides in size and temperature dependence with the hysteresis in the Dy electric polarisation shown in the upper part Fig. 1. Therefore we argue that in the lock-in regime, where the Dy moments order with the same periodicity as the Mn, the Dy moments contribute to the electric polarisation. Thus the increase in polarisation above the T_b value shown in Fig. 2 between 4.35 and 16 K appears to be due to a contribution from the Dy moments. Surprisingly, the two magnetic moments situated at completely different positions in the unit cell combine to induce an electric polarisation as if they simply summed up [6].

References:

- [1] N. A. Hill, J. Phys. Chem. B 104, 6694 (2000)
- [2] W. Eerenstein et al., Nature 442, 759 (2006)
- [3] T. Goto et al., Phys. Rev. Lett. 92, 25721 (2004)
- [4] M. Mostovoy, Phys. Rev. Lett. 96, 067601 (2006)
- [5] R. Feyerherm, Phys. Rev. B 73, 180401(R), (2006)
- [6] O. Prokhnenko et al., Phys. Rev. Lett., in press

In-situ X-ray scattering of single carbon fibres during creep

H. Rennhofer¹, S. Puchegger¹, O. Paris², R. Weiss³, H. Peterlik¹

¹ Fakultät für Physik, AG Streuung und Spektroskopie, Universität Wien

² Max-Planck-Institut für Kolloid- und Grenzflächenforschung, Abt. Biomaterialien, Potsdam

³ Schunk Kohlenstofftechnik GmbH, Gießen

1. Introduction

Carbon fibres are the most widely used material for aerospace-applications, where high mechanical strength at high temperatures and low weight is required. These fibers consist of long elongated ribbons of carbon crystallites with a dimension between 2 and 40 nm. The crystallites themselves are built up from several graphene sheets arranged in a so called turbostratic structure.

In recent experiments [1, 2] the mechanical properties and the creep behaviour of fibre bundles have been investigated up to temperatures of more than 2000 °C. However, no accompanying structural analysis was performed in these works. Whereas ex-situ structural investigations of fibre-bundles by X-ray diffraction after heat treatment are quite common [3,4,5], the structure of single carbon fibres could only be investigated by microbeam synchrotron radiation due to the small size of these fibres of about 7-10 microns [6]. The aim of this study was the *in-situ* investigation of structural changes within single fibres with applying simultaneously high load and high temperature.

2. Material

Two types of carbon fibres were investigated:

- HTA5131, based on polyacrylonitrile (PAN) -precursor, 7 µm diameter
- FT500, based on mesophase-pitch-precursor (MPP), 10 µm diameter

3. Experiment

A specially designed test equipment was developed, which allows the application of high stress for creep measurements to single carbon fibres while heating to temperatures up to more than 2000 °C (direct heating by electrical current through the fibre). The whole test equipment operates in vacuum (pressure smaller than 10^{-4} mbar) and is equipped with Kapton windows, which enables *in-situ* X-ray scattering. The measurements were performed at the µ-Spot beamline using a microfocus beam of about 15 µm diameter using a W/Si multilayer ($E=8.9$ keV, $\Delta E/E=0.01$) and a circular Bragg Fresnel lens. The setup consisted of the standard SAXS/WAXS setup of the beamline [7]. The structural changes were followed in dependence of time and temperature for a given specific stress.

4. Results

Two main structural parameters were obtained from the change of the 002 reflection originating from the stacking of the graphene layers: i) the interlayer spacing d_{002} , and ii) the azimuthal spread of this reflection (HWHM) that is indicative of the preferred orientation of the crystallites with respect to the fibre axis. Moreover, the orientation distribution of the slit-like pores with respect to the fibre axis can be estimated by the azimuthal distribution of the SAXS signal at low scattering angles.

HTA5131: The interlayer distance d_{002} decreases with increasing temperature. This effect is significantly larger than the thermal expansion (Fig. 1). For temperatures higher than 1400 °C, the structural change in the fibre is permanent: If one returns to room temperature, the interlayer distance remains at a significantly lower level. Additionally, the orientation of the pores (Fig. 2) and of the crystallites (Fig. 3) increases with increasing temperature.

FT500: No structural change is observed – only an increase of the interlayer distance d_{002} with increasing temperature, which is due to conventional thermal expansion (Fig. 4).

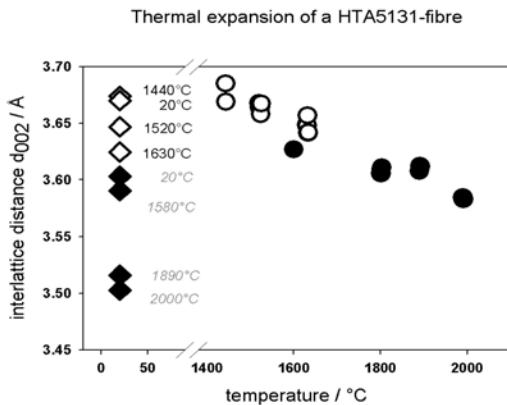


Fig. 1: HTA5131; Filled and empty symbols refer to two different specimens. Circles: high temperature measurements. Diamonds: room temperature measurements after being cooled down from the indicated temperature.

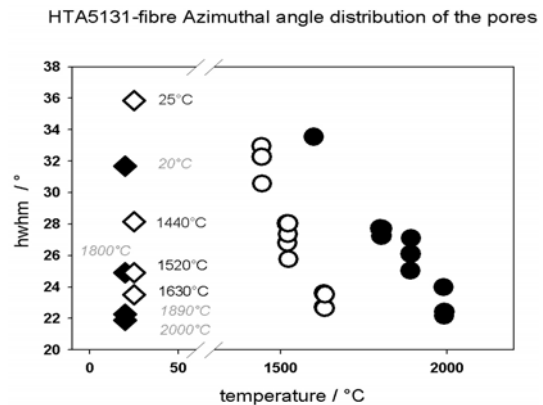


Fig. 2: HTA5131; Filled and empty symbols refer to two different specimens. Circles: high temperature measurements. Diamonds: room temperature measurement after being cooled down from the indicated temperature.

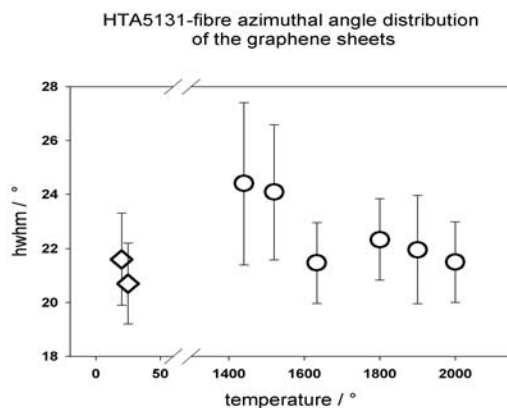


Fig. 3: Circles: HTA5131; Circles: measurements at high temperatures. Diamonds: room temperature measurement after treatment at 1800 and 2000 °C.

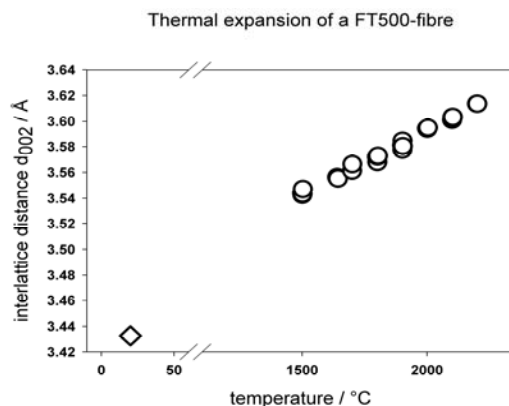


Fig. 4: Circles: FT500; Circles: measurements at high temperatures. Diamonds: room temperature measurement after treatment at 1500, 1600 and 1700 °C.

5. References

- [1] K. Kogure, S. Sines, J.G. Lavin, *J. Am. Ceram. Soc.* 79/1 (1996) 46-50.
- [2] C. Sauder, J Lamon, R. Pailler, *Comp. Sci. Techn.* 62 (2002) 499-504.
- [3] A. Gupta, I.R. Harrison, *J. Appl. Cryst.* 27 (1994) 627-636.
- [4] A.A. Ogale, C. Lin, R.P. Anderson, K.M. Kearns, *Carbon* 40 (2002) 1309-1319.
- [5] H. Rennhofer, D. Loidl, J. Brandstetter, K. Kromp, R. Weiss, H. Peterlik, *Fat. & Frac. Eng. Mat. & Struc.* 29/2 (2006) 167-172.
- [6] O. Paris, D. Loidl, H. Peterlik, *Carbon* 40 (2002) 551-555.
- [7] O. Paris, C. Li, S. Siegel, G. Weseloh, F. Emmerling, H. Riesemeier, A. Erko, P. Fratzl, *J. Appl. Cryst.* 40 (2007) in press.

6. Acknowledgement

The support of the Austrian Science Fund (P16315) is gratefully acknowledged.

Residual stresses in CrN/Fe structures at high temperature

E. Eiper^a, K.J. Martinschitz^a, M. Klaus^b, C. Genzel^b and J. Keckes^a

^a*Erich Schmid Institute for Materials Science, Austrian Academy of Sciences and Institute of Metal Physics, University of Leoben, Leoben, Austria*

^b*Hahn-Meitner-Institute, Berlin, Germany*

Hard coatings are routinely used to protect working tools from abrasion and corrosion. Residual stresses in the coatings as well as in the interface region of a working tool influence decisively the tool wear and thermal fatigue resistance, the coating adhesion and finally the lifetime of the component. Temperature cycling results usually in the annihilation of point defects in the coatings and relaxation of compressive stresses what negatively influences the lifetime. In order to design new coating/substrate systems with improved performance, it is of great importance to assess temperature-induced changes in the residual stresses occurring during temperature cycling.

In recent years especially hard coatings based on CrN have been used to increase wear and corrosion resistance of working tools. The optimization of thermal fatigue represents however still a challenging task and currently it is not known how CrN on steel behaves at high temperature and what kind of structural changes occur [1].

In this work, high-energy X-ray diffraction at EDDI beamline was used to characterize residual stresses in 3 μ m nanocrystalline CrN coatings deposited on shot-peened surfaces of steel in the temperature range of 25-800 C°. The CrN/Fe structures were thermally cycled using the heating stage DHS 900 [2] in N₂ atmosphere and changes in the residual stresses in the coating and the substrate were characterized.

A temperature dependence of residual stresses in the CrN coating obtained collected two temperature cycles is presented in Fig. 1. The results indicate that the coating behaves predominantly thermo-elastically and there is surprisingly no significant relaxation of the stresses caused by point defect annihilation. The slope of the stress-temperature dependence corresponds to the mismatch of coefficients of thermal expansion of CrN and Fe. About 600 °C, the stress in the coating is tensile what represent a critical point in the temperature behaviour of the coating.

In the case of underlying Fe substrate, it was possible to evaluate the temperature dependence of stress gradient during the temperature cycling. In Fig. 2, the results from the first temperature cycle are presented. Since the substrate was shot peened before the coating deposition, a relatively large compressive stress of about -900 MPa was observed in the surface region at room-temperature. Upon heating up, the residual stress relaxes especially about 600 degrees. When cooled down, the stress does not change what documents that the coating has no significant influence on the substrate stress.

In the future, the in-situ characterization of residual stresses will be devoted to multilayered hard coatings in order to assess the structural changes in distinct sublayers and an attempt will be made to evaluate residual stress depth gradients as a function of temperature.

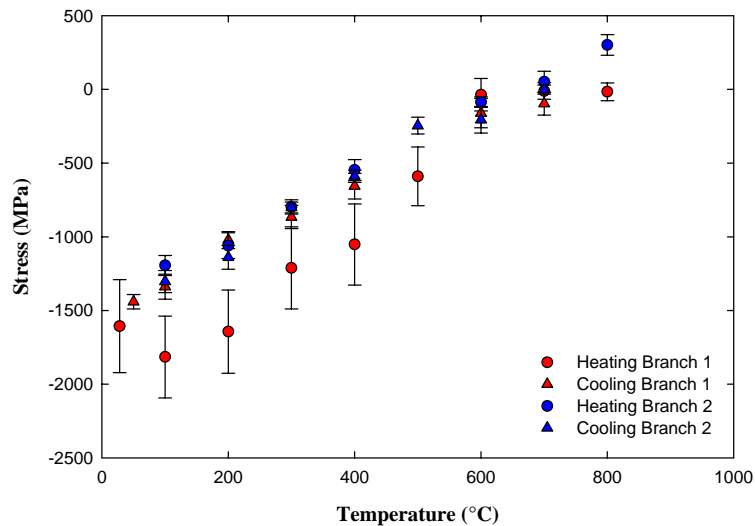


Figure 1 Temperature dependence of residual stresses in 3µm thick CrN coating on polycrystalline iron. The coating behaves during both temperature cycles thermo-elastically.

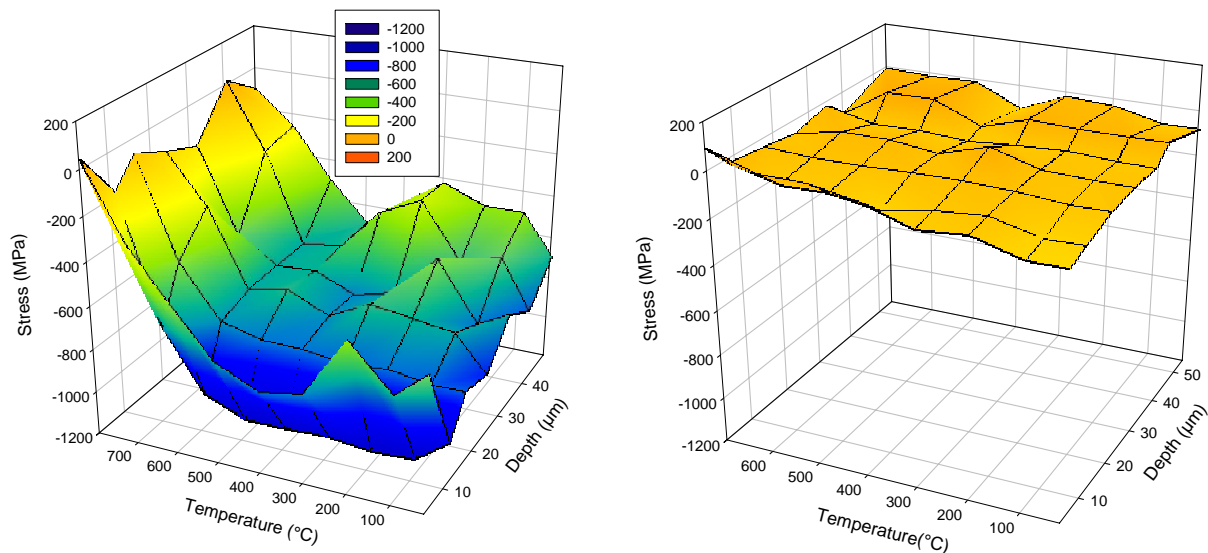


Figure 2 Temperature dependence of residual stress gradient in the surface region of a shot peened steel during first heating up (left) and cooling down (right). During the second cycle, the stresses in the substrate are below 100 MPa in the whole temperature range.

Acknowledgments

We gratefully acknowledge the European Community for a financial support grant through the Contract N° RII 3-CT-2004-506008. A part of this work was supported by the Austrian NANO Initiative via a grant from the Austrian Science Fund FWF within the project "StressDesign - Development of Fundamentals for Residual Stress Design in Coated Surfaces".

References

- [1] J. Jagielski *et al.*, *Appl. Surf. Sci.* **156** (2000) 47–64.
- [2] R. Resel, E. Tamas, B. Sonderegger, P. Hofbauer and J. Keckes, *J. Appl. Cryst.* **36** (2003) 80-85.

Position-Resolved μ -Laue Diffraction at EDR Beamline

J. Keckes^a, I. Zizak^b and W. Leitenberger^c

^a*Erich Schmid Institute for Materials Science, Austrian Academy of Sciences and Institute of Metal Physics, University of Leoben, Leoben, Austria*

^b*Hahn-Meitner-Institute, Berlin, Germany*

^c*University of Potsdam, Germany*

Position-resolved μ Laue diffraction provides an information on the local distribution of crystal orientations and strains. Synchrotron beamlines featuring the μ Laue technique are currently available only at ALS, APS and ESRF [1-3]. The aim of the present experiment was to perform a feasibility check and to analyze whether μ Laue could be performed principally also at the EDR beamline. Further, the experiment should help to determine which setup modifications and investments are necessary in order to establish μ Laue technique at BESSY.

The diffraction setup at the EDR beamline featured a white beam, x-y linear stage and an older type of CCD provided by BESSY. The experiments were performed at first with a capillary optics. The divergence of the beam from the optics was however too high and therefore not suited for μ Laue. Further on, pinholes with the diameters of 5, 10, 50 and 100 μm were used to shape the primary beam.

Position resolved μ Laue experiments were performed on bent Si(100) substrates with the thickness of 140 and 310 μm scanning the substrates across the edge. Additionally, a characterization of a 2 μm thick heteroepitaxial Al thin film deposited on Al_2O_3 substrate was performed at different sample positions. The results indicated that the μ Laue on the monocrystalline samples is possible applying the acquisition times below 20 seconds. To obtain a detectable signal from the Al film an acquisition time of 100 seconds was necessary. In Fig. 1, a comparison of the results obtained from the Al film at EDR and at 7.3.3 (<http://xraysweb.lbl.gov/microdif/>, ALS) beamlines is presented. An additional evaluation of the data is necessary in order to determine the strains in bent monocrystalline substrates numerically.

In general, the measurements indicated that the μ Laue diffraction can be performed at the EDR beamline. It was possible to obtain satisfactory Laue diffraction patterns from the monocrystalline wafers as well as from the epitaxial film applying the exposure times below 2 minutes. In order to apply the μ Laue technique in the future to analyze strains routinely and position resolved, investments in the primary optics (preferable KB mirrors with the focus distance of about 200 mm) and the usage of a CCD with higher dynamical range would be absolutely necessary. Additionally, in order to increase the accuracy of the measurements it would be useful to increase the energy range up to above 50 keV.

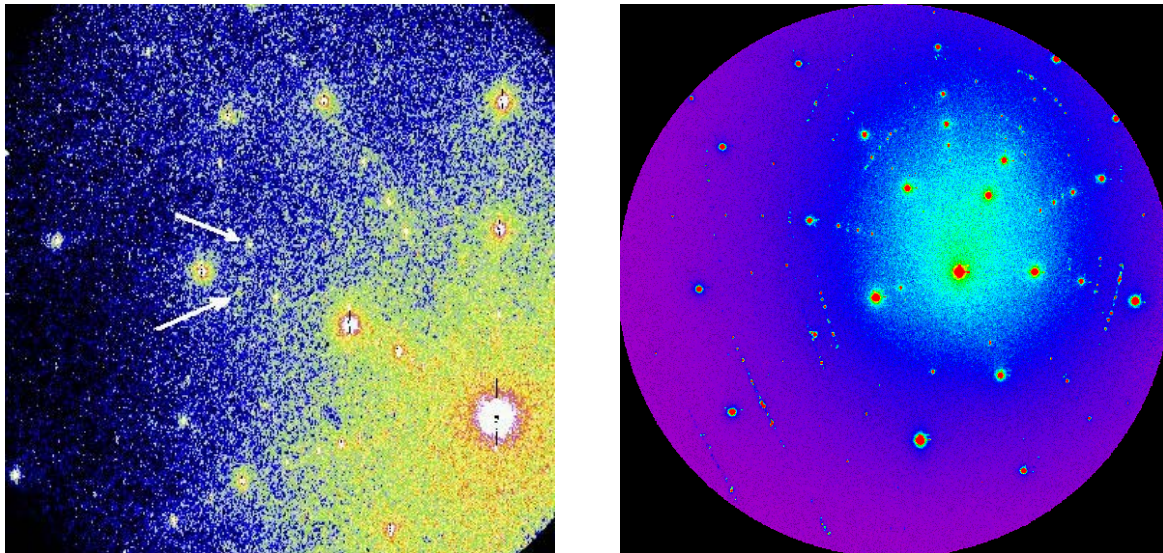


Figure 1 μ Laue diffraction patterns from the structure of 2 μ m heteroepitaxial Al thin film on Al₂O₃(0001). Left, a pattern collected at the EDR beamline applying a beam of 5 μ m in diameter and an acquisition time of 100 seconds. The arrows indicate the signal from the film while the strong maxima (partly saturated) correspond to the diffraction on the substrate. Right, a Laue pattern collected from the same structure at 7.3.3 beamline (ALS) using a beam of 2.3 μ m in diameter produced by KB mirrors and an acquisition time of 5 seconds.

Acknowledgments

We gratefully acknowledge the European Community for a financial support grant through the Contract N° RII 3-CT-2004-506008. A part of this work was supported by the Austrian NANO Initiative via a grant from the Austrian Science Fund FWF within the project "StressDesign - Development of Fundamentals for Residual Stress Design in Coated Surfaces".

References

- [1] B.C. Larson et al., *Nature* **415** (2002) 887.
- [2] N. Tamura et al., *J. of Synchrotron Radiation* **10** (2003) 137-143.
- [3] R.C. Rogan et al, *Nature Materials* **2** (2003) 379-381.

Residual stresses in Al thin films thermally strained down to -225 °C

E. Eiper, K.J. Martinschitz, and J. Keckes

*Erich Schmid Institute for Materials Science, Austrian Academy of Sciences and Institute of Metal Physics,
University of Leoben, Leoben, Austria*

Thermally induced mechanical stresses in small-scale structures, such as thin films on stiff substrates quite often exhibit values of several hundred MPa after processing or during service [1]. Such high stresses can induce defects in the thin film structures that may finally cause failure of the metal films or components in microelectronic devices. Therefore, a detailed understanding of thin film stress evolution is necessary including the effect of dimensional constraints and microstructural information.

Recent studies on stress evolutions of thin metal films reveal a strong dependency of the flow stresses on the film thickness and/or grain size [1]. In general, the flow stress increases with decreasing film thickness and/or grain size. This phenomenon was explained by Nix and Freund [1] as a consequence of geometrical constraints on dislocations in thin films.

In this work, a temperature cycling is applied 50nm to 2000nm thick Al films sputter-deposited on oxidized silicon (100) substrates. The experiments were performed at MAGS beamline in the temperature range from -225 to 60 °C. XRD was used to characterize lattice spacing of films at different sample tilt angles. The diffraction data were used to calculate residual stresses in the films as a function of film thickness using $\sin^2\psi$ method [2].

In Fig. 1, residual stress dependencies for polycrystalline Al thin films with the thickness of 50 and 1000 nm are depicted. The results indicate that, due to the temperature cycling, the residual stress at -225 °C in 1000 nm thick film reached about 350 MPa in tension in contrast to 800 MPa in 50 nm thick film.

Analyzing the stress-temperature dependency of films with different thickness, it was possible to identify the change from elastic to plastic behaviour and determine also the magnitude of the yield stress in Al thin films with different thickness (Fig. 2). The plot of yield stress versus inverse film thickness documents that the thinnest film (50 nm) exhibits the highest magnitude of the stress at -225 °C. For the thinnest film, the plastic limit was thus reached at about 800 MPa. The biaxial strength of Al film deposited on Si(100) is significantly higher than that of bulk (90 MPa). In the future, the analysis of the dislocation formation and movement using in-situ XRD is planned in order to understand deeper the size effects in thin films.

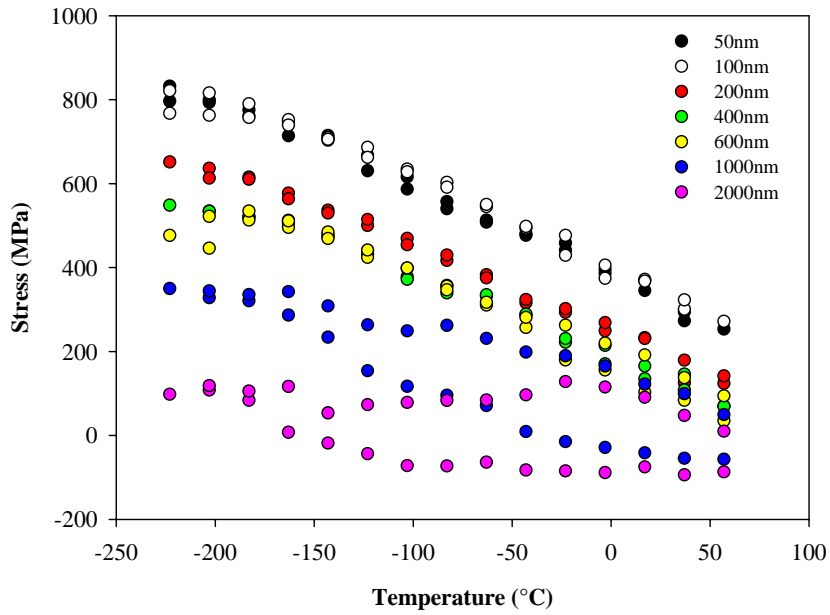


Figure 1 Temperature dependence of residual stressed in Al thin films with different thickness. The dependencies indicate that the 50 nm thick film exhibits very high tensile stresses of 800 MPa at -225 °C.

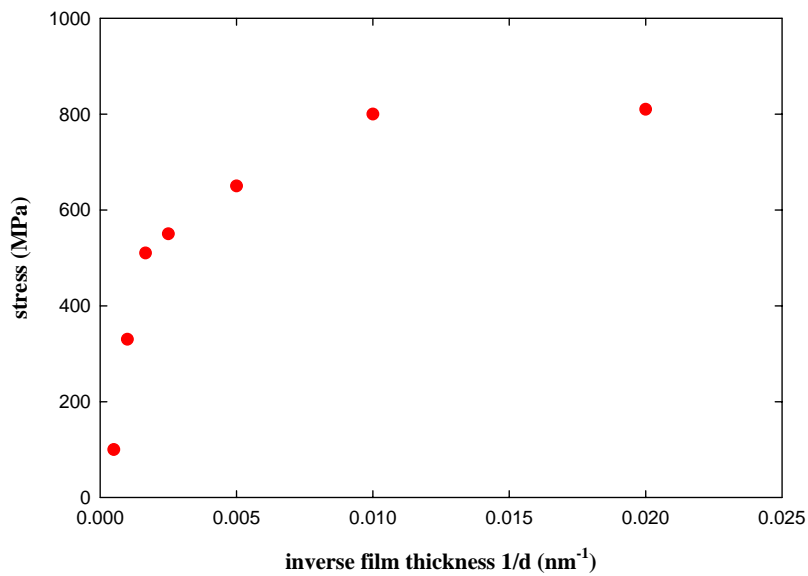


Figure 2 Yield stress in Al thin films on Si(100) as a function of inverse film thickness at -225 °C. The data document that 50 nm film exhibits the maximal tensile strength.

Acknowledgments

We gratefully acknowledge the European Community for a financial support grant through the Contract N° RII 3-CT-2004-506008.

References

- [1] W. D. Nix, *Metallurgical Transactions* 20A (1989) 2217.
- [2] J. Keckes, *J. Appl. Cryst.* 38 (2005) 311.

DIELECTRIC FUNCTIONS OF TRIGLYCINE SULPHATE CRYSTALS AT DIFFERENT TEMPERATURES NEAR THE FERROELECTRIC PHASE TRANSITION

B. Andriyevsky ^{a)}, N. Esser ^{b)}, A. Patryn ^{a)}, C. Cobet ^{b)}, W. Ciepluch-Trojanek ^{a)}

a) Faculty of Electronics and Computer Sciences, Koszalin University of Technologies, Śniadeckich Str. 2, PL-75-453, Koszalin, Poland

b) ISAS – Institute for Analytical Sciences, Department Berlin, Albert-Einstein-Str. 9, 12489 Berlin, Germany

The funding source and grant number: EU, R II 3.CT-2004-506008

The triglycine sulphate crystal (TGS), $(\text{NH}_2\text{CH}_2\text{COOH})_3\text{H}_2\text{SO}_4$, is a known ferroelectrics belonging to the monoclinic space group $P2_1$. Above the transition temperature it becomes paraelectric of the monoclinic group $P2_1/m$ [1]. The study of optical characteristics of TGS crystals in the range of electronic excitations can be particularly useful for the investigation of relations between the peculiarities of electronic structure and the ferroelectric state formation. Physical properties of TGS crystals were widely studied experimentally and theoretically. First measurement of the partially polarized reflectance spectra of TGS crystals in the range of 4...22 eV were done using the Lyman discharge light source with the relatively low accuracy of 10...30% [2]. First-principal calculations of the electronic band structure of TGS crystals were performed in the paper [3].

In the present paper, the results of theoretical first-principal calculations of the electronic band structure and optical spectra of TGS crystal have been presented on the basis of our study [3] together with the measurements of its optical properties in the range of 4...10 eV performed at different temperatures using synchrotron radiation.

Calculations of the band energy dispersion $E(k)$, density of electronic states (DOS), and dielectric functions $\varepsilon(\omega)$ of TGS crystal have been performed in a frame of the density functional theory (DFT) using the CASTEP code [4]. Details of these calculations are described in [3].

Measurement of the pseudo-dielectric function $\varepsilon = \varepsilon' + i\varepsilon''$ of TGS crystals have been done by spectroscopic ellipsometry using the synchrotron-ellipsometer [5] attached to the 3 m Normal Incidence Monochromator (NIM) of the Berlin Electron Storage ring for Synchrotron radiation BESSY II. Measurements were done in the spectral range of 4.0...9.9 eV with the resolution of 0.02 eV. The angle of incidence was $\sim 68^\circ$, while the polarization of the incident beam was chosen $\sim 20^\circ$ tilted with respect to the plane of incidence during the measurements. A MgF_2 polarizer and rotating analyzer, respectively, ensured a 99.998% degree of polarization. The cleaved (perpendicularly to Y -direction) and mechanically polished surfaces of TGS crystal were used for measurement.

The study of the band structure of TGS crystal has revealed the flat or low dispersive wave vector dependence of the electron energy $E(k)$ [3] corresponding to the weak inter-cell electronic interactions. The Mulliken population analysis of the TGS crystal have revealed a greater covalent character of chemical bonds in the glycine group of the unit cell than that found in the sulphate one.

Analysis of the DOS has revealed that the predominant part of DOS (92%) in the range of -3.0...0.5 eV is formed by the p -states of oxygen. In particular, the highest valence energy states at $E = -0.2$ eV are formed by the oxygen of SO_4 -groups and glycine-2 group. The lower part of the conduction band, 4.0...6.0 eV, is formed by carbon (53%), oxygen (30%), and hydrogen (16%). The part of the hydrogen electronic states in the range of 6.0...11.0 eV is the greatest and is equal to about 45%. The conduction band of the crystal is a mixed one regarding to the character (s -, and p -type) and origin (chemical elements) of the electronic states.

The most pronounced peak of $\varepsilon''(\omega)$ at the photon energy $\omega = 7.3$ eV is observed for the planes of incidence YX and ZX [3]. For the plane of incidence YZ this peak is smaller

(Fig. 1). The magnitudes of pseudo-dielectric function $\varepsilon'(\omega)$ at $\omega = 4$ eV agree within 10% with the square of refractive indices of TGS crystals [6].

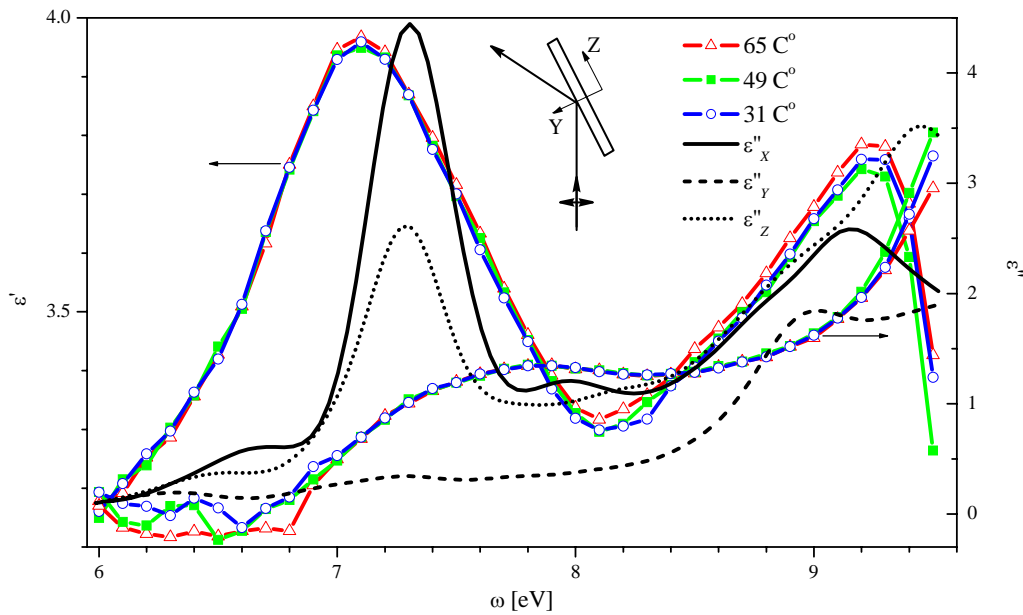


Fig. 1. Pseudo-dielectric functions $\varepsilon'(\omega)$ and $\varepsilon''(\omega)$ of TGS crystal experimentally obtained for the temperatures 31, 49, and 65 °C (points+lines) and the theoretical functions $\varepsilon''(\omega)$ for three principal directions X, Y, Z of optical indicatrix (lines).

The theoretical long-wave edge of fundamental absorption of TGS crystal determined by the $\varepsilon''(\omega)$ dependence is close to the experimental one when the scissor factor of 0.9 eV is used, that is typical for the DFT-based calculations. Analysis of the band structure has shown that the strong spectral band of $\varepsilon''(\omega)$ with maximum at $\omega = 7.3$ eV corresponds to the direct optical transitions at Γ^- , Y-, B, and E-points [3]. These transitions are associated with the valence p -states of oxygen and, predominantly, with the conducting states of hydrogen and carbon (Fig. 1). Similar analysis of the experimental and theoretical dielectric functions $\varepsilon''(\omega)$, band dispersion, and densities of states for TGS crystal gives possibility to assign the experimental maxima of $\varepsilon''(\omega)$ at 8.35 and 9.55 eV to the transitions between the oxygen valence p -states, probably partially delocalized, and lower lying delocalized states of the conduction band ($\omega > 6.0$ eV).

For the TGS samples of Y -cut and YZ incidence plane (YZ -geometry), the extrema of temperature dependencies of the real (χ'_{rel}) and imaginary (χ''_{rel}) parts of the relative susceptibility, $\chi''(T)/\chi''(65^\circ\text{C})$, $\chi = (\varepsilon - 1)$, of TGS crystal take place at the phase transition point for the energy of about $\omega = 9.5$ eV (Fig. 2). The temperature dependency of $\chi''_{rel}(T)$ in the vicinity of phase transition point demonstrates the critical-like behaviour, $\chi'' \sim (T - T_c)^{-\gamma}$, similar to the corresponding known dependency of static dielectric permittivity caused by the domain-like relaxation of TGS crystal. The increase of the relative susceptibility $\chi''_{rel}(T)$ at the temperature of 49 °C is equal to the considerable magnitude of 17%, that is approximately twice greater than the similar value for the temperature of 31 °C (Fig. 2). So, the probability of optical transitions near the energy of 9.5 eV at the temperature of ferroelectric phase transition (49 °C) is greater than that for the any other temperature around this point. It is interesting that the character of the temperature dependencies $\chi_{rel}(T)$ obtained (Fig. 2) is very similar to the temperature dependence of the relative optical path difference in the spectral range of the crystal's transparency ($\omega = 1.96$ eV) induced by the constant electric field along the polar Y -direction [7].

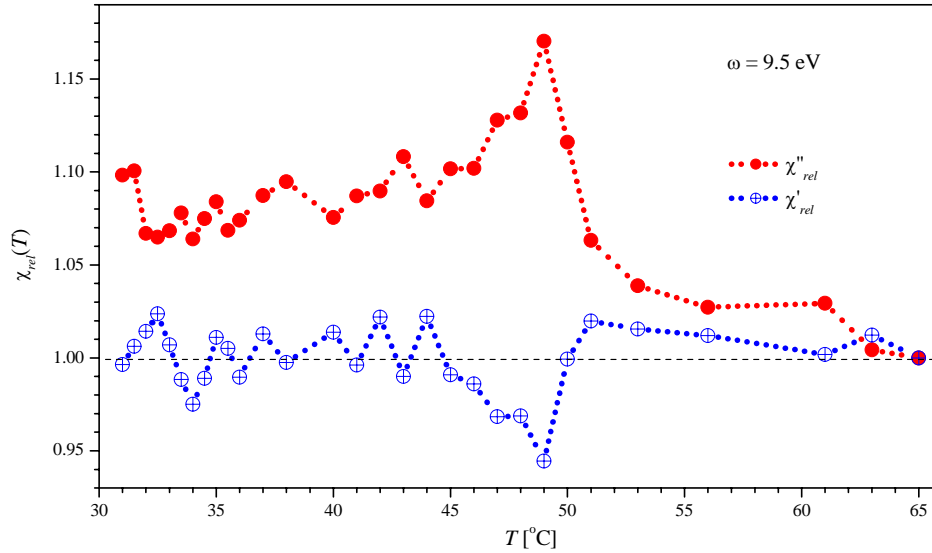


Fig. 2. Temperature dependencies of the real (χ'_{rel}) and imaginary (χ''_{rel}) parts of the relative susceptibility $\chi(T)/\chi(65^\circ\text{C})$ for YZ-geometry of TGS crystal and photon energy $\omega = 9.5$ eV.

One has to take into account that the extremum-like temperature dependency of dielectric permittivity and susceptibility of TGS crystal takes place only for YZ-geometry of experiment (Fig. 1), for which the Z-component of electric vector of light is considerable. For the geometries YX and ZX of experiment this Z-component of electric vector is relatively smaller. Taking into account the density of electronic states, one can suppose that the temperature dependency presented in Fig. 2 is associated with the electronic excitation of O-H...O bonds directed mainly along Z-axis between the glycine-2 and glycine-3 groups. At the temperature of ferroelectric phase transition, the hydrogen atoms of the O-H...O bonds are bound with neighbouring O atoms with the smallest strength. Then the electron population of the H atoms is probably the highest, and, therefore, the probability of the corresponding electronic excitations is the greatest.

The authors further gratefully acknowledge the support by BESSY.

- [1] S. Hoshino, I. Okaya, and R. Pepinsky, Phys. Rev. **115** (1959) 323.
- [2] N. A. Romanyuk, B. V. Andriyevsky, and I. S. Zheludev, Ferroelectrics **21** (1978) 333.
- [3] B. Andriyevsky, N. Esser, A. Patryn, *et al.*, Physica B: Physics of Condensed Matter **373** (2006) 328.
- [4] V. Milman, B. Winkler, J. A. White, *et al.*, Int. J. Quant. Chem. **77** (2000) 895.
- [5] T. Wethkamp, K. Wilmers, N. Esser, *et al.*, Thin Solid Films **313-314** (1998) 745.
- [6] N. A. Romanyuk, A. M. Kostetsky, and B. V. Andriyevsky, Physics of Solid State **19** (1977) 3095.
- [7] B. Andriyevsky, O. Myshchysyn, and M. Romanyuk, Physica Status Solidi (b) **203** (1997) 549.

Search for critical slowing down of heterophase fluctuations in a Au-Cd shape memory alloy by coherent x-rays

L. Müller^a, W. Leitenberger^b, U. Klemradt^a

^a II. Physikalisches Institut, RWTH Aachen University, 52074 Aachen, Germany

^b Institute of Physics, University of Potsdam, D-14469 Potsdam, Germany

The aim of this experiment was to observe heterophase fluctuations preceding (weakly first order) martensitic transformations (MT) in a bulk single crystal. In particular, the experiment aimed at distinguishing between conjectured “dynamic” and “static” fluctuations. In the dynamic case, a close analogy to second-order phase transitions is expected, implying a strong temperature dependence of the number of embryonic regions. In addition, an analogy to the well known effect of critical slowing down in 2nd order phase transitions [1] should be observable as well. The relevant time scales range from nanoseconds (phonon assisted nucleation) via very slow dynamics to the static, transformed sample [2, 3]. If dynamical fluctuations of embryonic regions exist, coherent x-rays should allow the observation of a fluctuating speckle pattern resulting from the different atomic arrangements.

Experimental

The temperature-dependent behaviour of a (001) oriented single crystal from the shape memory alloy Au_{50.5}Cd_{49.5} (denoted as Au-Cd) with a transformation temperature T_C of about 304 K was in the focus of the experiment. This alloy exhibits a MT which is even closer to a 2nd order transition than the MT of the model system Ni_{62.5}Al_{37.5}. The above mentioned effects should, therefore, be quite pronounced (if existing), provided the proper temperature close to T_C could be experimentally found.

For an experimental realization, a standard Bragg geometry was chosen for the observation of such fluctuations on a timescale of 100 s to 3000 s. A dedicated sample chamber provided a temperature stability better than ± 3 mK. For each temperature, the time characteristics of the intensity of the (001) Bragg reflection was measured with an integration time of 60 s in the first and 10 s in the second temperature cycle. This reflection is sensitive to the structural transformation. A vertical diffraction geometry was chosen due to a larger value of the spatial coherence in this direction. The used incident angle of 9.5° implied an energy of 11.2 keV for the first order diffracted beam. A $35\mu\text{m}$ pinhole was placed 30 cm in front of the sample to coherently illuminate a sample region. The reflected beam passed another $35\mu\text{m}$ pinhole 140 cm behind the sample.

Experimental data were taken at temperatures from approximately 10 K above the transition temperature in decreasing steps until the transition occurred. Thus a range of about one order of magnitude was covered in reduced temperature $t = \frac{T-T_C}{T_C}$. Since we are not aware of any similar experiment performed before, a more extended temperature range did not seem warranted for a first test. However, measurements at a temperature well above ($\Delta T = 40\text{K}$) and well below the transition ($\Delta T = -20\text{K}$) were included for reference. A typical set of data is shown in Fig. 1.

For the data evaluation the first order reflection is separated from each energy-dispersive spectra and then evaluated further by means of detrended fluctuation analysis (DFA). In essence, the recorded time series (denoted as $y(k)$) is integrated and divided into boxes of variable length n . In each of these boxes the local trend (a polynomial of order m , denoted

as $y_{n,m}(k)$ is subtracted. Finally the average fluctuation is calculated by $F(n) = \sqrt{\frac{1}{N} \sum_{k=1}^N (y(k) - y_{n,m}(k))^2}$ for all box sizes. A linear relationship between $\log(F(n))$ and $\log(n)$ indicates the presence of a power law, i.e. scaling behaviour [4-7]. A normalisation to the beam current is not necessary because the resulting trend is automatically taken care of by the detrending procedure, since DFA of order m does account for a trend in the data of order $m-1$. With the mostly predominant non-linear trends it is therefore required to use at least third order DFA, which is shown in Fig. 2 and 3.

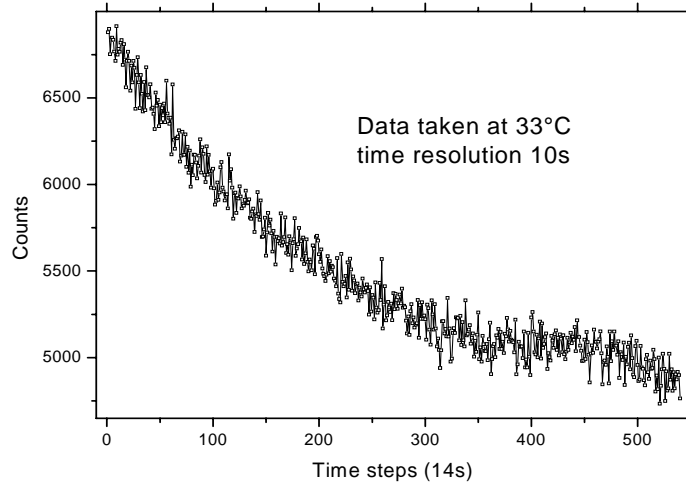


Fig. 1: Typical dataset for one temperature. Note that the trend in the data is not only caused by the decreasing incident beam intensity. The decrease in measured intensity is about 30% whereas the beam intensity decreased by only 15% during the measurement. Each time step corresponds to a 10s measurement with a following readout time of 4s.

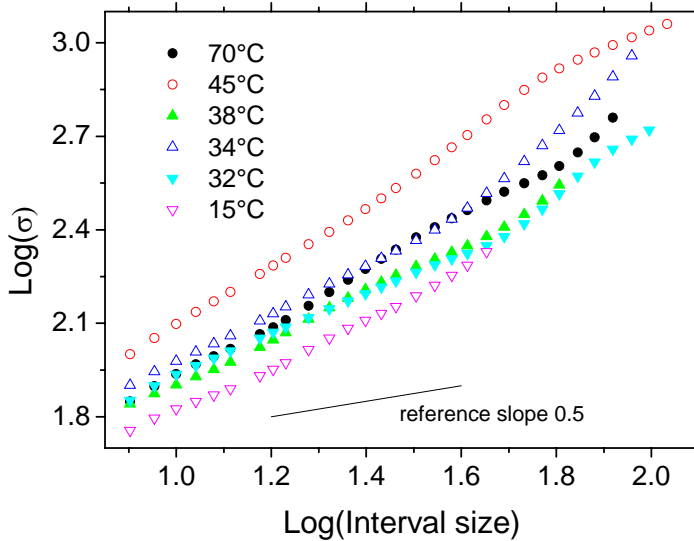


Fig. 2: Third order DFA of measurements with 60s time resolution. The slope is between 0.75 and 0.98 indicating a correlated fluctuation. Note the different slope in Fig. 3. The slope 0.5 corresponds to a random (uncorrelated) fluctuation.

Results

Obviously the results for the first run with 60s time resolution give very similar results for all temperatures (Fig.2). In the second run with 10s time resolution this behaviour is reproduced except for the measurement at 32°C (Fig. 3). The slopes of 0.75 - 0.98 indicate correlated behaviour of the fluctuation, with the slope corresponding to entirely uncorrelated fluctuations (0.5) shown in Fig. 2 for comparison. With a better time resolution, the slope is reduced to 0.7 - 0.67, still indicative of a correlated fluctuation (Fig. 3). However, very close to the MT a strong crossover to anticorrelated behaviour is observed (slope 0.28). This temperature agrees

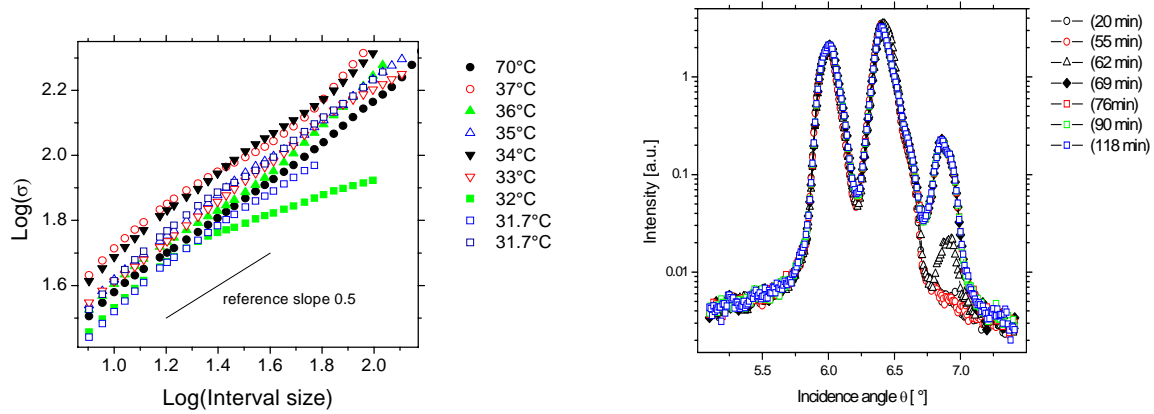


Fig. 3: *left* Third order DFA of measurements with 10 s time resolution. The slope is between 0.6 and 0.67. Note a crossover to anticorrelation (slope 0.28) at 32°C. The slope 0.5 corresponds to a random (uncorrelated) fluctuation. *right* Conventional diffraction measurements indicate a time dependent behaviour of the sample at a similar temperature. The times listed refer to the time after setting the temperature.

with the temperature range where anomalous nucleation behaviour has been observed in previous diffraction experiments with non-coherent x-rays (nucleation on isothermal holding for athermal martensites [8, 9]).

Conclusion

In conclusion, intensity fluctuations of a Bragg reflection sensitive to a MT have been observed on long time scales (100 s to 3000 s) by coherent x-rays. DFA shows that the fluctuations are not random but in general are correlated. In the vicinity of the MT, however, a crossover to anticorrelated fluctuations is observed. Whether this observation can be attributed to the conjectured critical slowing down is currently under investigation. Further scattering experiments are planned to shed (coherent) light on this behaviour.

Acknowledgement

This project has been supported by the BMBF via 05 ES3XBA/5.

References

- [1] R.A. Cowley, *Adv. in Phys.* **29** (1980) 1-110.
- [2] J.A. Krumhansl and R.J. Gooding, *Phys. Rev. B* **39**, 3047 (1989).
- [3] T. Davenport, L. Zhou, and J. Trivisonno, *Phys. Rev. B* **59**, 3421 (1999).
- [4] C-K. Peng, S.V. Buldyrev, S. Havlin, M. Simons, H.E. Stanley, A.L. Goldberger, *Phys. Rev. E* **49** (1994) 1685-1689.
- [5] J.W. Kantelhardt, E. Koscielny-Bunde, H.H.A. Rego, S. Havlin, A. Bunde, *Physica A* **295** (2001) 441-454.
- [6] K. Hu, P.C. Ivanov, z. Chen, P. Carpena, H.E. Stanley, *Phys. Rev. E* **64** (2001) 011114.
- [7] L.M. Stadler, B. Sepiol, J.W. Kandelhardt, I. Zizak, G. Grübel, G. Vogl, *Phys. Rev. B* **69** (2004) 224301.
- [8] T. Kakeshita, T. Fukuda, T. Saburi, *Scripta Mater.* **24** (1996) 147-150.
- [9] L. Müller, U. Klemradt and T.R. Finlayson, *Mat. Sci Eng. A* **438-440** (2006) 122-125.

Co nanodots on Au(887): An electronic structure outlook

C. Biswas, A. Varykhalov, and O. Rader

BESSY, Albert-Einstein-Straße 15, D-12489 Berlin, Germany

The research in low-dimensional systems offers unique opportunity for electronic device applications as well as a ground for experimenting with quantum effects. The advances in low-dimensional research have been assisted by nanofabrication techniques like self-assembly and proper templates for producing nanostructured solids with tailored properties [1]. The vicinal surfaces have proved to be important for tailoring the magnetic and electronic properties of nanostructured solids, for example, Co nanochains on the vicinal Pt(997) surface [2]. The angle-resolved photoemission is an ideal probe for investigating the electronic structure of low-dimensional structures.

Recently, Au vicinal surfaces like Au(23,23,21), Au(887), and Au(223) have been identified as suitable templates for growing 1D and 2D nanostructured solids [3]. The present experiment focuses on modifications of the electronic structure of Au(887) due to Co nanodots grown on the Au(887) vicinal surface at room temperature as well as low temperature. The Au(887) surface is characterized by a highly regular one-dimensional step array with terrace width (d) = 39 Å and step height (h) = 2.35 Å as shown in Fig 1(a). Au(887) has a miscut angle of 3.5° towards [111] and {111}-like steps (Fig. 1(a, b)).

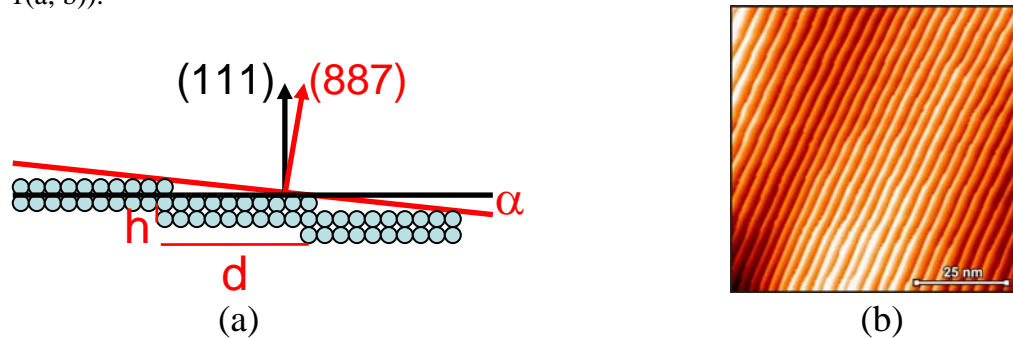
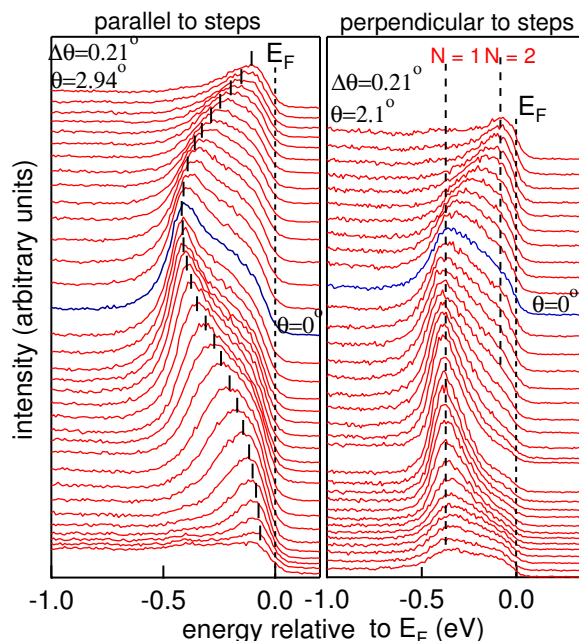


Fig.1. (a) The schematic representation of the side-view of the one-dimensional step array, where miscut angle, terrace width and step height are depicted. (b) STM picture from clean Au(887) shows a highly regular one-dimensional step array.

While the electronic structure of the Au(111) surface is defined by the two-dimensional free-electron-like surface state near the Fermi level, the Au(887) surface state has one dimensional character, i.e., it has a free-electron-like dispersion parallel to the steps and it becomes totally confined between two steps in the perpendicular direction as observed by the angle resolved photoelectron spectra in Fig 2. In



the perpendicular direction the free-electron-like surface state splits into two quantum well states at 0.4 eV ($N=1$) and 0.1 eV ($N=2$). The observed spectra agree with the previously reported results [4] for the Au(887) surface.

Fig.2. Au(887) surface state dispersion in the direction parallel and perpendicular to the steps. The one-dimensional character of the surface state with two quantum well levels in the perpendicular direction to the step is clearly observable. The spectra are recorded at $h\nu=30$ eV.

The Co, for sub-monolayer coverage deposited at room temperature, nucleates at the kinks of the Au(111) ($23 \times \sqrt{3}$) reconstruction geometry forming polygonal islands on Au(111) surface in

the $[1\bar{1}2]$ direction. Whereas, at sub-monolayer coverage, Co deposited on Au(887) forms an array of nanodots. At 140K deposition temperature the nanodot array is more ordered than that at room temperature [5]. Fig. 3 shows our STM picture of 0.2 ML coverage Co deposited on Au(887) at room temperature. Because the nanodots are formed at room temperature, the array does not have perfect long range ordering. Two kinds of dots co-exist on the surface (shown by arrows in Fig.3): small (A) and large (B), which is in agreement with the previously reported STM experiments [5].

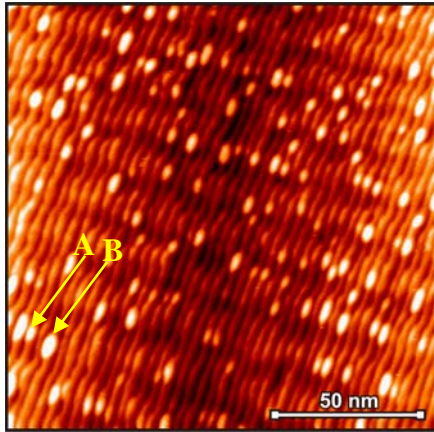
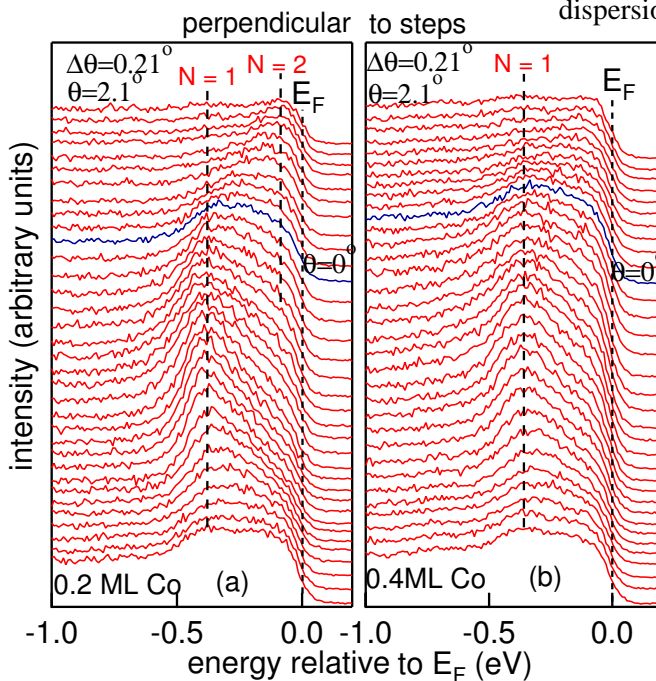


Fig.3. STM image of 0.2 ML Co deposition on Au(887) at room temperature. The image is obtained at room temperature.

The angle resolved spectra obtained for 0.2 ML Co deposited on Au(887) at room temperature still shows quantization in the perpendicular direction (Fig.4(a)) and free-electron-like dispersion in the parallel direction (not shown in figure).



As the Co coverage is increased to 0.4 ML at room temperature, it becomes more difficult to discuss the behaviour of the surface state due to increasing Co 3d spectral weight, but the quantization of the surface state perpendicular to the step appears to become weaker (Fig. 4(b)). The surface state behaviour parallel to the steps is also not free-electron-like (not shown in fig).

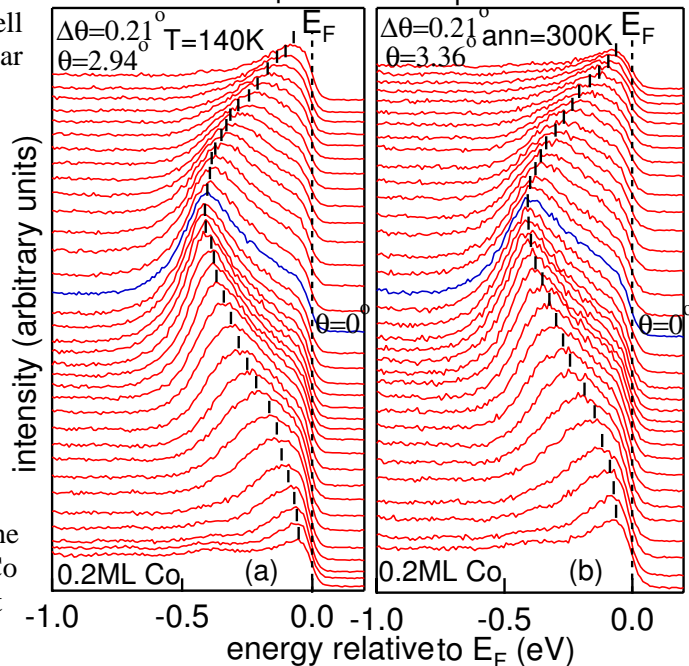
Fig.4. Angle-resolved photoemission spectra of the Au(887) surface state perpendicular to the steps for (a) 0.2 ML Co and (b) 0.4 ML Co coverage deposited at room temperature. The spectra are recorded at $h\nu = 30$ eV.

Whereas, for 0.2 ML Co coverage deposited at 140 K and consequently annealed to 300K, the surface state shows free-electron-like dispersion parallel to the steps

parallel to the steps (Fig. 5(a,b)) and two well distinguished quantum well states perpendicular to the steps (not shown in fig).

Fig.5. Angle-resolved photoemission spectra of the Au(887) surface state parallel to the steps for 0.2 ML Co coverage (a) deposited at 140K and (b) deposited at 140K with subsequent annealing at 300K. The spectra are recorded at $h\nu = 30$ eV.

The different behaviour of the surface state due to Co deposition at room and low temperatures might be due to different ordering and size of the Co nanodots on the Au(887) surface. The peak position of the surface state does not change with the Co coverage indicating no significant hybridization between the Au 6s,p and Co 3d states.



In conclusion, we confirm the appearance of an intense one-dimensionally confined surface state on Au(887). This state and its lateral quantization survives the formation of ordered Co nanodots of 0.2 and 0.4 ML nominal thicknesses at the optimum growth temperature of 140K and can be used to explore the possible electronic pathways of magnetic interdot coupling.

- [1] A. Varykhalov, C. Biswas, W. Gudat, and O. Rader, *Phys. Rev. B* 74, 195420 (2006).
- [2] P. Gambardella, A. Dallmeyer, K. Maiti, M. C. Malagoli, W. Eberhardt, K. Kern, and C. Carbone, *Nature* 416, 301 (2002).
- [3] A. Mugarza and J. E. Ortega, *J. Phys. Condens Matter* 15, S3281 (2003).
- [4] A. Mugarza, A. Mascaraque, V. Pérez-Dieste, V. Repain, S. Rousset, F. J. García de Abajo, and J. E. Ortega, *Phys. Rev. Lett.* 87, 107601 (2001).
- [5] S. Rohart, G. Baudot, V. Repain, Y. Girard, S. Rousset, H. Bulou, C. Goyhenex, and L. Proville, *Surf. Sci.* 559, 47 (2004).
- [6] N. Weiss, T. Cren, M. Epple, S. Rusponi, G. Baudot, S. Rohart, A. Tejada, V. Repain, S. Rousset, P. Ohresser, F. Scheurer, P. Bencok, and H. Brune, *Phys. Rev. Lett.* 95, 157204 (2004).

Part of this project supported by DFG: Grant no. RA-1041

C. B. is Marie Curie fellow of European Union: Grant No. MTKD-CT-2004-003178

NEXAFS study of carbon hard coatings tribo-tested under slip-rolling conditions

Ch.-A. Manier, D. Spaltmann, M. Woydt, A. Lippitz and W. E. S. Unger

Bundesanstalt für Materialforschung und –prüfung (BAM), 12203 Berlin, Germany

Tribo-chemical phenomena at hard coatings are extensively studied in recent materials science. Tools of surface analysis as photoelectron spectroscopy, time-of-flight secondary ion mass spectrometer and, last but not least, X-ray absorption spectroscopy have to be applied in order to derive chemical information for a more detailed understanding of tribo-chemical processes influencing the performance of the respective coated parts in machines, cars, hip joint endoprosthesis, etc.

Amongst the popular hard coatings ta-C, a-C:H (“DLC”) or nano-crystalline diamond play an increasing role. Therefore, in a DFG Project, the behaviour of these coatings under slip rolling conditions is studied with the goal to understand fundamental phenomena and failure mechanisms under consideration of surface chemistry. The coatings were deposited on the circumference of cylinders made of a typical bearing steel 52100. Different types of coatings, tetrahedral amorphous coating (ta-C), hydrogenated amorphous coating (a-C:H) and nano-crystalline diamond were supplied by different manufacturers. The coatings were tested under “mixed/boundary lubrication” conditions using different lubricants, paraffin oil or polyglycol, applying an Amsler type twin disc tribometer. It generates rolling movement with a slip rate of 10%. The counter disc was made of the same steel as the coated disc, but with a curvature which creates “ball on cylinder” contact geometry (Fig. 1a). This arrangement allows high initial Hertzian contact pressures. After testing two areas of interest can be differentiated on the coating at the circumference of the coated disk: Unstressed areas and the tribologically stressed track (Fig. 1b). The track is typically about 1.5 mm wide and accessible for surface analysis by NEXAFS spectroscopy. Comparisons of different coatings were made based on a common empirical failure criterion. Slices of the coated cylinders were cut, cleaned in an ultrasonic bath, using first iso-propanol and then ethanol to remove remaining lubricants used during the tribological tests, finally dried and analysed using the NEXAFS endstation at the HE-SGM beamline.

K-edge total electron yield (TEY) NEXAFS spectra were acquired with the photon beam impinging the surface at the magic angle. The spectra are normalized in units of the edge jump.

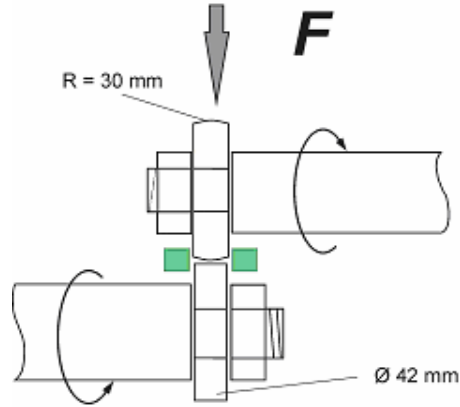


Fig. 1a: Schematic diagram of the Amsler type twin disc tribometer. The lower coated disc turns at a speed of 390 rpm, the upper uncoated disc at 354 rpm.

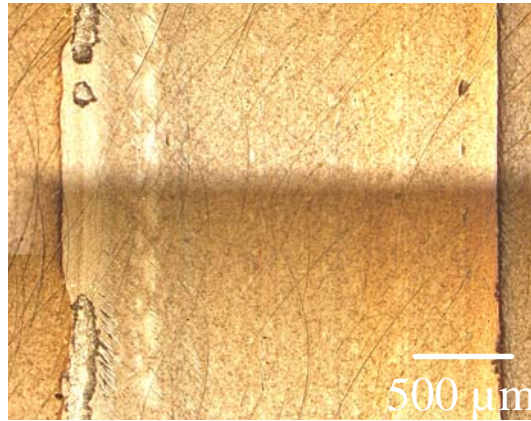


Fig. 1b: Circumference of the coated disk after testing showing the tribologically stressed track.

The surface concentration of sp^2 bonded carbon species in unstressed areas and the tribologically stressed track were compared for different tribo test conditions and different carbon hard coatings by using a graphite reference. The relative sp^2 concentrations were estimated according to:

$$sp^2 [\%] = \frac{sp^2}{sp^2 + sp^3} = \frac{I_{\pi^*}}{I_{ref\pi^*}} \cdot \frac{I_{Total\ ref}}{I_{total\ sample}}, \quad (1)$$

with I_{total} as the area of the whole spectrum between 280 and 330 eV, I_{π^*} and $I_{ref\pi^*}$ as the $sp^2 \pi^*$ resonance areas of the sample and the graphite as reference, respectively.

Fig. 2 shows an example of C K-edge NEXAFS spectra of a tribo tested a-C:H coating tested under 1.5 GPa with paraffin oil as lubricant. It reached 10 million cycles without any

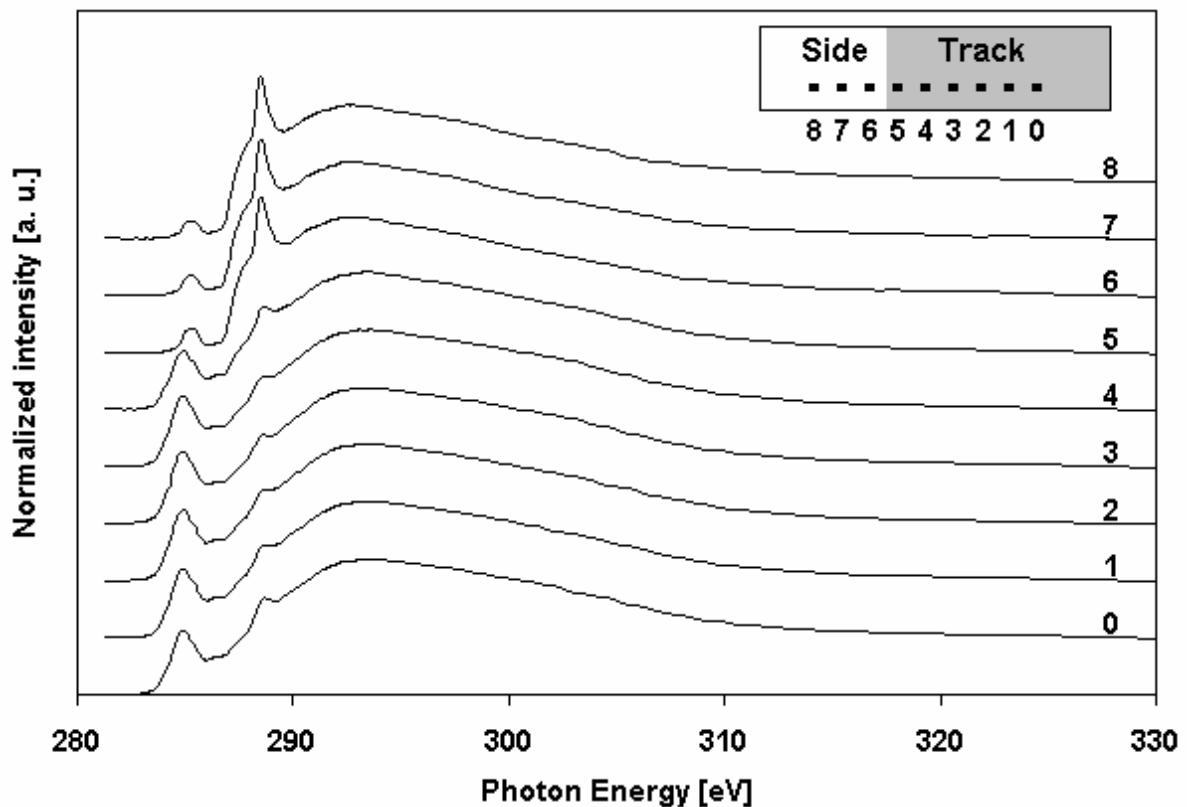


Fig. 2: NEXAFS TEY C K-edge spectra of an a-C:H coating measured by moving the X-ray spot stepwise from the wear track into the unstressed side area.

visible defects. The unstressed area outside the track is characterized by a relatively low surface concentration of sp^2 bonded species, pointing to a low level of concentration of graphitic species, together with signatures pointing to some oxidation of the surface layer. Moving the X-ray spot into the track region characteristic changes can be observed. The π^* resonance to be related to sp^2 bonded carbon species increases in intensity and the resonance energy shifts from 285.3 eV to 285.0 eV when the X-ray beam reaches the track. The change of the sp^2 carbon intensity and the energy shift can be explained in terms of a tribo-chemical reaction, i.e., by a graphitization of the coating in the track.

As mentioned above, a number of different coatings was investigated and evaluated in terms of graphitic character in the unstressed state and graphitization due tribological stressing later on. The spread of the character of the films in the as received state and after tribo testing is wide and a clear correlation with the performance is not yet found. Probably information on the sp^2 vs. sp^3 bonding character is not sufficient for an unequivocal classification of the films in terms of potential performance.

Acknowledgement: This work has been funded by the DFG (Kz. WO 521/6, Kurztitel: „Wälzbeständigkeit von DLC Schichten“)

Nickel L edge resonant Raman and Interference effects?

D.R. Batchelor¹⁾, Th. Schmidt¹⁾, R. Follath²⁾, C. Jung²⁾, R. Fink³⁾, M. Knupfer⁴⁾, A. Schöll¹⁾, B. Büchner⁴⁾ and E. Umbach¹⁾

¹⁾ Universität Würzburg, Experimentelle Physik II, Am Hubland, D-97074 Würzburg, Germany, ²⁾ BESSY GmbH, Albert-Einstein-Straße 15, 12489 Berlin, Germany, ³⁾ Physikalische Chemie II, Universität Erlangen-Nürnberg, Egerlandstraße 3, D-91058 Erlangen, German, ⁴⁾ IFW Dresden, D-01171 Dresden, Germany

Core hole excitation results in a complex dynamical multielectron response. This is in particular the case at and near threshold where the core excitation and decay of the hole cannot be viewed as separate events. In other words to calculate NEXAFS spectra requires an understanding of this multielectron response. Photoemission is a useful tool in this respect as one can monitor the changes in valence emission and Auger decay as the photon energy is varied and obtain valuable insight to electron correlation and the electron dynamics of the system. The technique of resonant photoemission has advanced considerably with the development of synchrotron sources and electron energy analysers. However due to the sequential stepping of the photon energy it suffers from long experimental times. Amemiya et. al. [1] first showed that dispersive NEXAFS was possible. We have followed on from their work at BESSY and have showed [2] that in addition to being able to do parallel NEXAFS there is sufficient flux and photon energy resolution to do resonant photoemission experiments i.e. Soft X-Ray dispersive CFS/CIS electron spectroscopy.

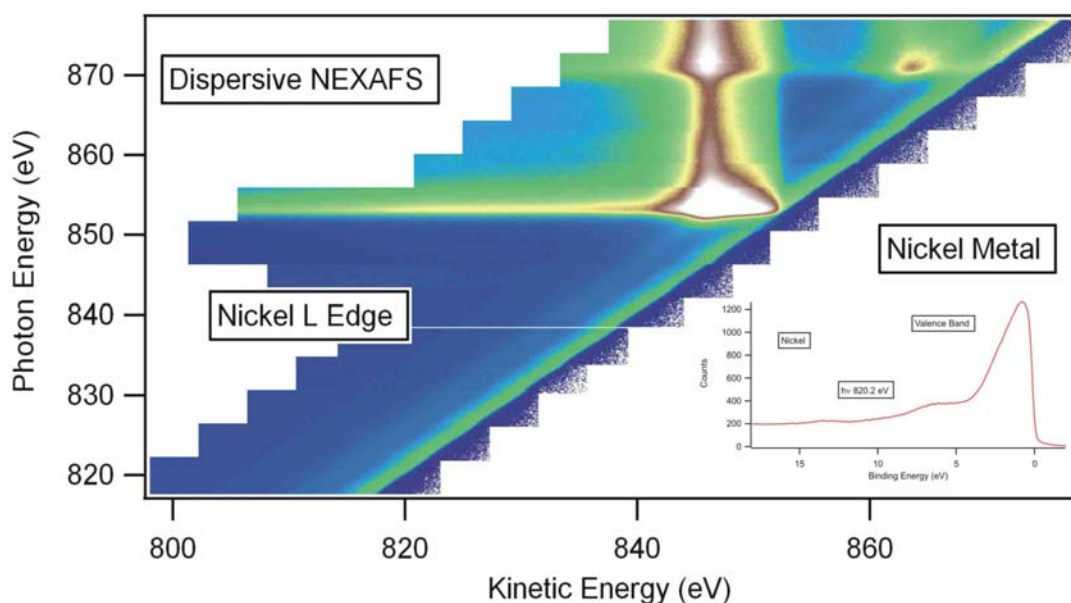


Figure 1. Dispersive CFS/CIS electron spectroscopy of the Ni LMM Auger and valence band over the $L_{2,3}$ edge. Insert shows the valence spectrum below threshold.

The idea is simple the polychromatic light strip of the grating monochromator is projected onto the sample which is then subsequently imaged by an imaging electron energy analyser. The analyser is mounted so that the electron energy is dispersed normal to the light dispersion and the spatially resolving direction of the analyser is parallel to the light dispersion. This requires the beamline focus to be at the sample rather than the more normal situation at the exit slit. With the present PGM monochromator however it is possible to extend the depth of focus by using low C_{ff} values and small source apertures. The drawback of course is that decreasing both, C_{ff} and ID apertures leads to a loss of photon flux. In addition there is a decrease in the available energy range due to a smaller undulator harmonic width. Our

present pilot setup is currently being updated [2] to a purpose built beamline which will allow both traditional photoemission and NEXAFS spectroscopy and the new dispersive spectroscopy by simply switching mirrors.

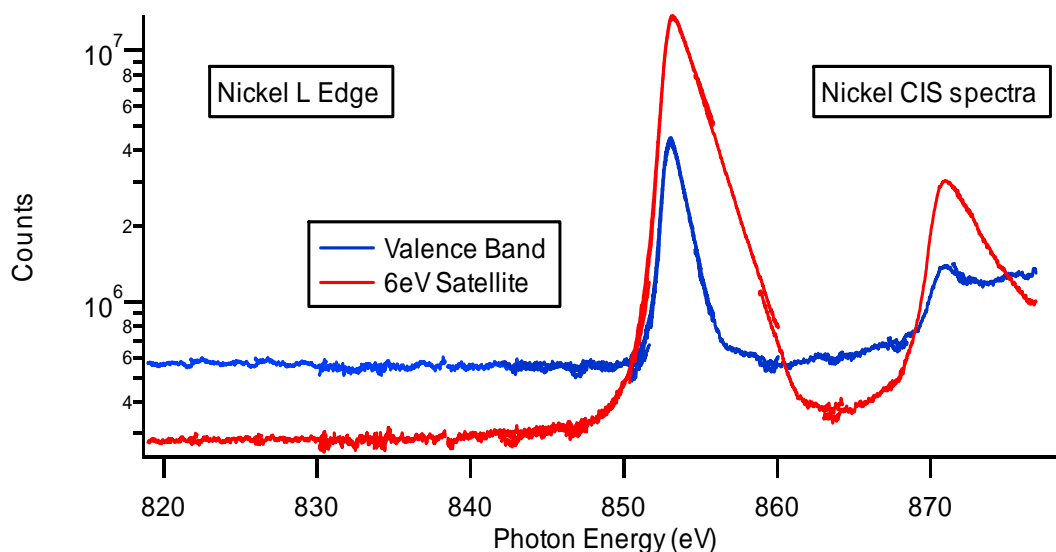


Figure 2. Intensity versus photon energy of the 3d8 satellite and valence band. The data are the results of integrating small windows of the dispersive data shown in Figure 1.

As an example of the technique we show in Figure 1, a map of the Nickel LMM Auger transition over the $L_{2,3}$ edges with a large pre-edge similar to the range covered by Weinelt et. al. [3]. They used a Ni(100) single crystal and exploited the variable polarisation of the undulator to accentuate Auger and photoelectron emission. Their experimental results show a clear dip in the pre-edge of the 3d8 photoemission satellite and valence band which was interpreted as due to a Fano resonance, an indication of interference between the direct photoemission process and an underlying continuum of states. In contrast our experiment used a polycrystalline foil which although averaging over the different crystalline orientations would still be expected to show some evidence of a fano profile in particular for the valence band where Wienelt et. al. [3] see a dramatic effect due to the absence of the autoionisation channel.

The data in Figure 1, have been corrected for a simple linear decrease in flux with photon energy in the displayed range. Figure 2 shows the results of integrating the 3d8 satellite and the valence band (see insert of Figure. 1.) over small energy windows. The data are plotted on a logarithmic scale to magnify the low intensity features and show no evidence of a characteristic Fano dip for the satellite or valence band. This result calls into question that interference effects characteristic of a Fano process are responsible for the resonance. At this point the origin of the maxima in the NEXAFS should be discussed. The kinetic energy of the 3d8 satellite and Auger emission were determined by a simple curve fitting algorithm and are shown in Figure 3. Below the L_3 threshold the energy of the 3d8 satellite disperses linearly until at threshold the decay of the core hole by autoionisation to this doubly ionised final state dominates. Above threshold the path of the photoemission feature is difficult to trace since it requires accurate curve fitting over almost two orders of magnitude. However in the low intensities of the Auger tail it is readily picked up again. At the L_2 edge the behaviour is similar but a shift to higher kinetic energies is observed which is presumably due to additional screening resulting from shake-up and the Koster-Kronig decay.

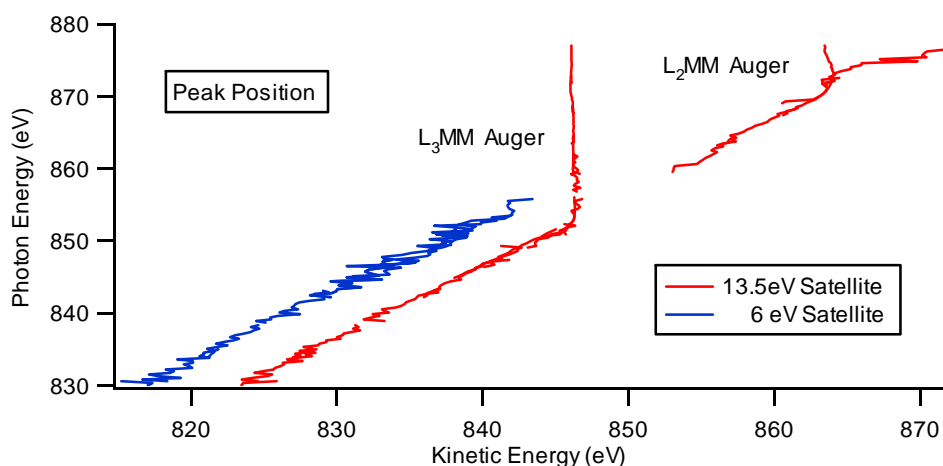


Figure 3. Energy position of the 3d8 6eV satellite and the LMM Augers together with the satellite at 13.5eV. The values were extracted from the data in Fig. 1. using a simple curve fitting routine over a small energy window.

In addition to the well known 3d8 satellite we observe an additional weak photoemission feature at 13.5eV which is also present in the data of Weinelt et. al. [3] and Tjeng et. al. [4]. The latter work attributes this to a 3d7 satellite. On tracking its energy dependence it is found to intersect with the maxima in the Nickel NEXAFS spectrum at 861eV. Again it is a shake-up satellite that is responsible for this feature in the NEXAFS. Similar effects are also seen with copper metal the maxima in the NEXAFS spectra correlate with photoemission features which can only be shake-up satellites i.e. they are not simply density of state effects in the unoccupied band structure.

The discrepancy with the work of Weinelt et. al. [3] needs to be pursued further. Although X-ray diffraction effects can be ruled out electron diffraction effects such as photoelectron diffraction may be responsible for the dip. The new dispersive measurements are already showing the advantage of the new multiplex technique. With the new beamline setup and its increased flexibility it will be possible to extend the experimental capabilities and improve the sensitivity even further.

References

- [1] K. Amemiya, H. Kondoh, T. Yokoyama, T. Ohta, *J. Electr. Spectr. Rel. Phenom.* 124 (2002) 151–164
- [2] D.R. Batchelor, Th. Schmidt, R. Follath, C. Jung, R. Fink, M. Knupfer, A. Schöll, B. Büchner and E. Umbach, *Bessy Annual Report 2005*, „An energy-dispersive VUV beamline for NEXAFS and other CFS/CIS studies“ submitted to NIMA
- [3] M. Weinelt, A. Nilsson, M. Magnuson, T. Wiell, N. Wassdahl, O. Karis, A. Föhlisch, and N. Mårtensson, J. Stöhr and M. Samant, *Phys. Rev. Lett.* 78 (1997) 96-970
- [4] L. H. Tjeng, C. T. Chen, P. Rudolf, G. Meigs, G. van der Laan, B. T. Thole, *Phys. Rev. B* 48 (1993) 13378-13382

Silica particle distribution in Styrol Butadien Rubber

G. Weidemann*, J. Goebbels*, H. Riesemeier*, G. J. Schneider**, D. Göritz**

*Federal Institute for Materials Research and Testing (BAM), Berlin;

**Institute of Physics, University of Regensburg

Due to the widespread use, studying the structure of silica is of general interest for fundamental research and for applications. For example, it is well known that rubber filled with silica can be used to improve the mechanical properties of the composite material. The goal of many different material models is to describe this so called reinforcement effect. The models depend on reliable information about the structure of the filler. However, the length scales involved range from nanometres up to millimetres and thus a complete study does not exist. The new salient synchrotron tomography experiments, available at BAMline, offer the unique possibility to investigate the structure down to 675 nm and thus to investigate the micro dispersion of silica in rubber.

The CT measurements are performed at an energy of 7 keV with a very low object to detector distance to minimise phase contrast. The voxel size of all data measured is 675 nm. The intensity was increased by bending the second multilayer of the double multilayer monochromator at BAMline.

For a better quantitative understanding of the attenuation contrast first Styrol Butadien Rubber (SBR) without silica particles was studied (Fig. 1 left). The average attenuation coefficient was found to be 8.0 cm^{-1} . From the chemical composition of SBR at 7 keV a value of 6.2 cm^{-1} is expected assuming a density of 1 g/cm^3 . The significantly higher value as well as the stronger attenuating particles found can be attributed to additives.

Furthermore a silica powder was studied (Fig. 1 right). It shows aggregates of particles with attenuation coefficients varying from 20 cm^{-1} to 32 cm^{-1} and a mean value of 24 cm^{-1} . Applying the mass attenuation coefficient of SiO_2 which is $53.6 \text{ cm}^2/\text{g}$ at 7 keV the density of the silica powder can be derived. It varies from 0.37 g/cm^3 to 0.60 g/cm^3 with a mean value of 0.45 g/cm^3 .

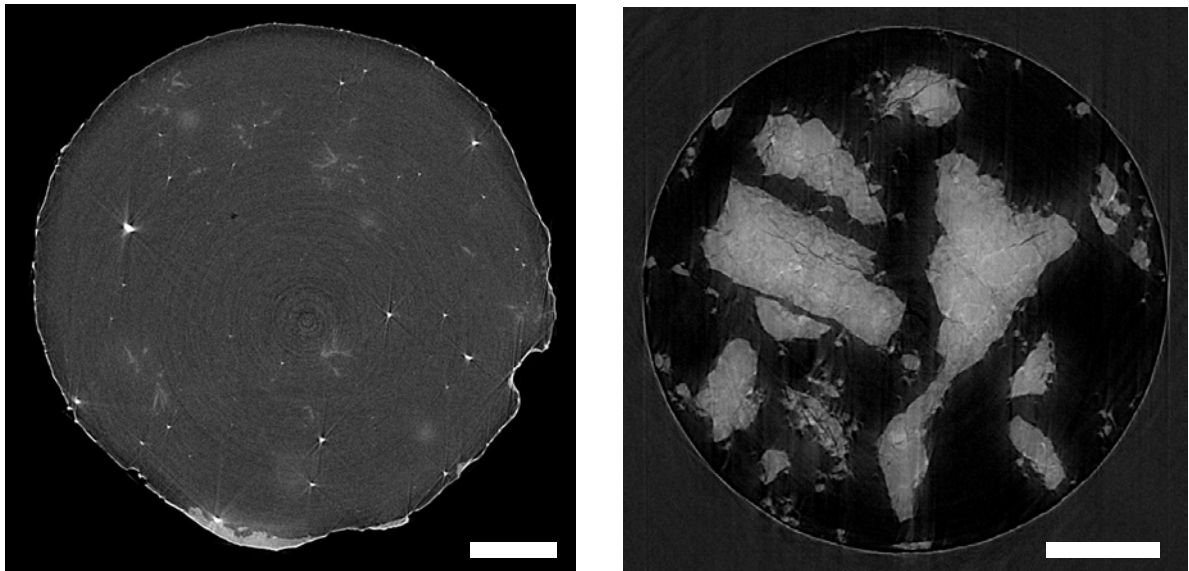


Fig. 1 Left: Cross section of SBR without silica particles. Right: Powder of silica particles in a polyethylene tube. The white bars represent 100 μm respectively.

Three samples with a varying content of silica particles are studied (Fig. 1, Table 1). The CT-slices of the samples with silica particles show a large number of aggregates of silica particles embedded in a quite homogenous matrix. The size of the particles ranges from a few microns up to 100 μm diameter. Aggregate diameters of 5 – 20 μm appear most frequently. The aggregates show nearly the same attenuation as the silica powder. The mean attenuation of aggregates is only slightly higher than the mean attenuation of the powder, which can be explained either by a penetration of the aggregates with styrol butadiene or by a selection of denser aggregates due to a higher resistivity against dissolution in the styrol butadiene matrix. The latter is in agreement with the variation range of density in the silica powder.

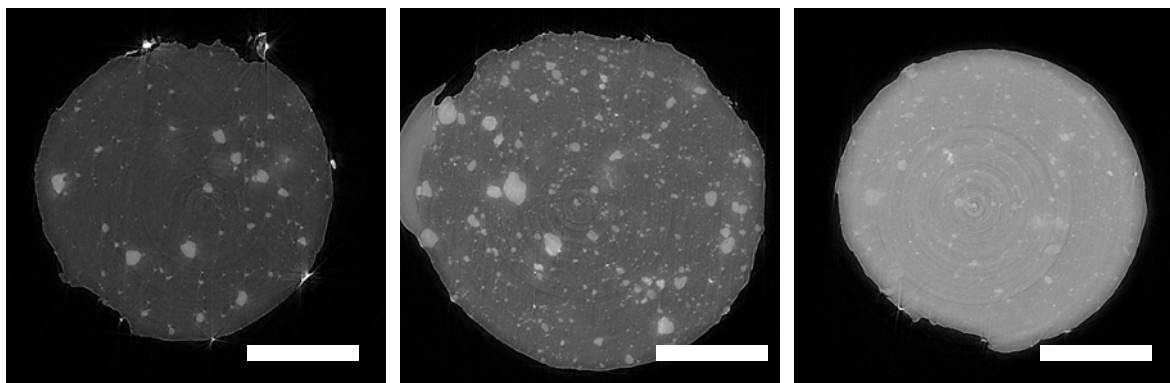


Fig. 2: Cross sections of samples S1-M2 (left), S1-M4 (middle), S1-M7 (right). The white bars represent 200 μm respectively.

Sample	Silica content		
	total (initial)		matrix (measured)
	vol. %	M %	[g/cm ³]
S1-M2	2	5	0.02
S1-M4	9	17	0.11
S1-M7	19	33	0.28

Table 1: Initial silica content of the samples measured and the silica content of the matrix material calculated from the attenuation values.

Additionally to the occurrence of aggregates an increased attenuation coefficient of the matrix is observed. The difference to the attenuation coefficient of the sample without silica allows to estimate the amount of particles distributed in the matrix material using the theoretical mass attenuation coefficient of SiO₂. The values derived from the matrix attenuation coefficient given in the right column of Table 1 are in good agreement with the initial content and the observed amount of aggregates. With an increase of the initial silica content first the number of aggregates increases strongly (Fig. 3). A further increase of the initial silica content of the matrix does not increase the amount of aggregates but the amount of silica particles distributed in the matrix. The high matrix attenuation reduces the contrast below the level which allows a reliable separation of matrix and aggregates for a surface representation.

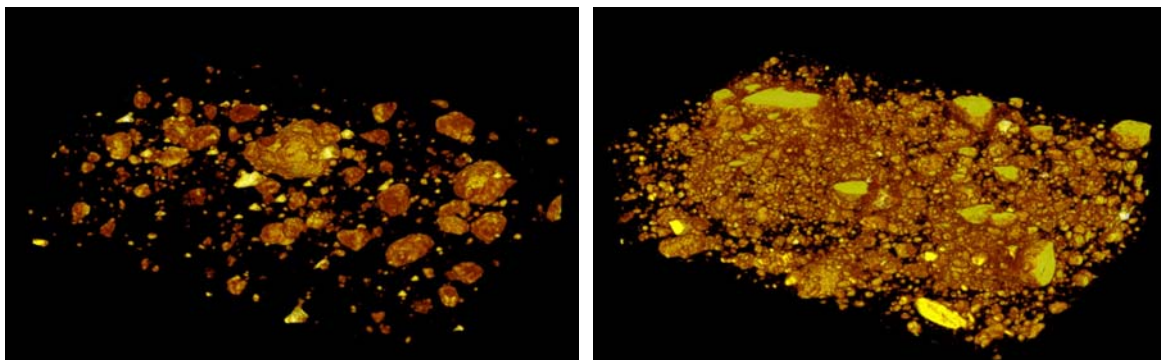


Fig. 3: The increase of particle becomes much more obvious in the surface representation of the silica aggregates within partial volumes of 270 μm × 170 μm × 68 μm of sample S1-M2 and S1-M4.

Electronic structure of self-assembled rare earth silicide nanostructures on Si(557)

M. Wanke, K. Löser, G. Pruskil, and M. Dähne

*Institut für Festkörperphysik, Technische Universität Berlin,
Hardenbergstr. 36, D-10623 Berlin, Germany*

Self-assembly of nanostructures is a powerful tool overcoming the limits of traditional lithographic fabrication of devices and data storage units. Hence new self-organized nanostructures are of special interest. On the Si(001)2×1 surface self-organized rare earth silicide nanowires can be formed [1,2], while Au chains can be prepared on Si(557) [3]. In the present investigation we observed the formation of different wire like rare earth silicide structures on the Si(557) surface. Clean Si(557) is characterized by a stepped structure consisting of (111) and (112) facets [4].

The rare earth silicide structures were prepared *in-situ* by deposition of dysprosium and erbium on clean Si(557) surfaces. Afterwards the sample was annealed to 500-800°C for several minutes, resulting in different wire types. To prevent oxidation, excellent ultra high vacuum conditions are necessary: The base pressure was lower than 5×10^{-11} mbar and did not exceed 2×10^{-10} mbar during the preparation process. The amount of rare earth exposure was determined by using a quartz-crystal microbalance with an accuracy of $\pm 20\%$. The temperature was measured using an infrared pyrometer with an accuracy of $\pm 10\%$. The ARPES experiments were performed at the BUS beamline (U125/2-SGM) at BESSY II with a Scienta SES 100 spectrometer at a photon energy of 41 eV. For the STM experiments we used a non-commercial setup with tunneling currents up to 3 nA and sample voltages between +3 V and -3 V.

In this work we show the band structure and topography of various dysprosium coverages on Si(557) samples. It should be noted that the STM and ARPES data of erbium silicide on Si(557) are essentially similar. STM images of the clean Si(557) sample show about 30 Å wide Si(111) terraces with a (7×7)-reconstruction. Depending on the coverage of dysprosium the width of the terraces is modified.

For coverages close to one monolayer, nanowires grow on the Si(111) terraces, as shown in Fig. 1(a). These nanowires are characterized by widths of 50-80 Å and lengths exceeding 1 μm, and show hexagonal terminations with clear straight edges along $\{\bar{1}10\}$ directions, as indicated by the ellipses in Fig. 1(a). These structural properties are characteristic for DySi₂/Si(111) [5], but the lacking atomic resolution does not allow a clear assignment on the basis of the STM data alone.

ARPES data of these nanowires for angles along the nanowire direction are shown in Fig. 1(b). The energy dispersion is characterized by parabolic bands crossing the Fermi energy at off-normal directions, while a wavy dispersion is found around $\bar{\Gamma}_{557}$ at about 1 eV binding energy. The dispersion perpendicular to the nanowires, as shown in Fig. 1(c), is characterized by parabolic bands close to the Fermi level. In Fig. 1(d), our data are compared

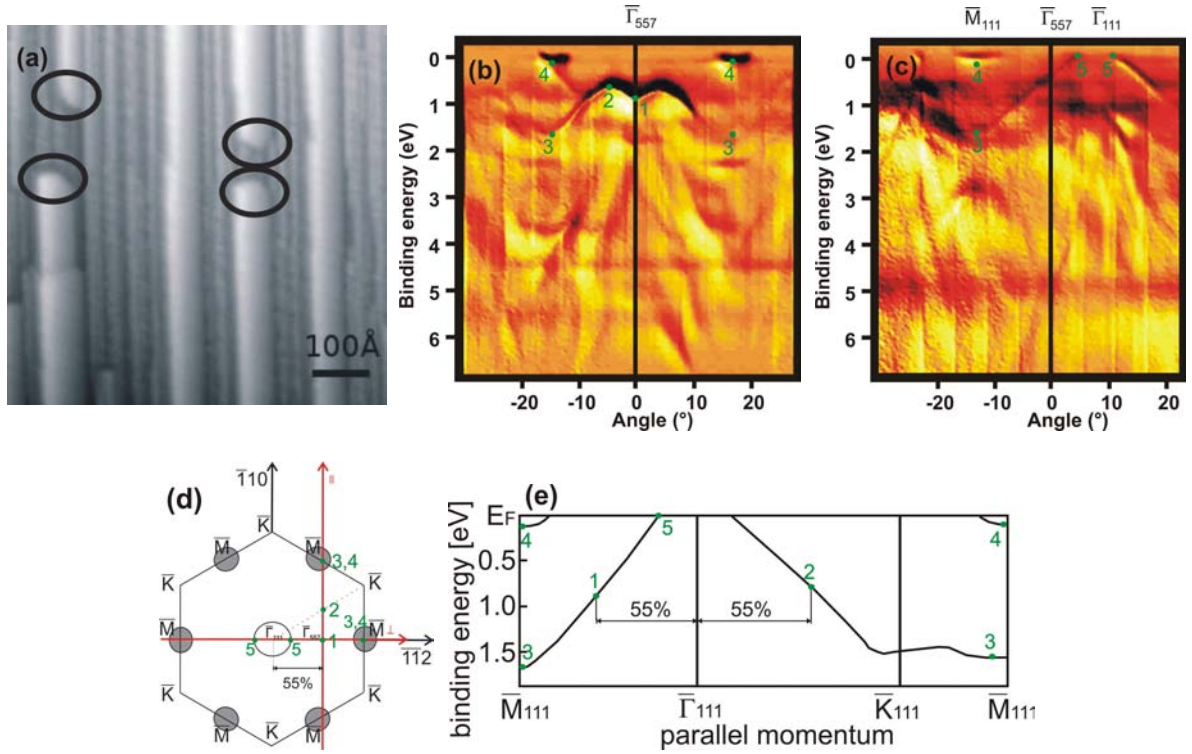


Fig. 1: (a) STM image, (b) ARPES data along and (c) perpendicular to the nanowire direction of DySi₂ nanowires on Si(557) prepared with 1,5 Å Dy and an annealing temperature of 700°C. (d) Assignment of the band structure to DySi₂ on Si(111) with a model of the surface Brillouin zone, (e) electronic structure of ErSi₂ on Si(111) [6].

with previous findings on ErSi₂/Si(111), which are shown in Fig. 1(e) [6]. On a first glance, the band structure on Si(557) also shows parabolic bands close to the Fermi level like those around the \bar{M}_{111} points on Si(111), but differs around normal direction. The latter is not surprising, since our data were taken around the surface normal corresponding to $\bar{\Gamma}_{557}$.

In Fig. 1(d), the surface Brillouin zone of ErSi₂/Si(111) is shown with the electron pockets around \bar{M}_{111} and the hole pocket around $\bar{\Gamma}_{111}$, as reported in Ref. [6]. The red lines indicate the directions around $\bar{\Gamma}_{557}$ where our data were taken. A detailed analysis shows an excellent agreement of our data taken along the nanowires with the ErSi₂/Si(111) band structure. This is manifested in particular by the green markers labeled 1 to 4. Marker 1 is the $\bar{\Gamma}_{557}$ point, which lies 55% away from the $\bar{\Gamma}_{111}$ point on the way to the \bar{M}_{111} point. Marker 2 lies on the way from the $\bar{\Gamma}_{111}$ point to the \bar{K}_{111} point. Markers 3 and 4 are located at the \bar{M}_{111} point. Perpendicular to the nanowires, the DySi₂/Si(111) band structure starting from $\bar{\Gamma}_{111}$ can be observed directly, as indicated by the markers 3, 4, and 5. The latter indicates the point where the hole-like state around $\bar{\Gamma}_{111}$ crosses the Fermi level.

For a higher amount of dysprosium of 3 Å the system shows a different behavior, as shown in Fig. 2. We have also found nanowires on Si(111) terraces, but with rounded terminations, as indicated by the ellipse, and a different band structure was determined. A strong and more complex dispersion of states crossing the Fermi level is observed both along and perpendicular to the nanowires. The silicide terraces are characterized by a $\sqrt{3} \times \sqrt{3}$ superstructure, as observed in LEED experiments. These observations indicate that the

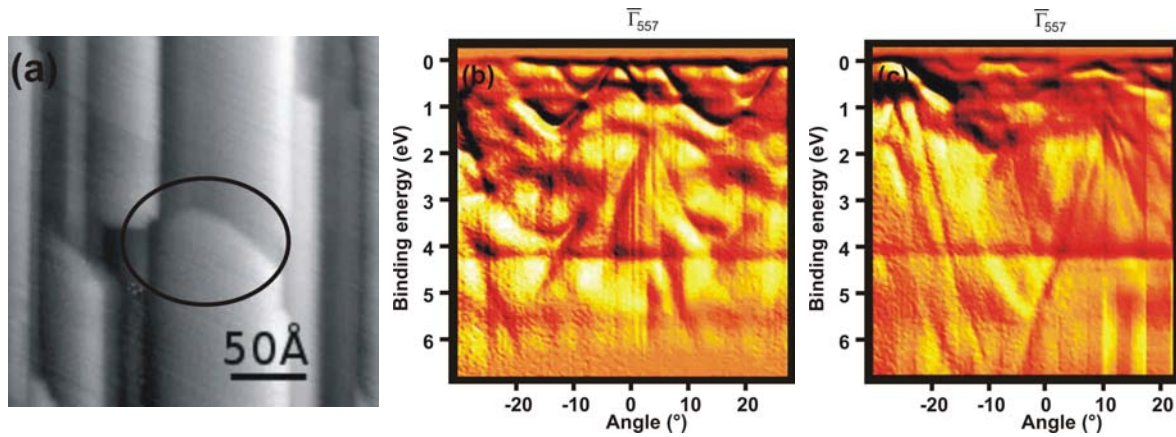


Fig. 2: (a) STM image and (b) ARPES data along nanowire direction, and (c) perpendicular to the nanowire direction of DySi_{2-x} nanowires on Si(557) prepared with 3 Å Dy and an annealing temperature of 700°C.

Si(111) terraces are now covered by Dy_3Si_5 multilayers. A detailed comparison with literature data is currently under way.

We have reported on different self-organized rare earth silicide nanostructures on the Si(557) surface. A dispersion of states crossing the Fermi energy was observed for different nanowire types, and an assignment to well-known silicide structures on the Si(111) surface could be made. However, the reported ARPES experiments could only be performed along specific directions in k-parallel space. A complete picture of the energy dispersion, also indicating possible quantum-size effects, could be derived from future measurements of the energy contours in k-parallel space.

This work was supported by the Deutsche Forschungsgemeinschaft, project number DFG Da408/11. We thank the group of G. Kaindl and E. Weschke for providing the experimental chamber, and BESSY is acknowledged for providing the beamtime.

References:

- [1] C. Preinesberger, S. Vandr , T. Kalka, and M. D hne-Prietsch, *J. Phys. D* **31**, L43 (1998).
- [2] J. Nogami, B.Z. Liu, M. Katkov, and C. Ohbuchi, *Phys. Rev. B* **63**, 233305 (2001).
- [3] I.K. Robinson, P.A. Bennett, and F.J. Himpsel, *Phys. Rev. Lett.* **88**, 0961041 (2002).
- [4] A. Kirakosian, R. Bennewitz, J.N. Crain, Th. Fauster, J.-L. Lin, D.Y. Petrovykh, and F.J. Himpsel, *Appl. Phys. Lett.* **79**, 1608 (2001).
- [5] I. Engelhardt, C. Preinesberger, S.K. Becker, H. Eisele, and M. D hne, *Surf. Sci.* **600**, 755 (2006).
- [6] L. Stauffer, A. Mharchi, C. Pirri, P. Wetzels, D. Bolmont, and G. Gewinner, C. Minot, *Phys. Rev. B* **47**, 10 555 (1993) .
- [7] C. Preinesberger, G. Pruskil, S.K. Becker, M. D hne, D.V. Vyalikh, S.L. Molodtsov, C. Laubschat, and F. Schiller, *Appl. Phys. Lett.* **87**, 083107 (2005).

Magnetism in Iron Nanoclusters

G. Ballentine, M. Heßler, M. Kinza, K. Fauth

Max Planck Institut für Metallforschung

Heisenbergstr. 3 Stuttgart, Germany 70569

Funding: Deutsche Forschungsgemeinschaft SPP 1153

Small magnetic nanoparticles are of interest for magnetic recording and other nanoelectronic and nanomagnetic applications. In order for small particles to display intrinsic ferromagnetism, they must either possess large magnetic anisotropy or be kept at very low temperatures (below their Curie temperature).

Surprisingly high Curie temperatures have been reported with ferromagnetic iron nanoclusters (with diameters of 2.4 – 3.7 nm) prepared on Cu(111) using buffered layer growth techniques [1]. In these experiments, the clusters also display a strong magnetic anisotropy, with the hard axis along the surface normal.

In order to investigate these claims, mass selected $\text{Fe}_{105\pm 2}$ was produced by laser vaporization of an iron target and deposited onto a Cu(111) surface at low temperatures (100 K) and small kinetic energies ($\ll 1$ eV/atom). The copper surface was prepared by a series of sputtering and annealing cycles until a sharp LEED pattern showed high surface quality. A coverage of $1.5(5) \times 10^4$ clusters/ μm^2 was achieved. X-ray magnetic circular dichroism (XMCD) and X-ray absorption (XAS) spectra recorded using the PM-3 beamline at the BESSY-II synchrotron by using the sample drain current (total electron yield) under x-ray illumination. XMCD curves were measured, as sensitive probes of magnetization, in applied magnetic fields of up to 2 T, at both normal incidence and 60° incidence with respect to the surface normal.

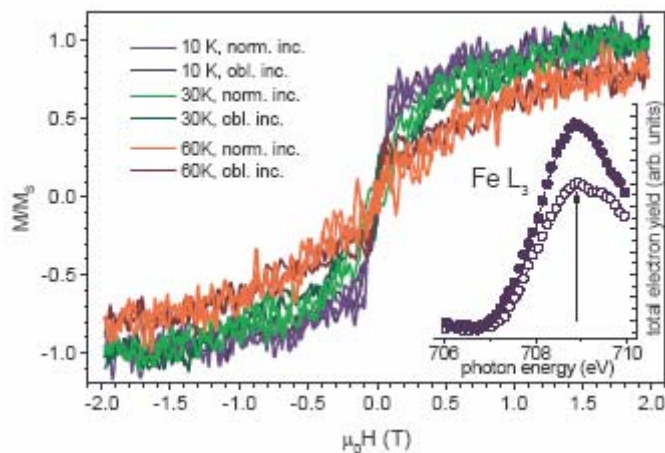


Fig. 1 Superparamagnetic XMCD magnetization curves, measured at normal and oblique (60°) incidence measured at temperatures of 10 K, 30 K and 60 K. The inset shows the Fe L_3 absorption spectra, measured at applied fields of ± 1 T at a 65 K temperature. Magnetization curves were measured at the photon energy where the largest difference (XMCD) is found between the two spectra (arrow).

The inset to Fig. 1 shows the Fe L_3 absorption curves measured at 65 K in applied fields of ± 1 T. This lineshape is characteristic of metallic Fe. All XMCD magnetization curves were measured at the point where the largest magnetic circular dichroism (arrow) is obtained.

Fig. 1 shows the magnetization curves of the $\text{Fe}_{105\pm 2}$ sample at temperatures of 10 K, 30 K and 60 K measured at both normal and oblique (60°) incidence. Clearly, all are superparamagnetic at all temperatures measured (remnant magnetization is not observed). The effect of temperature is clearly seen as the lower temperature curves have a much more sharp transition from a negative to positive magnetization state. Also, the measurements at normal and oblique incidence essentially fall on top of one another. Thus, we do not observe significant magnetic anisotropy (contrary to the claims of Pierce et al who find essentially zero out of plain magnetization at an applied magnetic field of 0.25 T). To further

substantiate our results, the experimental magnetization curves are fit to the model of classical Langevin paramagnetism to determine the magnetic moment per atom.

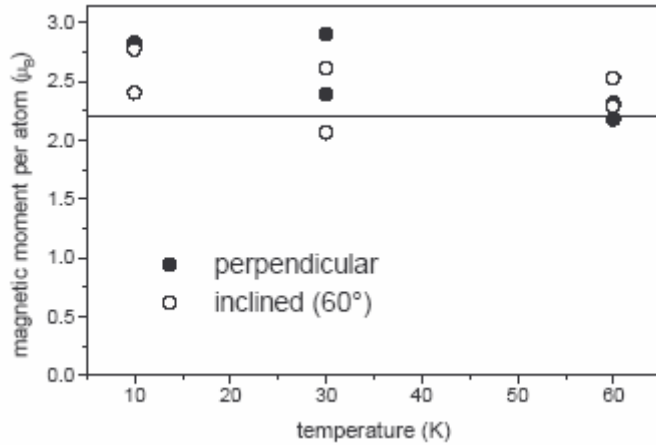


Fig 2. Magnetic moment per atom, as determined by least squares fit of the Langevin paramagnetic response. Full symbols correspond to out of plane (normal incidence) magnetization measurements and open symbols are taken at oblique incidence. The atomic moment of bulk bcc iron ($2.2 \mu_B$) is indicated by the horizontal line.

Fig. 2 shows the resulting total magnetic moments per atom of the clusters as a function of temperature, evaluated from the individual magnetization curves in Fig. 1. While there is some scatter in the experimental data, we see that atomic magnetic moments are consistently enhanced ($2.5 \pm 0.3 \mu_B$) with respect to the bulk limit ($2.2 \mu_B$), in particular at lower temperatures. This finding of enhanced magnetization in the clusters is consistent with observation of gas phase Fe clusters. Gas phase measurements yield even higher magnetic moments. Hybridization with the Cu(111) substrate has the effect of reducing the cluster magnetic moments compared to that of free particles.

We can estimate from the Pierce et al results a blocking temperature for our $Fe_{105 \pm 2}$ clusters of less than 3 K, if we assume that the effective Heisenberg Hamiltonian captures the indirect inter-particle exchange. Thus our finding of superparamagnetism is not at odds with their results. Since uniaxial magnetic anisotropy will be apparent if the anisotropy energy is on the same order as the thermal energy, we can state an upper bound to the anisotropy energy of 1 meV per cluster (or about $10 \mu eV$ per atom).

In conclusion, we find superparamagnetism in $Fe_{105 \pm 2}$ clusters deposited onto Cu(111) at temperatures as low as 10 K. This gives an intrinsic anisotropy energy smaller than 10^{-5} eV per atom. By Langevin analysis, we find an enhancement of magnetic moments by 10-20% from bulk iron. Experiments to compare magnetic clusters of similar sizes and densities and generated under various conditions are presently under development to further elucidate this aspect of nanomagnetism on surfaces.

[1] J.P. Pierce, M.A. Torija, Z. Gai, J. Shi, T.C. Schulthess, G.A. Farnan, J.F. Wendelken, E.W. Plummer, J. Shen, Phys. Rev. Lett. **92**, 237201 (2004)

Conversion of Functional Surface Groups on Aromatic Self-Assembled Monolayers on
UNCD by Soft X-Ray Radiation

Simon Quartus Lud^{*}, Peter Feulner[!], Jose Antonio Garrido Ariza^{*}, and Martin Stutzmann^{*}

^{*} Walter Schottky Institut, Technische Universität München, Am Coulombwall 3, 85748
Garching, Germany

[!] Physics Department E20, Technische Universität München, James-Franck-Strasse, 85748,
Garching, Germany

Diamond is considered an excellent electrode material for electrochemistry, with very low background current and the largest electrochemical potential window of all solids. Especially ultrananocrystalline diamond (UNCD) has received much attention for both biosensing applications and electron transfer investigations, since UNCD has the advantages of low production cost and the scalability to large area deposition. But the chemical modification of diamond or diamond-like surfaces remains difficult due to the almost inert nature of the substrate. In the last years aryl diazonium derivatives have recently attracted growing attention as promising candidates to functionalize diamond surfaces.

We investigate the reaction of 4'-nitro-1,1-biphenyl-4-diazonium tetrafluoroborate (NBD) and hydrogenated ultrananocrystalline diamond (UNCD) surfaces, which results in a homogeneous self-assembled monolayer of 4'-nitro-1,1-biphenyl (NB)¹. The proposed reaction is depicted in Figure 1a. NEXAFS experiments are suitable to investigate the presence of sp²-hybridized carbon on the modified diamond surface. All NEXAFS data were obtained at the U49-II-PGM-1 beamline. As depicted in Figure 1c (solid line), the NEXAFS spectrum of a NB-functionalized UNCD substrate shows unequivocally combined signals from both the grafted phenyl moiety and the diamond substrate. The strong peak (A') at 285 eV photon energy is assigned to the C1s→π* resonance, corresponding to sp² C-C bonds of the surface bonded biphenyl moieties, which is absent in the UNCD hydrogenated reference sample spectrum shown (dotted line). The peak of low intensity (B') at 288 eV can be attributed to C1s→Rydberg states or C1s→σ* transitions of C-H bonded carbon located on the phenyl rings of the biphenyl monolayer. Again, no corresponding feature can be detected for the non-modified surface. Spectral features at 292 eV (C') with several small peaks are

associated with the $C1s \rightarrow \sigma^*$ resonance of C-C bonds. Of high interest are especially alternative materials that allow the controlled modification of functional surfaces groups by a precisely adjustable parameter such as the irradiation dose. We have found that nitro groups on aromatic SAMs are selectively converted to amino groups under irradiation with X-rays (Figure 1b)². For the pristine NEXAFS spectra the X-ray beam was continuously moved over the samples throughout the data recording, for the purpose that, only non-irradiated parts of the diamond surfaces were illuminated and contributed to the spectra. For the investigation of the radiation induced conversion subsequent spectra were recorded by scanning the manipulator over an already scanned surface. Figure 1d represents a set of nitrogen K edge excitation spectra of the NB monolayer on UNCD. The soft X-ray synchrotron radiation (500 eV) gradually alters the intensity and ratio of the different resonances in N1s region with radiation time. Two low energy $N1s \rightarrow \sigma^*$ (N-H) resonances are observed at 398 eV (A'') and at 399 eV (B''). Increasing exposure increases the intensity of these two σ^* resonances, indicating the transformation process of the nitro group. The intensity of the two resonances at 404 eV (C'') and at 413 eV (D'') originating from the $N1s \rightarrow \pi^*$ (N-O) and $N1s \rightarrow \sigma^*$ (N-O) transitions decrease with longer irradiation times. Figure 1e shows the O1s NEXAFS of an irradiation sequence. The features A''' from the $O1s \rightarrow \pi^*$ (O=N) and B''' $O1s \rightarrow \sigma^*$ (O-N) transitions slightly diminish in intensity with increasing irradiation time, which is in accordance with the results found in the N1s region. Finally one can conclude that these NEXAFS studies showed that a major reaction pathway promoted by X-ray irradiation of surface grafted NB SAM involves the conversion of the functional nitro group to an amino group product on the surface.³

We thank S. Neppl, U. Bauer and the staff of BESSY, in particular O. Schwarzkopf, H. Pfau and W. Braun for help during the experiments. This work was supported by the German BMBF (05 ES3XBA/5) and by the Deutsche Forschungsgemeinschaft (Fe 346/1-3 and SFB 563 B15).

References

- (1) Stewart, M. P.; Maya, F.; Kosynkin, D. V.; Dirk, S. M.; Stapleton, J. J.; McGuinness, C. L.; Allara, D. L.; Tour, J. M., **Journal of the American Chemical Society** 2004, 126, (1), 370-378.
- (2) Eck, W.; Stadler, V.; Geyer, W.; Zharnikov, M.; Golzhauser, A.; Grunze, M., **Advanced Materials** 2000, 12, (11), 805-808.

(3) Lud, S. Q.; Steenackers, M.; Jordan, R.; Bruno, P.; Gruen, D. M.; Feulner, P.; Garrido, J. A.; Stutzmann, M., *Journal of the American Chemical Society* 2006, 128, (51), 16884-16891.

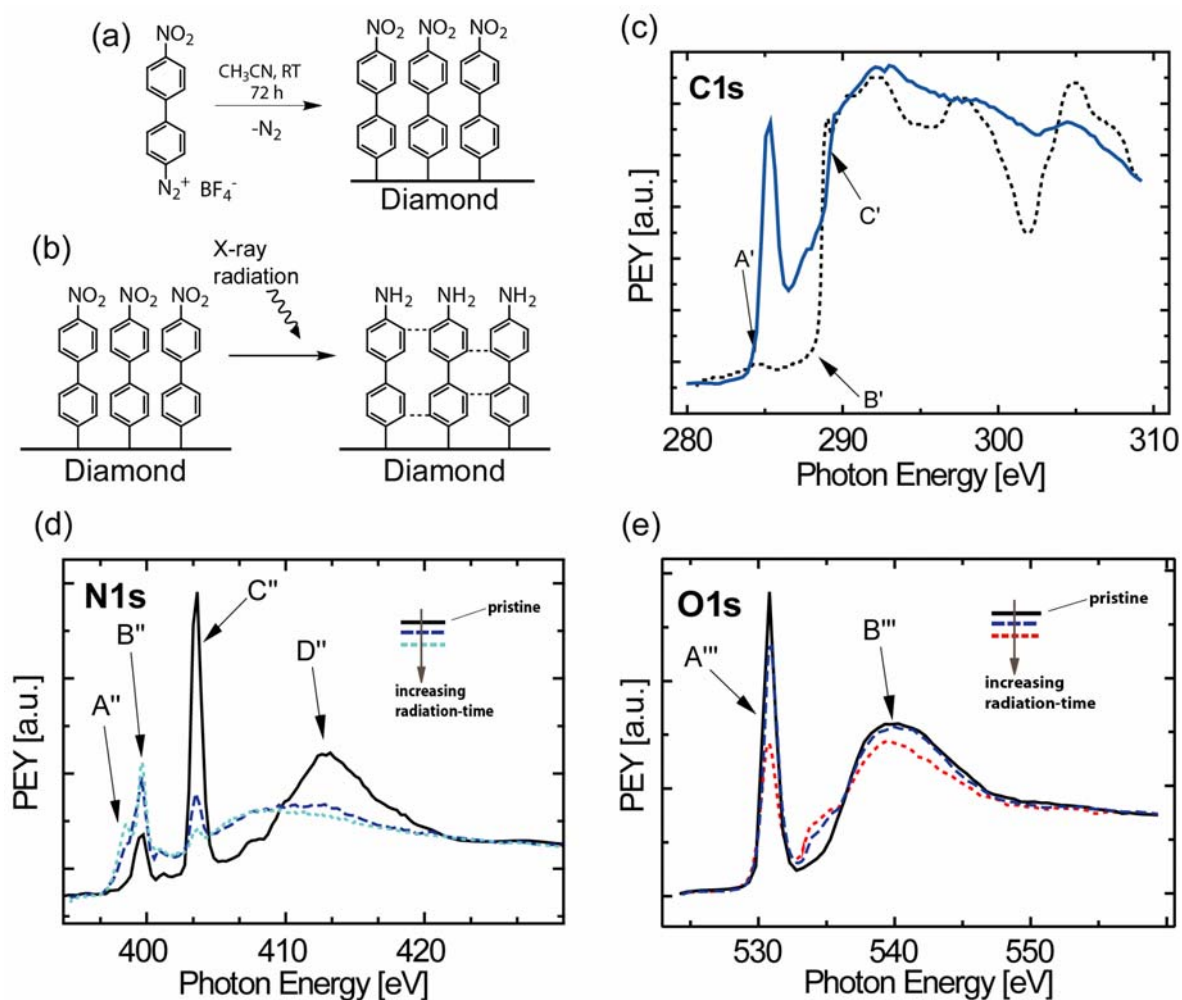


Fig. 1: (a) Reaction of the NBD with UNCD to form the SAM of NB. (b) Radiation induced conversion of the SAM of NB to the 4'-amino-1,1-biphenyl SAM. (c) Partial electron yield C1s NEXAFS spectra of a biphenyl grafted UNCD and a hydrogenated UNCD reference sample. (d) NEXAFS spectra recorded at the N1s edge of a biphenyl grafted UNCD. The subsequently recorded spectra show a radiation induced peak change of the σ^* and π^* resonances. (e) O1s NEXAFS spectra of a biphenyl grafted UNCD.

Following of Crystallization in a Levitated Droplet

Jork Leiterer¹, Franziska Emmerling¹, Wolfram Leitenberger², Andreas F. Thünemann¹ and Ulrich Panne¹

¹ Federal Institute for Materials Research and Testing, Richard-Willstaetter-Str. 11,12489 Berlin,

Germany

² University of Potsdam, 14469 Potsdam (Germany)

For the investigation of small sample volumes, the use of an acoustic levitator was tested as a ‘sample holder’ for hovering droplets in a synchrotron beam. It might be advantageous to use levitated droplets instead of samples confined in solid holders, especially for the study of crystallization processes where the influence of containing walls has to be minimized. These measurements indicate the possibility to investigate evaporation-induced crystallization with simultaneous observation of visible optical radiance. Acoustic levitation is a useful technique that can be applied without difficulty. Owing to its favourable properties, determinations of phase transformations, crystal structures and the physical properties of materials are no longer hampered by contamination from the sample container.

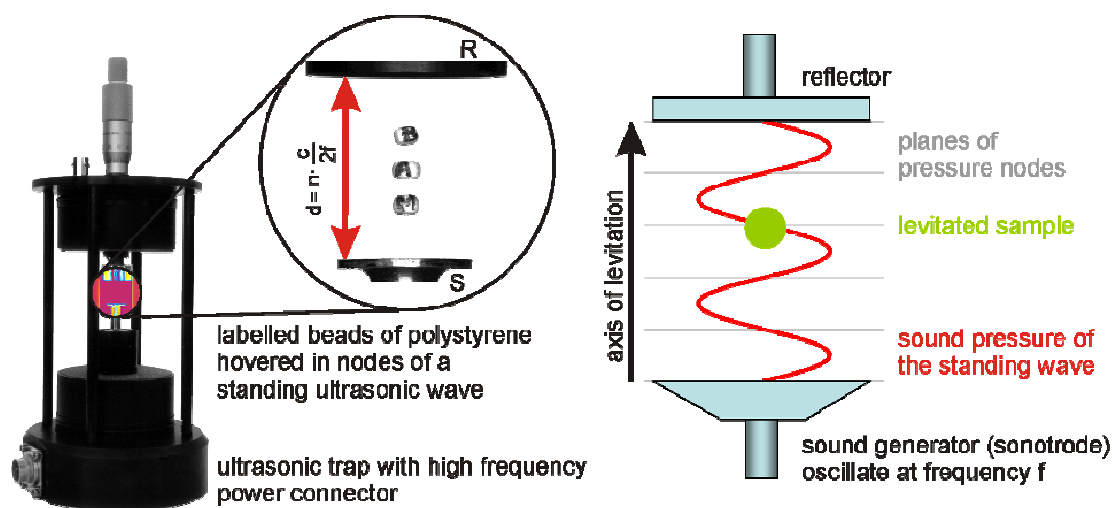


Figure 1. Setup and principle of the acoustic levitator in which sound level about 160 dB compensates for gravity

Experiments were carried out at the new BAM microfocus beamline¹ dedicated to scanning small (SAXS) and wide angle scattering (WAXS) and the EDR Beamline for energy-dispersive X-ray diffraction (EDXD)². In a first experiment, the crystallisation of sodium chloride in a small droplet of aqueous solution has been followed with a time resolution of 30 s. The collected diffraction peaks are compared with data in the ICSD database and the positions of the observed diffraction peaks agree with records from the ICSD database. Time resolved measurements at the BAM μ -Spot beamline in the second range can be obtained and additional information in the small angle range are available.

These measurements indicate the possibility to investigate evaporation-induced crystallization with simultaneous observation of visible optical radiance. Acoustic levitation is a useful technique that can be applied without difficulty. Owing to its favourable properties,

determinations of phase transformations, crystal structures and the physical properties of materials are no longer hampered by contamination from the sample container.

References:

- [1] O. Paris, C. Li, S. Siegel, G. Weseloh, F. Emmerling, H. Riesemeier, A. Erko, and P. Fratzl, *Journal of Applied Crystallography* **40** (2007).
- [2] U. Pietsch, J. Grenzer, T. Geue, F. Neissendorfer, G. Brezsesinski, C. Symietz, H. Möhwald, and W. Gudat, *Nuclear Instruments & Methods in Physics Research Section a-Accelerators Spectrometers Detectors and Associated Equipment* **467**, 1077-1080 (2001).
- [3] J. Leiterer, W. Leitenberger, F. Emmerling, A. F. Thünemann, and U. Panne, *Journal of Applied Crystallography* **39**, 771-773 (2006).

Molecular magnetism of metallo-supramolecular hierarchically ordered materials hosting mixtures of different transition metal ions

M. Lommel¹, U. Pietsch¹, G. Schwarz², D. G. Kurth², Y. Bodenthin³, W. Haase⁴, Z. Tomkowicz⁵

¹Institute of Physics, University of Siegen, Walter-Flex-Str. 3, 57078 Siegen, Germany

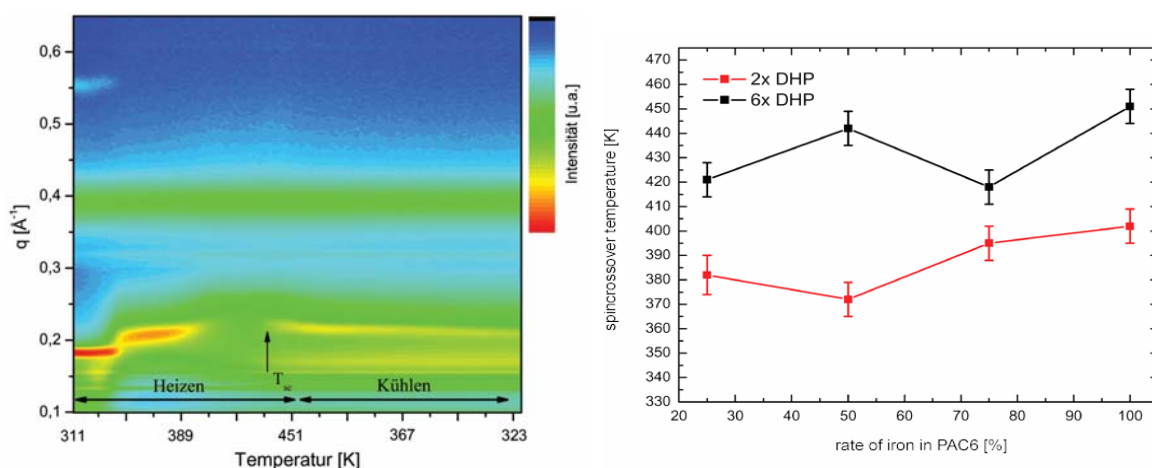
²Max Planck Institute of Colloids and Interfaces, 14424 Potsdam, Germany

³Swiss Light Source, Paul Scherrer Institute, CH-5232 Villigen PSI, Switzerland

⁴Institute of Physical Chemistry, Petersenstrasse 20, 64287 Darmstadt

⁵Institute of Physics, Jagellonian University, Reymonta 4, 30-059 Krakow, Poland

In contrast to the current paradigm in molecular magnetism to synthesizing molecules or clusters with large spins, the concept of designing supramolecular assemblies containing small magnetic units is flexible and tunable. An especially versatile approach relies on metallo-supramolecular polyelectrolyte amphiphile complexes self-assembled from bis-terpyridine ligands and amphiphilic molecules hosting octahedrally coordinated transition metal ions. Fe²⁺- and Co²⁺-ions can be induced to switch between a low-spin and a high-spin electronic state near room temperature, which is not possible for the Ni²⁺-ion. Using x-ray scattering, x-ray magnetic circular dichroism and magnetic measurements the spin transition of powdered materials has been identified as a transition from the S=0 (S = 1/2) low-spin state to the S=2 (S = 3/2) high-spin state of the Fe²⁺ (Co²⁺)-ions induced by a structural order-disorder transition of the amphiphilic matrix upon heating. The S=1 spin state of Ni²⁺ is not affected by the structural rearrangement. The temperature of the phase transition can be modified by the number and length of the amphiphiles attached to the polyelectrolyte backbone. In contrast to thin organized films the induced spin transition is not reversible but remains in the high-spin state, which might be stabilized by the disorder and interdigitation of amphiphilic molecules.



To explore the origin of the high-spin fraction we investigate the structure of PAC at the Energy Dispersive Reflectometer (EDR) at the BESSY II synchrotron. Small angle x-ray scattering (SAXS) patterns are collected as a function of temperature. The left figure summarizes the collected SAXS pattern for one heating and cooling cycle of the complex hosting 1:1 equivalents of Fe²⁺ and Ni²⁺-ions. The structural phase transition, indicated with T_{SC}, coincides with a spin crossover of the Fe²⁺- ions within the complex. The resulting new structural phase as well as the high spin state of the Fe²⁺-ions remains stable during cooling down to room temperature. On the right side, the evolution of the observed spin transition temperatures with increasing amount of Fe²⁺-ions within the complex. There is no linear dependency observed.

Acknowledgments: This work was supported by Deutsche Forschungsgemeinschaft as part of the priority program 1137 "Molecular Magnetism".

Native oxide, aging and magnetic properties of wet chemically prepared CoPt Nanoparticles

L.Glaser^a, M.Martins^a, C. Boeglin^c, V.Alesandrovic^b, H.Weller^b, W.Wurth^a

^aUniversität Hamburg, Department Physik, Luruper Chaussee 149, 22761 Hamburg

^bUniversität Hamburg, Department Chemie, Grindelallee 117, 20146 Hamburg

^cICPMS, GSI, 23, rue du Loess BP43, 67034 Strasbourg, France

Magnetic nano particles become of increased interest for applications. Especially in fields as magnetic storage devices, where grain sizes already reached the 10nm length scale, it is important that synthesis processes deliver a high output of equally sized and stoichiometric structured particles, as well as aging stability of the particle properties. Wet chemical processes have generally the advantage to evaporation or sputter processes, that the output is always macroscopic. However the nano-particles always come with organic ligands and native oxide outer layers. The chemists have by now overcome the obstacle of tailoring sizes. The sizes of the CoPt nano-particles measured by us were controlled with the hot organometallic synthesis. This method has two major advantages namely the freedom of choice of the organic ligands and the high reproducibility of particle size in different batches. The different sizes are controlled by the reaction temperature (Figure 1), allowing to tailor CoPt particles from 1.5nm up to 14nm in diameter, which is a broad range for wet-chemically synthesized nano particles. The entire synthesis process is discussed in detail in [1,2]. The

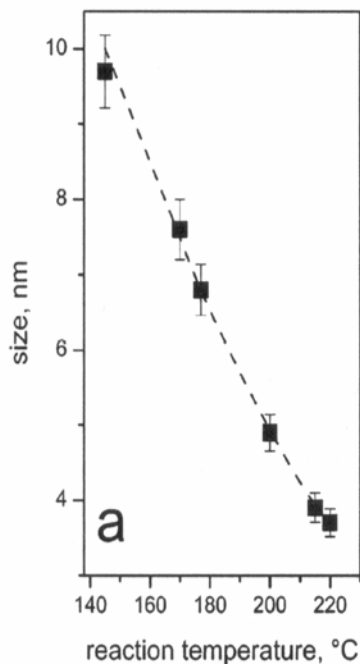


Figure 1: Temperature dependence of CoPt nano-particle synthesis[2]

The samples were produced in the institute of physical Chemistry in Hamburg. The Particles consist of a CoPt (decreasing with size from CoPt₃) core and an oxidized shell to which organic ligands are attached. Pictures taken with Scanning Electron Microscopy(SEM) and High resolution Transmission Electron Microscopy (TEM) have shown a sharp size distribution of 10% of the nano particles and a uniform crystallographic structure (GISAXS measurements have yet to be evaluated). There was no aging effects noticeable in TEM pictures of the same sample with time. During the preparation process and storage the reagents normally have contact with air and only the final synthesis process is under dry argon. To investigate the influence of the contact with air, we prepared and stored some samples completely in a nitrogen atmosphere. The entire synthesis process was carried out in a nitrogen pressurized glove box, as well as the cleaning of the silicon wafers with acetone and isopropanol, as well as spin coating with the diluted nano particle solution. A second goal of our measurements was to investigate whether or not there are aging effects measurable in the nano-particles, especially in respect to the magnetic properties. To do so we synthesized particles at different times before the measurement, the referred age in days in this report is the age of the sample after synthesis. All samples were measured with SEM before the measurement at the synchrotron, to ensure similar coverages. Some SEM pictures taken after the beamtime revealed that the organic seem not to suffer any damage under synchrotron radiation. We measured the total electron yield at the Co L_{2,3} – edge, keeping the constant external magnetic field parallel to the incoming light.

Switching the polarity of the light we measured spectra for X-ray magnetic circular dichroism (XMCD). Despite the different preparations at air and under nitrogen, the absorption spectra of equally sized nano particles show no distinguishable differences in their line shapes of the Cobalt L_3 edge, a measure of the oxidation state of the nano particle (Figure 2). Therefore the native oxidation can not be reduced by the nitrogen atmosphere during the synthesis process and storage.

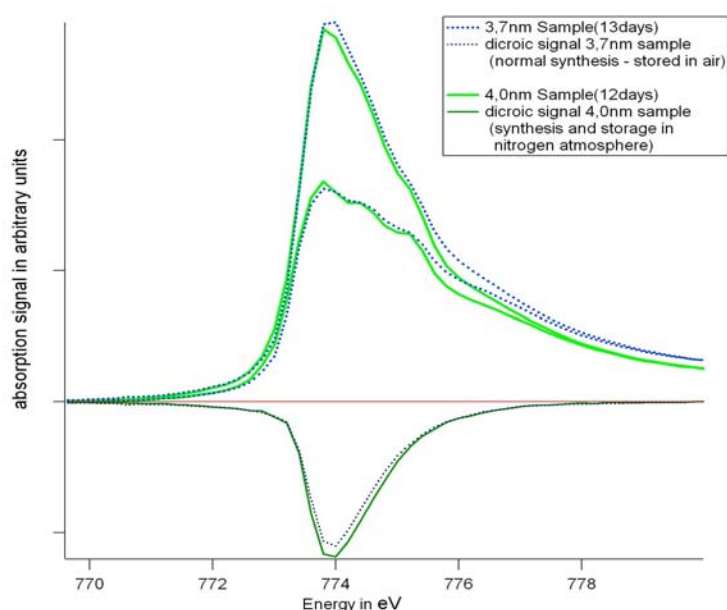


Figure 2: L_3 -edge absorption spectra and dichroic signals of a 3.7nm CoPt sample prepared and stored normally with contact to air and a 4.0nm CoPt sample synthesized and stored under nitrogen atmosphere until measurement

The oxidation of the particles increase with the time since synthesis, as it has been observed with other Co nano-particles, where it is reported that the oxide shell thickens with time up to 2.5nm[3,4]. However even particles of the same age differ in their native oxidation state [5]. The larger the particles are, the stronger they are oxidized. This correlates with the change in stoichiometric ratio of Co to Pt from 1:3 to 1:1 with the particle size. Having similar native oxide shells, the oxidized Cobalt detected in the adsorption spectrum scales with the stoichiometric probability of Cobalt to be in the outer shell, since the escape probability of the secondary electrons decreases from the surface towards the center of the particle.

Using the XMCD sum rules an increase of magnetic orbital to spin moment with increasing oxidation was detected[5]. This is expected since the ratio of CoO is about thrice of that of pure Co. This already shows that the magnetic properties of the material changes with time, but even further time dependence was detectable. Measuring the same 7.6nm particle sample at the age of 53 and 210 days, the oxidation remained the same. However an increase of the orbital to spin magnetic moment (Figure 3) from 0.14 to 0.16 with age is detectable. There are two aging effects, one that simply shows an increase of oxide in the absorption spectrum and a second that only reduces the orbital magnetic moment.

Acknowledgements

We are grateful for the support of the staff of beamline UE46 and UE56/2 of Bessy II and for the many valuable discussions with P.Imperia. This work has been financially supported by the German Ministry of Education and Research through grant 05 KS4 GUB/6.

References

- [1] E.Shevchenko et al, JACS 124 (2002) 11480-11485
- [2] E.Shevchenko et al, JACS 125 (2002) 9090-9101
- [3] Wiedwald et al, PRB 68 (2003) 064424
- [4] Wiedwald et al, ChemPhysChem 6 (2005) 2522-2526
- [5] L.Glaser et al, in preparation

In-situ X-ray diffraction during physisorption of dibromomethane in ordered mesoporous silica

Susanne Jähnert¹, Gerald A. Zickler², Oskar Paris² and Gerald H. Findenegg¹

¹Stranski Laboratory of Physical and Theoretical Chemistry, Technical University Berlin

²Department of Biomaterials, Max Planck Institute of Colloids and Interfaces, Potsdam

The physisorption and capillary condensation of an organic fluid in a periodic mesoporous silica material (SBA-15) was investigated by *in-situ* synchrotron small-angle diffraction. This work forms part of a longer-term study aiming at (i) a detailed characterisation of the pore structure of ordered mesoporous materials and (ii) elucidation of the different stages of pore filling during physisorption of vapours. SBA-15 is a silica powder in which the individual particles constitute a two-dimensional (2D) hexagonal array of cylindrical mesopores of uniform size embedded in an otherwise amorphous microporous silica matrix. In our study, powder small-angle diffraction patterns resulting from the regular packing of the cylindrical mesopores in SBA-15 are collected *in situ* as a function of vapour pressure of the fluid. A specially designed sorption cell housed in a thermostated specimen chamber (aluminium) (Fig.1) and connected with a gas dosing system with gas pressure sensors was developed for these studies. It allows step-by-step pressure changes or a continuous adsorption or desorption of the fluid [1]. The cell is temperature-controlled by Peltier devices for measurements from 260 K to ambient temperature. The cell windows are sealed with Kapton foil. The experimental parameters (pressure and temperature) are controlled and recorded by computer software.

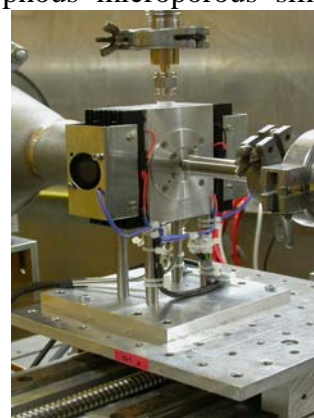


Fig.1. sample cell

SBA-15 silica was synthesized according to the procedure described by Zhao *et al.* [2]. The calcined material was characterized by nitrogen adsorption at 77 K and SAXD. The pore radius was derived from the nitrogen adsorption isotherm by means of the nonlocal density functional theory (DFT) [3]. SBA-15 powder was compacted to a stable pellet of 0.3 mm thickness and 3 mm diameter and placed into the sorption chamber. Fig. 2 shows the adsorption isotherm of dibromomethane (CH_2Br_2) in the SBA-15 material and SAXD curves for a series of gas pressures along the isotherm. Due to the similar electron densities of the silica matrix ($6.5 \times 10^{23} \text{ cm}^{-3}$) and liquid CH_2Br_2 ($6.75 \times 10^{23} \text{ cm}^{-3}$), this organic fluid is particularly well-suited to elucidate the sequence of stages of pore filling of the matrix. SAXD curves were measured *in-situ* at a series of gas pressures during continuous adsorption and desorption of the fluid (Fig. 2b).

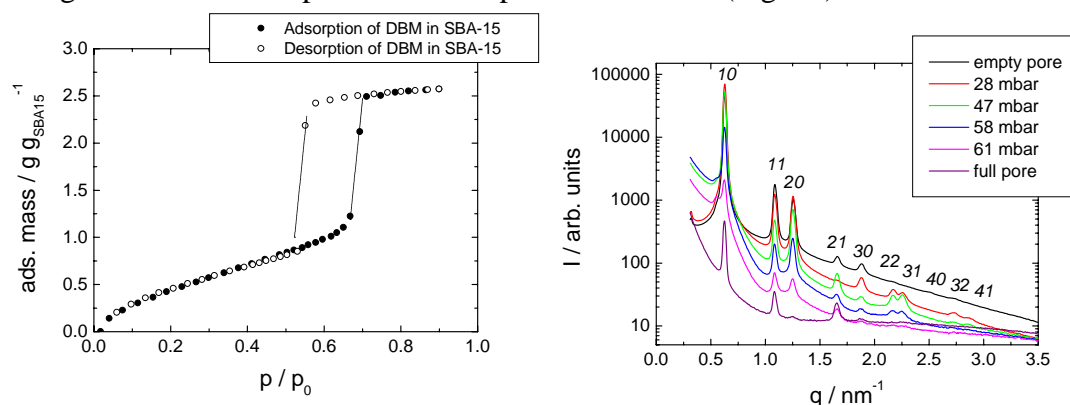


Fig. 2. Adsorption of dibromomethane in SBA-15: (a) sorption isotherm; (b) SAXD curves.

$a_s / \text{m}^2\text{g}^{-1}$	$v_p / \text{cm}^3\text{g}^{-1}$	$2R_{\text{DFT}} / \text{nm}$	a / nm	
SBA-15	800	1.04	8.1 ± 0.1	11.64

Characterization of SBA-15: a_s : specific surface area; v_p : specific pore volume; R_{DFT} : pore radius; a : lattice parameter of the 2D hexagonal pore lattice

In Fig. 2b, the powder diffraction peaks result from the 2D hexagonal packing of the cylindrical pores. Using synchrotron radiation at the BESSY μ -Spot beamline, ten diffraction peaks and the systematic changes of their intensity with the gas pressure can be resolved. The integrated intensities of the diffraction peaks are analyzed with a structural model of a core-shell cylinder with four density levels (ρ_0 to ρ_3) as shown in Fig.3 [1]. This model, which represents an extension of a model proposed for the pore structure of SBA-15 [4], provides quantitative information about the pore structure of the evacuated sample, the filling of the microporous corona (C), and the growing thickness of the liquid film (L) in the mesopores as the gas pressure is increased.

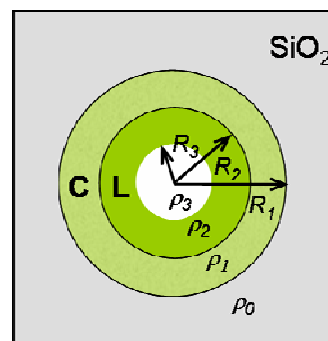


Fig. 3. Four-density-level model of SBA-15 silica.
C: microporous corona
L: adsorbed fluid film

From the integrated intensities of the diffraction peaks for the evacuated sample we derive a pore radius R_2 of 4.05 nm, in very good agreement with the pore radius R_{DFT} resulting from the nitrogen adsorption isotherm. Furthermore, we find a corona thickness $R_1 - R_2$ of 1.1 nm and a corona porosity P_c of nearly 40%. The parameters R_1 , R_2 and P_c are kept fixed in the subsequent data analysis. Gradual pore filling with the fluid is reflected in a gradual increase of the corona density ρ_3 (due to the filling of the corona) and the formation and growth of a liquid-like film of thickness $d = R_2 - R_3$ at the pore walls. From these parameters one can calculate the amount of fluid adsorbed in the cylindrical pores and their corona as a function of the gas pressure. However, it is found that the amount of adsorbed fluid calculated on the basis of this model is considerably smaller than the amount obtained by direct gravimetric adsorption measurements, or from *in-situ* X-ray transmission measurements [5]. This implies that a significant amount of the fluid must be adsorbed in disordered regions of the sample. A preliminary analysis of the diffuse small-angle scattering from the sample and its dependence on gas pressure supports this conjecture. We are planning to modify our structural model by allowing microporosity of the matrix outside the corona to account for these observations.

Acknowledgements: We wish to thank C. Li, S. Siegel and G. Weseloh for help and advice at the μ -Spot beamline. This work has been supported by the Deutsche Forschungsgemeinschaft in the framework of Sfb 448 "Mesoscopically Organized Composites".

- [1] G.A. Zickler, S. Jähnert, W. Wagermaier, S.S. Funari, G.H. Findenegg, and O. Paris *Phys. Rev. B* **73**, 184109 (2006).
- [2] D. Zhao, J. Feng, Q. Huo, N. Melosh, G. H. Fredrickson, B. F. Chmelka, and G. D. Stucky, *Science* **279**, 548 (1998).
- [3] P. I. Ravikovitch and A. V. Neimark, *J. Phys. Chem. B* **105**, 6817 (2001)
- [4] M. Impérator-Clerc, P. Davidson, and A. Davidson, *J. Am. Chem. Soc.* **122**, 11925 (2000).
- [5] G.A. Zickler, S. Jähnert, S.S. Funari, G.H. Findenegg, and O. Paris *J. Appl. Cryst.* **40**, in press (2007).

Hydrogen in germanates as high-pressure models of mantle silicates?

S.-M. Thomas, M. Koch-Müller

GeoForschungszentrum Potsdam, Telegrafenberg, 14473 Potsdam

There is considerable evidence from experiments that significant volumes of water may be stored in the Earth's mantle, either stoichiometrically bound in hydrous compounds, e.g. in dense hydrous magnesium silicates (e.g. superhydrous phase B, ringwoodite), or as hydroxyl point defects in nominally anhydrous minerals (e.g. olivine). The presence of dense hydrous magnesium silicates in the Earth's mantle could play a major role for a potential deep water cycle. Beyond this, experiments have also shown that even major mantle constituents that by their formulae do not contain any hydrogen, e.g. olivine and pyroxene are able to dissolve water in trace amounts. Due to the large volume of rock in the Earth's mantle, even such trace concentrations are sufficient to form a substantial water reservoir that would seriously influence the Earth's geodynamical processes as well as its water cycle. Even trace amounts of hydrogen have a major effect on physical mineral properties such as electrical conductivity and deformation strength. To understand those effects, it is crucial to know how hydrogen behaves at the atomic scale within the host phases.

To study mantle silicates, germanates have been extensively used as low-pressure analogues, applying the close crystal chemical relationship to the corresponding silicon compounds due to similar outer electron structures and ionic radii of tetravalent silicon and germanium ions [1]. Recent computer simulations of OH-defects in Ge-ringwoodite suggest to use germanium phases as models to understand the hydrogen incorporation in the high pressure silicates [2]. But experimentally up to now only dry Ge-anhydrous phase B (Ge-anhB) [3] and Ge-ringwoodite containing a few wt ppm water [4] could be synthesized as high-pressure models of the aforementioned silicates. Obtained data provided useful facts on structure, crystal chemistry, phase transformations, pT-stabilities, etc., however, specific hydrogen incorporation mechanisms in those phases remain unclear.

To get a more detailed insight in the system $\text{MgO-SiO}_2\text{-H}_2\text{O}$, feasible water concentrations and possible hydrogen incorporation mechanisms in mantle silicates as well as to verify the use of germanium models in studies of water-related defects and their effects on physical properties, our present work is focused on hydrogen incorporation in germanium equivalents.

Experiments were made in a piston-cylinder apparatus at 2 GPa and 950 and 1000°C with up to 23 wt% water. We synthesized the Ge-analogues of ringwoodite, anhydrous phase B and for the first time Ge-superhydrous phase B (Ge-shyB). Recovered single crystals were investigated by X-ray diffraction (XRD), electron microprobe (EMP), infrared (IR) and Raman spectroscopy as well as transmission electron microscopy.

Single crystal XRD of the samples confirmed the space groups as observed for the corresponding silicon phases but with slightly larger lattice parameters due to the presence of germanium. EMP analysis yielded the chemical formulas $\text{Mg}_{9.97}\text{Ge}_{3.01}\text{O}_{14}(\text{OH})_4$ (Ge-shyB) and $\text{Mg}_{13.89}\text{Ge}_{5.06}\text{O}_{24}$ (Ge-anhB), the latter indicating, that vacancies either at the Mg or the Ge sites, or both, exist. Single crystal IR spectra, taken in the spectral region 3000-4000 cm^{-1} , revealed the presence of hydroxyl point defects in Ge-ringwoodite, Ge-shyB and even in Ge-anhB (Fig. 1), whose silicon form is known to be absolutely dry. Our results indicate, that water content and hydrogen incorporation mechanism in Ge-shyB are identical to the Si-phase [5], but both, the water concentration and the OH incorporation mechanism of the nominally anhydrous phases Ge-anhB and Ge-ringwoodite differ significantly from the results obtained on the Si-phases. Water contents in Ge-anhB and Ge-ringwoodite were determined by polarized IR spectroscopy using the calibration of [6] to be about 0.5 wt% H_2O and 0.2 wt% H_2O , respectively. Polarized IR spectra of Ge-anhB were obtained using synchrotron radiation

(Fig. 1). Due to its high brilliance and a smaller beam diameter, compared to a conventional light source, it was possible to measure even 30 to 50 μm sized single crystals. The synchrotron beam was additionally used to study the OH distribution in the samples with a local resolution of $15 \times 15 \mu\text{m}$. The resulting chemical maps indicated no heterogeneities and thus verified the homogeneous distribution of hydrogen in the crystal lattice.

On the basis of our data we suggest new models for the OH incorporation in Ge-anhydrous phase B and Ge-ringwoodite. We propose two hydroxyl point defects for Ge-anhydrous phase B. The first defect (Fig. 2) is introduced into the structure by the hydrogarnet substitution – a vacant Ge2 tetrahedron with four OH groups, which give rise to three vibrations ν_1 , ν_2 , ν_3 and ν_3b . The second defect (Fig. 3) is most probably associated with the substitution of Mg1 by Ge^{4+} and two OH groups at the adjacent vacant Ge2 tetrahedron causing the vibrations ν_1 and ν_4 . The bands ν_1 , ν_2 , ν_3a , ν_3b and ν_4 can be explained by the vibration of dipoles O3-H1, O1-H2, O8-H3 and O8-H4, respectively (Fig. 1, 2, 3). The corresponding OH distances were estimated from the observed band positions using the correlation of OH stretching frequencies and O-H...O distances given in [7]. The proposed hydrogen positions match the structure very well. O3-H1 dipoles are involved in both defects, which reflects the high intensity of the associated vibration in the IR spectra (Fig. 1, 2, 3).

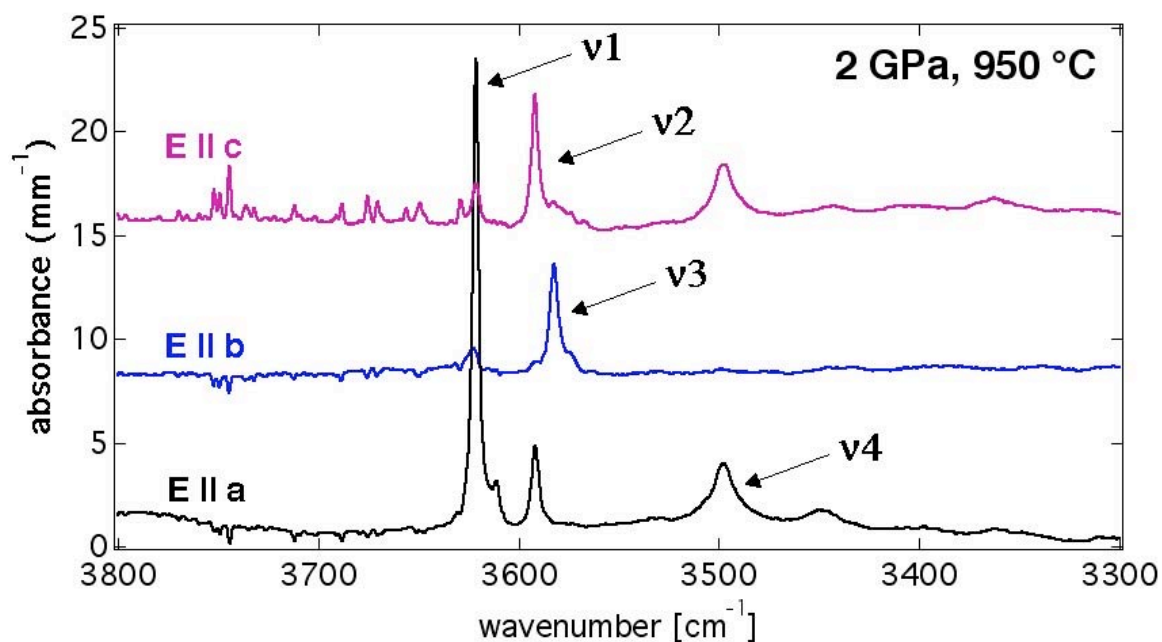


Fig. 1 Polarized IR spectra of Ge-anhB with E parallel to a, b and c pointing out the strong pleochroitic behavior of the OH-bands.

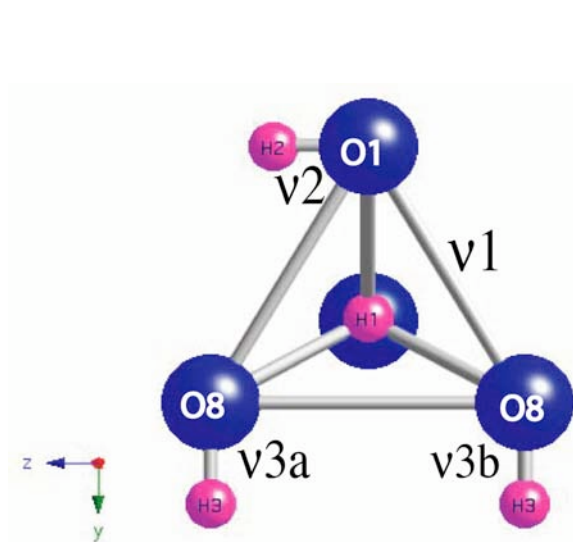


Fig. 2 Projection of a part of the structure of Ge-anhydrous phase B parallel (100) showing defect 2.

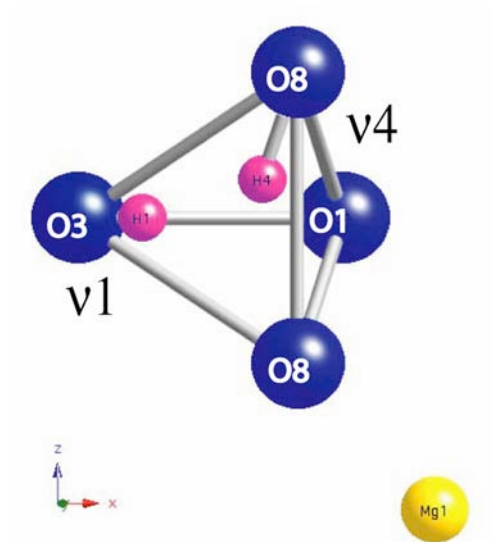


Fig. 3 Projection of a part of the structure of Ge-anhydrous phase B parallel (010) showing defect 2.

Our results on Ge-superhydrous phase B show its identical behavior in comparison to the Si-phase [5] and thus support suggestions to use Ge-analogues as silicate high-pressure models for hydrous phases. In contrast, water incorporation in the Ge-analogues of nominally anhydrous phases deviates significantly from the behavior of the Si-phases and is apparently governed by other factors like water fugacity, therewith pressure as well as intrinsic defects in their structures.

References

- [1] Ringwood, A. E. (1975): Composition and Petrology of the Earth's mantle, *Mc-Graw-Hill International Series in the Earth & Planetary Sciences*, New York, 618 p.
- [2] Blanchard, M., Wright, K., Gale, J.D. (2005): A computer simulation study of OH defects in Mg_2SiO_4 and Mg_2GeO_4 spinels. *Physics and Chemistry of Minerals*, 32, 585-593.
- [3] von Dreele, R. B., Bless, P. W., Kostiner, E., Hughes, R. E. (1970): The Crystal Structure of Magnesium Germanate: A Reformulation of Mg_4GeO_6 as $Mg_{28}Ge_{10}O_{48}$. *Journal of Solid State Chemistry*, 2, 612-618.
- [4] Hertweck, B., Ingrin, I. (2005): Hydrogen incorporation in a ringwoodite analogue: Mg_2GeO_4 spinel. *Mineralogical Magazine*, 69, 337-343.
- [5] Koch-Müller, M., Dera, P., Fei, Y., Hellwig, H., Liu, Z., Van Orman, J., Wirth, R. (2005): Polymorphic phase transition in Superhydrous Phase B. *Physics and Chemistry of Minerals*, 32, 349-361.
- [6] Libowitzky, E., Rossman, G. R. (1997): An IR absorption calibration for water in minerals. *American Mineralogist*, 82, 1111-1115.
- [7] Libowitzky, E. (1999): Correlation of O-H Stretching Frequencies and O-H...O Hydrogen Bond Lengths in Minerals. *Monatshefte für Chemie*, 130, 1047-1059.

OH-mapping of synthetic Enstatite-crystals

Elke Schlechter, Roland Stalder
Department of Geoscience, Göttingen University

Enstatite is the second most abundant mineral in Earth's upper mantle and is able to incorporate several tens ppm weight of hydrogen. The influence of hydrogen on the electrical conductivity of Earth's mantle is expected to be significant, but has so far not been investigated. Magnetotelluric measurements (electrical conductivity of Earth's deep interior) need systematic laboratory data on the influence of hydrogen on the electrical conductivity of mantle minerals for the interpretation of the data.

For this purpose, synthetic enstatite crystals of gem quality with cross section areas of about 1 - 2 mm² have been synthesized at the Department of Geosciences in Göttingen and have been checked for homogeneity applying an automatic X-Y-stage at the infrared beamline of BESSY II. Large homogenous crystals are necessary, because the electrical conductivity measurements require a minimum cross section area of about 500-2000 μm^2 for the mounting of the electrodes.

Hydrogen is incorporated in enstatite mostly in association with defect-forming cations, and forms hydroxyl molecules with oxygen atoms in the crystal lattice. Since the different mechanisms of hydrogen incorporation cause different absorption bands at several wavenumbers between 3000 and 3600 cm^{-1} , the infrared spectra give information about the spatial distribution of the different defect cations in the crystal. The enstatite crystals (chemical formula $\text{Mg}_2\text{Si}_2\text{O}_6$) contain a small amount of Fe^{2+} , Fe^{3+} and Al^{3+} . These cations participate in the formation of the abovementioned defects. An example for the graphical result of the mapping is shown in figure 1. Here, the peakheight at the wavenumber 3548 cm^{-1} has been measured systematically all over a partial area of an enstatite single-crystal. The size of the aperture was 400 μm^2 and the distance between the measuring points was 20 μm . The green area at the crystal rim do not indicate high absorbance but is a result of scattering of the IR-beam at the rough rim of the crystal. It is regarded as erroneous measurement. This is a common feature in our mappings of mm-size crystals with an irregular shape and affects only a narrow range at the rim of the crystals (some μm , see figure 1). Several of this mappings had been measured during the visit at BESSY II. Results from this hydrogen mappings clearly show that the distribution of the different mechanisms of hydrogen incorporation over the whole crystal can be regarded as homogeneous.

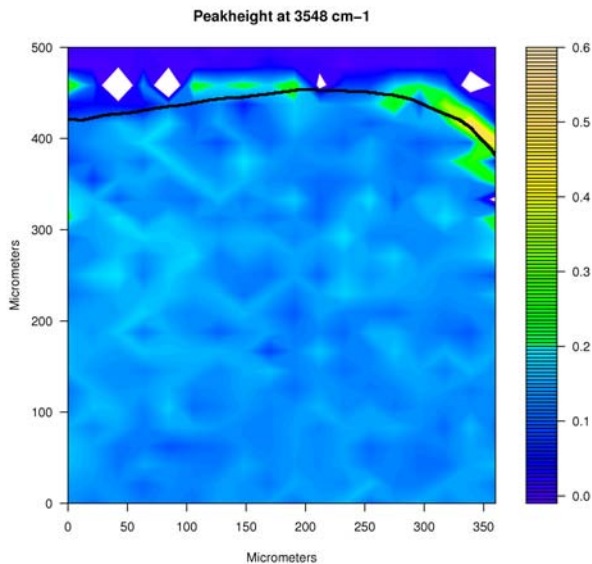


Figure 1: Mapping with respect to the peakheight at the wavenumber 3548 cm^{-1} , colors indicate the peakheight and the black line designates the crystal-rim

3D μ -SRXRF on monazite (CePO_4) for in-situ chemical dating

Schmitz, S.¹, Wilke, M.², Möller, A.², Bousquet, R.², Schefer, S.³, Malzer, W.⁴, Kanngießer, B.⁴

¹ JWG Universität Frankfurt M., Inst. f. Mineralogie, Germany, ² Universität Potsdam, Inst. f. Geowissenschaften, Germany, ³ Universität Basel, Geologisch-Paläontologisches Institut, Switzerland, ⁴ Technische Universität Berlin, Inst. f. Optik und Atomare Physik, Germany

Introduction

Monazite is an accessory LREE¹ Phosphate - mineral rich in U (≤ 5 wt. %) and especially Th (3 - 15wt. %). It is an ideal mineral for (chemical) dating of high temperature (HT) metamorphism in high-grade metasediments and granitic rocks [e.g. 1, 2] because the Th-Pb and U-Pb systems remain closed at high temperatures [3] and are therefore highly resistant to diffusive Pb loss.

The accuracy and precision of chemical age determination is dependent on the Pb concentration of the minerals and in the case of monazite the Pb content is assumed to be completely enriched by radioactive decay.

The use of *in-situ* chemical dating of especially young monazite has been restricted either by high detection limits (EMP² ca. 100 ppm) or low spatial resolution (μ -XRF ca. 150 μm). Here we propose the use of the 3D experimental set-up which was developed by Kanngießer et al. [4] at the μ -spot beamline at BESSY. This 3D set-up restricts the excitation volume and prevents the excitation of radiation from deeper parts of the sample which minimizes absorption effects and signals from other minerals.

The set-up was tested using several well-known reference samples of known age and was applied to monazites from high-temperature rocks (sapphirine-bearing granulites) from the Alps (Gruf Complex, N-Italy). The aim of the study was to gain a HT age for the sapphirine bearing granulites (granulitefacies event). Liati & Gebauer [5] reported SHRIMP³ zircon ages that are younger than or coeval with the Bergell Intrusion (BI; 30 - 32 Ma [6]), but concerning structural observations the age is assumed to be slightly older than the BI [7-9].

Experimental set-up, measurements and data reduction

The 3D μ -XRF set-up at the μ -spot beamline (7T WLS) is realized by a confocal arrangement of two polycapillary half lenses. The spot size is defined by overlapping of the foci (Fig. 1). The probing-volume can be moved along the surface of the sample and into the depth which allows a chemical insight of the sample [4].

Characterization of the probed volume was carried out with a thin W-foil that was moved through the micro-volume. The FWHM of the W intensity-curve is about 25 μm (at 18 keV).

For chemical dating, synchrotron X-ray fluorescence data were acquired for (1) isotopically well characterized reference samples (compositions and ages), (2) "internal" comparative reference samples dated by other verified methods and (3) monazite samples of unknown age from the Gruf Complex in the western

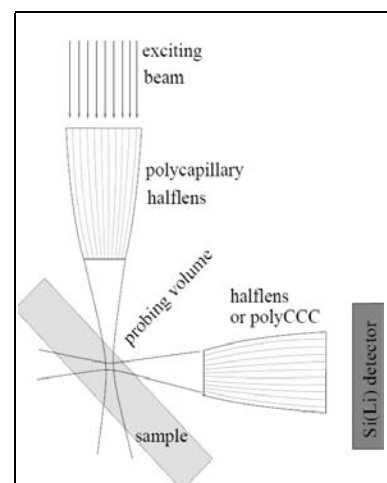


figure 1: confocal set-up with defined probing volume; [10]

¹ LREE – Light Rare Earth Elements

² EMP – Electron MicroProbe

³ SHRIMP – Sensitive High Resolution Ion MicroProbe

Alps. The 4 reference samples (number of measurement = 59) were measured for 500 – 1000 sec (depending on their age and Pb content) and the unknown samples (N = 18) for 1000 sec (including 10 % dead time).

Data reduction is based on the method of Engi et al. [11] who used the fluorescence lines Pb L_α, Th L₁ and U L₁. The intensities of the fluorescence peaks were determined at the beamline using a fitting program developed by Malzer et al. (unpubl.).

Three isotopically dated (e.g. by SHRIMP, ID-TIMS⁴) and chemically well characterized monazite reference samples and one “internal” comparative standard with ages between ~100 Ma and 1821 ± 0.6 Ma covering a wide range of U - Th - Pb compositions were used to calibrate the parameters of Ranchin’s formula [12].

$$Age = \frac{7550 k_{Pb} A_{Pb}}{k_U A_U + 0.36 k_{Th} A_{Th}}$$

with *k*: empirical parameters, *A*: peak areas, intensities of the elements

The values of the coefficient *k*_{Pb}, *k*_{Th} and *k*_U can be obtained with the help of the reference samples and are used later for age calculation of the unknowns. The values depend on the analytical conditions and differ between different minerals.

Analytical techniques

The reference standards are separated and polished grains that are placed in epoxy. The unknown monazites were measured in-situ within rock thin sections (with textural context) on glass holders. To avoid detecting signals of underlying minerals (in thin sections), we used half of the incoming counts instead the entire count rate, placing only half the excitation volume inside the analysed grains. This depth calibration had to be performed for each analysis.

Results

Fig. 2 shows a monazite XRF spectrum with the Pb, Th and U triplet which was used for the calculations.

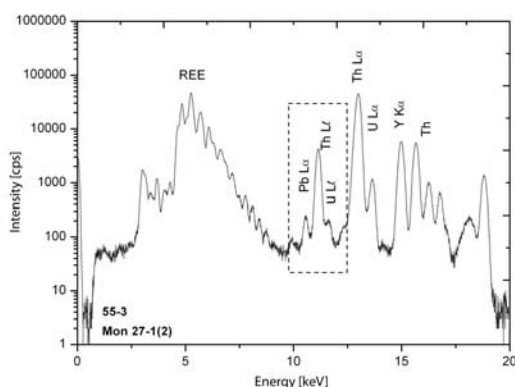


figure 2: monazite energy dispersive (EDS) spectrum for a 1000 sec measurement

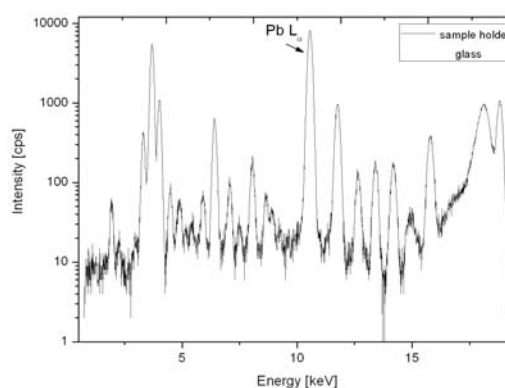


figure 3: XRF spectrum of the glass slide underneath the rock thin sections shows a strong Pb signal at 10.55 keV which would influence the monazite results in a non-confocal experimental set-up or if the radius of the excitation volume would be bigger than the thickness of the rock section.

⁴ ID-TIMS – Isotope Dilution Thermal Ionization MassSpectrometer

The age reproducibility of each single point is within 5 - 10% of the isotopic results, the average values have errors of 1 – 4 %. The difference between SRXRF method and reference methods is shown in tab. 1. The good reproducibility indicates that the Ranchin parameter can be used to determine the ages of the unknown monazites because the age of the younger reference sample (JUNCA) can be reproduced within 4 Ma. The relative minimum detection limit (MDL_{rel.}) was calculated for the reference samples F6 and 3345 (T=500 sec) and is below 10 ppm for Pb, allowing the determination of ages as young as ca. 10 Ma. The absolute DLs for a volume with d = 25 µm are in the pg range (MDL_{abs.}: Pb 50 ± 0.9 pg, Th 39 ± 20 pg, U 440 ± 6 pg).

Chemical U-Th-Pb ages obtained for the unknown monazites cover a range of 41 - 86 Ma, with the older dates interpreted as relics from protoliths, prograde remnants or artefacts by excess of common or radiogenic Pb. The large variation of these values might be explained with a strong Pb signal (Fig. 3) from the sample holder beneath the minerals which might influence the assumed low concentration of Pb in the sample and creates older ages. The youngest dates, clustering at 41 - 43 Ma, are interpreted to be the age of the HT event of the Gruf Complex because these grains are inclusions in HT-minerals. Concerning further analysis one should use sample holder which contain no Pb (or below DL?) to avoid contamination of the Pb signal.

Table 1: comparison of data obtained by the BESSY 3D µ-SRXRF set-up with reference methods (N = total number of points)

	Age reference (Ma)	SRXRF mean age ± 1s (Ma)	N	Δ
GM3	483.2 ± 1.5	470.8 ± 23.4	14	-12
F6	560 ± 1	569.8 ± 16.3	23	+10
3345	1821 ± 0.6	1834 ± 76	11	+13
JUNCA	100	104.3 ± 6.1	8	+4

Conclusion

Age determination with 3D µ-SRXRF shows much better results compared to EMP (DL for Pb > 100 ppm) or even conventional µ-XRF (~ 10 ppm MDL_{rel.}) and allows detection of much younger ages, making the technique useful for studies of recent mountain belts, such as the Alps, Andes and Himalayas. The spatial resolution is lower than EMP methods (~ 5 µm), but better than conventional µ-XRF (where only whole grain analysis is possible) and comparable to Laser-ICP/MS and ion microprobe.

For further analysis we plan to use Pb-free SiO₂ glass for sample holders and younger reference samples are required for the calibration.

- [1] F. Finger, I. Broska, M.P. Roberts & A. Schermaier: *Am Mineral* **83** (1998) 248-258.
- [2] G. Foster, P. Kinny, D. Vance, C. Prince & N. Harris: *EPSL* **181** (2000) 327-340.
- [3] R.R. Parrish: *Can J Earth Sci* **27** (1990) 1431-1450.
- [4] B. Kanngießer, W. Malzer & I. Reiche: *Nucl Instr and Meth B* **211** (2003) 259–264.
- [5] A. Liati & D. Gebauer: *Schweiz Mineral Petrogr Mitt* **83** (2003) 159-172.
- [6] F. von Blanckenburg: *Chem Geol* **100** (1992) 19-40.
- [7] R. Staub: *Beitr Geol Karte CH N.F.* **103** (1958).
- [8] C. Davidson, C. Rosenberg & S.M. Schmid: *Tectonophysics* **265** (1996) 213-238.
- [9] A. Berger, C. Rosenberg & S.M. Schmid: *Schweiz Mineral Petrogr Mitt* **76** (1996) 357-382.
- [10] W. Malzer: *The Rigaku Journal* **23** (2006) 40-47.
- [11] M. Engi, A. Cheburkin & V. Köppel: *Chem Geol* **191** (2002) 225-241.
- [12] G. Ranchin: *Sci Terre* **13** (1968) 161-205.

Study of samples from environmental and life science using the STXM at U41

G. Mitrea¹, J. Thieme¹, E. Novakova¹, S.-C. Gleber¹, P. Guttmann², S. Heim³

¹Institut für Röntgenphysik, Georg-August-Universität Göttingen,
Friedrich-Hund-Platz 1, D-37077 Göttingen

²Institut für Röntgenphysik, Georg-August-Universität Göttingen,
c/o BESSY GmbH, Albert-Einstein-Str. 15, 12489 Berlin

³BESSY GmbH, Albert-Einstein-Str. 15, 12489 Berlin

Introduction

Samples of chernozem and lipid bilayers have been studied using the Scanning Transmission X-ray Microscope (STXM) at BESSY II. The STXM provides a combination of high spatial resolution (60 nm) and spectral resolution ($E/\Delta E=1700$) for investigation of wet and dry samples. Chemical state mapping at the Carbon edge could be used to study the interactions between soil clay minerals and soil organic matter [1]. The elemental mapping of Carbon in the biological sample helps to study the morphology of the artificial lipid membrane-colloid composites and subsequently, the interactions between proteins and membranes. Spectra have been extracted from image stacks to obtain information about the chemical state. For the analysis of the latter, principal component analysis and cluster analysis have been applied. It was possible, for example, to discriminate clay particles from organic components.

Materials and Methods

An otherwise well characterized chernozem soil from an area close to Göttingen [2] has been taken as a first sample to demonstrate the performance of the STXM. Some general characteristics of this chernozem are homogeneity and alkalinity ($\text{pH} = 8.2 - 8.4$). The chemical composition of this soil shows a high organic content (4.1 %). A 1 % dispersion of chernozem has been made in deionized water. Thus, large associations of soil colloids fall apart, while small clusters of colloids in the range accessible to x-ray microscopy stay intact. A small quantity of approx. 50 μl of this dispersion has been placed on a 100 nm thick Si_3N_4 -membrane, and let dry. As a result, small clusters of soil colloids will be found on the membrane.

The second type of sample investigated with the STXM was lipid bilayers of DPPC/DPPS. Lipid bilayers are important as cell boundaries and are inherently complex forms of soft matter. Planar bilayer systems can serve as simple models for the much more complex biological counterparts. In our STXM experiment, colloidal particles (400nm latex microspheres) took the role of inclusions or adsorbed particles, which can in future be replaced by proteins specifically tagged by colloidal markers. We have prepared anionic lipids mixed with neutral lipids by vesicle fusion on 100 nm thin Si_3N_4 - foil. Then colloidal particles had been added and a second Si_3N_4 -foil was used to seal the wet sample chamber. STXM images have been taken below and above the K-absorption edge of Carbon.

The STXM has been described in detail elsewhere [3]. With this instrument the absorption of x-rays as they pass through the specimen is measured. By tuning the energy of the monochromator below and above the K-absorption edge of Carbon, and by subsequently dividing the resulting images, the distribution of that element within the sample can be mapped (see Figure 1).

The STXM can also be used for acquiring point spectra of samples by tuning

undulator and monochromator synchronously and recording on the detector the transmitted intensity as a function of energy (see Figure 2).

Another method which provides spectral and spatial information is to take a stack of images of the sample at many closely spaced energies (see Figure 3) [4]. In this way, not only an image of the sample is obtained for each energy but also a spectrum over the entire energy range can be extracted for each pixel.

Results

In Figure 1, images of an aqueous sample of unsaturated lipids DPPC/DPPS(4:1) and 400nm latex spheres have been taken at $E = 284$ eV (left) and $E = 314$ eV (middle) and the Carbon map has been created by division (right).

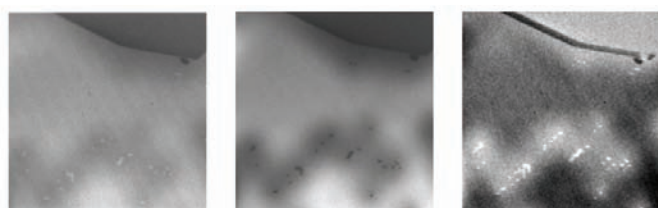


Figure 1: Aqueous sample of unsaturated lipids DPPC/DPPS (4:1) and 400nm latex spheres. Image size $40 \times 40 \mu\text{m}^2$, $200 \times 200 \text{ pixel}^2$, dwell time 6ms/pixel.

Figure 2 shows the NEXAFS spectrum of a 130 nm thick polyimide foil. The π^* resonances of the C-C, C-N and C=O bonds are clearly identified and in good agreement with literature values.

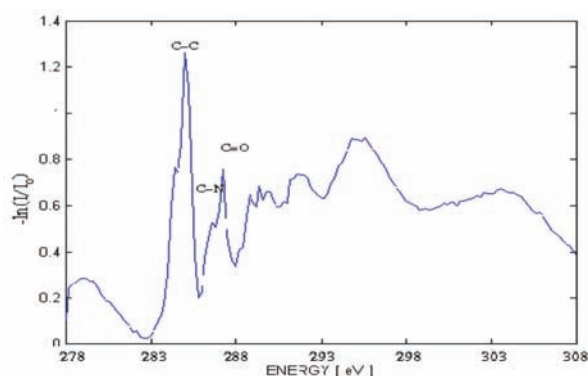


Figure 2: NEXAFS-spectrum of a polyimide foil. Plotted is the optical density $-\ln(I/I_0)$ as a function of energy. I is the transmitted x-ray intensity through the sample, and I_0 is the incident x-ray intensity.

Figure 3 shows some of a stack of images of the chernozem sample, taken around the K absorption edge of Carbon within the energy range 283-308 eV and with an energy step of 0.5 eV.

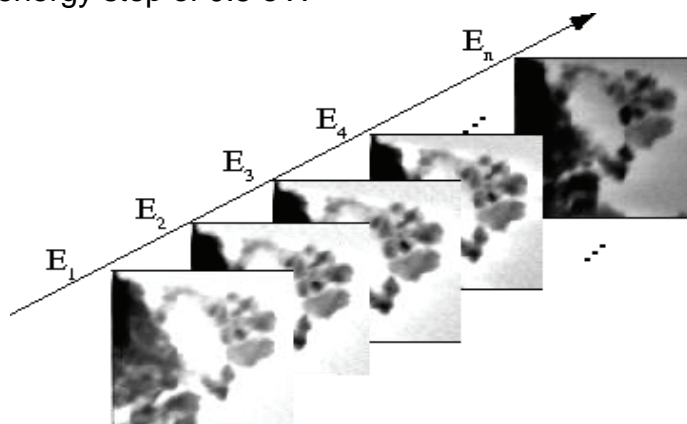


Figure 3: Some of a stack of images at closely spaced energies ($\Delta E = 0.5$ eV), showing colloidal structures within a chernozem soil. Image size $10 \times 10 \mu\text{m}^2$, $100 \times 100 \text{ pixel}^2$, dwell time 10 ms/pixel.

Three different analyzing methods can be applied to data sets obtained with the

STXM. Gaussian fitting can be used to identify functional groups in the sample. The principal component analysis reduces and noise-filters the data and the cluster analysis provides representative spectra and corresponding images [5]. As an example for results derived by the latter method, in figure 4 (left) the presence of Potassium as an indication for clay minerals in our specimen of figure 3 is clearly evidenced by the two absorption edges L_{III} and L_{II} . The organic components in the sample are spatially and spectrally separated as well.

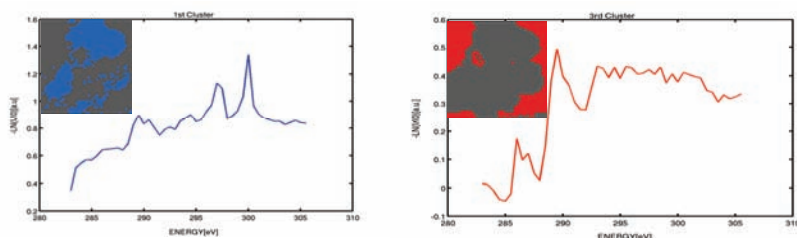


Figure 4: Applying cluster analysis to the stack of images seen in Figure 3 results in maps of the spatial distribution of Potassium indicating clay particles and of organics.

Outlook

Improvements will be made on the instrumental side as well as on the analytical side. The replacement of the monochromator will result in a higher monochromaticity and a better stability. Experiments at the K absorption edge of Nitrogen and Oxygen will be done using a Helium environment for the sample stage to avoid absorption by air.

Acknowledgements

This work has been funded by BMBF under contract number 05KS4MGB/7 and under contract number 02WU9893/0. We want to thank the staff of BESSY for excellent working conditions.

References

- [1] G.Mitrea, J.Thieme, P.Guttman, S.Heim, S.-C.Gleber: X-ray spectromicroscopy of soil colloids with the scanning transmission x-ray microscope at BESSY II, submitted.
- [2] C. Ahl, H.-G. Frede, S. Gäth, B. Meyer: Böden aus Löss. *Mitteilgn. Dtsch. Bodenkundl. Gesellsch.* 42 (1985) 359-434.
- [3] U. Wiesemann, J. Thieme, P. Guttman, R. Früke, S. Rehbein, B. Niemann, D. Rudolph, and G. Schmah: First results of the new scanning transmission X-ray microscope at BESSY-II. In: J. Susini, D. Joyeux, F. Polack, eds., *X-Ray Microscopy 2002*, *Journal de Physique IV* 104 (2003) 95–98.
- [4] C. Jacobsen, G. Flynn, S. Wirick, and C. Zimba: Soft x-ray spectroscopy from image sequences with sub-100 nm spatial resolution. *Journal of Microscopy* 197, no. 2, (2000) 173-184.
- [5] M. Lerotic, C. Jacobsen, J.B. Gillow, A.J. Francis, S. Wirick, S. Vogt and J. Maser: Cluster analysis in soft X-ray spectromicroscopy: finding the patterns in complex specimens. *Journal of Electron Spectroscopy and Related Phenomena* 144-147C (2005) 1137-1143.

Angle-resolved soft x-ray emission spectroscopy (SXES) for depth profiling of thin film systems

I. Lauermann⁽¹⁾, H. Mönig^(1,2), Ch. Camus⁽¹⁾, A. Grimm⁽¹⁾, S. Sokoll⁽¹⁾,
T. Kropp⁽¹⁾, Ch. Jung⁽³⁾, M. Ch. Lux-Steiner^(1,2), and Ch.-H. Fischer^(1,2)

⁽¹⁾Solarenergieforschung (SE 2), Hahn-Meitner-Institut, 14109 Berlin, Germany

⁽²⁾Freie Universität Berlin, 14195 Berlin, Germany

⁽³⁾BESSY GmbH, 12489 Berlin, Germany

Depending on the elemental composition of a material, SXES provides an information depth of 50 to 1000 nm. For studies of thin multilayer structures a tuning of this parameter is highly desirable. One possibility is the variation of the excitation energy, which is accompanied by a variation of the photoionisation cross sections. To avoid that, angle resolved SXES can be used to vary the information depth [1]. We are especially interested in chalcopyrite thin film solar cells, which are composed of multi-layer stacks with a typical structure of n^+ -ZnO/i-ZnO/buffer/Cu(In,Ga)(S,Se)₂/Mo/glass with layer thicknesses of several tens of nanometers up to several micrometers.

Model system Cu(In,Ga)Se₂/Zn(S,O)

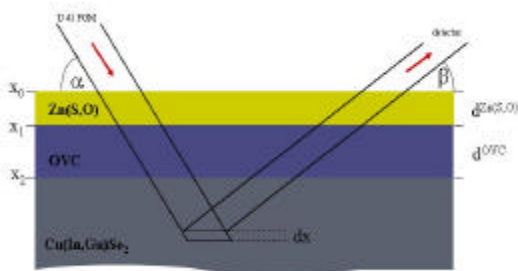


Figure 1: Layer structure used for modeling

To study the angle dependence in detail, we focused on the buffer material Zn(S,O) deposited on the chalcopyrite absorber Cu(In,Ga)Se₂ (“CIGSe”).

In Figure 1, the assumed layer structure used for the model is shown. It includes a Cu-poor surface region in the absorber (Ordered Vacancy Compound OVC [2]). SXES measurements on these samples were made in the CISSY end station using a Scienta Gammadata XES-300 spectrometer at the BESSY U 41 PGM Beamline with an excitation energy of 1200 eV. In the 3D color map in Figure 2, Cu, Zn and Ga emission lines at different exit angles β are shown. The spectra clearly display increased surface sensitivity at small (grazing exit) and at large exit angles (grazing incidence) which is due to the fact that the detector is fixed in a position perpendicular to the incoming beam.

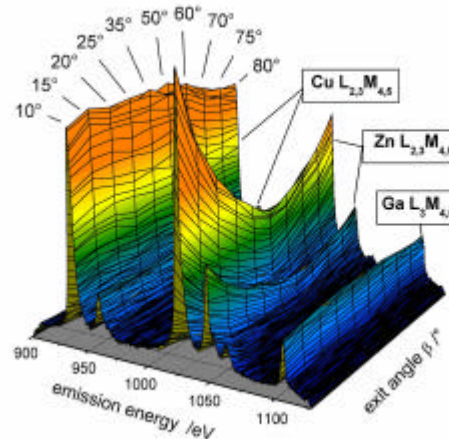


Figure 2: Cu, Zn and Ga emission lines at different exit angles β .

The mathematical relation

$$\frac{I_{1011}^{Zn}}{I_{930}^{Cu}} \propto \frac{\int_{x_0}^{x_1} e^{-x \left(\frac{1}{a_{att1200}^{Zn(S,O)} \sin a} + \frac{1}{a_{att1012}^{Zn(S,O)} \sin b} \right)} dx}{e^{-a^{Zn(S,O)} \left(\frac{1}{a_{att1200}^{Zn(S,O)} \sin a} + \frac{1}{a_{att930}^{Zn(S,O)} \sin b} \right)} \cdot \left[\int_{x_1}^{x_2} e^{-x \left(\frac{1}{a_{att1200}^{OVC} \sin a} + \frac{1}{a_{att930}^{OVC} \sin b} \right)} dx + e^{-a^{OVC} \left(\frac{1}{a_{att1200}^{OVC} \sin a} + \frac{1}{a_{att930}^{OVC} \sin b} \right)} \cdot \int_{x_2}^{\infty} e^{-x \left(\frac{1}{a_{att1200}^{ClGSe} \sin a} + \frac{1}{a_{att930}^{ClGSe} \sin b} \right)} dx \right]$$

describes a simple model based on Beer-Lamberts law and the geometry of our setup (SXES- spectrometer orthogonal to synchrotron beam, compare Figure 1). Based on x-ray fluorescence (XRF) measurements we considered a slightly modified stoichiometry of $\text{CuIn}_{0.72}\text{Ga}_{0.43}\text{Se}_{2.22}$ for the base layer of the absorber. Figure 3 displays both the experimental intensity ratio $\text{Zn } L_3M_{4,5} / \text{Cu } L_3M_{4,5}$ as a function of the emission angle β and the fit based on our model, which is in reasonable agreement with the data.

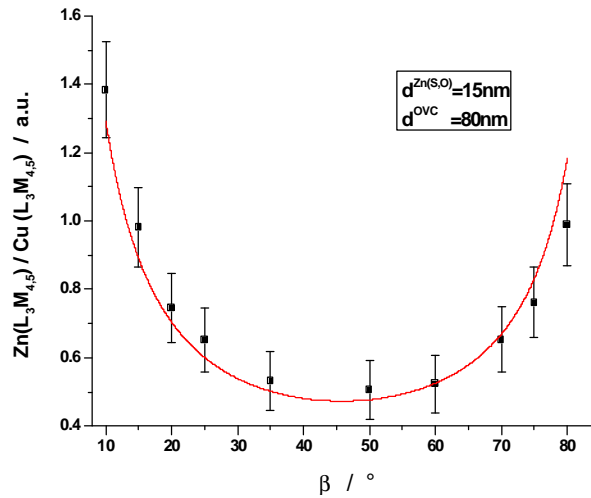


Figure 3: Intensity ratio $\text{Zn } L_3M_{4,5} / \text{Cu } L_3M_{4,5}$ as a function of β (black) and the fit (red) based on our model

References

1. Gålnander, B.; Käämbre, T.; Blomquist, P.; Nilsson, E.; Guo, J.; Rubensson, J.-E.; Nordgren, J., *Thin Solid Films* 343-344, 35-38, (1999).
2. Lehmann, S.; Bär, M.; Fuertes Marrón, D., Pistor, P.; Wiesner, S.; Rusu, M.; Kötschau, I.; Laueremann, I.; Grimm, A.; Sokoll, S.; Fischer, Ch.-H.; Schedel-Niedrig, T.; Lux-Steiner, M.Ch.; Jung, CH., *Thin Solid Films* 511-512, 623-627, (2006).

In-situ monitoring of the beam-induced corrosion of chalcopyrite surfaces in air by soft x-ray emission spectroscopy

I. Lauermann⁽¹⁾, H. Mönig^(1,2), S. Lehmann⁽¹⁾, A. Grimm⁽¹⁾, S. Sokoll⁽¹⁾, T. Kropp⁽¹⁾,
Ch. Jung⁽³⁾, M. Ch. Lux-Steiner^(1,2), and Ch.-H. Fischer^(1,2)

⁽¹⁾Solarenergieforschung (SE 2), Hahn-Meitner-Institut, 14109 Berlin, Germany

⁽²⁾Freie Universität Berlin, 14195 Berlin, Germany

⁽³⁾BESSY GmbH, 12489 Berlin, Germany

Chalcopyrite (“CIGSSe”) thin film solar cells with a typical layer structure n^+ -ZnO/i-ZnO/CdS/Cu(In,Ga)(S,Se)₂/Mo/glass are promising candidates for future low-cost, high efficiency power conversion devices [1]. Some functional materials in chalcopyrite thin film solar cells, e.g., buffer layers like CdS, are usually deposited wet-chemically. However, the exact mechanisms of material formation, inter-diffusion, and possible chemical changes of the absorber are often unknown. *In-situ* analysis is necessary to answer some of these questions. Therefore, we developed a UHV-compatible flow-through cell for in-situ soft x-ray emission spectroscopy (SXES) at liquid/solid or gaseous/solid interfaces. The set-up of the flow-through cell was shown in the BESSY annual report for 2005. A crucial part of the flow-through cell is the Si₃N₄ window with a membrane, which is only 100 nm thick (supplied by Silson Ltd, England). Yet it has to withstand a pressure difference of around 1000 mbar between the inside of the flow-cell (which is under ambient pressure) and the UHV in the analysis chamber. Therefore it was chosen to be as small as possible, i.e. the dimensions are 0.5 x 1 mm².

For two reasons the single membrane used so far has been unsatisfactory: First, prolonged irradiation of the membrane leads to its eventual rupture, which results in venting the UHV chamber. Secondly, a single, small membrane allows the analysis of only a single, small spot on the sample, which is also susceptible to irradiation damage. Therefore we designed a Si₃N₄ window with four 100 nm thick, 0.5 x 1 mm² membranes. This window is shown in Figure 1. Using this window we could, for the first time, detect a S L_{2,3} XES signal from a CIGSSe sample inside the wet cell in air. This spectrum is shown in Figure 2 together with a spectrum from the same sample obtained in UHV and a sulfate reference spectrum from a powder sample.

While in UHV a typical sulfide spectrum was recorded, the spectrum from the air-exposed sample shows emission lines typical of sulfate and hardly any sulfide signal. The signal to noise ratio of the spectrum recorded through the wet-cell window is much lower than that of the

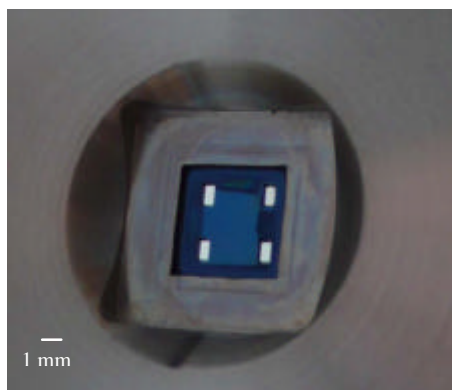


Figure 1: Detail of the wet cell window with four 100 nm membranes

UHV-sample due to absorption from the window. The acquisition time for this spectrum was 40 minutes. Furthermore, the energy resolution is poor as compared to the reference spectrum, because the spectrometer entrance slit had to be fully opened to increase the signal intensity.

Nevertheless, the spectrum gives clear evidence that a S L_{2,3} XES spectrum can be obtained even through a Si₃N₄ membrane with a rather strong absorption in this energy range. Furthermore, the fact that sulfate is detected rather than the expected sulfide, shows that even in air chalcopyrite surfaces suffer severe radiation damage when irradiated using a beam energy of 200 eV. The mechanism of this beam damage remains unknown but most likely the

presence of water vapour in the ambient air gives rise to photoelectrochemical reactions at the surface, leading to superficial oxidation. Similar reactions had been observed at irradiated chalcopyrite surfaces immersed in aqueous solutions [2] and at hydroxide-containing interfaces, e.g. ZnO/CIGSSe [3]. However, even direct oxidation by oxygen cannot be excluded, so future experiments will utilize different gas mixtures to shed light on this process. Sacrificial compounds such as alcohols will be added to liquid electrolytes used in the wet cell to avoid photoelectrochemical corrosion.

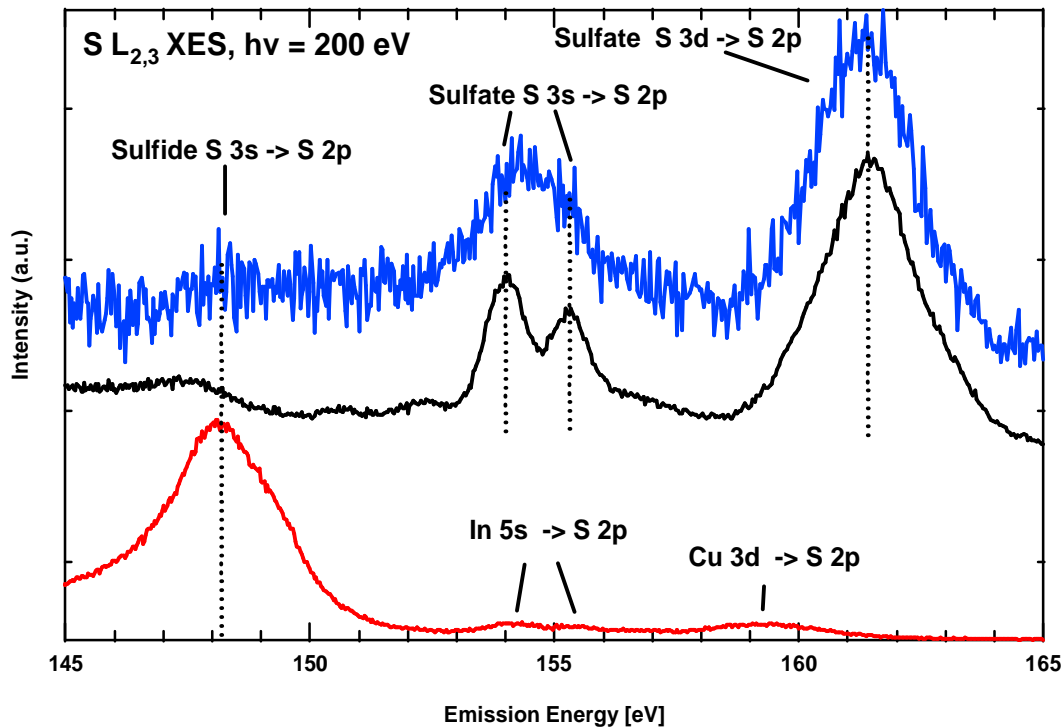


Figure 2: $S L_{2,3}$ spectra of CIGSSe in the wet cell in air (upper spectrum, blue) through 100 nm Si_3N_4 and in vacuum (lower spectrum, red). A sulfate spectrum is shown as reference (middle spectrum, black). Transitions leading to the observed peaks are denoted using the subshell with the main contribution to the valence band

References

1. Contreras, M.; Ramanathan, K.; AbuShama, J.; Hasoon, F.; Young, D. L.; Egaas, B.; and Noufi, R.; Prog. Photovolt: Res. Appl.; 13:209–216 (2005).
2. Heske, C., Groh, U., Fuchs, O., Weinhardt, L., Umbach, E., Schedel-Niedrig, T., Fischer, C.-H., Lux-Steiner, M. C., Zweigart, S., Niesen, T. P., Karg, F., Denlinger, J. D., Rude, B., Andrus, C., and Powell, F., J. Chem. Phys., 119(20), 10467 (2003).
3. Reichardt, J.; Bär, M.; Grimm, A.; Kötschau, I.; Lauer mann, I.; Sokoll, S.; Lux-Steiner, M. C.; Fischer, Ch.-H.; Heske, C.; Weinhardt, L.; Fuchs, O.; Jung, Ch.; Gudat, W.; Niesen, T. P., and Karg, F., Appl. Phys. Lett. 86, 172102 (2005).

SXPS at the Solid-Liquid Interface of Dye Sensitized Solar Cells

Schwanitz Konrad, Mankel Eric, Hunger Ralf, Mayer Thomas, and Jaegermann Wolfram

Darmstadt University of Technology, Material- and Geo-Science Institute

mayerth@surface.tu-darmstadt.de

Funded by DFG, Grant Number JA 859/3-3.

At BESSY we run the experimental station SoLiAS, dedicated to solid-liquid interface analysis. SoLiAS allows for the transfer of wet chemically prepared surfaces to the ultra high vacuum without contact to ambient air. In addition in situ (co)adsorption of volatile solvent species onto liquid nitrogen cooled samples is possible. SoLiAS proves to be very useful in analyzing the chemical and electronic structure of solid-liquid interfaces e.g. of dye sensitized solar cells. A monolayer of Ru(N3)-dye was adsorbed from ethanol solution under clean N₂ atmosphere in an UHV-integrated electrochemical cell (EC). Acetonitrile or benzene were adsorbed from the liquid in the EC or in situ from the gas phase. Ex situ sintered nanocrystalline anatase substrates as well as in situ deposited polycrystalline TiO₂ samples were used. Distinct reversible changes occur in synchrotron induced photoelectron valence band and core level spectra when the solvent is adsorbed to pristine and dye covered TiO₂ substrates. Based on the experimental results the alignment of electronic states ^[1] and a model on the dye-solvent interaction have been deduced ^[2].

The valence band maximum of nc-TiO₂ is found at $E_B = 3.6$ eV binding energy while the fundamental gap is 3.2 eV only. Surface gap states related to Ti³⁺3d¹ orbitals are found with a maximum at $E_B = 1.3$ eV and in addition just below the Fermi level. In the rigid band model these states are assigned to occupied conduction band states but may be due to substoichiometric TiO_{2-x}. Adsorption of acetonitrile is accompanied by quenching of the surface gap states (Fig. 1). This finding is confirmed in Ti2p core orbital spectra by the quenching of the Ti³⁺ low binding energy shoulder of the Ti⁴⁺ bulk emission. Coadsorption of acetonitrile (Fig. 2) shifts the dye HOMO by 150 meV from 2.0 eV binding energy to 2.15 eV.

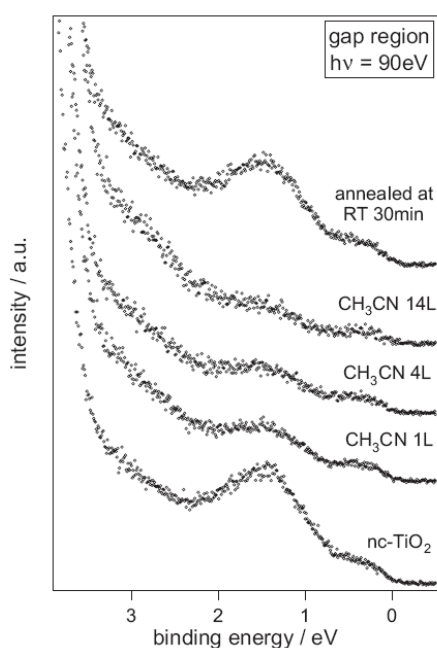


Fig. 1: Intensity normalized (O2p valence band) SXPS spectra of the gap states of nanocrystalline anatase TiO₂ in the course of acetonitrile adsorption and desorption.

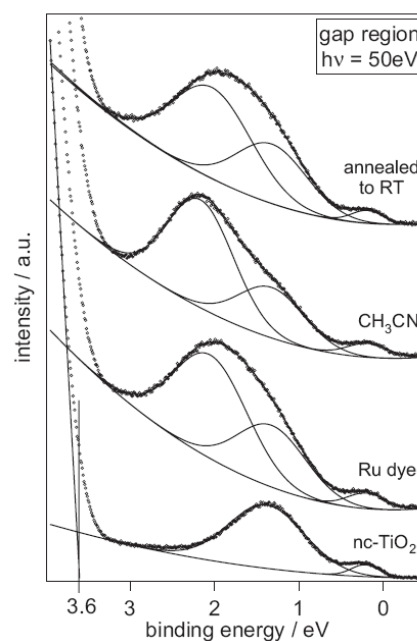


Fig. 2: SXPS spectra of the gap states of nanocrystalline anatase TiO₂ in the course of Ru(N3)-dye adsorption and acetonitrile coadsorption and desorption.

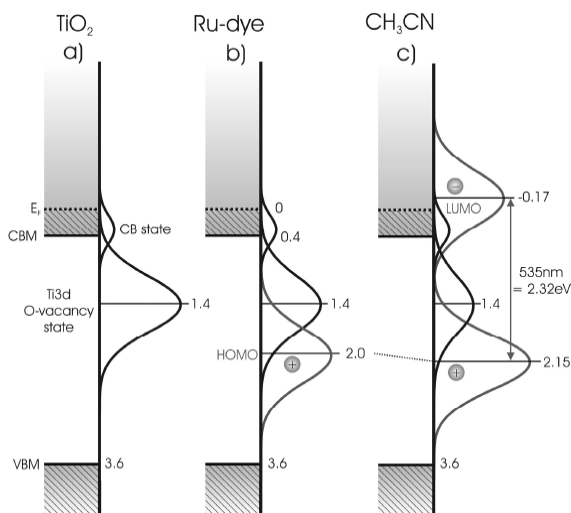


Fig. 3: Schematic of the photovoltaic-relevant valence states in the rigid band model a) the as prepared nanocrystalline TiO₂ anatase film, b) after dye adsorption from ethanol solution with HOMO position, c) after coadsorption of the solvent acetonitrile with the HOMO shifted by 150meV to higher E_B. Using the optical absorption maximum the LUMO is found 0.17 eV above the Fermi level.

A schematic representation of the photovoltaic-relevant valence states as deduced in the simple rigid band model is displayed in Fig.3. The measured HOMO corresponds to the position of the lowest energy hole-state created by the photoemission of an electron i.e. the HOMO of the molecular cation. Except for a Franck Condon shift of approximately 0.1 eV away from the Fermi level due to vibrational excitation in the photoemission process, this is the relevant energy position for rereduction by the redox system. For the electron injection process the alignment of the LUMO to the conduction band edge is crucial. Using the energy of the optical absorption maximum (535nm=2.32eV), the LUMO is found 0.17 eV above the Fermi level.

While the shape of the S2p line of the dye NCS group does not change when benzene is coadsorbed (Fig 4a right), the S2p emission counterintuitively sharpens upon CH₃CN coadsorption (Fig 4a left). In a simple model (Fig. 4b left) the polar solvent acetonitrile penetrates the dye layer and the interaction of the dye NCS groups with the TiO₂ surface and with neighbouring dye molecules is suppressed due to a solvation shell. The S2p intensity development in the course of CH₃CN adsorption suggests reorientation of the dye molecules pointing the NCS groups away from the surface towards the electrolyte. On the other hand nonpolar benzene just covers the dye layer (Fig. 4b right). The solvation and orientation of the dye by acetonitrile may be important for obtaining vectorial photovoltaic charge transfer of the electron from the dye LUMO to the TiO₂ conduction band and the hole from the dye HOMO to the electrolyte.

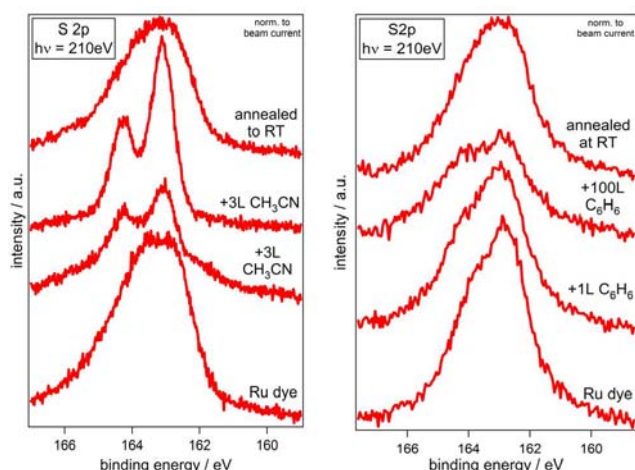


Fig. 4a: Ru(N3)-dye S2p level in the course of acetonitrile (left) and benzene (right) coadsorption and desorption.

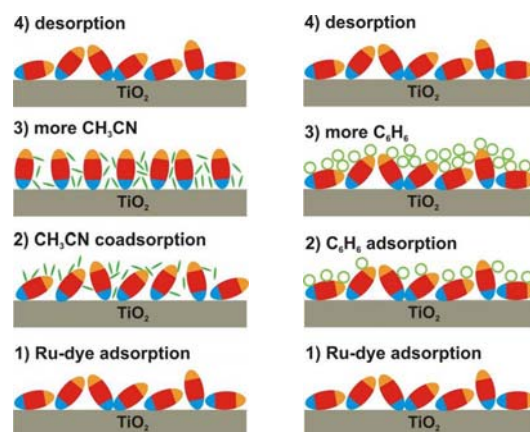


Fig. 4b: Cartoon of the Ru(N3)-dye/solvent interaction in the course of acetonitrile (left) and benzene (right) coadsorption and desorption.

[1] K. Schwanitz, U. Weiler, T. Mayer, and W. Jaegermann J. Phys. Chem. C, 111 (2007), 849-854

[2] K. Schwanitz, E. Mankel, R. Hunger, T. Mayer, and W. Jaegermann; BESSY Highlights 2005

Investigation of water evolution in operating fuel cells by means of in situ synchrotron radiography

Ch. Hartnig¹, I. Manke², H. Rieseemeier³, J. Banhart², W. Lehnert¹

¹Centre for Solar Energy and Hydrogen Research (ZSW)

²Institute of Materials Science and Technology, Technical University Berlin

³Federal Institute for Materials Research and Testing

Abstract:

The formation of liquid water in operating, unmodified fuel cells has been investigated by means of synchrotron X-ray radiography. The overall transport process is split in two parts: initial water clusters at the micrometer range are formed in the gas diffusion layer under the ribs of the fuel cell flow field; for the transition from the gas diffusion layer to the flow field channel a new mechanism is found: besides the continuous flow some filled pores are emptied by an eruptive mechanism where the water content is transported from the porous media to the flow field channel. The process of pore filling and emptying resembles a periodicity depending on the operating conditions and load profile.

Detailed report:

A well-balanced water management is the major precondition for an optimum performance of state-of-the-art fuel cells: on the one hand, water is essential for the conductivity of the membrane, whereas flooding is one of the main problems which limit the current density at high power requests and/or low temperatures. The gas diffusion layer (GDL) and the flow field are the main modules in a fuel cell which have to fulfil several functions to achieve this aim: the optimum supply of the reaction layer with reactants should not be blocked by excess liquid water which in turn has to be transported towards the outlet and a certain amount of gaseous and/or liquid water has to be retained in the GDL to moisturise the membrane.

In preceding ex-situ experiments the suitability of synchrotron tomography to resolve water structures in GDLs has been proved [1]. As a next step, the formation of liquid water has been observed in-situ. A state-of-the-art fuel cell setup has been employed for the measurements; the operating cell was investigated through small sealed holes of 8 mm diameter in the metallic end-plates of the cell. In previous investigations the water evolution in the same fuel cell was studied by means of neutron radiography to determine the most reactive areas inside the fuel cell; the resolution of this method is not sufficient to detect the initial spots of water formation, whereas a good choice has been made to select these areas for a detailed investigation to elucidate the process of water evolution. The flow field and the other components remained completely unmodified; thus the slight modification of the housing is assumed not to influence the thermal and electrical conductivity of the components and the water evolution and transport in the cell. The focus has been set on the formation of small water clusters in the GDL and the transition from the GDL to the flow field channels.

The process of liquid water formation is governed by two mechanisms: the mode of water transport varies thereby between different locations in the observed areas. An

eruptive transport mechanism was observed at some spots while the well-known continuous flow of water takes place at others. The eruptive transport describes a mechanism where many droplets of liquid water in the gas diffusion layer are ejected into the channel and merge there into a single drop within a short period. This process has been observed for the first time at the micrometer level; additionally, the repeat time of the periodic process has been determined in dependence of operating conditions and applied load profile.

In Figure 1, a series of images describing the eruptive transition from the gas diffusion media under the rib of the flow field to the channel is given. The initial formation of water under the land (yellow spots) can be identified (top). The next two consecutive images render the transition of the water droplets from the GDL to the channel of the flow field. The small water clusters merge and form a large droplet in the channel which evaporates (middle, bottom).

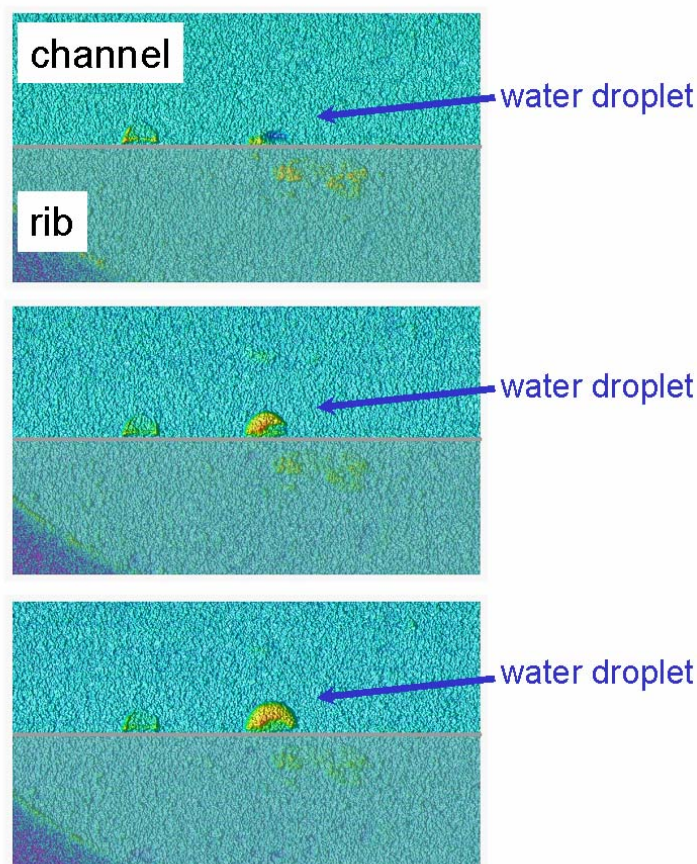


Abbildung 1: Eruptive water evolution and transition from the gas diffusion layer to the flow field channel. Initial water clusters (top) merge and form a large droplet in the channel of the flow field (middle, bottom).

The observed transport mechanism implies a periodicity where the eruption and evaporation steps follow each other; the frequency of this process is influenced by the utilization ratios (the percentage of fuel gas which is consumed along the reaction path) and the load profile (requested current) [2].

References:

- [1] Ch. Hartnig, I. Manke, Experimental report on proposal BESSY.05.2.ID-88
[2] I. Manke, C. Hartnig, M. Grünerbel, W. Lehnert, N. Kardjilov, A. Haibel, A. Hilger, H. Riesemeier, J. Banhart, Appl. Phys. Lett., submitted

Fragmentation of fluorinated fullerite C₆₀F₁₈ by synchrotron radiation

V.M. Mikoushkin, M.S. Galaktionov, V.V. Shnitov, and Yu.S. Gordeev
Ioffe Physical-Technical Institute, Russian Academy of Sciences, 194021, St.-Petersburg, Russia

S.L. Molodtsov, D.V. Vyalikh
Institut für Festkörperphysik, Technische Universität Dresden, D-01062 Dresden, Germany

O.V. Boltalina, I.V. Goldt
Chemistry Department, Moscow State University, Moscow, 119899, Russia

Abstract. Transformation of photoelectron spectra of C₆₀F₁₈ film has been studied under synchrotron radiation (SR). Fragmentation of C₆₀F₁₈ molecules accompanied by detachment of fluorine atoms has been revealed both under intensive flux of “zero-order” SR and low intensity beam of monochromatic X-ray. Mechanism of molecule excitation by photo-electrons is assumed to be the reason of the fragmentation. As a result, fluorinated fullerite was transformed into quite different material resembling some kind of amorphous carbon.

The project was supported by the bilateral program “Russian-German Laboratory at BESSY” and by the Russian Academy of Sciences (program “Influence of atomic structure on the properties of condensed matter”, project 2.14, and “Quantum nanostructures”, project 5-22).

Introduction

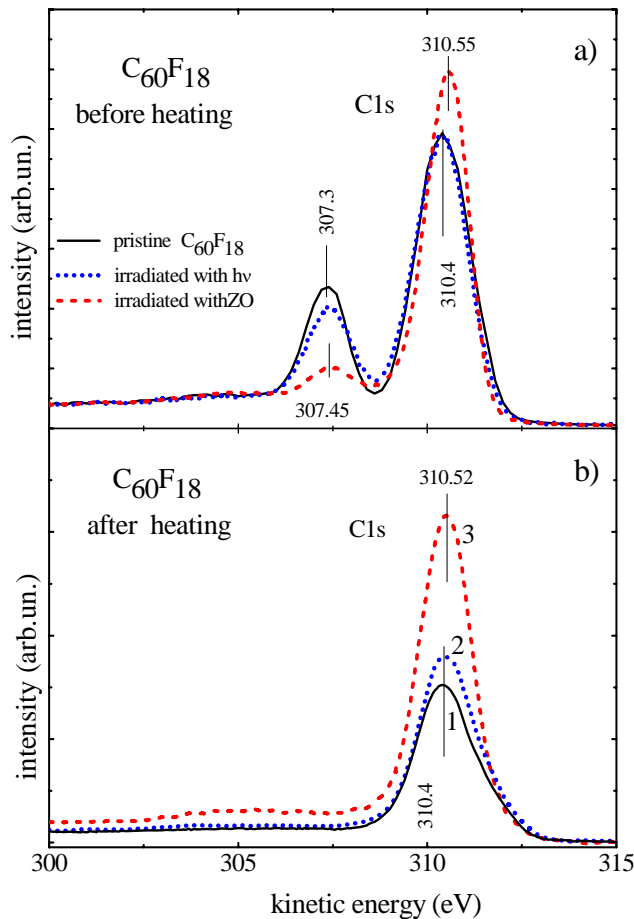
Radiation stability of molecules is their important physical characteristic and is of interest of some applied problems. Though fullerenes C₆₀ is considered to be exceptionally stable molecules [1], modification of films of condensed fullerenes (fullerite films) have been observed recently under synchrotron radiation (SR) [2-3]. There is no information about radiation stability of fullerene derivatives, such as fluorinated fullerenes C₆₀F₁₈. But one can expect essentially lower stability of fluorinated fullerenes as compared to pure fullerenes taking into account the lately obtained results of modification of solid C₆₀F₁₈ by electrons [4]. High modification rate of C₆₀F₁₈ film has been revealed under electron beam. As a result of modification, non-evaporable substance was created. The conclusion was made that the revealed process might be used in some kinds of electron lithography. The scientific goal of this research was to show that fluorinated fullerite C₆₀F₁₈ can be fragmented by synchrotron radiation and can be transformed into quite different material.

Experimental details

The experiment was performed at BESSY II storage ring (Berlin) on the Russian-German synchrotron radiation (SR) beamline equipped with the plane-grating monochromator (PGM) and the experimental station of the Russian-German laboratory [5]. Photoelectron spectra were collected using a hemispherical analyzer VG CLAM-4. About 10 monolayers (MLs) of solid C₆₀F₁₈ were grown on silicon oxidized surface in the preparation chamber by evaporation of pure fluorite C₆₀F₁₈ powder. In present experiment, we used the C₆₀F₁₈ soot which was utilized in our previous research of this material [4,7]. Native silicon-oxide layer on silicon wafer was chosen as a substrate to take a more difficult conditions of molecule attachment and to simulate conditions of fabrication of structures like “conductive cluster on insulator” for electronic devices. Core-level and valence band structure of pristine film as well as the film irradiated by monochromatic x-ray $h\nu = 300$ eV and intensive non-monochromatic (“zero-order”) synchrotron radiation were measured.

Transformation of C1s core-level and valence-band spectra of C₆₀F₁₈ film under SR

Modification of C₆₀F₁₈ film was observed in the course of irradiation. Extent of the film modification was controlled by measuring the number of fluorine atoms lost by fullerene cage. This number is proportional to the intensity of the photoemission line C1s of carbon atoms chemically bounded with fluorine atoms. Fig.1a shows C1s photoelectron spectrum of C₆₀F₁₈ molecule containing two peaks. One of them (right, $E_k = 310.55$ eV) corresponds to carbon atoms of fullerene cage being free of fluorine atoms, and another one, a satellite peak



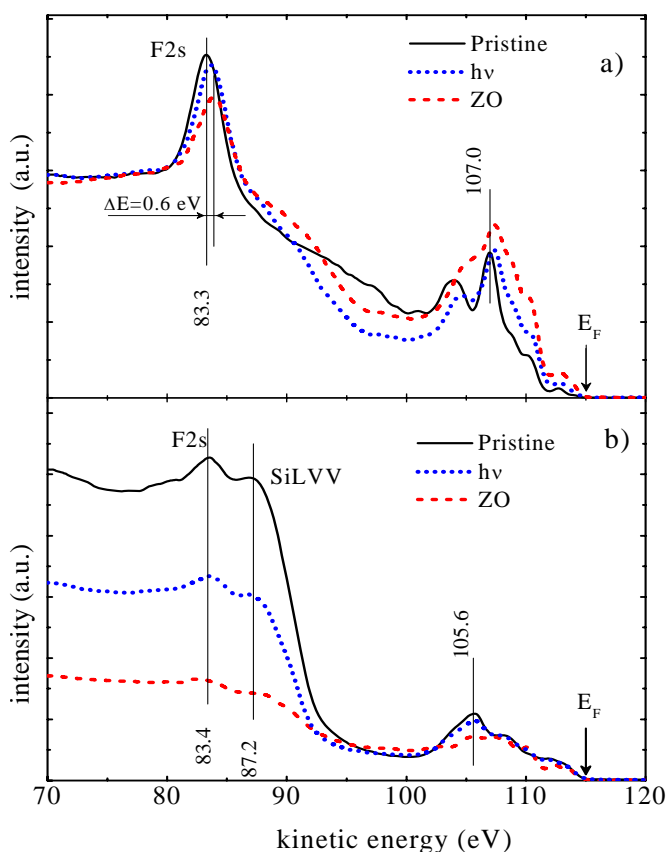
(left, $E_k = 307.45$ eV) is connected to the carbon atoms chemically bounded with fluorine atoms. One can see that the line intensity of the fluorine derived peak diminishes in the course of irradiation both by monochromatic (curve 2, blue) and intensive non-monochromatic “zero-order” synchrotron radiation (curve 3, red). Relative intensity of the satellite peak characterizes the average number of atoms remaining in molecule: ~ 14.5 fluorine atoms remain after monochromatic irradiation and only ~ 5 fluorine atoms - after “zero-order” irradiation. The conclusion can be made that modification of the film is connected with detachment of fluorine atoms from $C_{60}F_{18}$ molecules.

Fig. 1. Core level C1s photoelectron spectra of $C_{60}F_{18}$ film before (a) and after (b) heating. Solid line corresponds to pristine film, dotted line – to the irradiated one by monochromatic x-ray and dashed one – to the film irradiated by intensive “zero order” SR flux.

Fig.1b shows C1s photoelectron spectrum of $C_{60}F_{18}$ molecule after heating. Only one C1s peak corresponding to pure carbon bondings is observed in this case. This fact evidences for complete liberation of fluorine atoms from the molecule due to heating both in pristine and irradiated films. We can conclude that heating, as well as irradiation, results in fragmentation of molecule with complete or partial loss of fullerene atoms. The detached fluorine atoms probably form chemically stable molecules such as F_2 and CF_4 . The essential part of these molecules stays in the film, and a part of them remains in the film even after heating as it can be seen in the valence band spectra shown below (Fig. 2).

Modification of density of occupied valence states of $C_{60}F_{18}$ film due to irradiation by low-intensity monochromatic and intensive “zero-order” SR is shown in Fig.2a representing the valence band and adjoining photoelectron energy region. Intensity of fluorine shallow core F2s line ($E_k = 83.4$ eV) diminishes in the course of x-ray radiation. In addition, valence molecular peaks are smeared, density of states at the top of valence band becomes higher and the band gap gets narrower. Line shift to lower binding energy is also observed. The described tendencies become stronger for “zero-order” radiation pointing out to creation of the phase of amorphous carbon [3]. Mechanism of the observed modification should include excitation of valence electrons [3,4]. In the case of non-monochromatic “zero-order” radiation, adsorption of ultra-violet could result to this excitation. X-ray can not directly excite valence electron. Therefore, excitation by photo- and secondary electrons should be assumed.

Transformation of element composition of the substrate covered by $C_{60}F_{18}$ film was studied in the course of heating by analysis of the intensities of valence band structure and of Si LVV Auger line of substrate. This analysis led to the following conclusion for of non-irradiated film: the major part of $C_{60}F_{18}$ molecules are evaporated in heating, but about 1 ML of defected fullerene molecules and some amount of small fluorine rich molecules remain on the Si-oxide surface after heating. Behavior of the $C_{60}F_{18}$ film under heating proved to be similar to that of C_{60} film deposited to clean silicon surface when interface molecules are



strongly bounded to the surface due to charge transfer and 1 ML of molecules remain on the surface after heating. 1 ML of fragmented molecules of fluorinated fullerene was assumed to be strongly coupled with rather inert Si-oxide surface due to a number of broken bonds created by thermo-induced fragmentation.

Fig. 2. Photoelectron spectra of $C_{60}F_{18}$ film before (a) and after (b) heating. Solid line (black) corresponds to pristine film, dotted line (blue) – to the film irradiated by monochromatic x-ray and dashed one (red) – to the film irradiated by “zero order” SR flux.

We expected at the beginning of the research that $C_{60}F_{18}$ films modified by radiation would transform into quite different material - some kind of amorphous carbon which is not completely evaporated in heating. Indeed, this expectation was confirmed not only for intensive “zero-order” SR but

also for low intensity monochromatic radiation ($h\nu = 300$ eV). The thickness of residual layer after the sample heating is ~ 3.5 ML in the case of “zero-order” irradiation and 1.6 ML in the case of X-ray. Taking into account the 1 ML thickness of the background layer covering all the irradiated and non-irradiated areas of the surface, we can conclude that the thickness of the film area irradiated by x-ray beam is 0.6 ML of fullerenes or about 1 ML of carbon atoms. In spite of low thickness, this experiment has demonstrated the possibility of transformation of molecular crystal into amorphous substance by a set of single X-ray quanta.

Conclusions

Fragmentation of fluorinated fullerite $C_{60}F_{18}$ accompanied by detachment of fluorine atoms has been revealed both under intensive flux of “zero-order” synchrotron radiation and low intensity beam of monochromatic X-ray. Excitation of molecule by photo- and secondary electrons was assumed to be a reason of fragmentation. As a result of fragmentation, fluorinated fullerite was transformed into quite different material resembling some kind of amorphous carbon. This conclusion is confirmed by modification of valence band spectrum towards that of amorphous carbon and by the fact that, contrary to high evaporability of fullerite $C_{60}F_{18}$, the created substance is characterized by low evaporability, which makes possible fabrication of image of SR beam.

References:

1. E.E.B. Campbell, F. Rohmund, Rep.Prog.Phys. **63**, 1061 (2000).
2. V.M.Mikoushkin, V.V.Shnitov, V.V.Bryzgalov, et al., *BESSY Annual Report* (2004), 92.
3. V.M.Mikoushkin, V.V.Shnitov, et al., *Physics of the Solid State*, **46**, 2311 (2004).
4. V.V.Shnitov, V.M.Mikoushkin, Yu.S.Gordeev, S.Yu.Nikonov, O.V.Boltalina, I.V.Goldt, 14 Int. Symp. “Nanostructures: Physics and Technology”, St. Petersburg, 182 (2006).
5. S.I.Fedoseenko, D.V.Vyalikh, et al., *Nucl. Instr. and Meth., A* **505**, 718 (2003).
6. I.V.Goldt, O.V.Boltalina, L.N.Sidorov, et al., *Solid State Sciences*, **4**, 1395 (2002).

Influence of Restoration Treatments on Ink Corroded Manuscripts

Oliver Hahn¹, Birgit Kanngießer², Max Wilke³, Wolfgang Malzer²,
Bettina Nekat³, Timo Wolff^{1,2}, Alexei Erko⁴

¹ *Bundesanstalt für Materialforschung und –prüfung (BAM), 12200 Berlin*

² *Institut für Optik und Atomare Physik, Technische Universität Berlin, 10623 Berlin*

³ *Institut für Geowissenschaften, Universität Potsdam, Postfach 601553, 14415 Potsdam*

⁴ *BESSY GmbH, Albert-Einstein-Straße 15, 12489 Berlin*

Introduction: In order to determine the success of different restoration processes on ink corroded manuscripts we studied historical samples and artificial dummies before and after restoration treatments. The results of this ongoing project demonstrate that the success naturally depends on the restoration method. However, in addition it becomes apparent that the state of the historical ink-paper system itself determines the effectivity of the method.

Former investigations show that a combination of micro X-ray fluorescence analysis (micro-XRF) and micro X-ray absorption near edge structure spectroscopy (micro-XANES) is a step forward in the understanding of the complicate and complex paper degradation process in the context of iron gall ink corrosion [1]. With elemental mapping by micro-XRF the correlation of the minor elements zinc, manganese and copper in the ink to the major element iron was investigated. Along concentration profiles of iron micro-XANES measurements were carried out in order to determine the oxidation state of iron and its local environment. First results indicate that everal treatments influence the chemical composition of the inks and therefore change the archaeometrical fingerprint [2] of the historical sample.

Experimental: The experiments were carried out at the bending magnet beamline KMC-2 at BESSY. Final focussing to a spotsize of about 20 μm at the experiment was done by use of a polycapillary half-lens. In order to obtain higher fluorescence intensities and to decrease effects by sample inhomogeneities, the data were collected with a bigger spot size of 30 μm . The elemental mapping was performed with a step width of 50 μm . Micro-XANES spectra at the Fe K-edge were collected in fluorescence mode using an energy step width around the absorption edge of 0.5 eV. Total acquisition time for one absorption spectrum is about 15 minutes. The XANES spectra were corrected for background absorption by subtracting a polynomial function that was fitted to the spectral region before the pre-edge. The spectra were then normalized for atomic absorption by fitting an arc tangent function and a gaussian function to the spectra and setting the arc tangent function to equal step height for all spectra. According to former investigations, we used the inflection point of the absorption edge as a figure of merit for determination of the valence state. The inflection point indicates the energetic shift of the edge position if the bulk chemical composition is not changing.

Results: We measured different samples - originals as well as artificial samples. Due to the chemical composition of the ink, storage conditions, and the quality of the paper or parchment the investigations reveal distinguishable preservation states. If the $\text{Fe}^{2+}/\text{Fe}^{3+}$ ratio may be taken as a proxy for the degradation process, measurements of this ratio allow estimating the degree of decomposition as well as the hazard potential for a given manuscript (Fig. 1).

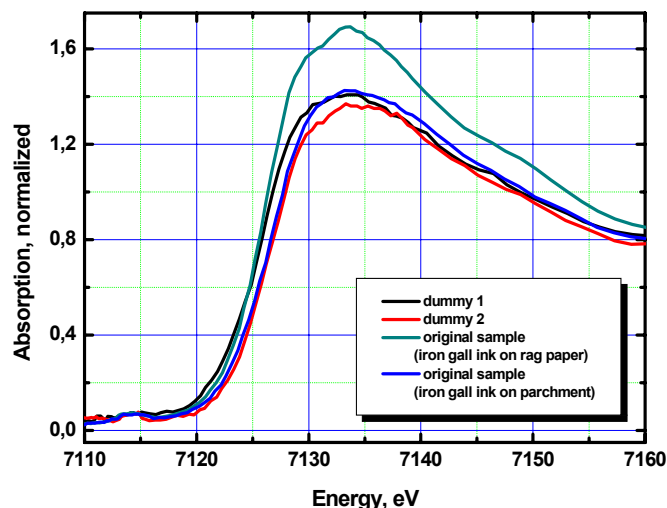


Fig. 1: Averaged XANES spectra of different iron gall ink samples. The first dummy contains only iron whereas the second one also contains copper ions. The first original iron gall ink sample on paper contains iron copper and zinc. The second original iron gall ink sample on parchment also contains iron copper and zinc.

Concerning the monitoring of restoration treatments, Figure 2 shows the results of the measuring series before treatment (black lines), after restoration (red), and after one year (blue). In accordance to former investigations [3], a local dependence of the $\text{Fe}^{2+}/\text{Fe}^{3+}$ ratio could be observed in the original ink material. In addition, a significant decrease of the $\text{Fe}^{2+}/\text{Fe}^{3+}$ ratio took place due to restoration. This new $\text{Fe}^{2+}/\text{Fe}^{3+}$ ratio shows no local dependence - it seems to be constant. However, after one year we could observe an obvious increase of the relative Fe^{2+} concentration.

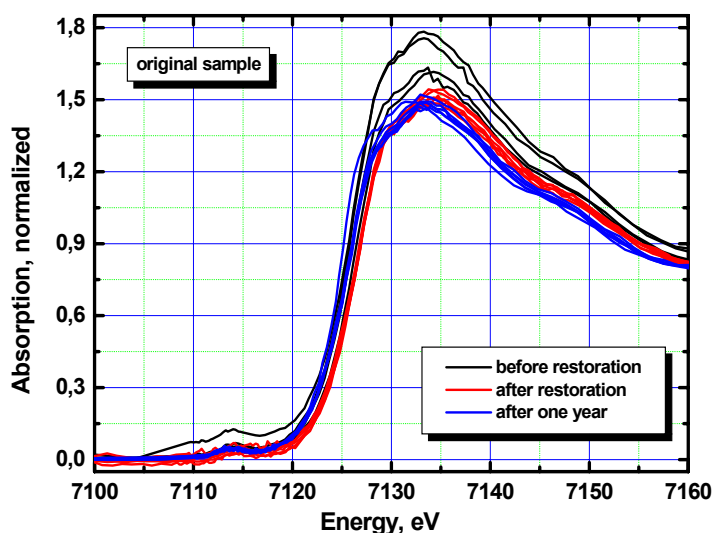


Fig. 2: XANES spectra of one historic iron gall ink sample (18th), taken from different sites. The investigations were carried out before restoration, after restoration, and after one year.

These measurements presented here describe again an equilibrium system which also was observed in former investigations. One may conclude that the restoration treatment affects an equilibrium state between Fe^{2+} and Fe^{3+} ions. This equilibrium state naturally depends on the chemical composition of the ink materials, storage conditions, and the quality of the paper or parchment. Aqueous restoration methods may reduce the concentration of the Fe^{2+} - and other soluble components. However, after a certain time the primary equilibrium is “re-installed”.

Conclusions: As demonstrated before, our results show that the combination of micro-XRF measurements with micro-XANES experiments is a versatile tool to monitor the impact of restoration treatments of ink corroded manuscripts.

Up to now the sustainability of the restoration methods shows a strong dependence of the chemical composition of the ink materials. In view of our results we have to ask the question if other restoration methods would obtain better results. In order to examine further trends our different samples have now to be stored for at least one year. In 2008, more investigations will continue this long-term research project. The publication of our present results is intended [4].

References

- [1] Kanngießner B, Hahn O, Wilke M, Nekat B, Malzer W, Erko A, Investigation of Oxidation and Migration Processes of Inorganic Compounds in Ink Corroded Manuscripts, *Spectrochimica Acta B*, Vol 59/10-11, 1511-1516 (2004).
- [2] Hahn O, Eisengallustinten – Materialanalyse historischer Schreibmaterialien durch zerstörungsfreie naturwissenschaftliche Untersuchung”, editio, Internationales Jahrbuch für Editions-wissenschaft, Niemeyer Verlag, Bd. 20, 143-157 (2006).
- [3] Hahn, O, Malzer W, Kanngießner B, Wilke M, Nekat B, and Erko A, Influence of restoration processes on ink corroded manuscripts, BESSY-Jahresbericht (2004).
- [4] Hahn O, Wilke M, Kanngießner B, Wolff T, Malzer W, Nekat B, Stiebel N, “Influence of restoration processes on archaeometrical investigations”, *Studies in Conservation*, in preparation.

Visualization of package induced deformations of ICs

Tilgner Rainer¹, Alpern Peter¹, Müller Bernd R.², Lange Axel², Harwardt Michael², Hentschel Manfred P.²
1) Infineon Technologies, Munich, 2) BAM, Berlin

Abstract

Within micro electronic power devices (switching currents ~1A) the integrated circuit (IC) is laid out as switching modules on a thin Silicon single crystal, encapsulated in epoxy resin and soldered to a copper sheet metal for cooling purposes. Temperature fluctuations lead to a flexural load of the Silicon crystal due to different thermal expansion coefficients of the constituent materials. The knowledge of the real deformation of the crystal is essential for the proof of Finite Element Method (FEM) calculations and the associated predictions concerning nano fracture mechanics. To visualize the real deformation of the crystal a new inspection method was developed at the materials research beam line (BAMline) of the German Federal Institute for Materials research and testing (BAM) at BESSY [1]. The method (Synchrotron Laue Contrast Radiography – SLCR) is based on the coherent scattering of monochromatic synchrotron radiation by the net planes of the silicon single crystal of the electronic device.

Introduction

Within a micro electronic component containing an IC the package establishes a link between switching entities of the chip such as pn-junctions implanted in silicon and the component's outer pins designated to become soldered to a printed circuit board (PCB). The mechanical interaction between package and chip (fig.1) induces deformations which may become starting points of mechanical flaws in principle [2-4]. Modern quality and reliability development ask for the extent of these interactions. The main reason for deformation of the chip is the layered structure of the overall system chip and package (OCP). To spread the heat from the chip switching currents of ~1A the silicon is soldered at 328°C by lead (its use is regulated by ROHS [5]) on a copper heat slug. Cooling down to room temperature the shrinking copper will distort the thermally more inert silicon chip. In a similar way a mold compound is used to fix and to cover the construction. It is processed at 175°C as a liquid which shrinks and hardens after cooling down. The final shape of the whole chip within the package can be evaluated non-destructively by hard x-rays.

Experiment

To explore the final shape of the whole chip the micro electronic device is placed in front of a CCD camera system (pixel size 14.4 μm x 14.4 μm) and irradiated by a parallel and monochromatic beam (55keV) delivered by the Double Multilayer Monochromator (DMM) of the BAMline, which is furnished with synchrotron radiation by a 7 Tesla Wave Length Shifter (7T WLS). The surface normal of the chip is parallel to the beam axis and the beam cross-section covers the entire chip (fig. 2, left).

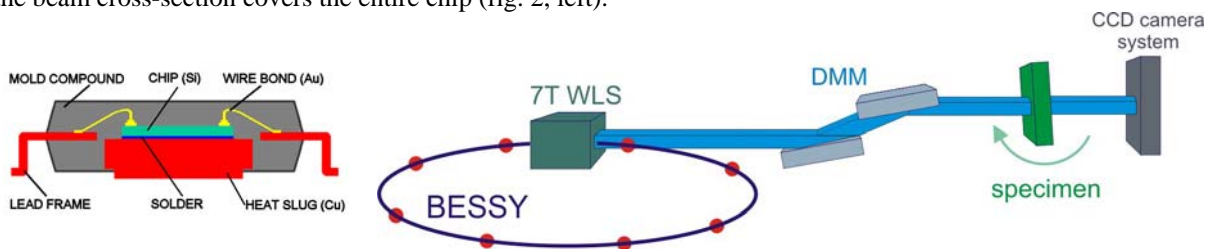


Fig. 1: Cross-section of a micro electronic power device.

Fig. 2: Experimental set up for SLCR measurements at the BAMline.

The measurement is performed by rotating the device around an axis while recording in parallel the radiographs of the device. The axis is oriented perpendicular to the beam. In most cases the CCD camera displays the radiograph of the absorbing gold bonding wires (fig. 3, left). But for specific orientations of the device dark bands across the silicon crystal become visible (fig. 3, right).



Fig. 3: Radiograph of the bonding wires, (left) without and (right) with dark bands, respectively

The observed phenomenon can be explained with the help of fig. 4. X-rays will be deflected by a single crystal if d (the spacing between the planes in the atomic lattice of the single crystal), λ (the wavelength of the synchrotron beam) and Θ (the angle between the incident beam and the scattering planes) fulfil the Bragg condition.

$n\lambda = 2d \cdot \sin(\Theta)$ For a perfectly flat single crystal the condition is fulfilled across the entire crystal simultaneously (fig. 4, left). Thus the whole radiograph becomes dark (pseudo absorption), but not because of absorption. In flexural loaded single crystals the scattering planes are distorted. Thus the Bragg condition is only fulfilled in some local areas of the crystal (fig. 4, right). This leads to more or less small dark bands in the radiograph (local pseudo absorption, fig. 3, right). The shape and the width of the local pseudo absorption bands depends on the shape and the radius of curvature of the flexural loaded crystal, respectively. By rotating the curved crystal the dark bands are moving across the radiograph. The measurement of one device takes a few minutes, so that e.g. time dependent (temperature) experiments can be performed.

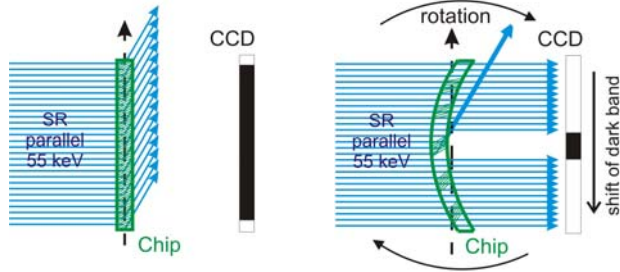


Fig. 4: Illustration of the pseudo absorption of single crystals. Left: x-rays are deflected across the whole flat single crystal due to diffraction. No x-rays arrive at the detector (the radiograph would be dark). Right: for curved crystals the Bragg condition is only fulfilled in local parts. This leads to dark bands in the radiograph (local pseudo absorption, see fig. 3, right). The position of the dark band can be moved by rotating the crystal.

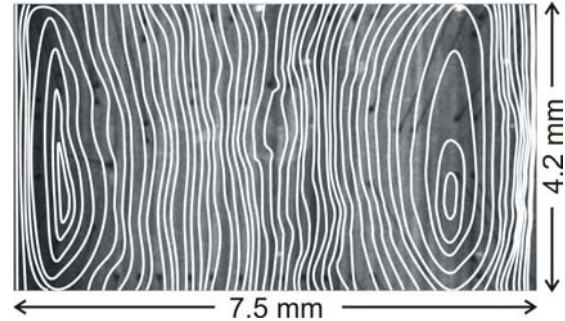


Fig.5: Aggregation of all dark band positions (isoclines) during rotation (angle range 0.11° , step width 0.001°). In the background the radiograph of the chip is shown. In the centre part of the radiograph a lead void is visible by the brighter grey coloured area.

The measurement of the electronic devices (photon energy 55 keV ($\lambda = 0.022$ nm), angle scan range 0.11° , step width 0.001°) yields a series of dark band positions (isoclines) across the whole crystal. They are aggregated in a 2D plot (fig. 5). The isoclines density represents the local radius of curvature of the crystal. It typically ranges between 5 m and 50 m (the higher the density the smaller the radius of curvature).

A 3D surface profile of the flexural loaded Silicon crystal can be derived from the 2D isoclines plot with a very high resolution of about ± 1 nm in height (fig. 6).

Result

The 3D surface profile of a chip just after packaging is shown in fig.6, left. As mentioned above, the temperature dependent shrinkage of the heat slug, which is situated beneath the profile, exceeds that of the chip and the mold compound. This leads to a smooth convex shape of the chip. The amplitude between the minimal and maximal height is about 1500 nm, which may not harm the functionality of the electronic device. A second device was measured after a stress treatment of 1000 temperature cycles from -55°C to $+150^\circ\text{C}$. The result is shown in fig.6, right. The shape has changed to a more irregularly profile (like a magic carpet) with a reduced height amplitude of about 300 nm. This is explained by a partial loss of the adhesive strength between the package and the chip caused by degradation e.g. of the solder during stress treatment.

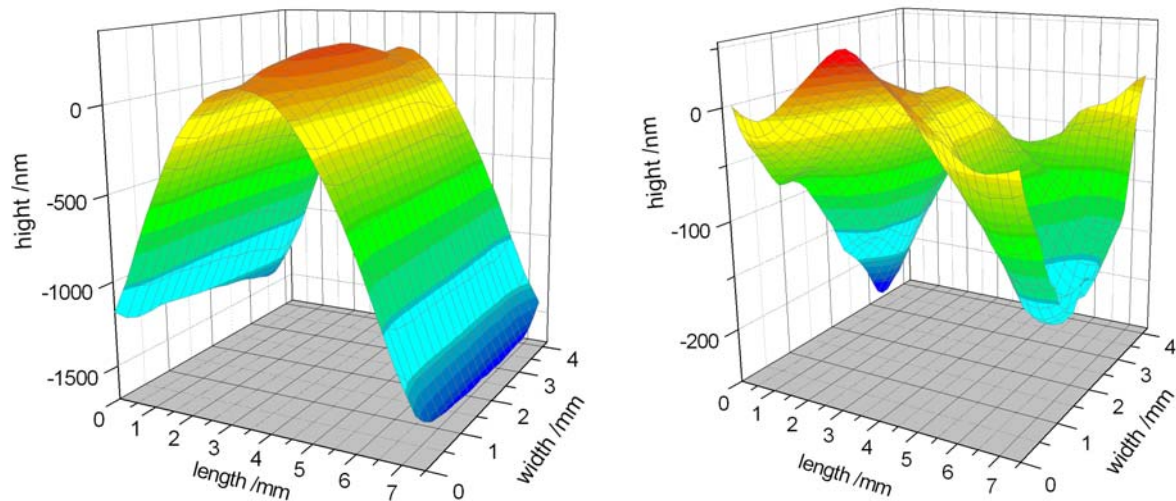


Fig. 6: 3D surface profiles (lateral resolution: $14.4 \mu\text{m} \times 14.4 \mu\text{m}$, height resolution: ± 1 nm) deduced from the isoclines plots (fig. 5). The Cu heat slug is situated beneath the profile. Left; chip just after packaging, right; chip after a stress treatment of 1000 temperature cycles from -55°C to $+150^\circ\text{C}$.

It remains, however, to ask for the limit of detect ability of more minute mechanical influences of the package. Thus, we choose the following influences:

- Gold wire bonds
- Voids within the solder die attach to fix the chip to the copper heat slug
- Higher order influences

A void was found within the lead solder from X-ray absorption radiography (background of fig. 7, left). The SLCR measurement discovers the mechanical effect of the gold wire bonds and the lead solder void on the surface of the silicon crystal impressively (fig. 7, left, distorted local pseudo absorption isoclines). Fig. 7, right shows the residual 3D surface profile of the crystal where a parabolic underground was subtracted. Notice, the height range is only within 10 nm. Finally even higher order effects such as interaction between void and bonding wires can be detected.

From these results SLCR can be considered as a new powerful inspection method to evaluate even minute degradation processes in electronic devices. This is an essential for any prognostic reliability work in the future.

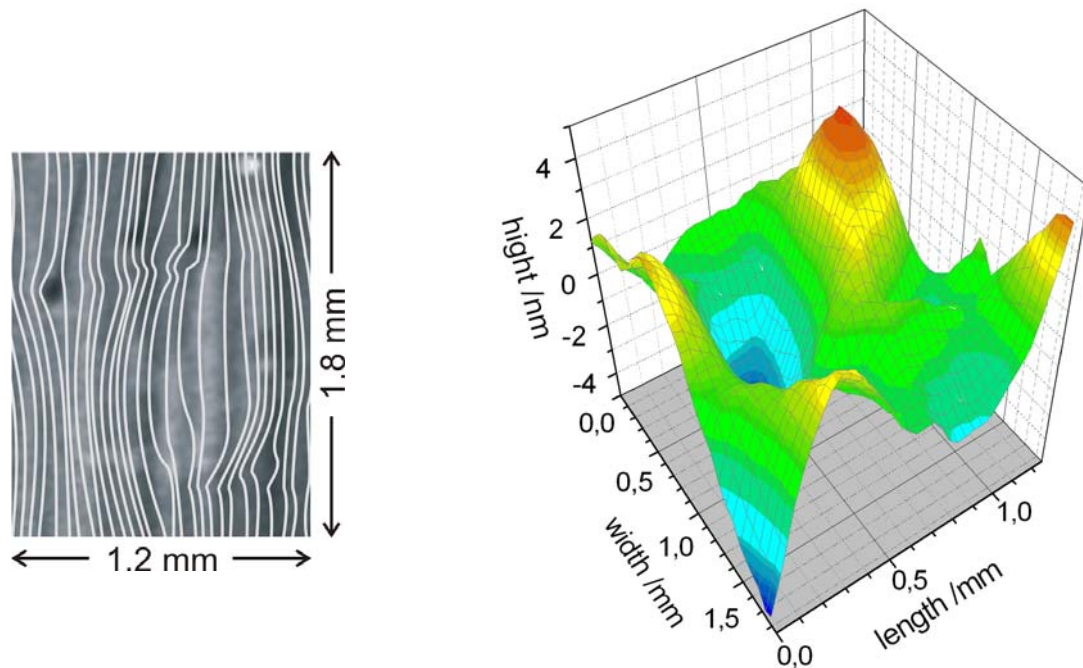


Fig. 7: left: Detection of a void in the lead solder by x-ray absorption (heightened centre part of fig 6). The SLCR measurement discovers the impact of the gold wire bonds and the lead solder void on the silicon crystal, left: 2D plot of the local pseudo absorption isoclines, right: 3D surface profile deduced from left plot. A parabolic underground is subtracted.

References

- [1] Müller, B.R., Görner, W., Hentschel, M.P., Riesemeier, H., Krumrey, M., Ulm, G. Diete, W., Klein, U., Frahm, R.; "BAMline: the first hard X-ray beamline at BESSY II", Nucl. Inst. and Meth. in Phys. Res. A, **467/468**, 703-706, (2001)
- [2] P. Alpern, V. Wicher and R. Tilgner; "A simple test chip to assess chip and package design in case of plastic assembling", IEEE Trans. CPMT **A17** (3) pp. 583-589 (1994); Erratum in 1995 **18**, 862-863
- [3] P. Alpern, H. Pape and R. Tilgner; "Schadensmechanismen bei kunststoffgekapselten integrierten Schaltungen unter Temperaturwechselbelastung", VTE **10** (1998) Heft 1, pp. 10-18
- [4] Z. Suo; „Reliability of Interconnect Structures“, Chapter in vol.8: *Interfacial and Nanoscale Failure* (W. Gerberich, W. Yang, Editors) *Comprehensive Structural Integrity* (I. Milne, R.O. Ritchie, B. Karihaloo, Editors-in-Chief) Elsevier 2003
- [5] Official Journal of the European Union, "Directive 2002/95/EC of the European Parliament and of the Council of 27 January 2003 on the restriction of the use of certain hazardous substances in electrical and electronic equipment" L37/19-23, Annex, point 7.

Contact: Bernd R. Müller, bernd.mueller@bam.de

KMC-1: a High Resolution and High Flux Beamline for HIKE-PES

F. Schäfers, M. Mertin, M. Gorgoi

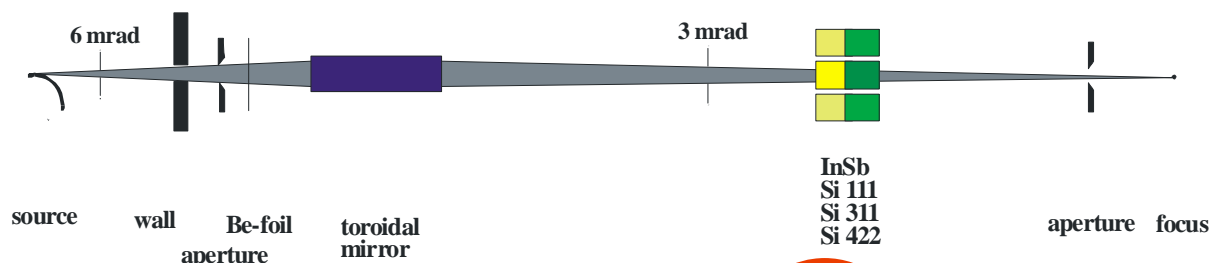
BESSY GmbH, Albert-Einstein-Strasse 15, 12489 Berlin, Germany

Electron spectrometers with highly stabilised high voltage power supplies are available nowadays which have an ultra-high resolution of not more than 20 meV at kinetic energies up to 15 keV. This high kinetic energy photoemission at hard x-rays (HIKE or HAX-PES) is an ideal – non-destructive - tool to look deeply into bulk material (>5 nm) and to study (buried) interface layers /1,2/. For this technique hard x-rays with similar ultra-high energy resolution at highest flux are required.

The BESSY bending magnet beamline KMC-1 /3/ has been used in the last years to successfully establish this HIKE technique employing a Gammadata Scienta R-4000 hemispherical analyzer /4,5,6/ optimized for high kinetic energy electrons up to 10 keV. Despite of the low photoelectron cross sections at high excitation energies, core levels of multilayer interfaces and “real” solar cell samples at probing depths of more than 10 nm could be investigated.

The reason for the good matching of this beamline to the experimental requirements is basically due to the facts that this beamline not only has a high flux (10^{11} - 10^{12} photons/sec) in a focus size of $0.3 \times 0.4 \text{ mm}^2$, which is well matched to the spectrometer acceptance, and a continuously tuneable working range between 1.7 and 12 keV, which fits ideally to the HIKE requirements, but also and - most important - a very good energy resolution. All this could be

top view



side view

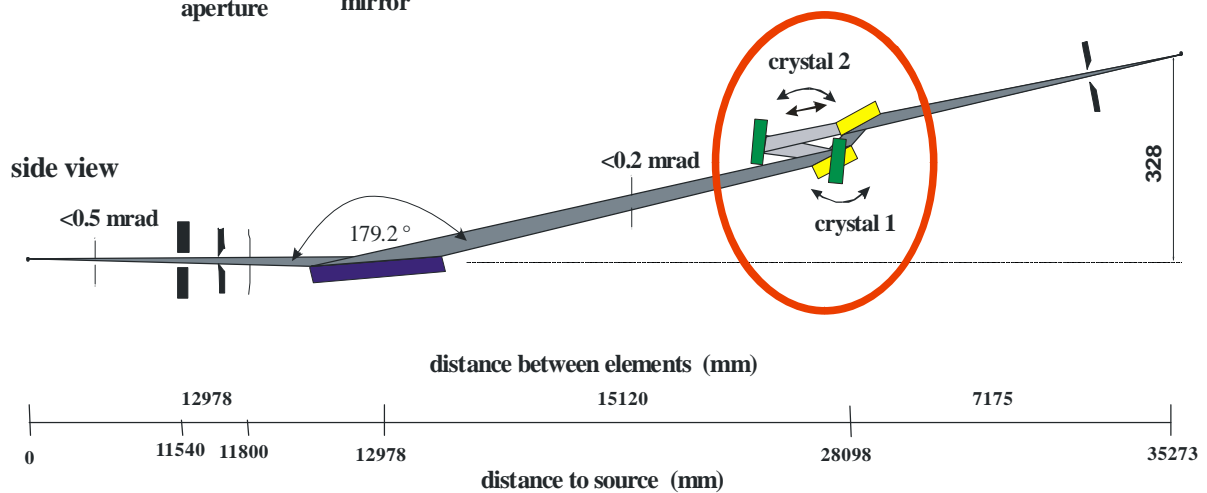


Figure 1 Bending magnet KMC-1 double crystal monochromator beamline with high resolution (crystal backscattering) option

achieved by (1) the windowless setup under Ultra-High-Vacuum conditions up to the experiment, (2) by the use of only three optical elements to minimise reflection losses, (3) by

collecting a large horizontal radiation fan with the toroidal premirror (6 mrad acceptance), and (4) the optimisation of the crystal optics to the *soft* x-ray range ($E_{\min} = 1.7$ keV@InSb, 2 keV@Si 111). According to the Bragg equation this lowest energy requires a maximum Bragg angle of 82 degrees. This “built-in” normal incidence crystal optics (back-scattering geometry) is intrinsically coupled to a high energy resolution according to

$$\Delta E = E\Delta\theta / \tan \theta, \quad \theta: \text{Bragg angle, } \Delta\theta: \text{rocking curve width.}$$

Thus any flux-consuming post-monochromatization employing Si (nnn) channelcut crystals is unnecessary in our case. The rocking curve width

$$\Delta\theta = \sqrt{\left((\Delta\theta_{cr})^2 + \psi^2 + (\phi^2 \tan \theta / 8)^2\right)}$$

is determined by the intrinsic crystal Darwin width $\Delta\theta_c$ and by the sagittal and meridional beam divergences ψ and ϕ . Thus, crystal limited resolution is achievable using collimated incident light, with ψ and ϕ being close to zero. At large angles, however, the tangent is dominating, the beam divergence does not affect the resolution significantly and crystal limited resolution is possible.

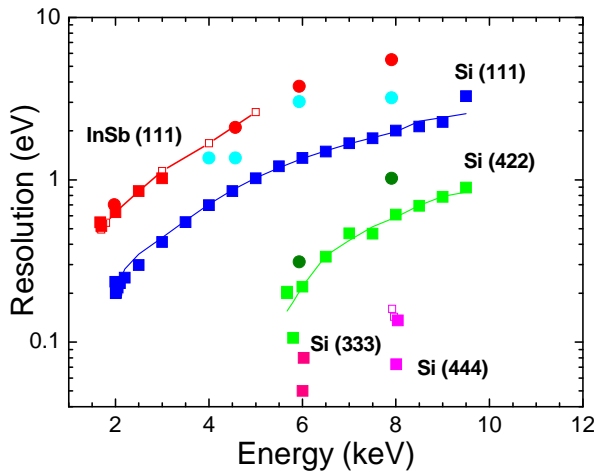


Figure 2 Calculated (open points and lines) and experimentally determined (solid circles, solid squares) resolving power of the KMC-1 monochromator crystals InSb (111), and Si with (111), and (422) orientations. Si (333) and Si (444) correspond to higher order radiation. The solid circles have been measured by the photocurrent absorption drop (FWHM) in a single-crystalline Si photodiode with (nnn) and (400) orientation operated in back-reflection /9/.

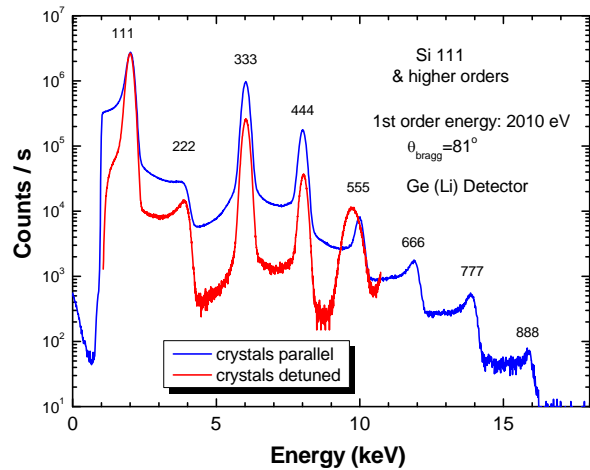


Figure 3 Higher order crystal reflections of Si (111) at a photon energy setting of 2010 eV for a parallel setting of both crystals (blue curve), and for the detuning case (red curve). Note that the 2nd order reflection is forbidden. Spectra were obtained with an energy-dispersive Ge(Li)-detector.

Figure 2 shows all the KMC-1 resolution data extracted from crystal-optical measurements and from HIKE photoemission. In the case of the HIKE measurements the Au 4f core levels were followed. The Au 4f_{7/2} line was fitted by a Doniach-Sunjic profile /7/ which - being a convolution of two functions, a Lorentzian and Gaussian - includes an asymmetry parameter. The Lorentzian function estimates the lifetime and the Gaussian function stands for the instrumental broadening given by spectrometer and beamline /8/ (see figure 4).

The tangent-like behaviour of the resolution is clearly seen. At 6 keV a beamline resolution of 50 meV using Si (111) in 3rd order has been measured. This corresponds to a resolving power $E/\Delta E$ of as much as 120.000.

By use of high crystal reflection orders (Si (333) und 444)) (see figure 3) this high resolution option ($\Delta E < 500$ meV) is available nearly *continuously* within the complete spectral range. Ultrahigh resolution ($\Delta E < 200$ meV) is available at selected photon energies ((2, 5.7, 6, 8 keV)). The third and fourth order excitation energy can be used *simultaneously* within a HIKE spectrum, such that in principle an in-situ depth profiling of a sample – *within* one scan - is possible. However, beamline optimisation for higher order intensity requires a slight detuning of the monochromator crystals. Taking into account that not only the flux in higher crystal orders, but also the cross section decreases dramatically with higher kinetic energy, the acquisition of typical high-resolution low-noise HAXPES-spectra such as Au 4f takes between one minute (Si (111)) and some hours (employing Si (333) or (444)) (see figure 4).

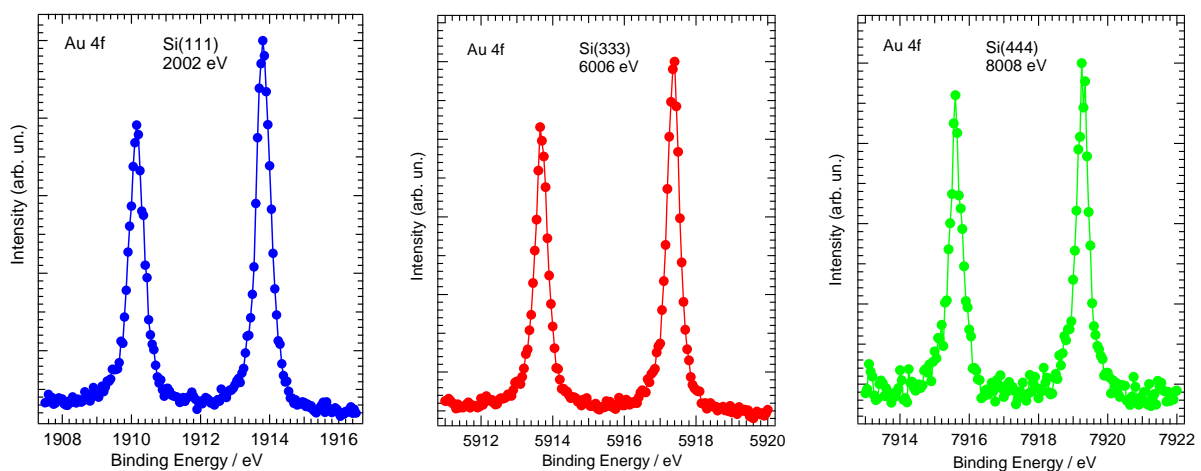


Figure 4 Photoelectron spectra of Au 4f_{5/2} and Au 4f_{7/2} valence bands obtained using the KMC-1 Si (111) crystal tuned to 2002 eV photon energy. Spectrometer passenergy 100 eV, entrance slit 0.5 mm

	1st order	3rd order	4th order
	Si (111)	Si (333)	Si (444)
Photon Energy	2002 eV	6006 eV	8008 eV
Acquisition time	4 min.	40 min.	180 min.
Lorentzian FWHM (eV)	0.348	0.348	0.348
Gaussian FWHM (eV)	0.243	0.135	0.185
Analyzer Resolution (eV)	0.125-0.140	0.125-0.140	0.125-0.140
Beamline Resolution (eV)	0.21±0.01	0.050±0.02	0.073±0.02

Concluding, soft x-ray bending magnet beamlines at medium energy storage rings provide good opportunities for HIKE spectroscopy. Especially the energy tuneability at high resolution is an exclusive option, since this is normally not available at undulator beamlines on high energy SR facilities, when fixed-energy channelcut monochromators are used.

- /1/ W. Drube et. al. Phys. Rev. Lett. **74**, 42 (1995)
- /2/ K. Kobayashi et al., Appl.Phys. Lett. **83**, 1005 (2003)
- /3/ http://www.bessy.de/users_info/02.beamlines/linespdf/D_01_1B.pdf
- /4/ P. Bressler et al., BESSY Annual Report, p. 254-255 (2004)
- /5/ P. Bressler et al., BESSY Annual Report, p. 476-478 (2005)
- /6/ E. Holmström et al., Phys. Rev. Lett. **97**, 266106-1-4 (2006)
- /7/ S. Doniach, M. Sunjic, J. Phys. C: Solid St. Phys. **3**, 285 (1970)
- /8/ L. Lindau et al. Nature **250**, 214 (1974)
- /9/ M. Krumrey, G. Ulm, Nucl. Instrum. Meth. **A467-468**,1175-1178 (2001)

First microbeam diffraction results from biological and biomimetic materials at the μ -Spot beamline

Oskar Paris¹, Chenghao Li¹, Stefan Siegel¹, Gundolf Weseloh¹, Helmut Cölfen², Peter Fratzl¹

¹Department of Biomaterials, and ²Department of Colloid Chemistry,
Max Planck Institute of Colloids and Interfaces, Potsdam

Introduction

The new microfocus beamline has recently been designed [1] and commissioned at the 7T wavelength-shifter source at BESSY II. An experimental station was developed and installed by the MPI of Colloids and Interfaces, in collaboration with BESSY, Bundesanstalt für Materialforschung und -prüfung (BAM) and the Technical University of Berlin. The goal of the MPI project part was to implement a microbeam scanning instrument for the combination of simultaneous small- and wide-angle scattering (SAXS/WAXS) and X-ray fluorescence (XRF) from thin sample sections. This unique combination of methods allows mapping of structural parameters from the atomic/molecular to the nanometre scale by combined SAXS and WAXS, simultaneously with chemical composition by XRF. The lateral resolution for SAXS/WAXS mapping is given by the minimum beam size in the order of 5-10 μm . In this report we present the experimental station layout for scanning SAXS/WAXS/XRF, together with first SAXS/WAXS data from biological and bio-inspired materials acquired at the μ -Spot beamline.

Experimental setup

The microbeam was defined by a toroidal mirror together with a W/Si double multilayer monochromator (DMM) at 15keV and a beam defining pinhole close to the sample. Due to the broad bandpass of the DMM, this option provided a high intensity at the sample ($> 10^9$ ph/s) at a beam size of $\approx 10 \mu\text{m}$, and a divergence of $\approx 1 \times 0.1$ mrad (h x v) [2]. Alternatively, a circular Fresnel zone plate in connection with the DMM delivered an intensity of $\approx 4 \times 10^8$ ph/s ($E=8.9$ keV) at a beam size of roughly $15 \mu\text{m}$. A large area detector with high pixel resolution (MarMosaic), in connection with a small beamstop and a short sample-detector distance (≈ 200 mm) allowed collecting the SAXS/WAXS signal simultaneously with a SAXS resolution of ≈ 50 nm and almost three orders of magnitude in the range of the accessible scattering vector [2]. No evacuated flight path was necessary due to the short distance between the sample and the beamstop (< 100 mm). An on-axis, long-distance optical microscope permitted to visualize the sample and to define regions of interest for subsequent microbeam SAXS/WAXS with an accuracy of about 2-3 μm . The specimens were typically mounted on a high resolution scanning stage (resolution 0.1 μm).

Scanning SAXS/WAXS of bone

The basic building block of bone can be considered as an organic/inorganic nanocomposite consisting of collagen fibrils reinforced with small, plate like calcium phosphate mineral particles. We studied the local structure of this composite in connection with bone diseases such as osteoporosis with scanning SAXS/WAXS using a microbeam of about 10 μm (Fig.

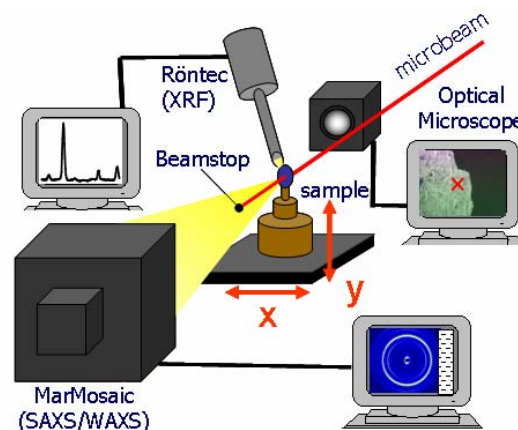


Fig.1: Sketch of the experimental setup for simultaneous SAXS/WAXS/XRF at the μ -Spot beamline.

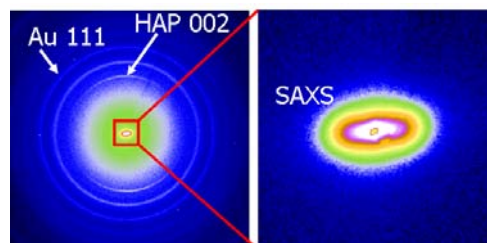


Fig. 2: 2D scattering pattern from a gold-coated, $\approx 10 \mu\text{m}$ thick bone section (left). The right side shows a magnification of the SAXS signal in the central region. The angular range covers $0.08^\circ - 40^\circ$, corresponding to a range of scattering vectors $0.1 \text{ nm}^{-1} < q < 50 \text{ nm}^{-1}$.

2). The WAXS signal provided local information about the crystallographic orientation of the mineral crystals (crystallographic texture), as well as the lattice parameter determined accurately by using a thin (300 nm) gold coating of the specimens as internal standard. Moreover, the SAXS signal allowed determining the local orientation and the mean thickness (T-parameter) of the mineral platelets. All these parameters were calculated by a semi automated data evaluation procedure [3], and maps of nanostructural parameters were created (Fig. 3) that can be compared with other imaging methods such as histology or backscattered electron microscopy. These maps provide crucial information about local microstructural changes due to bone diseases and their medical treatment.

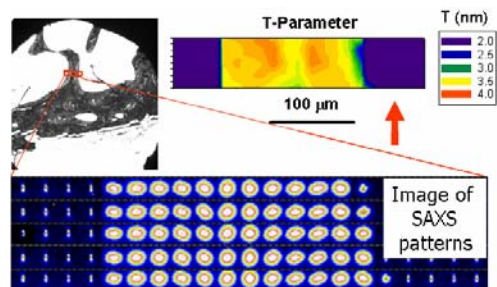


Fig. 3: Scanning SAXS of bone. The SAXS patterns were evaluated by a semi-automated procedure to provide maps of nanostructural parameters such as the thickness T of mineral platelets.

Biomimetic Mineralisation

Inspired by the concept of biomineralization, block copolymers can be used as effective templates for mineralisation of calcium carbonate crystals from solution. The particle morphology can be greatly influenced by type and concentration of the polymer and by the calcium concentration in the solution. We have investigated single calcite particles grown in the presence of poly(ethylene oxide)-block-poly(sodium 4-styrenesulfonate) [PEO₂₂-PNaStS₄₉]. The size of the particles was about 20 μm , ideally suited for microbeam SAXS/WAXS at the μ -Spot beamline using a 15 μm beam from a Fresnel zone plate (Fig. 4). We found that both, the SAXS and the WAXS signal differ considerably for different particles. Even though the particles look like polycrystalline aggregates in the scanning electron micrographs, the diffraction patterns show that they are strongly textured or they are even almost perfect single crystals. Application of different characterisation methods revealed for the first time a continuous structural transition in the product particles from polycrystalline, to mesocrystal to single crystal in the presence of the polymer at a fixed calcium/sulfonate molar ratio with variation in the calcium concentration. The existence of this structural sequence led us to the proposal of a unifying crystallization framework based on the aggregation of precursor subunits that span the limits from non-oriented aggregation of nanoparticles to classical ion-by-ion growth [4].

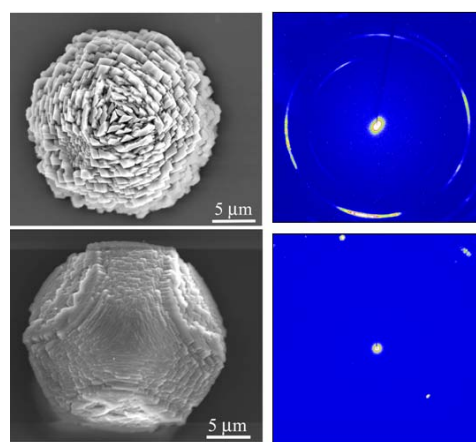


Fig. 4: SEM images (left) and corresponding SAXS/WAXS patterns (right) from biomimetic calcite particles. The Ca concentration (at fixed Ca / PEO₂₂-PNaStS₄₉ ratio) was 10 mM and 2.5 mM for the particles in the upper and lower row, respectively

Acknowledgements

We are grateful to H. Riesemeier (BAM), A. Erko (BESSY) and W. Malzer (TU Berlin) for their help with the commissioning. We acknowledge financial support from the Max Planck Society, BESSY GmbH, Bundesanstalt für Materialforschung und -prüfung, and the BMBF (project 05KS4KT1/6).

References

- [1] A. Erko, F. Schaefer, A. Firsov, W. B. Peatmann, W. Eberhardt, R. Signorato, *Spectrochimica Acta B* **59** (2004) 1543-1548.
- [2] O. Paris, C. Li, S. Siegel, G. Weseloh, F. Emmerling, H. Riesemeier, A. Erko, P. Fratzl, *J. Appl. Cryst.* **40** (2007) in press.
- [3] A. Gourrier, W. Wagermaier, M. Burghammer, D. Lammie, H. Gupta, P. Fratzl, C. Riek, T. Wess, O. Paris, *J. Appl. Cryst.* **40** (2007) in press.
- [4] A. N. Kulak, P. Iddon, Y. Li, S. Armes, H. Coelfen, O. Paris, R. M. Wilson, F. C. Meldrum, *J. Amer. Chem. Soc.* (2007) in press.

Transmissive Position Detectors for X-ray beamlines

Martin R. Fuchs¹, Karsten Holldack², Franz Schäfers², Frank Höft², and Uwe Mueller²

¹*Protein Structure Factory c/o BESSY, Free University Berlin,*

Albert-Einstein-Str. 15, 12489 Berlin, Germany and

²*BESSY GmbH, Albert-Einstein-Str. 15, 12489 Berlin, Germany*

We present the development of a new transmissive center-of-mass X-ray Beam Position Monitor (XBPM), based on a thinned-down duo-lateral Position Sensitive Diode (PSD). In measurements at the BESSY bending magnet beamline KMC-1, a first 3 mm x 3 mm detector prototype yielded signal currents of up to 3 μA / 100 mA ring current at 5 keV photon energy using the monochromatic beam. The detector thickness was measured to be 5 μm with a transmission of 93 % at 10 keV and 15 % at 2.5 keV. A proof-of-principle feedback system based on the detector signals and a piezo actuator was successfully commissioned. As it stands, this monitor design approach promises a generic solution for automation of state-of-the-art crystal monochromator beamlines.

Introduction

Contemporary X-ray beamlines based on crystal monochromators require excellent stability of the monochromatic beam. Moving further towards higher brilliance, microfocus and automated beamline operation, as in case of protein crystallography applications, beam monitoring and feedback schemes are crucial. For monitoring, XBPMs can provide information about intensity, position and shape of an X-ray beam along a beamline. While imaging monitors can provide all three parameters at once for beam adjustment, they are inherently limited in time resolution and occlude the beam in most cases.

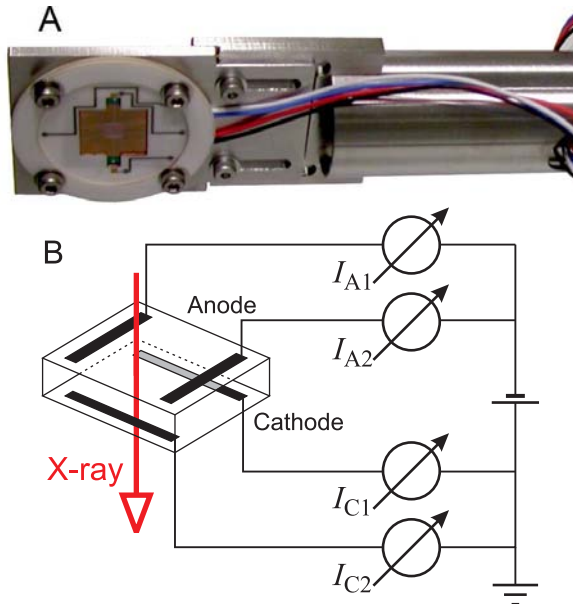


FIG. 1: Duo-lateral transmissive PSD-XBPM with 3 mm x 3 mm area as mounted for the experiment (A) and corresponding wiring scheme (B).

Most center-of-mass type XBPMs, on the other hand, can provide beam position information at high time-resolution, a parameter of central importance for monitors to be used in feedback schemes. In-situ operating XBPMs (allowing for on-the-fly intensity *and* position control) while

combining large active area at sub-micron resolution and full feedback capability are of great importance. Paving the way in that direction, we present first commissioning results from a new detector type based on a thinned-down Silicon-PSD detector developed within a joint project initiated at BESSY [1] and shared by a semiconductor manufacturer [2] and partners from several European Storage Rings (BESSY, DESY, DIAMOND, ESRF and SOLEIL). PSDs have proven their workability as position monitors for visible and infrared light. Their functional principle as depicted in Fig. 1 is the differential measurement of the photodiode surface resistance by comparing the photocurrents at a split anode or, in the duo-lateral detector case, split anode and cathode.

Beam-occluding 1D-PSDs (a so-called lateral diode) are already in use at BESSY beamlines in horizontal beamline stabilization schemes [3] in the VUV range. In order to extend the performance of PSDs to the X-ray range, 2D duo-lateral PSDs were manufactured on silicon thinned down to thicknesses of 5 μm – 10 μm at active areas of up to 100 mm². First prototypes (see image in Fig. 1A) have been recently studied at the crystal monochromator KMC-1 at BESSY with promising results described below.

Measurements

The tests with a first PSD-XBPM prototype were performed at the BESSY double crystal monochromator (DCM) beamline KMC-1 [5]. This beamline is on a bending magnet source and covers an energy range from 1.7 keV to 12 keV (InSb and Si-(111) crystals) at a maximum flux of 10¹¹ photons/s/(100 mA ring current). The beam-size at the monitor position was $\sim 500 \mu\text{m}$ and the spectral resolution $E/\Delta E = 2 \cdot 10^3$ at 5 keV.

The measured transmission curve (Fig. 2) with transmission values of 15 % at 2.5 keV, 84 % at 6 keV and 93 % at 10 keV corresponds to a Si thickness of $\sim 5 \mu\text{m}$. A scan over the whole detector area reveals a transmission variation over the detector area of under 2 % (Fig. 3).

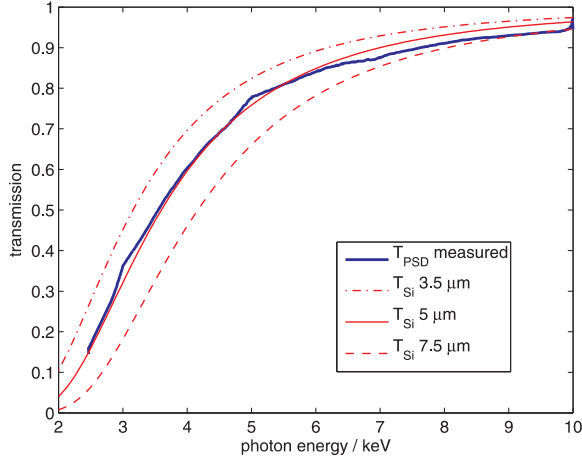


FIG. 2: Measured PSD-XBPM transmission (blue) versus the full KMC-1 beamline photon energy range. Calculated X-ray transmission curves [4] of 3.5, 5 and 7.5 μm thick Si foils are plotted in red for comparison

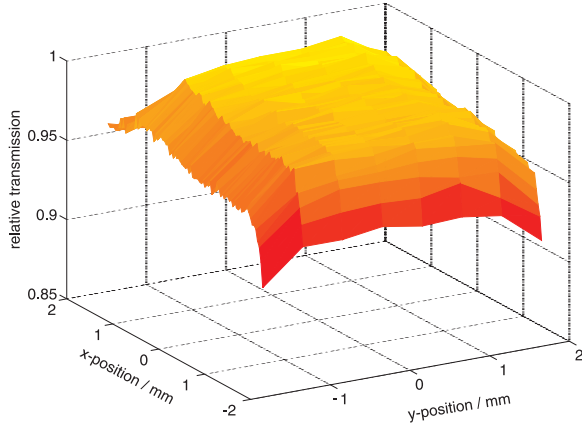


FIG. 3: Transmission relative to maximum transmission at 5 keV over the entire area of the PSD-XBPM measured with a second photo diode. The overall inhomogeneity is at least $\leq 2\%$.

The device tested was a 3 mm x 3 mm duo-lateral PSD mounted on a XYZ translation stage (Fig. 1A). In a duo-lateral PSD, both the cathode and anode are split, in orthogonal direction with respect to each other. This design minimizes crosstalk between the vertical and horizontal electrodes and thus results in a smaller position detection error compared to a tetra-lateral type. The anode and cathode currents were detected via four Keithley electrometers (models 6517A and 6514, Fig. 1 bottom) and the BESSY data acquisition computer.

For scans of the beam across the detector area, the detector was moved against the fixed beam in both horizontal and vertical direction via the manipulator stage. In addition, horizontal sweeps of the beam were performed via the piezo actuator voltage of the roll axis of the second monochromator crystal. The current signals observed during such a horizontal sweep are shown in Fig. 4, depicting the low crosstalk between horizontal (measured

at the anode side) and vertical (cathode side) directions. Short horizontal scans with piezo-mirror control show sub-micron position resolution of the detector.

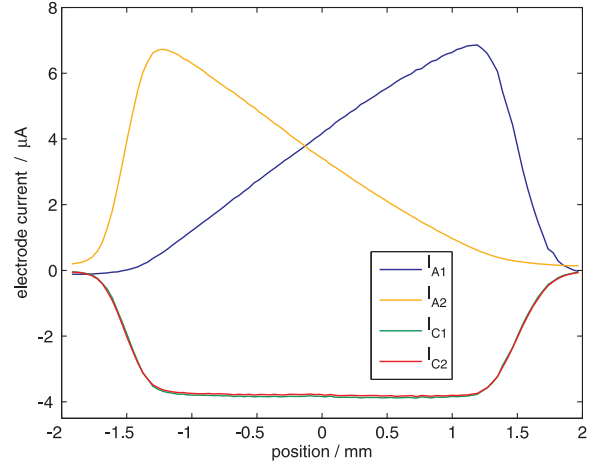


FIG. 4: Anode currents I_{A_i} and cathode currents I_{C_i} of the transmissive PSD-XBPM plotted against the beam position for a horizontal sweep of the beam at 5 keV.

Nonlinearities in the separate electrode signals cancel in the computation of the difference-over-sum (D/S) position signal according to

$$\frac{I_{E2} - I_{E1}}{I_{E1} + I_{E2}} = \frac{2x_E}{L_E} \quad (1)$$

with I_{E_i} being the electrode currents measured at contacts 1 and 2 of anode or cathode, x_E the distance from the detector center in the direction of the respective electrode and L_E the length of the active detector area in the direction of the respective electrode.

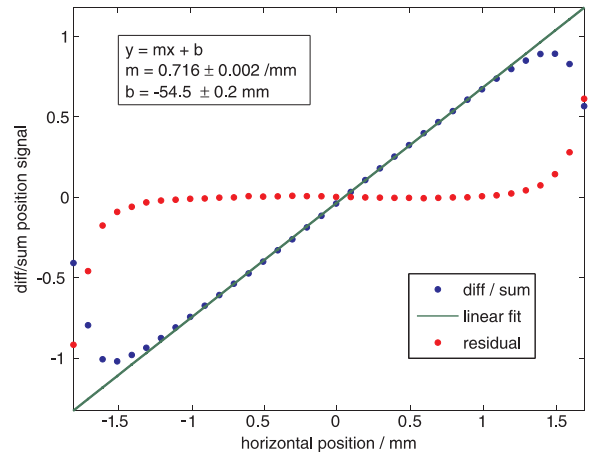


FIG. 5: Difference-over-sum (D/S) signal versus horizontal translation stage position with linear fit and residual. The linearity range of 2 mm was limited by the finite beam size.

A linear fit to the observed D/S position dependence of a horizontal sweep across the detector is shown in Fig. 5. The large region of excellent linearity over almost the entire 3 mm of the active

area highlights one of the great advantages of the PSD design in its use as an XBPM. The slight deviation of the slope from the expected value of $2/3 \text{ mm}^{-1}$ is due to a reduction of the apparent active region due to the finite X-ray beam diameter.

Measurements in the vertical direction revealed a position-independent constant cathode current resulting in a D/S slope diminished by a factor of 5. This lower sensitivity could be traced to an increased inter-cathode surface resistance. The manufacturing process is currently being modified to reduce this parameter into the same resistance range as the $\sim 6 \text{ k}\Omega$ inter-anode resistance. Alternatively, fabrication of a tetra-lateral detector with a four-fold split anode for 2D-position detection is being discussed.

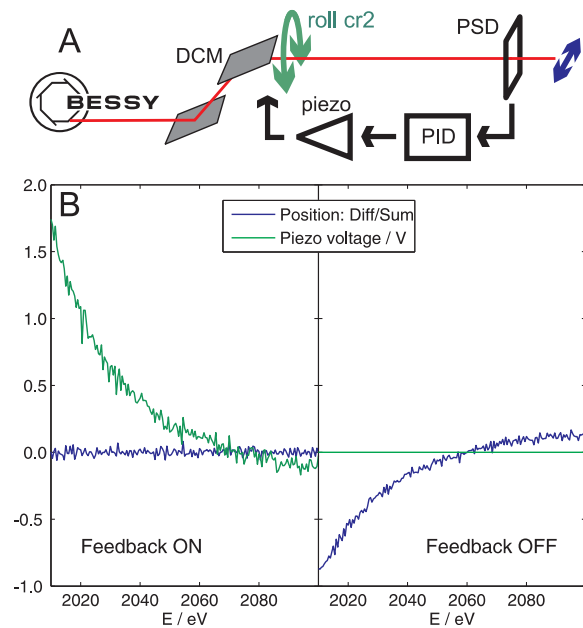


FIG. 6: A: Schematic of the KMC-1 beamline horizontal feedback loop. B: Piezo actuator voltage (green) and D/S position signal (blue) for feedback ON (left) and feedback OFF (right).

The horizontal D/S signal was employed subsequently in a PID feedback loop to stabilize beam drifts during energy sweeps. The piezo actuator voltage for the roll movement of the second crystal of the double crystal monochromator was controlled to minimize the D/S position signal and thus to lock the beam to the center of the PSD detector 6.5 m downstream (see Fig. 6A). While the photon flux within the monochromatic beam is regulated by an intensity-feedback [6], the horizontal angular travel of the beam is determined by the mechanical accuracy of the rotation and

translation stages of the DCM assembly. For beam stability the low energy end resembles the worst case: the change of the Bragg angle θ per energy is largest here (0.1 deg/eV). The translation of the second crystal T_2 is given by $T_2 = D/2\cos(\theta)$ where D is the mutual offset of the two crystals. Thus, an energy scan as shown in Fig. 6 requires a Bragg angle change from 70 to 80 deg and a translation $T_2=32 \text{ mm}$ of the second crystal producing a residual horizontal angular deviation of 0.18 mrad behind the DCM. At higher energies (i.e. smaller Bragg angles) this problem becomes negligible. A correction scheme based on the new PSD detector as depicted in Fig. 6A was employed here to fight the beam motion at low energies. In Fig. 6B the cases with feedback ON and feedback OFF are compared demonstrating that the feedback loop detects and locks the beam drift of up to 0.8 D/S signal, corresponding to a motion of 1.2 mm off the detector center.

In conclusion, the first detector prototypes for the transmissive PSD-XBPMs have already proven their great potential for a generic solution for beam monitoring and for their use in feedback schemes for crystal monochromator beamlines. Further studies, the long-term stability, the maximum time- and position-resolution and the final design for 2D operation (duo- versus tetra-lateral PSD) are underway.

This work was supported by the European Commission BIOXHIT Project, FP6 Project No LSHG-CT-2003-503420. We would like to thank John Morse, ESRF, for helpful discussions and D. Ponitz and M. Mertin (BESSY) for technical support.

-
- [1] within a joint project between BESSY and Free University Berlin (EC-FP6 integrated project BIOXHIT), <http://www.bioxhit.org>.
 - [2] Micron Semiconductor Ltd, Lancing, UK. <http://micronsemiconductor.co.uk>.
 - [3] K. Holldack, W. B. Peatman, and Th. Schroeter. Vertical photon beam position measurement at bending magnets using lateral diodes. *Rev. Sci. Instrum.*, **66**, 1889 (1995).
 - [4] F. Schäfers et al., REFLEC – a program to calculate VUV/X-ray optical elements and synchrotron radiation beamlines. TB 201, BESSY, Berlin, Germany (1996).
 - [5] F. Schäfers et al. to be published in 2007.
 - [6] F. Schäfers et al., this annual report.

3D Micro-XRF under cryo-conditions - a pilot experiment for trace element analysis in biological specimens

Gundolf Weseloh¹, Wolfgang Malzer², Marcel Pagels², Lars Lühl², Birgit Kanngießner²

¹Universität Heidelberg, Angewandte Physikalische Chemie, Im Neuenheimer Feld 253, 69120 Heidelberg

²Technische Universität Berlin, Institut f. Atomare Physik und Fachdidaktik, Hardenbergstr. 36, 10623 Berlin

Introduction:

Preparation of water-rich samples while preserving their microstructure and the spatial distribution of their constituents is a major challenge in biological imaging applications. Rapid freezing of water rich samples with high cooling rates under minimization of ice-crystal formation (vitrification) does not impose major modifications on sample structure and composition.

Three-dimensional Micro X-ray fluorescence analysis (3D-XRFA) allows tomography-like, spatial resolved analysis of trace elements in non-flat samples with dimensions of some hundred microns with a resolution of some 10 microns, depending on the X-ray energy of the exciting beam and the element detected [1]. The principle is shown in Fig. 1.

At the new BESSY microfocus beamline “ μ Spot” a confocal setup for 3D Micro-XRF was equipped with a nitrogen cryogenic stream allowing small samples being analyzed under cryogenic conditions nearly without any sample preparation. Thus, delicate, water-rich biological samples can be investigated in a near native state while preserving physiological structures and the distribution of trace elements.

For the first pilot experiment we selected a small rootlet of common duckweed (*Lemna minor*) as prototype for a delicate, water rich biological sample for investigation. The common duckweed is an important component of the aquatic food chain. The free floating plant grows on the surface of fresh water ponds and lakes. It readily takes up heavy metals and as such has been used for bioremediation of polluted waters and model organism for the study of the interaction between heavy metals and plants [2].

Experimental setup:

The μ Spot beamline is located at the 7 T wavelength shifter WLS1 [3]. For fluorescence and absorption spectroscopy, the beam is pre-focused by a mirror situated close to the source, and final focussing is performed by glass capillaries. For this experiment, the beamline was operated in a pink beam mode with the monochromator removed and an Al-filter for low energy cut off. In this set up, photon flux on the sample was estimated to be more than 2 orders of magnitude higher than using the multilayer monochromator, by which a photon flux of about 10^{12} ph/s is obtained. Detection of the X-ray fluorescence radiation from the sample was achieved by one element of an energy dispersive 7-element Si(Li) detector with digital signal processor. The polycapillary half-lenses for the confocal arrangement were purchased from IFG (Berlin, Germany), both with an X-ray focus of about $20\mu\text{m}$ at 15 keV and a focal distance of ca. 7.5 mm for excitation and 4 mm for the detection path.

The cryogenic system consists of a nitrogen cold gas source from KGW Isotherm (Karlsruhe, Germany) with a dry and CO_2 -free air sheath gas stream generated by a purge gas generator (CMC Instruments GmbH, Eschborn, Germany). The cold gas stream was operated at a temperature of 100 K at about 70 L cold gas/minute and the sheath gas was adjusted to 28 L/min. A sketch of the set up with cryo-jet, X-ray detector and focussing capillaries is shown in figure 2.

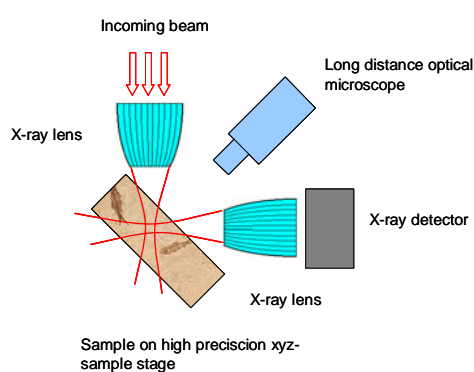


Fig. 1: Principle of 3D-XRF operating with two polycapillary half-lenses.

For sample preparation, one single root filament of duckweed was excised by stainless steel tweezers and mounted on a brass pin of a magnetic base from a small goniometer-stage by a small amount of bee's wax. The fresh root tip was immediately shock frozen in situ by the cold gas stream (fig. 3):

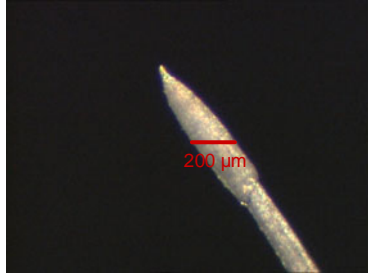


Fig. 3: Frozen duckweed root tip with scanned cross section, as seen from the sample stage microscope

For the determination of the elemental distribution the root tip was scanned along virtual cross sections with a step size of 10μm and an acquisition time of 2 seconds per sampling point. A complete cross section of the root took about 45 minutes. The X-ray fluorescence spectra were processed by a simple peak fitting algorithm and normalized to the beam current. The distribution of the elements is represented by the photopeak area of their K-line fluorescence radiation and visualized as contour plots.

Results:

A typical spectrum obtained in the center of the root is shown in Fig. 4. Under these experimental conditions, characteristic radiation of Ca, Fe, Cu, Zn, and Sr could be observed:

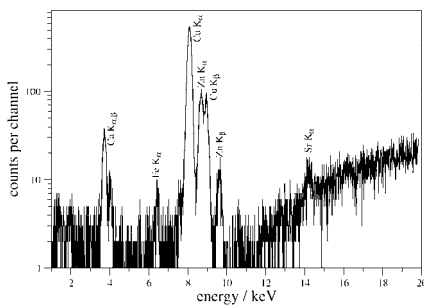


Fig 4: XRF spectrum from the center of the duckweed root with fluorescence peaks for Ca, Fe, Cu, Zn and Sr.

Contour plots of the distribution of two elements are shown in figure 5. Each pixel represents one sampling point. In particular, Cu and Ca show different distribution patterns inside the rootlet,

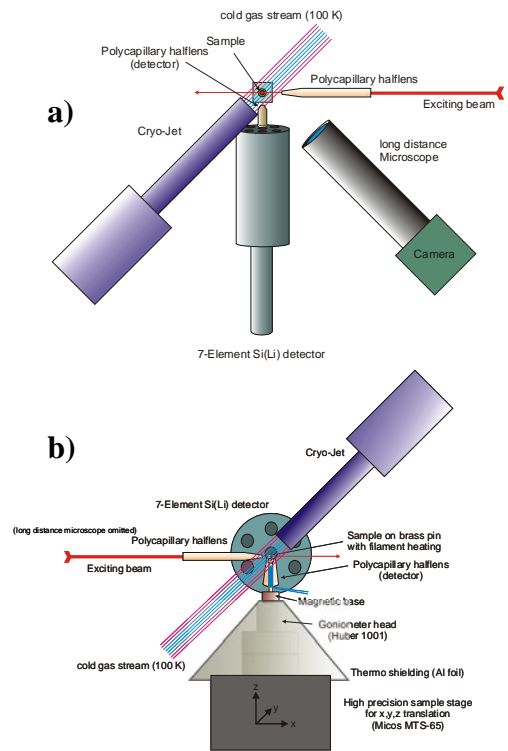


Fig. 2: Set-up of the cryo- system: a) top view b) side view (optical microscope omitted).

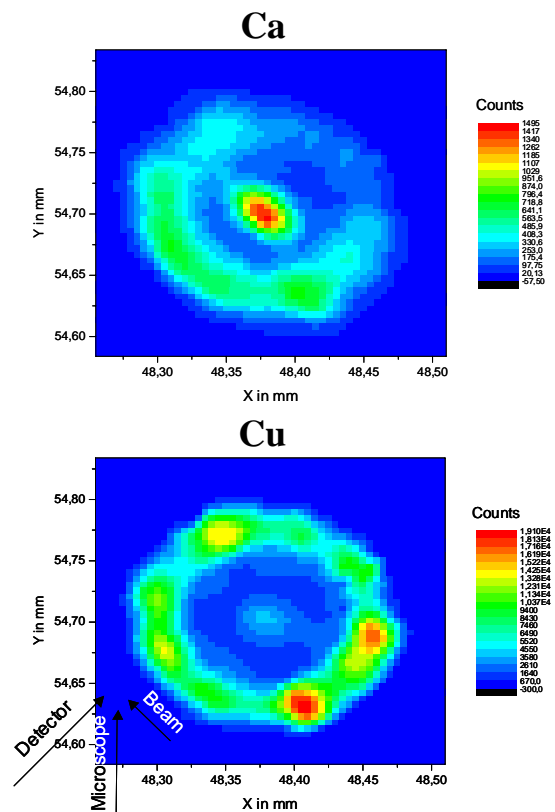


Fig. 5: Distribution of Ca and Cu in a virtual cross section of a root filament of *Lemna minor*. Arrows are indicating the position of detector, microscope and the direction of the incoming beam.

representing differences in the chemical and physiological behaviour of these elements. In the case of Cu, the highest elemental concentration is found in the peripheral part of the rootlet (epidermis or outer cortex), whereas the main amount of Ca is localized in the core of the rootlet, which harbours the central cylinder with one single tracheary xylem element surrounded by phloem tissue [4]. The asymmetry of the apparent distribution of Ca across the sample diameter is due to absorption of the Ca fluorescence inside the sample and does not represent a property of the specimen.

Conclusion and perspectives:

In this pilot experiment we demonstrated that it is possible to obtain 3D- images of trace element distributions in a biological, water rich sample without major sample preparation. The distribution of Iron, Copper, Zinc and Calcium was investigated by the new method of 3D Micro X-ray fluorescence analysis using cryogenic fixation by a nitrogen cold gas stream. Besides the *in situ* cryogenic fixation of the specimen, no further sample preparation was necessary. The next major improvement will be the transition to a continuous scanning mode, by which the acquisition time may be reduced to one quarter. Absorption correction and a full quantification procedure are under development. A more detailed description of this experiment can be found elsewhere [5].

The equipment for cryogenic investigations is available for general use at the μ Spot beamline and may be of interest not only for the investigation of samples from life sciences, but also for applications from various research areas, which benefit from measurements under cryogenic conditions down to about 80 K.

Acknowledgements:

We wish to express our thanks to Heinrich Riesemeier (BAM), Alexei Erko (BESSY), Stefan Siegel and Chenghao Li (MPI-KGF) for their help with the commissioning of the beamline and Andreas Balzers and Frank Höft (BESSY) for substantial technical support. Financial support is acknowledged from Max Planck Society, BESSY and BAM. Major parts of this work were funded by the BMBF (project no. 05KS4KT1/6).

References:

- [1] B. Kanngießer, W. Malzer, I. Reiche, *A new 3d micro x-ray fluorescence analysis set-up - first archeometric applications*, NIM B **211**, (2003) 259-264.
- [2] W. Wang, *Literature review on duckweed toxicity testing*, Environ. Res. **59**(1), (1990), 7-22.
- [3] A. Erko, F. Schaefers, A. Firsov, W. B. Peatmann, W. Eberhardt, R. Signorato, *The BESSY x-ray microfocuss beamline project*, Spectrochimica Acta B **59** (2004) 1543-1548.
- [4] J.E. Melaragno, M.A. Walsh, *Ultrastructural features of developing sieve elements in lemna minor l. - the protoplast*, Am. J. Bot. **63**(8) (1976), 1145-1157.
- [5] G. Weseloh, W. Malzer, M. Pagels, L. Lühl, B. Kanngießer, *3D Micro-XRF under cryo-conditions – a pilot experiment for trace analysis in biological specimens*, Micron, submitted.

Quantitative Evaluation of 3D Micro X-ray Fluorescence Measurements of Stratified Materials

W. Malzer¹, I. Mantouvalou¹, I. Schaumann², L. Lühl¹, R. Dargel²,
C. Vogt² and B. Kanngießner¹

1) Institut für Optik und Atomare Physik, TU Berlin,
Hardenbergstr. 36, 10623 Berlin, Germany

2) Institut für Anorganische Chemie, Leibniz Universität Hannover,
Callinstr. 9, 30167 Hannover, Germany

Introduction

3D micro X-ray fluorescence spectroscopy (3D Micro-XRF) is a recent development in X-ray fluorescence analysis [1, 2]. While a considerable number of experiments using the new technique for research in various fields are known, reliable quantification procedures were missing up to now.

With this work, a quantification procedure for stratified materials is proposed and validated. It facilitates the reconstruction of systems of layers, viz the computation of their thicknesses and their compositions, from the results of depth-sensitive measurements with a 3D Micro-XRF setup. Basis is a fundamental parameter expression for the count rate depending on the probing depth, which relies on an analytical model for the probing volume [3]. This expression was extended for stratified materials. In a series of experiments the validity of the equations was tested and the accuracy of the reconstruction was determined.

One of the obstacles was the lack of suitable reference materials. Therefore specific stacks of polymeres, containing varying amounts of metal, have been manufactured as stratified reference samples. This combination, metals in low-Z matrix, is typical for most applications of 3D Micro-XRF, like e.g. paint layers.

Theory

For a single homogeneous layer with boundaries at d_1 and d_2 the count rate $\Phi(x)$ for a chemical element depending on the probing depth x can be written

as:

$$\Phi(x) = \Phi_0 \tilde{\eta} \sigma_F \rho \exp(-\bar{\mu}_{\text{lin}} x) \exp\left(\frac{1}{2}(\bar{\mu}_{\text{lin}} \sigma_x)^2\right) \times \\ \times \frac{1}{2} \left[\operatorname{erf}\left(\frac{d_2 + \bar{\mu}_{\text{lin}} \sigma_x^2 - x}{\sqrt{2} \sigma_x}\right) - \operatorname{erf}\left(\frac{d_1 + \bar{\mu}_{\text{lin}} \sigma_x^2 - x}{\sqrt{2} \sigma_x}\right) \right]$$

The symbols have the following meaning:

Φ_0 is the incoming flux in counts per second.

σ_F is the production cross section (cm^2/g) for the respective X-ray line.

The production cross section includes all atomic processes leading to the emission of a specific X-ray line.

$\bar{\mu}_{\text{lin}}$ is the effective linear mass attenuation coefficient, which takes into account the attenuation of both, the incoming and the detected radiation.

The setup is characterized by two parameters per chemical element: the integrated sensitivity $\tilde{\eta}$ and the width of the profile σ_x in the scanning direction. According to the equation above, the count rate is governed by four terms:

The product of the first four factors including the local density ρ represents the intensity one would obtain in the absence of absorption.

The Lambert-Beer term stands for the decrease of the intensity due to absorption in probing depth x . The Lambert-Beer factor would be sufficient for an infinitesimal small probing volume. The second exponential corrects for its actual extension.

The error functions are of importance if the probing volume intersects the layer boundaries.

For a succession of n layers, this intensity equation must be extended by an additional factor for the absorption of radiation by the layer on top of a specific layer. If we designate the intensity contri-

bution from a specific layer l with thickness D as $\Phi_l(x)$, the overall count rate equates:

$$\Phi(x) = \sum_{l=1}^n \prod_{k=1}^l \exp(-\mu_{\text{lin},k} D_k) \Phi_l(x)$$

For each chemical element detected, such an equation exists. They are coupled via the absorption terms, because all elements contribute to the attenuation of the radiation.

The equations are solved by using least square fitting. For the calibration step a set of thick multielement reference materials is used. The composition and the mass density must be known. The integral sensitivity $\tilde{\eta}$ and the profile width σ_x are determined for each element. The values of missing elements can be interpolated.

For the purpose of quantification, the local densities ρ and the thicknesses of the layers are computed as free parameter of the least square fit. The number of layers and their qualitative composition must be given *a priori*. The fraction of light elements (H, O, etc.) or the stoichiometry of oxides must be given as well.

Experimental

The 3D Micro-XRF experiments have been carried out at the μSpot beamline, which has a dedicated setup for this type of chemical analysis. The polycapillary lens in the excitation channel has a focal FWHM of 24 μm . The FWHM of the lens in the detection channel is 12 μm . Both values are valid for a photon energy of 18 keV.

Homogeneous glass reference material (Breitländer) was used for calibration. The calibration was not only performed for the standard scanning direction (tilted 45° to the beam axis), but as well with 30° and 60°. In contrary to the profile width σ_x , the integrated sensitivity $\tilde{\eta}$ is predicted not to depend on this angle.

The quantification procedure was validated and tested with the glasses from Breitländer as bulk samples on the one hand, and with the above mentioned systems of polymer layers on the other hand.

The basic material for the polymer layers was ethylene propylene diene monomer rubber (EPDM) with additives for vulcanization and ZnO in varying amounts. Slabs with thicknesses from ca. 35 μm to 150 μm were produced and vulcanized to stacks. The lateral homogeneity was thoroughly tested with scanning Micro-XRF. The thicknesses were determined by light microscopy.

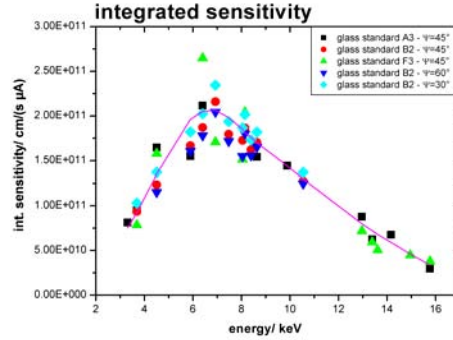


Figure 1: Integrated sensitivity $\tilde{\eta}$

Results

With the first step, the calibration, the integral sensitivity $\tilde{\eta}$ and the profile width σ_x are determined as the characteristic parameters of the 3D Micro-XRF spectrometer. Figure 1 shows an intercomparison of the calibration values for the sensitivity $\tilde{\eta}$ for three different glass reference materials and three scanning directions. The statistical spread of the sensitivity values is around 10%. In agreement with the prediction of our model, no dependency on the scanning direction can be observed. The values for the profile width σ_x (not depicted here) scatter with around 10%, as well. The sensitivity $\tilde{\eta}$ is plotted versus the energy of the emission lines, because interpolation of the characteristic parameters between K-line and L-Line series is possible.

In a second step, one of the glass reference material was excluded from the calibration procedure and treated like an unknown sample. The results show, that for major and minor constituents, the uncertainty is around 20%. For trace elements and for low Z elements it may increase up to ca. 50%. This is mainly caused by absorption effects.

Figure 2 shows a typical result for the reconstruction of a EPDM layer system. The black dots represent the count rates measured and the black line the computed ones. With the red line, the reconstructed weight percent profile is depicted. As general result from almost 60 depth scans we can summarize: The thicknesses obtained by repeated depth scans on the same sample scatter with ca. 10% to 15%.

The values for the layer thicknesses obtained by light microscope and by 3D Micro-XRF agree within their error bars.

The repeatability for the weight fractions is around

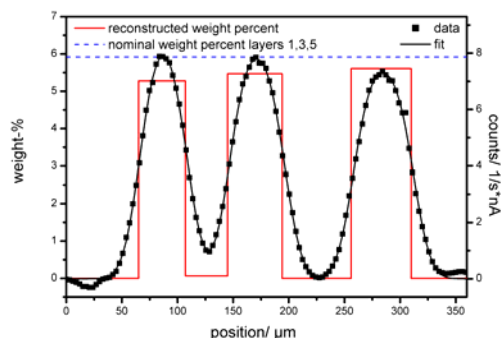


Figure 2: Reconstruction of a 5 layer system

6%. We observed a systematic deviation of the computed weight fraction to the nominal values. This deviation was 25% at most.

The dynamic range of concentrations between neighbouring layers can be up to ca. 100 for layer thicknesses of around 40 μm . For example, an Zn concentration of 0.1% can be determined adjacent to a layer containing 10% of Zn.

Conclusions and Perspectives

We proposed and validated a fundamental parameter equation for the reconstruction of stratified materials from depth-sensitive measurements with a 3D Micro-XRF setup. Schemes for calibration, measurement and evaluation have been established and render the confocal Micro-XRF into a quantitative analytical technique. Thicknesses and Compositions of layer can be determined. The uncertainties are around 20% to 30%. In less favourable situations, in particular trace elements and strong absorption, the uncertainty may increase substantially.

With the specimen made on the basis of EPDM, a suitable well characterised stratified material as reference for 3D Micro-XRF became available. The thickness of the layers and the concentration of the metals added can be varied within a wide range. Thus, it will be possible to produce specific reference materials for applications with edge requirements.

A more detailed publication of the results presented in this report is in preparation and will be submitted to Analytical Chemistry.

We plan to integrate these computations with the control software of the μSpot beamline. A user friendly graphical interface shall allow for convenient use.

Acknowledgment

This work was funded by the Federal Ministry for Education and Research (BMBF) of Germany, grant 05KS4KT1/6, and the German Research Foundation (DFG), grant KA 925/7-1-3004607.

References

- [1] B. Kanngießer, W. Malzer, and I. Reiche. Micro-xrf goes 3d: X-ray insights into mughal paintings. *Bessy Highlights*, pages 28 – 29, 2002.
- [2] Birgit Kanngießer, Wolfgang Malzer, and Ina Reiche. A new 3d micro x-ray fluorescence analysis set-up - first archaeometric applications. *NIM B*, 211:259 – 264, 2003.
- [3] W. Malzer and B. Kanngießer. A model for the confocal volume of 3d micro x-ray fluorescence spectrometer. *Spectrochim. Acta B*, 60:1334 – 1341, 2005.

Status of 5m-NIM Beamline

Thorsten Zandt, Christof Janowitz and Recardo Manzke

Institut f. Physik, Humboldt-Universität zu Berlin, Newtonstraße 15, 12489 Berlin

Introduction

Application of highly brilliant synchrotron radiation in a wide photon energy range from infrared up to the x-rays leads to an ever increasing number of important results in all scientific fields. This permanently growing scientific impact stands in close interrelation with the rapid development of new and more efficient sources of synchrotron radiation as well as steadily improving and changing experimental end stations, but also with a continuously prospering demand for well-trained young scientists.

In order to meet in parts the demands, our team of the Humboldt University started, in close collaboration with BESSY, with the implementation of the HU Research and Training Beamline (5m-NIM) at BESSY II. On this beamline it is planned to introduce and continuously qualify students and young scientists into the fascinating possibilities of synchrotron radiation research.

Description of the optical system

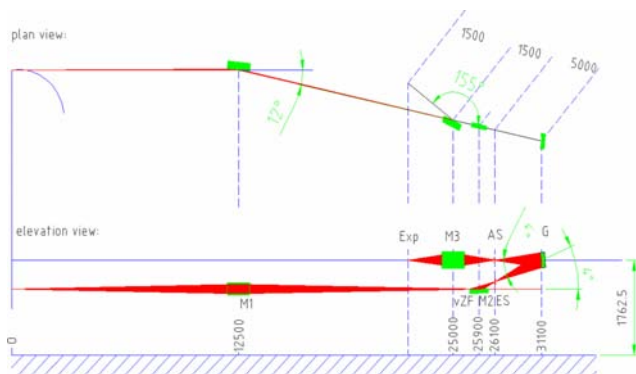


Figure 1: Optical lay-out of the 5m-NIM beamline

A 3m-NIM was up to then in successful user operation at the dipole magnet DIP3-1B. This 3m-NIM was replaced by our 5m-NIM. With the ray trace program 'Ray' [1] was calculated, which of the optical components can be reused and how new parts to have designed. According to the results of the computation, we used the old pre-

and post-monochromator optics of the 3m-NIM. Only the mirror M2 and the grating had to be exchanged.

The new beamline will cover the energy range from 10 to 40 eV with a resolving power of nearly 20.000 ($E/\Delta E$). The schematic layout of the 5m-NIM beamline is shown in figure 1. Optimal transmission is achieved with only one reflection at the grating under normal incidence. The pre-optics and the refocusing mirror are illuminated under grazing incidence, so that here only small losses arise.

The pre-monochromator optics consists of two mirrors. The first mirror M1 used from the old 3m-NIM [2]. M1 is a 1 m long toroid and is 12.5 m far away from the dipole source. The M1 is vertically lighted ($2\Theta = 168^\circ$) and producing in 12.5 m an intermediate vertical focus and in 13.6 m a horizontal focus. 0.9 m behind the intermediate vertical focus is situated the new mirror M2, a plane ellipse (130 mm x 20 mm), which is lighted under a angle of 176° , ergo the mirror deflect the beam 4° upward. The M2 produces a line focus in 0.2 m distance on the entrance slit. We use the mirror chamber of the 3m-NIM beamline with the cartesian 6-struct system [3].

By the monochromator opening angle of 4° , the light is after reflection on the grating at the exit slit again parallel to the ring level. The grating producing a 1:1 image on the exit slit. 1.5 m after the exit slit is the focusing mirror M3, which is vertically illuminate ($2\Theta = 155^\circ$). The toroidal mirror M3 produced 1m away a vertically and horizontally focus. The radius of M3 was chosen to produce the best spot for a photon energy of 21 eV in combination with a 1200 l/mm grating. On account of the monochromator opening angle of 4° the height in the experiment amounts to 1763 mm.

Monochromator

The monochromator is an off-Rowland circle normal incidence monochromator with a deflection angle of $2\Theta = 4^\circ$. Entrance slit and exit slit are fixed in position. The grating unit is 5 m far away from the slits. The monochromator action is performed by simultaneously rotating the grating in vacuum and translating the whole grating chamber in

air, whereas the translation only determines the degree of focusing [4].

The rotation is measured by an in-vacuum angle encoder (Heidenhain RON 905-UHV) with a resolution of $0.01''$, which is mounted to the rotation axis. A high precision worm gear transmission with a stepping motor enabled the translation of the grating chamber. The position of the chamber is measured with a linear encoder (Heidenhain 401R) with a resolution of $0.5 \mu\text{m}$.

On the grating unit it is possible to position three gratings, which are interchangeable in vacuum. At the beginning we will use one 1200 l/mm grating (W-coated, $\lambda_{\text{opt}} = 80 \text{ nm}$). In the future we plan to use a 600 l/mm (Al/MgF2-coated, $\lambda_{\text{opt}} = 150 \text{ nm}$) and a second 1200 l/mm or a 2400 l/mm grating (Pt-coated, $\lambda_{\text{opt}} = 40 \text{ nm}$).

Assembling of the beamline

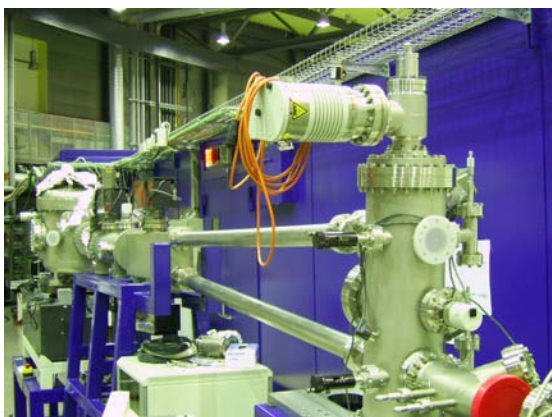


Figure 2: View from the slit chamber to the monochromator

All necessary hardware and instrumentation for this beamline has been designed and obtained. Either built, purchased or used from the old 3m-NIM. This includes all

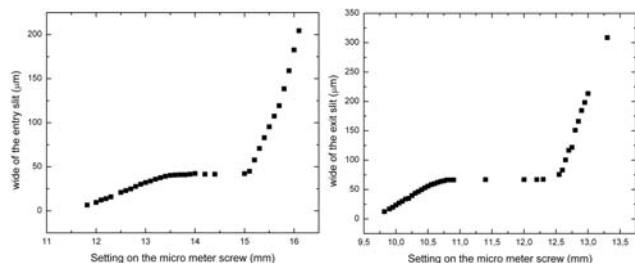


Figure 3: Width of entrance and exit slit versus micrometer screw setting

the optical and engineering design work, fabrication, installation and testing of the slit assembly, the monochromator and the vacuum chambers and programming a software under Windows 2000 for the monochromator action.

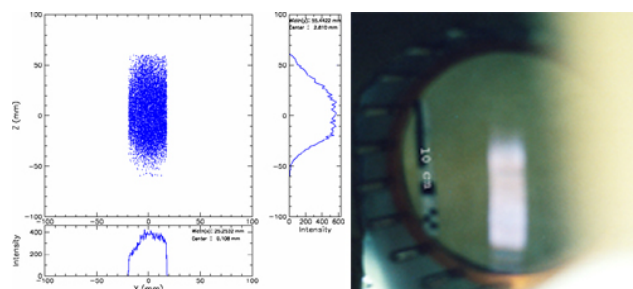


Figure 4: Size, shape and intensity on the grating as calculated with the program 'RAY' and camera picture of the light near the grating

Assembling started with the installation and testing of the new slit chamber (figure 3). The 1200 l/mm grating and the mirror M2 (all Carl Zeiss, Germany) were delivered and tested at BESSY in 2005. Until end of April 2006, the mirror M2 was installed in the mirror chamber of the old 3m-NIM beamline. The M2 chamber was mounted by a special flange on the new slit chamber. The following steps performed were the alignment of the slit chamber and all other vacuum chambers including the monochromator chamber. The first tests with white light agree very well with the ray trace calculations (figure 4).

At the beginning of the year 2007 we start with the installation of the grating and pumping the vacuum chambers. Afterwards we will start with the commissioning of the beamline.

Outlook

Initial operation of the 5m-NIM beamline on the Dipol DIP3-1B is planned for januar 2007. The beamline will then be available as a modern, high resolving beamline (figure 5) in the VUV range and will be an additional, state of the art beamline at BESSY II for measurements in the spectral energy range smaller than 40 eV. Therefore, this beamline is well suited for high-resolution photoemission, angle-resolved ultra-violet photoelectron spectroscopy (ARUPS) and Fermi surface mapping.

A new experiment station also belongs to the new beamline. The experimental station is equipped with a high-resolution photoelectron spectrometer SES-2002

from Gamma Data, with a resolution of $500 \mu\text{eV}$. A high precision manipulator equipped with a He cryostat and a high precision sample rotation stage is mounted on the experimental station. The manipulator allows angle-resolved measurements over 2π steradian below 10 K.

Furthermore an OMICRON photo emission electron microscope (PEEM) with a resolution of 20 nm is available as end station.

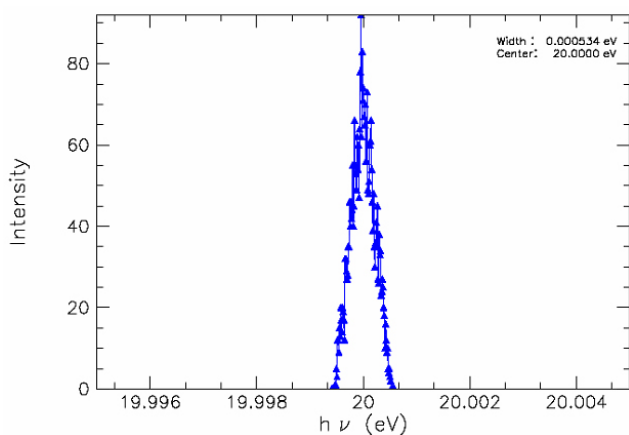


Figure 5: Approx $500 \mu\text{V}$ resolution at 20 eV photon energy for $20 \mu\text{m}$ slits (calculated with 'RAY').

The measurement time on this new beamline, about 20 weeks per year, are assigned in the context of a cooperation treaty with BESSY and our workgroup. In this time training courses for research with synchrotron radiation will be offered, which are addressed to students of the natural science departments and the new life science department in Berlin, but also with the perspective of performing courses for students from EU member states.

Today's planning provides besides the experiments for the advanced practical training also the possibility to do research for longer term projects like work on a thesis. The offer is rounded off by lessons and exercises at the Humboldt University.

Acknowledgement

We would like to thank the German Federal Ministry of Education and Research (BMBF), Project 05KS1KH11, for their financial help. The authors acknowledge the support from the staff of BESSY, especially Dr. G. Reichardt. Also we would like to thank to C. von Dewitz, R. Heimburger and S. Schmidt for technical assistance.

References

- [1] F. Schaefers and J. Feldhaus, authors of the Ray Trace Program 'RAY'. For information contact F. Schaefers, BESSY II.
- [2] R. Reichardt, T. Noll, I. Packe, P. Rotter, J. S. Schmidt and W. Gudat, *Nuc. Inst. and Meth. A* **467-468** (2001) 458–461.
- [3] T. Noll, Th. Zeschke, G. Reichardt, H. Lammert and W. Gudat *Nuc. Inst. and Meth. A* **467-468** (2001) 775–777.
- [4] J. Samson, *Techniques of Vacuum Ultra Violet Spectroscopy*, Wiley, New York (1967)

p-Reflectivity of different protective layers for Aluminium coatings above their transmission energy

G. Reichardt

BESSY, Albert-Einstein-Straße 15, 12489 Berlin, Germany

The refocussing optics of the high resolution monochromator U125/2-NIM consists of two toroidal mirrors with a platinum coating. Each mirror deflects the light by $2\Theta=155^\circ$ in p-geometry. This is the reason for a significant reduction in the transmission for light below a photon energy of 10 eV (fig.1). In the design phase for this beamline this behaviour was not of interest. Caution with respect to the influence of the undulator on the storage ring at high K-values and the immense heatload made the limitation of the onset energy to 15eV a reasonable decision for this beamline. But the operation of the beamline meanwhile showed that this onset can easily be shifted down to 3 eV without any negative influence. Thus, the optical coating of the refocussing mirrors is not well matching the capabilities of the source and needs some redesign.

In this low energy range Aluminium is a material with a very attractive high reflectivity. Unfortunately the rapid development of a natural oxide layer blemishes this attractive behaviour significantly. For most applications a protective layer of MgF_2 , SiO_2 or AlF_3 is deposited over the fresh Aluminium coating at the end of the production process. These materials are almost 100% transparent for low energy photons and preserve the high reflectivity of Aluminium in this range. Simulations with the code REFLEC [1] show that in the refocussing geometry of the U125/2-NIM these protective layers even become good reflectors with reflectivities almost equal to those of the existing Platinum coating (fig.1). So replacing the Platinum coating with a protected Aluminium coating would increase the obtainable flux by more than an order of magnitude below 10 eV without sacrificing much intensity on the high energy end.

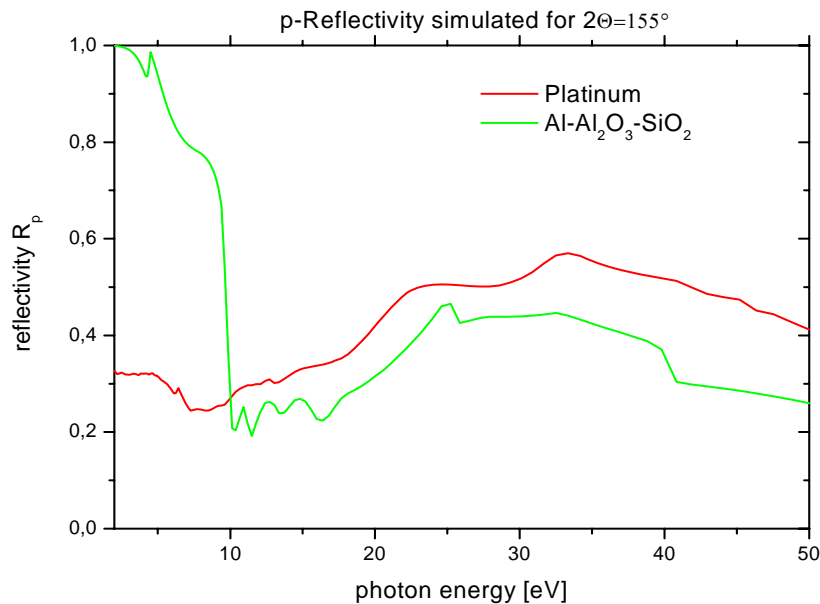


Fig.1: Simulated p-reflectivity of Platinum and Al-SiO₂(10nm)

The fact that these simulations are based on optical constants derived from crystalline materials and not from thin, in most cases porous films made some experimental investigations necessary. Three test mirrors Al-SiO₂ (Fa. Halle, SPS1), Al-SiO₂-uv-grade (Fa. Halle, SPS3) and Al-AlF₃ (FhG IOF, Jena) were investigated in a simple reflectometry set-up. By means of a GaAsP-photodiode the intensity delivered by the bending magnet monochromator 3m-NIM was recorded. For prevention of higher order contamination a MgF₂-Filter was used for the lower energy range. In a second step the SR was deflected by the test mirrors by 135° (given by the available test set-up). A photodiode of the same type was used to record these reflected intensities.

From these measurements the p-reflectivity of the coatings under test could be determined (fig.2) and compared to the simulation results. The obtained values are rather promising for an application in the refocusing optics of the U125/2-NIM system. Compared to the results obtained from simulations even better reflectivity values could be measured. The coatings Al-SiO₂ (SPS3) and Al-AlF₃ both yield reflectivities of above 80% for photon energies below the transmission limit of the protective coating. AlF₃ is even slightly more efficient in the range around 10 eV. Above 10 eV the reflectivity remains in the 20 to 30 % range up to more than 50 eV.

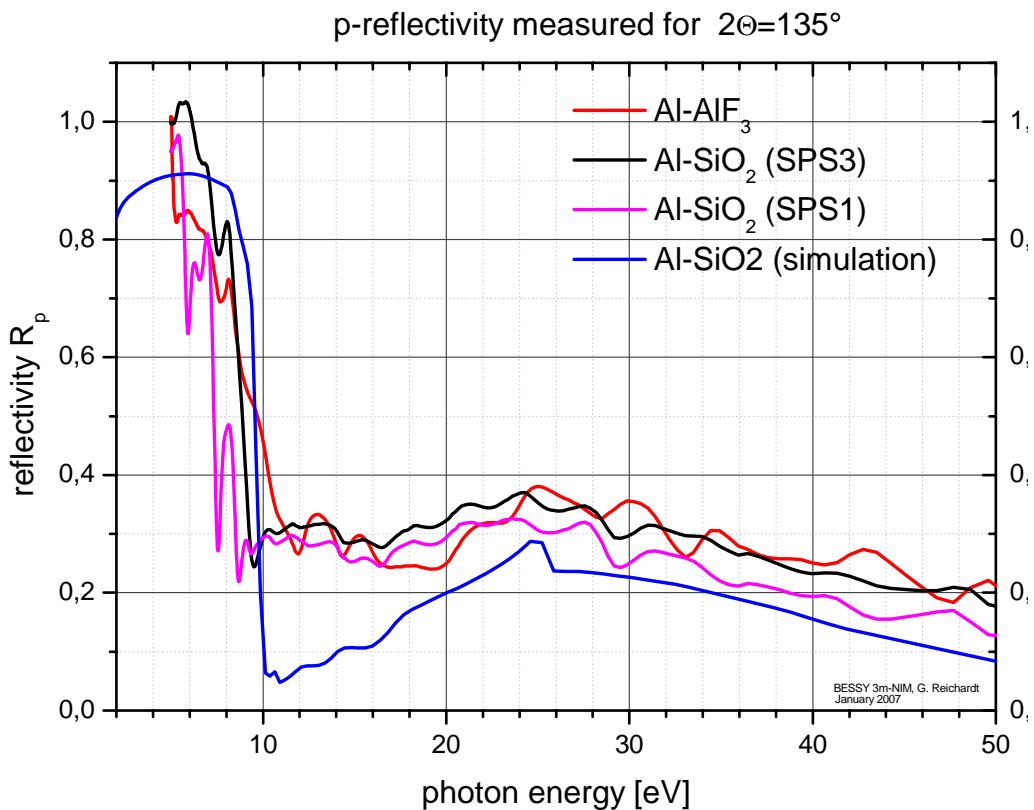


Fig. 2: measured p-reflectivity of the Aluminium samples under test.

The SPS1 coating shows significant oscillations in the reflectivity below 10eV. They can be understood in terms of an Al_2O_3 layer between the pure Aluminium and the SiO_2 protective layer. This behaviour makes SPS1 less attractive for the desired application.

Although the used simple reflectometry set-up definitely does not claim for highest precision, the obtained results are at least reasonable. Use of two different detectors, even if they are of the same type, bears a substantial risk of error. The imperfect removal of higher order contributions from the beamline (above 10 eV the MgF2-filter had to be removed from the optical path) is another error source. This error leads in general to a reduction of the measured reflectivity compared to measurements with light free of higher orders.

So it is even less understandable that we measured partially even a better reflectivity than predicted from the simulations. To some extent this can be attributed to the unknown thickness of the Al_2O_3 - and the SiO_2 -layers and their probably porous structure.

From the measurements we can conclude, that for the given geometry in the refocusing optics of the U125/2-NIM the p-reflectivity of the different protective layers for Aluminium coatings can serve as an attractive optical coating in the photon energy range up to 50 eV. For energies below 10 eV the unprecedented reflectivity of Aluminium will give rise to an intensity increase of more than an order of magnitude for the beamline U125/2-NIM, whereas above 10 eV no significant loss compared to the existing Platinum coatings has to be assumed.

[1] F. Schäfers, M. Krumrey, "REFLEC-A program to calculate VUV/X-ray optical elements and synchrotron radiation beamlines", Technischer Bericht, BESSY TB201 (1996)

The author would like to acknowledge D. Gräber and N. Kaiser (FhG IOF, Jena) for providing the Al-AlF₃ sample.

SPEEM at UE49 PGMa - commissioning status and first applications

F. Kronast, R. Ovsyannikov, A. Gloskovskii¹, G.H. Fecher¹, C. Felser¹,
H.A. Dürr and W. Eberhardt

BESSY GmbH Berlin

¹Institut für Anorganische Chemie und Analytische Chemie,
Johannes Gutenberg - Universität Mainz, D-55099 Mainz, German

Magnetic nanostructures are at the heart of modern data storage technology. Typical dimensions of magnetic bits are in the sub-100nm region. In addition novel magnetoelectronic devices such as magnetic random access memory junctions are operated on the sub- μm scale. For an understanding of magnetic properties of such low-dimensional structures spectro-microscopy tools capable of appropriate lateral resolution have to be used. The new nanospectroscopy end-station at BESSY achieves that goal by combining a novel spin-resolved photoemission microscope (SPEEM) with a dedicated microfocus PGM beamline with full x-ray polarization control (UE49-PGMa). A schematic view of the experimental setup is shown in Fig.1. The end-station is equipped with a commercial PEEM (Elmitec GmbH) capable of 20nm spatially resolution for x-ray excitation. The integrated imaging energy analyzer allows spatially resolved photoemission spectroscopy with an energy resolution of 0.4eV and it helps to minimize chromatic aberrations of the lenses. A specialty of this new instrument is the integrated spin analysis. Using two electrostatic deflectors the photoelectron beam can be deflected into one of the two attached Mott polarimeters. All three Cartesian components of the photoelectron spin can be measured using the Mott detectors. Confining the electron beam with an adjustable aperture in the last image plane of the microscope the spin polarization of areas with a minimum size down to 200nm can be analyzed.

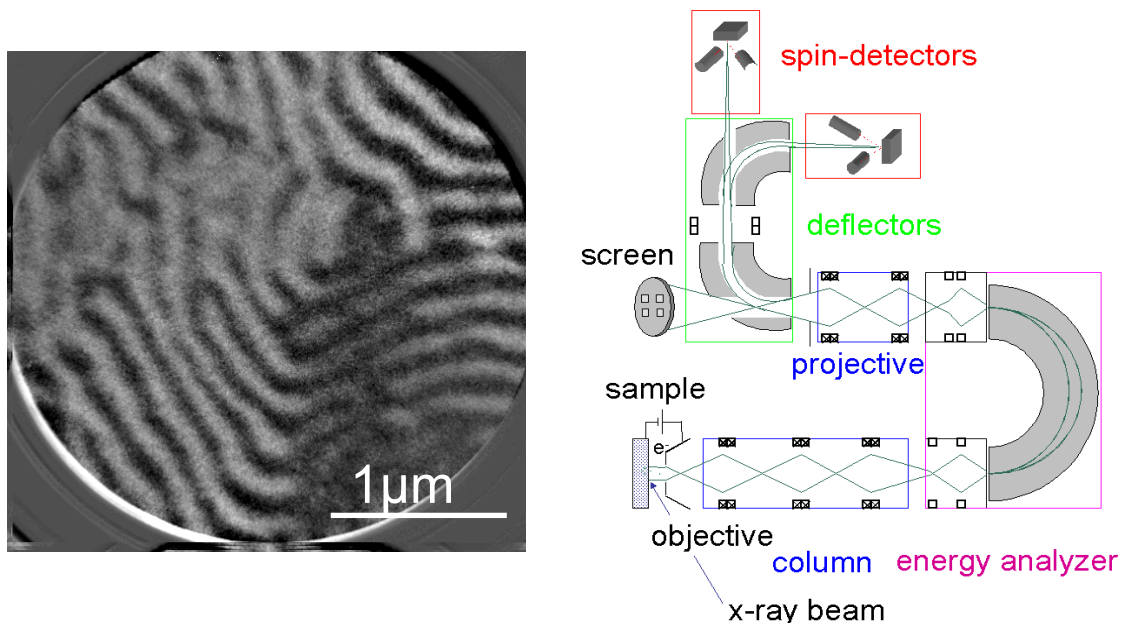


Fig. 1: The left side shows a high resolution image of magnetic domains in a Nickel film. It is the difference of two PEEM images recorded with opposite helicities at Nickel L_3 resonance. The right side schematic view of the SPEEM setup at the UE49 PGMa beamline.

The SPEEM experiment is set up at the new UE49PGMa microfocus beamline. This beamline delivers photons in an energy range from 110 to 1800eV with a flux of 10^{11} to 10^{13} ph/s/100mA and a spectral resolution $E/\Delta E$ of about 10000 at 700eV. Due to the full polarization control of the insertion device over the whole spectral range techniques like x-ray magnetic circular dichroism (XMCD) and x-ray magnetic linear dichroism (XMLD) can be employed to image magnetic domains in the PEEM mode. Dedicated optics of this beamline focus the x-ray beam onto the sample with a spot size of $8 \times 32\mu\text{m}$. Thus high photon densities at the sample surface enable reasonably short integration times in the high resolution PEEM mode and laterally resolved spin analysis.

One of the first high resolution images obtained with the SPEEM during the commissioning period in 2006 is shown on the left side of Fig. 1. It shows the magnetic domains of an in-situ prepared Nickel film, with magnetic domains of only about 100nm width. The presented image is the difference of two PEEM images recorded with opposite helicities at the Nickel L_3 resonance.

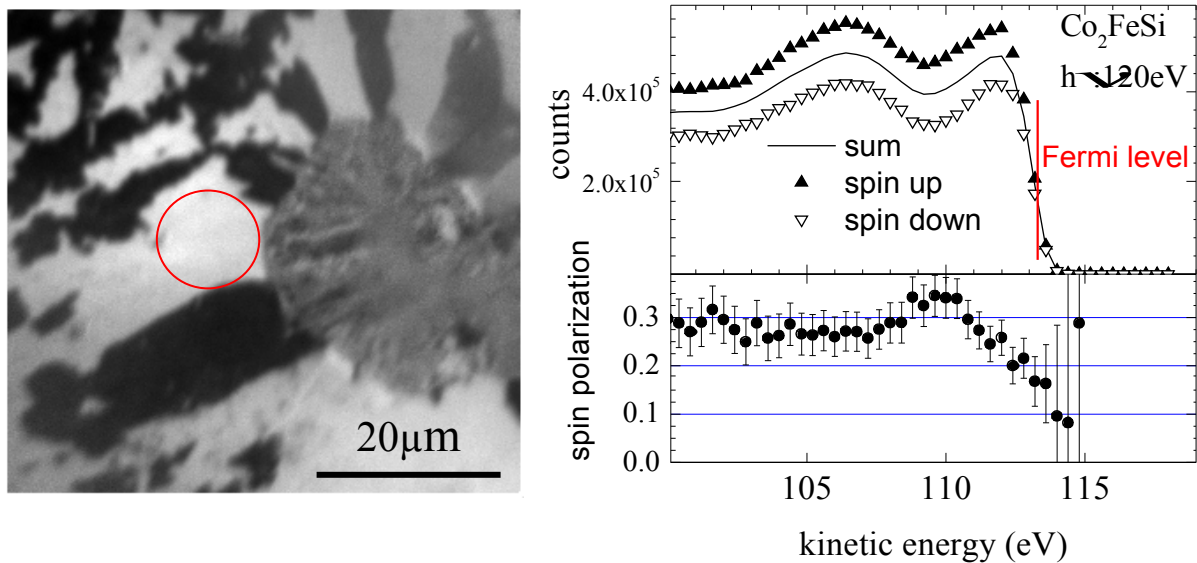


Fig.2: The PEEM image on the left shows the magnetic domain pattern in the Co_2FeSi single crystal. It is the difference of two images recorded with opposite helicities at the iron L_3 resonance. The right side shows the spin-resolved photoemission spectrum recorded from a single domain region indicated by the red circle in the left image .

The spin detection has been tested and calibrated for different magnification levels of the microscope. Since the Elmitec PEEM uses magnetic lenses to image the photoelectron distribution the in-plane spin components conduct a precessional motion while passing through the magnetic lenses of the microscope. The rotation angle of the in-plane spin components was determined for all relevant lens settings.

The potential of laterally resolved spin detection was demonstrated on a Heusler alloy single crystal of Co_2FeSi . This material is predicted to be a half metallic ferromagnet [1]. The high spin-polarization at the Fermi level in combination with a high Curie temperature makes such materials promising candidates for spintronics applications. Because of the difficult surface preparation and a complex domain pattern in remanence [2] a direct experimental prove of half-metallicity e.g. by spin-resolved photoemission is still missing. The magnetic domain pattern of the investigated Co_2FeSi single crystal is visible in the PEEM image of Fig. 2. The surface was cleaned in-situ by several cycles of Ar^+ ion sputtering and subsequent annealing at temperatures up to 500°C . This resulted in strongly reduced contamination levels of Carbon

and Oxygen as measured with laterally resolved XPS. But the surface was still showing non-stoichiometric defects like the one visible on the right side of the red circle in Fig. 2. These defects contain an increased amount of Cobalt and large magnetic domains are located around them. The magnetic domains pinned at the defect sites were selected for spatially resolved spin analysis. A spin resolved photoemission spectrum from single magnetic domain is shown in Fig. 2 (right side). Linear polarized light with a photon energy of 120eV was used for excitation. The diameter of the selected region was about 13 μ m as indicated by the red circle in Fig. 2.

The measured spin polarization at the Fermi energy of 16% is considerably higher than the one reported by Wang et al [3] for Co₂MnSi films (8-10%). But is still much lower than the expected 100% for an half metallic ferromagnet. The reduction of the spin polarization at room temperature may be caused by a thermal occupation of the minority conduction bands giving a hint on a partial loss of the half-metallicity in Co₂FeSi at elevated temperatures[4]. But the observed reduction of the spin polarization may also be caused by a non-stoichiometric surface. A fully equipped sample preparation chamber will be installed in the second half of 2007 allowing more detailed studies and in-situ preparation.

References

- [1] S. Wurmehl et al. Phys. Rev. B 72 184434 (2005)
- [2] C. Felser et al. J. of Phys. Cond. Matter 15, 7019 (2003)
- [3] W. H. Wang et al. Phys. Rev. B. 71, 144416 (2005)
- [4] A. Gloskovskii et al. Submitted to J. Phys. D: Appl. Phys.

X-ray stereo microscopy at BESSY II to study dynamics

S.-C. Gleber¹, J. Thieme¹, P. Guttman¹, S. Heim², G. Mitrea¹

¹Institut für Röntgenphysik, Georg-August-Universität Göttingen,
Friedrich-Hund-Platz 1, 37077 Göttingen

²BESSY GmbH, Albert-Einstein-Str. 15, 12489 Berlin

Introduction

X-ray microscopes using X-rays in the energy range of the water window are very well suited to image samples within aqueous media of several micrometer thickness. Now we want to extend the possibilities of X-ray microscopy into the field of the dynamical behavior of samples by using stereo methods where tomography is not applicable.

To study chemical changes as a function of time, we plan to insert soil colloids in aqueous media into the Scanning Transmission X-ray Microscope (STXM) at U41 and to take images at different energies for elemental mapping as a time series as well as at different tilting angles for stereo image processing [3].

Materials and methods

Stereo calculations can be done using the parallax equation:

$$h = \frac{\Delta Y}{2V \sin \theta}$$

This equation relates the parallax ΔY to the vertical distance h , the magnification V , and the tilting angle 2θ (θ is called stereo angle).

Based on the assumption of x-ray images as parallel projections and on the parallax equation, a program has been written to mark or select significant structures in a set of tilted x-ray images and derive information about the 3-D configuration, distances and lengths.

One possibility of a tiltable sample holder for samples in aqueous media is a thin glass capillary, used successfully in X-ray tomography [1, 2]. We took borosilicate glass capillaries of 1 mm outer diameter and 0.1 mm wall thickness. For easier filling, the capillaries have a 0.1 mm thick glass filament attached to the inner wall, increasing the capillary forces when filled with a liquid. By adjusting the parameters of the pipette pulling process, capillary tips were made with thicknesses down to 1 μm . The tips are short enough to avoid vibrations when inserted in the STXM.

For first experiments, the capillary was glued onto a standard sample holder ring (figure 2). For further dynamics studies, a holder has been designed consisting of two Si_3N_4 windows pressed together by the holder ring. A 3 μm thick photo resist layer will implement two channels of decreasing diameter from 400 to 200 μm . They will be filled with two different aqueous samples via tubes connected to the holder ring. The

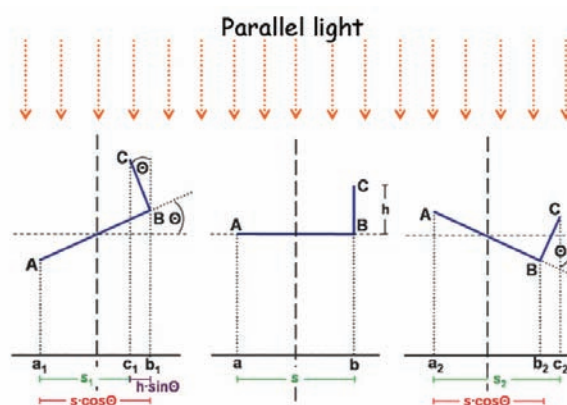


Figure 1: Parallel projection of a tilted object

liquids will meet in the middle of the holder. Images of this area will visualize the products of reactions between the two liquids.

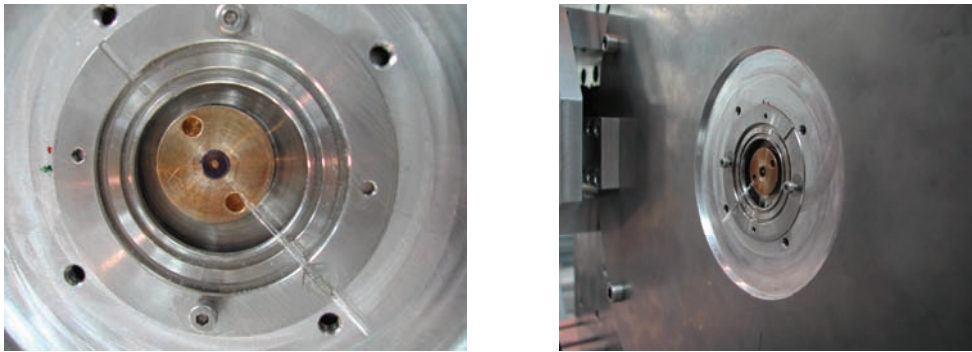


Figure 2: Capillary tip fixed improvised to standard sample holder

First experiments with capillaries and the STXM

First experiments with a capillary holder have demonstrated the suitability of the STXM for the planned experiments. No problems with sample drift or tip vibrations could be seen, and focus series showed clearly that an image focusing into the middle of the capillary includes all sample information.

The images were taken of a capillary with an outermost thickness of approx. $4 \mu\text{m}$ and a wall thickness of about $0.4 \mu\text{m}$. The glass filament is visible at the upper capillary wall. The X-ray transmission through the water filled capillary at the used energies is approx. 10 %

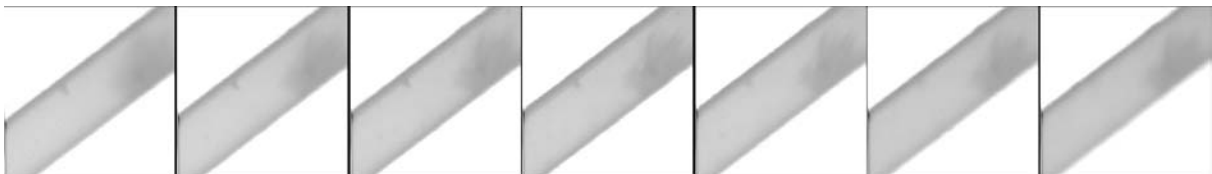


Figure 3: Capillary filled with a cluster of colloids from a chernozem soil in water. Images were taken using a zoneplate with $d_{r_n}=50\text{nm}$ at $E=400 \text{ eV}$. The dwell time was 10 ms/pixel and an area of $10 \times 10 \mu\text{m}^2$ was imaged with $200 \times 200 \text{ px}^2$. The focus stepsize is $3 \mu\text{m}$, the total time from first to last image of this series was 1 h.

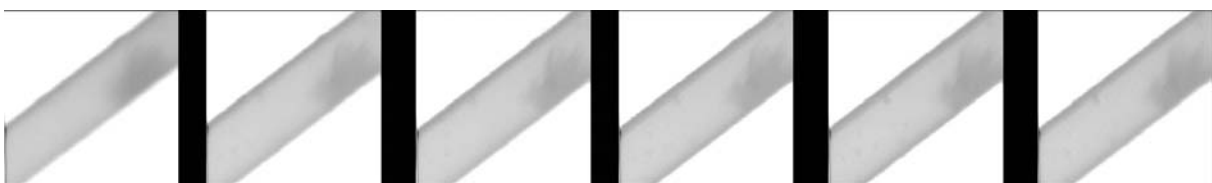


Figure 4: Same sample as in figure 3. Images taken at $E=390 \text{ eV}$ same size parameters as in figure 3. Total time of imaging the same position (figure 3 and 4) was 3 h.

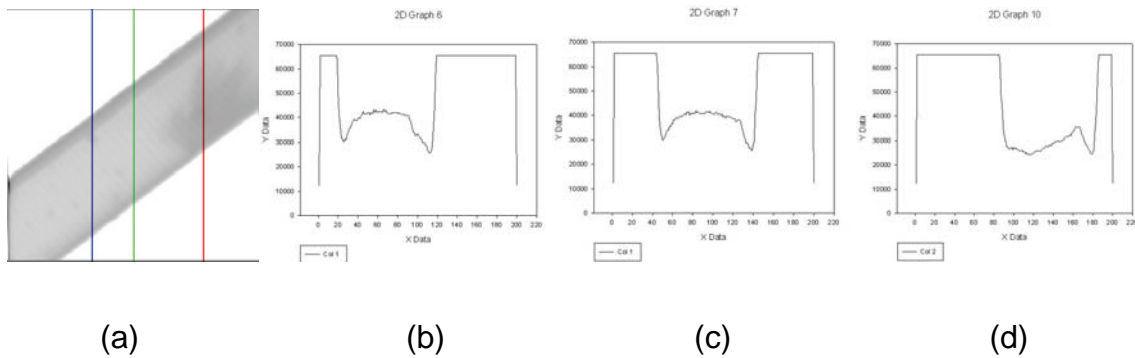


Figure 5: Line scans through 5th image of focus series shown in figure 4. (b) shows the blue line, (c) the green line, and (d) the red line visible in (a).

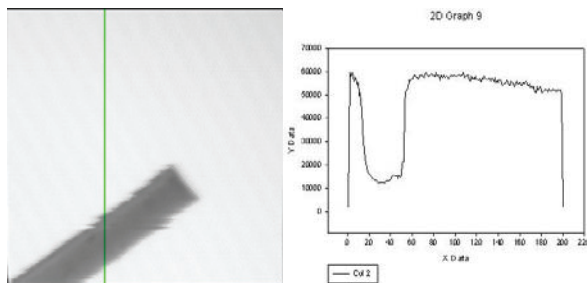


Figure 6: Micrograph of a capillary tip and a linescan through it along the green line. Image parameters as above, 6 ms exposure time per pixel.

Outlook

The STXM will be modified for controlled tilting the sample holder by a stepper motor. Further STXM improvements are described in G. Mitrea et al. in this volume.

Acknowledgements

This work has been funded by DFG under contract number Th 445/8-1. We would like to thank the staff of BESSY for providing excellent working conditions, as well as the technical staff of our institute for important technical and methodical support, and the Zoologisches Institut, Universität Göttingen, for providing their pipette puller.

References

- [1] J. Lehr: Entwicklung, Charakterisierung und Anwendung von dreidimensionalen Bildgebungsverfahren für die Röntgenmikroskopie, Dissertation, Institut für Röntgenphysik, Georg-August-Universität Göttingen, Shaker Verlag (1997)
- [2] D. Weiß: Computed tomography based on cryo X-ray microscopic images of unsectioned biological specimen, Dissertation, Institut für Röntgenphysik, Georg-August-Universität Göttingen, Cuvillier Verlag Göttingen (2000)
- [3] S. Gleber, C. Knöchel, J. Thieme, D. Rudolph, G. Schmahl: 3-D computer reconstruction of x-ray microscopy objects from stereo images, Journal de Physique IV, 104, 639 (2003)

Phase defect inspection of industrial multilayer masks for 13.5 nm optical lithography using PEEM in a standing-wave mode

J. Maul¹, J. Lin^{2,4}, A. Oelsner^{1*}, D. Valdaitsev^{1*}, N. Weber³, M. Escher³, M. Merkel³, U. Kleineberg^{2,4}, G. Schönhense¹

¹ Institut für Physik, Johannes Gutenberg-Universität, Staudingerweg 7, D-55128 Mainz,

² Fakultät für Physik, Universität Bielefeld, Postfach 100131, D-33501 Bielefeld,

³ Focus GmbH, Neukirchner Str. 2, D-65510 Hünstetten-Kesselbach,

⁴ Ludwig Maximilian-Universität, Am Coulombwall 1, 85748 Garching,

* Present address: Surface Concept GmbH, Staudingerweg 7, 55128 Mainz, Germany

Extreme ultraviolet lithography (EUVL) is widely considered to be most promising for the production of next generation semiconductor chips [1-3]. Synchrotron based techniques are well suited to investigate the performances of EUVL at a chosen photon energy. One central issue for chip production using EUVL is the quality of reflective masks with patterned absorbers, employed for the structuring of semiconductor elements. Here, the density and the properties of defects is essential [4]. For multilayer optics, two different types of defects are generally distinguished: amplitude defects and phase defects (or “buried defects”) distorting the standing electrical wave inside the multilayer and leading to variations in the field strength at the surface. In our study, we exploit synchrotron based EUV photoemission electron microscopy (EUV-PEEM) in a standing-wave mode for an “at wavelength” inspection of buried defects in multilayer mask blanks [5,6].

Fig. 1 shows the experimental scheme for EUV-PEEM measurements where the PEEM was designed for a sample illumination near normal incidence which resembles the geometry in an EUVL stepper. For this, a toroidal broadband Mo/Si multireflector (spectral range between 80eV and 100eV) was installed at an angle of 4° to the electron optical axis, near the diffraction plane of the microscope. The EUV-PEEM allows a field of view between 2.3μm and 1mm. EUV radiation from beamline UE112-PGM-1 was used in an energy range between 89eV and 97eV.

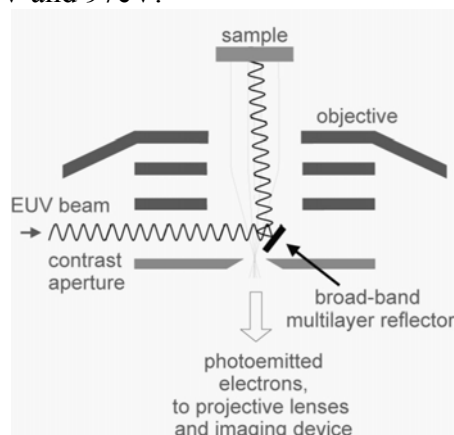


Fig. 1. Schematic of the EUV- and electron optical setup of the PEEM utilizing near normal incidence illumination.

For the resonant standing wave field arising from the superposition of incoming and reflected wave in multilayer mask blanks, the incident wave-field propagates several hundred nm deep into the Mo/Si multilayer-substrate interface. Thus, wave front distortions caused by defects can be probed with a PEEM at the multilayer surface taking advantage of high photoemission for surface regions being penetrated by standing wave antinodes and low photoemission for wave front nodes.

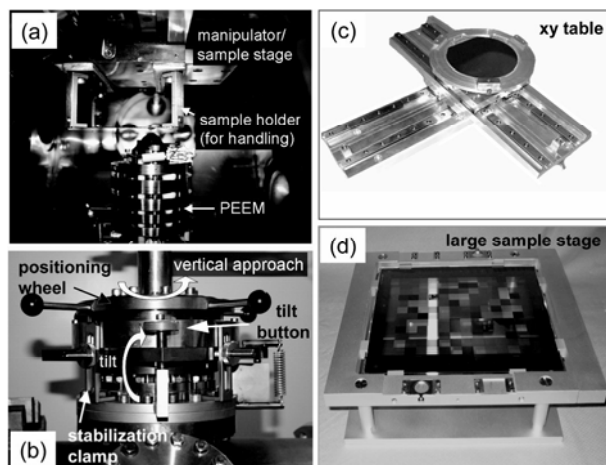


Fig. 2. Photographs of the sample positioning setup: (a) view into the UHV chamber demonstrating the adoption of sample positioning to the PEEM setup; (b) vertical approach and tilt mechanism, especially suited for large samples; (c) view of the xy-positioning table, (d) mount for six inches masks and mask blanks (for illustration, a six inches mask from AMTC GmbH & Co. KG is enclosed).

A new stage for larger samples up to six inches was required to fulfill the needs for industrial masks. The design of the novel sample positioning system and the present up-graded setup are described here. Photographs of the relevant building blocks are shown in Fig.2.

Basically, the novel repositioning system consists of a large motor-driven xy sample-positioning stage (free path of motion: 180mm*250mm, motors: Nanomotion Ltd., maximum velocity: 250mm/s, attainable resolution up to 100nm) mounted onto a vertical distance approach and tilt mechanism. Optical repositioning encoders are integrated into the xy-positioning system for a controlled sample movement, each with a resolution of 100nm. The entire unit is installed on top of the UHV chamber, the vertical distance approach and tilt mechanism thereby realizing the distance and angle adjustment relative to the PEEM installed beneath. Fig. 2a provides a view through the UHV chamber front window, the sample positioning unit mounted on top of the UHV chamber and the EUV-PEEM installed from below. Here, a provisional sample holder for first laboratory handling tests is shown. In Fig. 2b, a photograph of the vertical approach and tilt mechanism is shown. The positioning wheel for the vertical distance approach as well as one of both buttons for the tilting are marked. Fig. 2c shows the xy-positioning table. The sample holder is mounted onto the large disc visible in the center part. The large sample mount in Fig. 2d is conceived for six inches multilayer masks and mask blanks.

A six inches Mo/Si multilayer blank sample with 11nm silicon capping on top from Schott Lithotec was investigated (with 41 bilayers; each bilayer: 7nm thickness). These parameters define a nominal photon energy (i.e. reflection maximum) at 92eV (13.5nm wavelength) for 4° off-normal incidence. A field of view of $\sim 300\mu\text{m}$ in diameter was chosen for the PEEM images, and the illumination occurred within a frame of $\sim 100*300\mu\text{m}^2$ following the orientation of the exit slit in the beamline. PEEM images were recorded at different photon energies between 89eV and 97eV with energy increments of 0.5eV.

Fig. 3a gives a zoomed view of the defect, showing up from the enhanced brightness at the photon energy of $h\nu=92\text{eV}$. The linescans performed across the dotted line in Fig. 3a is shown in Fig. 3b. Here, a Gaussian curve is applied for fitting. The brightness enhancement of the defect for different photon energies is shown in Fig. 3c. It is defined by the baseline-subtracted peak maximum divided by the baseline value extracted from the direct vicinity of the defect, thus reaching values between zero and one for small brightness modulations on the baseline. At $h\nu=89\text{eV}$, only a shallow baseline modulation is recognized. At $h\nu=91\text{eV}$, a small but significant peak arises (signal-to-noise ~ 1) which notably increases for $h\nu=91.5\text{eV}$, 92eV and $h\nu=92.5\text{eV}$. It decreases for $h\nu=93\text{eV}$ and finally vanishes above $h\nu=96\text{eV}$.

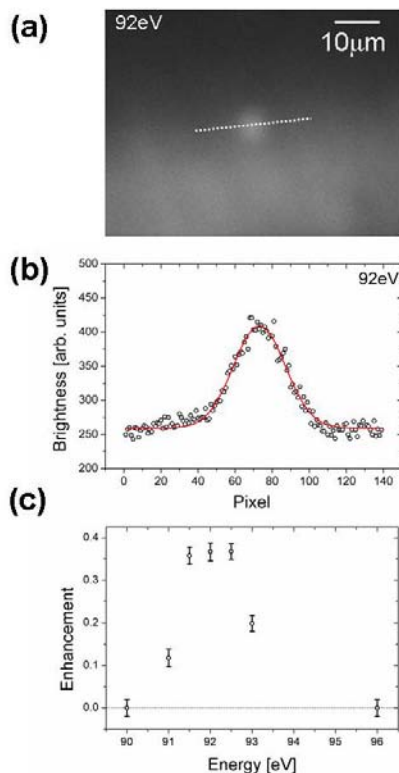


Fig. 3. Defect inspection on a six inches MoSi multilayer mask (Schott Lithotec AG).

(a) Enlarged and contrast-enhanced view of the defect. A dotted line for linescan extractions is indicated. (b) Linescan across the dotted line in (a) for a photon energy of 92eV. A Gaussian function is applied for fitting. (c) Brightness enhancement of the defect relative to the background as a function of photon energy.

From the FWHM width of the observed defect shown in Fig.3b the apparent diameter is determined to $\sim 7\mu\text{m}$ which appears to be significantly larger than the expected defect sizes of the defect in the range over several to some tens of nanometers. The defect exclusively emerged in the energy interval between 90eV and 94eV, with an energetic center position at 92eV corresponding to a wavelength of $\lambda=13.5\text{nm}$. The evolution of the brightness enhancement (Fig.3c) is clear indication of an interference-type contrast with the standing wave field at the surface. In order to check that the feature does not result from chemical contrast, the electron binding energies of elements are figured out for the relevant energy range between 90eV and 94eV, showing that the only entries correspond to Fe 3s (91.3eV) and to Zn $3p_{1/2}$ (91.4eV) [7] both materials being very unlikely on this surface.

Our results show that phase defects show up with high contrast at the nominal wavelength. Tunability is required to prove that we really observe phase defects (“buried defects”) and not structural defects like bumps or grains. Continuitive work is foreseen aiming at the use of laboratory X-Ray sources for defect inspection of multilayer masks.

This work is supported by the European Union (6th Framework program) within the project “Exploring new limits to Moore’s law- More Moore”.

References:

- [1] S. Hector and P. Mangat, *J. Vac. Sci. Tech. B* 19 (2001) 2612.
- [2] S. Bajt et al., *Opt. Eng.* 41 (2002) 1797.
- [3] G. Dattoli et al., *Nucl. Instr. Meth. A* 474 (2001) 259.
- [4] D.G. Stearns, P.B. Mirkarimi, E. Spiller, *Thin Solid Films* 446 (2004) 37.
- [5] U. Neuhausler et al., *Appl. Phys. Lett.* 88 (2006) 053113.
- [6] J. Maul et al., *Surf. Sci.*, in print.
- [7] A. Thompson et al. (Eds.), *X-Ray Data Booklet*, Center of X-Ray Optics, ALS Berkeley, USA (2006).

Optimization of a femtosecond VUV photon source based on high-order harmonic generation.

J.Gaudin*, S.Gode, K.Godehusen, O.Schwarzkopf, Ph.Wernet, W.Eberhardt

BESSY – Albert Einstein Str., 12489 Berlin

Introduction

Femtosecond lasers are nowadays a common and powerful tool for investigations of ultrafast phenomena in matter. This type of laser is nevertheless limited in terms of wavelengths to the IR and visible domain. Numerous processes such as photoemission spectroscopy however require more energetic photons in the VUV range. For these wavelengths synchrotron radiation is the best suited source but it is limited in terms of pulse duration to the picosecond range.

Two decades ago two groups showed [1,2] independently that interaction of a intense femtosecond (fs) laser pulse with a gas target enables generation of high order harmonics (HOH). This discovery paved the way for fs studies in the VUV and soft X ray domain. The high-order harmonic generation (HHG) activity at BESSY is twofold. A first experiment is optimized for investigations of ultrafast molecular dynamics with time resolved spectroscopy (see contribution of Ph. Wernet *et al.* in this report). In this experiment we use a static gas cell, which is one of the possible technical solutions for HHG. But other set-ups such as a gas jet [3] or a glass capillary also denoted hollow core fiber [4] are possible. In order to investigate and compare the HHG efficiency of these different solutions while using the same laser, we chose to build, optimize and characterize a new HHG source based on a hollow core fiber in a second experiment. Both experiments aim at adresssing science and technology of future free electron laser (FEL) sources.

Experimental results, theroretical modeling

The laser we used delivers pulses with energies up to 2,5 mJ and a duration of 60 fs (FWHM) at a 1 kHz repetition rate. The beam is focused by a 400 mm lens onto the capillary entrance. The alignment is achieved by maximizing the energy coupled through the capillary while keeping a Gaussian beam profile. The capillary itself is a simple glass tube where the gas is injected via 2 drilled holes. The aim is to get a homogeneous gas density along the beam path. The total, i.e. non monochromatized, photon flux was measured via a GaAs photodiode and a picoammeter. The

fundamental IR laser beam was blocked by a 150 nm thick Al filter. We also took images of the far field with a VUV CCD camera.

The main aim of the experiment was to determine the experimental parameters where the harmonic generation, i.e. the photon flux, is maximized. We have tested different diameters (200, 300 and 400 μm) and lengths (1,2,3...10 cm) of the capillary. The nature of the gas and its pressure are also important parameters: we have used xenon and argon. Figure 1 shows an example for the generated photon flux as a function of gas pressure. The quantum efficiency of the diode is wavelength dependent but since we do not monochromatize the harmonics, we can only give an estimation of the measured total flux. With xenon (argon) we estimate to generate up to $5 \cdot 10^7$ (10^6) photons per pulse, with a 1 cm long 400 μm capillary. The efficiency is comparable or even a bit higher than the one we obtained with the static gas cell.

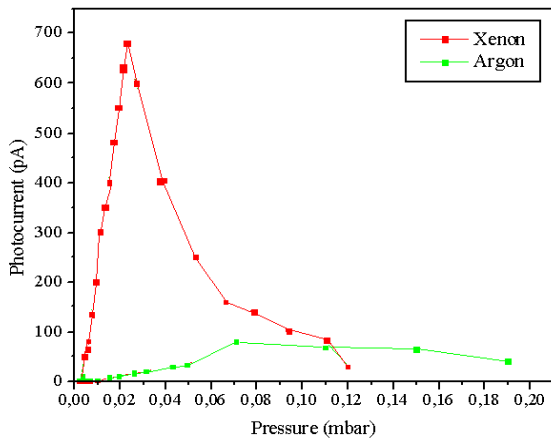


Figure 1: Photodiode signal as a function of pressure for xenon and argon. (fiber 8 cm long, 400 μm in diameter)

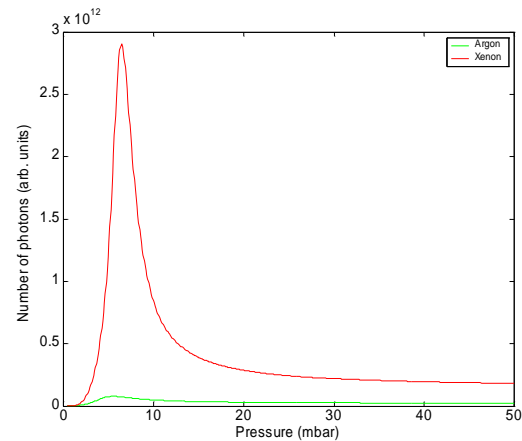


Figure 2: Calculated yield of harmonic 23 ($h\nu=35$ eV) for xenon and argon. (fiber 8 cm long, 400 μm in diameter)

In order to better understand the influence of the different parameters we simulated our results by using a simple 1D model [3]. This model enables to calculate the number of photons emitted for 1 harmonic on the propagation axis (figure 2). Starting from Maxwells equations it describes the propagation of both the fundamental laser and the harmonic beam. Even if this model is quite simple it already takes into account several parameters such as the microscopic response of the atoms (through calculated dipole moments), the effect of ionization of the medium, and the most important process on the macroscopic level: the phase matching between the fundamental and the harmonic field. This model is time dependent which allows us to take into account the fact that we deal with a Gaussian temporal profile. As can be seen in figure 2 we obtain a qualitative agreement between measured and calculated photon flux. The differences between measured and calculated pressures can

be explained by the fact that we did not measure the pressure in the capillary itself, but upstream in the gas line.

The far field harmonic beam profile generated with a 4 cm long fibre with 300 μm diameter shows a nearly Gaussian profile (see figure 3). The profile is similar for all tested fibres. We measured a full width at half maximum of 1.86 mm at a distance of 96 cm away from the source which gives a divergence of nearly 1 mrad.

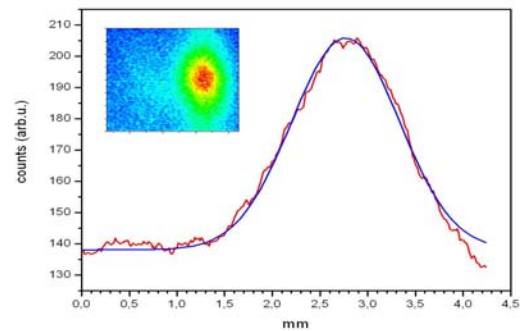


Figure 3
Profile and 2D image of far field beam.
(fiber 4 cm long, 300 μm in diameter)

Conclusions and perspectives.

We have investigated and demonstrated that HHG with a capillary is an efficient source for ultrashort VUV pulses. The generation process and the influence of various parameters such as the nature of the gas and the diameter of the capillary could be approximated with a 1D model.

The next step will be to use a deformable optical mirror in order to control the wavefront. By using an genetic algorithm we also hope to be able to enhance generation for the whole spectrum or for a specific harmonic. This could be combined with a more detailed model to get deeper insight into the HHG process.

Finally, we are investigating the possibility to use the harmonic beam for ultrafast x-ray imaging or coherent scattering. Taking advantage of the good optical properties of the beam (small divergence, Gaussian beam profile) we are planning to use diffractive optics (i.e. zone plates) to achieve femtosecond time resolved imaging with a spatial resolution of a few hundreds of nm.

References:

- [1] M. Ferray *et al.*, J. Phys. B **21**, L31 (1988).
- [2] A. McPherson *et al.*, J. Opt. Soc. Am. B **4**, 595 (1987).
- [3] Hergott *et al.*, PRA **66**, 021801(R) (2002).
- [4] A. Rundquist *et al.*, Science **29**, 1412 (1998).
- [5] E. Constant *et al.*, Phys. Rev. Let. **82**, 1668 (1999).

*contact: gaudin@bessy.de

Type I receptor recognition of GDF-5

Alexander Kotsch¹, Joachim Nickel¹, Walter Sebald^{1,2} and Thomas D. Mueller^{1,2}

¹Department of Physiological Chemistry II, Biocenter, University Wuerzburg, D-97074 Wuerzburg, Germany. ²Rudolf-Virchow Center (DFG Research Center), University Wuerzburg, D-97070 Wuerzburg, Germany

Growth differentiation factors (GDFs) and bone morphogenetic proteins (BMPs) belong to the transforming growth factor- β (TGF- β) superfamily of multifunctional cytokines. Members of this superfamily control many steps of the embryonal development and are also crucial for organ homeostasis in the adult organism. Due to their involvement in the control of bone and cartilage formation several BMP proteins are already used in therapeutic treatments. Their importance for organ homeostasis however makes them an attractive target for the so-called regenerative medicine.

Signaling of ligands of this superfamily is achieved by binding to two types of single transmembrane serine/threonine kinase receptor chains classified as type I and type II. Binding and activation of these receptors occurs usually via a sequential binding mechanism. The ligand binds first to its high-affinity receptor chain, depending on the ligand this can be either a type I or a type II receptor. Then the low-affinity receptor chain is recruited into the binary ligand-receptor complex initiating the intracellular signal cascade, e.g. via the SMAD signaling proteins. An interesting feature of all members of the TGF- β superfamily is that they can bind to more than receptor of a particular subtype. In addition a particular receptor can also bind more than one ligand. These special binding properties of members of the TGF- β superfamily result in a pronounced promiscuity of the ligand-receptor interaction. It is thus especially remarkable that for some of the ligands receptor specificity is absolutely crucial (Sebald et al., 2004). GDF-5 binds to the type I receptors BMPR-IA and BMPR-IB with only a 10-fold difference in affinity, but only binding to BMPR-IB results in GDF-5 signaling (Nickel et al., 2005). This is related to observations *in vivo* that mutations in either GDF-5 or BMPR-IB (but not in BMPR-IA) result in a similar phenotypic disease called brachydactyly or symphalangism.

We have crystallized two ligand-receptor complexes of GDF-5 bound to BMPR-IA and a chimeric variant of BMPR-IA resembling the BMPR-IB receptor. The complex of GDF-5 bound to BMPR-IA was obtained by using a GDF-5 variant GDF-5R57A that exhibits a 10-fold increased affinity for the BMPR-IA receptor. Interestingly despite the higher affinity this GDF-5 variant is still inactive in various cell-based assays showing that the lower affinity in the wildtype ligand-receptor interaction is not the reason for the lack of activity. The structure

of this complex could be determined from high-resolution data obtained at BESSY. The structure of the complex is highly similar to that of BMP-2 bound to BMPR-IA (Keller et al., 2004). The location of the receptor on both ligands is almost identical, similar intermolecular polar interactions (H-bonds and salt bridges) suggest that recognition of the GDF-5 variant and BMP-2 by BMPR-IA is highly similar.

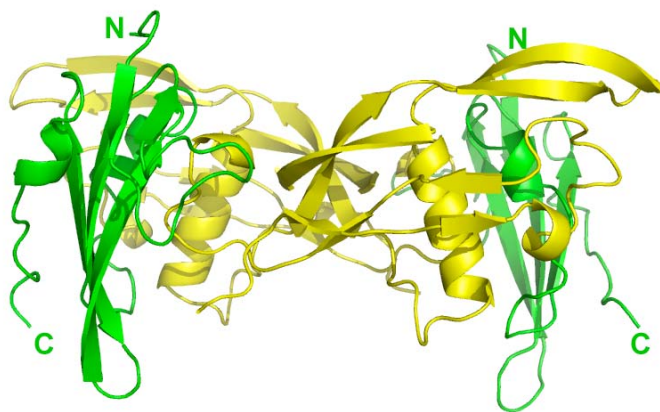


Fig. 1: Structure of the complex of GDF-5R57A (yellow) variant bound to two receptor ectodomains BMPR-IA (green). The N- and C-termini of the receptor ectodomains are indicated, both C-termini point towards the putative membrane surface.

In order to understand whether binding and recognition of GDF-5 by BMPR-IA and BMPR-IB are different, we have tried to crystallize the complex of GDF-5 bound to BMPR-IB, however, despite extensive screening all trials were unsuccessful so far. We have therefore used a chimeric variant of BMPR-IA in which all residues (18 residues) in the ligand binding epitope have been exchanged for those of BMPR-IB (Nickel et al., 2005). Analysis of the binding properties were tested with BMP-2 and GDF-5 showing that this chimeric variant (A3BEA6) exhibits all the binding properties of wildtype BMPR-IB and thus might be used as a model. Crystals of such a complex could be obtained, however initial analysis using molecular replacement techniques failed. We have therefore recorded a three wavelength MAD dataset using a Se-Met labeled GDF-5:A3BEA6 complex. Analysis of the complex structure is ongoing, but first results show that in both complexes the location of the receptor on the ligand is unchanged. The ligand itself seems not to adapt to the different receptor surface, but some parts of the receptor, BMPR-IA and the BMPR-IB-BMPR-IA chimera, exhibit different backbone and side chain conformations. The largest differences between both receptors are in the $\beta 1\beta 2$ -loop and the short helical element (see figs. 2a,b). The latter is especially noteworthy since the helical element carries the main-binding determinants for the ligand-receptor interaction, thereby possibly explaining the differences in the binding affinities of the ligand to both receptor molecules.

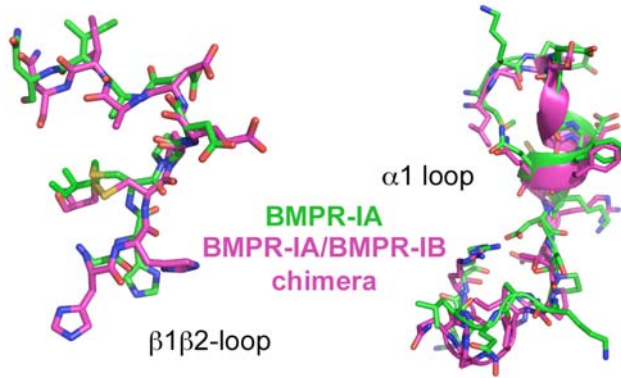


Fig. 2: Segments of the receptors BMPR-IA and BMPR-IA/BMPR-IB chimera that differ most in the ligand-receptor complex structures. The most prominent differences in the structures of both bound receptor molecules is the length of the helical element $\alpha 1$. In the receptor BMPR-IA the helix is longer and seems more stable, whereas in the chimera that resembles the binding properties of BMPR-IB this element is shortened. Since this element also carries the main binding determinants, this might explain the differences in binding affinities observed for the GDF-5 ligand receptor interaction.

1. Keller, S., Nickel, J., Zhang, J.L., Sebald, W. and Mueller, T.D. (2004) Molecular recognition of BMP-2 and BMP receptor IA. *Nat Struct Mol Biol*, 11, 481-488.
2. Sebald, W., Nickel, J., Zhang, J.L. and Mueller, T.D. (2004) Molecular recognition in bone morphogenetic protein (BMP)/receptor interaction. *Biol Chem*, 385, 697-710.
3. Nickel, J., Kotsch, A., Sebald, W. and Mueller, T.D. (2005) A single residue of GDF-5 defines binding specificity to BMP receptor IB. *J Mol Biol*, 349, 933-947.

Determination of the effective atomic number of human nails using X-Ray Transmission

E. Mavromati¹, M. Katsikini^{1,*}, F. Pinakidou¹, D. Ioannides², E.C. Paloura¹ and A. Erko³

¹*School of Physics, Aristotle University of Thessaloniki, Thessaloniki, 54124, Greece*

²*School of Medicine, Aristotle University of Thessaloniki, Thessaloniki, 54124, Greece*

³*BESSY mbH, Albert Einstein 15, 12489, Berlin, Germany*

We propose a method for the determination of the effective mass attenuation coefficient and the effective atomic number, Z_{eff} , of human nails using Synchrotron Radiation (SR) X-ray transmission. In materials with complex structure and composition, such as biological samples, the effective atomic number Z_{eff} is considered as the atomic number of an imaginary element that scatters and absorbs equivalently to the average of all the elements that comprise the nail¹. Scattered radiation is used to evaluate absorption effects from light element matrix in biological materials. In the analysis of environmental, biological and geological samples, where the presence of low - Z elements dominates the absorption effects, the X-ray transmission method can be applied in order to get an estimation of the mass absorption coefficient of the irradiated mass and consequently the effective atomic number².

The studied samples are nails that were collected from thirteen donors at the Hospital of Venereal and Dermatological diseases of Thessaloniki. Human nails, in a similar fashion to hair, are considered a modified type of epidermis that consists of compact layers of dead cells of epithelium formed by α – keratin. Both materials can be used to monitor the concentration of the essential for the organism elements which, on the basis of their concentration, are usually grouped as major (e.g. Mg, Ca) or trace (e.g. Cu, Zn). Thus, human nails can be viewed as layered materials that consist of relatively heavy elements embedded in a light matrix. In order to test the reliability of the applied method for the determination of the Z_{eff} , a PET (Polyethylene Terephthalate) sample of known composition ($\text{C}_{10}\text{H}_8\text{O}_4$) was used as a reference material. The PET sample was chosen because polymers consist of light elements and thus mimic the nail matrix. The thickness of the nails and the PET sample was measured using an electronic calliper. The X-ray transmission measurements were conducted at the KMC-II beamline. The intensity of the transmitted X-rays was measured at 7.5keV and 10.5keV with the sample positioned normal to the beam. The intensity of the impinging, I_0 , and the transmitted, I , beam was measured using two ionization chambers. The I/I_0 ratio was normalized with the corresponding ratio measured in the absence of any sample in order to account for the different characteristics of the detectors, as for example the internal and electronic amplification.

The attenuation of the X-ray beam after penetrating a sample of thickness d and density ρ is given by Beer's law $I = I_0 \exp[-\rho d(\mu/\rho)_{\text{eff}}]$ [eq. 1]. The subscript "effective" is referred to the mass attenuation coefficient of the irradiated mass. Thus, if the I/I_0 ratio is experimentally determined and the ρd product is known, the effective mass attenuation coefficient can be calculated. The value of the mass attenuation coefficient of an element is mainly determined by its atomic number. For a sample of known composition the effective atomic number, Z_{eff} , is

defined as¹ $Z_{\text{eff}} = \frac{\sum_i w_i A_i Z_i}{\sum_i w_i A_i}$ [eq. 2], where w_i , A_i and Z_i are the weight fraction, the atomic mass

and the atomic number of the element i , respectively. For a sample of unknown composition the Z_{eff} can be calculated after interpolating the known μ/ρ values of the elements in a specific range of values of Z .

As far as the PET sample is concerned the Z_{eff} was calculated using equation [2] and is found equal to 6.81. The corresponding values of μ/ρ were determined using the law of Beer and the values of $\rho = 1.37 \text{ gr/cm}^3$ and $d = 0.021 \text{ cm}$. The experimentally determined values of μ/ρ were found equal to $8.627 \pm 0.302 \text{ cm}^2/\text{gr}$ and $2.793 \pm 0.097 \text{ cm}^2/\text{gr}$ at 7.5 and 10.5 keV, respectively.

The Z_{eff} of PET can be graphically determined from the μ/ρ versus Z plots shown in Fig. 1, which were constructed using the data of absorption coefficients published by Henke *et al*³, for elements with Z ranging from 1 to 10. By performing least square fitting of the two curves shown in Fig. 1, using polynomial functions for $4 \leq Z \leq 10$, it is possible to determine the values of Z and the corresponding errors. Indeed, by following this procedure it is shown that the Z_{eff} of PET is equal to 6.947 ± 0.071 and 6.679 ± 0.068 at 7.5 and 10.5 keV, respectively. These values yield an average of $Z_{\text{eff}} = 6.86 \pm 0.09$ which is in very good agreement with the value of Z_{eff} which is determined using the analytical equation [2]. Therefore, by following the same procedure, we can determine the Z_{eff} of the nail samples. The variation of $\ln(I/I_0)$ on ρd for all studied nails at the energies of 7.5 keV and 10.5 keV is shown in Fig. 2.

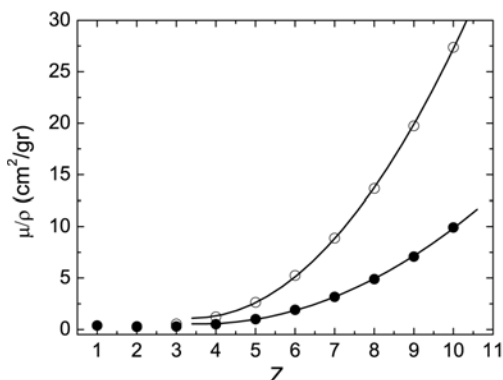


Figure 1: Dependence of the mass attenuation coefficient on the atomic number of the first 10 elements of the periodic Table at 7.5 keV (open circles) and 10.5 keV (solid circles).

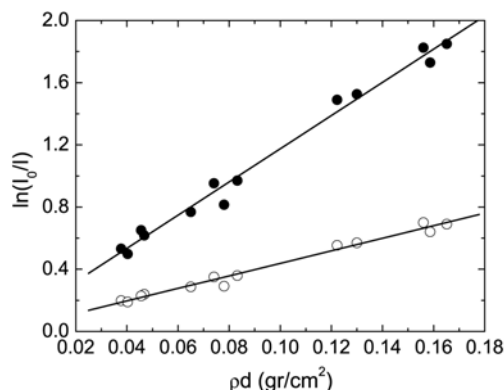


Figure 2: Neperian logarithm of the I_0/I as a function of the product of the density with the thickness of the nail samples at 7.5 keV (solid circles) and 10.5 keV (open circles).

The average effective mass attenuation coefficient of the nail samples can be determined from the slope of the curves shown in Fig. 2 and is found equal to 10.68 ± 0.37 and $4.03 \pm 0.16 \text{ cm}^2/\text{gr}$, at 7.5 keV and 10.5 keV, respectively. The assigned errors are the uncertainties in the determination of the slope with the least square fitting method. As in the case of the PET sample, the Z_{eff} of the nails at 7.5 and 10.5 keV can be determined from the curves shown in Fig. 1, either graphically or using the least square fitting method described above. Indeed, the value of the Z_{eff} is found equal to 7.399 ± 0.077 and 7.539 ± 0.090 , at 7.5 and 10.5 keV, respectively, resulting to an average Z_{eff} equal to 7.47 ± 0.07 . This value is very close to the Z_{eff} of hair which was found equal to 6.73 with the application of a similar method⁴.

The Z_{eff} of human nail is also calculated analytically using equation [2] and by taking into account the mass fractions of the various amino acids that are present in the nails. The concentrations of seventeen amino acids in human nails, which range from 0.7-16.7 wt % have been reported previously⁵. In particular, these amino acids are alanine ($\text{C}_3\text{H}_7\text{O}_2\text{N}$), arginine ($\text{C}_6\text{H}_{14}\text{O}_2\text{N}_4$), aspartic acid ($\text{C}_4\text{H}_7\text{O}_4\text{N}$), cysteine ($\text{C}_3\text{H}_7\text{O}_2\text{NS}$), glutamic acid ($\text{C}_5\text{H}_9\text{O}_4\text{N}$), glycine ($\text{C}_2\text{H}_5\text{O}_2\text{N}$), histidine ($\text{C}_6\text{H}_9\text{O}_2\text{N}_3$), isoleucine ($\text{C}_6\text{H}_{12}\text{O}_2\text{N}$), leucine ($\text{C}_6\text{H}_{13}\text{O}_2\text{N}$), lycine ($\text{C}_6\text{H}_{14}\text{O}_2\text{N}_2$), methionine ($\text{C}_5\text{H}_{11}\text{O}_2\text{NS}$), phenylalanine ($\text{C}_9\text{H}_{11}\text{ON}$), proline ($\text{C}_5\text{H}_9\text{O}_2\text{N}$), serine ($\text{C}_3\text{H}_7\text{O}_2\text{N}$), threonine ($\text{C}_4\text{H}_9\text{O}_3\text{N}$), tyrosine ($\text{C}_9\text{H}_{11}\text{O}_3\text{N}$) and valine ($\text{C}_5\text{H}_{11}\text{O}_2\text{N}$). Using the concentrations of the various amino acids reported by Greaves and Moll the value of the Z_{eff} is found equal to 7.47. These values are in very good agreement with the value of the Z_{eff} that is determined experimentally with X-ray transmission measurements.

¹ R. P. Alvarez, P. Van Espen, A. A. Quintana, *X-Ray Spectrometry*, **33**, 74 (2004).

² S. X. Bao, *X-Ray Spectrometry* **27**, 332 (1998).

³ B. L. Henke, E. M. Gullikson, J.C. Davis, *Atomic Data and Nuclear Data Tables*, **54**, 213 (1993).

⁴ H. Kubo, *Phys. Med. Biol.* **26**, 867 (1981).

⁵ M. S. Greaves, M. H. J. Moll, *Clinical Chemistry*, **22/10**, 1608 (1976).

NEXAFS Surface Chemical Characterisation of Atmospheric Pressure deposited N-rich Plasma-Polymer Films for Tissue Engineering

P.-L. Girard-Lauriault¹, M.R. Wertheimer¹, A. Lippitz² and W.E.S. Unger²

¹ *Department of Engineering Physics, Ecole Polytechnique, Montreal, Canada*

² *Bundesanstalt für Materialforschung und -prüfung (BAM), Berlin, Germany*

Biotechnological applications show an ever-increasing need for surfaces permitting control over cell functions. These so-called "smart" surfaces are specifically engineered to provide solutions to particular challenges. One possible solution involves the use of engineered surfaces that permit better control of the cell environment and thus obtaining phenotype conservation and control over gene expression. It is known that most cell types do not adhere to hydrophobic polymer surfaces like polyethylene, polypropylene, polystyrene or PTFE. However, hydrophilic surfaces, for example those functionalized by plasma or VUV treatments, are known to promote cell adhesion. We report a promising novel material, nitrogen-rich plasma-polymerised small hydrocarbons (PP:N), which are deposited on various substrates of interest, using an atmospheric pressure dielectric barrier discharge (DBD) apparatus [1]. Their characteristics, high nitrogen content and high surface energy, render them promising candidates for providing tailored solutions to the challenges described above. We have previously reported [1] that plasma polymerised ethylene films (PPE:N) with high nitrogen content ([N]) were particularly good at influencing cell processes. We demonstrated reproducible, selective adhesion for, e.g., U-937 human macrophages on PPE:N surfaces. We have also shown the critical importance of nitrogen concentration, [N], by correlating the adhesion of different cell types on surfaces with varying [N]. However, the mechanisms involved in these processes are still elusive. Given the high chemical complexity of PPE:N surfaces, careful analysis is required in order to proceed forward in our understanding of cell-surface interactions. In this case, the combined information yielded by many techniques is required in order to obtain a chemical mapping of the material's surface. In this short communication we demonstrate the effectiveness of near edge x-ray absorption spectroscopy (NEXAFS) for that purpose.

For the experiments reported here, PPE:N films were deposited on biaxially oriented polypropylene (BOPP) for cell culture experiments, on glass for XPS and FT-IR characterisations and on silicon wafers for NEXAFS. The atmospheric pressure plasma deposition system is described in detail in refs. [1]. Essentially it comprised a moveable aluminium plate electrode, on which substrates were uniformly coated by a dielectric barrier discharge (DBD). Using this apparatus, films containing a high and controllable total nitrogen content, [N], were deposited from the precursor gas mixture composed of nitrogen (N₂, 10 slm) and a small hydrocarbon such as methane, ethylene or acetylene (CH₄, C₂H₄, C₂H₂, from 10 to 60 sccm). The surface compositions of films were determined by XPS. Analyses of unsaturated groups were performed by NEXAFS (C, N and O K-edges) and FT-IR. Noteworthy is the partial characterization of chemical functionalities: derivatisation experiments have always given primary amine concentrations < 10% of [N]. Details of used cell culture methodology are available in refs. [1].

In order to demonstrate the great potential of PPE:N for cell culture and tissue engineering, a wide variety of experiments have been conducted, using nominally 200 nm of PPE:N with a certain N surface concentration, deposited on the substrate of particular interest. One of these experiments was testing the cell adhesion of U-937 macrophages. Coated substrates with [N] values ranging from 36.3% downward to 17.5% were then exposed to concentrated cell suspensions. Figure 1 show such micrographs of macrophages for the cases [N] = 25% and 23%, respectively. Obviously a "critical" value of nitrogen concentration, [N]_{crit}, exists between 25% and 23%, a value below which this cell-type does not adhere to PPE:N.

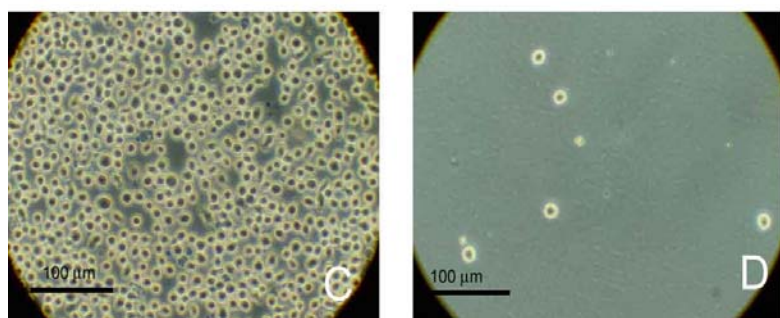


Figure 1: Cell culture results from refs. [1]: Adhesion of U-937 macrophages to PPE:N films on BOPP, after 1hr of culture: (C) 25% [N], (D) 23% [N]

Composition of PP:N films with regards to both elemental composition and specific functional groups was thoroughly investigated with the final goal to correlate cell adhesion with surface chemistry data. NEXAFS C, N and O K-edges were acquired at the HE-SGM beamline

for each of the PP:N films but, for length concerns, only the results gathered from PPE:N C K-edges are shown as an example here. First results revealed that for all films the structures originating from alkenyl, imine and nitrile groups were identified in accordance with the literature and standard materials such as poly(acrylonitrile), as a nitrile reference, and poly(ethyleneimine) as an amine reference. Obviously, the surface concentrations of unsaturated N species exceed that of amines in many cases. With the help of N K-edge NEXAFS different unsaturated N species can be semi-quantitatively differentiated and the influence of plasma parameters on these features can be studied. It is expected that this information will promote the understanding of cell adhesion phenomena.

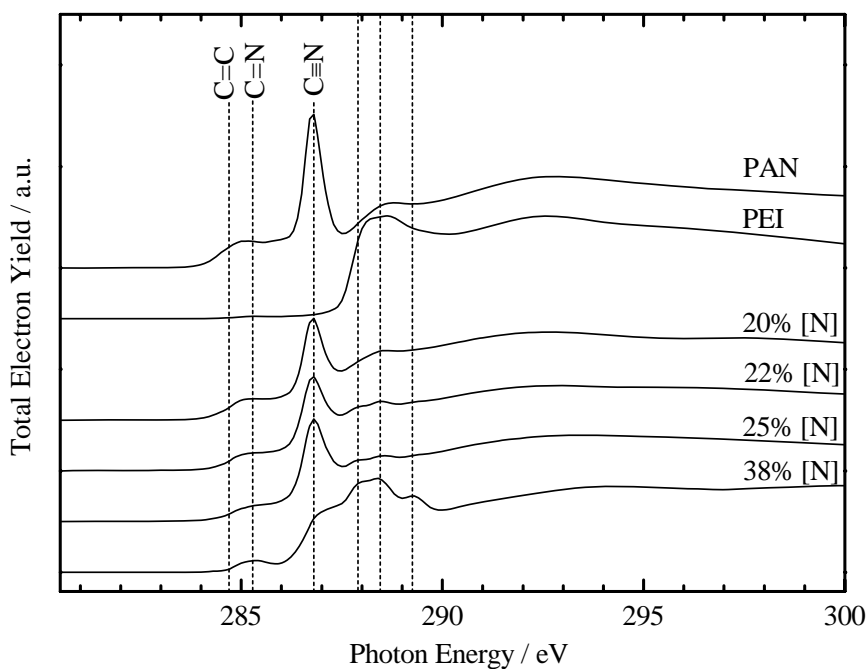


Figure 2: C K-edges of PPE:N films with [N] varying from 20% to 38%. The respective edges of the references poly(acrylonitrile), PAN, and poly(ethyleneimine), PEI, are given, too.

Acknowledgements: P.-L.G.-L. and M.R.W. gratefully acknowledge financial support from NanoQuebec and NSERC.

- [1] N. A. Bullett, D. P. Bullett, F.-E. Truica-Marasescu, S. Lerouge, F. Mwale, M. R. Wertheimer, *Appl. Surf. Sci.* **235**, 395 (2004), and P.-L. Girard-Lauriault, F. Mwale, M. Iordanova, C. Demers, P. Desjardins, M. R. Wertheimer, *Plasma Proc. Polym.* **2**, 263 (2005).

Nano-structure of different drug delivery systems studied by synchrotron radiation

M. Kumpugdee-Vollrath, P. Opanasopit¹, P. Guttman², I. Zizak³, A. Hoell³

Department of Pharmaceutical Engineering, University of Applied Sciences Berlin (TFH),
Luxemburger Str. 10, D-13353 Berlin, Germany, Email: vollrath@tfh-berlin.de,

¹Silpakorn University, Nakorn Pathom, Thailand,

²University of Goettingen, c/o BESSY, Albert-Einstein-Str. 15, D-12489 Berlin, Germany,

³Hahn-Meitner-Institute Berlin, Glienicker Str. 100, D-14109 Berlin, Germany

1. ABSTRACT

Nowadays several drug delivery systems are available e.g. liposomes, lipid emulsion, micellar solution, nanoparticles, etc. This present work is based on these systems in order to understand deeply their structures during formulations. Finally the most suitable system for being used as a site specific delivery system of the model drugs can be chosen. The determination of the structure in nanoscale was performed by using synchrotron radiation in different instruments e.g. SAXS and X-ray microscopy.

2. INTRODUCTION

Different nano-delivery systems e.g. liposomes, niosomes, lipid emulsion, micellar solution and nanoparticles are available as drug delivery systems in the pharmaceutical field. Advantages and disadvantages of these systems are discussed in the literature [1]. However, there are only few systems which work as an active site delivery system. Therefore the target of the project is to find out the most suitable system for delivery of model drugs (hydrophilic and hydrophobic drugs). Formerly researchers have mostly used the classical techniques e.g. light scattering, electron microscopy, etc. in order to characterize these delivery systems. The interpretation of the structure in nanoscale is mostly built up on the approximation base on theory. In this project the modern characterizing techniques such as small angle x-ray scattering (SAXS) and x-ray microscopy were used additionally to the classical one and the results can provide a better understanding in nanoscale of the structure of these delivery systems [2]. The modern synchrotron sources, like BESSY II, with their intense and highly collimated x-ray beams and the development of suitable lenses, i.e. Fresnel zone plates, have involved that x-ray microscopy is a powerful imaging method in different application fields. Nowadays, x-ray microscopy offers a lateral resolution of about 20 nm. Moreover the measurements can be performed with wet samples with only small volume (~ µl). The structure of the core and shell of the wet systems e.g. micelles or nanoparticles can be determined. On the other hand the SAXS technique can give information about the secondary structure (gel-, liquid crystalline-, hexagonal phase) as well as the phase transition temperatures.

3. MATERIALS

Different nano drug delivery systems e.g. polymer micelles, lipid emulsion and liposomes were investigated in this present work.

3.1 Polymer Micelles:

The synthetic polymer N-phthaloylchitosan-grafted poly (ethylene glycol) methyl ether was used to entrap different drugs (hydrophilic and hydrophobic) by a dialysis method [3].

3.2 Lipid Emulsion:

In order to prepare lipid emulsion the medium chain triglyceride, lecithin, surfactant, drug and water were mixed together by the emulsification method [4].

3.3 Liposomes:

The dry film method was used to prepare liposomes from different phospholipids. Different drugs were incorporated into the liposomes [5].

4. METHODS

4.1 Small Angle X-ray Scattering (SAXS)

The experiments were performed at the new SAXS instrument of the Hahn-Meitner Institute (7T-MPW-SAXS) installed at the synchrotron source BESSY in Berlin, Germany. The scattering patterns were acquired using a 2D position sensitive gas detector with delay line read out (Molecular Metrology). The samples (3.1-3.3) were measured at room temperature under vacuum conditions by using quartz capillaries of about 1 mm of thicknesses as sample holders (Fig. 2) at energy of 8000 eV. The resolution is about 1 nm.

4.2 X-ray Microscopy

The experiments were performed at the soft x-ray microscope (U41-TXM), BESSY, Berlin, Germany. About 5 μl of the sample (3.1) was placed in the sample holder (Fig. 4) and the thickness of the sample was adjusted to below 10 μm . The images were taken in amplitude contrast mode at the wavelength of 2.4 nm (~ 524 eV) at room temperature. The sample was placed vertically to the radiation with the dimension of maximum 3 mm. The lateral resolutions during the experiments were about 25 nm due to the objective in use.

5. RESULTS AND DISCUSSION

5.1 SAXS

The x-ray scattering curve (Fig. 2) of the liposomes loaded with the drug lidocaine HCl (water soluble) shows two peaks at different Q-values. The peak positions differ after addition of the drug to the liposomes which means that the structure of the liposomes had changed. The similar result was shown with the SAXS data from the lipid emulsion (Fig 3). The scattering curve of the polymer micelles showed a broad spectrum which means that the micelles has an small unilamellar structure (data not shown).

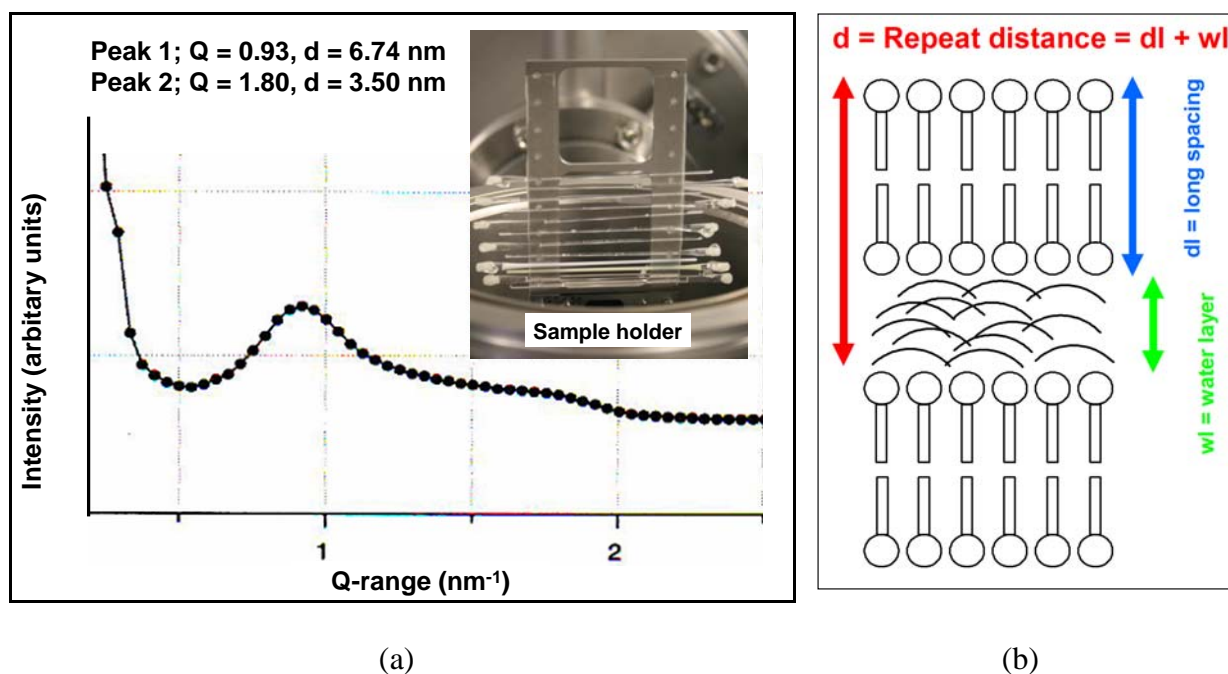


Figure 2: (a) SAXS data of liposomes loaded with the drug lidocaine HCl, the magnification of sample holders, (b) the repeat distance consists of lipid bilayer and water layer.

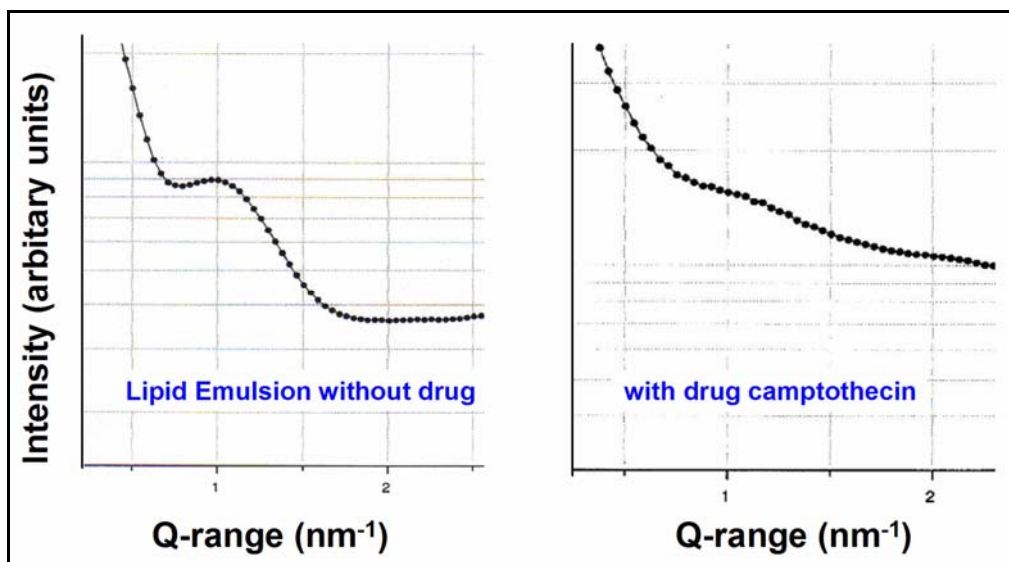


Figure 3: Lipid emulsion without drug ($Q = 1.07 \text{ nm}^{-1}$, $d = 5.89 \text{ nm}$) and with the drug camptothecin ($Q = 1.20 \text{ nm}^{-1}$, $d = 5.23 \text{ nm}$) studied by SAXS.

5.2 X-ray Microscopy

The direct imaging can give information of the structures formed by polymer micelles from chitosan loaded with a drug (Fig. 4). For this, x-ray microscopy will give additional input for the models of nano-delivery systems.

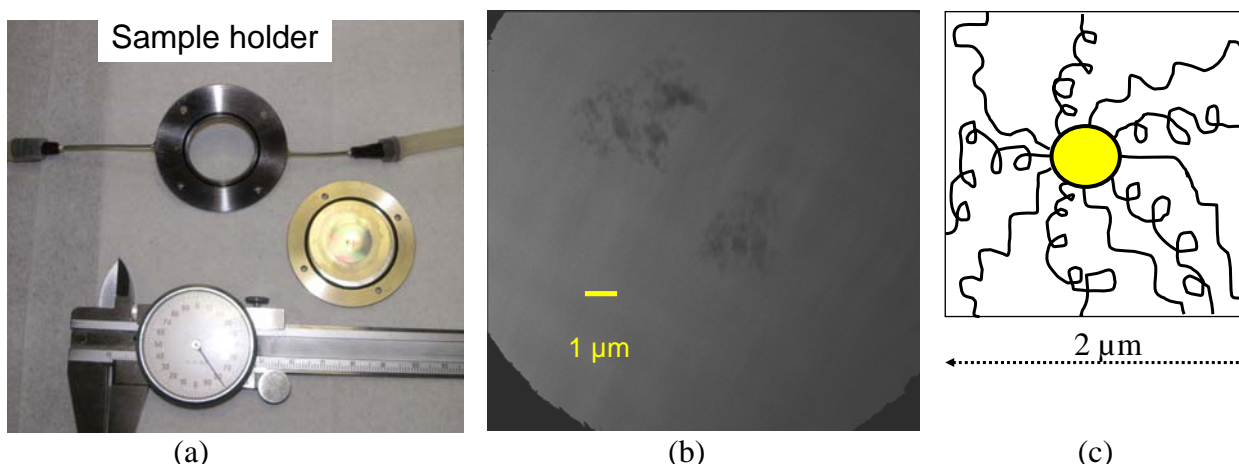


Figure 4: (a) a sample holder for x-ray microscopy, (b) x-ray micrograph and (c) scheme of the structure of polymer micelles from chitosan loaded with a drug. It can be seen that the structure of polymer micelles has a core with a diameter of about $0.5 \mu\text{m}$ and the shell with a thickness of about $1.0\text{-}1.5 \mu\text{m}$.

6. REFERENCES

1. Hillery, A.M., Lloyd, A.W. and Swarbrick, J. (Eds.), Drug Delivery and targeting for pharmacist and pharmaceutical scientists, Taylor&Francis, 2001
2. Lindner, P. and Zemb, T., Eds. Neutrons, x-rays and light scattering methods applied to soft condensed matter. Elsevier B.V., Amsterdam, Netherland. (2004)
3. Opanasopit, P., et al, European Journal of Pharmaceutics and Biopharmaceutics, 64(3):269-76. (2006)
4. Chinsriwongkul, A., et al, The 5th World Meeting on Pharmaceutics Biopharmaceutics and Pharmaceutical Technology, 27-30 March, Geneva, Switzerland. (2006)
5. Kumpugdee, M., et al, Proceeding of the International Meeting on Pharmaceutics, Biopharmaceutics and Pharmaceutical Technology, 15-18 March, Nürnberg, Germany, 121-122. (2004)

***In situ* research of radiation damage of thin bio-molecular films**

Yu.S. Gordeev, V.M. Mikoushkin, V.V. Shnitov

Ioffe Physical-Technical Institute, Russian Academy of Sciences, 194021, St.-Petersburg, Russia

F. Alvarado, R. Morgenstern, T. Schlathöler

KVI, Rijksuniversiteit Groningen, 9747 AA Groningen, The Netherlands

S.L. Molodtsov, D.V. Vyalikh

Institut für Festkörperphysik, Technische Universität Dresden, D-01062 Dresden, Germany

Abstract. Modification of thin films of thymine and adenine was revealed under irradiation by synchrotron radiation. The modification manifests itself in transformation of photoelectron spectra. It is accompanied by loosening nitrogen and oxygen atoms. X-rays of different wavelength modify these molecules differently. Mechanism of the modification includes molecular excitation by a swarm of secondary electrons generated by photoelectrons.

The project was supported by the bilateral program “Russian-German Laboratory at BESSY” and by the Russian Academy of Sciences (program “Influence of atomic structure on the properties of condensed matter”, project 2.14, and “Quantum nanostructures”, project 5-22).

Introduction

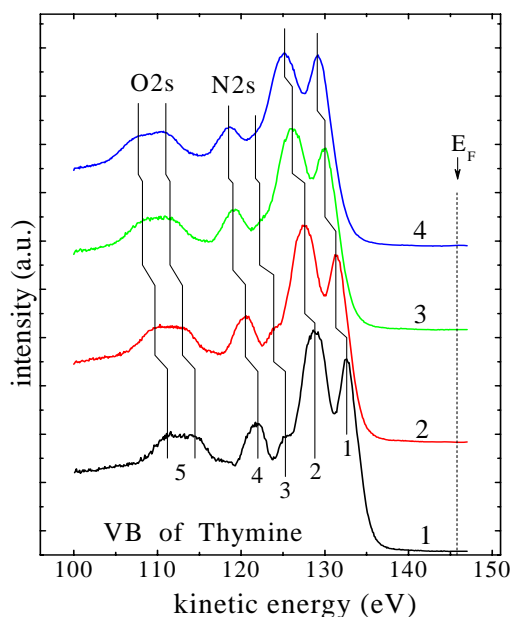
Radiation damages of bio-molecules play an important role in the life of cells. However, mechanisms of the damages are not completely clear yet. Ionization and electron excitation of molecule were considered to be important stages of the damage generation. An essential role of photoelectrons and secondary electrons can be assumed in this process. Indeed, attachment of low energy electrons (0-20 eV) was found to induce dissociation of DNA building blocks such as the nucleobases uracil and thymine [1]. Similar resonances as found for electron induced nucleobase dissociation have been observed before in study of low energy electron induced single- and double-strand-break formation of plasmid DNA deposited on surfaces [2]. It is now known that even electrons of almost zero kinetic energy can induce single strand breaks [3]. It might be concluded from the similarity between the nucleobase and the plasmid DNA results that one important step in biological radiation damage is dissociative electron attachment to single nucleobases. Pioneering studies of the last few years [e.g.1-3] showed that investigations focusing on the molecular level are an excellent tool to understand the basic processes involved in biological radiation damage. To clarify mechanisms of radiation damages, one needs *in situ* control of element composition, chemical state of atoms and electron structure of bio-molecules. There are only a few of such studies. Using electron and adsorption spectroscopy for such *in situ* control was a methodological approach of this research. Scientific goal of our project was to reveal changes in bio-molecular films under synchrotron radiation (SR) and to get information about mechanisms of creation of SR- induced damages.

Experimental details

The experiment has been carried out at BESSY using the plane-grating monochromator (PGM) beamline and the experimental facilities of the Russian-German laboratory. Experimental technique of *in vacuum* fabrication of thymine and adenine films was developed. Films of these nucleobases were grown on the silicon (100) surface cleaned by annealing up to 1100 °C. The films were repeatedly exposed to different doses of non-monochromatic SR provided by a “zero-order” mode of the PGM or of monochromatic SR with photon energy $h\nu = 150$ eV. Photoelectron spectra of the thymine and adenine films were measured in parallel with near edge x-ray absorption fine structure (NEXAFS) spectra, to our knowledge for the first time. Spectra were measured repeatedly after each of the radiation exposure.

Transformation of photoelectron valence-band spectrum of thymine under SR

Modification of thymine (C₅N₂O₂H₆) and adenine (C₅N₅O₂H₅) was revealed under irradiation by both monochromatic x-rays and non-monochromatic SR. Rapid changes in XPS

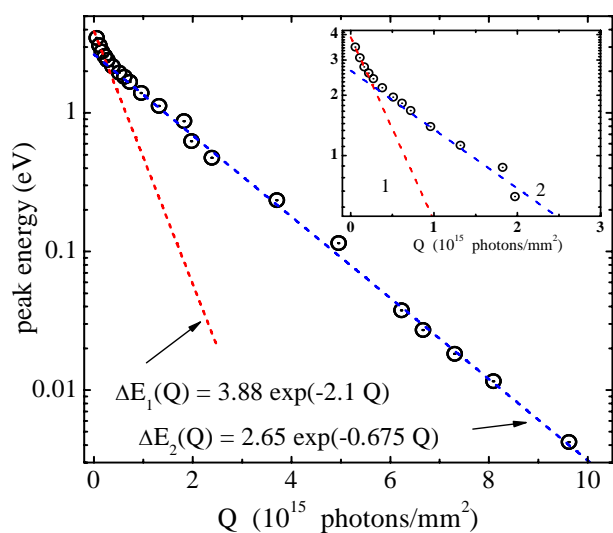


and NEXAFS spectra were observed in the first several minutes even under low intensity monochromatic irradiation. The fact of rapid modification should be taken into account in obtaining correct information about electronic structure of pristine bio-molecules.

Fig.1. Photoelectron valence-band spectra of thymine corresponding to pristine (1) and irradiated by monochromatic SR [$h\nu = 150$ eV] (2-4) films.

Fig.1 shows transformation of photoelectron valence-band spectrum of thymine under irradiation by x-rays with the energy $h\nu = 150$ eV and intensity $I_0 < 6 \cdot 10^{11}$ photons/s 1 mm 2 . Curve 1 corresponds to pristine film. Curves 2-4 correspond to increasing radiation doses. X-rays with the same energy were used to measure the spectra. Fig. 1 demonstrates drastic (3.5 eV) rigid shift of all molecular peaks to higher binding energies (to the left) and essential decreasing (1.75 times) the intensity of the nitrogen (N2s) and some of the carbon derived (2 and 3) signals. Dependence of the peak position on the irradiation dose is shown in Fig.2. The dependence is described by two exponents evidencing two stages of the modification. The dose dependence of nitrogen concentration (not shown here) is also described by two exponents in the same dose intervals. Therefore the conclusion was made that the observed line shift is strictly connected with losing nitrogen atoms, some of which can remain in the film as interstitial atoms. As a result, the ring hexagon structure of the molecule must be broken and can be transformed into pentagon ring. New states affecting the position of the Fermi level can be created, which can be one of the reasons of the observed rigid line shift. Taking into account the direction of the shift, these states are the n-type ones, e.g. that of N interstitial atoms.

One should notice that thymine film is a dielectric material with the band gap $\Delta = 5.2$ eV. Therefore photoelectron spectrum of pristine film (curve 1) is shifted to higher binding energies (to the left) due to static positive charging the film being initiated by photoionization. The charging line shift was estimated from Fig.1 to be 5.0 eV (if the Fermi level is in the middle of the band gap). Defect creation could enhance the conductivity, reduce charging and the observed line shift, but this is not the case according to Fig.1. Moreover, n-type state generation can be responsible only for a part of the observed line shift ($\Delta/2 = 2.6$ eV). The possi-



bility of radiation induced creation of the substance with higher dielectric properties must be assumed to explain the observed line shift by increasing charging the material.

Fig.2. Dependence of the peak position (1) on the irradiation dose of x-rays with the energy $h\nu = 150$ eV.

Modification of thymine under much more intensive “zero-order” SR looks quite differently. Fig.3 shows the transformation of the valence-band photoelectron spectrum of thymine. Curve 1 is the reference curve

corresponding to the film irradiated by monochromatic SR (curve 4 in Fig.1). Curves 2-5

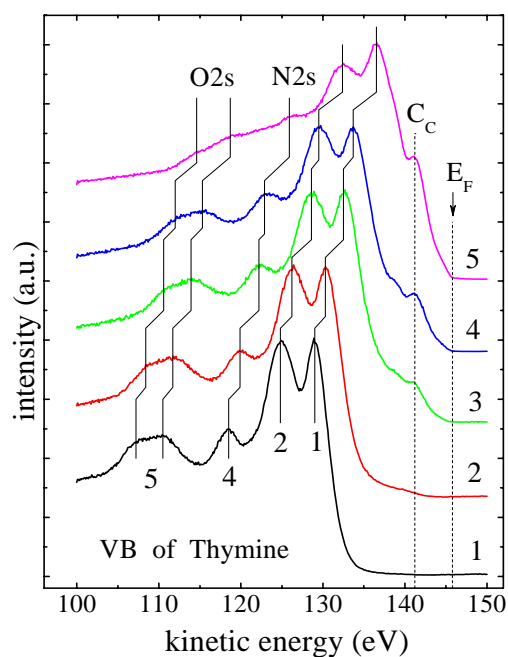


Fig.3. Photoelectron spectra of the thymine valence band. Curve 1 corresponds to the film irradiated by monochromatic SR. Curves 2-5 correspond to increasing “zero-order” irradiation doses.

losing nitrogen, and oxygen atoms is also seen. Finally, contribution of quasi-continuous background, new carbon-derived line (C_C) and quasi-metallic shape of photoelectron spectrum in the vicinity of the Fermi level arise. This background and new lines are related to the phase of some kind of conductive amorphous carbon, which is confirmed by the appearance of the satellite line in

the C1s core-level spectrum corresponding to C=C bonds. The constant energy position of the new line evidences for the absence of the static charging in this stage of the film modification. Thus, creation of p-type states (e.g. C- interstitial atoms) and diminution of static charging due to formation of the phase of amorphous carbon might be reasons for the observed line shift.

Analogous modification of adenine under monochromatic and non-monochromatic SR was observed. The first quick stage of the dose dependence is finished at the value of about $1 \cdot 10^{15}$ ph/mm² (Fig.2). Taking into account the cross section of the valence electron photoionization $\sigma \sim 2 \cdot 10^{-19}$ cm², the density of ionized atoms was estimated to be 10^{19} 1/cm³, that is less than 1% of the material atoms. Therefore x-ray can't be a direct cause of the observed modification with losing 20% of nitrogen atoms. Indeed, x-ray can't neither directly eject molecular atoms no directly excite valence electrons to initiate the first step of the molecular fragmentation. Therefore, the conclusion was made that thymine is modified by photoelectrons and by a swarm of secondary electrons. Electrons can excite anti-bonding states or can heat the molecule through electron-phonon interaction followed by evaporation of atom or fragment. Contrary to monochromatic x-rays, “zero-order” SR can directly excite valence electrons by ultra-violet or indirectly by photoelectrons of higher energies. This difference can be a reason of quite different modification behavior for these two types of SR: different wavelength or different energies of photoelectrons influence different atomic sites of the nuclear-bases.

Thus, modification of thymine and adenine was revealed under irradiation by both monochromatic and non-monochromatic (“zero-order”) synchrotron radiation for the first time. Modification is induced mainly by a swarm of secondary electrons and is accompanied by ejection of nitrogen and oxygen atoms. SR of different wavelength regions modifies these bio-molecules differently.

References:

1. M. A. Huels *et al.* J. Chem. Phys. **108**, 1309 (1998). G. Hanel *et al.* Phys. Rev. Lett. **90**, 188104 (2003). S. Denifl *et al.* Chem. Phys. Lett. **377**, 74 (2003). H. Abdoul-Carime *et al.* Phys. Rev. Lett. **92**, 168103 (2004).
2. B. Boudaiffa *et al.* Science **287**, 1658 (2000). X. Pan *et al.* Phys. Rev. Lett. **90**, 208102 (2003).

3. F. Martin *et al.* Phys. Rev. Lett. **93**, 068101 (2004).

Investigation of the catalytic mechanism of shikimate kinase from *M. tuberculosis*

Marcus D. Hartmann, Marc Bruning, Gleb P. Bourenkov, Attila Oberschall,
Nicolai Strizhov and Hans D. Bartunik

Max-Planck Unit for Structural Molecular Biology, MPG-ASMB c/o DESY, Hamburg

The shikimate pathway leading to chorismate as an intermediate compound in the production of aromatic aminoacids is essential for *Mycobacterium tuberculosis* (Parish and Stoker, 2002). The absence of the shikimate pathway in mammals makes the enzymes involved in it to interesting targets for a possible rational design of new antimicrobial drugs. Shikimate kinase, a P-loop kinase, catalyzes the ATP-dependent phosphorylation of shikimate (SKM) to shikimate-3-phosphate (S3P) as the fifth step of the pathway. In order to provide a structural basis for a detailed understanding of the catalytic functioning on a molecular level, we investigated enzymatic reaction states of shikimate kinase from *M. tuberculosis* (MtSK). After having determined several crystal structures of MtSK in different ligation states on the basis of cocrystallizations, we systematically explored possibilities to initiate the enzymatic reaction in crystals by soaking techniques and study phosphoryl transfer 3D. These exploratory experiments were carried out at the BESSY PX beamline BL14.1 and at the MPG beamline BW6 at DORIS. Diffraction data sets were measured under a number of different soaking and timing conditions, aiming to achieve high populations of intermediate states of catalytic turnover in the crystalline enzyme.

In the end we succeeded in starting a productive enzymatic reaction by diffusing MgATP into crystals of MtSK in complex with SKM. The initial structure exhibited a fully occupied SKM molecule bound to the ESB domain and a sulfate ion interacting with the P-loop. Flash-freezing of crystals after a number of different time points after soaking with ATP, the enzyme was trapped in two different intermediate states. The first showed the enzyme immediately after the catalytic step in complex with the in-situ formed products S3P and ADP. The second corresponded to the state after release of ADP to the solvent. The knowledge of the structures immediately before and after initiation of the enzymatic reaction in the crystal provided the basis for identifying the reaction as a predominantly associative in-line phosphoryl transfer (Hartmann et al., 2006) depicted in Figure 1. We further identified domain motions, which are required for proper orientation of the substrates for phosphotransfer and of the products prior to stepwise release, and synergic effects in the random sequential substrate binding.

The work was supported by the Bundesministerium für Bildung und Forschung, BMBF/PTJ, under grant number BIO/0312992A (to H.D.B.).

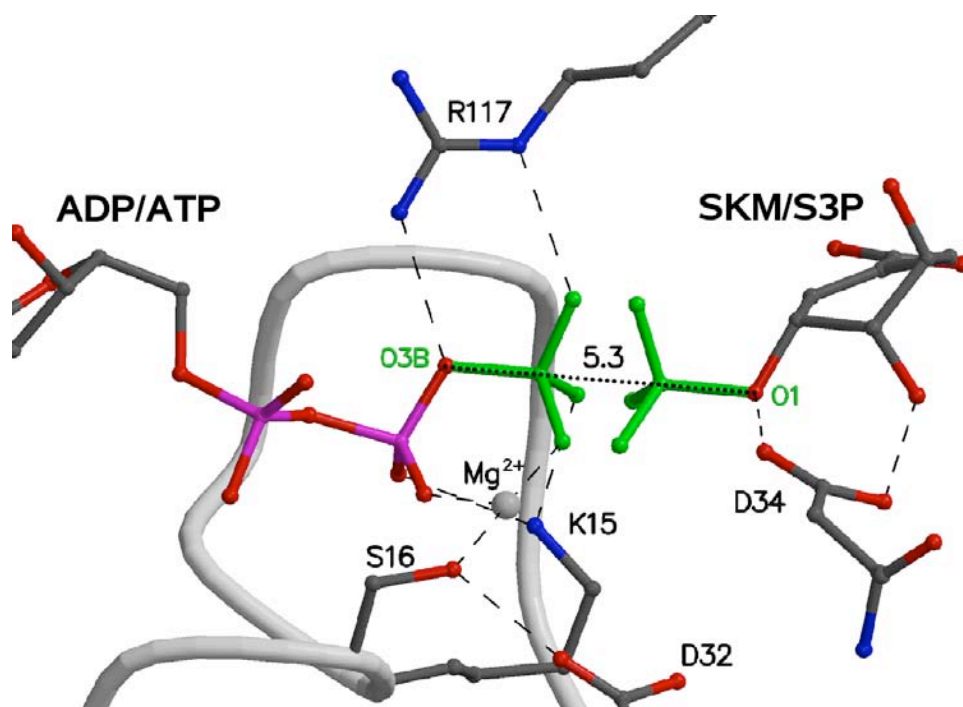


Figure 1:
Structural model of the phosphoryl transfer of the transition state for in-line associative phosphoryl transfer from crystal structures determined immediately before and after the catalytic reaction in the crystalline state. The P- loop is shown as a grey ribbon.

References

- Parish, T., Stoker, N.G. (2002). The common aromatic acid biosynthesis pathway is essential in *Mycobacterium tuberculosis*. *Microbiology* 148, 3069-77.
- Hartmann, M.D., Bourenkov, G.P., Oberschall, A., Strizhov, N., Bartunik, H.D. (2006). Mechanism of phosphoryl transfer catalyzed by shikimate kinase from *Mycobacterium tuberculosis*. *J Mol Biol.* 364(3):411-23.

Characteristics of bony tissue around biofunctionalised titanium implants using an osteoporotic animal model

R. Bernhardt¹, J. Dudeck¹, I. Manjubala², St. Rammelt³, G. Weidemann⁴, J. Goebbels⁴, G. Vollmer⁵, P. Fratzl², H. Worch¹, D. Scharnweber¹

¹Max Bergmann Center for Biomaterials, Technische Universität Dresden, Germany;

²Max Planck Inst. of Colloids and Interfaces, Dept. of Biomaterials, Potsdam, Germany;

³Department of Trauma and Reconstructive Surgery, University Hospital, Dresden, Germany;

⁴Federal Institute for Materials Research and Testing (BAM), Berlin, Germany;

⁵Institute for Zoology, Technische Universität Dresden, Germany

1 Introduction

The goal of the overall work of our project is to describe the mineral structure of newly formed bone surrounding implants in comparison to bone which was present before implantation but not influenced by the surgical procedure. An osteoporotic animal model with and without a hormone therapy was investigated. To describe mineral structure, the data of different analytical methods have to be combined to gain information on different hierarchical structure levels (mm to chemical relationships). In this study, based on SR μ CT-data, mechanical properties of bone mineral should be determined two-dimensionally as a function of the conditions 'healthy', 'osteoporotic' and 'hormone treated osteoporotic' with the help of nanoindentation measurements for selected areas of examined explants. Additionally, the influence of the implant biofunctionalisation on the characteristics of the mineral phase should be investigated. New knowledge is expected for the osseointegration of biofunctionalised titanium implants for normal as well as disordered bone regeneration.

2 Materials and Methods

Ovariectomised rats with and without hormone treatments were used as the animal model. Titanium wires with a diameter of 0.8 mm with biofunctional coatings of collagen-type I + chondroitin sulphate (CS), CS + Bone Morphogenetic Protein 4 (hBMP-4) and a blank control (cp-Ti) were placed in the tibia of ovariectomised rats for 4 weeks. After the animal experiments, the rat tibiae were freed from adherent soft tissue, fixed in paraformaldehyde and dehydrated in a series of ethanol solutions with gradually increasing ethanol content. The embedding was performed in Polymethylmetacrylate (PMMA). At the BAMline (BESSY II) 24 specimens in total, with 4 samples for each condition, were evaluated with Synchrotron Microcomputed Tomography (SR μ CT). For each sample 720 x-ray attenuation projections with a local resolution of 11 μ m were acquired using an x-ray energy of 30 keV. After investigation with SR μ CT, the specimens were cut within the measured CT-volume perpendicular to the bone length axis in 1 mm thick sections with an IsoMet low speed saw (Buehler GmbH, Düsseldorf, Germany). To locate differences in bone mineral density with an environmental scanning electron microscope (ESEM, QUANTA 600F, FEI, Hillsboro, USA) micrographs were made for each slice (Fig. 1). The nanoindentations were performed in a grid-like manner with a spacing perpendicular to the sleeve boundary of 10 μ m and of 50 μ m parallel to the sleeve. Afterwards, the reliability of the indents was checked with the ESEM. In order to obtain a suitable sample surface by the polishing process it was necessary to remove the implants. Afterwards the cavity of the former implant site was filled with Loctite 9434 (Henkel, Munich, Germany).

The nanoindentation was performed with a Triboindenter nanomechanical test instrument (Hysitron INC., Minneapolis, USA) equipped with a Berkovich diamond tip and coupled with an atomic force microscope (Nanoscope III, Digital Instruments). The indentations were performed with a maximum load of 5000 μN . The loading/unloading curves were used to calculate the reduced E-modulus (E^*). In order to transfer the x- and y-coordinates of the selected bone areas from the BSE images to the nanoindenter system, AFM-imaging (contact mode) was performed after a rough positioning with the instrument optics. After identifying osseous structures on AFM images, it was possible to determine the exact indenter position over the selected region of interest (ROI). The mechanical property maps created were digitally overlaid and matched with the BSE images of the same area (Fig. 3).

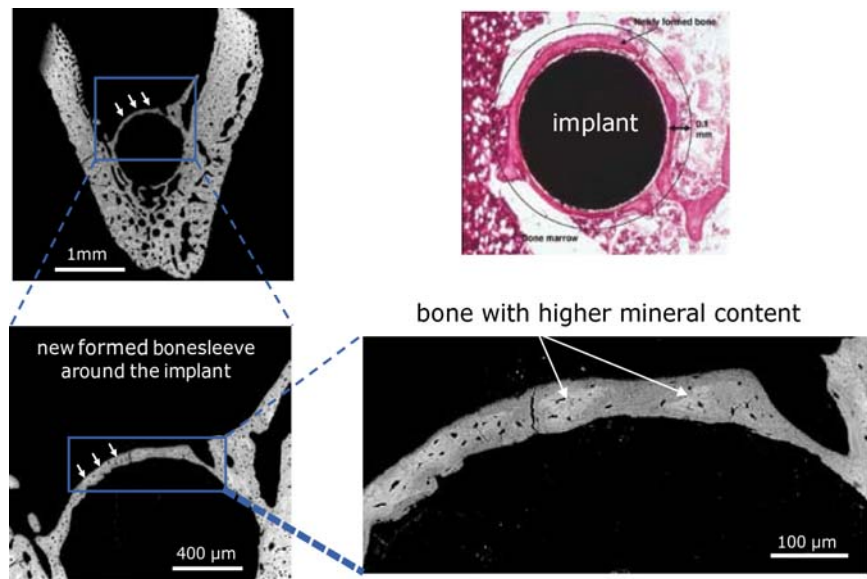


Figure 1: ESEM and histological images of tibial Diaphysis in an ovariectomised rat (sample CSO-481 with removed implant, H&E stain, original magnification 25x).

3 Results and Discussion

The SR μ CT reconstruction of the explants shows a detailed visualisation of bone formation around the titanium implants (Fig. 2). Assigning different colours to the attenuation (grey levels) of mineralised bone, local areas of higher (orange) and lower (yellow) mineral content are visible. The colour maps for the reduced E-moduli (E^*) of the hard tissue around the implant are in good relation to the density differences found in the SR μ CT- and ESEM-visualisations. The local areas of a higher and lower mineralization degree, which can be recognized by means of SR μ CT and SEM (Fig. 2 and 3), correspond with highly stiff areas (stiffness: 20.5 – 24.7 GPa) and areas with lower stiffness (9.6 – 15.9 GPa) respectively, as shown in the related colour maps (Fig. 3). The mean value of E^* with 19.45 ± 3.49 GPa for the newly formed bone around the implant shows a similar stiffness to the highly mineralized cortical bone (19.69 ± 1.92 GPa). In the present study we were able to show that the E^* -moduli of stationary and newly formed cortical bone is in the

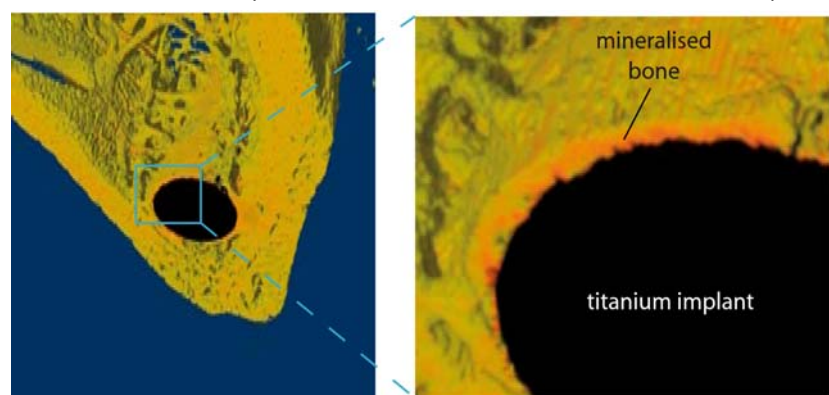


Figure 2: SR μ CT reconstruction of a titanium wire (black, diameter = 0.8 mm) coated with collagen and chondroitin sulphate inside a tibia of an ovariectomised rat after a healing time of 4 weeks (sample CSO-481).

range of the stiffness for stationary trabecular bone in ovariectomized rats which is given by the literature (15.8 -21.0 GPa [1]).

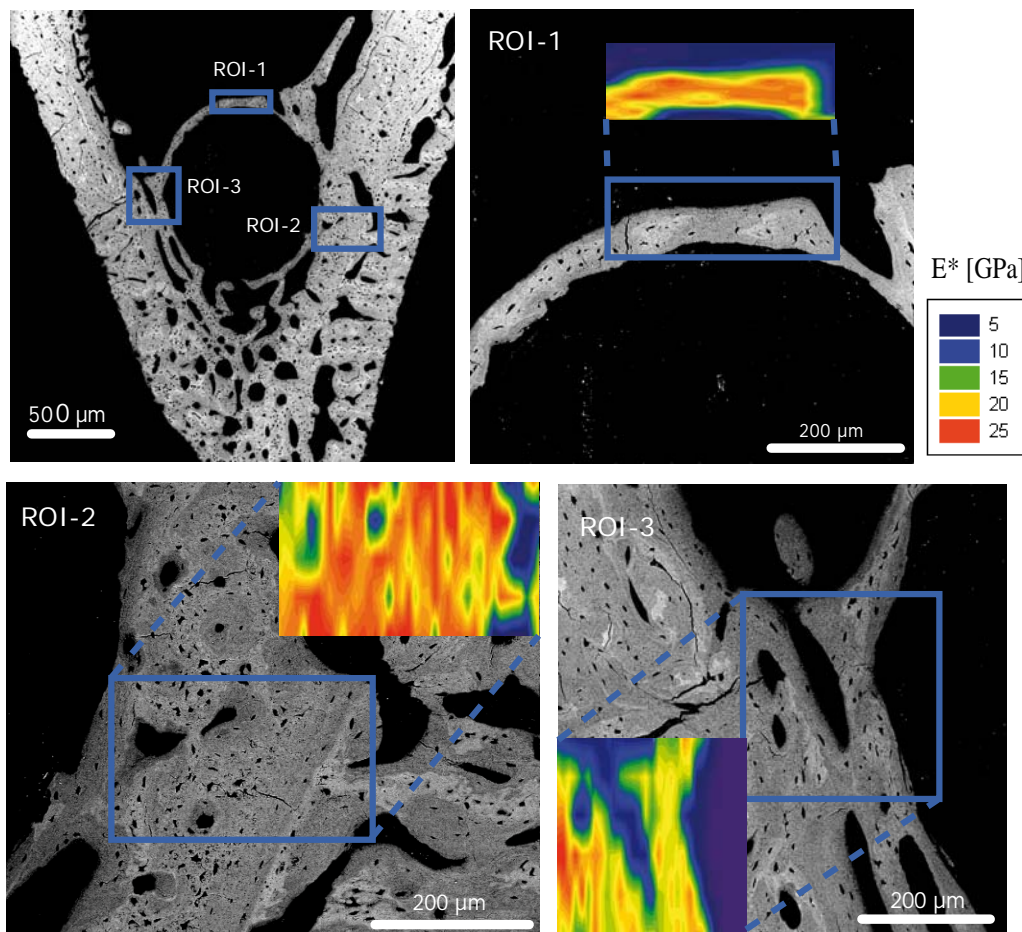


Figure 3: Imaging of the reduced E-modulus (E^*) in 3 different ROI's of the sample CSO-481 after removal of the implant from inside a tibia of an ovariectomized rat after a healing time of 4 weeks.

Using the E^* values of the embedding material (E^* -PMMA: 4.82 ± 0.21 GPa) as a reference value, we could prove the reliability of mechanical tests found in the literature (4.0 – 5.4 GPa [2]). The next steps in our investigations are to find out if there are relationships between the type of bone regeneration and/or biofunctional coatings and the mechanical properties of the newly formed bone around the implants. SAXS- and FT-IR-measurements should furthermore expand the understanding of the mineralisation process with this osteoporosis model.

4 Acknowledgements

The authors gratefully acknowledge the support of this work by the DFG (SCHA 570/9-1) and BESSY (Project 2006_1_50033).

References

- [1] X. E. Guo, et al., J Orthop Res 18 (2000) 333-336.
- [2] D. D. Wright-Charlesworth, et al., J Biomed Mater Res A 74 (2005) 306-314.

Determination of the Ionization Potentials of Security Relevant Substances with Single Photon Ionization Mass Spectrometry Using Synchrotron Radiation

E. Schramm¹, F. Mühlberger^{1}, S. Mitschke¹, G. Reichardt²,
R. Schulte-Ladbeck³, M. Pütz³, R. Zimmermann^{1, 4, 5}*

1. GSF – National Research Center, Neuherberg

2. BESSY - Berlin

3. BKA - Wiesbaden

4. BfA - Augsburg

5. University of Augsburg



1. Introduction

Recent world events have increased the interest in powerful detection methods for explosives and their precursors as well as chemical warfare agents (CWAs). But also drugs and their precursors are interesting to trace. It is security relevant to identify lowest concentrations of these substances not only in public transit terminals but also for identifying illegal drug laboratories or to discover land mines.

The main difficulty is that these security relevant substances appear in very low concentrations due to their low vapor pressures. One possibility to increase the concentration in a gaseous matrix is to increase the temperature. This implies that solid samples have to be taken and vaporized at high temperature. Wipe test desorbers, known from airports, are based on this technique. Thereby the surface of a suspicious object is wiped with a swab. This swab is put inside a thermal desorber where it is heated up and the substances on the swab vaporize into a hot flushing gas like nitrogen. As a result relatively high concentrations of the substances can be generated.

Unfortunately, not only the trace substances are collected on the swab but also a large amount of other substances in much higher concentrations leading to a complex matrix containing besides the flushing gas e.g. oils and fats. Thus, a separation of the matrix from the relevant trace compounds is necessary for a sensitive detection.

A possibility to detect low concentrations of different substances in complex matrices is single photon ionization mass spectrometry (SPI-MS). This method uses vacuum ultraviolet (VUV) photons for soft photon ionization. Thereby a single photon is absorbed by the molecule and if the photon energy is higher than the ionization potential (IP) of the molecule, an electron is separated. The charged molecule can then be detected by the mass spectrometer (MS). Hence, substances with an IP higher than the photon energy are not ionized and not detected. Most matrix molecules like nitrogen (IP = 15.58 eV), oxygen (IP = 12.06 eV), carbon dioxide (IP = 13.77 eV) and water (IP = 12.62 eV)^[1] have relatively high IPs. If the IPs of the security relevant substances are all below the IPs of the matrix components, it is possible to use an intermediate photon energy, thus, the matrix elements would not be ionized. This is very favorable as a high density of ions causes unwanted ion scatter and space charge effects in the MS resulting in an increase of the limit of detection (LOD) for the trace compounds due to high noise signals.

Choosing a photon energy just above the IPs of the relevant substances will have another advantage. Only little additional energy is transferred to the molecule resulting in little fragmentation (soft ionization) as the appearance energy (AE) of many fragments is not reached. The advantage of such a soft ionization technique is that the number of unwanted fragment signals

in mass spectra is reduced. Therefore labeling of signals from complex mixtures is more likely.

For soft ionization of trace compounds a wavelength between their IPs and the lowest IP of the matrix elements has to be applied. Unfortunately, for most security relevant substances the IPs are not known from literature. Therefore, the IPs of several security relevant substances were determined in this work. To detect the IPs, SPI spectra at various photon energies between 7 eV and 11.8 eV (177 nm–105 nm) were recorded and the onsets of the molecular ion peaks were determined.

The measurements described in this work were performed by using monochromatized synchrotron radiation from the “Berliner Elektronenspeicherring-Gesellschaft für Synchrotronstrahlung” (BESSY). The Federal Criminal Police Office of Germany provided 10 different drugs and drug precursors, 12 explosives and related substances as well as DIMP and DMMP as simulants for CWAs.

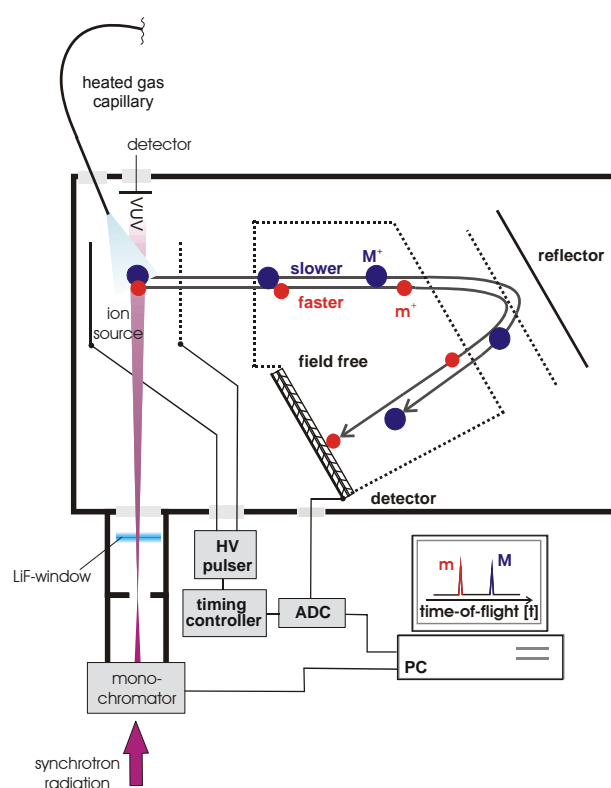


Fig. 1: Measurement Setup

IPs, it was necessary to maintain a constant concentration of the substances while recording the spectra. Two home made standard gas generators were used for that purpose.

3. Results and Discussion

Using the standard gas generators mentioned above concentrations of the substance could be held constant during the measurements. Thus photo ionization efficiency plots (PIEs) could be generated from single spectra at different wavelengths. Therefore signals were integrated, divided by the respective VUV light intensity and displayed vs. photon energy.

Finally, the lowest photon energy where the molecular ion could be detected was taken as IP. Unfortunately, for some substances the molecular ion peak could not be seen. However by determining the AE of a main fragment a rough estimate of the IP could be found. For the

2. Experimental Method

To obtain SPI spectra at different wavelengths, a time of flight mass spectrometer (TOFMS) was installed behind a monochromator at the beamline U125/2-NIM of BESSY^[2]. The 10 m normal incidence monochromator was designed for photon energies from 10 eV to 40 eV, but for the measurements performed here energies between 7 eV and 11.8 eV were used. Unfortunately, in this range some photons with wavelengths of higher order appeared which had to be blocked using a LiF-window.

The experimental setup is shown in Fig. 1. The gas streamed through a heated capillary (200 °C) effusively into the ion source where the security relevant substances were ionized by the VUV synchrotron photons. The ions were mass separated and detected with a reflectron time of flight mass spectrometer described in [3]. For determination of the

selection of the fragment it had to be ensured, that it is a photo ionization fragment and not a thermal decomposition product. Therefore only peaks which could be found in high levels in the EI spectrum as well were selected.

Due to the rather low signal to noise ratio and the width of the wavelength steps the IPs and AEs are not more accurate than ± 0.1 eV. This could have been improved by averaging more spectra at each wavelength and reducing the step width. Unfortunately, the beam time and the availability of the security relevant substances were limited and therefore the averaging time at every wavelength step was 10 s with 0.1 eV steps.

Fig. 2 shows exemplarily the EI spectrum with 70 eV^[1], a SPI spectrum measured at BESSY as well as the PIE plot of 2,4-DNT. It is a decomposition product of TNT. Due to its higher vapor pressure it is used to detect TNT.

The molecular ion peak (182 amu) appears at 10.0 eV which therefore is assigned as its IP (Fig. 2c) and it remains the main peak up to 10.6 eV. At higher photon energies three fragments at $m/z = 119$, 165 and 167 appear. All three fragments are present in the EI-Spectrum, as well. The signal at 119 m/z is caused by the separation of NO_2 and OH from the molecule. The fragment $m/z = 165$ results from the loss of OH and the one at 167 m/z results from a loss of the CH_3 -group.

As a summary of our measurements it can be said, that despite the problems with the low concentrations due to the low vapor pressure of the security relevant substances we were able to determine 12 new ionization potentials and to verify 6 known ones. None of the measured IPs was standing in discrepancy with available data from the NIST data base^[1]. For 7 substances only the AEs of fragments could be determined.

It can be concluded, that the IPs of the drugs are in the interval of 7 eV to 10 eV and the IPs of the explosives are in the interval from 8 eV to 11 eV. Hence, all yet known IPs from security relevant substances can be found below the IPs of the most common matrix molecules, amongst them oxygen shows the lowest with 12.06 eV^[1]. According to this it is possible to find a photon energy so that substances of interest can be detected in very low concentration without being screened due to the shielding of the matrix molecules.

4. References

- [1] G. Mallard et al., National Institute of Standards and Technology (NIST): <http://webbook.nist.gov/chemistry>, Vol. 2000, NIST database
- [2] G. Reichardt et al., Nuc. Inst. a. Meth. in Phys. Res. Sec. A, Vol. 467-468, Part 1, 21 July 2001, P. 462-465.
- [3] F. Mühlberger et al., Analytical Chemistry 2005, Vol. 77, P. 7408-7414.

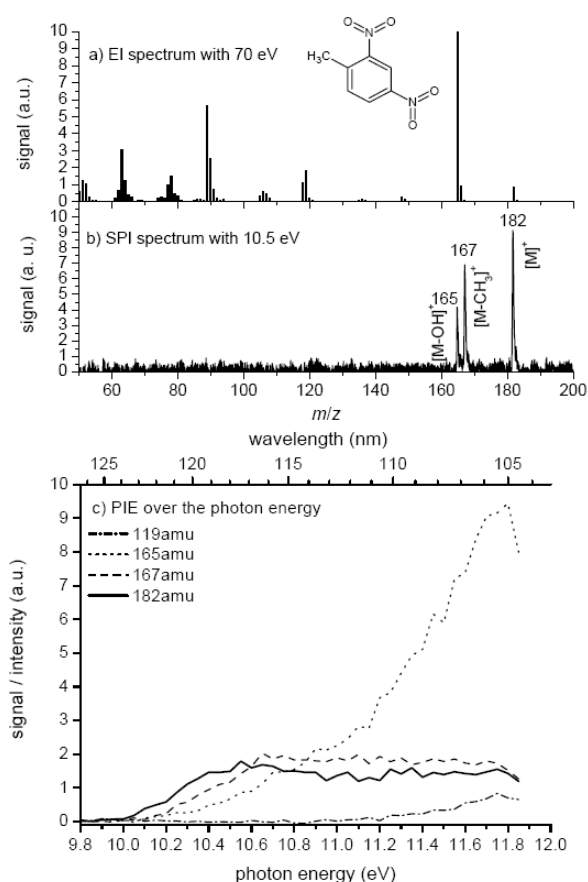


Fig. 2: a) EI spectrum^[1],

b) SPI spectrum and

c) PIE plot.

Structure of the Bet3:Tpc6B subcomplex of human TRAPP complex involved in vesicular transport

Daniel Kümmel^{1,2}, Jürgen J. Müller¹, Yvette Roske¹, and Udo Heinemann^{1,2}

¹Max-Delbrück-Center for Molecular Medicine, Berlin, Germany

²Chemistry and Biochemistry Institute, Free University, Berlin, Germany

Introduction

Living cells are separated from their surrounding by lipid bilayer membranes which fence off the interior of the cell, the cytosol, from the outside world. In addition, the cells of all higher organisms contain specialized compartments which are separated from the cytosol also by lipid membranes. The exchange of proteins and other molecules between different compartments or between the cell and the outside world is achieved by vesicular transport. The whole process of transporting a vesicle with a specific cargo from a donor compartment to an acceptor compartment can be considered a functional module [1]. The different trafficking pathways in eukaryotic cells are all organized based on the same underlying principle, but differ in their components. The individual steps that are required to fulfill this complex task are carried out by submodular entities, which work together in a coordinated concert. These include the sorting of cargo, budding and scission of the vesicle from the donor membrane, uncoating, and tethering, docking and membrane fusion at the acceptor compartment (Figure 1). Main regulators of vesicular transport are the Arf GTPases, which control vesicle budding, and the Rab GTPases, which coordinate membrane fusion.

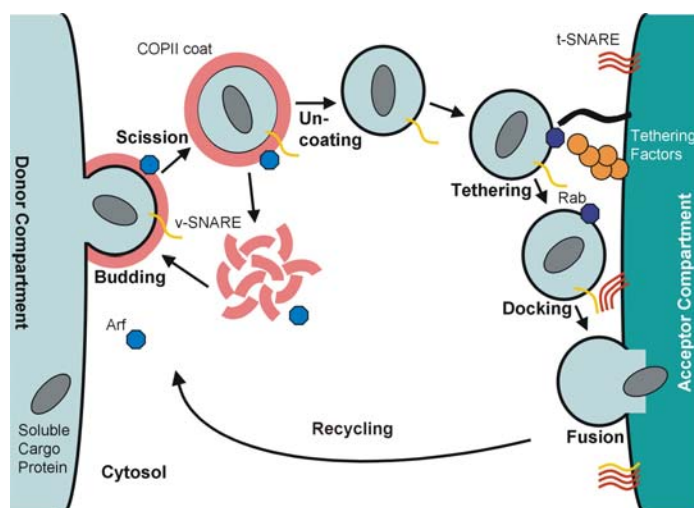


Fig. 1: The functional modul of vesicular transport can be dissected into submodular entities that constitute of conserved sets of proteins (after [1]).

We are interested in the TRAPP (Transport Protein Particle) tethering complex which is involved in the transport of vesicles from the endoplasmic reticulum (ER), where proteins are synthesized, to the Golgi network, where proteins are further processed. TRAPP was shown to interact with ER-derived vesicles and to promote nucleotide exchange of a regulatory protein, the Rab-GTPase Ypt1p.

The TRAPP subunits Bet3 and Tpc6 form a heterodimeric subcomplex of TRAPP

We had previously determined the crystal structures of the TRAPP subunits Bet3 [2] and Tpc6 [3] (Figure 2). Both proteins revealed a novel α/β -plait protein fold: the secondary structural elements are arranged in a topology constructed by a twisted, antiparallel, four-stranded β -sheet on one side, with helices forming the other side of the structural motif. Bet3 and Tpc6 form homodimers, which primarily involves the interactions between the helices $\alpha 1$ and $\alpha 2$. In spite of only 17% sequence identity, the superposition of the α -carbon backbones of the monomers of both proteins shows high similarity. Differences in structure are mainly confined to the loop regions, whereas the α/β -plait cores of both proteins show little divergence. The similarity between Bet3 and Tpc6 is especially prominent at the dimerization interfaces of the proteins leading to the intriguing possibility of a heterodimerization between Tpc6 and Bet3. Heterodimerization could be demonstrated by *in vitro* and *in vivo* association studies [3]. We pursued the crystallization of the heterocomplex of both proteins that was postulated based on these structural and biochemical data [4].

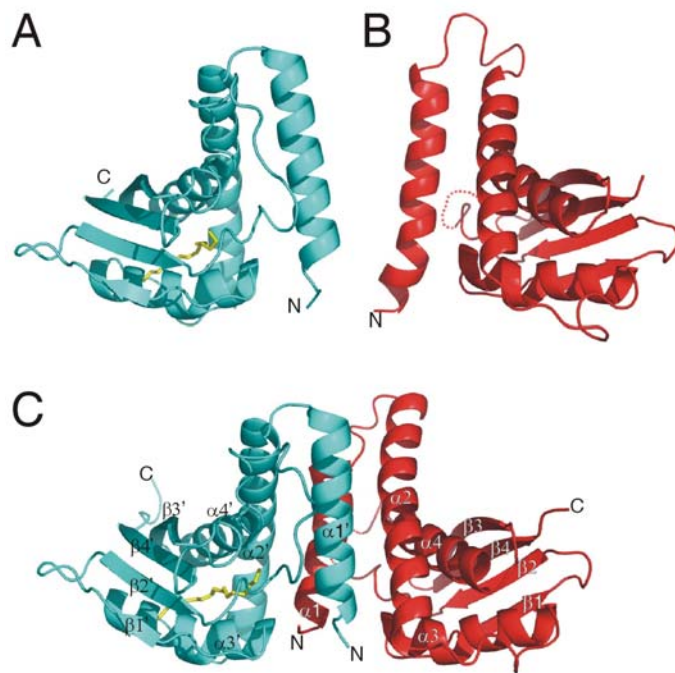


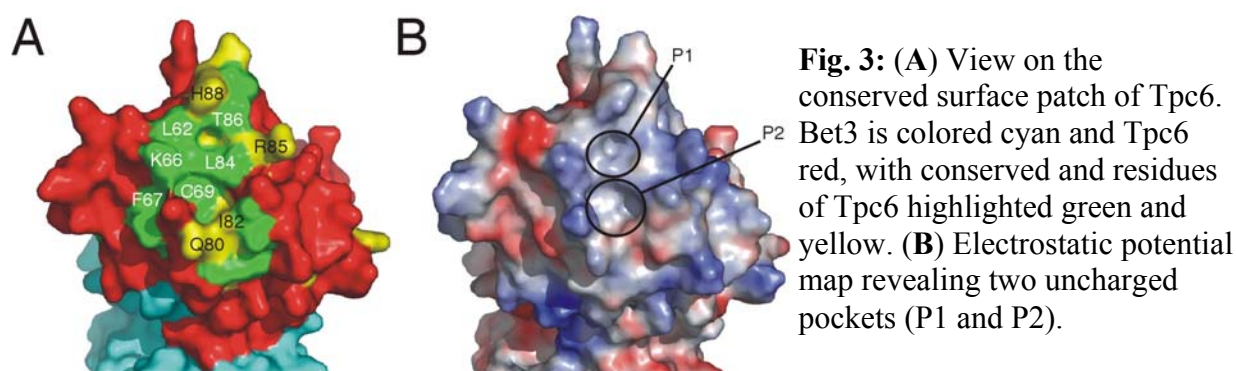
Fig. 2: Structure of the Bet3:Tpc6 complex. (A) Bet3 and (B) Tpc6 monomers as they are observed in the homodimer crystal structures are shown in comparison to (C) Bet3:Tpc6 with labeled secondary structure elements.

The structure of the Bet3:Tpc6 complex closely resembles the model proposed before (Figure 2). Only limited structural rearrangement in the $\alpha 1$ - $\alpha 2$ loop region of Tpc6 when compared with the homodimeric structures is observed. This leads to the formation of a groove in the heterocomplex that might represent a binding interface for a further TRAPP subunit or interacting protein. The buried surface area of the heterocomplex is smaller than that of Bet3 and similar to that of Tpc6 homodimers. Instead, more polar contacts are formed in the heterodimer, of which a conserved salt bridge between Bet3 Arg62 and Tpc6 Asp3 is the most prominent. These polar interactions seem to be responsible for a stabilization of the heterodimer compared with the homodimers as seen with the coexpression of Bet3 and Tpc6 which favored the formation of heterocomplexes.

A conserved surface patch of Tpc6 might mediate membrane association of TRAPP

Crystallographic studies have revealed the existence of two Tpc6 paralogs A and B that both can form a stable heterodimeric complex with Bet3 [3, 5]. Further experiments showed similar expression levels of both *tpc6* paralogs and that both isocomplexes are able to participate in TRAPP complex formation.

Sequence comparison of TPC6 paralogs and orthologs led to the identification of a conserved surface patch with uncharged pockets that, according to the current model, faces towards the membrane. Interestingly, the conserved patch is located at a structurally similar position where the entrance to a hydrophobic channel, which has been suggested to be involved in membrane association of TRAPP, is found in Bet3. Biochemical and genetic data show that the yeast Tpc6 homolog is indeed able to recruit Bet3 to the membrane and to suppress the growth defect of Bet3 mutants lacking proper membrane localization [5].



These studies suggest that Tpc6 helps anchoring Bet3 to a proposed anchoring moiety with residues located in the conserved patch of Tpc6. We envisage that the patch is involved in recruitment of TRAPP to the Golgi membrane *via* the interaction with an anchoring protein that might be the same moiety that binds to Bet3. This model could explain the additional contribution of Tpc6 for membrane binding of TRAPP, and the identification of the conserved patch might help find the anchor protein for TRAPP at the Golgi.

References

1. Hofmann, K.P., Spahn, C.M., Heinrich, R., and Heinemann, U. (2006) Building functional modules from molecular interactions. *Trends Biochem Sci* **31**: 497-508.
2. Turnbull, A.P., Kümmel, D., Prinz, B., Holz, C., Schultchen, J., Lang, C., Niesen, F.H., Hofmann, K.P., Delbrück, H., Behlke, J., Müller, E.C., Jarosch, E., Sommer, T., and Heinemann, U. (2005) Structure of palmitoylated BET3: insights into TRAPP complex assembly and membrane localization. *EMBO J* **24**: 875-884.
3. Kümmel, D., Müller, J.J., Roske, Y., Misselwitz, R., Büssow, K., and Heinemann, U. (2005) The structure of the TRAPP subunit TPC6 suggests a model for a TRAPP subcomplex. *EMBO Rep* **6**: 787-793.
4. Kümmel, D., Müller, J.J., Roske, Y., Henke, N., and Heinemann, U. (2006) Structure of the Bet3-Tpc6B core of TRAPP: two Tpc6 paralogs form trimeric complexes with Bet3 and Mum2. *J Mol Biol* **361**: 22-32.
5. Kim, M.S., Yi, M.J., Lee, K.H., Wagner, J., Munger, C., Kim, Y.G., Whiteway, M., Cygler, M., Oh, B.H., and Sacher, M. (2005) Biochemical and crystallographic studies reveal a specific interaction between TRAPP subunits Trs33p and Bet3p. *Traffic* **6**: 1183-1195.

Structure determination of bacterial cold shock proteins in complex with single-stranded nucleic-acid ligands

Klaas E.A. Max¹, Markus Zeeb^{2,5}, Ralf Bienert¹, Jochen Balbach^{2,3}
and Udo Heinemann^{1,4,*}

¹ Max-Delbrück-Centrum für Molekulare Medizin Berlin-Buch, Germany;

² Lehrstuhl für Biochemie, Universität Bayreuth;

³ Martin-Luther-Universität Halle-Wittenberg, Germany; Fachgruppe Biophysik, Fachbereich Physik, Germany;

⁴ Institut für Chemie und Biochemie, Freie Universität Berlin, Germany;

⁵ Department of Molecular Biology, The Scripps Research Institute, La Jolla, USA

Bacterial cold shock proteins (CSP) regulate cellular adaptation to cold stress. Functions ascribed to CSP include roles as RNA chaperones [1] and in transcription antitermination [2]. Using the BESSY PX beamlines 14.1 and 14.2 we have determined structures of the cold shock proteins *Bs*-CspB of *Bacillus subtilis* and *Bc*-Csp of *Bacillus caldolyticus* both complexed with hexathymidine DNA single strands at resolutions of 1.78 Å and 1.29 Å, respectively [3-5]. These are the first reported structures of proteins with cold shock domain in complex with an oligonucleotide ligand. In both structures, individual binding subsites interact with single nucleobases through stacking interactions and hydrogen bonding. The sugar-phosphate backbone and the methyl groups of the thymine nucleobases remain solvent exposed and are not contacted by protein groups. Fluorescence titration experiments monitoring the binding of oligopyrimidines reveal binding preferences at individual subsites and allow the design of an optimised heptapyrimidine ligand, which is bound with subnanomolar affinity. Based on crystallographic and biochemical studies of deoxyoligonucleotide binding to CSP, we suggest a common mode of binding of single-stranded heptanucleotide motifs to proteins containing cold shock domains, including the eukaryotic Y-box factors (Figure 1).

In addition to ligand binding, we observed a remarkable structural transition: *Bc*-Csp in the dT₆-complexed structure adopts the conformation of a domain-swapped dimer in which β-strands 1 to 3 associate with strands 4 and 5 from the other subunit to form a closed β-barrel and *vice versa* (Figure 2). The globular units of dimeric *Bc*-Csp closely resemble the well known structure of monomeric CSP. The structural re-organization from the monomer to the domain-swapped dimer involves a strictly localized change of the peptide bond linking Glu36 and Gly37 of *Bc*-Csp. Similar structural re-organizations have not been observed in any other CSP or OB-fold structures. Each dT₆ ligand is bound to one globular unit of *Bc*-Csp *via* an amphipathic protein surface. Although a similar arrangement of cold shock proteins has not yet been reported in solution, this rearrangement emphasizes their great structural flexibility and needs to be further analyzed in the context biological function.

Literature

1. Jiang, W., Hou, Y., and Inouye, M., CspA, the major cold-shock protein of *Escherichia coli*, is an RNA chaperone. (1997) *J Biol Chem.* **272**: 196-202.
2. Bae, W., Xia, B., Inouye, M., and Severinov, K., Escherichia coli CspA-family RNA chaperones are transcription antiterminators. (2000) *Proc Natl Acad Sci USA.* **97**: 7784-9.
3. Max, K.E., Zeeb, M., Bienert, R., Balbach, J., and Heinemann, U., T-rich DNA single strands bind to a preformed site on the bacterial cold shock protein Bs-CspB. (2006) *J Mol Biol.* **360**: 702-14.
4. Max, K.E., Zeeb, M., Bienert, R., Balbach, J., and Heinemann, U., Common mode of DNA binding to cold shock domains. (2007) *FEBS J.* **in press**, accession number: 17266726
5. Zeeb, M., Max, K.E., Weininger, U., Low, C., Sticht, H., and Balbach, J., Recognition of T-rich single-stranded DNA by the cold shock protein Bs-CspB in solution. (2006) *Nucleic Acids Res.* **34**: 4561-71.

Figures

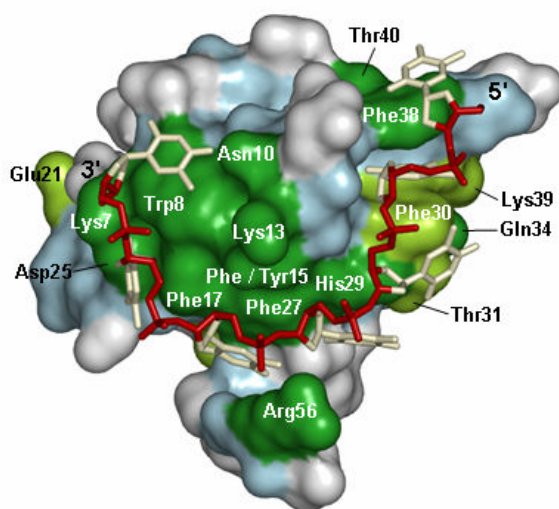


Figure 1: The ligand-binding surfaces of CSP and Y-box proteins are highly conserved. Most residues forming the ligand interaction site are conserved on the level of at least 75% identity (dark green) and similarity (light green). Invariant regions which originate from the protein backbone are colored light blue. In total 7 nucleobase binding subsites were identified which can interact with a single thymine-based heptanucleotides (sticks).

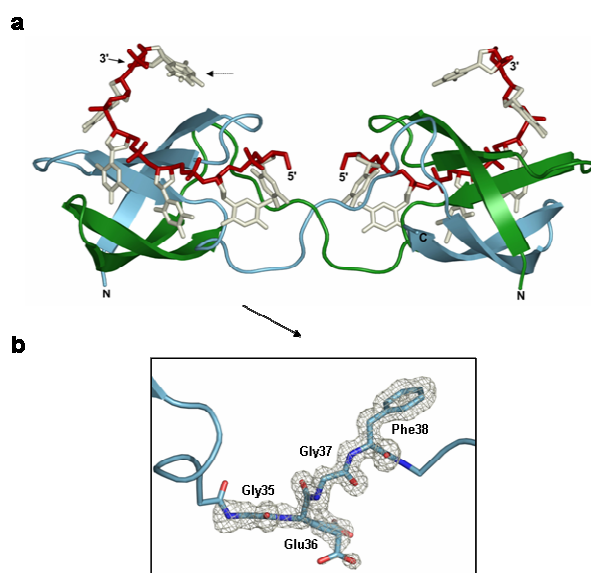


Figure 2: Crystal structure of the domain-swapped *Bc*-Csp-dT₆ complex. *a*) The DNA strands (backbone - red, bases - beige) bind to globular units of a swapped *Bc*-Csp dimer (chain A - green, chain B - blue). Each globular unit is composed of residues 1-35 and 38-66 of two different protein chains. The base of the terminal nucleotide T6 occupies two different positions in chain D (dotted arrow). *b*) The region of the domain swap in chain B revealed by $F_o - F_c$ difference electron density calculated from a model devoid of residues 35 to 38. The map (gray wireframe) was contoured at 2.5σ .

Acknowledgements

We are grateful to A. Feske (MDC, Berlin) for help with protein crystallization, and to the staff at BL 14/BESSY for help with X-ray diffraction experiments. This work was supported by a Kekulé fellowship (#668152) of the Fonds der Chemischen Industrie to K.M. and the Deutsche Forschungsgemeinschaft.

Crystal Structure of human Saposin D Involved in Sphingolipid Degradation in Lysosomes

Maksim Rossocha¹ and Timm Maier¹, Robert Schultz-Heienbrok¹, Joachim Behlke², Natascha Remmel³, Claudia Alings¹, Konrad Sandhoff³, Wolfram Saenger¹

¹ *Institut für Chemie / Kristallographie, Freie Universität Berlin, Takustr.6, 14195 Berlin, Germany*

² *Kekulé-Institut für Organische Chemie und Biochemie der Universität Bonn, Gerhard-Domagk Str.1, 53121 Bonn, Germany*

Saposins (Sap) A, B, C and D are homologous amphipathic glycoproteins involved in a variety of cellular processes accompanied by lipid transport and modulation of lipid bilayers. They are non-enzymatic activator proteins that belong to the large and divergent family of more than 200 known saposin-like proteins and domains containing the saposin fold. Saposins mediate amongst others the interaction between membrane-bound glycosphingolipids and water-soluble specific exohydrolases facilitating access of the active site of enzymes to short head groups of oligosaccharides. Inherited deficiencies of either lysosomal hydrolases or saposins give rise to more than 40 glycosphingolipid storage disorders, including Gaucher, Fabry and Niemann-Pick diseases. Besides the saposins themselves, which play a major role in mediating membrane degradation in the lysosome, saposin folds have been identified in proteins as diverse as cytolytic proteins from amoeba and human natural killer cells, jellyfish lens crystallin, lipopolysaccharide hydrolase, plant aspartic proteases, and neurotrophic factors. Despite their similar structures, each saposin promotes the degradation of specific sphingolipids in lysosomes. SapD for instance accelerates the sphingomyelinase activity and is involved in ceramide hydrolysis and the catabolism of glycosphingolipids containing alpha-hydroxylated acyl chains. It is a primary saposin that is stored in the liver of patients with Nieman-Pick disease.

We expressed the recombinant SapD and variant SapD-K9/E9 in the yeast *P. pastoris* expression system. After purification, the proteins were crystallised in acidic solution containing sulfate ions. Using synchrotron radiation from BESSY II / Berlin, we were able to obtain X-ray diffraction data from these crystals suitable for structure determination. The crystal structure allowed us not only to visualize the tertiary structures of human SapD and variant SapD-K9/E9, but also its higher structural (quaternary) organisation. SapD crystallises as dimer and adopts the well known compact saposin fold common to other non-liganded members of the family. Comparison of different crystal forms of SapD suggested the most likely physiological dimer interface (Fig. 1). Analytical ultracentrifugation experiments confirmed that SapD forms homo-dimers also in solution.

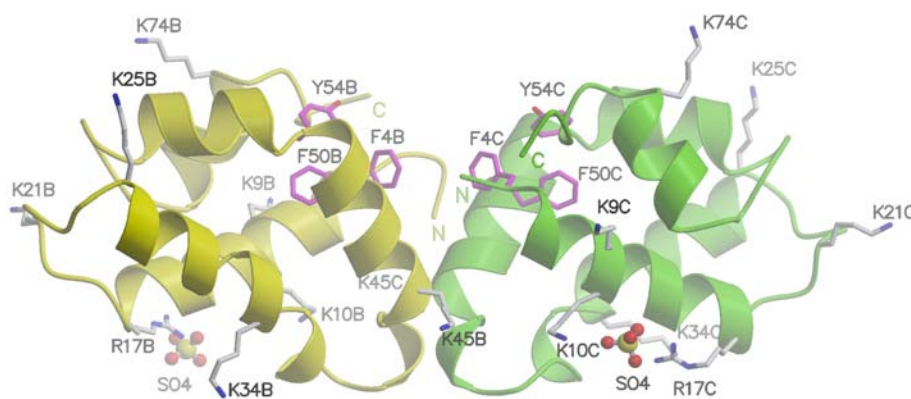


Fig 1. SapD forms a homo-dimer. The crystal structure of SapD revealed that Lys10 and Arg17 are binding sites for sulfate ion and may serve as one of the phosphate binding sites, promoting the initial binding of SapD to biological membranes. Conserved aromatic residues Tyr4, Phe50 and Tyr54 are proposed to be involved in specific protein-sphingolipid interactions.

Negatively charged lipids are known to be important for saposin-membrane interactions. At low pH, the cluster of positively charged amino acids lysine and arginine are supposed to promote the initial binding of saposins to negatively charged phosphate groups. The crystal structure of SapD revealed Lys10 and Arg17 as binding sites for sulfate and may serve as one

of the phosphate binding sites, promoting the initial binding of the saposin to biological membranes (Fig 2).

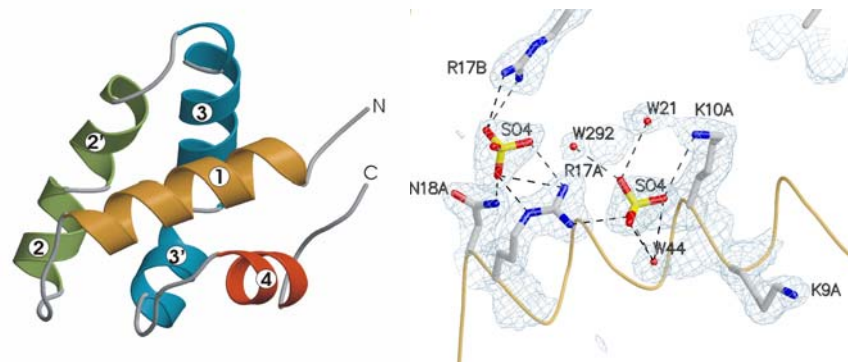


Fig 2. Crystal structure of the SapD monomer (left). Positively charged lysine and arginine residues of Helix 1 are involved in sulfate binding (right). The electron density surrounding the side chain atoms, sulfate ions and water molecules is contoured at 1σ .

Residue Lys9 is strongly conserved among SapD's from different organisms. Surprisingly no sulfate atoms were found bound at Lys9. To investigate the role of this residue we mutated the Lys9 to negatively charged glutamate. The crystal structure of this SapD variant revealed that the mutation did not affect the binding of sulfate ions to Lys10 and/or Arg17.

The crystal structure of SapD provides insights into the saposin-lipid interaction. These studies would also be of importance for the whole growing class of lipid binding proteins.

References

- [1] Timm Maier
X-Ray Structure Analysis of Proteins of Human Sphingolipid Metabolism
PhD Thesis, FU Berlin, 27.01.2004
- [2] Massimo Tatti, Rosa Salvioli, Fiorella Ciaffoni, Piero Pucci, Annapaola Andolfo, Angela Amoresano and Anna Maria Vaccaio
Structural and membrane-binding properties of saposin D
Eur. J. Biochem. **263**, 486-494 (1999)

Crystal structure of the FK506-binding domain of human FKBP38

C. Parthier¹, M. Maestre-Martínez², P. Neumann¹, F. Edlich², C. Lücke², M. T. Stubbs^{1,3}

¹Institut für Biochemie und Biotechnologie, Martin-Luther-Universität Halle-Wittenberg, Kurt-Mothes-Straße 3, D-06120 Halle (Saale), Germany

²Max Planck Forschungsstelle für Enzymologie der Proteinfaltung, Weinbergweg 22, D-06120 Halle (Saale), Germany

³Mitteldeutsches Zentrum für Struktur und Dynamik der Proteine, Martin-Luther-Universität Halle-Wittenberg

FKBP38 is a member of the the peptidyl prolyl cis/trans isomerase (PPIase) family of FK506-binding proteins (FKBPs). This enzyme class catalyzes protein folding processes by the interconversion of cis/trans peptide bonds preceding proline residues in the polypeptide chain. FKBP38 is also involved in immunosuppression by forming tight complexes with the low-molecular-weight compound FK506, which ultimately results in prevention of T-cell proliferation by inhibition of the protein phosphatase calcineurin.

FKBP38 possesses unique properties among the human FKBP38s in that its enzymatic activity was found to be calmodulin/Ca²⁺-dependent¹. Hence, FKBP38 is the only human FKBP that is regulated by a secondary messenger, implying different structural features compared to constitutively active FKBP38s. The elucidation of the three-dimensional structures of FKBP38 and its complexes will contribute to understanding the molecular basis of its biological function(s) and the mechanism(s) by which its enzymatic activity is controlled.

The structure of the FK506-binding domain of human FKBP38 was recently solved by NMR². In parallel, high-resolution structural analysis using X-ray crystallography were initiated, to study the interactions of the FK506-binding domain in complex with different ligands and inhibitors at molecular level.

The isolated FK506-binding domain was crystallized in the spacegroup P2₁ (see table Data collection statistics). A high-resolution dataset (1.05Å) was collected at BESSY BL14.1 and the structure solved by molecular replacement.

Data collection statistics	
Space group	P2 ₁
Cell dimensions	
a, b, c (Å)	29.06, 60.29, 30.84
α, β, γ (°)	90, 97.59, 90
Resolution (Å)	1.05
Completeness (%)	90.4 (52.4)
Unique reflections	18,643
R _{merge}	4.3 (11.8)
I / σ[I]	20.1 (5.6)

The values in parentheses are for the highest-resolution shell (1.05-1.11 Å).

Figure 1 represents the overall structure of the FK506-binding domain of FKBP38. It adopts the *half β -barrel fold*, consisting of an antiparallel β -sheet wrapped around a central α -helix that encloses the active site, thereby exhibiting the typical fold of FKBP domains.

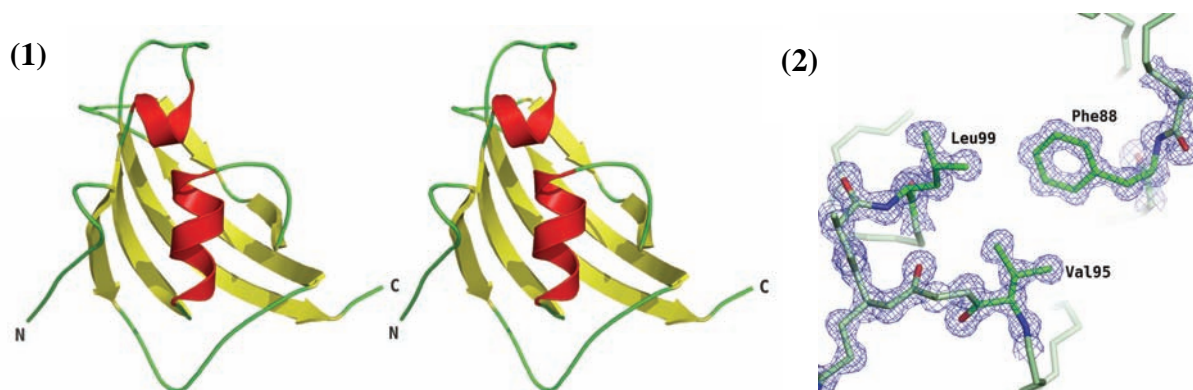


Figure (1) Stereo-view of the *half- β -barrel fold* adopted by the FK506-binding domain of human FKBP38. **(2)** $2F_o-F_c$ electron density map (blue mesh) contoured at 1.5σ shown for selected residues (stick representation) that form part of the interface between the β -sheet and central α -helix.

The key question why the FK506-binding domain of FKBP38 - in contrast to other FKBP - exhibits neither PPIase activity nor affinity to the inhibitor FK506 in the absence of calmodulin remains unclear. Further crystallographic studies on FKBP38 will help to understand the structural basis of its binding properties, and reveal how the enzyme is regulated by Ca^{2+} /calmodulin.

Acknowledgments This work was supported by the Sonderforschungsbereich 604 “Multifunctional signalling proteins” and the Graduiertenkolleg 1026 “Conformational transitions in macromolecular interactions”. We thank Melanie Kirchner for excellent technical support.

References:

1. Edlich, F. *et al.* Bcl-2 regulator FKBP38 is activated by Ca^{2+} /calmodulin. *EMBO J.* **24**, 2688-2699 (2005).
2. Maestre-Martinez, M. *et al.* Solution structure of the FK506-binding domain of human FKBP38. *J. Biomol. NMR* **34**, 197-202 (2006).

Fatty acid metabolizing enzymes

Susan Arent, Anette Henriksen

*The Biostructure Group, Carlsberg Laboratory, Gamle Carlsberg Vej 10,
DK-2500 Valby, Denmark*

Lipids constitute a diverse group of compounds of which some are involved in structural organization of the cell, some in intracellular signaling, and others in energy storage. The aims of experiments in this proposal are to investigate interactions between lipids and proteins in the peroxisomal β -oxidation pathway and in the fatty acid synthesizing pathways. The interplay between these opposing pathways determines the level of free fatty acids in the cell and is essential in regulation of cell viability versus apoptotic processes.

Enzymes involved in fatty acid synthesis have come into focus as targets for new antibiotics and in cancer treatment. The fatty acid synthase found in mammalian cytosol is multifunctional and encoded by a single gene, while mitochondria, plant chloroplast and bacteria fatty acid synthases (FASes) have the individual enzymatic activities encoded by discrete genes. A description of the exact role, electrostatic properties, and hydrogen bonding potentials of active site residues in the different FASes would facilitate inhibitor optimization and differentiation.

β -ketoacyl-ACP synthase (KAS) catalyze the first devoted step in fatty acid synthesis. KAS I from *Escherichia coli* represent the group of decarboxylating condensing enzymes with a cysteine nucleophile and two active site histidines (CHH enzymes) to which also the KAS domain of the mammalian FAS belongs. While mammalian FAS only have one type of KAS domain, bacteria most often have three or more KAS isozymes with different but overlapping substrate specificity. *In vitro* *E. coli* KAS I catalyzes all condensation reactions needed for synthesis of long chain fatty acids, except elongation of palmitoleoyl-ACP. Diffraction data have been collected on wild type KAS I crystals soaked with C10-CoA and C14-CoA. Data from the C10-CoA soaked crystals showed diffraction to 1.65Å resolution and the structure has been refined to $R_{\text{free}}/R_{\text{cryst}}$ of 0.17/0.19, respectively (Table 1). Several data sets from C14-CoA soaked crystals were collected. The crystals was soaked using a range of conditions as C14-CoA is not readily soluble in water. Data were collected 1.94 Å.

Table 1. Data collection and refinement statistics

	KASI:C10	KASI:C14
Resolution (Å)	27.00 - 1.65	45.60-1.94
R_{merge}	0.088	0.089
$I/\sigma I$	6.7	6.1
$R_{\text{free}}/R_{\text{cryst}}$	0.16/0.19	0.18/0.21
$\langle B \rangle$ (Å ²)	19.4	20.2
Rmsd bond lengths (Å)	1.19	0.93
Rmsd bond angles (°)	0.010	0.006

Although several studies have addressed inhibitor binding to *E. coli* KAS enzymes no systematic study of the acyl-binding pocket possibilities has been made. We are characterizing the acyl-binding pocket plasticity by introducing acyl chains of different length to the active site of *E. coli* KAS I and have obtained data suggesting that the arrangement of residues in the deep end of the acyl binding pocket does not allow substrates longer than twelve carbon atoms to bind to both subunits at the same time.

The peroxisomal β -oxidation pathway is responsible for the majority of fatty acid oxidation in plants. The products of the pathway are multifunctional and include jasmonic acid, indole-acetic acid, H_2O_2 and acetyl-CoA, the entry molecule for Krebs cycle. Control over fatty acid oxidation appears to be required for controlled production of specific fatty acids in plants and for incrementing the fatty acid level. Fatty acids enter the cycle in the form of acyl-CoA thioesters but are shortened by a two-carbon unit during one reaction cycle. One acetyl-CoA molecule is produced by each reaction cycle. The first and rate limiting step in the peroxisomal β -oxidation is the introduction of a double bond into the acyl-CoA substrate. This reaction is catalyzed by the FAD containing acyl-CoA oxidases (ACXs). The second (enoyl-CoA hydratase) and third (hydroxyacyl-CoA dehydrogenase) step in the reaction is catalyzed by multifunctional proteins, MFPs, while the last thiolytic cleavage of the carbon-carbon bond are catalyzed by thiolases (KATs). Crystal structures of peroxisomal ACXs and KATs are known.

We have collected native data from *Arabidopsis thaliana* MFP2 crystals to solve the structure of this enzyme and analyze enzyme interactions in the peroxisomal β -oxidation. Data in space group $P6_1/6_5$ were collected to 3.5 Å, with a completeness of 81% and a multiplicity of 2.4. Data analysis using the xtriage program shows the data to originate from twinned crystals and structure determination is being pursued with MR techniques and production of Se-Met protein.

Structure determination of biphenyl synthase (BIS)

P. Neumann¹, B. Epler¹, T. Raeth², T. Beuerle², L. Beerhues², M. T. Stubbs¹

- (1) Institut für Biochemie und Biotechnologie, Martin-Luther-Universität Halle-Wittenberg, Kurt-Mothes-Straße 3, D-06120 Halle (Saale), Germany
- (2) Institut für Pharmazeutische Biologie, Technische Universität Braunschweig, Mendelssohnstraße 1, 38106 Braunschweig, Germany
- (3) Mitteldeutsches Zentrum für Struktur und Dynamik der Proteine, Martin-Luther-Universität Halle-Wittenberg

Biphenyls and dibenzofurans are the phytoalexins of the Maloideae, a subfamily of the economically important Rosaceae. The most important fruits are apples, pears and stone fruits such as peach, apricot, cherry, plum and almond. Other members of the rose family are strawberries as well as blackberries and raspberries. Despite this considerable economic importance of rosaceous plants, their disease resistance mechanisms are relatively poorly understood. Following fungal infection, biphenyls and dibenzofurans accumulate as phytoalexins in the sapwood of a number of Maloideae species. In the leaves of *Sorbus aucuparia* the biphenyl aucuparin accumulate in response to biotic and abiotic elicitation. The carbon skeleton of the two classes of antimicrobial secondary metabolites is formed by biphenyl synthase (BIS). The homodimeric enzyme catalyzes the formation of the C12 skeleton of biphenyls and likely dibenzofurans (Hrazdina 2003).

BIS is a novel type III polyketide synthase (PKS) that shares about 60% amino acid sequence identity with other members of the enzyme superfamily. Its preferred starter substrate is benzoyl-CoA that undergoes iterative condensation with three molecules of malonyl-CoA to give 3,5-dihydroxybiphenyl via intramolecular aldol condensation. In contrast to the closely related chalcone synthase (CHS) BIS does not accept CoA-linked cinnamic acids such as 4-coumaroyl-CoA. In a phylogenetic tree, BIS group together closely with benzophenone synthase (BPS) that also uses benzoyl-CoA as starter molecule but cyclizes the common intermediate via intramolecular Claisen condensation.

BIS mechanism

The starter substrate for BIS is benzoyl-CoA a rare starter molecule for PKSs. Both BIS and BPS catalyze the iterative condensation of benzoyl-CoA with three acetyl units from malonyl-CoA to give identical linear tetraketides (Fig 1). While BPS cyclizes this intermediate via an intramolecular C6!C1 Claisen condensation, BIS catalyzes an intramolecular C2!C7 aldol condensation and decarboxylative elimination of the terminal carboxyl group. The two type III PKSs share 54% amino acid sequence identity over their approx. 400 amino acids. Biphenyl synthase and BPS each are inactive with CoA-linked cinnamic acids such as 4-coumaroyl-CoA, the preferred starter molecule for CHS and STS. Side products released by derailment after two and three condensation reactions with malonyl-CoA are frequently observed with type III PKSs, especially CHSs. Both benzoyl-CoA and 4-coumaroyl-CoA arise from cinnamic acid that is in turn derived from phenylalanine.

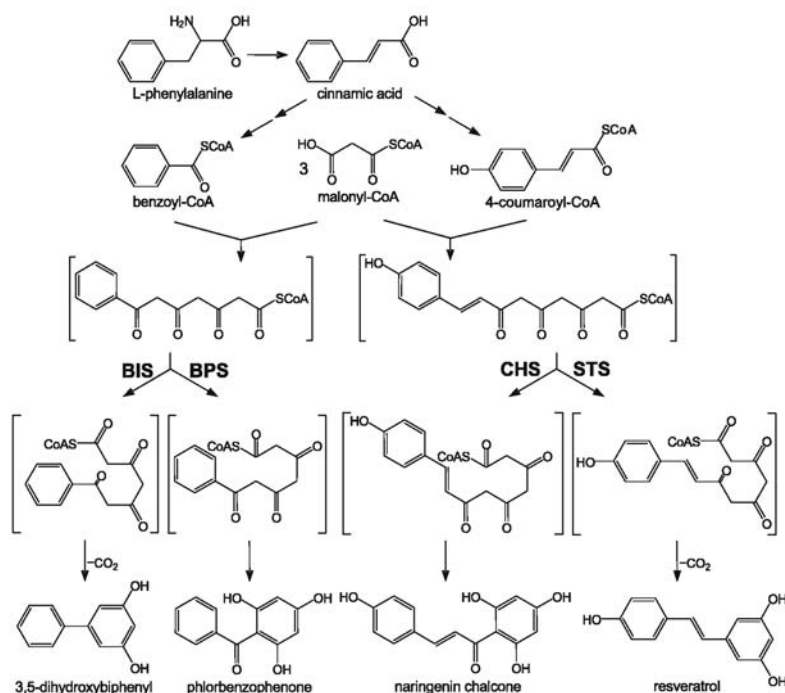


Fig. 1 Reactions catalyzed by type III PKSs. BIS biphenyl synthase, BPS benzophenone synthase, CHS chalcone synthase, STS stilbene synthase. The biogenic relationship of their starter substrates is also shown.

The structure solution

Biphenyl synthase (BIS) crystallizes in space group P2(1) with unit cell dimensions of $a = 73.182 \text{ \AA}$, $b = 117.306 \text{ \AA}$, $c = 92.223 \text{ \AA}$, $\beta = 112.670^\circ$ and four monomers (two independent dimers) in the asymmetric unit. The structure was determined by molecular replacement method (MR) and refined to a resolution of 3.0 \AA . The starting model for MR was the CHS monomer (Noel 1999). The final model contains residues from 15 to 392 for each of the monomers. The missing protein residues exhibit no interpretable electron density maps and are most likely disordered. The final R and R_{free} are 21.92% and 27.94% respectively.

The second crystal form of BIS crystallizes in space group P1 with unit cell dimensions of $a = 73.410 \text{ \AA}$, $b = 93.880 \text{ \AA}$, $c = 117.930 \text{ \AA}$, $\alpha = 73.27^\circ$, $\beta = 89.80^\circ$, $\gamma = 68.30^\circ$ and eight monomers (four independent dimers) in the asymmetric unit. The structure was also determined by MR and refined to a resolution of 3.0 \AA . The final R and R_{free} are 28.82% and 31.62% respectively.

Table 1. The crystallographic statistic for BIS in P2(1) and P1 space groups.

<i>Data collection</i>	<i>BIS P21</i>	<i>BIS P1</i>
Wavelength (Å)	$\lambda = 1.5418$	$\lambda = 1.5418$
Max. resolution (Å)	3.0	3.0
R_{merge}	0.232 (0.644)	17.4 (31.0)
% complete	98.0 (97.1)	95.7 (94.4)
No. of reflections	84844	104956
No. of unique reflections	28260	53385
$\langle I/\sigma(I) \rangle$	4.9 (1.8)	4.72 (2.6)

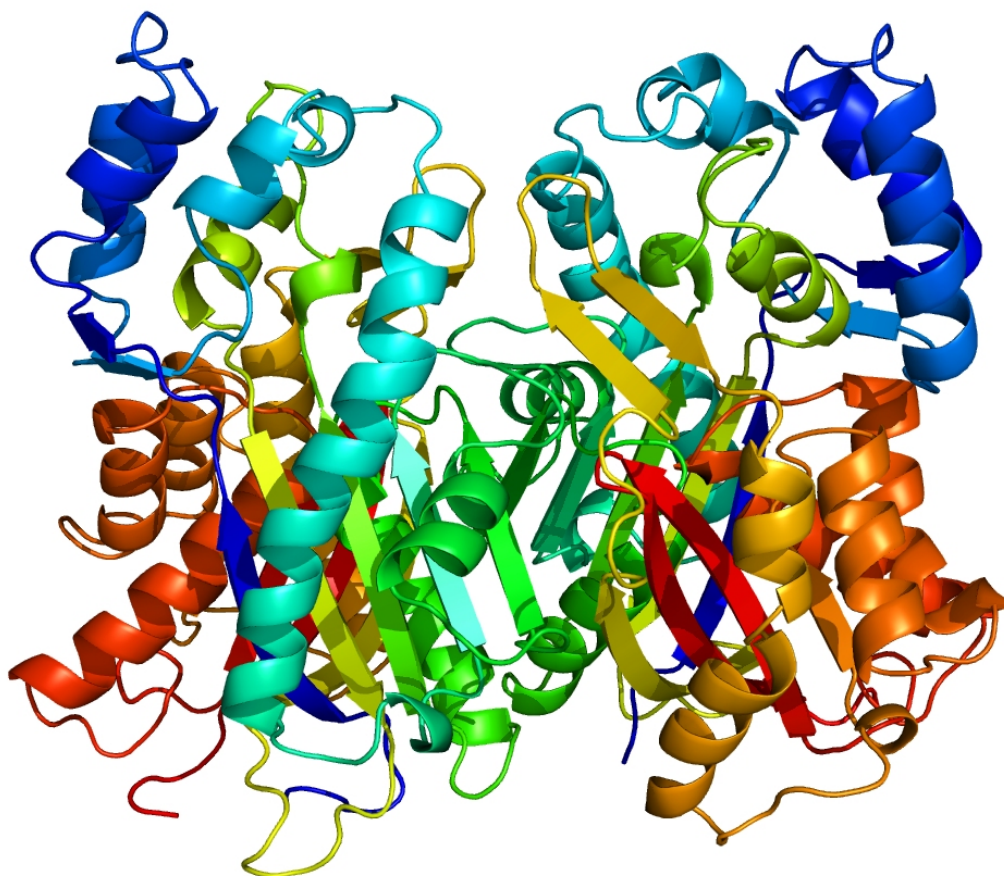


Fig 2. The BIS dimer, each monomer is colored according to the residue number.

Due to the problems with cryo conditions, we were not able to collect any higher resolution data at BESSY for either crystal form of BIS. This will be the major emphasis of our further work, together with ligand binding studies.

Acknowledgments This work was supported by the DFG Schwerpunktprogramm 1152 “Evolution metabolischer Diversität” and the Graduiertenkolleg 1026 “Conformational transitions in macromolecular interactions”.

Literature:

B. Liu, T. Raeth, T. Beuerle and L. Beerhues (2006) Biphenyl synthase, a novel type III polyketide synthase. *Planta* DOI 10.1007/s00425-006-0435-5

Hrazdina G (2003) Response of scab-susceptible (McIntosh) and scab-resistant (Liberty) apple tissues to treatment with yeast extract and *Venturia inaequalis*. *Phytochemistry* 64:485–492

Kokubun T, Harborne JB (1995) Phytoalexin induction in the sapwood of plants of the Maloideae (Rosaceae): Biphenyls or dibenzofurans. *Phytochemistry* 40:1649–1654

Ferrer JL, Jez JM, Bowman ME, Dixon RA, Noel JP (1999) Structure of chalcone synthase and the molecular basis of plant polyketide biosynthesis *Nat Struct Biol.* 1999 Aug;6(8):775-84.

Photosynthetic water oxidation: The protein-bound manganese complex of Photosystem II and biomimetic models studied by XAS at the Mn K-edge

Alexander Grundmeier¹, Boris Repen¹, Björn Süss¹, Thomas Tietz², Christian Limberg², Magnus Anderlund³, Ann Magnuson³, Michael Haumann¹, Holger Dau^{1*}

¹*Freie Universität Berlin, FB Physik, Arnimallee 14, D-14195 Berlin, Germany;*

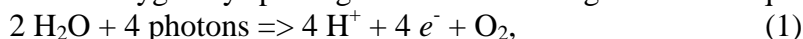
²*Humboldt-Universität Berlin, Inst. f. Chemie, Brook-Taylor-Strasse 2, D-12489 Berlin, Germany;*

³*Uppsala University, Molecular Biomimetics, Villavagen 6, S-752 36 Uppsala, Sweden;*

**Email: holger.dau@physik.fu-berlin.de*

Introduction

Driven by the absorption of four light quanta (photons), plants and cyanobacteria produce the atmospheric dioxygen by splitting of water according to the net equation:



where e^- denotes the electrons extracted from water (water oxidation), which eventually serve as reducing equivalents in the carbon fixation chemistry of the Benson-Calvin cycle. The locus of water splitting is a manganese-calcium complex bound to the proteins of Photosystem II (PSII) which cycle through various intermediate states [1-5]. Water oxidation by PSII is a process of fundamental importance for the atmosphere (O_2 production) and biosphere (primary biomass formation) of the Earth. Furthermore, it is foreseeable that biotechnological and biomimetic approaches for light-driven H_2 -production from water need to become a cornerstone in the worldwide endeavor to move from fossil fuels to hydrogen-based fuel technologies [6]. The crucial and chemically especially challenging step in light-driven H_2 production, namely the splitting of water according to Eq. 1, takes place in PSII. In this realm, elucidation of the mechanism photosynthetic water oxidation by PSII—including the light-driven assembly of the Mn_4Ca complex, photodestruction, photoprotection, and repair mechanisms—is of prime interest. Furthermore, studies on biomimetic model complexes do (i) promote an improved understanding of the PSII chemistry and (ii) are of interest in the effort to develop systems for artificial photosynthesis [7, 8]. Here we report, inter alia, the characterisation of two synthetic compounds at beamline KMC1 in an XAS-experiment for ultra-dilute samples.

Materials and Methods

XAS measurements were carried out at the bending-magnet beamline KMC-1 using a double crystal monochromator in a scan range of 6400-7200 eV. For X-ray fluorescence detection, a photodiode and an energy-resolving single-element solid-state detector were employed. Further details of the KMC1 experiment are described in [9]. The setup for XAS was improved with respect to previous measuring periods: (1) The cryostat was moved to the end of the beamline by ~4 m. The result was that the spot size of the X-ray beam on the sample was increased to about 5 mm x 0.5 mm, thereby reducing the problem X-ray induced modifications of the protein samples (2) A newly purchased heavy experimental table was employed to mount the cryostat system, improving the vibration resistance of the setup. (3) Besides of the energy-resolving detector we employed a photodiode for fluorescence measurements on high-concentration samples to avoid saturation effects. (4) As a next step, we are purchasing an high-stability ion chamber to be mounted in the vacuum line for enhanced precision of the I_0 -measurement.

Results

Two Mn compounds were studied by XAS: (1) A dimanganese complex (Fig. 1A) which catalyzes the oxidation of water by *tert*-butylhydrogenperoxide or cerium nitrate to dioxygen [10]. This complex is assumed to be stable in aqueous solution. (2) A tri-nuclear Mn complex

(Fig. 1B) in its crystalline form which previously has been studied by us in acetonitrile solution by XAS measurements at BESSY (Limberg and coworkers, unpublished). In addition, XAS measurements were performed on the native manganese complex of photosystem II. Respective PSII protein samples were prepared aiming at the population of intermediates in the light-driven assembly of the Mn complex [9].

XAS measurements were performed in a temperature range from 10 K to room temperature using a helium-cryostat system. The analysis of the temperature dependence of EXAFS spectra of model compounds and PSII was expected to provide information whether specific dynamics at the atomic level contribute to efficient Mn oxidation in photosystem II.

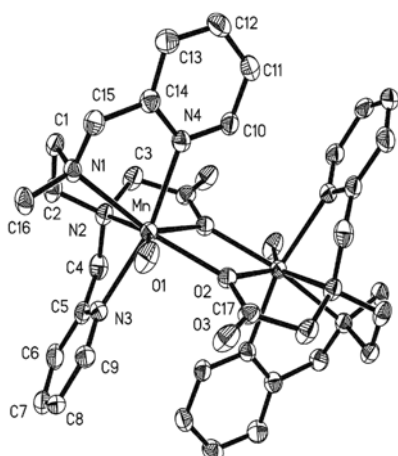


Fig. 1A: Crystal structure [3] of $[\text{Mn}^{\text{II}}_2(\text{mgbpen})_2(\text{H}_2\text{O})_2](\text{ClO}_4)_2$ which has been synthesized in the laboratory at Uppsala University. The Mn-Mn distance is ~ 4.1 Å.

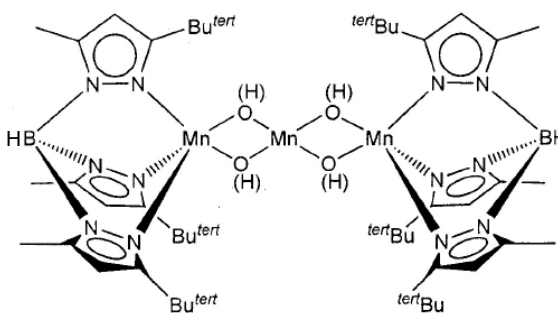


Fig. 1B: Crystal structure of a trinuclear Mn complex which has been synthesized in the group of Prof. C. Limberg at Humboldt University. Mn-Mn distances are on the order of 2.9 Å.

Fig. 2A shows a representative EXAFS spectrum of the compound in Fig. 1A measured at 20 K in aqueous solution. In the FT (Fig. 2B), two main peaks are resolved and weak features around 4 Å are discernable. Peak I is due to Mn-O/N vectors. Preliminary data analysis suggests that peak II may be attributable to multiple-scattering effects. The Mn-Mn vector presumably corresponds to peak III. A similar EXAFS spectrum was observed when the complex was measured in its crystalline state, proving that surprisingly it is stable in water. Fig. 3 shows the FT of a 20 K EXAFS spectrum of the complex in Fig. 1B in its crystalline state. Mn-Mn distances at ~ 2.9 Å are clearly visible. Comparison of Mn K-edge energies (not shown) revealed that a Mn(IV) atom becomes Mn(III) in acetonitrile solution. The temperature dependence of the EXAFS spectra of both complexes currently is analyzed.

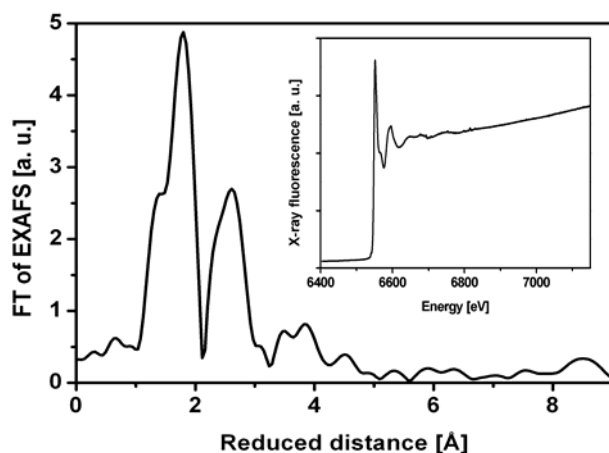


Fig. 2: FT of EXAFS of the dinuclear Mn complex in Fig. 1A at 20 K in aqueous solution. Inset: Raw EXAFS data.

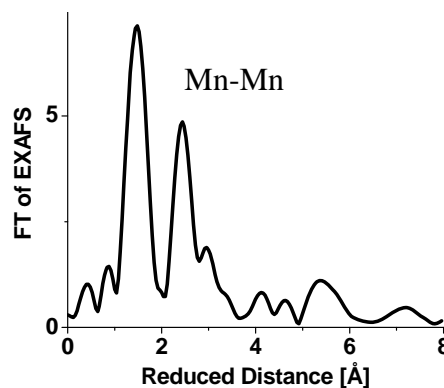


Fig. 3: FT of EXAFS of the trinuclear Mn complex in Fig. 1B (crystalline state) at 20 K.

Conclusion

EXAFS spectra of good quality were obtained on two Mn model compounds in solution and in the crystalline state and in a broad temperature range. Comparison of XANES and EXAFS spectra indicate that the complex of Fig. 1A is largely stable also in an aqueous environment (i. e. dissolved in water), in contrast to most synthetic Mn complexes. This property is of obvious importance for water oxidation by synthetic complexes. The measurements of the complex of Fig. 1B provided interesting insights in its structure, for various states of the molecule. The measurements on the Mn complex of PSII protein revealed that further upgrading of the setup is necessary to improve the spectra of ultra-dilute samples. Such improvements will be implemented during the next measuring period.

Acknowledgement

We gratefully acknowledge excellent support by the scientists at beamline KMC-1 Drs. Franz Schäfers and Marcel Mertin and funding by the DFG within SFB 498 (Berlin).

References

- [1] M. Haumann, P. Liebisch, C. Müller, M. Barra, M. Grabolle, H. Dau, Photosynthetic O₂ formation tracked by time-resolved X-ray experiments, *Science* 310 (2005) 1019-1021.
- [2] H. Dau, M. Haumann, Reaction cycle of photosynthetic water oxidation, *Science* 312 (2006) 1471-1472.
- [3] H. Dau, M. Haumann, X-ray absorption spectroscopy to watch catalysis by metalloenzymes: Status and perspectives discussed for the water-splitting manganese complex of photosynthesis, *J. Sync. Rad.* 10 (2003) 76-85.
- [4] H. Dau, P. Liebisch, M. Haumann, X-ray absorption spectroscopy to analyze nuclear geometry and electronic structure of biological metal centers - potential and questions examined with special focus on the tetra-nuclear manganese complex of oxygenic photosynthesis, *Anal. Bioanal. Chem.* 376 (2003) 562-583.
- [5] M. Haumann, C. Müller, P. Liebisch, L. Iuzzolino, J. Dittmer, M. Grabolle, T. Neisius, W. Meyer-Klaucke, H. Dau, Structural and oxidation state changes of the photosystem II manganese complex in four transitions of the water oxidation cycle (S₀→S₁, S₁→S₂, S₂→S₃, S_{3,4}→S₀) characterized by X-ray absorption spectroscopy at 20 K as well as at room temperature, *Biochem.* 44 (2005) 1894-1908.
- [6] N.S. Lewis, D.G. Nocera, Powering the planet: chemical challenges in solar energy utilization, *Proc Natl Acad Sci U S A* 103 (2006) 15729-35.
- [7] A. Magnuson, P. Liebisch, J. Hogblom, M.F. Anderlund, R. Lomoth, W. Meyer-Klaucke, M. Haumann, H. Dau, Bridging-type changes facilitate successive oxidation steps at about 1 V in two binuclear manganese complexes--implications for photosynthetic water-oxidation, *J Inorg Biochem* 100 (2006) 1234-43.
- [8] A. Magnuson, Y. Frapart, M. Abrahamsson, O. Horner, B. Åkermark, L. Sun, J.J. Girerd, L. Hammarström, S. Styring, A biomimetic model system for the water oxidizing triad in photosystem II, *J. Am. Chem. Soc.* 121 (1999) 89-96.
- [9] M. Barra, M. Haumann, P. Loja, R. Krivanek, A. Grundmeier, H. Dau, Intermediates in assembly by photoactivation after thermally accelerated disassembly of the manganese complex of photosynthetic water oxidation, *Biochem.* 45 (2006) 14523-14532.
- [10] C. Baffert, M.N. Collomb, A. Deronzier, S. Kjærgaard-Knudsen, J.M. Latour, K.H. Lund, C.J. McKenzie, M. Mortensen, L. Nielsen, N. Thorup, Biologically relevant mono- and di-nuclear manganese II/III/IV complexes of mononegative pentadentate ligands, *Dalton Transactions* (2003) 1765-1772.

IR - Synchrotron Mapping Ellipsometry for Characterisation of Biomolecular Films

K. Hinrichs^{1,6}, M. Gensch^{1,6}, G. Dittmar⁴, S. D. Silaghi¹, D.-M. Rosu¹, U. Schade³, D.R.T. Zahn², S. Kröning⁵, R. Volkmer⁵ and N. Esser¹

¹ Institute for Analytical Sciences- ISAS, Albert-Einstein-Str. 9, D - 12489 Berlin

² Chemnitz University of Technology, Semiconductor Physics, D- 09107 Chemnitz

³ BESSY GmbH, Albert-Einstein-Str. 15, 12489 Berlin, Germany

⁴ Sentech Instruments GmbH, Carl Scheele Str. 16, 12489 Berlin

⁵ Charité Universitätsmedizin Berlin, Institut für Medizinische Immunologie, Abteilung Molekulare Bibliotheken, Hessische Str. 3-4 , 10115 Berlin, Germany

⁶ present adress: Deutsches Elektronen-Synchrotron (DESY), Notkestr. 85, 22607 Hamburg, Germany

In previous synchrotron studies nanostructured and biomolecular films have been characterized by IR ellipsometry [1-5] and complementary methods (VUV ellipsometry, XRD and AFM) with respect to the thin film structure. Recently in cooperation with Sentech Instruments the IR synchrotron mapping ellipsometer was upgraded with a rotating retarder option (see Fig. 1). This rotating retarder delivers a continuous change of the introduced phase shift without changing the optical path of the reflected radiation. This additional phase shift e.g. allows more sensitive measurements when $\cos\Delta$ is close to one. Previously for this purpose a prism in ATR geometry was used, which afforded a change of the optical path.

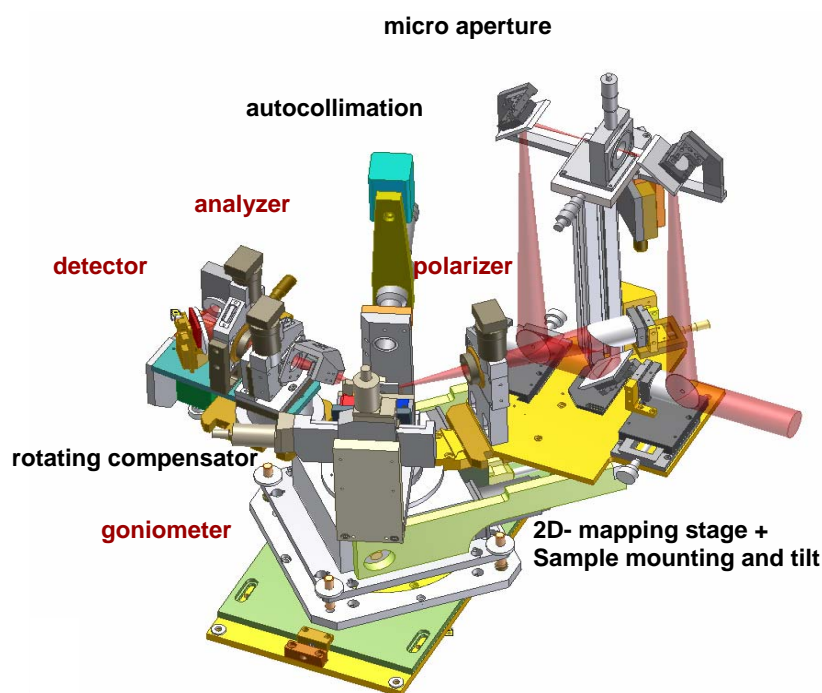


Fig. 1: Infrared (IR)-Mapping ellipsometer with 2-dimensional mapping stage, autocollimation, rotating retarder and microfocus unit at the IR synchrotron beamline at BESSY in Berlin.

In the following the first results taken with the upgraded IR synchrotron mapping ellipsometer are shown.

A) Biosensors

Currently used standard methods to read out microarrays are dependent on fluorescence and chemiluminescence-imaging techniques. These methods require labeling of a component by a marker and usually only detect the concentration of the marker molecule. A label-free imaging method that also enables a quantitative spectroscopic analysis of the composition and, moreover, possible interaction of components would be of great advantage. Therefore IR mapping ellipsometry (Fig. 1) was applied for the label-free imaging of a biochip before and

after incubation with peptide solution [3]. The general principle of such biosensors is based on the fact that peptides, proteins, enzymes, antibodies, antigens and DNA-fragments can be attached via specific linker molecules to a silicon chip. Electronic recognition of the specific adsorption site can serve for fast analysis of the samples under investigation. Our measurements show that IR ellipsometry is a sensitive tool for laterally resolved identification of the different materials and determination of the composition of a biosensor. The biosensor has been prepared by photo-electrochemical deposition of the linker (TFPAM-3 (*N*-(4-azido-2,3,5,6-tetrafluorobenzyl)-3-maleimidopropionamide)) on a hydrogen passivated silicon surface. After that, part of the linker covered wafer was incubated with peptide (Cys-GCN4) solution. Ellipsometric spectra of the biosensor were taken before and after incubation with the peptide solution. Fig. 2 shows maps (6 mm x 6 mm) of amplitudes of a linker specific band at 1288 cm^{-1} and a peptide specific band at 1547 cm^{-1} . From both maps linker and peptide covered regions of a sample surface are easily identified. As expected, the peptide was only found on those sample regions which were initially incubated by peptide solution, while the non-modified “linker regions” do not show the characteristic peptide band at 1547 cm^{-1} . Under certain assumptions (isotropic film, thickness independent structure of the films) the band amplitudes of a thin film directly correlate with the thickness of the film. Presently the qualitative interpretation of the band shapes is in agreement with an isotropic film structure. However, future work will be directed onto a more comprehensive evaluation of the experimental spectra by optical simulations.

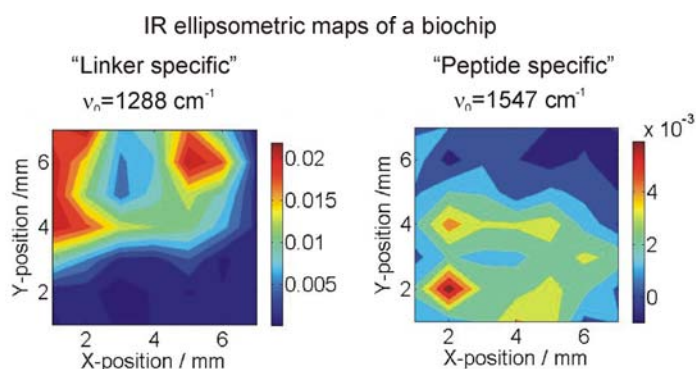


Fig. 2: Infrared ellipsometric maps of a biochip: $\tan \Psi$ band amplitudes of a linker specific band at 1288 cm^{-1} and a peptide specific band at 1547 cm^{-1} for a 6 mm x 6 mm area [3].

B) Thin cytosine film

In order to test the upgraded ellipsometer with rotating retarder a 110 nm thin cytosine film has been measured over an area of 3x3 mm^2 . The probed spots had a size of approx. 1 mm^2 in this case. By reducing the micro aperture 250x250 μm^2 lateral resolution can be achieved. Fig. 3 shows the average of the single spot spectra of the 3x3 mm^2 area in comparison to the lab measurement of the same sample.

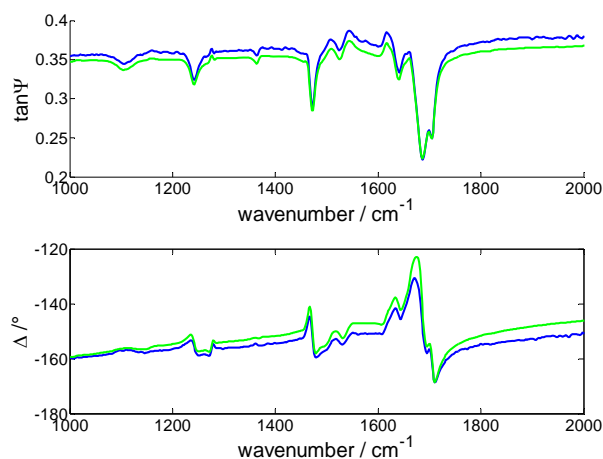


Fig. 3: Comparison of averaged synchrotron measurements (blue) of 1 mm^2 spots from a 3x3 mm^2 area and lab measurements (green) of a larger sample area ($\sim 7 \times 7 \text{ mm}^2$). The sample was 110 nm thick cytosine film on silicon.

A good agreement between lab and synchrotron measurements is found. However the spectra show slight deviations. This might be explained by the following reasons: 1) The high brilliance of the synchrotron radiation (e.g. smaller opening angle, less radiation is reflected from the backside of the transparent substrate on the detector); 2) selectively irradiated parts of not homogeneous optical elements (polarizer, detector) 3) in lab experiments the irradiated spot was larger than the sample area ($\sim 7 \times 7 \text{ mm}^2$), therefore also contributions of the inhomogeneous edges of the sample have to be considered in this case.

Fig. 4 shows maps of $\tan\Psi$ and Δ values at a frequency above the frequency range of vibrational bands of cytosine (at 1911 cm^{-1}). The maps prove that the prepared cytosine film is of homogeneous thickness. The maximum deviation of Δ is 0.2° .

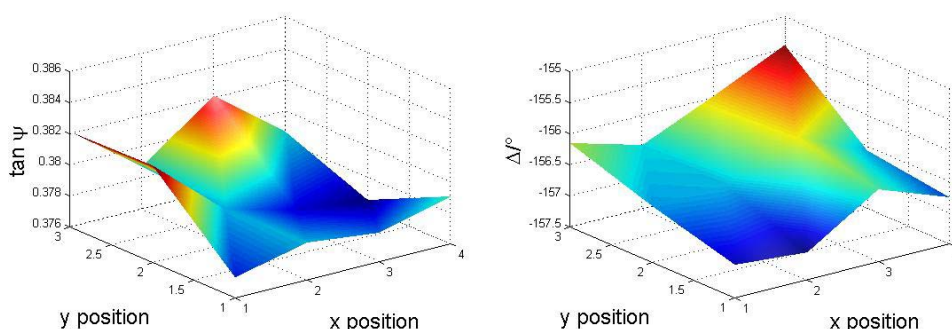


Fig. 4: Infrared ellipsometric maps of the thin cytosine film: absolute values of $\tan\Psi$ and Δ at 1911 cm^{-1} for an angle of incidence of 64° .

Support by the EU through SSA DASIM (ctr. Nr. 00055326) and through the EFRE program (ProFIT grant, contract nr. 10125494) is gratefully acknowledged. We thank Dr. A. Röseler for many valuable discussions.

[1] K. Hinrichs, M. Gensch, N. Esser (2005) *Appl. Spectroscopy* 59:272A-282A.

[2] M. Gensch, N. Esser, E. H. Korte, U. Schade, K. Hinrichs, *Infrared Physics and Technology* 49 (1-2) (2006) 39-44.

[3] K. Hinrichs, M. Gensch, N. Esser, U. Schade, J. Rappich, S. Kröning, M. Portwich, R. Volkmer, *Anal. Bioanalyt. Chem.* (2006) DOI 10.1007/s00216-006-08

[4] M. Gensch, K. Roodenko, K. Hinrichs, R. Hunger, A. Merson, J. Shapira, Th. Dittrich, J. Rappich, N. Esser, *J. Vac. Sci. Technol. B* 23 (2005) 1838.

[5] K. Hinrichs, S. D. Silaghi, C. Cobet, N. Esser and D. R. T. Zahn, *phys. stat. sol. b* 242 (2005) 2681.

Towards Crystal Structure of SMY2-GYF Domain in Free and Peptide Bound State

Miriam-Rose Ash¹, Michael Kofler¹, Tolga Helmbrecht¹, Yvette Roske²,
Katja Faelber³, Christian Freund¹

1 - AG Protein Engineering, 3 – AG Solid state NMR, Leibniz-Institut für Molekulare Pharmakologie (FMP), Robert-Rössle-Str. 10, 13125 Berlin; 2 – Proteinstrukturfabrik, Max-Delbrück-Centrum für Molekulare Medizin, Robert-Rössle-Str. 10, 13125 Berlin

GYF domains play an important role in mediating protein-protein interactions. The GYF domain is a eukaryotic protein domain, which recognizes proline-rich sequences. Two classes of GYF domains are structurally characterized, namely the CD2BP2-type and the SMY2-type. For the CD2BP2-GYF domain the binding of a peptide derived from CD2 has been characterized, whereas for the SMY2-type so far only the unbound structure of one representative (hypothetical protein At5g08430) has been determined.

Our goal was to determine the structure of the GYF domain of the SMY2 protein in free and peptide bound state.

Data collection at BESSY resulted in a 1.8Å resolution data set for crystals containing the free SMY2-GYF domain. Peptide bound SMY2-GYF crystals diffracted to 4.0Å. The data of the free SMY2-GYF domain showed hexagonal crystal lattice with cell dimensions of $a=68.2\text{Å}$, $b=68.2\text{Å}$, $c=111.1\text{Å}$, $\alpha=\beta=90^\circ$, $\gamma=120^\circ$, a completeness of 96.9% (86.9%), an average $I/\sigma(I)$ of 23.8 (4.4%) and an R_{sym} of 6.3% (49.9%). Data in brackets belong to highest resolution shell (1.77Å – 1.85Å).

Molecular Replacement failed to solve the structure using the existing NMR structure of the SMY2-type GYF domain (1WH2) as a model.

Recently we succeeded to obtain crystals with selenomethionine substituted SMY2-GYF domain. Crystals have not been tested for diffraction yet, but size and morphology look promising.

X-ray microscopy of stratum corneum – first results

S.-C. Gleber¹, J. Thieme¹, M. Noro², C. Harding², P. Guttman³

¹Institut für Röntgenphysik, Georg-August-Universität Göttingen,
Friedrich-Hund-Platz 1, D-37077 Göttingen

²Unilever R&D Port Sunlight Laboratory,
Quary Road East, Bebington, CH 633JW Wirral, United Kingdom

³Institut für Röntgenphysik, Georg-August-Universität Göttingen,
c/o BESSY GmbH, Albert-Einstein-Str. 15, 12489 Berlin

Introduction

The stratum corneum (SC) forms the outermost region of the epidermis, which makes it responsible for protection against external influences like substances or UV radiation, and against water loss. The basic structure of this 10 -20 μm thin skin layer reminds of a brick wall because of the order of lipid lamellar phase where keratin-rich corneocytes are embedded. Both physiology and kinetics are being investigated. For optical microscopic examination of the SC, various even noninvasive techniques have been developed like confocal laser scanning microscopy. For other microscopic investigation methods, thin samples are needed, which are easily gained by adhesive tape stripping, a common and well known technique to prepare certain skin samples.

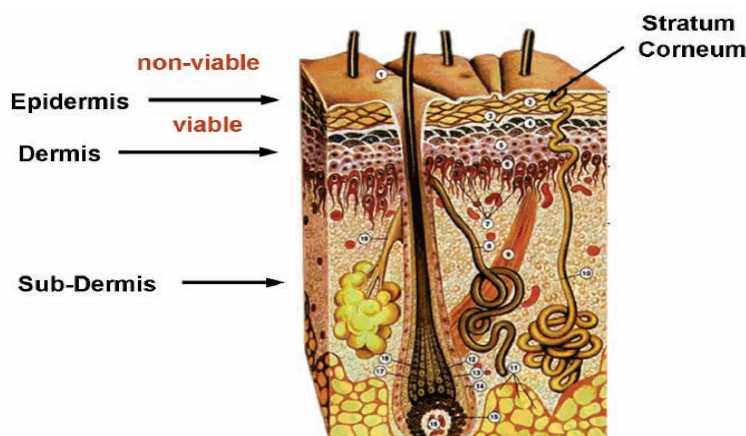


Figure 1: Scheme of skin structure

X-ray microscopy of stratum corneum

The examined samples were skin tissues taken with glue from the forearm by C. Harding. The adhesive was nearly completely removed and the remaining sample sent to Göttingen in small pieces of about 15 - 20 μm thickness (figure 2).

To compare the structures with fresh skin, skin samples were detached with tweezers from the experimentator's forearm (figure 3).

The Transmission X-ray Microscope (TXM) at undulator U41 was used to study these tissues. The images were taken at $\lambda = 2.4 \text{ nm}$ wavelength. With an outermost zone width of $dr_n = 25 \text{ nm}$ of the zoneplate the achievable resolution is around $\delta = 30 \text{ nm}$ and the depth of focus $\Delta f = 0.65 \mu\text{m}$. Smaller structures than 40 nm, however, could not be observed. The samples were held between two Si_3N_4 foils in air.

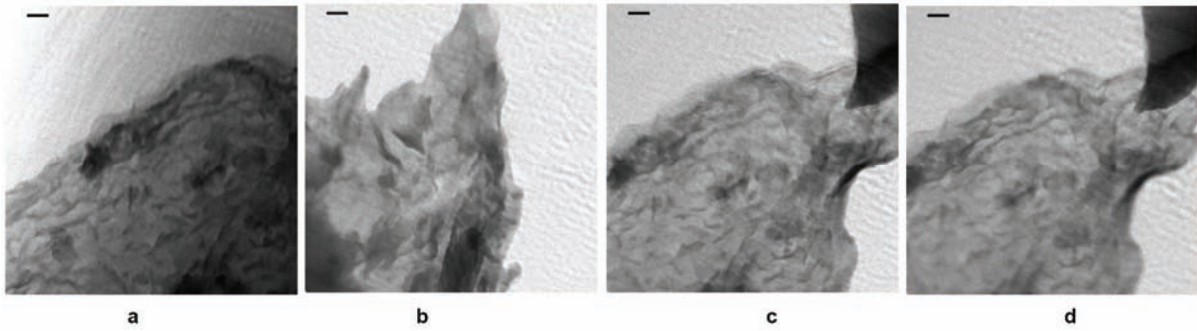


Figure 2: Micrographs of skin samples taken from a forearm. The images are taken with $t = 10$ s exposure time. (c) and (d): Images of the same sample region taken with a focus difference of 2 nm, so different layers of the skin are imaged in focus. Scale bar = $1\mu\text{m}$.

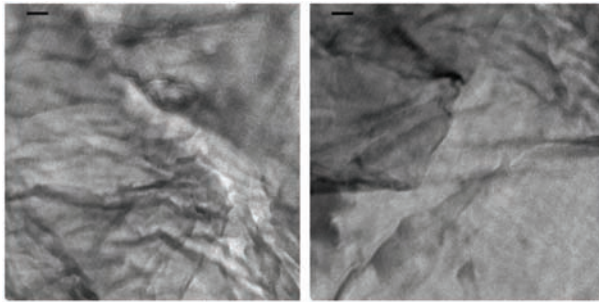


Figure 3: Micrographs of a fresh skin sample detached with tweezers from the forearm. The sample layer is about $10\text{-}15\ \mu\text{m}$ thick. The images were taken with the TXM with $t = 20$ s exposure time. Scale bar = $1\mu\text{m}$.

Results and outlook

The presented work is about using the advantages from x-ray microscopy to examine human skin cell structures. These first experiments were meant to show principle applicability and the requirements for sample preparation. The next step for imaging stratum corneum with x-ray microscopy will be a more appropriate sample preparation: most areas of the sample layers were thicker than $15\ \mu\text{m}$. A higher water content in the samples may lead to a lower density of then finer structure and thus to better visible structure in the images. Thinner layers would decrease the exposure time, so finer structures which are now not visible due to movements during long exposure time could be imaged sharply. Another aim of further work will be spectromicroscopy studies of skin samples using the Scanning Transmission X-ray Microscope at the undulator U41, obtaining spatially resolved information of chemical bonds in the skin.

Acknowledgements

This work has been funded by DFG under contract number Th 445/8-1 and is supported by the EU Network of Excellence “SoftComp”. We want to thank the staff of BESSY for excellent working conditions.

First-order phase transition near 40 °C in MnAs nanodisks

B. Jenichen, Y. Takagaki, and K. H. Ploog

*Paul-Drude-Institut für Festkörperelektronik,
Hausvogteiplatz 5-7, D-10117 Berlin, Germany*

N. Darowski, R. Feyerherm, and I. Zizak

Hahn-Meitner-Institut Berlin GmbH, Glienicker Strasse 100, D-14109 Berlin, Germany

The phase transition near 40 °C of both as-grown thin epitaxial MnAs films prepared by molecular beam epitaxy on GaAs(001) and nanometer-scale disks fabricated from the same films is studied. The disks are found to exhibit a pronounced hysteresis in the temperature curve of the phase composition. In contrast, supercooling and overheating take place far less in the samples of continuous layers.

Manganese arsenide on GaAs is a promising materials combination for spintronic applications based on spin injection [1]. MnAs is ferromagnetic at room temperature and has a large carrier spin polarization. It can serve as a source of spin polarized electrons. Furthermore MnAs may be applied for sensors and actuators thanks to its magnetoelastic response [2]. The room temperature ferromagnetic α -phase is metallic and crystallizes in the hexagonal NiAs($B8_1$) structure. Near 40 °C MnAs transforms into the orthorhombic β -phase exhibiting the MnP($B31$) structure. The temperature dependence of the magnetization near the transition was investigated in [2, 3], and a 20 K wide hysteresis loop was observed. At this first order structural phase transition a significant change in the lattice parameter a is found, which amounts to $\approx 1.2\%$ [4, 5].

During epitaxy [6, 7] the MnAs($1\bar{1}00$) film on GaAs(001) is attached by the side facet of the hexagonal unit cell, so that the c lattice direction MnAs[0001] is parallel to GaAs[$1\bar{1}0$]. The deformations in the layer lead to the phenomenon of phase coexistence, i.e. the phase content ξ does not change abruptly between zero and unity at a certain temperature as expected from the Gibbs phase rule. Two coexisting phases are found, on the contrary, in a wide temperature range [8]. Elastic domains of both phases form a periodic stripe pattern [9] in a self organized way. The domain period amounts to approximately five times the film thickness [10, 11]. Application of hydrostatic pressure [12, 13] or biaxial stress [14] has a considerable influence on the transition temperatures.

The phase transition can be affected further by imposing artificial constraints on the stripe pattern. Significant effects are expected from a lateral confinement when a film is patterned to small disks. Such disks with smaller sizes than the widths of the elastic domains enable elastic relaxation of the laterally periodic stresses accumulated inside the epitaxial layer. The tight restriction of the MnAs lattice along the interface is then released. As a consequence the formation of elastic domains in MnAs nanodisks seems to be no longer energetically favourable. The distribution of magnetic domains in such MnAs disks was investigated in [15]. The aim of the present work is to study in more detail the influence of such a lateral structuring on the phase coexistence of α and β MnAs. We investigate the temperature dependence of the phase composition in epitaxial MnAs films prior to and following the artificial modification using microfabrication technologies.

The MnAs layers were grown by solid source molecular beam epitaxy (MBE) as described elsewhere [7, 16, 17]. The nanostructuring was carried out using electron beam lithography and Ar ion milling. The resulting disks were assembled in the form of a square array. In this sample, the diameter of the disks is smaller than 100 nm, i.e. well below the equilibrium size of the elastic domains in the original continuous MnAs layer. Temperature dependent synchrotron x-ray diffraction experiments were performed at the MAGS beamline at the BESSY storage ring using a Si(111) double crystal monochromator and 8 keV radiation. A six circle diffractometer equipped with a special cryostat was employed for the measurements. Preliminary experiments were performed at a similar diffractometer of the KMC 2 beamline at BESSY. In addition we performed laboratory experiments using a Panalytical X'Pert System with Ge (220) hybrid monochromator and Ge (220) analyzer crystal.

The phase contents of the MnAs samples were obtained from the ratio of the integrated intensities of the corresponding α MnAs and β MnAs reflections measured in symmetrical $\omega/2\theta$ -scans. The ($\bar{3}300$) and (060) or the ($1\bar{1}00$) and (020) were analyzed [11, 18], and the layer reflections were fitted by Gaussian curves. The intensity ratio changes with temperature in the phase coexistence range [8]. The samples reached their equilibrium composition almost immediately after a certain temperature had been set, i.e. the relaxation times are significantly small. Samples consisting of MnAs disks having various diameters on the GaAs substrate were compared to their parent unstructured samples. The

lateral period of the domain structure of the original MnAs epitaxial layer can be obtained from the distance between satellite maxima $\Delta\omega_S$ in the x-ray triple crystal ω -scan. The period Λ_d is calculated from the formula $\Lambda_d=2\pi/(\Delta Q_x)=\lambda/(2\Delta\omega_S \sin \Theta_B)$, where ΔQ_x is the distance of the satellite maxima in reciprocal space, λ is the x-ray wavelength, and Θ_B is the Bragg angle [19]. The x -axis is defined to be perpendicular to the c -direction of MnAs and parallel to the interface. The angular distance of the satellite maxima measured at room temperature yields an average lateral period of the domain structure of 247 nm. The thickness of the original MnAs film was determined to be 38 nm using x-ray reflectivity measurements [11]. The equilibrium domain period is thus estimated to be 190 nm [9]. As the diameters of the smallest disks are sufficiently small (≈ 80 nm) only one elastic phase domain exists in an individual disk, which was confirmed at room temperature using magnetic force microscopy [15].

The full triangles in Fig. 1 show the temperature dependence of the phase content ξ of α MnAs in the unpatterned continuous epitaxial layer. As reported in [8] the heating and cooling curves roughly coincide and hence the temperature hysteresis in the range of phase coexistence is negligible. In the present sample this range extends quite broad between 270 and 315 K. The overall phase coexistence range amounts to 45 K. In the vicinity of the transition temperature of 315 K the α MnAs content rises from zero almost linearly. When lowering the temperature further the rise of the phase content weakens, and the content gradually reaches the saturation level at unity. The temperature dependence of the phase content ξ in the small MnAs disks is also shown in Fig. 1 (hollow symbols). When cooling down the MnAs disks, α MnAs first emerges in the disks only at a temperature as low as 298 K. We observe a significant supercooling of the disks, i.e. all of them remain to be in the β -phase. Subsequently, the α MnAs content rises with further cooling until all the disks are transformed to the α -phase at 270 K. Once the α -phase had been realized entirely in all the disks, the sample was heated. Similar to the cooling case the temperature was as high as 285 K when the disks began transforming into the β -phase. Therefore, a significant extent of overheating takes place in the disks in contrast to the continuous MnAs layer. The behavior of the MnAs nanodisks at the first order phase transition is similar to that of bulk MnAs [2, 3]. The same widths of the hysteresis in the temperature dependencies of the magnetization in bulk MnAs [2] and of the phase content $\xi(T)$ in the MnAs disk ensemble are found. Moreover no phase coexistence takes place in the individual disks [15]. Nevertheless, the phase transition in the disk ensemble does not occur abruptly at a certain temperature. The slope of the temperature curve $d\xi/dT$ has increased only by a factor of 2-3 compared to that of the layer curve. The fact that the experimental disks are not perfectly identical due to small fluctuations in their sizes and shapes and the random presence of defects may be responsible for the finite temperature window at the phase transition. The strong temperature hysteresis observed in the experiment (Fig. 1) manifests the supersaturation in individual disks.

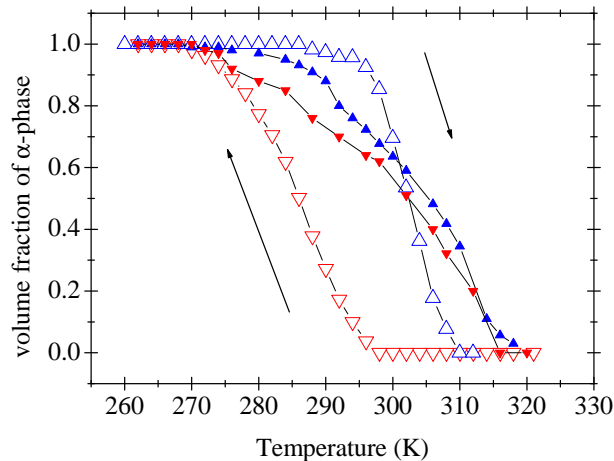


FIG. 1: Temperature dependence of the volume fraction ξ of the MnAs α -phase illustrating the coexistence of the two phases in the MnAs layer (full symbols) and the MnAs disk (hollow symbols) system. Upwards (downwards) directed triangles correspond to the heating (cooling) curve. The changes of the composition with temperature are more steep in the disk system than in the continuous layer system. The range of phase coexistence in the layer system is as large as 45 degrees and only a very small hysteresis is observed. The disk system changes from one phase to the other within 15 to 20 degrees and a strong hysteresis (width 20 ± 5 K) of the temperature curve is found.

The authors thank E. Dudzik, E. Wiebecke, C. Herrmann, V. M. Kaganer, L. Däweritz, and A. Erko for their support and for helpful discussions.

-
- [1] M. Ramsteiner, H. J. Hao, A. Kawahrazuka, H. J. Zhu, M. Kästner, R. Hey, L. Däweritz, H. T. Grahn, and K. H. Ploog, *Phys. Rev. B* **66**, 081304 (2002).
 - [2] V. A. Chernenko, L. Wee, P. G. McCormick, and R. Street, *J. Appl. Phys.* **85**, 7833 (1999).
 - [3] G. A. Govor, *J. of Magnetism and Magnetic Materials* **54**, 1361 (1986).
 - [4] B. T. Willis and H. P. Rooksby, *Proc. Phys. Soc. London Sect. B* **67**, 290 (1954).
 - [5] R. H. Wilson and J. S. Kasper, *Acta Cryst.* **17**, 95 (1964).
 - [6] M. Tanaka, J. Harbison, M. C. Park, Y. S. Park, T. Shin, and G. M. Rothberg, *J. Appl. Phys.* **76**, 6278 (1994).
 - [7] F. Schippan, A. Trampert, L. Däweritz, and K. H. Ploog, *J. Vac. Sci. Technol. B* **17**, 1716 (1999).
 - [8] V. M. Kaganer, B. Jenichen, F. Schippan, W. Braun, L. Däweritz, and K. H. Ploog, *Phys. Rev. Lett.* **85**, 341 (2000).
 - [9] V. M. Kaganer, B. Jenichen, F. Schippan, W. Braun, L. Däweritz, and K. H. Ploog, *Phys. Rev. B* **66**, 045305 (2002).
 - [10] T. Plake, M. Ramsteiner, V. M. Kaganer, B. Jenichen, M. Kästner, , L. Däweritz, and K. H. Ploog, *Appl. Phys. Lett.* **80**, 2523 (2002).
 - [11] B. Jenichen, V. M. Kaganer, C. Herrmann, L. Wan, L. Däweritz, and K. H. Ploog, *Z. Kristallogr.* **219**, 201 (2004).
 - [12] C. P. Bean and D. S. Rodbell, *Phys. Rev.* **126**, 104 (1962).
 - [13] N. Menyuk, J. A. Kafalas, K. Dwight, and J. B. Goodenough, *Phys. Rev.* **177**, 942 (1969).
 - [14] F. Iikawa, M. J. S. Brasil, C. Adriano, O. D. D. Couto, C. Giles, P. V. Santos, L. Däweritz, I. Rungger, and S. Sanvito, *Phys. Rev. Lett.* **95**, 077203 (2005).
 - [15] Y. Takagagi, B. Jenichen, C. Herrmann, E. Wiebecke, L. Däweritz, and K. H. Ploog, *Phys. Rev. B* **73**, 125324 (2006).
 - [16] M. Kästner, F. Schippan, P. Schützendübe, L. Däweritz, and K. H. Ploog, *J. Vac. Sci. Technol. B* **18**, 2052 (2000).
 - [17] L. Däweritz, L. Wan, B. Jenichen, C. Herrmann, J. Mohanty, A. Trampert, and K. H. Ploog, *J. Appl. Phys.* **96**, 5056 (2004).
 - [18] B. Jenichen, V. M. Kaganer, F. Schippan, W. Braun, L. Däweritz, and K. H. Ploog, *Mat. Science and Eng. B* **91**, 433 (2002).
 - [19] B. Jenichen, O. Brandt, and K. H. Ploog, *Appl. Phys. Lett.* **63**, 156 (1993).

The structural role of Fe in the formation of glasses containing Electric Arc Furnace Dust

F. Pinakidou, M. Katsikini, A. Mavromati, E. C. Paloura*

Aristotle University of Thessaloniki, School of Physics, 54124 Thessaloniki, Greece.

A. Erko

BESSY GmbH, Albert Einstein Str. 15, 12489 Berlin, Germany.

The volume of the solid waste that originates from the steel industry increases globally and thus its management must be efficient and environmentally friendly. Electric arc furnace dust (EAFD) is the largest solid waste stream produced by steel mills and it comprises mainly of heavy metals which are toxic when disposed to the environment. A simple and cost effective method used to stabilize these metals is vitrification which produces vitreous or glass-ceramic materials¹. Application of this process immobilizes metallic Zn and Fe and thus leads to the formation of safe for disposal EAFD-rich materials². Since the structural rigidity and hence the chemical stability of the final products is strongly correlated to the presence of the metals, it is crucial to study the structural role of Fe in the vitrified EAFD-rich industrial wastes, i.e. the type of polyhedra that Fe constitute the glassy matrix.

The studied samples are vitrified materials, rich in EAFD (which mainly consists of ZnO and ferric oxides ($ZnFe_2O_4$)), which is co-melted with SiO_2 , Na_2O and CaO and casted at $1400^\circ C$. The EAFD concentration in the resulting glasses increases with a step of 5wt% in the range 10 to 30wt% while the SiO_2/Na_2O ratio is equal to 11, i.e. in all samples the glassy network is a silica matrix. The Fe-K-EXAFS measurements were conducted at the KMC2 beamline and the spectra were recorded in the fluorescence yield mode using a Si-PIN photodiode. The fluorescence detector was positioned normal to the beam while the angle of incidence of the impinging X-rays was 85° , so as to limit self-absorption phenomena.

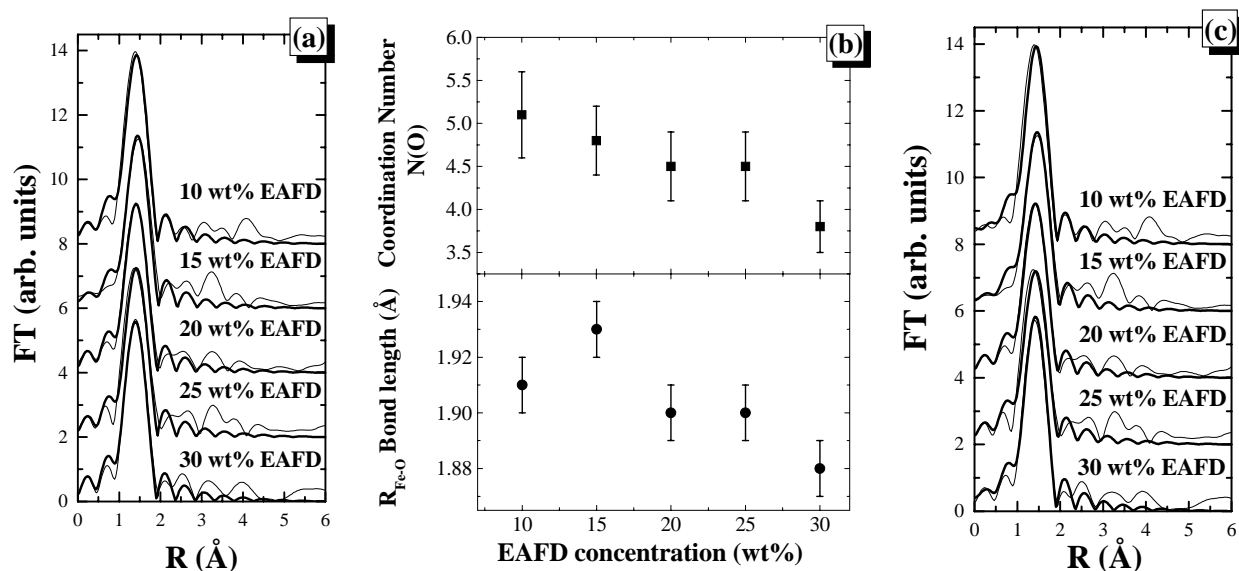


Figure 1: (a) The Fourier transforms (FT) of the $k^3 \times \chi(k)$ Fe-K edge spectra of all studied glasses. (b) Modulation of the Fe-O bondlength and coordination number of Fe as a function of the EAFD concentration in the glasses. (c) The FT of the $k^3 \times \chi(k)$ Fe-K edge spectra of all glasses where the fitting was performed using the mixed model. The raw data and the fitting are shown in thin and thick solid lines, respectively.

The Fourier transforms (FT) of the k^3 -weighted $\chi(k)$ Fe-K edge EXAFS spectra (k -range 2.8 - 9.5 \AA^{-1}) of all vitrified samples are shown in Fig 1(a). As it is evident from the profiles of the FTs

* E. C. Paloura, paloura@auth.gr, tel.:+302310998036, fax: +302310998036

only the 1st nearest neighbor (nn) shell is resolved indicating that the samples are amorphous and homogeneous. Therefore, the Fe-K EXAFS spectra of all the EAFD-containing glasses were fitted in the 1st nearest neighbor shell that consists of oxygen atoms. The EXAFS analysis reveals that the coordination environment around Fe changes with increasing the EAFD content. More specifically, as the EAFD concentration increases from 10 to 30 wt% the Fe-O bond length ($R_{\text{Fe-O}}$) decreases from 1.93 to 1.88Å while the number of O atoms attached to the FeO_x polyhedra ($N(\text{O})$) decreases from 5.1 to 3.8. The simultaneous decrease of the Fe-O bondlength and the coordination number of Fe as a function of the waste concentration, are shown in Fig. 1(b). Hence, the EXAFS analysis results demonstrate that the local coordination of Fe is mixed, i.e. Fe forms both FeO_4 tetrahedra and FeO_6 octahedra. The coordination environment of Fe changes gradually from octahedral to tetrahedral when the EAFD content increases. The intermediate role of Fe, i.e. the mixed tetrahedral and octahedral coordination of Fe, in the glass has been also reported in previous work conducted on Fe and Pb-rich vitrified industrial wastes³.

In an effort to determine the percentage of the different FeO_x polyhedra in the glassy matrix of the studied samples we fitted the Fe-K EXAFS spectra again using the mixed model, according to which X% of the Fe atoms belong to octahedral sites while the rest (100-X)% is bonded in tetrahedra. The fitting of the Fourier transforms (FT) of the k^3 -weighted $\chi(k)$ Fe-K edge EXAFS spectra (k -range 2.8-9.5Å⁻¹), using the mixed model, are shown in Fig 1(c). The spectra were fitted in the 1st nn shell and the fitting parameters were the percentage of the Fe tetrahedra and octahedra and the value of the Debye-Waller (DW) factor. The fitting was performed simultaneously for all the samples and the distance in the tetrahedral coordination was kept fixed to the value derived from the previous EXAFS analysis (1.88Å).

The EXAFS analysis results using the mixed model are listed in Table 1. The use of the mixed model discloses that in the glass with the lowest EAFD concentration (10wt%), approximately 50at% ($\pm 12\%$) of the Fe atoms are octahedrally coordinated in the vitreous matrix, while the rest constitute tetrahedra. The same percentage of Fe atoms that are bonded in octahedra is also detected in the glass with a slightly higher EAFD concentration (15wt%). But as the EAFD content increases further, the percentage of the FeO_4 polyhedra increases significantly, i.e. in the glasses with 20 and 25wt% EAFD, the percentage of the octahedrally coordinated Fe is approximately equal to 30at% ($\pm 7\%$), while it is drastically reduced to 19at% ($\pm 5\%$) when the EAFD content reaches the value of 30wt%. Thus, the intermediate role of Fe is also verified by the EXAFS results using the mixed model, i.e. Fe acts as a glass modifier and former when the EAFD content ranges from 10 to 30wt%. In particular, in the glass with the highest waste concentration (30wt%), the dominant role of Fe is that of network former since the number of the FeO_6 octahedra is only 19at%.

Table 1: Fe-K EXAFS results of the glasses with 10- 30 wt% EAFD, using the mixed model. The parameters that were fixed during the analysis are denoted with an asterisk (*).

Sample	Percentage of FeO_x polyhedra (at%)	$R_{\text{Fe-O}}$ (Å) (± 0.01 Å)	DW ($\times 10^{-3}$ Å ²)
10 wt% EAFD	$\text{FeO}_6 = 50 \pm 12$	1.95	5.4
	$\text{FeO}_4 = 53$	1.88*	4.1*
15 wt% EAFD	$\text{FeO}_6 = 58 \pm 9$	1.97*	5.4*
	$\text{FeO}_4 = 43$	1.88*	4.1*
20 wt% EAFD	$\text{FeO}_6 = 31 \pm 7$	1.97*	5.4*
	$\text{FeO}_4 = 69$	1.88*	4.1*
25 wt% EAFD	$\text{FeO}_6 = 35 \pm 7$	1.97	5.4*
	$\text{FeO}_4 = 65$	1.88*	4.1*
30 wt% EAFD	$\text{FeO}_6 = 19 \pm 5$	1.96	5.4*
	$\text{FeO}_4 = 81$	1.88*	4.1*

¹ F.G.F. Gibb, J. Geol. Soc., **157**, 27 (2000).

² M. Pellino, A. Karamanov, P. Piscicella, S. Criscussi and D. Zonetti, Waste Management, **22**, 945 (2002).

³ F. Pinakidou et al, J. Non-Crystal. Solids, **352**, 2933 (2006).

Charge order in a battery: electronic and ionic ordering in Na_xCoO_2

J. Geck^{1,2}, T. Kroll¹, H. Berger⁴, E. Dudzik³, L. Dunsch¹, R. Feyerherm³, M. Knupfer¹, C. Malbrich¹
and B. Büchner¹

¹*Department of Physics and Astronomy, University of British Columbia, Vancouver, Canada*

²*IFW Dresden, P.O. Box 270116, D-01171 Dresden, Germany*

³*Hahn-Meitner-Institut, Albert-Einstein-Str. 15, D-12489 Berlin, Germany*

⁴*Institut de physique de la matiere complex, EPF Lausanne, 1015 Lausanne, Switzerland*

Introduction: The interactions among the electrons in condensed matter lead to a plenty of fascinating physical phenomena of high technological potential. Recently, the Na_xCoO_2 cobalt oxides have garnered significant interest, thanks to their unusual physics. These materials consist of layers of covalent edge-sharing CoO_6 -octahedra, which alternate along the perpendicular stacking direction with ionic Na-layers (Fig.1). The CoO_2 -layers in these compounds constitute a realization of a correlated electron system based on a triangular lattice; a geometry which is known to be in favour of unconventional electronic ground states.

In addition to this, Na_xCoO_2 behaves very much like a rechargeable battery: sodium can be added or removed electrochemically, similar to the charging/discharging process of a battery. It is even possible to intercalate water molecules.

Adding Na adds electrons to the CoO_2 -layers, providing a convenient way to dope these correlated electron systems. Both changing x and water intercalation have dramatic effects on the electronic properties. Most notably, superconductivity emerges upon hydration and the non-hydrated compounds around $x=0.7$ display an anomalously high thermopower.

Aim: In this project we focus on the non-hydrated compounds Na_xCoO_2 with $0.5 \leq x \leq 0.9$. In these materials unconventional ordering phenomena associated with the CoO_2 -layers as well as strong tendencies towards sodium order have been reported recently.

In order to unravel the complex physics of Na_xCoO_2 , it is important to clarify whether or not the electronic ordering within the CoO_2 -layers is coupled to, or even induced by, the ionic ordering in the Na-planes. This relation is currently largely unclear and it is the aim of this project to shed light on this issue.

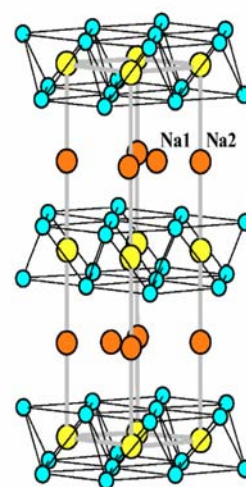


Figure 1: Crystal structure of $\gamma\text{-Na}_x\text{CoO}_2$ [1].

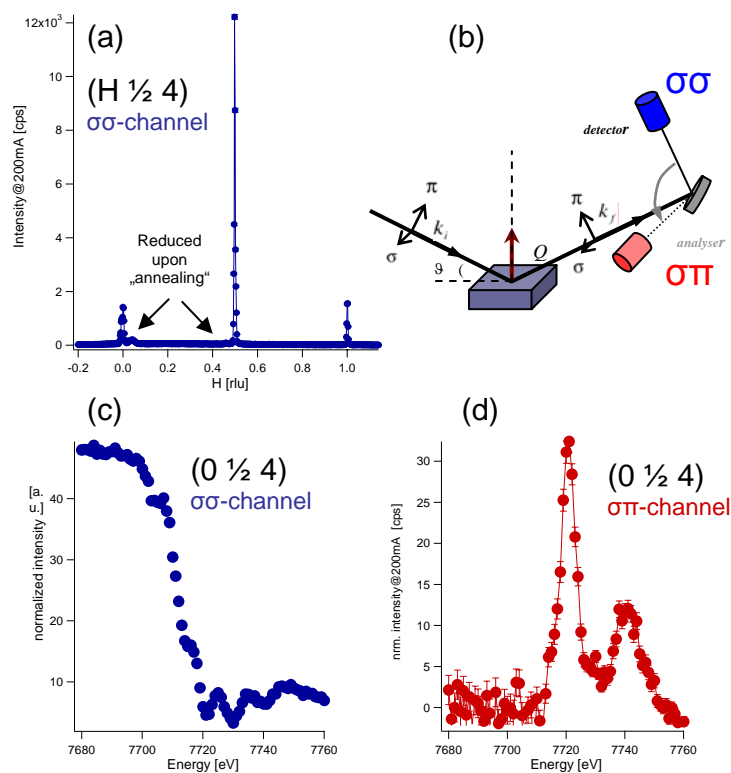


Figure 2: Data collected at $T=30$ K. (a): $(H \frac{1}{2} 4)$ -scan taken off-resonance. Well defined superlattice peaks are observed. The weak peaks at incommensurate positions are reduced after “annealing” at 350 K. (b): Illustration of a typical RXS experiment. (c): Energy dependence of the $(0 \frac{1}{2} 4)$ reflection in the $\sigma\sigma$ -channel (charge scattering). (d): Energy dependence of the $(0 \frac{1}{2} 4)$ reflection in the $\sigma\pi$ -channel after cross talk correction. This intensity is largest, when the charge scattering is lowest.

Experimental techniques: The experimental technique employed for this purpose is resonant hard x-ray scattering (RXS) at the Co K-edge (7710eV). Since the resonant scattering process at this energy involves $1s \rightarrow 4p$ transition, RXS is highly sensitive to local distortions around the Co-site. This means, however, that it does not provide a direct probe for Co-valence ordering. But since an ordering of Co-valences is connected to Co-sites with different local environments, RXS at the Co K-edge is very well suited to detect this type of charge ordering nonetheless. The advantage of this hard x-ray scattering experiment over the more direct resonant soft x-ray scattering is a larger region in reciprocal space that can be accessed and the possibility to perform an effective polarization analysis of the scattered beam.

The RXS experiments have been performed at the MAGS-beamline located at the 7T Wiggler of BESSY. Polarization analysis of the diffracted beam was performed using the (222) reflection of Al. Regarding the sample preparation the following approach was used: First, high-quality single crystals of Na_xCoO_2 with $x=0.75$ were prepared using chlorine flux methods. These crystals were then doped by electrochemical extraction or enrichment of Na in order to achieve different values of x .

Results: Here we will report the first RXS results obtained from an electrochemically doped $\text{Na}_{0.66}\text{CoO}_2$ single crystal. In Fig. 2, low-temperature RXS data for this crystal are shown. As demonstrated in Fig.2 (a) well defined superlattice peaks were observed off-resonance, which can be attributed to the ionic ordering within the Na-planes [2]. In addition, weak incommensurate reflections have also been observed. The intensity the incommensurate peaks could be considerably reduced upon

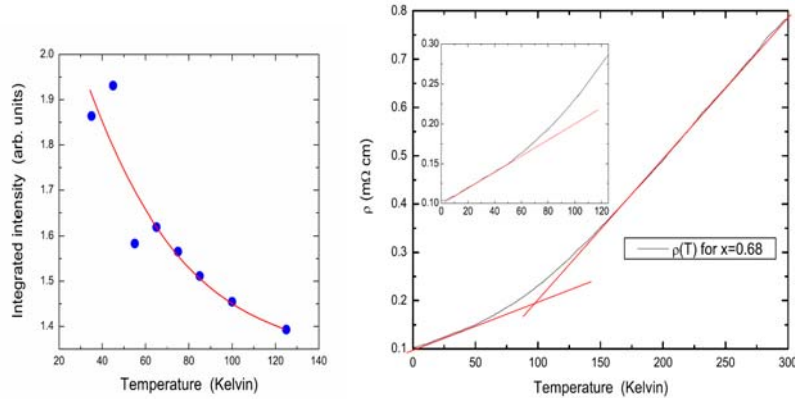


Figure 3: Comparison between the temperature dependences of the resonant $\sigma\pi$ -scattering at the $(0 \frac{1}{2} 4)$ position ($x=0.66$) and the electrical resistivity for $x=0.68$ (from Ref. 3)

“annealing” the sample at 350K. Most likely, the incommensurate peaks are related to Na inhomogeneities just after the electrochemical treatment.

In the following we focus on the $(0 \frac{1}{2} 4)$ reflection. The energy dependence of this reflection in the $\sigma\sigma$ -channel (cf. Fig.2 (b)) is shown in Fig. 2 (c). Below the Co K-edge, a high intensity at the $(0 \frac{1}{2} 4)$ position is observed, which is dramatically reduced due to absorption effects as the photon energy crosses the Co K-edge. The intensity in the $\sigma\sigma$ -channel is due to charge scattering caused by the ionic ordering of the Na-ions. In striking contrast to the behaviour of the $\sigma\sigma$ -intensity, we observe an enhancement around the Co K-edge in the $\sigma\pi$ -channel. Up to our knowledge, this is the first time that this is observed for Na_xCoO_2 .

The resonant enhancement of the $(0 \frac{1}{2} 4)$ reflection at the Co K-edge implies that the Na-order generates inequivalent Co-sites. This is not unexpected. However, the charge scattering observed in the $\sigma\sigma$ -channel is constant below 250 K, i.e. the Na-order does not change in this temperature regime. The resonant scattering in the $\sigma\pi$ -channel, on the other hand, is temperature dependent as shown in Fig. 3. In addition to this, the increase of the resonant scattering correlates with a cross-over behaviour observed in the electrical resistivity (Fig.3). This is strong evidence for charge correlations in the CoO_2 -planes induced by the Na-order.

The experiment described above demonstrates that RXS at the Co K-edge is capable to study the interplay of ionic and charge ordering in Na_xCoO_2 , which is important to develop a better understanding of these complex materials. In the future we plan to extend our studies to different doping levels. In particular, we want to study these effects for the commensurate doping $x=0.5$.

References:

- [1] D.P. Chen *et al.*, Phys. Rev. B **70**, 024506 (2004)
- [2] H.W. Zandbergen *et al.*, Phys. Rev. B **70**, 024101 (2004)
- [3] M.L. Foo *et al.*, Phys. Rev. Lett. **92**, 247001 (2004)

Nano-structure of shed snake skins compared to human skin studied by SAXS

M. Kumpugdee-Vollrath, T. Ngawhirunpat¹, A. Hoell², I. Zizak²

Department of Pharmaceutical Engineering, University of Applied Sciences Berlin (TFH),
Luxemburger Str. 10, 13353 Berlin, Germany, Email: vollrath@tfh-berlin.de, ¹Silpakorn
University, Nakorn Pathom, Thailand, ²Hahn-Meitner-Institute Berlin, Glienicke Str. 100,
14109 Berlin, Germany

ABSTRACT

It is reported that shed snake skins can be used successfully as model membrane for in-vitro (outside human body) studies. There are many types (species) of snakes that can be used for this purpose and the skins can be received without killing and without any cost from the snake-farm or zoo. Therefore many species are used in this project in order to determine which skins have similarity to human skin. These skins can then be used as alternative model membranes in in-vitro test of medical products e.g. transdermal drug delivery systems (TDDs) as creams, ointment, gel, etc. to observe their pharmacological activities. Because of the high resolution of the small angle x-ray scattering (SAXS), this technique was mainly used in this project. The data from shed snake skins from different species and human skin were finally compared.

INTRODUCTION

Shed snake skin has been reported to have many advantages more than other natural skins [1]. The permeability profiles through the shed snake skin closely match that through human stratum corneum. There are many advantages in using the shed snake skin as a model membrane. It can be obtained without killing the animal. The variation in permeability was lower than that of cadaver and fresh human skin. It can be kept for months under refrigeration. It releases fewer interfering substances in analytical procedure. The behaviour of the shed snake skin is also very similar to that of human stratum corneum. There are two parallel permeation pathways: lipid and pore pathways in shed snake skin as in human stratum corneum. The lipid content of the shed snake skin is nearly equal to the human stratum corneum [2]. The lack of hair follicles and skin appendage, however, as well as the existence of scale in shed snake skin are the main differences between shed snake skins and human skin.

There are some studies about shed snake skins, however, the basic permeation data of various drugs through the snake skin has been mainly performed by using shed snake skin of black rat snake *Elaphe obsoleta* [3] and found that it can be used as a model membrane for the in-vitro skin permeation studies of transdermal delivery systems (TDDs), especially lipophilic drugs. In Thailand are various species of Thai snakes such as Thai cobra (*Naja kaouthia*) and Thai python (*Python molurus bivittatus*), which were used in this present study compared to other skins. The small angle X-ray scattering (SAXS) can give details of the secondary structure up to nano-scale and was successfully used for characterizing the human stratum corneum [4]. Therefore SAXS was mainly used in this project.

MATERIALS AND METHODS

Materials

For this present study four species of shed snake skins i.e. *Naja kaouthia* (NK), *Viper calloselasma* (VC), *Python molurus bivittatus* (Pml) and *E. obsoleta* (EO) were obtained from Pata Department Store' Snake farm, Bangkok, Thailand. They were collected after the snake shed the skin from the body within 1 day. Human skin (human) was obtained from surgery department of a hospital. All the samples were stored at room temperature under dry conditions prior to use.

Method

Small Angle X-ray Scattering (SAXS)

The experiments were performed at the new SAXS instrument of the Hahn-Meitner Institute (7T-MPW-SAXS) installed at the synchrotron source BESSY in Berlin, Germany. The scattering patterns were acquired using a 2D position sensitive gas detector with delay line read out (Molecular Metrology). About 5 mg of dry skins of both parts (hinge and scale area) were measured by SAXS, while increasing the temperatures of the samples in steps of 5 °C from 25 °C to 100 °C at X-ray energy of 8000 eV under vacuum. The effect of swelling was determined by soaking the skins in sterile water for at least 14 h. The samples were mounted then into the sample holder between two sealed capton foils and measured at temperatures between 25 °C to 100 °C in steps of 5 °C. The difference was that a wet sample was purged with helium gas during measurement in order to reduce air scattering background in the sample chamber.

RESULTS AND DISCUSSION

Figure 1 shows that the morphology of the skin from different snakes is different in diameter and a number of hinge and scale region. These differences may affect the secondary structure, which will be studied in the next project by using the setup that can focus on a particular region. Figure 2 shows that there are differences between SAXS-patterns on shed snake and human skins. This means that the repeat distance of components e.g. lipids and proteins have different thicknesses because the peak maxima are at different scattering vectors (q). The heating has an effect on the structure both for shed snake and human skins, which can be seen in the shifting of the peak maxima to the right with increasing temperature. This means that the repeat distance gets smaller because the peak maximum is shifting to larger scattering angles or larger magnitudes of scattering vectors. This may be due to the fact that lipids are in both the skins which can be oriented in different forms e.g. gel-, crystalline-, hexagonal-phase. This hypothesis may be proved in further experiments. If the SAXS technique is combined with other techniques e.g. calorimetry (DSC) and spectroscopy (FTIR) a deeper understanding about the structure of the skins can be deduced. The data from DSC and FTIR were formerly shown in another report [5].

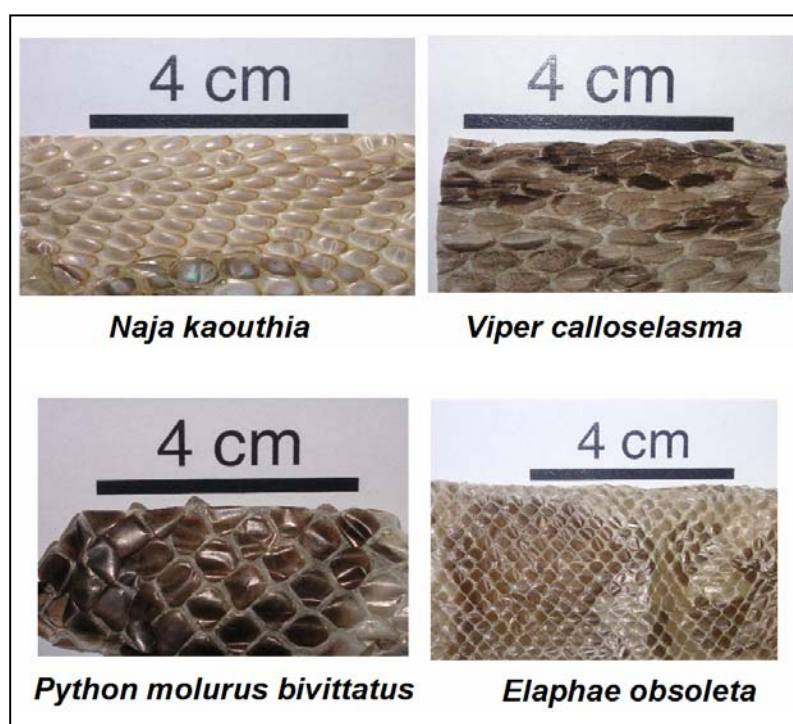


Figure 1: Photographs of different species of shed snake skins showing different diameters and a number of hinge and scale regions.

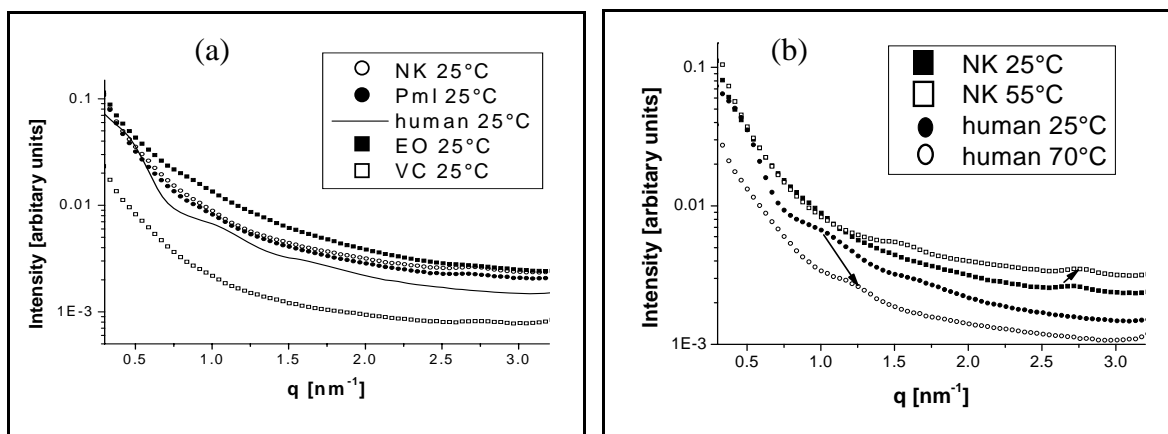


Figure 2: (a) SAXS curves show a significant difference of the shape of wet shed snake skins compared to human skin measured at 25°C, (b) SAXS curves of wet shed snake skins compared to human skin indicate a peak shifting to the right with increasing temperature.

CONCLUSION/PROSPECTIVE PLAN

The next step will be the challenge to find out the phase of lipids or lipid-mixtures by using the mathematical model. The effect of different surroundings during measurement to simulate the conditions, which will be used in in-vitro-test, will be studied as well. The further type of model skins e.g. shed snake skin from snake types existing in Germany e.g. Kreuzotter (*Vipera berus*), etc. will be studied and compared with other commonly used skins e.g. pig skin, synthetic skin. The data from SAXS and eventually combined with that from other techniques can give deeper understanding why the in-vitro-test with a model membrane from shed snake skins is comparable or even better than that from other commonly used skin models. The number of in-vivo-tests or direct tests at the human bodies can therefore be reduced.

ACKNOWLEDGEMENTS

The authors would like to thank the German Synchrotron Source in Berlin (BESSY), Dr. Tatchev and Mr. Haas for their experimental support during SAXS experiments. Thanks are also given to the Master-students Ms. Gögebakan, Ms. Bilek, Mr. Heckötter, Mr. Delissen, Mr. Hanusch and Mr. Wlosnewski for experimental help.

REFERENCES

- [1] Takahashi, K., et al, 1993. Percutaneous absorption of basic compounds through shed snake skin as model membrane. *J. Pharm. Pharmacol.* 45, 882-886.
- [2] Ngawhirunpat, T., et al, 2006. Comparison of the percutaneous absorption of hydrophilic and lipophilic compounds in shed snake skin and human skin. *Pharmazie* 61 (4), 331-335.
- [3] Itoh, T., et al, 1990. Use of shed snake skin as a model membrane for in vitro percutaneous absorption studies: comparison with human skin. *Pharm. Res.* 7, 1042-1047.
- [4] Gurny, R., Teubner, A., (Eds.) 1993. *Dermal and Transdermal Drug Delivery*. Wissenschaftliche Verlagsgesellschaft mbH, Stuttgart, Germany.
- [5] Kumpugdee-Vollrath, M., et al, Comparison of secondary structure of shed snake skins and human skin by small angle scattering (SAXS) technique, *Proceeding 13th International Pharmaceutical Technology Symposium*, 10-13/0972006, Antalya, Turkey.

Rudolf Winter¹, Daniel Le Messurier¹, Sylvio Haas², Armin Hoell²¹) Materials Physics, University of Wales Aberystwyth, Penglais, Aberystwyth SY23 3BZ, Wales²) Bereich Strukturforschung, Hahn-Meitner-Institut Berlin, Glienicke Str 100, 14 109 Berlin, Germany**Refractories.**

Refractories are used as linings in melting furnaces in the glass and metal producing industries. They are also used as coatings for sensors in hostile atmospheres and high-temperature environments as process control becomes more important to reduce waste and energy consumption. In some applications, clever nano-scale engineering can increase the mechanical strength of refractories as has been shown in the case of turbine blade coatings [1].

We are using a nano-scale analogue of an industrial alumina-zirconia-silicate refractory (cf. Fig. 1) as a physical model to understand the sintering and corrosion kinetics of this material class. The increased surface-to-volume ratio makes the model system ideally suited to kinetic investigations. We have studied this material by NMR [2] and SAXS [3], and we have recently published the first *in-situ* kinetic study of a heterogeneous material, silicate glass-forming batch, by NMR [4].

Refractory corrosion occurs when mobile ions from the glass melt penetrate into the amorphous binder phase of the refractory. We are looking into ways of increasing the viscosity of the refractory binder phase in order to reduce the penetration depth of the corrosives. One way to achieve this may be based on the mixed-alkali effect, the reduction of ionic conductivity when two mobile ions compete for conduction pathways in an amorphous structure [5] as ionic motion contributes to the flexibility of the network and hence decreases viscosity.



Fig. 1: Nano-scale refractory analogue: Alumina and zirconia nanoparticles embedded in a sodium / potassium silicate glass matrix.

Anomalous small-angle x-ray scattering.

Anomalous scattering is the chemical contrast enhancement that occurs around the absorption edge of a probe element due to the resonance between scattering and absorption [6]. Near the edge, an energy-dependent complex correction $f' + if''$ is applied to the scattering factor to account for this resonance. As a consequence, the total scattering function splits into three parts,

$$I(q, E) = I_0(q) + f' I_{0r}(q, E) + (f'^2 + f''^2) I_r(q, E), \quad (1)$$

i.e. the non-resonant, cross, and self terms.

There are only a small number of ASAXS studies reported in the literature so far, and even fewer attempt to monitor materials *in situ* while varying a process parameter. Systems that have been investigated by ASAXS so far are concerned with phase separation in alloys [7, 8], distribution of counter-ions in polymer-coated core-shell particles [9], and porosity of catalyst supports [10]. The only *in-situ* studies so far are a kinetic study of an organometallic reaction leading to the formation of nano-particles [11], degradation of an electrocatalyst in operation [12] (both at room temperature) and phase separation kinetics in an alloy at moderate annealing temperatures [13].

Not all of the previous ASAXS studies make full use of the potential inherent in eq.(1) to separate the cross term, which contains the correlation between the probe and the remaining scatterers, from the self term, which relates to the autocorrelation of the probes themselves, *i.e.* the pattern that one might expect if the phase containing the probe was in an otherwise perfectly index-matched environment. In order to solve eq.(1), measurements at a great deal more than three energies are required, and in addition to the usual corrections, the data need to be corrected for fluorescence, the width of the beam spectrum, and any chemical shifts of the edge occurring during an *in-situ* experiment [14].

Experimental.

The in-situ experiments were designed to repeat cycles of four beam energies plus edge scan while heating a sample at a fixed temperature up to 1000°C (cf. Fig. 2). To study corrosion, the refractory analogue was mixed with another glass, with a higher content of mobile ions than the refractory's matrix. This glass is known as the corrosive. While the corrosive is the same sodium-based glass in all experiments, versions of the nano-scale refractory analogue with both sodium and potassium based binder phases were used. We therefore contrast the conventional case, where there is a concentration gradient of Na⁺ ions from the melt into the refractory, with a situation where the total mobile ion concentration gradient is the same but Na⁺ ions diffuse into a K⁺-based structure.

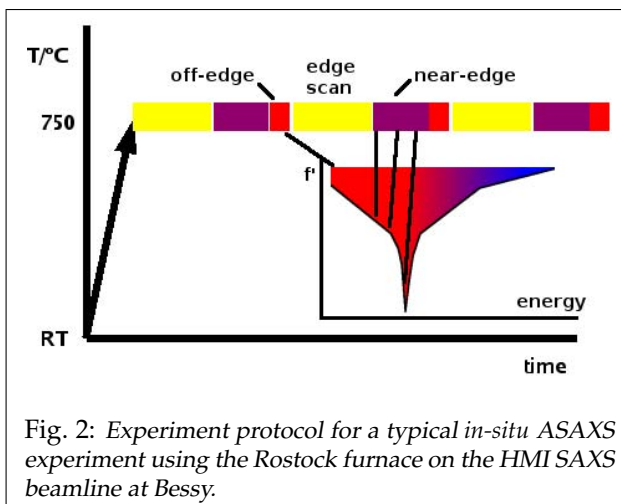


Fig. 2: Experiment protocol for a typical in-situ ASAXS experiment using the Rostock furnace on the HMI SAXS beamline at Bessy.

Results and Discussion.

We can see a difference in the energy dependence of the scattering pattern depending on whether a sodium or a potassium based corrosive is used. After the necessary corrections, radial averaging and absolute scaling of the scattering level by normalisation against an amorphous carbon sample, the straightforward difference is taken between runs near and well below the edge. A more detailed analysis is necessary but requires further software development, which is still work in progress. Figs. 3 and 4 show the difference plots for the sodium and the potassium based refractory, respectively, as three-dimensional data sets relating difference scattering intensity with momentum transfer (here shown as detector channel number) and time elapsed at a temperature of 820°C. Each time slice corresponds to about 3 min. Positive differences mean that the normalised scattering is stronger well below the Zr K edge than in the resonant region just below the edge, *i.e.* that scattering from Zr is greater than average in these positive-difference regions of the pattern. While a conclusive interpretation will require a more detailed analysis once the required software is available, the fact that the potassium corrosive shows an effect on the zirconium signal while the sodium corrosive does not is a significant result. Sodium is the only mobile ion in the refractory's glassy binder phase. A sodium-based corrosive, although containing a significantly higher amount of sodium ions, does not seem to affect the zirconia phase in the refractory. However, the potassium corrosive does change the zirconia nanostructure right from the beginning of the experiment, although an equilibrium is reached after about 15 min. The slight remnant curvature along the q axis suggests that the Guinier radius of the embedded zirconia particles is reduced during the initial reaction.

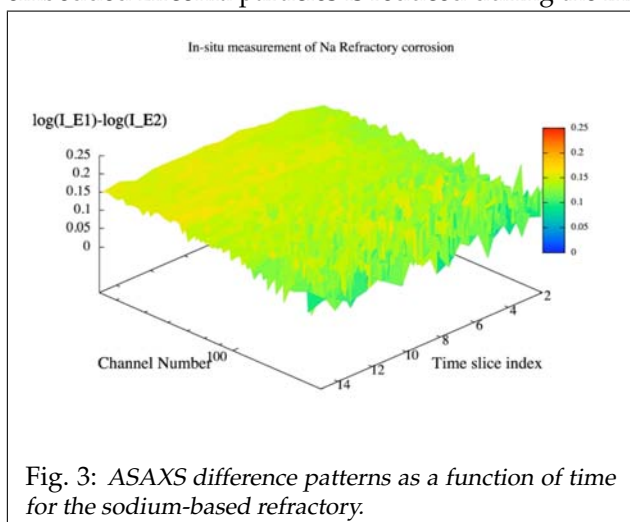


Fig. 3: ASAXS difference patterns as a function of time for the sodium-based refractory.

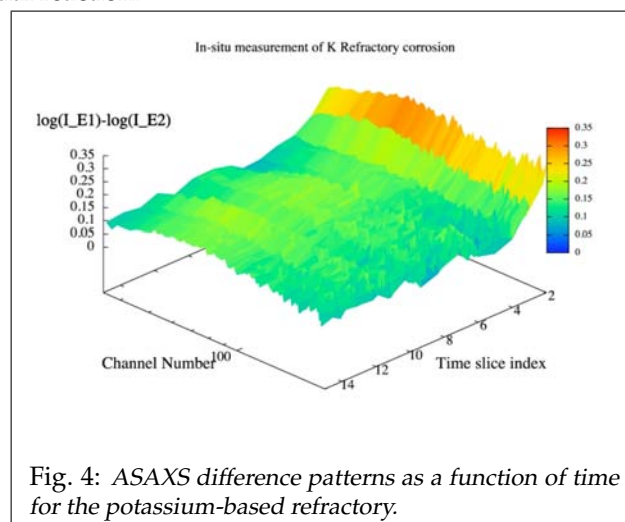


Fig. 4: ASAXS difference patterns as a function of time for the potassium-based refractory.

Conclusions and Outlook.

This first *in-situ* ASAXS experiment at the HMI SAXS beamline at Bessy has demonstrated that the beamline can provide the necessary time and energy resolution to enable us to study the kinetics of solid state reactions such as refractory corrosion. However, the temperatures available on the furnace used at the beamline at the time were not sufficient for the corrosion studies intended. Ways of improving and testing the furnace have been identified which will enable us to finish off this work in a follow-up experiment. These include operating the furnace with an inert gas atmosphere and placing the sample, which is a powder pellet, between two slivers of mica to improve mechanical stability.

Dissemination.

Preliminary results of this work have been presented at the European Society of Glass Science and Technology conference at Sunderland and at the Synchrotron Radiation User Meeting at Diamond, both in September 2006. A journal publication is underway but needs some further software development as indicated above. Follow-on beamtime at Bessy has been awarded and scheduled for March 2007, which will provide further in-situ ASAXS data on refractories to complete the picture.

References

- [1] JR Nicholls, RG Wellman, MJ Deakin; *Materials at High Temperatures* 20 (2003) 207
- [2] DA Le Messurier, N Sissouno, AR Vearey-Roberts, S Evans, DA Evans, R Winter; *Mater Sci Technol* 20 (2004) 975
- [3] R Winter, DA Le Messurier; *SRS Experimental Report* (2004) RB40 296
- [4] AR Jones, R Winter, P Florian, D Massiot; *J Phys Chem B* 109 (2005) 4 324
- [5] A Bunde, MD Ingram, S Russ; *Phys Chem Chem Phys* 6 (2004) 3 663
- [6] R Brückner, U Lembke, R Kranold; *Nucl Instr Meth Phys Res B* 97 (1995) 190
- [7] W Liu, WL Johnson, S Schneider, U Geyer, P Thiyagarajan; *Phys Rev B* 59 (1999) 11 755
- [8] A Hoell, A Wiedenmann, F Bley, JP Simon, A Mazuelas, P Boesecke; *Scripta Mater* 44 (2001) 2 335
- [9] B Guillaume, M Ballauff, G Goerigk, M Wittemann, M Rehahn; *Colloid Polym Sci* 279 (2001) 829
- [10] A Bóta, G Goerigk, T Drucker, HG Haubold, J Petró; *J Catal* 205 (2000) 354
- [11] K Angermund *et al.*; *J Phys Chem B* 107 (2003) 7 507
- [12] HG Haubold, XH Wang, G Goerigk, W Schilling; *J Appl Cryst* 30 (1997) 653
- [13] G Goerigk, HG Haubold, W Schilling; *J Appl Cryst* 30 (1997) 1 041
- [14] M Patel, S Rosenfeldt, M Ballauff, N Dingenouts, D Pontoni, T Narayanan; *Phys Chem Chem Phys* 6 (2004) 2 962

Organic-inorganic and organic-organic interfaces studied by NEXAFS

S. Berkebile, M. Oehzelt, G. Koller, M.G. Ramsey

Institute of Physics, Karl-Franzens-Universität Graz, A-8010 Graz, Austria

EU, R II 3-CT-2004-506008

Oligomers such as sexiphenyl (6P), sexithiophene (6T) and pentacene (5A) are attracting renewed interest not only as models for their related polymers, but also in their own right as active materials in organic devices such as FETs, LEDs and solar cells. The bonding interaction at the organic-inorganic interface has been shown to be important to the electronic properties via the band alignment [1], and there is much interest regarding molecular geometry in this interfacial region as it is crucial to many aspects of organic devices, from charge injection and transport to thin film growth. Further, organic devices often consist of a multiplicity of organic layers making the understanding of the organic/organic interface and organic-on-organic growth a technologically important issue. Here we report investigations into, first, a novel form of strain release at the 6P/Cu(110)-(2x1)O interface, followed by the growth of a 6P/5A/6T heterostructure. During the heterostructure growth, the orientation of 5A molecules from monolayer coverages to thin films (up to 25 nm) grown on a highly crystalline (20-3) oriented 6P film was monitored, as was the orientation of subsequently deposited 6T on the previous 5A film. The surfaces were prepared and investigated in the MUSTANG end station attached to the Russian-German beamline. C_K - and S_L - edge Auger yield Near Edge X-ray Absorption Spectroscopy (NEXAFS) spectra were obtained with a Phoibus 150 analyser from SPECS.

Low Temperature Scanning Tunneling Microscopy (LT-STM) studies have shown that the molecules in a monolayer (ML) of 6P on Cu(110)-(2x1)O are uniaxially oriented along the Cu[001] direction, i.e. along the oxygen rows. Further 6P growth results in crystallites where the 6P(20-3) plane of the bulk crystal structure is parallel to the underlying substrate surface in which the molecules maintain their orientation from the monolayer. [2,3] The 6P surface unit cell of the monolayer, however, shows a compression of -8.4% in the [1-10] direction and -1.1% in the [001] direction when compared to the two-dimensional unit cell of the 6P(20-3) plane. It is unlikely that the observed surface layer is simply a compressed (20-3) bulk plane forced by the substrate due to the high pressures this would require. One stress release mechanism which does not require simple compression would be a change of the inclination of the individual molecular planes with respect to the surface. A rotation of the molecular planes about the long molecular axis by only 4° is enough to allow commensurability without compromising the van der Waals spacing.[3] A change in the inclination of the molecular planes of this size should be measurable by NEXAFS.

Polarisation dependent C1s-NEXAFS spectra have been recorded to determine the molecular orientation and to check this hypothesis. If the molecules have the ability to release stress by increasing their tilt angle at the interface, then a different inclination angle in the monolayer and the 6P(20-3) crystallites that grow on it, should be detectable using the $C1s \rightarrow \pi^*$ resonance in the high resolution C1s-NEXAFS spectra. Figure 1 displays NEXAFS measurements performed with photon angles of incidence from normal ($\theta=0^\circ$) to grazing ($\theta=80^\circ$) along the high symmetry directions [001] and [1-10] for both a ML (Fig.1a) and a 32 nm thick film (Fig.1b) of 6P. For normal incidence with the polarisation plane parallel to

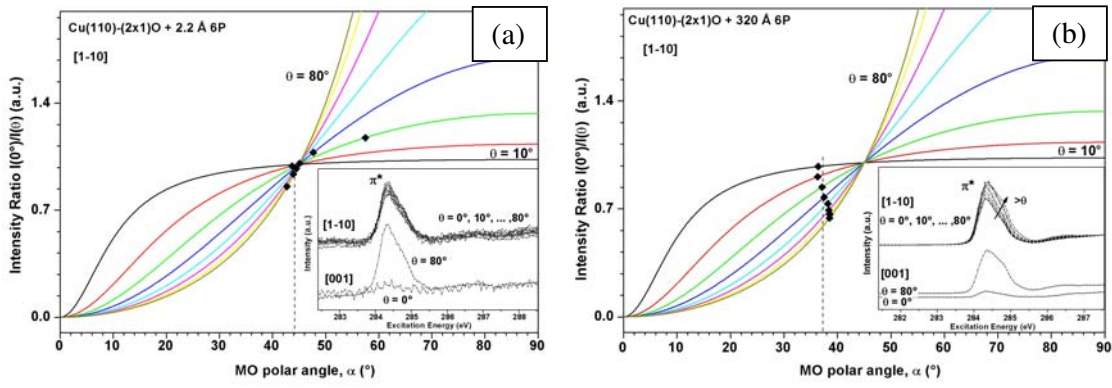


Figure 1: C_K -edge NEXAFS spectra for (a) 2.2 Å of p-6P and (b) 320 Å p-6P grown on Cu(110) – (2x1)O together with the calculated intensity ratio plots $I(\theta = 0^\circ)/I(\theta)$ as a function of the π^* -orbital (MO) tilt angle (α) for various X-ray incidence angles (taking the two-fold symmetry of the substrate into account). The dashed vertical lines indicate the derived molecular tilt angles with respect to the substrate. The respective NEXAFS spectra are shown in the inserts. ($\theta = 0^\circ \rightarrow$ normal incidence)

[001] the π^* excitation is largely forbidden for both the monolayer and the multilayer films indicating that the molecular axes are parallel to the surface and the [001] azimuthal direction, as observed in STM and XRD measurements [3]. In the [1-10] direction, perpendicular to the molecules, the inclination angle of the molecules with respect to the substrate can be determined from the π^* intensity variations. In the NEXAFS spectra of the monolayer the C1s $\rightarrow \pi^*$ resonance is strong and does not change upon changing the photon incidence angle θ as can be seen in the inset of Fig.1a. In contrast, the intensity of the C1s $\rightarrow \pi^*$ resonance for the thick layer changes considerably upon increasing the incidence angle θ as is shown in the inset of Fig.1b. To determine the molecular tilt angle, the calculated intensity ratio plots $I(\theta = 0^\circ)/I(\theta)$ are shown as a function of the π^* -orbital vector tilt angle α and for various X-ray incidence angles θ , together with the experimentally determined C1s $\rightarrow \pi^*$ transition ratios. The resulting tilt angle of the molecular plane in the case of the monolayer on the (2x1)-O reconstructed surface is determined to be $44^\circ \pm 5^\circ$. The same experiment for the thick film reveals an angle of $37^\circ \pm 5^\circ$. Although there is a systematic error making the results of both systems slightly larger than expected, the decrease in tilt angle from the monolayer to the thick bulk-like film is significant and reproducible and supports the proposed geometrical model.

The (20-3)-oriented 6P film shown in Fig.1b was used as the substrate for 6P/5A/6T heterostructure growth. The inset of Fig.2a shows C_K -edge NEXAFS spectra of a 250 Å thick 5A film grown on the 6P film at RT. As before, the spectra were recorded with the polarisation parallel to the [001] and [1-10] substrate azimuth and for incidence angles α between normal and grazing incidence. Some π^* features of 5A exist over a 1 eV range just before the 6P X-ray absorption edge. For normal incidence and polarisation along [001], these 5A features are very weak, whereas they are strong in [1-10] polarisation, indicating that the 5A molecules align parallel to the underlying 6P molecules (and to the Cu-O [001] direction). For both polarisation directions they have their maximum at grazing incidence, indicating that the molecular axis is parallel to the [001] azimuth and that the molecular plane is tilted with respect to the substrate surface. Nearly identical behavior was found for previous growth steps (not shown here) from the monolayer up to this coverage. A molecular orbital tilt angle

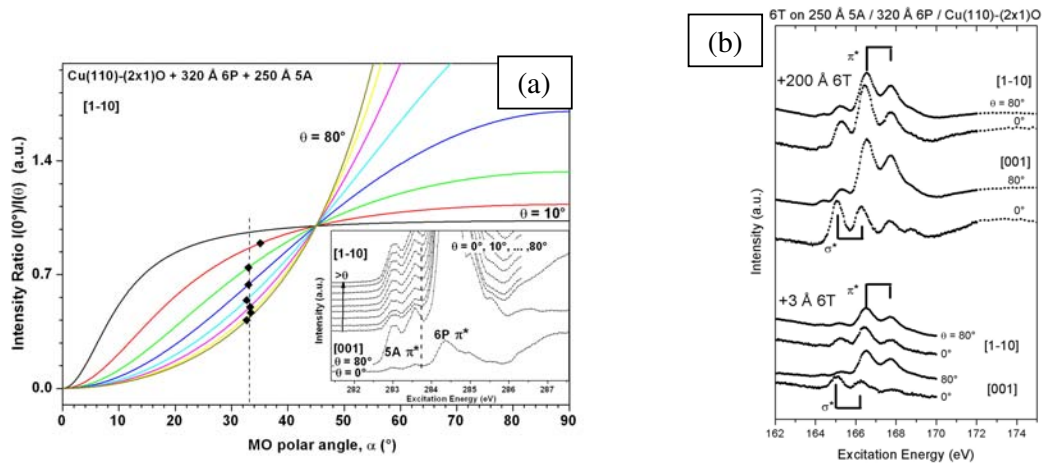


Figure 2: C_K -edge NEXAFS spectra for (a) 250 Å of 5A grown on 320 Å p-6P(20-3) together with the calculated intensity ratio plots $I(\theta = 0^\circ)/I(\theta)$ as a function of the π^* -orbital (MO) tilt angle (α) for various X-ray incidence angles (taking the two-fold symmetry of the substrate into account) and SL-edge NEXAFS spectra for (b) 3 Å and, subsequently, 200 Å α -6T grown on the film in (a). The dashed vertical line in (a) indicate the derived molecular tilt angles with respect to the substrate and the respective NEXAFS spectra are shown in the insert. ($\theta = 0^\circ \rightarrow$ normal incidence)

analysis, shown in Fig.2a, yielded a tilt of $33^\circ \pm 5^\circ$ of the molecular plane relative to the substrate surface and a value of $37^\circ \pm 5^\circ$ for the monolayer, which can be expected for uniaxially oriented 5A due to the herring-bone configuration of the bulk crystal structure.

In Fig.2b the S2p-NEXAFS spectra of a 3 Å and 200 Å thick 6T films grown on the oriented 5A layer at RT are shown. Comparable to the underlying 6P and 5A spectra little or no π^* features can be observed at normal incidence in [001] and the spectrum is dominated by the S2p to σ^* (C-S) resonance at 165.0 and 166.2 eV (spin-orbit splitting), while for x-ray polarisation along [1-10] in normal incidence both π^* and σ^* transition are strong. On increasing the incidence angle to G.I. the π^* transitions increase for both polarisations. This shows that the 6T molecules are aligned parallel to the Cu-O [001] direction and the underlying 5A molecules. C1s-NEXAFS of the completed heterostructure (not shown) reveal a superposition of 6P, 5A and 6T spectra, suggesting that islanding occurs during 5A and 6T growth. The uniaxial alignment of the long molecular axes of organic molecules in heterostructures, in which the orientation of the underlying organic substrate is imposed upon the overlayer molecules, appears to drive organic-on-organic growth for rod-like molecules [4,5].

Acknowledgments: This work has been supported by the Austrian Science Foundation (FWF) and the European Union (EU, R II 3-CT-2004-506008). The assistance of Gianina Gavrilă with the MUSTANG chamber (MUSTANG BMBF 05 KS4OC1/3) and the beamline staff at the RG-BL is gratefully acknowledged.

References:

- 1) G. Koller, R.I.R. Blyth, A. Sadar, F.P. Netzer, M.G. Ramsey, Appl. Phys. Lett. **76** (2000) 927.
- 2) for a similar example, see G. Koller, S. Berkebile, J. Krenn, G. Tzvetkov, G. Hlawacek, O. Lengyel, F.P. Netzer, M.G. Ramsey, C. Teichert, R. Resel, Adv. Mat. **16** (2004) 2159.
- 3) M. Oehzelt, L. Grill, S. Berkebile, G. Koller, F.P. Netzer, M.G. Ramsey, Nano Lett. submitted.
- 4) G. Koller, S. Berkebile, J.R. Krenn, F.P. Netzer, M. Oehzelt, T. Haber, R. Resel, M.G. Ramsey, Nano Lett. **6** (2006) 1207.
- 5) M. Oehzelt, G. Koller, J. Ivanco, S. Berkebile, T. Haber, R. Resel, F. P. Netzer, M. G. Ramsey, Adv. Mat. **18** (2006) 2466.

Identifying functional end-group features in π -conjugated supramolecular assemblies

Miguel Ruiz-Osés¹, Thorsten Kampen², Nora González¹, Iñaki Silanes¹, Andrés Arnau¹, André Gourdon³, Karsten Horn², and J. Enrique Ortega¹

¹Universidad del País Vasco, Manuel Lardizabal 4, E-20018 Donostia/San Sebastián, Spain

²Fritz-Haber-Institut der Max-Planck-Gesellschaft, Berlin, Germany

³CEMES-CNRS, Toulouse, France

Planar molecules with π -conjugated electron systems and end-group functionalization are frequently tested in the context of self-assembled monolayers on surfaces with specific electronic or geometric properties. Particularly, we investigate one-dimensional (1D) H-bonded structures made of pairs of molecules with linear shape and complimentary end-group functionalization. We have shown in a recent STM study [1], that 1D assembly is achieved in a 1:1 mixture of naphthalene tetracarboxylic diimide (NTCDI, $C_{14}H_8N_2O_4$), and 1,4-di(4,6-diamino-1,3,5-triazin-2-yl) benzene (BDG, $C_{12}H_{12}N_{10}$) adsorbed on Au(111).

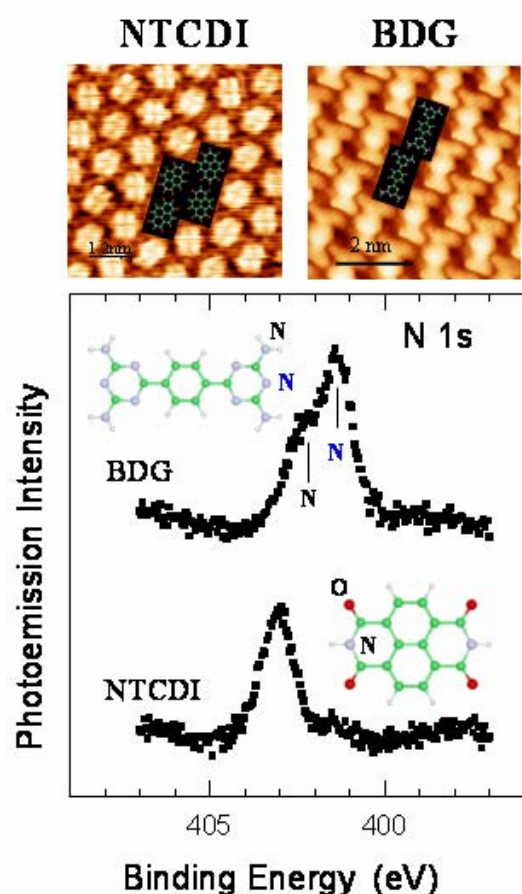


Figure 1: *N 1s* XPS spectra for NTCDI and BDG monolayers self-assembled on Au(111) (Top; STM topography). In BDG, two distinct components are observed for N in triazine rings (N) and amine groups (N'). In NTCDI the single N line characterizes the imide group.

Using X-ray photoemission spectroscopy (XPS) and near edge X-ray absorption fine structure spectroscopy (NEXAFS) we aim at understanding the underlying molecule/molecule and surface/molecule interactions. Our first experiments have been focused on the ability to assess the molecular level structure using NEXAFS. To achieve this, we have prepared monolayers of each molecule on Au(111). Both molecules self-organize forming the two-dimensional, H-bonded networks shown in the top panel of Fig. 1. The results are compared with ground state DFT calculations.

XPS and NEXAFS experiments were carried out at the UE56/2-PGM1 beamline using a SPECS Phoibos 100 analyser equipped with a CCD detector. NEXAFS spectra are recorded in Auger yield mode, using 100 eV pass energy and 260 eV, 375 eV, and 510 eV kinetic energies for C-, N-, and O- *K*-edges, respectively. BDG and NTCDI were deposited at room temperature from e-beam evaporators and the Au(111) substrate was prepared by standard sputtering-annealing cycles. The monolayer (ML) coverage was calibrated by the characteristic LEED patterns.

XPS is known to be element-specific and sensitive to the chemical environment. The bottom panel of Fig. 1 shows the *N 1s* XPS spectra for 1 ML NTCDI and BDG. In BDG the peak exhibits two different components at

402.2 eV and 401.2 eV, with approximately a 2:3 intensity ratio. That is indeed expected from

the proportion of N atoms within triazine rings (blue N in Fig. 1) and at amine groups (black N), respectively. For NTCDI only a single N atom is present in the imide group, and hence a single peak feature defines the *1s* spectrum. Similarly, a single component is observed in the *O 1s* emission (not shown).

Such simplicity in the *1s* spectra for O and N contrasts with the variety of shifted components in *C 1s*, which in turn reflect the different bonding configurations within the molecules. It suggests that NEXAFS at the O and N *K*-edges are better suited to explore molecular levels. The latter are expected to become very important in supramolecular structures since they are subject to changes upon weak intermolecular interactions.

In Fig. 2 we show the NEXAFS spectra for a NTCDI layer taken at the respective *K*-edges of N, O and C. The spectra are aligned with respect to the vacuum level, which in turn is straightforwardly determined from the binding energies of the respective XPS *1s* peaks [2]. For N and O, the series of empty molecular levels are well identified by comparing with the ground state DFT calculation for free-standing molecules. For C the NEXAFS spectrum is difficult to interpret beyond the LUMO peak, due to the presence of chemically shifted components in the XPS *1s* spectra (not shown).

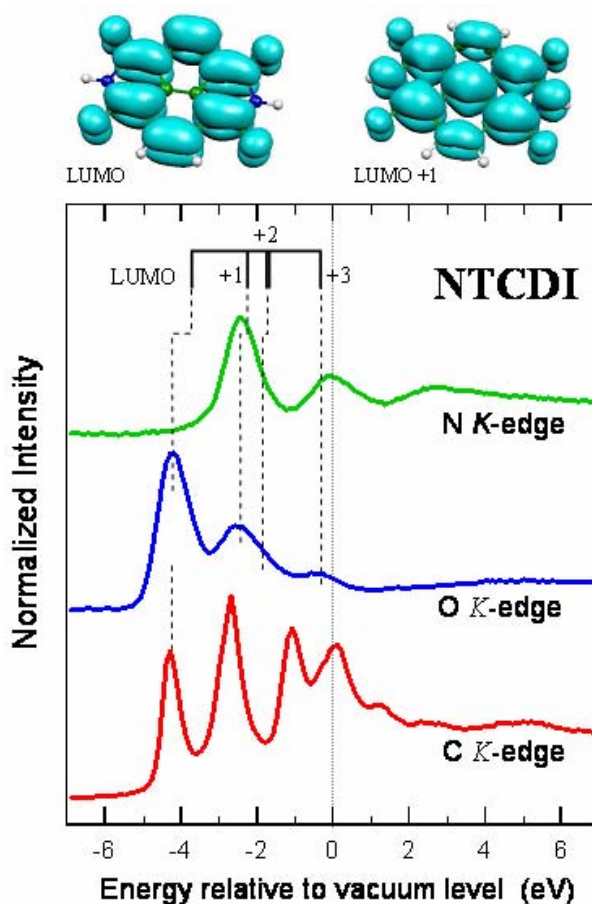


Figure 2: NEXAFS spectra at the different *K*-edges for NTCDI/Au(111). For the sake of comparison, the energy scale is referred to the vacuum level, which is determined from the respective XPS *1s* peaks. The different features are assigned to molecular levels by comparing with a theoretical calculation. On top we show the spatial distribution of charge in the lowest unoccupied levels. The quenching of the LUMO feature in the N spectrum is naturally explained by a local zero in the density of states.

Our calculation lacks an absolute energy scale, which can be obtained by matching theory and experiment at the LUMO+3 feature. Such orbital is the closest to the vacuum level, and hence it is expected to exhibit negligible core-hole effects. By comparing NEXAFS peaks and theoretical levels one can estimate the core-hole exciton energy, since that is not accounted for in the ground state calculation. In Fig. 2 one can observe an increasingly higher core-hole energy away from the vacuum level, i.e. from 0.10 eV to 0.26 eV and 0.60 eV for the LUMO+2, to LUMO+1 and LUMO levels, respectively. Such behaviour, as well as the relatively low core-hole energy value, is indeed expected for molecules adsorbed on metallic surfaces [2].

It is striking to observe that the LUMO and LUMO+2 emissions are quenched in the N spectrum. This is naturally explained by a locally depleted density of states at N sites, and hence by a lack of overlap between core-level and molecular orbital wave functions. On top of Fig. 2 we show the spatial charge distribution for LUMO and LUMO+1 orbitals in NTCDI molecules. The LUMO and LUMO+2 (not shown) charge density is zero at N sites (blue balls), in contrast to the significant charge density in the LUMO+1.

NEXAFS spectra in Fig. 3 correspond to the C and N K-edges for the BDG layer. Our ground state calculation gives three effective features. The LUMO, the LUMO+1,+2 levels that define a 0.1 eV band, and the LUMO +3,+4,+5 levels that lie within a 0.24 eV wide band. Such three features are well observed in the N spectrum of Fig. 3. Since the LUMO +3,+4,+5 is the closest to the vacuum level, it is used to define the absolute energy in the ground state calculation. Consequently we estimate both LUMO+1,+2 and LUMO core-hole energies at 0.40 eV. The calculation shows a significant charge density at N sites in all molecular levels, and hence no quenching is observed in NEXAFS, in contrast to NTCDI.

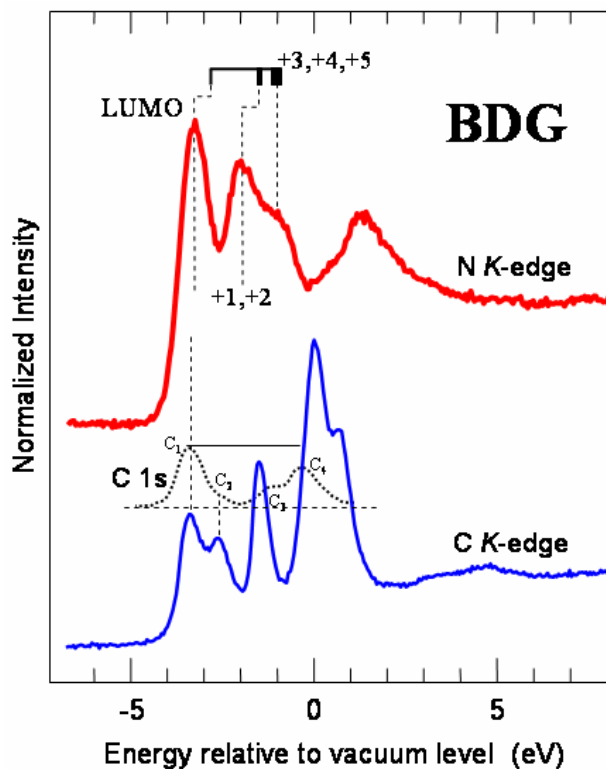


Figure 3: NEXAFS spectra at the N and C K-edges for a BDG layer on Au(111). In the N spectrum, the different peaks are assigned to molecular levels by comparing with a ground state, DFT calculation. In the C spectrum, the assignments are more complex due to the multiple core-level shifts in XPS (C 1s spectrum inserted, with the C₁ component aligned with the LUMO).

As in NTCDI, the peak assignment for the C K-edge spectrum for BDG in Fig. 3 is not straightforward. The LUMO displays a strong shoulder separated by 0.75 eV. In the C 1s XPS spectrum (superimposed, dotted line), a higher binding energy component (C₂) is in fact observed, shifted by 0.8 eV from the main C₁ peak. Beyond the LUMO, the complexity increases due to extra core-level emission at higher binding energies (C₃ and C₄), and hence NEXAFS peaks are difficult to assign following the molecular level calculation.

In summary, we have found a straightforward relationship between the series of molecular levels in theoretical calculations and NEXAFS peaks at the N K-edge and O K-edges of π -conjugated molecule layers. That is possible due to the presence of single chemical species of O and N within functional end-groups. In contrast C atoms exhibit a variety of bonding configurations across the molecule that give rise to chemically shifted components in XPS, and hence to more complex NEXAFS spectra.

Work at BESSY is supported by the European Community I3 Contract (RII 3-CT-2004-506008).

References:

- [1] M. Ruiz-Osés, N. González-Lakunza, I. Silanes, A. Gourdon, A. Arnau, J. E. Ortega, J. Phys. Chem. B **110**, 25573 (2006).
- [2] J. Stöhr in *NEXAFS Spectroscopy*, Springer Series in Surface Sciences, Ed. By G. Ertl, R. Gomer, and D. L. Mills, Springer-Verlag, Berlin-Heidelberg (2003).

Effect of MoO₃ on phase separation characteristics of a soda-lime-silica glass

Rainer Kranold¹, Armin Hoell², Dragomir Tatchev³, Sylvio Haas²

¹*Institute of Physics, Rostock University, D-18051 Rostock, Germany,*

²*Hahn-Meitner Institute, Glienicker Straße 100, D-14109 Berlin, Germany*

³*Institute of Physical Chemistry, BAS, Sofia 1113, Bulgaria*

1. Introduction

Glass-in-glass phase separation has been of interest, because it has an effect on numerous properties and the crystallization behaviour of glasses. The Na₂O-CaO-SiO₂ system, which is the basis of most commercial glasses, has a metastable miscibility gap in the high-silica corner of the ternary phase diagram. The glass investigated (NCS glass) with nominal composition 13 Na₂O-11CaO-76SiO₂ (mol%) separates via a binodal mechanism into droplet-like precipitates of nearly pure silica (Fig. 1) and a residual glass matrix [1]. The process has three stages which are nucleation, growth and Ostwald ripening. In previous small-angle X-ray scattering (SAXS) studies, we investigated the effect of minor anionic additives, Cl⁻ [2] and OH⁻ [3], on the phase separation behaviour of the NCS glass. Here, the effect of small amounts of MoO₃ on the phase separation characteristics of the NCS glass is studied. In particular, the influence of MoO₃ on the two competitive parameters thermodynamic driving force, $\Delta\mu$, and interface tension between droplet phase and matrix, σ , controlling the phase separation process is investigated.

2. Glass samples

The glasses investigated were prepared from the same batch mixed to obtain the pure NCS glass with nominal composition 13Na₂O-11CaO-76SiO₂ (mol%). To one part of this batch, a certain amount of MoO₃ was added in order to obtain NCS glass doped with 0.5 mol% MoO₃. Details of the glass melting procedure are given elsewhere [3]. By wet chemical analysis, a Na₂O deficit of 1.4 mol% and a CaO excess of 0.6 mol% with regard to the nominal composition has been determined. Therefore, $\Delta\mu$ is a little increased for the NCS glass (Fig. 4 and Table) in comparison with a glass of nominal composition [1]. (The glasses were prepared and analyzed in the Jena^{er} Glaswerk GmbH.)

In order to obtain comparable SAXS results (Figs. 3 and 4) from the glasses with and without MoO₃, the heat treatment of all glasses was performed simultaneously at 600 °C for each of the times indicated in Fig. 3.

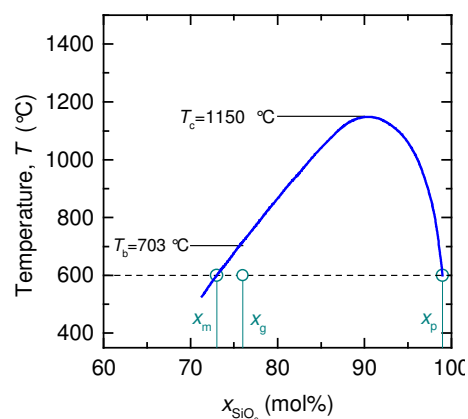


Fig. 1. Miscibility gap according to the quasibinary tie line SiO₂-[(13/24)Na₂O-(11/24)CaO] given in Ref. [1]; T_c=critical temperature, T_b=binodal temperature. For T=600°C, the silica concentrations of the homogeneous glass, x_g=0.76, of the precipitates, x_p=0.99, and of the matrix, x_m=0.73, are marked.

3. Interface tension

The effect of MoO₃ on the interface tension, σ , was established by determining the wetting angle, α , at $T=1200$ °C of a drop of the liquid NCS melt, without and with 0.5 mol% MoO₃, on the flat surface of pure silica glass. It was estimated that the value of σ for the pure NCS glass at 600 °C amounts to about 0.08 N/m, that of the doped glass is nearly 40% higher.



Fig. 2. a) Drop of the pure NCS glass; $\alpha = 30^\circ$. b) Drop of the glass doped with 0.5 mol% MoO₃; $\alpha=37^\circ$.

4. Kinetics by SAXS

The kinetics of the phase separation process has been studied by conventional SAXS measurements using a Kratky instrument. A description of the SAXS experiment and of the analysis of the scattering data is given in [4].

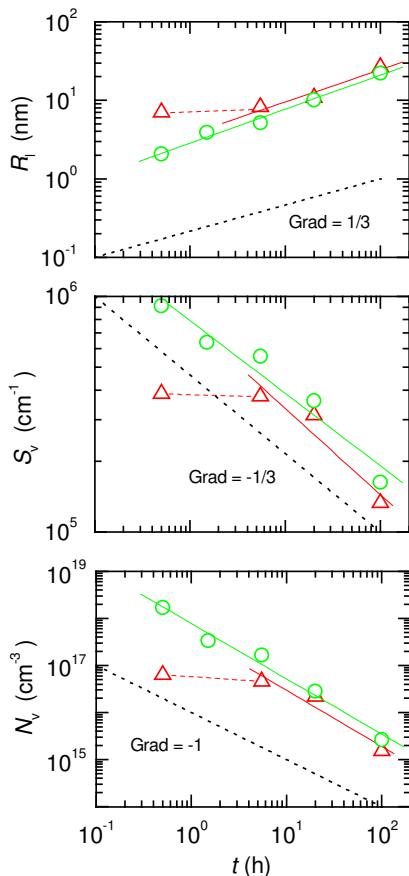


Fig. 3. Average droplet radius, R_i , internal surface per unit volume, S_v , and particle number density, N_v , of the pure NCS glass (\circ) and NCS glass doped with 0.5 mol% MoO₃ (Δ) as a function of the time, t , of isothermal heat treatment at 600 °C. The black dotted lines correspond to the power laws of the classical theory [5] of diffusion controlled Ostwald ripening.

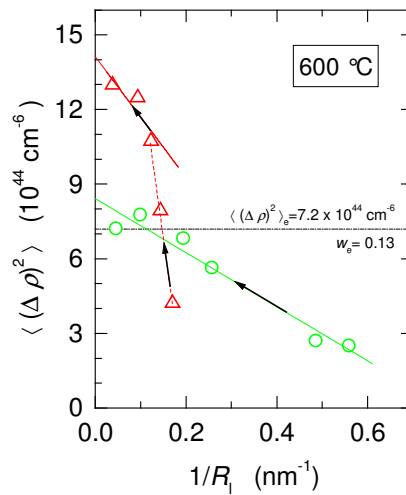


Fig. 4. Mean square of electron density fluctuations, $\langle(\Delta\rho)^2\rangle$, versus reciprocal average radius of the droplets. Plotted data are obtained from samples of the pure NCS glass (\circ) and of NCS glass doped with 0.5 mol% MoO₃ (Δ) phase separated at 600 °C in the time interval $0 \text{ h} \leq t \leq 100 \text{ h}$. The arrows illustrate the direction of increasing time of heat treatment. The equilibrium value of the volume fraction of the precipitates, w_e , and the corresponding value $\langle(\Delta\rho)^2\rangle_e$ for 600 °C calculated from the miscibility gap data (Fig. 1) is indicated by the dashed-dotted line.

MoO ₃ content (mol%)	$\langle(\Delta\rho)^2\rangle_e$ (10^{44}cm^{-6})	R^* (nm)
0	8.4	1.3
0.5	14.1	1.7

Fig. 3 demonstrates that during heat treatment both the pure and the doped NCS glass get to the stage of Ostwald ripening [5] but with varying kinetics. In Fig. 4, the SAXS parameters R_l and $\langle(\Delta\rho)^2\rangle = w(1-w)(\Delta\rho)^2$ are fitted with the expression $\langle(\Delta\rho)^2\rangle = \langle(\Delta\rho)^2\rangle_e - \langle(\Delta\rho)^2\rangle_e R^*/R_l$, developed for the first non-asymptotic stage of Ostwald ripening [2,6], where $R^* \sim \sigma/\Delta\mu$ is the critical Gibbs-Thomson radius. It has been estimated that the scattering contrast, $(\Delta\rho)^2$, cannot account for the largely increased value of $\langle(\Delta\rho)^2\rangle_e$ for the MoO_3 containing glass (Table). So, we have to conclude that the volume fraction, w , of the precipitated droplet phase is larger than that of the pure NCS glass.

5. Binodal temperature, T_b , by in situ high-temperature SAXS

In order to find out the cause of the increased precipitation of silica-rich droplets in the NCS glass doped with MoO_3 , in situ high-temperature SAXS measurements were performed at the HMI SAXS beamline at BESSY, Berlin.

Fig. 5 shows that the silica precipitates in the pure NCS glass dissolve completely during a heat treatment at 710°C , i.e. $T_b < 710^\circ\text{C}$ (compare Fig. 1). By contrast, during heat treatment

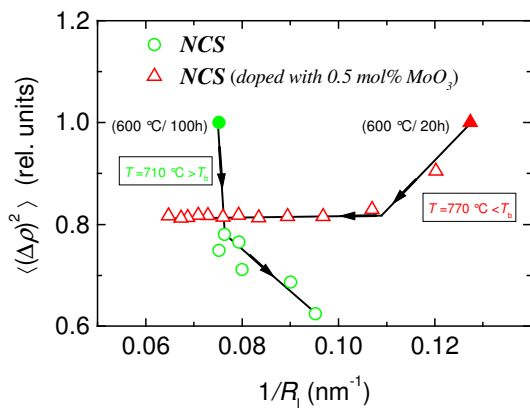


Fig. 5. Mean square of electron density fluctuations versus reciprocal average radius of the droplets. Plotted data points are obtained from glass samples, phase separated previously at 600°C (filled symbols), in the course of in situ SAXS experiments at 710°C and 770°C , respectively, in vacuum. The arrows illustrate the direction of increasing time of heat treatment.

of the NCS glass with 0.5 mol\% MoO_3 at 770°C , two processes can be observed. At first, the silica precipitates shrink in a reversion process until the silica concentration in the matrix reaches its new equilibrium value. Afterwards, the largest droplets grow again by slow ripening, i.e. $T_b > 770^\circ\text{C}$. Obviously, the MoO_3 content of the glass gives rise to a shift of the miscibility gap to higher temperatures.

Therefore, the increased value of $\langle(\Delta\rho)^2\rangle_e$ of the MoO_3 containing glass (Table) is caused by an increased precipitated volume fraction, w , resulting from a higher thermodynamic driving force, $\Delta\mu \sim (T_b - 600^\circ\text{C})$.

6. Conclusions

The presence of small amounts of MoO_3 in the NCS glass alters the kinetics as well as the equilibrium state of phase separation. Both the competitive parameters, thermodynamic driving force and interface tension, increase by an addition of MoO_3 to the base glass. The increased thermodynamic driving force results in a shift of the miscibility gap to higher temperatures and so to an increase of the precipitated volume fraction of the droplet phase.

References

- [1] J.J. Hammel, J. Chem. Phys. 46(1967)2234.
- [2] R. Kranold, M. Kammel, A. Hoell, J. Non-Cryst. Solids 293-295(2001)642.
- [3] R. Kranold, M. Kammel, A. Hoell, Glass Technol. 43C(2002)207.
- [4] A. Hoell, R. Kranold, U. Lembke, J. Aures, J. Non-Cryst. Solids 208(1996)294.
- [5] J.M. Lifshitz, V.V. Slyozov, J. Phys. Chem. Solids 19(1961)35.
- [6] J. Schmelzer, Phys. Status Solidi B 161(1990)173.

Photomission studies of ferroelectric thin films

Robert Schafranek and Andreas Klein,

Darmstadt University of Technology, Institute of Materials Science, Darmstadt, Germany

Emmanuel Arveux and Mario Maglione,

Institute of Condensed Matter Chemistry (ICMCB), Bordeaux, France

Thin films of Barium Strontium Titanate (BST) in the paraelectric state are used for tunable microwave devices as phase shifters, band pass filters and matching networks while ferroelectric BST thin films are applied in ferroelectric memories. Although the interfaces of these materials are known to have a significant impact on device performance, these are only poorly understood so far.

We have performed $\text{Ba}_x\text{Sr}_{1-x}\text{TiO}_3$ photoemission experiments of in-situ deposited films using the SoLiAS experimental station at the U49/2-PGM-2 beamline. Thin films of BST and Pt were prepared by rf-magnetron sputtering in a deposition chamber connected to the SoLiAS. The BST films ($x=1, 0.6$) were deposited from ceramic targets with 1% oxygen in the sputter gas at 650°C substrate temperature. In Fig. 1a the dependence of the Ba 4d emission of the surface of a BaTiO_3 thin film on excitation energy is presented. Two barium components, Ba(I) at 88.9 eV and Ba(II) at 89.9 eV are observed. The intensity of Ba(II) is clearly reduced with respect to Ba(I) with increasing excitation energy. Obviously the high binding energy component Ba(II) is due to a surface species. Using a simple bi-layer model, the thickness of the surface layer containing the Ba(II) species is calculated to be ~ 0.5 nm thick. A mean free path for the electrons as proposed by Tanuma, Powell and Penn has been used in this calculation.

Fig 1 (b) and (c) shows the Ba 4d emission of a $\text{Ba}_{0.6}\text{Sr}_{0.4}\text{TiO}_3$ and a BaTiO_3 thin film in the course of increasing Pt deposition. The spectra were recorded with an excitation energy of $h\nu=140\text{eV}$ yielding maximum surface sensitivity. With increasing Pt deposition the energy difference between the two Ba components is clearly reduced and only one Barium component is observed for a Pt thickness larger than $\sim 1\text{nm}$.

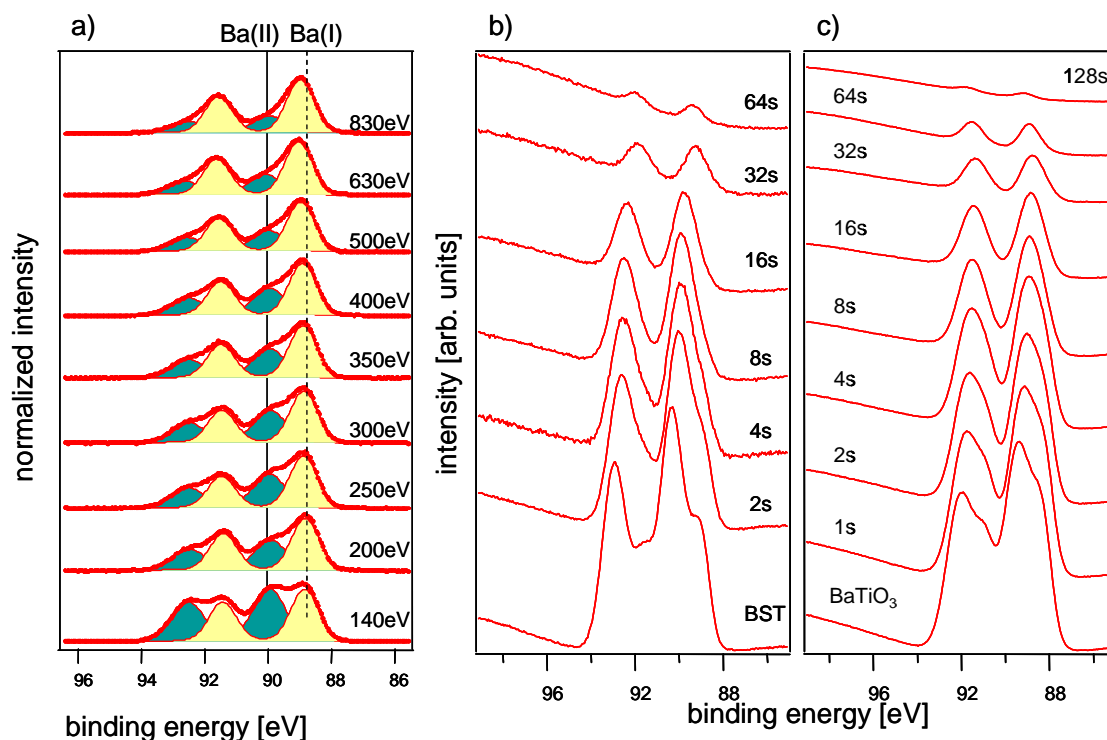


Fig. 1: (a) background subtracted Ba4d emission of a BTO thin film with varying excitation energy. The intensity of the Ba(II) component decreases with increasing excitation energy. Ba4d emissions of a BST (b) and BTO (c) thin film in the course of Pt-deposition. The energy difference between the two Ba components is reduced with increasing Pt coverage.

The surface Ba component at higher binding energies has been explained by various models such as a structurally relaxed surface layer [1], a surface core level shift [2], BaO, BaCO₃ and others. None of these explanations are likely in the light of the present results. First, our surfaces are free of carbon contaminations ruling out BaCO₃. Second, the surface layer is too thick to be explained by a surface core level shift as it is known for many semiconductors. In addition, deposition of Pt on top of a defective surface layer or a BaO surface species should preferentially change the surface Ba(II) component and not decrease the binding energy difference between the two species. Unfortunately, no explanation of the surface species can be given yet. However, as binding energies in photoemission are associated with atomic charges, it seems likely that the two components have an electronic, rather than a structural origin.

The relative band edge positions of Strontium Titanate (STO) and BaTiO₃ (BTO) are important to understand the different contact behaviour of these materials. We have therefore determined the band alignment between STO and BTO by stepwise deposition of BTO on a STO single crystal doped with 0.05 wt% Nb. The XP-spectra are shown in Fig. 2. The valence band maximum of the clean SrTiO₃ surface is found at 3.0 eV and only a small (100 meV) downward band bending is observed in the SrTiO₃ substrate in the course of BTO deposition. As the valence band maximum of the thick BTO films is observed at 3.3 eV binding energy, it is found 0.4 eV below the valence band maximum of STO. This result is in good agreement with recent calculations in literature if transitivity of the calculated band alignments is assumed [3]. The lower valence band maximum of BTO suggest larger barrier heights for electrons at the contact. This corresponds well with measurements of the STO/Pt and BTO/Pt interface which were also performed during the beamtime.

In Fig. 2, the Ba 4d level does not show the characteristic splitting discussed above. Currently, we assign this difference to the different Fermi level position in the film. Due to the band gap of BTO of 3.2 eV, a valence band maximum at 3.3 eV corresponds to a Fermi level inside the conduction band, which will modify the charge distribution and be in accordance with the suggestion of an electronic origin for the splitting of the Ba level. However, the dependence of the splitting of the Ba level on the Fermi level position remains to be studied more systematically.

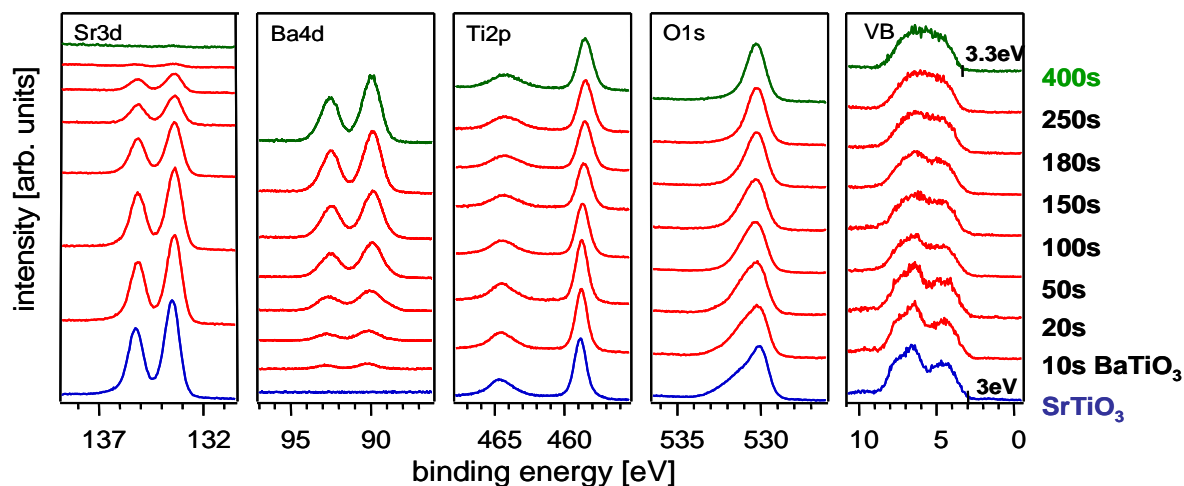


Fig. 2: Core level as well as valence band spectra of a SrTiO₃ single crystal during stepwise deposition of BaTiO₃. Spectra are excited with $h\nu = 630$ eV.

The experiments were supported by the DFG Graduate School *Tunable Integrated Components for Microwaves and Optics* (TICMO) and by the European Network of Excellence *Functionalized Advanced Materials and Engineering of Hybrids and Ceramics* (FAME).

- [1] V. Craciun and R. K. Singh, Appl. Phys. Lett. 76, 1932 (2000).
- [2] J. D. Baniecki, M. Ishii, T. Shioga, et al., Appl. Phys. Lett. 89, 162908 (2006).
- [3] J Junquera, M. Zimmer, P. Ordejón, and P. Ghosez, Phys. Rev. B **67**, 155327 (2003).

Self-screening of the polarization charge at the surface of conductive BaTiO₃

I. Konovalov, L. Makhova

Wilhelm Ostwald Institute for Physical and Theoretical Chemistry, Universität Leipzig, Linnéstr. 2, D-04103 Leipzig, Germany

Properties of ferroelectric oxides have been thoroughly studied since years for possible applications in microelectronics. Ferroelectric oxides are usually considered as switchable dielectrics. Since these oxides can also be made semiconductor by doping [1,2], the question arises whether switchable p-n- or Schottky diode structures can be prepared using them. This would be beneficial e.g. for a further miniaturization of non-volatile memories. We would like to study the relation between the direction of the spontaneous polarization and the transversal carrier transport in heterojunctions between BaTiO₃ and metals or semiconductors in the future. The carrier transport is determined by the band diagram of the junction, in particular by the band bending and by the band offsets at the interface. These effects should depend on the spontaneous polarization state in the ferroelectrics, as it can be predicted from theories of band discontinuities [3]. Using photoelectron spectroscopy, we observed shifts of the core spectral lines which can be interpreted as a change in the abrupt band bending after heating the BaTiO₃ crystal above the Curie temperature, explained in the following in more detail.

The experimental setup included ROSA experimental chamber equipped with a photoelectron energy analyzer and with a field plate. This field plate could be pressed in vacuum towards the surface of a conductive BaTiO₃ single crystal while the plate was electrically grounded. The sample could be electrically biased and simultaneously heated. The sample treatment sequence included: 1) heat treatment of the sample 2) applying a negative sample bias of about a hundred volts while cycling the temperature to above the Curie temperature and cooling down to the room temperature under the field plate 3) deposition of 3 Å CuI 4) applying a positive bias of about a hundred volts while cycling the temperature to above the Curie temperature under the field plate. Between the steps of the sample treatment, the field plate was removed and the photoelectron spectroscopy measurements at several kinetic energies were performed using Ba3d₅, Ti2p₃ and O1s core levels of the substrate, as well as Cu2p₃ and I3d₅ levels of the film. The figure shows Ba3d₅ and O1s core line spectra of the substrate. The energy resolution of about 2 eV along with a significant noise due to a small sensitivity makes exact interpretation of the spectra difficult. A significant core level shift was observed at large kinetic energies in all spectral lines of the substrate after the initial heating of BaTiO₃. Surprisingly, this shift is absent at lower kinetic energies of photoelectrons. A possible interpretation by a poor reproducibility (~3eV) of the excitation energy of the U41PGM beamline at energies above 1000 eV does not explain why the reproducibility improves during the subsequent measurements after the initial heating. Our interpretation is that the core level shift is caused by an abrupt band bending near the surface due to a double layer of polarization and self-screening charge [4], explained in the following. The internal spontaneous polarization state may cause an external electric field around a non-conductive material. In our experiment, BaTiO₃ was made conductive by an intrinsic doping. The surface charge due to the spontaneous polarization is screened by the redistribution of the free carriers, so that the external electric field is not observed [4]. However, the bulk of the material remains in the polarized state. Due to this surface dipole, the core level energies in the surface region are strongly depth dependent, as soon as the information depth of the XPS becomes larger than the correlation length. For BaTiO₃, the correlation length was estimated as 2 nm [4] and it is larger than the information depth at 50 eV kinetic energy, but it is typical for larger kinetic

energies of photoelectrons. This interpretation is also supported by the observation of the linewidth of the shifted emission line at the large kinetic energies, which is larger than at small kinetic energies, due to contributions from various depth regions with different potential. The energy of the photoelectron lines was found independent from an external static external electric field. No distinct trend was concluded from the minor shifts observed. The probable reason is that the static external field was screened by the conductivity in the sample.

In conclusion, using the variable kinetic energy in photoelectron spectroscopy measurements we observed shifts of core levels depending on the kinetic energy, which can be interpreted in terms of the internal screening in the conductive ferroelectric material. The estimate of the thickness of the screening sheet is close to the correlation length and to the lattice constant. These preliminary results need however to be additionally confirmed as to the effectiveness of the measures taken for changing the polarization of the sample.

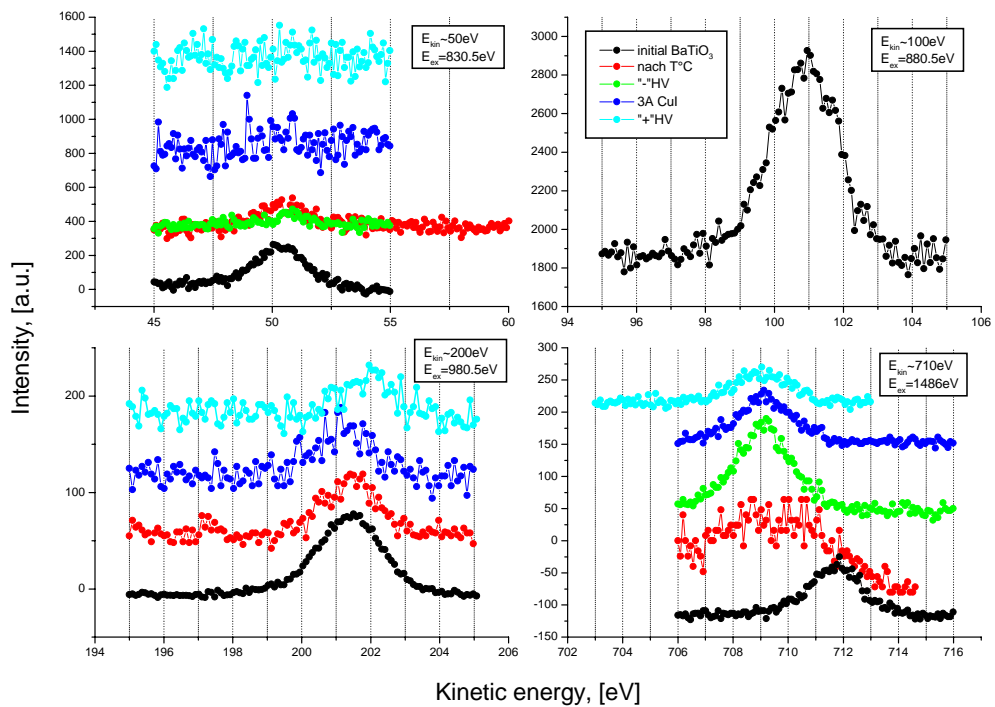
[1] J. Nowotny, M. Rekas, *Ceramics International* 1994, 20 225.

[2] J. I. Itoh, D. C. Park, N. Ohashi, I. Sakaguchi, I. Yashima, H. Haneda, J. Tanaka, *Jap. J. Appl. Phys.* 2002, 41 3798.

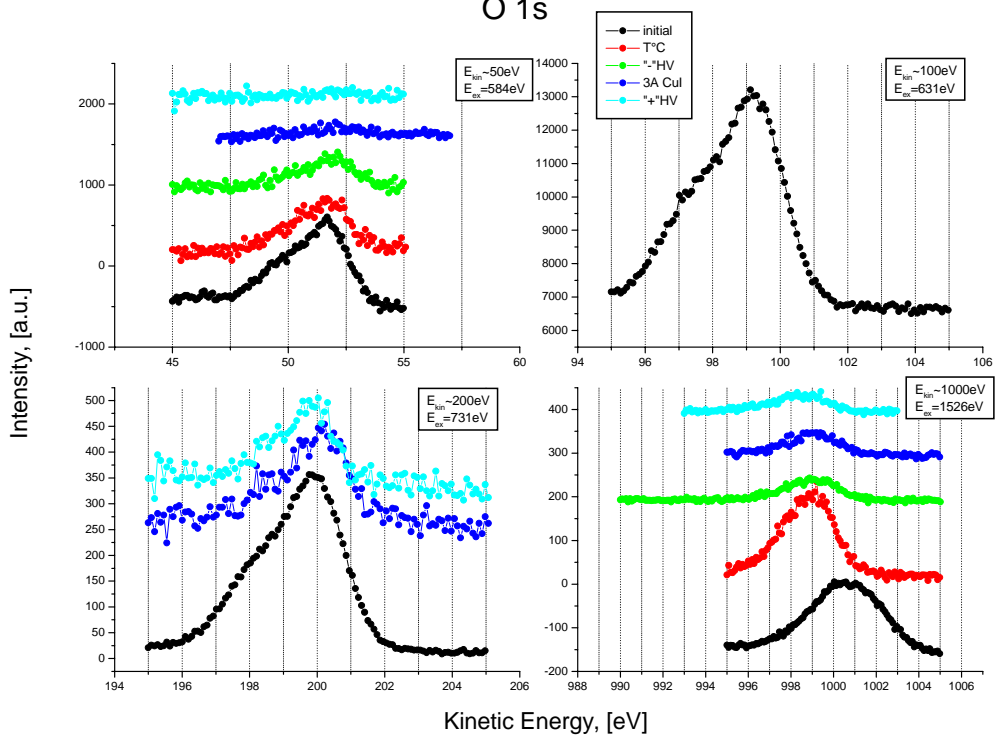
[3] F. Capasso, A. Y. Cho, K. Mohammed, P. W. Foy, *Appl. Phys. Lett.* 1985, 46 664.

[4] V. M. Fridkin, *Ferroelectric semiconductors*. New York: Consultants Bureau, 1980.

Ba 3d5



O 1s



VUV Spectroscopic Ellipsometry of Spiro-linked Organic Derivatives

Simona D. Silaghi¹, Till Spehr², Christoph Cobet¹, Christoph Werner¹, Josef Salbeck², Sven Peters³, Walter Braun⁴, and Norbert Esser¹

¹ISAS - Institute for Analytical Sciences, Department Berlin, D-12489 Berlin, Germany

²Institut für Chemie, Universität Kassel, D-34132 Kassel, Germany

³SENTECH Instruments GmbH, D-12489 Berlin, Germany

⁴BESSY-GmbH, D-12489 Berlin, Germany

Organic-based devices have the advantage of lower fabrication costs, large-area scalability, efficient visible-UV-VUV light emission, and low operating voltages making them suitable for colour displays and lighting applications [1].

The spiro-linkage concept is employed to modify the steric demands of small molecular organic compounds to improve their processability and morphologic stability, while their electronic properties are retained [1]. Spiro-linked organic materials have been proven to be very stable candidates [1] for organic optoelectronics and can be employed in charge transport and emitting layers of organic light-emitting diodes (OLEDs) [2] as well as solid-state lasers [3]. They form stable nonpolymeric organic glasses with high glass transition temperatures, usually associated with amorphous polymers. Currently, special attention is paid to those spiro-linked derivatives with strong absorption in the UV-VUV energy range. Compared to green-light-emitting materials, many efforts are still needed to further improve the performance of organic blue-light-emitting materials. Especially, information about the effective refractive index is needed in the case of organic (spiro derivatives) solid-state UV-lasers based on distributed feedback (DFB) resonators. The emission of such DFB lasers strongly depends on the period of the Bragg grating Λ and the effective refractive index n_{eff} of the waveguide [3]. Thus, the knowledge of optical constants is indispensable for optimizing the design of spiro-based electronic and optoelectronic devices.

Novel organic compounds of e.g. **Octo1** (2,2',4,4',7,7'-hexaphenyl-9,9'-spirobifluorene) and **Octo2** (2,2',4,4',7,7'-hexakis(biphenyl-4-yl)-9,9'-spirobifluorene) were synthesized at Universität Kassel in the group of Prof. Dr. Josef Salbeck. The molecular structure of a typical spiro-linked molecule i.e. **Octo1** is presented in the fig. 1. The thin films were grown by organic molecular beam deposition (OMBD) on silicon substrates kept at room temperature. The source materials were deposited under ultrahigh vacuum conditions with an evaporation rate of 1 Å/sec on the rotating substrate in order to avoid thickness inhomogeneities.

Fig. 2(a) shows an example of the measured and simulated ellipsometric spectra for a thin film of **Octo1**. The optical response of the organic films was described by an isotropic model based on a sum of Tauc-Lorentz oscillators. These types of oscillators work particularly well for amorphous materials [4], even though they were employed only in the case of inorganic materials so far.

The optical constants calculated from the ellipsometric parameters, Ψ and Δ , of the investigated spiro-linked organic films of **Octo1** (130 nm) and **Octo2** (170 nm) are displayed in the fig. 2(b). The OMBD prepared organic films on SiO₂ substrates are found to be smooth, homogeneous and optically isotropic as expected since the spiro-linkage approach suppresses the crystallization giving rise to amorphous organic films (see fig. 2). The strongest light

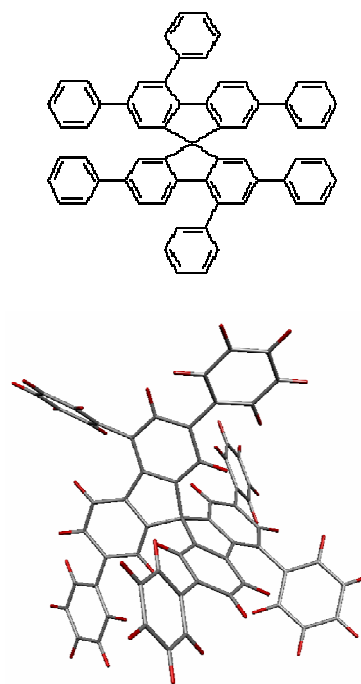


Fig.1 Molecular structure of 2,2',4,4',7,7'-hexaphenyl-9,9'-spirobifluorene (C₆₁H₄₀)→**Octo1**.

absorption occurs for both types of spiro-molecules in the deep UV energy range above 6 eV. As expected, the more effective π -conjugation of the **Octo2** molecule red shifts its absorption edge by 200 meV compared to **Octo1**. On the other hand, the increased non-planarity of the **Octo2** leads to a decrease of the electronic absorption or optical constants *i.e.* **n** and **k** (see fig.2b). For a thorough understanding of the optoelectronic behaviour of these spiro-molecules, density functional theory (DFT) calculations must be employed.

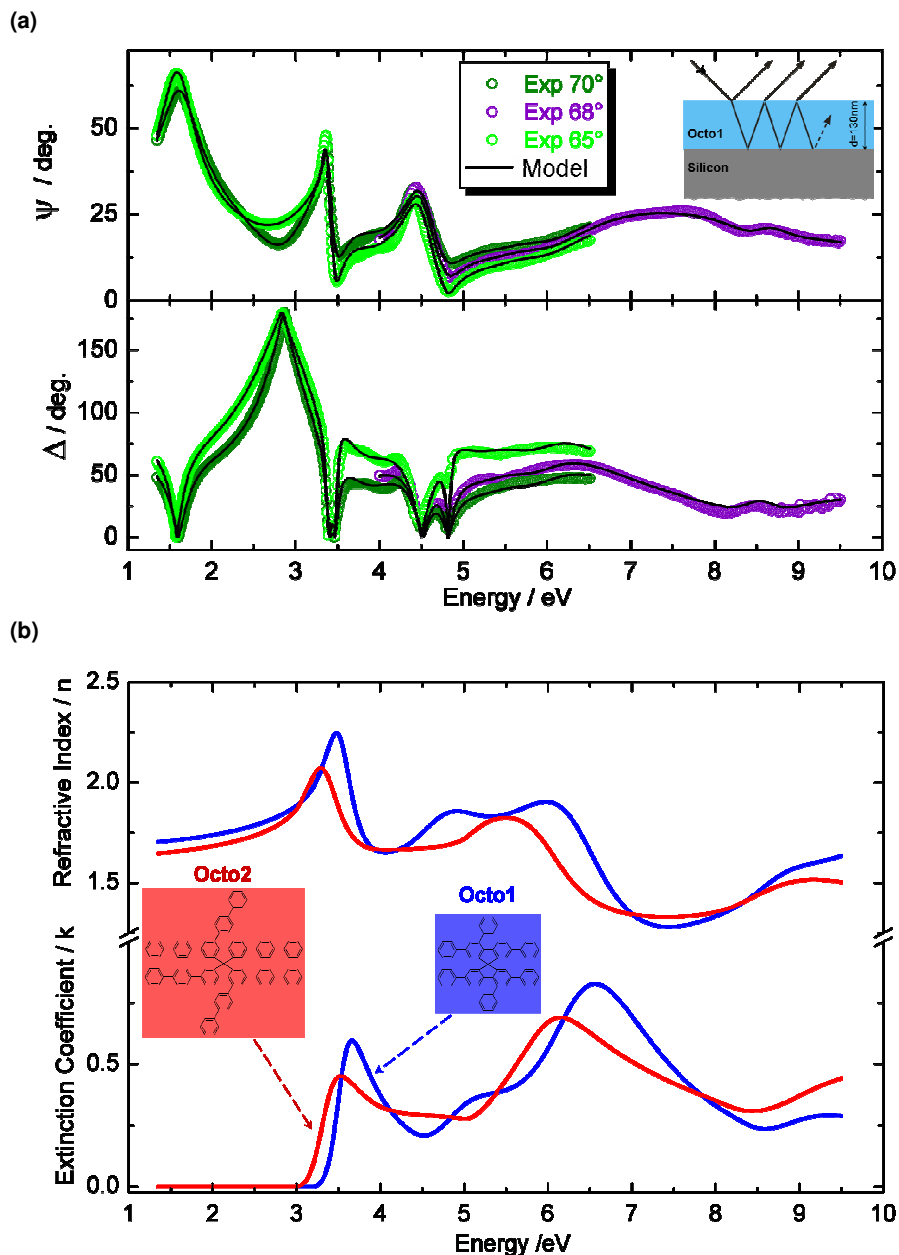


Fig.2 (a) Example of measured and simulated Ψ and Δ spectra of **Octo1** thin film (130 nm) on silicon substrate. **(b)** Determined optical constants of **Octo1** and **Octo2**.

References:

- [1] J. Salbeck, N. Yu, J. Bauer, F. Weissörtel, H. Bestgen, *Synth. Met.* **91** (1997) 209
- [2] D. Gebeyehu, K. Walzer, G. He, M. Pfeiffer, K. Leo, J. Brandt, A. Gerhard, P. Stöbel, H. Vestweber, *Synth. Met.* **148** (2005) 205
- [3] T. Spehr, A. Siebert, T. Fuhrmann-Lieker, J. Salbeck, T. Rabe, T. Riedl, H.H. Johannes, W. Kowalsky, J. Wang, T. Weimann, P. Hinze, *Appl. Phys. Lett.* **87** (2005) 161103
- [4] G.E. Jellison Jr., F.A. Modine, *Appl. Phys. Lett.* **69** (1996) 2137

Structural investigation of Carbon Supported Ru-Se Based Catalysts using Anomalous Small Angle X-Ray Scattering (ASAXS)

S. Haas ¹, A. Hoell ^{1*}, G. Zehl ², I. Dorbandt ², P. Bogdanoff ² and S. Fiechter ²

Hahn-Meitner-Institut Berlin, Glienicker Str. 100, 14109 Berlin, Germany,

¹ Dept. of Structural Research SF-3

² Dept. of Solar Energetics SE-5

Worldwide demand for energy is growing at an increasing rate. Currently, this demand is being met largely by fossil fuels, particularly crude oil. However, those reserves are diminishing and their exploration will become increasingly expensive. Hydrogen and methanol as energy carriers can be produced from both, fossil and renewable energy sources. By direct conversion into energy through an electrochemical reaction, fuel cells extract more power out of the same quantity of fuel when compared with traditional combustion. Due to their high activity, the use of platinum-based electrocatalyst in low temperature proton exchange membrane fuel cells (PEMFC) is present state of the art. However, the fact that commercial applicability of PEMFC technology is almost exclusively bound to this expensive and rare metal, may become a prohibitive factor for the successful adoption of fuel cells as mass-produced units.

As recently successfully demonstrated, Ruthenium based catalysts modified with Selenium also exhibit high catalytic activity for the oxygen reduction reaction [1]. One advantage of Ruthenium is that it is by a factor of 40 more common in the earth crust and its price presently amounts to only 17% of that of platinum. Furthermore, in direct methanol fuel cells (DMFC) the undesired crossover of methanol through the membrane from the anode space into the cathode compartment is still an unsolved issue. Therefore, platinum cathode catalysts suffer from activity losses due to methanol oxidation. As alternative, carbon supported Ruthenium nano-particles modified with Selenium feature absolute methanol tolerance. Although intense studies of these catalysts were performed during the last decade, no definite conclusion with respect to the nature of the catalytically active sites and the constitution of the RuSe nano-particles could be drawn. However, only a better understanding of the underlying principles is believed to pave the way towards higher active catalysts, thus making DMFCs more efficient and reliable.

Investigating RuSe electrocatalysts, data about the Selenium distribution over the catalyst's surface are particularly necessary, because catalytic efficiency depends strongly on the Selenium content of the catalysts. Anomalous Small Angle X-ray Scattering (ASAXS) represents a powerful tool for element sensitive analysis of nano-structured catalytic materials, whereas also useful data about the chemical composition in the sub-nanometer scale can be obtained. Using the ASAXS technique one takes advantage of the so-called anomalous or resonant behaviour of the atomic scattering amplitude of an element near its absorption edge to separate the scattering from different elements.

* to whom correspondence should be addressed: hoell@hmi.de

To clarify the structural features of these catalytically active Se-modified Ruthenium nano-particles, such materials were prepared by thermolysis of $\text{Ru}_3(\text{CO})_{12}$ in an organic solvent with and without the presence of dissolved Selenium. The resultant Ruthenium nano-particles were supported on the commercial Black Pearls 2000[®] carbon black from Cabot.

We investigated with ASAXS a complete set of samples, including the final working RuSe catalyst supported on a commercial carbon black, and some intermediate preparation states such as non-modified (Selenium free) Ruthenium nano-particles or the bare carbon support. The scattering curves were taken in the vicinity below the Selenium and the Ruthenium K absorption edges, respectively.

Figure 1a shows that Ru and Se form nano-structures that alter the shape of the Black Pearls scattering curve dramatically. The sample which contains Selenium (Fig. 1 b) shows a small hump at $Q \sim 7 \text{ nm}^{-1}$ that is visible also at the Ru-K edge (Fig. 1 a). It was deduced that Selenium within the sample generates structural features clearly detectable and analysable by ASAXS (Fig. 1 c).

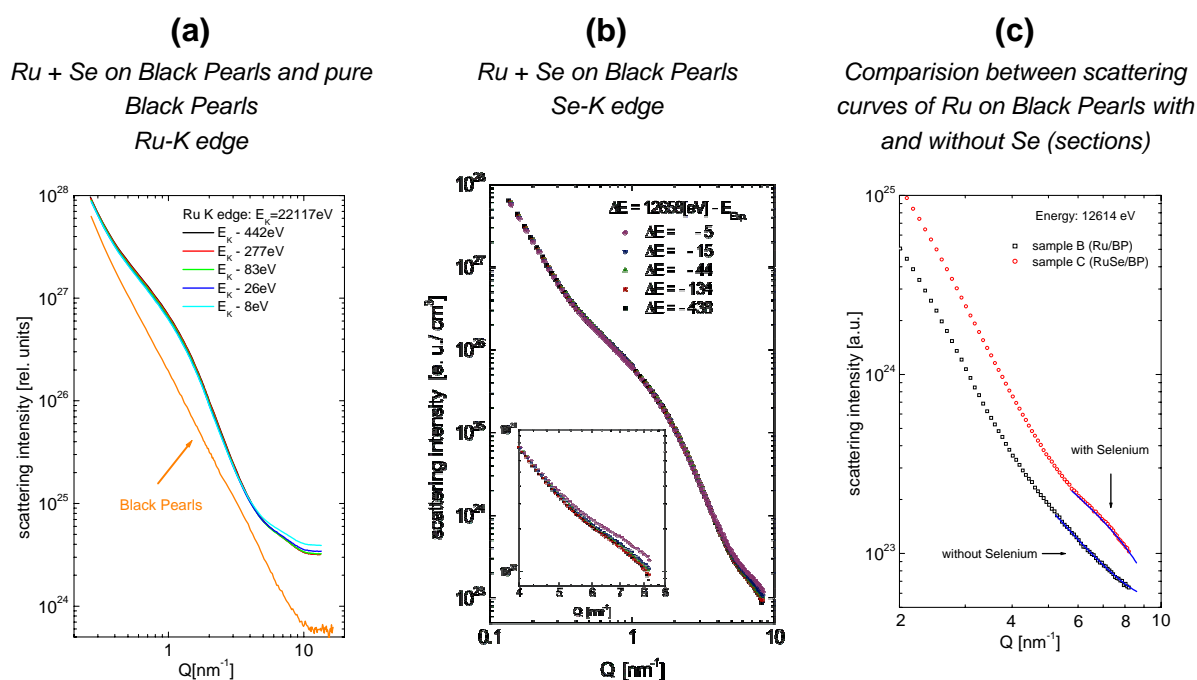


Figure 1: ASAXS scattering curves measured near below the K-absorption edges of Ruthenium (a) and Selenium (b and c).

Taken into account the anomalous dispersion effect, in the vicinity of the Se- and the Ru-edge as well, of the scattering intensity of all measured samples, a structure model of the catalytically active metallic nano-particles has been deduced. That model suggests a nearly spherical Ru particle with a mean diameter of 2.3 nm decorated with Se aggregates. These structures onto the Ruthenium nanocrystallites feature a diameter around 0.5 nm. The results are supported by data from XRD, XPS, and EXAFS measurements, obtained from the same materials [2, 3]. Even so, the real shape of these small Selenium clusters is not yet finally clarified.

However, free Selenium clusters of few atoms will form symmetric ring structures [4].

We also confirmed that the Selenium modified Ruthenium nano-particles are extremely resistant against agglomeration and particle growth. Even after annealing at 800°C the average particle size of the Ruthenium particles was found to remain below 2.5 nm in diameter.

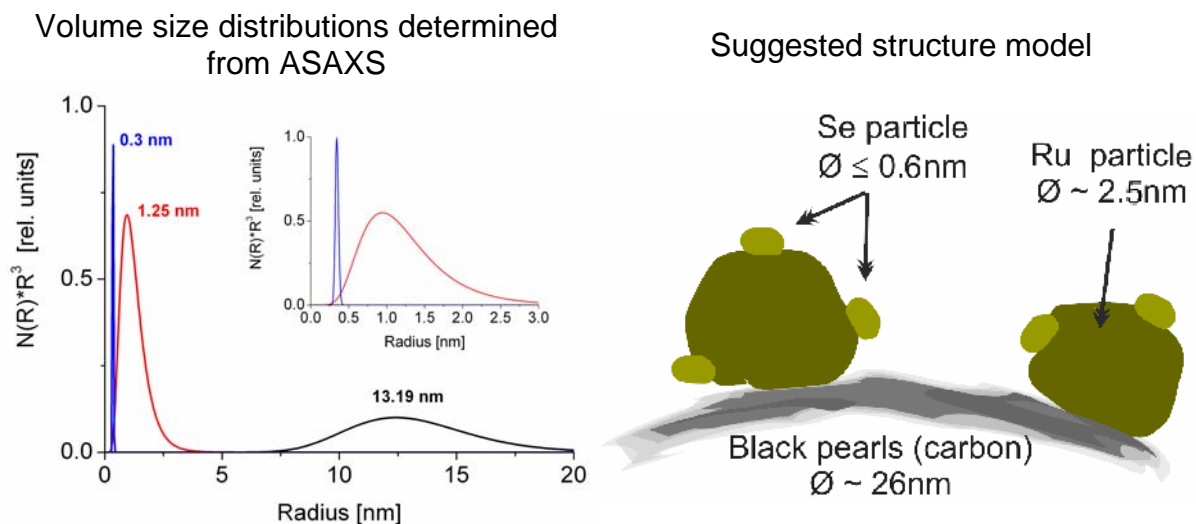


Figure 2: Structural model for Ruthenium based electrocatalysts supported on activated carbon and modified with Selenium at 800°C.

Conclusions [5]

ASAXS revealed nano sized features of the samples that are hidden for SAXS or SANS methods alone. A structure model of the catalytically active metallic nano-particles has been deduced suggesting a Ruthenium core, with an average diameter of 2.3 nm, decorated with Selenium aggregates.

The Selenium structures onto these Ruthenium nano-crystallites feature a diameter less around 0.5 nm. Therefore, no closed Selenium coverage of the Ruthenium core particles could be affirmed.

Selenium modified Ruthenium nano-particles are extremely resistant against agglomeration and particle growth. Even after annealing at 800°C the average particle size was found to remain below 2.5 nm in diameter.

- [1] Alonso-Vante, N.; Bogdanoff, P.; Tributsch, H.: On the Origin of the Selectivity of Oxygen Reduction of Ruthenium - Containing Electrocatalysts in Methanol - Containing Electrolyte; J. Catalysis 190 (2000) 240.
- [2] Fiechter, S.; Dorbandt, I.; Bogdanoff, P.; Zehl, G.; Schulenburg, H.; Tributsch, H.; Bron, M.; Radnik, J.; Fieber-Erdmann, M.: Surface modified Ruthenium nanoparticles: structural investigation and surface analysis of a novel catalyst for oxygen reduction; Journal of Physical Chemistry C, in press.
- [3] Zehl, G.; Dorbandt, I.; Fiechter, S.; Bogdanoff, P.: On the Influence of Preparation Parameters on the Catalytic Properties of Carbon Supported Ru-Se Electrocatalysts; Journal of New Materials for Electrochemical Systems, submitted.
- [4] Becker, J.; Rademann, K.; Hensel, F.: Ultraviolet photoelectron studies of the molecules Se₅, Se₆, Se₇ and Se₈ with relevance to their geometrical structure; Z. Phys. D. - Atoms, Molecules and Cluster 19 (1991) 229.
- [5] Haas, S; Hoell, A.; Zehl, G.; Dorbandt, I.; Bogdanoff P. and Fiechter S.: Structural investigation of Carbon Supported Ru-Se Based Catalysts using Anomalous Small Angle X-Ray Scattering; 211th ECS Meeting, Chicago, Illinois, May 6-11, 2007, accepted.

Valence and spin states of 3d ions in complex oxides $\text{La}_{1-x}\text{Ca}_x\text{Mn}_{0.5}\text{Co}_{0.5}\text{O}_3$ determined by X-ray absorption and X-ray photoelectron spectroscopies

V. R. Galakhov^{1*}, S. N. Shamin¹, A. S. Shkvarin¹, M. Raekers², C. Taubitz²,
M. Prinz², M. Neumann², M. A. Melkozerova³, T. I. Chupakhina³,
G. V. Bazuev³, Yu. S. Dedkov⁴, and S. L. Molodtsov⁴

¹*Institute of Metal Physics, Russian Academy of Sciences —
Ural Division, 620041 Yekaterinburg GSP-170, Russia*

²*Fachbereich Physik, Universität Osnabrück, D-49069 Osnabrück, Germany*

³*Institute of Solid State Chemistry, Russian Academy of Sciences —
Ural Division, 620041 Yekaterinburg GSP-145, Russia*

⁴*Institut für Festkörperphysik, Technische Universität Dresden, D-01062 Dresden, Germany*

The solid solution system $\text{LaMn}_{1-y}\text{Co}_y\text{O}_3$ has recently attracted much attention owing to ferromagnetic interactions dominating for intermediate values of y [1–7]. Although the Mn and Co ions are in trivalent states in the ternary compounds LaMnO_3 and LaCoO_3 , there is a tendency towards charge disproportionation in the quaternary materials $\text{LaMn}_{1-y}\text{Co}_y\text{O}_3$ (i.e., a combination of Mn^{4+} and Co^{2+}). Magnetic properties of $\text{LaMn}_{1-y}\text{Co}_y\text{O}_3$ are discussed in terms of competition between the ferromagnetic $\text{Mn}^{3+}\text{--O--Mn}^{4+}$, $\text{Mn}^{3+}\text{--O--Mn}^{3+}$, $\text{Co}^{2+}\text{--O--Mn}^{4+}$, and antiferromagnetic $\text{Mn}^{4+}\text{--O--Mn}^{4+}$, $\text{Co}^{2+}\text{--O--Co}^{2+}$, $\text{Mn}^{3+}\text{--O--Co}^{2+}$, superexchange interactions, considering also a tendency to $\text{Co}^{2+}/\text{Mn}^{4+}$ ionic ordering of the NaCl type [1–7].

According to the XPS and XAS studies, dopant Co ions in these compounds are divalent [8–11]. It means that the Mn ions are in a $\text{Mn}^{3+}\text{--Mn}^{4+}$ mixed valence and that the ferromagnetic interactions were attributed to the double exchange between Mn^{3+} and Mn^{4+} . On the other hand, it has been shown that magnetic properties of $\text{LaMn}_{0.5}\text{Co}_{0.5}\text{MnO}_3$ and valence states of Co and Mn ions depend on the synthesis conditions [3–5].

The phase prepared by the low-temperature nitrate method at 700 °C (P1) undergoes a transition to the ferromagnetic state at the Curie temperature $T_c \approx 230$ K. The phase synthesized by solid state reaction at 1300 °C (P2) has the Curie temperature $T_c \approx 150$ K [3–5]. Core-level Mn and Co $2p$ X-ray photoelectron spectroscopic studies at room temperature and magnetical measurements indicate that the spin states of Mn and Co are different in these two phases of $\text{LaMn}_{0.5}\text{Co}_{0.5}\text{MnO}_3$: Mn and Co ions are both in their trivalent states with Co in the low-spin configuration in the P1 phase and as Mn^{4+} and high-spin Co^{2+} in the P2 phase [4, 5].

Here we report the XAS and XPS studies of the two phases of $\text{La}_{1-x}\text{Ca}_x\text{Mn}_{0.5}\text{Co}_{0.5}\text{O}_3$. The phases P1 were prepared by a low-temperature citrate method at 700 °C. The samples P2 were synthesized by a ceramic method at 1300 °C. The oxygen content of the samples was determined by means of a thermogravimetric analysis during reduction in hydrogen flow at 900 °C. The Co $2p$ and Mn $2p$ x-ray absorption spectra (XAS) were carried out at the Russian-German Beam Line at the BESSY storage ring. The spectra were normalized to the incident current as measured from a gold grid located at the entrance chamber. The Mn $3s$ X-ray photoelectron spectra were measured using a PHI 5600 ci multitechnique system. The Al $K\alpha$ radiation was monochromatized by a double-focusing monochromator.

Figure 1 shows the Mn $2p$ X-ray absorption spectra of two phases of $\text{La}_{1-x}\text{Ca}_x\text{Mn}_{0.5}\text{Co}_{0.5}\text{MnO}_3$, P1 and P2, in comparison with the spectra of some manganites. The spectra of the P1 and P2 phases of $\text{La}_{1-x}\text{Ca}_x\text{Mn}_{0.5}\text{Co}_{0.5}\text{MnO}_3$ are more closely to those of $\text{La}_{0.07}\text{Ca}_{0.93}\text{MnO}_3$ than to those of

*e-mail: galakhov@ifmlrs.uran.ru

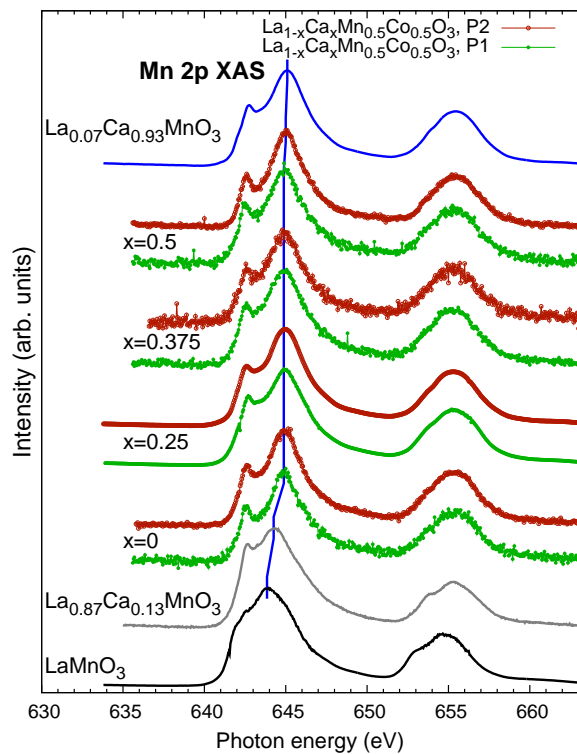


Fig. 1: Mn 2*p* X-ray absorption spectra of the phases P1 and P2 of $\text{La}_{1-x}\text{Ca}_x\text{Mn}_{0.5}\text{Co}_{0.5}\text{O}_3$. For comparison, the Mn 2*p* XAS spectra of some manganites are shown.

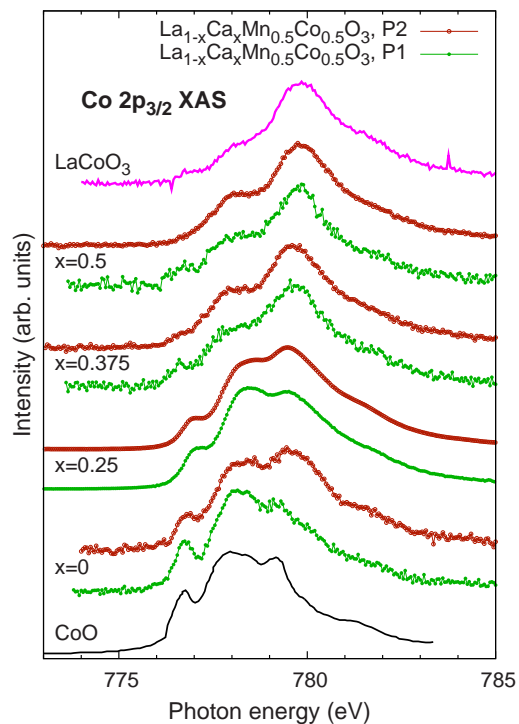


Fig. 2: Co 2*p*_{3/2} X-ray absorption spectra of the phases P1 and P2 of $\text{La}_{1-x}\text{Ca}_x\text{Mn}_{0.5}\text{Co}_{0.5}\text{O}_3$. For comparison, the Co 2*p* XAS spectra of some cobaltites are shown.

LaMnO_3 . Therefore, valence states of manganese ions in both phases of $\text{La}_{0.75}\text{Ca}_{0.25}\text{Mn}_{0.5}\text{Co}_{0.5}\text{MnO}_3$, P1 and P2, are closer to 4+ than to 3+.

We have performed Co 2*p* X-ray absorption measurements to investigate the valence of Co ions in these compounds (see Fig. 2). One can see that the spectrum of the phase P1 of $\text{LaMn}_{0.5}\text{Co}_{0.5}\text{O}_3$ is almost identical to the spectrum of CoO (Co²⁺ ions). The doping with Ca leads to a transformation of the spectra, and the spectra of the samples with $x = 0.5$ are practically identical to the spectrum of LaCoO_3 , where Co³⁺ ions are in the low-spin state. Assuming that the Co ions in the sample P1 of $\text{LaMn}_{0.5}\text{Co}_{0.5}\text{O}_3$ are in the 3+ state, we have estimated the valence states of Co ions in other samples of $\text{La}_{1-x}\text{Ca}_x\text{Mn}_{0.5}\text{Co}_{0.5}\text{MnO}_3$.

Valence states of Mn ions were estimated using the Mn 3*s* level splitting obtained by means of X-ray photoelectron spectroscopy (see Fig. 3). The magnitude of the splitting is proportional to $(2S + 1)$, where S is the local spin of the 3*d* electrons in the ground state. One can see that the magnitude of the Mn 3*s* splitting increases with decreasing x . Using both the Mn 3*s* XPS and Co 2*p* XPS data, we have estimated valence states of Mn and Co ions in the phases P1 and P2, of $\text{La}_{1-x}\text{Ca}_x\text{Mn}_{0.5}\text{Co}_{0.5}\text{MnO}_3$. The results are presented in Fig. 4. The fact that the mean valence states of (Mn+Co) ions are less than that expected from the chemical contents of the samples, can be described to the oxygen nonstoichiometry of the samples. Note that the samples P1 prepared by the low-temperature citrate method are nanocrystalline [5] with an average grain size of about 40–160 nm [6]. One can suggest that the change of the valence states of Co and Mn ions going from P2 to P1 is due to the nanoparticle nature of the P1 phase. It is known that nanooxides are more defective than bulk oxides. Deficiencies of oxygen atoms must lead to the increase of the mean 3*d* valences.

This work was supported by the grant “Cooperation between the Ural and Siberian Divisions of the Russian Academy of Sciences”, the Research Council of the President of the Russian Federation (Project NSH-4192.2006.2), and by the bilateral Program “Russian-German Laboratory at BESSY”.

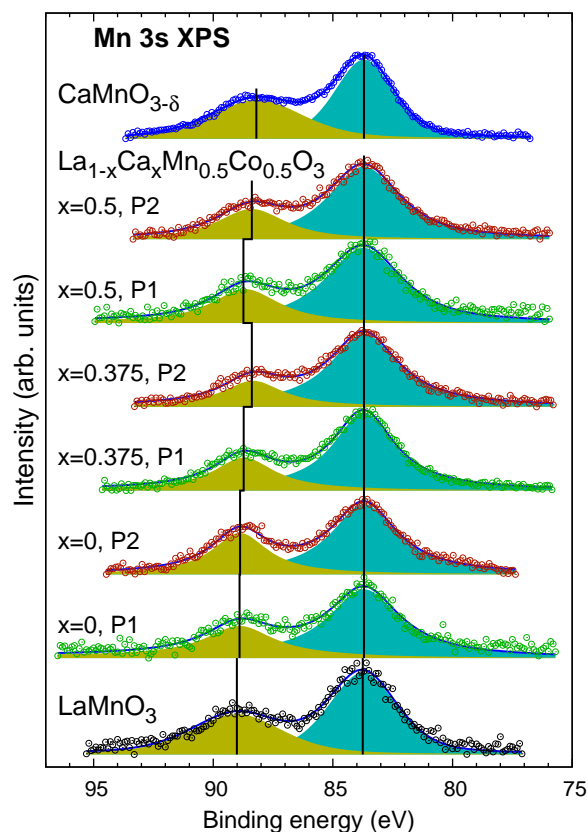


Fig. 3: Mn 3s X-ray photoelectron spectra of some manganites and the phases P1 and P2 of $\text{La}_{1-x}\text{Ca}_x\text{Mn}_{0.5}\text{Co}_{0.5}\text{O}_3$.

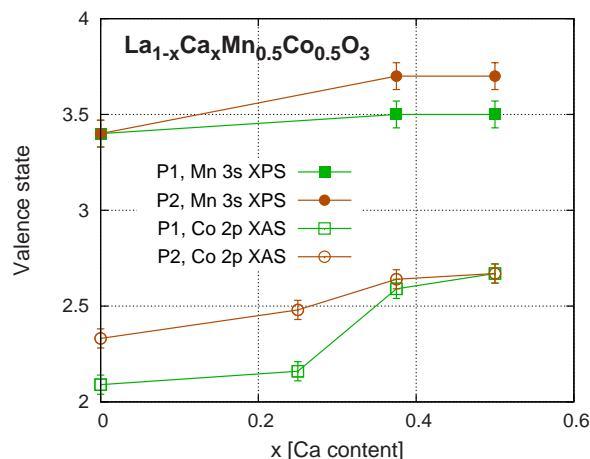


Fig. 4: The evolution of the average valence states of Mn and Co ions in the samples P1 and P2 of $\text{La}_{1-x}\text{Ca}_x\text{Mn}_{0.5}\text{Co}_{0.5}\text{O}_3$ derived from the Mn 3s X-ray photoelectron and Co 2p X-ray absorption spectra, respectively.

- [1] J. B. Goodenough, A. Wold, R. J. Arnett, and N. Menyuk, *Phys. Rev.* **124**, 373 (1961).
- [2] I. O. Troyanchuk, L. S. Lobanovsky, D. D. Khalyavin, S. N. Pastushonok, and H. Szymczack, *J. Magn. Magn. Mater.* **210**, 63 (2000).
- [3] P. A. Joy, Y. B. Kholam, and S. K. Date, *Phys. Rev. B* **62**, 8608 (2000).
- [4] V. L. J. Joly, P. A. Joy, S. K. Date, and C. S. Gopinath, *J. Phys.: Condens. Matter* **13**, 649 (2001).
- [5] V. L. J. Joly, Y. B. Kholam, P. A. Joy, C. S. Gopinath, and S. K. Date, *J. Phys.: Condens. Matter* **13**, 11001 (2001).
- [6] R. Mahendiran, Y. Breard, M. Hervieu, B. Raveau, and P. Schiffer, *Phys. Rev. B* **68**, 104402 (2003).
- [7] R. I. Dass and J. B. Goodenough, *Phys. Rev. B* **67**, 014401 (2003).
- [8] J.-H. Park, S.-W. Gheon, and C. T. Chen, *Phys. Rev. B* **55**, 11072 (1997).
- [9] M. C. Falub, V. Tsurkan, M. Neumann, I. O. Troyanchuk, V. R. Galakhov, E. Z. Kurmaev, H. H. Weitering, *Surface Science* **53**, 488 (2003).
- [10] O. Toulemonde, F. Studer, A. Barnabe, A. Maignan, C. Martin, and B. Raveau, *Eur. Phys. J. B* **4**, 159 (1998).
- [11] M. Sikora, C. Kapusta, K. Knizek, Z. Jirak, C. Autrer, M. Borowec, C. J. Oates, V. Procharzka, D. Rybicki, and D. Zajac, *Phys. Rev. B* **73**, 094426 (2006).

Formation of optically active gold nanoparticles in soda lime silica glasses: ASAXS studies of synchrotron activated growth.

A. Hoell¹, D. Tatchev², K. Rademann³, M. Eichelbaum³, S. Haas¹,

¹Hahn-Meitner-Institut, Department of structural research, D-14109 Berlin

²Institute of Physical Chemistry, Bulgarian Academy of Science, BG-1 113 Sofia

³Humboldt-Universität zu Berlin, Institut für Chemie, D-12489 Berlin

Abstract

Gold nanoparticles in soda lime silica glass were prepared by doping the glass precursors with small amounts of AuCl₃ and a following melting process at 1450°C, irradiation of the polished glasses with x-rays and subsequent annealing. Enhanced particle formation is observed in the irradiated areas. Anomalous small-angle x-ray scattering reveals that the gold particles are homogeneous. The determined volume fraction of the particles is in the range of 10⁻⁵ to 10⁻³ %. The amount of the precipitated gold is about 0.0007 mol%. The determined particle radii range from 0.5 nm after 20 minutes to 2.3 nm after 60 minutes annealing at 550°C.

Introduction

Metal nanoparticles have attracted the scientists' attention in the last years due to their exceptional magnetic, catalytic and optical properties. The production and conservation of especially very small metal clusters is however a difficult process. An effective way to produce metallic nanoparticles and to study their optical properties is to precipitate them in a transparent glass. Gold and silver clusters with monodisperse size distributions can be generated by synchrotron irradiation of glass samples and a subsequent annealing process [1]. This way, noble metal clusters even smaller than one nanometer become accessible, which reveal extraordinary optical properties like high quantum yield photoluminescence.

A system of Au or Ag particles in glass is suitable for small-angle x-ray scattering since the heavier metal atoms provide high scattering contrast against the light element matrix. According to TEM investigations, the particle shape is spherical [1, 2], which facilitates the SAXS data analysis.

Experimental

Gold and silver nanoclusters were produced by local activation of soda lime silica glasses with X-rays provided by the dipole scanner DEX02 at the AZM beamline in co-operation with Dr. Löchel. The glass composition was 70SiO₂-20Na₂O-10CaO (mol%). The gold and silver contents were 0.01 and 0.04 mol%, respectively. The gold containing samples for SAXS measurement were annealed at 550°C for 1, 3, 5, 10, 20, 30, 45, and 60 minutes. Small-angle x-ray scattering experiments were performed at the 7T-MPW-SAXS beamline. Anomalous scattering was measured at energies near the Au absorption edge of 11919 eV.

Results and discussion

During heat treatment, gold particles grow only in the activated glass areas. For longer annealing times, the activated areas colour in ruby red due to the surface plasmon resonance at 525 nm of gold nanoparticles. Significant SAXS scattering over the background is observed after 20 minutes of annealing – Figure 1. The curves show both increase of the scattered intensity as well as growth of the size of the scattering objects. The intensity increase at high q values is the tail of the first wide angle scattering peak of the glass matrix.

The anomalous SAXS effect near the gold absorption edge (11919 eV) is depicted in Figure 2 for one sample. The decrease of the scattered intensity with the energy approaching the edge reveals the presence of gold in the particles. Guinier plots [3] of the samples annealed longer times contain extended linear parts from which the particle radius can be extracted. Figure 3 shows the Guinier plots of a sample annealed for 45 min at 550°C. The

slope of the linear fits corresponding to the different x-ray energies is the same within the accuracy of the measurement. The calculated Guinier radius and spherical particle radius are 1.68 ± 0.02 and 2.16 ± 0.02 nm correspondingly. The fact that the Guinier radius does not depend on the x-ray energy proves that the gold particles are homogeneous, i.e. the system has typical two-phase behaviour.

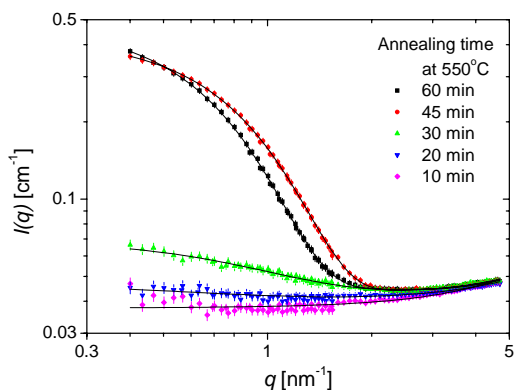


Figure 1. Scattering curves obtained from synchrotron activated gold containing glasses annealed for different time periods at 550°C.

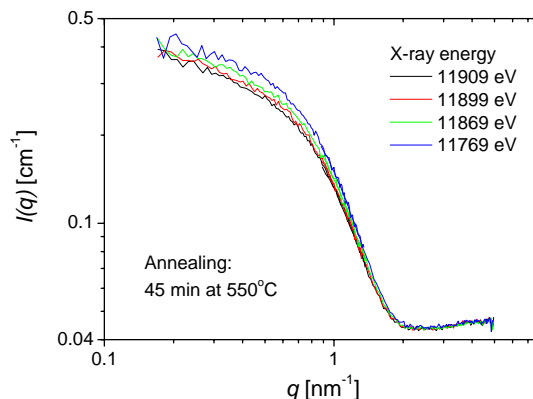


Figure 2. Anomalous SAXS effect at the Au absorption edge for a Au glass activated and annealed for 45 minutes at 550°C.

The solid lines in Figure 1 represent fits obtained by a model of pure Au spherical particles with a log-normal size distribution. The scattering of the glass matrix was approximated with an $A+Bq^2$ term [4]. The so obtained size distributions are shown in Figure 4, and the particle mean radii, particle numbers per unit volume and volume fractions in Figure 5. After approximately 35 minutes annealing at 550°C, the particle growth rate starts to diminish, the volume fraction levels to a constant, but the number of particles decreases. This behaviour is typical for the Ostwald ripening stage of the phase separation. To be noted is that the volume fraction is rather low in the ripening regime. An estimate shows that maximum 7% of the added gold, or only 0.0007 mol% had precipitated. X-ray fluorescence analysis of the glass however showed that only about 10% of the added gold (0.01 mol%) or 0.001 mol% remains in the as prepared glass. The rest of the added gold is lost during the glass preparation. During the Ostwald ripening process, the content of the gold remaining in the glass matrix should approach the equilibrium solubility at the annealing temperature.

Small angle scattering measurements were also done on silver containing glasses. The determined particle radii range between 0.5 and 0.6 nm.

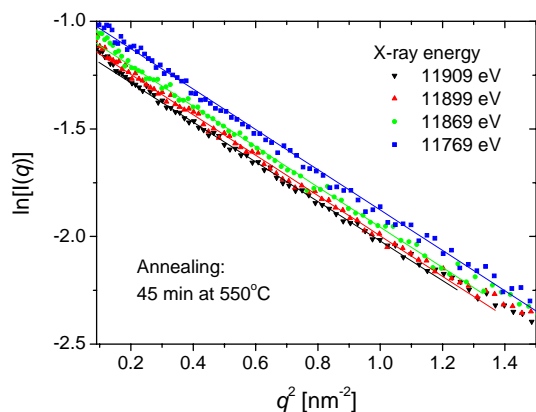


Figure 3. Guinier plots of a synchrotron activated Au glass annealed for 45 minutes at 550°C at 4 different x-ray energies. The determined radius of the spherical particles from all curves is 2.16 ± 0.02 nm.

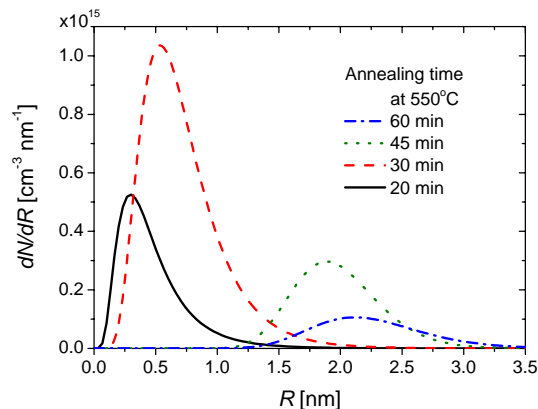


Figure 4. Size distributions of gold clusters in synchrotron activated glasses after different annealing times at 550°C.

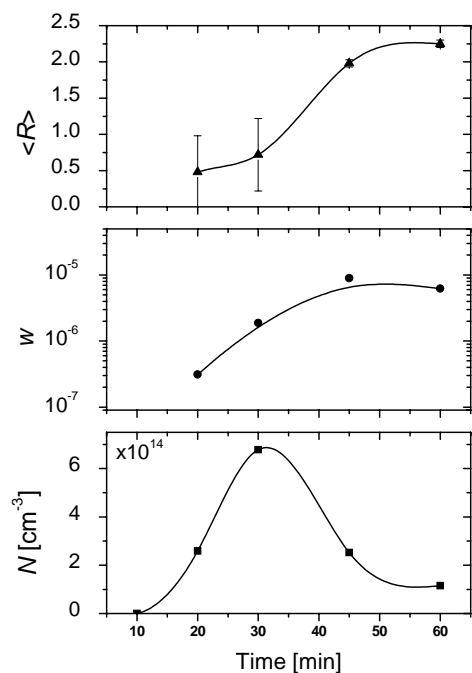


Figure 5. Mean particle radius, $\langle R \rangle$, volume fraction, w , and number of particles per unit volume, N , as a function of the annealing time at 550°C.

Supposing the Au particle has the mass density of the bulk gold, the number of atoms in a particle with 0.5 nm radius is about 31. This number is still high enough to approximate the particle electron density as a continuum. Moreover, the data accuracy and the signal to background ratio are currently low enough to distinguish between uniform and non-uniform particle electron density. This is manifested by the large error of the particle radii at annealing times of 20 and 30 minutes. Despite the large scattering contrast the attempt to reveal the very initial stages of phase formation has always to deal with vanishing volume fraction and consequently decreasing scattering intensity.

Conclusions

Gold particles with radii between 0.5 and 2 nm and narrow size distributions can be generated on demand in soda lime silica glasses by X-ray irradiation and subsequent annealing. For the Au particles, the Ostwald ripening stage of the phase separation already starts after 30-40 minutes annealing at 550°C. The maximum volume fraction of the particles obtained at the ripening stage is about 10⁻³ %. The anomalous small-angle scattering effect indicates clearly that the particles are homogeneous and the system is well described by the two-phase approximation.

References

1. M. Eichelbaum, K. Rademann, R. Müller, M. Radtke, H. Riesemeier, W. Görner, *Angew. Chem. Int. Ed.* (2005), **44**, 7905-7909; W. Görner, M. Eichelbaum, R. Matschat, et al., *INSIGHT* (2006), **48**, 540-544.
2. H. Hofmeister, G. L. Tan, M. Dubiel, *J. Mater. Res.* (2005), **20**, 1551-1562.
3. O. Glatter, O. Kratky, *Small Angle X-ray Scattering*, (1982) Acad. Press, p. 25.
4. D. L. Weinberg, *Phys. Lett.* (1963), **7**, 324-325.

CuPc Electronic Structure: Calculations and Resonant Photoemission Measurements

V.Yu. Aristov^{1,2}, O.V. Molodtsova¹, V. Maslyuk³, D.V. Vyalikh⁴, V.M. Zhilin²,
Yu.A. Ossipyan², T. Bredow⁵, I. Mertig³, and M. Knupfer¹

¹*IFW Dresden, D-01069 Dresden, Germany*

²*Institute of Solid State Physics, Russian Academy of Sciences, Chernogolovka, 142432, Russia*

³*Martin-Luther-Universität at Halle-Wittenberg, Fachbereich Physik, Germany*

⁴*Institute of Solid State Physics, TU Dresden, D-01069 Dresden, Germany*

⁵*Institute for Physical and Theoretical Chemistry, Bonn University, D-53115 Bonn, Germany*

The future trends of applications of organic semiconductor thin films (OMTF's) in electronic and optoelectronic devices [1, 2] has initialise significant research activity since about twenty years. Among them, the family of the phthalocyanines (Pc's) plays an essential role [3]. Thus the information about their electronic structure and properties, obtained by standard modern techniques as well as by calculations, is of crucial significance for both understanding of the fundamental physics and many applications.

In this work we have studied the electronic valence band structure of CuPc molecules and CuPc thin films. The CuPc molecule (Fig. 1) consists of the central Cu atom, which is surrounded by four pyrrole nitrogen atoms (N₁); four other nitrogen atoms (N₂) – bridging aza and 32 carbon atoms – the pyrrole (C₁) and the benzene (C₂, C₃ and C₄). The investigations were performed by using a combination of experimental and theoretical techniques, by means of near-edge x-ray absorption fine structure (NEXAFS), conventional and resonant photoemission spectroscopy (PES and ResPES), and by first principles calculations.

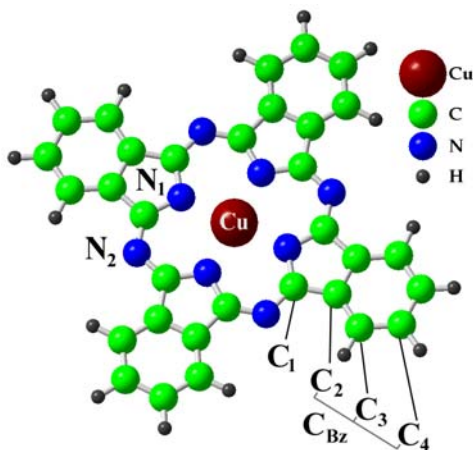


Figure 1. Schematic representation of the molecular structure of the CuPc molecule.

The UHV electron spectrometer on the Russian-German high energy resolution dipole beam line of the Berliner Speicherring für Synchrotronstrahlung (BESSY) was used for the deposition of the CuPc film on Au(001) substrate and the soft x-ray photoemission and absorption spectroscopy measurements. All other experimental details can be found elsewhere [4]. The theoretical investigation was done within the linear combination of atomic orbitals (LCAO) formalism based on density functional theory and was carried out with CRYSTAL package of GGA [5]. We used the Gaussian-type basis sets, namely 6-311+G** [6] for C, N and H atoms and TZVP [7] for Cu, and the hybrid B3LYP functional [8] for calculations.

Fig. 2 (a, upper panel) shows the experimental photoemission VB spectrum taken from a thin (70 Å) CuPc film together with the calculated spectra of CuPc molecules. In order to

align the spectra the first occupied peak was shifted to the binding energy position of the experimental peak arising from highest occupied molecular orbital. The Fig. 2 (a, lower panel) presents the DOS projected onto various atomic species. Each curve corresponds to a DOS summarized for both spin channels. The CuPc electronic structure is weakly modified by inter-molecular interaction in the solid state [9] and the measured spectra and the calculated ground-state molecular orbitals can be interrelated. Fig. 2 (b) shows the charge distribution (red) characteristic for the corresponding peaks of the valence band. In this way and taking into account the DOS projected onto various atomic species, we obtain a proper assignment of the different VB peaks.

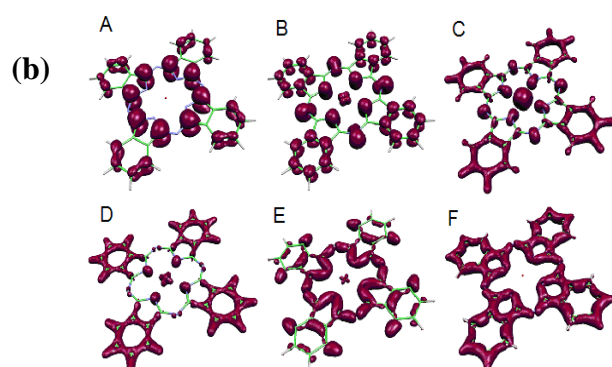
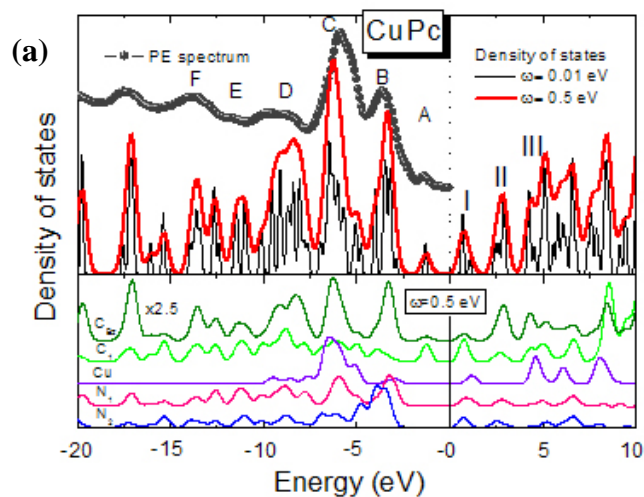


Figure 2 (a). Circles: PES of the VB of the CuPc film grown under UHV conditions on a clean (100) surface of a Au single crystal (normal emission, $h\nu = 110$ eV). 0 eV of the energy scale corresponds to the Fermi level. Thick/thin line: calculated DOS spectrum of isolated CuPc molecules, after application of a Gaussian function to each calculated state with a FWHM = 0.5/0.01 eV. Lower panel presents the DOS projected onto various atomic species. Note, the calculated DOS is the sum of the density of states for both spin-channels.

(b). CuPc molecules and calculated charge distribution contributing to corresponding peaks of the valence band (as labeled).

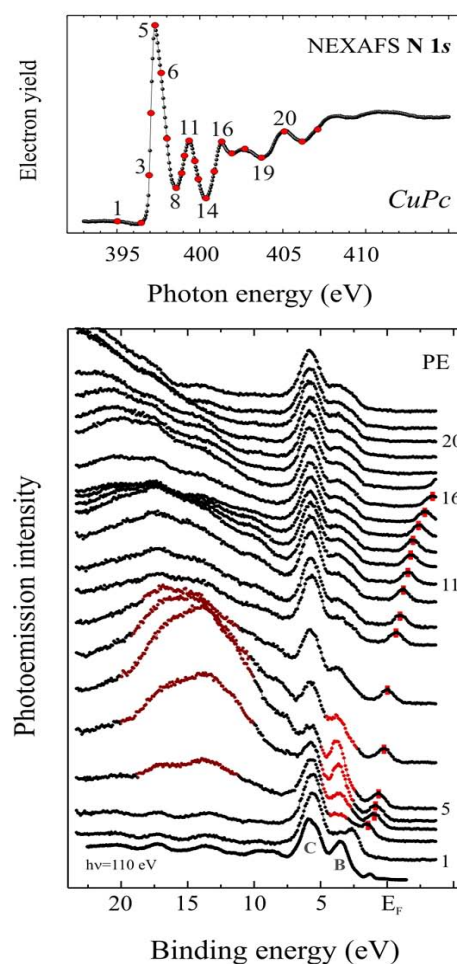


Figure 3. Spectra from a pristine CuPc film of 70 Å thickness, deposited on a Au(100) surface under UHV conditions.

Top panel: N 1s NEXAFS spectrum.

Bottom panel: valence band spectra, recorded at excitation photon energy around resonance ($N 1s \rightarrow \pi^*$). The bottom VB spectrum was recorded using $h\nu = 110$ eV.

For example, the HOMO (labeled with A) is mainly comprised of the spectral weight from the wave functions of carbon pyrrole C₁ atoms (see Fig. 1). Additional contributions to the HOMO stem from the benzene atoms C₃ and C₄. The analysis of molecular orbitals allows to separate peak B into three independent groups. The first two groups situated in the same energy range from -2.55 to -3.77 eV reflect contributions from hybrid Cu ($d_{x^2-y^2}$) and N₁ (p_x , p_y) orbitals as well as benzene and pyrrole π states. This is in contradiction with other theoretical results at LDA level [9, 10], where the Cu ($d_{x^2-y^2}$) state is the HOMO. We have reproduced these results by using the same local-density exchange-correlation functional.

Since it is known that LDA has deficiencies in the description of localized highly correlated electronic configurations, particularly for 3d transition metals, we conclude that the ordering of levels obtained with LDA is an artifact. The third group arises from σ - bonding orbitals between bridging aza N₂ and pyrrole C₁, with main contribution from the nitrogen atoms.

A deeper understanding of valence-band peaks was achieved utilizing resonant photoemission [11, 12]. Typical resonant photoemission spectra of CuPc thin films obtained by tuning the photon energy across the N 1s absorption edge are depicted in the bottom panels in Fig. 3. The VB spectra in Fig. 3 show resonant enhancement of the sharp VB spectral feature B (3.7 eV binding energy) as $h\nu$ is varied across the first N 1s - π^* excitation, which is marked by 5 in the N 1s NEXAFS spectrum (Fig. 3, top panel). According to our wave-function analysis the resonance is a result of a filling of N 1s core hole by the electron initially excited in the pyrrole π^* state. Simultaneously an intense hump appears at higher binding energies. This feature is assigned to spectator decay.

Regarding the HOMO peak, we cannot draw any conclusion, because the N 1s core-level emission excited by second order light overlaps the HOMO signal.

In conclusion, we have presented results of our studies of the occupied electronic states (valence band) of copper phthalocyanine by means of NEXAFS, photoemission, as well as resonant photoemission spectroscopy. The experimentally obtained valence-band features of CuPc are in very good agreement with *ab initio* density of states results, allowing the derivation of detailed site specific information.

Acknowledgements

This work was supported by the DFG under grant no. 436RUS17/52/06. Two of the authors (V.M.Z & V.Y.A) thank the RFBR (Grant N^o 05-02-17390).

References

- [1] R.H. Friend et al., Nature (London) **397** (1999) 121.
- [2] G. Horowitz, J. Mater. Research **19** (2004) 1946.
- [3] S.R. Forrest, Chem. Rev. **97** (1997) 1793, and references therein.
- [4] V.Yu. Aristov, O.V. Molodtsova, V.M. Zhilin, D.V. Vyalikh, M. Knupfer, Phys. Rev. B. **72** (2005) 165318.
- [5] V.R. Saunders et al., CRYSTAL2003 User's Manual, (University of Turin, Turin, 2003).
- [6] R. Krishnan et al., J. Chem. Phys. **72** (1980) 650.
- [7] A. Schaäfer, C. Huber and R. Ahlrichs, J. Chem. Phys. **100** (1994) 5829.
- [8] A.D. Becke, J. Chem. Phys. **98** (1993) 5648.
- [9] L. Lozzi, et al., J. Chem. Phys. **121** (2004) 1883.
- [10] M.-S. Liao, S. Scheinera, J. Chem. Phys. **114** (2001) 9780.
- [11] J. Kikuma, B.P. Tonner, J. Electron Spectrosc. Relat. Phenom. **82** (1996) 41.
- [12] S. Hüfner, Photoemission spectroscopy, Springer Verlag, (1995).

Static speckle experiments at the EDR beamline of BESSYII

Tushar Sant ^a, Tobias Panzner ^a, Gudrun Gleber ^a, Wolfram Leitenberger ^b
and Ullrich Pietsch ^a

^a Solid State Physics, University of Siegen, Germany

^b Institute of Physics, University of Potsdam, Germany

The third generation x-ray source BESSY II provides coherent x-ray radiation which can be used for static speckle analysis. Continuing our work on coherent x-ray scattering using white beam at EDR beamline [1-3] static speckle experiments were performed to verify the phase retrieval algorithm. Static speckle patterns from smooth and patterned semiconductor surfaces under grazing-angle incidence were measured over a wide energy range simultaneously. The inverse Fourier-transform of the speckle pattern can then be used to obtain the real height distribution of the surface.

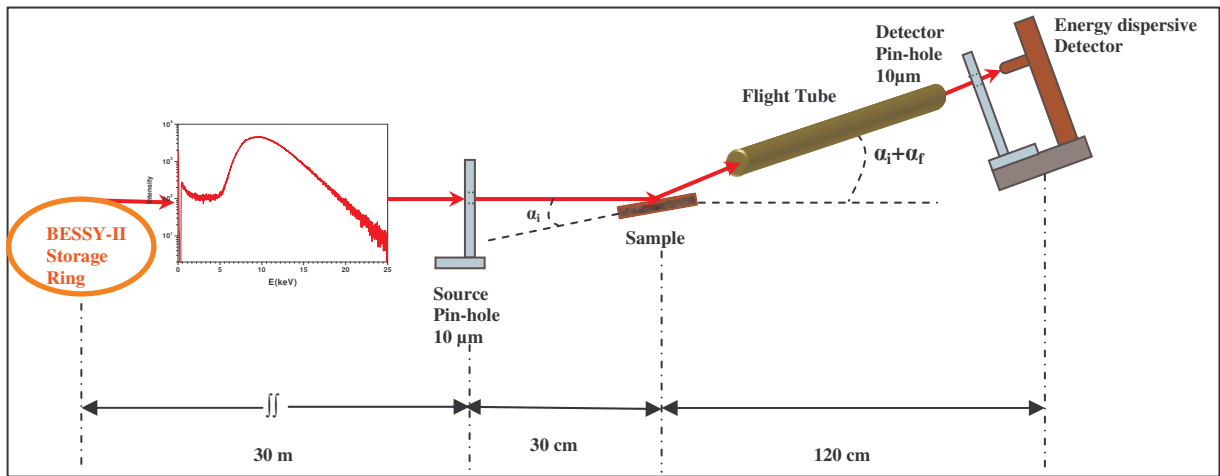


Fig. 1: Scheme of the different set ups for coherent experiments at the EDR-Beamline.

The static speckle pattern is influenced by the incident beam spectrum which already contains features of Fresnel diffraction of the initial pinhole. Therefore the approximation that the incident beam is a Gaussian is no longer justified. The measurement of illumination function was performed earlier [3, 4]. There is a good agreement between measured and calculated illumination function for diffraction at circular aperture. The amplitude and the phase of the incoming radiation calculated using Lommel formalism [5] are used to replace the Gaussian function for data analysis [6, 7] in future.

This formalism is tested for real surfaces. As test structure, we used a surface grating created by photolithography on GaAs. The grating lateral spacing is $D_0 = 500$ nm and the depth is 100 nm. The sample surface was inspected at a fixed incidence angle of $\alpha_i = 0.1$ degree. Reciprocal space maps were recorded by collecting the spectra while moving the detector at different z positions perpendicular to the incident beam. $z = 5$ mm corresponds to maximum exit angle $\alpha_f = 0.143$ degree. The inspected z -range corresponds to the maximum lateral momentum transfer of $q_{x,max} = \pm 3 \mu\text{m}^{-1}$. The peaks due to the grating are expected at positions $z \neq 0$ at $\Delta q_x = 2\pi/D$, where $D = D_0/\cos\omega$ is the projection of D_0 to the incident beam direction obtained by rotation of the grating vector by an azimuth angle ω . Fig.2 shows the reciprocal space map of the sample recorded under coherent illumination condition using a incident pinhole with diameter $\delta = 10 \mu\text{m}$ and a detector pinhole of same diameter. The map exhibits a series of line parallel q_z . Due to the small incident angle used (the critical q_{zc} of

total external reflection is $q_{zc} = 0.046 \text{ \AA}^{-1}$) the 1st order grating peaks (see vertical dotted lines) at $\Delta q_x = 0.17 \mu\text{m}^{-1}$ are hardly visible. The bent red and green lines mark the gallium and arsenic K-absorption lines (Ga, As) and their respective pile-ups (Ga*, As*). Nevertheless, the other lines appear more or less equidistant in q_x direction. Their separation changes when

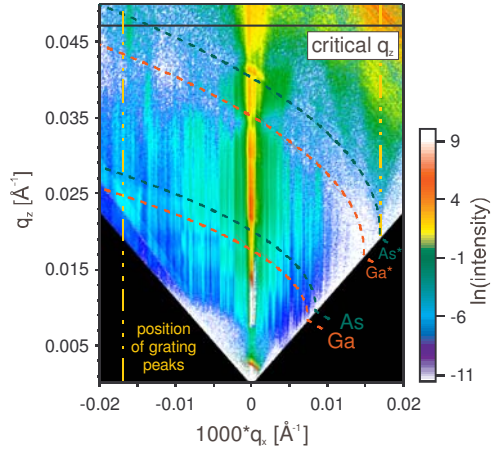


Fig. 2: Coherent reflectivity map of a GaAs-surface grating

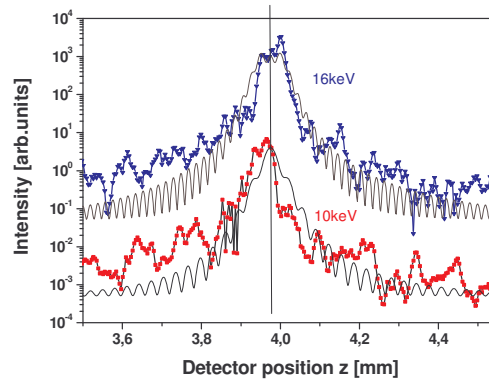


Fig. 3: Line scans for 10keV and 16keV extracted from (E,z) map and simulated Fresnel intensities

another pinhole diameter (not shown here) is used. Fig. 3 shows line scans for 10 keV (red) and 16 keV (blue) extracted from the measured (E,z) map, i.e. before re-calculation into the reciprocal space. The line scans exhibit a series of pronounced peaks decreasing in distance for increasing energy proportional to $(E\delta)^{-1}$. Therefore these peaks are mainly due to diffraction from the incident pinhole. However, not all peaks appear equidistant. Several of them are merging together caused by the speckle like scattering from the sample surface. The black lines in fig. 3 show the Fresnel function for a pinhole diameter of 10 μm . Only a few peaks of simulation match the experiment. Nevertheless, several of measured peaks display the same peak width as the Fresnel function changing as function of energy. All deviations from pure Fresnel behaviour may identify speckle from the sample.

In order to de-convolute the height- height fluctuation from the speckle pattern one has to consider the correct illumination function. Unfortunately the inversion procedure published recently [7] has less chance of success considering the correct illumination function instead of a Gaussian as input. . Therefore we try to determine the height-height fluctuation of the sample by direct simulation of the complex scattering amplitude $A(q_x)$

$$A(q_x) \cdot e^{i\alpha(q_x)} = \frac{1}{2\pi} \int_{-\infty}^{\infty} B(r, \phi) \cdot e^{iq_z h(x)} \cdot e^{-iq_x x} dx$$

for a set of q_z -values assuming a model surface where individual grating ridges are fluctuating in height.

References:

- [1] T.Panzner, W. Leitenberger, J. Grenzer, Y. Bodenthin, Th. Geue and U. Pietsch, H. Möhwald, BESSY Annual Report (2002) 345.
- [2] T. Panzner, W. Leitenberger, J. Grenzer, , K. Morawetz, U. Pietsch, H. Möhwald , BESSY Annual Report (2003) 319.
- [3] T. Panzner, G. Gleber, U.Pietsch, BESSY Annual Report (2005) 325.
- [4] T. Panzner, G. Gleber, T. Sant, W.Leitenberger, U. Pietsch, Thin Solid Films in press.
- [5] K.D. Mielenz, J. Res. Natl. Inst. Stand. Technol. 103, (1998) 497.
- [6] I. A. Vartanyants, J. A. Pitney, J. L. Libbert, I. K. Robinson, Phys.Rev. B55, 19,(1997) 13193.
- [7] U. Pietsch, T. Panzner, W. Leitenberger, I. A. Vartanyants, Physica B357 (2005) 45.

Time and energy resolved coherent X-ray reflectivity measurements

G. Gleber¹, T. Panzner¹, T. Sant¹, W. Leitenberger², A. Pucher², U. Pietsch¹

¹Institute of Physics, University of Siegen, D-57068 Siegen, Germany

²Institute of Physics, University of Potsdam, D-14469 Potsdam, Germany

The third generation X-ray source BESSY II (Berlin, Germany) provides coherent radiation which can be used for statistic and dynamic speckle analysis.

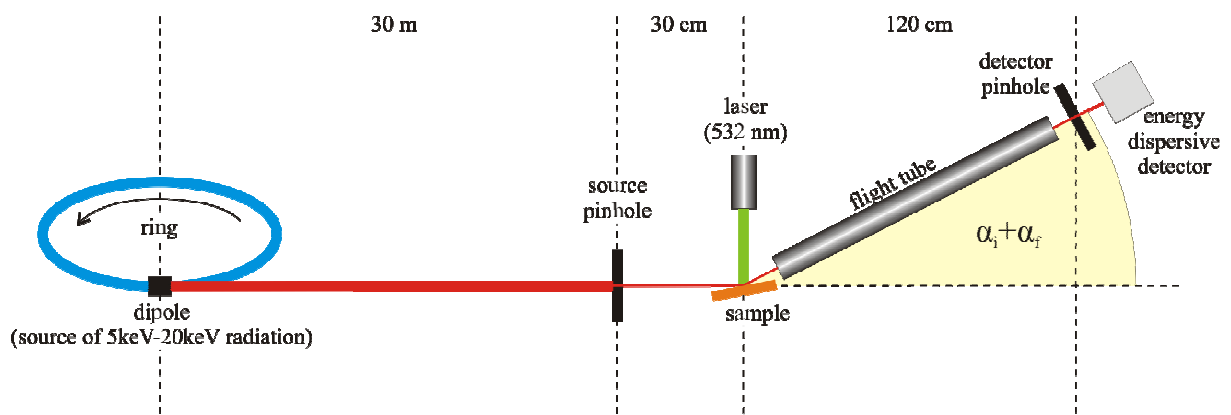


Figure 1: The experimental setup at the EDR beam line at the BESSY II in Berlin, Germany

Preventing thermal effects at the experimental setup like expansion of the sample table and other movements we choose a light sensitive polymer [1] as sample. To induce a slow surface changing process this polymer is illuminated by a laser. A slow process is needed because the time resolution is restricted by the used detector to 2.7 seconds (1 second is minimum of detector illumination time and 1.7 seconds for the read-out of the spectra to the computer). The time resolved energy spectra are measured at an off-specular position in a coherent reflectivity set up (shown in Figure 1). These spectra gives access to the observation of dynamic speckle movement (important technique for the investigation of time depending sample surface processes). The result of one of these measurements is shown in Figure 2. One

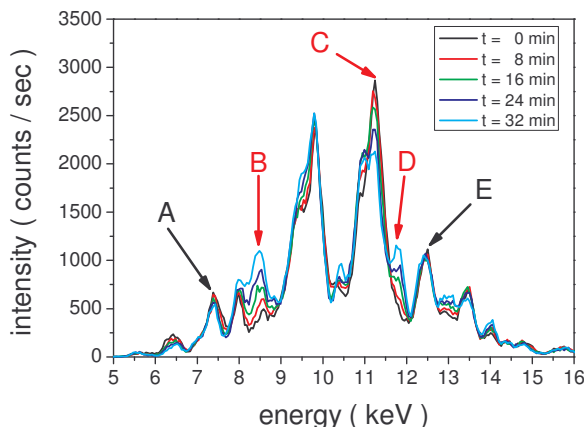


Figure 2: Time resolved energy spectra taken from a coherent reflectivity experiment. The intensities for some energies are changing (label B to C) there others stays constant (label A and E). This can be interpreted as dynamic speckle behaviour for the positions B, C and D.

can clearly identify different time behaviours for different energies. The constant peaks (labelled A and E) are purely caused by the Fresnel rings of the illumination function. The changing peaks (B to C) are caused by the illumination function as well but additionally convoluted with time depending speckles. This can be interpreted as a real dynamic process in the polymer induced by the illumination with laser light and therefore as a dynamic speckle observation in energy dispersive set up mode. The calculated autocorrelation function like map, which is shown in Figure 3, shows cosine-like oscillation only for some energies. It seems that there is also a different behaviour for the surface itself (below the critical energy) and the sub surface regions (above the critical energy). Due to these promising results the work in this direction of coherent experiments with a white X-ray beam will be continued in future.

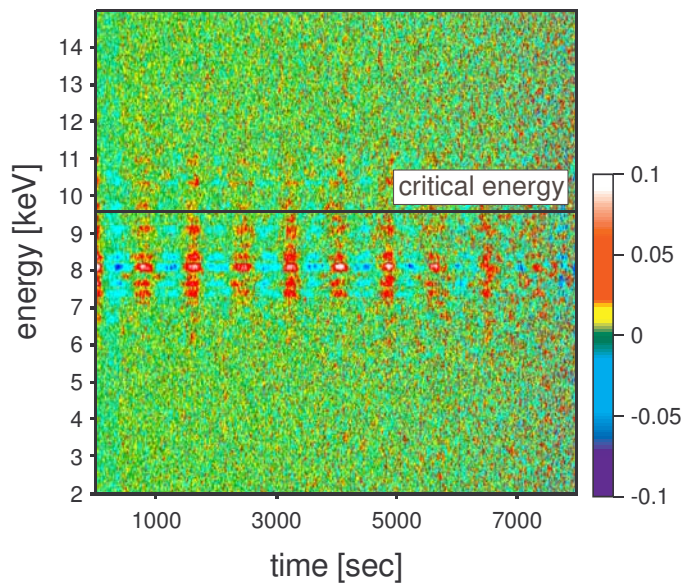


Fig. 3: Autocorrelation-like map for the whole data set from the time resolved coherent experiment. One can clearly see the oscillations in the range from 7 keV to 9.5 keV. The time behaviour above the critical energy seems to differ from the one below.

- [1] O. Henneberg, L.F. Chi, Th. Geue, M. Saphiannikova, U. Pietsch, P. Rochon, & A. Natansohn, A., Appl. Phys. Lett. 79 (15) 2357-59 (2001)

Temperature dependent molecular orientation of zinc phthalocyanine on polycrystalline gold

H. Peisert¹, I. Biswas¹, A. Haug¹, M. Knupfer², D. Batchelor,³ T. Chassé¹

¹University of Tübingen, IPTC, Auf der Morgenstelle 8, 72076 Tübingen, Germany

²Leibniz Institute for Solid State Research Dresden, P.O. Box 270116, D-01171 Dresden

³Universität Würzburg, Am Hubland, D-97074 Würzburg, Germany

It is well known, that the ordering and orientation of organic molecules is crucial for charge transport properties and thus for essential for the efficiency of devices based on these materials. Different mechanisms for the charge transport are debated, depending on the system under consideration. The localization energy based on electron-phonon coupling decreases significantly at low temperature, as a consequence different transport channels are possible: a band-like transport in organic materials e.g. is favoured at low temperatures [1]. The increase of electron-phonon coupling at higher temperatures may furthermore cause a reduction of width of electronic bands, which was shown experimentally for pentacene [2]. In this report we study whether these phenomena are accompanied by changes of the intermolecular interaction and thus the orientation of the molecules. We compare the orientation of zinc phthalocyanine (ZnPc) molecules on polycrystalline gold using polarization dependent X-ray absorption spectroscopy. The measurements were performed at the UE 52-PGM beamline. The energy resolution was set to 80 meV at a photon energy of 400 eV. The absorption was monitored indirectly by measuring the partial electron yield using a channeltron with an applied bias voltage of 360 V (N 1s edge). The raw data are corrected by the energy dependent photon flux and by an additional linear background due to energy dependent cross sections for the absorption. The spectra were normalized to have the same absorption edge step height well above the threshold.

In Fig. 1 we compare N1s excitation spectra for ZnPc evaporated on Au foil as a function of polarization of the synchrotron radiation. For flat sp^2 -hybridised carbon systems, such as phthalocyanines, a maximum intensity for dipolar transitions into groups of individual π^* states is observed if the electric field vector E is perpendicular oriented with respect to molecular plane. In our experiment, the direction of E of the incoming light was changed at grazing beam incidence, see insets of Fig. 1c. For standing molecules, as observed recently for CuPc on gold foil [3], we expect the most intense π^* resonances ($E < 402$ eV) for s-polarized light (i.e. the electric field vector is parallel to the beam – sample surface plane) and the opposite behavior is expected for the $1s \rightarrow \sigma^*$ resonances.

The spectra for a ZnPc evaporated on gold at room temperature show only a weak variation of the N1s- π^* intensity for p- and s-polarized light (Fig. 1a), indicating a relatively ill defined orientation. The preferred orientation of the ZnPc molecules is perpendicular with respect to the sample surface (standing molecules). In contrast, after cooling to about 20 K a clear dependence of the π^* resonance intensity on the polarization of the incoming light can be recognized, the degree of ordering is obviously increased. And finally, after reheating to room temperature differences between spectra for p- and s-polarization are reduced. The corresponding π^* resonance intensity ratios (p/s-polarized light) are 1/1.4 at room temperature

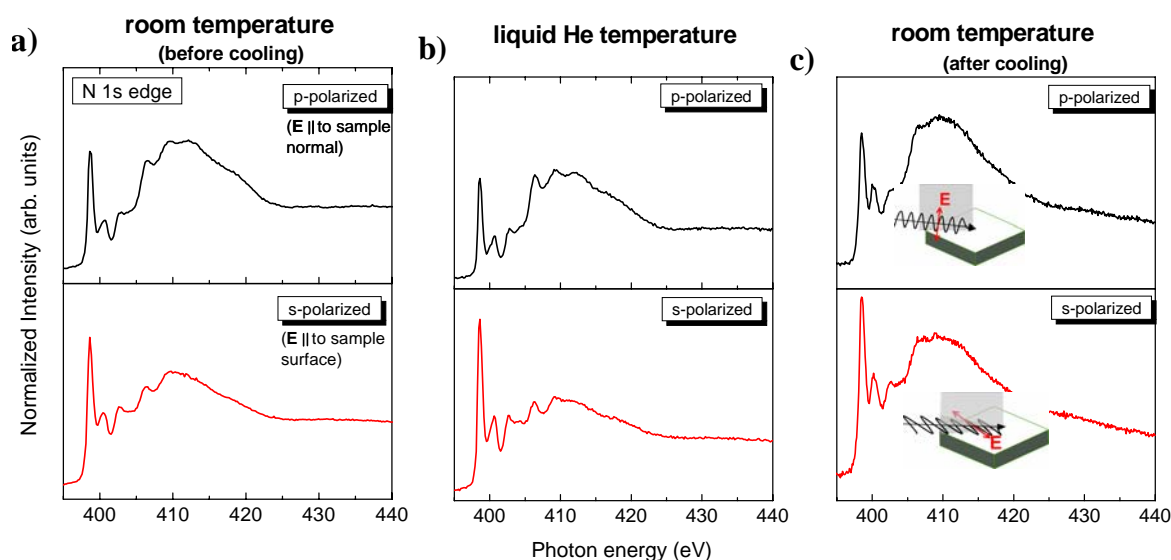


Fig. 1 N1s excitation spectra for 8 nm ZnPc on polycrystalline gold a) at room temperature, b) at liquid He temperature (~ 20 K), and c) at room temperature after cooling. The comparison of the N1s- π^* intensity ratios for s- and p-polarized light reveal that the degree of orientation is significantly higher during cooling.

(before and after cooling) and 1/1.8 at liquid helium temperature. A similar behavior was observed for preferred lying ZnPc molecules on Au (the orientation of the molecules depends on the substrate preparation conditions): the degree of ordering increases at lower temperature.

The increase of molecular ordering at low temperatures can be understood by an increase of the intermolecular interaction and by a decrease of the electron-phonon coupling. The changes of the orientation may therefore contribute to experimentally observed variations in the electronic band widths as a function of the temperature.

For valuable discussions and technical assistance we thank Ch. Jung, S. Pohl, W. Neu and R. Hübel. Financial support by BESSY is gratefully acknowledged.

References:

- [1] N. Karl, *Synthetic Metals* **133–134** (2003) 649.
- [2] N. Koch, A. Vollmer, I. Salzmann, B. Nickel, H. Weiss, J. P. Rabe, *Phys. Rev. Lett.* **96** (2006) 156803.
- [3] H. Peisert, T. Schwieger, J. M. Auerhammer, M. Knupfer, M. S. Golden, J. Fink, P. R. Bressler, and M. Mast, *J. Appl. Phys.* **90** (2001) 466.

In-situ study of microstructure changes at room temperature and elevated temperatures in nanocrystalline electrodeposits

Karen Pantleon, Karsten Hansen

Technical University of Denmark, Department of Manufacturing Engineering and Management IPL Building 204, DK – 2800 Kgs. Lyngby, Denmark

Electrochemical deposition has become the method of choice for manufacturing functional thin copper films, because it provides excellent filling behavior for small vias and trenches as required for the ongoing miniaturization of advanced microelectronic devices. The functionality and reliability of electrochemically deposited thin films depend on their microstructure – however, the thermodynamically non-equilibrium state of as-deposited films causes substantial changes of the microstructure and related properties with time already at room temperature and/or at elevated (operating) temperatures.

Copper, which has become the dominant material for interconnects in integrated circuits in microelectronics, is unstable even at room temperature; this phenomenon is called self-annealing. Recently, in-situ studies applying conventional X-ray diffraction with simultaneous measurements of the electrical resistivity have been carried out to investigate the evolution of the microstructure in electrodeposited copper layers [1]. It has been reported [1] that considerable growth of the as-deposited nanocrystalline grains and a drastic weakening of the crystallographic texture occur as function of time at room temperature and multiple twinning was suggested as the mechanism for self-annealing in copper electrodeposits [1,2].

In contrast, electrodeposited nickel, a promising material to realize movable structures for micro-electro-mechanical applications, is relatively stable at room temperature, but well-known for changes of the internal structure at elevated temperatures resulting in a dramatic deterioration of mechanical properties. Annealing the nickel layers in a conventional furnace or oil bath with subsequent microstructure characterization (ex-situ), as usually applied, allows just a comparison between as-deposited and annealed microstructures, but does not yield information on its time dependent evolution, which, however, is essential for understanding the mechanisms of (self-)annealing.

The factors controlling these processes in the nanocrystalline thin films and limiting their long-term applicability are at present largely unknown. In-situ experiments applying synchrotron diffraction were carried out in order to supplement current research work on electrochemically deposited copper, silver and nickel layers.

At BESSY at the beamline EDDI (part of ID 7T-MPW), the room temperature evolution of the microstructure was investigated for copper and silver layers. Great importance was attached to start the experiments before the onset of self-annealing; for this purpose, the as-deposited layers were frozen down to -20°C and first subjected to room temperature when the experiments were ready to start. For investigations of the self-annealing kinetics room temperature atmosphere was essential, i.e. radiation induced heat input into the

sample had to be avoided. By inserting appropriate absorbers in the primary beam path, the temperature could be reduced down to about 25°C, whereas without absorbers the sample would have been subjected to a temperature of 85°C, which would have triggered self-annealing considerably. The kinetics of self-annealing was studied with energydispersive diffraction by repeating measurements of the complete energy spectra both for copper and for silver layers with various thicknesses in the range of a few micrometers. Energydispersive diffraction spectra were collected at a fixed diffraction angle of $2\Theta = 15^\circ$, for which a multitude of reflections was expected in a wide energy range. As an example, Fig. 1 shows a part of an energy dispersive diffraction spectrum recorded within only 30s (i.e. information can be obtained extremely fast) for a 2.6 μm thick copper layer deposited onto a Si-wafer with a Au-film on top.

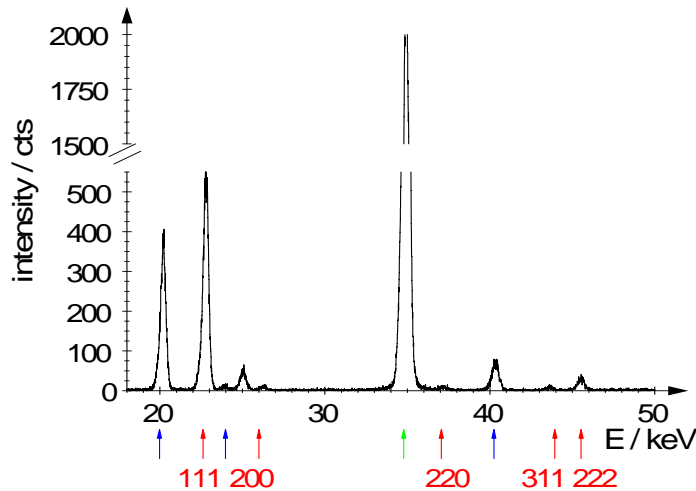


Fig. 1: Energy dispersive diffraction spectrum measured for a copper layer with 2.6 μm thickness electrochemically deposited onto a Au covered Si-wafer. Various diffraction lines are marked: Cu (red), Au (blue), Si (green). Only part of the spectrum is shown, although lines can be identified up to about 100 keV.

For the analysis of lattice strain (stress) the samples were tilted applying azimuth angles $0 \leq \psi \leq 89^\circ$ with a step size of $\Delta\psi = 5^\circ$, which allows to determine residual stresses according to the $\sin^2\psi$ -method. The variety of information contained in the energy spectra (a multitude of reflections corresponding to different lattice planes is recorded simultaneously and each reflection originates from a specific penetration depth) allows the determination of stress gradients perpendicular to the surface [3] and additionally, due to repeated measurements over the period of about one week, the evolution of stresses can be followed with time. Furthermore, the room temperature evolution of the microstructure can be followed with time by line profile analysis, i.e. separating the effects of grain size (size of coherently diffracting domains) and microstrain on the broadening of the measured diffraction lines. Evaluation of the diffraction spectra measured for the electrodeposits, however, indicated that diffraction line profile analysis for the interesting copper phase is not straightforward because of partly overlapping lines and weak intensities due to the very low layer thicknesses. Furthermore, line profile analysis for energydispersive diffraction is not a standard technique yet and the relatively broad instrumental profile as measured on a standard Si-powder (NIST 640c) as well as the even broader lines of the samples requires careful profile fitting, which is still the subject of current work.

For nickel electrodeposits preliminary diffraction studies with conventional X-rays revealed that the microstructure of nickel layers is stable at room temperature, in contrast to the behavior of copper and silver layers. At BESSY, the behavior of nickel at elevated temperatures was investigated in-situ at the beamline MagS (part of ID 7T-MPW) applying a heating facility for temperatures up to 800 K. Measurements were carried out applying a monochromated beam with photon energies of 12.4 eV (wavelength $\lambda = 0.1$ nm). Different temperature regimes were applied: i) isothermal annealing at different times (3h...8h) at various temperatures (400K...600K) and ii) isochronal annealing between 300K and 750K with temperature intervals of 50K. During the isothermal experiments, line profiles were successively measured for the 111, 222, 200, 400 and 311 reflections of nickel and measurements were repeated until no further changes of the line profiles could be detected. For the isochronal experiments, one series of the various nickel reflections was measured at each temperature, i.e. the holding time at the individual temperatures amounted to a few minutes only. Line profile analysis was applied to separate the various contributions to line broadening: the size of coherently diffracting domains, which is interpreted as the grain size, and microstrains were determined as a function of time and/or temperature. Furthermore, the evolution of preferred grain orientations was evaluated based on the integrated intensities of the various reflections. Fig.2 shows some examples of observed changes of the measured diffraction lines.

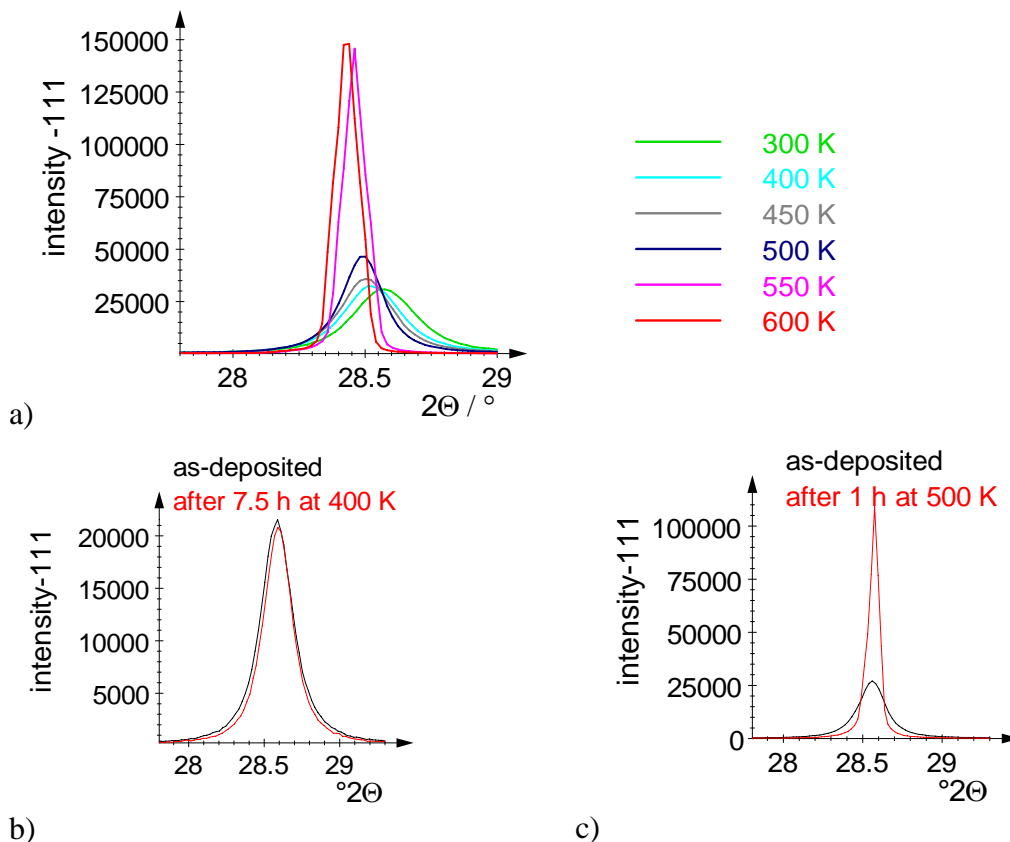


Fig.2: Examples of diffraction lines measured for electrochemically deposited nickel layers as function of time and/or temperature: stepwise increase of the temperature from 300 K to 600 K (a) and isothermal annealing at 400 K (b) or 500 K (c).

Fig.2a indicates that only temperatures above 400K yield considerable changes of the line profiles (similarly as shown here for the 111 diffraction line, it also was observed for the 222, 200, 400 and 311 lines), i.e. grain growth and crystallographic texture changes occurred more pronounced for higher temperatures. Figs.2b and c also emphasize the effect of the temperature: while during isothermal annealing at 400K no changes of the line profiles were observed even after several hours indicating a stable microstructure at that temperature, at 500K grain growth occurred immediately (actually, it started already during the heating phase) and was completed after isothermal holding of less than one hour. The as-deposited nanocrystalline grains with grain sizes of about 20 nm increased by grain growth during annealing to grain sizes of up to 180nm as obtained for the annealed microstructure. The kinetics of grain growth was found to be strongly affected by the applied temperature regime, while it was less dependent on both the electrochemical deposition parameters of the nickel layers and the applied substrate. From the observed annealing behavior of the nickel layers during isothermal and isochronal annealing the activation energy of grain growth was calculated based on the kinetics and the temperature dependence of the evolution of the line profiles, respectively. The obtained results will essentially contribute to a model description of (self-) annealing in electrochemically deposited films taking into account the effect of surface, interface and grain boundary energies on the driving force.

- [1] K. Pantleon, M.A.J. Somers, *J. Appl. Phys.* 100 (2006) 114319-1-7.
- [2] K. Pantleon, A. Gholinia, *Proc. of the EBSD Users meeting 2006*, Oxford Instruments HKL Technology, 47-49.
- [3] Ch. Genzel, I.A. Denks, M. Klaus, *Mat. Sci. For.* 524-525 (2006) 193-198.

We are grateful to Esther Dudzik and Ralf Feyerherm (HMI, Berlin) for experimental support at the beamline MagS and acknowledge Manuela Klaus and Ingwer Denks (HMI, Berlin) for experimental assistance at the beamline EDDI. The organisation of Danish users of hard X-ray synchrotron facilities (DANSYNC) is gratefully acknowledged for financial support.

Measurements of residual stresses in plasma-sprayed nano-hydroxyapatite coatings on titanium alloy

Renghini Chiara¹, Manescu Adrian¹ and Calbucci Vittorio¹

¹ *Dipartimento di Scienze Applicate ai Sistemi Complessi, Universita' Politecnica delle Marche and CNISM, Via Brecce Bianche, 60131 Ancona, Italy.*

Key words: Residual stress; Plasma spray; Hydroxyapatite; Coating

1. Introduction

Clinical application of hydroxyapatite (HA)-coated Ti-6Al-4V implants has attracted considerable attention because such implants can promote good bonding with natural bone owing to the bioactive hydroxyapatite coatings (HACs) [1,2].

Many deposition methods have been proposed to coat HA on Ti-alloy substrate including thermal spraying, hydrotherm and electrodeposition, etc. [3–6]. Among these methods, HACs processed by electrodeposition can achieve high crystallinity, few impurity phases and aqueous immersion stability [6], as compared with plasma-sprayed coatings [7,8]. Plasma spraying is a widely adopted process mainly due to its high deposition rate and the good bonding strength of the coatings [9–11].

It is well known that in this kind of process the final mechanical performances are determined by microstructural features such as porosity and residual stresses [12] of the deposited powder. The HA/substrate interface or HA itself can be fractured even under a relatively low stress because of the low adhesion strength and brittleness of the sprayed layer itself. Therefore, the use of nano-particulate materials has been proposed to solve this problem. In fact, it is known that, compared with conventionally crystallized HA, nano-crystallized HA can promote osteoblast adhesion and proliferation, osseointegration, and the deposition of calcium-containing minerals on its surface [13]. It is also believed that nano-structured HA can improve sintering kinetics because of higher surface area and subsequently improve mechanical properties.

In this study we investigated the structural characteristics of the nano-hydroxyapatite coating, including the surface morphology, phase, crystallinity and porosity. To evaluate the mechanical state of the coatings, the residual stress was measured. Because residual stress measurements by conventional X-ray techniques are limited to just surface states, the analysis of the residual stresses both in the coatings and in the substrate was done by performing an energy dispersive diffraction experiment, which allows the determination of stress gradients in a non-destructive way.

2. Materials and methods

2.1 Samples preparation

Nanosized HA powders used are composed by nanocrystalline agglomerates (50–100 nm) particles [14]. These powders were added to aqueous solution of 10% gelatin content that was prepared by dissolution of 10 g in 100 ml distilled water at 39 °C. The slurry prepared from this powder mixture was dispersed in oil in a flask by stirring with a glass paddle stirrer at 1000 rpm at oil temperature of 25 °C to form micrometer-sized granules (50–200 µm). The granules so obtained were subsequently sprayed on to commercial Ti6Al4V substrate. Coatings of thickness in the range 50–100 µm were obtained.

2.2 X-ray diffraction \sin^2 method

The residual stresses formed in the nano-HAC coatings were analyzed by energy dispersive X-ray diffraction. The measurements have been performed at the beamline EDDY of the BESSY Synchrotron (Berlin, Germany).

Diffraction measurements were taken at a fixed 2θ angle of 5° and at sixteen ψ values (ψ is the angle of tilt for the specimen, $\psi = 0, 5, 10, 15, 20, 25, 30, 35, 40, 45, 50, 55, 60, 65, 70, 75^\circ$).

The analysis was done for the different samples described in Table 1.

Table 1
Characteristics of the plasma-sprayed HACs

Sample	Powder	Thickness coating (μm)
HA275_S1	Nano-HA	100
HA296_S1	Nano-HA	80
HA311_S1	Nano-HA	50
HA309_S1	Commercial HA	50

3. Results and discussion

The residual stress data measured from the $\sin^2\psi$ method are shown in Fig.1 and in Fig.2.

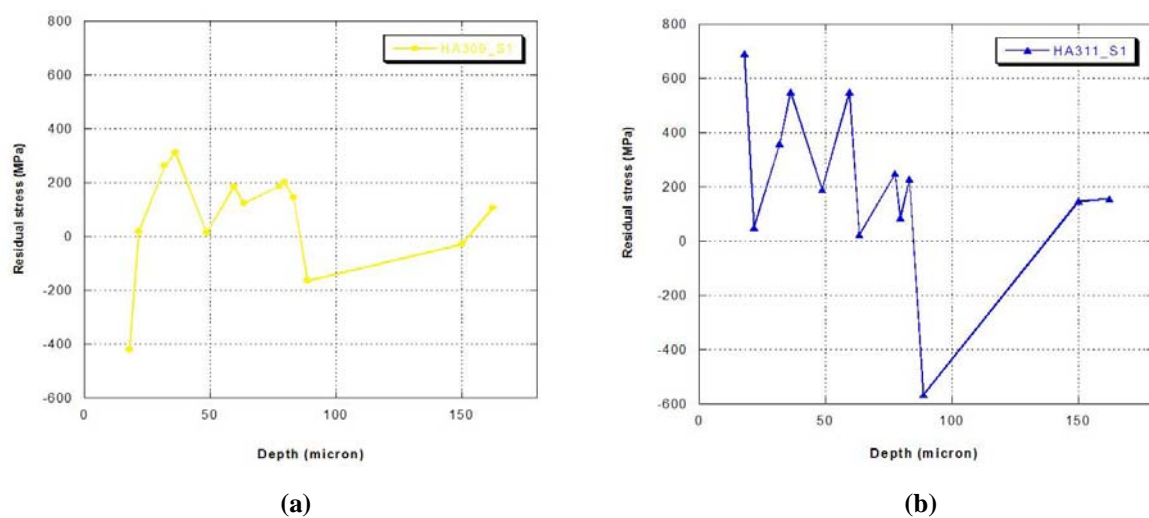


Fig.1: Residual stress distribution in the commercial HA coating (a) and in the nano-HA coating (b).

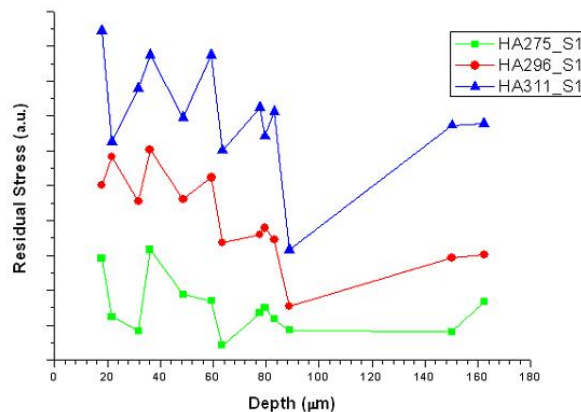


Fig.2: Residual stress distribution in the nano-HA coatings with different thickness

The result are concluded as below:

- Consistently tensile stress states were obtained in the all samples;
- The tensile residual stresses obtained for thinner coatings have higher values than those in the thicker coatings;

- For the all HACs, the residual stresses close to the top surface are higher than those closer to the interface between the HAC and Ti substrate.

4. Conclusion

There were several studies undertaken to determine residual stresses of plasma-sprayed HA coatings. From the past literature, different results were obtained. In this study, consistently tensile stress states were obtained in the HACs. The present results are supported by Tsui et al. [16], Tadano et al. [17] and Han et al. [19], but were opposed by Millet et al. [15], Heimann et al. [18] and partly by Sergio et al. [9], who calculated compressive residual stresses in the HACs. These contradictory results are in dispute still.

Acknowledgements

This experiment was supported by funds from the FP6 R II 3 CT-2004-506008 BESSY IA-SFS Acces Programme.

The authors wish to acknowledge the ICE project (Sviluppo di una nuova classe di rivestimenti bioceramici nanostrutturati per applicazioni biomediche), the INTAS Project (Innovative bioceramics systems for application in surgery and drug delivery: further development, production and utilisation) and the EU KMM-NOE Project (NOE 502243-2) for financial support.

References

1. J.A. Jansen, J.P.C.M. van de Waerden, J.G.C. Wolke, K. de Groot, J. Biomed.Mater.Res.25 (1991) 973.
2. B.W. Schreurs, R. Huiskes, P. Buma, T.J.H. Slooff, Biomaterials 17 (1996) 1176.
3. S.J. Ding, C.P. Ju, J.H. Chin Lin, J. Biomed. Mater. Res. 47 (1999) 551.
4. L.Cleries, J.M.Fernandez Pradas, J.L. Morenza, Biomaterials 21 (2000) 1861.
5. H. Ishizawa, M.Ogino, J.Mater . Sci. 34 (1999) 5893.
6. Y.Han, T. Fu, J.Lu, K.Xu, J.Biomed.Mater . Res. 54 (2001) 96.
7. B.C. Wang, E. Chang, T.M. Lee, C.Y. Yang, J. Biomed. Mater. Res.29 (1995) 1483.
8. J.E.Dalton, S.D. Cook, J.Biomed. Mater.Res. 29 (1995) 239.
- 9 V. Sergio, O.Sbaizer o, R.David, Biomaterials 18 (1997) 474.
10. C. Knabe, F.Klar , R.Fitzner , R.J. Radlanski, U. Gross, Biomaterials 23 (2002) 3235.
11. A.E. Porter, L.W. Hobbs, V. Benezra Rosen, M. Spector, Biomaterials 23 (2002) 725.
12. Y.C.Yang, E.Chang. Thin Solid Films 444 (2003) 260–275.
13. M.Thorwarth, S.Schultze-Mosgau, P.Kessler, J.Wiltfang and K.A.Schlegel. J. Oral and Maxillofacial Surgery, Vol.63, n.11 (2005) 1626-1633.
14. Fomin A.S., Komlev V.S., Barinov S.M., Fadeeva I.V., Renghini C. Advanced Materials. 2006. (in press).
15. P. Millet, E. Girardin, C. Braham, A. Lodini.J. Biomed. Mater. Res. 60 (2002) 679.
16. Y.C. Tsui, C. Doyle, T.W. Clyne. Biomaterials 19 (1998) 2015.
17. S. Tadano, M. Todoh, J. Shibano, T. Ukai, JSME Int. J. Ser. A Mech. Mater. Eng. 40 (1997) 328.
18. R.B. Heimann, O. Grassmann, M. Hempd, R. Bucher, M. Harting. Appl. Mineralogy, vol. 1, Balkema, Rotlcrdam, Brookfield, 2000, p. 155.
19. Y. Han, K. Xu, J. Lu. J. Biomed. Mater. Res. 26 (2001) 596.

Energy dispersive x-ray diffraction for the *in situ* investigation on the rapid thermal processing of CuInS₂ for thin film solar cell fabrication

I.M. Kötschau, H. Rodriguez Alvarez, C. Streeck, A. Weber, M. Klaus, I.A. Denks, J. Gibmeier, Ch. Genzel, H.W. Schock

Hahn-Meitner-Institut Berlin GmbH, Glienicker Straße 100, D-14109 Berlin

Highly efficient thin film solar cells based on chalcopyrite materials such as Cu(In,Ga)Se₂ show record efficiencies of up to 19.5% on the laboratory scale [1]. Solar cells made of plain CuInS₂ have not reached these record efficiencies yet but are also of significant interest due to a number of advantages in comparison with the more widely investigated selenium containing chalcopyrites. The main advantage lies in the much faster deposition process. CuInS₂ thin films are deposited by a rapid thermal process, whereby sputtered Cu/In precursors are completely sulphurized within a few minutes. Both, solar cells made of Cu(In,Ga)Se₂ as well as CuInS₂, are on the verge to large scale industrial production. A detailed understanding of the deposition process is indispensable.

The high flux available at the recently commissioned EDDI beam line facilitates energy dispersive X-ray diffraction (EDXRD) experiments at fixed geometry with a rather short acquisition time of typical 10sec per spectrum. Thereby the *in situ* monitoring of the solid state reactions during the rapid thermal process (RTP) of metallic precursors (i.e.: Cu and In) with elemental sulphur or selenium is possible. The analysis of a whole series of EDXRD

spectra gives valuable information on the reaction pathway leading from the metallic precursors to the chalcopyrite thin films. The aim of the experiment is to investigate RTP type processes for the synthesis of chalcopyrite and chalcopyrite related thin films. Of particular interest is the influence of the maximum pressure of the chalcogen during the reaction.

A special reaction chamber was constructed, suitable for *in situ* EDXRD experiments at the EDDI beam line. Glass substrates with metallic precursors are placed in an evacuated graphite reactor which is enclosed itself in a vacuum chamber equipped with two banks of high performance quartz lamp heaters (Fig. 1). The graphite reactor has a quartz glass window at top and on the bottom and can be sealed with graphite valve. Maximum heating rates are up to 250K/min. The temperature is monitored by two thermocouples placed close to the quartz lamp heaters and directly at the graphite reactor. Depending on the amount of elemental sulphur the maxi -

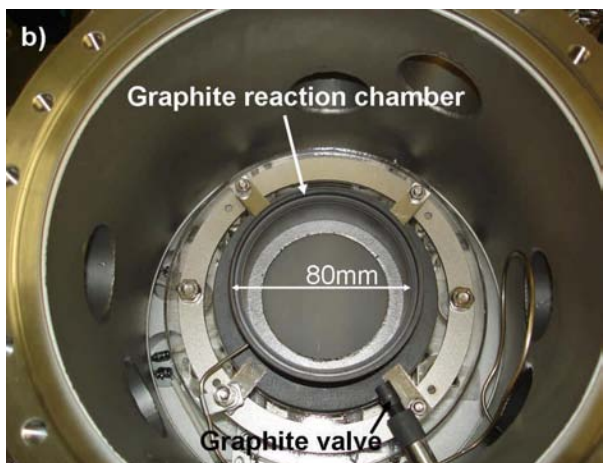
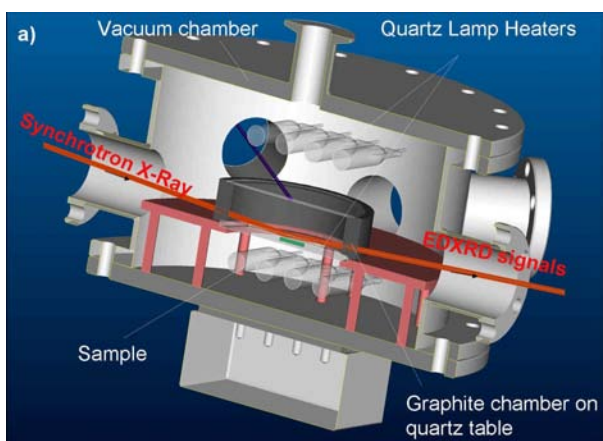


Figure 1: a) Schematic drawing of the *in-situ* EDXRD rapid thermal processing reaction chamber. b) View inside the vacuum chamber with the inner graphite reaction chamber.

imum pressure during the reaction can be adjusted. Metallic precursors were deposited by sequential sputtering of the elements on molybdenum coated soda lime glass according to the HMI baseline process for CuInS_2 solar cells [2]. Copper is supplied in excess ($\text{Cu/In}=1.6$) and segregates during the sulphurization as binary Cu-S phase on top of the CuInS_2 thin film. It can be removed after the process by etching in a suitable KCN solution. A well defined amount of elemental sulphur (40% excess) is placed on the bottom of the graphite reaction chamber next to the precursor substrate. The graphite reaction chamber is closed with a quartz glass window and the vacuum chamber is closed and evacuated to a pressure below 1×10^{-4} mbar. Subsequently the graphite valve is closed and the computer controlled RTP-process is started while simultaneously acquiring EDXRD spectra. The maximum pressure in the reaction chamber of about 1.5 mbar and corresponds to the state when all sulphur is completely evaporated but not consumed by the solid state reaction. The angle of the incident and emerging x-ray beam with the sample surface is the same (3.7°) and is kept fixed during the whole experiment (see Fig. 1a). The diffractometer setup at the EDDI beamline allows the arrangement of a nearly perfect parallel beam geometry. Thus, the sample position can be optimized easily for high count rates of the thin film and low background of the (amorphous) signal of soda-lime glass. This is important because small movements of the sample due to thermal expansion of the entire sample stage (in the RTP zone) may be compensated during the experiment without loss of accuracy in the position of diffraction peaks ($\Delta E < 10 \text{ eV}$ @ 40 keV). Figure 2 shows two typical EDXRD spectra of the Cu/In precursor ($\text{Cu/In}=1.8$) before and after the sulphurization. The comparison shows that the metallic CuIn_2 phase disappears in favour of a single chalcopyrite CuInS_2 phase at the end of the process. The signal very high since the spectra were acquired for 240 sec prior to the start and after the end

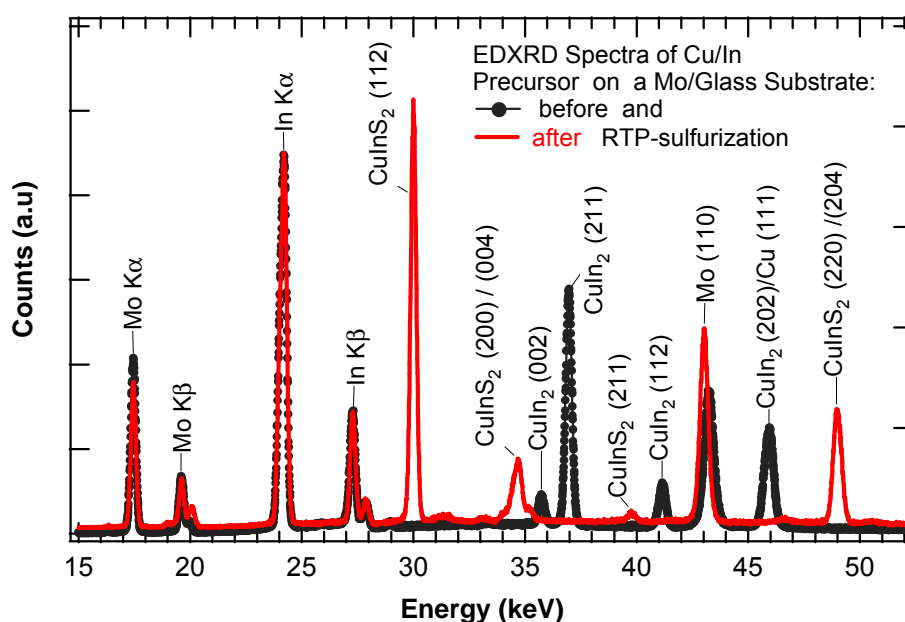


Figure 2: Typical in-situ EDXRD spectra before and after sulphurization of a sputtered Cu/In precursor on a Mo/Glass substrate. The metallic phases like CuIn_2 and Cu are completely consumed and single phase CuInS_2 is formed after the RTP process.

of the RTP process. So far the information can also be obtained by conventional laboratory based XRD experiments (not energy dispersive). However, the power of using the synchrotron lies in the high flux available and the short time necessary to acquire a spectrum which entails the qualitative information of all crystallographic phases present in the thin film at a particular time during the solid state reaction. Figure 3 shows a whole series of EDXRD spectra in a 2D representation which is obtained if the consecutively recorded spectra are plot-

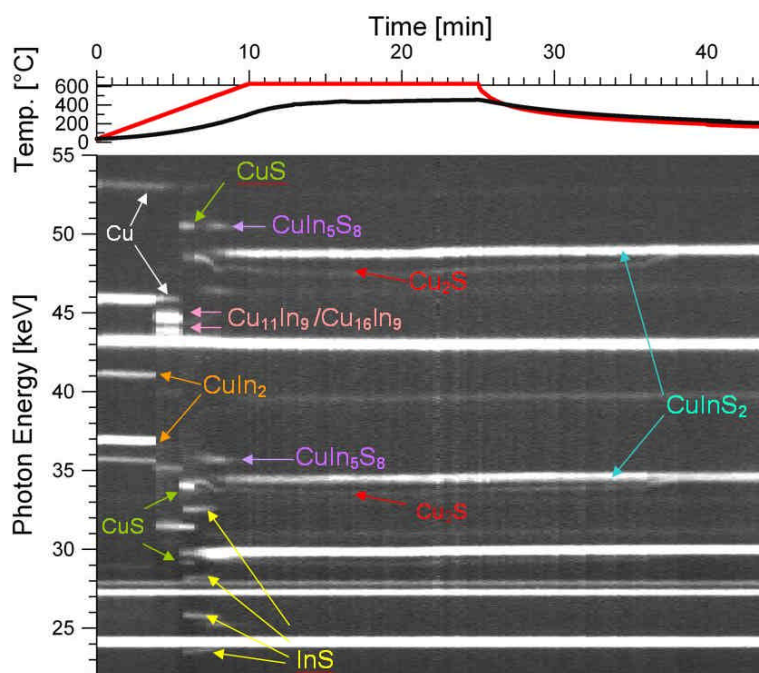


Figure 3: 2D representation of a whole series of EDXRD patterns of the RTP processing of a metallic Cu/In precursor thin film under sulphur atmosphere. The plot shows directly the phase predominance in the thin film at a given time. Thereby the dominant reaction pathway of the solid state reaction can be identified. The temperature of the sample lies between the nominal temperature of the heaters (red) and the graphite reactor (black).

ted next to each other as a line in a grey scale format. The top axis shows the process time (? spectrum number) and the left axis identifies the photon energy. The intensity of the diffraction pattern is represented by the grey scale. Brighter areas signify diffraction peaks with higher intensity. On top the nominal temperatures of the heater (red) and the graphite box (black) are shown as a function of process time. The heating rate for this particular experiment was 63K/min with a subsequent annealing time of 15 min. at a top temperature of 630°C. The chosen representation as 2D image allows very quickly to discern the qualitative phase predominance at a given time and thereby to identify the various stages of the absorber formation. During the sulphurization of the Cu-rich Cu/In precursor different crystallographic phases can be identified: Cu, CuIn₂, Cu₁₁In₉, Cu₁₆In₉, CuS, Cu₂S, InS, CuIn₅S₈ and finally CuInS₂. In contrast to other experiments carried out at much lower sulphur partial pressure ($p_{\max} < 10^{-3}$ mbar) [3] the reaction pathway follows the formation of the chalcopyrite from binary intermediate phases (CuS and InS) via a Cu-deficient defect phase (CuIn₅S₈) [4]. Other experiments with a much higher amount of elemental sulphur show a different behaviour in the onset of the chalcopyrite phase in comparison to the binary phases InS and CuS. The first results of this new experiment already confirm that the chalcogenide thin film formation is very sensitive to the vapour pressure in the gas phase during the solid state reaction. The experiment allows to systematically control this parameter and to study the absorber formation very close to the industrial process conditions. Therefore the optimization of the process conditions can be significantly accelerated and principle features of the growth mechanism can be identified. Preliminary experiments have shown that the time for the spectral acquisition can be further reduced to 3-5 seconds per spectrum. Real time experiments very similar to the HMI baseline RTP process with a much shorter the heat up phase of 2 min (instead of 10 min) will then be investigated by *in situ* EDXRD.

References:

- [1] M. A. Contreras, K. Ramanathan, J. AbuShama, F. Hasoon, D. L. Young, B. Egaas and R. Noufi, *Prog. Photovolt: Res. Appl.* **13** (2005); p. 209–216
- [2] K. Siemer, J. Klaer, I. Luck, J. Bruns, R. Klenk, D. Bräunig, *Solar Energy Materials & Solar Cells*, **67**, (2001), p. 159-166.
- [3] Ch. von Klopmann, J. Djordjevic, E. Rudigier, R. Scheer, *Journal of Crystal Growth* **289** (2006), p. 121-133
- [4] F.O. Adurodiya, J. Song, S.D. Kim, S.K. Kim, K.H. Yoon, *Jpn. J. Appl. Phys. Vol.* **37** (1998) p. 4248-4253

XANES study of fullerene-based coatings.

R. Torres¹, Z. Martín², R. Gago³ and I. Jiménez^{1,2}.

¹ Instituto de Ciencia de Materiales de Madrid (ICMM- CSIC), Cantoblanco, 28049 Madrid (Spain)

² Instituto de Ciencia y Tecnología de Polímeros (ICTP-CSIC). Juan de la Cierva 3, 28006 Madrid (Spain)

³ Centro de Microanálisis de Materiales, Universidad Autónoma de Madrid, 28049 Madrid, (Spain).

Within the framework of the European project "Fullerene-based Opportunities for Robust Engineering: Making Optimized Surfaces for Tribology (FOREMOST)", we have studied by XANES a variety of carbon-based coatings with an intrinsic fullerene-based structure, and also nanocomposite coatings containing fullerene-like nanoparticles. The experiments were conducted at beamline PM4. Some results are described as follows.

A. Monolythic fullerene-like (FL) coatings based on Carbon and BCN.

The term fullerene-like (FL) material is applied to layered solids with curved planes that may form either closed cages or extended structures, based on the similarity with the carbon fullerenes. A monolythic FL coating is a single phase thin films formed by an extended layered compound with curved and interconnected basal planes. The curvature and interconnection of basal planes provides a significant improvement on the physical properties (mainly mechanical) of the FL coating compared to thin films of the same compound in conventional plane-layered form [1].

We have studied the XANES spectra of carbon, carbon nitride [2] and BCN coatings with FL structures in comparison with conventional planar hexagonal structures. The samples were prepared as Thin Films by Physical Vapor Deposition (PVD) [3] and Chemical Vapor Deposition (CVD) techniques [4].

Here, we report on the XANES spectra for partially hydrogenated carbon films prepared by CVD techniques, with and without a FL structure. There is a significant improvement of the tribomechanical properties for the FL sample compared to the conventional, with an change in hardness from 2 to 17 GPa, in elastic modulus from 30 to 150 GPa, in friction coefficient from 0.3 to 0.1 for tests against a WC/Co counterface, and in the wear coefficient from 10^{-3} to 10^{-7} mm³/Nm. The XANES spectra for both samples, labeled as polymeric-carbon and FL-carbon are show in Figure 1, together with references from graphite, diamond, C60 and a tetrahedral amorphous carbon. Clearly, new features appear in the FL sample, that can be directly compared with the features of the C60 molecule. .

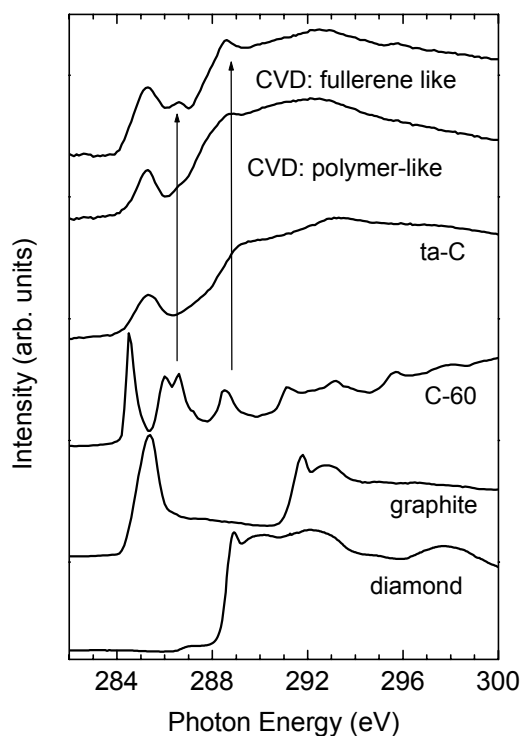


Fig.1. C(1s) XANES from carbon films with fullerene-like and polymer-like structures, compared to different reference materials.

Similar studies have been performed for the carbon nitrides and ternary BCN compounds.

B. Nanocomposite coatings based on fullerene-like particles.

A second family of fullere-based coatings is that in which FL particles are incorporated into a matrix material, hence forming a composite material. If the FL are particles have nanometric size, the resulting coating is a nanocomposite.

In our work we have considered several nanoparticles, including carbon nanotubes (CNT), C_{60} fullerene, BCN nanoparticles prepared by ball milling [5], and inorganic fullerene-like WS_2 (IF- WS_2). This last material consists in an onion-like structure of the layered chalcogenide WS_2 with concentric curved planes, yielding particles with an average diameter of 80 nm. The IF- WS_2 particles have been incorporated into various materials, namely carbon, CN and BCN films, and thermoplastic polymer coatings.

Regarding the performance of the nanocomposite, an important point is the interfacial interaction between the matrix material and the nanoparticle, which can be modified by surface treatments of the nanoparticles or the addition of surfactants. One of the possible methods for surface modification is a plasma oxidation of the nanoparticles. Here, we present in Figure 2, the XANES data for the Oxygen plasma modification of the IF- WS_2 nanoparticles.

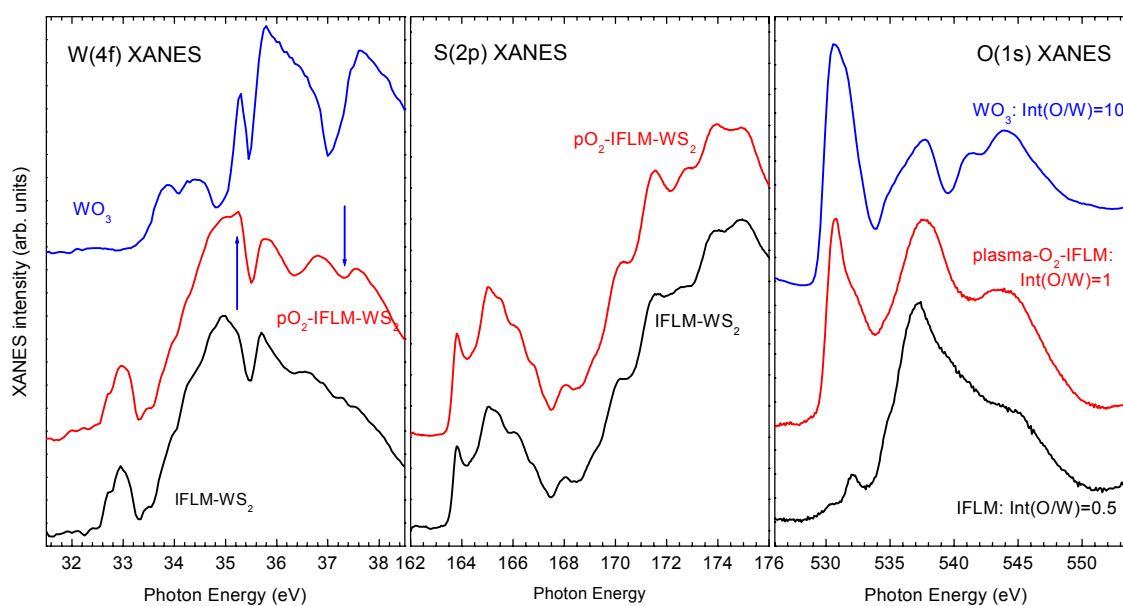


Fig. 2. XANES data from inorganic fullerene WS_2 particles treated with an O_2 plasma for controlled oxidation of the surface layer.

Different types of nanoparticle surface modification were performed on all the materials considered in this study, including plasma treatment with different gases and chemical treatments. XANES appears as a well suited method to characterize the surface modification induced in the nanoparticles, and to follow if this surface treatments remains in the nanocomposite.

Acknowledgements.

The XANES work was performed at beamline PM-4 using the SURICAT endstation. We are indebted to Dr. Antje Vollmer for her help and assistance with the experiment. This work has been partially financed by the European Union-6th Framework Program, Project FOREMOST under contract NMP3-CT-2005-515840. The synchrotron work was supported by the European Community - Research Infrastructure Action under the FP6 "Structuring the European Research Area" Programme (through the Integrated Infrastructure Initiative Integrating Activity on Synchrotron and Free Electron Laser Science - Contract R II 3-CT-2004-506008).

References.

- [1] H. Sjöström, S. Stafström, M. Boman, J. E. Sundgren, *Phys. Rev. Lett.* 75 (1995) 1336.
- [2] R. Gago, I. Jiménez, J. Neidhardt, B. Abendroth, I. Caretti, L. Hultman, and W. Möller, *Correlation between bonding structure and microstructure in fullerene-like carbon nitride thin films*, *Phys. Rev. B* 71 (2005) 1254514.
- [3] I. Caretti, J.M. Albella and I. Jiménez, *Tribological study of BC₄N coatings*, *Diamond. Relat. Mater.* 16 (2007) 63-73.
- [4] M. Camero, J.G. Buijnsters, C. Gómez-Aleixandre, R. Gago, I. Caretti and I. Jiménez, *The effect of nitrogen incorporation on the bonding structure of hydrogenated carbon nitride films*, *J. Appl. Phys.* (2007) in press.
- [5] R. Torres, I. Caretti, R. Gago, Z. Martín, and I. Jiménez, *Bonding structure of BCN nanopowders prepared by ball milling*, *Diamond. Relat. Mater.* (2007) in press.

Decomposition and oxidation behaviour of ZrH₂ powder for metal foaming

Jimenez Catalina, Garcia-Moreno Francisco, Zizak Ivo, Schumacher Gerhard, Banhart John

Introduction

The Powder Metallurgical (PM) route is one of the most successful methods to produce metallic foams. Basically the PM route consists of admixing metal powders and 0.5-1 wt% blowing agent, e.g. hydrides or carbonates. Then, the mix is hot pressed, yielding a dense compacted precursor. The foaming process is initiated by heating the precursor up to the foaming temperature. Next, there is an isothermal stage to stabilize the liquid foam. And finally, the metallic porous structure is retained by cooling in air to room temperature. By now, pre oxidized TiH₂ for 3 hours at 480 °C has proved to be the best choice to make aluminum or aluminum-based alloy foams through the PM route. The oxide layer shifts the gas release onset of H₂ to higher temperatures. It also provides one single peak in the curve of H₂ evolution measured by mass spectrometry as a function of temperature [1, 2]. However in the large scale, pre oxidizing TiH₂ leads to important hydrogen losses. Lower costs alternative blowing agents are eager to be found. ZrH₂ has been considered as a suitable blowing agent for some aluminum alloys [3] and Zn.

KMC-2 beamline at Bessy synchrotron light source has shown successfully in-situ phase transformation and oxide formation in TiH₂ [4]. In our measurements, the 6-circle diffractometer and its 2D detector permitted to follow in-situ phase transformations of ZrH_x at high temperatures. Time resolution was high enough to heat up far faster than 10 °K/min, under Ar atmosphere, thus approximating better the conditions during foaming.

Experimental

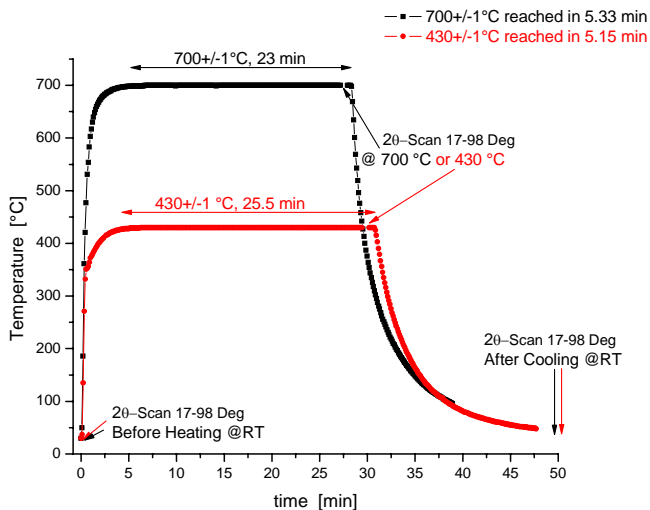


Fig 1. Heating profiles of samples held at 430 and 700 °C.

As received ZrH₂ powders with an average size of 8 μm, were sieved to get from a second powder of particle size $r < 25 \mu\text{m}$. Tablets of 0.2 g and 6 mm diameter were cold compacted using both powders. A hole of 0.6 mm diameter was drilled on the surface of the sample to insert a thermocouple beside the beam path. The tablet was tightened to a Tantalum plate, which was subsequently mounted on a resistive heater. The whole system was sealed within a Beryllium dome. The samples were heated up with the temperature profile shown in Fig 1. A high purity Ar flow was used to keep the atmosphere at normal pressure. 430 °C is a typical foaming

temperature for Zinc, and 700 °C permitted to follow the sequence of phase transformations. Cooling down to room temperature was also done under Ar flow. The photon energy used was 12 keV, which corresponds to $\lambda = 1.03 \text{ \AA}$. The projected beam size on the specimen was between 0.7-0.8 mm. In order to obtain diffractograms containing the main peaks of fct $\epsilon\text{-ZrH}_2$, fcc $\delta\text{-ZrH}_x$, bcc $\beta\text{-Zr}$, $\alpha\text{-Zr}$ and monoclinic ZrO₂, the 2θ range selected was 17-33 degrees. The acquisition time per frame, i.e. per diffractogram, was 5 seconds. Scans in 2θ between 17-98

degrees were performed before heating, at the holding temperature, and after cooling, as indicated also in Fig 1.

Results

In Fig. 2, 2θ scans between 17- 98 degrees corresponding to the sample heated up to 430°C are plotted. These 2θ scans were performed without the Beryllium dome, at room temperature, before heating, and after cooling. No phase transformations from ϵ -ZrH_x to δ -ZrH_x, or to α -Zr were observed. After

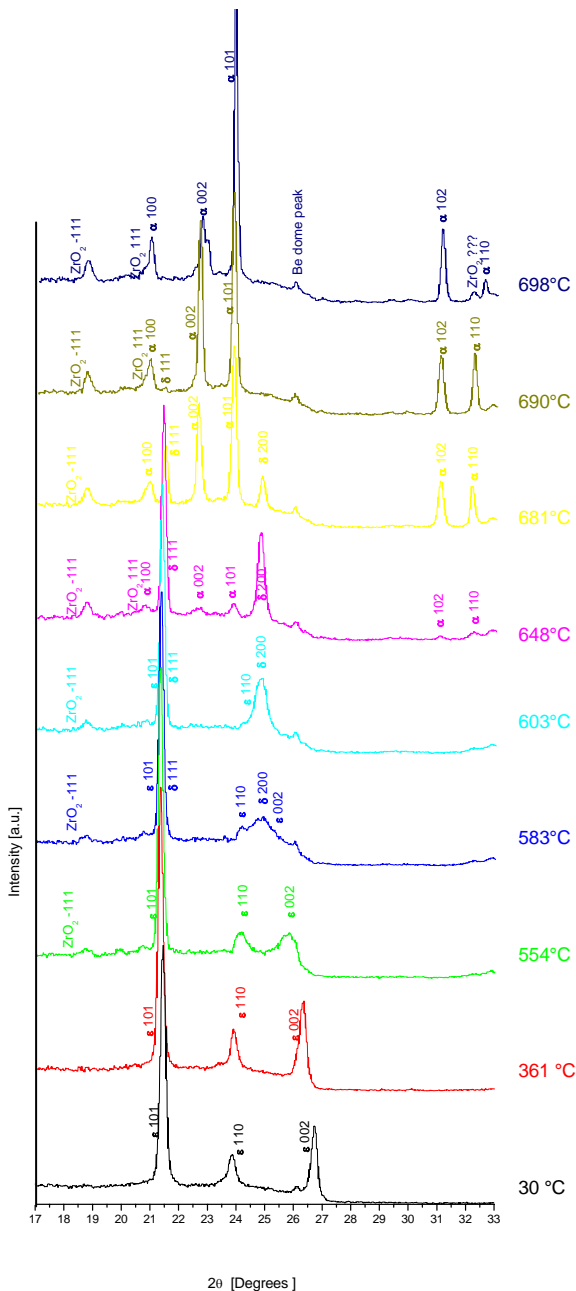


Fig 3. Sequence of phase transformations for ZrH_x during heating up to 700°C under Ar atmosphere.

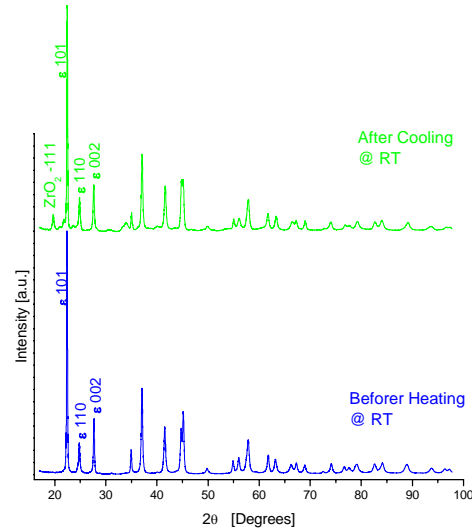


Fig 2. 2θ scans of the sample held at 430 °C.

cooling, it was possible to identify peaks of the monoclinic ZrO₂ and ϵ -ZrH_x.

The tablets heated up to 700 °C under Ar atmosphere presented all the phases expected except β -Zr, which was not observed. Fig. 3 shows the sequence of phase transformation for ZrH_x acquired in-situ during heating.

The fct phase ϵ -ZrH₂ was observed from room temperature to 603 °C. The fcc phase δ -ZrH_x, was observed in range of temperatures 583-690 °C. The metallic hcp phase, α -Zr, appeared at 648 °C. The monoclinic oxide ZrO₂ appeared at 554 °C. Both of them, α -Zr and ZrO₂ are the final products, i.e. no further phase transformations were observed during the isothermal step, or during cooling.

At around 26 degrees of 2θ , there is a little peak that comes from the Beryllium dome. At 698 °C, slightly above 32 degrees of 2θ , there is a group of peaks corresponding most probably to the ZrO₂ phase.

Discussion

The use of ϵ -ZrH₂ as blowing agent to foam Zn, was found not to be the best choice. After foaming Zn with ZrH₂, at 430 °C, most of the hydrogen would remain in the foam as hydride, which is inefficient. That leads to possible secondary expansions of the foam, and or crack development in the cell walls.

In-situ experiments under Ar atmosphere, at normal pressure holding at 700 °C permitted to follow in-situ the decomposition of the hydrides and the oxidation at high temperatures. It is extensively reported that oxygen, especially at high temperatures, stabilizes α -Zr and destabilizes β -Zr. It is therefore not surprising that β -Zr did not appear. However, in the selected range of 2θ for the in-situ measurements, bcc β -Zr has only one peak, the 110. That peak is rather close to the angle where the peak 101 of the hcp phase α -Zr has appeared. Thus, overlapping of both main peaks is not discarded.

At least two additional experiments should be done: first, in-situ acquisition in a wider range of 2θ , to figure out whether β -Zr appears or not. Second, heating rates of 10 K/min going to 430°C, 700 °C or even higher temperatures, to attempt to correlate this phase transformations with standard techniques of thermal analysis, like differential scanning calorimetry and thermal gravimetry. Additional information, like mass spectroscopy is necessary to determine, through the hydrogen signal, the mechanisms that govern the decomposition behavior of ZrH₂ in metal foams.

References

- [1] B. Matijasevic, J. Banhart, S. Fiechter, O. Görke, N. Wanderka, *Acta Materialia* 54 (2005) 1887-1900.
- [2] B. Matijasevic, J. Banhart, *Scripta Materialia* 54, 503-508 (2006)
- [3] B. Matijasevic, O. Görke, H. Schubert, J. Banhart, *Conf. Proc. MetFoam 2005/ JIMIC-4*, Ed. by H. Nakayima and N. Kanetake. (2006) 107-110
- [4] B. Matijasevic, J. Banhart, I. Zizak, N. Darowski, G. Schumacher, *BESSY Annual Report* (2003) 443-444.

Chemical reactions in polyelectrolyte brush - interaction of PAA brush with monovalent cation

Yulia Mikhaylova¹, Katy Roodenko¹, Leonid Ionov⁵, Michael Gensch^{1,4}, Norbert Esser¹, Manfred Stamm¹, Ulrich Schade³, Klaus-Jochen Eichhorn², Karsten Hinrichs^{1*}

¹ISAS - Institute for Analytical Sciences, Department Berlin, Albert-Einstein-Str. 9, 12489 Berlin, Germany

²Leibniz Institute of Polymer Research Dresden, Hohe Str. 6, 01069 Dresden, Germany

³Berliner Elektronenspeicherring-Gesellschaft für Synchrotronstrahlung m.b.H (BESSY), Albert-Einstein Str.15, 12489 Berlin, Germany

⁴present address: Deutsches Elektronen-Synchrotron (DESY), Notkestr. 85, 22607 Hamburg, Germany

⁵Max-Planck-Institute of Molecular Cell Biology and Genetics Pfotenhauerstrasse 108, 01307 Dresden, Germany

* corresponding author: hinrichs@ansci.de

Modification of a solid surface with thin covalently attached polymeric coatings (brush) has received increasing interest in chemistry, physics in and in biology, particularly in the area of sensor development - especially for “chemical sensors”. The polyelectrolyte brushes represent a very attractive group of surface immobilized polymer coatings. In particular, polyelectrolyte brushes are very promising for biotechnological applications because their properties can be switched in aqueous environment by changing pH, ion strength, temperature, etc. In this work we chose the pH as a variable parameter to determine the structural changes of a poly(acrylic acid) (PAA) brush which can show strong response to the presence of low molecular weight electrolytes (KOH, pH 10). For instance, Treat et al. [1] characterized the swelling behaviour of PAA brush in the electrolyte solutions of different pH by ellipsometry. They found that dissociation of PAA carboxylic groups leads to the conformational changes of polymer chains due to repulsive forces between fully ionized carboxylic groups.

The FT-IR ellipsometer at the IRIS beam-line utilizes the high brilliance of the synchrotron source for the investigation of small samples or sample areas [2,3]. Infrared spectral range is dedicated for investigations of the vibrational bands and thus the molecular structure of the film. We monitored vibrational bands of the 3.3 nm thick PAA brush on a gold-covered glass substrate which was partially dipped into KOH solution (pH 10). Figure 1 shows mapping results in two orthogonal directions (3x4 spots, 2 mm lateral step scan). As expected, the $\nu(\text{C}=\text{O})$ stretching vibration of carboxyl groups was strongly influenced by the environment. In the part of the sample that was brought in contact with a KOH solution, a band belonging to the asymmetric stretching vibration (1586 cm^{-1} , $\nu_{\text{as}}\text{COO}^-$) of carboxylate groups of PAA anion is clearly seen. By these spectral differences two chemically different areas can be clearly distinguished. The concentration of PAA molecules in the brush decreases from Col. 1 to Col. 3.

Future work will be focused on research of biosensor application and composition-dependent structural properties of gradient brushes.

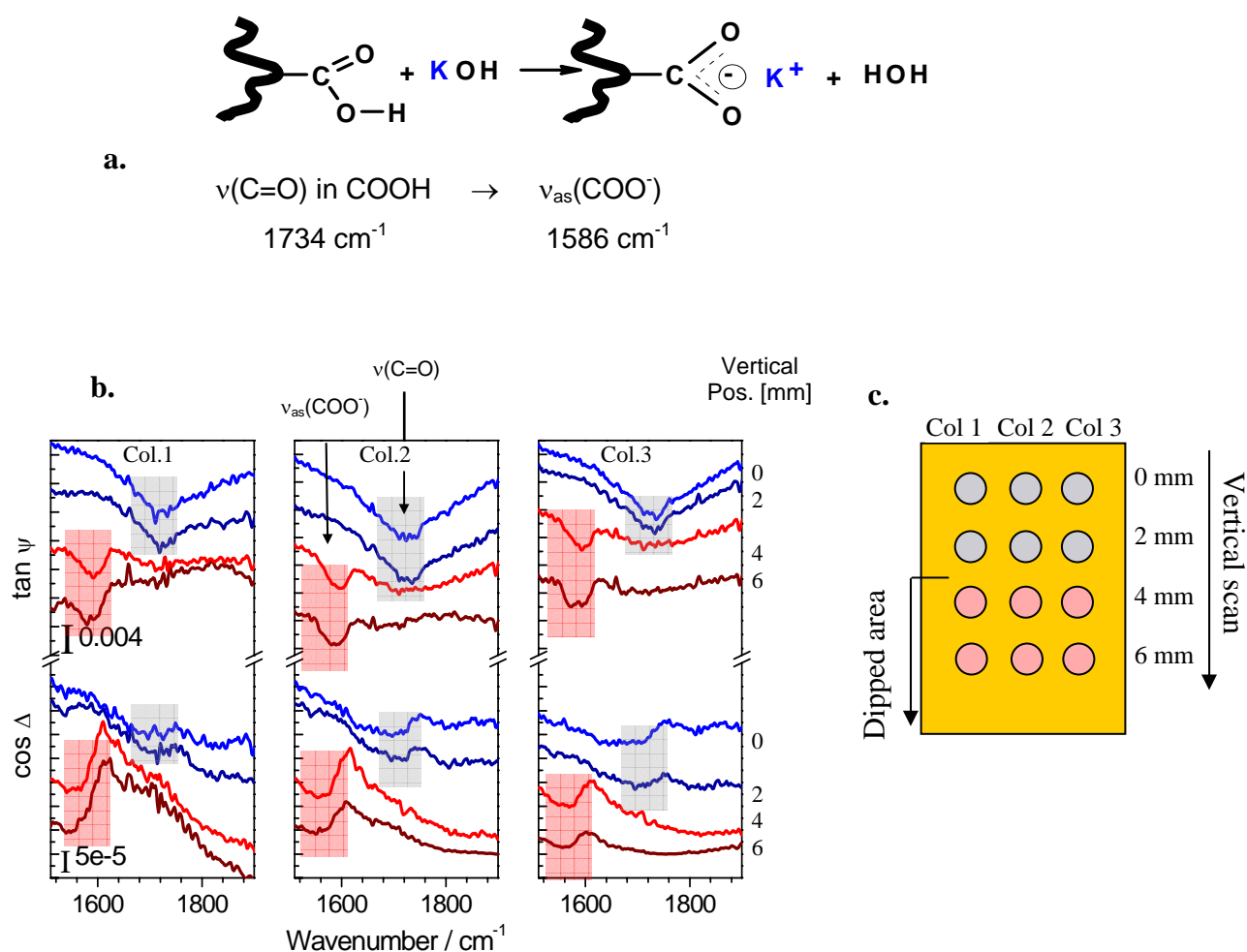


Figure 1 (a) Reaction and peak assignment upon a dip of the PAA brush into a KOH solution (pH 10). (b) Ellipsometric parameters ($\tan \psi$ and $\cos \Delta$) of the sample. Blue: spectra from the non-dipped area; red: spectra from the dipped area of the sample. Several lines were scanned for homogeneity check in two dimensions. A clear discrimination between the immersed part and non-dipped part into the KOH is seen in all spectra. (c) Schematic drawing of the sample and of the performed scan.

References

- [1] N.D. Treat, N. Ayres, S.G. Boyes, W.J. Brittain, *Macromolecules*, **39**, 26 (2006)
- [2] M. Gensch, E. H Korte, N. Esser U. Schade, K. Hinrichs, *Infrared Phys. and Technol.* **49**, 74 (2006)
- [3] K. Hinrichs, M. Gensch, N. Esser, *Appl. Spectrosc.* **59**, 272A (2005)

Acknowledgments

We acknowledge support by the EU through EFRE program (ProFIT grant, contract nr. 10125494). K. Roodenko gratefully acknowledges support from the Minerva foundation.

Electronic Structure of Molecular Magnets

N.Schmidt¹, B.Graf¹, A.Scheurer², R. Prakash², R.W. Saalfrank², E.Goering³, R.Fink¹

¹ Physikalische Chemie II, Univ. Erlangen, Egerlandstr. 3, 91058 Erlangen

² Organische Chemie II, Univ. Erlangen, Henkestr. 42, 91054 Erlangen

³ Max-Planck-Institut für Metallforschung, AG Schütz, Heisenbergstr. 3, 70569 Stuttgart

Molecular nanomagnets like Mn_{12} and Fe_8 are interesting objects because of their peculiar magnetic properties. Below about 1 K these materials show remanent magnetization and spin tunnelling leading to steps in hysteresis loops due to quantum coherence effects [1]. They are regarded as promising candidates for ultra-high-density magnetic storage devices and quantum computing applications.

We have investigated the electronic structure and spin state of the so-called “ferric star”(Fe₄) [1] and several “manganese wheels”[2] using NEXAFS and XMCD spectroscopy. These compounds feature four Fe³⁺ ions (for Fe₄) respectively four Mn³⁺ and three Mn²⁺ ions (for Mn₇), the coordination sphere being distorted octahedra of oxygen, nitrogen and chloro donors. Both prototype complexes have a blocking temperature T_B of around 1 K. In order to distinguish the spectral contribution of Mn ions in the two different oxidation states, two partially In-substituted Mn_3In_4 and $\text{Mn}_4\text{In}_3(\text{PPh}_4)^+$ substances were investigated, both containing Mn²⁺ only. The substances were prepared in a straightforward one-pot synthesis and cleaned by recrystallization except for the heteronuclear Mn-In compounds. The samples were prepared by drop-coating from chloroform solutions onto Au-plated Si wafers and handled under inert gas atmosphere.

Room temperature NEXAFS measurements were carried out at the UE52-PGM beamline. To reduce radiation damage, advantage was taken of single-bunch mode. The open 3d shell of Mn²⁺ (d^5), Mn³⁺ (d^4) and Fe³⁺ (d^5) gives rise to a strong XMCD effect. The XMCD measurements were carried out at UE46-PGM and PM3 beamlines with a static magnetic field up to 6.5 Tesla and a switched magnetic field of 2 T at temperatures of about 1.5 K (or higher). Unfortunately, no equipment was available to reach temperatures below T_B .

Results and Discussion

The NEXAFS and XMCD data of Fe₄ are shown in Fig. 1 together with its structural formula.

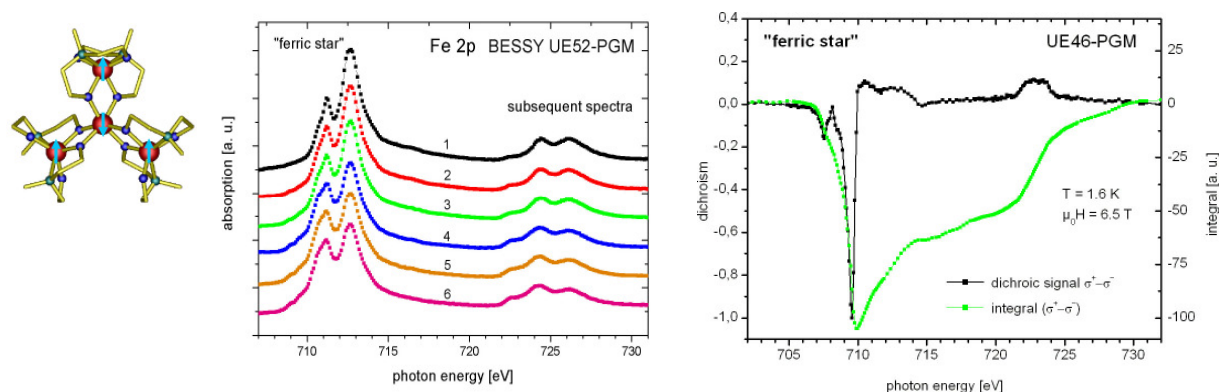


Fig. 1: (a) Structural formula of the investigated polynuclear Fe₄ complex. (b) Sequence of Fe L-edge NEXAFS spectra. (c) XMCD spectrum of Fe₄ measured for two different magnetic field orientations.

As demonstrated in Fig. 1b, the material is very sensitive to radiation. The ratio of the two resonances at the Fe L₃ edge changes with increasing dose, which is interpreted as a radiation induced reduction, because the low energy resonances are regarded to be an indication for Fe²⁺ rather than Fe³⁺ (as expected for pristine Fe₄). A possible explanation for the pronounced sensitivity is the insufficient core-

hole shielding for the metal ions within these weakly coupled supramolecular aggregates or reduction of the Fe ion by transferring a ligand electron to the Fe 2p hole upon destructive oxidation of a ligand molecule (as observed in C 1s NEXAFS). On the other hand, this might lead to an oxidic Fe species with much stronger ligand field. Note that the experimental NEXAFS spectra of Fe₄ do not resemble a calculated multiplet spectrum for Fe³⁺ in a weak octahedral field [3]. Therefore, a better quantitative understanding of the present spectra requires multiplet calculations taking the unsymmetric special coordination spheres into account.

XMCD spectra in Fig. 1c reflect only a summation over the (non-interacting) four Fe³⁺ ions since the temperature was not low enough for quantum effects to be effective. XMCD shows a negligible orbit momentum using the sum rules[4], which is usually expected for d⁵-high spin systems.

Fig. 2 shows NEXAFS and XMCD data of the Mn₇ and Mn_xIn_y compounds.

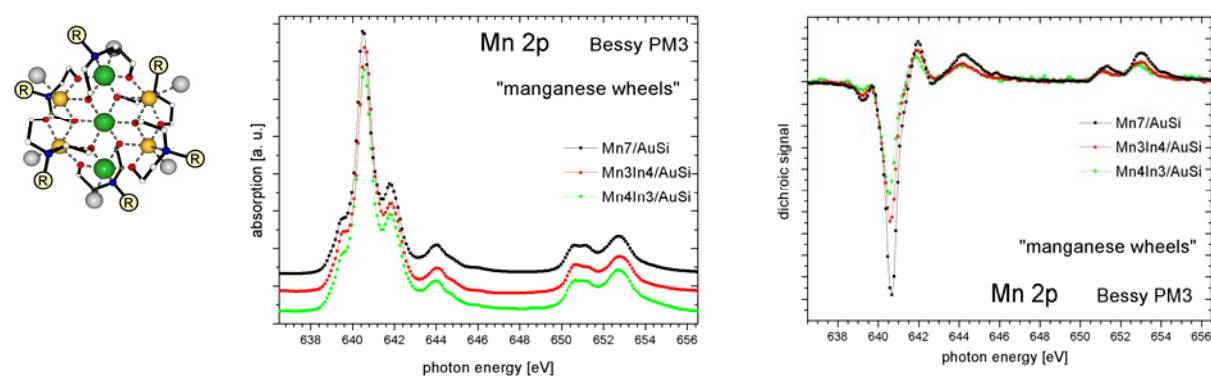


Fig. 2: (a) Structural formulae of the investigated polynuclear Mn₇/Mn_xIn_y clusters. (b) Mn L-edge NEXAFS spectra for the various Mn_xIn_y-wheels. (c) Comparison of the respective XMCD spectra.

Astonishingly, the Mn L-edge NEXAFS of Mn₇ and its In derivatives are very similar and resemble a calculation for Mn²⁺ (d⁵) (Fig. 2b). This was expected for Mn₃In₄- and Mn₄In₃-“wheels”, since both contain Mn²⁺ only. However, Mn₇ wheels also should have contributions from Mn³⁺, so the spectrum should definitely differ from the other two substances. From this experimental finding one may speculate about a much higher radiation sensitivity of Mn³⁺ compared to Fe³⁺. XMCD spectroscopy of all “manganese wheels” (again a summation over all uncoupled Mn ions, since T > T_B) clearly shows a small but easily detectable orbit momentum ($\mu_L : \mu_S = 1 : 7$). The dichroic effect is roughly proportional to the number of Mn ions per molecule, strongest for Mn₇ (Fig. 2c).

The major drawback of the present investigations is the fact that we could not reach temperatures below the blocking temperature to investigate the magnetic correlations within the nanomagnets. Radiation sensitivity can be overcome using single-bunch rather than multibunch mode.

Acknowledgements

We gratefully acknowledge assistance of S. Sperner (Univ. Erlangen), K. Fauth (MPI Stuttgart), D. Schmitz (HMI Berlin), P. Saintavit (CNRS), F. Kronast (Bessy GmbH, Berlin), and D. Batchelor (UE52-PGM, Uni Würzburg) for preparation of the substances, assistance during the experiments and discussion of the results. The work was financially supported by the DFG (within SFB 583) and BMBF (contract 05 ES3XBA/5).

References

- [1] R. W. Saalfrank, A. Scheurer, I. Bernt, F. W. Heinemann, A. V. Postnikov, V. Schünemann, A. X. Trautwein, M. S. Alam, H. Rupp, P. Müller, *Dalton Trans.* **2006**, 2865-2874.
- [2] R. W. Saalfrank, R. Prakash, H. Maid, F. Hampel, F. W. Heinemann, A. Trautwein, L. H. Böttger, *Chem. Eur. J.* **2006**, *12*, 2428.
- [3] G. van der Laan, I. W. Kirkman, *J. Phys: Condens. Matter* **1992**, *4*, 4189-4204.
- [4] E. Pellegrin, *Nachr. FZ Karlsruhe* **2000**, *32*, 4, 349.

Alkyl-modified Si(111) surfaces for sensing applications in wet-FETs

Ralf Hunger^{a,*}, Daisuke Niwa^b, So Kudo^b, Mariko Matsunaga^b, Yosi Shacham-Diamand^c, sWolfram Jaegermann^a, Tetsuya Osaka^b

^aInstitute of Materials Science, TU Darmstadt, Petersenstr. 23, D-64287 Darmstadt, Germany

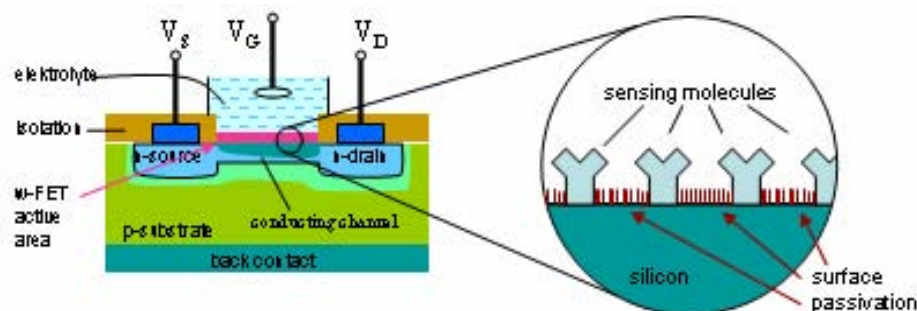
^bDepartment of Applied Chemistry, Waseda University, 3-4-1 Okubo, Shinjyuku, Tokyo 169-8555, Japan

^cDepartment of Physical Electronics, Tel-Aviv University, Ramat-Aviv 69978, Israel

Figure 1 shows the schematics of a “wet” field-effect transistor (w-FET) acting as a biochemical sensor [1]. The central idea of this device is that biochemical sensor molecules with highly specific binding properties are attached on the gate electrode of a w-FET. This is the active region of the electrochemical sensing device, which is contacted by an electrolyte. Realizing this device in silicon technology requires two technological preconditions: a) The gate electrode surface needs to be stable against the electrolyte (corrosion resistance) [2]. b) sensor molecules need to be fixed to the gate electrode in a defined way, and (lateral) spatial pattern, thus “chemical lithography” is required [3].

Figure 1:

Schematics of an electrochemical, “wet” field effect transistor, w-FET, for biosensing applications.



Alkyl-modified silicon surfaces are one interesting class of materials considered for surface passivation and structuring [2-4]. Cyclic voltammograms of various alkyl-modified Si(111) surfaces are shown in Figure 2. The onset of electron transfer from the semiconductor to into the $Fe^{2+/3+}$ redox electrolyte depended on the type of organic termination. The charge transfer is easiest, i.e. the onset of cathodic current is observed for lowest overpotentials for methylated Si(111) [5]. Apart from that, a remarkable property Si(111)- CH_3 is its p-type surface channel action in “wet” or humid conditions which makes this modification particularly interesting for w-FET sensing applications [6]. The mechanism leading to p-type surface channels is not yet understood and serves as a further starting point for our investigations. Another particularity is of Si(111)- CH_3 is the fact that it is the only alkyl species by which a 100% surface termination, i.e. chemical saturation of every Si(111) surface atom is accomplished [7]. All longer alkyl chain moieties appear to fail to give a full monolayer coverage due to steric hindrances (cf. Figure 3).

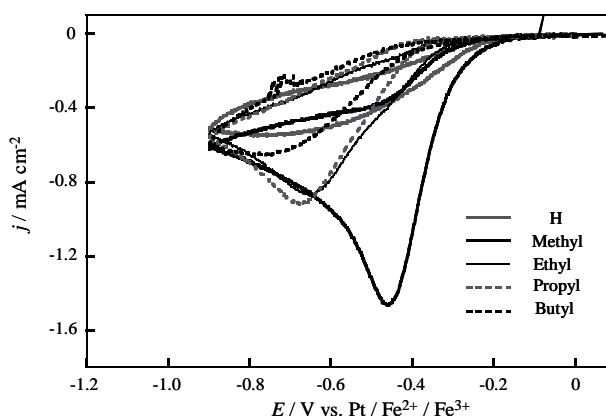


Figure 2: Cyclic Voltammograms (1st scan, cathodic branch only) of differently modified Si(111) surfaces in contact with a $Fe^{2+/3+}$ redox electrolyte

Alkylated Si(111) surfaces were prepared in a wet chemical two-step process, where the Si(111) surface is first chlorinated, and subsequently alkylated in Grignard reagent solutions e.g. CH_3MgCl in THF [2, 5]. The samples were analysed by photoemission in the SoLiAS station [8] on the U49/2-PGM2 beamline of

the CRG BTU Cottbus-HMI-TUDarmstadt. Spectra were acquired in normal emission using a Phoibos 150 MCD 9 analyser, and referenced to the Fermi level.

Figure 3 shows photoelectron spectra of differently modified silicon surfaces in the valence band and the C 1s core level regions. The direct bonding of the terminator group to surface Si atoms is evidenced by the emission from the $\sigma_{\text{Si-C}}$ bond (or analogously the $\sigma_{\text{Si-H}}$ bond) at around 5 eV [9]. Another characteristic feature of direct Si-C linkage is the low BE component C_{Si} at around 284.3 eV (silicon-bound carbon) in the C 1s emission. The second component C_{CH_2} at 285.0 eV is related to C-C or C-H bonded, aliphatic species. With increasing alkyl chain length the intensity of the aliphatic component increases (Data for ethylated-Si from [10]). For ethylated Si(111), the ratio $C_{\text{CH}_2} / C_{\text{Si}}$ is about 1:1, for butylated Si 1:3 in accordance with expectations.

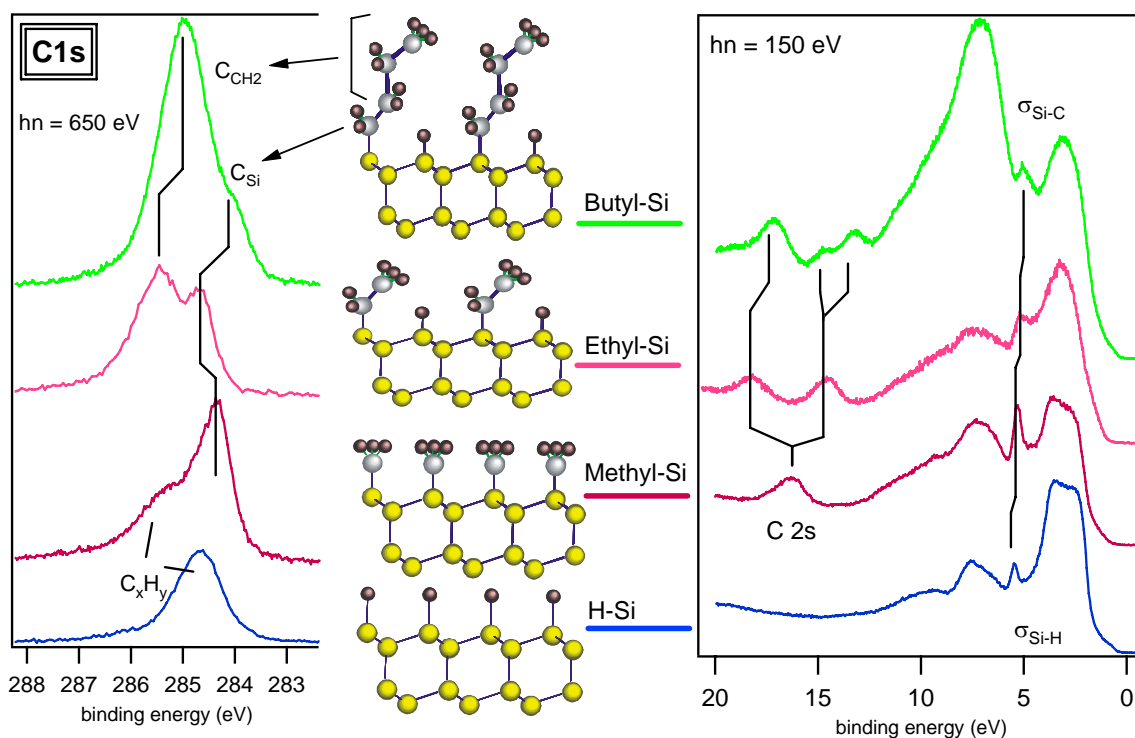


Figure 3: Photoelectron spectra of various alkylated Si(111) surfaces. The direct Si-C linkage is evidenced by the the surface state emission from the $\sigma_{\text{Si-C}}$ bond orbital and the C_{Si} labelled low BE component in the C 1s emission, which is associated with silicon-bound aliphatic carbon. C_{CH_2} corresponds to aliphatic, only C-C and C-H coordinated carbon.

As mentioned above, one important issue concerning organic modification, which is related to its stability in a humid environment, is the degree of termination, i.e. the question of how many of the surface Si dangling bonds are saturated by methyl/methylene bonding. Usually, such surface coverage quantification is derived from an intensity analysis. The data shown in Figure 4, however, illustrate that such approaches have to be undertaken with great care. An excitation energy-scan of the Si 2p and C 1s emissions of methylated Si(111)-CH₃ was performed, where the excitation energy was varied from 300 eV to 470 eV in steps of 5 eV. A substantial modulation of detected photoelectron intensity due to photoelectron diffraction (PED, [11]) was evidenced. The large modulation amplitude reflects the high structural perfection of the methyl monolayer which is as well monitored by LEED [9]. The contamination level from non-silicon-bound hydrocarbons C_xH_y is much lower than in earlier PED studies [11]. Concludingly, for the quantification of surface coverage, excitation energies no too close to the ionization threshold of C 1s are recommended in order to minimize PED effects [10].

In summary, very interesting organic monolayer termination structures of Si(111) can be prepared by chemical processing. In future studies, the contact behaviour of such alkyl-modified surfaces with electrolytes and organic or inorganic semiconductors will be investigated.

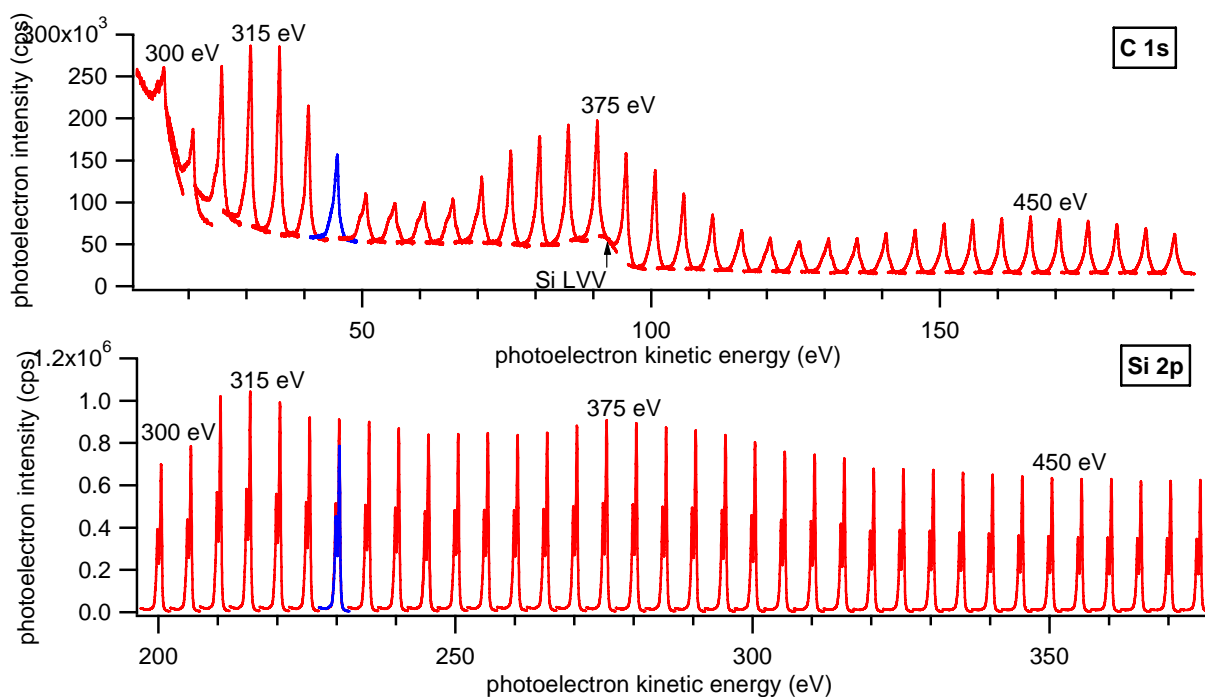


Figure 4: *C1s* and *Si2p* photoelectron spectra series of *Si(111)-CH₃* measured in normal emission, where the excitation energy was varied from 300 to 470 eV in steps of 5 eV. The periodic intensity modulation of the core level emissions is caused by photoelectron diffraction. At around 90 eV kinetic energy the *C1s* core level emissions pass across the substrate *Si LVV* Auger emission structure.

Acknowledgements: This work was supported by the BMBF, contract number 05 KS4RDA/0 (SoLiAS), and the FAME Network of Excellence WP6.

References

- [1] Niwa, D., Yamada, Y., Homma, T., Osaka, T.: *Formation of Molecular Templates for Fabricating On-Chip Biosensing Devices*. *J. Phys. Chem. B* **108**(10) (2004), p. 3240-3245.
- [2] Niwa, D., Inoue, T., Fukunaga, H., Akasaka, T., Yamada, T., Homma, T., Osaka, T.: *Electrochemical Behavior of Methyl- and Butyl- Terminated Si(111) in Aqueous Solution*. *Chem. Lett.* **33**(3) (2003), p. 284.
- [3] Yamada, T., Takano, N., Yamada, K., Yoshitomi, S., Inoue, T., Osaka, T.: *Alkyl monolayers on Si(111) as ultrathin electron-beam patterning media*. *J. Electroanal. Chemistry* **532**(1-2) (2002), p. 247-254.
- [4] Yamada, T., Yamada, K., Takano, N., Inoue, T., Osaka, T.: *Evaluation of Organic Monolayers Formed on Si(111): Exploring the Possibilities for Application in Electron Beam Nanoscale Patterning*. *Japanese Journal of Applied Physics* **40**(Part 1, 8) (2001), p. 4845-4853.
- [5] Osaka, T., Matsunaga, M., Kodo, S., Niwa, D., Shacham-Diamand, Y., Jaegermann, W., Hunger, R.: *Electric and electrochemical properties of alkyl-monolayer modified Si(111) in the presence of water*. *Journal of the Electrochemical Society* (submitted).
- [6] Niwa, D., Fukunaga, H., Homma, T., Osaka, T.: *Surface Conductivity in Methyl-monolayer/Si Heterojunction Structure in the Presence of Water*. *Chemistry Letters* **34**(4) (2005), p. 520-521.
- [7] Nemanick, E.J., Hurley, P.T., Brunshwig, B.S., Lewis, N.S.: *Chemical and Electrical Passivation of Silicon (111) Surfaces through Functionalization with Sterically Hindered Alkyl Groups*. *J. Phys. Chem. B* **110**(30) (2006), p. 14800-14808.
- [8] Mayer, T., Lebedev, M.V., Hunger, R., Jaegermann, W.: *Elementary processes at semiconductor /electrolyte interfaces: perspectives and limits of electron spectroscopy*. *Appl Surf. Sci.* **252** (2005), p. 31.
- [9] Hunger, R., Fritsche, R., Jaekel, B., Jaegermann, W., Webb, L.J., Lewis, N.S.: *Chemical and electronic characterization of methyl-terminated Si(111) surfaces by high-resolution synchrotron photoelectron spectroscopy*. *Physical Review B* **72**(4) (2005), p. 045317-7.
- [10] Jaekel, B., Hunger, R., Lim, T., Jaegermann, W., Webb, L.J., Lewis, N.S.: *High-Resolution Synchrotron Photoemission Studies of the Electronic Structure and Thermal Stability of CH₃- and C₂H₅-Functionalized Si(111) Surfaces*. *Journal of Physical Chemistry B* (submitted).
- [11] Terry, J., Linford, M.R., Wigren, C., Cao, R., Pianetta, P., Chidsey, C.E.D.: *Determination of the bonding of alkyl monolayers to the Si(111) surface using chemical-shift, scanned-energy photoelectron diffraction*. *Applied Physics Letters* **71**(8) (1997), p. 1056-1058.

Anomalous widths of surface XPS peaks observed in free Xe clusters

G. Öhrwall,¹ W. Pokapanich,¹ S. Barth,² V. Ulrich,²
S. Joshi,² T. Lischke,² S. Marburger,² O. Björneholm,¹ and U. Hergenhahn²

¹Uppsala University, SE-751 21 Uppsala, Sweden

²IPP, Euratom Assoziation, 85748 Garching, Germany

The core level photoelectron spectrum of free rare gas clusters is fairly well understood. It contains peaks attributed to surface and to bulk atoms [1]. The largest contribution to the width of these peaks is due to binding energy differences between inequivalent sites in a cluster [2]. On the surface of a cluster, there is a larger variation in coordination than in the bulk. For this reason it is expected that the surface peak is wider than the bulk peak, which also is observed.

We have recorded the Xe 4d photoelectron spectrum for free Xe clusters of several sizes at the beamline UE112-lowE-PGM-a, using a Scienta SES-200 spectrometer. The spectrometer was mounted in the so-called magic angle to the polarization of the ionizing radiation, to decrease the angular distribution effects on relative intensities. In Fig. 1, the surface and bulk peak widths of the Xe 4d photoelectron lines for a series of different cluster sizes are shown.

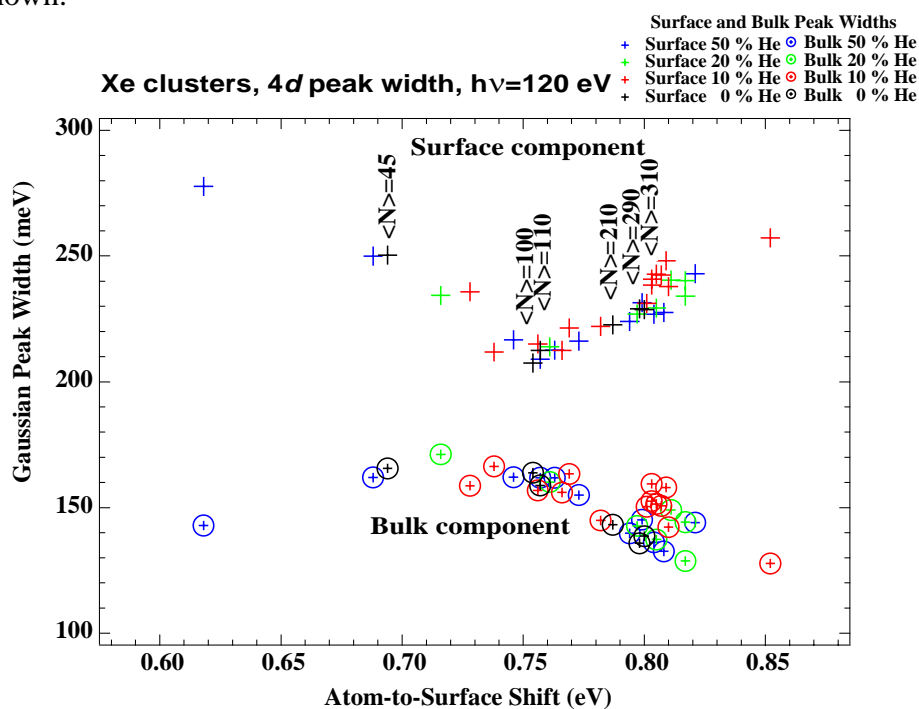


Fig.1. Xe 4d photoelectron spectra of clusters produced by expansion of pure Xe (black symbols) and several mixtures of Xe and He (blue, green and red symbols). We show the widths of the bulk and surface components of the photoemission lines as obtained from a curve fit. Data are plotted against energy difference of the surface peak to the atomic reference signal. This quantity is a monotonous function of cluster size. Cluster sizes obtained from a scaling law [3] are shown for pure clusters.

The experimental broadening from spectrometer and photon band width, (in total ≈ 80 meV), has been deconvoluted.

One would further expect that the variations in coordination decrease with size, both for surface and bulk atoms. This would lead to a narrowing of the peaks for larger clusters. For Xe clusters, this narrowing is essentially observed for the bulk peak, but the surface peak exhibits an anomalous behavior: For small sizes, the surface peak width decreases with size as expected, but for clusters larger than 100 atoms, the width increases (see Fig. 1).

To investigate if this observation is an effect of entropy, we have attempted to vary the Xe cluster temperature by co-expansion with a buffer gas – He – in various fractions. But as seen in Fig. 1, the He cooled clusters exhibit a very similar behavior. This indicates that temperature is not affecting the width of the surface peak to any large degree.

In Fig. 2, the ratio of the surface and bulk peak areas are plotted. It shows a monotonous decrease as a function of size, which is the expected behavior. This supports the observation that the increase of the surface width with size is a physical effect, and not an artifact of the curve fitting.

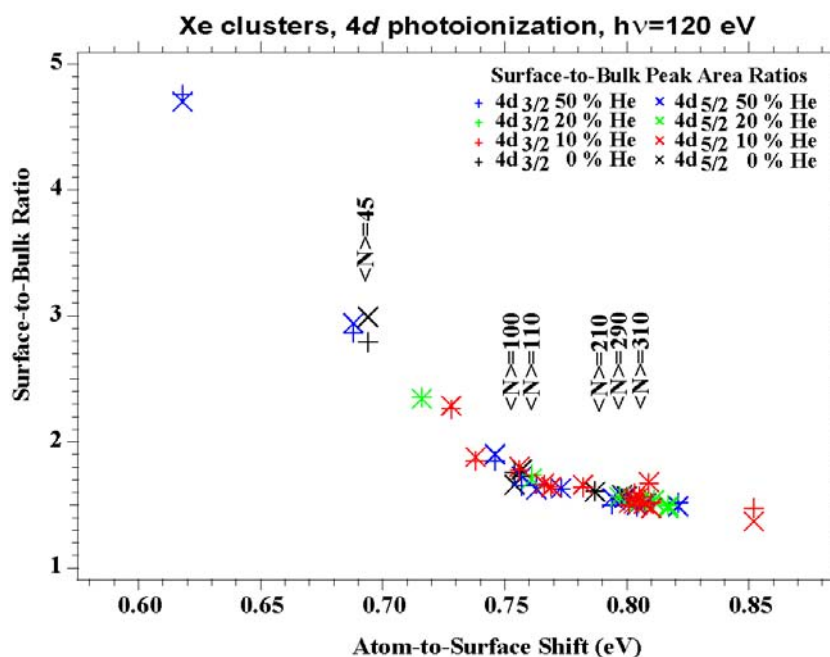


Fig. 2. The ratio of surface and bulk peak areas for the same data as in Fig. 1. The data for the two Xe 4d spin-orbit components are presented separately.

It has been suggested that free rare gas clusters go through a series of phase changes, from icosahedral to decahedral to fcc crystal structure, as a function of size [4]. These phase changes are due to the competition of strain inside the bulk of the cluster and the drive to minimize the surface area: For small sizes the gain in surface energy by using the icosahedral structure is larger than the strain induced in the bulk. In the size range of a transition from one structure to another, the spectra will contain contributions from both types of structures. For the bulk, the phase change should mean a smaller variation in inequivalent sites, but this need not be the case for the surface. However, it is expected that the first phase change occurs for clusters of many hundred or even thousand atoms, clearly at odds with the present observation. Further experimental and theoretical investigations are in progress to shed light on the issue.

- [1] O. Björneholm, F. Federmann, F. Fössl, and T. Möller, Phys. Rev. Lett. 74, 3017 (1995).
- [2] H. Bergersen, M. Abu-samaha, J. Harnes, O. Björneholm, S. Svensson, L.J. Sæthre, K.J. Børve, PCCP 8, 1891 (2006).
- [3] U. Buck and R. Krohne, J. Chem. Phys. 105, 5408-15 (1996).
- [4] J. P. K. Doye and F. Calvo, J. Chem. Phys. 116, 8307 (2002).

Electronic structure of Mn₁₂ derivatives on the clean and functionalized Au surface

S. Voss¹, M. Fonin¹, M. Burgert², Yu. S. Dedkov³, U. Groth², and U. Rüdiger¹

¹Fachbereich Physik, Universität Konstanz, 78457 Konstanz, Germany

²Fachbereich Chemie, Universität Konstanz, 78457 Konstanz, Germany

³Institut für Festkörperphysik, Technische Universität Dresden, 01062 Dresden, Germany

The ongoing miniaturization of electronic circuits has motivated the study of a possible use of single molecules in the design of logic or memory units of future electronic devices. Implementation of single molecules in electronic components demands an understanding of their electronic properties which ensures the possibility to control the electronic transport through single molecule junctions. With respect to this, single molecule magnets (SMMs) like Mn₁₂-acetate [1, 2] and its derivatives, combining low-temperature magnetic hysteresis and quantum effects, represent a material class with a promising perspective for application in ultra-high density data storage devices or quantum computing. The ability to deposit intact spatially isolated single molecule magnets on surfaces is an indispensable prerequisite to perform electronic transport measurements on individual molecules. So far, the investigation of Mn₁₂ clusters on surfaces had mostly been limited to scanning probe and core-level x-ray photoelectron spectroscopy (XPS) studies (e.g. Ref. [3]). Scanning probe results on Mn₁₂ clusters revealed hints of a possible fragmentation of the molecular magnets while core-level XPS could not be used for the unambiguous determination of the chemical integrity of such complex molecules.

In this work, we performed a combined scanning tunneling microscopy (STM), x-ray absorption spectroscopy (XAS) and resonant photemission (ResPES) study on two Mn₁₂ derivatives: Mn₁₂-thiophene-3-carboxylate (Mn₁₂-th) and Mn₁₂-biphenyl-carboxylate (Mn₁₂-biph) [Fig. 1]. The Mn₁₂ clusters were grafted to Au(111) surfaces [(111) oriented Au layer on a silicon wafer with Ti adhesion layer] via ligand exchange reaction with 4-mercapto-tetrafluorobenzoic acid (4-MTBA) and via physisorption due to a strong S-Au interaction between the thiophene ligands and the Au substrate. Previous STM measurements revealed the presence of a sub-monolayer of nearly identical sized clusters on the surface after deposition via ligand exchange reaction while small molecular fragments were visible after direct deposition of Mn₁₂-th onto Au(111) [Fig. 2]. However, XPS measurements

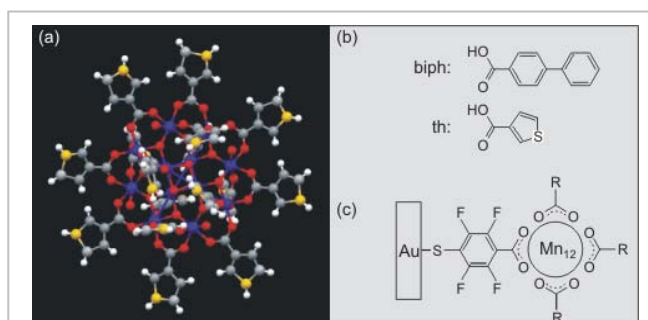


Fig.1. (a) Crystallographic structure of Mn₁₂-thiophene-3-carboxylate (Mn₁₂-th). (b) Schematic representation of thiophene and biphenyl ligands. (c) Schematic representation of the grafting procedure via ligand exchange reaction with 4-MTBA.

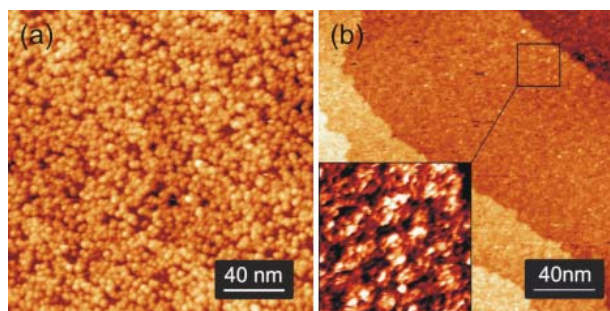
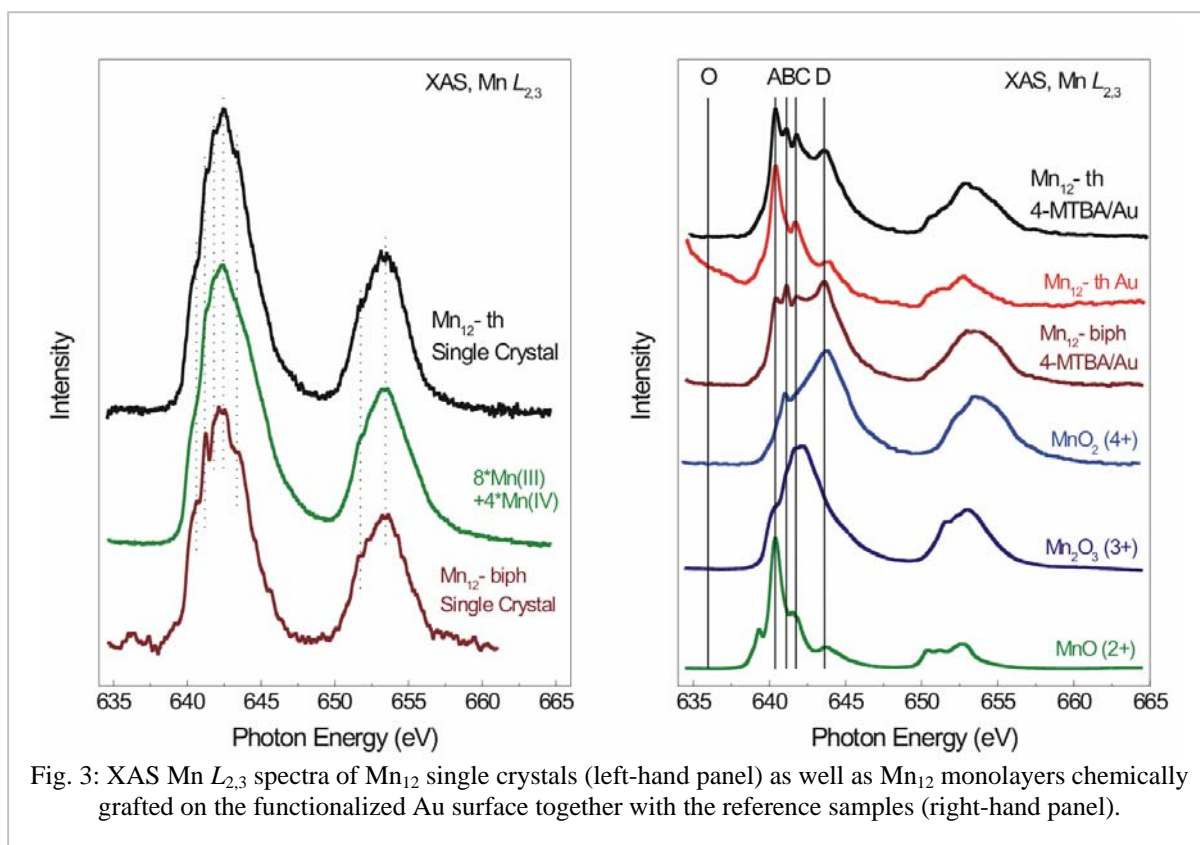


Fig. 2. (a) 200 × 200 nm² STM image of Mn₁₂-th on functionalized Au(111). (b) 200 × 200 nm² STM image of Mn₁₂-th on clean Au(111).



showed no difference in PES spectra obtained from monolayers prepared by either of the preparation techniques. Thus STM and XPS measurements alone cannot be used to determine the chemical and structural integrity of Mn₁₂ molecules on surfaces. To this end, XAS provides a tool for the determination of the oxidation states of Mn ions within the Mn₁₂ core.

Mn $L_{2,3}$ XAS measurements were performed at the RGLB-PGM (BESSY) beam line since this beam line provides low-intensity radiation continuously distributed over a wide energy range and is thus suitable for spectroscopic studies of fragile molecular samples. XAS spectra were obtained in total electron yield mode. Sample spectra recorded within 2 hours were compared to each other and showed no hints of any change of the spectral line shape due to radiation damages to the molecules. The results derived from XAS measurements revealed a significant difference in the Mn $L_{2,3}$ line shape depending on the selected preparation technique. Furthermore a significant deviation from the usual Mn₁₂ single crystal XAS spectra was observed in case of Mn₁₂ monolayers (Fig. 3). Instead of sole Mn³⁺ and Mn⁴⁺ contributions to the XAS spectrum a clear Mn²⁺ peak occurred giving evidence for a Mn₁₂ core reduction or fragmentation after surface deposition. In case of the direct deposition of Mn₁₂-th on clean Au(111) the XAS Mn $L_{2,3}$ line shape was nearly identical to that of a MnO (Mn²⁺) XAS reference spectrum suggesting a complete destruction of the Mn₁₂ core.

In addition, we performed ResPES measurements on Mn₁₂-th and Mn₁₂-biph deposited on functionalized surfaces via ligand exchange reaction by tuning the photon energy over the $2p \rightarrow 3d$ excitation threshold. The photoelectron intensity which is proportional to the Mn $3d$ partial density of states (PDOS) of the Mn₁₂ monolayers [Fig. 4] was obtained by subtracting the off-resonance spectra taken around 635.6 eV excitation energy [corresponding to label "O" in Fig. 3] from the on-resonance one [corresponding to label "D" in Fig. 3]. Due to the strong Mn²⁺ intensity in the XAS spectra [see Fig. 3] only the $D-O$ difference spectra can be attributed to purely Mn³⁺ and Mn⁴⁺ contributions and thus to possibly intact Mn₁₂ clusters. The PDOS is spread uniformly over a range of about 10 eV while a band gap sets in about 1 eV below the Fermi level, supporting the insulating nature of Mn₁₂ clusters. The comparison of experimentally obtained difference curves with previous LDA + U calculations on Mn₁₂ for

$U=4$ eV [4, 5] showed a very good agreement between theory and experimental results [6]. This result provides evidence for the presence of a finite number of intact Mn_{12} single molecule magnets on suitably functionalized surfaces. Due to the good agreement between experimental and theoretical results the assumption of coexisting Mn_{12} molecules and molecular fragments seems to be adequate and thus the monolayers prepared by the ligand exchange technique are suitable for both spectroscopic and scanning probe studies offering a possibility to address magnetism and quantum effects on a molecular scale. Further studies concerning the electronic and magnetic properties of spatially isolated Mn_{12} clusters on surfaces are now under way.

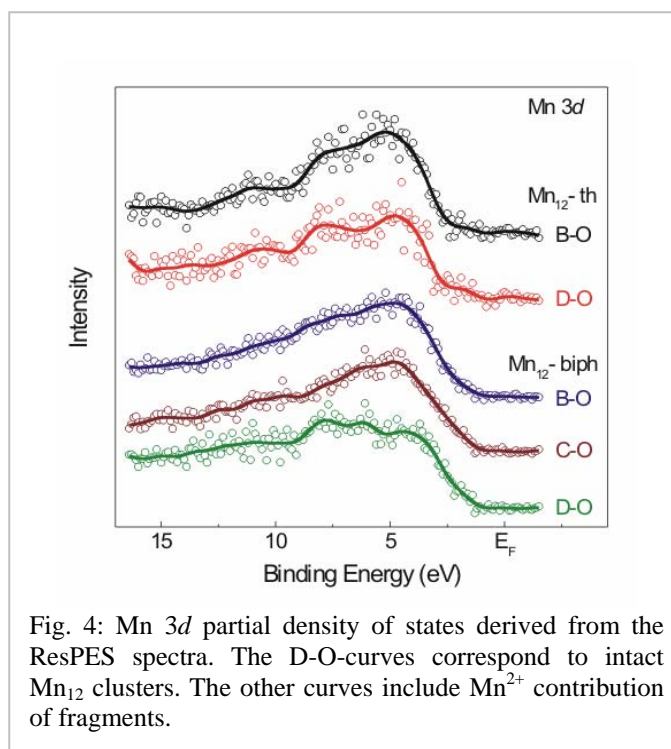


Fig. 4: Mn 3d partial density of states derived from the ResPES spectra. The D-O-curves correspond to intact Mn_{12} clusters. The other curves include Mn^{2+} contribution of fragments.

This work was supported by the Deutsche Forschungsgemeinschaft (DFG) through Sonderforschungsbereich (SFB) 513.

- [1] R. Sessoli *et al.*, Nature (London) **365**, 141 (1993).
- [2] L. Thomas *et al.*, Nature (London) **383**, 145 (1996).
- [3] A. Cornia *et al.*, Angew. Chem. **115**, 1683 (2003).
- [4] U. D. Pennino *et al.*, Surf. Sci. **600**, 4185 (2006).
- [5] D. W. Boukhvalov *et al.*, J. Electron Spectrosc. Relat. Phenom. **137-140**, 735 (2004).
- [6] S. Voss *et al.*, Phys. Rev. B **75**, 045102 (2007).

DOUBLE AUGER DECAY AFTER INNERSHELL IONISATION IN ARGON ATOMS AND IN SELECTED MOLECULES

L.Andric¹, G.Gamblin¹, P.Lablanquie¹, J.Palaudoux¹, F.Penent¹,
U. Becker², M. Braune², J.Viefhaus^{2,3}, J.H.D.Eland⁴

¹ LCPMR, Université Pierre et Marie Curie, 75252 Paris 5, France,

² Fritz-Haber-Institut, Faradayweg 4-6, 14195 Berlin, Germany

³ HASYLAB at DESY, Notkestrasse 85, 22603 Hamburg, Germany

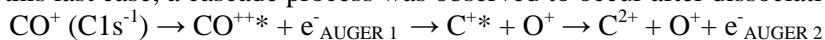
⁴ Physical and Theoretical Chemistry Laboratory, Oxford, OX1 3DW, U.K.

The non-radiative decay of inner shell holes by emission of an Auger electron has been extensively studied by Auger spectroscopy. Less known are the processes whereby two or more Auger electrons are released. Their interest arises from the strong electronic correlation mechanisms that are at their origin, especially in the case of a 'direct' double Auger decay where two Auger electrons are simultaneously released. Conventional coincidence experiments with low angular acceptance electron spectrometers are limited to the detection of only two electrons. They can give important information in well defined cases (such as angular correlations [1]) but generally they fail to give a complete picture of the process. A complete coincidence detection of all released electrons is required for that.

Our experimental set-up [2] consists in a time of flight spectrometer of the magnetic bottle type developed by J. Eland et al [3]. Its magnetic mirror configuration allows detection of all electrons emitted over the full 4π solid angle. This gives a high efficiency suitable for the observation of all the electrons released in multiple ionization events in a multi-coincidence mode. The single bunch operation of the BESSY synchrotron with a long time period of 800ns between light pulses was essential to separate overlapping processes. With our week of beam time in November 2006 at the UE125/2-SGM beam line we concluded our experiments on the 2p hole decay in argon [4] and the 3d one in krypton [5], and studied the Br 3d decay in CH₃Br. We will present here in more details the Argon results.

Figure 1 shows the two dimensional map of the double Auger decay after 2p inner shell ionization in argon and corresponds to triple coincidences since the two Auger electrons are selected by the 2p_{1/2} or 2p_{3/2} photoelectron. Coincidences are located on diagonal lines corresponding to specific Ar³⁺ final states. The weak continuous structure is associated to the previously investigated [1] direct Double Auger process. Most of the intensity is due to Auger electron pairs of energies around (10eV, 150eV), and originates from cascade processes. The electrons of E_{kin} ~150eV correspond to the first emitted Auger electron, associated to a transition between the 2p level and intermediate Ar²⁺ states. They are broadened by the 2p lifetime. This is not the case for the second step electrons of ~10eV for which, moreover, a high resolution can be achieved thanks to the time of flight technique. As a result, analysis of the second step electrons leads to a high resolution spectroscopy of the Ar²⁺ intermediate steps. This is shown in Figure 2 for the Ar 2p_{3/2} decay. It gives evidence for Ar²⁺ states of high binding energies, embedded in the triple ionization continuum. They are attributed to satellite states of 3s⁻² configuration.

Double Auger decay was also observed after 3d ionization in Kr [5], Br 3d decay in CH₃Br and C 1s ionization in CO. In this last case, a cascade process was observed to occur after dissociation, namely:



Autoionization occurs in the C^{+*} fragment after dissociation.

References

- [1] J. Viefhaus et al, Phys. Rev. Lett. **92**, 083001 (2004).
- [2] F. Penent, et al, Phys. Rev. Lett. **95**, 083002 (2005)
- [3] J. H. D. Eland, et al, Phys. Rev. Lett. **90**, 053003 (2003).
- [4] P. Lablanquie et al, J.Electron Spectroscopy Rel. Phen. (2007) in press
- [5] J. Palaudoux, PHD thesis, Université Pierre et Marie Curie, Paris (December 2006)

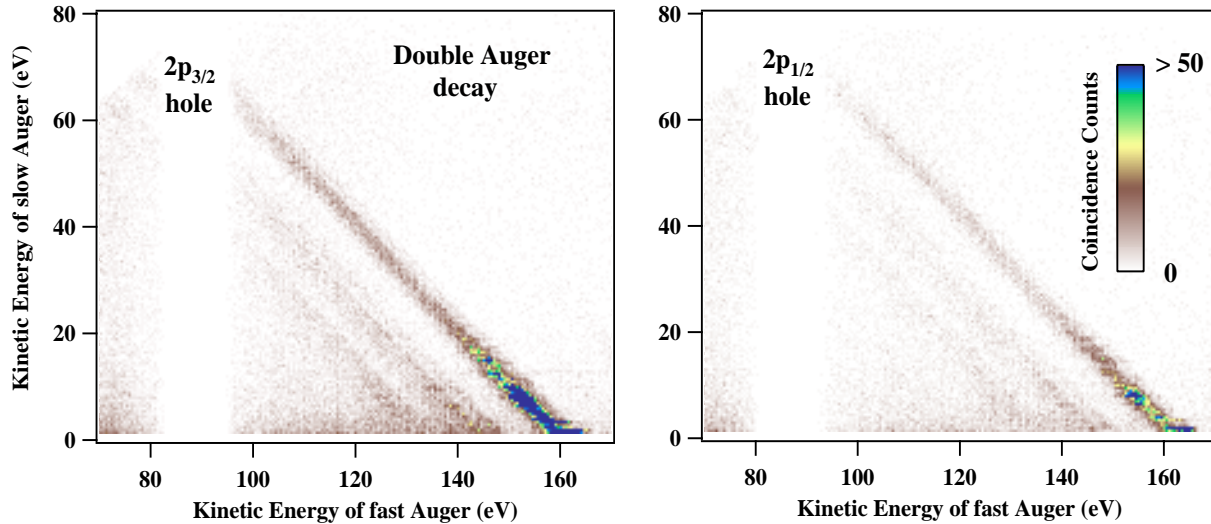


Figure 1: Decay of argon 2p holes by emission of two Auger electrons. Ionization was by photons of $h\nu=337\text{eV}$. Coincidence detection of the 3 released particles (the 2p photoelectron and the two Auger electrons) allows us to separate the double Auger spectra associated with the decay of the $2p_{3/2}$ or $2p_{1/2}$ hole. These data were obtained in 2005 at the UE56/2-PGM1 beamline [4].

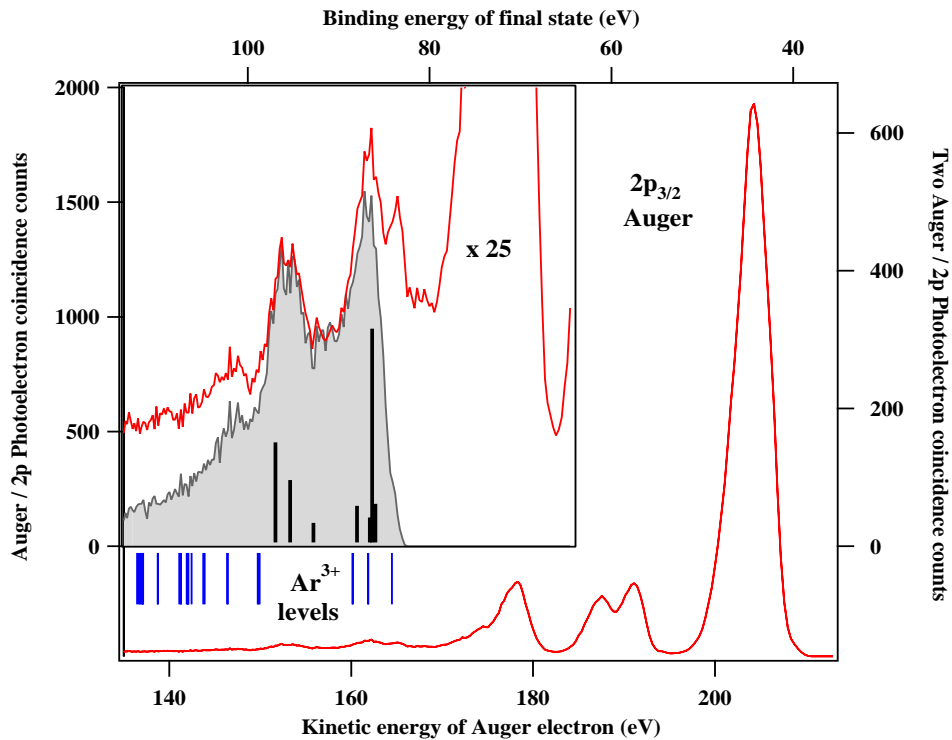


Figure 2: Complete coincidence Auger spectrum of argon associated with the decay of the $2p_{3/2}$ hole (red lines) obtained from 2 particles photoelectron / Auger coincidences. The grey part (inset) gives the contribution of the double Auger decays populating $\text{Ar}^{3+} 3p^{-3}$ states, deduced from the 3 particles coincidences from Figure 1. Thick black vertical bars indicate the Ar^{2+} intermediate states involved in the cascade double Auger decay, they are resolved thanks to the observation of their secondary decay. Blue vertical bars give the position of Ar^{3+} levels from the literature (NIST).

pH dependent N 1s binding energies of the amino acid lysine in aqueous solution

Dirk Nolting,^a Niklas Ottosson,^b Emad F. Aziz,^c Manfred Faubel,^d Ingolf V. Hertel,^a and Bernd Winter^a

^a Max Born Institute, Max-Born-Str. 2a, 12489 Berlin, Germany. E-mail: bwinter@mbi-berlin.de

^b Göteborg University, 405 30 Göteborg, Sweden.

^c BESSY mbH., Albert Einstein Straße 15, 12489 Berlin, Germany

^d Max Planck Institute for Dynamics and Self-Organization, Bunsenstraße 10, 37073 Göttingen, Germany.

The interaction of the protic and polar solvent water with solutes is complex, and comprises (de)protonation, dipole-dipole interactions and hydrogen bonding. For amino acids there is chemical equilibrium between protonated and deprotonated species with a conversion rate on the picosecond timescale. The equilibrium position depends on pH, and thus the mole fraction for several different charge states can be controlled, e.g. by sequential protonation. This gives unique access to species which are neither present in the gas phase nor in the solid state. Here, we observed pronounced chemical shifts of the N 1s caused by protonation of the amino groups. Photoelectron spectroscopy is combined with the liquid microjet technique. A 10 μm diameter liquid microjet is generated in a high-vacuum environment yielding nearly collisionless evaporation [1]. The jet, having a temperature of 4 °C, is formed by injecting the liquid at 20 bar through a 10 μm diameter orifice [1, 2]. For 3-5 mm downstream from the nozzle the beam is laminar, having a smooth surface [1, 3]. The photoelectron (PE) measurements were performed at the undulator beamline U41 PGM.

S(+)-lysine monohydrochloride (for synthesis) was purchased from Merck, and was used without further purification. A 0.5 molal solution of lysine monohydrochloride in highly demineralized

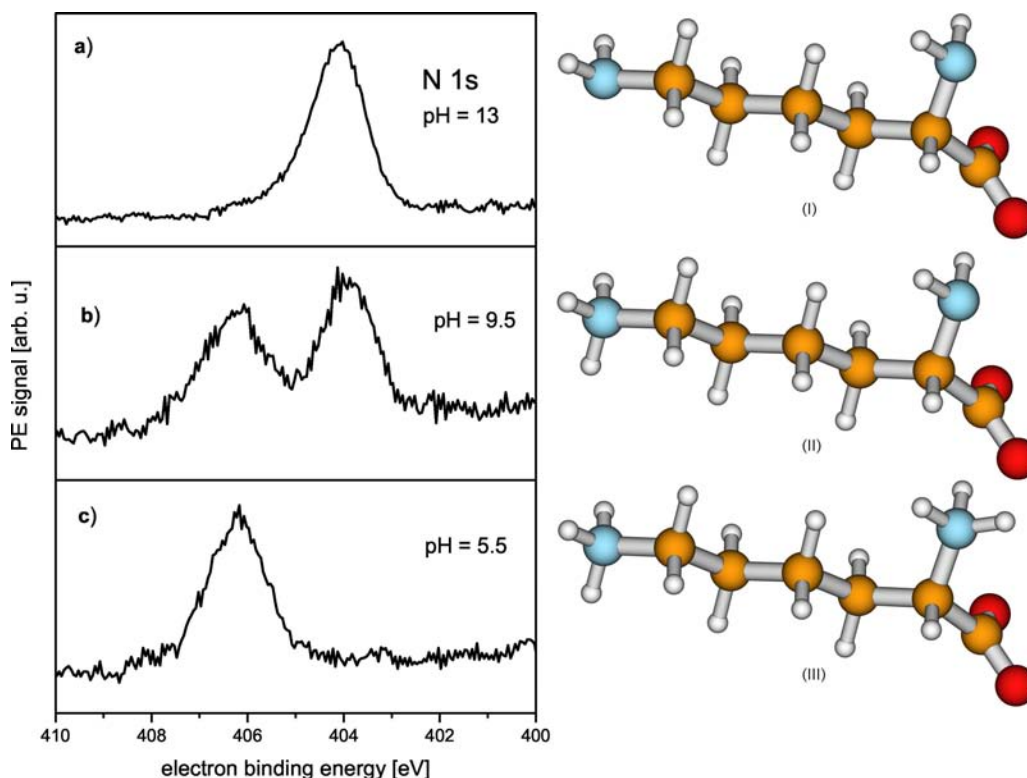


Figure 1: The N 1s PE spectra at different pH with the corresponding structures. a) At pH 13 both amino groups are neutral and have the same BE. b) At pH 9.5 Protonation of one amino groups increases its BE by 2.2 eV. As one amino group remains neutral the peak splits. c) At pH 5.5 the second amino group is also protonated and again only one peak appears.

water was used for all experiments.

At pH 13 more than 99% of lysine is present in the anionic form (I). Both nitrogens are neutral and show the same BE of 404.3 eV. Lowering the pH value to 9.5 causes the protonation of the nitrogen in the side chain. At this pH 75% of all lysine molecules are in the zwitterionic form (II) and the remaining molecules are in the charge states (I) and (III) at equal amounts. The protonation leads to a higher binding energy (BE) due to columbic attraction between the PE and the additional positive charge on the nitrogen. Hence, a second peak appears in the PE spectrum in Fig. 1b with a 2.2 eV higher BE, at 406.5 eV. The isoelectric point of lysine is 9.74, i.e. close to the pH in Fig. 1b, and both peaks have similar intensities. The small

discrepancy is caused by the measurement uncertainty of the pH value. At pH 5.5 (Fig. 1c) both nitrogens are protonated in more than 99% of all lysine molecules. Thus only one peak at 406.5 eV appears in the PE spectrum.

The sequential protonation enables the clear assignment of the two peaks in Fig. 1b: The peak at 404.3 eV corresponds to the neutral, and the peak at 406.5 eV to the protonated nitrogen. Hence, protonation causes a chemical shift in the N 1s level of 2.2 eV to higher binding energies. It is noteworthy to mention that chemical shifts are also observed for the carbon atoms (data not shown). Through-bond interaction induces a shift of ≈ 0.3 eV for carbons adjacent to the amino group. Hence, the sequential protonation of lysine allows a clear assignment of the measured BE to moieties of the molecule.

References

- [1] M. Faubel and T. Kisters, *Nature*, 1989, **339**, 527–529.
- [2] B. Winter, R. Weber, W. Widdra, M. Dittmar, M. Faubel, and I. V. Hertel, *J. Phys. Chem. A*, 2004, **108**, 2625–2632.
- [3] M. Faubel, B. Steiner, and J. P. Toennies, *J. Chem. Phys.*, 1997, **106**(22), 9013–9031.

THE PHOTOABSORPTION AND PHOTOIONIZATION OF BROMINE REVISITED.

R. Locht¹, B. Leyh¹, H.W. Jochims², H. Baumgärtel².

¹ *Molecular Dynamics Laboratory, Department of Chemistry, Institute of Chemistry, University of Liège, Sart-Tilman par B-4000 Liège 1, Belgium.*

² *Institut für Physikalische und Theoretische Chemie, Freie Universität Berlin, Takustrasse 3, D-14195 Berlin, Germany.*

During the last few years we proceeded with the investigation of the ionization and dissociation dynamics of bromine derivatives of ethylene [1]. Photoabsorption spectroscopy (PAS), photoionization mass spectrometry (PIMS) and photoelectron spectroscopy (PES and TPES) were applied. The disubstituted derivatives 1,1-C₂H₂Br₂ and cis- and trans-1,2-C₂H₂Br₂ are suspected to be more sensitive to photodissociation than their corresponding difluorinated and dichlorinated compounds. Atomic Br or molecular Br₂ could thus contaminate the spectra. This has been observed, e.g., in the PAS of CH₃Br [2].

To be able to ensure the purity of the spectra of the above mentioned brominated derivatives, the molecular Br₂ has been reinvestigated by PAS and PIMS in the 5-15 eV photon energy range.

The PAS of Br₂ has been reported by Venkateswarlu [3] between 8.183eV and 10.538 eV using a 10m concave grating spectrograph. PIMS has been applied to Br₂ by Dibeler et al. [4,5] between 10 eV and 13 eV photon energy. These authors studied the Br⁺ fragment ion formation between 10 eV and 12.5 eV. Only the ion-pair formation Br⁺/Br⁻ takes place in this range. More recently, Yencha et al. [6] published a synchrotron radiation work on Br₂. The ion-pair process is reported between 10.332 eV and 10.875 eV and discussed in detail. These authors also measured the TPES of Br₂ at high resolution [7].

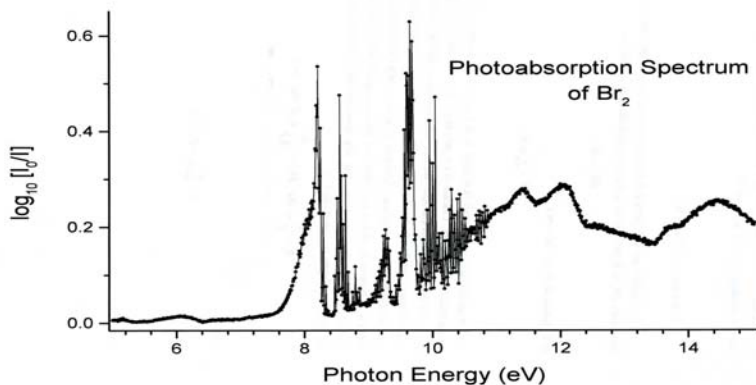


Fig. 1: Photoabsorption Spectrum of Br₂ in the 5.0 eV to 15.0 eV photon energy range.

We investigated the PAS and the PIMS of Br₂ by using the BESSY synchrotron radiation dispersed by a 3m-NIM monochromator. For recording the PAS, slits were set at 40μm whereas for the PIMS work, 200 μm slits were used. Fig.1 shows the PAS spectrum as observed

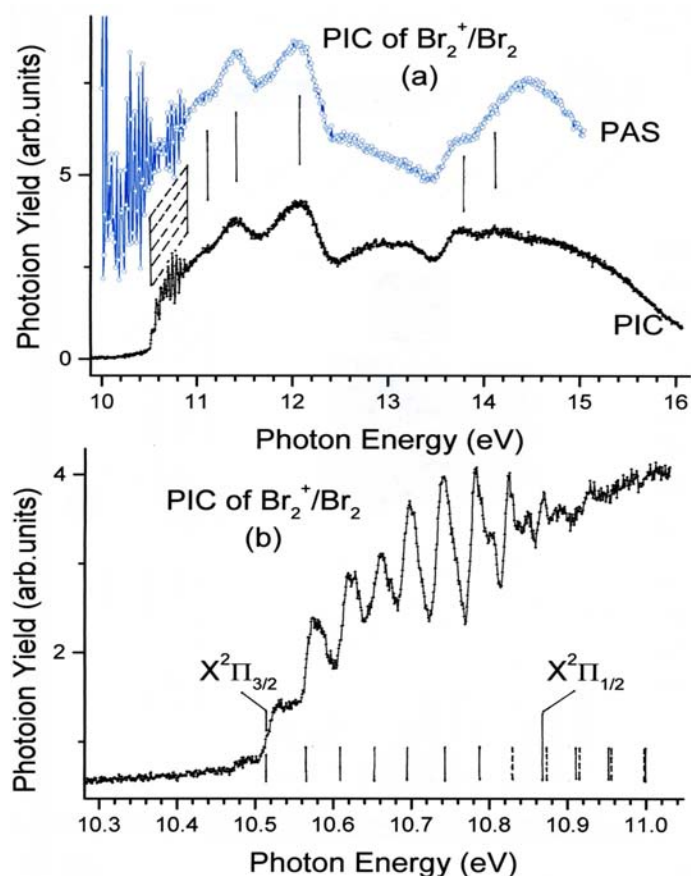


Fig. 2: Photoionization efficiency curve of $\text{Br}_2^+/\text{Br}_2$.

has already been analyzed in great detail by Venkateswarlu [3].

At high energy (10.5-15.0 eV) several weak sharp as well as weak broad features are observed. Fig. 2(a) clearly shows the close correlation between the structures observed in the PAS and the photoionization (PIC) as indicated by vertical bars. The dashed region corresponds to the dense fine structure measured in the threshold region.

Fig. 2(b) shows the ionization threshold region of Br_2 on an expanded energy scale. Vertical bars are positioned at critical energies corresponding to the two adiabatic ionization energies $X^2\Pi_{3/2}$ - $^2\Pi_{1/2}$ and to the vibrational progression observed in Br_2^+ determined by TPES [7]. Direct ionization as well as vibrational autoionization is involved. The lowest adiabatic ionization energy has been measured at 10.517 eV in excellent agreement with ZEKE-PFI-measurements [8].

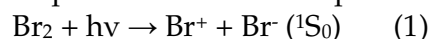
The efficiency of Br^+ production from Br_2 has been measured between 10eV and 15 eV photon energy. At high photon energy, i.e., above 14.0 eV the Br^+ ion current steeply increases reaching a maximum near 14.8 eV. Critical energies are measured at 13.98 eV, 14.1 eV, 14.26 eV, 15.51 eV and 15.62 eV and should correspond to the dissociative ionization Br_2 into $\text{Br}+\text{Br}^+$.

in the 5-15 eV photon energy range.

At low photon energy two broad bands are spread from 5.8 eV to 6.4 eV and 7.0 eV to 8.0 eV. The former is weak and structureless whereas the latter shows one or more vibrational progressions. This region has been measured carefully with 0.5 meV energy increments. About 50 vibrational levels are observed. Their analysis is in progress.

The medium (8.0-10.8 eV) photon energy range is characterized by numerous very sharp and strong to weak peaks. These are analyzed in terms of Rydberg series. The 8.2-10.5 eV region

Below 14 eV the ionization efficiency shows fairly strong resonance shaped features corresponding to the production of an ion-pair Br^+/Br^- through the reaction



where Br^+ is produced in its ground configuration $4p^4$ giving rise to $^3\text{P}_2$, $^3\text{P}_1$, $^3\text{P}_0$, $^1\text{D}_2$

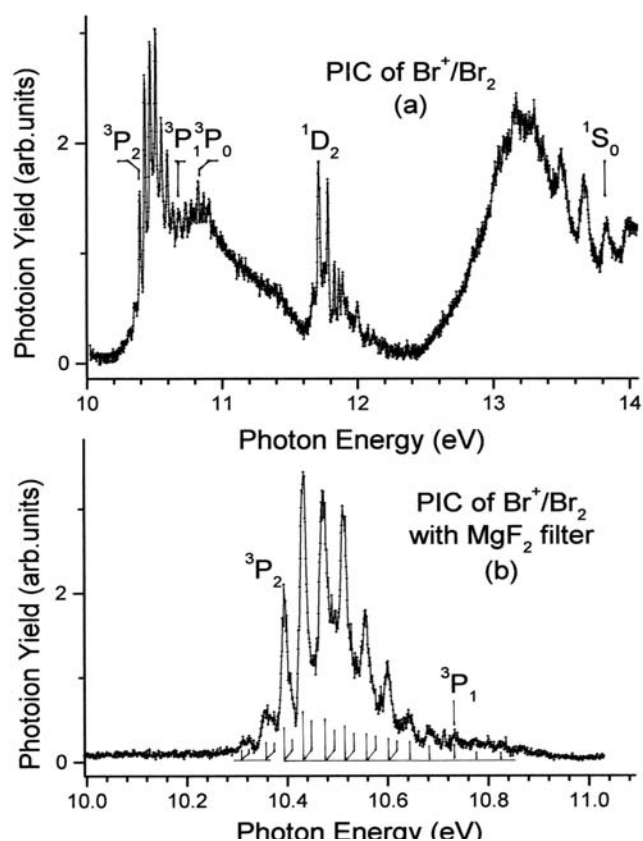


Fig. 3: The PIC of Br^+/Br_2 between 10-14 eV.

and $^1\text{S}_0$ electronic states. The corresponding thermochemical onsets of reactions (1) are displayed in Fig. 3(a). Furthermore, a fairly extended fine structure is observed upwards from the successive thresholds. The first band is shown on an expanded energy scale in Fig. 3(b) as recorded with a MgF_2 filter having a cutoff at 10.8 eV. A vibrational progression is observed with a characteristic wavenumber of $322 \pm 24 \text{ cm}^{-1}$ in very good agreement with earlier observations [6]. The resolution obtained in the present work allows us to highlight several "doublets" in this band corresponding to a second progression with the same wavenumber of 322 cm^{-1} but blue-shifted by 12 meV (96 cm^{-1}). Further analysis and assignment are in progress.

Acknowledgments.

The authors are indebted to the FNRS and the EU (Contract n°RII3-2004-506008) for financial support.

References.

- [1]. R. Locht, B. Leyh, H.W. Jochims, H. Baumgärtel, BESSY Annual Report (2005) 56.
- [2]. R. Locht, B. Leyh, H.W. Jochims, H. Baumgärtel, Chem. Phys. 317 (2005) 73.
- [3]. P. Venkateswarlu, Can.J.Phys. 47 (1969) 2525.
- [4]. J.D. Morrison, H. Hurzeler, M.G. Inghram, J.Chem.Phys. 33 (1960) 821.
- [5]. V.H. Dibeler, J. Walker, K.E. McCulloh, H.M. Rosenstock, J.Chem.Phys. 53 (1970) 4715; *ibid.* Intern.J.Mass Spectrom.Ion.Phys. 7 (1971) 209.
- [6]. A.J. Yencha, D.K. Kela, R.J. Donovan, A. Hopkirk, A. Kvaran, Chem.Phys.Letters 165 (1990) 283.
- [7]. A.J. Yencha, A. Hopkirk, A. Hiraya, R.J. Donovan, J.G. Goode, R.R.J. Maier, G.C. King, A. Kvaran, J. Phys.Chem. 99 (1995) 7231.
- [8]. T. Ridley, D.A. Beattie, M.C.R. Cockett, K.P. Lawley, R.J. Donovan, PCCP 4 (2002) 1398.

THE VUV PHOTOABSORPTION SPECTROSCOPY AND PHOTOIONIZATION OF HALOGENATED ETHYLENES: BROMO-DERIVATIVES.

R. Locht¹, B. Leyh¹, H.W. Jochims², H. Baumgärtel².

¹ *Molecular Dynamics Laboratory, Department of Chemistry, Institute of Chemistry, University of Liège, Sart-Tilman par B-4000 Liège 1, Belgium.*

² *Institut für Physikalische und Theoretische Chemie, Freie Universität Berlin, Takustrasse 3, D-14195 Berlin, Germany.*

For several years we investigate halogenated derivatives of methane and ethylene with focusing on the dynamics of highly excited states of their cations. For this purpose photoabsorption (PAS), photoelectron spectroscopies (PES, TPES and CIS), photoionization mass spectrometry (PIMS) and fragment ion translational energy (TES) spectroscopy are applied. Discharges in rare gases and synchrotron radiation are used as light sources. The VUV-PAS, PIMS, PES and TPES study of CH_3X ($\text{X}=\text{F}, \text{Cl}, \text{Br}$) [1,2,3] and $\text{C}_2\text{H}_3\text{X}$ ($\text{X}=\text{Cl}, \text{Br}$) [4,5] have been reported.

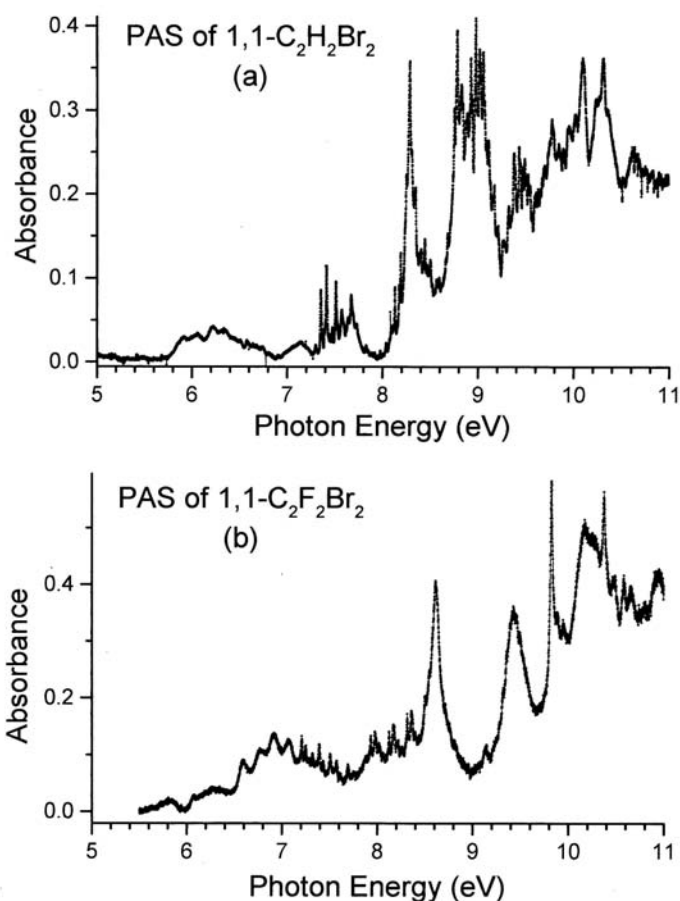


Fig. 1: VUV absorption spectrum of $1,1\text{-C}_2\text{H}_2\text{Br}_2$ compared with that of $1,1\text{-C}_2\text{F}_2\text{Br}_2$.

Almost all disubstituted derivatives of ethylene corresponding to $\text{C}_2\text{H}_2\text{X}_2$, where $\text{X}=\text{F}$ and/or Cl , have been extensively investigated by Kaufel [6] using synchrotron PIMS. Almost all fragment ions have been recorded and thermochemical data have been deduced.

In the frame of the present ongoing project, the PAS, PES, TPES and CIS spectra have been reported earlier for $1,1\text{-C}_2\text{H}_2\text{F}_2$ and the three isomers of $\text{C}_2\text{H}_2\text{Cl}_2$ [7]. However, data about the disubstituted bromoethylenes are very scarce. To the best of our knowledge only the VUV-PAS of *trans*- $1,2\text{-C}_2\text{H}_2\text{Br}_2$ [8] is available in the literature. PES spectra have been reported by Wittel and Bock [9]. PIMS work on *cis*- and *trans*-

$C_2H_2Br_2$ has been published by Momigny [10].

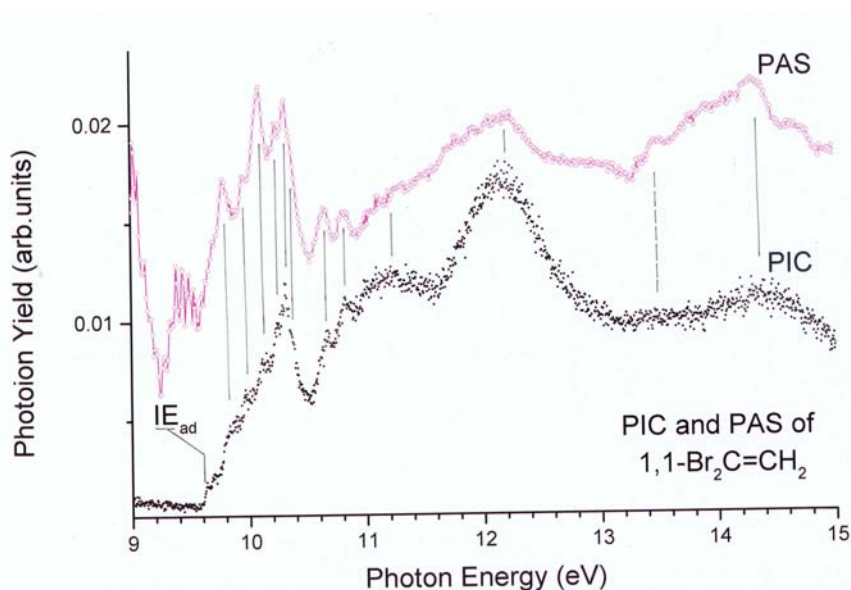


Fig. 2: Photoionization (PIC) and Photoabsorption (PAS) of 1,1- $C_2H_2Br_2$ between 9-15 eV photon energy.

The photoabsorption spectrum of 1,1- $C_2H_2Br_2$ has been recorded on the 3m-NIM beamline between 5 eV and 15 eV photon energy. The result is shown in Fig. 1(a) for the 5-11 eV photon energy range. Above the usual $\pi \rightarrow \pi^*$ valence transition, the Ryd-

berg transitions start up from 7.2 eV. The detailed analysis of this part of the spectrum is in progress. Interesting is the comparison with the corresponding difluorinated compound 1,1- $C_2F_2Br_2$ as displayed in Fig. 1(b) and recorded under the same conditions. Both spectra clearly show similarities but (i) the $\pi \rightarrow \pi^*$ transition is stronger and blue-shifted and (ii) several peaks, e.g., at 8.2 eV, 8.8 eV and near 10 eV in $C_2H_2Br_2$ are blue shifted in $C_2F_2Br_2$. This has very likely to be ascribed to the expected perfluoro-effect. It is also highly interesting to compare the PAS of these two latter compounds to those characterizing 1,1- $C_2H_2X_2$ and 1,1- $C_2F_2X_2$ (with X= F and/or Cl). These VUV spectra have been measured earlier [11].

The photoionization mass spectrum of 1,1- $C_2H_2Br_2$ recorded at 20 eV photon energy essentially shows three ions, i.e., $C_2H_2Br_2^+$, $C_2H_2Br^+$ and $C_2H_2^+$. Fig. 2 displays the photoionization efficiency curve (PIC) of $C_2H_2Br_2^+$ between 9.0-15.0 eV photon energy. The PAS of 1,1- $C_2H_2Br_2$ as measured in the high photon energy range is also displayed in Fig. 2. Vertical bars highlight the close correlation between the features observed in the PIC of the molecular ion and the PAS of the neutral molecule. IE_{ad} indicates the position of the adiabatic ionization energy $IE_{ad}(1,1-C_2H_2Br_2) = 9.612 \pm 0.010$ eV. This value is lower than the PES value of 9.63 eV reported by Wittel and Bock [9]. However, these authors do not mention the error limits on their reported measurements. At higher photon energies the vibrational structure is visible but more and more embedded in the autoionization structure.

Acknowledgments.

The authors are indebted to the FNRS and the EU (Contract n°RII3-2004-506008) for financial support.

References.

- [1]. R. Locht, B. Leyh, A. Hoxha, D. Dehareng, H.W. Jochims, H. Baumgärtel, Chem. Phys. 257 (2000) 283; R. Locht, J. Momigny, E. Rühl, H. Baumgärtel, Chem. Phys. 117 (1987) 305.
- [2]. R. Locht, B. Leyh, A. Hoxha, H.W. Jochims, H. Baumgärtel, Chem. Phys. 272 (2001) 259; R. Locht, B. Leyh, A. Hoxha, D. Dehareng, K. Hottmann, H.W. Jochims, H. Baumgärtel, Chem. Phys. 272 (2001) 293.
- [3]. R. Locht, B. Leyh, H.W. Jochims, H. Baumgärtel, Chem. Phys. 317 (2005) 73; R. Locht, B. Leyh, D. Dehareng, K. Hottmann, H.W. Jochims, H. Baumgärtel, 323 (2006) 458.
- [4]. R. Locht, B. Leyh, K. Hottmann, H. Baumgärtel, Chem. Phys. 220 (1997) 207.
- [5]. A. Hoxha, R. Locht, B. Leyh, D. Dehareng, K. Hottmann, H.W. Jochims, H. Baumgärtel, 260 (2000) 237; *ibid.* Chem. Phys. 256 (2000) 239.
- [6]. R. Kaufel, Ph.D. Dissertation, FU Berlin (1985).
- [7]. R. Locht, B. Leyh, H.W. Jochims, H. Baumgärtel, BESSY Jahresbericht (1996) 156; B. Leyh, R. Locht, K. Hottmann, H. Baumgärtel, BESSY Jahresbericht (1995) 163.
- [8]. K. Wittel, W.S. Felps, L. Klasinc, S.P. Glynn, J. Chem. Phys. 65 (1976) 3698.
- [9]. K. Wittel, H. Bock, Chem. Ber. 107 (1974) 317.
- [10]. J. Momigny, Bull. Classe Sci. Acad. Roy. Belg. 46 (1960) 686.
- [11]. R. Locht, B. Leyh, H.W. Jochims, H. Baumgärtel, BESSY Jahresbericht (2005) 56.

Lamellar Structured Nanoparticles formed by Complexes of a Cationic Block Copolymer and Perfluorodecanoic Acid

André Laschewsky^{1,2}, Murat Mertoglu¹, Stefan Kubowic^{2,3}, and Andreas F. Thünemann⁴

¹ University of Potsdam, Institute of Chemistry, Karl-Liebknecht-Str. 24-25, 14476 Potsdam-Golm, Germany, laschews@rz.uni-potsdam.de

² Fraunhofer Institute of Applied Polymer Research IAP, Geiselbergstr. 69, 14476 Potsdam-Golm, Germany, laschewsky@iap.fhg.de

³ Max Planck Institute of Colloids and Interfaces, Am Mühlenberg 1, 14476 Golm, Germany

⁴ Federal Institute for Materials Research and Testing, Richard-Willstaetter-Str.11, 12489 Berlin, Germany

Being interested in nanoparticulate polymeric carriers for biomedical uses, we explored the complexation of sodium alkanoates as model ionic surfactants with a cationic double hydrophilic block copolymer. We present the initial step of a long term project aimed at the understanding of the influence of BICs on the secondary structure of proteins and peptides.

A double hydrophilic block copolymer was synthesized by controlled free radical polymerization, namely by the RAFT method, from a poly(ethylene oxide) macromonomer and a cationic acrylate. Stoichiometric complexes with sodium decanoate (H-BIC) and with sodium perfluorodecanoate (F-BIC) were prepared by self-assembly. Both complexes are soluble in water forming core-shell nanoparticles with hydrodynamic radii of 54 nm and 22 nm, respectively, and neutral zeta potentials. The complex containing decanoate decomposed upon dilution, while the complex with perfluorodecanoate is stable even against dialysis and in salt solution.

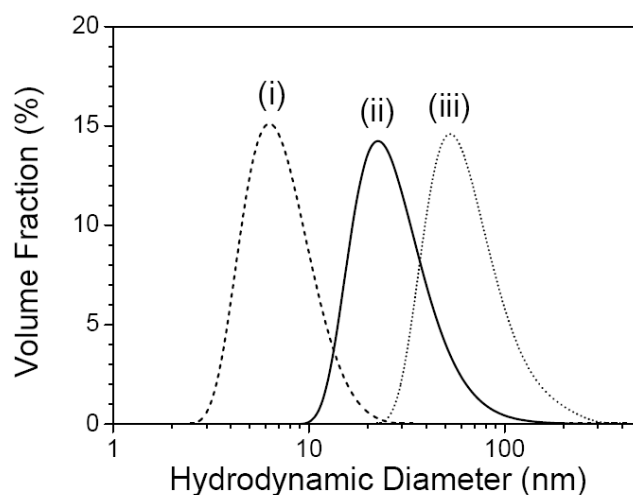


Figure 1-DLS analysis of (i) polyM1-block-M2 (dashed line), (ii) the F-BIC (solid line) and (iii) H-BIC (dotted line) in aqueous solution. The maxima are at 6 nm, 22 nm and 54 nm, respectively.

Only the nanoparticles containing perfluorodecanoate show a strong contrast in small-angle X-ray scattering (SAXS). It is produced from their cores that have an elliptical shape (short axes = 8.5 nm, long axis = 23.3 nm) and a sharp density transition to the shell.

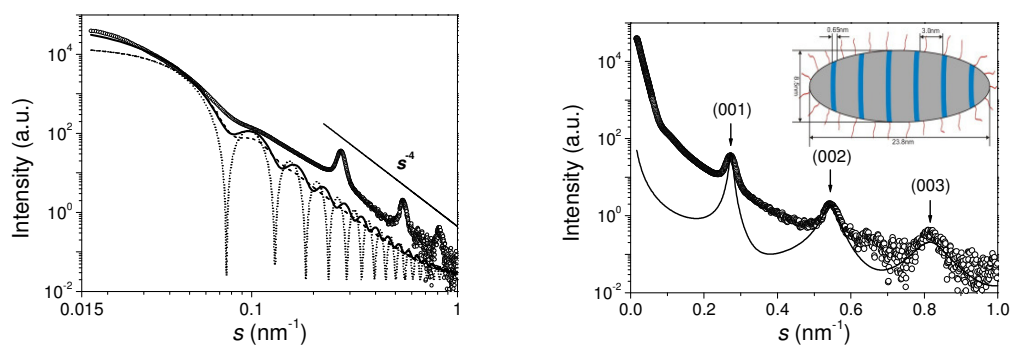


Figure 2 a) Small-angle X-ray scattering of F-BIC nanoparticles (symbols) and the scattering curves of monodisperse spheres ($R = 9.5$ nm, dotted line), polydisperse spheres ($R = 9.5$ nm, $\sigma = 0.14$, dashed line) and prolate ellipsoids (short semiaxis = 8.5 nm, long semiaxis = 23.8 nm, $\epsilon = 2.8$ nm, solid line). b) Arrows indicate the scattering maxima at 0.274, 0.544 and 0.820 nm⁻¹. The solid line corresponds to a stack of lamellae with a periodicity of $L = 3.65$ nm and with thicknesses $d_1 = 3.00$ nm and $d_2 = 0.65$ nm of the lamellae rich in perfluoroalkyl groups and ionic groups, respectively ($\sigma_1 = \sigma_2 = 0.2$ nm). The inset shows a sketch of the core structure of F-BIC nanoparticles.

The cores exhibit an internal lamellar structure with a long period of 3.65 nm consisting of fluorocarbon rich lamellae ($d_1 = 3.00$ nm) and lamellae enriched in ionic groups ($d_2 = 0.65$ nm). These fluorinated nanoparticles coexist in physiological buffer with human serum albumin and fibrinogen without inducing aggregation. Moreover, the content of α -helix of these serum proteins increased when in solution with the fluorinated nanoparticles.

The F-BIC nanoparticles exemplify the potential of functional/complex polymers which can be synthesized via RAFT in water. For any biomedical application of polymer-based nanoparticles, the structure of such a polymer should be well defined, and this can be achieved via RAFT polymerization in water. Importantly, all the steps for the preparation of nanoparticles including polymer synthesis were carried out in water. Therefore, the risk of having residual organic solvents in hydrophobic core of particles, which may cause serious problems for any in vivo application, can be excluded in this strategy, as well.

- [1] A. Laschewsky, M. Mertoglu, S. Kubowic, A. F. Thünemann, *Macromolecules* **2006**, 39, 9337-9345

Femtosecond VUV Photon Pulses for Time-resolved Photoelectron Spectroscopy

Philippe Wernet, Jérôme Gaudin, Kai Godehusen, Olaf Schwarzkopf, Wolfgang Eberhardt

BESSY, Albert-Einstein-Strasse 15, D-12489 Berlin, Germany

1. Introduction

At synchrotron radiation sources such as BESSY photons with energies of 20-2000 eV (62-0.62 nm) allow for unique insights into the electronic structure of materials with x-ray spectroscopy. A new dimension could be added to these investigations with ultrashort x-ray pulses by studying the evolution of the electronic structure in real time with pump-probe schemes. The application of synchrotron radiation to ultrafast processes, however, is limited by the intrinsic picosecond pulse length. X-ray free electron lasers (FELs) promise great progress and first results on pump-probe spectroscopy at such a source have been obtained recently [1]. We use high harmonic generation (HHG) in rare gases [2-5] as a laser-based source of femtosecond (fs) vacuum ultra violet (VUV) and soft x-ray pulses to help developing tools needed for future ultrafast spectroscopy at FELs [6-8]. Our aim is to explore the potential of ultrafast x-ray spectroscopy for the study of electronic structure in real time.

2. Experiment

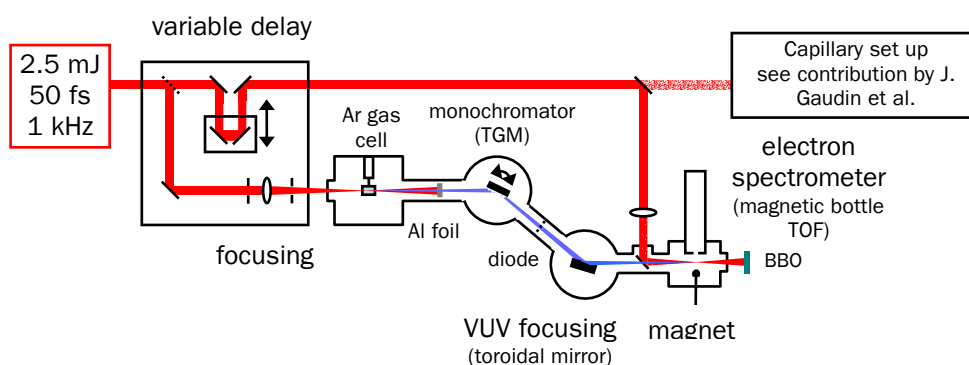


Fig. 1. Setup for ultrafast photoelectron spectroscopy in the gas phase based on HHG.

Our HHG source is driven by a fs laser (maximum pulse energy 2.5 mJ, 1 kHz, 50 fs, 800 nm Ti:Sa, multipass amplifier). The higher harmonics are generated in Xe or Ar gas cell and a grating monochromator is used to select single harmonics. The VUV radiation is

focused with a toroidal mirror to a spot size of about $50 \times 100 \mu\text{m}^2$. Up to 10^{10} photons/(s · 250 meV bandwidth · 100 μm spot size) are generated with pulse durations down to 60 fs. Photoelectrons are detected with a magnetic bottle type time of flight electron spectrometer. Figure 1 schematically depicts the experimental setup. IR (800 nm)-pump and VUV-probe beams intersect in the source volume of the electron spectrometer. Sidebands in rare-gas photoelectron spectra [9] are used to temporally characterize the VUV pulses.

3. Results and Discussion

Figure 2 depicts 3p photoelectron spectra of Ar gas. Side bands (red) [9] between the main lines (blue) that originate from the different harmonics indicate temporal overlap between pump and probe pulses. They result from two-photon ionization where an IR photon is absorbed or emitted simultaneously with the absorption of the VUV photon. Their intensity is used to characterize the temporal resolution of our set up (cross correlation).

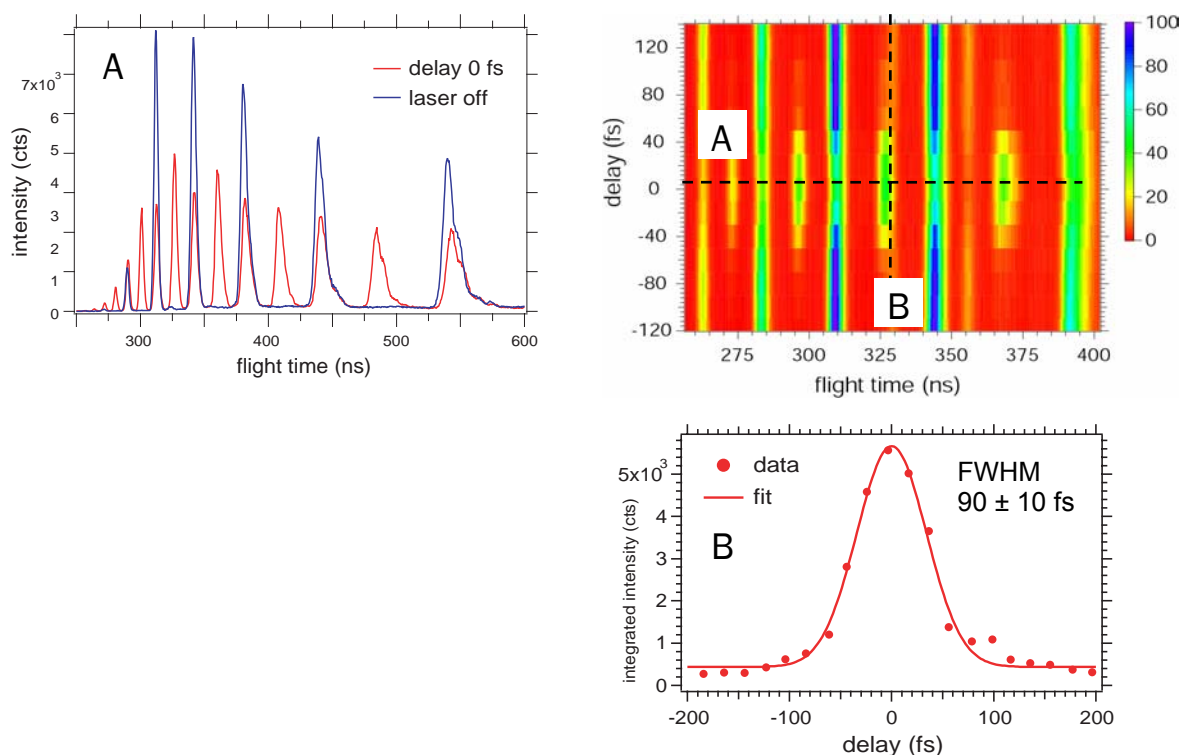


Fig. 2. Ar 3p photoelectron spectra (intensity vs. time of flight) taken in zero order of the monochromator for zero pump-probe delay (upper left panel). The 2D plot (upper right panel) depicts photoelectron intensities as a function of flight time and pump-probe delay. The side bands between the main lines and concomitant depletion of the main lines are clearly visible. The lower right panel corresponds to a section through the 2D plot for one of the side bands. A Gaussian fit to the data points with FWHM of 90 fs indicates a VUV pulse length of around 60 fs.

A cross correlation measurement for monochromatized harmonics is shown in figure 3. Through diffraction on the grating the 60 fs VUV pulses are stretched in time resulting in a duration of the monochromatized pulses of around 120 fs.

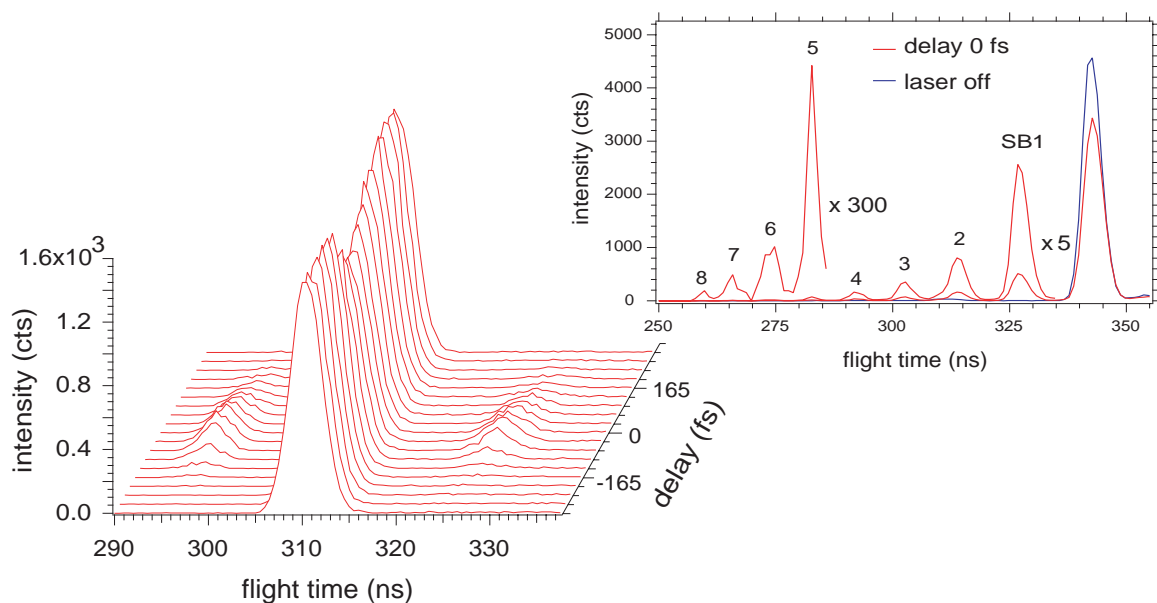


Fig. 3. Ar 3p photoelectron spectra (lower left panel) taken with one harmonic as a function of pump-probe delay. A fit to the side band intensities (not shown) reveals a FWHM of 120 fs. Ar 3p spectra are compared in the panel on the upper right for zero delay and for laser off. Up to eight sidebands are observed.

4. Conclusions

Femtosecond VUV pulses were generated with intensities suitable for ultrafast photoelectron spectroscopy. Our results demonstrate the possibility to include both versatility of the source for spectroscopy by being able to choose from different harmonics (photon energies) and high temporal resolution in the fs regime. Following pioneering investigations with fs VUV pulses for gas phase [7] and surface spectroscopy [8] we aim at investigating the electronic structure of various materials in real time with ultrafast photoelectron spectroscopy. Besides getting unprecedented insights into ultrafast phenomena this approach helps developing tools and methods for future x-ray FEL sources.

References

- 1 M. Meyer et al. *Phys. Rev. A* **74**, 011401(R) (2006).
- 2 E. Constant et al., *Phys. Rev. Lett.* **82**, 1668 (1999).
- 3 M. Schnürer et al., *Phys. Rev. Lett.* **83**, 722 (1999).
- 4 E. Takahashi et al., *Phys. Rev. A* **66**, 021802 (2002).
- 5 E. Gibson et al., *Phys. Rev. Lett.* **92**, 033001 (2004).
- 6 A. L’Huillier et al., *Eur. Phys. J. D* **26**, 91 (2003).
- 7 L. Nugent-Glandorf et al., *Phys. Rev. Lett.* **87**, 193002 (2001).
- 8 M. Bauer et al., *Phys. Rev. Lett.* **87**, 025501 (2001).
- 9 E. S. Toma et al., *Phys. Rev. A* **62**, 061801(R) (2000).

X-ray absorption spectroscopy on Na_xCoO_2

T. Kroll¹, J. Geck², H.J. Grafe¹, M. Knupfer¹, D. Batchelor³, C. Malbrich¹, L. Dunsch¹, H. Berger⁴, C.T. Lin⁵, D.P. Chen⁵, and B. Büchner¹

¹*IFW Dresden, P.O. Box 270016, 01171 Dresden, Germany*

²*University of British Columbia, Vancouver, Canada*

³*BESSY, 12489 Berlin, Germany*

⁴*Institute of Physics of Complex Matter, EPFL, CH-1015 Lausanne, Switzerland*

⁵*Max-Planck-Institut für Festkörperforschung, 70569 Stuttgart, Germany*

Introduction:

The discovery of an unexpectedly large thermopower accompanied by low resistivity and low thermal conductivity in Na_xCoO_2 [1] raised significant research interest in these materials. This interest has strongly been reinforced by the discovery of superconductivity in the hydrated compound $\text{Na}_{0.35}\text{CoO}_2 \cdot 1.3\text{H}_2\text{O}$ in 2003[2]. The similarity of the Na cobaltates to the high temperature superconductors (HTSC) - both are transition metal oxides and adopt a layered crystal structure with quasi-two-dimensional $(\text{Cu},\text{Co})\text{O}_2$ layers - is an important aspect of the research activities. In contrast to the HTSC cuprates however, the CoO_2 layers consist of edge sharing CoO_6 octahedra which are distorted in a way that the resulting symmetry is trigonal. In trigonal symmetry, the formerly degenerate t_{2g} states are split into an a_{1g} orbital pointing along the (111) direction, and a two-fold degenerate e_g' level.

Experimental details:

The NEXAFS measurements of the absorption coefficient were performed at the UE52-PGM beamline at the synchrotron facility BESSY II, Berlin, analyzing the drain current. The energy resolution was set to 0.09 eV and 0.16 eV for photon energies of 530 eV and 780 eV, respectively. We performed measurements on different nonhydrated single crystals with a sodium content between $x=0.4$ and $x=0.75$ at various temperatures and different polarizations of the incident synchrotron light at the oxygen K -, cobalt $L_{2,3}$ -edge, and sodium K -edge. For simplicity reasons, results from only two samples will be shown. All the crystals were of the same size of about 3mm x 3mm area and 1 mm thickness. Crystals were freshly cleaved *in situ* under ultrahigh vacuum conditions (about $2 \cdot 10^{-10}$ mbar at 25 K), which resulted in shiny sample surfaces.

Results:

In Fig. 1 experimental spectra of the Co $L_{2,3}$ -edges for $x=0.4$ and $x=0.6$ are shown, which display three main features at each edge: one strong central peak (peak b and b') with a shoulder towards higher energies (peak c and c') and a peak or shoulder towards lower energies (peak a and a'). Comparing these results to the similar compound LiCoO_2 and performing cluster calculations, one can assign the low energy features a and a' to excitations into a_{1g} levels of Co^{4+} , peaks b and b' to excitations into Co^{3+} e_g levels, and peaks c and c' to excitations into Co^{4+} e_g levels [3,4,5,6]. This interpretation is furthermore supported by the doping dependence of the L -edge as the low energy peak appears stronger for lower sodium doping, i.e. (higher Co^{4+} concentration) and weaker for higher sodium doping (i.e., lower Co^{4+} concentration) [5].

The a_{1g} orbital of the ground state in trigonal symmetry points along the (111) direction of the distorted CoO_6 octahedra, i.e., parallel to the crystallographic c axis, while the two e_g orbitals point perpendicular to it. From polarization dependent measurements with the \mathbf{E} vector of photons parallel and 70° to the crystal c axis one observes the a_{1g} peak of Co^{4+} to be stronger for $\mathbf{E} \parallel c$ as compared to $\mathbf{E} \perp c$. This behavior is expected for a local trigonal distortion, where the t_{2g} ground states split into states with a_{1g} and e_g' symmetry, whereas the e_g states remain untouched and therefore should not show a strong polarization dependence. Different

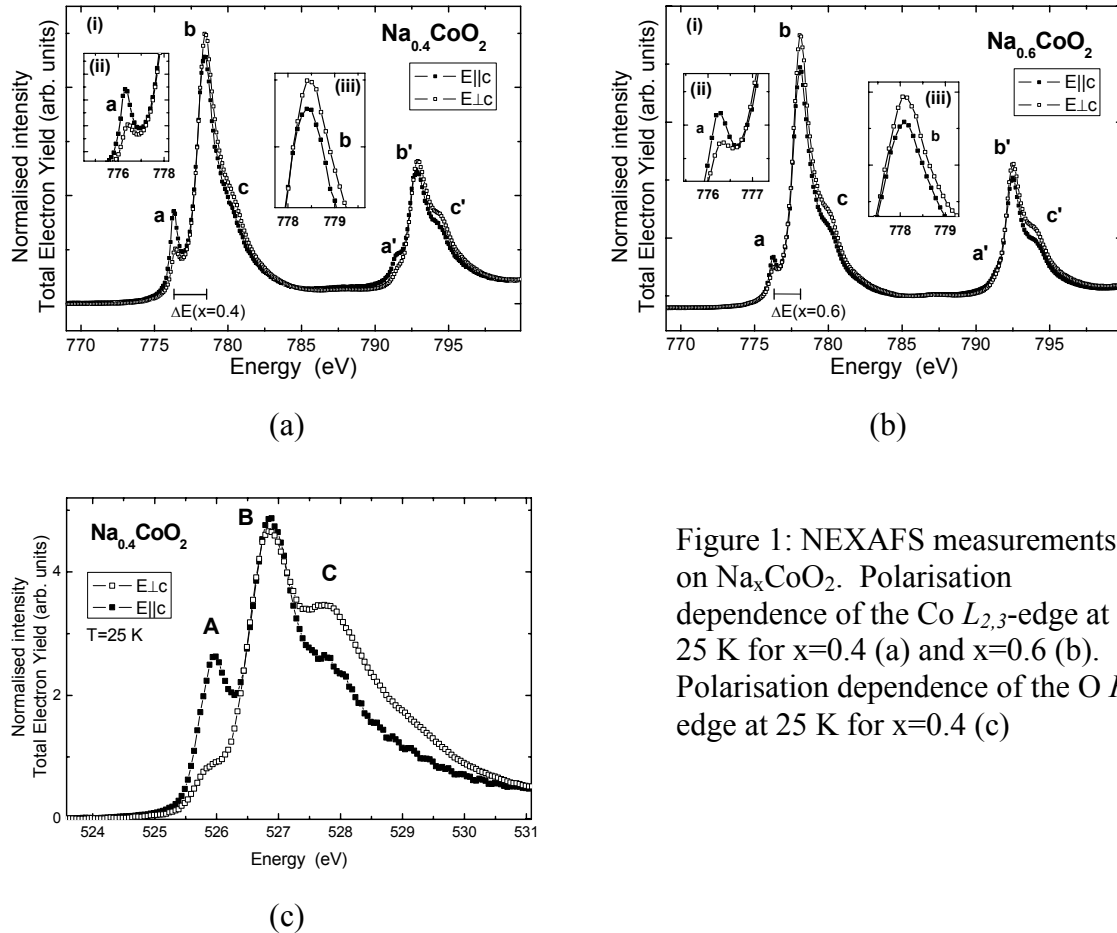


Figure 1: NEXAFS measurements on Na_xCoO_2 . Polarisation dependence of the Co $L_{2,3}$ -edge at 25 K for $x=0.4$ (a) and $x=0.6$ (b). Polarisation dependence of the O K -edge at 25 K for $x=0.4$ (c)

from that, the intensity of the Co^{3+} central peak is significantly larger for $E\perp c$ compared to $E||c$ (Fig. 1(a) and (b)), which is unexpected from symmetry arguments and also from the calculations done. This effect points to an additional distortion that splits the e_g levels. Note that no significant temperature dependence has been observed at the Co $L_{2,3}$ -edge for temperatures between 25 and 732 K [5].

NEXAFS measurements of the O K -edge showed three peaks (see Fig. 1(c)). Peak A results from excitations into unoccupied a_{1g} levels of Co^{4+} , peak B from excitations into e_g levels of Co^{4+} , and peak C from excitations into e_g states of Co^{3+} [4,5]. As it can be seen in Fig. 1(c), peak A is stronger for light polarised parallel to the crystallographic c -axis and peak B does not show a significant polarisation dependence, as expected for trigonal symmetry. However, peak C exhibits a clear polarisation dependence with a higher intensity for $E\perp c$ than for $E||c$, similar to the Co $L_{3,2}$ -edge. This finding supports the idea, that for octahedra containing a nominal Co^{4+} central ion, the local symmetry is indeed trigonal, whereas for octahedra containing a nominal Co^{3+} central ion, the local symmetry is additionally distorted. This additional distortion has to lead to a splitting of the formerly degenerate e_g levels. Note that even in this case a polarisation dependence is the effective valence at the Co ion is less than the nominal valence of $3+$, i.e. only in case of large hybridization. Theoretically, a large hybridization has indeed been found from cluster calculations [6].

Bibliography:

- [1] Terakasi *et al.*, Phys. Rev. B **56**, R12 685 (1997)
- [2] K. Takada *et al.*, Nature **422**, 53 (2003)
- [3] J. van Elp *et al.*, Phys. Rev. B **44**, 6090 (1991)
- [4] W.B. Wu *et al.*, **94**, 146402 (2005)
- [5] T. Kroll *et al.*, Phys. Rev. B **74**, 115123 (2006)
- [6] T. Kroll *et al.*, Phys. Rev. B **74**, 115124 (2006)

Orbital/Spin moment ratio dependence of Co-Pt nanoparticles upon Pt concentration and preparation conditions

P. Imperia^{a,b}, P. Andreazza^c, J. Penuelas^c, C. Andreazza-Vignolle^c

^aUniversität Hamburg, Institut für Experimentalphysik, Luruper Chaussee 149, 22761 Hamburg, Germany

^bHahn-Meitner-Institut-Berlin, Glinicker Str. 100, 14109 Berlin, Germany

^cCentre de Recherche sur la Matière Divisée, UMR6619, CNRS-University of Orléans, 1B rue de la Férollerie, 45071 Orléans Cedex 2 France

Co-Pt and pure Co nanoparticles of ~ 2 nm diameter having different composition and crystal structure have been studied by X-ray magnetic circular dichroism (XMCD) at the Co $L_{2,3}$ edges at beam line UE46 PGM of the synchrotron radiation facility BESSY, Berlin with the high magnetic field chamber of the Hahn-Meitner-Institut. The magnetic properties of the samples measured at 3.4 K and covered with a thin protecting layer of Al_2O_3 , depend on the composition and crystallographic order. Furthermore, a small oxide contamination has a huge impact on the calculated orbital and spin moment values. While pure Co nanoparticles reveal an orbital to spin moment ratio of about $\mu_l/\mu_s = 0.10$ in perfect agreement with the value expected for Co thin films, Co-Pt mixed nanoparticles show a μ_l/μ_s ratio that depends on the relative amount of Co and Pt, linearly increasing from $\mu_l/\mu_s = 0.11$ for nanoparticles having 91% of Co and 9% Pt, to $\mu_l/\mu_s = 0.14$ when the Co amount is reduced to only 38%. Samples having a core of Pt and the Co segregated at the surface show μ_l/μ_s values similar to the disordered mixed samples of the same composition. The samples with a small CoO contamination show a very high μ_l/μ_s ratio with, for example, $\mu_l/\mu_s = 0.25$ in a sample having 71% Co mixed with 29% Pt. The annealing of the samples increases the dimension of the nanoparticles promoting their aggregation and, interestingly, it increases also the orbital to spin moment ratio, with respect to the non annealed samples of similar composition, induced probably by the formation of an ordered L10 phase.

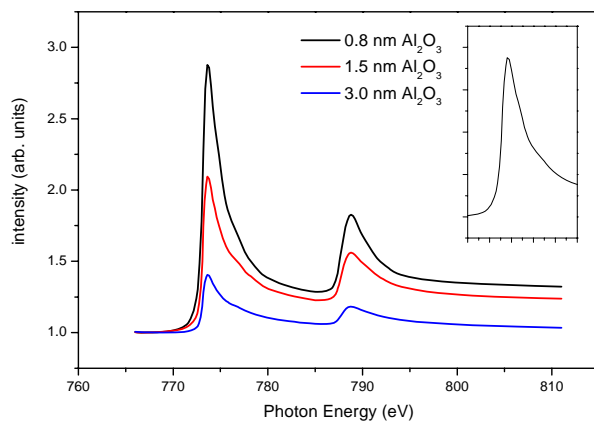


Figure 1: Absorption spectra at different Al_2O_3 coverage.

The development of metal thin film media containing small particles of tight size distribution, optimized in composition and crystallographic structure is one key feature for the progress in ultra-high-density magnetic recording devices. Surface-supported nanoparticles offer additional degrees of freedom to tune the magnetic properties by controlled modifications of the particle size, shape and interactions with the substrate. These characteristics make nanosized systems attractive for fundamental studies as well as for applications.

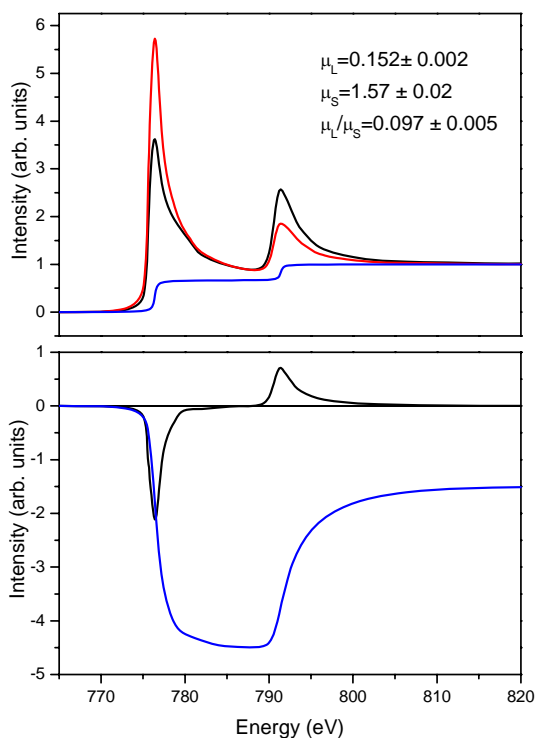


Figure 2: 100% Co sample.

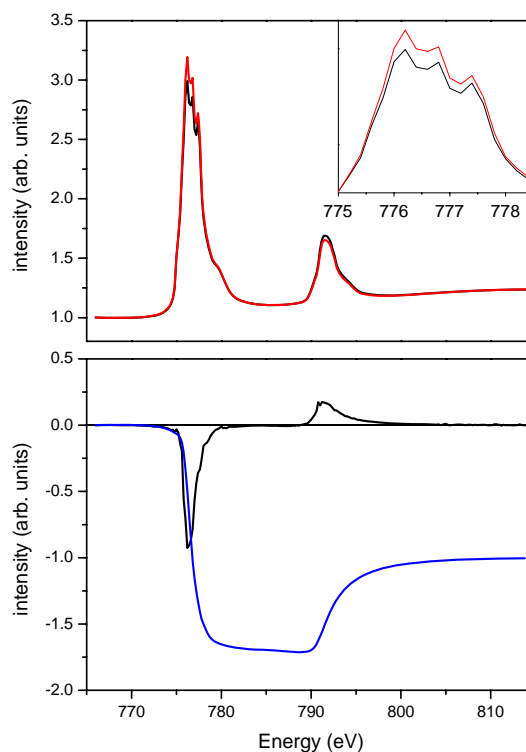


Figure 3: CoO contaminated sample.

The magnetic anisotropy energy or the orbital moment are very sensitive to the atomic neighbouring (surface or interface atoms) of magnetic Co atoms contained in nanosized particles. By assembling cobalt nanoparticles containing less than 40 atoms (smaller than 1 nm size) on Pt substrate [1], the latter parameters display an increase with the decreasing of Co atoms coordination. Also studies of thin films and multilayers have shown that adding platinum to cobalt gave materials with very high magnetocrystalline anisotropy. The Co-Pt system maximizes the magnetic anisotropy energy of the Co 3d ferromagnetic phase, owing the strong spin-orbit coupling of Pt 5d states making it particularly interesting. Co-Pt alloys can be obtained over a wide range of compositions as bulk. For either cobalt or platinum rich alloys, Co_3Pt and CoPt_3 , a chemically ordered (L12 structure) as well as a disordered structure can be observed. For the compositions near 50/50, a face centred cubic (fcc) disordered phase and a face centered tetragonal (fct) L10 ordered phase can be obtained by annealing at the correct temperature. This latter structure can be described as alternate cobalt and platinum (001) planes, giving rise to a magnetocrystalline anisotropy along the (001) axis.

A vapour deposition setup has been used to produce the Co and Co-Pt nanoparticles. The Si substrate with a thin SiO_2 over-layer has been chosen to limit the cluster-substrate interactions. The possibility of tuning the growth in term of nanoparticles morphology, density and size in the range of 1 to 4 nm is very suitable to prepare materials of controlled assemblage [2]. The growing parameters allow a great versatility regarding morphology and atomic arrangement [3]. The Co and Co-Pt nanoparticles were formed in ultra high vacuum conditions. Before deposition the substrates were degassed for 15 minutes at 650°C . The sample preparation conditions are described in reference [4]. After preparation the samples have been capped in situ with few MLs of Al_2O_3 . Figure 1 shows

the absorption spectra of the pure Co nanoparticles at the L-edges for 3 different Al₂O₃ thicknesses. Already 0.8 nm of Al₂O₃ corresponding to 4 MLs are enough to completely avoid sample oxidation [5]. The XMCD measurements have been done applying a static field of 6.5 T at 3.4 K. Figure 2 shows an example of the absorption spectra for parallel ($\mu+$, red line) and antiparallel ($\mu-$, black line) photon helicity (upper panel) and the corresponding XMCD signal together with its integral (blue line, in the lower panel) of a pure Co sample. This 100% Co reference sample, 4.0 \pm 0.2 nm diameter nanoparticles, shows a ratio $\mu_l/\mu_s = 0.097\pm 0.005$ as for thin layers. Increasing the amount of Pt mixed with the Co atoms the orbital spin moment ratio increases almost linearly. It goes to $\mu_l/\mu_s = 0.11$ with 78% Co and 22% Pt and to $\mu_l/\mu_s = 0.12$ when the proportion of Co-Pt is 74% and 26%, respectively. Finally, samples prepared mixing Co and Pt in a ratio of 38/62 have $\mu_l/\mu_s = 0.140\pm 0.005$. Samples having the Co segregated at the surface of the nanoparticles and a Pt core follow the same linear increases of the ratio μ_l/μ_s as the simply mixed samples [6] while one sample having a Co core and Pt shell of 2.5 nm diameter shows a much higher ratio $\mu_l/\mu_s = 0.20$.

An example of a CoO contaminated sample is shown in figure 3. Previous studies of Co nanoparticles prepared ex situ by chemical synthesis demonstrated that the presence on the surface of a small amount of CoO strongly enhances the orbital to spin moment ratio [7]. Also in this case the mixed samples have always higher values of the μ_l/μ_s ratio with respect to the same composition non contaminated ones. Samples with a Co core and Pt shell contaminated with a small amount of CoO show an enhanced ratio $\mu_l/\mu_s = 0.25$ at RT and $\mu_l/\mu_s = 0.28$ at 3.4 K. In the reversed configuration with a Pt core and a complete Co shell, where the CoO is probably on the Co surface, the enhancement of the μ_l/μ_s ratio caused by the simultaneous increases of the orbital moment and decreases of the spin moment reaches the high value of $\mu_l/\mu_s = 0.33$ at 3.4 K.

Already few monolayers of Al₂O₃ are enough to protect the nanoparticles from oxidation, the increase of quantity of Pt in the Co-Pt system seems to increase linearly the orbital to spin moment ratio and a very small amount of CoO on the surface increases this value considerably. Particular care must be taken when evaluating the magnetic properties of nanoparticles: small CoO contaminations have a strong impact on the magnetic properties measured by a surface sensitive technique like XMCD.

Acknowledgments

D. Schmitz, S. Rudorff and the BESSY staff are kindly acknowledged for their support during the measurements. Financial support of SFB 668 is gratefully acknowledged.

References

- [1] P. Gambardella, S. Rusponi et al., Science 300 (2003) 1130.
- [2] P. Brault et al., Eur. Phys. J.: Appl. Phys. 19 (2002) 83.
- [3] P. Andreatza et al., J. Nanopart. R. submitted.
- [4] J. Penuelas et al., J. Appl. Phys. submitted.
- [5] P. Imperia et al., J. Magn. Magn. Mater. accepted for publication (2006).
- [6] P. Imperia et al., paper in preparation.
- [7] P. Imperia et al., Phys. Rev. B 72 (2005) 014448.

Resonant inelastic x-ray scattering study of TCNQ and F4-TCNQ molecular solids

J.-J. Gallet¹, F. Bournel¹, N. Jaouen², F. Rochet¹, J.-M. Mariot¹

¹Laboratoire de Chimie Physique–Matière et Rayonnement (UMR 7614), Université Pierre et Marie Curie, 11 rue P. et M. Curie, 75231 Paris Cedex 05, France

²Synchrotron SOLEIL, L'Orme des Merisiers, Saint-Aubin, BP 48, 91192 Gif-sur-Yvette Cedex, France

Introduction

An important route to the enhancement of the functionality of electronic devices is to combine the characteristics of organic and inorganic materials within a single device. Thus the study of the structural and electronic properties of organic molecules deposited on semiconducting substrates is crucial.

In this report we present results of near-edge x-ray absorption fine structure (NEXAFS) spectroscopy and of high-resolution resonant inelastic x-ray scattering (RIXS) at the C and N 1s edges of tetracyano-quinomethane (TCNQ) (see inset to Fig. 1) and tetrafluoro-tetracyano-quinomethane (F4-TCNQ) deposited on silicon. In both techniques an incoming x-ray photon with an energy in the vicinity of a core electron binding energy is absorbed. In NEXAFS the strength of the dipolar absorption as a function of the photon energy is studied. This allows one to probe the unoccupied electronic states projected onto the atom involved, thanks to the localized character of the core hole left behind. In addition, by changing the orientation of the electric vector of the light relative to the surface, information on the orientation of the organic molecules within the deposited film is obtained. The high brilliance of modern synchrotron radiation sources also opens up the opportunity to study the energy spectrum of the radiative decay of the excited state created in the absorption process. The whole process has to be seen as a RIXS in which excitations above the neutral ground state are measured, again with the advantage of atomic element specificity. Finally it should be mentioned that the NEXAFS and RIXS signals are free from any contribution from the substrate, making both techniques very well suited to explore the electronic structure of adsorbates.

Experimental

The experiments were performed at BESSY on the high brilliance U41-PGM beamline and using a newly built plane-grating flat-field soft x-ray spectrometer [1]. Molecular solid films were deposited under ultra-high vacuum by evaporation onto a silicon wafer. During acquisition the sample was moved continuously with respect to the x-ray spot to limit the radiation damage. For both molecules, a RIXS spectrum at the N and C 1s edges was acquired in less than 15 min each spectrum with a resolution of ≈ 250 meV (emitted photons).

Results and discussion

The C and N 1s NEXAFS spectra of TCNQ are shown in Fig. 1 for grazing and normal incidence of a linearly polarised photon beam.

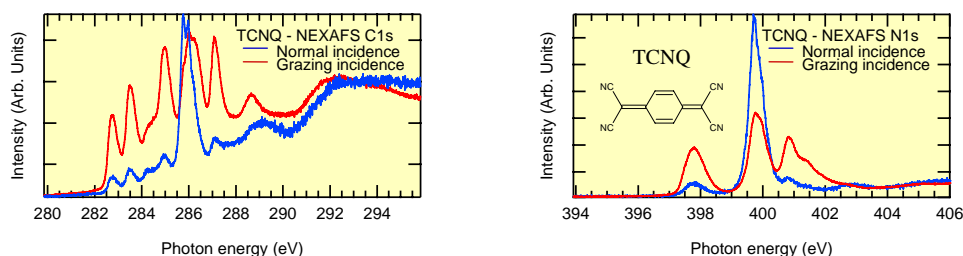


Fig. 1: C and N 1s NEXAFS spectra of TCNQ.

The three resonances at the N 1s edge vary strongly in intensity when the direction of the light polarization relative to the surface is changed. They correspond to transitions to molecular orbitals oriented either in (main central resonance) or out of (the other two resonances) the molecular plane. This strong linear dichroism – also observed for F4-TCNQ – shows that the molecules are not randomly oriented but lay rather flat on the surface of the substrate.

Because of the presence of numerous non-equivalent carbon atoms, the assignment of the C 1s edge structures to specific unoccupied molecular orbitals is much more difficult without the help of model calculations (underway) (see, e.g., Refs. 8, 9). The corresponding RIXS spectra are shown in Figs. 2 and 3 for excitations at the N 1s and C 1s edges respectively for TNCQ (left panels) and F4-TCNQ (right panels).

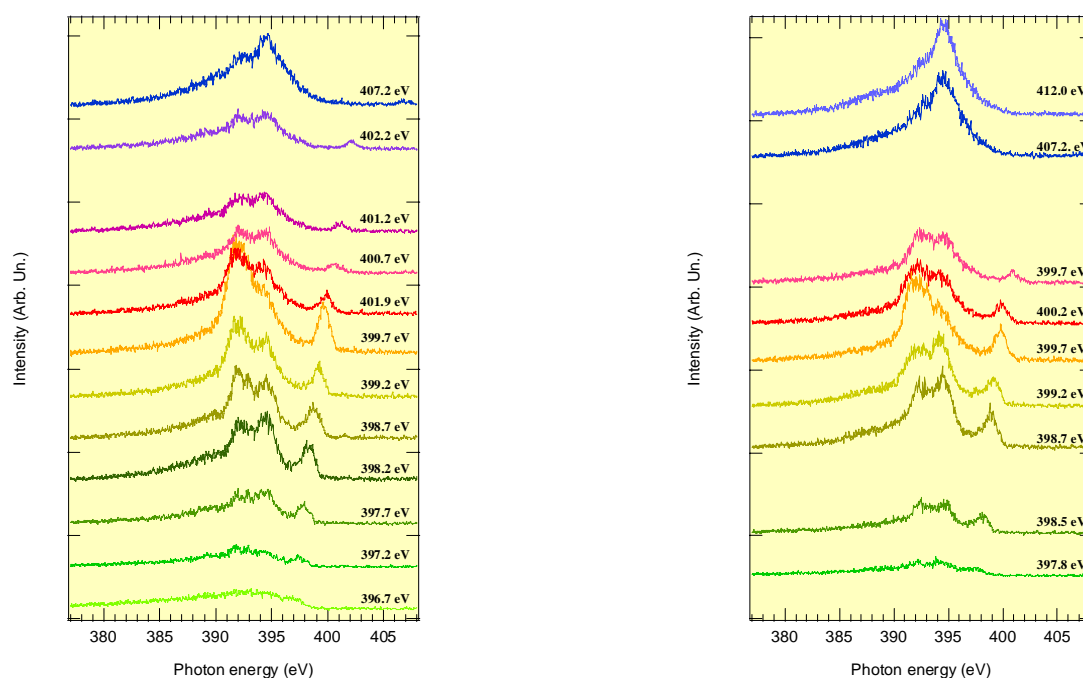


Fig. 2: RIXS spectra at the N 1s edge of TCNQ (left panel) and F4-TCNQ (right panel).

The RIXS spectra at the N 1s edge are very similar for both molecules. This means that the fluorine atoms bonded to the central ring have a limited influence on the nitrogen π states. No dispersive features are observed on the “spectator part” (excited “optical” final state). This is surprising as the promoted electron in the π^* NEXAFS final state should remain localized around the core hole.

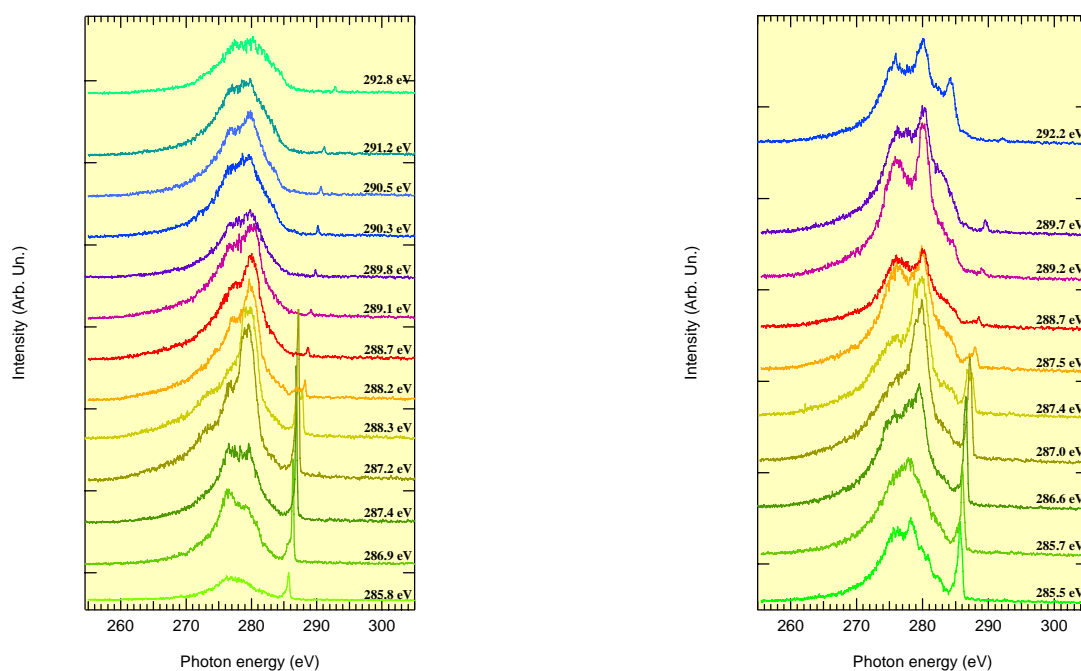


Fig. 3: RIXS spectra at the C 1s edge of TCNQ (left panel) and F4-TCNQ (right panel).

At the C 1s edge the resonant spectra are more complex due to the difference in chemical environment of the carbon atoms. Nevertheless the more structured emission spectra of F4-TCNQ differ strongly from that of TCNQ molecule. The large changes in shape and intensity of the various features have to be analyzed in more details with the help of calculations (these are underway).

At the C 1s edge (285–288 eV) low energy-loss features are present for both molecules. They are not observed for excitations at the N 1s edge (see Fig. 4). We attribute these energy-loss features to vibrational excitations. The strong dependence on the excitation energy of these features can be explained by the change in the scattering duration when the excitation energy is varied. On resonance the duration of the scattering process is long enough to allow the nuclear wave packet to evolve, allowing vibrational motion during scattering [4]. The contribution to these different vibrational levels appears in the emission spectra as energy-loss features, the shape of which is extremely sensitive to the excitation energy. Beyond the resonance only a single elastic peak is observed as detuning the excitation energy away from the resonance shortens the duration time of the scattering process; which suppresses the vibrational motion. This type of behaviour has already been reported on condensed ethylene [5].

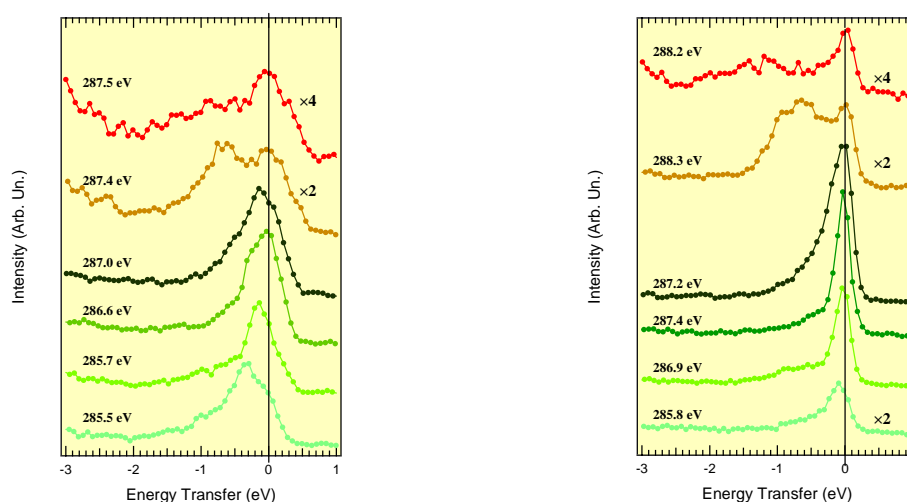


Fig. 4: RIXS spectra at the C 1s edge of TCNQ (left panel) and F4-TCNQ (right panel).

Acknowledgements

This work has been supported by the European Community Research Infrastructure Action [contact RII3-CT-2004-506008 (IA-SFS)].

References

- [1] C. F. Hague, J. H. Underwood, A. Avila, R. Delaunay, H. Ringuenet, M. Marsi, and M. Sacchi, *Rev. Sci. Instrum.* 76 (2005) 023110.
- [2] M. Bäessler, R. Fink, C. Buchberger, P. Väterlein, M. Jung, and E. Umbach, *Langmuir* 16 (2000) 6674.
- [3] J. Fraxedas, Y. J. Lee, I. Jiménez, R. Gago, R. M. Nieminen, P. Ordejon, and E. Canadell, *Phys. Rev. B* 68 (2003) 195115.
- [4] F. Gel'mukhanov and H. Ågren, *Phys. Rep.* 312 (1999) 87.
- [5] F. Hennies, S. Polyutov, I. Minkov, M. Nagasono, F. Gel'mukhanov, L. Triguero, M.-N. Piancastelli, W. Wurth, H. Ågren and A. Föhlisch, *Phys. Rev. Lett.* 95 (2005) 163002.

X-ray absorption study of electronic structure of Ni(II) phthalocyanine and porphyrins

S.A. Krasnikov^{1,2}, A.B. Preobrajenski^{1,3}, N.N. Sergeeva⁴, M.M. Brzhezinskaya¹, M.A. Nesterov¹, A.A. Cafolla², M.O. Senge⁴ and A.S. Vinogradov¹

¹ V.A. Fock Institute of Physics, St. Petersburg State University, 198504 St. Petersburg, Russian Federation

² School of Physical Sciences, Dublin City University, Glasnevin, Dublin 9, Ireland

³ MAX-lab, University of Lund, P.O. Box 118, S-22100 Lund, Sweden

⁴ School of Chemistry, SFI Tetrapyrrole Laboratory, Trinity College Dublin, Dublin 2, Ireland

Porphyrins (Ps) and phthalocyanines (Pcs) constitute a unique class of compounds that are ubiquitous in nature and function in a wide variety of roles ranging from oxygen transport, electron transfer, and oxidation catalysts to photosynthesis [1]. 3d transition metal (TM) Pcs and Ps are widely used in many technological applications due to their unique properties. The synthesis of novel TM porphyrins has received great attention in the last few years [2], while spectroscopic characterization of their electronic structure remains a less well investigated area. The central part of these complexes (3d-atom and its nearest neighbours) is known to be their most reactive component and to define their most important applications. The occupied and empty 3d electron states of the TM atom, located near the Fermi level and involved in chemical bonding, are essentially responsible for the interesting properties of these 3d compounds. A detailed knowledge of the 3d-related features of chemical bonding can be obtained with X-ray absorption (XA) spectroscopy due to its site and symmetry selectivity. The present work is aimed at revealing the chemical bonding features in NiPc and Ni porphyrins by studying the unoccupied electronic states in these compounds with high-resolution Ni 2p absorption spectra.

The XA measurements on the Ni(II) phthalocyanine (NiPc), Ni(II) tetrabenzoporphyrin (NiTBP), Ni(II) octaethylporphyrin (NiOEP), Ni(II) tetraisobutylporphyrin (NiTiBuP), Ni(II) diphenylporphyrin (NidPP) and Ni(II) diisobutylporphyrin (NidiBuP) were performed at the Russian-German beamline, BESSY II in the total electron yield detection mode. The metal sample was a nickel foil cleaned in vacuum. The samples of other compounds were in powder form. The photon-energy resolution at the Ni 2p (N 1s) absorption threshold was better than 150 meV (70 meV). The spectra were normalized to the incident photon flux monitored by a gold grid. The photon energy at the Ni 2p and N 1s edges was calibrated using the known positions of the first narrow peaks in the Ti 2p (459.0 eV) and F 1s (683.9 eV) absorption spectra of K₂TiF₆ [3].

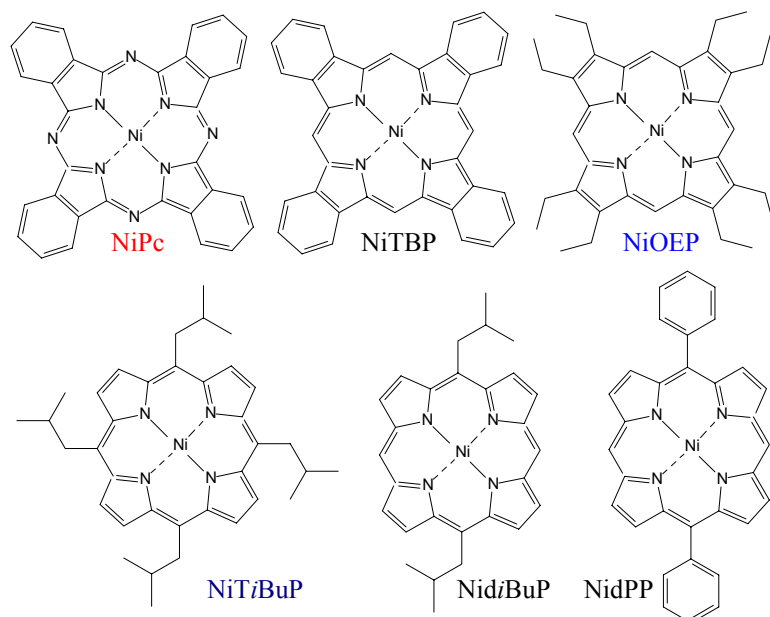


Fig. 1. Structural formulas of the studied Ni compounds.

NiPc and NiPs represent a class of flexible molecules with nearly square planar core conformation. The molecular structures of the Ni compounds under study are shown in Fig.1. Here we will mainly focus on the Ni atom and its nitrogen-type coordination spheres taking into account the symmetry (deviation from planarity) of the main part of NiP (Pc) – porphyrin (phthalocyanine) macrocycle. The studied Ni compounds have mainly the D_{4h} symmetry of the

macrocycle except for the ruffled porphyrins NiTzBuP (D_{2h}) and NiOEP (D_{2d}). The nickel atom formally has the electron configuration of the Ni^{2+} ion $[(3d_{xz,yz}e_g)^4(3d_{z^2}a_{1g})^2(3d_{xy}b_{2g})^2]$ in these Ni(II) compounds with D_{4h} symmetry.

The measured Ni 2p XA spectra for the studied Ni compounds are displayed in Fig. 2. The intensities of the absorption structures in the spectra have been normalized to the intensity of the main absorption line A.

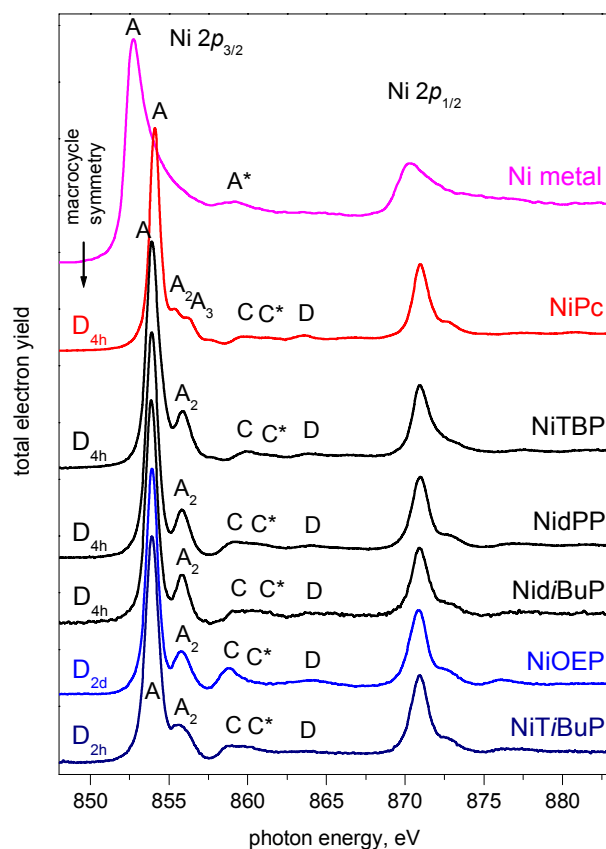


Fig. 2. Ni 2p XA spectra of the NiPc and NiPs compared to Ni 2p XAS of the Ni metal.

following comparative analysis of the Ni 2p and N 1s spectra of the NiPc and NiOEP, the main line A can be associated with transitions of Ni $2p_{3/2}$ electrons to the LUMO, which is weakly antibonding σ molecular orbital (MO) of b_{1g} symmetry with predominantly Ni $3d_{x^2-y^2}$ character (almost pure intra-atomic Ni $2p_{3/2} - 3d_{x^2-y^2}$ electron transitions), while the structures A_2 , C, C^* and D – with transitions to the empty states with hybridized Ni $3d - N 2p$ character (some contribution to the MOs responsible for the XA structures C, C^* and D can be due to the Ni $4s$, p states). The high-energy shift of the Ni 2p absorption in going from Ni metal to NiPc (1.4 eV) and NiPs (1.2 eV) is a result of a decrease in the effective number of 3d electrons on the Ni atom due to the strong Ni $3d - N 2p$ covalent bonding of the π type. This effect is well known as the back-donation [6], namely, an additional $3d\pi - 2p\pi^*$ charge transfer from the 3d atom to ligands with low-lying unfilled antibonding $2p\pi^*$ molecular orbitals. This metal-to-ligand charge transfer in the case of NiPc and Ni porphyrins occurs from the occupied Ni $3d_{xz,yz} \pi (e_g)$ orbitals to the unoccupied N $2p\pi^* (e_g)$ orbitals, resulting in the corresponding absorption bands (A_2 , A_3) in the Ni 2p XA spectra.

There are three main differences between the Ni $2p_{3/2}$ XA spectra (Fig. 3) of the NiPc and NiPs: (i) the reliably detected high-energy shift of the main absorption line A by 0.2 eV in the NiPc compared to NiPs, (ii) the increase in the energy separation between the A and A_2 absorption lines $\Delta E(A-A_2)$ from 1.3 eV to 1.8 – 2.0 eV in going from the NiPc to NiPs and (iii) the presence of the additional line A_3 separated in energy by 0.8 eV from A_2 in the XA spectrum of the NiPc. The first finding reflects larger transfer of the 3d electron density from the Ni atom to the ligands and the stronger Ni $3d\pi - N 2p\pi$ covalent bonding in the case of the

intensity of the main absorption line A. Examining the series of Ni $2p_{3/2}$ absorption spectra of the NiPc and NiPs one can see that the spectra are quite similar: the main absorption line A accompanied by a high-energy lines A_2 , C – D. In contrast to the NiPc and NiPs the Ni $2p_{3/2}$ XA spectrum of metallic Ni consists of only one main line A accompanied by the so-called “6-eV” satellite A^* that assigned to multiple scattering from the environment at intermediate range [4]. The difference between the absorption spectra of the Ni metal and the Ni(II) compounds can be understood within the framework of a quasi-molecular approach [5] with inclusion of the covalent mixing between the Ni and ligand atom valence electron states inside the quasi-molecule (NiN_4). The covalent bonding between the Ni and N atoms with participation of the Ni $3d$, $4s$ and N $2p$ electrons is responsible for the appearance of the additional $2p_{3/2}$ absorption bands in going from Ni metal to the NiPc and NiPs.

On the basis of comparison with the Ni 2p XA spectrum of Ni metal and the

NiPc compared to the NiPs. The splitting of the π -bonding related band A_2 in the NiPs into two structures A_2 and A_3 in the case of the NiPc may be explained by the presence of four additional N atoms in the *meso* positions of the Pc macrocycle. Thus, in the NiPc there are two different nitrogen sites (pyrrole and bridging N atoms), and it is reasonable to suppose that there are two corresponding low-lying unfilled antibonding N $2p\pi^*$ molecular orbitals.

As can be seen, the absorption structure A_2 has a broader shape in the case of NiTiBuP and NiOEP.

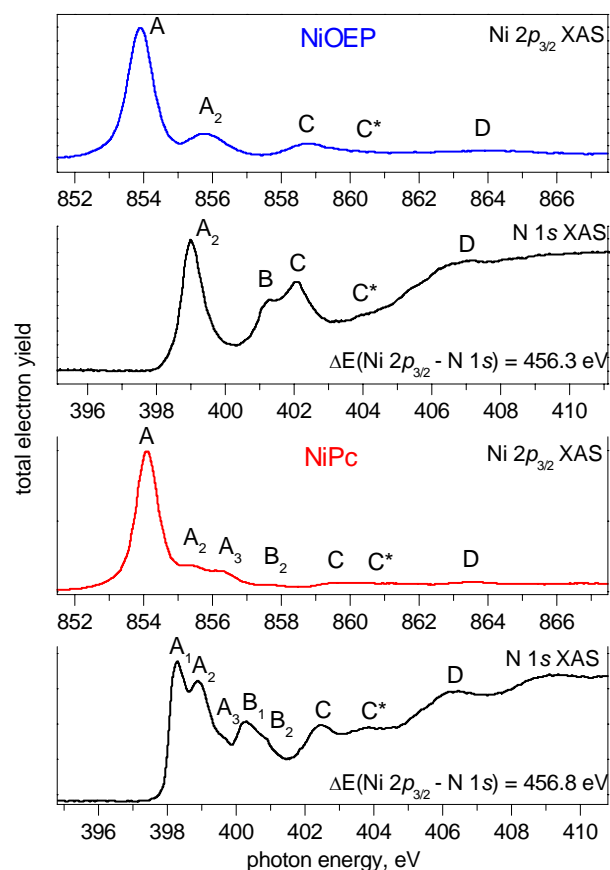


Fig. 3. Ni $2p_{3/2}$ and N 1s absorption spectra of the NiOEP and NiPc.

the pyrrole rings. The most intense absorption band (A) in Ni $2p_{3/2}$ spectrum, which corresponds to the lowest unoccupied state b_{1g} , has no analogue in the N 1s spectrum. This indicates that the b_{1g} MO has an almost pure Ni $3d_{x^2-y^2}$ character.

Absorption band A_1 , present in the N 1s XAS of the NiPc only, corresponds to electron transitions to the empty nonbonding MO having the N and C $2p\pi$ character, where N atoms are in the *meso* positions on the Pc macrocycle and C atoms are nearest neighbours. In turn, the structure A_3 , observed both in the Ni $2p_{3/2}$ and the N 1s XAS of the NiPc, reflects the electron transitions to the empty MO with mixed Ni $3d$ - N $2p$ character (N atoms in the *meso* positions). Thus, applying a quasi-molecular approach to the more complicated NiPc requires a larger quasi-molecule for which nitrogen atoms in the third coordination sphere around Ni atom must be taken into account.

This work was supported by the Russian Foundation for Basic Research (Grant No 06-02-16998), the bilateral Program “Russian-German Laboratory at BESSY” and the Irish Higher Education Authority PRTL program. M.O. Senge gratefully acknowledges a Science Foundation Ireland Research Professorship.

References:

1. K.M. Kadish, K.M. Smith, R. Guillard (Eds.), The Porphyrin Handbook, Academic Press, San Diego, 2000.
2. M.O. Senge, Chem. Commun. (2006) 243.
3. A.Vinogradov, *et. al.*, Fiz. Tverd. Tela (St. Petersburg) 24 (1982) 1417 [Sov. Phys. Solid State 24 (1982) 803].
4. A.I. Nesvizhskii, A.L. Ankudinov, J.J. Rehr, K. Baberschke, Phys. Rev. B 62 (2000) 15295.
5. A.S. Vinogradov, S.I. Fedoseenko, S.A. Krasnikov, *et. al.*, Phys. Rev. B 71 (2005) 045127.
6. A.S. Vinogradov, A.B. Preobrajenski, *et. al.*, J. Electron Spectrosc. Rel. Phen. 114-116 (2001) 813.

from D_{4h} in planar Ps to D_{2h} and D_{2d} in the ruffled NiTiBuP and NiOEP, respectively, in which the pyrrole rings are significantly tilted. This tilt probably leads to a decrease of the overlap between the Ni $3d\pi$ and the N $2p\pi$ orbitals and a respective weakening of the π bonding. The latter is reflected in the intensity decreasing and broader shape of the absorption structure having the Ni $3d\pi$ - N $2p\pi$ hybridized character (A_2).

In Fig. 3 we compare the Ni $2p_{3/2}$ and the N 1s XA spectra of the NiOEP and NiPc. Analysing NiOEP spectra within the framework of a quasi-molecular approach [5] it is reasonable to assume that the structures A_2 , C - D are of the same nature reflecting the electron transitions to hybridized Ni $3d\pi$ - N $2p\pi$ unoccupied states (N atoms in pyrrole rings) of NiN_4 quasi-molecule in NiOEP (some contribution to the MOs responsible for the XA structures C, C* and D may be due to the Ni 4s, p states). In turn, the absorption structure B can be associated with the electron transition to the empty nonbonding MO formed by the N and C $2p\pi$ orbitals of

Spin polarization of oxygen atoms in cobalt-doped ZnO

N. Akdogan¹, A. Nefedov¹, R. I. Khaibullin², L. R. Tagirov^{2,3}, H. Zabel¹

¹Ruhr-Universität Bochum, 44801 Bochum, Germany

²Kazan Physical-Technical Institute of RAS, 420029 Kazan, Russia

³Kazan State University, 420008 Kazan, Russia

The recently discovered class of ZnO-based dilute magnetic semiconductors (DMSs), which can be formed by doping 3d transition metal atoms in ZnO, offers an interesting combination of electrical, optical, and magnetic properties. Of special interest is the possibility to join aspects of semiconductor and magnetic effects to develop new device concepts. According to suggestion of Dietl *et al.* [1], the ZnO-based DMSs can order ferromagnetically at room temperature. However, a consensus on the origin of the ferromagnetic coupling has not been achieved yet. To shed more light on the microscopic mechanism of long range magnetic coupling in TM-doped ZnO we have studied in detail the magnetic properties of Co-doped ZnO films for different implantation doses.

For the growth of ZnO we used epi-polished single-crystalline a-plane sapphire wafers. The nominal thicknesses of the sputter deposited ZnO films were in the range of 500 Å, according to the deposition time [2]. In order to increase the crystallinity of the ZnO films, we have carried out post-growth annealing in an oxygen atmosphere with a partial pressure of up to 2000 mbar and a temperature of 800 °C. After annealing, ZnO samples were implanted in ILU-3 ion accelerator (KPTI of RAS) with 40 keV Co⁺ ions to a dose range of 0.25 – 2.00 × 10¹⁷ ion/cm². The magnetic properties of cobalt implanted ZnO thin films were investigated using soft x-ray resonant magnetic scattering (XRMS) technique at room temperature. The XRMS experiments were carried out at the undulator beamline UE56/1 of BESSY II in Berlin using the UHV diffractometer ALICE [3].

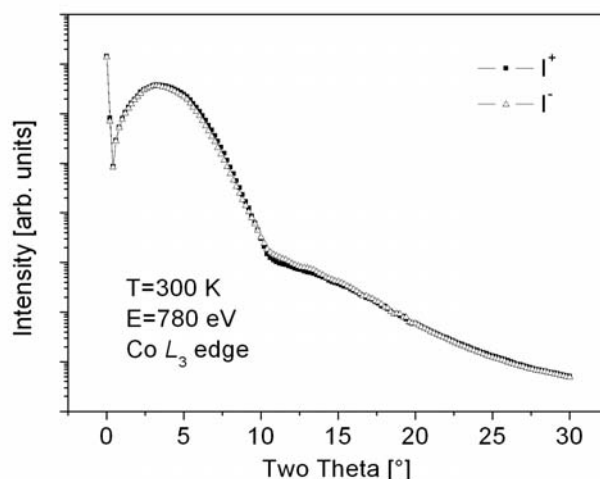


Figure 1: Reflectivity scans of Co-doped ZnO. The measurements were taken at room temperature and with a magnetic field applied in the sample plane parallel (I⁺, solid line) and antiparallel (I⁻, dash line) to the photon helicity.

In Fig. 1 we show reflectivity scans of the Co:ZnO system. As a compromise between high scattering intensity and high magnetic sensitivity for the investigation of the magnetic properties at the Co *L* edges, the scattering angle was fixed at the position of $2\theta=8.2^\circ$.

For measurements at the O K edge the scattering angle was fixed at $2\theta=12^\circ$, which corresponds to the same scattering vector in the reciprocal space. The energy dependence of the intensity around the Co $L_{2,3}$ edges measured in saturation at positive (closed symbols) and negative (open symbols) fields are shown in Fig. 2. It is well known that in the case of metallic films the resonant scattering peak consists of a single component. However, in Fig. 2 a fine structure of the Co L_3 peak ($E=780$ eV) is clearly seen. This fine structure of the Co L_3 peak is similar to that observed before for Co-doped TiO_2 films [4], as well as for Co-doped ZnO by Kobayashi et al.[5] and it is indicative of a Co 2^+ state.

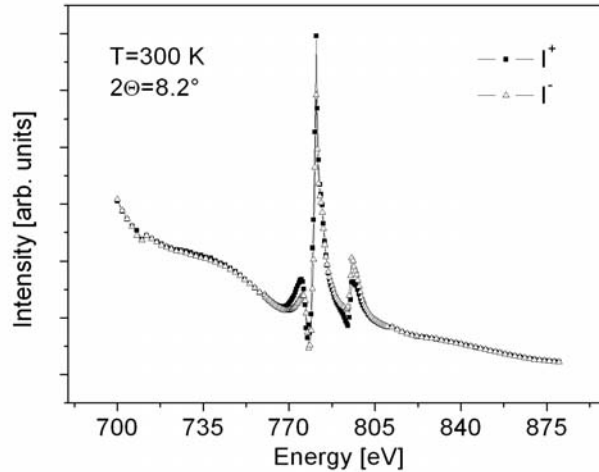


Figure 2: Energy dependence of scattering intensities at the Co L edges.

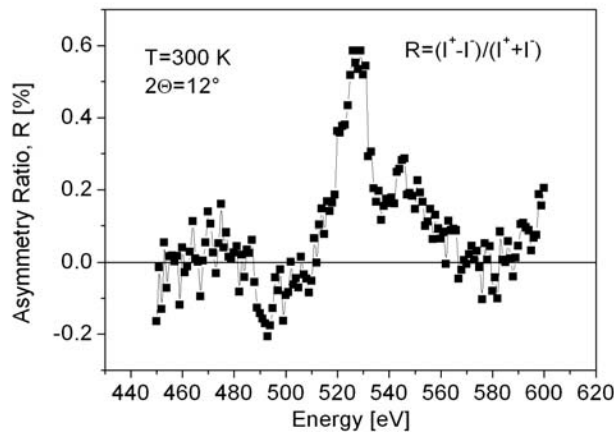


Figure 3: XMCD signal (asymmetry ratio) measured at the oxygen K edge.

We have also investigated the magnetic signal at the Zn $L_{2,3}$ and the O K edges. Within the sensitivity limit no magnetic signal could be recorded for Zn; however, at the O K edge, a clearly visible magnetic signal was observed. The XMCD signal (the asymmetry ratio) measured in reflection geometry is depicted in Fig. 3. Note that the maximum in the XMCD signal of oxygen is much smaller than the XMCD signal of cobalt.

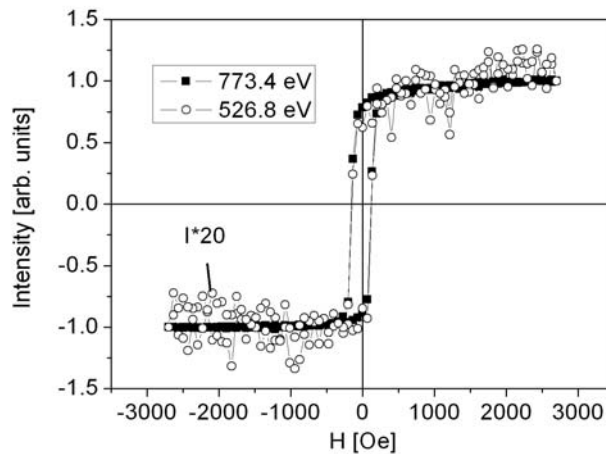


Figure 4: Hysteresis curves measured at Co L (closed symbols) and O K (open symbols) edges. The intensity of the oxygen signal has been multiplied by a factor of 20 for clarity.

In Fig. 4 we show the magnetic hysteresis recorded at the O K edge (open symbols). The shape of this hysteresis curve is the same as the one recorded at the Co L edge (closed symbols), including the coercive field, but the intensity is much lower. This implies that the oxygen atoms in close proximity to Co atoms are polarized ferromagnetically.

In conclusion, we have analyzed the element specific magnetic hysteresis curves of Co, Zn and oxygen in Co-implanted ZnO films. Magnetic dichroism was observed at the Co $L_{2,3}$ edges, as well as at the O K edge, indicative of a spin polarization of oxygen atoms in the ZnO host matrix.

This work was partially supported by BMBF through Contracts Nos. 05KS4PCA and 05ES3XBA/5, by DFG through SFB 491, by RFBR through the grant No 04-02-97505, and by TUBITAK through the project No 104T176. N. Akdogan acknowledges a fellowship through the IMPRS "SurMat".

References

- [1] T. Dietl *et al.*, *Science* **287**, 1019 (2000)
- [2] M. Ay, A. Nefedov and H. Zabel, *Appl. Surf. Sci.* **205**, 329-335 (2003)
- [3] J. Grabis, A. Nefedov, and H. Zabel, *Rev. Sci. Instrum.* **74**, 4048 (2003)
- [4] A. Nefedov, N. Akdogan, R.I. Khaibullin, L.R. Tagirov and H. Zabel, *Applied Physics Letters* **89**, 182509 (2006)
- [5] M. Kobayashi *et al.*, *Phys. Rev. B* **72**, 201201(R) (2005)

Investigation of Surface Acoustic Wave Fields in Langatate Crystals by High-Resolution X-Ray Diffraction

Dmitry Roshchupkin,¹ Luc Ortega,² and Alexei Erko³

¹*Institute of Microelectronics Technology RAS, 142432 Chernogolovka, Moscow district, Russia*

²*Laboratoire de Cristallographie, CNRS, BP 166, 38042 Grenoble Cedex 09, France*

³*BESSY GmbH, Albert-Einstein Str. 15, 12489 Berlin, Germany*

Introduction

Langatate (LGT, $\text{La}_3\text{Ga}_{5.5}\text{Ta}_{0.5}\text{O}_{14}$) is one of the new piezoelectric materials of langasite family for telecommunication systems based on acoustoelectronic devices and operating with digital signals in a real time mode. LGT crystal combining the best acoustic properties of LiNbO_3 (high value of electromechanical coupling coefficient) and quartz (low value of thermal expansion coefficient) permits to design the acoustoelectronic components with unique properties.

This study presents an experimental investigation of x-ray Bragg diffraction on the Y cut of a LGT crystal modulated by a $\Lambda = 12 \mu\text{m}$ surface acoustic wave (SAW). X-ray radiation is very sensitive to crystal lattice distortions and can be used for studding acoustic wave fields in crystals [1-2]. Synchrotron radiation source coupled with high-resolution diffraction techniques provide an interesting tool for the investigation of SAW propagation in crystals. X-ray diffraction on SAW-modulated crystals can be characterized by diffraction satellites appearing around the Bragg peak. The angular positions and intensity of these diffraction satellites depends on both the wavelength and SAW amplitude.

Experimental results

X-ray diffraction from a SAW-modulated LGT crystal was studied in a double axis x-ray diffractometer scheme at the beamline KMC-2 at the BESSY (Fig. 1). X-ray energy was selected by a double Si(111) monochromator. Primary and secondary slits with horizontal and vertical gaps of 1×1 and 0.1×0.1 mm, respectively, were used for x-ray beam collimation. LGT is a piezoelectric crystal of space group symmetry 32. The crystal lattice is similar to the one of quartz with the parameters $a = 8.235 \text{ \AA}$ and $c = 5.128 \text{ \AA}$ [3].

An Y cut [(100) atomic planes parallel to the crystal surface] was used for this experiment. To excite a Rayleigh SAW, an interdigital transducer (IDT) was deposited on the crystal surface by photolithography technique. The SAW amplitude can be changed linearly from 0 to few angstroms by varying the amplitude of high-frequency electrical signal supplied to the IDT. At the resonance excitation frequency $f = 168.796 \text{ MHz}$, the SAW wavelength was $\Lambda = 12 \mu\text{m}$, and the propagation velocity was $V = 2025 \text{ m/s}$.

SAW propagation causes a sinusoidal deformation of a crystal lattice. The SAW penetration depth inside the crystal is approximately one SAW wavelength ($\Lambda = 12 \mu\text{m}$).

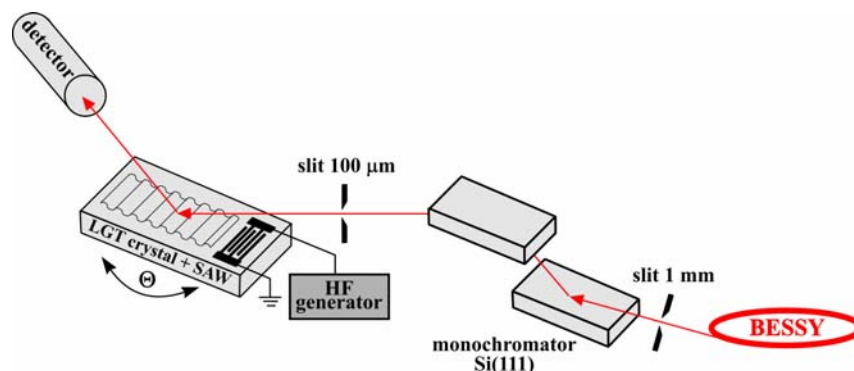


Fig. 3. Experimental setup.

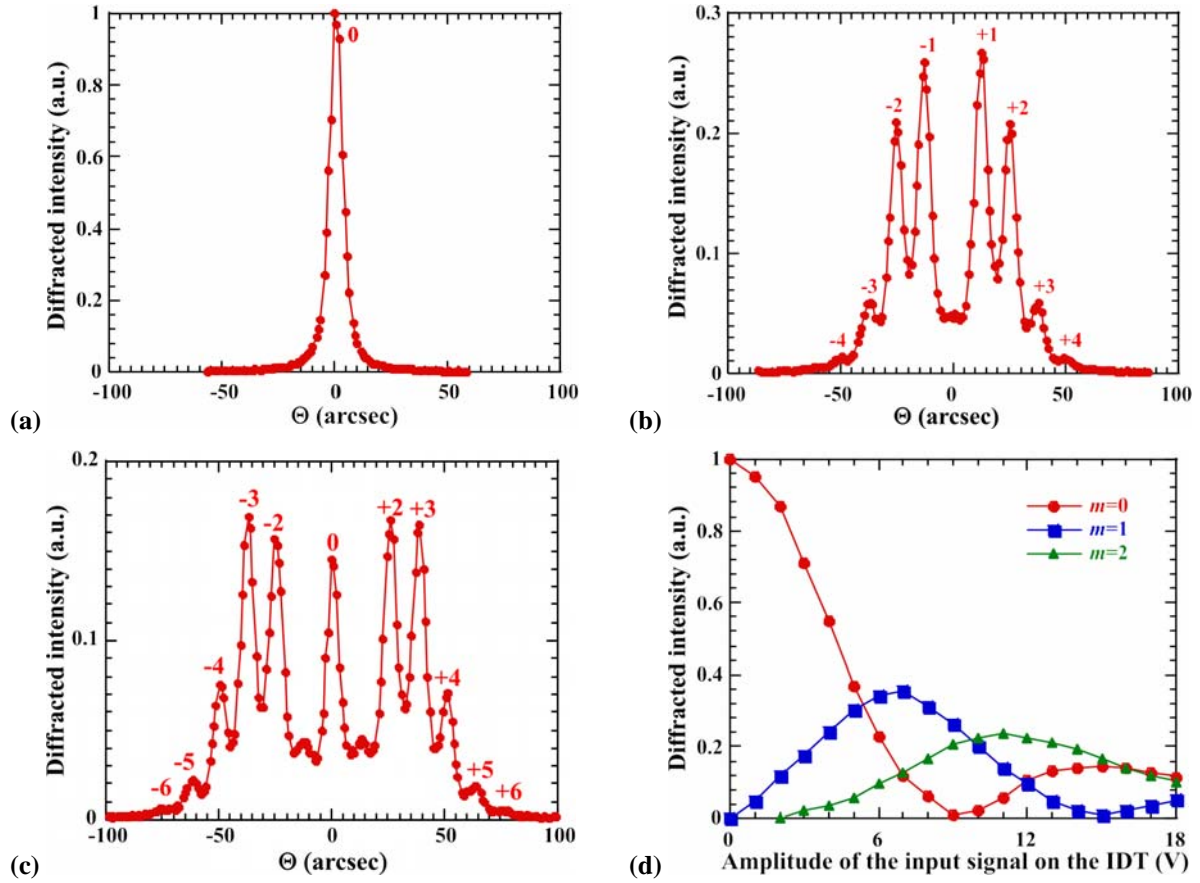


Fig. 2. Rocking curve measured for different amplitude of the input signal supplied to the IDT: (a) $U=0$ V, (b) $U=9$ V, (c) $U=15$ V, (d) intensities of the diffraction satellites versus amplitude of the input signal supplied to the IDT. $E=11.5$ keV; $\Lambda=12$ μm ; (100) reflection.

Since the SAW velocity is much smaller than x-ray photon velocity, acoustic deformation can be considered as quasistatic.

X-ray diffraction on acoustically modulated atomic planes gives rise to diffraction satellites on both sides of the Bragg diffraction peak. The angle between adjacent satellites measured on a rocking curve can be calculated from the equation

$$\delta\Theta_{mRC} = md/\Lambda, \quad (1)$$

where d is the interplanar spacing, Λ is the SAW wavelength.

Rocking curves were measured at various SAW amplitudes. The x-ray energy was $E=11.5$ keV. Interplanar spacing for the (100) reflection in LGT is $d = 7.1385$ \AA . In the kinematic approximation x-ray penetration depth inside the crystal depends on the absorption in LGT crystals as a function of energy $\mu_z^{-1}(E) = \sin[\Theta_B(E)]/2\mu_l(E)$, where μ_l is the linear absorption coefficient and Θ_B is the Bragg incident angle. The K -edge of Ga at 10.47 keV causes a drastic change in the absorption coefficient. At $E=11.5$ keV, x-ray penetration depth in LGT crystals reaches only $\mu_z^{-1} = 0.5$ μm , which is much less than the SAW penetration depth inside the crystal.

Fig. 2 shows selected rocking curves for LGT crystal modulated by a $\Lambda = 12$ μm SAW measured at various input signals supplied to the IDT. The Bragg incident angle is $\Theta_B = 4.283^\circ$. The full width at half maximum of the Bragg peak without SAW excitation is 6 arc sec [Fig. 2(a)]. Fig. 2 shows that the number of diffraction satellites on the rocking curve increases with the amplitude of the input signal supplied to IDT. The angular divergence between two diffraction satellites $\delta\Theta_{mRC}$ is 12.1 arc sec, which agrees quite well with the value 12.2 arc sec calculated from eq. (1). Intensities of the $m=0, 1, 2$ diffraction satellites as a

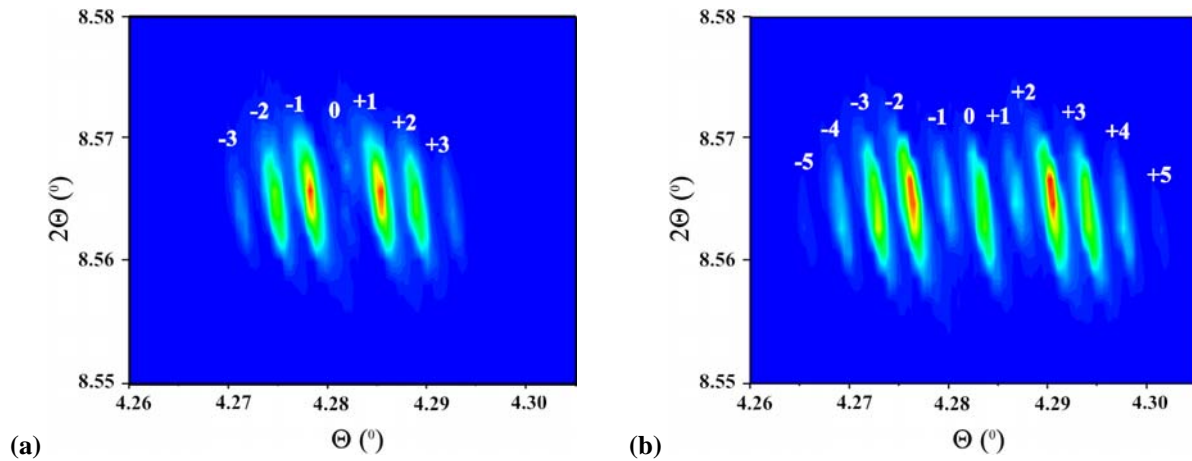


Fig. 3. Two-dimensional distribution of the diffracted x-ray intensity excited by SAW-modulated LGT crystal: (a) $U=9$ V, (b) $U=15$ V. $E=11.5$ keV; $\Lambda=12$ μm ; (100) reflection.

function of the input high-frequency signal on IDT are shown in Fig. 2(d). A diffraction satellite (except satellite $m=0$) grows up as soon as the SAW amplitude reaches a threshold value increasing with the diffraction order. After reaching a maximum rapidly, the satellite intensity decreases smoothly and oscillates. The maximum intensity (38% of the intensity of the Bragg peak without SAW excitation) of the $m=+1(-1)$ diffraction satellites was obtained at $U=7$ V. It can be seen [Fig. 2(b)] that the intensity of the $m=0$ satellite is equal to zero for LGT at $U=9$ V. For these amplitudes, the phase shift of the x-ray radiation diffracting into the zero satellites from the SAW minima and maxima is equal to π . This effect can only be observed if the acoustic wave field probed by x-rays is very homogeneous in amplitude. This is therefore only possible if the x-ray absorption is very strong. The extinction of the $m=+1(-1)$ satellites is observed at more high SAW amplitude [$U=15$ V, Fig. 2(c)]. Fig. 3 shows the two-dimensional distributions of the diffracted x-ray intensity obtained at different SAW amplitudes corresponding to extinction of the $m=0$ diffraction satellite at $U=9$ V (a) and extinction of the $m=+1(-1)$ satellites at $U=15$ V (b).

Summary

This experiment has shown that x-ray diffraction can be used to study the SAW propagation in piezoelectric crystals. Furthermore the extinction of the $m=0$ diffraction satellites in LGT crystals excited at specific SAW amplitudes is very interesting tool to design the high frequency acoustic modulator with 100% modulation depth [3].

Acknowledgement

This work has been supported by a joint program between the BESSY and the IMT RAS. One of us (D.V.R.) is indebted to the Russian Foundation for Basic Research (Contract No. 06-02-22005).

References

- 1 I.A. Schelokov, D.V. Roshchupkin, D.V. Irzhak, R. Tucoulou, Dynamical theory for calculation of X-ray spectra from crystals modulated by surface acoustic waves, *Journal of Applied Crystallography* **37** (2004) 52-61.
- 2 D.V. Roshchupkin, H.D. Roshchupkina, and D.V. Irzhak, X-Ray topography analysis of acoustic wave fields in the SAW-resonators structures, *IEEE Transaction on Ultrasonics, Ferroelectrics, and Frequency Control* **52** (2005) 2081-2087.
- 3 R. Tucoulou, D.V. Roshchupkin, O. Mathon, I.A. Schelokov, M. Brunel, E. Ziegler, and C. Morawe, High-frequency x-ray beam chopper based on diffraction by surface acoustic waves, *J. Synchrotron Rad.* **5** (1998) 1357-1362.

Magnetic EXAFS Study of Fe on Ag(100): Experiment and Theory

J. Kurde¹, N. Ponpandian¹, J. Luo¹, C. Sorg¹, K. Baberschke¹, P. Srivastava^{2,*} and H. Wende^{1,2}

¹Institut für Experimentalphysik, Freie Universität Berlin, Arnimallee14, 14195 Berlin, Germany

²Angewandte Physik, FB Physik, Universität Duisburg-Essen, Lotharstrasse.1, 47048 Duisburg, Germany

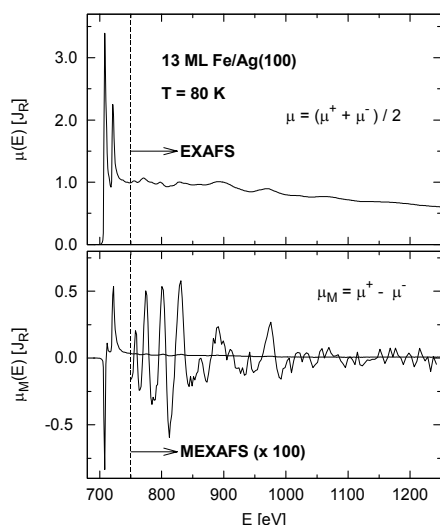


Figure 1: Experimental EXAFS and MEXAFS $\mu(E)$ spectra.

Studies providing information related to dynamic and local magnetic disorder are of immense interest, particularly for systems that show magnetic phase transitions. In the past decade, X-ray absorption spectroscopy in the extended energy range using linear and circularly polarized light has become the technique of choice to draw such kind of information. The temperature-dependence of magnetic EXAFS (MEXAFS) and EXAFS yields the local magnetic disorder (spin-fluctuations) and the dynamic disorder (lattice vibrations) [1]. For systems containing $3d$ elements, measurements at their $L_{2,3}$ -edges are of relevance since thereby the important $3d$ states can be probed. In the past we have conclusively established that the overlap between L_3 - and L_2 -edges can be described very accurately by *ab initio* calculations [1-2]. Furthermore, a procedure to deconvolute the experimental spectra into their L_3 - and

L_2 -edge contributions was developed [2], which enabled us to study higher spin-spin correlations. In the present work, EXAFS and MEXAFS measurements have been carried out at the $L_{2,3}$ -edges of Fe in bcc Fe film (13 ML) on Ag(100) substrate at BESSY on UE56/PGM beamline [3]. This system is well established with respect to its magnetic and structural properties (see e.g. [4]). The Ag substrate is chosen since no other absorption edges of the substrate are found in the Fe EXAFS/MEXAFS range of about 700-1500 eV. The measurements were carried out at 300 K and 80 K. The absorption spectra were recorded in a k -range up to 12 \AA^{-1} . As the regular EXAFS is

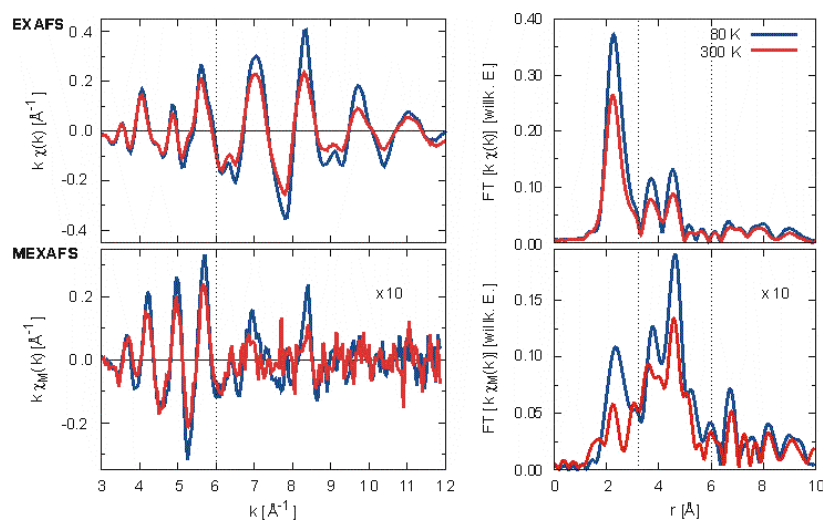


Figure 2: EXAFS and MEXAFS oscillations $\chi(k)$ and $\chi_M(k)$ and the corresponding Fourier transforms recorded at 80 K (blue) and 300K (red). The temperature-dependent damping can be clearly seen.

automatically recorded when measuring magnetic EXAFS, an attempt is made to directly compare structural properties with the local magnetic structure.

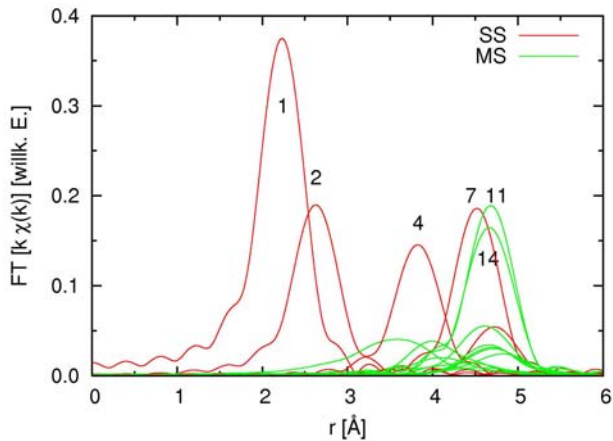


Figure 3: FEFFIT calculation for the single Fe L_3 -edge. Each peak corresponds to one scattering path. The dominating single and multiple scattering paths for the EXAFS are (see also figure 4):

1	(A - 1a - A)	R = 2.4825 Å
2	(A - 2a - A)	R = 2.8665 Å
4	(A - 3a - A)	R = 4.0538 Å
7	(A - 4a - A)	R = 4.7536 Å
11	(A - 5a - 1a - A)	R = 4.9649 Å
14	(A - 1a - 5a - 1a - A)	R = 4.9649 Å

the $L_{2,3}$ -edges and (ii) enhanced multiple-scattering. Apart from this, significant intensities for distances larger than 6 Å in the Fourier transform can be observed, which have been identified so clearly for the first time. To achieve a more fundamental understanding of the spin-selective scattering phenomena that determine the MEXAFS, we applied two theoretical models: (i) *ab initio* calculations and (ii) the rigid band model [1].

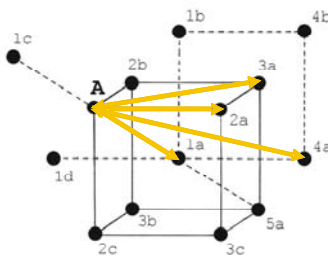


Figure 4: Corresponding Fe lattice with various scattering paths.

For the *ab initio* calculations the FEFF82 code [5] was employed. The enveloping intensity of the oscillation as well as most of its fine structures are reproduced quite well (not shown). Similar conclusions can be drawn for the magnetic spectra. One can deduce from the analysis that at high photo-electron energies ($k > 10 \text{Å}^{-1}$) mainly long distance ($r > 6 \text{Å}$) single scatterings contribute, which is however not predicted by theory [for details see 3]. We tried to identify all scattering paths that contribute to the EXAFS signal. The required information can be found in the intensity and position of the related peaks in the Fourier transform, which we calculated for each scattering path using the FEFFIT code. Figures 3 and 4 show the result for the L_3 -edge and paths with $R \leq 5 \text{Å}$. One can clearly see the dominance of single and forward scattering paths, although other multiple scattering paths also contribute.

The spin-dependent scattering of the photo-electron can be modelled by the scattering potential for the spin-averaged case. The spin up/down potential can be simulated by shifting this potential in energy. The rigid band model [6,7] predicts an analogous spin-dependent energy shift (ΔE) of the density of final states ($Z(E)$). This energy shift is temperature dependent, since for

The experimental EXAFS and MEXAFS spectra $\mu(E)$ recorded at 80 K are shown in figure 1, clearly depicting a good quality MEXAFS signal. The Fourier transform (FT) of the oscillations $\chi(k) = (\mu(k) - \mu_0(k)) / \mu_0(k)$ is related to the radial pair distribution functions of each scattering shell (Figure 2). The spin-averaged EXAFS measurements confirm that Fe film has a bcc structure. In this case the main peak includes contributions from the nearest and second nearest neighbours. The two smaller peaks at $r > 3 \text{Å}$ are related to longer path lengths including multiple scattering paths. For MEXAFS, the amplitude in the range of the high frequency oscillation at $k < 6 \text{Å}^{-1}$ is larger than in the normal EXAFS. This is also visible in the Fourier transform, where the main peak is smaller than the two following peaks. These differences between the EXAFS and MEXAFS signal are due to (i) overlapping of

the $L_{2,3}$ -edges and (ii) enhanced multiple-scattering. Apart from this, significant intensities for distances larger than 6 Å in the Fourier transform can be observed, which have been identified so clearly for the first time. To achieve a more fundamental understanding of the spin-selective scattering phenomena that determine the MEXAFS, we applied two theoretical models: (i) *ab initio* calculations and (ii) the rigid band model [1].

randomly oriented spins ($T > T_C$) the magnetic interaction cancels out. Since the absorption coefficient is related to $Z(E)$, one can calculate the MEXAFS spectrum from the experimental EXAFS spectrum as follows [1]:

$$\chi_{\text{MEXAFS}}(E) = \chi_{\text{EXAFS}}(E - \frac{1}{2} \Delta E(T)) - \chi_{\text{EXAFS}}(E + \frac{1}{2} \Delta E(T)).$$

Recently this method has been applied to the calculated EXAFS spectra [8]. We have simulated MEXAFS spectra recorded at two different temperatures using this model with the experimental EXAFS spectra and the results are shown in Figure 5. It is clear that the agreement of experiment and this model is quite good even for distances $r > 6 \text{ \AA}$. Hence the magnetic

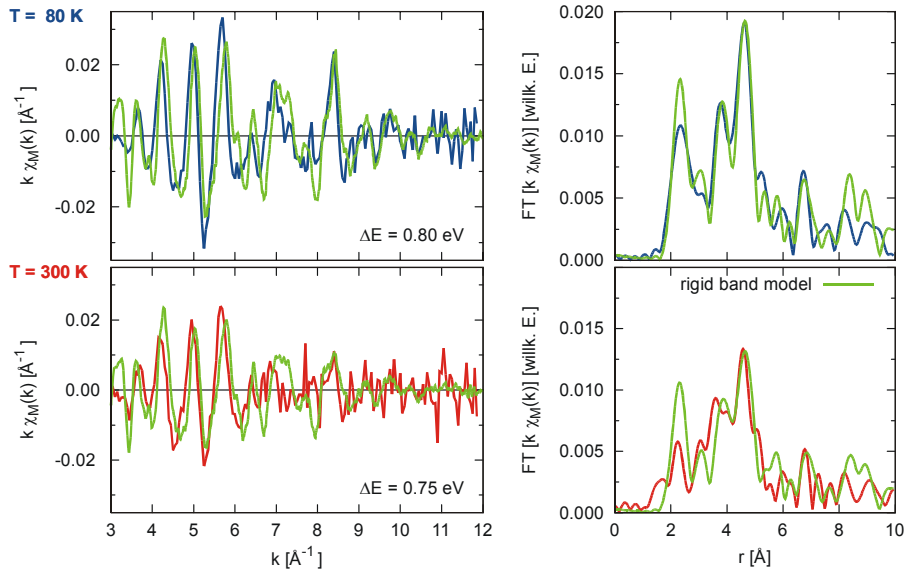


Figure 5: Experimental (blue and red) and simulated (green) MEXAFS oscillations $\chi_M(k)$ and corresponding Fourier transforms for spectra recorded at 80 K and 300K.

EXAFS can indeed be described by the density of scattering states, which is energy shifted due to magnetic exchange coupling. It is to be noted that $\Delta E(T)$ is nearly constant as $M(T)$ is not expected to change significantly in this (80 K-300K) temperature range for a 13 ML Fe film. Therefore, the observed temperature dependence is mainly due to a change in the Debye-Waller factor.

In summary, the present work shows high quality EXAFS and MEXAFS data resulting into significant intensities for distances larger than 6 \AA in corresponding Fourier transforms. The detailed scattering path analysis shows significant intensities for single and forward scatterings. It is shown that the rigid band model works quite well to reproduce MEXAFS data. This work is supported by BMBF (05 KS4 KEB 5) and DFG (Heisenberg-Stipendium).

References

*Permanent Address: Department of Physics, IIT Delhi, Hauz Khas, New Delhi 110 016 (India).

- [1] H. Wende, Rep. Prog. Phys. **67**, 2105-2181 (2004).
- [2] H. Wende et al., J. Appl. Phys. **83**, 7028-7030 (1998).
- [3] J. Kurde, Diploma Thesis, FU Berlin (2006), unpublished
- [4] M. Stampanoni et al., Phys. Rev. Lett. **59**, 2483-2485 (1987).
- [5] A. L. Ankudinov et al., Phys. Rev. B **65**, 104107 (2004).
- [6] J. L. Erskine and Stern, Phys. Rev. B **12**, 5016 (1975).
- [7] C. Brouder et al., Phys. Rev. B **54**, 7334 (1996).
- [8] H. H. Rossner et al., Phys. Rev. B **74**, 134107 (2006).

**Martin Güngerich^a, Tobias Niebling^a, Wolfram Heimbrodt^a, Peter J. Klar^b,
Stanko Tomić^c, Stefan G. Ebbinghaus^d, Armin Reller^d, David Batchelor^e**

^a*Fachbereich Physik und Wissenschaftliches Zentrum für Materialwissenschaften, Philipps-Universität, Renthof 5, D-35032 Marburg*

^b*I. Physikalisches Institut, Justus-Liebig-Universität, Heinrich-Buff-Ring 16, D-35392 Gießen*

^c*Computational Science and Engineering Department, CCLRC Daresbury Laboratory, Keckwick Lane, Warrington, Cheshire WA4 4AD, United Kingdom*

^d*Lehrstuhl für Festkörperchemie, Institut für Physik, Universität Augsburg, Universitätsstraße 1, D-86159 Augsburg*

^e*EP 2, Universität Würzburg, c/o BESSY, Albert-Einstein-Straße 15, D-12489 Berlin*

Funding was provided by the DFG Research Group “Metastable Compound Semiconductors and Heterostructures”.

Our research at BESSY in 2006 has focused on zincblende III-V semiconductor materials where a small fraction (percent range) of the group-V atoms has been isovalently replaced by nitrogen. We investigated GaN_{0.021}P_{0.979}, GaN_{0.085}As_{0.915} and GaN_{0.015}Sb_{0.985} epitaxial layers as well as a zincblende GaN reference sample by XAS experiments in fluorescence mode in the spectral range of the nitrogen K edge. Our aim is to obtain information about the local bonding properties as well as clustering effects of N atoms in these metastable alloys.

Our experiments have shown that XAS is possible on the N K-edge in dilute nitride materials even at N concentrations of about 1%. The XAS data of the series of samples show a clear trend in the near-edge (NEXAFS) region, when the atomic mass and radius of the host group-V atoms increase in the order GaN, GaNP, GaNAs, GaNSb. As depicted in fig. 1 (left panel), a red shift of the edge energy is found for increasing atom size and also the fine structure of the near-edge spectra shows significant changes in the sample series. The untreated EXAFS spectra are shown in the right panel of fig. 1. It is worth noting that the XAS data of the GaNAs sample with 8.5% of N do not show as clear signatures in the EXAFS region as the GaNP and GaNSb samples with lower N concentrations around 2%. The most probable reason for this is that N statistics become more important with increasing N content and the relative number of isolated N atoms decreases. This leads to an EXAFS spectrum containing contributions from N atoms in different environments with different bond lengths and therefore the EXAFS features are washed out compared to the spectra of the less N-containing crystals.

A major problem is the difficulty of clearly separating NEXAFS and EXAFS region on the N K-edge. A further, even more severe complication arises for the dilute nitrides from the native oxide on the surface. Because of the close vicinity of oxygen K-edge and N K-edge, the range of the EXAFS oscillations detected at the N K-edge is restricted to approximately 100 eV.

Concerning the quantitative analysis, we have so far focused on the EXAFS region. We used the software DL_Excurv (issued by CCLRC Daresbury Laboratory (UK)) in close cooperation with Dr. Stanko Tomić. This program allows a modeling of EXAFS spectra with complex structural models including self-consistent potentials of the scattering species. The results for the GaN EXAFS data, obtained by an ordered shell model with self-consistent potentials, are shown in fig. 2 and the corresponding parameters are given in tab. 1 up to the 4th shell. The distances of the first three shells agree well with the values expected from the known lattice constant of GaN and the geometry of the zincblende structure.

As a first attempt, an equivalent model was assumed for GaNSb, which means that a possible disorder on the group-V shells (i.e. the formation of N-N pairs of different spatial separations) has not yet been taken into account. The results are shown in fig. 3 and parameters up to the 4th shell presented in tab. 2. Despite the simplicity of the structural model, the obtained shell radii show a

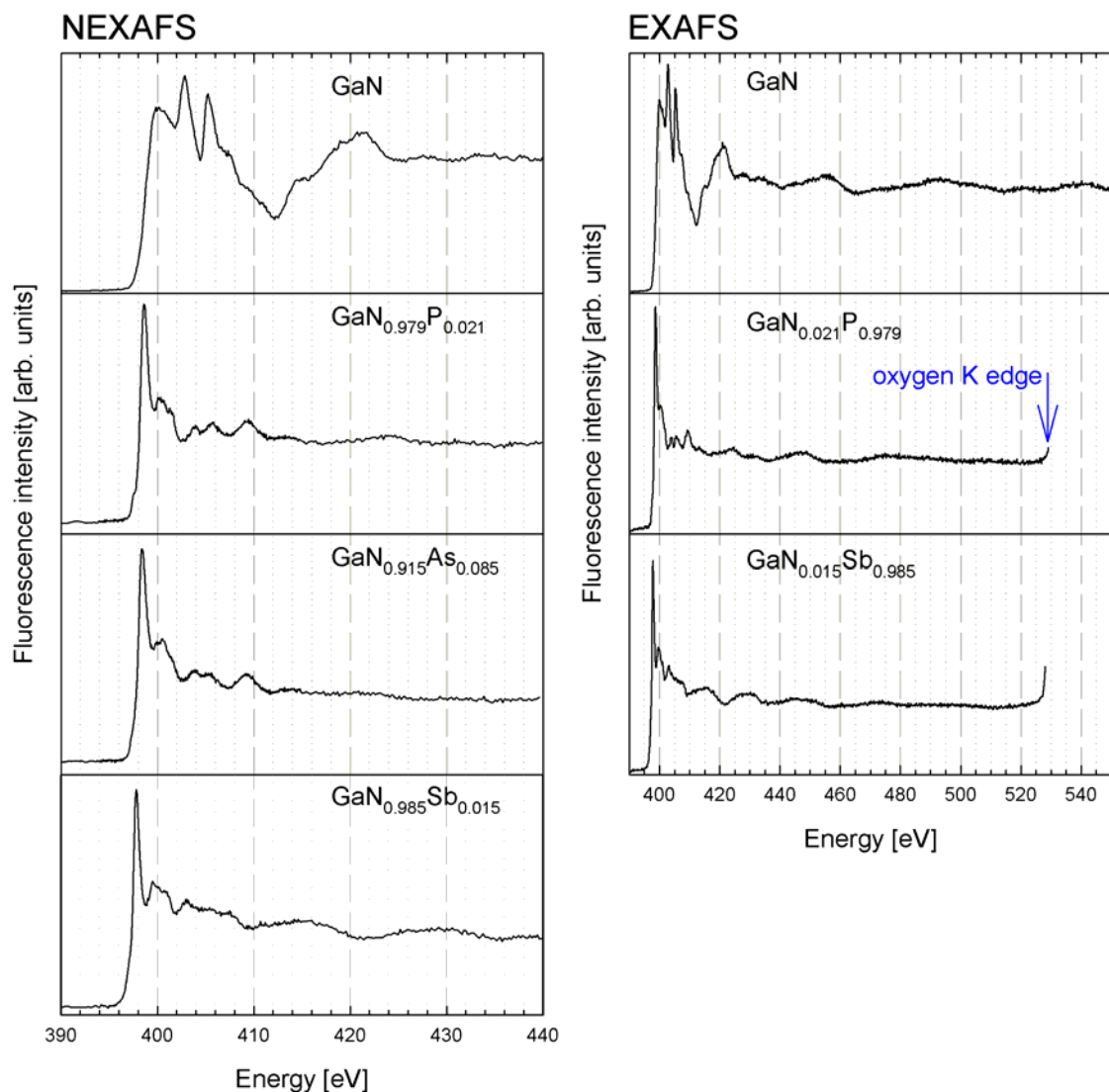


Fig. 1: NEXAFS (left panel) and EXAFS (right panel) raw data of zincblende GaN and several dilute-N III-V semiconductor alloys. Each spectrum shown is an average of several scans.

reasonable trend for the first three shells. As expected, the distances of neighbouring atoms around the N atom, being small compared to the Sb atom it replaces, are significantly smaller than the corresponding distances in the surrounding of a Sb atom. Obviously, the N atom “pulls” its neighbours towards itself, causing a strong local lattice distortion.

The next step of our analysis will focus on modeling the GaNP EXAFS spectrum, again with the help of self-consistent potentials provided by Daresbury Lab. Further steps will include disorder on the shells of the group-V atoms and additionally investigate the influence of multiple-scattering effects. The latter are expected to give a better refinement of the structural model and to allow further conclusions concerning the influence of N on the local crystalline symmetry.

Outlook

We will try to extract information about the electronic structure from the series of NEXAFS spectra by the use of self-consistent potentials.

To complete the series of EXAFS data, it is necessary to repeat the measurement of GaNAs using a sample containing less N. EXAFS experiments of dilute nitrides without native oxide would be highly desirable to provide a longer range of oscillations and to facilitate a more reliable refinement of the structural models.

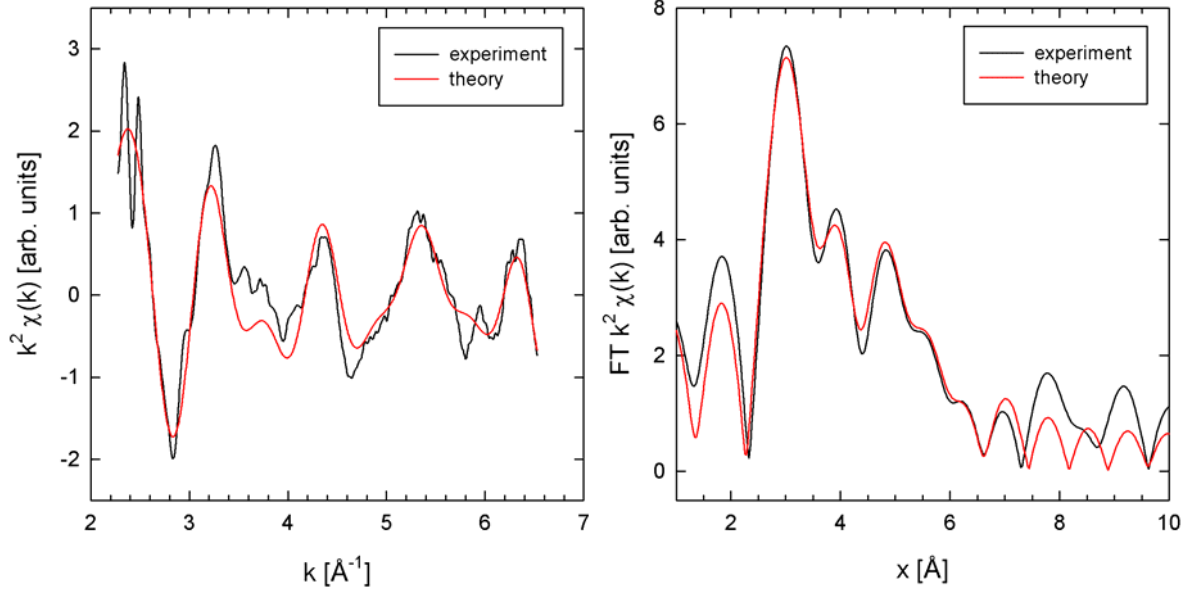


Fig 2: Experimental and theoretical EXAFS data for GaN in k-space (left panel) and their Fourier transforms (right panel).

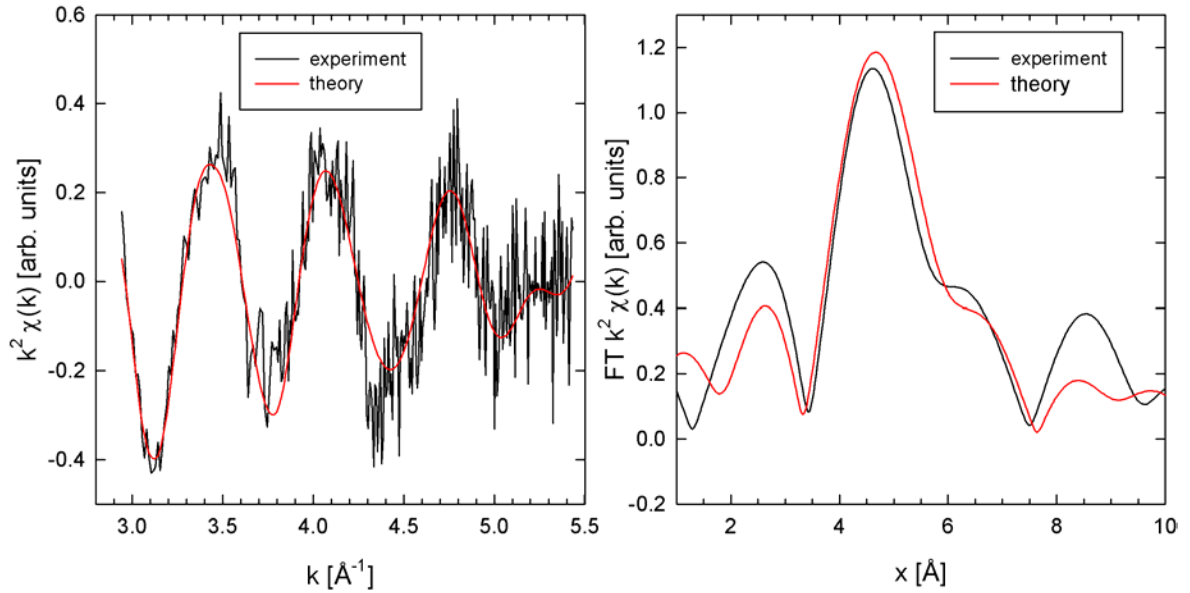


Fig 3: Experimental and theoretical EXAFS data for GaN_{0.015}Sb_{0.985} in k-space (left panel) and their Fourier transforms (right panel).

S	N	Element	r_E [Å]	r_{Lit} [Å]	D
1	4	Ga	1.971	1.9486	0.062
2	12	N	3.154	3.1820	0.044
3	12	Ga	3.804	3.7312	0.044
4	6	N	3.905	4.5000	0.133

Tab. 1: Parameter table for zincblende-GaN. S is the shell number, N the occupation of the shell. r_E denotes the shell radius obtained from EXAFS refinement, while r_{Lit} is the radius calculated from the known lattice constant (literature value) and the structural geometry. D is the Debye-Waller factor of the shell.

S	N	Element	r_E [Å]	r_{Lit} [Å]	D
1	4	Ga	2.346	2.6396	0.222
2	12	Sb	4.067	4.3105	0.110
3	12	Ga	4.847	5.0545	0.037
4	6	Sb	6.243	6.0959	0.036

Tab. 2: Parameter table for GaN_{0.015}Sb_{0.985}. The literature values r_{Lit} are those for GaSb.

Characterization of a Fresnel bimirror for hard X-rays

W. Leitenberger & U. Pietsch*

Universität Potsdam, Inst f. Physik, Am Neuen Palais 10, D -14469 Potsdam, Germany
** Universität Siegen, FB 7 - Physik, 57068 Siegen, Germany.*

Some Fresnel bimirrors (FBM) made on top of a flat glass and silicon substrate were already successfully used to investigate the coherence properties of X-rays in the energy range of 5 to 50 keV [1,2]. This device acts similar to an Young double slit and produces the well known two beam interference fringes with high intensity contrast. The coherence properties of the X-ray beam could be determined from the quantitative evaluation of the interference pattern [1,3].

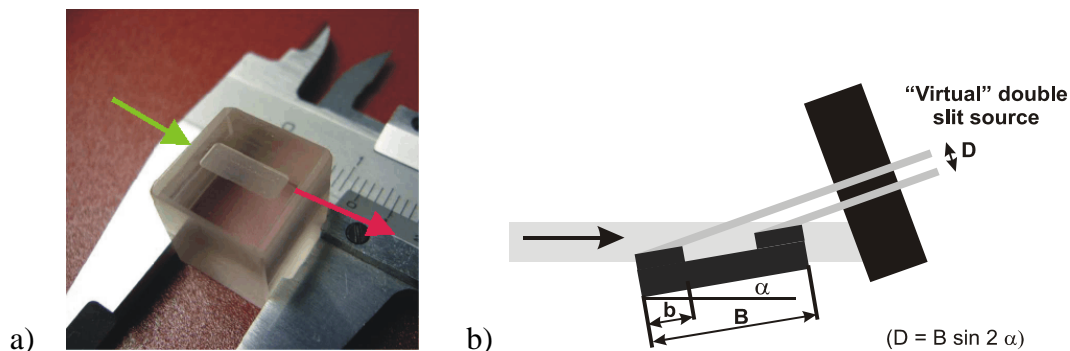
The quality of the previous X-ray measurements was limited by the non exact parallel alignment of the two mirrors due to a small curvature of the substrate after preparation of the mirrors. A new FBM was prepared by Fa. Jenoptik. It was made on top of a monocrystalline quartz cube. The initial surface was polished with a maximum roughness of 0.46 nm. The FBM structure was created by grinding a 500 μm deep groove into this surface (see Fig. 1,2). The midpoints of the two remaining mirrors are 9 mm apart from each other. Using this device at shallow incidence angles of typically 0.1 degree and below we obtain in good approximation a double slit of dimensions in the micrometer range where diffraction phenomena at Ångström wavelength can be observed.

We characterized the FBM by two methods.

(i) By micro-interferometry we determined the height profile of a mirror plane and found a maximum height difference between the centre and rim of the mirror of about 10 nm. At 1 mm mirror width this coincides to a curvature of about 2 arcsec.

(ii) The X-ray interferogram in Fig. 2 was recorded in a distance of 1.3 m behind the mirror. A pinhole of 5 μm diameter was scanned with high accuracy in front of an energy dispersive detector. The tilt angle was determined from the separation of the two diffraction pattern of 5 arcsec.

We can conclude that compared to the previous Fresnel bimirror the bending of the actual quartz mirror is a factor of 4 weaker. A Fresnel bimirror is a simple and effective method for characterization of the coherence properties of X-rays at a SR-beamline.



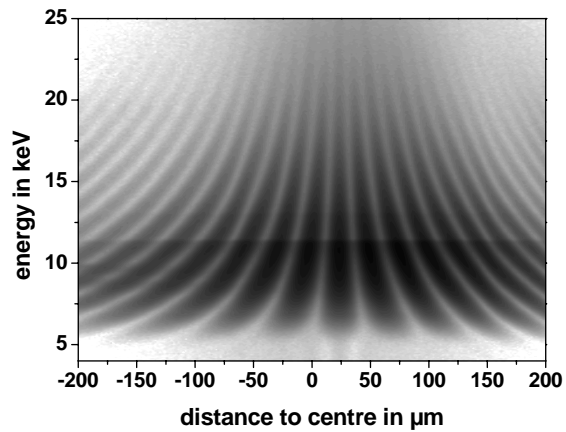


Fig 1 a) Photograph of the Fresnel bimirror
 b) principle of generating narrow beams
 c) diffraction pattern of a bimirror in the energy range of 5 to 25 keV

- [1] Leitenberger, W., Pietsch, U. (2007) *A monolithic Fresnel bimirror for hard X-rays and its application for coherence measurements. J. Synchrotron Rad.* In press
- [2] Pietsch U, Panzner T, Leitenberger W, Vartanyants IA: *Coherence experiments using white synchrotron radiation. Physica B* 2005; **357**, 45-52.
- [3] Leitenberger W, Wendrock H, Bischoff L, Weitkamp T; *Pinhole Interferometry with Coherent Hard X-rays. J. Synchrotron Rad.* 2004; **11**, 190-197.

Interface magnetization of ultrathin epitaxial $\text{Co}_2\text{FeSi}(110)/\text{Al}_2\text{O}_3$ films

M. Kallmayer,¹ H. Schneider,¹ G. Jakob,¹ H.J. Elmers,^{1,*} B. Balke,² and S. Cramm³

¹*Institut für Physik, Johannes Gutenberg-Universität, D-55099 Mainz, Germany*

²*Institut für Anorganische und Analytische Chemie,*

Johannes Gutenberg-Universität, D-55099 Mainz, Germany

³*Institut für Festkörperforschung, Forschungszentrum Jülich GmbH, D-52425 Jülich, Germany*

Heusler alloys recently attracted scientific interest because theory has predicted ferromagnetic halfmetallic properties for some of these alloys. Heusler alloys with complete spin-polarization of conduction electrons would be ideal materials for spin electronic devices. As a reason for the lack of experimental proof of the half metallic properties structural deviations from the ideal $L2_1$ structure in particular at the interfaces of thin films are suspected. Our aim in this project is the determination of element-specific magnetic properties of thin films separated between properties at the interface and in the core of the films using X-ray circular dichroism (XMCD). We focus on epitaxial ultrathin films of the Heusler alloy Co_2FeSi grown on $\alpha\text{-Al}_2\text{O}_3$. It was recently shown that Co_2FeSi is a very good candidate for providing a high spin-polarization [1]. The material exhibits a very high Curie temperature of 1100 K and a magnetic moment of $6 \mu_B$ per formula unit. The compound is special in regards to its Curie temperature and magnetic moment because both values are the highest observed until now in this class of materials. Band-structure calculations based on the local density approximation with additional consideration of electron correlation (LDA+U) showed that an effective Coulomb exchange interaction $U = 2 - 5$ eV leads to halfmetallic ferromagnetism and to an integer magnetic moment [2], in contrast to the case of $U = 0$ where no half-metallic behavior and a smaller magnetic moment of $5.3 \mu_B$ per formula unit was found

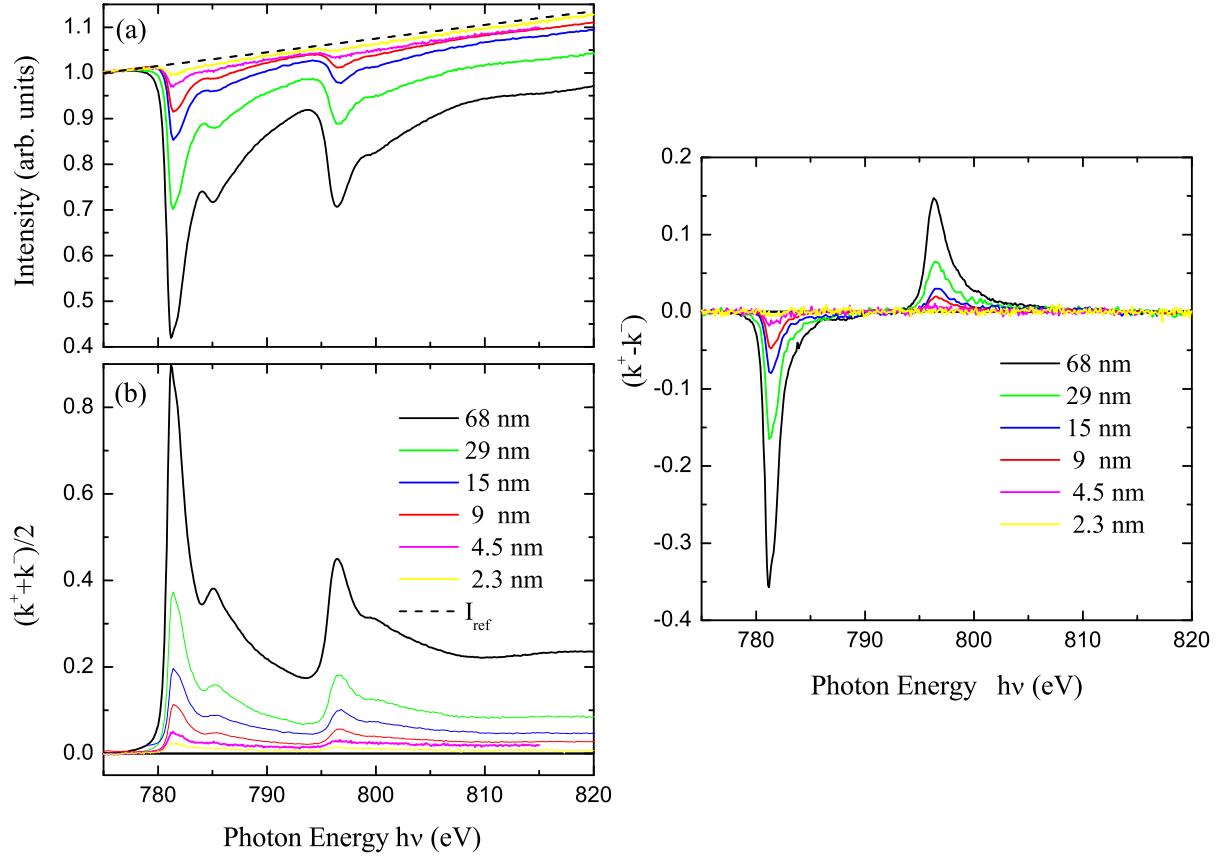


FIG. 1: (Left panel) (a) Intensity of the luminescence light emerging from the substrate measured at the Co $L_{2,3}$ -edge of Co_2FeSi films on Al_2O_3 . Thicknesses of the films are indicated in the figure. The intensity was normalized at the pre-edge. (b) Corresponding absorption coefficient $k = -\ln(I/I_{ref})$ for various film thicknesses. (Right panel) Circular magnetic dichroism signal $(k^+ - k^-)$ for thicknesses indicated in the Figure.

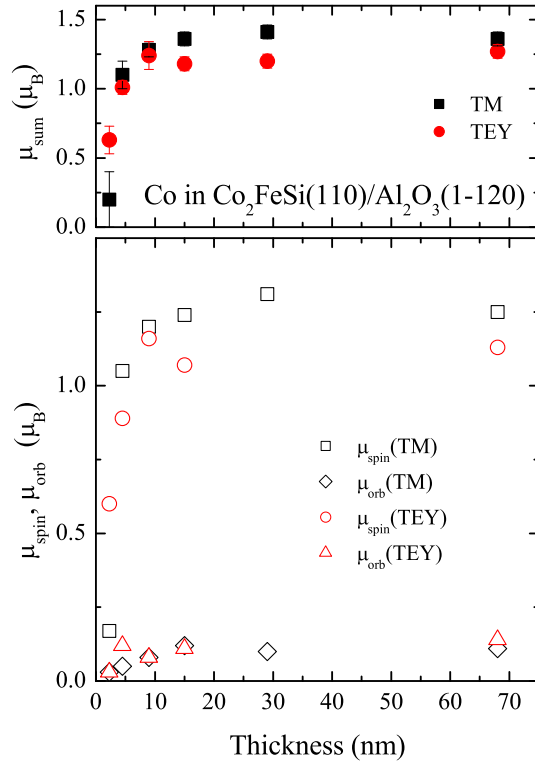


FIG. 2: Effective spin moment, μ_{spin} , orbital moment, μ_{orb} , and total moment, μ_{sum} , for Co in Co_2FeSi Heusler alloy films from transmission and TEY as a function of film thickness.

[3].

Our experimental approach is based on X-ray magnetic circular dichroism (XMCD) in the X-ray absorption spectroscopy (XAS), measured simultaneously by the total electron yield (TEY) and in transmission (TM) [4]. We have deposited Co_2FeSi thin films on Al_2O_3 (11 $\bar{2}$ 0) substrates by RF magnetron sputtering with a rate of 5 $\text{\AA}/\text{s}$ [5]. The films were finally covered with 4 nm of aluminium at a temperature of 350 $^\circ\text{C}$ in order to prevent oxidation.

Fig. 1(a) shows the incident-photon-flux-normalized transmission XAS spectra of $\text{Co}_2\text{FeSi}/\text{Al}_2\text{O}_3$ Heusler alloy films for thicknesses $d = 2.3$ nm to $d = 68$ nm averaged over the two magnetization directions. Assuming that the luminescence signal of the substrate I_{lum}^\pm is proportional to the transmitted X-ray intensity, the X-ray absorption coefficient k can be calculated using the equation $k^\pm(h\nu) = -\ln[I^\pm(h\nu)/I_{ref}(h\nu)]$ (Fig. 1(b)). The reference spectra $I_{ref}(h\nu)$ was measured by the bare substrate crystal and found to increase linearly with the photon energy. $I_{ref}(h\nu)$ was then normalized at the pre-edge region of the corresponding element.

Fig. 1 shows the corresponding XMCD signal ($k^+ - k^-$) for different film thicknesses calculated from the two spectra measured with opposite magnetization direction.

The minimum X-ray penetration depth at the Co L_3 edge is $\lambda_{x,min}(\text{Co}) = 752$ \AA and can be used to correct the total electron yield data [6]. The absorption signal for TM and TEY does not show pronounced differences, independent of the film thickness. The main difference is that the TEY signal is independent of the thickness while the TM signal decreases with decreasing thickness. Element specific magnetic moments shown in Fig. 2 were derived by a sum-rule analysis [6] assuming numbers of d -holes $n_d(\text{Fe}) = 3.4$, $n_d(\text{Co}) = 2.5$ as reported for the pure elements. [6].

From the transmission measurement we obtain a magnetic moment averaged along the surface normal. This fact allows a calculation of the magnetic moment m per area A of the film: $m/A = d\mu/V_u$ (V_u is the unit cell volume). From an evaluation of m as a function of thickness, contributions from the bulk

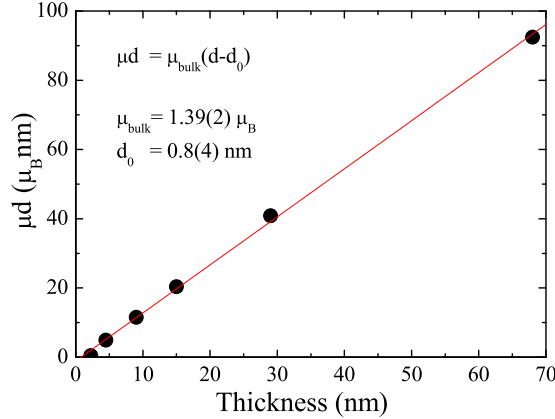


FIG. 3: Magnetic moment of Co atoms multiplied by the thickness, μd , versus thickness for a series of Co_2FeSi films on $\text{Al}_2\text{O}_3(1120)$ (dots). The full line represents a linear fit to the data.

of the film and excess moments at the surfaces can be separated according to Ref. [7]. From a linear fit of the data shown in Fig. 3 we determined a moment deficiency equivalent to a magnetic thickness of $d_0 = (0.8 \pm 0.4)$ nm attributed to both interfaces of the film. Our experimental value of d_0 is an order of magnitude larger compared to surface effects measured for pure element films. If the observed surface effect is caused by the upper interface one would expect a smaller magnetic moment determined by the surface sensitive TEY method, which was in fact observed. The expected ratio of moments determined by TEY and TM is roughly given by $\mu(\text{TEY})/\mu(\text{TM}) = 1 - d_0/\lambda_e = 0.6$, which is much smaller compared to the experimental value of $\mu(\text{TEY})/\mu(\text{TM}) = 0.92$. Thus we conclude that the contribution of the lower interface to the dead layer thickness d_0 is even larger. The corresponding contribution d_0^1 of the upper interface between film and capping layer to d_0 is given by $d_0^1 = 0.15$ nm. For the lower interface we obtain $d_0^2 = d_0 - d_0^1 - d(T) = 0.55$ nm, assuming a size effect of $d(300\text{K}) = 0.1$ nm.

The observed attenuation of interface magnetization observed here for a single $\text{Co}_2\text{FeSi}(110)$ film is comparable to the number of dead layers observed in the case of $\text{Co}_2\text{MnGe}(110)/\text{Au}$ and $\text{Co}_2\text{MnGe}(110)/\text{V}$ multilayers [8, 9]. We clearly find the same trend of a stronger attenuation of interface magnetization at the bottom of the film compared to the upper interface, although the difference between upper and lower interface seems to be larger in our case.

The authors would like to thank for financial support from the Deutsche Forschungsgemeinschaft (EL-172/12-2).

* eMail: elmers@uni-mainz.de

- [1] S. Wurmehl, G. H. Fecher, H. C. Kandpal, V. Ksenofontov, and C. Felser, *Phys. Rev. B* **72**, 184434 (2005).
- [2] H. C. Kandpal, G. H. Fecher, C. Felser, and G. Schönhense, *Phys. Rev. B* **73**, 094422 (2006).
- [3] I. Galanakis, P. H. Dederichs, and N. Papanikolaou, *Phys. Rev. B* **66**, 174429 (2002).
- [4] M. Kallmayer, H. Schneider, G. Jakob, H. Elmers, K. Kroth, H. Kandpal, U. Stumm, and C. Cramm, *Appl. Phys. Lett.* **88**, 072506 (2006).
- [5] H. Schneider, G. Jakob, M. Kallmayer, H. J. Elmers, M. Cinchetti, B. Balke, S. Wurmehl, C. Felser, M. Aeschliemann, and H. Adrian, e-print cond-mat/0606666 (2006).
- [6] R. Nakajima, J. Stöhr, and Y. U. Idzerda, *Phys. Rev. B* **59**, 6421 (1999).
- [7] K. Wagner, N. Weber, H. J. Elmers, and U. Gradmann, *J. Magn. Magn. Mater.* **167**, 21 (1997).
- [8] J. Grabis, A. Bergmann, A. Nefedov, K. Westerholt, and H. Zabel, *Phys. Rev. B* **72**, 024438 (2005).
- [9] A. Bergmann, J. Grabis, A. Nefedov, K. Westerholt, and H. Zabel, *J. Phys. D* **39**, 842 (2006).

Correlation of structural and electronic properties of epitaxial Ni₂MnGa/Al₂O₃ films

M. Kallmayer,¹ T. Eichhorn,¹ K. Hild,¹ H. Schneider,¹ G. Jakob,¹ H.J. Elmers,^{1,*} and S. Cramm²

¹*Institut für Physik, Johannes Gutenberg-Universität, D-55099 Mainz, Germany*

²*Institut für Festkörperforschung, Forschungszentrum Jülich GmbH, D-52425 Jülich, Germany*

Martensitic phase transitions have a long history of scientific interest because of their technological importance. The martensitic phase transition is a displacive, first-order transformation from a cubic high-temperature phase to a tetragonally distorted martensite structure at low temperature that occurs in many metal alloys. Recently, Ni₂MnGa has attracted scientific interest because of its potential application as a shape memory alloy. Because Ni₂MnGa is ferromagnetic the martensitic phase transition in this Heusler compound can be induced by a magnetic field. An enormous field induced strain of up to 9.5 % has been reported for this system [1].

The structural phase transition in Ni₂MnGa has been extensively investigated by neutron and X-ray diffraction [3, 4]. The martensitic transition temperature is 210 K, while the Curie temperature is 370 K. In the high temperature phase, the structure of Ni₂MnGa is L2₁ with $a = 5.825 \text{ \AA}$. The structure can be described as a bcc lattice with Ni atoms at the corner sites and Mn and Ga atoms alternately in the center of it. In the martensitic phase, Ni₂MnGa shows a tetragonal distorted structure with $a = 5.92 \text{ \AA}$, $c = 5.56 \text{ \AA}$ and $c/a = 0.94$. An additional modulation in the structure with five or seven layer periodicity has been found [4].

Attempts to understand the martensitic phase transition in Ni₂MnGa from ab-initio calculations turned out to be difficult [2, 5, 6]. While Zayak et al. [6] found a global energy minimum of the martensitic phase for a ratio $c/a > 1$, a stable martensitic phase at $c/a = 0.97$ was reported by Barman et al. [2]. The change of the electronic structure at the phase transition mostly involves Ni derived minority states. The Ni $3d$ states with e_g symmetry that are degenerated in the cubic phase split in the martensitic phase into Ni $3dz^2$ and $3dx^2 - y^2$ states [2]. The minority-spin DOS at EF varies with c/a , while the majority spin DOS is unaffected. This could have important implication in spin polarized transport where the tailoring of the minority-spin DOS can be used [2]. Besides variations of the density of states (DOS) with the c/a ratio, the removal of degeneracies causes changes of the Ni magnetic moments, while Mn moments remain unaffected.

The exceptionally large change of the c/a ratio at the martensitic phase transition of Ni₂MnGa offers the possibility for a direct experimental observation of changes of the spin-resolved DOS and the magnetic moments. Observable changes of the X-ray absorption spectra were predicted by Ayuela et al. [5].

A precondition for a detailed comparison of theoretical predictions and experimental results are single crystalline samples. We prepared epitaxial Ni₂MnGa films using magnetron sputtering on single crystalline substrates. The films showed the martensitic phase transition at slightly higher temperatures ($\approx 250 \text{ K}$) compared to the bulk value as confirmed by X-ray diffraction. In order to test the theoretical predictions [5] we performed X-ray absorption spectroscopy and determined the X-ray magnetic circular

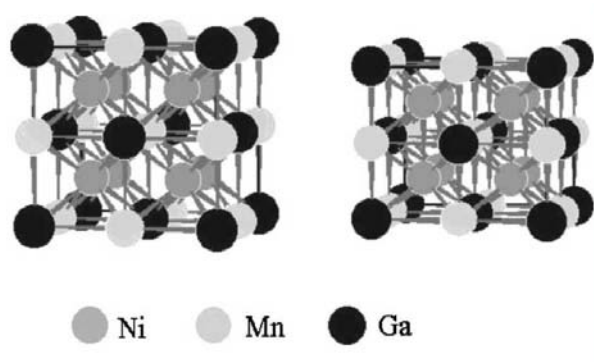


FIG. 1: The crystal structure of Ni₂MnGa in austenitic (left) and martensitic (right) phase. The tetragonal distortion in the martensitic phase is magnified to highlight the structural difference between the two phases. The modulation in the martensitic phase is not shown (taken from Ref. [2]).

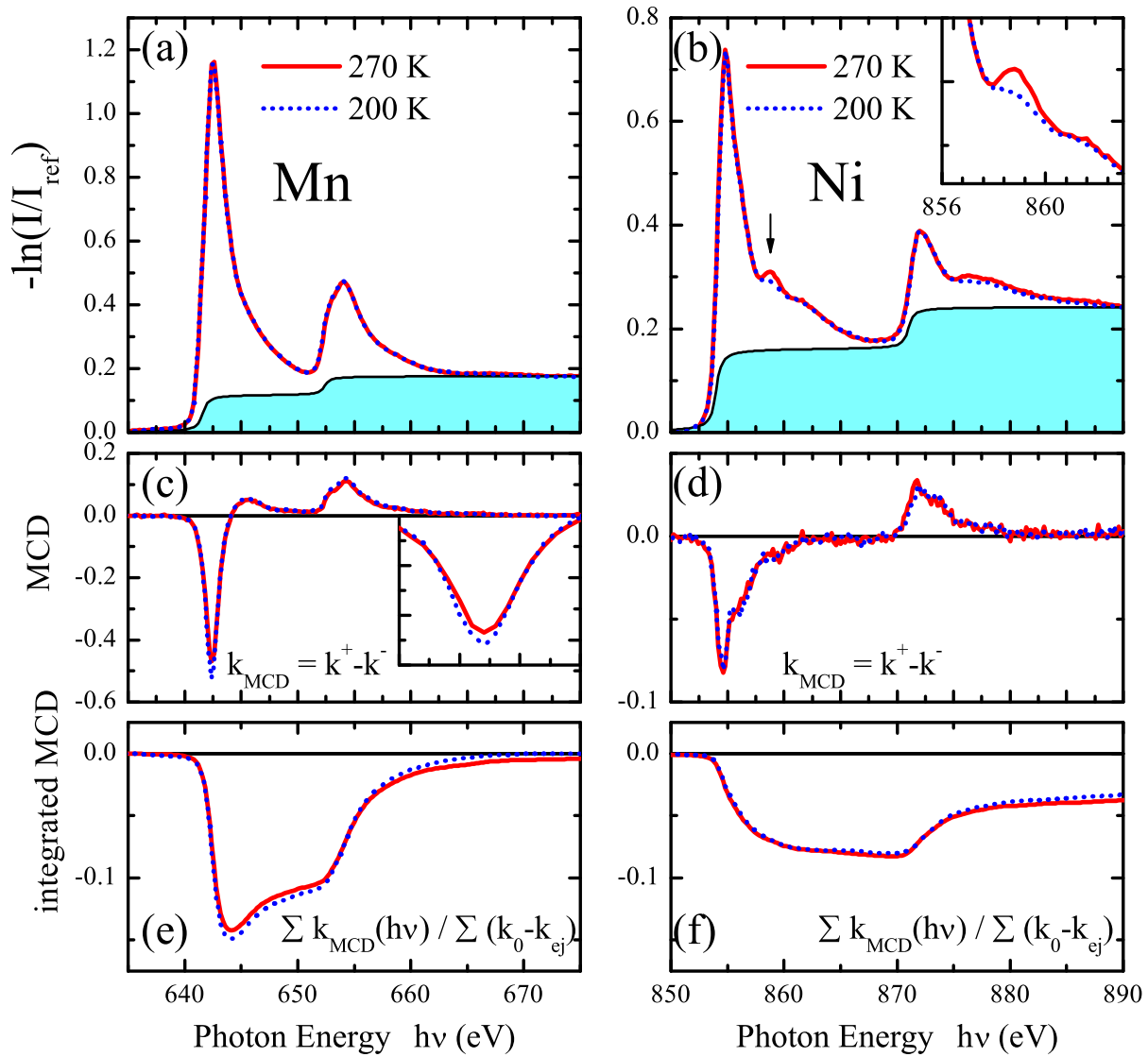


FIG. 2: (a) Absorption coefficient $k = -\ln(I/I_{ref})$ of X-ray light transmitted through a 83 nm $\text{Ni}_2\text{MnSi}(110)$ film on $\alpha\text{-Al}_2\text{O}_3$ at the Mn $L_{2,3}$ edge. (b) Corresponding data measured at the Ni $L_{2,3}$ edge. The inset emphasizes the difference of the extra peak 5 eV above the edge for temperature below and above the phase transition. Circular magnetic dichroism signal ($k^+ - k^-$) for Mn (c) and Ni (d). The inset in (c) shows the L_3 maximum revealing the temperature induced decrease of the XMCD signal. (e) Integrated Mn XMCD spectrum normalized by the integrated 3d - absorption spectrum (step function subtracted). (f) Corresponding data measured at the Ni $L_{2,3}$ edge.

dichroism (XMCD) at the Mn and Ni L - edges. We measured simultaneously the total electron yield (TEY) and the transmitted X-ray intensity (TM) [7]. An external field of 1.6 T was applied normal to the surface and parallel to the X-ray beam.

Fig. 2 show data calculated from the incident-photon-flux-normalized transmission XAS spectra of a $\text{Ni}_2\text{MnGa}(110)/\text{Al}_2\text{O}_3$ Heusler alloy film at temperatures below and above the martensitic phase transition. Assuming that the luminescence signal of the substrate I_{lum}^\pm is proportional to the transmitted X-ray intensity, the X-ray absorption coefficient k is calculated by $k^\pm(h\nu) = -\ln[I^\pm(h\nu)/I_{ref}(h\nu)]$ (Fig. 2(a) and (b)). The reference spectra $I_{ref}(h\nu)$ increases linearly with the photon energy. The absolute value of $I_{ref}(h\nu)$ was then normalized at the pre-edge region of the corresponding element. Fig. 2(c) and (d) show the corresponding XMCD signals for the elements Mn and Ni calculated from the two spectra measured with opposite magnetization direction.

The intensity of the extra peak in the Ni absorption signal (indicated by the arrow in Fig. 2(b)) clearly depends on the structural phase. While this peak is well pronounced in the cubic phase above the transition temperature it is nearly suppressed in the tetragonally distorted phase at lower temperatures. This is in full agreement with the theoretical prediction [5].

The sum rule analysis results (see integrated XMCD data shown in Fig. 2(e) and (f)) in spin magnetic moments for Ni of $\mu_{\text{spin}}/N_h = 0.175 \mu_B$ at low temperature and $\mu_{\text{spin}}/N_h = 0.176 \mu_B$ at high temperature. The orbital to spin ratio amounts to $\mu_{\text{orb}}/\mu_{\text{spin}} = 0.13$ and $\mu_{\text{orb}}/\mu_{\text{spin}} = 0.14$, respectively. Within the error limits there is no temperature dependence present for the Ni magnetic moments. For Mn we obtain values $\mu_{\text{spin}}/N_h = 0.335 \mu_B$ at low temperature and $\mu_{\text{spin}}/N_h = 0.313 \mu_B$ at high temperature. The orbital moment nearly vanishes for both cases. The decrease of the Mn moment with increasing temperature reflects the usual magnetization decrease with increasing excitation of spin-waves. Surprisingly, the Ni moment remains constant. This is in contradiction to the theoretical prediction [2]. Barman et al. [2] calculated a 20 % decrease of the Ni moment at the transition from the tetragonally distorted phase to the cubic phase.

In summary we found a correlation of structural and electronic properties at the martensitic phase transition of Ni₂MnGa. The lift of degeneracies of Ni 3d related unoccupied electronic states in the tetragonally distorted phase leads to a characteristic decrease of the corresponding peak in the X-ray absorption spectra. The Ni magnetic moment increases with respect to the Mn moment at the transition from the distorted to the cubic phase.

The authors would like to thank for financial support from the Deutsche Forschungsgemeinschaft (EL-172/12-2).

* eMail:elmers@uni-mainz.de

- [1] A. Sozinov, A. A. Likhachev, N. Lanska, and K. Ullakko, Appl. Phys. Lett. **80**, 1746 (2002).
- [2] S. R. Barman, S. Banik, and A. Chakrabarti, Phys. Rev. B **72**, 184410 (2005).
- [3] V. V. Martynov and V. V. Kokorin, J. Phys. III **2**, 739 (1992).
- [4] P. J. Brown, J. Crangle, T. Kanomata, M. Matsumoto, K.-U. Neumann, B. Ouladdiaf, and K. R. A. Ziebeck, J. Phys.: Condens. Matter **14**, 10159 (2002).
- [5] A. Ayuela, J. Enkovaara, and R. M. Nieminen, J. Phys.: Condens. Matter **14**, 5325 (2002).
- [6] A. T. Zayak, P. Entel, J. Enkovaara, and R. M. Nieminen, J. Phys.: Condens Matter **15**, 159 (2003).
- [7] M. Kallmayer, H. Schneider, G. Jakob, H. Elmers, K. Kroth, H. Kandpal, U. Stumm, and C. Cramm, Appl. Phys. Lett. **88**, 072506 (2006).

Time-resolved XMCD experiments at ALICE diffractometer

Stefan Buschhorn, Frank A. Brüßing, Alexei Nevedov, Hartmut Zabel
*Experimentalphysik IV, Ruhr-Universität Bochum,
Universitätsstrasse 150,
44780 Bochum, Germany*

Magnetic recording and data storage devices have become a matter of large interest within the last years. The precession of the magnetic moments is a natural limit for magnetic switching of single domains, and thus a thorough understanding of precession dynamics in magnetic structures is indispensable in order to access high writing and reading times. X-ray magnetic circular dichroism (XMCD) provides a very powerful tool as different layers in a heterostructure can be distinguished via element selectivity, and the time structure of a synchrotron opens a possibility to measure in a stroboscopic manner. In this way, precession frequency and phase relation for different elements are accessible by sweeping the x-ray flash with respect to an excitation of the system [1; 2].

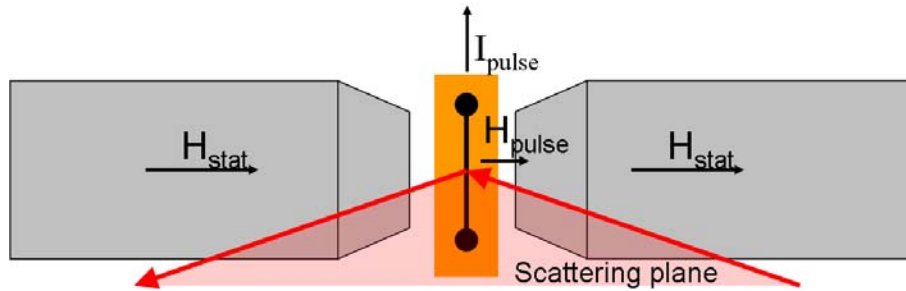


Figure 1: Geometry of the sample and external magnetic fields The stripline with the Py layer is perpendicular to the scattering plane, thus the pulsed field H_{pulse} is parallel to the external static field H_{stat} .

The scattering geometry is shown in Figure 1. An ideally rectangular shaped current pulse is provided through a stripline, and a short-living magnetic field is produced perpendicular to the current direction. The stripline is perpendicular to the scattering plane, and the pulsed magnetic field is parallel to the existing static field H_{stat} . If the magnetic moments are initially aligned parallel to the stripline by an external field, this pulse sets an angle between the magnetic moment and applied static field direction. The precession of the magnetic moment can then be monitored by means of XMCD. In order to set up such a system, we prepared a Cu stripline of 500 nm thickness and 200 μm width on a 1x1 cm^2 sapphire substrate by ion-beam sputtering in UHV vacuum system with an Ar pressure of $9.4 \cdot 10^{-7}$ mbar. For the magnetic layer Py was chosen and deposited directly on top of the stripline *in-situ* to get a maximum field amplitude, which decreases with $1/r$, where r is the distance from the center of the stripline. The current pulse is provided by a pulse generator and can be changed in length and position with respect to an arbitrary zero point. An oscilloscope is used to control the signal shape, i.e. voltage amplitude and width of the pulse. The experiments were carried out with the ALICE chamber at beamline UE52-SGM at BESSY, Germany, in single-bunch mode. Sample and detector are set to specular reflectivity condition with $\Theta = 10^\circ$, and the sample position in the

beam is verified by an energy scan, where the resonant reflection of both Fe and Ni at the energies corresponding to the $L_{3,2}$ transitions can be seen. Then we measured hysteresis loops of the sample by varying the static field H_{stat} without any additional field, and in a *quasi-static* mode. In this way, the maximum current pulse height provided by the generator, leading to a current of about 2 A, is applied for pulses of $718 \mu s$ width, the maximum pulse length provided by the pulse generator at a period of $8 \mu s$. The latter two hysteresis loops are shown in Figure 2. Obviously, the curves have the same shape but are shifted by 2.5 Oe in opposite directions. Hence, we are able to produce an additional field of 2.5 Oe at the Py film perpendicular to the stripline.

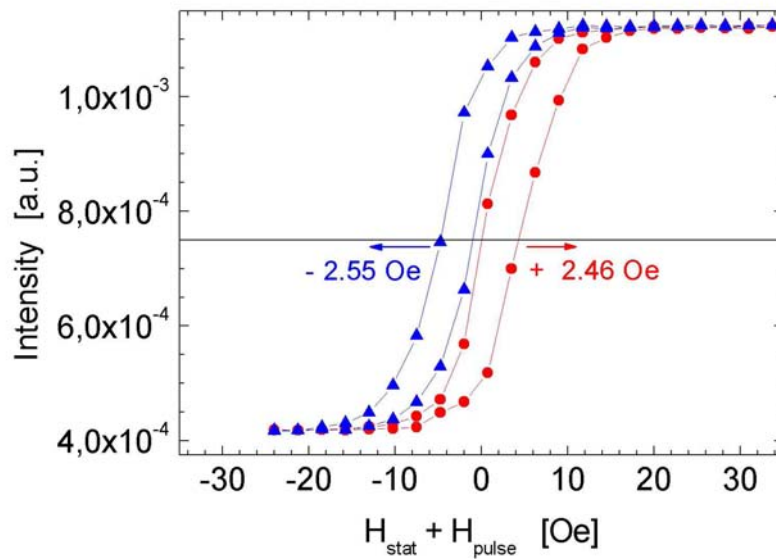


Figure 2: The shift of the Fe hysteresis loop gained by a quasi-constant current through the stripline. Depending on the current direction, a shift of ≈ 2.5 Oe in both directions is realised.

As next step we applied short current pulses of 5 – 35 ns length as is shown in the upper part of Figure 3. The x-ray flash is represented by stars, showing 800 ns periodicity. The current pulse can be changed in width τ and position Δt with respect to an arbitrary zero point that has a fixed phase relation to the flash. The bottom part of Figure 3 shows the resulting timescan: In the first part $\Delta t = 640$ ns is fixed, and each line marks an increase of 5 ns for the width of the pulse τ . As from $t = 448$ s on, $\tau = 35$ ns is kept constant and the current pulse is shifted to later times in steps of 5 ns. The intensity decreases linearly, but from $\tau = 15$ ns on the intensity drops down stepwise with increasing pulse width. By shifting the pulse backwards in time in the second half, the intensity increases stepwise again. These steps are attributed to a stepwise change of the magnetisation direction of the Py film from an antiparallel to an orientation parallel to the pulsed field. The magnetisation changes as long as the pulsed field is applied, where a pulse shift produces a change in intensity. The magnetisation direction is directly measured at a certain time, and by changing Δt in steps of about 100 ps the magnetisation of the film after applying can be monitored with time. In the future we plan to implement a second static field parallel

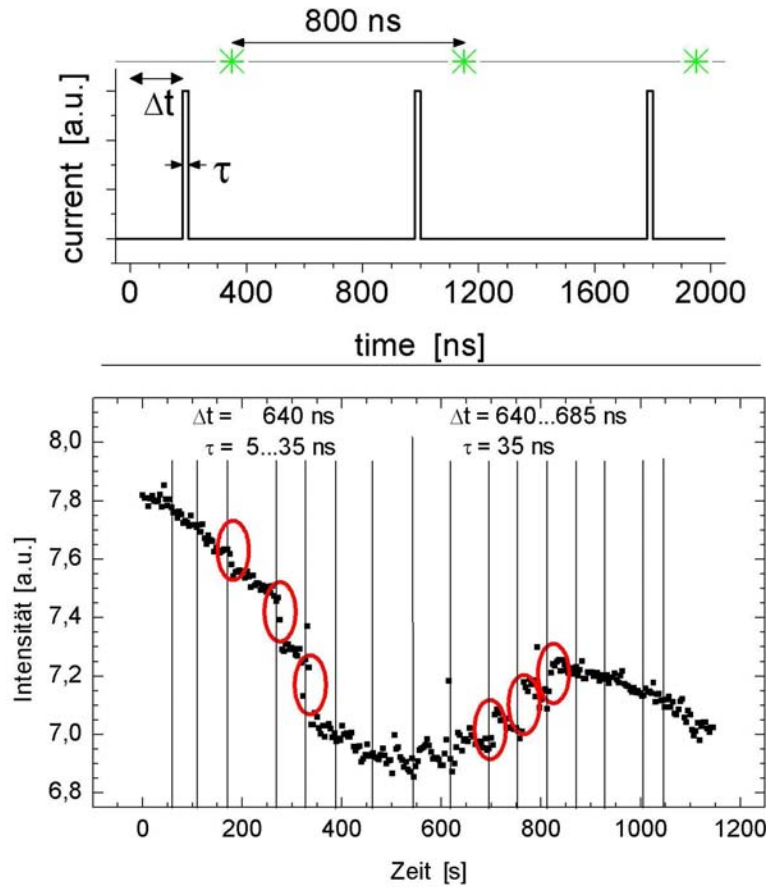


Figure 3: Schematic view (top) and timescan (bottom) of experiments with short current pulses. For details, see text.

to the stripline. Then the magnetic moment will precess around the field axis on a cone surface rather than switch the direction. As a consequence the vector component parallel to the pulsed field is sinusoidal in time. This component can again be monitored, a change of the magnetisation component leads to a change in intensity. The time delay between current pulse and x-ray flash has to be changed by much less than the time needed for a full rotation, and the oscillation in intensity is then a direct measure for the precession frequency.

This work was supported by the BMBF under contracts 05KF4PCA (ALICE diffractometer) and 05ES3XBA/5 (travel to BESSY).

References

- [1] M. Bonfim, G. Ghiringhelli, F. Montaigne, S. Pizzini, N. B. Brookes, F. Petroff, J. Vogel, J. Camarero, and A. Fontaine, *Phys. Rev. Lett.* **86**(16), 3646–3649 (2001)
- [2] W. E. Bailey, L. Cheng, D. J. Keavney, C.-C. Kao, E. Vescovo, and D. A. Arena, *Phys. Rev. B* **70**(17), 172403 (2004)

The initial stages of oxide-mediated growth of iron silicides on silicon

M.V. Gomoyunova ¹, I.I. Pronin ¹, D.E. Malygin ¹, A.S. Voronchihin ¹, D.V. Vyalikh ²,
S.L. Molodtsov ²

¹ A.F.Ioffe Physico-Technical Institute, 194021, St. Petersburg, Russia

² Institut für Oberflächenphysik und Mikrostrukturphysik Fachrichtung
Physik Technische Universität Dresden, D-01062 Dresden, Germany

Much attention has been paid to ternary Fe-O-Si systems in the recent years [1–3], and particularly to the problem of oxygen influence on the initial stages of iron silicides formation. The high-temperature solid-phase reaction between iron and silicon was studied for two different systems: Fe₂O₃ films deposited on the silicon surface and oxidized Fe/Si

multi-layer structures. However, there are no any experiments on thin Fe films deposited on the surface of oxidized silicon so far. Such kind of investigations was performed for another 3d-metal – cobalt [4, 5], and it was shown, that the reaction of silicide formation proceeds under the oxidized layer, that notably improves quality of CoSi₂ films. The aim of the present work was to study the initial stages of iron silicides formation in the ternary system Fe/SiO_x/Si(100).

The experiments were carried out in vacuum $\sim 5 \times 10^{-11}$ mBar using the beams with the energy of 110–540 eV. The overall energy resolution of the electron energy analyser and the monochromator was ~ 100 meV. The substrates used were Si(100) wafers with a misorientation of less than 0.1°. The samples were flashed up to 1200°C and cooled slowly, that ensured the sharp 2×1 LEED pattern and the absence of C and O contaminations. The oxidation of the sample surface was carried out at 500°C by exposing it to an oxygen (10 L). Iron films were deposited from an electron bombardment evaporator at a rate of ~ 1 ML/min.

The Si 2p spectrum obtained after deposition of 4 ML of iron on the oxidized silicon surface as well as the spectra measured during the graduated sample annealing are shown in Fig.1. The dots represent the experimental data, while solid lines are the fitting results and fitted components. Besides

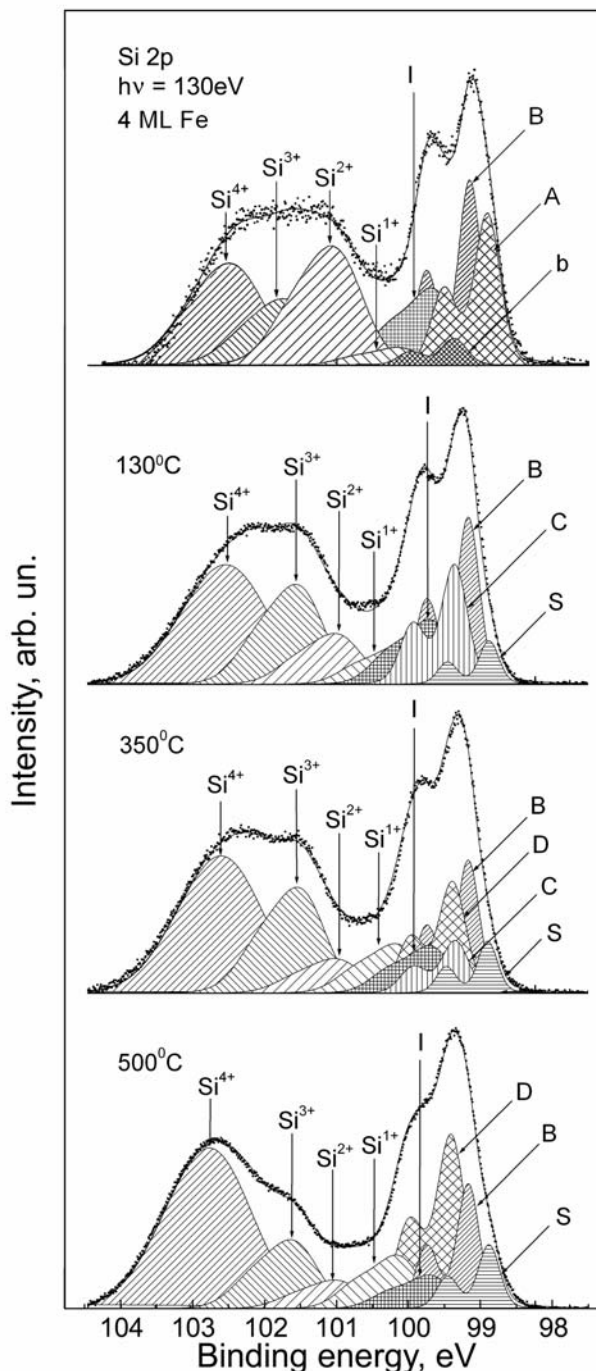


Figure 1.

different oxide components the first spectrum contains A mode with the negative energy shift -0.25 eV, as well as I mode with the energy shift of 0.5 eV. According to [6], the A mode corresponds to the Fe-Si solid solution formed under the oxide layer, while the I mode is due to a ternary interface phase consisted of Fe, O and Si atoms.

The first low-temperature (60°C) annealing leads to the transformation of the significant part of the solid solution into a new silicide phase, characterized by C mode with the positive energy shift of 0.2 eV. This fact proves that the solid-phase reaction between Fe and Si atoms starts. It should be emphasized that the cobalt silicides formation occurs at higher temperature (250°C), showing greater reactivity of the Fe/Si interface as compared with the Co/Si interface. Subsequent temperature increase up to 130°C results in the growth of C mode intensity and decrease of A mode intensity. The further annealing of the sample until 250°C does not change Si 2p spectrum, demonstrating the constancy of the phase composition of the analyzing area. The next process stage takes place at 350°C , when a new D mode appears with the energy shift of ~ 0.25 eV, and C mode intensity decreases significantly. The last mode disappears completely after annealing temperature reaches 420°C , and D mode becomes dominant in the spectrum. The spectrum structure remains during the subsequent temperature increase up to 630°C .

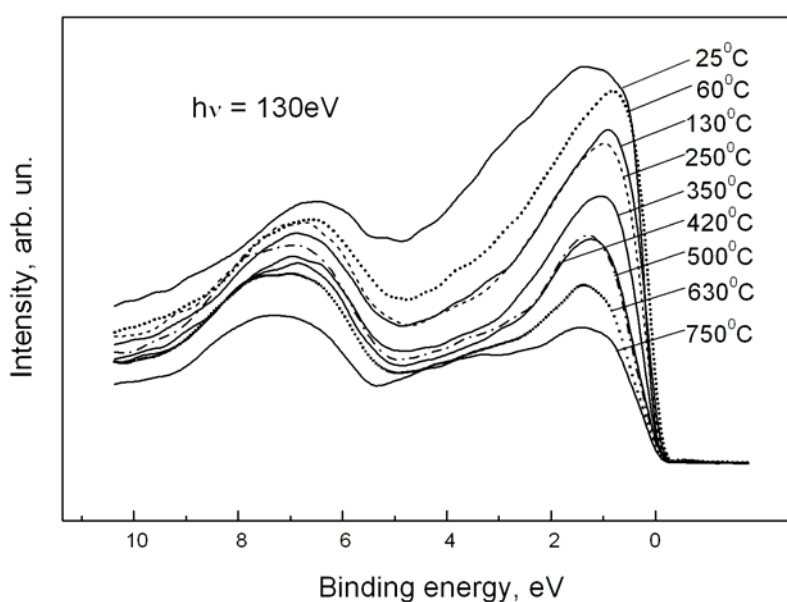


Figure 2.

The valence band spectra obtained in the experiment are shown in Fig. 2. As it is seen, the spectra observed in the ranges of temperature $130^{\circ}\text{C} - 250^{\circ}\text{C}$ and $420^{\circ}\text{C} - 500^{\circ}\text{C}$ are very similar, so two different iron silicides are formed in these intervals. We have compared valence band spectra of these silicides with the standard ones. As it was found out, low-temperature iron silicide characterized by C mode is the metastable FeSi phase with the CsCl structure. Regarding higher-temperature

iron silicide (D mode), it can be identified as the semiconducting disilicide $\beta\text{-FeSi}_2$. Finally, it should be noticed that the considered solid-phase reaction is accompanied by modification of the silicon oxide layer. The most important tendency is the increase of Si^{+4} and Si^{+1} silicon oxide components and the decrease of Si^{+2} mode.

The work was supported by RFBR (grant № 04-02-17651) and the Russian-German laboratory at BESSY.

References

1. K. Prabhakaran, Y. Watanabe, K.G. Nath et al. *Surf. Sci.* **545**, 191 (2003).
2. M.G. Garnier, T. de los Arcos, J. Boudaden et al. *Surf. Sci.* **536**, 130 (2003).
3. B.A. Orłowski, B.J. Kowalski, K. Fronc et al. *J. Alloys and Comp.* **362**, 202 (2004).
4. R.T. Tung. *Jpn. J. Appl. Phys.* **36**, 1650 (1997).
5. M.V. Gomoyunova, I.I. Pronin, D.E. Malygin et al. *Surf. Sci.* **600**, 2449 (2006).
6. M.V. Gomoyunova, D.E. Malygin, I.I. Pronin. *Technical Physics.* **51**, 1243 (2006).

EXAFS and MEXAFS above the L_3 -edge of Ni

H.H. Rossner, D. Schmitz, N. Darowski,
Hahn-Meitner-Institut Berlin,
Glienicke Str. 100, D-14109 Berlin, Germany

In previous work [1] the relation between spin-averaged extended x-ray absorption fine structure (EXAFS) energy spectra and magnetic EXAFS (MEXAFS) energy spectra has been shown for the overlapping L -edges of Fe. This relation is based on the rigid band model (RBM) and describes the MEXAFS signal $\mu^M = \mu_{L_2}^M + \mu_{L_3}^M$ by the spin-averaged EXAFS-components μ_{L_2} and μ_{L_3} shifted by an exchange-like energy ΔE :

$$\mu^M(E) \approx \frac{1}{4} \left[\mu_{L_3}(E + \frac{\Delta E}{2}) - \mu_{L_3}(E - \frac{\Delta E}{2}) \right] - \frac{1}{2} \left[\mu_{L_2}(E + \frac{\Delta E}{2}) - \mu_{L_2}(E - \frac{\Delta E}{2}) \right]. \quad (1)$$

This approximation was now tested for the overlapping L -edges of Ni with larger spin-orbit split energy and smaller magnetic moment compared to Fe. A Ni film with thickness of roughly 120 Å was grown in UHV at room temperature on clean Cu(100) substrate. Energy spectra of spin-averaged and spin-polarized EXAFS data were measured above the L_3 -edge of Ni at temperatures of 30 K and 300 K. The data were taken at the elliptical undulator beamline UE46-PGM using the gap-scan technique with circularly polarized light in the energy range of $850 \text{ eV} \leq E \leq 1400 \text{ eV}$.

For the analysis of the EXAFS data we applied the Bayes-Turchin procedure described in Ref. [2]. This procedure takes into account experimental as well as model uncertainties, determines the atomic-like background by cubic-spline functions, and represents the EXAFS Debye-Waller parameters σ^2 by structural disorder components σ_{struct}^2 and thermal disorder components σ_{therm}^2 , $\sigma^2 = \sigma_{\text{struct}}^2 + \sigma_{\text{therm}}^2$. The thermal disorder is described by a force-field model using two spring constants, and the *a priori* values of these constants are fitted to the vibrational density of states extracted from inelastic neutron scattering. The phonon frequency spectrum at 298 K was calculated from 18 Born-von Karman parameters which had been fitted to dispersion relations [3]. It is not expected that the two-parameter force-field model with the nearest neighbor spring constant κ_1 and the next-nearest neighbor spring constant κ_2 can reproduce all details of the frequency spectrum build from 18 parameters of five shells. However, as shown in Fig. 1, the two parameter model with $\kappa_1 = 36.5 \text{ N/m}$ and $\kappa_2 = 0.5 \text{ N/m}$ in fact approximates the result of the 18 parameter model very well.

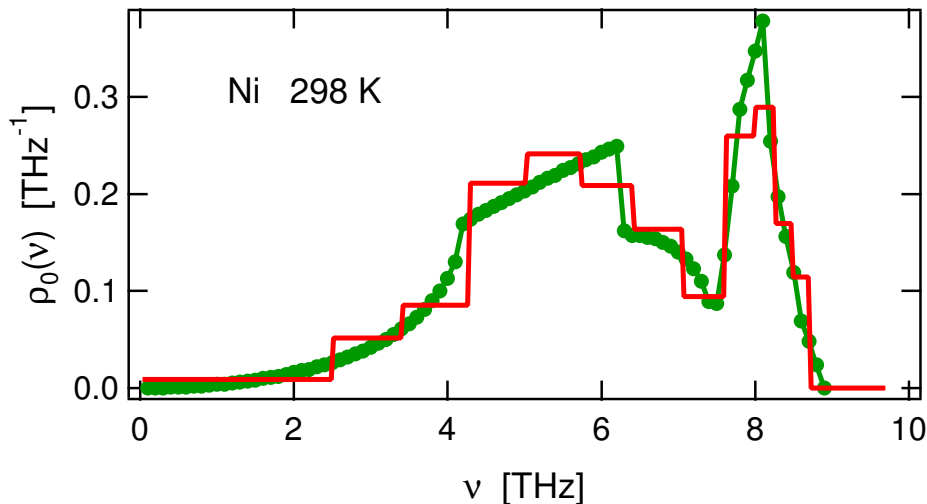


Figure 1: Comparison of vibrational density of states deduced from inelastic neutron scattering (dots) and results of a two-parameter force-field model (histogram).

In the analysis procedure a Ni cluster of radius 8 Å was considered. Due to the misfit of 2.6 % between the crystal parameters of Ni ($a_{Ni} = 3.524$ Å) and Cu ($a_{Cu} = 3.615$ Å) a tetragonal distortion is expected in the Ni film. This distortion is modelled by two lattice parameters a_{xy} and a_z . Starting from an ideal fcc-crystal structure the *a priori* value of a_{xy} was set assuming an inplane lattice expansion by 1 %. The out-of-plane contraction of a_z follows from volume conservation. To reduce the number of fit parameters, the following assumptions were made: a) the amplitude reduction factor was fixed to 0.9, b) the spin-orbit split energies were taken from the FEFF code, c) all third cumulants $C_{3,j}$ of paths j were set to zero, except $C_{3,1}$ which was included in the fit serving as sensor for anharmonicities of the scattering potential, d) the variations of the shell radii were calculated from variations of the lattice parameters a_{xy} and a_z , and e) the Debye-Waller parameters of all scattering paths were calculated from σ_{struct}^2 , κ_1 and κ_2 , which were treated as fit parameters using *a priori* values of 0.0 Å², 36.5 N/m, and 0.5 N/m, respectively. The *a priori* value of the reference energy E_0 was set to 860 eV, resulting in overlapping positions of the first EXAFS oscillation of model and data. With 16 support points for the cubic-spline correction-functions of the atomic-like background μ_0 we thus end up with 23 fit parameters.

The Bayes-Turchin analysis procedure uses probability distributions for experimental data and model parameters to account for uncertainties. The experimental uncertainties were assumed to be 0.5 % of the measured absorption coefficient, except in the edge regions, where the failure of the multiple-scattering approach requires the elimination of the data from the fit. Thus, very large uncertainties were attributed to the data in the L_1 -edge region between $6.3 \text{ \AA}^{-1} \leq k \leq 7.3 \text{ \AA}^{-1}$. The model uncertainties of scattering amplitudes f , scattering phases Φ , and effective mean free path λ were assumed to be $\Delta f/f = 7 \%$, $\Delta\Phi = 0.07$ rad, and $\Delta\lambda/\lambda = 10 \%$, respectively. The uncertainties caused by the truncation of the multiple scattering series have been taken into account for each edge separately as explained in Ref. [2] and added quadratically to the other uncertainties.

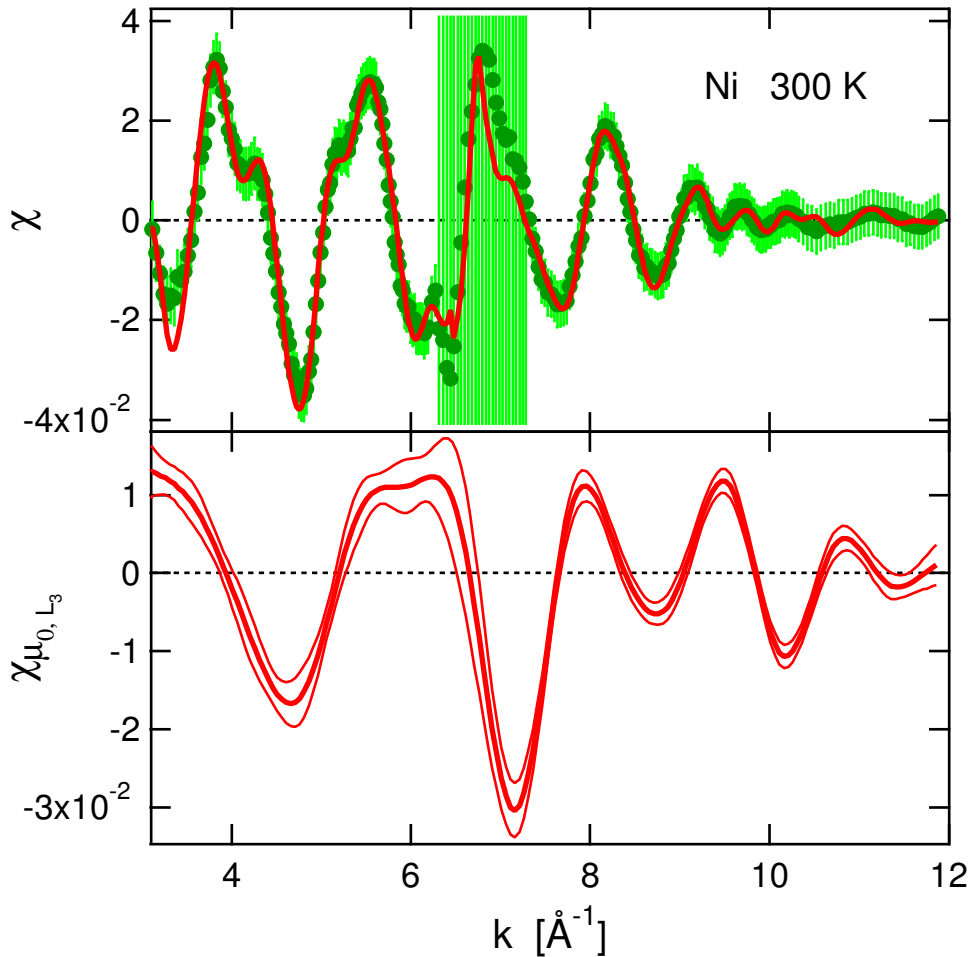


Figure 2: Upper panel: Comparison of experimental EXAFS signal (dots with error bars) and *a posteriori* model EXAFS signal. Lower panel: *a posteriori* normalized background oscillation with error band.

The fitting procedure is applied to the measured absorption coefficient μ_{exp} which was normalized to the smoothed model function $\mu_{0,\text{FEFF}}$ calculated by FEFF. It yields the contributions χ_{L_s} and $\mu_{0,L_s} + \delta\mu_{0,L_s}$ for all L_s -edges, $s = 1, 2, 3$. In Fig. 2 preliminary results for the room temperature data are shown. The background oscillations for the L_3 -edge are defined as $\chi_{\mu_{0,L_3}} = \delta\mu_{0,L_3}/\mu_{0,L_3}$, and have amplitudes similar to the EXAFS oscillations. They are interpreted as combination of atomic background oscillations and systematic disturbances of the undulator beam. The large amplitudes strongly underline the importance of the background determination. The analysis yields *a posteriori* lattice parameters with *a posteriori* errors of $a_{xy} = 3.63 \pm 0.01 \text{ \AA}$ and $a_z = 3.28 \pm 0.02 \text{ \AA}$. The value of a_{xy} is very close to the lattice parameter of Cu and suggests that the lattice-parameter misfit of 2.6 % even exists at relatively thick Ni films. Within *a posteriori* error bars this result is independent of the number of cubic spline support points N in the range $14 \leq N \leq 20$. The *a posteriori* parameters of σ_{struct}^2 , κ_1 , and κ_2 are $0.0046 \pm 0.0006 \text{ \AA}^2$, $36.5 \pm 1.1 \text{ N/m}$, and $0.5 \pm 1.1 \text{ N/m}$, respectively, indicating a moderate structural deformation. It is noted, that the force-field parameters are not changed by the fit implying that the data do not require any modifications of these parameters. As expected, the third cumulant $C_{3,1}$ stays at zero.

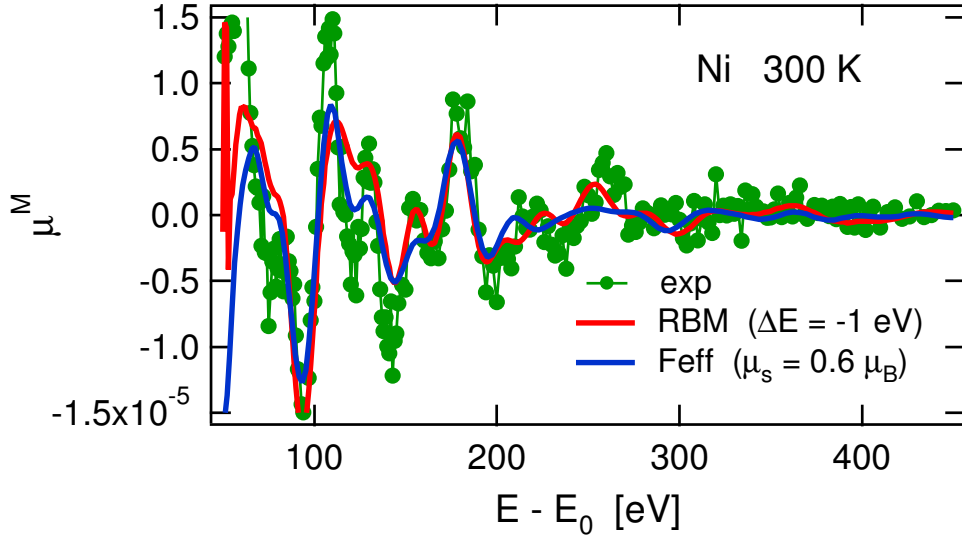


Figure 3: Upper panel: Comparison of experimental MEXAFS signal (dots), rigid band model approximation (red line), and FEFF calculation (blue line).

With the components $\mu_{L_3}(E)$ and $\mu_{L_2}(E)$ deduced from $\mu_{\text{exp}}(E)$ the approximation of Eq. (1) can be applied. The comparison of the experimental MEXAFS signal with this rigid band model approximation using $\Delta E = -1 \text{ eV}$ is shown in Fig. 3. Also shown in this figure is the FEFF calculation for magnetic EXAFS performed for a lattice distortion of 2.6 %. It is noted that the Ni MEXAFS data are not sensitive to this distortion because of poor statistics. A good agreement between FEFF calculation and experimental data is achieved when the magnetic moment is set antiparallel to the beam direction, opposite to the situation for the XMCD signal in the edge region. This finding corroborates the rigid band model result of a negative exchange-like energy ΔE . The absolute value of ΔE is proportional to the magnetic spin moment μ_s averaged over all scattering paths. We observe that $|\Delta E| = 1 \text{ eV}$ corresponds to $\mu_s = 0.6 \mu_B$.

References

- [1] H.H. Rossner, D. Schmitz, P. Imperia, H.J. Krappe, and J.J. Rehr, Phys. Rev. B **74**, 134107 (2006).
- [2] H.J. Krappe and H.H. Rossner, Phys. Rev. B **66**, 184303 (2002).
- [3] G.A. DeWit and B.N. Brockhouse, J. Appl. Phys. **39**, 451 (1968).

Cross sections for the ionisation continuum of H₂ in the 15.3-17.2eV energy range

M. Glass-Maujean¹, S. Klumpp², L. Werner², A.Ehresmann² and H. Schmoranzner³

¹LPMAA, Université P. et M. Curie /CNRS, 4, pl Jussieu, F-75252 Paris Cedex 05, France

²Institut für Physik, Universität Kassel, D-34132 Kassel, Germany

³Fachbereich Physik, Technische Universität Kaiserslautern, D-67653 Kaiserslautern, Germany

We recorded the absorption and ionisation spectra of H₂, at very high resolution, in the 72 to 81 nm spectral range (15.3-17.2 eV energy range), at low pressure and room temperature. The photoionisation and absorption cross sections of H₂ have been measured absolutely several times above 18 eV.^{2,3} Near threshold, however, either the studies yield absolute values at very low resolution only and so integrate over strong autoionisation structures or, at high resolution, they give relative values only.⁴ We will present here the first measurements of absolute values at high resolution for the cross sections of the ionisation continuum at low energy (15.3 to 17.2 eV). The ionisation energy threshold (from the rotational $J''=0$ level) is located at 15.4257 eV⁵ and the dissociative ionisation energy threshold, i.e. the dissociation energy of the H₂⁺ ions, lies at 17.2 eV (referring to the rotational $J''=0$ level of H₂). Between these two energies, the $X^2\Sigma_g^+$ state of the ion exhibits a progression of 18 vibrational levels; each of them corresponds to a threshold which induces a step in the photoionisation cross section.^{6,7}

The VUV photons from the undulator beamline U125/2-10m-NIM of BESSY II were dispersed by a 10m-normal incidence monochromator equipped with a 1200-lines/mm grating. At the third order, with 45µm-wide slits, a resolution of 0.0012 nm was achieved. These photons were focused into a differentially pumped 39 mm-long gas cell containing H₂ at a pressure of 20 mT (27 µbar) measured by a baratron gauge, at room temperature. A photodiode located at the back of the cell enabled to measure the intensity of the transmitted light. The intensity of the incident light was monitored by the ionisation signal from a focussing mirror in front of the cell. A small voltage of 10 V was applied to an electrode in the target cell in order to collect the photoions. Their current is scanned simultaneously with the transmitted light signal as a function of the incident-photon energy leading to the ionisation excitation and absorption spectra.

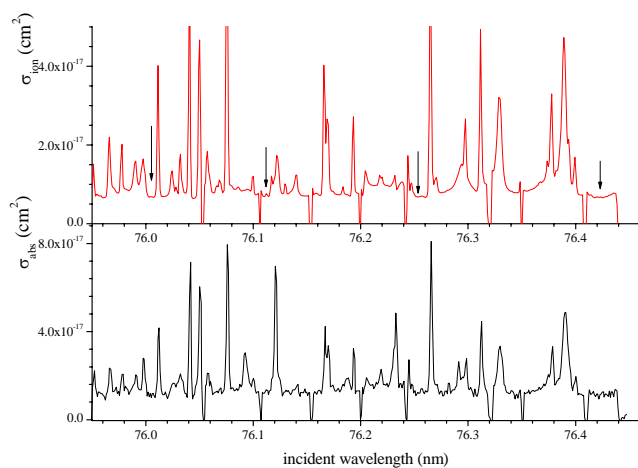


Fig.1: A typical section of the measured absorption (upper panel) and ionisation (lower panel) spectra. The zero pressure points are used as calibration marks. The arrows indicate the measured points.

From the known pressure and absorption length, the absorption spectrum is directly calibrated. For most of the scans, additional data points were registered without gas at the beginning, at the end and even during the scans. The ionisation cross section can be calibrated with an uncertainty of 6% to be added to the error due to the noise at each point which is of the order of a few 10^{-20}cm^2 .

The high resolution allowed us to distinguish the continuum from the lines in most of the wavelength ranges but not everywhere. Fig. 1 displays small parts of the spectra with the points at zero pressure as markers. The results of the continuum measurements are summarized in fig. 2.

There is important theoretical literature on the H₂ photoionisation cross section. Most of the papers concern either the energy range higher than 18eV or fixed

energy values (21.2 eV).⁹⁻¹³ The threshold region is sketched only in few references.^{6,7} From the graph in ref. 7, we extracted the data displayed in fig. 2 for comparison. We shifted the calculated threshold to adjust it to the absorption from the $J''=1$ level, the most populated rotational level (66%) of the ground state (the rotational structure is always neglected in these calculations). We investigated the first threshold region where we were able to distinguish the rotational thresholds (fig. 3). The curve shown in fig. 3 was calculated with steps located at the theoretical positions of the respective thresholds from the various rotational levels of the ground state; as a first approximation, the steps's

intensities were taken proportional to the rotational populations in the ground state and to the

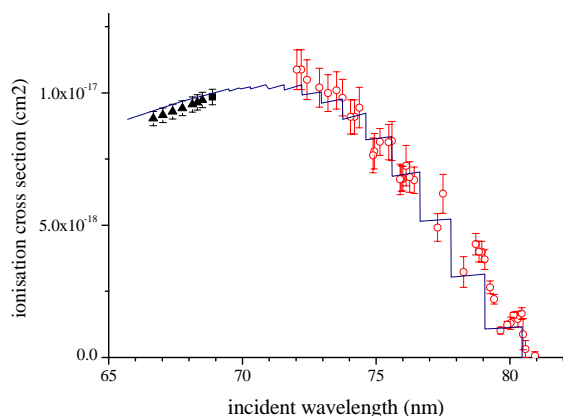


Fig. 2 Ionisation cross section for the continuum vs the incident-photon wavelength. Theoretical values (line) are from ref. 7. Experimental values: open circles are present data, full triangles data from ref 2;

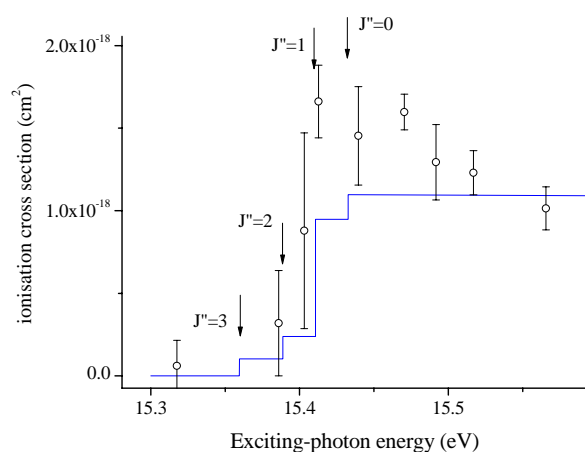


Fig. 3: Ionisation cross section for the continuum near the threshold showing the rotational thresholds, ($J''=0$ to $J''=1$, $J''=1$ to $J''=0$, $J''=2$ to $J''=1$ and $J''=3$ to $J''=2$); Theoretical values (line) see text, experimental values: open circles are present data.

theoretical value from ref. 7. The deviation of the point located just below the $J''=1$ threshold with quite a large ionisation cross section may be due to the ionisation of high Rydberg states in the weak electric field used to detect the ions ($\sim 3\text{V/cm}$). The experimental points reproduce well the steps but they suggest that the shape of the ionisation cross section at threshold is not a mere flat step but may include a short bump. That may be also the case for the second vibrational threshold.

The absorption continuum is not only due to ionisation but also to dissociation. Therefore, the measurements of the absorption continuum cannot lead to a precise determination of the ionisation cross section, in addition to the fact that the absorption continuum is much noisier. The $\text{H}(n=2)+\text{H}(1s)$ dissociation channel opens at 85nm; its continuum cross section slowly decreases at shorter wavelengths; around 80nm, it amounts to roughly 1 Mbarn (or 10^{-18}cm^2). At 75nm, the $\text{H}(n=3)+\text{H}(1s)$ dissociation channel opens with a dissociation cross section of the same order of magnitude, very small compared to the ionisation cross section.

We determined the continuum ionisation cross section of H_2 near the threshold in absolute values in a high resolution excitation spectrum. The successive vibrational thresholds were clearly put in evidence. The agreement between experimental values and theoretical ones is very good except around the first and second vibrational thresholds where the experimental data exceed the theoretical ones. The effect of the rotation can be clearly seen. Its neglect in the calculations may be the origin of the discrepancy.¹⁴

- ¹ J.W. Gallager, C.E. Brion, J.A.R. Samson, and P.W. Langhoff, *J. Chem. Phys. Ref. data* **17**, 9 (1988) and references therein
- ² Y.M. Chung, E.-M. Lee, T. Masuoka, and J.A.R. Samson, *J. Chem. Phys.* **99**, 885 (1993)
- ³ J.A.R. Samson and G.N. Haddad, *J. Opt. Soc. Am.* **B11**, 279 (1994)
- ⁴ P. M. Dehmer and W.A. Chupka, *J. Chem. Phys.* **65**, 2243 (1976)
- ⁵ G. Herzberg and Ch. Jungen *J. Mol. Spectrosc.*, **41**, 425 (1972)
- ⁶ S.V. O'Neil and W.P. Reinhardt, *J. Chem. Phys.* **69**, 2126 (1976)
- ⁷ G. Raseev and H. Le Rouzo, *Phys. Rev. A* **27**, 268 (1983)
- ⁸ U. Fano, *Phys. Rev.* **124**, 1566 (1961)
- ⁹ P.H.S. Martin, T.N. Rescigno, V. McKoy and W.H. Henneker, *Chem. Phys. Lett.* **29**, 496 (1974)
- ¹⁰ H. Tai and M.R. Flannery, *Phys. Rev* **A16**, 1124 (1977)
- ¹¹ C.M. Dutta, F.M. Chapman, Jr and E. F.Hayes, *J. Chem. Phys.* **67**, 1904 (1977)
- ¹² J.A. Richards and F.P. Larkins, *J. Phys.* **B19**, 1945 (1986)
- ¹³ I. Ceelli, R. Moccia and A. Rizzo, *J. Chem. Phys.* **98**, 8742 (1993)
- ¹⁴ M. Glass-Maujean, S. Klumpp, L. Werner, A.Ehresmann and H. Schmoranzler, *J. Chem. Phys.* in press

Observation of the oscillating absorption spectrum of a double-well state: the $B''\bar{B}^1\Sigma_u^+$ state of H_2

M. Glass-Maujean¹, S. Klumpp², L. Werner², A. Ehresmann² and H. Schmoranzner³

¹LPMAA, Université P. et M. Curie /CNRS, 4, pl Jussieu, F-75252 Paris Cedex 05, France

²Institut für Physik, Universität Kassel, D-34132 Kassel, Germany

³Fachbereich Physik, Technische Universität Kaiserslautern, D-67653 Kaiserslautern, Germany

Direct photodissociation of a bound state of a diatomic molecule takes place typically at an internuclear distance shorter than the equilibrium distance of that state. The inner limb of the potential curve of that state has a steep slope and, hence, the continuum absorption cross section shows its typical triangular shape. This is commonly described by the reflection principle. For double-well potential states, however, the situation is more complicated and it is interesting to study deviations from this picture- the reflection principle- which are likely to occur.

The $B''\bar{B}^1\Sigma_u^+$ state of H_2 is the lowest double-well state with *ungerade* symmetry observed only recently in a triple-resonance laser experiment where the energies of a number of rovibrational states in the outer well and above the barrier ($v'_o = 21$ to 35) [1] ($v'_o = 36$ to 45) [2] were measured with high precision. The double well of the $B''\bar{B}^1\Sigma_u^+$ state results from the interaction of more than two configurations. The Franck-Condon region for absorption out of the molecular ground state corresponds to the inner part of the inner well (Fig.1). This situation is quite common for diatomic molecules.

We performed the first direct vuv absorption measurement into the full vibrational series of the discrete states and the dissociation continuum of the $B''\bar{B}^1\Sigma_u^+$ state out of the $X^1\Sigma_g^+$ molecular ground state. The VUV radiation from the undulator beamline U125/2-10mNIM was monochromatized by a 10m-normal-incidence monochromator equipped with a 1200 lines/mm grating, at a bandwidth of 0.0012 nm at 78nm. These photons were focused into a differentially pumped gas cell of 39 mm length containing H_2 at a pressure of 20 mTorr (26.7 μ bar) at room temperature. The transmitted light intensity was detected by a photodiode located at the back of the cell. Lyman- α or Balmer- α fluorescence radiation from the H(n=2) or H(n=3) atomic fragments, respectively, was detected simultaneously with the transmitted light. In addition, photoions were collected by applying a voltage of 10 V to one of two electrodes in the target cell. The comparison of the absorption spectra with all the H(n=2) and H(n=3) dissociation and ionization excitation spectra enables the calibration of these channels. The estimated uncertainties are about 10%.

In order to interpret the experimental results, we calculated the discrete absorption spectrum of the $B''\bar{B}^1\Sigma_u^+$ state completely. The potential curves of the $B''\bar{B}^1\Sigma_u^+$ and $X^1\Sigma_g^+$ states [3,4] and the

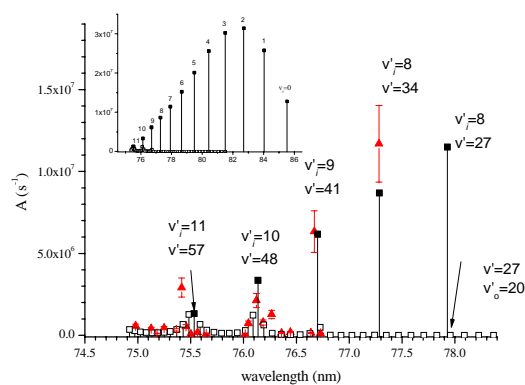


Fig.1: Transition probabilities A_v for the discrete spectrum (R(1) lines). The lines corresponding to the inner well $v'_i = 0 \dots 11$ (see inset) present noticeable A values. Full triangles: measured A values with their associated error bars.

$B''\bar{B}^1\Sigma_u^+$ dipole transition moment function are known theoretically with a high precision [5]. The calculation of the discrete part of the spectrum and of the dissociation continuum is straightforward. For $v' > 3$, the calculated spectrum shows vibronic levels located in the outer well or the inner well. We can easily number the levels for each well [1] and follow the v'_i (inner well) from 0 to 8 and v'_o (outer well) from 0 to 36. At the expected wavelength of the transition to the $v'_i = 9$ level, we find two absorbing $J=2$ levels instead of one. The “outer-well” character pollutes the “inner-well” progression. The energy of these levels exceeds the potential barrier. Although they are not any more “inner” or “outer” levels, their absorption keeps the signature of the different wells. At the expected $v'_i = 10$ position, three $J=2$ levels are absorbing and at $v'_i = 11$, there are five. The absorption becomes more and more

diluted. The calculated discrete spectrum shows clearly two vibrational frequencies, namely that related to v'_o which is small and connected to the wide outer well and that related to a large vibrational frequency v'_i connected to the narrow inner well. According to the calculations, the “inner-well” character is still localized. The calculated photodissociation cross section exhibits the same behaviour with oscillations at two frequencies, namely the two frequencies related to v'_o and v'_i . In Fig.2 we display both the discrete and the continuous spectra giving an arbitrary width to the lines to fit the same scale. The continuity is striking. As the excess energy above the dissociation limit is increased, the dissociation time decreases. Therefore, the widths of the resonances are increasing, smoothing away the fast frequency.

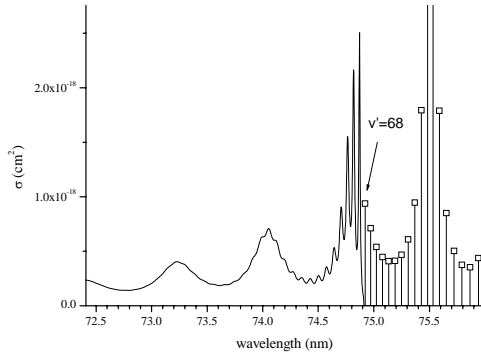


Fig.2: Calculated discrete and continuous absorption cross sections of the $B''\bar{B}'^1\Sigma_u^+$ state of H_2 for a R(1) transition (the width of the discrete lines was appropriately chosen in order to fit the same scale in the figure)

any fitting at all of the amplitudes and the positions. The fast oscillations of the continuum can be clearly seen above the threshold (from $J''=1$ at 74.911nm). The noise of the measurement amounts to about $\pm 1 \times 10^{-19} \text{ cm}^2$ whereas the oscillation amplitudes amount typically to $6 \times 10^{-19} \text{ cm}^2$. The oscillation amplitudes agree well, the positions are in rather good agreement, too, even if the calculated cross section does not reproduce perfectly the measurement. It should be mentioned here, that energy differences between calculated and measured positions of discrete levels have been observed to increase as v' increases above the potential barrier [1,2].

The only previous measurement concerning the H_α emission has been made at 5 wavelengths between 68.6 and 72.3 nm [6]. However, these authors have assumed a monotonous and smooth decrease of the absorption cross section with increasing energy, i.e. there was no indication of structures or oscillations. Their absolute value of $0.19 \pm 0.07 \text{ Mb}$ for the σ_{H_α} cross section at 72.3 nm may be compared to our value of $\sigma_{n=3} = 0.45 \pm 0.10 \text{ Mb}$. at 73.0 nm with 30% ($\pm 10\%$) of H(3p) atoms[7] which corresponds to $\sigma_{H_\alpha} = 0.33 \pm 0.10 \text{ Mb}$ with a quantum efficiency for Balmer radiation of 74% ($\pm 10\%$).

We have shown that a double-well state (e.g., the $B''\bar{B}'$ state of H_2) shows an absorption spectrum which reflects the characters of both wells and may maintain them distinct above the internal potential barrier, and even beyond the discrete spectrum, in the continuous one, too. The experimental results corroborate the theoretical ones and the two wells appear to represent a situation reminding of two very weakly coupled classical oscillators[8].

[1] A. de Lange, W. Hogervorst, W. Ubachs and L. Wolniewicz, Phys. Rev. Lett. **86**, 2988 (2001)

[2] R.C. Ekey, Jr. A. Marks, and E. F. McCormack, Phys. Rev. A **73**, 023412 (2006)

[3] W. Kolos and L. Wolniewicz, J. Mol. Spectrosc. **54**, 303 (1975)

[4] E. Reinhold, W. Hogervorst, W. Ubachs and L. Wolniewicz, Phys. Rev. A **60**, 1258 (1999) and http://www.fizyka.ump.pl/ftp/publications/ifiz/luwo/bbhh_state.98

[5] L. Wolniewicz and G. Staszewska, J. Mol. Spectrosc. **217**, 181 (2003)

[6] L.C. Lee and D.L. Judge Phys. Rev. A **14**, 1094 (1976)

[7] H. Liebel, H. Schmoranzler and M. Glass-Maujean BESSY Annual report 1999, p143

[8] M. Glass-Maujean, S. Klumpp, L. Werner, A. Ehresmann and H. Schmoranzler, J. Phys. B **40**, F19 (2007)

To compare the calculations with the experiment, we had to sum up all the contributions for the $D\ 3p\pi\ ^1\Pi_u$ and $B''\bar{B}'^1\Sigma_u^+$ states and from the various J'' rotational states. This cross section is represented in fig. 3 with the experimental dissociation cross section in this wavelength range, evaluated from the detected fluorescence intensity of the atomic fragment on the $H(n=3) \rightarrow H(n=2)$ transition, the H_α line.

The dissociation spectrum is dominated by structures, The broad maxima at low frequency are hardly distinguishable, due to the scale, from the underlying continuum whereas the high-frequency structures remain visible. The other structures, some of them being very narrow, are due to predissociations. It is striking that far above the ionisation threshold the relatively slow dissociation can still occur with high efficiency.

The measured underlying continuum can be compared with the calculated continuum on an absolute scale, without

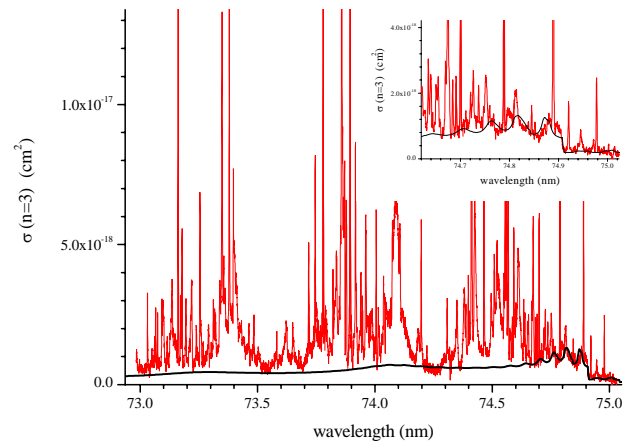


Fig.3: Dissociation cross sections above the $H(n=3)+H(n=1)$ limit (from the initial rotational state $J''=1$). The experimental cross section was evaluated from the measured H_α intensity. The theoretical cross section was calculated from the contributions of the D and $B''\bar{B}'$ states (thick line).

Outstanding spin-orbit activated interchannel coupling in the Ba $3d$ photoemission

T. Richter, E. Heinecke, P. Zimmermann

Institut für Optik und Atomare Physik, Technische Universität Berlin

D. Cubaynes, M. Meyer

LIXAM, Centre Universitaire Paris-Sud

The importance of interchannel coupling on the atomic photoionization for outer and inner electrons over a wide range of kinetic energies is generally accepted (see for example [1, 2] and references therein). In general, pronounced effects occur when the transition matrix elements of a weak channel are modified by mixing with a strong channel and can be observed in the photoionization spectra of all states of matter from atoms to solids.

A completely new type of interchannel coupling has been discussed for the $3d$ photoionization of Xe, Cs and Ba [3, 4] where in the vicinity of the $3d_{3/2}$ threshold the $3d_{5/2}$ channel is strongly influenced by mixing with the $3d_{3/2}$ channel. It was stimulated by an experimental investigation on the Xenon $3d$ photoionization [5]. Predictions were made for Cs and Ba.

This interchannel coupling is a supposedly general effect fed by the spin orbit interaction. The calculations use a modified version of the spin-polarized random phase approximation with exchange (SPRPAE) methodology. While theory was based on experimental Xe photoionization cross section data, its implications on Cesium were confirmed previously for the cross section [6] and cross section as well as anisotropy parameter [7]. The data on Cesium show some discrepancies between the SPRPAE predictions and the independent experimental results.

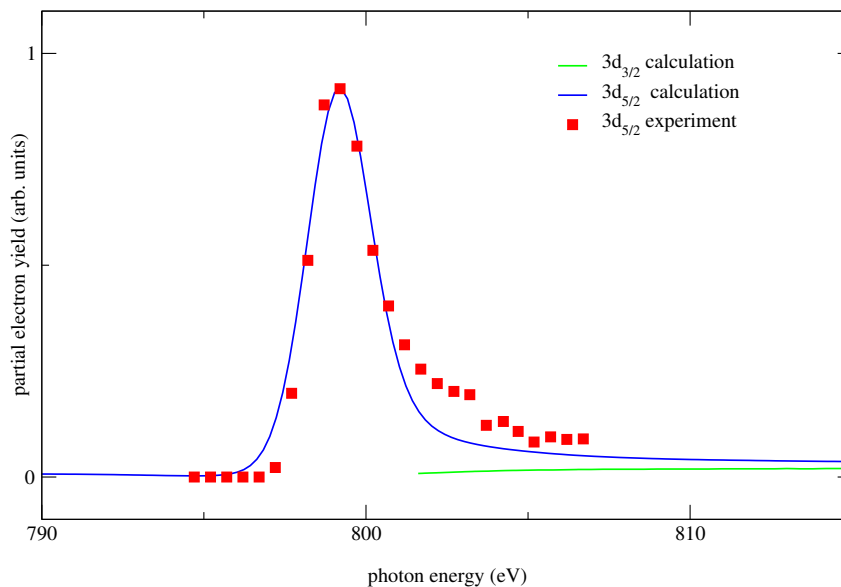


Figure 1: Photoelectron yield measured for Ba $3d_{5/2}$, calculated for both spin-orbit doublets

We now report on experimental data for the Barium $3d$ photoionization, that strongly supports predictions based on the spin orbit activated intra channel coupling. The partial cross section of the Ba $3d_{5/2}$ photoelectrons shows a pronounced maximum in the vicinity of the $3d_{3/2}$ threshold. This extra feature is not reproduced by uncorrelated numerical calculations (e.g. Hartree-Fock).

The experiments were carried out at the UE52-SGM beamline. A Scienta SES-2002 electron analyser was used to separate energetically the different photoelectrons. For the determination of the partial cross section only electrons emitted under the magic angle ($54^\circ 44'$) with respect to the linear polarization vector of the synchrotron radiation were observed. The intensity of the $3d_{5/2}$ photoline was recorded as a function of the exciting photon beam with proper normalization to the photon flux and the energy dependent transmission of the analyzer.

We have measured the $3d_{5/2}$ photoionization cross section of Ba in the region around the $3d_{3/2}$ threshold at about 800 eV excitation energy (Figure 1). The solid lines represent the SPRPAE calculation by Amusia et al. [3], which have been convoluted by a Gaussian distribution of 1.9 eV width to match the experimental resolution and have been shifted to overlap in the cross section maximum at 799.2 eV. Experimental and theoretical curve are in very good agreement demonstrating thereby the strong interchannel coupling effect also for the $3d_{5/2}$ cross section in Ba. But this observed resonance is of completely different origin than for Xe and Cs, since the resonance maximum is situated *below* threshold. The shape of the resonance profile is almost symmetric and closely resembles the form of the absorption curve [8]. The collapse of the $4f$ wavefunction upon $3d$ excitation causes the strong discrete $3d_{3/2} \rightarrow 4f$ resonance, which is seen in the $3d_{5/2}$ cross section. Unfortunately the proposed strong changes in the β value [4] coincides with a vanishing $3d_{5/2}$ cross section. That made an experimental verification of the theoretical β results impossible and leaves it as an extremely challenging task for the future.

In summary our experimental findings verify qualitatively the theoretical predictions [3, 4] which suggests an interpretation of the results for Ba completely different from the discussion on Xe and Cs. For a more detailed treatment of the topic see our upcoming paper [9].

We are thankful for the support of the BESSY staff. This work was funded both by the Deutsche Forschungsgemeinschaft (DFG Zi 183/22-1) and through BESSY-EC-IA-SFS Contract EU R II 3-CT-2004-506008.

- [1] O. Hemmers, S. T. Manson, M. M. Sant'Anna, P. Focke, et al. Phys. Rev. A, **64** 022507 (2001).
- [2] P. C. Deshmukh. Rad. Phys. Chem., **70** 515 (2004).
- [3] M. Ya. Amusia, L. V. Chernysheva, S. T. Manson, A. Z. Msezane, et al. Phys. Rev. Lett., **88** 093002 (2002).
- [4] M. Ya. Amusia, A. S. Baltenkov, L. V. Chernysheva, Z. Felfli, et al. J. Phys. B, **37** 937 (2004).
- [5] A. Kivimäki, U. Hergenhahn, B. Kempgens, R. Hentges, et al. Phys. Rev. A, **63** 012716 (2000).
- [6] H. Farrokhpour, M. Alagia, M. Ya. Amusia, L. Avaldi, et al. J. Phys. B: At. Mol. Opt. Phys., **39** 765 (2006).
- [7] T. Richter, P. Zimmermann, K. Godehusen, and M. Yalçinkaya. BESSY Jahresbericht (2006).
- [8] U. Arp, K. Iemura, G. Kutluk, T. Nagata, et al. J. Phys. B: At. Mol. Opt. Phys., **32** 1295 (1999).
- [9] T. Richter, E. Heinecke, P. Zimmermann, K. Godehusen, et al. Phys. Rev. Lett., **in print** (2007).

The study of the $B''\bar{B}^1\Sigma_u^+$ state of H_2 : transition probabilities from the ground state, dissociative widths and Fano parameters.

M. Glass-Maujean¹, S. Klumpp², L. Werner², A. Ehresmann² and H. Schmoranzner³
¹LPMAA, Université P. et M. Curie /CNRS, 4, pl Jussieu, F-75252 Paris Cedex 05, France
²Institut für Physik, Universität Kassel, D-34132 Kassel, Germany
³Fachbereich Physik, Technische Universität Kaiserslautern, D-67653 Kaiserslautern, Germany

Being the third-lowest $^1\Sigma_u^+$ state, with a dipole allowed transition from the ground state; the $B''\bar{B}^1\Sigma_u^+$ state shows a rather strong absorption of vuv photons. Its vibrational levels with $v' \geq 1$ are predissociated into excited $H(n=2)$ atoms¹. This process may be important in determining the thermal balance of interstellar diffuse clouds². The $B''\bar{B}^1\Sigma_u^+$ state of H_2 is also the lowest double-well state of H_2 with *ungerade* symmetry.

The absorption, ionisation and dissociation spectra were recorded with a very high resolution (0.0012nm) in the wavelength range from 81nm to 74nm in steps of 0.00002nm on the undulator beamline U125/2-10m-NIM of BESSY. The absorption spectrum is directly calibrated from the known pressure and absorption length with an uncertainty of 6% to be added to the error due to the noise at each point. We determined the Ly_α detection efficiency (with an uncertainty of 12%) from the comparison of the absorption and dissociation on a the line known to be totally predissociated ($D^1\Pi_u^+ - X^1\Sigma_g^+ R(1)$ lines). In order to cross-check the various calibrations we rebuilt the absorption cross section as the sum of the dissociation and ionisation cross sections.

Only the positions of the rotational levels of the $v'=0$ to 6 vibrational progression in the inner well are known.^{3,4,5} Levels of the outer well have been observed only recently in a triple-resonance laser experiment where the energies of rovibrational states in the outer well were measured at high precision for energies below the internal barrier or just above ($v' = 24$ to 50)^{6,7}.

In order to interpret the experimental results, we calculated the discrete absorption spectrum of the $B''\bar{B}^1\Sigma_u^+$ state completely, (see previous report).

As expected, the inner-well levels have a strong absorption probability while the outer-well levels show no absorption (see Figure 1).

The calculated predissociation widths reproduce the same character. They are negligible for levels lying in the outer well, as expected, since the coupling occurs at small internuclear distance. As expected, they show very little rotational dependence, as the coupling inducing the dissociation is of the homogeneous type (vibrational interaction).

The calculated Fano parameters of the $B''\bar{B}^1\Sigma_u^+ - X^1\Sigma_g^+$ lines have values between 20 and 30 for the inner-well levels lying below the internal potential barrier and between 16 and 20 for the levels lying above the internal potential barrier. For the levels with B'' character, nearly no rotational dependence was found.

We were mainly interested in the $B''^1\Sigma_u^+ v_i' - X^1\Sigma_g^+ v''=0$ lines which show noticeable absorption probability, i.e. in lines

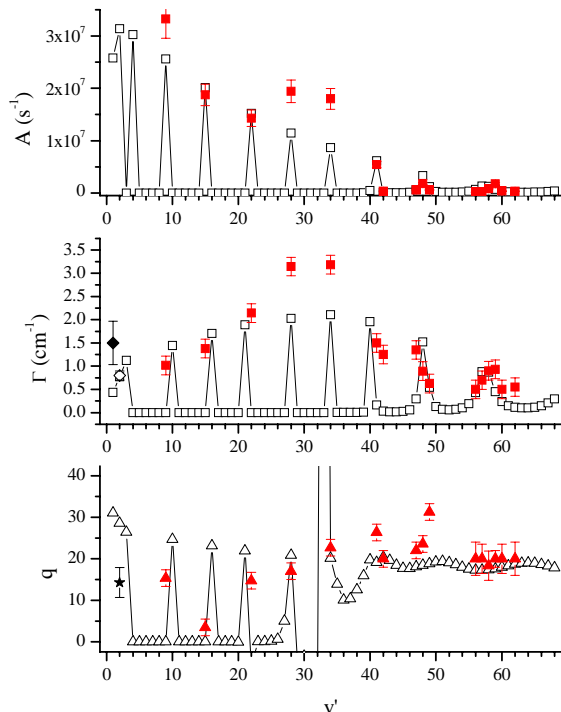


Fig. 1: Transition probabilities $A_{v',v''=0}$, dissociative widths Γ and Fano parameter q as function of the vibrational quantum number of the $B''\bar{B}^1\Sigma_u^+$ state.

connecting the vibrational $v''=0$ ground state level to the vibrational v_i' levels lying in the inner well. The first task was to assign the observed lines for $v_i' > 6$. The positions of the lines observed in

the dissociation excitation spectrum were first compared with the calculated positions. To make sure of the assignment, the intensity of the line, its width and its asymmetry parameter were taken into

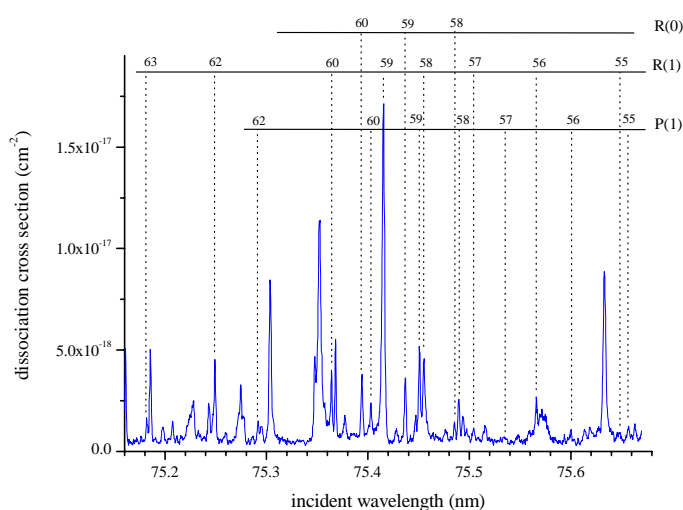


Fig. 2: Dissociation spectrum: Rotational lines within the $v' = 11$ band. The B'' character is partly spread over the levels of the outer well.

account. More than 40 lines corresponding to rotational lines of the v'_i progression with v'_i from 5 to 11 were assigned for the first time. The uncertainty of the measured wavelength is ± 0.005 nm (or 8 cm^{-1}). The energy difference between the measured and the calculated positions reached up to 80 cm^{-1} . These deviations are mostly due to accidental perturbations ignored in the calculation.

The $B''\bar{B}^1\Sigma_u^+ - X^1\Sigma_g^+$ lines are observed in the dissociation spectrum as fully predissociated. The measured predissociation widths are comparable to the Doppler width. They can be determined through deconvolution of the observed profile. The fitting process enabled to determine the predissociation

width, the Fano asymmetry parameter q and the area of the profile yielding the transition probability A .

We observed a dispersion of the parameter values within a rotational band due to local perturbations. In order to obtain the vibrational behaviour, we averaged the parameters q , Γ , and A over the rotational lines for a given v' value.

The transition probabilities of the various vibrational bands from the $X v'' = 0$ ground state were measured over the complete vibrational progression, showing clearly that only the inner-well state with $B'' 4p\sigma$ character can absorb vuv light. The absolute values of these transition probabilities agree well with *ab-initio* calculations if one takes into account that the calculations neglect non-adiabatic couplings. Contrary to the assumptions in refs. 6 and 7, the predissociation was observed to be the major deexcitation channel.

As predicted by the calculations, only a partial delocalisation of the B'' character was observed in the $B''\bar{B} v'$ -progression above the potential barrier and the last $B'' v'_i = 10$ and 11 rotational levels could be assigned and their parameters could be measured, even if the positions of the v'_i levels in the v' progression are not always perfectly reproduced by the calculations: e.g., the more intense absorption occurs on the $v' = 47$ R(1) line instead of on the $v' = 48$ R(1) line, so that the $v' = 48$ R(1) line could not be assigned. (see Figure 2)

For the study of the $\text{H}_2 B''\bar{B}^1\Sigma_u^+ - X^1\Sigma_g^+$ system, our measurement, with a 10m-normal-incidence monochromator and detecting the absorption, ionisation and dissociation spectra simultaneously, is complementary to double-resonance laser studies. Whereas the precision of the line position measurement is superior in the laser experiment, our experiment enabled to measure the transition probabilities, to assign more than 40 new lines and to follow the inner-well levels over the whole vibrational progression.⁸

¹ G. Herzberg Topics in modern physics, a tribute to Condon, E.U.P. 191 Colorado Press 1971

² J.M. Ajello, I. Kanik, S.M. Ahmed, and J.T. Clarke, J. Geophys. Res. **100**, 26411 (1995)

³ A Monfils J. Mol. Spectrosc. **15**, 265 (1965)

⁴ G. Herzberg and Ch. Jungen, J. Mol. Spectrosc. **41**, 4251 (1972)

⁵ Ch. Jungen and O. Atabek, J. Chem. Phys. **66**, 5584 (1977)

⁶ A. de Lange, W. Hogervorst, W. Ubachs and L. Wolniewicz, Phys. Rev. Lett. **86**, 2988 (2001)

⁷ R.C. Ekey, Jr. A. Marks, and E. F. McCormack, Phys. Rev. A **73**, 023412 (2006)

⁸ M. Glass-Maujean, S. Klumpp, L. Werner, A. Ehresmann and H. Schmoranzler, submitted to J. Chem. Phys.

Transition probabilities from the ground state of the $np\pi^1\Pi_u^-$ state of H_2

M. Glass-Maujean¹, S. Klumpp², L. Werner², A. Ehresmann² and H. Schmoranzner³

¹LPMAA, Université P. et M. Curie /CNRS, 4, pl Jussieu, F-75252 Paris Cedex 05, France

²Institut für Physik, Universität Kassel, D-34132 Kassel, Germany

³Fachbereich Physik, Technische Universität Kaiserslautern, D-67653 Kaiserslautern, Germany

Molecular hydrogen emission is an important astrophysical process. Since Voyager and IUE flights and later on with the Hubble Space Telescope and the Galileo spacecraft, it has been known that H_2 emission is the primary VUV and EUV emission process in the atmospheres of outer planets^{1,2}. The determination of the lines' positions and of the transition moments is an important tool for the computation of simulated spectra used in astrophysical studies³.

The aim of this work is to measure the absorption probability of a larger number of levels all of them belonging to the $^1\Pi_u^-$ symmetry.

The absorption, ionisation and dissociation spectra were recorded with a very high resolution (0.0012nm) in the wavelength range from 81nm to 74nm in steps of 0.00002nm on the undulator beamline U125/2-10m-NIM. The absorption spectrum is directly calibrated from the known pressure and absorption length with an uncertainty of 6% to be added to the error due to the noise at each point.

The $np\pi^1\Pi_u^-$ $v, J = 1$ levels are excited from the ground state levels through Q lines. Due to their symmetry, these levels cannot be coupled to the $np\sigma^1\Sigma_u^+$ $v, J = 1$ levels, the only possible couplings are with $n'p\pi^1\Pi_u^-$ $v' \neq v, J = 1$ levels. In a first approximation, only the couplings with $\Delta v = \pm 1$ are effective; so the couplings are expected to be quite limited, and the line positions can be predicted.

In order to interpret the experimental results, we calculated the discrete absorption spectrum of the $np\pi^1\Pi_u^-$ state completely from ab-initio data for the $n=3, 4$ and 5 $np\pi^1\Pi_u^-$ states with a quantum defect approach for the higher n values.

The absorption spectrum was studied from 81.2nm to 72.4nm, more than 90 Q(1) lines have been assigned; their intensity and width have been measured.

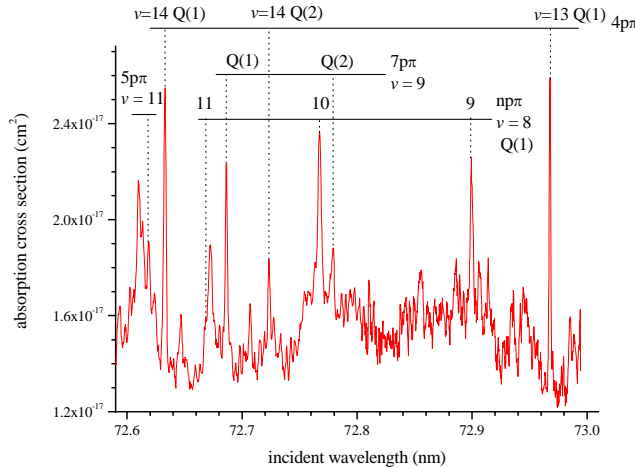


Figure 2: H_2 absorption cross section around 72.8nm, above the $v^+ = 7$ ionisation threshold

In many cases, the ionisation and the dissociation excitation spectra help us to isolate lines superposed in the absorption spectrum. The Q(1) lines are narrow, the measured widths are quite small, for energies below the $H(n=3)+H(1s)$, all the widths (HMHM) are found to be smaller than 1.5 cm^{-1} (the uncertainty of our measurement is of the order of $\pm 0.5 \text{ cm}^{-1}$). The $^1\Pi_u^-$ levels are known to be very stable, and they may give molecular fluorescence even if located at energies above the ionisation limit^{4,5}. For $\lambda < 73.0 \text{ nm}$ the Q lines are the main clear structures visible on the absorption spectrum, see Fig 1.

The results for the A emission probabilities of the D $3p\pi$, D' $4p\pi$, and D'' $5p\pi^1\Pi^-$ v levels to the X $v''=0$ state are gathered in Figure 2, from both the Q(1) and Q(2) lines. The agreement with the calculated values is very good except in a few cases. The discrepancies are due to local non adiabatic couplings.

The local couplings which may be ignored on the position of the levels, are efficient on the transition probability, as expected. For instance, the D $3p\pi^1\Pi^-$ $v=6$ level is perturbed by the nearby $7p\pi^1\Pi^-$ $v=1$, the coupling being due to the vibrational interaction acting between $\Delta v = 5$ levels,

such Δv value is expected to give very weak coupling values nevertheless, the effect is obvious on the D level. The D' $4p\pi$ $^1\Pi$ $v=3$ level may be perturbed by the nearby $n p\pi$ $v=0$ levels (with $v>12$), once again the interaction is through $\Delta v = 3$ interaction. We are far from the approximation usually used which leads to neglect all the vibrational interactions with $\Delta v \neq 1$.

The results for the A emission probabilities of the $n p\pi$ $^1\Pi_u^-$ $J=1$ levels with $n=6$ to 11 are

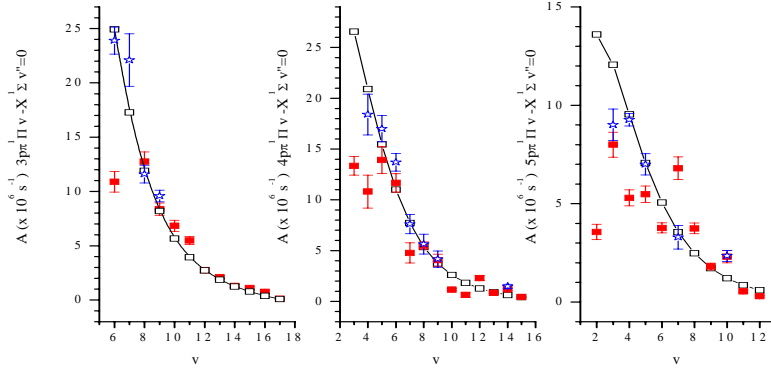


Figure 2: A emission probabilities of the D $3p\pi$, D' $4p\pi$, and D'' $5p\pi$ $^1\Pi_u^-$ v J levels to the X $v''=0$ $J''=J$ levels: open squares and full line for the calculated values, full square are for Q(1) lines i.e. $J=J''=1$, open stars are for Q(2) lines $J=J''=2$.

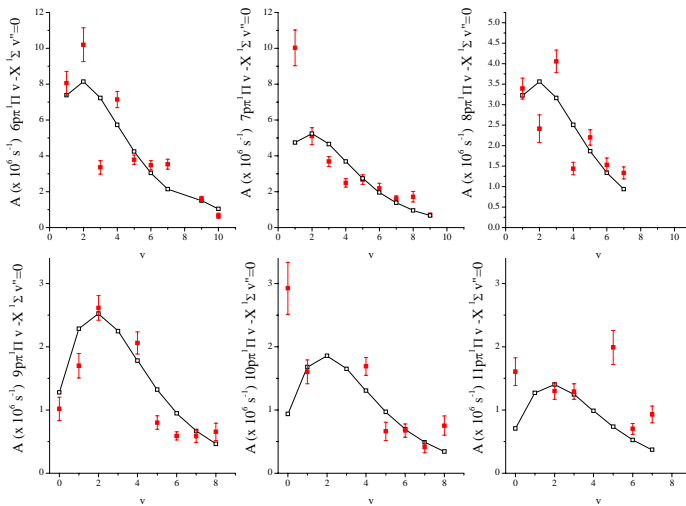


Figure 3: A emission probabilities of the 6 to 11 $p\pi$ $^1\Pi_u^-$ v $J=1$ levels, to the X $v''=0$ $J''=1$ levels: full line for the calculated values, same as fig2.

transitions (with $n \geq 3$). These transition probabilities are found in good agreement with calculated values. The main discrepancies may well be explained by local non-adiabatic couplings which were not included in the calculations. Vibrational couplings between levels with very large Δv values up to $\Delta v = 5$ may be observed on the transition probabilities. Only an extended MQDT calculation of the spectrum would be able to reproduce the observed values.⁶

are displayed in Figure 4 and 5. For these levels, the transition moment functions used in the calculation are not ab-initio calculated but, following Ch. Jungen in ref 4, approximated using the quantum defect. The global agreement is very good if we take the D'' $5p\pi$ $^1\Pi$ state as reference data and use equation 1 with $n=5$.

Once again some A values are clearly due to local perturbations; for instance the $10p\pi$ $^1\Pi_u^-$ $v=2$, $J=1$ level is strongly perturbed by the nearby $6p\pi$ $^1\Pi_u^-$ $v=3$ $J=1$ and $4p\pi$ $^1\Pi$ $v=5$ $J=1$ levels and takes its transition probability from both of them. We can see that the $7p\pi$ $^1\Pi_u^-$ $v=1$ $J=1$ level is effectively perturbed by the D $3p\pi$ $^1\Pi_u^-$ $v=6$ $J=1$ from which it takes an added transition probability.

From an absorption spectrum taken between 81.3nm and 72.2 nm, at very high resolution using a 10m-NIM monochromator on a synchrotron radiation source, we have been able to measure the transition probabilities of most of the $n p\pi$ $^1\Pi_u^-$ $v, J - X$ $^1\Sigma_g^+$ $v''=0, J''=J$

¹ A.L. Broadfoot et al., Science, **204**, 709 (1979)

² J.T. Clarke, H.W. Moos, S.K. Atreya and A.L. Lane, **ApJ** **241**, 179 (1980)

³ X. Liu, D.E. Shemansky, J.M. Ajello, D.L. Hansen, C. Jonin and G.K. James, **ApJS** **129**, 267 (2000)

⁴ J. Breton, P.M. Guyon, and M. Glass-Maujean, Phys. Rev. **A** **21**, 1909 (1980)

⁵ M. Glass-Maujean, J. Breton, B. Thièblemont and K. Ito, Phys. Rev. **A** **32**, 947 (1985)

⁶ M. Glass-Maujean, S. Klumpp, L. Werner, A.Ehresmann and H. Schmoranzner, submitted to Molec. Phys.

Studies of the spectral dependences of the absorption cross sections in Ca2p edge of CaF₂ by total electron yield method.

V.N. Sivkov^a, S.V. Nekipelov^a, D.V. Vyalikh^b, R. Follath^c, S.L. Molodtsov^b

^a Syktyvkar State University, Syktyvkar 167001, Russia;

^b Institut für Festkörperphysik, Technische Universität Dresden, D-01062 Dresden, Germany

^c BESSY, D-12489 Berlin-Adlershof, Germany.

Atoms of the $3d$ transition elements are constituents of a wide variety of nanocomposite materials and nanostructures and define their electric and magnetic properties, which are strongly determined by the partly filled $3d$ -shell. The effective atomic potential for d -electrons in the free $3d$ atom has the positive potential barrier, what results in the collapse effect of the d -orbital with increasing nuclear charge along the $3d$ -atom series. The collapse appears very rapidly and starts with Sc ($Z=21$) at the beginning of the series of the free $3d$ atoms [1]. In X-ray absorption spectra the collapse causes changes of the oscillator strength distribution between discrete and continuous parts of the spectrum and the rise of the very intense $2p_{3/2}$ and $2p_{1/2}$ absorption lines [2]. The influence of the $2p$ -hole results in the shift of the collapse from Sc ($Z=21$) to Ca ($Z=20$) and K ($Z=19$) both for the solid metals [3] and the free atoms [4]. Therefore the information about the complete distribution of dipole oscillator strength for the $3d$ transition metals over the wide spectral range and the oscillator strengths for individual electron transitions are of considerable fundamental and practical interest since they characterize quantitatively the interaction processes of photons of certain energy with metals and allow one to test results of theoretical calculations. Recently we have investigated the distribution of the dipole oscillator strength in the vicinity XANES $2p$ absorption spectra of $3d$ metal films from Sc to Cu [5]. The studies show that, when the atoms of the $3d$ elements are considered instead of the Ar atom, the collapse of the d -orbitals manifests itself as a sharp increase of the integral oscillator strength for the $2p_{1/2}$, $2p_{3/2} \rightarrow 3d$ transitions in the spectra of metals. The integral oscillator strength reaches its peak for the Sc metal. The near-linear dependence of the oscillator strength sum in the range from 0 to 80 eV above the $2p_{1/2}$, $2p_{3/2}$ -absorption edge on the number of unfilled $3d$ states in separated atoms is established experimentally for a series of metals from Ca to Ni. The result shows that the partial sums of the oscillator strengths of the x-ray transitions in the $2p$ -absorption spectra of the $3d$

metals present a sensitive tool for characterizing the states of the d -orbitals in the atoms and, thus, can be used in experimental studies of the properties of transition metal atoms in compounds.

The studies of the compounds by transmission method are difficult task because the samples need to be done as the thin films and layers with the thickness 30-100 nm at the transparent substrates. It is possible only for the bounded amount of the compounds. In that case the studies of the solid materials spectra are carried by monitoring the total electron yield (TEY) from samples that are prepared by rubbing powders of the solid materials into the scratched surface of a clean copper plate or by vacuum evaporation method on the surface of the conducting hard substance. The total electron yield is proportionate to the product of the intensity of x-ray monochromatic radiation and absorption cross section (σ). So the absorption cross section in arbitrary units can be obtained by means of the division the TEY by the monochromatic radiation intensity in arbitrary units. At that the monochromatic radiation intensity in arbitrary units can be obtained using the TEY of matter with appointed σ . Reduction σ to absolute scale can be fined by calibration using the known values of the atomic cross section [6]. The correct measurements of TEY and the monochromatic radiation intensity in arbitrary units in soft-x-ray range present considerable experimental difficulties. Extraneous stray light and high-order light from monochromator gratings normally hinder measurements of these values. Measurements near $h\nu \sim 250 - 600$ eV are particularly difficult on soft-x-ray beamlines, since there are significant second- and third-order components and contaminations on optical elements that can introduce additional structures. To make absolute cross-section measurements, these extraneous contributions to photoabsorption must be well characterized or removed entirely. Recently we have found that the titanium filter method can be used to solve this problem [7]. The investigations have shown that this experimental procedure enables one to measure

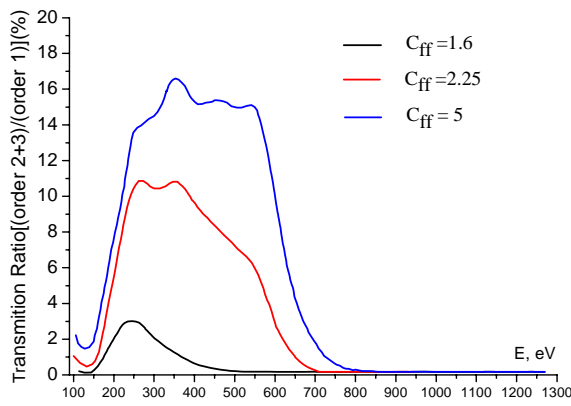


Fig.1. The ratio of higher-orders (second plus third order) to the first-order light transmission of RGLB.

the photoabsorption cross sections using the radiation of Russian–German soft-x-ray beamline at BESSY-II near $h\nu \sim 250\text{--}450$ eV [7,8]. In present work the method of the absolute cross section measurement by TEY is illustrated at example $\text{Ca}2p$ –absorption spectrum CaF_2 . The samples are the polycrystalline films prepared by thermal vacuum evaporation on the surface of a clean copper plate. Ti - filter were prepared in the form of free film (diameter 14 mm) on Au – gauze with small mesh. The intensity of the incident synchrotron radiation was measured using a TEY from a clean Si photocathode. A TEY was divided into value σ of the atomic Si [6]. The energy resolution, photon flux and the degree of higher-diffraction order light suppression of Russian-German beamline (RGLB) is determined by the fix-focus ratio $C_{ff} = \cos\beta/\cos\alpha$ (α and β are the incidence and the diffraction angles relative to the grating normal, respectively). And with decrease of C_{ff} the degree of higher-diffraction order light suppression is increase. It is shown in Fig.1 as calculated ratio orders (second plus third order) to the first order light transmission [9].

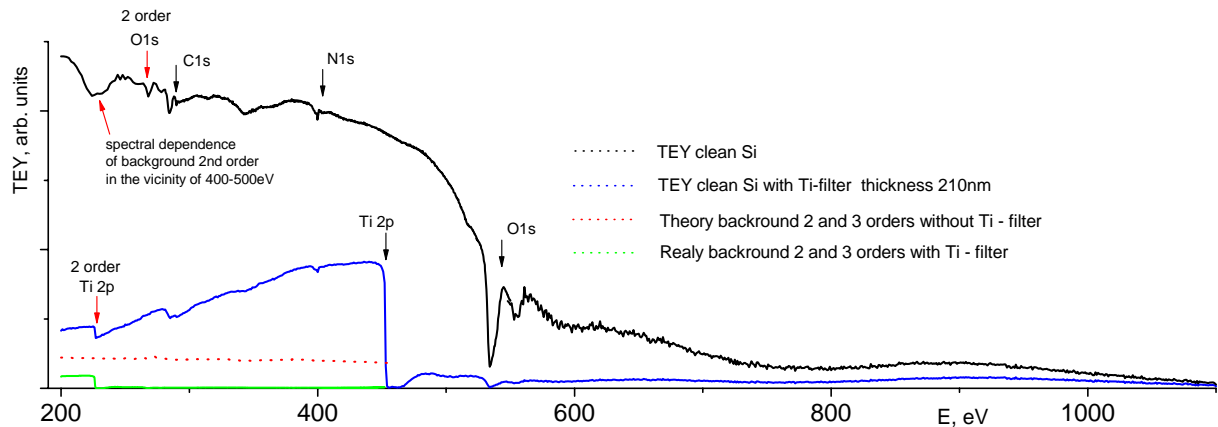


Fig.3. The spectral dependence TEY of clean Si and the value of the high-order light without (black and red lines) and with (blue and green lines) Ti–filter (thickness 210 nm).

Fig.1 shows that the intensity of higher orders is about 10% for $C_{ff}=2.25$ in the photon–energy range 250–450 eV. The energy resolution of the monochromator in the region of the $\text{Ca}2p$ –absorption edge (350 eV) at $C_{ff} = 2.25$ did not exceed 0.05 eV. In the fig.2 is shown, that Ti-films have high absorption coefficients in the area 10–100 eV [10,11] and 450–900 eV [12] at the good transmission in the range 250–450 eV. In the Fig.3 is shown the spectral dependence TEY of clean Si in the wide range 200–1100 eV without (black line) and with (blue line) Ti – filter (thickness 210 nm). Evidently, that Ti – filter carry out full suppression of high orders background in the area of the $2p_{1/2}$ and $2p_{3/2}$ absorption lines (454–460 eV) and therefore the scattered nonmonochromatic radiation is absent.

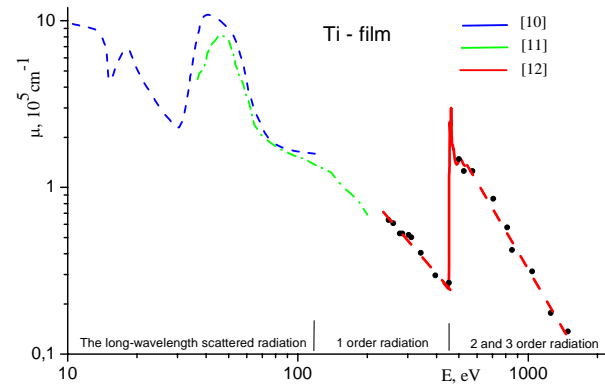


Fig.2. The absorption coefficient spectral dependence of the free Ti-films [10–12].

The red line in fig.3 shows the value of the theory background of 2nd and 3rd orders without Ti – filter, which was calculated in accordance with the data [9] (fig.1). The Ti - filter decrease the background of 2nd and 3rd orders in the area 237–450 eV nearly to zero (green line). From the fig.3 we can see, that in the area 200–450 eV the spectral dependence TEY of clean Si without

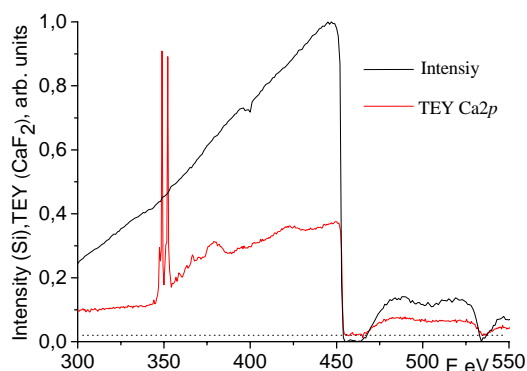


Fig.4. The spectral dependence of intensity synchrotron radiation (ratio TEY Si/atomic absorption cross section Si) and TEY in range Ca2p-edge CaF₂.

Ti – filter have the structure connected with the shortwave background. With the Ti - filter the spectral dependence TEY of Si become monotonous and shown the jump in the area of

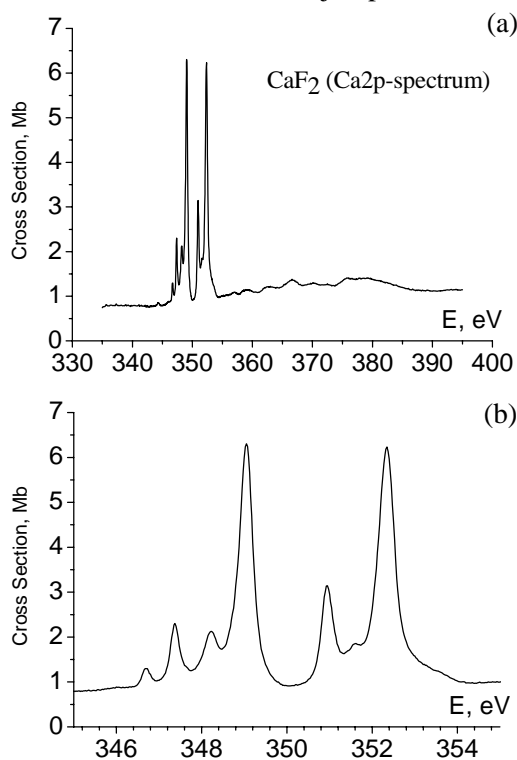


Fig.5. The spectral dependence of absorption cross section in range Ca2p-edge CaF₂.

the second order Ti2p-edge (227 eV). In fig.4 is shown the spectral dependence intensity of synchrotron radiation in the arbitrary units, which was obtained from the TEY of the clean Si dividing by σ of the atomic Si (black line), and the spectral dependence of TEY in the vicinity Ca2p-edge CaF₂ (red line). Evidently, that the both dependences have a large slope with quantum energy change. That slope issues from absorption synchrotron radiation in Ti-film. In fig.5a,b shown the spectral dependence of σ (Mb) in the vicinity XANES Ca 2p-absorption edge, which was reduced to absolute scale by means of

the calibration using the known values of the atomic cross section [6] sum before Ca 2p-edge CaF₂. It is essentially that the measurement cross sections with the long-length side (341.3eV) and with the short-length side (392.4eV) from Ca 2p-edge good correlate with the dates obtained by laboratory spectrometer using emission lines CaL _{α} (0.78 Mb) and TiL _{ℓ} (1.7 Mb). At that exists the great difference between the measurement by TEY σ and atomic cross section sum on the shortwave of the Ca 2p-edge in CaF₂. That suppression of absorption edge is the characteristic feature for XANES of the central atoms in the fluoride compounds. In conclusion it is necessary to note that the problem of the reduction to the absolute scale of absorption cross section obtained by TEY-method is not solved. Solution of this problem requires the additional investigations.

Acknowledgements:

This work was supported by the RFBR (Grants No 04-02-17216); the Target Program of the DSPHS (Grant NRP 2.1.1.3425), and by the Bilateral Program of the Russian--German Laboratory at BESSY II.V.N. Sivkov gratefully acknowledge the financial support by BESSY-II and the Technische Universität Dresden.

References

1. Latter R., Phys. Rev. **99**, 510(1955).
2. Karazia P.I., Uspehi Fizicheskikh Nauk (in Russian), **135**, №1, 79(1981).
3. Barth J., Gerken F., Kunz C., Phys. Rev. B, **28**, N6, 3608(1983).
4. Mansfield M.W.D., Proc. R. Soc. London A, **346**, 555(1975).
5. V.N. Sivkov, S. V. Nekipelov, D. V. Sivkov, A.S. Vinogradov, Izvestia RAN (in Russian), 71, N1, **81** (2007).
6. B.L. Henke, E.M. Gullikson, J.L. Devis., At.Data.Nucl.Data.Tables. **54**, 181(1993).
7. V. N. Sivkov, A. S. Vinogradov, S. V. Nekipelov, D. V. Sivkov, D. V. Vyalykh, S. L. Molodtsov, Optika i Spektroskopiya **101**,N5 782 (2006).
8. Sivkov V.N., Vinogradov A.S., Nekipelov S.V., Sivkov D.V., Vyalikh D.V., Molodtsov S. L. BESSY Annual Report, 2004, p.167-169.
9. D.A. Gorovikov, S.L. Molodtsov, R. Follath, Nucl.Instr. and Meth. **A411**,506 (1998).
10. D.A. Shirley, Phys. Rev. B, **3**, 4709 (1972).
11. F.S. Broun, R.Z.Bachrach, A.Bianconi, Chem. Phys. Lett., **54**, 425(1979).
12. V.N. Sivkov, A.S. Vinogradov, Poverkhnost' (in Russian), N1,151(2002).

Oscillator strengths of the vibrational and Rydberg transitions in the 1s absorption spectrum of a nitrogen molecule

V.N. Sivkov^a, A.S. Vinogradov^b, S.V. Nekipelov^a, D.V. Sivkov^a, D.V. Vyalikh^{b,c}, S.L. Molodtsov^{b,c}

^a *Syktvykar State University, Syktvykar 167001, Russia;*

^b *V.A. Fock Institute of Physics, St.Petersburg State University, St.Petersburg 198504, Russia;*

^c *Institut für Festkörperphysik, Technische Universität Dresden, D-01062 Dresden, Germany.*

The x-ray absorption near-edge structure (XANES) of the 1s spectrum of a nitrogen molecule has become subject of extensive experimental and theoretical investigations [1--3]. Due to the use of high-power synchrotron radiation sources and spectrometers with a high instrumental resolution, the vibronic transitions in the region of the π_g and σ_u resonances, diversified Rydberg structure, and doublet [4] and triplet [5] excitations were revealed in the XANES of the 1s -absorption spectrum of N₂. Study of the XANES of the 1s - absorption spectra of clusters formed by nitrogen molecules revealed the differences in the vibrational structures of the clusters and free molecules [6]. However, these works did not involve consideration of the absolute absorption cross sections and oscillator strengths of the x-ray transitions in N1s - spectrum, which are the fundamental spectroscopic parameters because the oscillator strength equals, to within a constant factor, the probability of the corresponding transition and can be calculated theoretically. These data are important for understanding the phenomena arising from the absorption of an x-ray quantum by a molecule, such as the resonance x-ray photoemission, resonance x-ray fluorescence, photochemical processes in the upper atmosphere, and photodynamic processes in molecular clusters. The lack of experimental data on the oscillator strengths for series of the vibrational and Rydberg transitions in a nitrogen molecule results from the fact that the appropriate measurements appear to be a complex experimental problem. To cope with this problem, not only the background radiation and instrumental distortions should be adequately taken into account, but the measurements should be carried out with a high energy resolution. To date, this is possible only using synchrotron radiation. The energy resolution $\Delta E = 0.04$ eV, which is necessary for obtaining contrast vibrational and Rydberg structures, can be attained at the Russian-German beamline only at a high value of the constant of the fix focus ratio, $C_{ff} = 12$. In this case, the second- and third-order

short-wavelength radiation intensities occur high enough in the region of the N1s ionization threshold (400 eV) [7]. The presence of the anomalously intense band in the XANES of the 1s - spectrum calls for measuring the cross sections within a wide range of the optical densities of nitrogen. Under such conditions, the transmittance measurements of the cross sections appear difficult, and it becomes preferable to study the photoionization spectra at low nitrogen pressures of 10^{-1} to 10^{-2} torr in a measuring cell. In this case, the "thickness effect" and photoelectron transport on the spectral dependence of the cross sections can be ignored. Then, for structureless incident radiation, the spectral dependence of a partial cross section within a narrow range 400 to 410 eV near the 1s - ionization threshold of N₂ can be derived by a simple subtraction of the absorption by the upper shells. Further, the partial spectral dependence of the cross section obtained in relative units can be reduced to the absolute scale of cross sections by normalizing the latter to the oscillator strength of the π_g shape resonance measured on a laboratory spectrometer in the limit of the "zero" optical density with due account of the nonmonochromatic background [8]. The XANES of the 1s - absorption spectrum of N₂ was obtained using an ionization chamber at the Russian - Geman soft-x-ray beamline at BESSY-II [7, 9]. The energy resolution of the monochromator in the region of the N1s absorption edge (400 eV) at $C_{ff} = 12$ did not exceed 0.04 eV. The measurements were carried out at a nitrogen pressure of $4 \cdot 10^{-2}$ torr in the ionization chamber, which was separated from the working volume by a separating slit with a vacuum-tight polyamide membrane. In order to determine the inherent structure of the absorption spectrum of the membrane near the N1s absorption edge, it was studied in the incident synchrotron radiation within the 395-420 eV quantum energy range. A change in the synchrotron radiation intensity in the incident beam after passing through the polyamide membrane was by 2-3%, which is negligibly small in comparison with the relative change in the cross sections within the studied spectral range

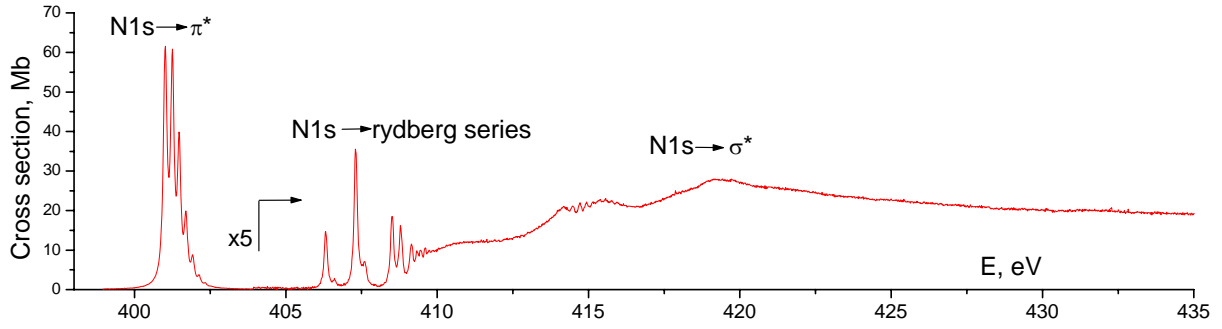


Fig.1. The spectral dependence of the absorption cross section N_2 in the vicinity $1s$ - absorption edge.

(Fig. 1). The spectral dependence of the partial $1s$ cross sections in terms of relative units was derived by subtraction of the contribution of the upper shells from the obtained spectral dependence of the photoionization current. The absolute measurements of the spectral distribution of the cross sections of a nitrogen molecule were carried out by the transmission method using an x-ray spectrometer-monochromator RSM-500 with $\Delta E = 0.3$ eV. The cross section measuring technique was

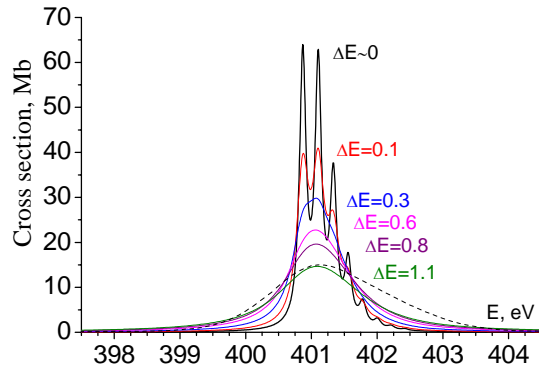


Fig.2. The simulation of the "thickness effect" of the dispersion instrumental function with different half-widths ΔE for the "zero" gas pressure.

described in detail in [8]. To determine the oscillator strength of the π_g shape resonance, we used the known relationship between the absorption cross section σ (in Mb) and the spectral oscillator strength density df/dE $\sigma(E) = (\pi e^2 h/mc)(df/dE) = 109.8 (df/dE)$, where E is the energy (in eV) of the absorbed x-ray quantum [10].

$$\sigma(E) = k \int_{-\infty}^{+\infty} \sigma'(E') f(E - E') dE', \quad (1)$$

In our previous study [8], we demonstrated that, on passage to the "zero" pressure in the case of a small change in the incident radiation intensity within the width of the instrumental function and a fast drop of the cross section with departure from the peak of an absorption band, where $\sigma(E)$

and $\sigma'(E)$ are the measured cross section and the true cross section, respectively; $f(E - E')$ is the instrumental function of a spectrometer; and k is the normalization constant with dimensions of the inverse energy. Note that E is measured from the peak of an absorption band. Taking into account the normalization of the instrumental function to unity and integrating Eq (1) over energy, we obtain the following equation for a quantity proportional to the oscillator strength of a transition:

$$\int_{-\infty}^{+\infty} \sigma(E) dE = \int_{-\infty}^{+\infty} \sigma'(E) dE, \quad (2)$$

It can be seen from Eq. (2) that the overall oscillator strength of an isolated band examined at the zero optical density of a sample is independent of the instrumental function and coincides with its true magnitude. This makes it possible to compare measurement results obtained with the use of different spectrometers. Equation (2) can be simplified by integrating over a finite range from E_1 to E_2 rather than over the infinite range:

$$\int_{E_1}^{E_2} \sigma(E) dE = \int_{E_1}^{E_2} \sigma'(E) dE, \quad (3)$$

where the range of integration (E_1, E_2) is larger than the band width and $(E_2 - E_1) \gg \delta$ being the width of the instrumental function. There is a narrow selected band in the $1s$ - absorption spectrum of a nitrogen molecule (Fig.1), which allows us to use Eqs. (1) - (3). For comparison, we took the $1s$ - absorption spectrum recorded on the RSM-500 spectrometer with the low energy resolution $\Delta E = 0.3$ eV in the absolute units (the dashed curve in Fig.2) and the spectrum studied using synchrotron radiation with the high resolution $\Delta E = 0.04$ eV in the relative units. To convert the latter spectrum to the absolute scale, we used Eq. (3). The oscillator strength of the band with all the vibrational peaks within the range from $E_1 = 398$ eV to $E_2 = 405$ eV was normalized to 0.29 [8]. Fig. 1 depicts the $1s$ -

absorption spectrum converted to the absolute scale using the above procedure. Simulation of the effect of the dispersion instrumental function on the spectral distribution of the oscillator strength in the region of the $1s$ - absorption edge of nitrogen for the zero pressure is illustrated in Fig.2. In this case, the spectral dependence obtained with the high resolution and converted to the absolute scale was taken as the true $\sigma'(E)$ distribution in Eq. (1). It can be seen from Fig.2 that, as the width of the instrumental function successively increases to 0.8 eV, a gradual change-over is observed from the spectrum studied with the high energy resolution using synchrotron radiation to the spectrum recorded at $\Delta E = 0.3$ eV. The observed difference in ΔE between the experimental and calculated spectra is quite natural, given the approximate choice of the instrumental function and the error in ΔE in the experiment. Each vibrational peak (Fig.3)

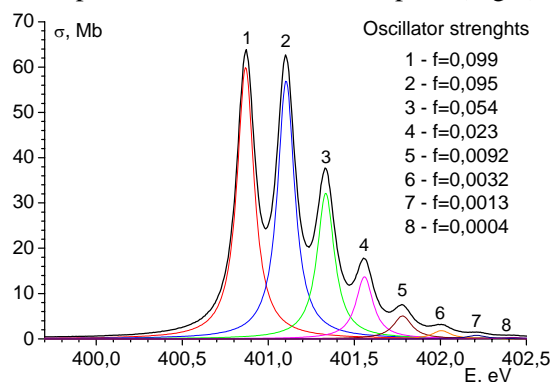


Fig.3. Spectral dependences of the absorption cross sections in the regions of vibrational transitions π_g shape resonance.

was approximated by a dispersion function of a certain width and height at maximum, so that the sum of the dispersion functions reproduce the original behavior of the cross sections. As a result of the integration, the following values of the oscillator strengths of the vibrational transitions were obtained (the inset). The Rydberg structure was resolved into components by representing each of 14 peaks by a Gaussian of a certain width and height (Fig. 4), the $N1s$ - absorption edge being approximated by arc tangent. The parameters of these functions were varied so that the total absorption cross section be in agreement with the experimental curve. The oscillator strengths of the Rydberg transitions were found to be the following (the inset). Our study has demonstrated that the conversion of the molecular x-ray spectra recorded with a high energy resolution using synchrotron radiation to an absolute cross section scale basing on

measurements with laboratory spectrometers makes it possible to evaluate the oscillator strengths of the vibrational and Rydberg transitions.

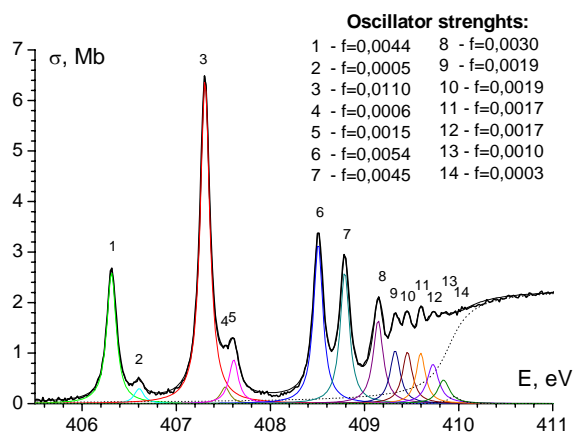


Fig.4. Spectral dependences of the absorption cross sections in the regions of the Rydberg transitions.

Acknowledgements:

This work was supported by the RFBR (Grants No 04-02-17216 and 06-02-16998); the Target Program of the DSPHS (Grant NRP 2.1.1.3425), and by the Bilateral Program of the Russian--German Laboratory at BESSY II.

References

1. M. Nacamura, M. Sasanuma, S. Sato, et al., *Phys. Rev.* **178**, 80 (1969).
2. M.J. Van der Wiel, Th.M. El-Sherbini, and C.E. Brion, *Chem. Phys. Lett.* **7**, 161 (1970).
3. A.S. Vinogradov, B. Shlarbaum, and T.M. Zimkina, *Opt. Spektrosk.* **36**, 658 (1974).
4. C.T. Chen, Y. Ma, and F. Sette, *Phys. Rev. A* **40**, 6737 (1989).
5. F. Shigemasa, T. Gejo, M. Nagasono, et al., *Phys. Rev. A* **66**, 022508 (2002).
6. B. Flech, A. A. Pavlychev, J. J. Neville, et al., *Phys. Rev. Lett.* **86**, 3767 (2001).
7. S.A. Gorovikov, S.L. Molodtsov, and R. Follath, *Nucl. Instrum. Methods Phys. Res. A* **411**, 506 (1998).
8. V.N. Sivkov and A.S. Vinogradov, *Opt. Spektrosk.* **93** (3), 430 (2002) [*Opt. Spectrosc.* **93** (3), 395 (2002)].
9. S.I. Fedoseenko, D.V. Vyalikh, I.E. Iossifov, et al., *Nucl. Instr. Methods Phys. Res. A* **505**, 718 (2003).
10. U. Fano and J. W. Cooper, *Rev. Mod. Phys.* **40**, 441 (1968).

Characterization of metal marker layers with sub-nanometer depth resolution using x-ray waveguide structures

N. Darowski¹, I. Zizak¹, A. Gupta², C. Meneghini³, A. Erko⁴

¹*Hahn-Meitner-Institute Berlin, Berlin, Germany*

²*UGC-DAE Consortium for Scientific Research, Indore, India*

³*University of Rome, Rome, Italy*

⁴*BESSY, Berlin, Germany*

Information obtained through x-ray diffraction techniques is usually averaged over the penetration depth of the probing x-rays, i.e., several microns for standard geometries. Depth selectivity can be obtained by generating x-ray standing waves (XSW) inside a layered structure by exploiting the effect of total reflection from a bottom layer of a high Z element. The intensity of the generated wave field is localized in the anti-nodal region. Thus, a change of the position of these regions in the nanostructure by changing the angle of incidence provides weighted information from different depth below the sample surface [1]. Depth selectivity

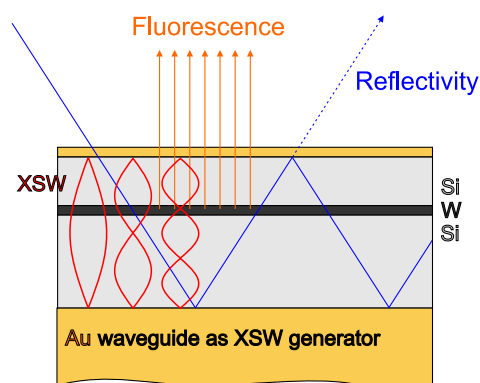


Figure 1: Experiment geometry.

can be further enhanced by making use of waveguide structures [2]. The geometry of the experiment is sketched in figure 1 together with the excitation modes of the x-ray standing wave.

Here the high-resolution capability of this *optics inside the sample* is demonstrated for a thin metal marker layer embedded into silicon. The objective of the synchrotron radiation study was to investigate intermixing in the Si/W/Si trilayer induced by swift heavy ion irradiation. In recent years swift heavy ion irradiation has been used for controlled modification of thin films and multilayer structures. In metallic systems swift heavy ions are known to produce damage above a certain threshold value of electronic energy loss.

X-ray fluorescence patterns of the samples were recorded prior to and after irradiation with 600 MeV Au ions from the ion beam laboratory ISL at Hahn-Meitner-Institute Berlin to determine the structure of the thin metal film in an unambiguous manner. Depth resolved information about the various phases formed after irradiation are valuable in understanding the mechanisms of mixing, i.e., give insights into the interaction between high energetic ions and solid matter.

Waveguide structures were deposited on commercial Si substrate using magnetron sputtering. Details of the multilayer sample structure are given in figure 2(a). Two Au layers form the walls of a waveguide. The graded-crystal monochromator beam line KMC-2 at BESSY was used to set up the nanoprobe XAFS system. The x-ray beam in an energy range of 10 keV to 14 keV was monochromatized by a double-graded-crystal monochromator and collimated in both directions using two slit systems and a collimating mirror. The beam size at sample position was $100\mu\text{m}$ horizontal and $700\mu\text{m}$ vertical. PIN diode detectors were used for measurement of the reflected beam as well as for detection of the fluorescence signal from the sample.

Figure 2(c) shows the calculated electrical wave field inside the sample structure, i.e. its intensity distribution along z , versus the scattering vector together with the expected fluorescence signal (figure 2(b)). The scattering vector is defined as $\mathbf{q} = 4\pi \sin \vartheta / \lambda$, ϑ denoting the angle of incidence and λ the wavelength of the probing x-rays.

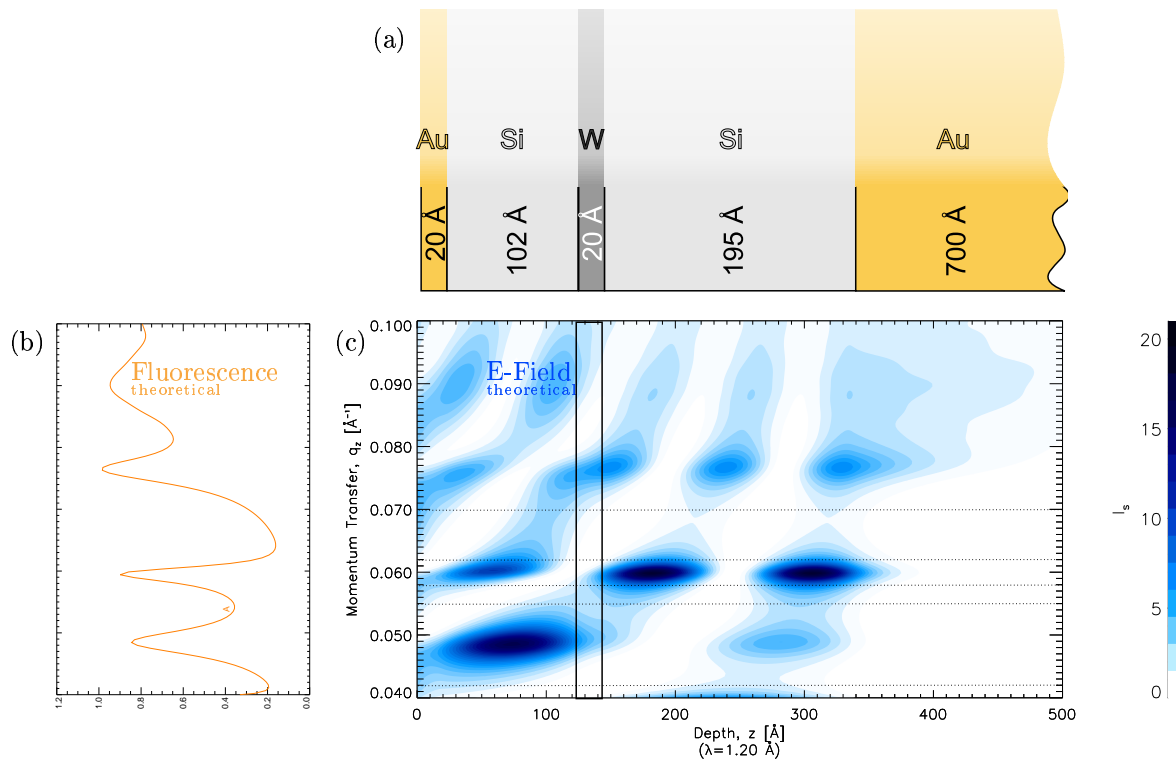


Figure 2: Calculated intensity distribution of the electrical wave field inside the sample versus the scattering vector (c) together with the theoretical fluorescence signal (b). Details of the multilayer structure are given in (a).

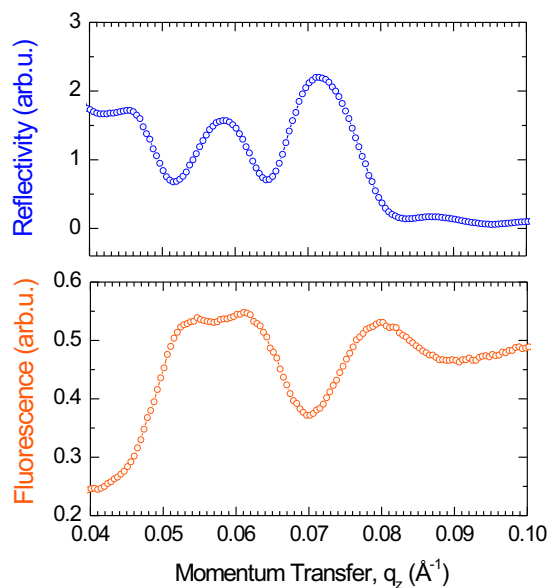


Figure 3 shows the experimentally recorded and normalized tungsten L-edge fluorescence and reflectivity intensity curves versus momentum transfer q_z recorded at 10.3 keV incidence energy. With varying q_z the wave field intensity inside the multilayer changes, thus const- q_z -scans recorded at different momentum transfer provide weighted information from different depths. Maxima in fluorescence yield occur whenever an anti-nodal region of the XSW field coincides with the tungsten marker layer. Different maxima correspond to different modes of the XSW. For the reflectivity signal an inversed behaviour is expected and experimentally observed.

Figure 3: Experimentally recorded fluorescence and reflectivity signal.

Figure 4(a) shows tungsten L-edge data for two selected only slightly different momentum transfer together with the contributions which were taken into account for fitting. The corresponding Fourier transform is given in figure 4(b). The experimental XAFS data of the pristine as well as irradiated samples were fitted with a three shell model: i) a W-Si shell, which is the main contribution to the whole XAFS signal, ii) a W-W shell around 0.27 nm, similar to the W-W nearest neighbor distance in metallic W, and iii) a W-W shell around 0.32 nm which is similar to the W-W next nearest neighbor distance in metallic W.

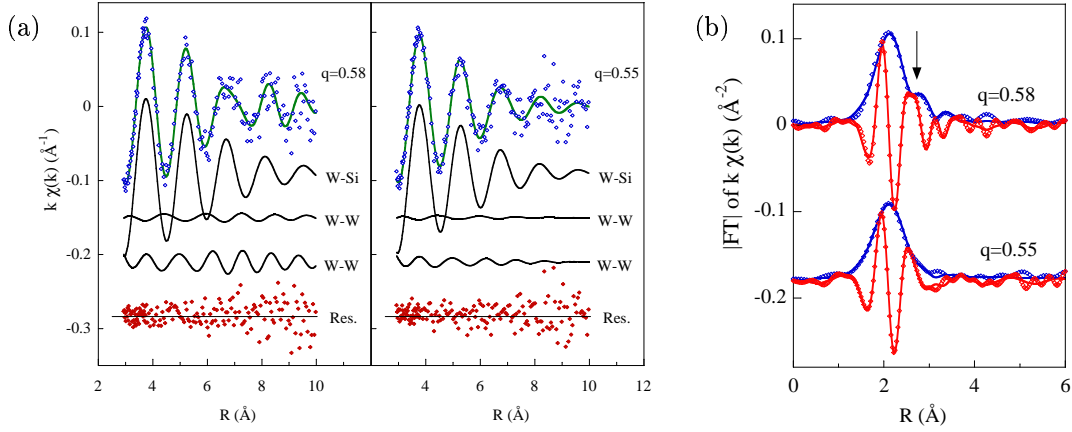


Figure 4: XAFS data of selected q_z with according fitting contributions (a) together with the corresponding Fourier transform (b).

The XAFS data of the pristine sample suggest about 60% W in metallic environment and 40% in WSi_2 . Irradiation provokes partial dissolution of W in Si giving rise to a higher fraction of W-Si correlation. Figure 5 shows the variation of (a) fraction of W-Si bonds and (b) the W-Si bond length as a function of q_z . A minimum of $x_{\text{W-Si}}$ is found at $q_z = 0.57 \text{ nm}^{-1}$, i.e., the position of the W marker layer. $R_{\text{W-Si}}$ clearly depends on the irradiation fluence Φt . For $\Phi t \geq 1 \times 10^{13} \text{ Au/cm}^2$ W-Si correlations dominate while metallic W contribution decreases. Φt is depth independent, indicating large intermixing. For $\Phi t < 1 \times 10^{13} \text{ Au/cm}^2$ Φt is systematically shorter and increases with depth. A small $R_{\text{W-Si}}$ value is consistent with W-rich structures as W_5Si_3 , whereas larger W-Si distances point to Si-rich WSi_2 phase.

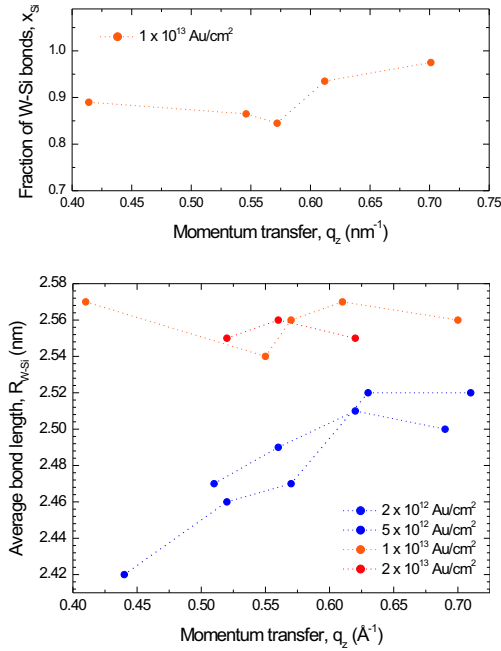


Figure 5: $x_{\text{W-Si}}$, (a) and $R_{\text{W-Si}}$ (b) as function of q_z

The combination of XAFS and an X-ray standing wave field generated by a wave guide structure provides sub-nanometer depth resolution with extremely high sensitivity to the layer structure. This combination of methods is also very promising for investigation of different kinds of diffusion processes as well as interfaces of different materials in layered structures.

- [1] S.K. Ghose, B.N. Dev, and A. Gupta *Physical Review B* **64** (2001) 233403.
- [2] A. Gupta, P. Rajput, V.R. Reddy, M. Gupta S. Bernstorff, and H. Amenitsch *Physical Review B* **72** (2005) 075436.

Probing the magnetic coupling between Fe and CoO by means of dichroic X-ray absorption spectroscopy

R. M. Abrudan^{1,2}, J. Miguel², M. Bernien², C. Tieg^{1*}, M. Piantek², W. Kuch², J. Kirschner¹

¹ Max-Planck-Institut für Mikrostrukturphysik, Weinberg 2, D-06120 Halle

² Freie Universität Berlin, Institut für Experimentalphysik, Arnimalle 14, D-14195 Berlin
DFG-KU 1115/7-2

Since the discovery of the exchange bias phenomenon by Meiklejohn and Bean early in the 50's [1], the focus of interest in the field of coupling between an FM (ferromagnetic) and an AFM (antiferromagnetic) material has been on the understanding of the role of the FM/AFM interface. Many modern devices in the field of magnetic data storage or sensors exploit the exchange bias effect in order to tune the switching of the FM layer coupled to an AFM layer. Even though widely used, the main effect is not yet fully understood; experimental and theoretical papers contribute to the study of the exchange bias but are still far away from solving the complete puzzle. The answer has to be sought at the atomic level, therefore single crystalline interfaces and substrates have to be used as model systems to investigate the fundamental coupling mechanism. This way one can reduce the superimposed influence of the grain size and roughness.

In this work we make use of the element selectivity of the x-ray absorption spectroscopy, employing X-ray Magnetic Circular Dichroism (XMCD) and X-ray Magnetic Linear Dichroism (XMLD) to separately probe the magnetism of FM and AFM layers, respectively, of an FM/AFM bilayer. In our case the studied system were ultra-thin Fe/CoO bilayers epitaxially deposited on a Ag(001) single crystal. XMCD is the proper technique to be used for probing the magnetization of a ferromagnetic or ferrimagnetic unidirectional magnetic system, while XMLD can be used studying antiferromagnetic uniaxial magnetic systems.

The transition metal oxide CoO, same as its equivalents MnO, NiO, forms an ionic, antiferromagnetic crystal with rock-salt structure. The antiferromagnetic order of bulk CoO is that what is known as a type II antiferromagnetism - in the Co (fcc) lattice, following the [100] direction, one can find Co spins (separated by oxygen atoms) being antiferromagnetically aligned.

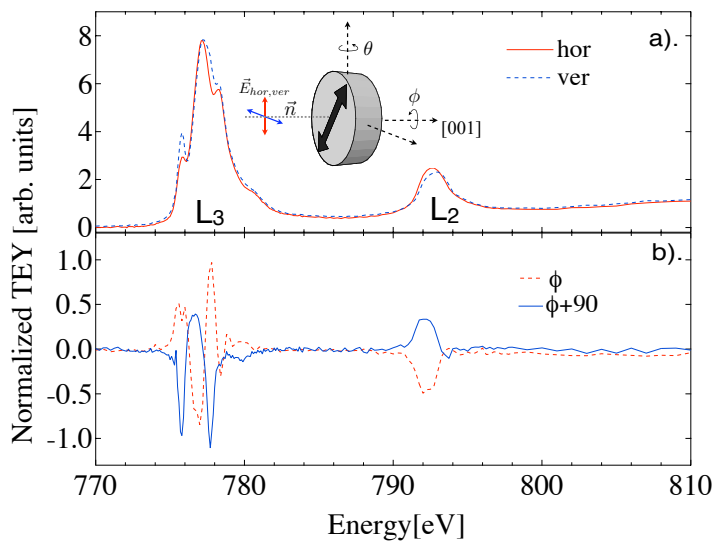


Fig. 1 Co x-ray absorption spectra measured on 6 ML Fe/8 ML CoO/Ag(001) for different linear polarization (a) and XMLD signal for two complementary azimuth angles ϕ (b).

*Present address: European Synchrotron Radiation Facility (ESRF), F-38043, Grenoble

In general, the $\langle 111 \rangle$ planes are having the spins ordered ferromagnetically; adjacent $\langle 111 \rangle$ planes show an antiferromagnetic ordering of the spins. The Néel temperature (T_N) for bulk CoO was reported to be 289 K [2].

Deposited as thin films on Ag(001), the CoO films suffer a vertical lattice expansion from $a_{\text{bulk}} = 2.13$ Å to $a_{\text{film}} = 2.17$ Å due to the lattice mismatch between the CoO and Ag (approximately 5%). The spin structure of the CoO is also changed, the magnetic spins are in this case aligned in the film plane [3].

The X-ray absorption spectra presented in Fig. 1 (a) were measured at 150 K, keeping the incoming synchrotron light normal to the sample surface. The clear difference in the spectra for horizontally and vertically polarized light is visible in both, the L_3 and L_2 edges. The XMLD signal presented in Fig. 1 (b) reverses with the azimuth angle, thus proving the 2-fold symmetry of the CoO antiferromagnetic order.

Fig. 2 shows the angular dependence of XMCD and XMLD for various azimuth angles. Continuous lines are fits using $\cos(\phi)$ and $\cos(2\phi)$ based functions for circular and linear dichroism, respectively. One can deduce from this graph the sense of direction of the Fe magnetic moments at room temperature and at low temperatures, but also the orientation of the CoO spin axis below T_N .

All measurements were done in remanence after magnetically saturating the sample at room temperature with an external magnetic field. The decrease in the XMCD intensities at low temperature (red points) may be attributed to a partial break-up into domains of the Fe film when CoO develops the AFM state.

In conclusion, the in-plane spin direction of CoO films in contact to ferromagnetic Fe was probed by means of XMLD. The measured signal can be correlated to the XMCD signal of Fe, measured at the same time. This way it is possible to deduce the magnetic coupling at the Fe/CoO interface. We found that both the AFM spin axis of CoO and the Fe moments in the ferromagnetic film are parallel aligned along the $[110]$ direction.

[1] W. H. Meiklejohn and C. P. Bean, Phys. Rev. 102, 1413 (1956).

[2] M. D. Reichtin and B. L. Averbach, Phys. Rev. B 6, 4294 (1972).

[3] S. I. Csiszar, M. W. Haverkort, Z. Hu, A. Tanaka, H. H. Hsieh, H.-J. Lin, C. T. Chen, T. Hibma, and L. H. Tjeng, Phys. Rev. Lett. 95, 187205 (2005).

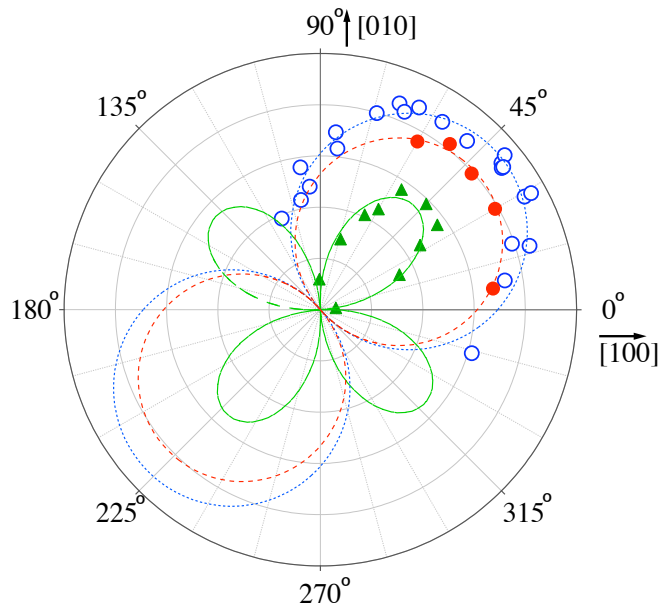


Fig. 2 Dependence of the Fe XMCD signal at room temperature (blue, open circles) and at 150 K (red, filled circles) on the azimuthal angle as well as the Co XMLD signal (green triangles) at 150 K. Data recorded from 7 ML Fe/ 10 ML CoO/ Ag(001).

Resonant photoemission and inelastic x-ray scattering of $\text{Ga}_{1-x}\text{Mn}_x\text{As}$

O. Rader, S. Valencia, A. Zimina, R. Könnecke, S. Eisebitt, K. W. Edmonds¹
BESSY, ¹School of Physics and Astronomy, University of Nottingham

$\text{Ga}_{1-x}\text{Mn}_x\text{As}$ which was found to be ferromagnetic ten years ago is the prototype material in the class of diluted ferromagnetic semiconductors. It is well known that $\text{Ga}_{1-x}\text{Mn}_x\text{As}$ adopts the zincblende structure of GaAs where Mn occupies Ga sites and provides both magnetic moments and charge carriers. Yet, there is no agreement on the origin of the ferromagnetic order in this system. In this work two recent results from the literature are critically investigated for state-of-the-art $\text{Ga}_{1-x}\text{Mn}_x\text{As}$ samples with high Curie temperature (150 K).

Theory has been explaining ferromagnetism in $\text{Ga}_{1-x}\text{Mn}_x\text{As}$ based on two different models. The double-exchange model [1] applied to $\text{Ga}_{1-x}\text{Mn}_x\text{As}$ postulates an interaction where Mn 3d electrons hop via As 4p states. This leads to a substantial density of Mn 3d states at the Fermi energy as appears in local density calculations [2]. An alternative approach employs the Zener model of ferromagnetism [3] which means indirect exchange via polarized As 4p states. The Zener model resembles the RKKY interaction in metals.

Photoemission studies of the Mn 2p core level [4] and of the Mn 3d spectral weight in the valence band [5,6,7] showed strong photoemission satellites, a low Mn 3d density of states, and a high binding energy (~4 eV) of the Mn 3d main peak. The electron configuration respectively the number of d electrons was determined as $\text{Mn}3d^{5.3\pm 0.1}$ [4].

Recently, it has been argued that in situ grown samples would constitute a better realization of $\text{Ga}_{1-x}\text{Mn}_x\text{As}$ [8]. Photoemission spectra showed a high density of states near E_F , a Mn 3d main peak at lower energy (~3 eV), and no satellite [8]. All in all, good agreement with local-density theory was found and the description by a localized model [4-7] was considered unnecessary [8].

Because our previous studies [4-7] were performed on samples with low (~50 K) Curie temperature, a new study on low-temperature postannealed and HCl-etched samples with high (150 K) Curie temperature is called for. Another reason is that early x-ray absorption and XMCD spectra were dominated by non-intrinsic contributions. This became clear from XMCD of HCl-etched samples [9] and it is also evident from XAS of samples well prepared by Ar-ion sputtering and annealing [7] and from the magnetic-field dependence of XMCD of untreated surfaces [10].

Fig. 1(b) shows the Mn3d spectral weight from our low-temperature-annealed high- T_C $\text{Ga}_{1-x}\text{Mn}_x\text{As}$ samples after HCl surface treatment produced, as usual, by subtracting spectra at 50 and 48 eV photon energy (a). Except for reduced intensity around 2 eV, the data agree very well with published data [5] and show a strong satellite at ~7 eV, a large main-peak binding energy (~4 eV), and vanishing Mn3d contribution at E_F . The data are therefore fully in agreement with a localized description of the electronic structure and with ferromagnetism based on the Zener model in contrast to the claims from the recent literature [8]. We also studied the effect of higher annealing temperatures (c,d). The Mn3d spectral weight changes strongly, increases in absolute units indicating surface segregation of Mn, and resembles the Mn3d spectral weight obtained recently for concentrated MnAs of zincblende structure [11]. This transformation is interesting since MnAs usually forms the NiAs structure with very different electronic and magnetic properties.

There is other recent data apparently supporting the double-exchange model for ferromagnetism in $\text{Ga}_{1-x}\text{Mn}_x\text{As}$. In fact, RIXS data from $\text{Ga}_{1-x}\text{Mn}_x\text{As}$ shown in Fig. 2(a) have been interpreted as proving that double exchange causes the ferromagnetism [12]. A prominent peak not accounted for by an atomic Mn^{2+} calculation (orange arrow in a) has been assigned to a Mn^{3+} configuration. Therefore also the RIXS measurements have been repeated on new samples with a high Curie temperature (150 K) and surface preparation by HCl etching. The XAS data (b) shows that the sample is free from the extrinsic contributions discovered earlier [7,9,10]. The RIXS data (c) shows that the feature in question is indeed intrinsic (orange arrow). Does this feature require reconsideration of the interpretation of previous data and of the origin of ferromagnetism in $\text{Ga}_{1-x}\text{Mn}_x\text{As}$ as the authors [12] suggest? Fig. 2(e) shows results from a resonant-photoemission calculation based on the configuration-interaction theory on a Mn-As cluster model [7]. The energy relative to main peak in resonant photoelectron spectroscopy (e) can be identified with the energy-loss scale in RIXS (a,c). It is seen that the feature in question (orange arrow) is already accounted for by the existing theory with a $3d^{5.3}$ configuration. Thus it is not necessary to invoke Mn^{3+} and double-exchange ferromagnetism.

- [1] C. Zener, Phys. Rev. 82, 403 (1951).
 [2] H. Akai, Phys. Rev. Lett. 81, 3002 (1998).
 [3] T. Dietl et al., Science 287, 1019 (2000).
 [4] J. Okabayashi et al., Phys. Rev. B 58, R4211 (1998).
 [5] J. Okabayashi et al., Phys. Rev. B 59, R2486 (1999).
 [6] J. Okabayashi et al., Phys. Rev. B 64, 125304 (2001).
 [7] O. Rader et al., Phys. Rev. B 69, 075202 (2004).
 [8] H. Åsklund et al., Phys. Rev. B 66, 115319 (2002).
 [9] K. W. Edmonds et al., Appl. Phys. Lett. 84, 4065 (2004).
 [10] O. Rader et al., J. El. Spectr. 144-147, 789 (2005).
 [11] J. Okabayashi et al., Phys. Rev. B 70, 233305 (2004).
 [12] Y. Ishiwata et al, Phys. Rev. B 71, 121202(R) (2005).

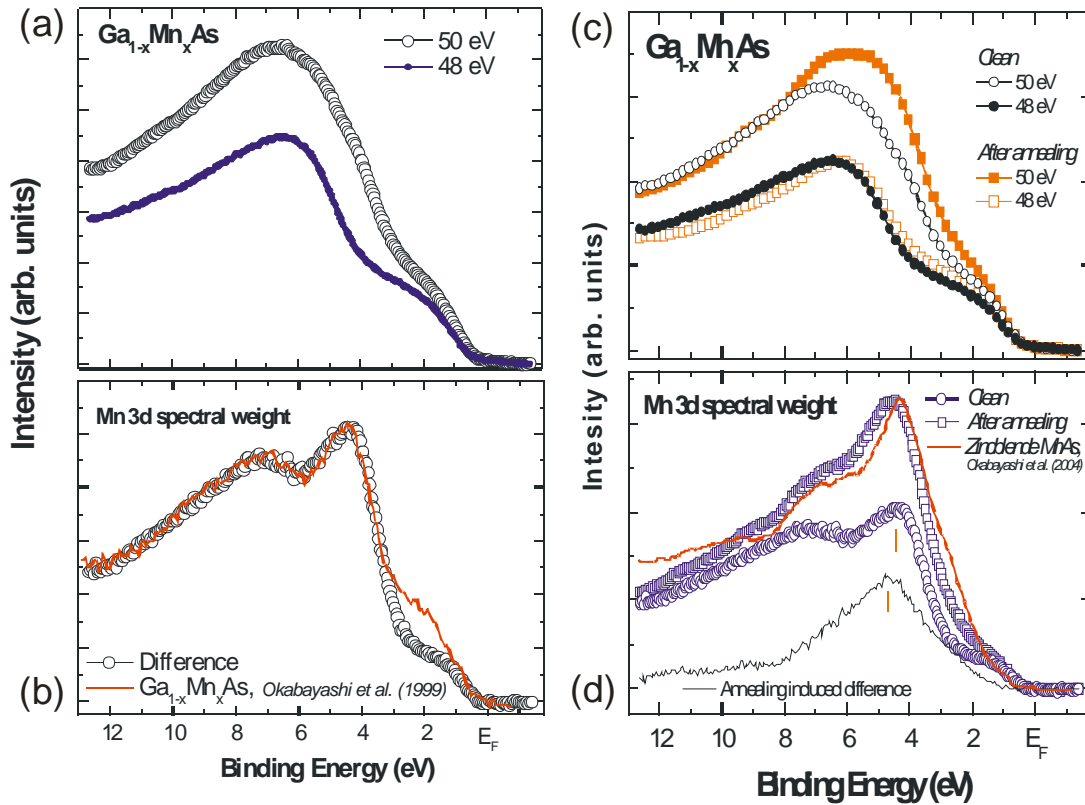


Fig. 1. Resonant photoemission spectra of high- T_c $\text{Ga}_{1-x}\text{Mn}_x\text{As}$ at the Mn 3p excitation threshold (a). The spectra are truly angle integrated. The difference between 50 eV and 48 eV spectra (b, circles) is in good agreement with the literature (b, red line [5]). (c): Resonant photoemission spectra before (black, taken from a) and after annealing (orange) reveal changes in the Mn3d spectral weight (shift to higher binding energy, reduced satellite intensity, d) which are assigned to surface segregation of Mn. The resulting 3d spectral weight (d) resembles data [11] from MnAs of zincblende structure.

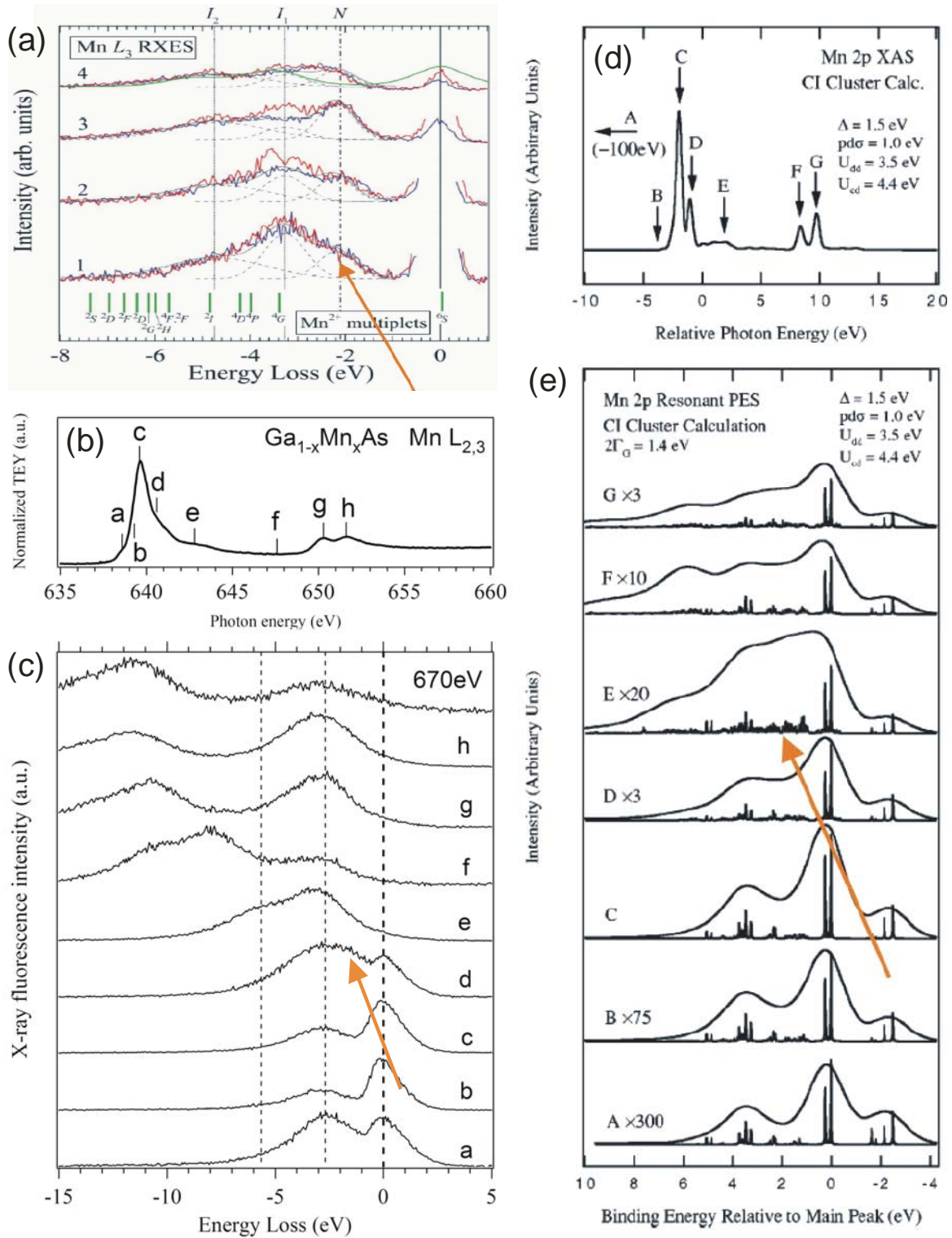


Fig. 2. (a) Literature data [12]: RIXS spectra are compared with an atomic model for Mn^{2+} . The peak not accounted for by the Mn^{2+} configuration (orange arrow) is assigned to a Mn^{3+} configuration based on another atomic calculation. This was interpreted as proving double exchange [12]. Our electron yield XAS (a) and RIXS data (b) of high- T_c (150 K) samples show that the extra peak not accounted for by the atomic Mn^{2+} (orange arrow) is intrinsic. (d,e): Calculations of XAS (d) and resonant photoemission (e) based on a configuration-interaction cluster model for $Mn3d^{5.3}$ [7]. If we identify the energy loss scale in RIXS with energy relative to main peak in resonant photoelectron spectroscopy, it is evident that the feature in question is already accounted for by the existing theory.

High resolution crystal optics schemes for HIKE-PES tested at the 7T Wiggler MAGS Beamline

F. Schäfers¹, M. Mertin¹, M. Gorgoi¹, E. Dudzik², D. Korytar³

¹BESSY GmbH, Albert-Einstein-Strasse 15, 12489 Berlin, Germany

²Hahn-Meitner Institute, Berlin

³Institute of Electrical Engineering, SAS, Piestany, Slovakia

Electron spectrometers are available nowadays with ultra-high resolution of up to 20 meV@10 keV kinetic energies. Hard x-ray photoemission at high kinetic energy (HAX-PES or HIKE) is an ideal tool to look deeply into bulk material (>5 nm) and to study (buried) interface layers [1].

For this technique hard x-rays with similar ultra-high energy resolution at highest flux are required. The energy resolution of a monochromator crystal is obtained by differentiating the Bragg equation $n\lambda = 2d \sin \theta$ which yields

$$\Delta E = E\Delta\theta / \tan \theta \quad (1)$$

with the rocking curve width

$$\Delta\theta = \sqrt{\left((\Delta\theta_{cr})^2 + \psi^2 + (\phi^2 \tan^2 \theta / 8)\right)} \quad (2)$$

For a small ΔE , the rocking curve width $\Delta\theta$, the crystal reflection curve must be small. The total width is determined by the intrinsic crystal Darwin width $\Delta\theta_c$ and by the sagittal and meridional beam divergences ψ and ϕ . So crystal limited resolution is achievable using collimated incident light, with ψ and ϕ being close to zero.

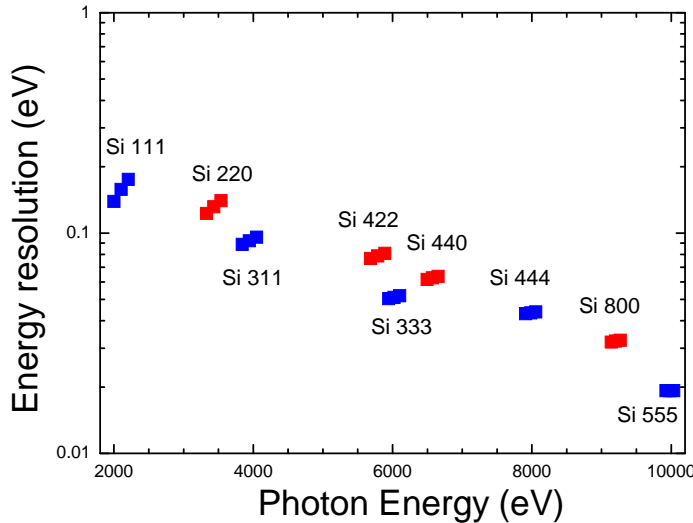


Figure 1 Calculated crystal-limited resolution of high-indexed Si lattice planes in back-reflection geometry.

the crystal limited resolution data achievable with high indexed Si lattice planes in back-reflection geometry.

Alternatively to achieve a small ΔE , the tangent can be made large. Close to 90 degrees the tangent dominates. So at large Bragg angles (backscattering), which is connected with low energy, crystals have the optimum – crystal limited resolution. In addition, in this case any beam divergence does not affect the resolution significantly.

The Darwin widths - crystal limited - resolutions of high-indexed Si lattice planes can be as high as $E/\Delta E=10^6$. However, only in backscattering geometry a significant integral reflection remains, so that this ultra-high resolution is achievable only at selected energies. Figure 1 shows

To test such high resolution schemes, the 7T Wiggler MagS-beamline of the HMI was used together with a postmonochromator and the HIKE experimental chamber (figure 2). The MagS-beamline is equipped with a Si (111) Double Crystal Monochromator, a collimating bendable premirror and a bendable refocussing mirror. Horizontal focussing is achieved by bending the 2nd crystal and by these bending options the outgoing beam profile can be manipulated between collimation and focussing. The focus position can be moved to any

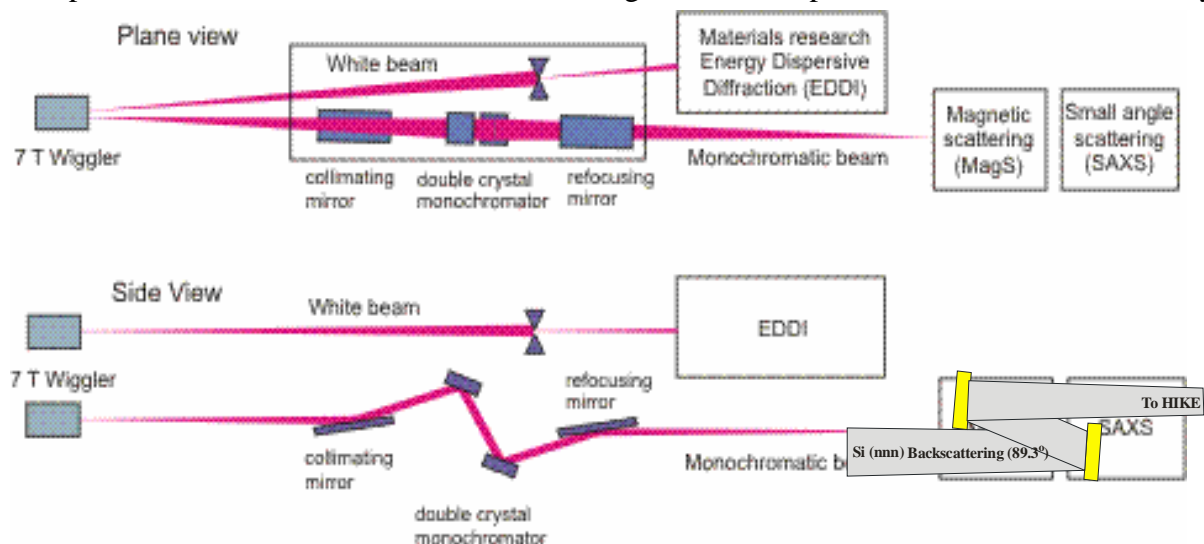


Figure 2 7T Wiggler MAGS-Beamline with Si (nnn) Postmonochromator

point along the beampass.

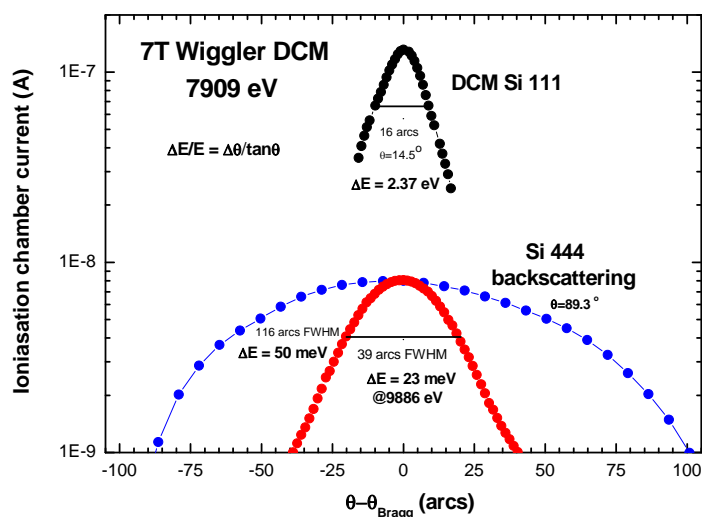


Figure 3 Rocking curves of the DCM at 7,9 keV (black curve) and of the Si (nnn) Postmonochromator with n=4 (blue curve, 7.9 keV) and n=5 (red curve, 9.9 keV). A fit to eq. 1 yields a resolution of 60 meV@7.9 keV and 23 meV@9.9 keV, resp.

The double crystal Si (nnn) postmonochromator was mounted in backscattering (89.3 degrees) – under atmospheric pressure - onto the 6-circle Huber goniometer stage inside the experimental hutch, which allowed independent setting of both crystals for easier alignment. The beampath in between the crystals was pumped down and the vacuum was separated by Kapton windows.

Figure 3 shows the rocking curves of the DCM and of the postmonochromator and photon energies corresponding to the Si (444) (7.9 keV) or Si (555) reflection (9.9keV). The DCM rocking curve width is much smaller than the one including

the postmonochromator, however, if the tangent function is deconvoluted according to eq. 1, a resolution of 60 meV at 7.9 keV and of 23 meV at 9.9 keV, respectively is obtained. This corresponds to a resolving power $E/\Delta E$ of as much as 130.000 and 430.000, respectively and this is very close to the numbers expected by raytracing simulations (figure 4).

This ultra-high resolution of $E/\Delta E = 158.000$ is confirmed by a photoelectron spectrum obtained with the HIKE experimental chamber under these experimental conditions. We were able to measure the Au Fermi edge at room temperature and the fit delivered a beamline resolution of approximately 60 meV (figure 5).

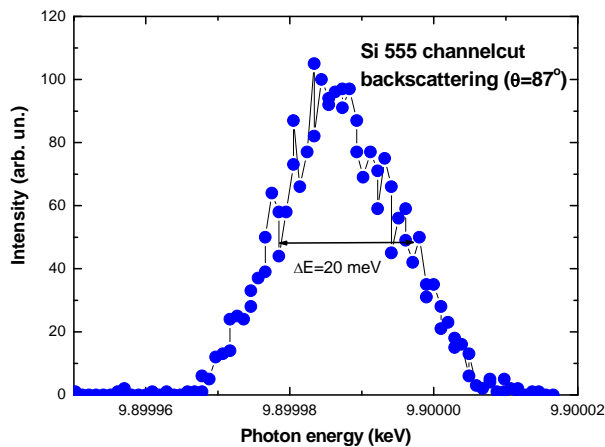


Figure 4 Raytracing result for the energy resolution of the MAGS beamline including a Si (555) post-monochromator operating at 9.9 keV

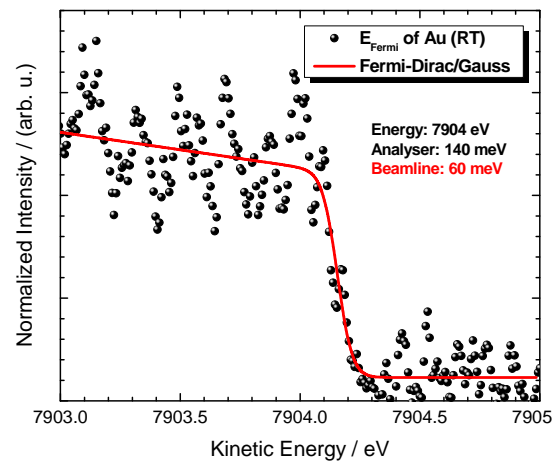


Figure 5 Au Fermi-edge at room temperature obtained with the HIKE spectrometer at a pass energy of 100 eV and a spectrometer slit of 0.5 mm. The Fermi-Dirac fit convoluted with an instrumental Gaussian profile delivered a beamline resolution of 60 meV@7.9 keV

In conclusion it was demonstrated that ultrahigh energy resolution in the hard x-ray region is possible at high intensity Wiggler beamlines even with the radiation not being strictly collimated. This was used successfully for High Kinetic Energy Photoelectron Spectroscopy which has a large potential for non-destructive investigations on buried layers and interface systems.

References

- /1/ E. Dudzik, R. Feyerherm, W. Diete, R. Signorato, Ch.Zilkens, *The new HMI beamline MAGS: an instrument for hard x-ray diffraction at BESSY*, Journal of Synchrotron Radiation, **13**, 421 (2006)
- /2/ E. Holmström et al., *A sample preserving deep interface characterization technique*, Phys. Rev. Lett. **97**, 266106-1-4 (2006)

Sodium superlattice formation in Na_xCoO_2 ($x = 0.8$)

E. Dudzik¹, R. Feyerherm¹, D. A. Tennant², D.J.P. Morris³

¹*Hahn-Meitner-Institute, c/o BESSY, 12489 Berlin, Germany*

²*Hahn-Meitner-Institute, 14109 Berlin, Germany*

³*Department of Physics, University of Liverpool*

The alkali cobaltate Na_xCoO_2 currently raises considerable interest as model compound for the doping of triangular transition metal oxide layers in comparison with the well-known square layered cuprate high-temperature superconductors. Extensive research efforts were initiated by the observation of superconductivity with T_C of up to 5 K in hydrated $\text{Na}_{0.35}\text{CoO}_2$ [1]. In Na_xCoO_2 the basic effect of a variation of the sodium concentration x is a simultaneous control of the magnetic and electronic degrees of freedom of the quasi two dimensional triangular CoO_2 sheets. For the stoichiometric $x = 1$ material, Co is in the Co^{3+} state with $S = 0$ in a low spin (LS) configuration. Compositions with $x < 1$ nominally are $\text{Co}_x^{3+}/\text{Co}_{1-x}^{4+}$ mixed valence systems where Co^{4+} has a LS $S = 1/2$ configuration. This provides control for both the electronic and magnetic properties of these materials in a natural way, where the Na content x controls both the charge carrier concentration and the amount of magnetic ions. Consequently, the system Na_xCoO_2 exhibits a rich phase diagram as function of x with a wealth of interesting electronic and magnetic ground states [2].

In addition to providing a way of doping the CoO_2 sheets, variation of the Na content has been shown to result in various types of ordered Na superstructures, as demonstrated first by electron diffraction studies on a broad series of Na_xCoO_2 samples with x ranging from 0.15 to 0.75 [3]. Sodium ion ordering may affect the electronic and magnetic properties of these compounds considerably, because it may impose electronic constraints on the CoO_2 layer. Despite the importance of Na superstructure formation, the number of corresponding structure investigations is limited [3-6].

We therefore started a project with the aim of studying the sodium superlattice formation in the series Na_xCoO_2 ($x = 0.3 - 1$) by combined X-ray and neutron diffraction experiments. First X-ray diffraction results on a sample with $x = 0.48$ have been reported already in the BESSY Annual Report 2005, p. 295f. Here we report on results on a sample with nominal stoichiometry $x = 0.75$ obtained in January 2006 on the HMI operated 7 Tesla wiggler beamline MAGS, which is equipped with a six circle goniometer. The experiment was carried out using an X-ray energy of 12.4 keV. Since the sample was a relatively thin plate (0.15mm), this high energy allowed for X-ray diffraction experiments in transmission (Laue geometry). The sample was mounted to a closed-cycle cryostat.

In the diffraction experiment we focused on searching for superlattice reflections within the basal plane of the hexagonal structure, i.e., reflections of type (h k 0). The basic result of our study was the observation of various superlattice reflections related to sodium ordering below 285K belonging to two sets, namely a “commensurate” set, e.g., (0.4, 0.4, 0), and a seemingly “incommensurate” set, e.g., (0.065, 0.735, 0). The accurate determination of the position of the latter reflections was most important for the following analysis.

The temperature dependence of the intensities of these two types of reflection revealed that they vanished at exactly the same temperature, $T_c = 285$ K, suggesting that they may arise from a single complex superlattice. A detailed analysis showed that all observed reflections could be explained assuming a single supercell of $\mathbf{a}' = \mathbf{a} + 3\mathbf{b}$ and $\mathbf{b}' = 4\mathbf{a} - 3\mathbf{b}$, where \mathbf{a} and \mathbf{b}

are the original hexagonal unit cell vectors in the basal plane. This experimental result was an important ingredient for the verification of similar experimental results from neutron diffraction on the same sample, which, however, did not give an accurate enough determination of the positions of the “incommensurate” reflections. It also was important for checking theoretical considerations concerning an organizational principle for understanding the sodium superlattice formation. In the theoretical studies, the screened Coulomb interaction among Na ions was identified as primary driving force for the Na ordering which appears to be governed by pure electrostatics. An organizational principle was derived that involves stabilization of charge droplets, namely di- and tri-vacancy clusters that order long range. Energetically the observed superstructure is within a few K of the most stable phase for the $x = 0.80$ tri-vacancy model. The deviation of the model value for x from the nominal value 0.75 points to a possible phase separation of the sample into regions with different x .

The complete work is published in Nature [7], where the present X-ray diffraction results entered as supplementary information.

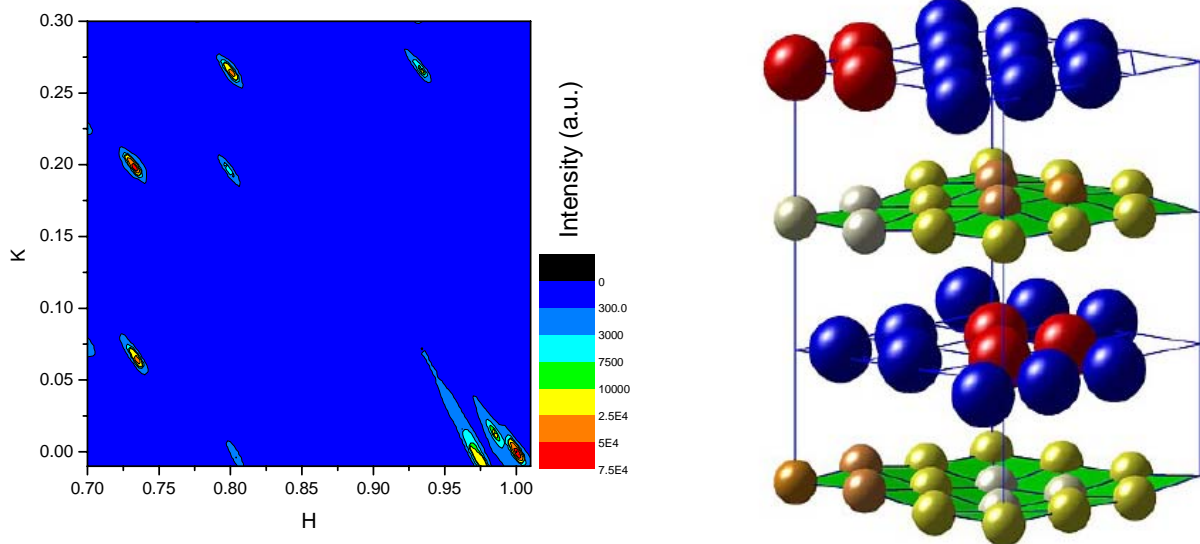


Figure 1: (left) section of reciprocal space showing strong superlattice reflections like $(0.065,0.735,0)$ and $(0.2,0.735,0)$ besides weak reflections like $(0.8,0,0)$; (right) real space superstructure related to an $x=0.80$ tri-vacancy model fitting the experimental data. Blue are Na ions, red are Na vacancies clustered in triplets. Only Co ions are shown for CoO_2 sheets marked green.

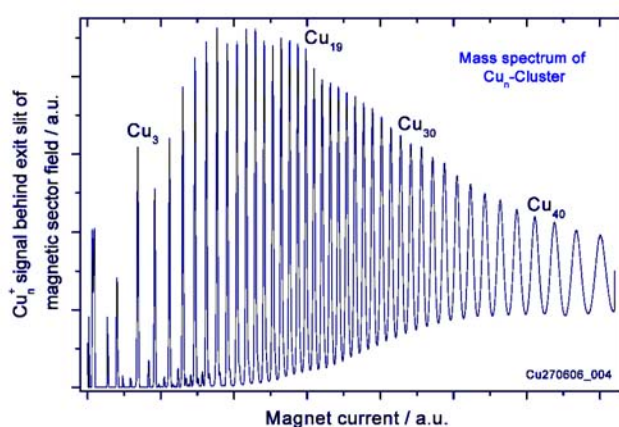
References

- [1] K. Takada, H. Sakurai, E. Takayama-Muromachi, F. Izumi, R. A. Dilanian, and T. Sasaki, Nature (London) **422**, 53 (2003).
- [2] M. L. Foo et al., Phys. Rev. Lett. **92**, 247001 (2004).
- [3] H. W. Zandbergen, M. L. Foo, Q. Xu, V. Kumar, and R.J. Cava, Phys. Rev. B **70**, 024101 (2004).
- [4] Q. Huang, M. L. Foo, J. W. Lynn, H.W. Zandbergen, G. Lawes, Yayu Wang, B. H. Toby, A. P. Ramirez, N. P. Ong, R.J. Cava, J. Phys.: Condens. Matter **16**, 5803 (2004).
- [5] D. N. Argyriou, P. G. Radaelli, C. J. Milne, N. Aliouane, L. Chapon, A. Chemseddine, J. Veira, S. Cox, N. D. Mathur, P. A. Midgley, J. Phys.: Condens. Matter **17**, 3293 (2005).
- [6] J. Geck, M. v. Zimmermann, H. Berger, S. V. Borisenko, H. Eschrig, K. Koepfner, M. Knupfer, and B. Büchner, Phys. Rev. Lett. **97**, 106403 (2006)
- [7] M. Roger, D.J.P. Morris, D.A. Tennant, M.J. Gutmann, J.P. Goff, J.-U. Hoffmann, R. Feyerherm, E. Dudzik, D. Prabhakaran, N. Shannon, B. Lake and P.P. Deen, Nature (London) **445**, 631 (2007).

X-ray absorption and core-shell ionization of mass-selected Cu-clusters on Si

B. Balkaya, N. Ferretti, M. Neeb, and W. Eberhardt
BESSY, Albert-Einstein Str. 15, D-12489 Berlin-Adlershof

XANES (L_3) and XPS ($2p$) spectra of deposited Cu-clusters of up to 70 atoms have been measured at the Optics-BL PM4 and compared with the respective bulk spectra. The clusters were produced by a home-built magnetron sputter cluster source and mass-selected prior to deposition by a magnetic sector field. A typical Cu-mass spectrum, as measured behind the

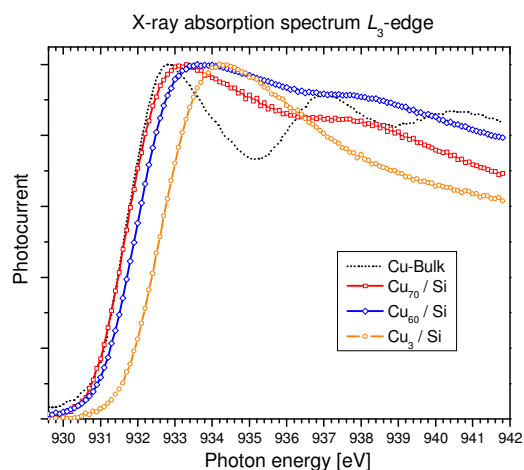


exit slit of the magnetic mass filter, is shown in the adjoining figure.

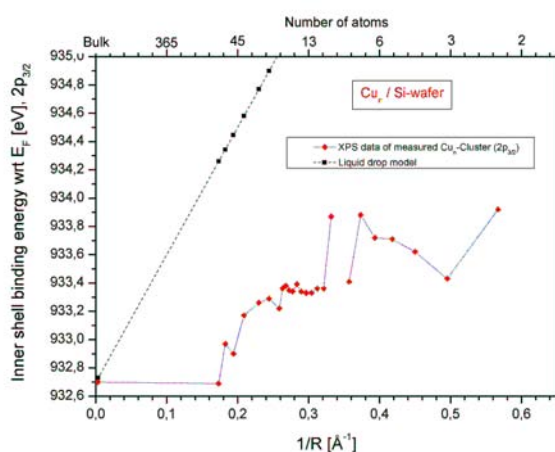
After passing the mass filter an individual cluster mass was softly landed (~ 1 eV/atom) onto a biased Si-substrate ($1 \times 1 \text{ cm}^2$). Depending on the cluster size a coverage of 10^{11} - 10^{12} cluster/ cm^2 was reached within 10-30 minutes for each sample, i.e. < 1 atom% of a monolayer. During deposition the

cluster current was recorded on the sample by an electrometer (10-100 pA). The cluster covered samples were transferred from the cluster machine to the photoemission chamber SURICAT at PM4 by a battery driven mobile UHV suitcase. A pressure of $< 5 \times 10^{-9}$ mbar was maintained during deposition and transfer.

XANES spectra (Cu- L_3 -edge) of individual cluster sizes are exemplarily shown in the adjoining figure. With respect to the bulk, the L_3 -edge for all clusters is shifted to a higher absorption energy by 1-2 eV for small clusters [1] and converging smoothly towards the bulk value with increasing cluster size. Similarly, a blue shift of the core electron binding energy is observed which amounts to ~ 1 eV for small clusters and converge towards the bulk value with increasing cluster size. The absorption



energy is located within the ionization continuum, i.e. above the $2p$ -XPS threshold, indicating a closed d -shell of the supported Cu-clusters. Upon oxidation, as experimentally shown for an oxidized Cu_{10} -sample, an excitonic peak below the $2p$ -XPS threshold reveals a charge transfer from the filled d -band towards oxygen. Another distinct difference between the XANES



spectra of the bulk and cluster is the missing fine structure [2,3] beyond the L_3 edge at energies >936 eV for sizes smaller than 10 atoms. At a cluster size ≥ 13 atoms a second absorption feature arises at ~ 938 eV (see figure above: X-ray absorption spectrum) indicating a morphology change from flat to icosahedral structures [4]. Furthermore the band gap of the supported clusters has been estimated from a rigid band model.

A strong interaction between the Si-wafer and the Cu cluster is indicated by a clear deviation from the liquid drop model (ionization potential versus inverse cluster radius $1/R_{\text{cluster}}$) as seen by the corresponding plot.

- [1] N. Ferretti, B. Balkaya, A. Vollmer, M. Neeb, W. Eberhardt, J. Electron Spect. Relat. Phenom., in press.
- [2] H. Ebert, J. Stöhr, S. Parkin, M. Samant, A. Nilsson, Phys. Rev. B **53**, 16067 (1996).
- [3] T. Tiedje, J.R. Dahn, Y. Gao, K.M. Colbow, E.D. Crozier, D.T. Jiang, W. Eberhardt, Solid State Comm. **85**, 161 (1993).
- [4] M. Kabir, A. Mookerjee, A.K. Bhattacharya, Phys. Rev. A **69**, 043203 (2004) and A.V. Soldatov, University Rostov, Russia.

Lifetime interference effects observed in the NO^+ ($A^1\Pi - X^1\Sigma^+$) fluorescence in the vicinity of the $1s^{-1} \rightarrow \pi^*$ resonance

L Werner¹, W Kielich¹, S Klumpp¹, A Ehresmann¹, Ph V Demekhin^{1,2}, V L Sukhorukov^{2,4}, K-H Schartner³ and H Schmoranzner⁴

¹ Institut für Physik, Universität Kassel D-34132 Kassel, Germany

² Rostov State University of Transport Communications, 344038 Rostov-on-Don, Russia

³ I Physikalisches Institut, Justus-Liebig-Universität, D-35392 Giessen, Germany

⁴ Fachbereich Physik, Technische Universität Kaiserslautern, D-67653 Kaiserslautern, Germany

E-mail: ehresmann@physik.uni-kassel.de

In (Ehresmann *et al* 2006a, Ehresmann *et al* 2006b) we could show that the investigation of the N_2^+ ($C - X$) fluorescence via photon-induced fluorescence spectroscopy (PIFS) (Schmoranzner *et al* 2001) after excitation of an innershell electron gives information about the decay mechanism of the N_2 $1s^{-1}\pi^*$ resonance into the C -state of the N_2^+ ion. With a high enough fluorescence resolution it was even possible to distinguish individual band sequences. Through determined emission cross sections the influence of lifetime vibrational interference effects (LVI) can be investigated. In case of the different N_2 $1s^{-1}\pi^*$ (v_r) resonance vibrational levels the effects are expected to be small due to their vibrational spacing of about 230 meV (Chen *et al* 1989) in contrast to their natural width of about 115 meV (Prince *et al* 1999), which has been confirmed by measurements of (Ehresmann *et al* 2006b, Marquette *et al* 1999).

When looking at the similar N^*O (v_r) and NO^* (v_r) resonances the vibrational spacing is 1.5 times larger than their natural widths of 124 meV (Prince *et al* 1999) in the former case, and with 150 meV in contrast to the natural width of 170 meV (Püttner *et al* 1999) already smaller in the latter case. Therefore LVI effects are expected to be seen in the emission cross sections of the NO^+ ($A^1\Pi \rightarrow X^1\Sigma^+$) fluorescence populated after innershell resonance excitation of the NO molecule, especially in the case of the NO^* (v_r) resonance excitation and their subsequent de-excitation.

The experiment, performed at the UE 56/2 PGM beamline at BESSY II, Berlin, has an experimental setup similar to (Ehresmann *et al* 2006a, Ehresmann *et al* 2006b) and only the essential points will be described here. Monochromatized synchrotron radiation was focused into a differentially pumped target cell filled with molecular nitric oxide at room temperature and at a pressure of 27.6 μbar . The pressure was chosen to be in the linear regime of the fluorescence intensity-pressure function, to avoid artifacts, such as photoelectron impact induced fluorescence. The exciting-photon energy was varied around the vicinity of the $\text{N}^*\text{O}(1s^{-1}\pi^*)$ resonance and $\text{NO}^*(1s^{-1}\pi^*)$ resonance in steps of 50 meV. A bandwidth of the exciting radiation of about 100 meV and 130 meV FWHM at 400 eV and 530 eV, respectively, was chosen, as a compromise of high fluorescence flux and small bandwidth of the exciting photons. The exciting-photon energy was calibrated to the energy positions of the vibrational levels of the $\text{N}^*\text{O}(1s^{-1}\pi^*)$ (Wang *et al* 2001) and $\text{NO}^*(1s^{-1}\pi^*)$ (Püttner *et al* 1999) resonances. The dispersed fluorescence radiation was detected by a position sensitive CsI microchannel plate detector between $118 \leq \lambda_{fluor} \leq 142$ nm and was observed perpendicularly to the exciting-photon beam and parallel to the \vec{E} - vector of the linearly polarized exciting radiation. The fluorescence resolution of the 1 m-NIM monochromator, equipped with a 1200 l/mm grating, and detector combination was about $\Delta\lambda_{fl} = 0.2$ nm.

Likewise to (Ehresmann *et al* 2006a, Ehresmann *et al* 2006b) relative doubly integrated emission cross sections for the $A(v') \rightarrow X(v'')$ fluorescence bands have been determined by integrating the corresponding fluorescence intensities, $I(\omega, \lambda)$, corrected for the quantum efficiency of detector over a wavelength interval of 0.6 nm centered at the wavelength $\lambda_{exp}^{v',v''}$ and over the present exciting-photon energy range ($\omega_1 - \omega_2$) around the innershell resonances:

$$\bar{\sigma}_{Av'}^{Xv''} = \int_{\omega_1}^{\omega_2} \sigma_{Av'}^{Xv''}(\omega) d\omega = \int_{\lambda_{exp}^{v',v''} - 0.3 \text{ nm}}^{\lambda_{exp}^{v',v''} + 0.3 \text{ nm}} \sigma_{Av'}^{Xv''}(\lambda) d\lambda, \quad (1)$$

$$\sigma_{Av'}^{Xv''}(\omega) = \int_{\lambda_{exp}^{v',v''} - 0.3 \text{ nm}}^{\lambda_{exp}^{v',v''} + 0.3 \text{ nm}} I(\omega, \lambda) d\lambda, \quad (2)$$

$$\sigma_{Av'}^{Xv''}(\lambda) = \int_{\omega_1}^{\omega_2} I(\omega, \lambda) d\omega, \quad (3)$$

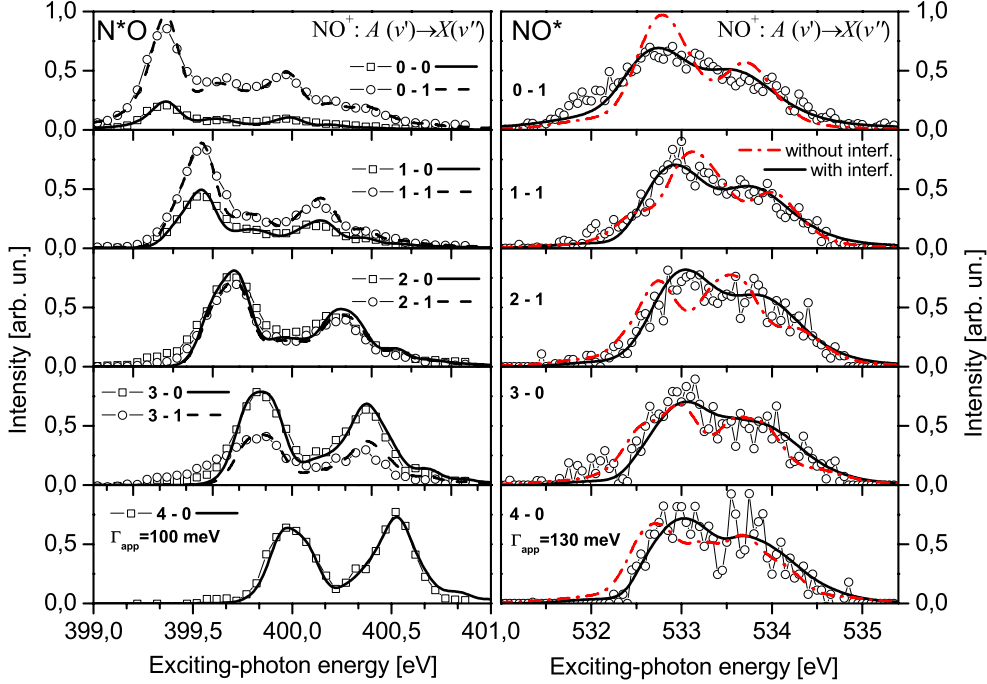


Figure 1. Comparison between measured and computed cross sections for $A\ ^1\Pi(v') \rightarrow X\ ^1\Sigma^+(v'')$ fluorescence excited via the N^*O (left) and NO^* (right) resonances. The computed cross sections were additionally convolved with a Gaussian of 100 meV and 130 meV FWHM, respectively. For better comparison of shapes the areas of computed cross section were equalized to the respective areas of measured one. The fluorescence cross sections calculated neglecting the vibrational interference are shown for the NO^* case by the red dash-dot line.

where the $\sigma_{Av''}^{Xv'}(\omega)$ and $\sigma_{Av''}^{Xv'}(\lambda)$ are the integrated cross sections for $A(v') \rightarrow X(v'')$ fluorescence at a given exciting-photon energy, ω , or fluorescence wavelength, λ , respectively. When calculating the emission cross sections for the $A\ ^1\Pi(v') \rightarrow X\ ^1\Sigma^+(v'')$ fluorescence an approach beyond the Franck-Condon approach is needed to be introduced because the electronic transition moment $\mathbf{D}_A^X(R)$ exhibits a strong dependence on the internuclear distance R .

In figure 1 the computed cross sections (lines) of the $\sigma_{Av''}^{Xv'}(\omega)$ for the $A\ ^1\Pi(v') \rightarrow X\ ^1\Sigma^+(v'')$ fluorescence are compared to the experimental results (open circles, open squares). The computed cross sections were additionally convolved with Gaussians of 100 meV and 130 meV FWHM, respectively, for N^*O and NO^* core-excitations and to compare the computed and measured cross sections their respective areas has been equalized. As can be seen in figure 1 the shape of the computed and measured $\sigma_{Av''}^{Xv'}(\omega)$ cross sections agree very well. Neglecting LVI effects changes the shape of the emissions cross sections clearly as can be seen in figure 1 for the NO^* excitation by the red dash-dot line. Relative values of the doubly-integrated cross sections $\bar{\sigma}_{Av''}^{Xv'}$ observed in the present experiment (corrected for the QE of CsI detector), normalized to $\bar{\sigma}_{Av''=1}^{Xv''=1} = 100\%$, in comparison with the calculated ones are given in table 1. The strong discrepancy between theory and experiment for the (0,1) band is due to their overlap with a NI atomic line and the (3,3) band. Missing experimental values of the $\bar{\sigma}_{Av''}^{Xv'}$ cross sections for the NO^* resonance excitation are because they could not be resolved in the present measurement.

Table 1 illustrates for the case of the N^*O and the NO^* intermediate resonance the influence of the interference effects on the calculated $\bar{\sigma}_{Av''}^{Xv'}$ values and shows a good agreement between measured and calculated $\bar{\sigma}_{Av''}^{Xv'}$ values. In case of the NO^* intermediate resonance one can recognize that taking LVI effects into account improve the agreement between computed and measured doubly-integrated cross sections. For instance, accounting for the LVI decrease computed values of $\bar{\sigma}_{A4}^{X0}$ and $\bar{\sigma}_{A3}^{X0}$ by the factors of 2.5 and 1.8, respectively. For the remaining difference between theory and experiment cascade effects in populating the A state in the NO^+ ion after resonant excitation of an inner-shell electron are being examined at the moment.

This work was supported by the Deutsche Forschungsgemeinschaft (DFG) and by the Bundesministerium für Bildung und Forschung (BMBF) (Förderkennzeichen 05 ES3XBA/5 and IB/DLR RUS 02/037). The authors gratefully acknowledge the help of Dr. Gerd Reichardt, Dr. Olaf Schwarzkopf and Dr. Rolf Follath during their experiments.

Table 1. Doubly-integrated cross sections $\bar{\sigma}_{Av'}^{Xv''}$, equation (1), of vibrational bands (relative to $\bar{\sigma}_{A1}^{X1}$ in %) observed in the $A - X$ fluorescence of NO^+ after $1s^{-1}\pi^*$ resonant N^*O or NO^* Auger decay and calculated in different approximations.

Bands $A(v') \rightarrow X(v'')$	N^*O			NO^*		
	Theor. ^a	Theor. ^b	Exper. ^c	Theor. ^a	Theor. ^b	Exper. ^c
4 - 0	24	17	7	131	53	15
3 - 0	44	34	22	107	60	33
2 - 0	59	50	46	79	60	
3 - 1	15	12	12	37	21	
1 - 0	50	50	48	50	50	
2 - 1	57	49	40	77	58	40
0 - 0	17	21	21	17	21	
1 - 1	100	100	100	100	100	100
0 - 1	61	74	132 ^d	61	73	151 ^d

^a) Vibrational interference is neglected;

^b) Vibrational interference is accounted for;

^c) Experimental data are corrected for QE of CsI detector.

^d) Experimental value of $\bar{\sigma}_{A0}^{X1}$ is too large because this molecular band is strongly overlapped with NI atomic line and (3,3) band.

References

- Chen C T, Ma Y and Sette F 1989 *Phys. Rev. A* **40**, 6737.
- Ehresmann A, Werner L, Klumpp S, Lucht S, Schmoranzer H, Mickat S, Schill R, Schartner K-H, Demekhin P V, Lemeshko M P and Sukhorukov V L 2006 *J. Phys. B: At. Mol. Phys.* **39**, 283-304.
- Ehresmann A, Werner L, Klumpp S, Demekhin P V, Lemeshko M P, Sukhorukov V L, Schartner K H and Schmoranzer H 2006 *J. Phys. B: At. Mol. Phys.* **39**, L119.
- Marquette A, Meyer M, Sirotti F and Fink R F 1999 *J. Phys. B: At. Mol. Opt. Phys.* **32**, L325.
- Prince K C, Vondráček M, Karvonen J, Coreno M, Camilloni R, Avaldi L and de Simone M 1999 *J. Electr. Spectr. Relat. Phenom.* **101-103**, 141.
- Püttner R, Domingue I, Morgan T J, Cisneros C, Fink R F, Rotenberg, Warwick T, Domke M, Kaindl G and Schlachter A S 1999 *Phys. Rev. A* **59**(5), 3415.
- Schmoranzer H, Liebel H, Vollweiler F, Müller-Albrecht R, Ehresmann A, Schartner K-H and Zimmermann B 2001 *Nucl. Instrum. Methods in Phys. Res. A* **467-468**, 1526.
- Wang H, Fink R F, Piancastelli M N, Hjelte I, Wiesner K, Bässler M, Feifel R, Björneholm O, Miron C, Giertz A, Burmeister F, Sorensen S L and Svensson S 2001 *J. Phys. B: At. Mol. Phys.* **34**, 4174.

Ultrafast precessional dynamics excited by femtosecond laser pulses in ferromagnetic Nanoparticles.

Beaurepaire Eric, Boeglin Christine, Bigot Jean-Yves, Stamm Christian, Dürr Hermann A., Pontius Niko J.

The main objective during this beam time was to study the ultra-fast magnetization dynamics in nanometric superparamagnetic cobalt clusters. These experiments consisted in performing XMCD experiments at the Co $L_{2,3}$ edges at the UE 56/1 beam line, using a femto second laser excitation and an external magnetic field of ± 0.4 Tesla. In this project we focused mainly in the magnetization dynamics of superparamagnetic particles as a function of particle size and temperature. The XMCD was measured in the transmission mode as a function of the pump-probe delay in the 0-1ns range.

Composite films made of Co nanoparticles embedded in a dielectric medium have been deposited on Si₃N₄ membranes. The first part of our beam time was devoted to the optimisation of the samples with respect to the quantity of Co in order to ensure a reasonable transmission of the x-ray beam. The first results have shown that the transmission experiment is feasible with thin Co films of 10 nm thickness as well as 7 nm superparamagnetic Co particles (fig.1). The second part of the beam time was devoted to the optimisation of the laser fluence in the pump probe experiment. The best results have been obtained for a laser fluence of 130 mJ/cm² on Co nanoparticles with a diameter of ~8 nm. Our first results display two main temporal components. The first one corresponds to a demagnetization of the Co particles within about 100ps. It is limited by the temporal resolution of the beam line. The second one corresponds to the re-magnetization of the Co particles associated to a thermal diffusion to the environment.

The temperature dependency ($80\text{K} < T < 300\text{K}$) shows that the re-magnetization time of Co nanoparticles is faster at low temperature ($T = 80\text{K}$). For technical reasons (cryostat limited to liquid N₂) the blocking temperature (50-60 K) of the superparamagnetic Co particles could not be reached. For this reason we were not able to investigate the magnetization dynamics in this interesting and unexplored regime. The new set up of the beam line available in 2007 will allow us to perform these experiments.

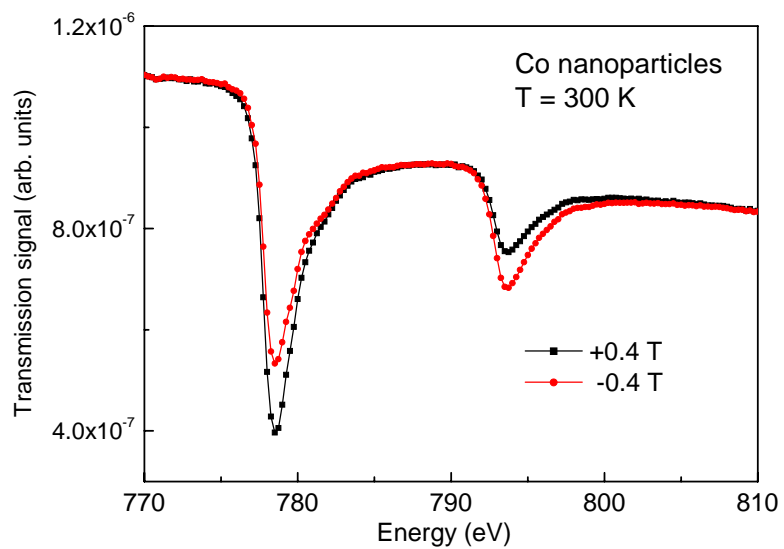
A second important limitation of the experiment was the 60ps time resolution achievable in the used multi bunch operation mode. The overall dynamics that we observed on the Co particles did not allow us to resolve the first step of the demagnetization (below 1ps). In addition the multi bunch mode did not allow to investigate the size and temperature dependency of the Co magnetization dynamics.

Beside the time resolved magnetization dynamics experiments we performed XMCD spectroscopy at the Co L_3 edge for selected delays between the pump and probe. This experiment was performed in order to study the electronic shift and broadening of the Co $L_{2,3}$ edges. We found that the dynamics of these edges show striking differences when comparing thin Co films with Co nanoparticles.

In order to investigate the precession dynamics of our Co nanoparticles we performed tests experiments with the existing field orientation (parallel to the x-ray beam). The outcome of these tests shows that a transverse field is mandatory in order to induce a precession that could be compared with the magneto-optical measurements performed in Strasbourg.

Several limitations (low temperatures, transverse fields) that we encountered in this first beam time will be overcome in the next beam time allocated in spring 2007. The improvement of the limited time resolution requires the low alpha mode, which is the object of the next project.

Fig. 1: Transmission signal obtained on Co nanoparticles of 7nm diameter for ± 0.4 Tesla field applied along the out of plane axis of the sample.



Photoelectron correlation spectroscopy ($\gamma,2e$) on Xe/Cu(111)

C. Winkler, M. Muñoz-Navia, K. Hünlich, H. Chang,
R. Patel and J. Kirschner

Max-Planck-Institut für Mikrostrukturphysik, Weinberg 2, D-06120 Halle

1 Introduction

Correlation between electrons is a fundamental characteristics of systems containing many electrons. The influence of correlation on the electronic structure of solids manifests itself in enhanced or suppressed magnetic susceptibilities of paramagnetic metals, large electronic coefficients of the heat capacity, or in differences between experimental and theoretical one-electron band widths, to name only a few examples. A quite promising way to investigate these correlation effects is to study the double photoemission (DPE), where the absorption of a single photon leads to the simultaneous excitation and emission of two (correlated) electrons. This simultaneous two-orbital excitation following the absorption of one VUV photon is exclusively caused by the interelectronic interaction because in the case of excitations by electron dipole transitions, a photon can only interact with one electron at a time[1],[2]. The main obstacle in experiments on correlation effects is a low-counting coincidence rate of two *correlated* electrons as compared to the large amount of *uncorrelated* secondary electrons that appear as a huge background. This, finally, leads to quite long aquisition times in order to collect spectra with a reasonable statistics.

In the present work, the energy-distributions of correlated photoelectrons ejected from Xe adsorbed on a Cu(111) single crystal surface were studied experimentally. A rare-gas solid was chosen because it is known that double photoemission is a very efficient process in the gas phase[3]. Since solid rare-gases are formed by weak Van-der-Waals interaction, double photoemission should be comparable to the gas phase, leading to reasonable measuring times. Electron correlation spectroscopy (e,2e) experiments on Xe/Cu(111) actually show a rather high coincidence count rate compared to clean copper over a broad

range of kinetic energy of the incoming electron[4]. In a further experiment which was carried out at the beamline CP-NIM during the single bunch (SB) operation of BESSY II in autumn 2004, we confirmed that Xe adsorbed on Cu(111) is also a promising sample with respect to the coincidence rate in the case of photoelectron correlation spectroscopy[5].

To date, we got a reasonable data set for different primary energies on (e,2e) measured in our lab and some data on comparable photon primary energies on (γ ,2e), latter acquired at the dipole beamline CP-NIM of the BESSY II synchrotron radiation source in Berlin in the single-bunch-mode. A preliminary comparison of the (e,2e) to the (γ ,2e) data is given in this report.

2 Experimental details

In the present experiment, the time-of-flight (TOF) technique was utilised to determine the energy of the electrons released from the surface by an incoming electron or photon, respectively. The experimental setup with the TOF-spectrometer is presented in detail already elsewhere[6],[7]. The sample was prepared by dosing 20 L Xe onto a Cu(111) single crystal surface, which was held continuously at a temperature of $T_s \simeq 30$ K during the measurement. The Xe film was refreshed every eight hours. A schematic view of the experimental set up is given in fig.1.

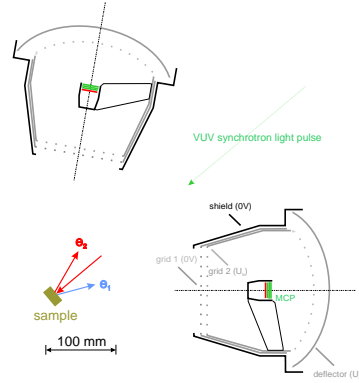


Figure 1: Schematic view of the experimental set up. e1, e2: photoelectrons, MCP: multichannelplate.

3 Results

The energy distributions of Xe/Cu(111) for a (γ ,2e) and an (e,2e) experiment with comparable photon/primary energies are shown in Fig. 2. It is interesting to note that both spectra reveal a striking difference: while the (e,2e) data show a clearly resolved region of high intensity along the Fermi-edge with $E_{kin1} + E_{kin2} + W = E_p$ (W : work-function of the sample), the (γ ,2e) spectrum is dominated by inelastic processes with $E_{kin1} + E_{kin2} + 2W < h\nu$. The work function deduced from this data is slightly shifted

to lower values compared to that of clean Cu. This very observation was also made for another pair of corresponding energies, namely $h\nu = 35$ eV and $E_p = 30$ eV, and, at first glance, this observation suggests a rather low Xe coverage with ≤ 1 ML. In this case contributions of the Xe/Cu *and* the Cu substrate have to be taken into account for a more detailed data analysis. This requires an elaborated analysis procedure which is currently underway.

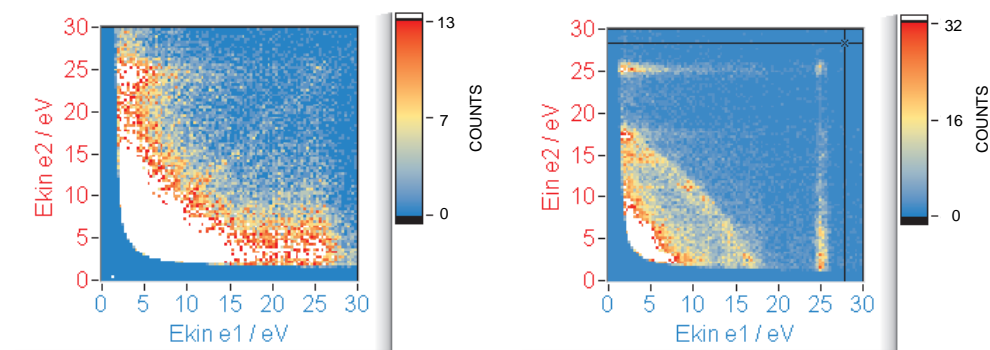


Figure 2: Energy distributions for Xe/Cu(111) at $T_p \approx 30$ K for $(\gamma, 2e)$ (left, $h\nu = 30$ eV) and $(e, 2e)$ (right, $E_p = 25$ eV).

References

- [1] J. Berakdar, *Phys. Rev B* **58** (1998) 9808
- [2] J. Berakdar, *Appl. Phys. A* **69** (1999) 497
- [3] H.W. Biester, M.J. Besnard, G. Dujardin, L. Hellner and E.E. Koch, *Phys. Rev. Lett.* **59** (1987) 1277
- [4] C. Winkler and J. Kirschner, *Verhandl. DPG (VI)* **40 2/2005** (2005) 476
- [5] C. Winkler, K. Hünlich and J. Kirschner, *Bessy Annual Report* (2004)
- [6] C. Winkler, G. Kerherve and J. Kirschner, *Verhandl. DPG (VI)* **39 2/2004** (2004) 399
- [7] J. Kirschner, G. Kerherve and C. Winkler, *Rev. Sci. Instr.* to be published

Interplay between structural properties and electronic ground states in the organic superconductor κ -(BEDT-TTF) $_2$ Cu[N(CN) $_2$]Br

A. U. B. Wolter¹, R. Feyerherm¹, E. Dudzik¹, S. Süllow², Ch. Strack³, M. Lang³, D. Schweitzer⁴

¹Hahn-Meitner-Institut GmbH, c/o BESSY, 12489 Berlin, Germany

²Institut für Physik der Kondensierten Materie, TU Braunschweig, 38106 Braunschweig, Germany

³Physikalisches Institut, J. W. Goethe Universität, 60438 Frankfurt am Main, Germany

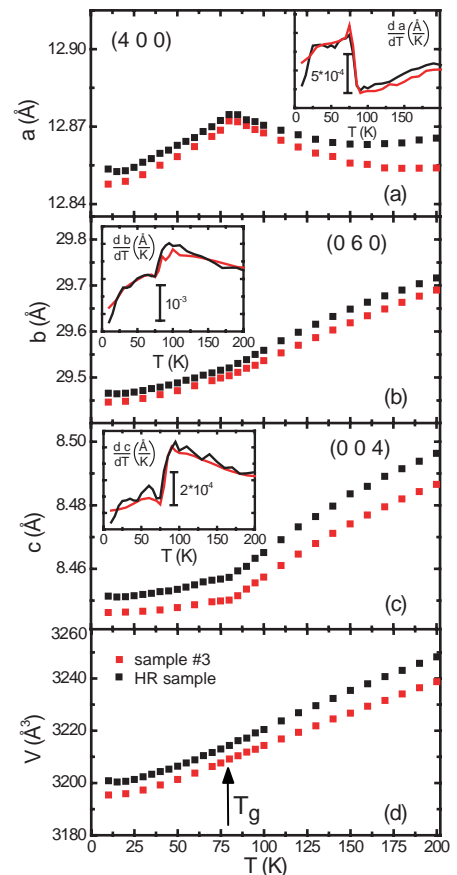
⁴Physikalisches Institut, Universität Stuttgart, 70550 Stuttgart, Germany

Funded by the DFG under contract no. SU229/8-1.

Due to their exotic superconducting and normal-state properties, resembling those of the high- T_c cuprates, the organic charge-transfer salts κ -(BEDT-TTF) $_2$ X, X = Cu(NCS) $_2$, Cu[N(CN) $_2$]Br and Cu[N(CN) $_2$]Cl have been intensively studied in recent years. Resulting from a layered crystal structure, consisting of alternating planes of conducting (BEDT-TTF) $_2^+$ cations and insulating anions X, the electronic properties of these materials are quasi two-dimensional. This leads to electronic ground state properties for the series of materials which are commonly summarized within a conceptual phase diagram, with the antiferromagnetic insulator X = Cu[N(CN) $_2$]Cl and the correlated metals X = Cu[N(CN) $_2$]Br, Cu(NCS) $_2$ on opposite sites of a bandwidth-controlled Mott transition [1].

In recent thermal expansion measurements on κ -(BEDT-TTF) $_2$ Cu[N(CN) $_2$]Br (abbreviated κ -Br hereafter) three kinds of anomalies have been identified [2]: one associated to the superconducting transition at $T_c = 11.6$ K, a phase-transition-like anomaly at $T^* \sim 40$ K, and a kinetic glass-like transition at $T_g = 77$ K. The origin of the glass-like transition is still unclear and led to various hypotheses [2-4], from which the idea of a configurational freezing-out of the terminal ethylene groups (CH $_2$) $_2$ of the BEDT-TTF molecule taking place at T_g received most support. In this material, the terminal ethylene groups can adopt two possible configurations, with either an *eclipsed* or *staggered* relative orientation of the outer C-C bond. Then, the “glassy” state below T_g would be characterized by the level of frozen-in disorder of the two configurations, and which – by way of the history dependence of the freezing process – accounts for the pronounced cooling-rate dependencies of various bulk properties observed for this organic superconductor. These facts in combination with the striking sample-to-sample variations in the resistivity [5] above T_g , which have been linked to real structure effects (disorder, defects) [6], and the importance of information about the (local) structural properties for theoretical models to account for superconductivity in these compounds, lead to an increased interest in the local structure. Therefore synchrotron x-ray diffraction experiments have been performed on two single crystals of κ -Br using the 7 T multipole wiggler beamline MAGS. To

Fig. 1(a)-(d) The T dependence of the lattice parameters a , b , c and of the volume V for sample #3 and the HR sample of κ -Br. In the insets the derivative of the lattice parameters is shown, indicating a structural anomaly at ~ 80 K.



avoid sample heating as well as irradiation damages the power of the beam (full beam intensity 10^{12} photons/s at 10 keV) was reduced using appropriate absorber foils. The single crystals were grown by an electrochemical technique using different solvents for both synthesis routes, which may cause variations in the purity of the material and the structural perfection. They have been characterized in full detail including resistivity experiments [5] (sample #3 and sample labelled HR). Whereas the HR sample exhibits a broad maximum in the resistivity around 100 K, sample #3 has a lower resistivity and no maximum has been observed. Apart from this sample-dependent, extrinsic scattering contribution, however, the different variants behave almost identically with regard to the glass-like transition at T_g , abrupt changes in the resistivity data at T^* and the superconducting transition at $T_c \sim 12$ K. In an attempt to search for possible structural differences of the two single crystals, the presence of local structural disorder and to establish if the structural parameters control the electronic ones in κ -Br, we have performed a detailed mapping of various Bragg peaks and measured the lattice parameters as function of temperature. All temperature dependencies were measured on heating in order to avoid hysteresis effects, with cooling and subsequent heating rates of ~ 2 K/min for these investigations. From our data we do not observe any indication of splitting of Bragg reflections down to 10 K, excluding the possibility of a significant (monoclinic) distortion at the T^* or T_g transitions.

The temperature dependent results for the a , b and c parameters are depicted in Fig. 1. The data for the three principal axes show a highly anisotropic behavior. Surprisingly, only the quantitative behavior of the lattice parameters appears to be different, with the one from the HR sample being somewhat larger. For both samples, upon heating, for the a axis an upturn is observed. After reaching its maximum at T_g , the lattice constant abruptly decreases again up to ~ 200 K. In contrast, for the b and c directions we find a monotonic increase up to 200 K, with only a small kink at 80 K. However, as result of compensating lattice parameter anomalies, no anomaly in the unit cell volume $V(T)$ is observed at T_g for both crystals. The anomalous behavior of the a lattice parameter suggests an anomalous change in the bond angle of --CN--Cu--NC-- in the polymeric chain in the temperature range well above T_g . This in turn might induce a change in the hydrogen bonding --CH \cdots N—between terminal ethylene groups and nitrogen atoms on the polymer, thus affecting the electronic properties of κ -Br.

Another important question concerns the relationship between the ethylene ordering and a possible superstructure formation below $T = 200$ K [4,7]. In order to check for a superstructure formation we performed high-resolution synchrotron x-ray diffraction experiments at 28 K on sample #3. According to Ref [7], claiming that the wave vector of the displacive structural distortion doubles the lattice parameter along c and the reciprocal wave vector of all observed reflections has a sizeable a^* component, the following reflections have been examined in our work: (3 0 0.5), (5 0 0.5), (7 0 0.5), (6 0 3.5), (7 0 3.5), (8 0 3.5). We found no evidence for any superstructure formation for the crystal used in our work in contrast to former x-ray “monochromatic” Laue photographic studies claiming a commensurate lattice modulation with a propagation vector $0.5 c^*$. This leads us to believe that these kind of materials are extremely sensitive regarding their thermal history and handling in that sense that slow and rapid cooling through the glass-like transition may modify the local potential of the ethylene groups and thus the overall properties of the system. Parts of the above results will be published in the near future [8].

[1] K. Kanoda, *Hyperfine Interact.* **104**, 235 (1997).

[2] J. Müller *et al.*, *Phys. Rev. B* **65**, 144521 (2002).

[3] X. Su *et al.*, *Phys. Rev B* **57**, R14056 (1998).

[4] M. A. Tanatar, T. Ishiguro, T. Kondo, G. Saito, *Phys. Rev. B* **59**, 3841 (1999).

[5] Ch. Strack *et al.*, *Phys. Rev. B* **72**, 054511 (2005).

[6] M. Lang *et al.*, ISCOM 2005 Conference: <http://dx.doi.org/10.1007/s10909-006-9018-x>

[7] Y. Nogami *et al.*, *Solid State Comm.* **89**, 113 (1994).

[8] A. U. B. Wolter *et al.*, *Physical Review B* in print (2007).

Observation of two ferromagnetic phases in Co-implanted ZnO

N. Akdogan¹, A. Nefedov¹, R. I. Khaibullin², L. R. Tagirov^{2,3}, H. Zabel¹

¹Ruhr-Universität Bochum, 44801 Bochum, Germany

²Kazan Physical-Technical Institute of RAS, 420029 Kazan, Russia

³Kazan State University, 420008 Kazan, Russia

According to suggestion of Dietl *et al.* [1], the ZnO-based dilute magnetic semiconductors (DMSs) can order ferromagnetically at room temperature. However, the origin of ferromagnetic coupling in the ZnO-based DMSs has not been very well understood yet. Some investigations showed that observed ferromagnetism originates from substitution of doped magnetic ions in Zn sites, while in other publications the origin of ferromagnetism is reported to be due to the precipitation of metallic clusters. To understand the microscopic mechanism of long range magnetic coupling in TM-doped ZnO, we have investigated the magnetic properties of Co-doped ZnO film at room temperature.

For the growth of ZnO we used epi-polished single-crystalline a-plane sapphire wafers. The nominal thicknesses of the sputter deposited ZnO films were in the range of 500 Å, according to the deposition time [2]. In order to increase the crystallinity of the ZnO films, we have carried out post-growth annealing in an oxygen atmosphere with a partial pressure of up to 2000 mbar and a temperature of 800 °C. After annealing, ZnO samples were implanted in ILU-3 ion accelerator (KPTI of RAS) with 40 keV Co⁺ ions to a dose of 1.50×10^{17} ion/cm². The magnetic properties of cobalt implanted ZnO were investigated using magneto-optical Kerr effect (MOKE) and soft x-ray resonant magnetic scattering (XRMS) technique at room temperature. The XRMS experiments were carried out at the undulator beamline UE56/1 of BESSY II in Berlin using the UHV diffractometer ALICE [3].

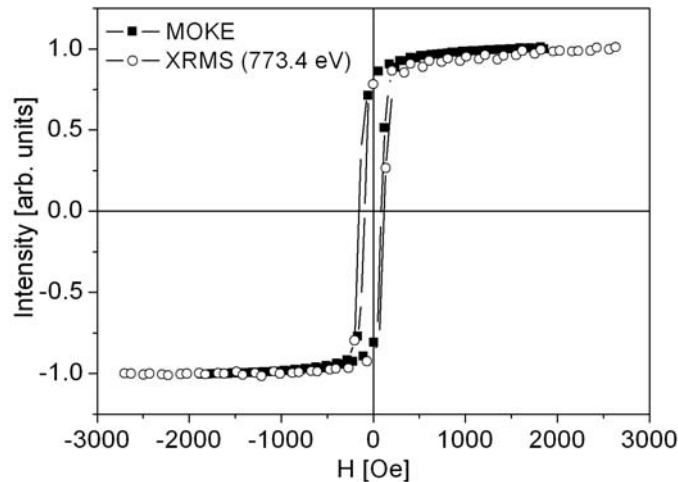


Figure 1: Hysteresis curves of the implanted ZnO film measured at room temperature using MOKE and XRMS techniques.

In Fig. 1 we show the magnetic hysteresis curve recorded using MOKE technique (closed symbols). This hysteresis curve indicates that after cobalt implantation non-magnetic ZnO is getting ferromagnetic at room temperature. To study in detail the observed ferromagnetic behavior, we measured XMCD signal (asymmetry ratio) at the Co $L_{2,3}$

edges in scattering geometry (Fig. 2). Strong ferromagnetic signal (up to 30%) is clearly observed confirming the results obtained by MOKE. Then we measured three hysteresis loops for different photon energies (shown by open circles in Fig. 2) and we observed systematic change of hysteresis loop shape with increasing photon energy. The shape of hysteresis curve taken at 773.4 eV (open symbols in Fig. 1) is practically the same as the one measured by MOKE, but the coercive field is slightly larger.

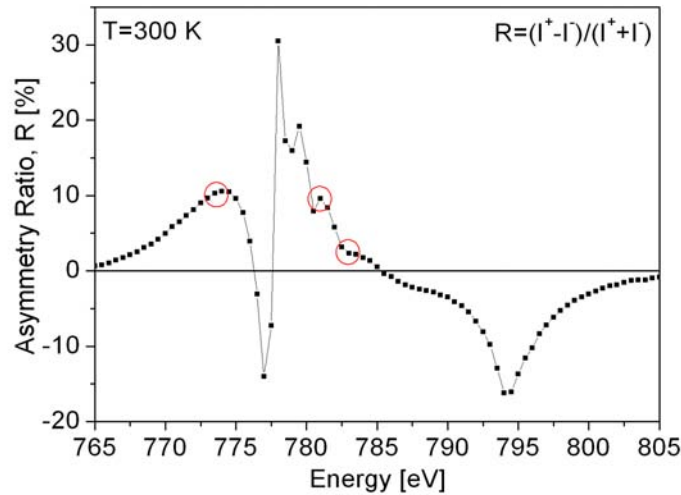


Figure 2: XMCD signal (asymmetry ratio) taken at the Co *L* edges. Open circles show the energies, where we observed different hysteresis curves.

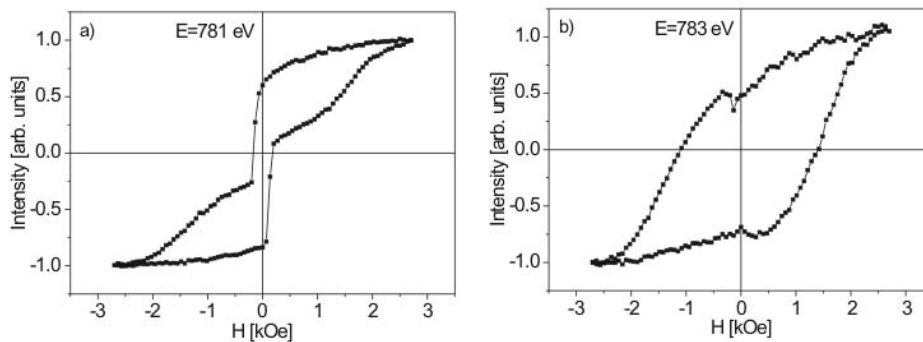


Figure 3: (a) Hysteresis loop measured at the energy of 781 eV shows the superposition of two different phases of cobalt in host material. (b) Hysteresis loop taken at the energy of 783 eV indicates metallic phase of cobalt with a large coercive field.

However, when we increase the incoming photon energy up to 781 eV and 783 eV, we have observed two hysteresis loops which are different from each other and the one measured at 773.4 eV. In Fig. 3 (a) we present the hysteresis curve recorded at 781 eV. At this energy the hysteresis curve has another component with a larger coercive field. At the higher energies low coercive field component decreases and at the energy of 783 eV (Fig. 3 (b)) hysteresis curve has practically a large coercive field component only.

In conclusion, we have studied the magnetic properties of Co-implanted ZnO using magneto-optical Kerr effect and x-ray resonant magnetic scattering techniques. The observed room temperature ferromagnetism is contributed by two phases of cobalt atoms in the implanted region. One is the substitutional phase with a relatively small coercive field (discussed in [4]) and the second one is formation of cobalt clusters.

This work was partially supported by BMBF through Contracts Nos. 05KS4PCA and 05ES3XBA/5, by DFG through SFB 491, by RFBR through the grant No 04-02-97505, and by TUBITAK through the project No 104T176. N. Akdogan acknowledges a fellowship through the IMPRS "SurMat".

References

- [1] T. Dietl *et al.*, *Science* **287**, 1019 (2000)
- [2] M. Ay, A. Nefedov and H. Zabel, *Appl. Surf. Sci.* **205**, 329-335 (2003)
- [3] J. Grabis, A. Nefedov, and H. Zabel, *Rev. Sci. Instrum.* **74**, 4048 (2003)
- [4] N. Akdogan, A. Nefedov, R.I. Khaibullin, L.R. Tagirov and H. Zabel, *Bessy Annual Report* (2006)

X-ray absorption spectra and resonant Ni 3d, 3p and 3s photoelectron spectra at the Ni 2p absorption edge for nickel phthalocyanine NiPc

A.S. Vinogradov¹, S.A. Krasnikov^{1,2}, A.B. Preobrajenski^{1,3}, M.M. Brzhezinskaya¹, S.I. Fedoseenko¹, E.V. Nikolaeva¹, D.A. Zverev¹, S.L. Molodtsov^{1,4} and R. Püttner⁵

¹ V.A. Fock Institute of Physics, St. Petersburg State University, St. Petersburg, 198504 Russia;

² School of Physical Sciences, Dublin City University, Glasnevin, Dublin 9, Ireland;

³ MAX-lab, Lund University, S-22100 Lund, Sweden;

⁴ Institut für Festkörperphysik, Technische Universität Dresden, D-01062 Dresden, Germany

⁵ Institut für Experimentalphysik, Freie Universität Berlin, Berlin, Germany

Transition metal phthalocyanines (MPc's) and porphyrins (MP's) are very stable complex compounds that function in a wide variety of roles ranging from oxygen transport, electron transfer, and oxidation catalysts to photosynthesis [1,2]. As a result, their electronic structure remains a subject of intense research during last decade [3]. The main aim of the present work, which continues our previous investigation of NiPc [4], was to gain a deeper insight into the nature of chemical bonding between the nickel atom and its environment and electronic structure features for nickel phthalocyanine NiPc. To do this, we have carried out high-resolution, uniformly calibrated measurements of the Ni 2p and N 1s absorption spectra for NiPc and related Ni compound - nickel tetrabenzoporphyrin, NiTBP, as well as those of the Ni 3p, Ni 3s and valence-band PE spectra for NiPc recorded in the wide range of the excitation photon energies, including those of resonance excitations at the Ni 2p_{1/2,3/2} and 3p absorption edges.

All measurements on NiPc and NiTBP were performed at the Russian-German beamline at BESSY II. The Ni PC and NiTBP chemicals were purchased from Aldrich Inc. and Frontier Scientific Inc., respectively. The samples were thin (30-50 nm) polycrystalline NiPc and NiTBP films prepared by thermal evaporation *in situ* onto a clean Si(100) substrate covered with ultra-thin layer of natural oxide. The NEXAFS spectra of all the compounds were obtained in the total electron yield mode by detecting a sample current. The photon-energy resolution was set to 300 meV at the Ni 2p_{3/2} edge (~850 eV) and 80 meV at the N 1s edge (~400 eV). The photon energy was calibrated using the known energy position of the

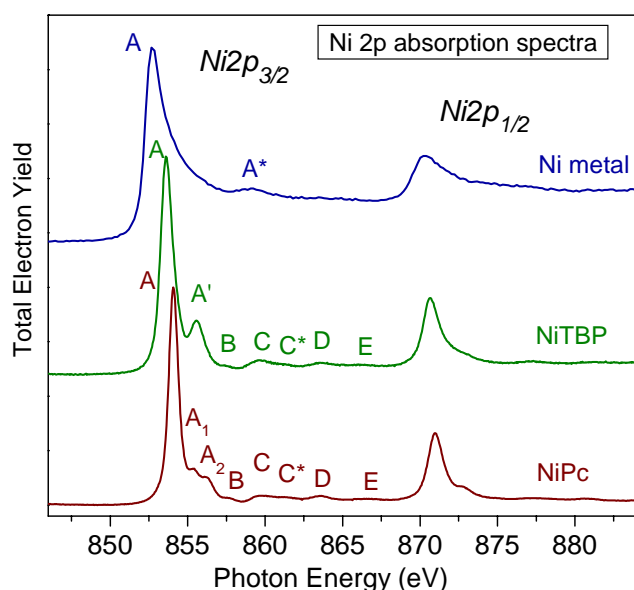


Fig. 1. Ni 2p absorption spectra of nickel complexes NiPc and NiTBP and metallic Ni.

the total electron yield from a clean gold crystal.

Figure 1 shows Ni 2p absorption spectra of NiPc, NiTBP and Ni metal measured at the incident angle of 45° to the sample surface. These Ni complexes are planar (D_{4h}) aromatic

first narrow peak in the Ne 1s absorption spectrum (Ne 1s \rightarrow 3p; 867.13 eV [5]) and in the Ti 2p_{3/2} absorption spectrum of solid K₂TiF₆ (Ti 2p_{3/2} \rightarrow t_{2g}; 459.0 eV [6]). Valence-band and core-level photoelectron spectra for NiPc were collected in the angle-integrated mode with a VG CLAM 4 electron analyzer. The total energy resolution was about 120 meV for the PE spectra at the photon energies of 50-200 eV using the 400 grs/mm diffraction grating and ~0.8 – 1.0 eV for the Res PE spectra at the Ni 2p_{1/2, 3/2} edges (h ν ~850-885 eV) with the 1200 grs/mm grating. The absorption and photoemission spectra were normalized to the incident photon flux, which was monitored by detecting

systems (macrocycles), in which the central nickel atom is surrounded by four isoindole units (compositions of the pyrrole and benzene molecules) that are linked by four aza (bridge) nitrogen or carbon atoms in NiPc and NiTBP, respectively. Thus, in both structures, each Ni

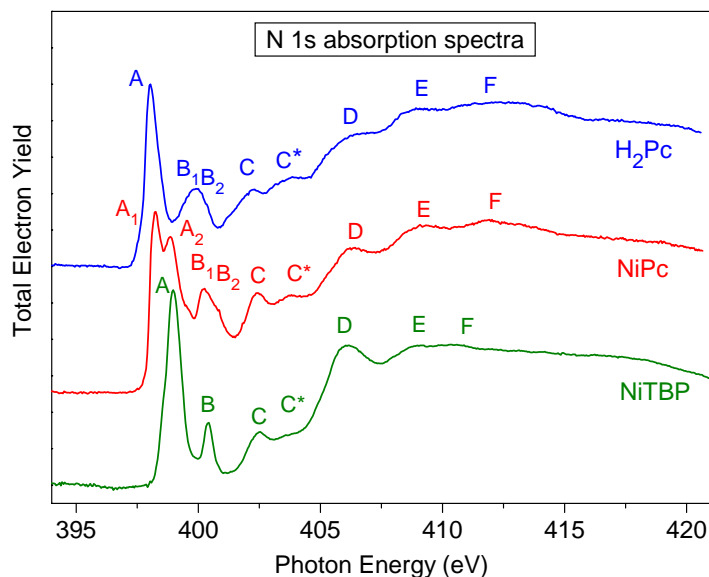


Fig. 2. *N 1s* absorption spectra of metal-free phthalocyanine H_2Pc and nickel complexes $NiPc$ and $NiTBP$.

atom is coordinated to four nitrogen atoms and structural differences between these complexes are available only in the third coordination shell (different bridge atoms of nitrogen or carbon). As a result the most interesting Ni $2p_{3/2}$ spectra of these complexes are alike each other in overall spectral profile: they are characterized by an intense low-energy absorption band A attributed to the intra-atomic Ni $2p_{3/2} \rightarrow 3d_{x^2-y^2}$ electron transition and by several high-energy structures A' (A_1 , A_2) - E that are associated

with the Ni $2p_{3/2}$ electron transitions to unoccupied Ni $3d - N2p$ hybridized electron states (unfilled antibonding MO's of π and σ type) of the complex [4]. At the same time, important changes are observed in the Ni $2p_{3/2}$ absorption spectra in going from NiTBP to NiPc: the main band A undergoes a ~ 0.5 -eV high-energy shift as well as the band A' is split into two structures A_1 and A_2 separated in energy by 0.8 eV. These findings reflect changes in an energy distribution of the Ni $3d$ electron states over the unfilled MO's and thus the ones in the electronic structure for NiTBP and NiPc as well as in the chemical bonding between the Ni and neighboring N atoms in these complexes. As a result the chemical state of the Ni atom in NiPc and NiTBP is

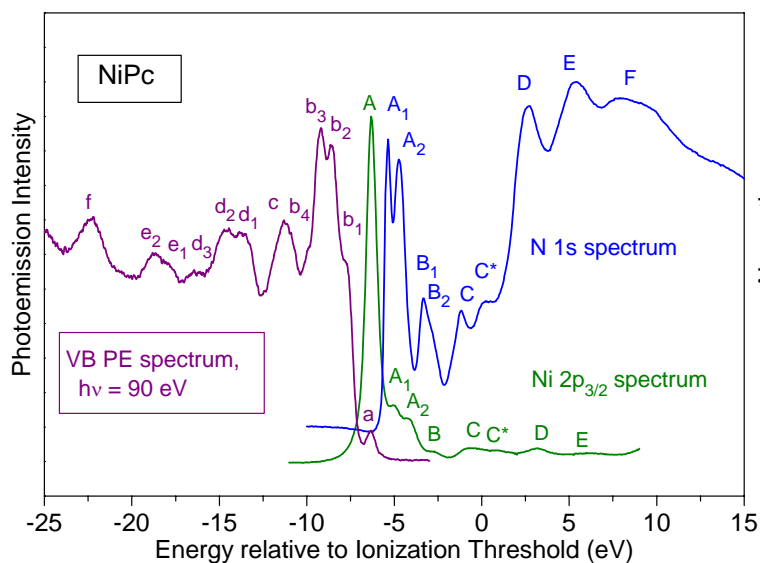


Fig. 3. Valence-band PE spectrum, $Ni 2p_{3/2}$ and $N 1s$ absorption spectra for $NiPc$ aligned in energy at the energy positions of the IP's.

different despite the fact that the metal atom has the same valence of two and its ground-state electron configuration is expected to be formally the one of the Ni^{2+} ion, namely, $[Ar]3d^8$. In this case the high-energy shift of the intra-atomic transition A observed in going from NiTBP to NiPc can be considered as an evidence for an additional transfer of the $3d$ electron density from the Ni atom to the ligands and a strengthening of chemical bonding between the Ni atom and the macrocycle in NiPc in comparison to NiTBP. This result is reasonable in light of the smaller Ni-N bond length in NiPc (1.966 Å in NiTBP vs. 1.887 Å in NiPc [7]). Finally it should be also noted that the energy of the intra-atomic transition A for complexes NiTBP

(853.6 eV) and NiPc (854.1eV) is considerably more than that for metallic Ni (852.7 eV). This is in good agreement with the known fact that the ground-state electron configuration of the nickel atom in the metal is $[Ar]3d^94s$ [8], that is, it contains larger $3d$ electron number in comparison to complexes.

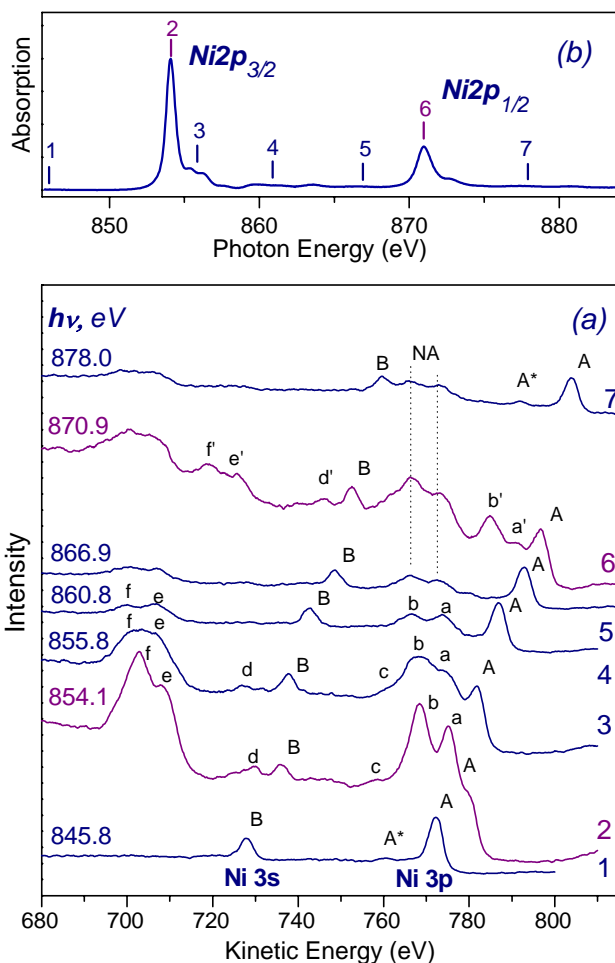


Fig.4. Non-resonant and resonant Ni 3p and 3s PE spectra (a) at various photon energies at the Ni2p absorption edge (b) of NiPc.

German Laboratory at BESSY II". We thank Dr.Yu. Dedkov and Dr. D. Vyalikh for valuable technical assistance D.A. Zverev acknowledges the financial support by the Freie Universität Berlin within the Leonhard-Euler fellowship program.

References

1. C.C. Leznoff, A.B.P. Lever, *Phthalocyanines, Properties and Applications*. Vol. 3, VCH Publishers, Inc., NY, 1993.
2. K.M. Kadish, K.M. Smith, R. Guilard, Eds, *The Porphyrin Handbook*, Vol. 1, Acad. Press, San Diego, 2000.
3. G. Dufour, C. Poncey, F. Rochet, et al., *J. Electron Spectrosc. Rel. Phenom.* **76**, 219 (1995); H. Yoshida, K. Tsutsumi, N. Sato, *ibidem* **121**, 83 (2001); T. Okajima, Y. Yamamoto, Y. Ouchi, K. Seki, *ibidem* **114-116**, 849 (2001); G. Polzonetti, V. Carravetta, G. Iucci, et al., *Chem. Phys.* **296**, 87 (2004); M.P. de Jong, R. Friedlein, S.L. Sorensen, et al., *Phys. Rev. B* **72**, 035448 (2005).
4. A.S. Vinogradov, A.B. Preobrajenski, D.A. Zverev, et al., *BESSY Annual Report 2004*, p.201.
5. R.N.S. Sodhi, C.E. Brion, *J. Electron Spectrosc. Relat. Phenom.* **34**, 363-372 (1984).
6. A.S. Vinogradov, A.Yu. Dukhnyakov, V.M. Ipatov, et al., *Sov. Phys. Solid State* **24**, 803-806 (1982)
7. C.J. Schramm, R.P. Scaringe, D.R. Stojakovic, et al., *J. Amer. Chem. Soc.* **102**, 6702 (1980).
8. M. Weinelt, A. Nillson, M. Magnusson, et al., *Phys. Rev. Lett.* **78**, 967 (1997).

Similar conclusions concerning the chemical bonding and electronic structure features in NiTBP and NiPc result from a consideration of N 1s absorption spectra of NiTBP, NiPc and H₂Pc (Fig. 2) as well as from a comparative study of Ni 2p_{3/2} and N1s absorption spectra of NiPc aligned in energy using measured energy separation (456.8 eV) between the Ni and N core levels (Fig. 3).

Figure 4a shows resonant photoelectron spectra for NiPc in the Ni 3s and Ni 3p ionization region for several resonant excitations (2-7) as marked in the Ni 2p absorption spectrum (Fig. 2b) together with an off-resonant photoelectron spectrum (1). The Ni 3p and 3s core-ionized states are dominant in the non-resonant spectrum and are not enhanced at all by the resonant excitation. On the other hand, series of satellites bands, a-f, in the Ni 3p and 3s ionization region are enhanced by resonant excitation.

Acknowledgements

This work was supported by RFBR (Project Nos. 04-02-17646, 06-02-16998) and the bilateral program "Russian-

Modulated X-ray photoconductivity and origin of deep electronic states in ternary copper chalcogenide semiconductors

I. Konovalov, L. Makhova

Wilhelm Ostwald Institute for Physical and Theoretical Chemistry, Universität Leipzig, Linnéstr. 2, D-04103 Leipzig, Germany

It is important to know and to control recombination through deep electronic states in the band gap of semiconductors. A particularly large variety of different defect states is predicted in ternary and multinary semiconductors. Defect spectroscopy methods allow direct measurements of only the electrical parameters of the defect states, namely their energy and capture cross sections. The control over the defect states requires an additional knowledge of the defect structure, not only the electrical properties. We succeeded in measuring the localization and the symmetry of several defect states in a transparent in visible p-type semiconductor CuAlO_2 (potential use in blue light emission devices and as a transparent conductive coating) and in CuInSe_2 (material for solar cells). Until very recently, there was no possibility of a direct experimental observation of the localization and of the symmetry of defect electronic states. Our approach is to utilize the effect of trap-related modulated x-ray photoconductivity (MPC), which we discovered recently [1], for determination of the localization and of the symmetry of the defect states in these materials. The idea is that if the defect states become populated (directly or via the partial band states) from the core levels through excitation by synchrotron radiation, the symmetry and the local selection rules are applicable.

Figure 1 demonstrates one of our measurements on CuAlO_2 samples. We measured the amplitude of the alternating component of the voltage across the sample under current flow and under the influence of a periodic synchrotron radiation (single bunch mode). The amplitude of the photoconductivity modulation in CuAlO_2 is presented vs. temperature with synchrotron excitation in the energy region of Cu2p, Cu2s and O1s core levels. Only in the case of Cu2p excitation, we detect signals which are both energy and temperature dependent, which is typical for processes of electron re-emission from the defect states. Three observed defect states show the characteristic temperatures of 130 K, 200 K and 300 K. All the three states can be excited effectively using a narrow spectrum around 936 eV close to Cu2p absorption edge (excitation bandwidth is about 2 eV). Assuming a direct filling mechanism of the defect states, its symmetry should be s- or d-like and the localization includes the vicinity of the copper atoms at the defect. Additionally, mostly in the case of the defect at 200 K, the amplitude signal is also sensitive to the energy variation in the vicinity of O1s edge, which can be tentatively interpreted as a defect in the interstitial position between Cu and O sites. In the case of oxygen we see an edge-like energy dependence, suggesting an indirect excitation mechanism. If we assume excitation of donors through the partial density of oxygen states in the conduction band (see [1] for details), the localization of the 200 K defect states includes the oxygen lattice sites. In this case they have s-like symmetry. An alternative interpretation is possible here assuming filling of the core hole by electrons from oxygen as acceptor having p-like symmetry.

Figure 2 demonstrates one of our results on thin single crystalline CuInSe_2 film on GaAs substrate. Again, the amplitude of the photoconductivity modulation is shown vs. the temperature. In this material we observe several gap states sensitive to the excitation at the Cu2p absorption edge. They were detected below 80K, at around 200K and above 330K. The energy dependence is always of the edge type, suggesting the indirect (through the conduction band or filling of the core hole from an acceptor) excitation mechanism. The nature of possible electron defect states was studied theoretically for a CuInSe_2 crystal before [2]. For a

convincing comparison of our measurements results with this calculation, we need to study CuInSe_2 additionally, with small deliberate deviations from the stoichiometry in this material.

We have tentatively identified the nature of the increase of the background typical for temperatures above 300K, as seen for example in all graphs of fig. 2. Figure 3 shows the same measurement on another CuAlO_2 sample, repeated twice – from cold to hot (left) and from hot to cold (right) temperatures. The difference at temperatures above 250K is clearly visible and it is obviously related to “glow” effects: when the sample is in its cold state, the excitation fills the trap states, but the temperature is still too low in order for carriers to escape from them. When the sample is heated to the room temperature, the trapped carriers are emitted into the band and they increase the background conductivity in the band, independently of the excitation in the hot state. This “tail” is absent, if measured hot-to-cold. During the next beamtime we plan to study the magnitude of the glow effect with respect to the excitation energy in the cold state, in more detail.

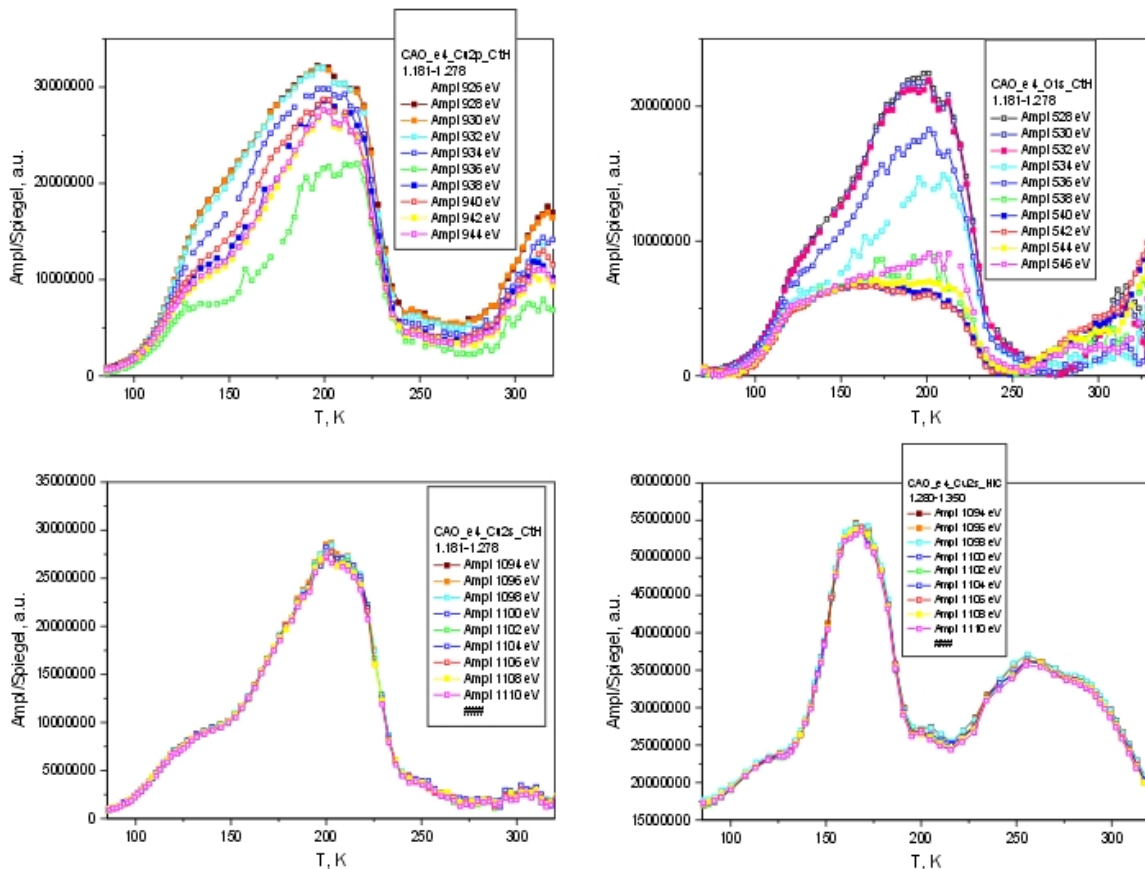


Figure 1. MPC spectra of CuAlO_2 . Three defect states in CuAlO_2 with characteristic temperatures of 130 K, 200 K and 300 K are both energy and temperature sensitive in the $\text{Cu}2p$ energy region.

In conclusion, for the first time we observed the trap-related effects of the synchrotron radiation on the modulated photoconductivity in two ternary copper chalcogenides CuAlO_2 and CuInSe_2 . The background signal in this measurements is tentatively related to the glow effect, which should be studied in more detail.

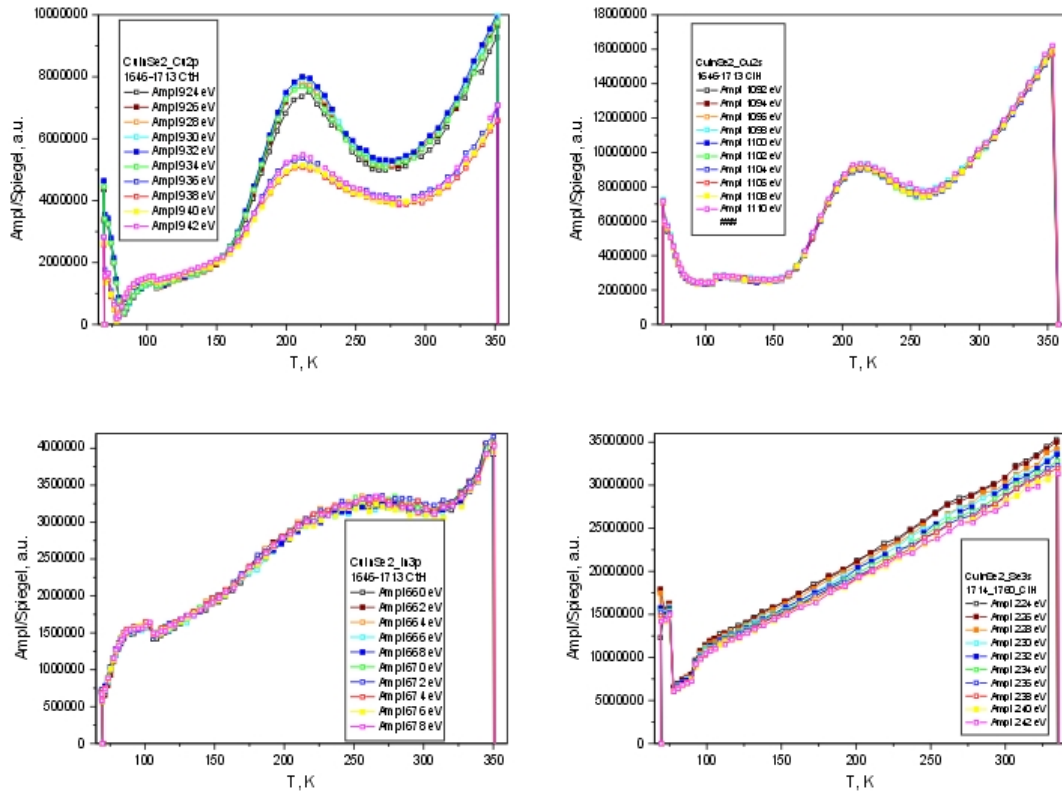


Figure 2. MPC spectra of CuInSe_2 . The amplitude of the conductivity signal in CuInSe_2 is both energy and temperature sensitive in the $\text{Cu}2p$ energy region of the excitation.

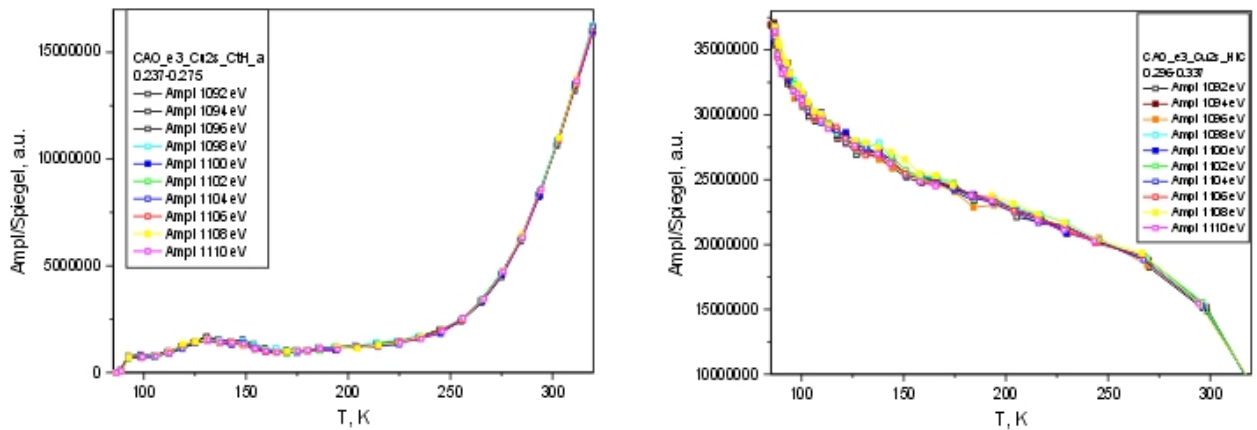


Figure 3. Glow effects on the background signal in the modulated photoconductivity effect: measurement cold-to-hot (left) and hot-to-cold (right) of the same CuAlO_2 sample.

- [1] I. Konovalov, L. Makhova, D. Wett, K.-H. Hallmeier, R. Szargan, R. Mitdank
X-ray photoconductivity due to trap-sensitive relaxation of hot carriers,
Appl. Phys. Lett. 88 (2006) 222106
- [2] S. B. Zhang, Su-Huai Wei, Alex Zunger, H. Katayama-Yoshida,
Defect physics of the CuInSe_2 chalcopyrite semiconductor,
Phys. Rev. B 57 (1998) 9642

Bulk sensitive photo emission spectroscopy of $C1_b$ compounds.

Benjamin Balke, Andrei Gloskovskii, Joachim Barth,
Gerhard H. Fecher, and Claudia Felser

*Institut für Anorganische Chemie und Analytische Chemie,
Johannes Gutenberg - Universität, 55099 Mainz, Germany*

Abstract

This work reports about bulk-sensitive, high energy photoelectron spectroscopy from the valence band of CoTiSb excited by photons from 2.5 to 5 keV energy. The high energy photoelectron spectra were taken at the KMC-1 high energy beamline of BESSY II employing the recently developed PHOIBOS 225 HV analyser. It is shown that the high energy spectra reveal the bulk electronic structure better compared to low energy XPS spectra.

Photo emission spectroscopy is the method of choice to study the occupied electronic structure of materials. Low kinetic energies result in a low electron mean free path being only 5.3 Å at kinetic energies of 100 eV or 26 Å at 1.2 keV (all values calculated for CoTiSb using the Tamuna-Powel-Penn (TPP-2M) equations [1]). In the hard X-ray region of about 5 keV one will reach a high bulk sensitivity with an escape depth being larger than 84 Å (corresponding to 15 cubic cells). Lindau *et al* [2] demonstrated in 1974 the possibility of high energy photo emission with energies up to 8 keV, however, no further attention was devoted to such experiments for many years. High energy photo emission (at about 15 keV excitation energy) was also performed as early as 1989 [3] using a ^{57}Co Mößbauer γ -source for excitation, however, with very low resolution only. Nowadays, high energy excitation and analysis of the electrons become easily feasible due to the development of high intense sources (insertion devices at synchrotron facilities) and multi-channel electron detection. Thus, high energy X-ray photo emission spectroscopy (HXPS) was recently introduced by several groups around the world as a bulk sensitive probe of the electronic structure in complex materials. In the present work, excitation energies of $h\nu = 1.2 \dots 5$ keV were used to study the density of states of CoTiSb.

CoTiSb samples have been prepared by arc-melting of stoichiometric amounts of the constituents in an argon atmosphere at 10^{-4} mbar. Details and results of the structural and magnetic properties are reported elsewhere [4]. Details of the electronic structure have been explored experimentally by means of high energy X-ray photo emission spectroscopy. The measurements have been performed at the KMC-1 beamline of the storage

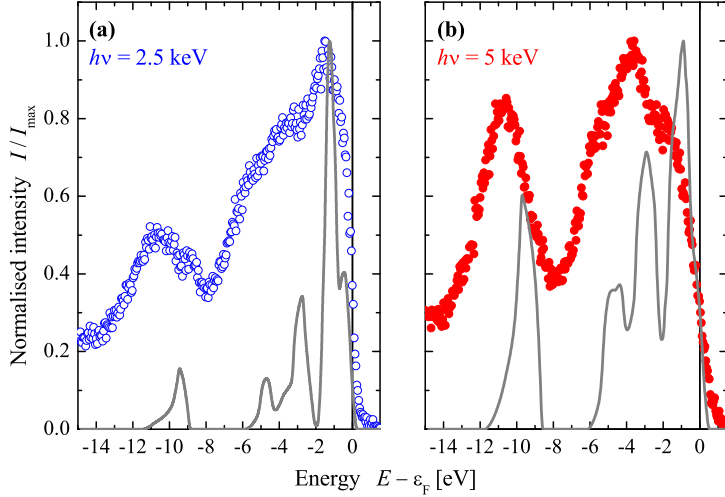


Fig. 1. High energy valence band spectra of CoTiSb. Shown are spectra taken at 2.5 keV (a) and 5 keV (b) excitation energy (symbols) and the DOS weighted by the photo emission cross section (lines).

ring BESSY II (Berlin, Germany). As electron analyser, a recently developed hemispherical spectrometer with 225 mm radius has been used (PHOIBOS 225 HV). The analyser is designed for high resolution spectroscopy at kinetic energies up to 15 keV. For the present study, a 2D-CCD detector has been employed for detection of the electrons. The analyser is prepared for parallel 2D (energy and angle) and simultaneous spin-detection using a combination of a 2D-delay-line detector with a low energy Mott-detector. Under the present experimental conditions an overall resolution of 240 meV at 2 keV photon energy has been reached (monochromator plus electron detector), as was determined from the Fermi edge of Au(100) [5]. Due to the low cross-section of the valence states from the investigated compounds, the spectra had to be taken with E_{pass} from 50 eV to 150 eV and a 1 mm entrance slit for a good signal to noise ratio. The polycrystalline CoTiSb samples have been cleaned in-situ by Ar⁺ ion bombardment before taking the spectra to remove the native oxide layer. Core-level spectra have been taken to check the cleanliness of the samples. No traces of impurities were found. All measurements have been taken at room temperature (≈ 300 K).

The results from high energy photo emission are displayed in Figure 1 and compared to the total density of states (DOS) weighted by the partial cross sections. For better comparison, the weighted DOS is additionally broadened by a Gaussian of 0.25 eV (0.5 eV) width to account roughly for the experimental resolution at 2.5 keV (5 keV) excitation energy. Both high energy spectra reveal clearly the low lying *s*-states at about -11 eV to -9 eV below the Fermi energy, in well agreement to the calculated DOS. These low lying bands are separated from the high lying *d*-states by the $C1_b$ -typical hybridisation gap being clearly resolved in the spectra as well as the calculated DOS. The size of this gap amounts typically to $\Delta E \approx 3 \dots 4$ eV in Sb containing compounds. Obviously, the emission from the low lying *s*-states is pronouncedly enhanced compared to the emission from the *d*-states. This can be explained by a different behaviour of the cross sections of the *s*, *p*, and

d states with increasing kinetic energy as was recently demonstrated by Panaccione *et al* [6]. In particular, the cross section for d -states decreases faster with increasing photon energy than the ones of the s or p -states. This behaviour influences also the onset of the d -bands at about -7 eV to -6 eV. Just at the bottom of those d -bands, they are hybridised with sp -like states, leading to a high intensity in this energy region. At $h\nu = 2.5$ keV, the structures of the weighted DOS have approximately the same heights, whereas the strong enhancement of the s states is clearly visible if comparing Fig. 1 (a) and (b). The structure of the high energy spectra in the range of the d states agrees roughly with the structures observed in the total DOS although the high density at -5 eV and -3 eV is not well resolved. Overall the emission from the d states covers a larger energy range compared to the calculated DOS, what gives indicates an underestimation of correlation effects in the local density approximation. However, one also has to account for lifetime broadening and the experimental resolution if comparing that energy range. At 2.5 keV excitation, the emission is still dominated by the high dense d -states at about -1.5 eV. Increasing the excitation energy to 5 keV has the result that the intensity in this energy range becomes considerably lower. At the same time, the emission from the bands at about -3 eV becomes strongly enhanced. As both structures in the DOS emerge, at least partially, from flat d -bands, the transfer of the intensity maximum might be not only explained by pure cross section effects.

Overall, the measured photoelectron spectra agree with the calculated density of states. Small shifts of the peaks in the measured spectra compared to the calculated DOS indicate an incomplete treatment of correlation effects in the local density approximation.

Acknowledgments:

Financial support by the Deutsche Forschungs Gemeinschaft (project TP 7 in research group FG 559) as well as by BESSY (BMBF 05 ES3XBA/5) is gratefully acknowledged.

References

- [1] S. Tanuma, C. J. Powell, and D. R. Penn. : *Surf. Interf. Anal.*, 21:165, 1993.
- [2] I. Lindau, P. Pianetta, S. Doniach, and W. E. Spicer. *Nature*, 250:214, 1974.
- [3] W. Meisel. *Hyperfine Interact.*, 45:73, 1989.
- [4] K. Kroth, B. Balke, G. H. Fecher, V. Ksenofontov, C. Felser, and H.-J. Lin. *Appl. Phys. Lett.*, 89:202509.
- [5] G. H. Fecher, A. Gloskovskii, K. Kroth, J. Barth, B. Balke, C. Felser, F. Schäfers, M. Mertin, W. Eberhardt, S. Mähl, and O. Schaff. *J. Electron Spectrosc. Related Phenom.*, page in print, 2007.
- [6] G. Panaccione, G. Cautero, M. Cautero, A. Fondacaro, M. Grioni, P. Lacovig, G. Monaco, F. Offi, G. Paolicelli, M. Sacchi, N. Stojic, G. Stefani, R. Tommasini, and P. Torelli. *J. Phys.: Condens. Matter*, 17:2671, 2005.

Broadband Multilayer Elements for EUV Polarization Analysis

A.G. Michette, A.K. Powell, S.J. Pfauntsch

King's College London, Department of Physics, Strand, London, WC2R 2LS, UK

Z. Wang, H. Wang, J. Zhu, F. Wang, Z. Gu, L. Chen

Institute of Precision Optical Engineering, Tongji University, Shanghai 200092, China

F. Schäfers, A. Gaupp

BESSY GmbH, Albert Einstein Straße 15, D-12489 Berlin, Germany

M. Macdonald

CCLRC Daresbury Laboratory, Warrington WA4 AD, UK

Studies of magnetic scattering and magneto-optics of synchrotron radiation require knowledge of the beam polarization, which is also necessary to characterize EUV optical elements at off-normal incidence angles. The ability to analyze the polarization state of the beam is of practical importance in evaluating the performances of insertion-device synchrotron sources. Experimental control and evaluation of a beam's polarization state can be obtained with optical devices such as phase retarders and linear analyzers. Periodic multilayers are commonly used to study the polarization state of EUV beams, but they must be changed or rotated to perform broadband polarization analyses because of their intrinsically narrow wavelength acceptances. This situation could be improved by utilizing aperiodic multilayer elements, which can greatly extend the bandwidth without the necessity of changing the incidence angle. The design of aperiodic polarizers, phase retarders and analyzers and their manufacture using a magnetron sputtering system have been described previously [1,2,3,4]. This report summarizes further characterization of these elements using the high-precision polarimeter at BESSY.

Several different aperiodic multilayers were designed, made and characterized for various wavelength ranges. The calculated and measured properties of Mo/Si broadband multilayer polarizers over the wavelength ranges of 13–19 nm, 14–18 nm and 15–17 nm, at grazing incidence angle of 50°, are shown in table 1. The degree of polarization, P , is defined in terms of the s- and p-reflectivities, R_s and R_p , by

$$P = \frac{R_s - R_p}{R_s + R_p}. \quad (1)$$

The errors in the means of R_s and R_p arise since the reflectivities vary with wavelength; an example is shown in Fig.1. The differences between the calculated and measured values are due to interlayer roughness and/or diffusion, with a length scale of ~ 1 nm.

Table 1. Design parameters and calculated and measured performances of Mo/Si multilayer polarizers for different spectral bandwidths.

λ [nm]	No. of bilayers	Mean R_s [%]		Mean R_p [%]		Mean P	
		Calc.	Meas.	Calc.	Meas.	Calc.	Meas.
13–19	30	30.4±1.2	18.2±3.6	0.24±0.16	0.20±0.16	0.985	0.980
14–18	31	35.0±0.1	21.1±2.5	0.18±0.14	0.16±0.16	0.990	0.986
15–17	32	50.0±0.2	36.6±0.7	0.17±0.07	0.24±0.08	0.993	0.987

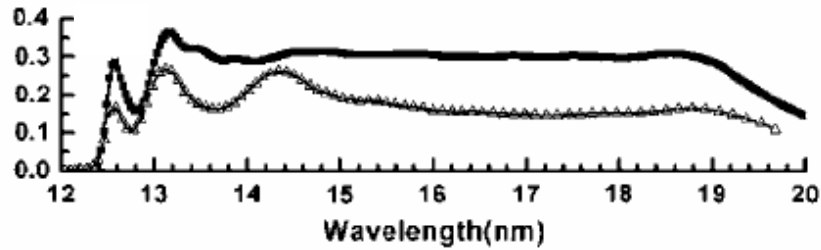


Figure 1. The variation of s-reflectivity with wavelength of the Mo/Si polarizer. The upper curve shows the calculated values and the lower the measured values.

Similar multilayers may be used as analyzers [2,3]; the performances of Mo/Si and Mo/Y mirrors are summarized in table 2. The Mo/Y mirrors for the ranges 8.5–10.1 nm (at 46° grazing angle) and 9.1–11.7 nm (at 45°) have mean design $R_s \sim 10\%$ [5]; this is $\sim 3\times$ less than the peak reflectivity of a periodic multilayer, but the bandpasses are $\sim 5\times$ larger. As these systems work at a fixed angle over a range of wavelengths, they must (according to the Bragg law) work at a fixed wavelength over a range of angles. Similar multilayers for 13 nm and 45–49° using Mo/Be have design $R_s \sim 45\%$ [2]. For shorter wavelengths (5.2 nm, 44–46°) Ni/C is a suitable combination, with design $R_s \sim 20\%$ [2].

Table 2. Calculated and measured performances of multilayer analyzers.

λ [nm]	Grazing angle [°]	Mean R_s [%]		Mean R_p [%]		Mean P	
		Calc.	Meas.	Calc.	Meas.	Calc.	Meas.
Mo/Si 13	45–49	64.99±0.18	50.7±2.3	0.29±0.23	0.0026±0.0011	0.991	1
Mo/Y 8.5–10	46	9.3±0.2	5.5±1.4			1	0.988±0.003
Mo/Y 9.3–11.7	45	9.9±0.3	6.1±0.7			0.99±0.02	0.965±0.007

Multilayers deposited on transmitting substrates may be used as phase retarders. An example of a Mo/Si phase retarder is shown in Fig. 2, where the measured phase shifts at grazing angles of 47° and 54° agree well with those calculated [6].

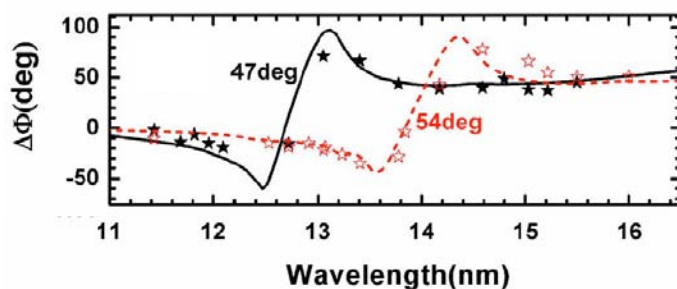


Figure 2. The variation of phase shift with wavelength of a Mo/Si phase retarder at two incidence angles.

In addition to measuring the properties of individual components a combination of a transmission multilayer phase retarder and a reflection analyzer has been used to analyse the polarisation state of the BESSY UE56/1-PGM beamline radiation in the wavelength range 12.7–15.5 nm [7]. Fig. 3 shows a typical angular distribution of the transmitted intensity as a function of the polarizer azimuthal angle α for four settings of the analyzer azimuthal angle β . The fitted Stokes-Poincaré parameters P_1 (one direction of linear

polarization), P_2 (orthogonal direction) and P_3 (circular polarization) are 0.001 ± 0.001 , -0.089 ± 0.002 and 0.999 ± 0.001 , respectively, with a phase shift of $\Delta\Phi = 38.4 \pm 0.2^\circ$, a ratio of transmission through the phase retarder $T_p/T_s = 0.910 \pm 0.001$, and for the analyzer $R_p/R_s = 0.019 \pm 0.003$. The variations of the Stokes-Poincaré parameters as functions of the undulator (i.e., polarization) settings are shown in Fig. 4; these are in good agreement with the expected variations from the known undulator parameters.

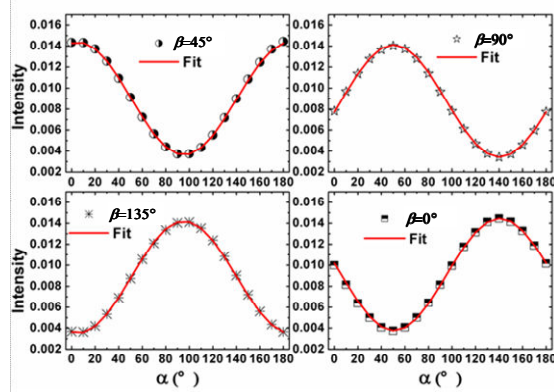


Figure 3. A typical angular distribution of the transmitted intensity as a function of the polarizer azimuthal angle α for four settings of the analyzer azimuthal angle β .

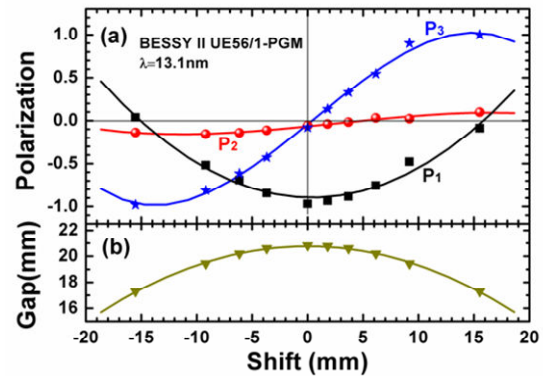


Figure 4. (a) Measurement of Stokes-Poincaré parameters of the radiation from the BESSY UE56/1-PGM beamline. (b) The gap values as functions of the undulator shift at $\lambda = 13.1$ nm.

In conclusion, it can be seen that the broadband polarizing elements work as predicted, so long as interlayer roughness / diffusions of ~ 1 nm is taken into account.

Acknowledgements: This work was supported by the National Natural Science Foundation of China (contract nos. 60378021 and 10435050), by the National 863-804 Sustentation Fund, by the Program for New Century Excellent Talents in University (NCET-04-037), by the Royal Society, London (NC/China/16660), Tongji University scientific fund, and by the European Union through the BESSY-EC-IA-SFS contract (BESSY-ID.05.2.165).

1. Z Wang, H Wang, J Zhu, F Wang, Z Gu, L Chen, AG Michette, AK Powell, SJ Pfauntsch, F Schäfers 2006 *J Appl. Phys.* **99** 056108-1
2. Z Wang, H Wang, J Zhu, F Wang, Z Gu, L Chen, AG Michette, AK Powell, SJ Pfauntsch, F Schäfers 2006 *Opt. Express* **14** 2533
3. H Wang, J Zhu, Z Wang, Z Zhang, S Zhang, W Wu, L Chen, AG Michette, AK Powell, SJ Pfauntsch, F. Schäfers, A. Gaupp 2006 *Thin Solid Films* **515** 2523
4. AG Michette, AK Powell, SJ Pfauntsch, Z Wang, H Wang, J Zhu, F Wang, Z Gu, L Chen. F. Schäfers 2005 *BESSY Annual Report*
5. Z Wang, H Wang, J Zhu, Y Xu, C Li, F Wang, Z Zhang, Y Wu, X Cheng, L Chen, AG Michette, SJ Pfauntsch, AK Powell, F Schäfers, A Gaupp, M MacDonald 2006 *App. Phys. Lett.* **89** 241120
6. Z Wang, H Wang, J Zhu, Z Zhang, S Zhang, Y Xu, S Zang, W Wu, F Wang, B Wang, L Chen, AG Michette, SJ Pfauntsch, AK Powell, F Schäfers, A Gaupp, M MacDonald 2007 *App. Phys. Lett.* **90** 031901
7. Z Wang, H Wang, J Zhu, Z Zhang, S Zhang, F Wang, W Wu, L Chen, AG Michette, SJ Pfauntsch, AK Powell, F Schäfers, A Gaupp, M Cui, L Sun, J Zhu, M MacDonald 2007 *App. Phys. Lett.* (in press)

The bonding configuration of Cyclopentene and 1,4-Cyclohexadiene on GaAs(001) surfaces

R. Paßmann^{1,2}, T. Bruhn², C. Friedrich², G. Gavrila³, D. R. T. Zahn³, W. Braun⁴,
W. Richter^{2,5}, N. Esser^{1,2}, P. Vogt²

¹ISAS – Institute for Analytical Sciences – Department Berlin, Albert-Einstein- Str. 9, 12489 Berlin, Germany

²Institute of Solide State Physics, TU Berlin, Hardenbergstr. 36, 10623 Berlin, Germany

³Institut für Physik, TU Chemnitz, 09107 Chemnitz, Germany

⁴BESSY GmbH, Albert-Einstein-Straße 15, 12489 Berlin, Germany

⁵Universita degli Studi Roma “Tor Vergata”, Via della Ricerca Scientifica 1, 00133 Roma, Italy

During the last year we investigated the adsorption and bonding configuration of Cyclopentene (C₅H₈) and 1,4-Cyclohexadiene (C₆H₈) on InP(001) and the c(4x4), (2x4) and (4x2) surface reconstructions of the GaAs(001) surface. Our aim was to obtain information which helps to elucidate the important role of the surface dimer configuration and the influence of the number of double bonds within organic hydrocarbon ring molecules on the interface formation. Yet, no comprehensive study of these parameters on the important organic/inorganic interfaces can be found in literature and most of the work available was obtained on Si(001)(2x1) surfaces. On the other hand III-V (001) semiconductor surfaces exhibit the potential of different surface stoichiometries with different atomic surface structure (i.e. dimer structure) and different electronic and optical properties. In this report we will focus on the results concerning GaAs(001). Here, we could demonstrate that the surface dimer structure indeed influences the bonding configuration of 1,4-cyclohexadiene and Cyclopentene on GaAs(001) significantly. These results are also important for an understanding of the interface formation between organic molecules and semiconductor surfaces in general. In order to clarify the chemical composition and surface bonding sites for the molecules on the different surfaces SXPS measurements were carried out at the PM-RD and PM3 beamlines at BESSY.

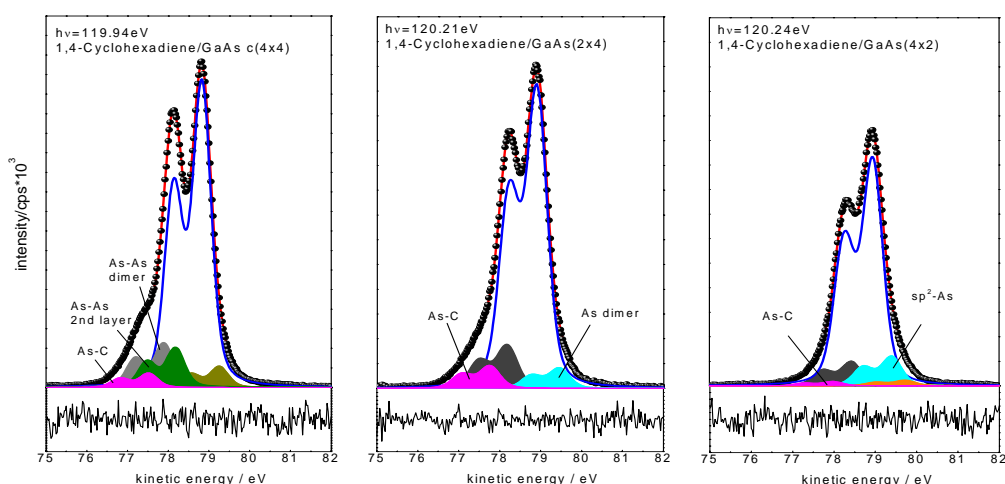


Fig.1:
Core-level of As3d for the with 1,4-Cyclohexadiene saturated GaAs(001)c(4x4) on the left, (2x4) middle and (4x2) on the right, respectively.

1,4-Cyclohexadiene adsorption on GaAs(001) surfaces

After the deposition of 1,4-Cyclohexadiene the saturated surface was characterized by SXPS. The line shape of the clean core level is comparable to previous work. The As3d core level are depicted in Fig 1. An additional component (As-C) was observed

for all three surfaces at the lower kinetic energy side with respect to the bulk component. It is reasonable to conclude that this component can be assigned to As-atoms which are bonded to C-atoms from the Cyclopentene molecules. Within the Ga3d core level emission line no additional components can be observed. The analysis of the C1s core levels for the three GaAs(001) surfaces saturated with 1,4-Cyclohexadiene is shown in Fig. 2.

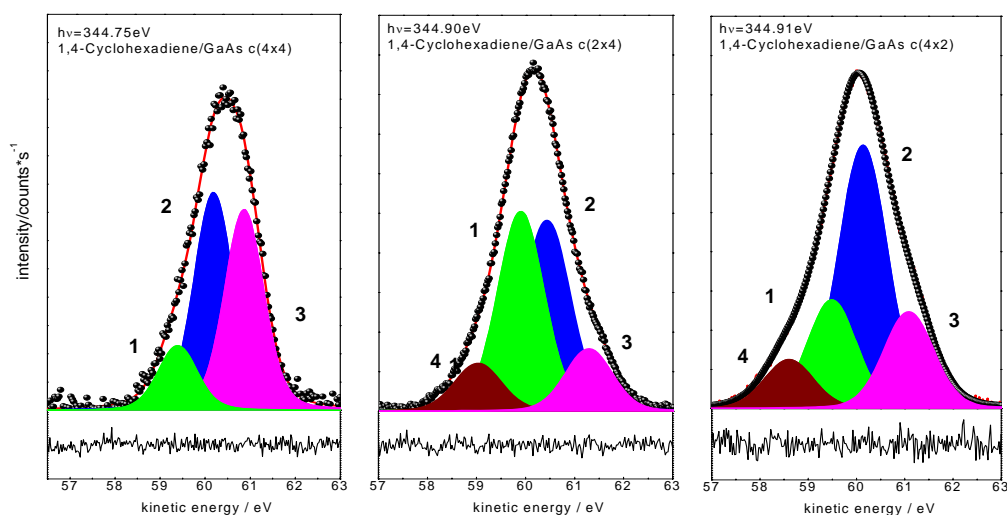


Fig.2: Core-level of C1s for the with 1,4-Cyclohexadiene saturated GaAs(001)c(4x4) on the left, (2x4) middle and (4x2) on the right, respectively.

In all three cases three main components within the C1s line shape are found by numerical analysis and a fourth one for the (2x4) and (4x2) reconstructed surfaces. The component 1 can be related to electrons which are included in the carbon-carbon double bond and the component 2 is related to the electrons of carbon atoms which are involved in the single carbon-carbon bond. The component labelled with 3 and 4 for the (2x4) and (4x2) reconstructed surfaces can be assigned to the electrons of the carbon atoms which are involved in the C-As bondings to the first and second layer As-atoms. Therefrom we can conclude that the 1,4-Cyclohexadiene molecules bonds to the topmost As-atoms of each surface reconstruction. In all three cases it is obvious that beside the chemisorption also physisorption is found indicated by component (1) which is related to electrons of the C=C double bond. This component is very pronounced for the (2x4) reconstructed surface indicating more carbon double bonds and thus more 1,4-Cyclohexadiene molecules which stay intact on this surface after deposition. This is a hint towards a physisorption on the (2x4). For the c(4x4) and (4x2) this component is not as pronounced as for the (2x4).

Cyclopentene adsorption on GaAs(001) surfaces

An additional component was also found in the core level line shape of the As3d emission. No additional component appeared in the numerical analysis for Ga3d. The C1s core level spectra of Cyclopentene adsorbed on the GaAs(001) surfaces are shown in Fig. 3. Also for each surface reconstruction the core levels were fitted with three components with numerical analysis similar as for the adsorption of 1,4-Cyclohexadiene while for the (4x2) four components were necessary. Again for each reconstruction the component 3 was observed which is related to the electrons in an As-C bond.

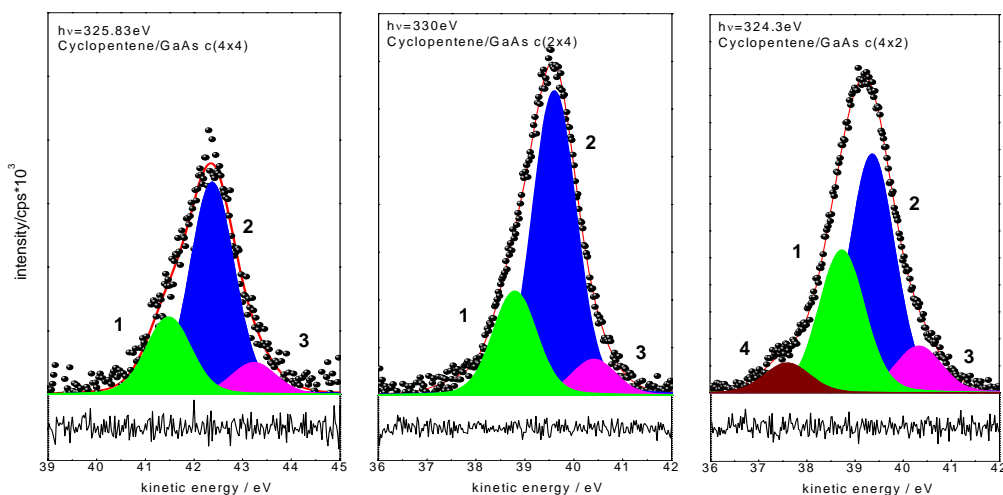


Fig.3: Core-level of C1s for the with Cyclopentene saturated GaAs(001)c(4x4) on the left, (2x4) middle and (4x2) on the right, respectively.

The additional component 4 for the (4x2) reconstructed surface indicates bonding not only to the topmost As atoms but also to the second layer As atoms as in the case of 1,4-Cyclohexadiene. Component 1 should not appear in case of Cyclopentene because if the molecule bonds covalently to the surface the double bond should be broken. Therefrom we can conclude that besides the chemisorption also a physisorption of the molecules takes place.

Summary and conclusion

For both molecules it can be concluded that the molecules chemisorb but also physisorb on the surfaces. In all cases a new component appears only in the As3d core level line shape and no additional component for the Ga3d core level was found. Therefrom we can conclude that it is much more attractive for the hydrocarbon ring molecules to form a bond to the filled dangling bonds of the topmost As-atoms than to the Ga-atoms. The amount of additionally physisorbed molecules is different for each surface reconstruction. In the case of 1,4-Cyclohexadiene it is also difficult to distinguish between chemisorption and the additional C=C bond within the organic molecule. It can be concluded that both molecules interact with their C=C double bond and the surface topmost As-atoms. This last finding is important since the gallium-atoms/dimers seem to play no role in the interface formation in these cases. Furthermore it should be pointed out that the organic hydrocarbon ring molecules used in this work do not destroy the surface reconstruction and form an atomically abrupt interface. The molecules can be thermally removed by annealing and a clean well reconstructed GaAs(001) surface is formed again as verified by SXPS and RAS. Our SXPS results are supported by RAS measurements [4] and STM results.

We would like to acknowledge financial support by the BMBF under grant number – MUSTANG BMBF 05 KS40C1/3.

References

- [1] W. G. Schmidt, F. Bechstedt, W. Lu, J. Bernholc, Phys. Rev. B 66, 085334 (2002), [2] W. G. Schmidt, F. Bechstedt, K. Fleischer, C. Cobet, N. Esser, W. Richter, J. Bernholc, G. Onida, Phy. Stat. Sol (a) 188, 1401 (2001), [3] W. G. Schmidt, N. Esser, A. M. Frisch, P. Vogt, J. Bernholc, F. Bechstedt, M. Zorn, T. Hannappel, S. Visbeck, F. Willig, W. Richter, Phys. Rev. B 61, R16335 (2000), [4] R. Passmann, M. Kropp, T. Bruhn, B.O. Fimland, F. L. Bloom, A. C. Gossard, W. Richter, N. Esser, P. Vogt, Applied Physics A, in print (2007).

Ion-Beam Induced Nano-Sized Ag-Metal Clusters in Glass

H.-E. Mahnke^{1,2*}, B. Schattat¹, P. Schubert-Bischoff¹, I. Zizak¹, N. Novakovic^{1,3}, V. Koteski^{1,3}

¹Hahn-Meitner-Institut Berlin GmbH, Bereich SF, Glienicker Str.100, D-14109 Berlin, Germany,

²FU Berlin, Fachbereich Physik, D-14195 Berlin, ³VINČA, POB 522, 11001 Belgrade, Serbia

Glasses containing metal clusters have attracted attention both in cluster research and in possible applications of such clusters for magnetic or optoelectronic purposes. Nanometer-sized clusters of noble metals in glasses exhibit strong absorption of visible light which, in addition, may be highly polarization dependant depending on size and shape with special alignment of the clusters [1, 2]. Various preparation methods are pursued to obtain control of the mechanisms to form such clusters. A promising approach is the irradiation of glasses containing the wanted metal as a metal oxide with heavy-ion beams at MeV/amu energies [3,4,5]. At such velocities the energy deposited along the ion path leads to track formation in the material. In the following, we show how synchrotron radiation techniques help to characterize ion-beam induced materials modifications.

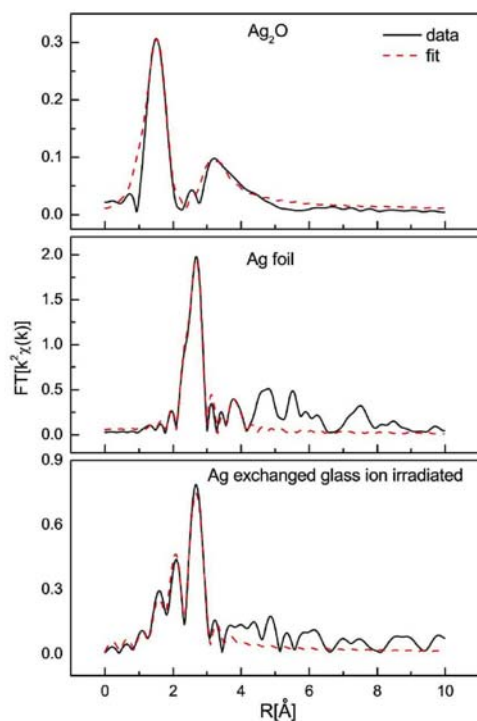


Figure 1: Fourier transformed EXAFS signal (k^2 -weighted): The irradiated glass sample (bottom) shows the ion beam induced formation of metallic Ag. The EXAFS signature for Ag metal (middle) and for Ag_2O (top) are given for comparison.

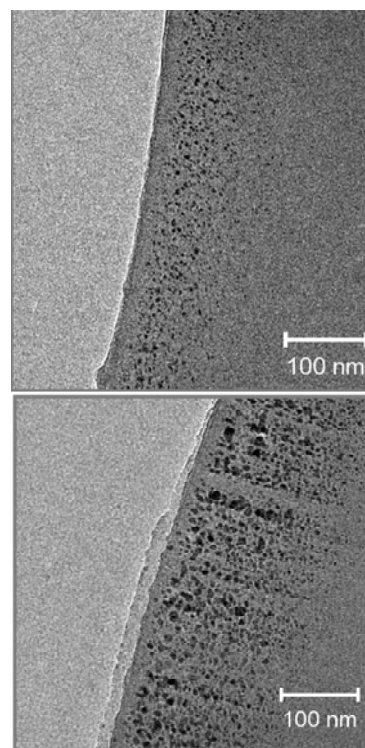


Figure 2: TEM picture of irradiated (bottom) and non-irradiated (top) glass samples: After irradiation with gold ions and subsequent annealing, clusters of metallic silver are visible arranged in chains along the direction of the ion beam. The TEM was operated at 120 kV.

We have studied the formation of Ag-metal clusters in soda lime glass induced by heavy ion irradiation with x-ray absorption spectroscopy (XAS), while the shape of the formed clusters were studied both with transmission electron microscopy (TEM) and with small angle x-ray scattering (SAXS). Silver was introduced by ion exchange into 0.1-mm thick glass platelets (see [4]). We have irradiated these Ag-containing glass platelets kept at LN₂ temperature with 600-MeV Au ions with fluences around 10¹² ions/cm² at the ion beam laboratory ISL. The ion flux was kept below 10¹⁰ ions/cm²s.

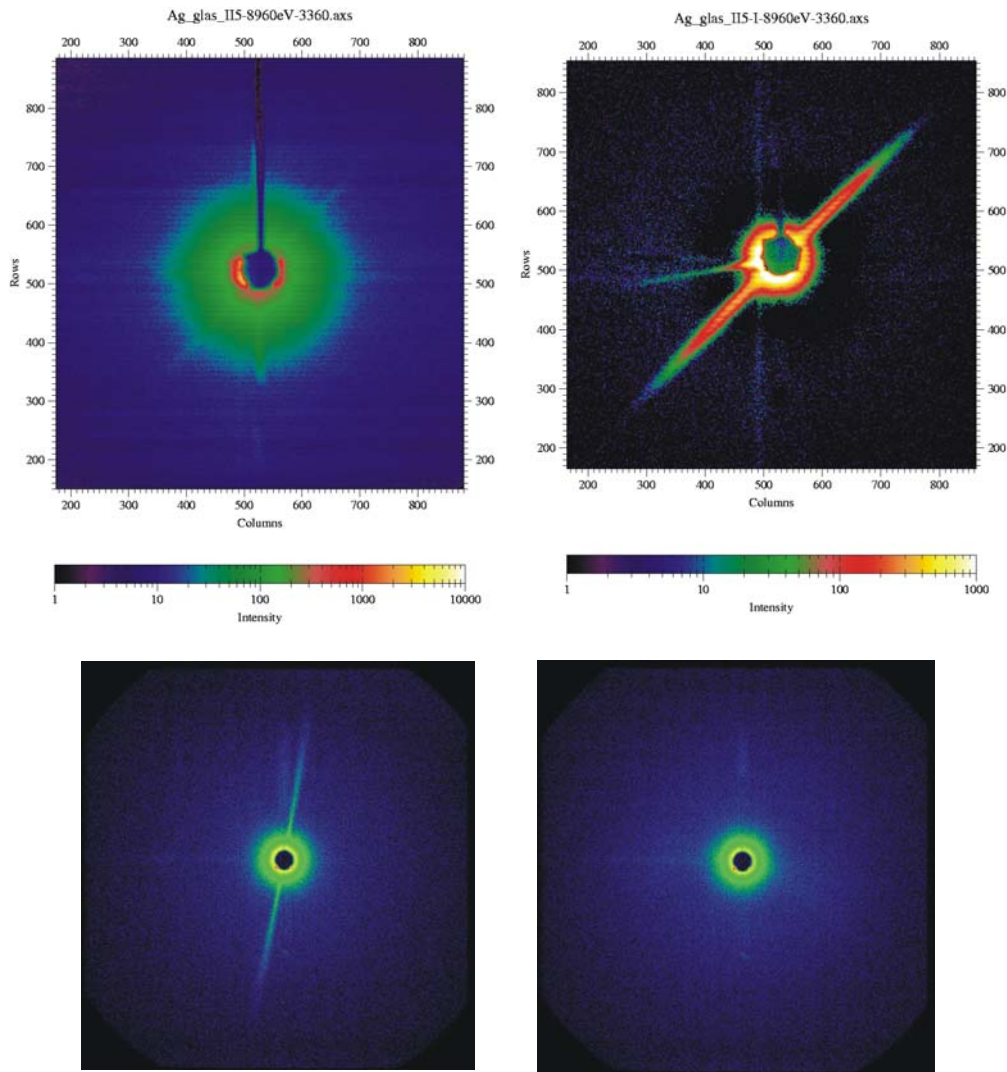


Figure 3: SAXS images of ion-irradiated (upper right) and non-irradiated (upper left) Ag containing glass samples revealing a column-like structure by the disc-like image. The dimensions in q space correspond to a diameter of the "columns", the arrangement of Ag droplets along chains in the ion direction, of around 7 nm. SAXS images on ion irradiated glass samples without Ag show ion tracks in glass (lower left) which disappear when annealed (lower right).

Following the ion irradiation, the samples were investigated with X-ray absorption spectroscopy at the Ag K-edge. The EXAFS experiment, performed at the X1 beamline of HASYLAB, revealed the transformation of Ag from the oxidic type local structure after the ion-exchange proc-

ess into the metallic form following the swift heavy ion irradiation and annealing (see Fig. 1, for details see ref. [6]).

First information on the shape of the formed clusters was obtained by transmission electron microscopy (TEM) on thin slices of some 10 nm cut out of the samples parallel to the ion impact and deposited onto a fine grid (see Fig. 2). For a more detailed study of the arrangement, the shape, and the formation process SAXS experiments including in-situ experiments at varying annealing temperatures are under way at the 7-T MPW beam line at BESSY.

While annealing under a reducing atmosphere of argon with a few % H₂ alone already leads to the formation of metal clusters (we annealed for 30 minutes at 340°C), such clusters are not very uniform in size and are randomly distributed over the Ag-containing glass volume. The comparison presented in Fig.2 illustrates the significant influence of the ion irradiation: (i) the metal clusters have grown and their size distribution has become more uniform, but the most remarkable feature is that (ii) the clusters are arranged in chains parallel to the direction of the ion beam.

A more quantitative description of the arrangement seen in the TEM images can be achieved by SAXS measurements performed at the newly commissioned 7-T MPW beam-line of the HMI at BESSY. An illustration of the first experiment is given in Fig.3. The ion fluence in this case was 10¹¹cm⁻², the sample was heat treated after the ion irradiation in the same way as the sample in Fig. 2. A glass platelet without Ag also shows ion tracks when ion irradiated at LN temperature. However, they disappear when the same annealing procedure is applied. Thus, the small angle scattering confirms the arrangement and shape of the Ag metal clusters as induced by the ion irradiation and proves to be a very valuable complementary way to study such ion induced structures.

Since some of the chains consist of clusters very similar in diameter and almost in contact, one is tempted to speculate that a totally columnar structure may be obtained by controlling the influencing parameters such as the ion fluence and the annealing parameters. First in-situ experiments to follow the subsequent annealing procedure are being analyzed.

The authors are grateful to the HASYLAB staff at DESY, in particular to J. Wienold and E. Welter. We very much appreciate P. Szimkowiak's help in sample preparation. Special thanks are expressed to the colleagues from the department SF3 of the HMI, A. Höll, S. Haas and D. Tachev, who helped as scientists at the HMI SAXS 7-T MPW beam line at BESSY.

References

- [1] K. L. Kelly et al. , J. Phys. Chem. **B 107** (2003) 668
- [2] A. Podlipensky et al., J. Phys. Chem. **B 108** (2004) 17699
- [3] E. Valentin et al., Phys. Rev. Lett. **86** (2001) 99
- [4] G. Bataglin et al., Nucl. Instr. and Meth. in Phys. Res. **B 200** (2003) 185
- [5] J.J. Penninkhof et al., Appl. Phys. Lett. 83 (2003) 4137
- [6] H.-E. Mahnke et al., Nucl. Instr. and Meth. in Phys. Res. **B 245** (2006) 222

Defect Induced Low Temperature Ferromagnetism in $\text{Zn}_{1-x}\text{Co}_x\text{O}$ Films

E. Biegger,¹ G. Mayer,¹ M. Fonin,¹ Yu. S. Dedkov,² and U. Rüdiger¹

¹ *Fachbereich Physik, Universität Konstanz, 78457 Konstanz, Germany*

² *Institut für Festkörperphysik, Technische Universität Dresden, 01062 Dresden, Germany*

Diluted magnetic semiconductors (DMSs) produced by the doping of transition metal ions into nonmagnetic semiconductors have become recently the subject of an intensive research due to the possibility to utilize both charge and spin degrees of freedom in the same material making DMS promising candidates for the next generation spintronic devices [1]. The prediction of the Curie temperature (T_C) of Mn-doped ZnO exceeding room temperature (RT) [2], stimulated numerous experimental works on the preparation of RT ferromagnetic transition-metal-doped ZnO [3]. However, the recent reports on the nature of magnetism in Co/ZnO and Mn/ZnO have been quite contradictory. For nominally identical systems reports of high T_C coexist with those excluding intrinsic ferromagnetism [3]. Moreover, the origin of the ferromagnetism in doped magnetic ZnO and related DMS materials is still under strong debate. Recently, the formation of a shallow spin-split impurity band upon coalescence of bound magnetic polarons (BMPs) constituted by donor defects has been proposed to explain the origin of RT ferromagnetism for oxide DMSs [3]. A number of experiments showed the correlation between the ferromagnetic behavior and the concentration of structural defects, either Zn-interstitials [4] or oxygen vacancies [5], incorporated into the ZnO host lattice giving an evidence that ferromagnetism in $\text{Zn}_{1-x}\text{Co}_x\text{O}$ is mediated by donor-bound carriers.

In this work, we performed a combined near edge x-ray absorption fine structure spectroscopy (NEXAFS) and photoemission spectroscopy (PES) study on ferromagnetic as well as paramagnetic epitaxial $\text{Zn}_{1-x}\text{Co}_x\text{O}$ films. All NEXAFS and PES experiments were carried out at RT at the RGLB-PGM beamline (BESSY). The UHV system with the base pressure of 1×10^{-10} mbar was equipped with a 127° CLAM4 analyzer. The total energy resolution in the XPS measurements was set to 150 meV. The position of the Fermi energy (E_F) was determined from the valence-band spectrum of a polycrystalline Au foil in electrical contact with the sample. All spectra were normalized to the incident photon flux. NEXAFS spectra were collected in the total electron yield mode and normalized to the maximum intensity. The energy resolution in the NEXAFS experiments was set to 100 meV.

High quality 100-200 nm thick epitaxial $\text{Zn}_{0.9}\text{Co}_{0.1}\text{O}$ films were prepared by magnetron sputtering on $\text{Al}_2\text{O}_3(0001)$ substrates. Two different preparation routes, i.e. sputtering in Ar-atmosphere (samples referred to as *S1*) and sputtering in Ar/O₂ atmosphere in conjunction with a postannealing step (samples referred to as *S2*) were used in order to control the concentration of oxygen vacancies in the ZnO host lattice. Magnetization measurements indicated ferromagnetic behavior at low temperatures for the samples prepared in oxygen-poor conditions (*S1*) whereas the samples prepared in oxygen-rich conditions (*S2*) did not show ferromagnetic behavior. After introducing the samples into the UHV chamber at BESSY their surface was cleaned by Ar⁺ sputtering.

Fig. 1 (a) shows NEXAFS spectra of the Co-doped ZnO samples *S1* and *S2* measured at Co $L_{2,3}$ absorption edge. The Co $2p_{3/2}$ peak at 778 eV and the Co $2p_{1/2}$ peak at 793 eV are clearly separated by the large $2p$ core-hole spin-orbit interaction. The line shape of NEXAFS spectra from samples *S1* and *S2* are clearly different from that of the Co metal showing the absence of any Co clustering. Thus these data rule out phase segregation as the source of ferromagnetism in Co-doped ZnO and point to an intrinsic origin. The observed NEXAFS line shape is similar to that of the previously reported spectra from both ferromagnetic [6] and nonmagnetic [7] Co-doped ZnO as well as to several atomic multiplet configuration interaction calculations confirming that Co ions are present in the high-spin Co^{2+} state under

tetrahedral coordination, indicating a proper incorporation into the ZnO host lattice. Although the samples *S1* and *S2* should differ in the oxygen content only a very small difference in the spectral line shape is visible. The inset of Fig. 1 (a) shows Co 2*p* core level PES spectra of both *S1* and *S2* Zn_{0.95}Co_{0.05}O samples taken at $h\nu=1000$ eV. The Co 2*p* spectra of both samples are similar to that of CoO supporting the presence of Co²⁺ ions in the samples. Fig. 1 (b) shows valence band PES spectra of the *S1* Zn_{0.95}Co_{0.05}O obtained at 774 eV (off-resonance) and 777 eV (on-resonance) which are similar to that of ZnO showing a broad feature between 3 and 8 eV of binding energy (BE) corresponding to O 2*p* band. No PES intensity was observed in the E_F region confirming the insulating nature of the sample. Similar spectra were obtained for the *S2* samples. Thus the charge carrier mediated ferromagnetism based on the Ruderman-Kittel-Kasuya-Yosida (RKKY) mechanism or related Zener mechanism, in which itinerant free carriers interact with localized *d* electrons on isolated dopant ions can be ruled out. By subtracting the off-resonance spectrum from the on-resonance one, the Co 3*d* partial density of states (PDOS) can be obtained. The difference curve presented in Fig. 1 (c) shows a peak at about 3.5 eV of BE which is in good agreement with previous studies [6,7]. These results show that in ferromagnetic (*S1*) as well as in paramagnetic (*S2*) Co-doped ZnO samples (not shown) the Co 3*d* states are located near the top of the valence band at about 3.5 eV of BE.

In order to provide the evidence that ferromagnetic behavior in Co-doped ZnO is donor carrier mediated and thus can be explained in the frame of the BMPs model a direct relationship between the ferromagnetic behavior and the oxygen vacancies concentration of different samples should be established. Here we used O *K* edge NEXAFS measurements on both sets of samples (*S1* and *S2*) to probe the local structure of Co-doped ZnO and especially the oxygen-related defects in the ZnO host lattice. Figure 2 shows the comparison of O *K* edge NEXAFS spectra from the undoped reference ZnO sample, the Zn_{0.9}Co_{0.1}O sample *S1*, and the Zn_{0.9}Co_{0.1}O sample *S2*. Good agreement exists between the present NEXAFS spectra and those from ZnO powder [8] or PLD grown Co-doped ZnO [9]. The region between 530 and 538 eV can be attributed to the hybridization between O 2*p* and Zn 4*s* states followed by the region between 539 and 550 eV which is due to the hybridization between O 2*p* and Zn 4*p* states. Above 550 eV the spectrum can be assigned to the hybridization between O 2*p* and Zn 4*d* states. Krishnamurthy *et al.* [9] recently showed that broadening of the spectral features at 537, 540 and 543 eV can be assigned to the presence of oxygen vacancies, which means that the sample *S1*, prepared in oxygen poor conditions, indeed contains more oxygen-related

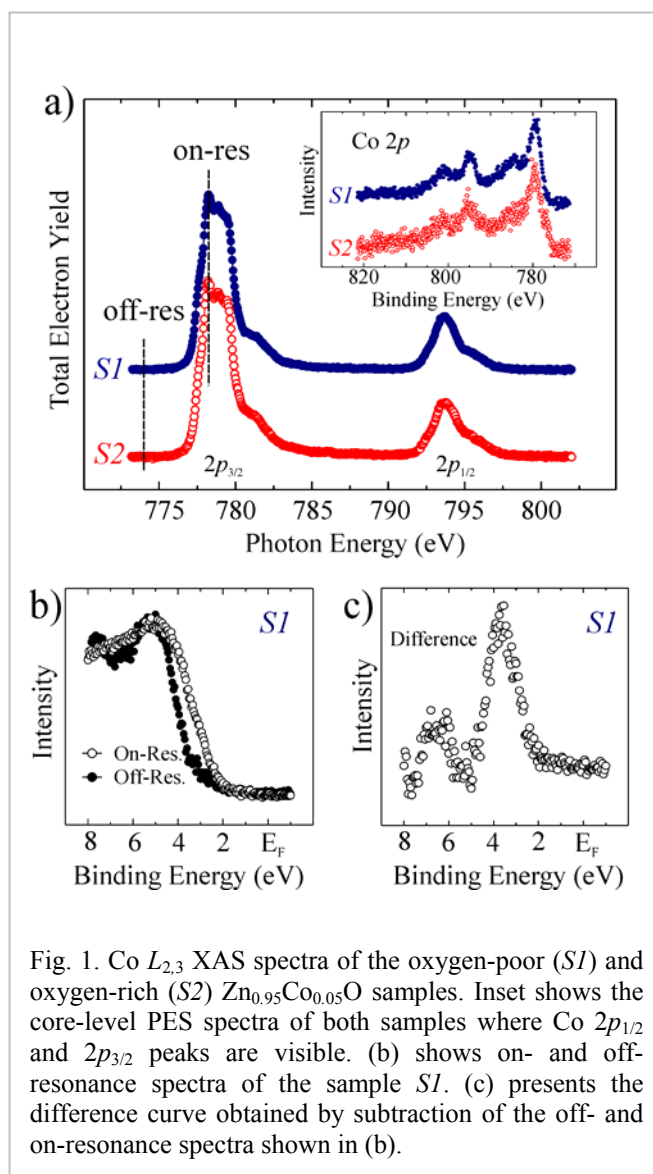


Fig. 1. Co *L*_{2,3} XAS spectra of the oxygen-poor (*S1*) and oxygen-rich (*S2*) Zn_{0.95}Co_{0.05}O samples. Inset shows the core-level PES spectra of both samples where Co 2*p*_{1/2} and 2*p*_{3/2} peaks are visible. (b) shows on- and off-resonance spectra of the sample *S1*. (c) presents the difference curve obtained by subtraction of the off- and on-resonance spectra shown in (b).

defects compared to the sample *S2*, prepared in oxygen rich conditions as well as to the undoped reference sample. The inset of Fig. 2 shows the Zn $L_{2,3}$ NEXAFS spectra which agree well with those of ZnO nanorods [10] and crystalline ZnO [11] ruling out significant ZnO defect related features in the sample like Zn interstitials. Thus defects due to oxygen are predominant. Comparing the NEXAFS results with those from magnetization measurements it can be concluded that ferromagnetism is strongly correlated with the oxygen vacancies concentration, supporting the BMP model, because a higher density of oxygen vacancies leads to a larger volume occupied by BMPs. Thus the probability of overlapping of the BMPs is increased and more Co ions are present in ferromagnetic areas, contributing to ferromagnetism.

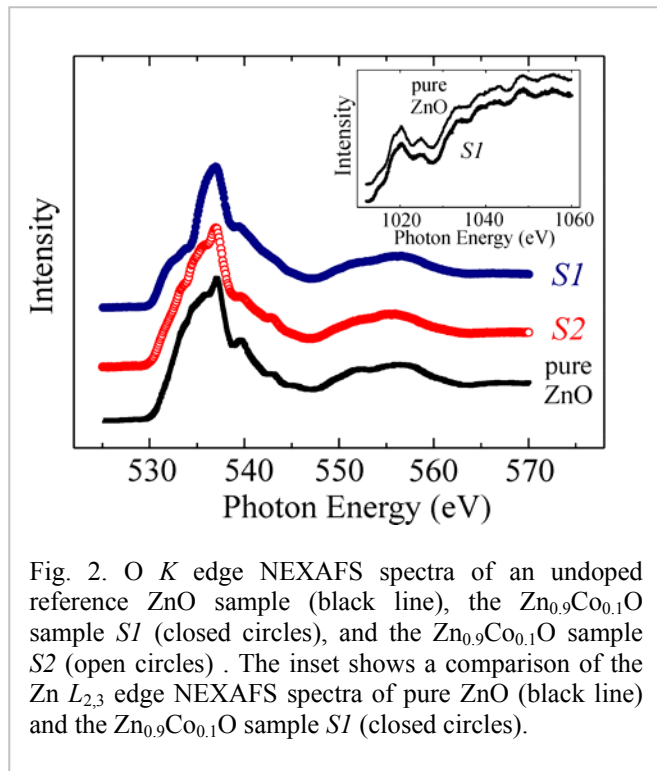


Fig. 2. O K edge NEXAFS spectra of an undoped reference ZnO sample (black line), the $Zn_{0.9}Co_{0.1}O$ sample *S1* (closed circles), and the $Zn_{0.9}Co_{0.1}O$ sample *S2* (open circles). The inset shows a comparison of the Zn $L_{2,3}$ edge NEXAFS spectra of pure ZnO (black line) and the $Zn_{0.9}Co_{0.1}O$ sample *S1* (closed circles).

This work was supported by the Deutsche Forschungsgemeinschaft (DFG) through Sonderforschungsbereich (SFB) 513 and Kompetenznetz „Funktionelle Nanostrukturen“ des Landes Baden-Württemberg. E. B. and M. F. would like to thank BESSY for financial support.

1. H. Ohno, *Science* **281**, 951 (1998).
2. T. Dietl, H. Ohno, F. Matsukura, J. Cibert, and D. Ferrand, *Science* **287**, 1019 (2000).
3. J. M. D. Coey, M. Venkatesan, and C. B. Fitzgerald, *Nature Mater.* **4**, 173 (2005).
4. K. R. Kittilstved, W. K. Liu, and D. R. Gamelin, *Nature Mater.* **5**, 291 (2006).
5. H. S. Hsu *et al.*, *Appl. Phys. Lett.* **88**, 242507 (2006).
6. M. Kobayashi *et al.*, *Phys. Rev. B* **72**, 201201(R) (2005).
7. S. C. Wi *et al.*, *Appl. Phys. Lett.* **84**, 4233 (2004).
8. C. McGuinness *et al.*, *Phys. Rev. B* **68**, 165104 (2003).
9. S. Krishnamurthy *et al.*, *J. Appl. Phys.* **99**, 08M111 (2006).
10. J. W. Chiou *et al.*, *Appl. Phys. Lett.* **85**, 3220 (2004).
11. J.-H. Guo *et al.*, *J. Phys. : Condens. Matter* **14**, 6969 (2002).

Rotational Structure of Nitrogen Ions after Resonant $1s\text{-}\pi^*$ Photoexcitation

M. Meyer¹, J. Plenge², A. Wirsing², R. Flesch², and E. Rühl²

¹LIXAM, Centre Universitaire Paris-Sud, Bâtiment 350, F-91405 Orsay Cedex, France

²Physikalische und Theoretische Chemie, Institut für Chemie und Biochemie, Freie Universität Berlin, Takustr. 3, 14195 Berlin

The electronic relaxation of core-excited nitrogen molecules has been studied by means of UV/VIS fluorescence spectroscopy. The spectral analysis of the fluorescence from excited ionic states has shown to provide valuable information on the dynamics of inner-shell excited atoms, molecules, and clusters [1] and is complementary to the generally used high-resolution electron spectroscopy, which allows the vibrational structure of the molecular ion to be resolved [2]. Since the spectral resolution attainable in dispersed fluorescence spectra does not depend on the energy and the bandwidth of the exciting photons, the investigation of the rotational structure of diatomic molecular ions (level spacing of some ten μeV) is possible even after excitation of core-hole resonances (energies of several hundred eV). The present study is aimed at the investigation of the UV/VIS fluorescence from the N_2^+ $A^2\Pi_u$ and $B^2\Sigma_u^+$ ionic states formed after electronic relaxation via resonant Auger decay and autoionization of the $1s^{-1}\pi^*$ resonance of nitrogen.

The experiments were carried out at the beamline UE-52-SGM at BESSY. Fluorescence was produced in the region of interaction between the synchrotron radiation and a free gas jet,

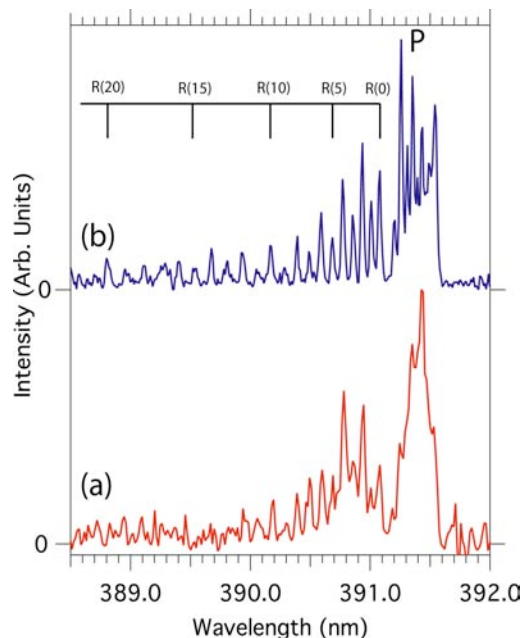


Fig. 1: Rotationally resolved fluorescence spectra of the N_2^+ ($B^2\Sigma_u^+$, $v'=0$) \rightarrow ($X^2\Sigma_g^+$, $v=0$) transition recorded upon photoexcitation at (a) 395.0 eV and (b) 400.88 eV. Further details: see text.

which produces a high density of rotationally cold ($T_{\text{rot}} = 40$ K) N_2 molecules. The UV/VIS photons were collected in the direction perpendicular to the synchrotron radiation and focused onto the entrance slit of a high-resolution fluorescence spectrometer (Jobin Yvon HRS460). The spectra are recorded by using a large area (2000 x 800 pixels), liquid nitrogen cooled CCD detector.

Fig. 1 shows the rotationally resolved fluorescence spectra recorded after excitation at photon energies of (a) 395 eV, i.e. in the region below the $1s$ resonances and ionization threshold, where the ions are produced only by direct valence-shell ionization, and (b) 400.88 eV, i.e. after excitation to the lowest vibrational level ($v''=0$) of the N_2 $1s\text{-}\pi^*$ resonance. The observed

rotational band structure is assigned to the transition $B^2\Sigma_u^+, v'=0 \rightarrow X^2\Sigma_g^+, v=0$ of the N_2^+ ion and reveals two branches (P and R), which is typical for Σ - Σ transitions. The two fluorescence spectra show marked differences when comparing the relative intensities of the individual lines in both branches indicating a change in the rotational population of the $N_2^+(B^2\Sigma_u^+)$ ion formed via autoionization of $1s^{-1}\pi^*$ resonance (Fig. 1a) or via direct valence-shell ionization (Fig. 1b).

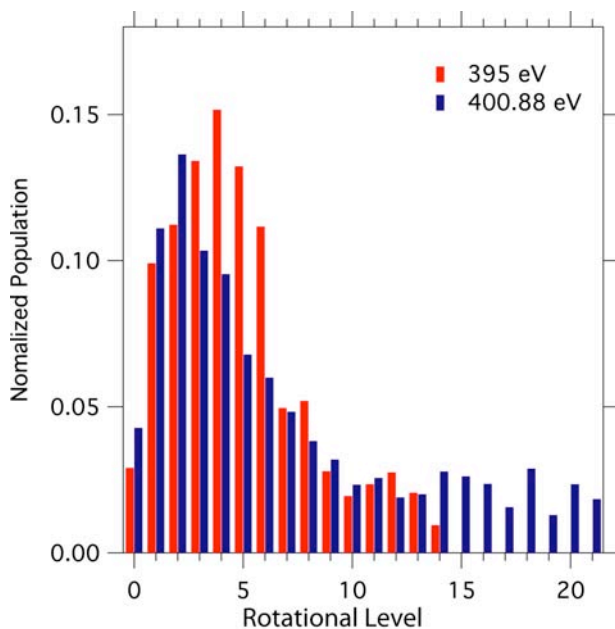


Fig. 2: Population of the rotational levels of $N_2^+(B^2\Sigma_u^+, v'=0)$ formed upon excitation of N_2 at 395.0 eV (red) and 400.88 eV (blue). Further details: see text.

For a quantitative analysis, the rotational population of the $N_2^+(B^2\Sigma_u^+)$ ions was deduced from the experimental fluorescence spectra (Fig. 2). For each spectrum the population of all rotational levels was normalized to unity for ease of comparison. Clear evidence is found for the population of higher rotational levels up to $J=21$ after excitation of the $1s^{-1}\pi^*$ state (blue histogram) compared to valence-shell photoionization at 395 eV ($J < 14$) (red histogram). It has been shown earlier [3] that significant changes in the rotational distribution of N_2^+ , which are formed by valence-shell photoionization, occur as a function of photon energy in the region from 20 to 200 eV [3]. These results have been

explained by a theoretical analysis showing an increasing importance of higher angular momentum for the outgoing photoelectron. Our investigations extend these studies to even higher photon energies (up to 500 eV) and highlight the particular case of resonant $1s\text{-}\pi^*$ excitation, which has never been treated before. Additional theoretical work is currently under way in order to obtain more detailed insight into the electronic relaxation dynamics of $1s^{-1}\pi^*$ excited N_2 with respect to the rotational excitation of N_2^+ in the final state $B^2\Sigma_u^+$.

The project was funded through BESSY-EC-IA-SFS Contract (EU R II 3-CT-2004-506008).

References

- [1] M. Meyer, A. Marquette, A. Grum-Grzhimailo, R. Flesch, and E. Rühl, *Surf. Rev. Lett.* **9**, 141 (2002); I. L. Bradeanu, R. Flesch, M. Meyer, H. W. Jochims, and E. Rühl, *Eur. Phys. J. D* **36**, 173 (2005); M. Meyer, P. O'Keeffe, J. Plenge, R. Flesch, and E. Rühl, *J. Chem. Phys.* **125** (2006).
- [2] M. N. Piancastelli, R. F. Fink, R. Feifel, M. Bäessler, S. L. Sorensen, C. Miron, H. Wang, I. Hjelte, O. Björneholm, A. Ausmees, S. Svensson, P. Salek, F. K. Gel'mukhanov, and H. Agren, *J. Phys. B* **33**, 1819 (2000).
- [3] E. D. Poliakoff, H. C. Choi, R. M. Rao, A. G. Mihill, S. Kakar, K. H. Wang, and V. McKoy, *J. Chem. Phys.* **103**, 1773 (1995).

Spectroscopic investigation of the coupling between an antiferromagnetic and a ferromagnetic film: NiMn/Co/Cu(001)

C. Tieg^{1,3}, R. M. Abrudan^{1,2}, M. Bernien², W. Kuch², J. Kirschner¹

¹ Max-Planck-Institut für Mikrostrukturphysik, Weinberg 2, D-06120 Halle, Germany

² Freie Universität Berlin, Institut für Experimentalphysik, Arnimallee 14, D-14195 Berlin, Germany

³ present address: European Synchrotron Radiation Facility, BP 220, F-38043 Grenoble Cedex, France

Non-volatile magnetic data storage in modern information technology relies on complex devices made of stacks of magnetic layers with engineered functionality. An important role in these multilayered structures plays the magnetic coupling between an antiferromagnetic (AFM) and a ferromagnetic (FM) material, whereas by definition the former carries no net magnetisation. The purpose of the AFM layer is to tune the magnetic switching behaviour of the adjacent FM layer to be non-symmetric with respect to externally applied magnetic fields. This coercive field tuning of the FM layer exploits the *exchange bias effect*, discovered in the middle of the last century. Though intensively studied on many systems in the last decade [1], a full understanding of the coupling phenomenon in AFM/FM systems is still missing. A promising step to tackle the problem is the study of simple model systems based on epitaxial films which allow to control and modify the interface properties [2]. In addition, single-crystalline bilayers reduce the complexity of the coupling due to the absence of structural grains in the individual films.

In our work we have studied the epitaxial bilayer system of metallic antiferromagnet NiMn films in contact to ferromagnetic Co films on a single crystalline Cu(001) substrate. The objective of our work is the study of the orientation of the magnetic moments in the antiferromagnetic and ferromagnetic layer. To address this, we employed the spectroscopic method of polarisation dependent soft x-ray absorption at the element specific $L_{3,2}$ absorption edges. In short, x-ray magnetic circular dichroism (XMCD) was used to measure the orientation of the magnetic moments in the FM layer, while x-ray magnetic linear dichroism (XMLD) was used to probe the orientation of the AFM layer. NiMn was deposited after saturating the Co film on Cu(001) by an external magnetic field along the [110] in-plane direction, being the magnetic easy axis of this system. We were interested in the following questions. First, does the subsequent deposition of NiMn induce a rotation of the magnetisation direction of the underlying Co film as observed in FeMn/Co/Cu(001) systems [4], and second, what is the direction of the antiferromagnetic spin axis of NiMn adjacent to a saturated Co layer.

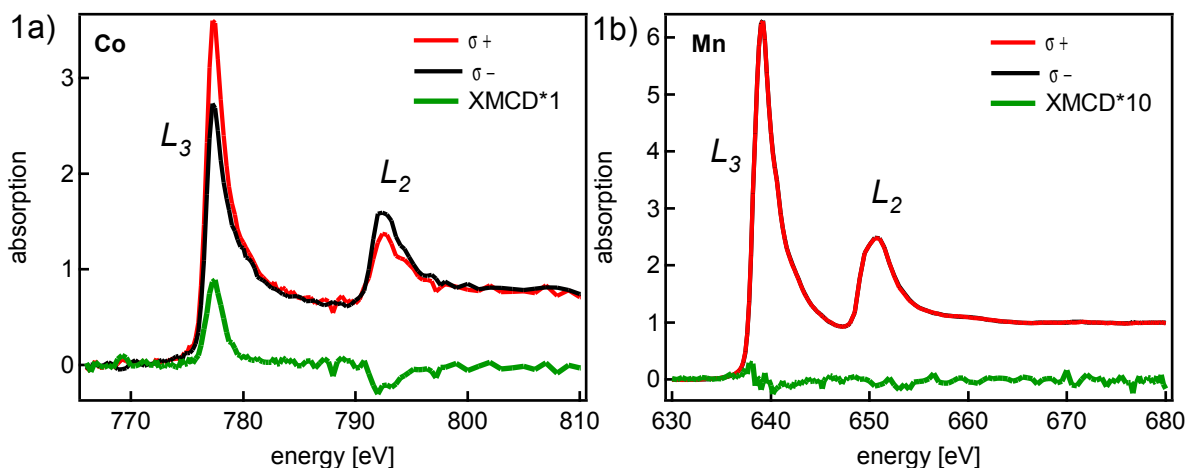


Fig 1) Absorption spectra at the Co and Mn L_3 and L_2 edges for left and right circularly polarised light (σ^+ , σ^-) together with the XMCD difference spectra obtained from a 22 ML NiMn/6 ML Co/Cu(001) sample. The spectra were normalised to the edge jump. The initial magnetisation direction and the photon beam direction make an angle of 60° . Note that the measured Mn XMCD signal is shown magnified by a factor of 10.

Films were prepared in-situ by thermal deposition on Cu(001) at room temperature. The alloy was grown by co-deposition of its constituents from separate evaporation sources. The Néel temperature of bulk NiMn, which exhibits a $L1_0$ crystal structure, is far above room temperature (1070 K). Thin films of NiMn were found to grow layer-by-layer on Cu(001), and to show a $c(2 \times 2)$ low energy electron diffraction pattern [3].

The absorption measurements using total electron yield detection were done at the beamline UE 56/2-PGM2. For XMCD measurements we chose an off-normal incidence angle of 30° , allowing a non-vanishing projection of the Co magnetisation onto the incoming beam direction. Figure 1a) and 1b) show the absorption spectra together with the dichroism at the Co and Mn absorption edges, respectively, for a 22 ML NiMn/6 ML Co/Cu(001) sample. As expected, we found a non-vanishing Co XMCD and a vanishing Mn XMCD signal. While the former proves that the Co film retained its initial magnetisation direction, the later shows that the Mn moments do not exhibit ferromagnetic ordering.

The XMLD measurements were performed in normal incidence geometry. Absorption spectra were recorded with horizontally and vertically polarised light relative to the storage ring plane. Absorption spectra together with XMLD difference curves for Co and Mn for a 20 ML NiMn/6 ML Co/Cu(001) sample being oriented with the [110] direction parallel to the horizontal plane are given in Figure 2a) and 2b), respectively. We observe a characteristic plus-minus feature in the XMLD spectrum at the Co L_3 edge. In comparison to the results of our XMCD measurements, which shows that the Co moments point along the [110] direction, the observed Co XMLD magnitude and sign are indicative for a fully saturated Co film [5].

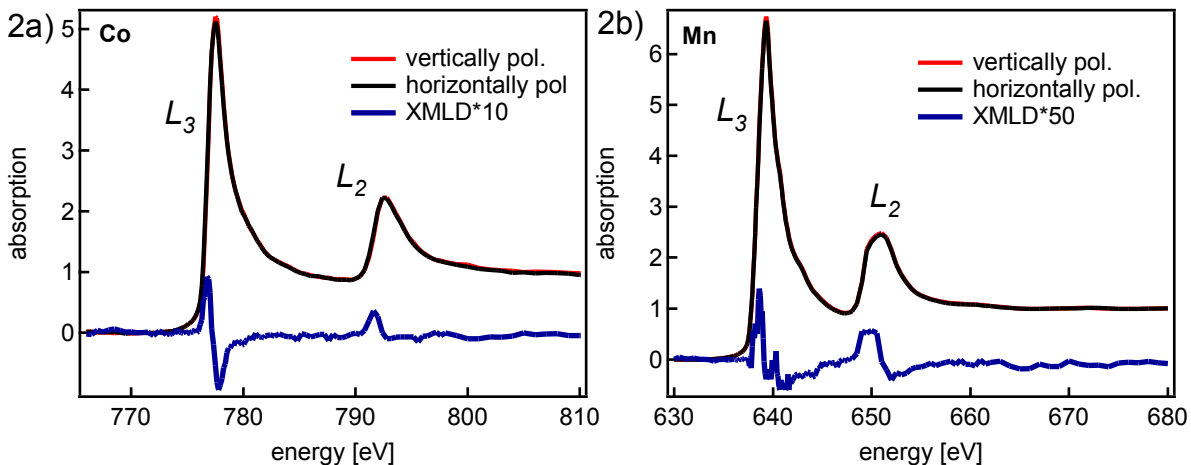


Fig 2) Absorption spectra at the Co (a) and Mn (b) L_3 and L_2 edges for vertically and horizontally polarised light together with the XMLD difference spectra obtained from a 20 ML NiMn/6 ML Co/Cu(001) sample. Note the different scaling factors of both XMLD spectra.

As can be seen in Fig. 2b), a small but detectable XMLD was found at the Mn absorption edges. This was not expected since the spectral contributions from Mn atoms belonging to the two structural 90° domains in the NiMn film cancel each other under the assumption of random distribution of both domains and mutually orthogonal orientation of their spin axes. In this picture we assume a bulk-like spin structure with an in-plane orientation of the spin axes. However, the spectral cancellation of both contributions is incomplete if the spin axes in both domains deviate from their orthogonal in-plane orientation. Such a deviation might be present in our system. Taking into account that the NiMn film is in contact with a saturated Co film, the AFM spin axis may be tilted towards the Co magnetisation due to the exchange coupling at the interface.

We wish to acknowledge the support by F. Helbig¹, B. Zada¹, W. Mahler (FHI) and by the BESSY staff.

[1] J. Nogués and I. K. Schuller, *J. Magn. Magn. Mater.* **192**, 203 (1999)

[2] W. Kuch, L. I. Chelaru, F. Offi, J. Wang, M. Kotsugi, and J. Kirschner, *Nature Mater.* **5**, 128 (2006)

[3] C. Tieg, W. Kuch, S. G. Wang, and J. Kirschner, *Phys. Rev. B* **71**, 094420 (2006)

[4] F. Offi, W. Kuch, L. I. Chelaru, K. Fukumoto, M. Kotsugi, and J. Kirschner, *Phys. Rev. B* **67**, 094419 (2003)

[5] W. Kuch, L. I. Chelaru, F. Offi, J. Wang, M. Kotsugi, and J. Kirschner, *Phys. Rev. Lett.* **92**, 017201 (2004)

Photoelectron-Auger electron coincidence spectra of CO and CF₄

Volker Ulrich, Silko Barth, Sanjeev Joshi, Toralf Lischke and Uwe Hergenahn^a

Max-Planck-Institut für Plasmaphysik, EURATOM association, Boltzmannstr. 2, 85748 Garching

Auger spectroscopy is widely used as an element-specific probe in material science. More information, e.g. about potential curves of the final state and about dynamics in the intermediate state, is contained in principle in the Auger spectrum, but is difficult to extract because the number of dicationic final states is typically large, and because an Auger spectrum, conventionally recorded, is composed of a convolution of all accessible intermediate states. A technique that can overcome this natural barrier is two electron coincidence spectroscopy [1].

Experimental: Our set-up used to record the photoelectron and the Auger electron from an inner shell transition in a small molecule in coincidence has been described earlier [2]. Briefly, we use a large, hemispherical electron analyser, in order to record the fast Auger electron with good energy resolution, in conjunction with several simple time-of-flight spectrometers, in order to obtain a larger solid angle for detection of the photoelectron. The flight time of the photoelectrons can either be referred to the BESSY bunch marker in single bunch operation, or to the arrival time of the Auger electron. With the latter scheme, measurements can be conducted also in the multi-bunch mode of BESSY. Spectra presented here were recorded at the UE52-SGM beamline, since our detector geometry requires the use of vertical linearly polarized light.

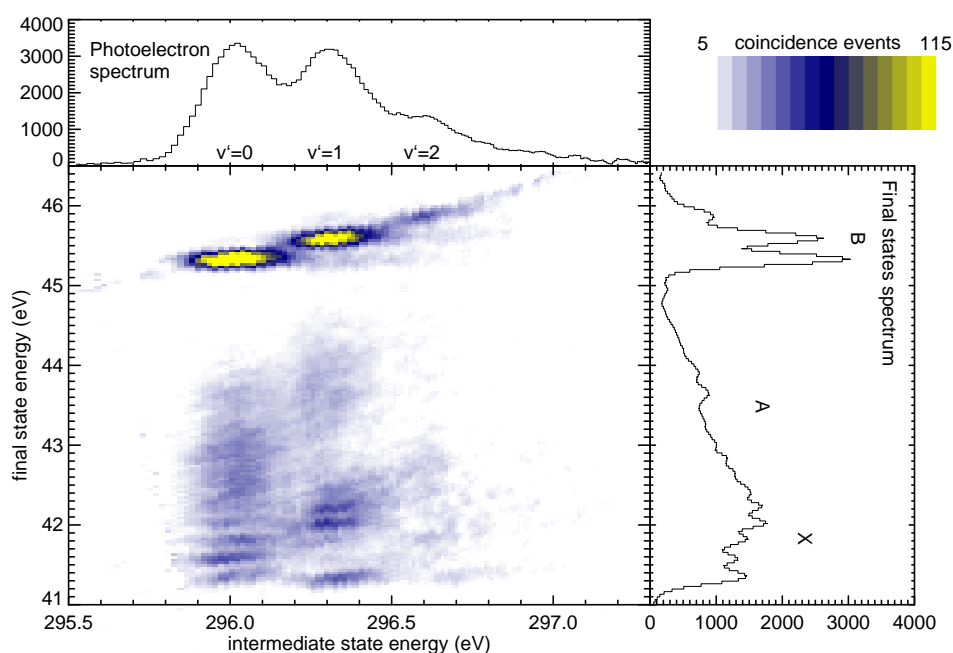


Figure 1: Intensity map of photoelectron-Auger electron pairs for C 1s ionization of carbon monoxide. The photon energy was set to 305 eV. The joint emission probability for each combination of energies of the two states involved in the decay is presented in the two-dimensional map. Spectra shown in the top and right hand panel pertain to summations over all final states or all photoelectron energies, respectively. The top panel compares well to published non-coincident spectra. The right hand side panel can be compared to pair energy dependent yields from direct photo double ionization [3] (see text).

^a Mailing address: IPP, c/o BESSY, Albert-Einstein-Str. 15, 12489 Berlin, email: uwe.hergenahn@ipp.mpg.de

Results: An example of data recorded in 2006 is shown in Figure 1. To give a better insight, the Auger electron kinetic energies measured in our experiment were converted to final state energies. The instrumental broadening for these data corresponds to 200 and 300 meV for the photoelectron and the Auger electron, respectively. At that resolution, the vibrational structure in the dicationic X state (the least energetic singlet state of CO^{2+}) can be clearly resolved around a final state energy of 41-42 eV. For the B state, transitions between pairs of vibrationally resolved intermediate and final states are clearly separated as well. As they would appear at practically identical Auger energy, it can be concluded that the potential curves of both states are parallel.

In the carbon monoxide example discussed so far, the intermediate state ($\text{CO}^+ \text{C}1s^{-1}$) is bound, and the final states of CO^{2+} shown here possess local minima in their potential curves as well (although asymptotically they are dissociative). A different regime of coincident photo + Auger emission is shown in Figure 2, which shows the coincident two-electron intensity for F 1s ionization of CF_4 . The intermediate state thus reached is strictly dissociative, and no vibrational structure is observed in the F 1s photoelectron spectrum. Nevertheless, strong propensity rules seem to exist that allow the population of most Auger final states only at certain energies of the photoelectron. This behaviour can be seen as the analogue to the ‘core hole clock’ effect in resonant Auger decay, where the time dependence of the decay within the lifetime of the core hole is well established.

In comparison to studies of the dicationic states by direct photo double ionization, here a much wider range of the final state potential curve can be reached [3].

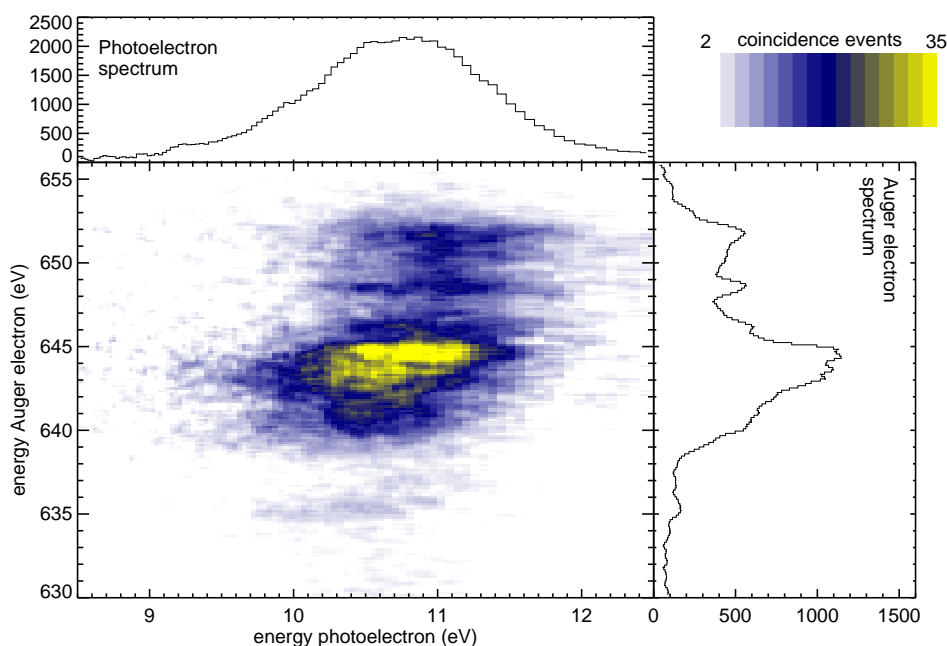


Figure 2: Intensity map of photoelectron-Auger electron pairs for F 1s ionization of carbon tetrafluoride. The right hand side panel compares well to the non-coincident Auger spectra.

References

- [1] H. W. Haak, G. A. Sawatzky, and T. D. Thomas, *Phys. Rev. Lett.* **41**, 1825 (1978).
- [2] O. Kugeler, S. P. Marburger, and U. Hergenhahn, *BESSY Annual report 2002*; *Rev. Sci. Instrum.* **74**, 3955 (2003).
- [3] J. H. D. Eland, M. Hochlaf, G. C. King, P. S. Kreynin, R. J. LeRoy, I. R. McNab, and J.-M. Robbe, *J. Phys. B* **37**, 3197 (2004); R. Feifel, J. H. D. Eland, L. Storchi, and F. Tarantelli, *J. Chem. Phys.* **125**, 194318 (2006).

Partial funding by the DFG under project He 3060/3-1,2 is gratefully acknowledged.

Valence photoelectron spectra of free clusters

Silko Barth,¹ Volker Ulrich,¹ Sanjeev Joshi,¹ Toralf Lischke,¹ Gunnar Öhrwall,²
Wandared Pokapanich,² Olle Björneholm,² and Uwe Hergenhahn^{1a}

1: Max-Planck-Institut für Plasmaphysik, EURATOM association, Boltzmannstr. 2, 85748 Garching

2: Uppsala University, Department of Physics, Box 530, SE-751 21 Uppsala

The electronic properties of clusters are interesting to study, as these small quantum systems are often in-between the isolated atom or molecule and the solid state. Numerous experiments have been carried out with *i.e.* laser photoionization or fluorescence spectroscopy, while straight-forward measurements of the photoelectron spectra are – in comparison – still lacking. We report here systematic studies of the $3p$ valence photoionization of Ar clusters, and a size-dependent study of the HOMO peak of water clusters. These spectra were recorded within three weeks of multi-bunch beamtime at the UE112-lowE-PGM-a beamline allotted for the study of cluster photoionization.

Ar clusters: The rare gas solids have earlier been referred to as ideal model systems for bulk state insulators, and the study of their valence bands was a pioneering application of synchrotron radiation [1]. Here, we report the evolution of the $3p$ photoelectron lines from medium sized Ar clusters ($\langle N \rangle = 900$) at the ionization threshold. Contrary to the more strongly bound $3s$ and $2p$ orbitals, these spectra cannot be explained by adding two broadened, quasi-atomic peaks with an energy difference resulting from polarization screening.

Ar clusters were produced by expansion of the gas through a LN₂ cooled copper nozzle into an expansion chamber that is separated from the main chamber by a conical skimmer. Electrons were recorded with a commercial hemispherical analyser (Scienta ES 200). Further details of the set-up have been published [2].

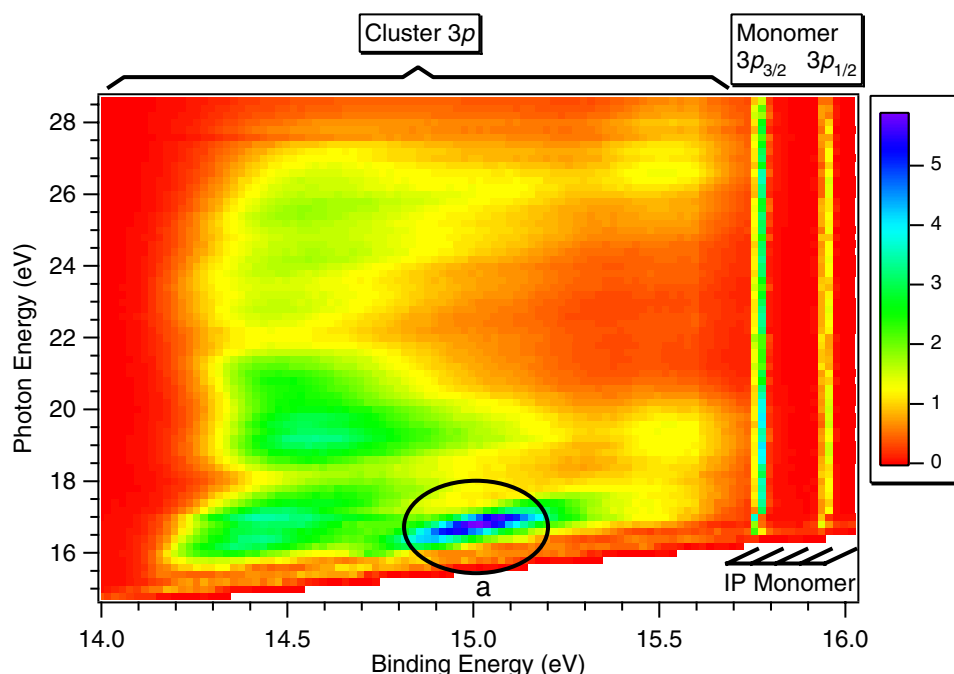


Figure 1: Series of $3p$ photoelectron spectra from medium sized Ar clusters at the ionization threshold. The large mean free path of the photoelectrons at this low energy promotes the bulk sensitivity of this method.

Our experimental results are shown in Fig. 1. The part of the spectrum related to $3p$ photoemission from clusters is broad, and shows a pronounced photon energy dependence. In

^a Mailing address: IPP, c/o BESSY, Albert-Einstein-Str. 15, 12489 Berlin; email: uwe.hergenhahn@ipp.mpg.de

earlier work on $\langle N \rangle = 1000$ clusters of Ar [3], in which a constant photon energy was used, the question was left open whether their $3p$ spectra should be interpreted in terms of band structure formation, or in terms of the older ‘ion core’ model. The latter postulates the formation of ionic oligomers, $(Ar_{13})^+$ in the case of Ar clusters [4], around the ionized site. Our spectra qualitatively are similar to series of electron spectra from 50-200 Å thick Ar films [1]. Moreover, features not hitherto observed in the solid state with a sharp photon energy dependence show up, such as the pronounced near threshold band marked ‘a’ in Fig. 1. We attribute these to final state effects in a band-like model of the photoemission process, and suggest that the band structure in Ar clusters of that size is fully developed.

Water clusters: A source for clusters from hydrogen bonded liquids was added to our set-up in 2005 [2], and was improved in 2006 by changing to conical nozzles of 1100 μm length.

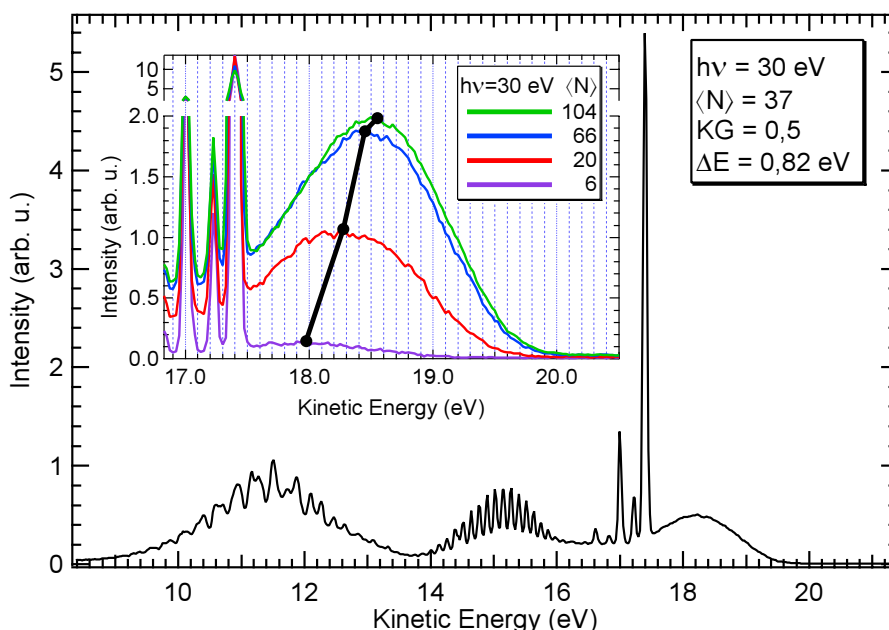


Figure 2: Full outer valence photoelectron spectrum of water clusters and energy shift of the HOMO peak (0.58, 0.88, 1.05 and 1.15 eV) in dependence of cluster size (inset).

In Figure 2 we report the valence photoelectron spectrum of water clusters, which is similar to spectra reported earlier at a somewhat worse resolution [4]. Sharp features are from uncondensed water molecules being present in the beam. The dependence of the energy shift of the cluster peak on cluster size has been recorded in detail, and is shown in the inset of the figure. The HOMO peak even for the smallest cluster size has a large energetical width, which results from the strong geometry change when this orbital, which is responsible for formation of the hydrogen bridge bonds, is ionized.

References

- [1] N. Schwentner, F.-J. Himpsel, V. Saile, M. Skibowski, W. Steinmann, and E. E. Koch, *Phys. Rev. Lett.* **34**, 528 (1975).
- [2] S. P. Marburger, O. Kugeler, and U. Hergenhan, in *Proceedings of the SRI 8, AIP Conference Proceedings Vol. 705*, p. 1114; BESSY Annual Reports 2002, 2005.
- [3] R. Feifel, O. Björneholm *et al.*, *Eur. Phys. J. D* **30**, 343 (2004).
- [3] F. Carnovale, J. B. Peel, R. G. Rothwell, J. Valldorf, and P. J. Kuntz, *J. Chem. Phys.* **90**, 1452 (1989).
- [4] O. Björneholm, F. Federmann, S. Kakar, and T. Möller, *J. Chem. Phys.* **111**, 546 (1999); G. Öhrwall, R. F. Fink, O. Björneholm *et al.*, *J. Chem. Phys.* **123**, 054310 (2005).

Partial funding within DFG project He 3060/3-1,2 is gratefully acknowledged.

Observing the heavy fermions in CeCoIn₅

A. Koitzsch^{1,2}, S. V. Borisenko¹, D. Inosov¹, J. Geck¹, V. B. Zabolotnyy¹, H. Shiozawa¹, M. Knupfer¹, J. Fink¹, B. Büchner¹, E. D. Bauer³, J. L. Sarrao³ and R. Follath⁴

¹*IFW Dresden, P.O. Box 270116, D-01171 Dresden, Germany*

²*Institute for Solid State Physics, TU Dresden, D-01062 Dresden, Germany*

³*Los Alamos National Laboratory, Los Alamos, New Mexico 87545, USA*

⁴*BESSY GmbH, Albert-Einstein-Strasse 15, 12489 Berlin, Germany*

The material class CeTIn₅ with ($T = \text{Co, Ir, Rh}$) shows a number of remarkable properties such as heavy fermion behavior, superconductivity and quantum criticality [1, 2]. In particular, the compound CeCoIn₅ ($T_c = 2.3 \text{ K}$) holds the high temperature record among all ambient pressure heavy fermion superconductors.

Here we investigate the electronic structure of CeCoIn₅ by angle-resolved photoemission spectroscopy (ARPES). We directly monitor the 4f-derived band which is responsible for the heavy fermion behavior of the compound by resonant ARPES. We find a pronounced temperature and k-dependence of this band.

The ARPES experiments were carried out using radiation from the U125/1-PGM beam line and an angle multiplexing photoemission spectrometer (SCIENTA SES 100) at the BESSY Synchrotron Radiation Facility. We present photoemission data taken with $h\nu = 90$ and 121 eV with an energy resolution of 40 meV and an angular resolution of 0.2° . Single crystals of CeCoIn₅ were grown in In flux. For the measurements the crystals were cleaved *in situ* at room temperature.

In Fig. 1 we study the angle dependence of the f-weight near E_F . Fig. 1a shows the off resonant energy dependence of the spectral weight parallel to the AR symmetry direction of the tetragonal unit cell at a photon energy of $h\nu = 90 \text{ eV}$. We observe an electron like band in agreement with bandstructure calculations and de-Haas-van Alphen measurements [3, 4, 5]. Summing up the spectral intensity along the k-axis results in the integrated spectra shown in Fig. 1b. No f-related peaks are found in the vicinity of E_F . Now we compare the off resonant measurement in panel (a) to the on resonant measurement taken with $h\nu = 121 \text{ eV}$ presented in panel (c). Again the electron-like band which consists mainly of Co 3d and In 5p states is detected. Additionally, we find an intense flat band at E_F and a weak sideband at $E = -0.3 \text{ eV}$. Since these features appear under the resonance condition only they are derived from 4f

states. We identify the flat band as part of the Fermi surface sheet which contains the heavy fermions. The integrated spectrum in panel 3d clearly shows the $4f_{5/2}$ derived peak at the Fermi energy and its $4f_{7/2}$ spin orbit component at $E = -0.3$ eV. Increasing the temperature decreases the intensity of the peak at the Fermi energy as shown in panels 1e-h. At $T = 105$ K the band is still visible. At $T = 180$ K the peak at E_F has nearly vanished but the sideband is still noticeable although it is broadened compared to lower temperatures. Thus our data directly reveal the evolution of the heavy mass quasiparticle band going to lower temperatures. Closer inspection of Fig. 1c reveals that the distribution of f-electrons over k is not uniform. It concentrates instead outside the parabola of the normal band, whereas it is much weaker inside.

Now we compare the data to theoretical models. The overall dispersion of the non-f valence bands is well described by LDA calculations [6]. For the theoretical description of the distribution of the spectral f-weight shown in Fig. 1c we approach the electronic structure from a different point of view, which roots in the Anderson lattice model [7]. We assume a normal non f-band which cuts E_F with a sizable slope (see Fig. 2a). The f-sites are modeled by a dispersionless state at a renormalized energy ϵ_f' above E_F . A finite hybridization opens a gap and results in two branches E_1 and E_2 . The Fermi vector is renormalized from k_F to k'_F to accommodate the additional f-electrons and the Fermi velocity is reduced, leading to an increase of the effective mass. The hybridization gap pushes spectral weight towards E_F “outside” the normal band and away from E_F “inside” the normal band. Panel b shows the spectral weight one expects then for an off resonant photoemission experiment. It is dominated by the conventional non-f band. On the other hand, for the on resonant condition (panel c), the spectrum is dominated by the f-weight outside the conventional band. This is in agreement with experiment (see Fig. 2c).

To conclude, we have explicitly observed the high effective mass 4f-derived band and studied its temperature dependence. The results compare favourably with simple theoretical models. We acknowledge financial support by the DFG SFB 463 and BMBF Project 05KS4OD2/8. Work at Los Alamos was performed under the auspices of the U.S. DOE. We would like to thank S. L. Molodtsov, Yu. Kucherenko, I. Opahle, S. Elgazar and M. Richter for valuable discussions.

References

- [1] C. Petrovic et al., *J. Phys.: Condens. Matter* **13**, L337 (2001)
- [2] V. A. Sidorov et al., *Phys. Rev. Lett.* **89**, 157004 (2002)

- [3] D. Hall et al., Phys. Rev. B **64**, 212508 (2001)
 [4] Settai et al., J. Phys.: Condens. Matter **13**, L627 (2001)
 [5] S. Elgazaar et al., Phys. Rev. B **69**, 214510 (2004)
 [6] A. Koitzsch et al., *unpublished*
 [7] M. J. Rozenberg et al., Phys. Rev. B **54**, 8452 (1996)

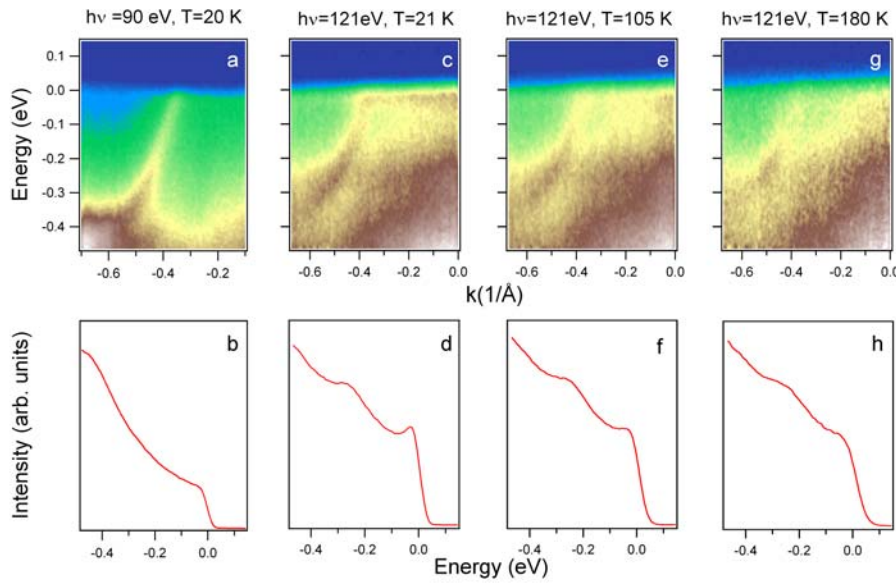


Fig. 1: (Upper row) Energy distribution maps (EDM's) along the blue line in Fig. 1 measured off and on resonance as a function of temperature. Note the appearance of the flat band for panel (c). (Lower row) Angle-integrated spectra of the EDM's in the upper row.

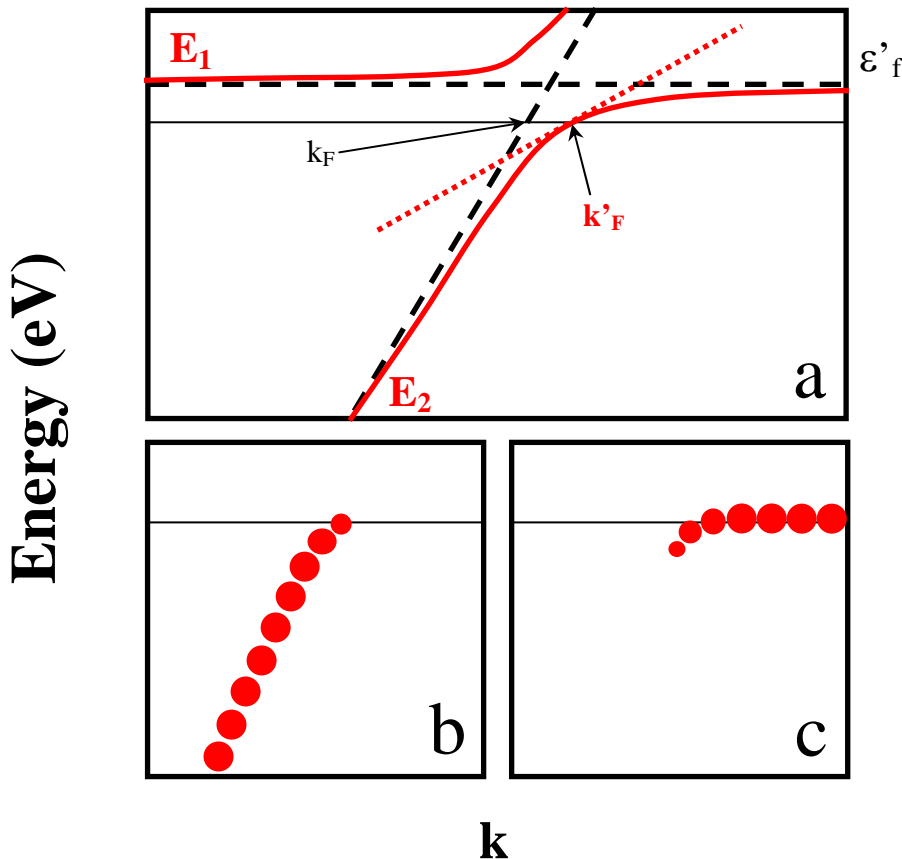


Fig. 2: (a) Schematic view on the Periodic Anderson model. The dashed lines are a dispersing valence band and the dispersionless renormalized f-states above the Fermi energy. For a finite hybridization, a gap opens and two branches with k -dependent orbital weight are formed (E_1 , E_2). The E_F crossing is adjusted to accommodate the additional f -electrons. The Fermi velocity is reduced and the effective mass enhanced. (b) Off resonant spectral weight as seen by photoemission. (c) On resonant spectral weight.

Hole states in BaCeO₃ and SrCeO₃ protonic conductors

V. R. Galakhov^{1*}, M. Raekers², C. Taubitz², N. Damnik², M. Neumann²,
T. I. Chupakhina³, R. Ovsyannikov⁴, and S. L. Molodtsov⁵

¹*Institute of Metal Physics, Russian Academy of Sciences —
Ural Division, 620041 Yekaterinburg GSP-170, Russia*

²*Fachbereich Physik, Universität Osnabrück, D-49069 Osnabrück, Germany*

³*Institute of Solid State Chemistry, Russian Academy of Sciences —
Ural Division, 620041 Yekaterinburg GSP-145, Russia*

⁴*BESSY GmbH, Albert-Einstein-Str. 15, D-12489 Berlin, Germany*

⁵*Institut für Festkörperphysik, Technische Universität Dresden, D-01062 Dresden, Germany*

It is well known that perovskite-type oxides of general formula ABO₃ (CaZrO₃, SrTiO₃, SrCeO₃ etc.) exhibit protonic conductivity at high temperatures when acceptor ions are doped in the B⁴⁺ site [1–6]. Crystalline structure of BaCeO₃ is shown in Fig. 1. Protonic conductors are important materials for a wide range of electrochemical applications, such as hydrogen fuel cells and sensors. Theoretical and experimental investigations of the mechanism of proton migration have been reported in perovskite-type protonic conductors. In Y³⁺-doped SrCeO₃ and Sc³⁺-doped SrTiO₃, proton migration in the bulk state has been confirmed [6, 7].

It is proposed that the proton migrates by hopping from site to site around the oxygen ion [8–11]. In recent years, the electronic structure of some protonic conductors (SrCe_{1-x}Y_xO₃, SrCe_{1-x}Yb_xO₃, SrTi_{1-x}Sc_xO₃, CaZr_{1-x}In_xO₃) has been studied by means of O 1s X-ray absorption spectroscopy [9], O K α X-ray emission spectroscopy [12], resonant photoemission spectroscopy [11]. It was found that in Sc-doped SrTiO₃ [8, 9], In-doped CaZrO₃ [10], Y-doped SrCeO₃ [11, 12], the hole states and the acceptor-induced levels due to acceptor doping are observed at the top of the valence band and above the Fermi level. Hydrogen acted as donor must compensate the hole created at the top of the valence band by acceptor doping [12]. Despite of many papers devoted to the study of protonic conductors, the electronic structure of these compounds has not been clarified.

The samples of BaCeO₃, BaCe_{0.9}Ga_{0.1}CeO₃, and BaCe_{1-x}In_xCeO₃ ($x = 0.1$ and 0.5), and SrCe_{0.95}Y_{0.05}O₃ were prepared by conventional solid-state reactions at about 1450 °C for 50–70 h. The samples were examined by X-ray diffraction analysis. The measurements of O 1s spectra of were performed in the total-electron-yield (TEY) mode at the Russian-German Beamline at BESSY. The samples were in the form of polycrystalline pressed pellets. The data were normalized to TEY spectra of Au in order to account for variations of the incident flux as a function of the photon energy.

Figure 2 displays the O 1s X-ray absorption spectra of BaCeO₃, BaCe_{1-x}In_xO₃ ($x = 0.1, 0.5$), BaCe_{0.9}Ga_{0.1}O₃, and SrCe_{0.95}Y_{0.05}O₃. The spectra are normalized by the A peak. The pre-edge peak A at about 531 eV reflects transition of a 1s core electron to 2p-hole states in the narrow 4f-dominated bands resulting from strong Ce 4f–O 2p hybridization in the ground states of tetra-

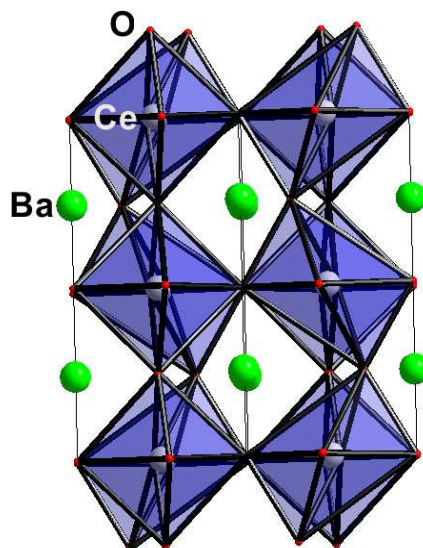


Fig. 1: Crystalline structure of BaCeO₃.

*e-mail: galakhov@ifmlrs.uran.ru

lent Ce compounds (see, for comparison, the O 1s X-ray absorption spectra of CeO₂ and BaCeO₃ presented in [13]). The peaks B/C and D in the spectrum of BaCeO₃ are assigned to Ba 5*d* and Ba 6*p* states, respectively. The intensity of these peaks increases with increasing In concentrations in In-doped Ba cerates. Therefore, the peaks B/C should be assigned to In 5*p* + Ba 5*d* states. In Ga-doped BaCeO₃, the peaks B/C reveal both Ga 4*p* and Ba 5*d* states.

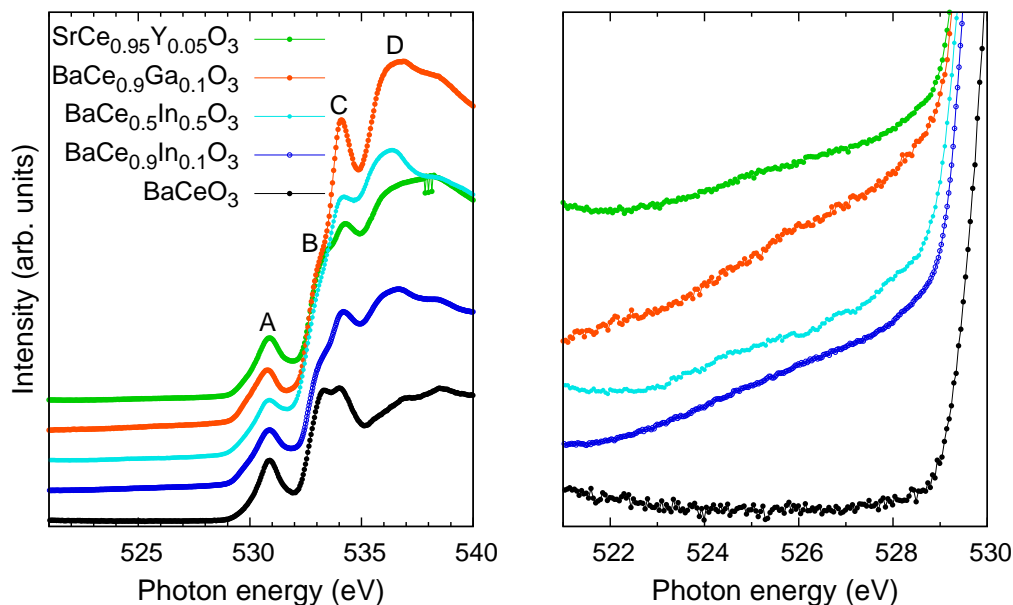


Fig. 2: O 1s X-ray absorption spectra of BaCeO₃, BaCe_{0.9}Ga_{0.1}O₃, BaCe_{1-x}In_xO₃ ($x = 0.1, 0.5$), and SrCe_{0.95}Y_{0.05}O₃.

It is known that the energy band gap of BaCeO₃, as it was derived from optical absorption spectra in [14], is 4.1 eV. There is no structure in the band gap of non-doped BaCeO₃ (see right panel in Fig. 2). However, features in the energy area from 522 to 529 eV are observed in the spectra of doped Ba and Sr cerates. These features might be assigned to the acceptor-induced levels. In the cerates, doping with 3+ ions should lead both to oxygen ion vacancies and electronic holes. Effects of atomic nonstoichiometry in BaCeO₃ was studied in [15,16]. In our work, we have found electronic holes produced by 3+ ion doping.

In conclusion, the holes induced by In, Ga or Y impurities in the BaCeO₃ and SrCeO₃ oxides were directly observed in O 1s X-ray absorption spectra in the form of the pre-edge features. The nature of the defect-induced structure would be one of the most important subjects for the mechanism of protonic conduction.

This work was supported by the grant “Cooperation between the Ural and Siberian Divisions of the Russian Academy of Sciences”, the Research Council of the President of the Russian Federation (Project NSH-4192.2006.2), and by the Bilateral Program “Russian-German Laboratory at BESSY”.

-
- [1] H. Iwahara, T. Esaka, H. Uchida, and N. Maeda, *Solid State Ionics* **3–4**, 359 (1980).
 - [2] J. Guan, S. E. Dorris, U. Balachandran, and M. Liu, *Solid State Ionics* **110**, 303 (1998).
 - [3] Xiwang Qi and Y. S. Lin, *Solid State Ionics* **120**, 85 (1999).
 - [4] Xiwang Qi and Y. S. Lin, *Solid State Ionics* **130**, 149 (2000).
 - [5] T. Norby and Y. Larring, *Solid State Ionics* **136–137**, 139 (2000).
 - [6] H.H. Huang, M. Ishigame, and S. Shin, *Solid State Ionics* **47**, 251 (1991).

- [7] N. Sata, K. Hiramoto, M. Ishigame, S. Hosoya, N. Nimura, and S. Shin, *Phys. Rev. B* **54**, 15795 (1996).
- [8] T. Higuchi, T. Tsukamoto, K. Kobayashi, S. Yamaguchi, Y. Ishiwata, N. Sata, K. Hiramoto, M. Ishigame, and S. Shin, *Phys. Rev. B* **65**, 33201 (2002).
- [9] T. Higuchi, T. Tsukamoto, N. Satam, M. Ishigame, K. Kobayashi, S. Yamaguchi, and S. Shin, *Solid State Ionics* **154–155**, 735 (2002).
- [10] T. Higuchi, S. Yamaguchi, K. Kobayashi, T. Takeuchi, S. Shin, and T. Tsukamoto, *Jpn. J. Appl. Phys.* **41**, L938 (2002).
- [11] T. Higuchi, T. Tsukamoto, S. Yamaguchi, N. Sata, M. Ishigame, and S. Shin, *Jpn. J. Appl. Phys.* **42**, 3526 (2003).
- [12] T. Higuchi, S. Yamaguchi, N. Sata, S. Shin, T. Tsukamoto, and S. Shin, *Jpn. J. Appl. Phys.* **42**, L1265 (2003).
- [13] Z. Hu, R. Meier, C. Schüßler-Langeheine, E. Weschke, G. Kaindl, I. Felner, M. Merz, N. Nücker, S. Schuppler, and A. Erb, *Phys. Rev. B* **60**, 1460 (1999).
- [14] T. He, P. Ehrhart, P. Meuffels, *J. Appl. Phys.* **79**, 3219 (1996).
- [15] J. Wu, R. A. Davies, M. S. Islam, and S. M. Haile, *Chem. Mater.* **17**, 846 (2005).
- [16] J. Wu, S. M. Webb, S. Brennan, and S. M. Haile, *J. Appl. Phys.* **97**, 054101 (2005).

X-ray absorption measurements of the valence states of the spinel $\text{Fe}_{1-x}\text{Cu}_x\text{Cr}_2\text{S}_4$

C. Taubitz^{1*}, M. Raekers¹, N. Damnik¹, V. R. Galakhov², V. Tsurkan³, M. Neumann¹, R. Ovsyannikov⁴, and S. L. Molodtsov⁵

¹*Fachbereich Physik, Universität Osnabrück, D-49069 Osnabrück, Germany*

²*Institute of Metal Physics, Russian Academy of Sciences — Ural Division, 620041 Yekaterinburg GSP-170, Russia*

³*Institute of Applied Physics, Academy of Sciences of Moldova — MD 2028, Chisinau, R. Moldova*

⁴*BESSY GmbH, Albert-Einstein-Str. 15, D-12489 Berlin, Germany*

⁵*Institut für Festkörperphysik, Technische Universität Dresden, D-01062 Dresden, Germany*

Our measurements were carried out at the Russian German Beam Line at BESSY. The aim of our investigation was to gain information about the valence states in $\text{Fe}_{1-x}\text{Cu}_x\text{Cr}_2\text{S}_4$. As a colossal magneto resistance (CMR)-compound the $\text{Fe}_{1-x}\text{Cu}_x\text{Cr}_2\text{S}_4$ is a very interesting material. The magneto resistance (MR) is the change in the electrical resistance of a conductor by an applied magnetic field (H). There are many different kinds of MR effects, but the so called colossal magneto resistance (CMR) effect is the biggest one. It can reach up to several 100% or 1000%. An important step in the attempt to understand the CMR-effect is to reveal the electronic structure of the $\text{Fe}_{1-x}\text{Cu}_x\text{Cr}_2\text{S}_4$ spinel. Although investigated for quite a long time the ion valence state in these crystals is still in discussion. There are two models that try to describe the valency states in the mothercompound CuCr_2S_4 . Goodenough [6] developed a model in which the Cu-site is divalent [$\text{Cu}^{2+}\text{Cr}_2^{3+}\text{S}_4^{-2}$]. But in a different model Lotgering [7,8] claims the Cu-site to be monovalent and the Cr-site to be in a mixed valence state [$\text{Cu}^{1+}\text{Cr}^{3+}\text{Cr}^{4+}\text{S}_4^{-2}$]. For the $\text{Fe}_{1-x}\text{Cu}_x\text{Cr}_2\text{S}_4$ system the situation becomes even more complicated, since there are several possibilities for the substitution of Cu by Fe, depending on whether Cu is monovalent or divalent. Recent XAS and Moessbauer measurements reveal contradictory results for the Fe-valence [1,2] and even XAS measurements done by different workgroups seem to differ from each other [2,3].

We performed X-ray absorption measurements of $\text{Fe}_{1-x}\text{Cu}_x\text{Cr}_2\text{S}_4$ for $x=0.2$, $x=0.6$, $x=0.75$ at 80K and room temperature. It is found that the shape of the spectra is not affected by the change in the measuring temperature. As shown in figure 2 there is no change in the Cr 2p lines for all the samples, indicating Cr to be trivalent. In figure 1 one can see the Fe 2p XAS measurements together with FeO and Fe_2O_3 measurements adapted from [4] and [5]. The Fe XAS spectra for $x=0.2$ show Fe in a divalent state, which is in agreement with Ref. [2]. For $x=0.6$ and $x=0.75$ the Fe 2p spectra reveal additional lines at higher photon energies on the L_2 and L_3 edge, which could indicate the measurement of a mixed $\text{Fe}^{2+}/\text{Fe}^{3+}$ valence state. Comparison with multiplett calculations will help to prove this.

*e-mail: ctaubitz@web.de

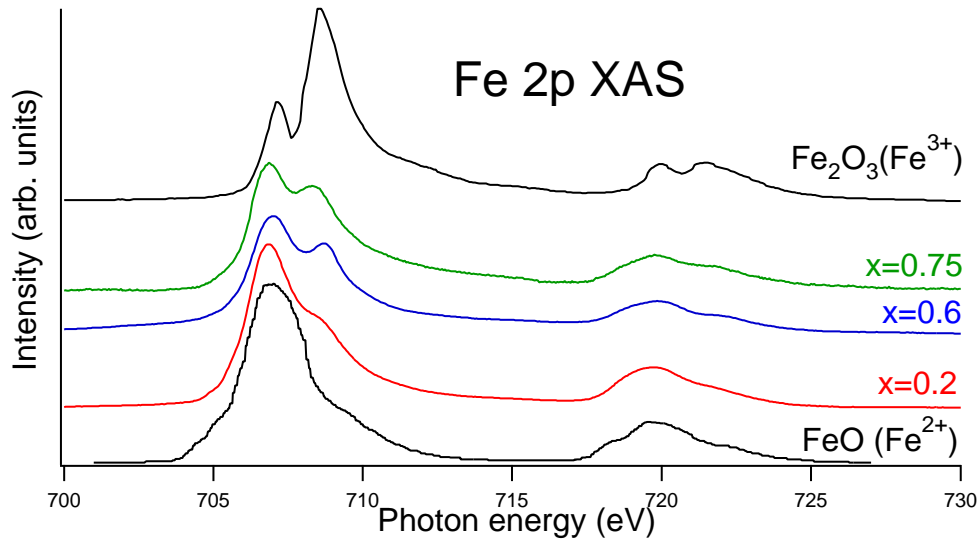


Figure 1: Fe 2p XAS measurement of $\text{Fe}_{1-x}\text{Cu}_x\text{Cr}_2\text{S}_4$ compared with FeO (adapted from [4]) and Fe_2O_3 spectra (adapted from [5]).

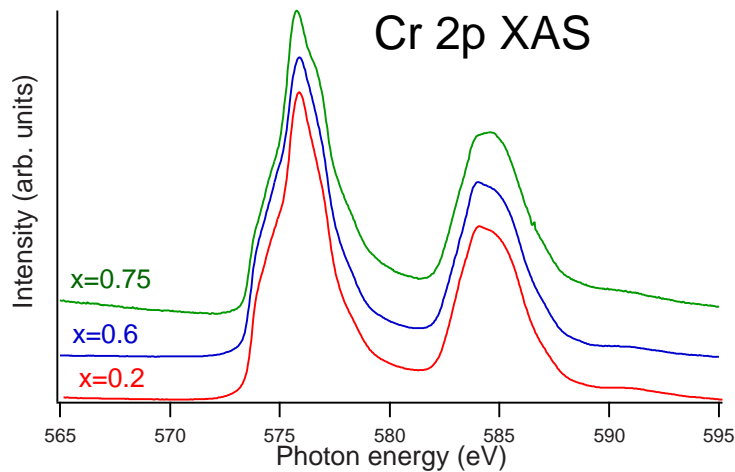


Figure 2: Cr 2p XAS measurement of $\text{Fe}_{1-x}\text{Cu}_x\text{Cr}_2\text{S}_4$.

-
- [1] S. J. Kim, B. S. Son, B. W. Lee, C. S. Kim, *Journal of Applied Physics*. Volume 95, Number 11, (2004)
 - [2] S.W. Han et al., *J. Phys.: Condens. Matter* 18(2006) 7413–7426
 - [3] Aniruddha Dep et al., *Phys. Rev. B* 68 (2003)
 - [4] S. S. Lee et al., *Journal of Applied Physics* 97, 10A309 (2005)
 - [5] K. C. Prince, M. Matteucci, K. Kuepper, S. G. Chiuzaian, S. Bartkowski, M. Neumann, *Phys. Rev. B* 71, 1 (2005)
 - [6] J. B. Goodenough, *J. Phys. Chem. Solids* 30 (1969), 261–280.
 - [7] F. K. Lotgering and R. P. van Stapele, *Solid State Communic.* 5 (1967), 143–146.
 - [8] F. K. Lotgering, R. P. van Stapele, G. H. A. M. van der Steen, and J. S. van Wieringen, *J. Phys. Chem. Solids* 30 (1969), 799–804.

HIKE experiments at KMC-1: Recent Analysis of Thin Film Nanocomposites

E. Lewin¹, E.M.J. Johansson², A. Sandell², M. Gorgoi³, F. Schäfers³, W. Braun³,
H. Siegbahn², M. Stüber⁴, U. Jansson¹, S. Svensson⁵, W. Eberhardt³

¹Dept. of Materials Chemistry, Uppsala University

²Dept. of Physics, Uppsala University

³BESSY GmbH, Berlin

⁴Inst. for Materials Research I, Forschungszentrum Karlsruhe

⁵BESSY and Dept. of Physics, Uppsala University

The following experiments were performed in October 2006 at the KMC-1 beam line [1], using a high kinetic energy XPS, of which the details have been described previously [2]. In this study thin film samples of nanocrystalline TiC (nc-TiC) embedded in an amorphous carbon (a-C) matrix were analyzed, making use of the increased sampling depth of HIKE XPS compared to standard XPS (i.e. with Al K α or Mg K α radiation sources).

Previous studies on nc-TiC/a-C samples have revealed an additional peak in the C1s spectra, besides those assigned to the C-C and C-Ti bonding (see figure 1). This peak has an unclear origin, see [3] and references therein. Since the peak designated C-Ti* in figure 1 mainly has been reported for samples which have been sputter-etched one possible explanation is damage induced during sputter-etching. Standard XPS instruments do not have the sampling depth required to sample beneath the contaminated and oxidized surface layer (up to approximately 10 nm for the analyzed samples). Hence the motivation of using the HIKE experiment is to achieve a greater sampling depth with a truly non-destructive method.

The analyzed samples were deposited at the department of Material Chemistry, Uppsala university (UU) [3], and at the Institute for Materials Research I at Forschungszentrum Karlsruhe (FZK) [4], respectively. In both cases non-reactive magnetron sputtering were used. The two analyzed samples differ slightly in different grain sizes and composition. Additionally, earlier measurements indicate that the surface oxidized layer might be thinner on the FZK-sample.

At KMC-1 spectra were attained using either the Si(111) or the Si(422) monochromators, the former operating with first or third order Bragg angles to maintain a high energy resolution also at high excitation energies. Excitation energies of 2 keV, and 6 keV were used to vary the sampling depth. Figure 2 shows the resulting spectra for samples from UU and FZK.

In figure 1 three contributions to the spectra are separated. The contributions C-C_{matrix} at 284.5 eV, and C-Ti at 281.7 eV are easily identified with the a-C matrix and the nc-TiC particles, respectively [5]. The third contribution, C-Ti*, is the interesting one which origin we are investigating. For the spectra in figure 2 both C-C_{matrix} and C-Ti contributions are readily identified and present for both excitation energies. The presence of surface components gives two extra contributions (C-O,H and C-C,H_{surface}) which, as expected are more pronounced for the lower excitation energy. The C-Ti component increases with increased excitation energy, which suggest that the TiC-particles are not preferentially situated in the near surface region of the sample. This is in agreement with ARXPS studies in literature [6].

A component between the C-C_{matrix} and C-Ti components is present at higher kinetic energies, indicating the presence of a C-Ti* component in the bulk of the sample. The relative intensity of this component is, however, much smaller than in the spectra from the sputter-

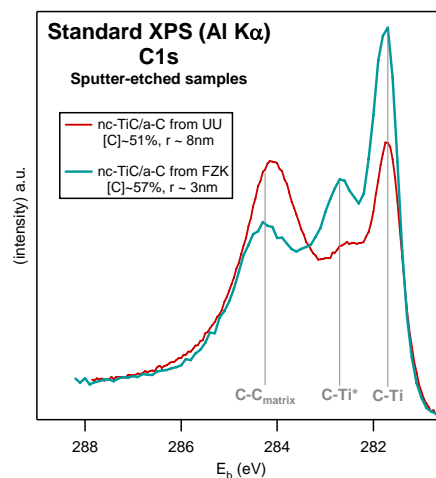


Fig 1 C1s spectra from a standard XPS system (Physical Electronics Quantum 2000, using monochromatic Al K α) of sputter-etched nanocomposite samples from UU (red) and FZK (blue-green)

etched samples. There are hence two possible models for the explanation of these results: 1) there might exist a chemical surrounding for some C-atoms in the samples that is the cause of the C-Ti* component in the spectra, and this type of chemical surrounding is promoted by sputter-etching; or, 2) there could be two overlapping, components, one feature of the nanocomposite and one the result of damage during sputter-etching. The reason for different intensities of the C-Ti* component for the two samples is not clear, but it is noted that several micro-structural parameters differ for the samples.

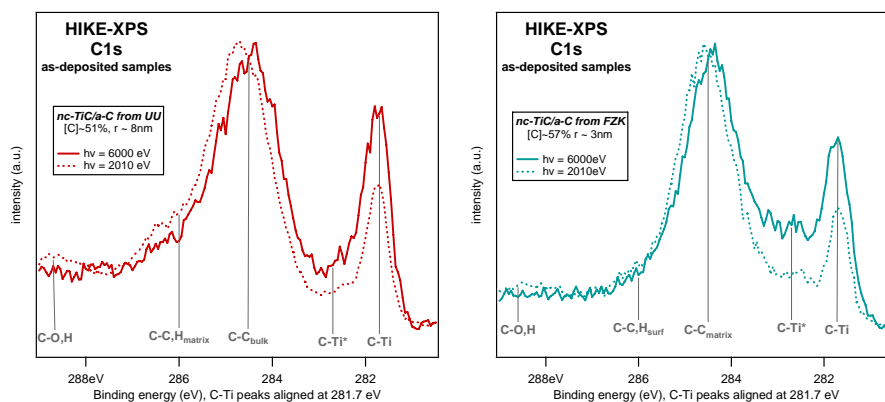


Fig 2 C1s spectra from the HIKE set-up at KMC-1. The same samples as in Fig 1, from UU (left) and from FZK (right). Spectra aligned to the carbidic peak at 281.7 eV. Normalisation has been done on the C-C-peak.

This study illustrates the danger of uncritical use of sputter-etching for spectroscopic bulk characterization and depth profiling. Furthermore the enhancement of the C-Ti* component during sputter-etching casts doubt over the analysis of ternary nanocomposite systems such as Ti-Si-C [7] and Ti-Al-C [8]. For such coatings C-Si or C-Al contribution to the C1s spectra are expected on a position overlapping the sputter-induced C-Ti* component. There might not be any real possibility to quantify chemical information from the C1s peak of such nanocomposites whilst using sputter etching. Hence instruments like the KMC-1 HIKE set-up have great importance in providing sampling of the bulk of samples in a truly non-destructive manner.

Future work may include further analysis of the observed 'true' C-Ti* component, and its possible variation between samples with different chemical and microstructural constitution, with the goal to identify what is the origin of the C-Ti* component. Additionally it could be interesting to use the combination of high resolution and depth sampling of HIKE at KMC-1 to investigate if it is possible to separate a sputter-induced from a 'true' C-Ti* component.

References

- ¹ http://www.bessy.de/users_info/02.beamlines/linespdf/D_01_1B.pdf
- ² P. Bressler et al., *HIKE-experiment at KMC-1: Progress and Proposed Experiments*, BESSY Annual Report 2005.
- ³ E. Lewin et al., *Journal of Applied Physics* **100**, 054303 (2005).
- ⁴ M. Stüber et al., *The correlation between the constitution, microstructural evolution and properties of non-reactively magnetron-sputtered TiC/a-C nanocomposite coatings – a review*, poster presentation at PSE 2006, Garmisch-Partenkirchen, Germany, 10-15 September 2006
- ⁵ *Handbook of X-ray Photoelectron Spectroscopy*; edited by J. Chastain and R. C. King Jr. (Physical Electronics, Inc., 1995).
- ⁶ B. Hornetz et al., *Fresenius Journal of Analytical Chemistry* **349**, 233-235 (1994).
- ⁷ E.g. P. Eklund et al, *Structural, Journal of Vacuum Technology and Science B* **23**, 2486-2495 (2005).
- ⁸ E.g. O. Wilhelmsson et al., *Design of nanocomposite low-friction coatings*, *Advanced Functional Materials*, accepted October 2006.

Non-interacting FePt nanoparticles: Size dependence of the A1-L10 phase transformation

U. Wiedwald, L. Han, B. Kern, A. Klimmer, H.-G. Boyen, and P. Ziemann
Institut für Festkörperphysik, Universität Ulm, Albert-Einstein-Strasse 11, 89069 Ulm, Germany

K. Fauth

Max-Planck-Institut für Metallforschung, Heisenbergstrasse 3, 70569 Stuttgart, Germany

Much effort has been spent over the last years to produce hardmagnetic nanoparticles due to their possible use as an ultrahigh storage medium. The equiatomic FePt alloy system stands in the focus of research since these particles can be prepared by self-assembly on flat substrates by chemical methods in large amounts at low cost. After preparation, however, FePt particles crystallize in the low-anisotropy A1 (fcc) phase and need a high temperature annealing at $T > 600^\circ\text{C}$ to transform towards the highly anisotropic L1₀ (fct) phase. This necessary annealing step is usually accompanied by the formation of larger agglomerates leading to the loss of array quality due to the small separation of particles of 1-3 nm. One simple ansatz to avoid agglomeration is the enhancement of particle separations.

Here, we report on metallic FePt particles with fairly large interparticle spacings of 20-100 nm. The particles are prepared by the self-assembly of metal-salt loaded reverse micelles on Si(001) and MgO(001) substrates. After deposition, the treatment of the specimen by oxygen plasma removes the organics and nucleates the metal salt to metal-oxide particles. A successive hydrogen plasma reduces them to pure metallic particles. In Figure 1 scanning electron microscopy images of 9 nm (a) and 5 nm (b) particles after H plasma treatments are shown. (c) presents the particle ensemble of (b) after annealing at 650°C for 90 min. Obviously, the quality of the array was maintained during this process. The autocorrelation functions were found very similar for the smaller particles before and after annealing, as shown in the corresponding insets. (d) shows the bright-field TEM cross-section image (large scale) of the nanoparticle

ensemble shown in (a) after annealing to 650°C for 45 min. The particles were capped by a silicon oxide film to avoid oxidation. High resolution TEM revealed that most of the nanodots (75–80 %) were single domain (e) with a small fraction of twinned particles (f). Diffractograms are presented in the left top corners of (e) and (f), showing the corresponding crystal structure together with reflections based on Fe₅₀Pt₅₀ bulk alloys (open circles). The FePt particles were brought in ambient conditions to bending magnet beamline PM3 where we attached a custom-built plasma etching system to the beamline end station. After reduction in hydrogen plasma we characterized the particles in

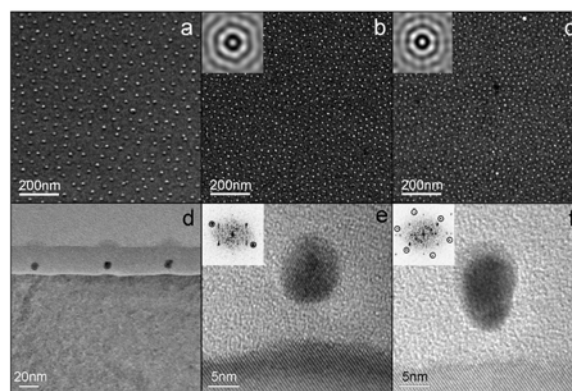


Figure 1 (adopted from [1]): Morphology of Fe₄₈Pt₅₂ nanoparticle arrays on Si(001) substrates prepared by using a micellar method. SEM images of 9 nm particles (a) and 5 nm particles (b), deposited by using a dip-coating process after the different plasma steps. Image (c) presents the ensemble shown in (b) after annealing to elevated temperatures in order to induce the transformation into the L1₀ phase. TEM images were taken by J. Biskupek and U. Kaiser, Univ. of Ulm.

the total electron yield mode in external fields of up to 3 Tesla. Element-specific hysteresis loops were taken at the maximum dichroic signal of the Fe-L₃

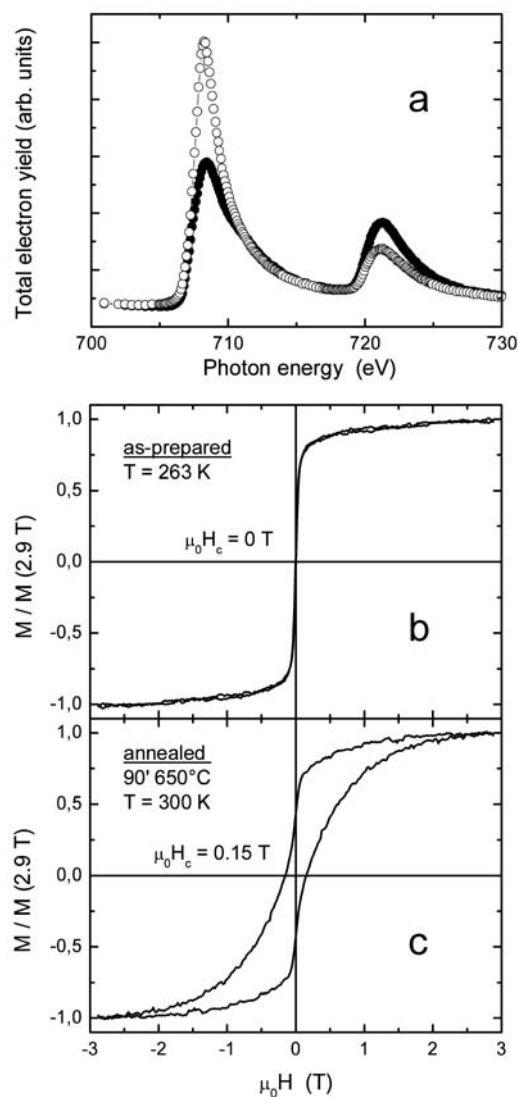


Figure 2 (adopted from [1]): (a) X-ray absorption spectra of metallic FePt nanoparticles in a magnetic field of $\pm 3T$. (b) and (c) show element-specific hysteresis loops taken at the maximum dichroic signal before and after annealing of the particles, respectively.

edge. Within the two beamtimes in 2006 FePt particle ensembles of 3, 4, 5, 7, and 9 nm diameter were characterized. Figure 2 (a) shows Fe-L_{3,2} x-ray absorption spectra of the 9 nm particles in external magnetic fields of $\pm 3T$. The spectral response clearly reveals the absence of any iron oxides. The magnetic moment evaluation of different sized particles is still under consideration. However, by taking element-specific hysteresis loops at different temperatures it becomes possible to track the phase transformation from A1 to L1₀ structures. Figure 2 (b) shows the initial magnetic hysteresis loop of 9 nm particles. At T =

263 K these show a superparamagnetic response while after annealing at T = 650°C for 90 minutes the particles partially transform into the L1₀ structure as indicated by an coercive field of $\mu_0 H = 0.15$ T at room temperature. Further treatment at higher temperatures increases the coercive field (not shown). Size and temperature dependent hysteresis loops revealed the remarkably result that in particles smaller than 6 nm the magnetic anisotropy energy does not rise as high as needed for stable magnetization at room temperature although for all sizes we find an enhanced coercive field after annealing at temperatures above 600°C. Since only magnetically decoupled particles were investigated we applied a modified Stoner-Wohlfarth type of simulation to extract the effective magnetic anisotropy energy K_{eff} from the hysteresis loops. In the A1 state all sizes show a small K_{eff} in the range 1-4 $\times 10^5$ J/m³. After different steps of annealing the evaluation of K_{eff} becomes more complicated since anisotropy distributions have to take into account. Each single particle seems to have its own transition temperature. Further, one has to consider fluctuations of the composition of the alloy particles. Details will be published elsewhere.

From an application point of view it is most desirable to lower the L1₀ ordering temperature of the nanoparticles as much as possible. As previously observed in FePt films this reduction might be achieved by He⁺ ion irradiation producing defects in the material. In a first test experiment, 7 nm FePt particles were bombarded with 350 kV He⁺ ions at a fluence of 10¹⁶ ions/cm² and compared to a non-bombarded reference sample. In Figure 3 the evolution of coercive fields as a function of the annealing temperature is shown. A clearly decrease of the onset of ordering by more than 100 K is observed. The experimental finding of a reduced annealing temperature necessary to form L1₀ ordered particles can be discussed in terms of reduced activation energy of diffusion after He⁺ ion irradiation. Starting from a fully disordered A1

FePt particle towards $L1_0$ chemical order by subsequent annealing allows the extraction of the activation energy of diffusion E_D for constant annealing time t_A . The characteristic diffusion length λ depends on the coefficient of diffusion D and the annealing time t_A , reading $\lambda = (D \cdot t_A)^{1/2}$ with $D = D_0 \cdot \exp(-E_D / k_B \cdot T_A)$. Here, D_0 is the diffusion constant, k_B Boltzmann's constant and T_A the annealing temperature. For alloys with a large uniaxial K_{eff} it has experimentally been demonstrated that the K_{eff} has a nearly linear dependence on degree of chemical order. Using this proportionality for Stoner-Wohlfarth type of particles the coercive field is directly proportional to the degree of chemical order, reading $H_C \sim K / M$. M is the magnetization of a particle. Thus, it becomes possible to determine the activation energy of diffusion E_D from hysteresis loops of non-interacting FePt particles. The slopes of the Arrhenius plots of the coercive field give activation energies of 0.7 eV for He^+ ion irradiated sample and 1.6 eV for the reference sample. These energies are significantly smaller than the volume diffusion energy of 3.0 eV / atom reported for Pt in FePt. Generally, the activation energy in nano-

particles can appear smaller, since the limited dimensions also allow reorganization of atomic structure by surface diffusion. The lowered diffusion energy for He^+ ion irradiated particles can be understood in terms the rigorous enhancement of electronic defects within the particles. Future studies will elucidate whether the ordering temperature can be further lowered by an increased fluence of He^+ ions.

The authors thank P. Walther for access to the SEM and the BessyII staff for their support during beamtime. This project is supported by the Deutsche Forschungsgemeinschaft within SFB 569, Zi317/21-1, and GRK 328 and the Ulmer Universitäts-gesellschaft.

- [1] A. Ethirajan, U. Wiedwald, H.-G. Boyen, B. Kern, L. Han, A. Klimmer, F. Weigl, G. Kästle, P. Ziemann, K. Fauth, G. Schütz, C. Jun, J. Behm, M. Büttner, A. Romanyuk, P. Oelhafen, P. Walther, J. Biskupek, U. Kaiser *Adv. Mater.* **19**, 406 (2007)
- [2] U. Wiedwald, A. Klimmer, B. Kern, L. Han, K. Fauth, H.-G. Boyen, and P. Ziemann, *Appl. Phys. Lett.* **90**, 062508 (2007)

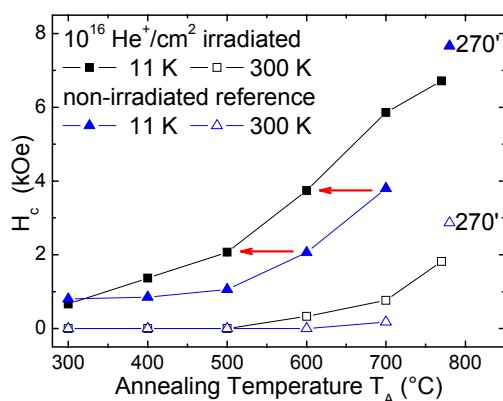


Figure 3 (adpoted from [2]): Experimentally determined coercive fields as a function of 30 min annealing time at temperature T_A for He^+ ion irradiated and reference sample at $T = 11$ K and $T = 300$ K. Additionally H_C is also given after 270 min annealing at $T_A = 775^\circ\text{C}$ for the non-irradiated sample.

HIKE experiments at KMC-1: Studies of Solar Cell Materials

E.M.J. Johansson¹, C. Platzer-Björkman², H. Rensmo¹, A. Sandell¹, H. Siegbahn¹, L. Stolt², M. Gorgoi³, S. Svensson^{1,3}, E. Lewin⁴, F. Schäfers³, W. Braun³ and W Eberhardt³

¹Dept. of Physics, Uppsala University

²Dept. of Engineering Sciences, Solid State Electronics, Uppsala University

³BESSY GmbH, Berlin

⁴Dept. of Materials Chemistry, Uppsala University

Considerable research effort is currently directed towards development of new solar cell devices. These are multilayer structures where both bulk and interface properties need to be appropriately designed for optimal performance. Thin-film solar cells based on $\text{Cu}(\text{In,Ga})\text{Se}_2$ (CIGS cells) contain a thin buffer layer of CdS in their standard configuration. CdS is an n-type semiconductor, which together with the n-type ZnO top-contact layers form the pn-junction with the p-type $\text{Cu}(\text{In,Ga})\text{Se}_2$. In order to avoid cadmium in the device for environmental reasons, Cd-free alternatives are currently investigated. ZnO-based films, containing Mg or S, grown by atomic layer deposition (ALD), have been shown to be viable alternatives to CdS¹. From device modeling it is known that a buffer layer conduction band (CB) position of 0-0.4 eV above that of the $\text{Cu}(\text{In,Ga})\text{Se}_2$ layer is consistent with high photovoltaic performance. For the $\text{Cu}(\text{In,Ga})\text{Se}_2/\text{ZnO}$ interface this position has been measured to -0.2 eV, resulting in increased interface recombination. By including sulfur into ZnO, a favorable CB position to $\text{Cu}(\text{In,Ga})\text{Se}_2$

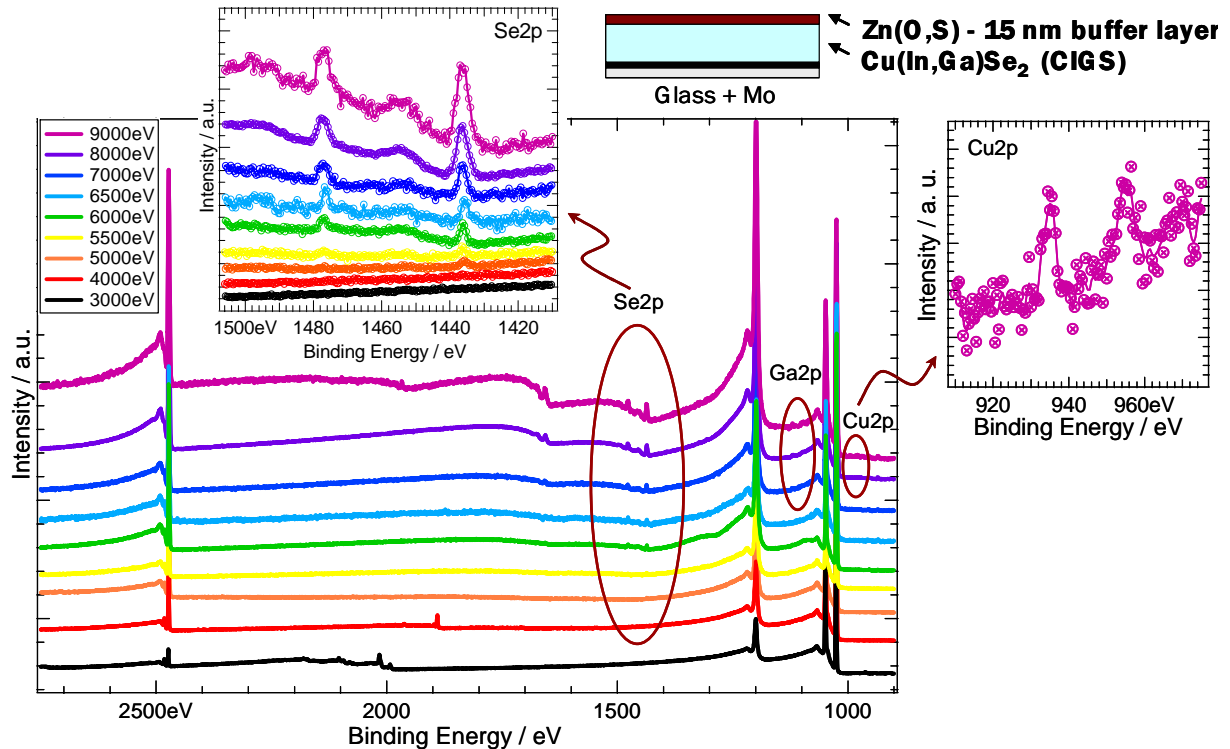


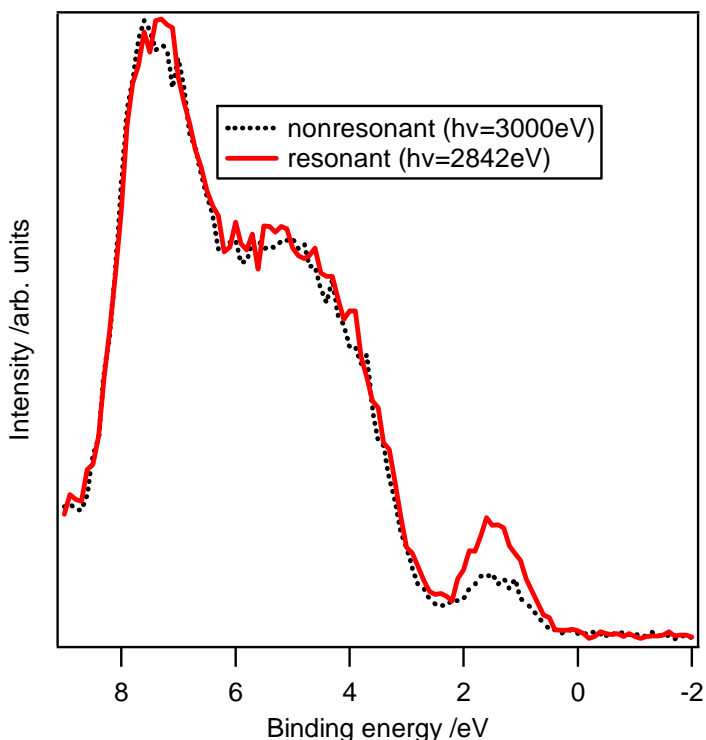
Fig. 1. Overview spectra obtained at photon energies 3000-9000 eV from CIGS film with 15nm Zn(O,S) buffer overlayer.

can be obtained for appropriate sulfur contents, and device efficiencies of up to 16.4% have been

¹ e.g. C. Platzer-Björkman, Band alignment between ZnO-based and $\text{Cu}(\text{In,Ga})\text{Se}_2$ thin films for high efficiency solar cells (PhD thesis, 2006) and references therein

demonstrated¹. The shift in the valence and conduction bands of Zn(O,S) have been shown to be non-linear with respect to the sulfur content, resulting in a large band gap bending. It is thus of considerable interest for the further development of this type of solar cell to study the structure of the buffer Zn (O,S) layer and its energy level alignment as function of composition. Fig. 1 shows HIKE spectra of a CIGS film with Zn (O,S) buffer layer obtained in the energy range 3000-9000 eV. As can be seen, the spectra allow an in-depth scan of the device structure to be made. In particular, the successive appearance of the CIGS film signals (Se2p, Cu2p, Ga2p) with increasing photon energy through the 15nm thick buffer layer can be nicely monitored. These results open up completely new possibilities for the study of properties of real devices of this type, relating structural and electronic properties to device performance.

A different example is shown in Fig. 2, a study of a dye-sensitized solar cell (DSSC) electrode. Such electrodes are synthesized from the assembly of nanoparticles (generally TiO₂) that interconnect and thereby allow for electronic conduction.² The electrodes are modified using molecular components (dyes) and the nanostructured material soaked with electrolytes forming film materials with a huge internal interfacial area, i.e. bulk heterojunctions. An essential aspect of the solar cell function is the initial step photoinduced charge transfer from the HOMO of the dye to the semiconductor conduction band. This process occurs on the fs time scale. This time scale is accessible using the core-hole clock technique³. The use of different core-hole states having different life-times for probing such dynamics is thus of large interest. Fig. 2 shows the valence levels of a TiO₂ electrode sensitized with a dye Ru polypyridine complex, where the HOMO (Ru 4d-derived) peak is located at 1.8 eV. The spectrum excited at the Ru2p-Ru4d energy is seen to



resonantly enhance the HOMO, which indicates that the excited electron is not injected into the semiconductor conduction band during the Ru2p core hole life-time (≈ 300 as). The prospect of higher energy excitation thus provides for a broadened basis for the core hole clock method of determining charge transfer times in these and other related systems, where also injection states of different character may be probed.

Fig. 2 Valence levels of dye-sensitized TiO₂ film

resonantly enhance the HOMO, which indicates that the excited electron is not

injected into the semiconductor conduction band during the Ru2p core hole life-time (≈ 300 as). The prospect of higher energy excitation thus provides for a broadened basis for the core hole clock method of determining charge transfer times in these and other related systems, where also injection states of different character may be probed.

² M. Grätzel, Nature 2001, 414, 338

³ J. Schnadt, P. A. Bruhwiler, L. Pattey, J. N. O'Shea, S. Södergren, M. Odellius, R. Ahuja, O. Karis, M. Bäessler, P. Persson, H. Siegbahn, S. Lunell, N. Mårtensson, Nature 418 (2002) 620-623.

X-ray microscope with mono-capillary condenser

S. Heim, P. Guttman*, S. Rehbein, B. Niemann*, G. Schneider

BESSY GmbH, Albert-Einstein-Str. 15, 12489 Berlin

*IRP, Univ. Göttingen c/o BESSY, Albert-Einstein-Str. 15, 12489 Berlin

Introduction

X-ray microscopy at 3rd generation synchrotron sources is a powerful imaging method for life, materials and environmental sciences [1]. The penetration depth of x-rays through matter permits to study whole biological cells, fully passivated electronic devices or metal layers in an applied magnetic field, to name modern topics of x-ray microscopy research. Many applications in biology require 3-D information, whereas in other scientific fields temporal resolution is essential, e.g., for magnetic storage devices.

The development of a new full-field transmission x-ray microscope (TXM) was motivated by different application fields which we outline first in order to describe their demands on an object stage. Among many scientific questions in life sciences, the cell nucleus which is a vital and complex organelle is still a mystery. How the DNA it contains and its associated proteins are arranged and packaged to fit within this ~10 μm diameter organelle is still unknown. Other questions of packaging concern how much "free" space for diffusion is available in the nucleus.

The current full-field x-ray microscope installed at the undulator U41 was developed for samples in air, e.g., wet cells. Therefore, two pinholes carrying vacuum windows separate the condenser and the x-ray objective chambers. Due to the strong absorption of soft x-rays in air, the distance between these pinholes is typically 300 μm . With such a setup it was possible to perform tomography experiments with samples in small glass tubes [2,3]. However, many samples, e.g., adherent cells, do not fit into a capillary holder and require a specific setup.

Another application field for x-ray microscopy which is of fundamental interest in materials science is electromigration in advanced copper interconnects buried in low- k dielectric materials [4]. In this case, time-resolved x-ray tomography of interconnect structures at about 250°C temperature and at current densities of 10^7 A/cm^2 has to be performed to determine the exact location of void nucleation and migration as well as to measure quantitatively the mass transport. In order to heat and tilt samples, an x-ray microscope with objects in vacuum is advantageous.

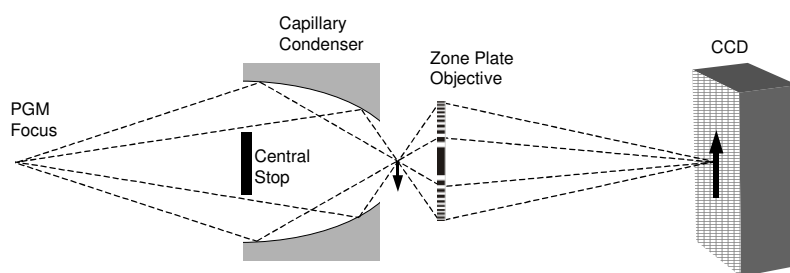


FIGURE 1. X-ray optical setup of the new BESSY full-field TXM with glass capillary condenser and tomography stage for flat sample holders.

During the beam time at the U41-PGM beam line extensive characterizations of different mono-capillary condensers fabricated by the IfG, Berlin, were performed. The results of the steps of a typical alignment procedure are shown in Fig. 3.

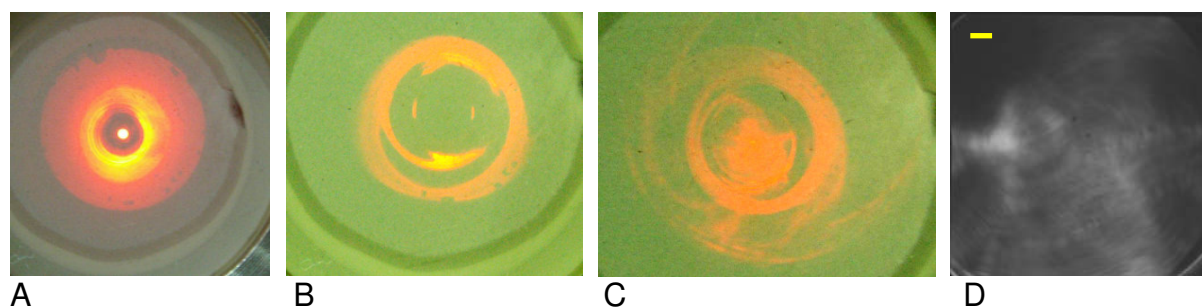


FIGURE 3. A-C: luminescent screen 147 mm behind the object position. A: aligned capillary; B: 15 μm pinhole in focus position; C: enlarged focus using a MZP. D: X-ray microscopy image of the focus (scale bar = 1 μm).

To demonstrate the spectromicroscopy possibilities of the new x-ray microscope an IC sample from AMD was used to record x-ray microscopy images over a wide energy range without changing or moving the mono-capillary condenser (Fig. 4).

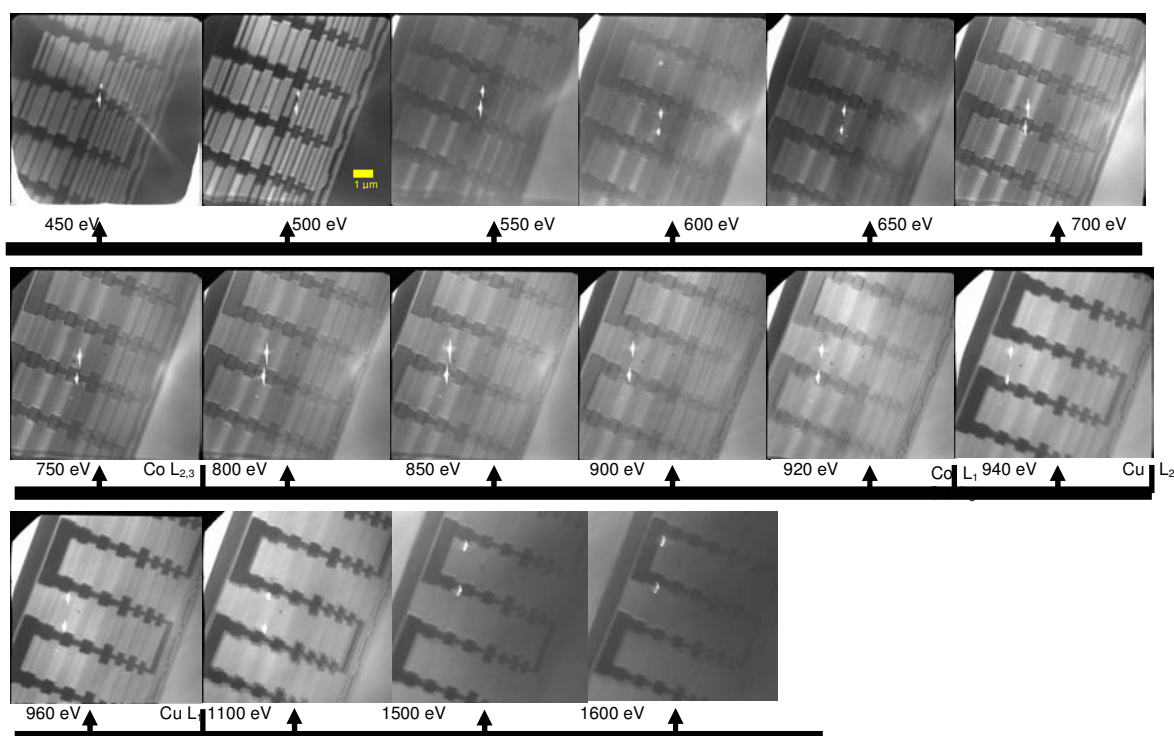


FIGURE 4. X-ray microscopy images of an IC Cu interconnect stack from AMD were recorded in the photon energy range between 450 eV and 1600 eV. Note that different materials in the IC stack are visualized depending on the photon energy.

Conclusions

We demonstrated for the first time that elliptically shaped glass capillaries are well suited as condensers in soft x-ray microscopes. The new BESSY TXM offers the possibility for spectromicroscopy with high energy resolution, because it uses a plane grating monochromator in front of the capillary condenser. In addition, the new optical setup of the TXM supports high resolution tomography of cryogenic or heated samples as it requires no pinhole close to the object plane. In comparison with other full-field x-ray microscopes, the features of the new BESSY TXM are unique.

Acknowledgements

The authors are indebted to D. Bjeoumikhov and N. Langhoff, IfG, Berlin, for the support in fabricating the mono-capillaries, E. Zschech, AMD, Dresden, for providing the IC sample and the beam line staff at the UE46-PGM, namely D. Schmitz, and U41-PGM, namely M. Mast for their great support. Additionally, the authors like to thank S. Werner and D. Eichert for their assistance. This work was supported in part by the BMBF under Contract No. 05KS4BY1/7.

References

1. J. Susini, D. Joyeux and F. Polack, *X-Ray Microscopy*, edited by J. Susini, et al., Proceedings of the 7th International Conference on X-Ray Microscopy, *J. Phys. IV*, **104**, Paris, France, 2003.
2. D. Weiss, G. Schneider, B. Niemann, P. Guttman, D. Rudolph and G. Schmahl, *Ultramicroscopy* **84**, 185-197 (2000).
3. G. Schneider, E. Anderson, S. Vogt, C. Knöchel, D. Weiss, M. LeGros, and C. Larabell, *Surf. Rev. Lett.*, **9**, 177-183 (2002).
4. G. Schneider, S. Rudolph, A.M. Meyer, E. Zschech, and P. Guttman, *Future Fab International* **19**, 115 (2005).

Photoelectron spectroscopy of size- and shape selected, neutral diamond clusters (diamondoids) in the gas-phase

K. Klünder,¹ C. Bostedt,¹ T. M. Willey,² T. van Buuren,² J. E. Dahl,³ S. G. Liu,³
R. M. K. Carlson,³ T. Richter,² P. Zimmermann,¹ T. Möller¹

¹ TU Berlin IOAP, Hardenbergstraße 36, 10623 Berlin, Germany

² Lawrence Livermore National Laboratory, Livermore CA 94550, U.S.A.

³ MolecularDiamond Technologies, Chevron, Richmond CA 94802, U.S.A.

Diamondoids, and in particular higher diamondoids, are ideal, surface passivated diamond clusters [1]. The first diamondoid, adamantane ($C_{10}H_{16}$), consists of the smallest possible single cage unit excised from the diamond lattice with the dangling bonds terminated by hydrogen atoms. The diamondoids are classified by the number of such closed diamond cages. Each subsequent diamondoid adds one additional face-fused cage, which, in the higher diamondoids may be shared by multiple cages. In a broader scientific context the diamondoids, especially the higher ones, are perfect ~nanometer-sized, diamond clusters. They form the link between molecules and semiconductor (nano-) crystals.

We have investigated the occupied density of states for the series of diamondoids from adamantane to cyclohexamantane in the gas phase by means of photoelectron spectroscopy. The experiments were carried out at the Max-Planck Undulator beamline UE56/2-PGM2. As spectrometer a Scienta SES-2002 hemispherical analyzer has been used. The samples were evaporated with a temperature stabilized oven and guided to the interaction region with a heated nozzle.

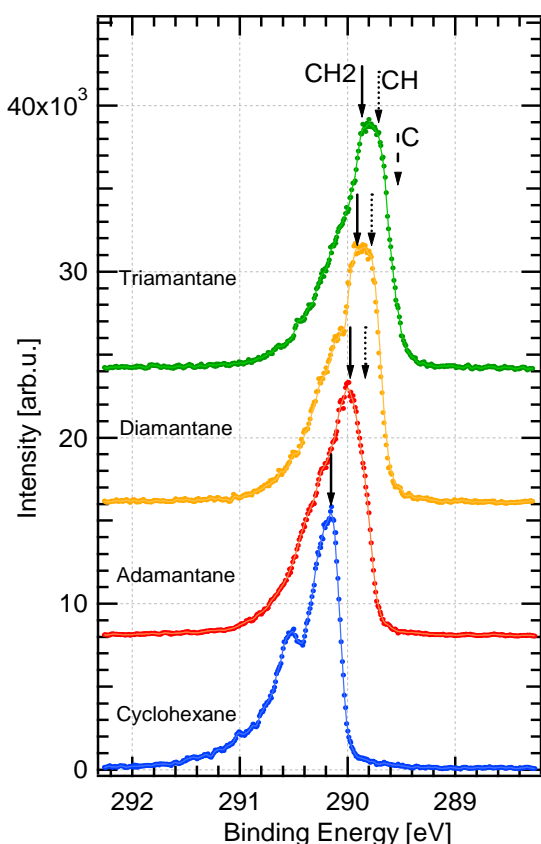


Fig. 1: C1s core level photoemission spectra for the diamondoids series from ada- to triamantane and a cyclohexane reference.

In Fig. 1 the C1s core level spectra for the diamondoid series from adamantane (one cage) up to triamantane (three cages) and a cyclohexane (C_6H_{12}) reference are shown. The spectra have been taken with photon energies of $h\nu=330$ eV. The photon energies have been calibrated with the argon 2p level at 248.4 eV binding energy. The joint resolution of beamline and spectrometer has been determined to be about 120 meV. The cyclohexane reference is comparable to previous high resolution photoemission measurements [2]. The spectrum exhibits the main line at 290.2 eV of a carbon atom with two carbon and two hydrogen neighbors (CH_2 -coordinated). Further, it exhibits clearly resolved vibrational structure from CH stretch modes at 290.6 eV of the core-ionized carbon atom. The broadened tail towards higher binding energies can be attributed to the excitation of additional CCH bending and stretching modes involving the neighboring atoms [2]. For the first diamondoid, adamantane, an additional contribution from CH-coordinated, i.e., three carbon and one hydrogen neighbor, carbon atoms becomes visible.

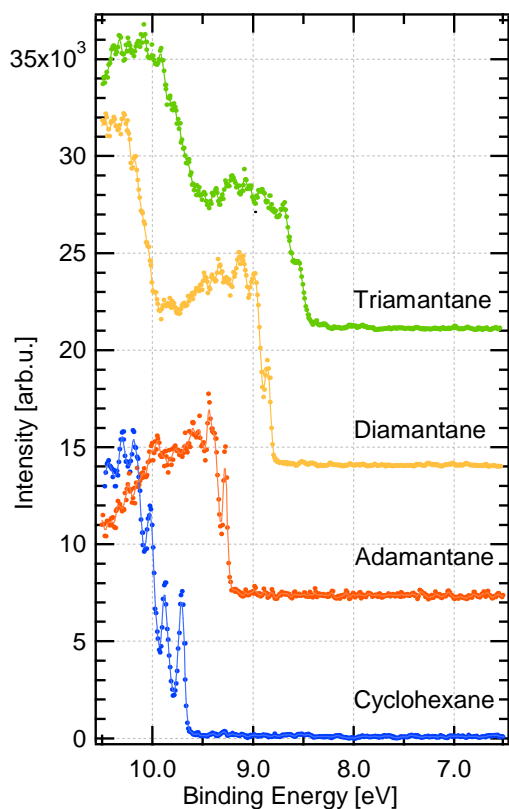


Fig. 2: Valence band photoemission spectra for the diamondoids series from ada- to triamantane and a cyclohexane reference.

This contribution is indicated with the dotted arrow in Fig. 1. With increasing diamondoid size, this contribution grows in line with the atomic coordination ratios in the clusters. For triamantane an additional component due to the existence of one bulk-coordinated carbon atom can be identified as indicated with the dashed arrow. The vibrational features are smeared out in the clusters compared to the cyclohexane reference.

In Fig. 2 photoelectron spectra of the highest occupied states for the same samples are shown. The spectra have been taken with a photon energy of $h\nu=80$ eV. The joint beamline and spectrometer resolution has been determined to be about 50 meV. The highest occupied states clearly shift to lower binding energies with increasing cluster size. The shift from adamantane to diamantane is 430 meV and from diamantane to triamantane 350 meV. Further, for the cyclohexane reference sharp features on top of the valence band are apparent which diminish for increasing cluster sizes. These features can again be attributed to vibrational excitations.

Size dependent changes in the electronic structure and quantum confinement effects in sub-nanometer sized diamond clusters have been subject to discussion recently. For the interpretation of our photoemission valence data we need to take size dependent screening effects into account [3]. In first approximation, changes in the screening function can be extrapolated from the core level shifts, i.e., subtract the core level shifts from the valence band data. This way we deduce valence band edge shifts of about 300 meV between adamantane and diamantane and about 250 meV between diamantane and triamantane. These findings are in reasonable agreement with previous x-ray fluorescence measurements on deposited diamondoids [4], and they agree with experimental investigations [5] and theoretical predictions [6] that quantum confinement effects in sub-nanometer diamond occur in the valence band only.

We gratefully acknowledge the support of all Bessy staff, especially from Willy Mahler and Birgit Zada for their help during the beamtime. T.M. Willey and T. van Buuren acknowledge support from the Office of Basic Energy Sciences, Division of Materials Science, under the auspices of the U.S. Department of Energy by the University of California, Lawrence Livermore National Laboratory under Contract No. W-7405-ENG-48.

References

- [1] J. E. Dahl, S. G. Liu, and R. M. K. Carlson, *Science* **299**, 96 (2003).
- [2] V. M. Oltedal et al., *Phys. Chem. Chem. Phys.* **6**, 4254 (2004).
- [3] J. J. Pireaux et al., *Phys. Rev. A* **14**, 2133 (1976).
- [4] T. M. Willey, C. Bostedt, T. van Buuren, et al., *Phys. Rev. B* **74**, 205432 (2006).
- [5] T. M. Willey, C. Bostedt, T. van Buuren, et al., *Phys. Rev. Lett.* **95**, 113401 (2005).
- [6] N. D. Drummond, A. J. Williamson, R. J. Needs, et al., *Phys. Rev. Lett.* **95**, 096801 (2005).

Electronic Properties of Highly Ordered CuPc Thin Films

Gianina Gavrila¹, Stefan Seifert¹, Walter Braun² and Dietrich R.T. Zahn¹

¹Chemnitz University of Technology, Semiconductors Physics Department, D-09107, Chemnitz.

²BESSY GmbH, Albert-Einstein-Straße15, D-12489, Berlin.

Highly ordered organic crystals or thin films usually show to improved transport properties and that the orientation of organic molecules is crucial for device efficiency. One intriguing way to control the ordering and the molecular orientation of organic molecules on inorganic substrates is by designing the geometric structure of the substrate surface, e.g. by the steps and terraces of vicinal surfaces.

Consequently the present work was directed towards a comprehensive study of the electronic properties and of the molecular orientation of highly ordered organic thin films, *i.e.* copper phthalocyanine (CuPc) on antimony (Sb) passivated vicinal silicon surfaces. We therefore performed a series of photon energy dependent photoemission measurements and a systematic Near Edge X-ray Absorption Fine Structure (NEXAFS) spectroscopy study of thin CuPc layers grown on Sb passivated Si(111)-1x1. The measurements were performed at the Multi-User-Multi-Purpose-STage for Angular Resolved Photoemission (MUSTANG) at the Russian German beam line at BESSY. The substrates were passivated *in situ* by antimony. The resulting antimony passivated Si(111) surfaces, from now on being denoted as Sb-Si(111)-1x1, exhibit a 1x1 surface reconstructions as judged by low energy electron diffraction. Additional details about the passivation process and surface reconstruction are given elsewhere [1]. The CuPc layers were deposited by organic molecular beam deposition (OMBD) onto substrates kept at room temperature. The nominal layer thickness was monitored by a quartz micro balance. The C-K edge NEXAFS measurements were performed by sweeping the excitation energy between 280 eV and 320 eV and recording electrons having a selected kinetic energy of 50 eV. The measured data were corrected for the photon flux by division of the spectra by the electron yield of the clean Sb-Si(111)-1x1 sample and normalized to the absorption step edge at 320eV. Valence band photoemission spectra (VB-PES) were measured at normal emission with an incident angle of light of 45°. The total resolution of the VB-PES spectra over the whole energy range used in the present measurements was better than 0.08 eV as estimated from the Fermi edge spectra of gold.

Figure 1 shows the photon energy dependence of normal emission VB-PES spectra in the HOMO and HOMO-1 region of 10 nm CuPc film deposited onto Sb-Si(111)-1x1. The HOMO feature near 1.5 eV hardly shows any shift in its position, while a more pronounced shift of about 0.25 eV is observed for the HOMO-1 feature above 3 eV. An indication for the origin of this shift as a function of the excitation energy is given in figure 1(b) which shows a comparison between the experimental data and the calculated DOS using Gaussian '03 [2]. It can be seen that the molecular orbitals (MOs) below 4 eV predominantly have π character. While a dispersion of the HOMO feature, which has a single π -character is hardly noticeable, the richness of HOMO-1 feature in π - molecular orbitals (between 3.2 eV and 3.6 eV there are six MOs with π -character) most probably explains the relatively strong peak shift as a function of excitation energy. It is worth noticing that there is almost no change in the shape of HOMO-1 as a function of the excitation energy. This finding indicates that the photoionization cross

section of the contributing MOs at different photon energies varies at the same rate. Therefore changes in the position of the HOMO-1 feature due to the photon energy dependent cross section of the contributing MOs can be excluded.

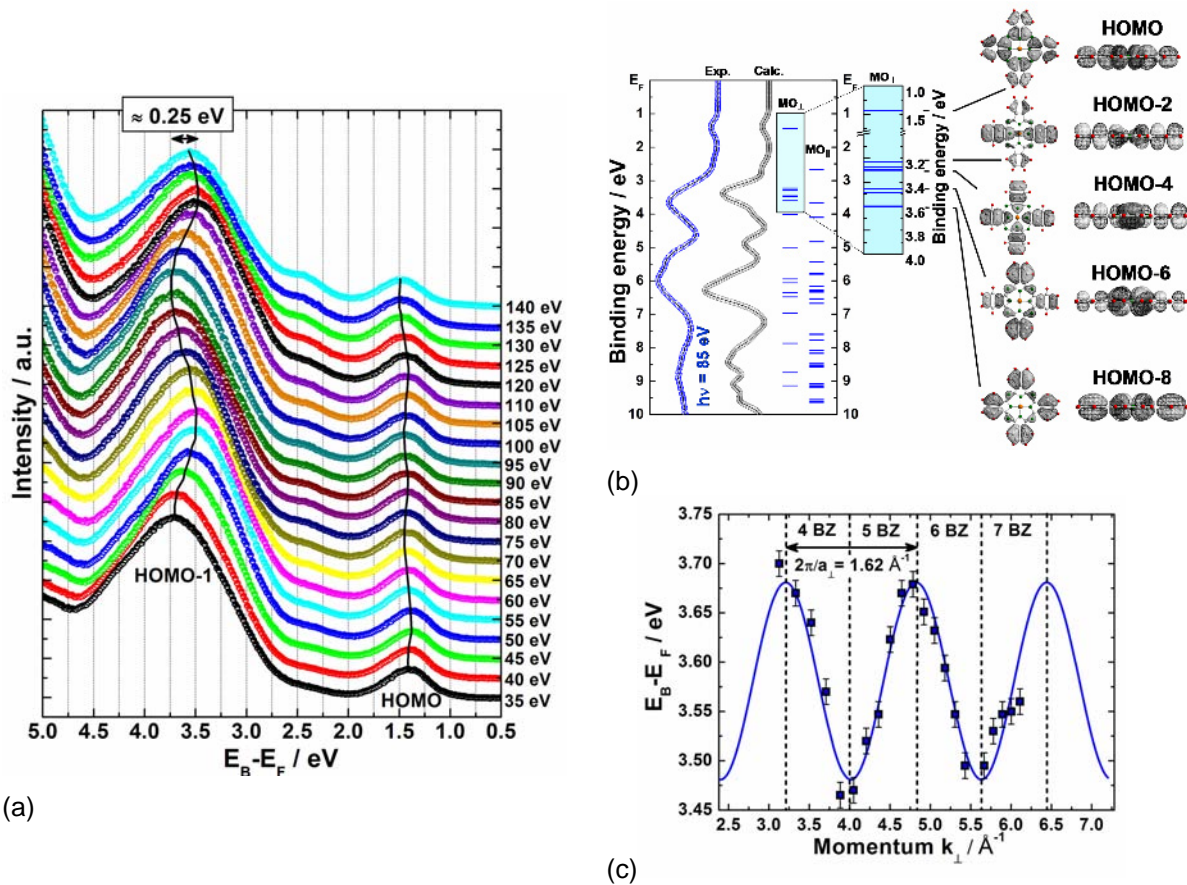
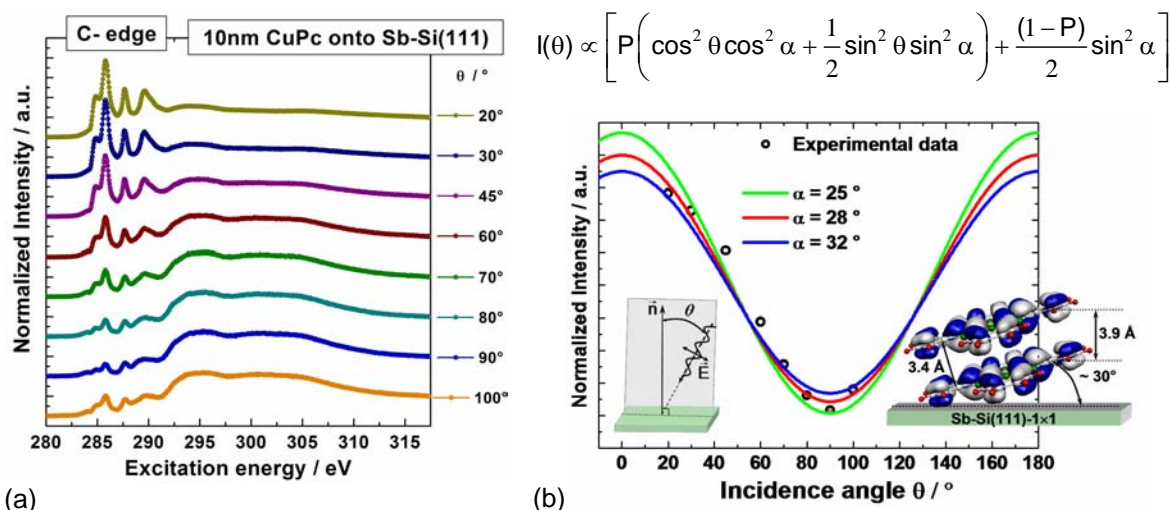


Figure 1. (a) Measured valence band spectra of 10 nm CuPc film deposited onto Sb passivated Si(111)-1x1 surfaces in the photon energy range of $35 \leq h\nu \leq 140\text{eV}$. (b) Valence band spectra measured at 85 eV and the calculated DOS of CuPc using a Gaussian broadening of the energy levels with a FWHM of 0.4 eV. Right side- the MO energies shown by horizontal bars and selected by their character (π - perpendicular to the molecular plane (MO_\perp) or σ - parallel to the molecular plane (MO_\parallel)). In order to picture the π symmetry of the MOs the charge contour of some selected MOs with side and top view are presented as well. (c) Experimental dispersion for the HOMO-1 band (filled squares) and the best fit curve (line) in the tight-binding model.

The energy band dispersion relation for CuPc is obtained by applying a one-dimensional tight-binding theory to the HOMO-1. For the formation of a 1D energy band it is assumed that a unit, *i.e.* a molecule, is repeating along an axis x with a period a_\perp . The interaction only takes place with the nearest neighbours its strength being defined by the value t , the transfer integral. By analogy to the Hückel theory, the energy E_B for the HOMO-1 is expressed in terms of wave vector k_\perp as: $k_\perp = [2m^* \times (h\nu - E_B - V_0)]$ and $E_B(k_\perp) = E_B^0 + 2t\cos(a_\perp \times k_\perp)$, where m^* is the effective mass of the electron and V_0 the inner potential which is treated as a fit parameter. Using the normal emission spectra and these two equations the energy of HOMO-1 band and its momentum can be calculated. The results of the best fit for the dispersion along with the experimental data are shown in figure 1(c). A cosine fit of the experimental data was performed where the inner potential V_0 and the transfer

integral t are the two parameters. The best fit between calculated and experimental data is provided by the following set of parameters – inner potential $V_0 = -5.9$ eV and transfer integral $t = 0.045$ eV. However, information on the intermolecular spacing of the present system, a_{\perp} , is necessary and this can be provided by the NEXAFS results.



(a) Figure 2 (a) The Carbon K-edge NEXAFS spectra of a 10nm CuPc film on Sb-Si(111)-1x1 as a function of the angle of incidence. (b) Normalized resonance intensity of the π^* orbitals as a function of the incidence angle θ – experimental data and fit. The sketches illustrate the experimental geometry for the polarized light (left) and the orientation of the molecules on the substrates together with the calculated intermolecular spacing $a_{\perp} = 3.9$ Å.

The angular dependent carbon K-edge NEXAFS spectra of a 10nm thick layer of CuPc onto Sb-Si(111)-1x1 are shown in figure 2 (a). Their quantitative analysis is provided in figure 2 (b). The normalized resonance intensity of the π^* orbitals is fitted using the formula given above figure 2(b), where P is the degree of polarization, θ is the angle of incidence and α the molecular tilt angle. The fitted curve is presented in figure 2(b). The average molecular tilt angles of the CuPc molecules with respect to the substrate surface is determined to be $(30^{\circ} \pm 3^{\circ})$.

With the distance between the intermolecular planes of 3.4 Å, as experimentally determined [3], we can calculate the length of repeating units (lattice spacing normal to the surface) as $a_{\perp} = 3.9$ Å as depicted in the figure 2 (b). The calculated a_{\perp} gives rise to the best fit of the energy dispersion to the experimental data using an inner potential V_0 of -5.9 eV and the transfer integral of 0.045 eV. As shown in this work, we succeeded to observe the HOMO-1 band dispersion for CuPc along the surface normal. The energy-band dispersion is extended over more than three Brillouin zones (4th, 5th, 6th and 7th zone) with a bandwidth of about 0.25 eV.

The authors would like to use this opportunity to thank all BESSY staff members for their assistance during beam times. We also acknowledge the financial support granted by the BMBF (FK MUSTANG 05KS40C1/3, FK 05KS1OCA1).

[1] S. Seifert, G.N. Gavrilu, D.R.T. Zahn, W. Braun, BESSY Jahresbericht, 221, 2005.
 [2] Gaussian 03 (Revision A.1), Gaussian Inc., Pittsburgh PA, 2003.
 [3] R. Hiesgen, M. Rabisch, H. Böttcher, and D. Meissner, Sol. Energ. Mat. Sol. C. 61, 73, 2000.

Time-Resolved UV/VIS Fluorescence of 2p-excited Argon Clusters

R. Flesch, A. Wirsing, J. Plenge, M. Meyer*, E. Rühl

Institut für Chemie u. Biochemie, Freie Universität Berlin, Takustr. 3, 14129 Berlin

* LIXAM, Centre Universitaire Paris-Sud, Bâtiment 350, F-91405 Orsay Cedex, France

Fluorescence spectroscopy has recently been shown to be a versatile tool to study the dynamics of inner-shell relaxation processes of atoms [1], molecules [2], and clusters [3]. The main advantage of fluorescence spectroscopy is an extremely high spectral resolution, since the radiative decay is independent of the energy and the bandwidth of the exciting photon.

We have recently studied fluorescence yields and dispersed fluorescence spectra of 2p-excited argon clusters [3]. These studies, however, were time-independent so that no information on the lifetime of the radiating systems could be obtained. We extend this work towards time-resolved studies so that temporal profiles of cluster fluorescence are obtained.

The experiments are carried out at the U49/2 PGM1 beamline at BESSY. A Seya monochromator ($f=20$ cm) in combination with a cooled photomultiplier (Hamamatsu R 6060) is used to disperse and detect fluorescence light. Clusters are prepared by an adiabatic expansion of neat argon through a continuous nozzle ($d=50$ μm). The jet is not skimmed so that it contains a significant amount of atomic argon. Calibration of the fluorescence monochromator is carried out by utilizing the well-known B-X transitions in N_2^+ [4]. The excitation energy is set to 290 eV for most experiments since Ar cluster fluorescence is known to be intense above the Ar 2 p ionization threshold [3].

Fig. 1 shows the fluorescence of the sample under conditions where only atomic argon is present in the beam. Fluorescence is recorded at $\lambda=212$ nm where cluster fluorescence is known to be strong. The observed temporal profile is interpreted as a convolution between the known instrumental response function and the decay function of the radiating system. It is found that the decay occurs monoexponentially with a time constant $\tau=3.44$ ns. It is assumed that the observed emission is due to doubly charged argon. Ar^{++} shows a set of strong emission lines around 212 nm [5]. Normal LMM Auger spectra of Ar have indicated earlier that a manifold of Ar^{++} states occur as satellite lines, resulting from a variety of shake channels [6].

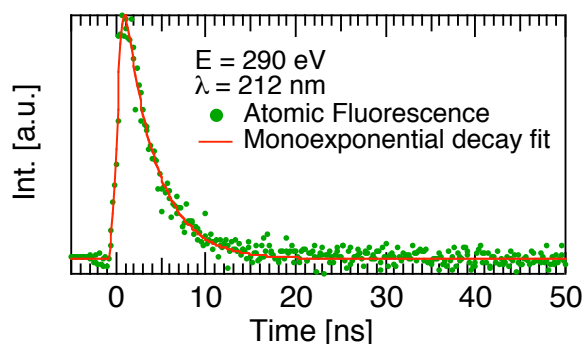


Fig. 1: Temporal profile of atomic argon fluorescence after 2p-excitation.

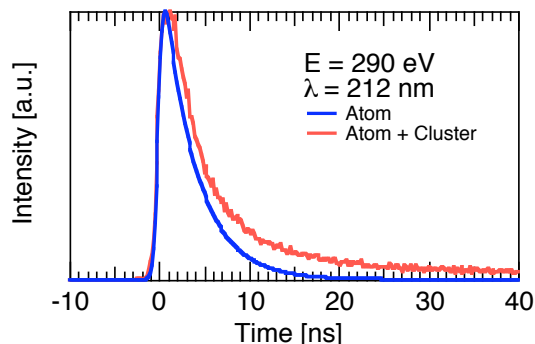


Fig. 2: Temporal profiles under different expansion conditions. See text for details.

Fig. 2 displays the time-resolved fluorescence under conditions where clusters are present in the beam (red profile) together with atomic fluorescence (blue curve). The profile under cluster conditions is significantly broadened compared to the atomic spectrum. It is concluded that the experimental data contain a significant amount of fluorescence from clusters *in addition* to an atomic signal.

Results of a fit over the temporal profile under cluster conditions are shown in Fig. 3. The cluster contribution to the temporal profile is suitably described by a sequential decay function which contains two time constants, where $\tau_1=18.9$ ns, and τ_2 is on the order of 1–2 ns. The following conclusions are consistent with these findings:

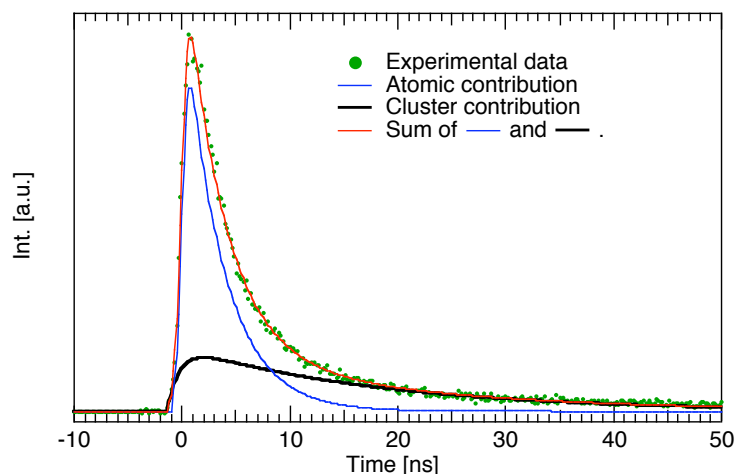


Fig. 3: Analysis of the temporal profile of a mixture of 2p-excited argon atoms and clusters.

(a) The atomic contribution is significant also under cluster conditions, and ~60% of the total signal intensity within the first 50 ns come from atomic emission. This is of importance when fluorescence yields are considered.

(b) The observed cluster fluorescence occurs in a cascade of steps where the first step is very slow compared to atomic fluorescence.

Additional experiments have been carried out under similar conditions, but for different fluorescence wavelengths. These will be analyzed in the near future to obtain a consistent picture of radiative decay processes in these core-excited clusters.

References

- [1] R. Flesch, H.-W. Jochims, J. Plenge, E. Rühl, *Phys. Rev. A* 61, 62504 (2000).
- [2] M. Meyer, P. O’Keeffe, J. Plenge, R. Flesch, E. Rühl, *J. Chem. Phys.* 125, 314206 (2006).
- [3] I. L. Bradeanu, R. Flesch, M. Meyer, H.-W. Jochims, E. Rühl, *Eur. J. Phys. D* 36, 173 (2005).
- [4] K. P. Huber, G. Herzberg, *Molecular Spectra and Molecular Structure, IV. Constants of Diatomic Molecules*, Van Nostrand, New York (1979).
- [5] Yu. Ralchenko, A.E. Kramida, J. Reader, *NIST Atomic Spectra Database, NIST Standard Reference Database #78* (2006) (<http://physics.nist.gov/PhysRefData/ASD/index.html>).
- [6] E. J. McGuire, *Phys. Rev. A* 11, 1880 (1975) and references cited therein.

Identification of complex energy features in AAFM $\text{La}_1\text{Sr}_2\text{Mn}_2\text{O}_7$

H. F. Li,¹ Y. Su,¹ A. Nefedov,² Tapan Chatterji,³ J. Persson,¹ P. Meuffels,¹ and Th. Brückel¹

¹Institut für Festkörperforschung, Forschungszentrum Jülich GmbH, D-52425 Jülich, Germany

²Institut für Experimentalphysik/Festkörperphysik, Ruhr-Universität Bochum, Germany

³Institut Laue-Langevin, BP 156, F-38042 Grenoble Cedex 9, France

I. INTRODUCTION

Strongly correlated electron systems such as 3d transition-metal oxides present exciting fundamental properties, e.g. the extraordinary colossal magnetoresistance (CMR) effect or the multiferroic behaviour in manganites. Their rich structural, magnetic and electronic properties are governed by the interplay of lattice, spin, charge and orbital degrees of freedom. Identification of the ordered phases is a prerequisite for understanding the physical properties and unusual phenomena. The emerging resonant soft x-ray scattering (RSXS) technique is a powerful method for probing these phases individually [1-3]. Meanwhile, the development of correct theoretical models is also the key step to make the real physics clear. To extract the meaningful information from the observed energy dependences, a theoretical modeling to the orbital and magnetic ordering spectra of $\text{La}_{2-2x}\text{Sr}_{1+2x}\text{Mn}_2\text{O}_7$ with multiplet calculations in a crystal field shows the presence of a relatively weaker Jahn-Teller distortion in addition to possible Mn^{3+} and Mn^{2+} -like valence fluctuations [4]. However, this simulation cannot even describe the main experimental resonant signals correctly, saying nothing of the subtle features. Thus identifying the origins of various features in the energy spectra is critical important. In this report, we have performed a systematic study on the energy and temperature dependences of the (0 0 1) *A*-type antiferromagnetic (AAFM) reflection in 50% hole-doped $\text{La}_1\text{Sr}_2\text{Mn}_2\text{O}_7$ manganite. RSXS experiments were carried out with the two-circle ALICE diffractometers [5] equipped with our goniometer at the UE56/1-PGM-b beamline of BESSY-II, Germany.

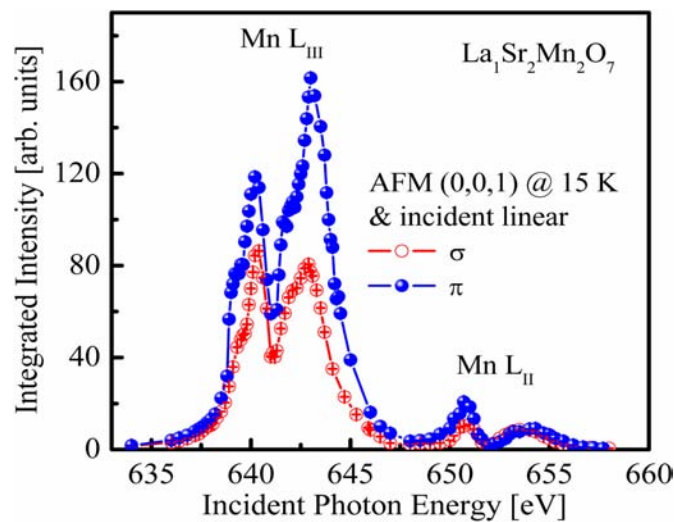


FIG. 1. Energy dependence of (0 0 1) superlattice reflection of a $\text{La}_1\text{Sr}_2\text{Mn}_2\text{O}_7$ single crystal recorded over the Mn $L_{\text{II, III}}$ edges at constant wave vector with incident linear σ and π polarizations at 15 K.

II. RESULTS AND DISCUSSION

Figure 1 shows the energy dependence of the integrated intensity at a fixed wave vector $Q = (0\ 0\ 1)$ over the Mn $L_{\text{II, III}}$ edges ($2p$ to $3d$) where it is expected to probe the $3d$ electronic states directly. The (0 0 1) reflection corresponds to the long range AAFM ordering along the c axis ($I4/mmm$). Both spectra at incident linear σ and π polarizations are dominated by scattering at the Mn L_{III} edge. There four distinct features are present: two peaks and their respective shoulders. The intensity ratio between the two main

features 2 and 4 at the Mn L_{III} edge is inverted with different polarizations. Polarization dependence is thought to be a sensitive measurement to probe the Mn valence states. Comparing the rude theoretical calculation [4], the energy spectrum with π polarization is probably ascribed to the Mn³⁺/Mn⁴⁺ type, while with σ polarization it mostly comes from the Mn³⁺/Mn²⁺ type. The temperature dependences of the AAFM (0 0 1) superlattice reflection recorded at the six energies corresponding to the six clear features 1, 2, 3, 4, 5 and 6 as labeled in Fig. 1. are shown in Figure 2. All of them display a similar temperature dependence indicative of the same origin: magnetic order parameter. The Néel temperature is thus determined as $T_N \approx 160$ K. The step feature around 130 K in temperature dependence is probably related to the setting up of CE-type spin ordering, consistent with neutron diffraction studies [6].

Meanwhile, we tried to search for the possible resonant magnetic exchange scattering at the oxygen K edge. However, no resonance of AAFM (0 0 1) above the background exists over the oxygen K edge.

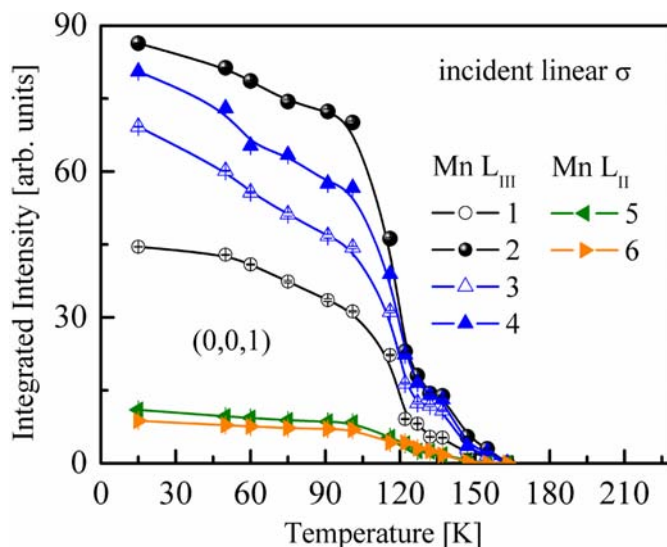


FIG. 2. Temperature dependent integrated intensity (measured in the longitudinal direction) of the AAFM (0 0 1) superlattice reflection of a $La_1Sr_2Mn_2O_7$ single crystal recorded at the six energies corresponding to the six clear features 1, 2, 3, 4, 5 and 6 as labeled in Fig. 1.

III. SUMMARY

We have investigated the spin ordering of a bilayered $La_1Sr_2Mn_2O_7$ single crystal by RSXS at the Mn $L_{II,III}$ edge. Huge resonances were observed in the AAFM (0 0 1) superlattice reflection with strong incident linear polarization dependence at 15 K. In particular, we have confirmed that six obvious features exist in the energy spectra of (0 0 1). The temperature dependences demonstrate that the six features purely originate from the spin ordering, supporting definitive experimental data for establishing the correct theoretical model.

ACKNOWLEDGEMENTS

We are grateful for the excellent technical support from BESSY-II, Germany. This work was partially supported by the BMBF under contract No O3ZA6BC2.

REFERENCES

- [1] S. B. Wilkins, P. D. Spencer, P. D. Hatton, *et al.*, Phys. Rev. Lett. 91, 167205 (2003).
- [2] K. J. Thomas, J. P. Hill, S. Grenier, *et al.*, Phys. Rev. Lett. 92, 237204 (2004).
- [3] J. H. Martin, J. Garcia, G. Subias, *et al.*, Phys. Rev. B 73, 224407 (2006).
- [4] S. B. Wilkins, N. Stojic, T. A. W. Beale, *et al.*, J. Phys.: Condens. Matter **18**, L323 (2006).
- [5] J. Grabis, A. Nefedov, and H. Zabel, Rev. Sci. Instr. 74, 4048 (2003).
- [6] M. Kubota, H. Yoshizawa, Y. Moritomo, *et al.*, J. Phys. Soc. Jpn. **68**, 2202 (1999).

The hole density of single crystals Pb-Bi2201 determined by XAS

A.K. Ariffin, B. Müller, R. Mitdank, L. Dudy, H. Dwelk, A. Krapf, C. Janowitz, and R. Manzke

Humboldt-Universität zu Berlin, Institut für Physik, Newtonstr. 15, D-12489 Berlin

In order to understand superconductivity in the oxide-based high temperature superconductors, which is assumed to be carried by holes, it is important to know the hole content of these materials. The x-ray absorption spectroscopy has been proven as a reliable technique to evaluate the hole content n_H in the oxide-based polycrystalline high temperature superconductor materials. This method has been employed successfully for polycrystalline LSCO [1] and BSCCO [2-4]. However, for single crystals this absorption signal is dependent on the orientation of the electrical field vector of the incident synchrotron light. This dependence on the polarization geometry has been investigated for single crystals Bi(Pb)-2201 with La concentration ranging from $x=0$ to 0.62. Then the hole content was determined

Samples were grown out of a stoichiometric melt by standard metallurgical methods. The chemical compositions and transition temperature, T_c of the samples were studied by measuring EDX and ac susceptibility respectively. The La content analyzed by EDX varied from $x=0.0$ to $x=0.62$. The superconducting properties were determined by ac susceptibility measurements. An example for ac susceptibility result is given in figure 1 below.

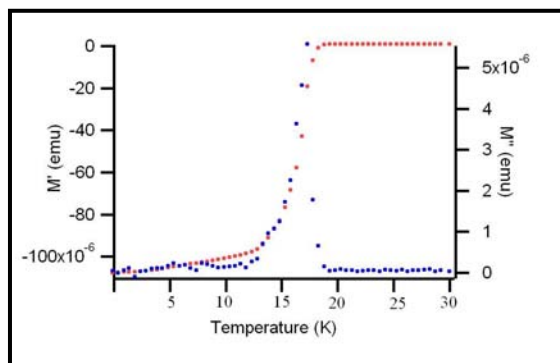


Figure 1: AC susceptibility measurement at optimum doping ($x=0.4$). Red M' (real part) and blue M'' (imaginary part of susceptibility)

The analysis was done at different levels of La doping. We took 3 particular samples, with La concentrations, $x=0$, 0.4, and 0.62. The transition temperature was, $T_c=0$ K for sample with $x=0$ and 0.62 and $T_c=18.0$ K for sample with $x=0.4$. All the samples were grown under identical growth conditions to achieve comparability. These conditions do not lead to highest T_c possible for optimum doping, which should be at La concentration of $x=0.4$. The orientation of single crystals was determined by LEED.

The XAS measurements were performed at the BESSY PM3 beamline using an XAS-chamber where both, total electron yield and the fluorescence signal, can be recorded simultaneously. The vacuum in the chamber was maintained to be in the range of 10^{-9} mbar. All measurements were conducted at room temperature. The X-ray beam was incident normal to the sample and therewith also normal to the CuO_2 -plane. The XAS signal was recorded at the Cu- L_3 edge ($E=925-938$ eV), which was then evaluated for a quantitative study of the hole contents. The signal consists of a so called “white line”, representing the excitation of Cu-2p-electrons into Cu-3d states, and a satellite peak, appearing as a high energy shoulder, with an intensity varying according to the hole content of the sample as shown in figure 2 below.

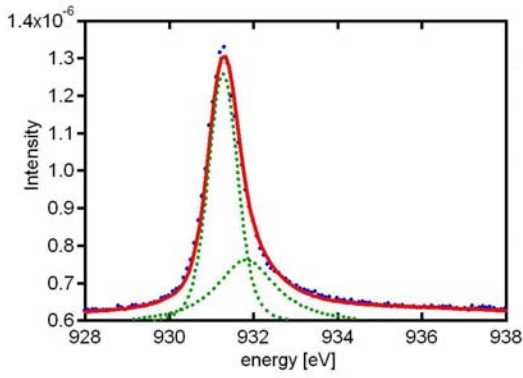


Figure 2: Exemplary Cu- L_3 XAS-spectrum of the Bi(Pb)-2201 sample with $x=0.62$. The spectrum was taken at a rotation angle of 71° around the surface normal. Blue dotted lines are the experimental data; red dotted lines refer to the fits by Voigt function with baseline. Two fitted peaks of Cu white line and satellite peak are represented by green dotted lines

To obtain a numerical value for the hole content the ratio of the intensity of the satellite peak to the intensity of white line plus satellite peak has to be evaluated [4] and it is given as

$$n_h = \frac{I_{\text{satellite}}}{I_{\text{satellite}} + I_{\text{whiteline}}} \quad (1)$$

The procedure gave good results for polycrystalline materials [2]. However, from the first measurements done on Bi(Pb)-2201 single crystals where the data were collected at random polarization geometry within the CuO_2 -plane, the results did not exhibit the same behaviour as polycrystalline material [4]. Considering that, the fluorescence and the electron yield signal were measured simultaneously at normal incidence while rotating the sample continuously around the sample normal and thereby altering the polarization geometry defined by the orientation of the electrical field vector of the photon beam and the orbitals in the CuO_2 -plane. The modulations for the analyzed samples are shown in figure 3 below. The modulations for the shown samples of a La concentration of $x=0.4$ and $x=0.62$ respectively, show some similarity, where the peaks occur at ΓM direction. The angle between two peaks is approximately 90° .

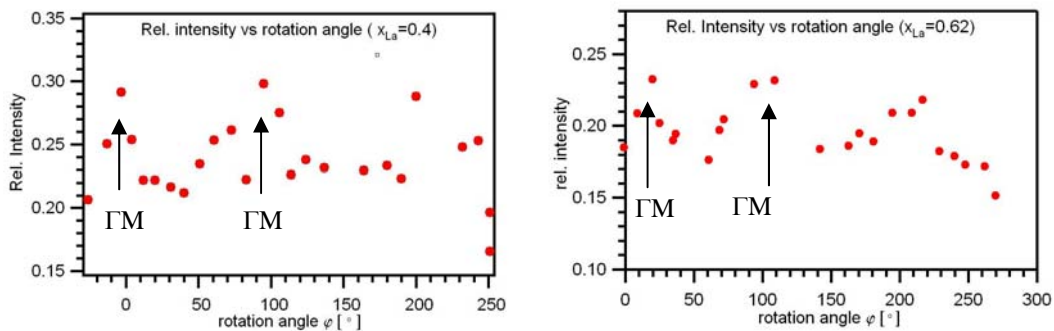


Figure 3: The relative intensity over angle for different La concentration $x=0.4$ and $x=0.62$

However, that characteristic is not observed clearly for the sample with La concentration $x=0$ which is a highly hole-overdoped sample, i.e. in the Fermi liquid regime. Further studies with higher angular resolution and better signal to noise ratio are under way to explain that

behaviour. The hole concentration as mean value over angle was calculated using equation (1). The value was then divided by 1.5 to take the measurement geometry into account. The results are presented in table 1 below.

Sample	La. Cont, x	T_c	\bar{n}_h
a	0.62	0	0.123
b	0.40	18	0.157
c	0.00	0	0.127

Table 1: Average relative intensity calculated for all polarization angles

By comparison the value of the right column for sample (a) fits well to the value of $1/8=0.125=\bar{n}_h$ assumed for a La concentration of $x=0.62$. Also at almost optimally doping, sample (b) the value of 0.157 is very close to the expected value of ≈ 0.16 . In accordance to the data on polycrystalline samples [4] the evaluated value for the hole content decreases instead of increasing after certain value, as can be seen for sample (c). This can be understood in the framework of one-band Hubbard model calculations [5]. However further studies with wide range of La concentration need to be done.

As conclusion, the polarization i.e. angular dependence of the main and satellite peak at the Cu-L₃ edge of Pb-Bi2201 was studied by XAS over a wide range of hole concentrations. Especially the optimum and the underdoped sample show modulations corresponding with the antinodal direction of the Brillouin zone

This work is based upon research conducted at BESSY. We gratefully thank the staff of BESSY, especially Dr. T. Kachel, for the support during the measurements. A. K Ariffin would like to thanks Ministry of Higher Education, Malaysia for the scholarship and Universiti Pendidikan Sultan Idris for granting the study leave.

- [1] M. Ronay et. al. Solid State Comm. **77**, 699 (1991)
- [2] A. Q. Pham et. al., Phys. Rev. B **48**, 1249 (1993)
- [3] P. Ghigna et. al., Phys. Rev. B **57**, 13426 (1998)
- [4] M. Schneider et. al., Phys. Rev. B **72**, 014504 (2005)
- [5] Duffy et al. Phys. Rev. B **56**, 5597 (1997)

Optical properties of neodymium- and yttriumhydride

A. Awada, B. Lobbenmeier, M. Marutzky, H. Schröter, S. Weber, and J. Schoenes

Institut für Physik der Kondensierten Materie, TU Braunschweig,
Mendelssohnstr. 3, D-38106 Braunschweig, www.ipkm.tu-bs.de

Ellipsometric spectroscopy is a powerful, nondestructive tool to analyze the optical and the electronic structure of materials. It has various advantages in comparison to many other forms of optical spectroscopy, for example a lower dependence on the surface properties of the samples than simple reflectivity measurements because the polarisation state of the reflected light is detected and not the intensity. Furthermore it simultaneously provides the real and the imaginary part of the optical functions without requiring a Kramers-Kronig-transformation which is necessary when only the reflectivity is measured.

Many rare earth metals undergo a metal-insulator transition upon hydrogenation. The dramatic change in the electronic properties are accompanied by changes of the optical properties: thin metallic film become transparent. In the context of yttrium the term of “switchable mirrors” has been established [1].

For neodymium this metal-insulator transition is in addition accompanied by a phase transition from an antiferromagnetic metal to a ferromagnetic semiconductor. Thus our studies on NdH_3 and YH_3 represent the optical characterisation of two rare earth metalhydrides with and without magnetic phase transition during hydrogenation.

Neodymium hydride

The neodymium films have been grown by molecular beam epitaxy onto CaF_2 -substrates. They need a palladium cap-layer to prevent the samples from corrosion in ambient air as neodymium is a very reactive rare earth metal. Furthermore the palladium-layer allows an ex-situ loading of the samples to higher H-concentrations. To avoid unloading of the samples in vacuum or even ambient air an additional CaF_2 layer is used on top of the films.

This multilayer structure of the samples doesn't allow a direct measurement of the dielectric function of $\text{NdH}_{3-\delta}$. The measured data are the pseudodielectric function of the samples which need further processing with a multilayer model to reveal the optical properties of $\text{NdH}_{3-\delta}$.

Figure 1 shows the pseudodielectric function of two samples with different hydrogen concentration. At approximately 9 eV and 8.5 eV, respectively, a major structure in the spectra can be seen which depends strongly on the hydrogen concentration by energy, strength and width. Furthermore, a weak shoulder appears at about 7.5 eV in the spectra. Negative values of ϵ_2 originate from interference effects at the interfaces between the different layers.

As our measurements show the optical properties of $\text{NdH}_{3-\delta}$ for the first time there are no data which can be compared in order to estimate the hydrogen content. A precise assignment of the spectra to hydrogen concentrations is not possible, yet.

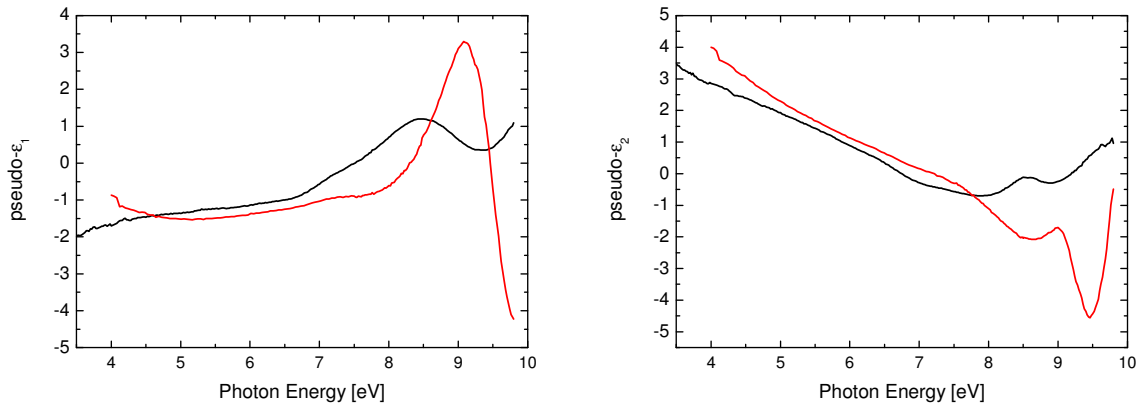


Fig.1: Real- and imaginary parts ϵ_1 and ϵ_2 of the pseudodielectric function of $\text{NdH}_{3-\delta}$ for two different hydrogen concentrations

Yttrium hydride

The YH_x films have been grown on $\text{CaF}_2(111)$ by Pulsed Laser Deposition (PLD).

Figure 2 shows the real and imaginary parts of the dielectric function measured in the range from 4 to 35 eV for YH_2 (black curve) and $\text{YH}_{2.2}$ (red curve), whereas the imaginary part ϵ_1 is the dispersive part, the real part ϵ_2 is the absorptive part. These are the first measurements on the new PLD grown layers. They took place in two sessions at the VUV/XUV ellipsometer at the BESSY II. During the first measurement session at the 3m-NIM1 beamline we determined the dielectric function from 4 to 9.5 eV.

In the second session at the TGM-4 beamline we determined the dielectric function from 11 to 35 eV. It has to be recognized, that a difference of only $x=0.2$ in the hydrogen concentration leads to clear changes of the dielectric function.

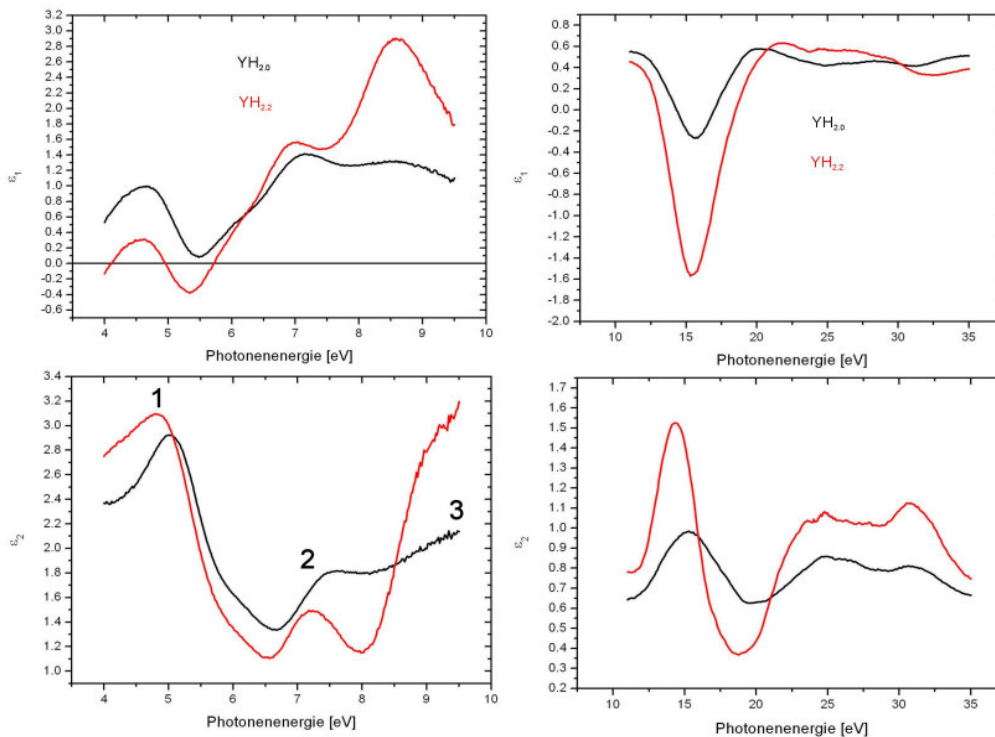


Fig. 2: Real and imaginary parts of the dielectric function obtained from ellipsometric spectroscopy

Structures in ε_2 originate from interband transitions which is demonstrated here for three peaks in the spectra of YH_2 . This can be interpreted in the framework of the band structure calculations shown in figure 3 [2]. The prominent peak at approximately 5 eV can be assigned to a transition from Γ_2' to Γ_{12} . The structures at approximately 7.5 and 9.5 originate from transition at the L - and X -point, respectively.

With the available band structure of YH_2 the allocation of interband transitions for energies over 10 eV is not possible.

For hydrogen concentrations above YH_2 no band structure calculations exist. For the further interpretation of the spectra new calculations from theoretical side are necessary.

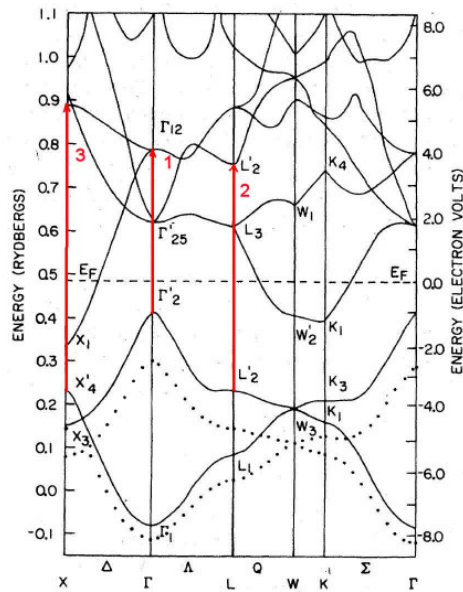


Fig. 3: Band structure of YH_2 and possible optical transitions [2]

Acknowledgments

We would like to thank the research group of Dr. N. Esser, especially Dr. C. Cobet, for the possibility to use the VUV ellipsometer and the BESSY company for beam time and BMBF for financial support (Förderkenzeichen 05 ES3XBA/5).

- [1] J. N. Huiberts, R. Griessen, J. H. Rector, R. J. Wijngaarden, J. P. Dekker, D. G. de Groot, and N. J. Koeman, *Nature (London)* **380** (1996), 231
- [2] D. D. Peterman et al. *PRB* **19** 4867 (1979)

Dielectric function and band structure of cubic InN

R. Goldhahn¹, P. Schley¹, J. Schörmann², D.J. As², K. Lischka²,

F. Fuchs³, F. Bechstedt³, C. Cobet⁴, N. Esser⁴

¹Institut f. Physik und Inst. f. Mikro- und Nanotechnologien, TU Ilmenau, PF 100565, 98684 Ilmenau, Germany

²Department Physik, Universität Paderborn, Warburger Str. 100, 33098 Paderborn, Germany

³Institut für Festkörperteorie und Theoretische Optik, FSU Jena, Max-Wien-Platz 1, 07743 Jena, Germany

⁴Institute of Spectrochemistry and Applied Spectroscopy Berlin, Albert-Einstein-Str. 9, 12489 Berlin, Germany

InN represents the least studied compound among the group-III nitride semiconductors. Determination of the complex dielectric function (DF) $\bar{\epsilon}(\hbar\omega) = \epsilon_1(\hbar\omega) + i \cdot \epsilon_2(\hbar\omega)$ of InN from the infrared into the VUV spectral region by spectroscopic ellipsometry (SE) has become one of the most powerful methods for studying absorption related properties of In-compounds both around the band gap as well as in the range of the high-energy critical points (CP) of the band structure [1-3]. By analysing the optical anisotropy around the absorption edge we demonstrated unambiguously that the band gap of hexagonal InN (h-InN) amounts to only 0.68 eV at room temperature which is much lower than the long-time accepted value of 1.9 eV. Theoretical calculations of the DF for the range of the high-energy CP's proved that the anisotropy and the peak positions can only be reproduced if electron-hole interaction is consequently taken into account [4].

So far, much less is known about the cubic counterpart (c-InN). Only recently, high quality epitaxial films became available. Preliminary ellipsometry studies [5] revealed an even lower band gap than for h-InN of about 0.61 eV, which is very close to the theoretical predictions of 0.59 eV [4] and 0.53 eV [6]. Here, we report for the first time on the experimental determination of the DF for c-InN up to photon energies of 10 eV and a comparison to numerical results.

The investigated films were grown by plasma-assisted molecular beam epitaxy. First, a 600 nm thick c-GaN buffer layer was deposited on (001)-oriented 3C-SiC substrate. Then, for the two studied samples c-InN films of 75 nm or 130 nm were grown. High-resolution X-ray diffraction proved the high crystalline quality of the films. Only 5% and 9% of hexagonal inclusions were found. Further growth details and results of the structural characterisation can be found elsewhere [5]. The ellipsometric data above 4 eV were recorded with BESSY ellipsometer attached to the 3m-NIM-monochromator, excellent matching to the data for the energy range from 0.74 up to 4.5 eV obtained with a commercial ellipsometer (J.A. Wollam Co., Inc.) was achieved.

Determination of a reliable DF becomes only possible if the peculiarities of the semiconductor surface are taken into account. In a first step, organic contaminations and the native oxide has to be removed. As demonstrated by our previous studies of h-InN it can be achieved by heating the sample to about 350 °C for 10 minutes. Figure 1(a) shows a comparison of the measured imaginary parts of pseudo-DF at room temperature for the as-grown sample (red) and cleaned film (blue). From the increase of the peak intensities after treatment a removal of about 3 nm oxide is estimated. It emphasises the necessity of surface preparation. In the second step, the post-annealing data are fitted by multi-layer approach which takes the surface roughness into account in order to get the DF of c-InN. The final results for the real and imaginary part of the DF are shown in Fig.1(b) by the red and blue lines, respectively. The spectral dependence up to 4 eV is very similar to the behaviour found for h-InN [1]. We find a sharp increase of ϵ_2 around the gap followed by a plateau. The shape of ϵ_2 above 4 eV is however markedly different to both, the ordinary and extraordinary DF of h-InN. A pronounced double-peak structure is found between 5 eV and 6.5 eV followed by a shoulder at 7 eV and a third peak at 9 eV.

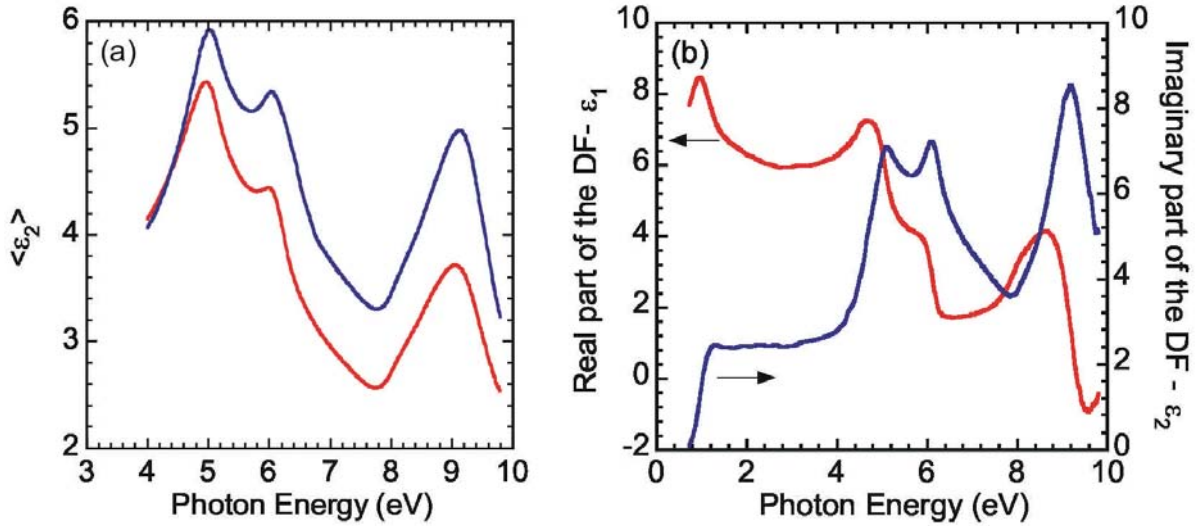


Fig. 1: (a) Comparison of the imaginary parts of the pseudo-DF prior (red) and after (blue) heating under UHV conditions. The data refer to room temperature. (b) Fitted real (red) imaginary part (blue) of the DF for cubic InN at room temperature.

Theoretical calculations of the optical properties of cubic InN starts from careful study of the quasi-particle band structure which has been described in more detail in Ref. 4. Taking the computed single-electron energies and wave functions only, one obtains an imaginary part of the DF as shown by the black line in Fig.2(a). Features attributed to transitions in the vicinity of the CP's are clearly. However, their spectral position deviates up to 800 meV from the experimental results (blue line). The discrepancy is lifted, if instead the electron-hole pair Hamiltonian is used for the DF calculation. Both, the peak positions and the peak intensity ratios, are in excellent agreement. As already observed for h-InN, only the magnitudes differ slightly to the experimental data. The current results for cubic InN are a further manifestation of our previous observation that the inclusion of excitonic effects over the whole spectral range is fundamental for the understanding of optical properties of nitride semiconductors.

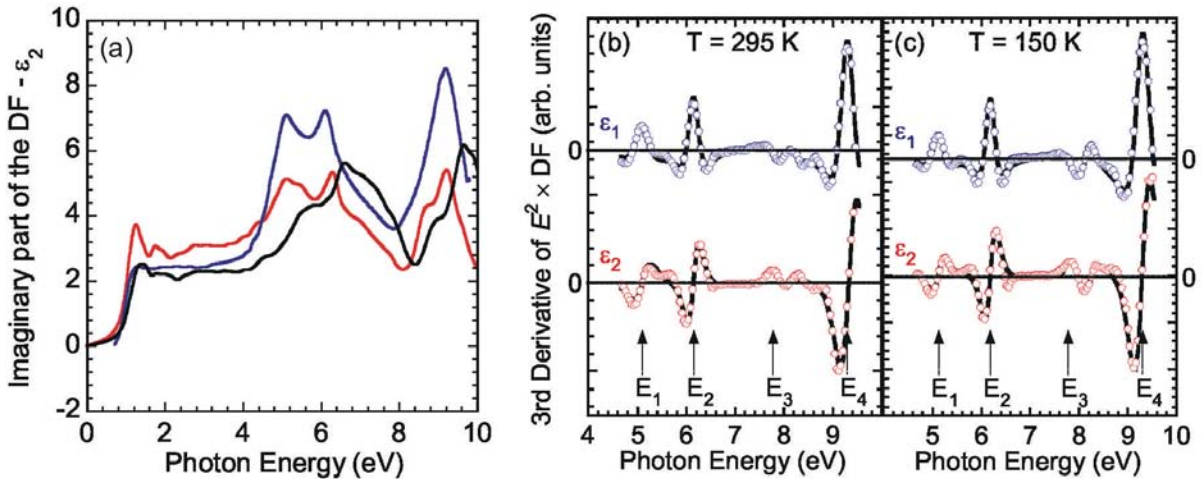


Fig. 2: (a) Imaginary part of the DF of cubic InN. Comparison of Coulomb-correlated electron-hole pairs (red) and independent quasiparticles spectra (black) to the experimental result (blue). Fit of the third derivative of the DF for room temperature (b) and $T=150\text{ K}$ (c). The circles represent the experimental data, and solid lines are the best fit. The transition energies of the critical points are marked by arrows.

For a high-resolution determination of the transition energies of the critical points following accurate approach was used. One calculate the third derivative of the point-by-point obtained DF (after surface roughness correction) multiplied by the square of the photon energy E . The resulting spectra can be fitted [7] via

$$\frac{d^3}{d(\hbar\omega)^3} \left((\hbar\omega)^2 \bar{\epsilon} \right) = \sum_{j=1}^4 e^{i \cdot \phi_j} \cdot \frac{C_j}{(\hbar\omega + i \cdot \Gamma_j - E_j)^{n/2}}, \quad (1)$$

where ϕ_j , C_j , Γ_j , and E_j denote the phase angle, the magnitude, the broadening energy, and the transition energy of the j -th CP, respectively. With $n=6$ corresponding to a two-dimensional critical point, we get the fit results for $T=295$ K and $T=150$ K as depicted in Fig. 2(b) and (c), respectively. At room temperature, the transition energies amount to 5.09 eV (E_1), 6.14 eV (E_2), 7.83 eV (E_3), and 9.28 eV (E_4). Especially the E_3 transition becomes much sharper in the numerical derivatives if the sample temperature is reduced to $T=150$ K. The low-temperature spectrum is characterized by Van Hove singularities at 5.12 eV (E_1), 6.18 eV (E_2), 7.85 eV (E_3), and 9.31 eV (E_4), i.e. the average shift between both temperatures amounts to about 30 meV. For comparison, similar studies of hexagonal InN yielded 40 meV.

In summary, we have determined the DF of cubic InN exhibiting a band gap of only 0.61 eV. Efficient surface cleaning was achieved by heating the samples up to 350 °C under UHV conditions. The DF shows in the high-energy part of spectrum contributions from at least four critical points of the band structure. Between 295 K and 150 K the transitions undergo a shift to higher energies by about 30 meV. It was demonstrated that the experimentally determined spectral dependence of the DF is well reproduced by theoretical calculation if electron-hole interaction is consequently taken into account.

The work at BESSY was supported by the BMBF grants 05KS4KTB/3 and 05ES3XBA/5. R.G. and the Ilmenau group acknowledge support by the DFG (GO 1378/2,3) and by Thüringer Ministerium für Wirtschaft, Technologie und Arbeit (B509-04011). The work at Jena was supported by the DFG (Be 1346/18-1) and the European Community in the framework of the network of excellence NANOQUANTA (NMP4-CT-2004-500198). The authors would like to thank H. Nagasawa and M. Abe from HOYA Corporation, SiC Development Center, for supplying the 3C-SiC substrates.

References

- [1] R. Goldhahn, A.T. Winzer, V. Cimalla, O. Ambacher, C. Cobet, W. Richter, N. Esser, J. Furthmüller, F. Bechstedt, H. Lu, and W.J. Schaff, *Superl.&Microstruc.* **36**, 591 (2004).
- [2] R. Goldhahn, P. Schley, A.T. Winzer, G. Gobsch, V. Cimalla, O. Ambacher, M. Rakel, C. Cobet, N. Esser, H. Lu, and W.J. Schaff, *phys. stat. sol. (a)* **203**, 42 (2006).
- [3] R. Goldhahn, P. Schley, A.T. Winzer, M. Rakel, C. Cobet, N. Esser, H. Lu, and W.J. Schaff, *J. Cryst. Growth* **288**, 273 (2006)
- [4] J. Furthmüller, P.H. Hahn, F. Fuchs, and F. Bechstedt, *Phys. Rev B* **72**, 205106 (2005).
- [5] J. Schörmann, D.J. As, K. Lischka, P. Schley, R. Goldhahn, S.F. Li, W. Löffler, M. Hetterich, H. Kalt, *Appl. Phys. Lett.* **89**, 261903 (2006).
- [6] P. Rinke *et al.*, *Appl. Phys. Lett.* **89**, 161919 (2006).
- [7] D.E. Aspnes, *Phys. Rev. Lett.* **28**, 168 (1972); D.E. Aspnes and J.E. Rowe, *Phys. Rev. B* **5**, 4022 (1972).

Dominant multi-electron transitions in the photoionization of laser-excited Li atoms

D. Cubaynes¹, S. Diehl-Guilbaud¹, F. J. Wuilleumier¹, M. Meyer¹,
T. Richter², E. Heinecke² and P. Zimmermann²

¹*LIXAM, Centre Universitaire Paris-Sud, Bâtiment 350, F-91405 Orsay Cedex, France*
²*Technische Universität Berlin, Institut für Optik und Atomare Physik, Hardenbergstraße 36,
10623 Berlin, Germany*

Detailed information on the complex electronic interaction governing the photoionization of atoms and molecules can be obtained by the combination of laser and synchrotron radiation [1]. The precise manipulation of the electronic cloud by the laser makes it possible to modify in a controlled way the interactions between the electrons in the atom and to probe these changes through inner-shell photoionization by XUV synchrotron radiation. In the present study, we have investigated by means of high-resolution spectroscopy the 1s photoionization of Lithium atoms, which were initially in the $1s^2s^2S_{1/2}$ ground state or laser-prepared in the excited $1s^22p^2P_{3/2}$ or $1s^23p^2P_{3/2}$ states. Already several years ago, theory has predicted a strong dependence of the photoionization cross section from the excited state (i.e. 2p or 3p) as well as from the energy of the ionizing radiation [2]. Experimental verification was missing up to now, in particular due to difficulties to obtain high laser intensities in the UV wavelength region allowing to prepare a sufficiently high density of Li atoms into the 3p excited state.

The experiments have been performed at the UE52-SGM beamline at BESSY using a high-resolution electron analyzer (SCIENTA SES-2002) for the analysis of the photoelectron energies. The Li atoms were excited to the $1s^22p^2P_{3/2}$ and $3p^2P_{3/2}$ states using a c.w. ring dye laser, and further ionized by monochromatized synchrotron radiation in the photon energy region between 80 and 140 eV. For the excitation of the $1s^22p$ level at 670.8 nm, a DCM dye providing up to 300 mW average power was used. In order to induce the $2s \rightarrow 3p$ transition at 323.4 nm, the radiation from the dye laser was frequency doubled in an external ring cavity and an average laser power of about 35 mW was obtained in the UV range. With these conditions about 30% of the Li atoms could be excited in the 2p and about 1% in the 3p excited state, which made it possible to record photoelectron spectra of good quality.

A typical photoelectron spectrum recorded after laser excitation to the $Li^* 1s^23p^2P_{3/2}$ state is shown in figure 1. The photoionization of the $Li 1s^22s$ ground state atoms, which are still present in the vapor, leads to the formation of the $Li^+ 1s2s^1S$ photolines as well to the less intense $Li^+ 1s2p^1P$ and $1s3l^1L$ satellite lines. Dramatic differences are observed when the intensity of the lines arising from the photoionization of the excited $Li^* 1s^23p$ atoms is investigated. First of all, the spectrum is more complicated due to the fact that via radiative relaxation also the $Li^* 1s^23s$ (and $Li^* 1s^22p$) levels are populated giving rise to additional structures in the photoelectron spectrum. But the most striking feature is the extremely strong $Li^+ 1s4p$ shake-up satellite, which

is about one order of magnitude stronger than the $\text{Li}^+ 1s3p$ photoline. The recorded photoelectron spectra of laser-excited Li demonstrate therefore for the first time that multi-electron transitions (ionization plus excitation) can dominate the direct photoionization of a very simple, few-electron atom. After excitation to the $\text{Li}^* 1s^2 2p$ level, the situation is completely different, the $\text{Li}^+ 1s2p$ main line is the strongest line and only about 40% of the intensity is found in the $\text{Li}^+ 1s3p$ shake-up state.

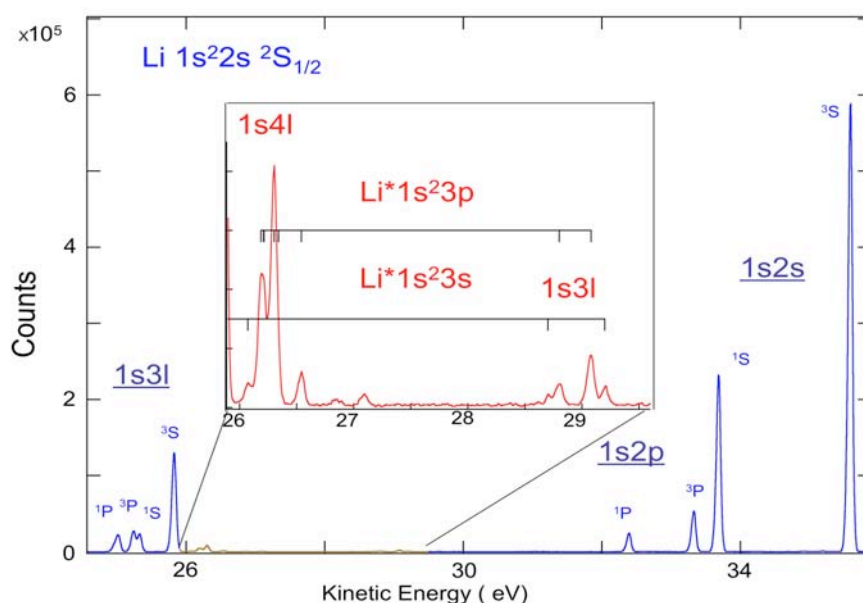


Fig. 1: Photoelectron spectrum of atomic Li in the $1s^2 2s$ ground (blue) and in the $1s^2 3p$ laser excited state (red) recorded after photoionization at $h\nu(\text{SR}) = 100\text{eV}$. The configurations of the final ionic states are indicated.

In addition, we have experimentally determined the energy dependence of the shake-up intensity, showing smaller values in the threshold region than at higher photon energies, in qualitative agreement with the results of Multi-configuration Hartree-Fock (MCHF) calculations [3]. In general, the observed effect can be related to the spatial overlap of the wavefunctions in the initial and final state of the photoionization process. The strong increase of the $\text{Li}^+ 1s4l$ shake-up intensity is therefore caused by the collapse of the nl -wavefunction in the ionized states. A quantitative analysis of the experimental data and a detailed comparison with the theoretical results are in progress

The project was funded through BESSY-EC-IA-SFS Contract (EU R II 3-CT-2004-506008).

References

- [1] F. J. Wuilleumier and M. Meyer, *J. Phys. B* 39, R425 (2006).
- [2] Z. Felfli and S. Manson, *Phys. Rev. Lett.* 68, 1687 (1992).
- [3] H. L. Zhou, S. T. Manson, L. Vo Ky, P. Faucher, F. Bely-Dubau, A. Hibbert, S. Diehl, D. Cubaynes, J.-M. Bizau, L. Journel, and F. J. Wuilleumier, *Phys. Rev. A* 59, 462 (1999).

Magnetization dynamics of Gadolinium probed by linear dichroism in 4f photoemission

A. Melnikov¹, H. Prima², M. Lisowski¹, R. Schmidt², C. Gahl², R. Weber³,
U. Bovensiepen¹, and M. Weinelt^{1,2}

1. *Freie Universität Berlin, Fachbereich Physik, Arnimallee 14, 14195 Berlin, Germany*

2. *Max-Born-Institut, Max-Born-Straße 2 A, 12489 Berlin, Germany*

3. *BESSY-GmbH, Albert-Einstein-Str. 15, 12489 Berlin, Germany*

In current technical implementations changes in the magnetization of ferromagnetic materials are induced thermally or magnetically. While this conventional switching happens on a nanosecond timescale, various experiments corroborated in the last decade that the spin system of itinerant ferromagnets exhibits a reduced magnetization within a few hundred femtoseconds (fs) after laser excitation [1]. Yet the underlying microscopic processes are not understood [2].

Gadolinium with its half-filled 4f core shell is a particular prototype system to study magnetization dynamics. In the Heisenberg ferromagnet Gd the strongly localized $4f^7$ electrons carry most of the magnetic moment of $7.55 \mu_B$ per atom. They spin-polarize the 5d valence electrons resulting in the extra contribution of $0.55 \mu_B$ per atom. This intraatomic 4f – 5d exchange coupling in turn mediates magnetic order within the 4f system below the Curie temperature of 293 K. Recent experiments employing non-linear magneto-optics demonstrate ultrafast magnetization dynamics also for gadolinium [3]. Linear and non-linear optics only probe the spin polarization of the valence states.

Here we report on a combined laser-synchrotron pump-probe experiment which aims at a direct measure of the temporal evolution of the 4f contribution to the magnetization. After excitation with an ultrashort laser pulse the transient magnetization is monitored by linear magnetic dichroism of the Gd 4f photoemission line [4]. We observe a loss in magnetization after laser excitation and find similar time scales for relaxation of the magnetization to the equilibrium value as in the non-linear optical studies [3].

Gd(0001) films of 100 Å thickness have been prepared by epitaxial growth on a W(110) substrate. The easy axis of magnetization lies in-plane. Figure 1 depicts 4f core-level spectra recorded at a photon energy of 60 eV and a sample temperature of 80 K, i.e. in the ferromagnetic state. The Gd film was remanently magnetized in opposite in-plane directions, as indicated in Fig. 1, inset. Spectra in Fig. 1a are measured without laser excitation, while spectra in Fig. 1b have been recorded for overlapping laser pump (100 fs, $h\nu = 1.53$ eV) and synchrotron probe pulses (40 – 80 ps, $h\nu = 60$ eV). For details of the experimental setup see Ref. [5]. Evidently, the 4f spectral shape and intensity $I \uparrow$ and $I \downarrow$ depend on the magnetization directions $M \uparrow$ and $M \downarrow$. The linear dichroism is thus a signature of the 4f spin system's magnetic order.

Three effects happen upon laser excitation (cf. Fig. 1b): the spectra shift to higher kinetic energy, they broaden slightly, and the overall dichroic signal decreases. In order to better visualize and quantify these effects we introduce a dichroic and an average spectrum according to $S_D = (I \uparrow - I \downarrow)/2$ and $S_A = (I \uparrow + I \downarrow)/2$. The corresponding spectra in Figs. 1c and d have been evaluated subtracting a Shirley background from the raw data of Figs. 1a and b. Most obvious is the shift between the spectra recorded without laser excitation (grey solid line) and the spectra obtained for overlapping pump and probe pulses (black solid line). The pump-induced broadening is best seen in the average spectra in Fig. 1d; the peak areas are equal but the peak maxima and thus widths differ slightly.

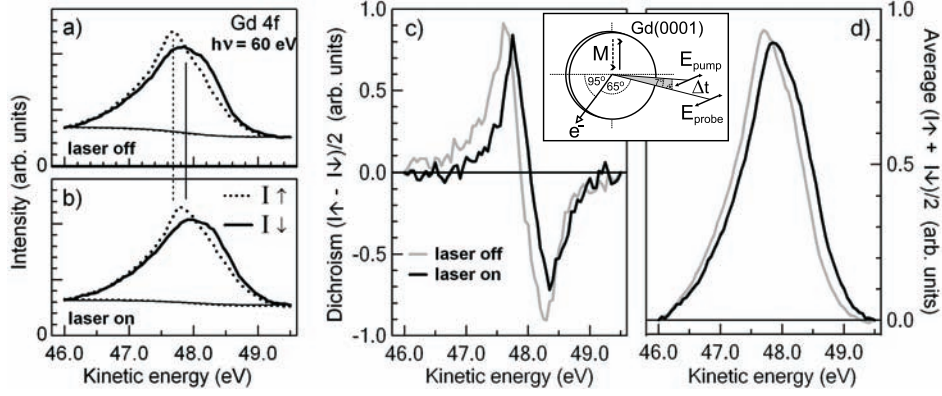


Figure 1: Gd 4f core-level spectra recorded for opposite magnetization directions ($M \uparrow$ and $M \downarrow$, see inset) at an angle of $\sim 5^\circ$ with respect to normal emission (a) without laser excitation and (b) for overlapping pump and probe pulses. (c) Dichroic spectra $(I \uparrow - I \downarrow)/2$ and (d) average spectra $(I \uparrow + I \downarrow)/2$ evaluated from the raw data in Fig. 1a and b (grey and black lines).

We attribute shift and broadening of the spectra to the formation of a transient space charge layer. The space charge originates from multiphoton photoemission driven by the p-polarized pump pulse (cf. inset in Fig. 1). For the angle of incidence of 70° we estimate the absorbed fluence to be 10 mJ/cm^2 . In this intensity range multiphoton ionization sets already in and creates a background of photoemitted electrons with low kinetic energy. This background was unavoidable, as fluence and polarization are necessary to reasonably demagnetize the Gd film.

Most important, Fig. 1c reveals a noticeable reduction of the dichroic signal upon laser excitation. We define the magnetic linear dichroic contrast as

$$M_D = \sqrt{\frac{\int dE S_D^2(E)}{\int dE S_A^2(E)}} = \sqrt{\frac{\int dE s_D^2(E)}{\int dE S_A^2(E)}} \cdot M \equiv \gamma \cdot M \quad (1)$$

where we assume $S_D(E) \propto s_D(E) \cdot M$, with $s_D(E)$ representing the spectral dependence. To justify Eq. 1 we have measured the temperature dependence $M_D(T)$ between 80 and 320 K. The dichroic contrast possesses a typical ferromagnetic behavior and in particular decreases to zero at T_C . This suggests that the dichroic contrast indeed reflects the magnetization of the sample and allows us to monitor the magnetic order of the 4f spin system of gadolinium. Finally, the pump-induced relative change of the magnetic order for delay Δt between laser pump and synchrotron probe pulses is evaluated according to

$$\frac{\Delta M_D(\Delta t)}{M_D} = \frac{M_D^{ON}(\Delta t) - M_D^{OFF}}{M_D^{OFF}} = \frac{\gamma^{ON}(\Delta t) M^{ON}(\Delta t) - \gamma^{OFF} M^{OFF}}{\gamma^{OFF} M^{OFF}}. \quad (2)$$

The result is shown in Fig. 2a along with the transient shift and broadening of the spectra in Figs. 2b and c. The latter have been evaluated calculating first and second moments of the average spectrum $S_A(\Delta t)$. From Eq. 2 it follows that the magnetic order reflects the true magnetization dynamics $\Delta M(\Delta t)/M$ as long as $\gamma^{ON}(\Delta t) = \gamma^{OFF}$. This holds for homogenous broadening of the spectrum [6]. Note, that the average dichroic signal is unaffected by the space-charge-induced overall shift, since the latter is independent of M .

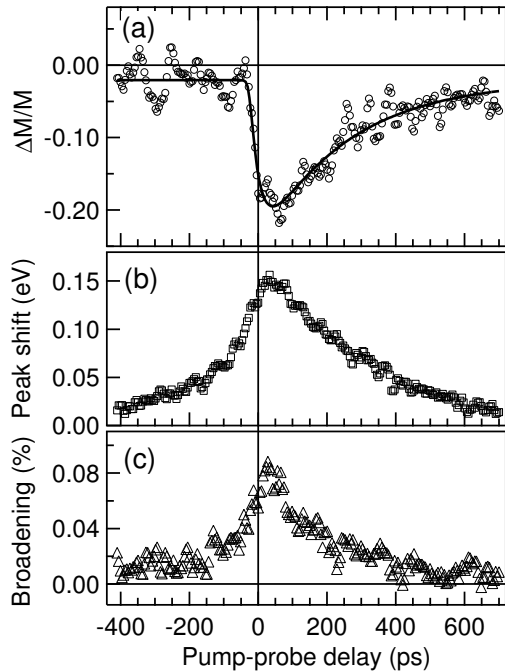


Figure 2: a) Relative change of the magnetization as a function of pump-probe delay. The solid line is an exponential fit convoluted with a Gaussian broadening to describe the pump pulse. b) Transient peak shift and c) peak broadening.

ics of ultrafast demagnetization. As the drop in $\Delta M/M$ simply reflects the time resolution of the experiment it only defines an upper limit of 50 ps in which ultrafast demagnetization occurs. Nevertheless, the experiment displays the potential of time-resolved core-level photoemission spectroscopy once femtosecond soft X-ray sources become available.

As the broadening is significantly smaller than the change of spin polarization, residual artifacts in $\Delta M(\Delta t)/M$ should be considerably smaller than the space charge effect itself. Furthermore, while the magnetization shows a clear drop at zero pump-probe delay (cf. Fig. 2a), shift and broadening in Fig. 2b and c exhibit a much broader onset. Electrons photoemitted at negative delay, i.e. at a point in time before the pump pulse excites the sample, are still accelerated by the negative space charge created later on at zero delay. The magnetization and thus the dichroic contrast remain, however, unchanged at negative pump-probe delay.

In conclusion, we have established that the transient dichroic spectrum of the 4f core-level monitors the magnetization dynamics in gadolinium. We observe a drop of the magnetization of about 20 % upon laser excitation. The magnetization recovers in about 250 ps. This timescale is consistent with the earlier magneto-optical experiment and is attributed to heat diffusion after laser excitation. Unfortunately, the duration of the synchrotron electron-bunches of 40 – 80 ps in single bunch operation does not allow to unravel the dynam-

- [1] E. Beaurepaire et al., Phys. Rev. Lett. **76**, 4250 (1996); L. Guidoni, E. Beaurepaire, and J.-Y. Bigot, Phys. Rev. Lett. **89**, 017401 (2002); B. Koopmans, M. van Kampen, and W. J. M. Jonge, J. Phys.: Condens. Matter **15**, S723 (2003); J.-Y. Bigot et al., Phys. Rev. Lett. **93**, 077401 (2004).
- [2] J. Hohlfeld et al., Phys. Rev. Lett. **78**, 4861 (1997); B. Koopmanns, in *Topics in Applied Physics*, edited by B. Hillebrands and K. Ounadjela (Springer, Berlin, 2003), Chap. 8, p. 253; M. Cinchetti et al., Phys. Rev. Lett. **97**, 177201 (2006).
- [3] A. Melnikov et al., Phys. Rev. Lett. **91**, 227403 (2003); M. Lisowski et al., Phys. Rev. Lett. **95**, 137402 (2005).
- [4] O. Krupin, PhD thesis, Fachbereich Physik, Freie Universität Berlin, Germany (2004).
- [5] T. Gießel et al., Rev. Sci. Instrum. **74**, 4620 (2003).
- [6] A. Melnikov et al., submitted to Phys. Rev. B.

The ferromagnetic nature of Co doped ZnO

E. Goering, T. Tietze, S.Brück, and G.Schütz

Max-Planck-Institut für Metallforschung, Heisenbergstrasse 3, 70569 Stuttgart, Germany

M. Gacic, G. Jakob,C. Herbort, and H. Adrian

Institute of Physics, University of Mainz, Staudinger Weg 7, 55099 Mainz, Germany

The existence of room temperature ferromagnetism in the wide gap semiconductor ZnO is a controversial issue. Utilizing X-ray magnetic circular dichroism with a very high sensitivity, we have detected pure paramagnetic Co 3d magnetism and no indication for Zn 3d magnetism. Our observation clearly rules Co, diluted and/or in metallic clusters, to be responsible for the observed room temperature ferromagnetism. As the Co-atoms show a pure paramagnetic magnetic behavior, we attribute the ferromagnetism to a spontaneously spin impurity band induced by oxygen vacancies and defects due to the transition metal doping.

Recently ZnO has attracted enormous interest, stimulated by important findings as p-type doping by N, ferromagnetism (FM) above room temperature (RT), and the opportunity to grow thin epitaxial films[1,2][3]. While the p-type doping gives rise to possible important applications like blue and UV lasers[4] and transparent conductive oxides, the observation of ferromagnetism at room temperature is very promising for future room temperature spintronic applications [2]. This is in strong contrast to other diluted ferromagnetic semiconductures like Mn doped GaAs, which show ferromagnetism only at temperatures well below room temperature. Unfortunately ferromagnetic ordering and the magnetic moment per dopand-ion are strongly depending on the preparation method, which is one reason preventing a clear and simple interpretation of the FM ordering.

Many old and recent band structure calculations have been performed to understand the electronic structure, magnetic coupling and the nature of defect induced in gap states and their influence to magnetic ordering [5-11]. However, all these publications have in common one basic assumption: Magnetic ordering of the impurity ions is mediated by the ZnO lattice. On the other hand, some magnetic features of the DMS are not simply explained on such a basis. For example, why is TM doped ZnO about to be ferromagnetic for nearly all 3d elements, including nonmagnetic ions [12]? Why is RT ferromagnetism appearing far below the percolation threshold? How can observed FM moments per dopand exceed the spin only value many times at low concentrations [13]? Why are Curie temperatures not scaling with the dopand concentration, and why are very large variations of the abso-

lute magnetic moments present, for differently prepared samples [14]?

We present experimental results clearly demonstrating the absence of magnetic transition metals long range order, while on the other hand a clear ferromagnetic moment is present, possibly due to a spontaneously spin split impurity band induced by the defect structure of the laser ablated $Zn_{0.95}Co_{0.05}O_x$ films.

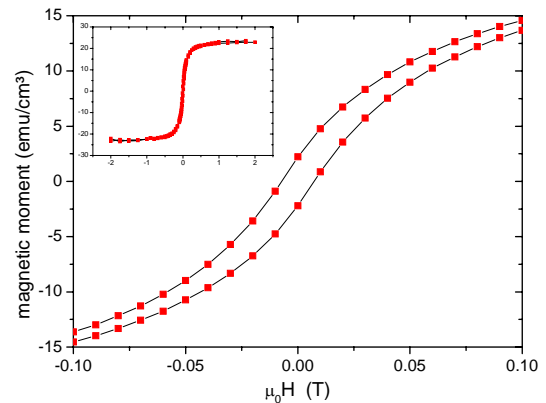


Figure 1: SQUID Hysteresis loop of a 5% Co-doped ZnO thin film measured at 300 K showing a remnant magnetic moment

Experimental

Thin films of $Zn_{0.95}Co_{0.05}O$ have been prepared by pulsed laser deposition (PLD) on Al_2O_3 substrates at 600°C in argon ambient pressure of 0.1 mbar. X-ray diffraction (XRD) measurements showed a ZnO single phase in (110) orientation. Impurity phases were not observed. The sample

magnetization has been monitored by VSM and SQUID. The Curie temperature lies above 300 K and the ferromagnetic saturation moment was up to 1.25 Bohr magnetons per Co atom at a nominal concentration of 5%. All XMCD and XAS spectra were recorded in the total electron yield mode at the bending magnet beamline PM III at Bessy II with an energy resolution of about $E/\Delta E=5000$. We used a new superconducting magnet system, providing fast field switching in less than 6sec at ± 2 T. All spectra have been measured in applied magnetic field, which has been flipped at each energy data point. This provides a sensitivity of the XMCD signal up to 10^{-6} , just at the pure photon statistics of the absorption process itself. This very high sensitivity allows the investigation of paramagnetic XMCD spectra for diluted Co at the Co $L_{2,3}$ edges down to about $10^{-4} \mu_B$. Further details of the total electron yield measurement and data analysis have been published elsewhere [15].

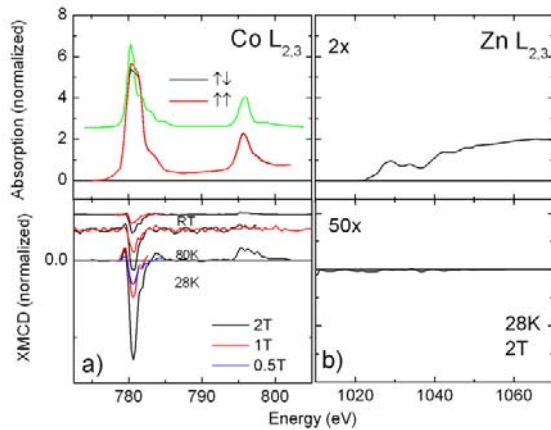


Figure 2: Co $L_{2,3}$ (a) and Zn $L_{2,3}$ XAS and XMCD spectra of a 5% Co-doped ZnO thin film.

In Fig. 1 a typical RT magnetization curve is shown. A clear remnant magnetic moment could be observed, which excludes superparamagnetism as a source of the magnetic moment. To access the microscopic ferromagnetism x-ray circular dichroism (XMCD) and x-ray absorption spectroscopy (XAS) measurements have been performed. XAS and XMCD spectra at the Co $L_{2,3}$, and the Zn $L_{2,3}$ edges of a 5% Co doped ZnO thin film sample are shown in Fig. 2. The Co $2p \rightarrow 3d$ absorption is shown in Fig. 2a. The spectral shape of the resonant XAS lines (red and black) is quite different to typical metallic spectra [16] and in good agreement to a theoretical multiplet spectrum of Co in tetrahedral coordination (from Ref. [17], Fig. 13, Co $3d^7$ configuration, T_d symmetry, and $Dq=1.5eV$), which is also reproduced in Fig.2a for direct comparison (green curve). This provides a consistent description of Co ions located at the Zn site in tetrahedral

coordination, as given by the crystal structure. For octahedral coordination, the theoretical XAS spectra (also in Ref. [17]) are in much less agreement to the tetrahedral coordination, especially for the $3d^7$ configuration, which is the most likely one of diluted Co in ZnO. These results and the conclusion of tetrahedrally coordinated Co ions in a $3d^7$ configuration are in excellent agreement with other published experimental results and theoretical XAS calculations, supporting the n-type non clustered Co $3d^7$ ion picture [18,19].

While the XMCD signal is about to be proportional to the magnetic field, a strong decrease as a function temperature could be observed (Fig. 3). These observations are typical for paramagnetic materials and unexpected for a ferromagnetic system. This will be discussed on a quantitative basis below. Similar to the observation above, the XMCD spectral shape is clearly different to metallic Co spectra [16], which [20] also confirms the Co $3d^7$ ion picture, and is in good agreement to other Co doped ZnO XMCD results, published so far [18]. This observation shows that Co clusters are not present in a significant way, and are not responsible for the ferromagnetic behaviour in our Co doped ZnO sample.

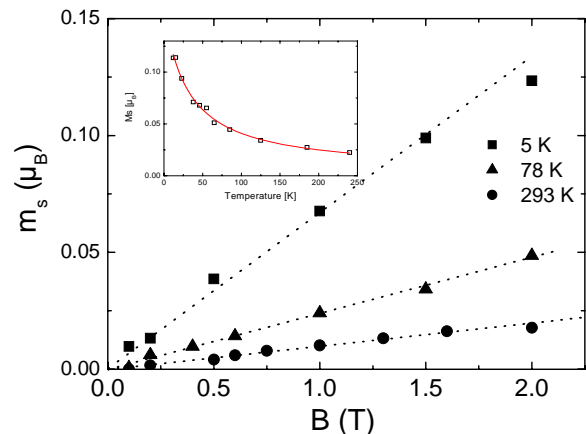


Figure 3: Temperature and field dependence of the Co L_3 XMCD signal.

Figure 2b shows the Zn $L_{2,3}$ edge spectra, probing the unoccupied Zn $3d$ site. The resonance of the Zn $L_{2,3}$ XAS lines is very weak, indicating a Zn $3d^{10}$ configuration, as expected. The lower part of Fig 2b shows the corresponding Zn $L_{2,3}$ XMCD, again in an expanded view. No significant Zn XMCD signal could be observed, consistent to the non resonant spectral line shapes of the corresponding XAS spectra shown above. This clearly demonstrates the absence of Zn $3d$ magnetism in doped ZnO.

We will now focus on the quantitative discussion of the XMCD Co magnetic moments, which have

been derived by the use of sum rules, using a number of holes $n_h=3$ consistent to the above discussed XAS and XMCD multiplet picture [16,18,21,22]. In an applied magnetic field of 2T and at a temperature of 28K, Co provides a projected 3d spin moment/ion of $m_S = 0.141 \mu_B$, and an orbital projected moment of $m_L = 0.036 \mu_B$ (RT at 2T: $m_S = 0.026 \mu_B$ $m_L = 0.008 \mu_B$). The spin values at both temperatures are quite close to a pure paramagnetic moment of a spin 3/2 system. In order to prove the paramagnetic behaviour of Co, the field dependence of the Co XMCD signal has been monitored by XMCD as shown in Fig. 3 for three different temperatures and different in applied magnetic fields up to 2T. No ferromagnetic or remnant behaviour could be observed. The inset in Fig. 3 shows the temperature dependence at 2T. A clear Curie law behaviour (red line) has been observed, with no indication of any constant (remnant or antiferromagnetic) magnetization contribution.

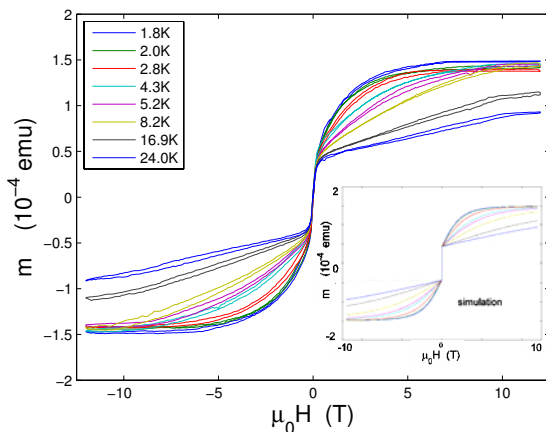


Figure 4: VSM low temperature and high field magnetization measurements compared with a simple paramagnetic simulation (inset).

To exclude surface effects we have performed extensive VSM magnetisation measurements before and after the XMCD measurements. The low temperature magnetisation measurements, shown in Fig. 4 clearly indicate the coexistence of a paramagnetic and a ferromagnetic contribution to the total signal. We have simulated the temperature and field dependent paramagnetic behaviour from Fig 4 [Co^{2+} with $J=S=1.5$; $g\text{-factor}=2$) by a Brillouin function, while the ferromagnetic contribution has been approximated by a temperature independent step function (inset of Fig. 4). The simulation is in perfect and also quantitative agreement to the VSM results.

On the basis of our shown and consistent XMCD and VSM data, Co shows pure paramagnetic behaviour. Therefore, we could clearly rule out Co or Zn 3d shell electrons as the main source for the

ferromagnetism observed in Co doped ZnO. This supports the idea, that defects or strain, as induced by the doping of the 3d metal ion, results in a long range magnetic polarisation of the O 2p shell, responsible for room temperature ferromagnetism of ZnO. Further details and additional Hall effect and magnetoresistance measurements will be published elsewhere [24]. In addition, we have found a very small but sizable temperature independent O K edge XMCD signal (not shown), which suggests oxygen as a possible source for FM in such systems.

Summary

We have found only paramagnetic behaviour of the Co 3d magnetism, down to low temperatures, excluding Co as the origin of the RT ferromagnetism, as shown in Fig. 1. Our results are in strong contrast to other published XMCD results, which found a mixture of antiferromagnetically and ferromagnetically coupled Co ions [18]. We would like to emphasize that it is essential to have a very high signal to noise ratio present at the XMCD system, to measure paramagnetic and strongly diluted magnetic moments at higher temperatures.

We would like to thank T. Kachel and all BESSY staff members for kind support during the beam time, and the Max-Planck-Society for financial support.

References

1. Ü. Özgür *et al.*, J.Appl.Phys. **98**, 041301-1 (2005).
2. S. J. Pearton *et al.*, Progress in Materials Science **50**, 293 (2005).
3. C. Klingshirn *et al.*, Superlattices and Microstructures **38**, 209 (2005).
4. M. H. Huang *et al.*, Science **292**, 1897 (2001).
5. K. Sato *et al.*, Phys.Stat.Sol. **229**, 673 (2002).
6. Q. Wang *et al.*, Appl.Phys.Lett. **84**, 4170 (2004).
7. L. Pisani *et al.*, cond-mat, 0601226-1 (2006).
8. S. Massida *et al.*, Phys.Rev.B **52**, R16977 (1995).
9. Yu. Uspenskii *et al.*, J.Magn.Magn.Mater. **258-259**, 248 (2003).
10. D. H. Lee *et al.*, Phys.Rev.B **24**, 6899 (1981).
11. I. Ivanov *et al.*, Phys.Rev.B **24**, 7275 (1981).
12. J. M. D Coey, Solid State Sciences **7**, 660 (2004).
13. C. Song *et al.*, Phys.Rev.B **73**, 024405-1 (2006).
14. J. M. D Coey, J.Appl.Phys. **97**, 10D313-1 (2005).
15. E. Goering *et al.*, J.Sync.Rad. **8**, 434 (2001).
16. C. T. Chen *et al.*, Phys.Rev.Lett. **75**, 152 (1995).
17. G. van der Laan *et al.*, J.Phys.: Condens.Matter **4**, 4189 (1992).
18. M. Kobayashi *et al.*, Phys.Rev.B **72**, 201201-1 (2005).
19. J. Okabayashi *et al.*, J.Appl.Phys. **95**, 3573 (2004).
20. S. S. Dhesi *et al.*, Phys.Rev.B **60**, 12852 (1999).
21. B. T. Thole *et al.*, Phys.Rev.Lett. **68**, 1943 (1992).
22. P. Carra *et al.*, Phys.Rev.Lett. **70**, 694 (1993).

Capacitance Transient X-ray Absorption Spectroscopy of Semiconducting structures

O. Vyvenko¹, N. Bazlov¹, A. Novikov¹, R. Ovsyannikov², A. Bondarenko¹,
A.S. Vinogradov¹

¹ - V.A. Fok Institute of Physics, St.-Petersburg State University, ²-BESSY

The state-of-art semiconductor devices utilize the properties of multi-layer structures of diverse elemental compositions. The local elemental content and atomic environment within every particular layer or at their interfaces define useful properties of the devices and need to be monitored. X-ray absorption spectroscopy (XAS- XANES/EXAFS) is a powerful technique for local atomic arrangement studies in various materials. The most common techniques to get absorption spectra in the soft X-ray region are total electron yield (TY) or fluorescence yield (XRFY) measurements since direct transmission measurements need to prepare thin films. In turn, the usage of TY and XRFY has also well known restrictions to get information from burned layers of the structures grown on massive substrates.

A natural way to make XAFS-information more directly useable in semiconductor physics and technology is to measure the spectral response of one of the semiconducting properties of the structure arose from a particular site of the structure. A few attempts of such kinds of measurements were reported during last decade.

The detection of X-ray absorption fine structure near K-edges Ga and As by photoconductivity[1], photodiode current [2, 3] and the diode photocapacitance[3-5] was previously reported for GaAs. It was shown that the photoconductivity and the diode photocurrent contained the same information as the XRF signal when appropriate corrections were applied [1, 2]. Contrary to that the measurements of stationary photocapacitance changes due to X-ray induced emptying of deep level defects revealed significant distinction of the capacitance XAFS-spectra from the XRFY spectra[5]. It was suggested [5] that the capacitance XAFS-signal arose due to direct transitions between the inner core level and the local defect level in the semiconductor band gap and carried the information about the local atomic environment of the defect. This interpretation was doubted in [3] where the time constants of the photocapacitance transients under X-ray excitation was measured at low temperatures in GaAs with EL2 deep level defect. Capacitance transient time constant spectrum obtained in [3] coincided well with the X-ray absorption spectrum of the GaAs matrix though the local atomic arrangement of EL2-defect differed significantly from one of the ideal GaAs lattice.

Another technique based on capacitance measurements that was developed recently [6] was called synchrotron-radiation deep level transient spectroscopy (SR-DLTS). The technique consisted of the measurements of thermal emission transients after the filling of the deep level traps with minority carriers created with the pulsed X-ray radiation.

We report about the development of another new technique for the detection of X-ray absorption in the layer structures that we called Capacitance Transient X-ray Absorption Spectroscopy (CapTXAS). CapTXAS technique consists of the periodical filling of local levels with majority carriers with short electrical pulses of the proper chosen amplitude and of subsequent measurements of the first derivative of the capacitance transient signal originated from the emptying of the levels as the result of X-ray absorption with the atoms of the semiconductor structure. We installed this technique at BESSY Russian-German Beam Line and applied to measurements on two test semiconductor structures: Au-nickel-phthalocyanine-silicon (Au-NiPc-Si) and Al- (silicon bonded wafer). Besides, the measurements of photocurrent spectra on diverse semiconducting structures were performed.

Fig. 1 represents the results of the measurements of the first derivative of the capacitance transients obtained on the sample of silicon bonded wafer of p-type conductivity. The dislocations at the bonded interface give rise to the appearance of the deep level states

with the energy of their levels from 0.15eV to 0.4 eV above the top of the valence band of silicon of the density of few 10^{11} cm^{-2} as it was established by means of deep level transient spectroscopy[7].

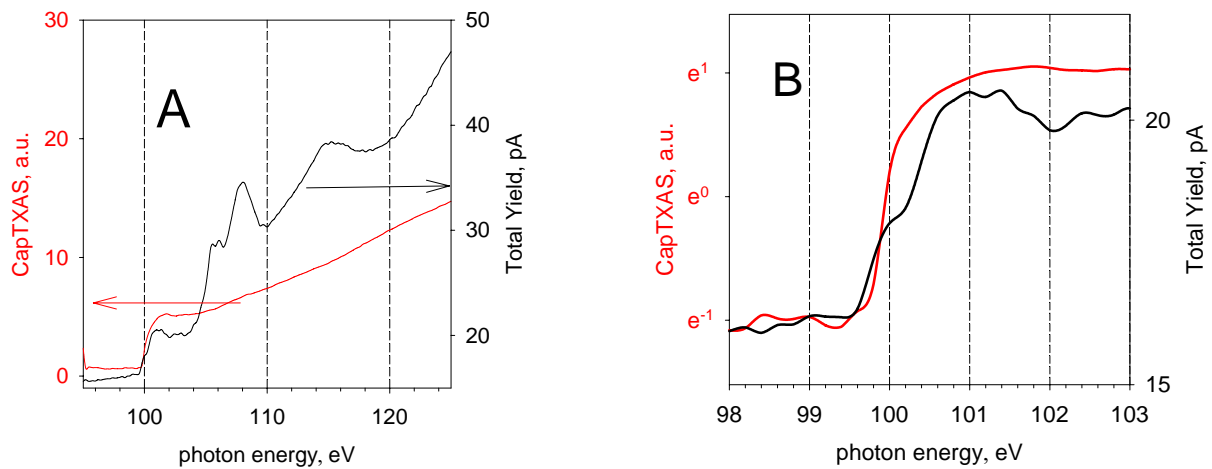


Figure 1. A,B: Red- capacitance transient X-ray absorption spectrum of o Al/50nmSi/Si bonded wafer taken at the reverse bias voltage $U_b=0V$, refilling forward voltage pulse level of $+0.6V$, refilling pulse duration/period of $10\mu s/1ms$ and at the room temperature. Black - total electron yield from the free surface of the same silicon. Note the logarithmic scale for CapTXAS in Fig. 4B.

The CapTXAS spectrum of the sample consist of the step at 99 eV correspondent to the 2p absorption edge of crystalline Si and a smooth increase of the capacitance transient signal toward higher photon energies. One can note from Fig.2 that the absorption peaks above 105 eV due to the presence of the native oxide on silicon surface registered with total yield technique does not reveal with capacitance measurements. That is because the capacitance changes are only due to the capture of the holes that were generated by X-ray absorption in the substrate as it was expected from the model and the theory presented above. Indeed the top bonded layer and the native oxide play a role of a filter for the X-ray radiation. Accordingly, since the thickness of the top bonded wafer (50nm) is much larger that the thickness of the native oxide the latter gives the minor contribution to the measured signal. Fig 2B reproduce a part of the spectra shown in Fig. 4A where the CapTXAS spectrum is presented in logarithmic scale since $\alpha_s d_s$ is now of about 0.5 and exponential dependence of the capacitance signal on absorption coefficient must be taken into account . The careful examination of the Fig.4B reveals some differences of the fine structure from the one of TY-spectrum. The origin of these differences is not established firmly up to now. Our tentative explanation is that might be due to mechanical strains that increase closer to the bonded interface.

CapTXAS and TY absorption spectra of NiPc layer at the N 1s edge are presented in Fig. 2. The fine structure of both spectra coincide well with the well known transition that were identified previously [8].

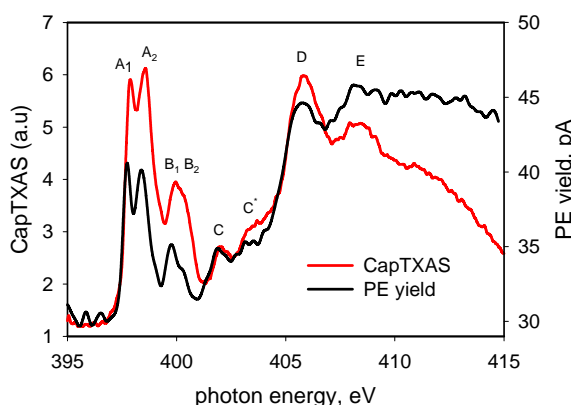


Figure 2. Absorption spectra of NiPc layer at the N 1s edge: red – capacitance transient measurements on Au-NiPc-Si structure, reverse bias voltage $U_b=-4V$, refilling forward voltage pulse level of $-4V$, refilling pulse duration/period of $10\mu s/0.5ms$ and $T=80K$. Black – total electron yield current from the free surface of NiPc layer on silicon.

There are obvious differences in the relative amplitudes of the particular peaks

measured with two techniques. The most conspicuous is the ratio of the signals between peaks A and D. According to previous data [8] the ratio of the intensity A/D peaks varied strongly depending on the polarization of the incident radiation with respect to the NiPc molecule plane. So, we could assume that there exist regions with different molecule orientation in our layer. Unfortunately, based on existing data it is impossible to differentiate whether the orientation inhomogeneity is lateral or across the sample thickness. Hence, additional experiments are needed to clarify this point.

Summary Local intensity of the synchrotron radiation beam of RGLB focused on the investigated Schottky-diode was found to be sufficient to produce the capacitance changes due to refilling of the carrier traps in our samples with the time constants of few milliseconds.

The short time constants of the capacitance transient allows one to use conventional lock-in correlation technique and for the first time one to realize a new method of the X-ray absorption measurements that we called Capacitance Transient X-ray Absorption Spectroscopy (CapTXAS).

CapTXAS can be applied measurements of the absolute absorption coefficients of thin layers, burned layers in multiplayer semiconductor structures, implanted layers. Both conductive and non-conductive layers bases on semiconducting substrate can be investigated with capacitance related techniques.

The quantitative model for the experimental data treatment obtained with the photocurrent- and photocapacitance- related techniques has to include the more precise treatment of the effects of hot carriers created under X-ray excitation on the recombination phenomena.

References

1. Hu, T.D., Y.N. Xie, S. Qiao, Y. Hai, Y.L. Jin, and D.C. Xian, *Photoconduction extended x-ray-absorption fine structure of GaAs*, Physical Review B, 1994. **50**(4): p. 2216 LP - 2220.
2. Boehme, R.F., G.S. Cargill III, W. Weber, and T. Jackson, *Diode current detection of extended x-ray absorption fine structure in gallium arsenide*, Journal of Applied Physics, 1985. **58**(2): p. 811-815.
3. Weber, J., J. Bollmann, S. Knack, V. Kotestki, H.-E. Mahnke, and W. E., *Capacitance-Transient detection of X-ray absorption fine structure: a possible toll to analyze the structure of deep-level centers?*, Solid state phenomena, 2004. **95-96**: p. 483-488.
4. Ishii, M., Y. Yoshino, K.-i. Takarabe, and O. Shimomura, *Site-selective x-ray absorption fine structure: Selective observation of Ga local structure in DX center of Al_{0.33}Ga_{0.67}As:Se*, Applied Physics Letters, 1999. **74**(18): p. 2672-2674.
5. Ishii, M., *Site-specific x-ray absorption spectroscopy of electron traps by x-ray-induced displacement current measurement*, Physical Review B (Condensed Matter and Materials Physics), 2002. **65**(8): p. 085310.
6. Fujioka, H., T. Sekiya, Y. Kuzuoka, M. Oshima, H. Usuda, N. Hirashita, and M. Niwa, *Synchrotron-radiation deep level transient spectroscopy for defect characterization of semiconductors*, Applied Physics Letters, 2004. **85**(3): p. 413-415.
7. Yu, X., T. Arguirov, M. Kittler, W. Seifert, M. Ratzke, and M. Reiche, *Properties of dislocation networks formed by Si wafer direct bonding*, Materials Science in Semiconductor Proc. 11th Int. Conf. on Defects - Recognition Imaging and Physics in Semiconductors (DRIP-XI) Sept. 13-19 in Beijing, 2006. **9**(1-3): p. 96-101.
8. Rocco, M.L.M., K.-H. Frank, P. Yannoulis, and E.-E. Koch, *Unoccupied electronic structure of phthalocyanine films*, The Journal of Chemical Physics, 1990. **93**(9): p. 6859-6864.

Time- and layer-resolved magnetization dynamics in magnetic multilayered systems

D. Bayer¹, J. Miguel², J. Sanchez-Barriga³, M. Piantek², B. Heitkamp³,
H. Dürr³, W. Kuch², M. Aeschlimann¹

¹ University of Kaiserslautern, Department of Physics, 67663 Kaiserslautern, Germany

² Freie Universität Berlin, Institut für Experimentalphysik, Arnimallee 14, 14195 Berlin, Germany

³ BESSY GmbH, Albert-Einstein-Straße 15, 12489 Berlin, Germany
(BMBF Nr. 05 KS4UK1/4)

For both fundamental and application points of view, the switching time and behaviour of a trilayer system consisting of a ferromagnetic/non magnetic/ferromagnetic trilayer (as used e.g. for magnetoresistive devices) is of utmost significance. In microstructured magnetic multilayer systems a clear view of the reversal dynamics has not been achieved experimentally because it needs a technique offering at the same time a high temporal and lateral resolution. Time-resolved XMCD-PEEM represents a state-of-the-art way of getting ultrafast time resolution (low picosecond regime) and simultaneously layer **and** spatially resolved information of the investigated magnetic multilayered structures. The magnetization can be excited by a short magnetic field pulse that can be achieved in principle through different pump-probe methods. In the actual applications we used a laser-induced electrical field pulse in a Au stripline.

The transient local magnetization dynamics was studied by time-resolved XMCD-PEEM in a stroboscopic pump-probe technique as shown in Fig. 1. Magnetic microstructures deposited on a Au stripline are magnetically disturbed by a short magnetic field pulse. The ultrashort magnetic field pulse is provided by an electric current pulse flowing through the stripline underneath the microstructure, triggered by an optical switch by means of a femtosecond laser pulse. This part of the technique, in combination with the length of the synchrotron bunch, is responsible for the time resolution of the experiment. Therefore, an important point is the synchronization between the pump laser pulse (triggering the optical switch and creating the field pulse) and the synchrotron bunch probing the magnetic structures.

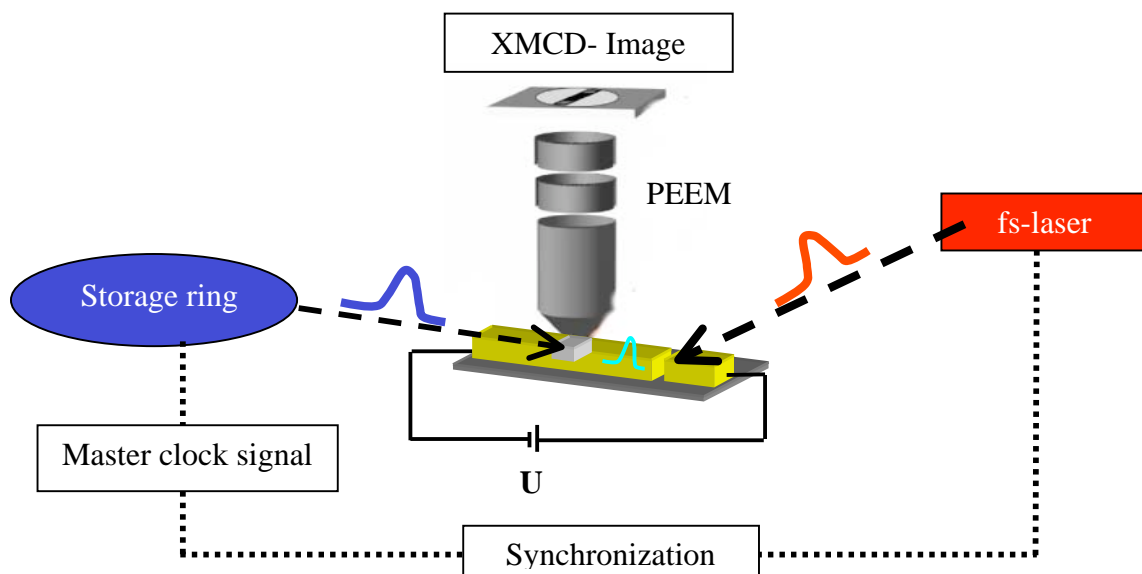


Fig. 1 Schematic of the time-resolved XMCD PEEM measurement.

Fig. 2 presents the sample design (optical switch, stripline and magnetic microstructures). As substrate we used low-temperature (lt) grown GaAs. The high defect density in lt-GaAs results in a short lifetime of the photoexcited carriers, leading to a short current pulse and, hence, to the desired short magnetic field pulse.

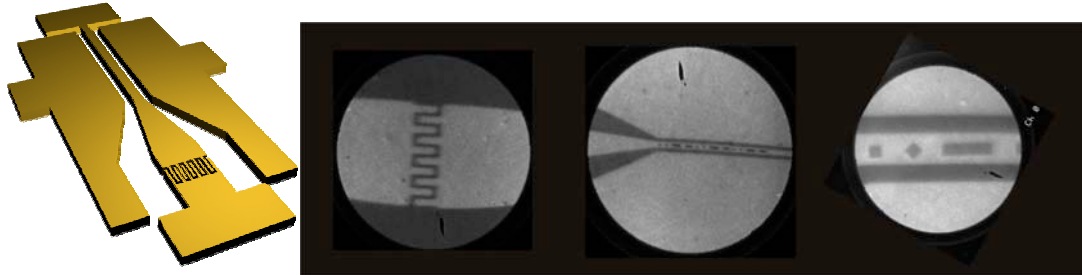


Fig. 2 The left side shows a sketch of the used switch and stripline combination used in the experiments. On the right side PEEM images of the switch (finger length 10 μm , width 5 μm , gap 5 μm), the stripline including the magnetic microstructures in survey mode, and the magnetic structures are shown (from left to right, fields of view are $\sim 100 \mu\text{m}$, 250 μm and 50 μm).

The laser-induced transient electric field pulse in the stripline leads to a small apparent shift of the stripline in the PEEM image, which can be used to obtain the temporal shape of the current pulses. By increasing the time delay between the laser pump pulse and the synchrotron bunch, a series of PEEM images of the Au stripline (close to the microstructures) was taken. By plotting the observed shift as a function of the pump–probe time delay, the temporal shape of the magnetic field pulse can be revealed.

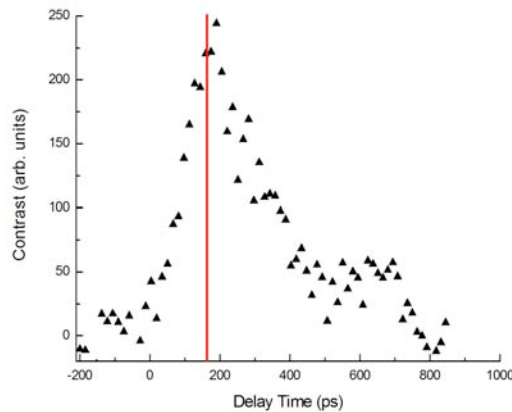


Fig.3 Transient shift of the Au stripline in the PEEM image as a function of the pump–probe delay time.

As shown in Fig. 3, the typical rise time of the transient shift, and hence the field pulse, is in the order of 100 ps, which is based on a convolution of the bunch pulse width (isolated electron bunch, $t_{\text{FWHM}} \approx 50 \text{ ps}$), the current pulse width, and the jitter between the laser and synchrotron pulse.

The investigated magnetic spin valve systems consist of 4 nm FeNi/4 nm Cu/4 nm Co trilayers, sputter deposited on the Au stripline. In order to control and optimize the magnetic coupling properties of the different magnetic layers, MOKE measurements on extended films and arrays of microstructures were performed. From such studies we obtain the coercive fields for both layers ($H_{\text{C}}^{\text{Co}} = 20 \text{ mT}$, $H_{\text{C}}^{\text{Py}} \sim 3 \text{ mT}$), and an exchange bias field for the Py layer, $H_{\text{E}}^{\text{Py}} \sim -6 \text{ mT}$.

In static XMCD-PEEM measurements, the domains of the different magnetic layers could be clearly resolved as shown in Fig. 4, revealing the perfect match of the corresponding domain structures.

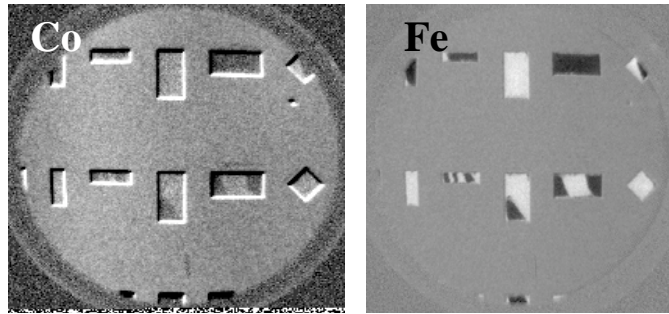


Fig. 4: Layer resolved static XMCD-PEEM images of magnetic microstructures (4 nm Py/4 nm Cu/8 nm Co trilayers). Although the underlying Co layer is covered by 10 nm Cu, the magnetic contrast is clearly visible (field of view: 130 μm).

Fig. 5 shows the first experimental time-resolved results. The series of images taken at the energy of the Fe- L_3 edge shows the microstructures at different pump-probe time delays.

A clear change in the domain pattern of the structures as a function of the pump-probe time delay is visible, as can be seen in the structure marked by a red rectangle. As the time delay increases, so does the magnetic field in the direction perpendicular to the stripline, and a darker domain develops in the left part of the structure. However, when the pump-probe delay was set back to the onset of the pulse, the initial magnetization pattern in the structure was not directly recovered. This suggests the presence of changes in the domain pattern of the magnetically hard Co layer on a timescale of hours, much longer than the magnetic response to single pulses.

We are currently working to improve the magnetic behavior of the samples, the maximum field strength and the temporal width of the pulses.

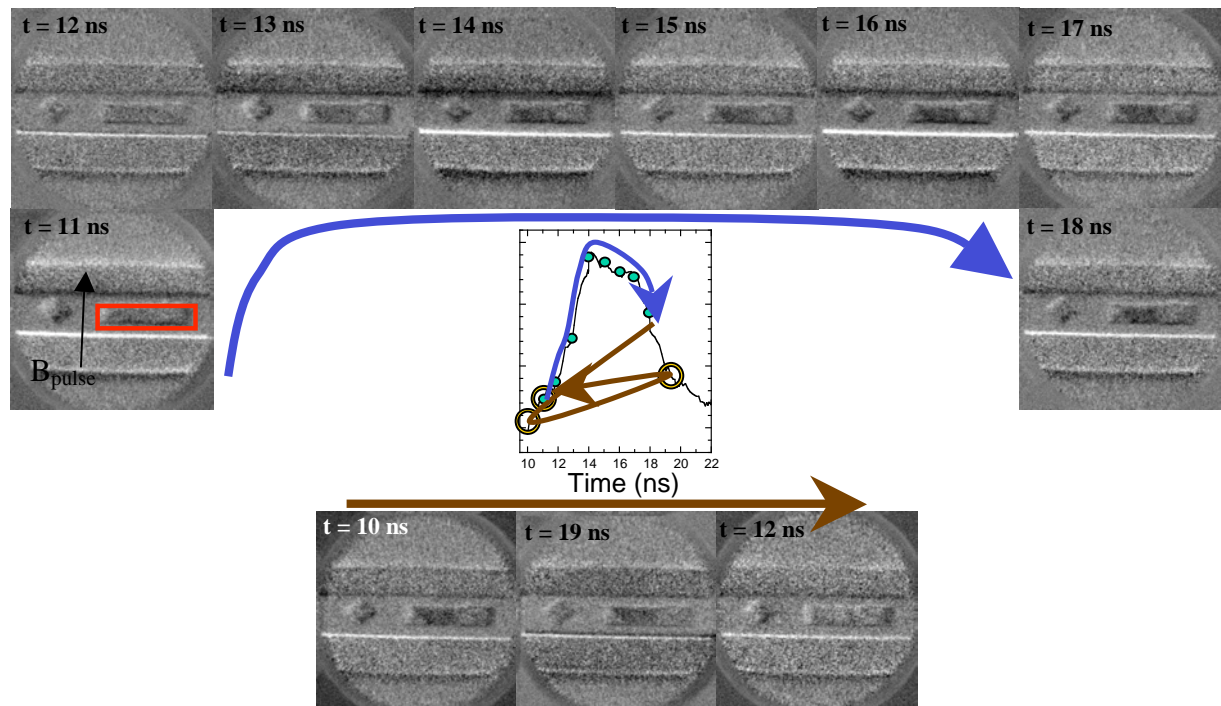


Fig. 5 Selected XMCD-PEEM images showing the time evolution of the magnetic domain structures during the magnetic pulse, shown in the inset (black line). The blue and brown arrows indicate the order in which the images were taken.

Direct observation of charge and orbital order in magnetite*

J. Schlappa,¹ C. Schüßler-Langeheine,¹ C. F. Chang,¹ H. Ott,¹ A. Tanaka,² Z. Hu,¹
M. W. Haverkort,¹ E. Schierle,³ E. Weschke,³ G. Kaindl,³ and L. H. Tjeng¹

¹*II. Physikalisches Institut der Universität zu Köln, Zùlpicher Str. 77, 50937 Köln*

²*ADSM, Hiroshima University, Higashi-Hiroshima 739-8530, Japan*

³*Institut für Experimentalphysik, Freie Universität Berlin, Arnimallee 14, D-14195 Berlin*

Funded by the DFG through SFB 608, TP C4
and the BMBF through project 05 ES3XBA/5

Magnetite, Fe_3O_4 , is one of the most fascinating materials in solid state physics. Besides being the first magnetic material known to the mankind, it is also the first example for an oxide to show a first order anomaly in the temperature dependence of the electrical conductivity at $T_V \approx 120$ K, the famous Verwey transition [1]. It is accompanied by a structural phase transition from the cubic spinel to a distorted structure, leading to the appearance of superstructure diffraction peaks mainly characterized by the wave vectors (001) and $(00\frac{1}{2})$ with respect to the cubic unit cell. One usually connects this transition with the charge ordering (CO) of Fe^{2+} and Fe^{3+} ions on the octahedrally coordinated, so called, B-sites. However, the detailed pattern of the CO in Fe_3O_4 , or in general the crystal structure, is still a matter of debate.

It was the recent diffraction study by Wright, Attfield and Radaelli using neutron and synchrotron-radiation from powder [2], which has triggered a flurry of new theoretical and experimental studies. The authors found long-range charge order from the pattern of shorter and longer bond lengths between B-site Fe and oxygen ions below T_V . Resonant x-ray diffraction experiments at the Fe K -edge, however, found contradicting results [3,4].

To resolve controversies about electronic order phenomena, resonant x-ray diffraction using soft-x-rays is most likely the better tool since the relevant valence orbitals are directly involved in the intermediate states of the process [5] thanks to the dipole allowed transitions. Indeed resonant soft-x-ray diffraction (RSXD) at the O K -edge has revealed the existence of the $(00\frac{1}{2})$ diffraction peak, which has been interpreted as evidence for Fe 'charge-orbital' ordering [6]. However, unlike for the cuprates, the oxygen- K resonance is a very indirect probe for the relevant transition-metal valence and orbital occupations in magnetite, because of the weak hybridization between the O- p and the Fe- t_{2g} orbitals.

We therefore performed a direct experimental determination of the Fe t_{2g} charge and orbital order by RSXD at the Fe $L_{2,3}$ edges. This approach has the major advantage that the $3d$ -electronic states of the transition-metal ion are probed directly. At this Fe resonance, the assignment of the resonance properties can be made right from the spectral shape without involving band-structure or multiple-scattering calculations. We studied the two diffraction peaks characteristic for the low-temperature phase of magnetite, $(00\frac{1}{2})$ and (001). The

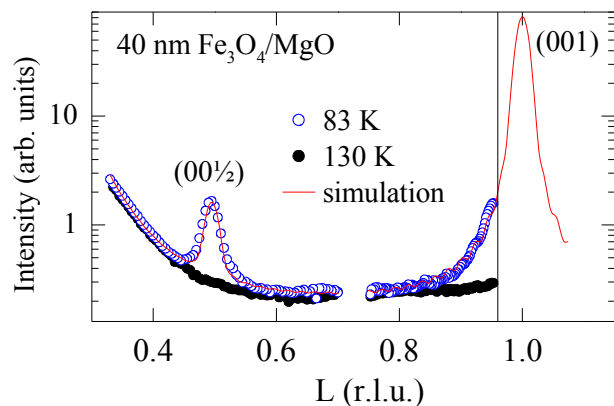


Fig. 1: Scan long L below (open symbols) and above T_V (filled) symbols. The red line is a simulation.

resonances of both peaks are also much stronger than the ones at the Fe K and O K edges providing an excellent spectroscopic signal with low background.

For this study we chose a magnetite film rather than a bulk crystal for two reasons. Firstly, diffraction features in a thin film are broadened along the surface normal. This broadening allows us to study the resonance of the (001) peak, whose peak maximum cannot be reached at the $L_{2,3}$ resonance. Secondly, the volume probed by the scattering experiment is determined by the film thickness rather than by the photon penetration depth. Since the latter changes strongly across resonances in the soft x-ray range, this change may obscure the resonance effect. A 40-nm film of Fe_3O_4 was grown ex-situ by molecular-beam epitaxy (MBE) on epi-polished MgO. In order to separate the specular reflectivity from the c -direction of Fe_3O_4 , a substrate with about 6° miscut was used. RSXD experiments were carried out at the BESSY beamline UE52-SGM using the UHV diffractometer built at the Freie Universität Berlin. Fig. 1 shows a reciprocal-space scan along the [001] or L direction taken at 83 K (blue open symbols), *i.e.* below T_V , revealing the $(00\frac{1}{2})$ diffraction peak, and the onset of the (001). Even though the maximum of the (001) cannot be reached at the Fe- $L_{2,3}$ resonance, where the maximum momentum transfer is $L=0.96$ as indicated by the vertical line in Fig. 1, the broadening of the (001) peak transfers some intensity into the reachable momentum space. The red solid line through the data points is a simulation including two peaks of the same shape but different intensity and the Fresnel reflectivity, which causes the increasing background at low L -values. This model describes the data reasonably well, even though the oscillations of the Laue profile are not resolved in the data. Both peaks disappear when the sample is heated to 130 K (filled symbols), *i.e.* above T_V .

The spectra obtained from the peaks after background subtraction are presented as symbols in Fig. 2 b) and c). The shapes of the spectra for the two peaks are distinctly different: the L_3 part of the $(00\frac{1}{2})$ spectrum has a sharp resonance maximum at 708.4 eV, while the spectrum of the (001) peak shows a double peak structure, one peak at 708.6 eV, *i. e.* almost the same energy as the maximum of the $(00\frac{1}{2})$ spectrum, and the second one at 710.1 eV. The L_2 parts of the spectra, on the other hand, are more similar with two maxima at 720 eV and 721.4 eV. For comparison the Fe $L_{2,3}$ XAS spectrum is presented in Fig. 2a), which looks clearly different from the diffraction spectra.

To interpret the spectroscopic results, we resort to the existing literature on the XAS of Fe_3O_4 [7,8] with emphasis on the strong magnetic circular and linear dichroism effects therein. The sharp structures in the dichroic spectra allow for a clear decomposition of the XAS spectrum in terms of contributions coming from the different Fe sites in magnetite. This decomposition is given in Fig. 2a): the spectrum from the B-site Fe^{2+} ion is shown by the red solid line, the A-site Fe^{3+} by in magenta, and the B-site Fe^{3+} in blue. The maximum in the L_3 white line of each of these ions occurs at quite differ-

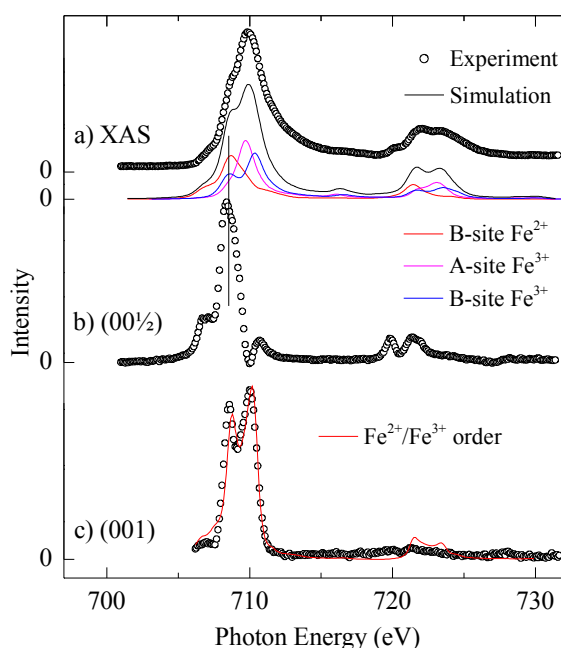


Fig. 2 a) x-ray absorptions spectrum (symbols) with contributions of the different ion sites (sub-spectra), b) resonance of the $(00\frac{1}{2})$ peak, c) resonance of the (001) peak with the result of a simulation (red line).

ent energies, an aspect which we will utilize next to interpret the spectra (001) and (00 $\frac{1}{2}$) diffraction peaks.

The maximum of the (00 $\frac{1}{2}$) diffraction peak spectrum occurs at essentially the same energy as that of the B-site Fe²⁺ XAS. This means that the (00 $\frac{1}{2}$) diffraction peak is due to an order, which involves only B-site Fe²⁺ ions. This in turn implies that orbital order of the t_{2g} electrons is at play here, since this is the only degree of freedom available which could make one B-site Fe²⁺ ion to be different from another B-site Fe²⁺ ion. In $P2/c$ or Cc symmetry the (00 $\frac{1}{2}$) diffraction peak is glide-plane forbidden with the consequence that only off-diagonal elements of the scattering tensors contribute. These elements can be expected to be much stronger for the Fe²⁺ (d^6) ions than for the more spherical Fe³⁺ (d^5) ions, explaining indeed why the resonant enhancement of the (00 $\frac{1}{2}$) peak occurs only for photon energies which are characteristic for the Fe²⁺ sites. We note that this orbital-order finding does not exclude the existence of charge-order associated with other, not glide-plane forbidden peaks related to the doubling of the unit cell along c as observed in Ref. 4.

In contrast to (00 $\frac{1}{2}$), the (001) spectrum shows two peaks which essentially occur at the energies of the maxima of the two B-site resonances. Such a double-peak structure is exactly the resonance shape to be expected from charge order involving the two B-site ions. The experiment is sensitive to differences in the scattering amplitudes of the different ions. For two resonances well separated in energy, as it is the case for the B-site Fe²⁺ and Fe³⁺ ions, this difference is large near the two resonance maxima leading to such a two-peak feature. To illustrate this we show as the red line in Fig. 2c) the result of a simulation using the complex scattering amplitudes for the B-site ions, which we have extracted from the subspectra in Fig. 2a). From the very good agreement between experiment and simulation we conclude that there is indeed B-site charge order with a (001) wave vector.

Summarizing, using resonant soft x-ray diffraction at the Fe- $L_{2,3}$ threshold from a film of magnetite grown on stepped MgO we were able to establish directly that there is t_{2g} orbital order on the B-sites Fe²⁺ ions and that this is reflected in the existence of the (00 $\frac{1}{2}$) diffraction peak. We have also been able to show that charge order of the B-site ions is the reason for the appearance of the (001) diffraction peak, thereby settling the contradicting claims from Fe K -edge resonant diffraction studies.

We are grateful to M. Braden, H.-H. Hung, P. G. Radaelli, P. Abbamonte, G. A. Sawatzky, and especially D. I. Khomskii for very helpful discussions and L. Hamdan for her skillful technical assistance.

* A more detailed report of these results can be found on [arXiv.org:cond-mat/0605096](https://arxiv.org/cond-mat/0605096).

- [1] E. J. W. Verwey, *Nature (London)* 144, 327 (1939).
- [2] J. P. Wright, J. P. Attfield, and P. G. Radaelli, *Phys. Rev. B* 66, 214422 (2002).
- [3] G. Subías *et al.*, *Phys. Rev. Lett.* 93, 156408 (2004).
- [4] E. Nazarenko *et al.*, *Phys. Rev. Lett.* 97, 056403 (2006).
- [5] C. W. M. Castleton and M. Altarelli, *Phys. Rev. B* 62, 1033 (2000).
- [6] D. J. Huang *et al.*, *Phys. Rev. Lett.* 96, 096401 (2006).
- [7] P. Kuiper, B. G. Searle, L.-C. Duda, R. M. Wolf, and P. J. van der Zaag, *J. Electron Spectrosc. Relat. Phenom.* 86, 107 (1997).
- [8] J. Chen, *et al.*, *Phys. Rev. B* 69, 085107 (2004).

A spatially resolved investigation of the local, micro-magnetic domain structure of Co₂FeSi single crystal.

Andrei Gloskovskii¹, Joachim Barth¹, Benjamin Balke¹, Gerhard H. Fecher¹, Claudia Felser¹, Fabiano Bernardi², Florian Kronast³, Ruslan Ovsyannikov³, Hermann Dürr³, Wolfgang Eberhardt³, Gerd Schönhense⁴

¹ Institut für Anorganische Chemie und Analytische Chemie, Johannes Gutenberg - Universität Mainz, D-55099 Mainz, Germany

² Instituto de Física, Universidade Federal do Rio Grande do Sul, Porto Alegre, 91501-970, Brazil

³ BESSY GmbH, Albert-Einstein-Straße 15, 12489 Berlin, Germany

⁴ Institut für Physik, Johannes Gutenberg - Universität Mainz, D-55099 Mainz, Germany

The X₂YZ Heusler compounds consist mostly of two transition metals (X₂, Y) and one main group (Z) element crystallising in the L₂₁ structure (space group $Fm\bar{3}m$). They have attracted scientific and technological interest for their potential use as materials for magneto-electronic devices [1]. Reason is the exceptional electronic structure found in many of those compounds, in particular the ones based on cobalt. The Heusler compound Co₂FeSi has attracted particular interest because it is predicted to have a large minority spin band gap in the order of 1 eV [2, 3] and, at T_C = 1100 K [4, 5], it has one of the highest Curie temperatures among the known Heusler compounds. Bulk Co₂FeSi has been stabilised in the L₂₁ structure with a saturation magnetisation of 6 μ_B at 5 K [4, 5].

We report on the study of the micro-magnetic structure of Co₂FeSi single crystal, using photo emission electron microscopy combined with X-ray magnetic circular dichroism as contrast mechanism. The micro-spectroscopic measurements were performed at the UE56-SGM beamline. The slits were set to 130 μm resulting in a spot-size at the sample of 30 μm with an energy dispersion of 0.65 eV across the spot at the Co L₃ edge. All measurements reported below were performed for non-magnetised samples.

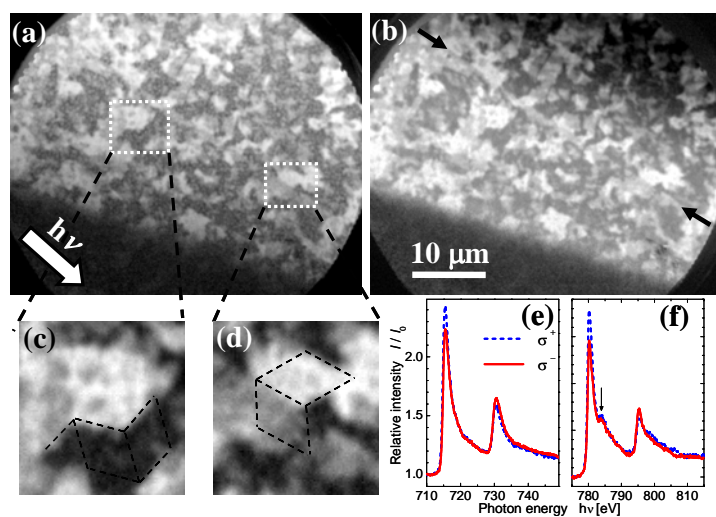


Fig. 1. XMCD-PEEM image showing the magnetic domain pattern of Co₂FeSi(110). The images are obtained at the Fe L₃ (a) and the Co L₃ (b) edges. The projection of the photon impact direction is denoted by $h\nu$. (c, d) show details of two domain structures that are rotated with respect to each other. The arrows in (b) point on a line-like defect. Local XMCD taken at the Fe (e) and Co (f) L-edges. Solid and dashed lines show the spectra measured with opposite photon helicity. The arrow in (f) assigns a structural feature that is typical for Heusler compounds.

Fig. 1 shows XMCD-asymmetry images of the (110) single crystal surface with an orientation better than 0.1° (MATECK). The images were acquired at the Fe L₃ edge (a)

and Co L_3 edge (b). The ferromagnetic coupling between Fe and Co is evident by the similar magnetic contrast of the domains measured at the corresponding absorption edges and clearly visible from Figs. 1(a) and (b). The surface exhibits an irregular pattern of domains with a size of a few μm . Close inspection reveals that the local patterns reflect nearly threefold symmetry. The two zoomed areas (c, d) show patterns that look like a cube viewed along the space diagonal. The orientation of the two cubes is rotated by about 35° . This corresponds to the angle between $\langle 111 \rangle$ and $\langle 110 \rangle$ -like directions. The larger angle drawn in the figure corresponds to about 110° that is the angle between $\langle 111 \rangle$ -like directions. The stray field minimisation of the local out-of-plane magnetisation directions results in small domains with different magnetisation directions.

In order to investigate the element specific magnetic properties and compare them with theoretical predictions, measurements of the magnetic circular dichroism in the soft X-ray core-level absorption of the Fe and Co 2p excitation were carried out. XMCD spectra of the Co and Fe $L_{2,3}$ edges are shown in Fig. 1(e, f). They were obtained by integrating over a region of interest in the XMCD-PEEM image while scanning the photon energy (bright area in Fig. 1(c) with a size of about $5 \times 5 \mu\text{m}^2$). The spectra reveal a high XMCD asymmetry with opposite sign at the L_3 and L_2 edges. In particular, the Co spectrum reveals an additional structure above the L_2 edge (see arrow in Fig. 1(f)) that is indicative for the L_{21} -structure. The spectra give no indication of oxidation that would show up in terms of a pronounced splitting of the L lines [6].

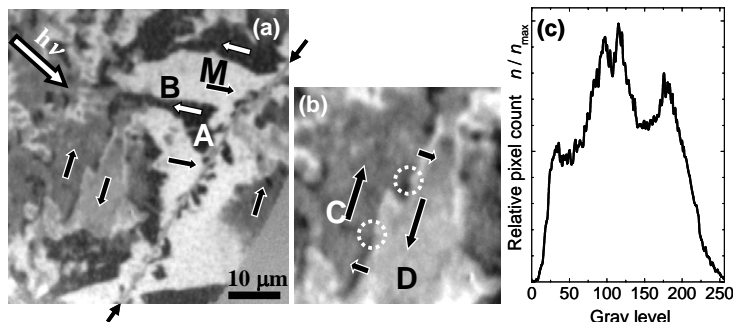


Fig. 2. (a) the domains from a different surface region compared to Fig.1. The arrows indicate the local magnetization direction. (b) is a detail showing the asymmetric Bloch walls between regions C and D. Arrows outside of (a) denote a crystal defect line. Histogram (c) of the grey levels in XMCD-PEEM image of the single crystal displayed in (b).

Fig. 2 shows the domain pattern of a different part of the surface. In this case the magnetisation lies obviously completely in the surface plane. The image reveals extended domains with sizes up to several $10 \mu\text{m}$ (note that the sample was not magnetised). Large areas showing the same grey levels are indicative of a uniform magnetisation within the domains and an in-plane easy axis. The local magnetization directions are denoted by arrows. Due to the tilted angle of incidence (see arrow at $h\nu$) domains of four equivalent orientations can be distinguished in the contrast. This is also evident from the histogram plotted in Fig. 2(c). Domains A and B are parallel to the photon impact direction yielding an almost black-white contrast. Domains C and D (see (b)) are not perpendicular to the photon impact direction resulting in two different grey levels. The 180° domain boundaries appear as asymmetric Bloch walls as is clearly seen in the zoomed image (b). Note that the sense of rotation of the in-plane magnetisation changes along a wall as indicated by the circles. The domains C and D are separated by a Bloch wall that, in the surface region turns in-plane similar to a Néel wall. The images exhibit also a few head-to-head 180° walls, in particular between regions A and B. Image (a) exhibits a crystal

defect running as line with irregular small domains across the image as is indicated by the arrows outside of the image. As this line crosses several larger domains of homogeneous magnetization distribution, it is interpreted as a surface defect, whose magnetisation pattern does not penetrate deeply into the bulk.

The authors acknowledge financial support from the Deutsche Forschungs Gemeinschaft (project TP7 in research unit FG 559) and partial funding by BESSY (BMBF 05 ES3XBA/5) and Materialwissenschaftliches Forschungszentrum, Mainz.

References:

- [1] C. Felser, G.H. Fecher, B. Balke. *Angew. Chemie (Int. Ed.)* **46** (2007) 668.
- [2] H. C. Kandpal, G. H. Fecher, C. Felser, G. Schönhense. *Phys. Rev. B*, **73** (2006) 094422.
- [3] B. Balke, G. H. Fecher, H. C. Kandpal, C. Felser, K. Kobayashi, E. Ikenaga, J.-J. Kim, S. Ueda. *Phys. Rev. B*, **74** (2006) 104405.
- [4] S. Wurmehl, G. H. Fecher, H. C. Kandpal, V. Ksenofontov, C. Felser, H.-J. Lin, J. Morais. *Phys. Rev. B*, **72** (2005) 184434.
- [5] S. Wurmehl, G. H. Fecher, H. C. Kandpal, V. Ksenofontov, C. Felser, H.-J. Lin. *Appl.Phys. Lett.*, **88** (2006) 032503.
- [6] C. Felser, B. Heitkamp, F. Kronast, D. Schmitz, S. Cramm, H. A. Dürr, H.-J. Elmers, G. H. Fecher, S. Wurmehl, T. Block, D. Valdaitsev, S. A. Nepijko, A. Gloskovskii, G. Jakob, G. Schönhense, and W. Eberhardt. *J. Phys.: Condens. Matter*, **15** (2003) 7019.

Time-resolved visualization of the heat flow in VO₂/Al₂O₃ films

Lee J. S.,¹ Ortolani M.,¹ Chang Y. J.,² Noh T. W.,² and Schade U.¹

¹ *Berliner Elektronenspeicherring-Gesellschaft für Synchrotronstrahlung m.b.H. (BESSY),
Albert-Einstein-Straße 15, 12489 Berlin, Germany*

² *ReCOE, School of Physics and Astronomy, Seoul National University, Seoul 151-747, Korea*

Thermodynamics related with a heat flow is one of the most fundamental topics in the physics community and is of particular importance for the micro-/nanoscale electrical devices where the generated heat should be managed to maintain their functional reliabilities [1]. While macroscale heat transfer is well explained by the Fourier law of the heat conduction, micro-/nanoscale heat transfer requires microscopic energy-transfer models since the characteristic length scale of a device (or the thermal diffusion length) is comparable to or smaller than the heat carrier mean-free-path and heat conduction processes are no longer local phenomena, but radiative phenomena.

In order to investigate this issue, we exploited the mid-infrared microscopy using the highly brilliant infrared synchrotron radiation [2], which allows us to achieve a diffraction-limited spatial resolution. We performed resistance switching of a VO₂ film grown on the Al₂O₃ substrate by applying an electric pulse. As a consequence Joule heating of about 1 W has been induced in a 15 × 50 μm² area between the two electrodes. We monitored the local temperature variation between 56 °C and 75 °C, where the optical response of the VO₂ film exhibits a huge change owing to the insulator-metal transition around 64 °C [3]. Figure 1 shows the temperature (T)-dependent reflectivity $R(\omega)$ of the VO₂/Al₂O₃ film in the infrared region as a function of the photon frequency. As the temperature increases, $R(\omega)$ exhibits a large increase consistently with the fact that the high reflectivity in the infrared region should be attributed to the free carrier response. The inset shows that the reflectivity integrated over the spectral range of 550 – 8000 cm⁻¹, $\text{Int}(R)$, monotonically increases with temperature between 58 and 75 °C. This behavior allows monitoring the temperature by observing the $\text{Int}(R)$.

Figures 2(a)-2(c) display the mercury-cadmium-telluride (MCT) detector signal for time-dependent mapping investigations at $t=10$ μs, 30 μs, and 50 μs, respectively. The yellow dotted lines represent the boundary of the Au/Cr electrodes. Since the MCT signal S_{MCT} is proportional to the temperature of the sample in the 56 – 75 °C range, this result clearly demonstrates how the temperature distribution changes with time. First, as the time elapses, the red area having the large S_{MCT} value becomes wider and forms a circular distribution indicating an isotropic propagation of the heat. Second, the boundary region between the red and blue false colours in Fig. 2(a)-2(c) seems to be rather sharp having a thickness of about 10 μm.

In order to explain these experimental observations, we performed numerical calculations of the temperature distribution. Heat flow can be modelled by using the Fourier equation.

$$\rho C_p \partial T / \partial t = k \nabla^2 T + Q \quad (1)$$

Here, ρ is the material density, C_p is the specific heat, and k is the thermal conductivity. Q is the heat flux density. Because of the small thicknesses of the VO₂ film (~ 55 nm) and Au/Cr electrodes (~150 nm), the heat flow should mainly occur through the sapphire substrate. Therefore, we adopted the material constants of Al₂O₃. Figures 2(d)-2(f) show the modeled temperature distributions of the topmost surface corresponding to the VO₂ film. The result of our calculations is comparable to our experimental results in terms of the spatial temperature distributed and its time-dependency.

In order to complete the comparison between the experimental and simulation results, we have also to compare the front edge of the heat flow. Figure 3 shows a line scan of the detector intensity, S_{MCT} , and the temperature values at $t=10 \mu\text{s}$, $30 \mu\text{s}$, and $50 \mu\text{s}$. As expected, the trend of reflectance values measured along the scan are consistent to the temperature trend calculated, which confirms again the fact that the optically obtained signal represents the temperature of the sample, and the heat flow in the VO₂/Al₂O₃ films can be well explained, at least in the micrometric length scale, in terms of the Fourier law [5].

We expect that the present result is useful for several applications where a local temperature control is needed, for example, temperature-dependent spectroscopic experiments of living cell arrays. While the narrow temperature range of only 56 – 75 °C was monitored in this work, one can extend the temperature windows down to room temperature since the transition temperature of VO₂ can be lowered by post-annealing, by strain control, and by other techniques [4]. Finer tools like near-field spectroscopy could provide information of the heat flow mechanism in the nanometer scale. Such improvement will provide the chance to use this scheme for the thermal characterization of nanoscale samples.

We acknowledge J. Kouba, D. Schondelmaier, R. Horn, and A. Ginolas for their supports by the preparation of the electrodes and the electric circuit for the transport measurements. This work was partly supported by the Korean Research Foundation Grant and by the Korean Ministry of Science and Technology through the Creative Research Initiative program.

[1] C.-L. Tien, A. Majumdar, and F. M. Gerner, *Microscale Energy Transport* (Taylor & Francis, Washington, DC, 1988), pp. 229–294.

[2] U. Schade, A. Röseler, E. H. Korte, F. Bartl, K. P. Hofmann, T. Noll, and W. B. Peatman, *Rev. Sci. Instr.* **73**, 1568 (2002).

[3] F. J. Morin, *Phys. Rev. Lett.* **3**, 34 (1959).

[4] K. Nagashima, T. Yanagida, H. Tanaka, and T. Kawai, *J. Appl. Phys.* **100**, 063714 (2006).

[5] J. S. Lee, M. Ortolani, U. Schade, Y. J. Chang, and T. W. Noh, *Appl. Phys. Lett.* **90**, 051907 (2007).

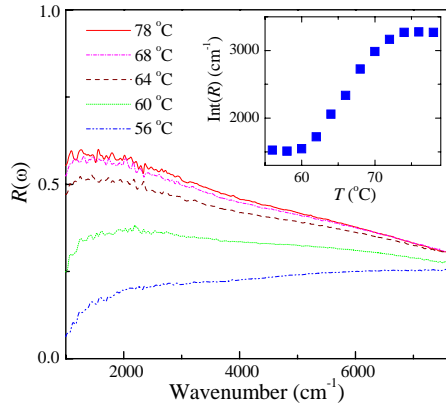


FIG. 1. Temperature dependent reflectivity spectra in the mid-infrared region obtained during the heating process. As the temperature increases, the reflectivity increases since the free carrier response becomes dominant. The inset shows the temperature-dependent changes of the integrated reflectivity, $\text{Int}(R)$. The integrated reflectivity linearly increases with temperature.

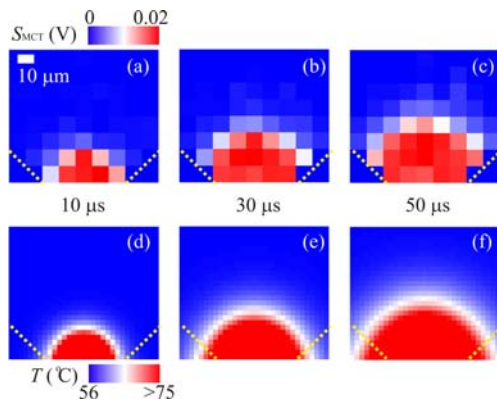


FIG. 2. Mapping data of the MCT detector signal, S_{MCT} , (a)-(c) and the predicted temperatures (d)-(f) at $t=10 \mu\text{s}$, $30 \mu\text{s}$, and $50 \mu\text{s}$. The yellow dotted line corresponds to the edge of the Au/Cr electrodes.

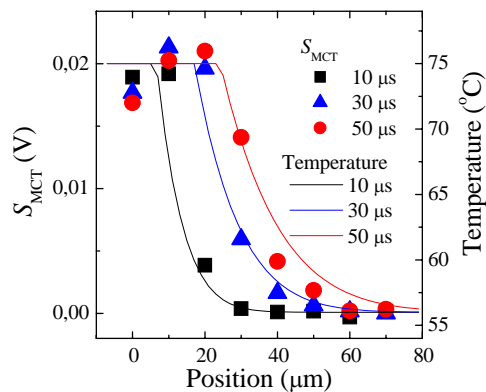


FIG. 3. Line scan curves for the MCT detector signal, S_{MCT} , and the calculated temperature profiles at $t=10 \mu\text{s}$, $30 \mu\text{s}$, and $50 \mu\text{s}$.

Doping dependence of the low-temperature order-disorder transition of the stripe phase in $\text{La}_{2-x}\text{Sr}_x\text{NiO}_4$

C. Schüßler-Langeheine,¹ R. Feyerherm,² E. Dudzik,² M. Benomar,¹ M. Braden,¹ L. H. Tjeng¹

¹II. Physikalisches Institut der Universität zu Köln, Zùlpicher Str. 77, 50937 Köln

²Hahn-Meitner-Institut c/o BESSY, Albert-Einstein-Str. 15, 12489 Berlin

Funded by the DFG through SFB 608, TP C4
and the BMBF through project 05 ES3XBA/5

Sr doped La_2NiO_4 shows an intriguing ordering of spin and charge degrees of freedom at low temperature, the famous stripe phase, which is also found in isostructural high-temperature superconductors. The crystal structure (Fig. 1) consists of NiO_2 layers, which are separated by double layers of LaO. Replacing La by Sr introduces holes into the system. At low temperatures, the doped holes arrange themselves in parallel lines, which run diagonally through the NiO_2 planes and form antiphase domain walls for the antiferromagnetic order on the hole-poor Ni sites in between. This superstructure causes additional reflections in the diffraction pattern.

The hole concentration in the hole stripes is essentially constant so that different doping levels lead to different spacings between stripes. While the stripe order can be incommensurate, each stripe has to be in register with respect to the lattice. These two conflicting tendencies lead to frustration. Incommensurate order is realized by a statistical sequence of commensurate stripe spacings such that on average the stripe spacing matches the doping level. The situation is similar for the arrangement of stripes in neighboring layers: Coulomb repulsion favors an anti-phase arrangement, which can be readily realized when the spacing in the NiO_2 layer is commensurate and an odd multiple of the lattice spacing. In all other cases the arrangement has to be partially disordered as well.

One particularly puzzling observation in these compounds is the different temperature dependence of the stripe order as found by neutron diffraction and by x-ray diffraction, respectively: While in neutron diffraction experiments the intensity of the stripe order peaks saturates at low temperatures resembling the $M(T)$ curve of a conventional ferromagnet [1], x-ray diffraction finds a maximum intensity of the diffraction peak at intermediate temperatures and a decay of the peak when the sample is cooled further [2] (c.f. upper panel of Fig. 3). This decay towards lower temperatures is accompanied by a broadening of the diffraction features indicating a loss of spatial coherence. From a careful analysis of soft x-ray diffraction data from a sample with a Sr content (x) of 0.2, we found that the *integrated* intensity of the charge and spin order peak, which is a measure of the average order parameter of the phase, essentially stays constant upon cooling; the decay of the peak height is mainly due to the broadening of the peak [3]. From this we conclude that upon cooling the phase breaks into smaller and smaller domains while the character of the order and its periodicity within each domain is con-

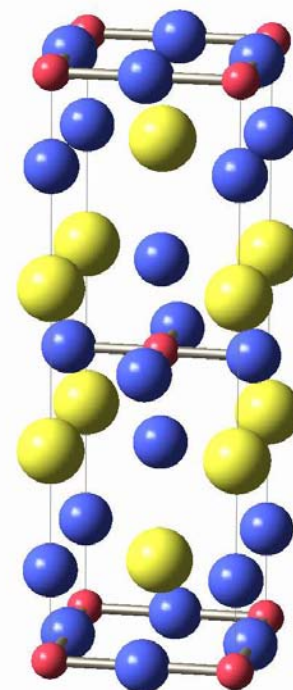


Fig. 1: Crystal structure of the parent compound La_2NiO_4 . Ni ions are red, O blue, La yellow. The NiO_2 planes are indicated by the Ni-O bonds.

served.

Such an order-disorder transition at low temperatures has been theoretically discussed for stripe phases, and two different mechanisms have been considered. One of them is a pinning of the stripes at low temperatures at the disorder potential created by the randomly distributed dopant ions [4]. The other mechanism is an intrinsic effect due to frustrations in the stripe phase that would lead to disorder at low temperatures even in a clean system [5].

In order to probe the relevance of both scenarios it is instructive to compare the order-disorder transition in differently doped samples. We chose one sample with $x \approx 1/3$, where the order is essentially commensurate and best defined and one sample with a lower doping level, $x = 0.2$, which shows incommensurate order. While the amount of intrinsic disorder is considerably different for the two samples, the influence of the dopant ions should be comparable.

The experiments were carried out at the *MAGS*-beamline of the Hahn-Meitner-Institute at BESSY at the Ni *K*-resonance around 8340 eV. The energy dependence of the $(2-2\epsilon, 0, 3)$ charge-order peak is presented in Fig. 2 (red line) together with that of the fundamental (204) Bragg peak (black) and the fluorescence signal (blue). The notation for the diffraction peaks is such that the H direction is along the modulation direction of the stripes in the NiO_2 plane, the K direction along the length of the stripes and the L direction perpendicular to the NiO_2 planes along c^* .

The charge-order spectrum shows a sharp resonance characteristic for an electronic modulation [6] with a moderate resonant enhancement of about 50 percent. In contrast to that, for the fundamental Bragg peak the loss of scattering volume caused by the reduced photon means free path above the resonance threshold is dominating and leads to an overall decreasing intensity.

At the Ni-*K* edge a wide part of the momentum space can be reached and the six-circle diffractometer at the *MAGS* beamline allows one to study the peak width in all three directions of reciprocal space. The results along L are presented in the lower panel of Fig. 3. Two different temperature scales are used for the two samples to account for the doping de-

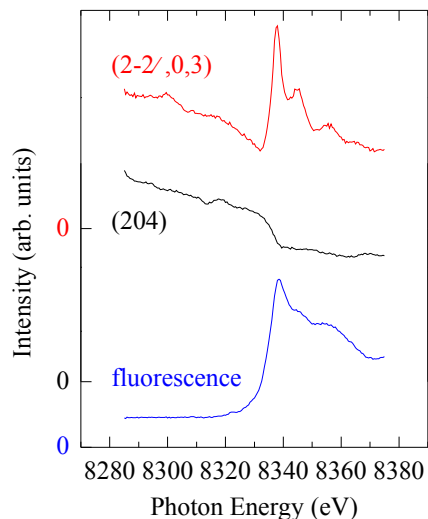


Fig. 2: Ni-*K* Resonance of the $(2-2\epsilon, 0, 3)$ charge order peak in $\text{La}_{1.8}\text{Sr}_{0.2}\text{NiO}_4$ (red) compared to the energy dependence of the fundamental (204) Bragg peak (black) and the fluorescence signal (blue).

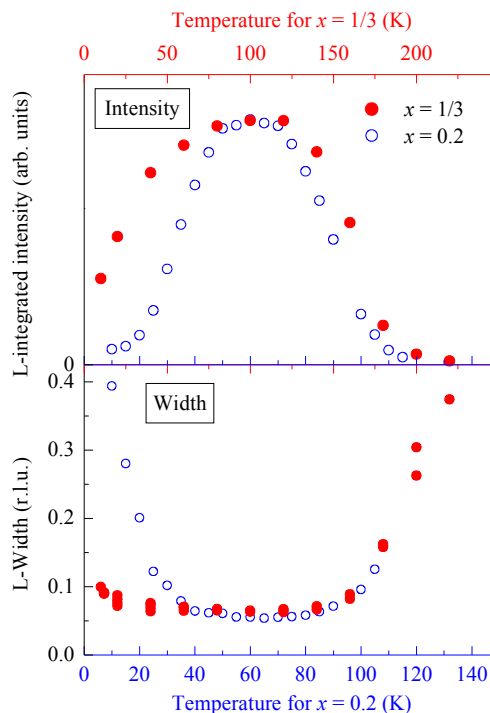


Fig. 3: L-integrated intensity (upper panel) and width along L (lower panel) vs. temperature for the two studied samples.

pendence of the transition temperatures. Presented in this way the high- and intermediate-temperature behavior of both samples are very similar. In the low-temperature region, however they curves look different. The incommensurate sample shows a dramatic loss of spatial coherence with the width at the lowest studied temperature being about 8 times larger than the minimum width around 60 K. Also the commensurate sample shows a loss of coherence, but the effect is much weaker, which is also reflected in the less prominent loss of peak height (upper panel). We can therefore assume that the influence of the disorder potential caused by the Sr ions is not the dominating cause of the broadening and that the intrinsic disorder is more important here.

It is interesting to consider, why the low-temperature order-disorder transition is not observed in neutron diffraction experiments. The intensity of a diffraction peak is distributed in a certain region of momentum space. An diffraction experiment integrates the intensity inside a volume given by the momentum resolution, *i.e.* by the detector acceptance and the beam divergence. If this probing volume is larger than the volume of the peak, a peak broadening will not affect the detected intensity as long as the peak is fully inside the probing volume. Usually, the resolution in neutron diffraction is worse than in synchrotron x-ray diffraction experiments. But the broadening, *e.g.* of the 0.2 sample is so strong that it should be visible even with very moderate resolution. The discrepancy between x-ray and neutron results must therefore have a different explanation and may be related to the different scattering cross sections and time scales probed in the respective experiments.

In conclusion, we observed a striking difference in the low-temperature order-disorder transition in doped La_2NiO_4 between a sample with nearly commensurate and one with incommensurate order. From this we conclude that the intrinsic disorder of the stripe phase is driving this transition rather than the disorder potential of the dopant ions. The change of the coherence length in the incommensurate sample is too strong to assign the fact, that neutron diffraction does not observe this transition, to the low momentum resolution in neutron experiments.

- [1] J. M. Tranquada, D. J. Buttrey and V. Sachan, Phys. Rev. B 54, 12318 (1996).
- [2] P. D. Spencer *et al.*, Eur. Phys. J. B 46, 27 (2005).
- [3] J. Schlappa *et al.*, to be published.
- [4] S. Bogner and S. Scheidl, Phys. Rev. B 64, 05417 (2001).
- [5] J. Schmalian and P. G. Wolynes, Phys. Rev. Lett. 85, 836 (2000).
- [6] Y. Murakami *et al.*, Phys. Rev. Lett. 80, 1932 (1998).

Exchange bias and uncompensated moments in fcc Co/FeMn/Cu(001)

D. Schmitz, D.A. Tennant
Hahn-Meitner-Institut Berlin c/o BESSY, Albert-Einstein-Str. 15, 12489 Berlin

M. Gruyters
Humboldt-Universität Berlin, Institut für Physik, Newtonstr. 15, 12489 Berlin

Exchange bias occurs in systems where a ferromagnet (FM) and an antiferromagnet (AFM) are in contact [1, 2]. We studied epitaxially grown ferromagnetic Co (5 ML thick) on antiferromagnetic $\text{Fe}_x\text{Mn}_{1-x}$ (12 ML thick) on Cu(001), using the excellent results obtained in Ref. [3, 4] as a starting point, in order to elucidate the role of uncompensated Fe and Mn moments at the interface to Co. Epitaxially grown systems have the advantage to exhibit a much better defined interface as compared with polycrystalline systems prepared by sputtering. Per definition, spins of one antiferromagnetic sublattice are called "uncompensated" if moments of the other antiferromagnetic sublattice, oriented into the opposite direction and therefore usually compensating the moment from the first sublattice, are missing. If the magnetization direction of the FM is reversed, one part of the uncompensated moments of the AFM follows because the coupling to the FM dominates. Another part of the uncompensated moments does not reverse with the FM because the coupling to the AFM dominates. This is the so-called "pinned fraction" of uncompensated moments which has been supposed to be crucial for exchange bias [5].

The uncompensated moments can be detected and quantified by X-Ray Magnetic Circular Dichroism (XMCD) in absorption and X-Ray Resonant Magnetic Scattering (XRMS) in reflection. We performed XMCD and XRMS measurements by reversing the helicity of the synchrotron radiation in well defined magnetization states of the samples, *e.g.*, magnetized after deposition, after field cooling and after reversing magnetization after field cooling. Magnetizing after deposition creates a well defined state of the magnetization of the FM, field cooling activates the exchange bias, reversing the magnetization reverses rotatable uncompensated spins whereas the pinned fraction keeps the initial magnetization, and reversing the magnetization a second time serves to test whether the initial reversal behaviour is maintained. The sample was prepared and checked with XMCD at room temperature in the spectroscopy chamber at UE46-PGM, capped with 3 nm Pt, and transferred through air to the high-field end station at UE46-PGM where it was finally measured.

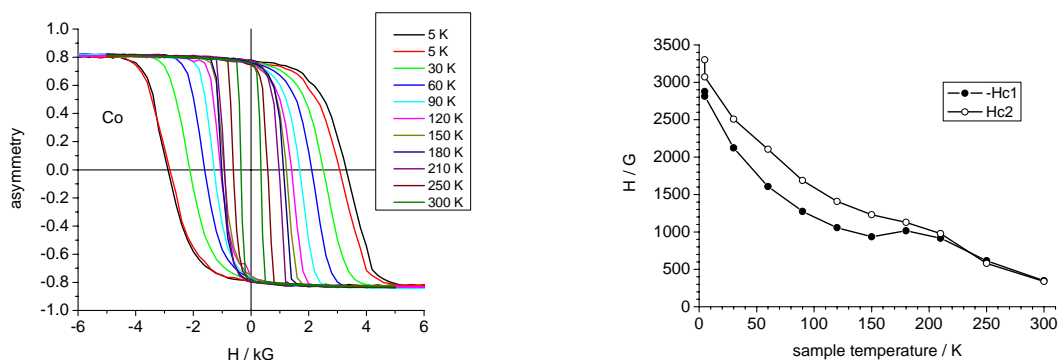


Fig.1: Hysteresis loops (left) and coercive fields (right) of Co measured as a function of temperature after field cooling to 5 K in -5 kG.

In Fig.1 the hysteresis loops (left) of Co measured in reflection as a function of temperature after field cooling to 5 K in -5 kG and the corresponding coercive fields $-H_{c1} > 0$ and $H_{c2} > 0$ (right) are shown. The exchange bias field is $H_{eb} = (H_{c1} + H_{c2})/2$. $H_c = (-H_{c1} + H_{c2})/2$ at 5 K is nine

times larger than at 300 K, and between 50 K and 150 K H_c is seven times larger than H_{eb} . These observations indicate that the hysteresis loops are dominated by the anisotropy of the AFM.

In detail, after field cooling to 5 K a coercive field H_c of about 3000 G and an exchange bias field H_{eb} of about 200 G are observed. After several hysteresis loops at 5 K H_{eb} decreases to 130 G, *i.e.*, there is a training effect. For increasing temperature H_{eb} first increases to 250 G at 60 K and then decreases to 0 G at about 230 K. At this blocking temperature a local maximum appears in $-H_{c1}$ and also but less pronounced in H_{c2} . This local maximum is usually explained by a decrease of the anisotropy of the AFM, so that more AFM moments rotate with the FM, resulting in an increase in H_c .

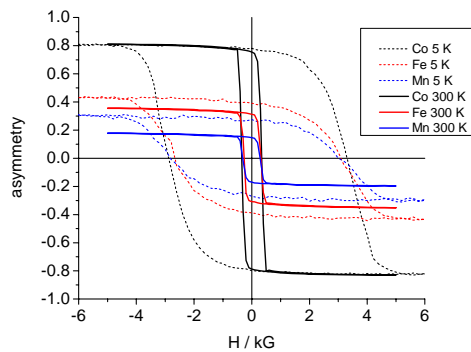


Fig.2: Hysteresis loops of Co, Fe and Mn at 5 K and 300 K after field cooling to 5 K in -5 kG (left).

Hysteresis loops of the three elements Co, Fe and Mn are shown in Fig.2 for 5 K and 300 K after field cooling to 5 K in -5 kG. The saturation magnetization of Co at 5 K and 300 K is similar because both temperatures are far below the Curie temperature of the FM. Contrary, the saturation magnetization of uncompensated Fe and Mn is significantly lower at the higher temperature of 300 K. This might be the case because the higher temperature is close to the Néel temperature of the AFM which is 380 K for the present film thickness of 12 ML FeMn.

Even at 5 K there is no significant vertical shift of the hysteresis loops, neither for Fe nor for Mn, indicating that the pinned fraction of uncompensated moments of the AFM is small, *i.e.*, at most 2%. This small fraction of uncompensated moments pinned to the AFM is in agreement with the relatively small exchange bias field of 200 G compared to the coercive field of 3000 G. In addition, the XMCD asymmetries measured at 5 K for Fe are tiny, *i.e.*, at most 0.45% at the L_3 resonance. According to a simple estimate, this value of the asymmetry corresponds to a small number of uncompensated Fe moments of 0.05 ML.

- [1] W.H. Meiklejohn, C.P. Bean, Phys. Rev. 102 (1956) 1413, Phys.Rev. 105 (1957) 904
- [2] W.H. Meiklejohn, J. Appl. Phys. 33 (1962) 1328
- [3] F. Offi, W. Kuch, J. Kirschner, Phys. Rev. B 66 (2002) 064419
- [4] F. Offi, W. Kuch, L.I. Chelaru, K. Fukumoto, M. Kotsugi, J. Kirschner, Phys. Rev. B 67 (2003) 094419
- [5] H. Ohldag, A. Scholl, F. Nolting, E. Arenholz, S. Maat, A.T. Young, M. Carey, J. Stöhr, Phys. Rev. Lett. 91 (2003) 017203

The comparative study of titanium fluorides, TiF₃ and TiF₄, using x-ray absorption: the effect of the filling onset of 3d electron shell

M.M. Brzhezinskaya^{1,2}, A.B. Preobrajenski^{1,3}, S.A. Krasnikov^{1,4}, and A.S. Vinogradov¹

¹ V.A. Fock Institute of Physics, St. Petersburg State University, St. Petersburg, 198504 Russia;

² BESSY GmbH, 12489 Berlin, Germany;

³ MAX-lab, Lund University, S-22100 Lund, Sweden;

⁴ School of Physical Sciences, Dublin City University, Glasnevin, Dublin 9, Ireland

An unambiguous identification of the electronic structure features in an individual transition metal (TM) system can be performed only by the systematic comparative spectroscopic investigation of the electronic structure in a reasonably large number of related compounds with the gradually varying parameters of their atomic and electronic structure. By the proper choice of the model compounds one can vary such parameters as symmetry of the TM atom surroundings, covalence degree of the bonding between the TM atom and the ligands, interatomic distances, etc. For simplification of the assignment of the spectra and correct understanding of electronic structure of the TM compounds it is highly desirable to exclude at least some of these factors and to reduce the real complex situation to a simplified one.

With this approach we have observed recently (i) the important role of the π -back-donation effect in the formation of low-energy unoccupied electron states in 3d metal cyanide complexes [1,2]; (ii) the necessity of considering covalent bonding in the description of unoccupied electron states in the iron and nickel compounds [2,3]; (iii) the hybridized TM 3d – F 2p character of empty electron states near the bottom of the conduction band in highly ionic 3d TM fluorides, ScF₃ – ZnF₂, [4-6]; (iv) the effect of the 3d shell filling on the TM atom 2p absorption spectra along the series of acetylacetonate complexes M(acac)₃ {acac=C₅H₇O₂ and M=Sc, V, Cr, Mn, Fe, Co} with the almost ideal oxygen octahedron of the nearly same size around the TM atom [7]; (v) the effects of the chemical bonding, the size and shape of ligand polyhedron on the TM atom 2p spectra in Sc compounds in which the scandium atom has no 3d electrons nominally in the ground state [8], etc.

The main goal of this investigation was to observe and to analyse in detail the effects of the filling onset of the 3d electron shell on x-ray absorption spectra as well as on electronic structure of solid titanium fluorides, TiF₄ and TiF₃, which are characterized by the similar (slightly distorted) octahedral fluorine surroundings around the Ti atoms and by different ground-state (GS) electron configurations of the titanium atoms [Ar]3d⁰ and [Ar]3d¹, respectively.

All measurements have been performed at the Russian-German beamline. We have taken high-resolution Ti 2p and F1s absorption spectra from powder samples of K₂TiF₆ and TiF₃ as well as from TiF₄ (powder sample and thin film deposited *in situ* with a molecular beam from a single water-cooled effusion cell of Knudsen type onto a clean polished copper plate). The NEXAFS spectra of these compounds were obtained in the total electron yield mode by detecting a sample drain current. The photon-energy resolution was set to 100 meV at the Ti 2p_{3/2} edge (~450 eV) and 150 meV at the F 1s edge (~680 eV). The photon energy was calibrated using the known energy position of the first narrow peak in the F 1s and Ti 2p_{3/2} absorption spectra of solid K₂TiF₆ (F 1s, Ti 2p_{3/2} → t_{2g}; 683.9 eV and 459.0 eV [9]). The TM atom 2p absorption spectra of VF₃ and CrF₃, which are structurally similar to TiF₃ and have an alternate 3d electron number, have been measured additionally.

In Fig. 1 the 2p_{1/2,3/2} absorption spectra of the Ti and Sc atoms, which have no 3d electrons in the GS electron configurations in the case of solid K₂TiF₆, TiF₄ and ScF₃ [8], are compared. The TM atom 2p_{1/2} structures were labeled by letters with asterisks. As is well seen, the spectra for ionic compound ScF₃ and molecular anion TiF₆²⁻ (in solid K₂TiF₆) are strongly similar in their spectral shape. Taking into account the similar octahedral fluorine environment of the metal atom in these compounds and the quasi-molecular analysis of the

spectra for TiF_6^{2-} [6], the main absorption bands a and b in $\text{Sc } 2p_{3/2}$ absorption spectrum of ScF_3 can be also associated with core electron transitions to the empty weakly antibonding MOs t_{2g} and e_g of the octahedral ScF_6 quasi-molecule formed by the Sc atom and the surrounding fluorine atoms. These MOs result from the covalent mixing between the Sc $3d$ electron states, which are split into $3dt_{2g}$ and $3de_g$ components in the field of the fluorine octahedron, and the $2p$ states of the fluorine atoms. Within the framework of this consideration, the weak low-energy structures α and β are described as a result of the $2p^6 3d^0 - 2p^5 3d^1$ electron transitions from the singlet ground state to the triplet final ones, while the low-intense high-energy bands $\gamma\delta$ and $\gamma^*\delta^*$ are associated with double electron excitations (the $2p - 3dt_{2g}$, $3de_g$ transitions with simultaneous valence electron excitations). The main difference between the spectra under comparison is the different energy spacing between the bands a and b (the $3dt_{2g}$ and $3de_g$ splitting components) in the spectra of TiF_6^{2-} (2.58 eV) and ScF_3 (1.83 eV). It is evidently due to the different interatomic distances between the metal and fluorine atoms in these compounds: $R(\text{Ti-F})=1.92\text{\AA}$ and $R(\text{Sc-F})=2.01\text{\AA}$.

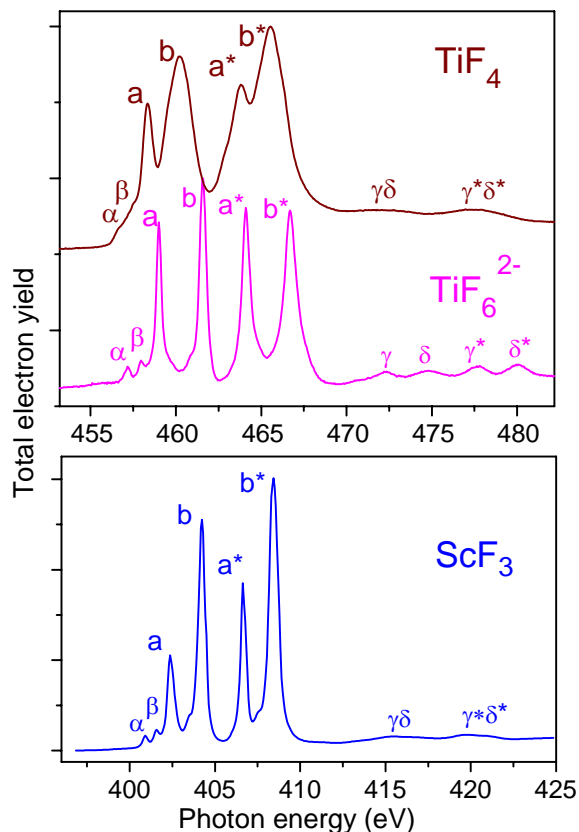


Fig. 1. Comparison between the $2p$ absorption spectra of the $3d^0$ TM atoms in TiF_4 , TiF_6^{2-} and ScF_3 .

of the titanium tetrafluoride, TiF_4 , can be described by arrays of layers of TiF_6 octahedra with a considerable tetragonal (C_{4v}) distortion linked by four shared equatorial corners [10]. Thus, it is reasonable to assume that the broadening of the absorption structures observed in the Ti $2p$ spectrum of TiF_4 as compared to that of TiF_6^{2-} is caused by this distortion which results in an additional splitting of the Ti $3d$ electron states by the fluorine environment. Indeed, there is the splitting of the absorption bands a ($3dt_{2g}$ component) and b ($3de_g$ component) into two subbands: $3de+3db_2$ components and $3da_1+3db_1$ components, respectively.

The most drastic change in the Ti $2p_{1/2,3/2}$ absorption spectrum is observed in going from the molecular anion TiF_6^{2-} and the ionic crystal TiF_4 to another ionic compound TiF_3 (Fig. 2): the number of main absorption structures is doubled. It should be noted that the crystal

In going from TiF_6^{2-} and ScF_3 to ionic TiF_4 , one can see in Fig. 1 that its Ti $2p$ spectrum conserves essentially the spectral shape of the ones of TiF_6^{2-} and ScF_3 , but all absorption structures are considerably increased in their width. The crystal structure

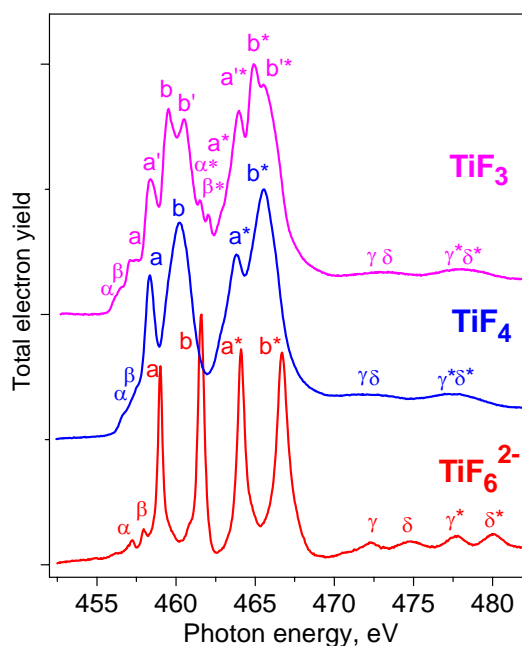


Fig. 2. $2p$ absorption spectra of Ti atom with the different GS electron configurations $[\text{Ar}]3d^0$ (TiF_4 , TiF_6^{2-}) and $[\text{Ar}]3d^1$ (TiF_3).

structure of TiF_3 is similar to that of ReO_3 , where oxygen (fluorine) octahedra are linked via their corners. Thus, the Ti atom in the compounds under consideration has the similar octahedral environment by the fluorine atoms and, consequently, the small differences in the atomic structure can not cause the significant change in absorption structures observed in the Ti $2p$ spectrum of TiF_3 . Evidently, these findings reflect a complication in electronic structure of TiF_3 because of the availability of $3d$ electrons in the GS electron configuration of the trivalent Ti(III) atom, $[\text{Ar}]3d^1$. In this case the exchange interaction between the $3d$ electrons should be taken into account in the final-state electron configuration, $[\text{Ar}]3d^2$. Calculations of the electronic structures of $3d$ -TM oxides [11] show that consideration of the exchange

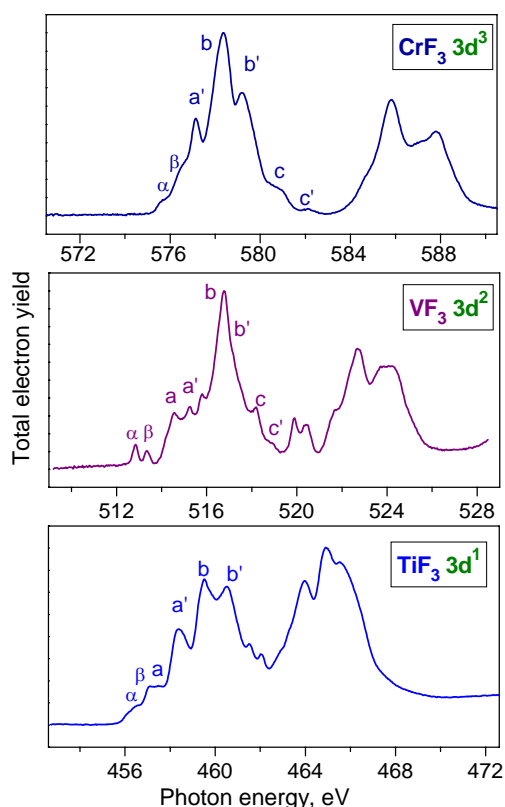


Fig. 3. Metal atom $2p$ absorption spectra of TiF_3 , VF_3 and CrF_3 .

absorption spectra (Fig. 3) which can be regarded as a result of the successive occupation of MO $t_{2g}\uparrow$ by $3d$ electrons.

Finally, it should be emphasized that the quasi-molecular analysis of the F $1s$ absorption spectra of TiF_6^{2-} , TiF_4 and TiF_3 leads to similar conclusions.

The work was supported by the Russian Foundation for Basic Research (Grant No 06-02-16998) and the bilateral Program "Russian-German Laboratory at BESSY.

References

1. A.S. Vinogradov, A.B. Preobrajenski, et al. *J. Electron Spectr. Relat. Phenom.* **114-116**, 813 (2001).
2. A.S. Vinogradov, A.B. Preobrajenski, S.A. Krasnikov, et al. *Surface Rev. & Lett.* **9**, 359 (2002).
3. A.S. Vinogradov, S.A. Krasnikov, A.B. Preobrajenski, et al. *BESSY Annual Report 2003*, p.158-160.
4. A.S. Vinogradov, S.I. Fedoseenko, D.V. Vyalikh, et al. *Optics & Spectroscopy* **93**, 862-869 (2002).
5. A.S. Vinogradov, S.I. Fedoseenko, S.A. Krasnikov, et al. *Physica Scripta* **T115**, 510 (2005).
6. A.S. Vinogradov, S.I. Fedoseenko, S.A. Krasnikov, et al. *Phys. Rev. B* **71**, 045127 (2005).
7. A.S. Vinogradov, A.B. Preobrajenski, S.A. Krasnikov, et al. *BESSY Annual Report 2004*, p.198-200.
8. A. Zimina, A.S. Vinogradov, *BESSY Annual Report 2004*, p.229-231.
9. A.S. Vinogradov, A.Yu. Dukhnyakov, V.M. Ipatov, et al., *Sov. Phys. Solid State* **24**, 803 (1982).
10. A. Wells, *Structural Inorganic Chemistry*, 5th ed. (Oxford University Press, Oxford, UK, 1984).
11. C. Suzuki, J. Kawai, H. Adachi, T. Mukoyama, *Chem. Phys.* **247**, 453 (1999).

X-ray magnetic linear dichroism in resonant absorption and reflection of soft X-rays

N. Ponpandian, A. Kleibert, S. Gutzeit, S. Polei and K.-H. Meiwes-Broer
*Institut für Physik, Universität Rostock, Universitätsplatz 3, D-18051
Rostock*

Supported by BMBF 05KS1HR2/4.

According to a theoretical work, a new magneto-optical "sum rule" connects the resonant XMLD in absorption with the anisotropy of the spin-orbit-interaction [1]. This tool can be used to determine the magnetic anisotropy energy (MAE) of ferromagnetic samples [2]. Since XMLD is quadratic in magnetization it enables for investigations on antiferromagnetic samples, and thus is well suited for studies on complex magnetic systems. In the important case of the 3d transition metals however, the XMLD in absorption is usually a quite weak effect. First *ex situ* feasibility studies of our group revealed strongly enhanced (by one order of magnitude) XMLD-type effects on iron and cobalt samples when detecting the intensity of the reflected radiation instead of the corresponding absorption signal. Thus, these effects possess a high potential for investigations on magnetic nanoparticles or clusters. Here we report on recent *in situ* experiments on ultrathin cobalt films grown on W(110). These films have atomically flat surfaces and sharp interfaces and thus are ideally suited for a quantitative analysis of reflectivity data [3].

The present experiments have been carried out at the UE56/2 PGM1 undulator beamline using a special UHV chamber designed for *in situ* T-MOKE measurements. The Co films have been prepared by means of molecular beam epitaxy (MBE) at room temperature. The W(110) substrate was cleaned by cycles of heating in oxygen atmosphere. The base pressure during the evaporation was maintained at 5×10^{-10} mbar at an evaporation rate of 1ML/min. The prepared Co films were annealed at 375 K for several minutes to ensure smooth film surfaces. The structural quality of the films was checked by means of LEED. X-ray absorption spectra (XAS) as well as x-ray reflectivity spectra have been recorded in the vicinity of Co $L_{2,3}$ edges using linearly polarized light. The angle of incidence was fixed at 20° with respect to the surface plane. The polarization of the incident radiation has been varied in order to measure the *s*- and *p*-polarized reflectivity of the samples. Simultaneously, XAS spectra were recorded via total electron yield detection. The samples have been oriented with the W[1 $\bar{1}$ 0]-axis parallel to the plane of incidence. An external magnetic field of up to 0.5 Tesla could be applied perpendicular to the scattering plane allowing for magnetic saturation of the sample along the W[001]-axis, i.e. the magnetic hard axis.

In Fig. 1 a) we present thickness-dependent reflectivity spectra obtained in transverse geometry, i.e. the magnetization oriented perpendicular to the plane of incidence. The dashed (red) curves show the *s*-polarized reflectivities. In the *p*-polarized case the transverse magneto-optical Kerr-effect gives rise to intensity changes being linear with the magnetization. Averaging the data for opposite magnetization yields the *p*-polarized reflectivity given by the solid black lines. The XMLD-type effect in reflection is presented in Fig. b) for the case of the 6 ML cobalt film. The upper panels show the *s*- and *p*-polarized reflectivity for

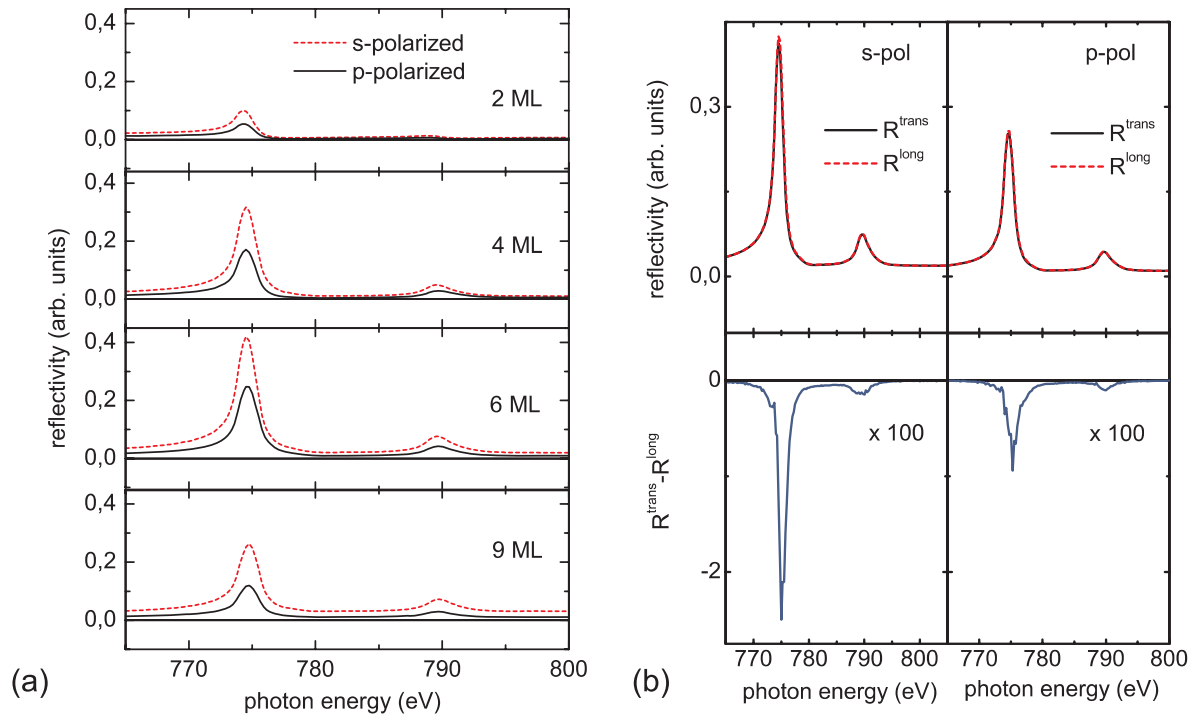


Figure 1: (a) Thickness-dependent reflectivity for Co/W(110) in the vicinity of the $L_{2,3}$ -edges. The magnetization has been saturated transverse to the plane of incidence. (b) Top: Reflectivity for s - and p -polarized light with transverse and longitudinal orientation of the magnetization, respectively. Bottom: Reflectivity difference for longitudinal and transverse magnetization.

longitudinal and transverse magnetization R^{long} and R^{trans} , respectively. The corresponding difference spectra given by $R^{\text{trans}} - R^{\text{long}}$ are shown in Fig. 1b). The observed effects correspond to the XMLD-type effect in reflection, but are somewhat smaller than those found in our previous experiments. However, we find a noticeable difference in the XMLD-type spectra when comparing the s - and p -polarized case. Since the electric field vector probes two orthogonal axes of the sample this difference is ascribed to a corresponding anisotropy of the magnetic properties of the sample [4]. We furthermore observe a remarkable thickness dependence of the XMLD in reflection as well as of the anisotropy of the XMLD. The detailed quantitative analysis of these absorption and the reflectivity spectra and the comparison of these results together with the calculations based on the Fresnel formalism will be published in the near future.

References:

- [1] G. van der Laan *et al.*, Phys. Rev. Lett. **82**, 640 (1999).
- [2] S. S. Dhesi *et al.*, Phys. Rev. Lett. **87**, 067201 (2001).
- [3] A. Kleibert *et al.*, Phys. Rev. B **72**, 144404 (2005).
- [4] J. Kunes and P. M. Oppeneer, Phys. Rev. B **67**, 024431 (2003).

Matrix-Element Effects in Valence Band Photoemission on Fe_xTiS_2 Using Circularly Polarized Light

*M. Marczynski-Buehlow*¹, *J. Buck*¹, *K. Rossnagel*¹, and *L. Kipp*¹
*N. Janke-Gilman*², *A. Walter*², *L. Broekman*², and *J. Riley*²

¹*Institut für Experimentelle und Angewandte Physik, Universität Kiel, D-24098 Kiel, Germany.*

²*Department of Physics, La Trobe University, Victoria 3086, Australia.*

The effect of iron intercalation on the structural, magnetic and electronic properties of the layered transition metal dichalcogenide TiS_2 is an interesting and extensively studied question [1]. Of particular interest is whether and to what extent Fe intercalation leads to modifications of the host valence band structure, such as increased band filling, hybridization between the Fe 3d orbitals and the host Ti 3d and S 3p orbitals, or new Fe 3d-derived electronic states below the Fermi energy.

We investigated the valence band structure of Fe_xTiS_2 ($x = 0; 0.1; 0.33$) by angle-resolved photoemission spectroscopy taking advantage of a second generation toroidal electron spectrometer with fast data acquisition [2].

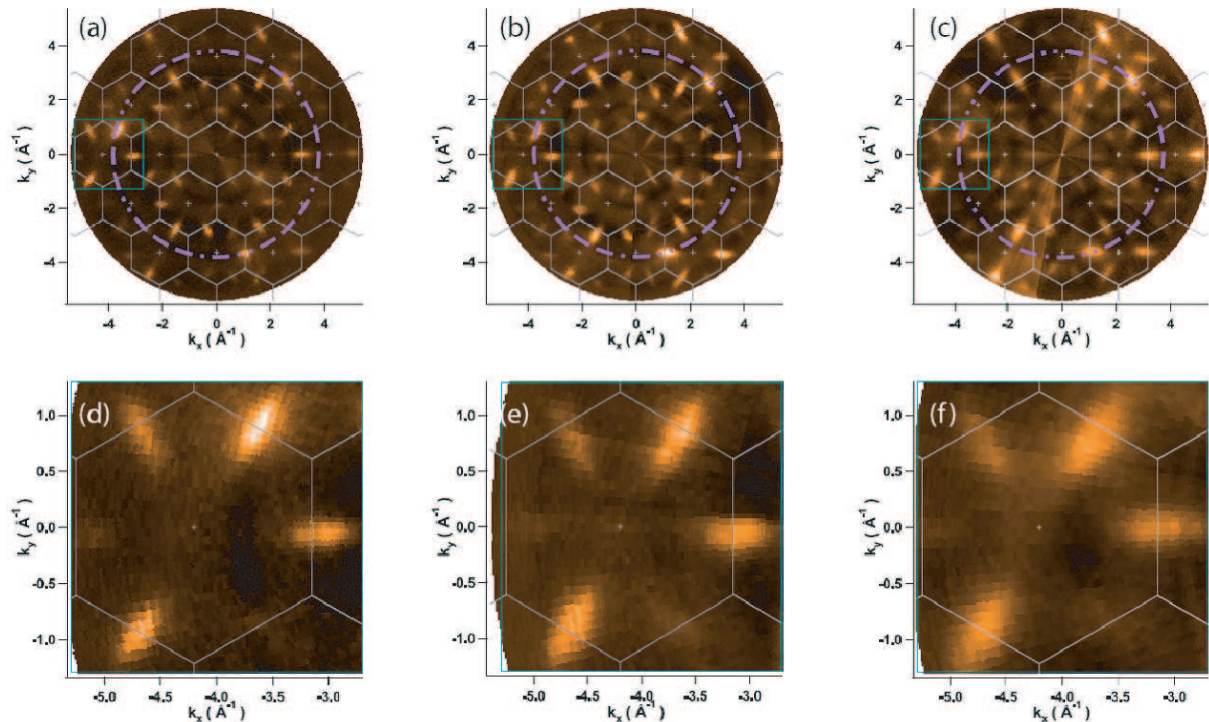


Figure 1: Fermi surface maps of TiS_2 (a+d), $\text{Fe}_{0.1}\text{TiS}_2$ (b+e) and $\text{Fe}_{0.25}\text{TiS}_2$ (c+f) taken at a photon energy of 116 eV with left circularly polarized light. Grey lines represent the Brillouin zone boundaries. Violet circles indicate the position of the azimuthal scan profiles in Figure 3.

Our main aim in this work was to reveal possible spin polarization effects at the Fermi energy by using fully circularly polarized light from beamline U56/2-PGM1 ($h\nu = 89$ to 1328 eV) at BESSY [3]. Although we were not able to answer the question concerning spin polarization,

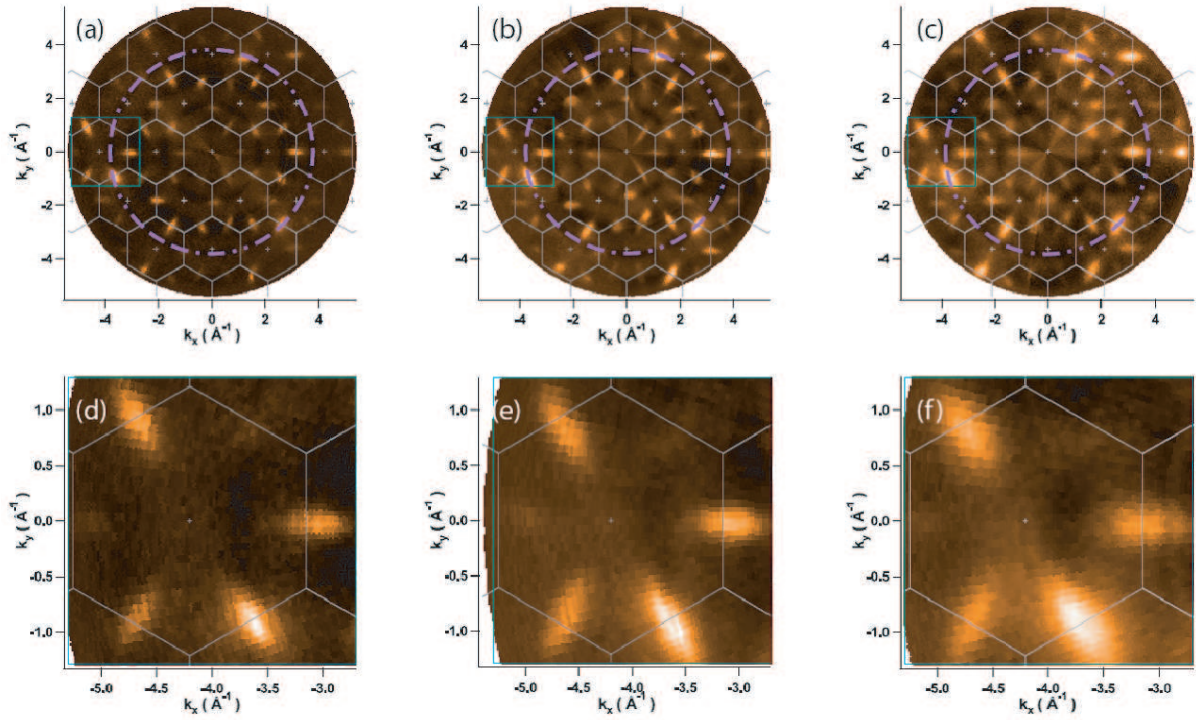


Figure 2: Fermi surface maps of TiS_2 (a+d), $\text{Fe}_{0.1}\text{TiS}_2$ (b+e) and $\text{Fe}_{0.25}\text{TiS}_2$ (c+f) taken at a photon energy of 116 eV with right circularly polarized light. Grey lines represent the Brillouin zone boundaries. Violet circles indicate the position of the azimuthal scan profiles in Figure 3.

interesting matrix-element effects were observed for the iron intercalated as well as for the pristine TiS_2 compounds.

In figure 1 and 2 we present Fermi surface maps of TiS_2 and its Fe intercalates measured with differently circularly polarized light. The crossings of the lowest Ti 3d band with the Fermi energy lead to the typical cigar shaped electron pockets around the M(L) points of the Brillouin zone. In both figures the growth of these electron pockets with increasing Fe concentration is clearly visible. This is a sign of electron transfer from the intercalated Fe to the host material. Additional modification of the host valence band structure could not be resolved in this experiment.

Various polarization dependent matrix-element effects are observed in the Fermi surface maps as well as in the valence band structure measurements not shown here. In particular it is eye-catching that these effects are getting more and more obvious in the higher Brillouin zones. Figure 3 shows azimuthal angle scans through the third Brillouin zone indicated as violet circles in figure 1 and 2. Beside the above mentioned growing of the electron pockets with increasing Fe intercalation, the intensity profiles measured with left and right circularly polarized light show mirror symmetry about the $\Gamma\text{M(AL)}$ -direction. This effect directly reflects the three-fold symmetry of the crystal. Further changes in the matrix-element effects due to increasing Fe concentration could not be observed.

This work was supported by the DFG Forschergruppe 353.

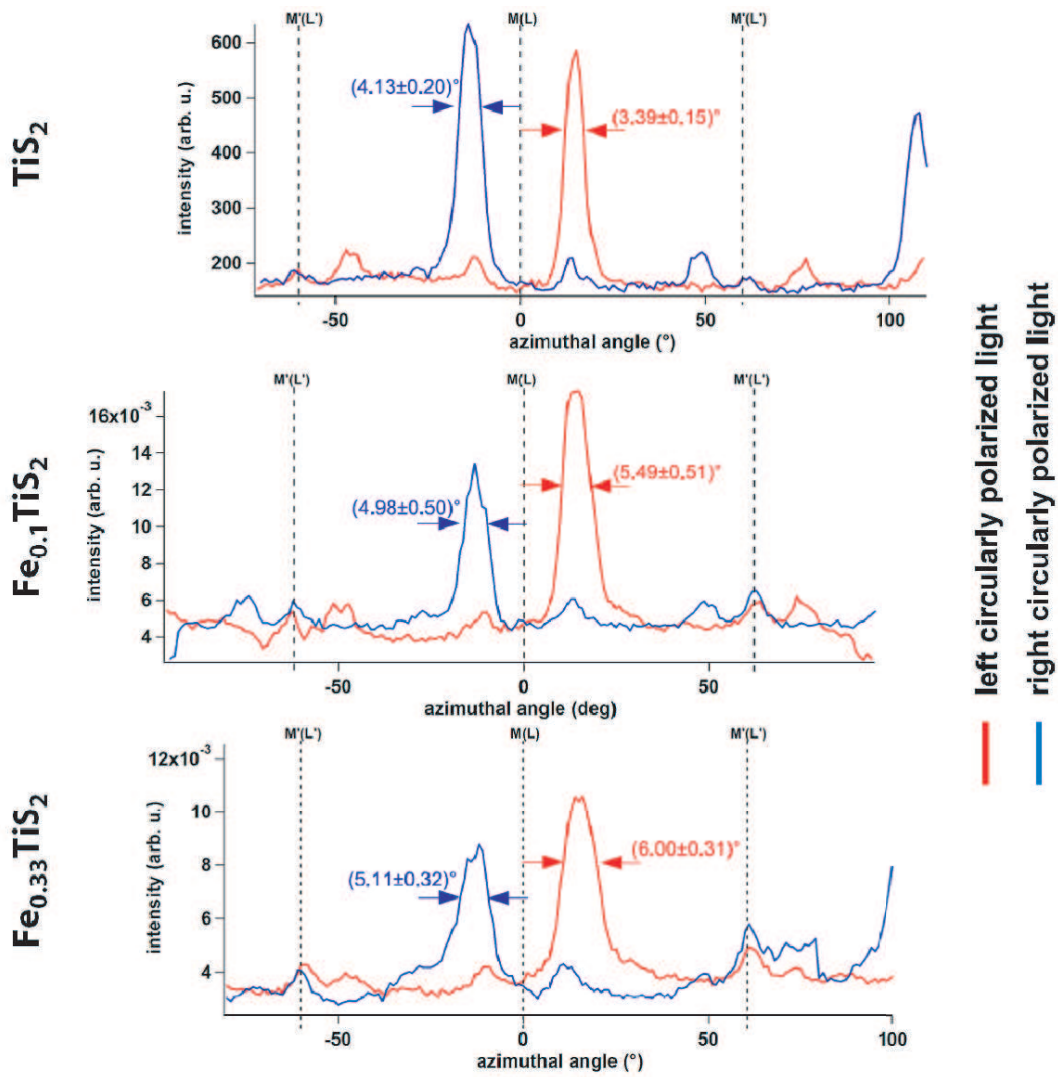


Figure 3: Azimuthal scan profiles through the 3rd Brillouin zones extracted from Fig. 1 (a,b,c) and Fig. 2 (a,b,c). The azimuthal angle of 0° points in the $-k_x$ -direction. High-symmetry directions are indicated by the dashed lines.

References

- [1] M.Inoue, H.P. Hughes, A.D. Yoffe, *Advances in Physics* 38, 565 (1989).
- [2] A. Tadich, L. Broekman, E. Huwald, R. Leckey, J. Riley, T. Seyller, L. Ley: *BESSY Annual Report 2003*, p. 515.
- [3] M.R. Weiss, R. Follath, K.J.S. Sawhney, F. Senf, J. Bahrtdt, W. Frentrup, A. Gaupp, S. Sasaki, M. Scheer, H.-C. Mertins, D. Abramsohn, F. Schaefers, W. Kuch, W. Mahler, *Nucl. Instr. and Meth. A* 467-468 (2001) 449-452.

Electronic structure of gold nanoclusters on the oxidized Ni(755) surface

A.G. Rybkin¹, D.U. Usachev¹, A.M. Shikin¹, V.K. Adamchuk¹

¹ *Institute of Physics, St.-Petersburg State University, St.-Petersburg, 198504, Russia*

A. Varykhalov², O. Rader²

² *BESSY*

The electronic structure of gold nanoclusters grown on the oxidized stepped (755) surface of fcc Ni has been investigated experimentally. It has been shown that oxidization of the Ni(755) surface leads to the development of a well-ordered uniform structure similar to the (2×2)O structure which forms on flat Ni(111). Deposition of gold on this oxidized stepped surface leads to the formation of gold nanoclusters with sizes determined by the surface terrace width. Comparison between Au 4f core-level photoemission from gold nanoclusters on pure and on oxidized Ni(755) shows for the oxidized system the appearance of spectral components Au^{+δ} different from those characteristic of the metallic state. We assume that these are connected to partial oxidation of gold atoms under participation of surface defects in the stepped relief of the Ni substrate.

Recently nanoclusters of the noble metals Au and Ag supported on various oxide surfaces have been attracting considerable interest since they can exhibit high catalytic activity, particularly in the oxidation of carbon monoxide [1, 2]. Several theories have been suggested to describe this effect. One of them emphasizes the role of ionic noble-metal species in the catalytic reaction. According to these, the presence of this ionic noble metal determines the catalytic activity of the system consisting of noble metal nanoclusters and the oxide support [3, 4]. In several experiments the ionic state of gold atoms has been archived on defect-rich surfaces with oxygen vacancies or with steps [5, 6].

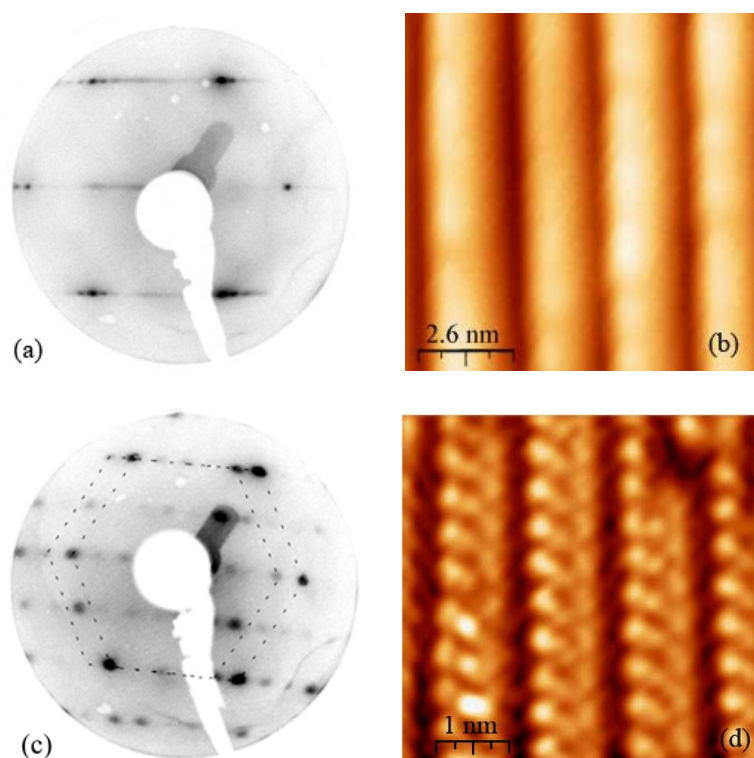


Fig.1: Results of the LEED and STM studies;
(a) *diffraction pattern obtained from clean Ni(755), $E_p = 96.3$ eV;* (b) *STM image of clean Ni(755);* (c) *diffraction pattern obtained from oxidized Ni(755), $E_p = 96.4$ eV;* (d) *STM image of oxidized Ni(755).*

The aim of the present work was to prepare an oxidized stepped surface Ni(755) with defects and to investigate the electronic structure of gold clusters on this surface. We assumed that the cluster size on such stepped surfaces will be controlled by the terrace width which may lead to a more uniform size distribution. The high-Miller-index crystal surface Ni(755) is geometrically characterized by well-ordered steps with monatomic height and a terrace width of 1.3 nm. The confirmation of this surface geometry by a superlattice splitting in the LEED is shown in Fig. 1(a,c). Fig. 1(a) presents the diffraction pattern from clean Ni(755) typical of a clean and well-ordered stepped surface. Fig. 1(b) shows STM data of Ni(755). One can clearly see that the terrace width is not 1.3 nm but 2.6 nm. This means that the steps are of double layer height. The Ni(755) surface was oxidized at an average temperature of 650 K and a partial O₂ pressure of 5×10^{-8} torr during 10 min. It was found that at ~520 K a reconstruction of the Ni(755) surface takes place and the width of terraces becomes 1.3 nm which corresponds to steps of monatomic height. Since for oxidation of Ni temperature higher than 520 K was used, the terrace width during oxidation was 1.3 nm. Fig. 1(c) shows the LEED pattern from oxidized Ni(755). The Ni LEED spots in the figure are combined into hexagons. The distance between split Ni spots is twice as large as for clean Ni(755), consequently the terrace width of oxidized Ni is half that of clean Ni. The LEED pattern also allows for conclusions on the structure of adsorbed oxygen. The structure of oxygen atoms prevent the reconstruction of the nickel surface so that at room temperature an oxidized Ni(755) surface with a terrace width of 1.3 nm is obtained. In fig. 1(d) the (2×2) superstructure of oxygen is directly observed within the limits of terrace.

We measured normal-emission photoelectron spectra of the valence band under deposition of Au on oxidized Ni(755). We started from submonolayer coverages and went up to 4 ML. In brief, we made the following observations:

- Ni3d-derived features are less strongly suppressed by deposited gold than expected. This indicates an island-like mechanism of growth.

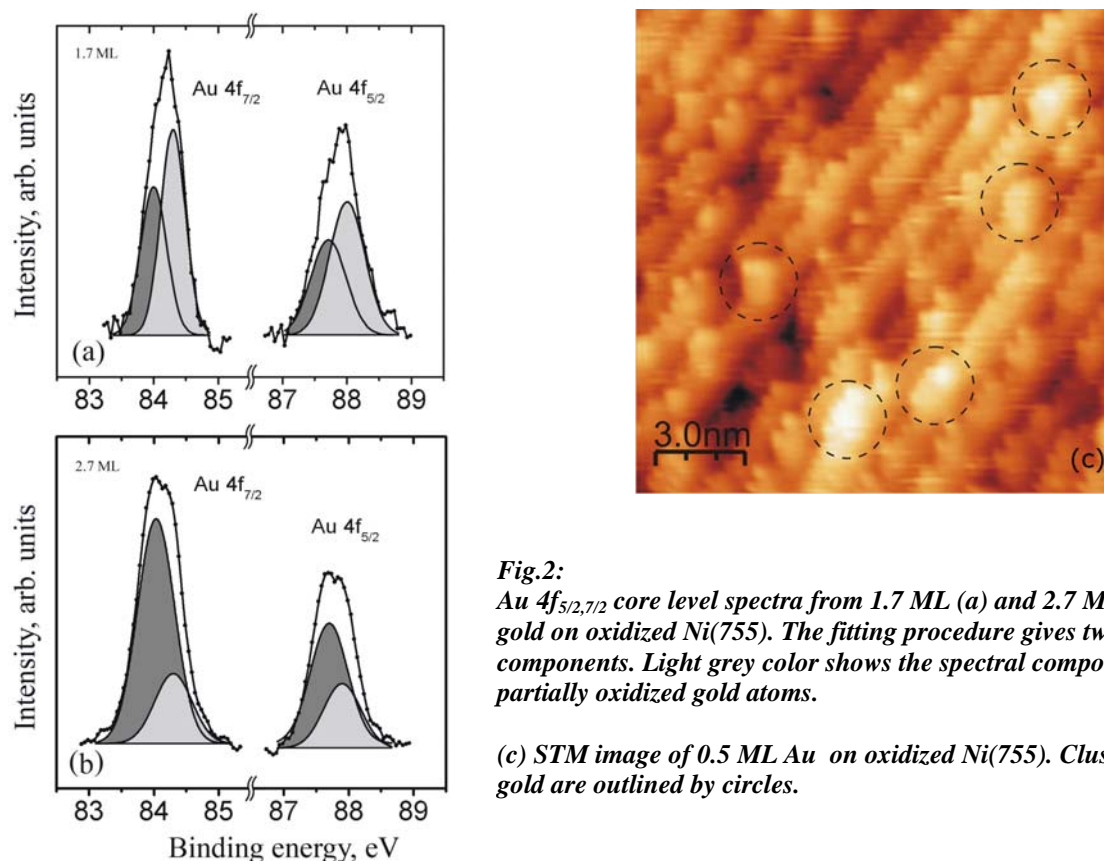


Fig.2: Au 4f_{5/2,7/2} core level spectra from 1.7 ML (a) and 2.7 ML (b) of gold on oxidized Ni(755). The fitting procedure gives two spectral components. Light grey color shows the spectral component for partially oxidized gold atoms.

(c) STM image of 0.5 ML Au on oxidized Ni(755). Clusters of gold are outlined by circles.

- Under deposition of Au on oxidized Ni(755) we observe the formation of several features in the upper part of Au5d-band (binding energies ~3 eV and 2.4 eV). This indicates the formation of quantum-well states which testify the formation of clusters of uniform size. The appearance of these features suggests that the oxidized stepped surface can lead to the formation of uniform noble metal clusters. The size of these clusters is probably limited by the terrace width if diffusion of Au across step edges is negligible.

The formation of gold clusters limited by the terrace width is supported by our STM investigations. Fig.2(c) displays an STM image of 0.5 ML Au on oxidized Ni(755). The gold clusters are outlined by circles.

Au 4f core-level spectra from 1.7 ML (a) and 2.7 ML (b) nominal gold coverage on oxidized Ni(755) are shown in figs. 2(a,b), respectively. The fitting procedure gives two spectral components: for Au 4f_{7/2} 84.0±0.1 eV and 84.3±0.1 eV, for Au 4f_{5/2} 87.7±0.1 eV and 87.9±0.1 eV. The spectral components with binding energies 84.0±0.1 eV and 87.7±0.1 eV are characteristic of bulk metallic gold. Comparing Au 4f spectra for the two systems Au on clean Ni(755) and Au on oxidized Ni(755) we find that on oxidized nickel two additional spectral components appear with energies 84.3±0.1 eV and 87.9±0.1 eV. We assume that this is due to partial oxidation of gold atoms under participation of surface defects inherent in the stepped relief of the Ni substrate. This conclusion is supported by the observation that the "partially oxidized" component is stronger for lower Au coverages. Consequently, we conclude that the formation of Au clusters on oxidized Ni(755) leads to two states of Au which possibly play an important role in the catalytic activity of the Au clusters on such oxidized stepped surfaces.

[1] M. Haruta, *Catal. Today* 36, 153 (1997)

[2] M. Valden, X.Lai, D.W. Goodman, *Science* 281, 1647 (1998)

[3] H.J. Freund, *Surf. Science* 500, 271 (2002)

[4] Q. Fu, H. Saltsburg, M. Flytzani-Stephanopoulos, *Science* 301 (5635), 935 (2003)

[5] A.Varykhalov, O. Rader, V. K. Adamchuk, W. Gudat, B. E. Koel, A. M. Shikin, *Phys. Rev. B* (in press)

[6] N. Lopez, J.K. Norskov, T.V.W. Janssens, A. Carlsson, A. Puig-Molina, B.S. Clausen, J.D. Grunwaldt, *J. Catal.* 225, 86 (2004)

Inner-Shell Photoionization and Photofragmentation of Free Selenium Clusters

T. Arion, R. Flesch, J. Neville*, and E. Rühl

Physikalische und Theoretische Chemie, Institut für Chemie und Biochemie, Freie Universität Berlin, Takustr. 3, 14195 Berlin

* Department of Chemistry, University of New Brunswick, P.O. Box 45222, Fredericton, NB, Canada E3B 6E2 Canada

Inner-shell excitation of free clusters has been studied during the past years, where the emphasis was put on size-effects of van der Waals clusters [1,2]. Such cluster systems are on one hand easy to prepare in adiabatic expansions; on the other hand this approach produces the clusters in wide size distributions. Clusters from covalent species have the inherent advantage that they are often formed with well-defined sizes [3-5]. Often, this requires the evaporation of the solid samples.

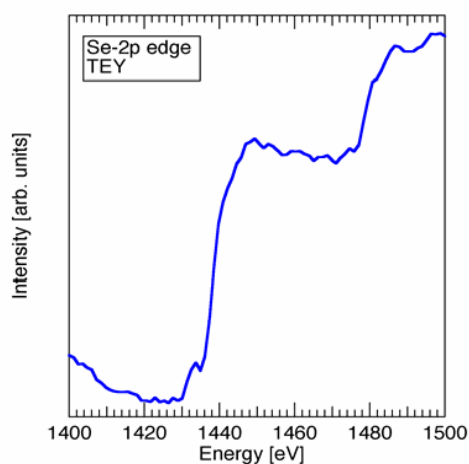


Fig. 1: Total electron yield of selenium clusters in the gas phase near the Se 2p-edge.

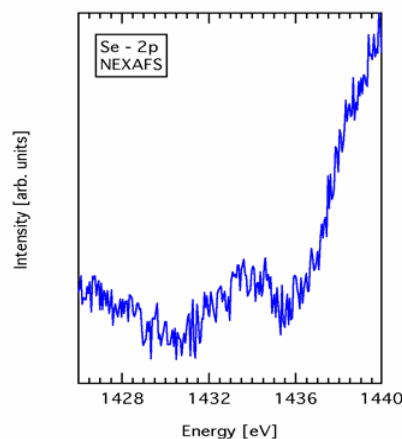


Fig. 2: Enlarged portion of the 2p-NEXAFS spectrum of selenium clusters.

Selenium clusters have been studied before in the Se 1s-regime (12.5-13.5 keV), where the X ray absorption fine structure has been used to determine the structure of the clusters [3]. The present work focuses on the Se 2p-regime, which is a continuation of previous work, where we investigated sulfur clusters in the core level regime [4,5].

The experiments are carried out at the U49/2-PGM1 beamline at BESSY. Selenium clusters are produced from neat selenium in a two-stage oven at different heating temperatures. The oven is connected via a pinhole to a vacuum recipient, where the effusive cluster jet crosses the dispersed undulator radiation. The oven temperature is chosen such that the clusters in the gas phase are dominated by Se_6 with minor contributions from Se_7 and Se_2 [6]. Total ion yield

(TIY) and total electron yield (TEY) spectra are recorded under static extraction conditions of charged species from the ionization region, where the cluster beam crosses monochromatic synchrotron radiation. Coincidence spectra are recorded by utilizing a time-of-flight mass spectrometer. Both TEY and the TIY show almost no edge jump at the 3p edge (160-180 eV regime), so that the 3p-edge is barely visible in energy scans of the charged particles. Near-edge features are found in the 3p regime with weak intensity. However, distinct features are observed above 1420 eV, where the Se 2p electron excitation is known to occur. Fig. 1 shows the TEY in the vicinity of the Se 2p edge (1400-1500 eV). The edge jump is observed at 1438.5 eV ($2p_{3/2}$) and 1479.5 eV ($2p_{1/2}$), respectively. These energies are somewhat higher than electron binding energies of elemental Se (1433.9 eV and 1474.3 eV) [7] indicating that

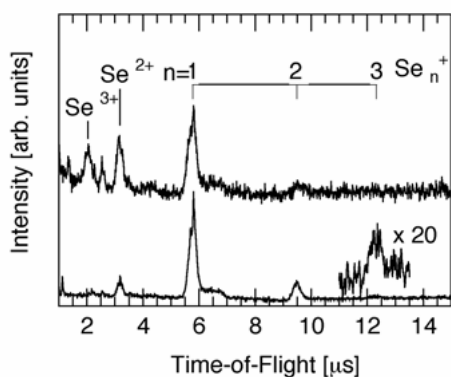


Fig. 3: Time-of-flight mass spectra of Se clusters recorded at 150 eV (bottom) and 1450 eV (top).

there is a considerable chemical shift in clusters.

A broad resonant feature of weak cross section is observed in the pre-edge regime (1432-1436 eV). This is shown in greater detail in Fig. 2. We assign this feature to transitions into unoccupied valence orbitals, which is in analogy to previous work on 2p-excited sulfur clusters [4]. A detailed assignment, however, requires the use of model calculations, which are currently in progress. Fig.

3 shows two time-of-flight mass spectra of Se clusters. The bottom spectrum is obtained from $E=150$ eV, which is located in the Se 3d-continuum. The heaviest cation that is detected in the mass spectrum is Se_3^+ . The distribution of neutrals in the beam indicates that the singly charged cations come most likely from fission of larger clusters. Double and triply charged atomic fragments are observed with high intensity upon Se $2p_{3/2}$ -continuum excitation (see Fig. 3(top)). Fission in core-excited Se clusters is studied by photoion-photoion-coincidence (PIPICO) and photoelectron photoion-photoion coincidence (PEPIPICO) spectra.

This project has been supported by the BMBF (contract No. 05-KS4WWD/0) and the Fonds der Chemischen Industrie.

References

- 1 E. Rühl, *Int. J. Mass Spectrom.* **229**, 117 (2003).
- 2 I.L. Bradeanu, R. Flesch, N. Kosugi, A.A. Pavlychev, E. Rühl, *Phys. Chem. Chem. Phys.* **8**, 1906 (2006); A.A. Pavlychev, X.O. Brykalova, R. Flesch, E. Rühl, *Phys. Chem. Chem. Phys.* **8**, 1914 (2006).
- 3 N. Nagaya, M. Yao, T. Hayakawa, Y. Ohmasa, Y. Kajihara, M. Ishii, Y. Katayama, *Phys. Rev. Lett.* **89**, 243401 (2002).
- 4 C.M. Teodorescu, D. Gravel, E. Rühl, *J. Chem. Phys.* **109**, 9280 (1998).
- 5 E. Rühl, R. Flesch, W. Tappe, D. Novikov, N. Kosugi *J. Chem. Phys.* **116**, 3316 (2002).
- 6 J. Berkowitz, W. A. Chupka, *J. Chem. Phys.* **45**, 4289 (1966).
- 7 G.P. Williams in: *X-Ray Data Booklet*, Berkeley (1986).

Molecular Chirality uncovered - Circular Dichroism of Adsorbed Chiral Molecules

Thorsten U. Kampen¹, Philipp Martin Schmidt¹, Jeong Won Kim², Hugo Dil¹,
and Karsten Horn¹

¹Fritz-Haber-Institut der Max-Planck-Gesellschaft, Berlin, Germany

²Nano-Surface Group, Korea Research Institute of Standards and Science, Daejeon, Korea

One of the most intriguing aspects in three-dimensional molecular structure is the occurrence of chirality. A molecule is called chiral if it is not superimposable on its mirror image. Apart from an interest in this property from a fundamental point of view, the chiral nature of specific materials also plays an important role in practical applications. For example, the chiral discrimination in modern drug production has become so crucial that the proportion of single enantiomer drugs has been rapidly increasing, and has reached a level of up to 75 % [1]. This chiral discrimination is achieved by heterogeneous catalysis where active metal surfaces covered with chiral molecules serve as catalysts.

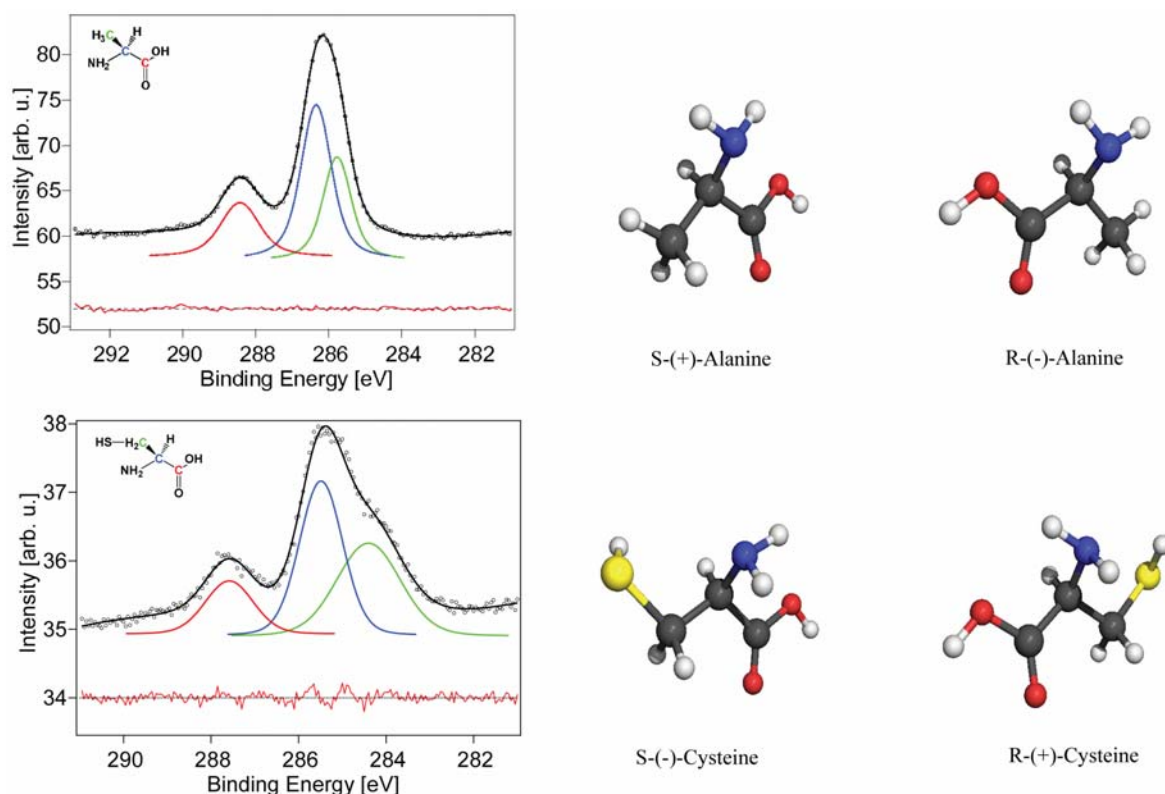


Figure 1: C1s core level photoemission spectra and chemical structure of alanine and cysteine

In general, chirality is detected by optical activity, that is, how the linear polarization of light is rotated upon passing through a solution or a crystal consisting of chiral molecules. Linearly polarized light can be regarded as a superposition of coherent left and right circularly polarized light beams. Optical activity is then due to different molecular coefficients of absorption for left and right hand circularly polarized light. The difference in those coefficients is a measure of the intensity of circular dichroism. It should be mentioned that optical activity and magnetic optical activity, which can occur in all media and is induced

by longitudinal magnetic fields, both have the potential for magnetically induced enantioselectivity in chemical reactions. It has been shown experimentally, that magnetochiral anisotropy—an effect linking chirality and magnetism—can give rise to an enantiomeric excess in a photochemical reaction driven by unpolarized light in a parallel magnetic field, which suggests that this effect may have played a role in the origin of the homochirality of life [2].

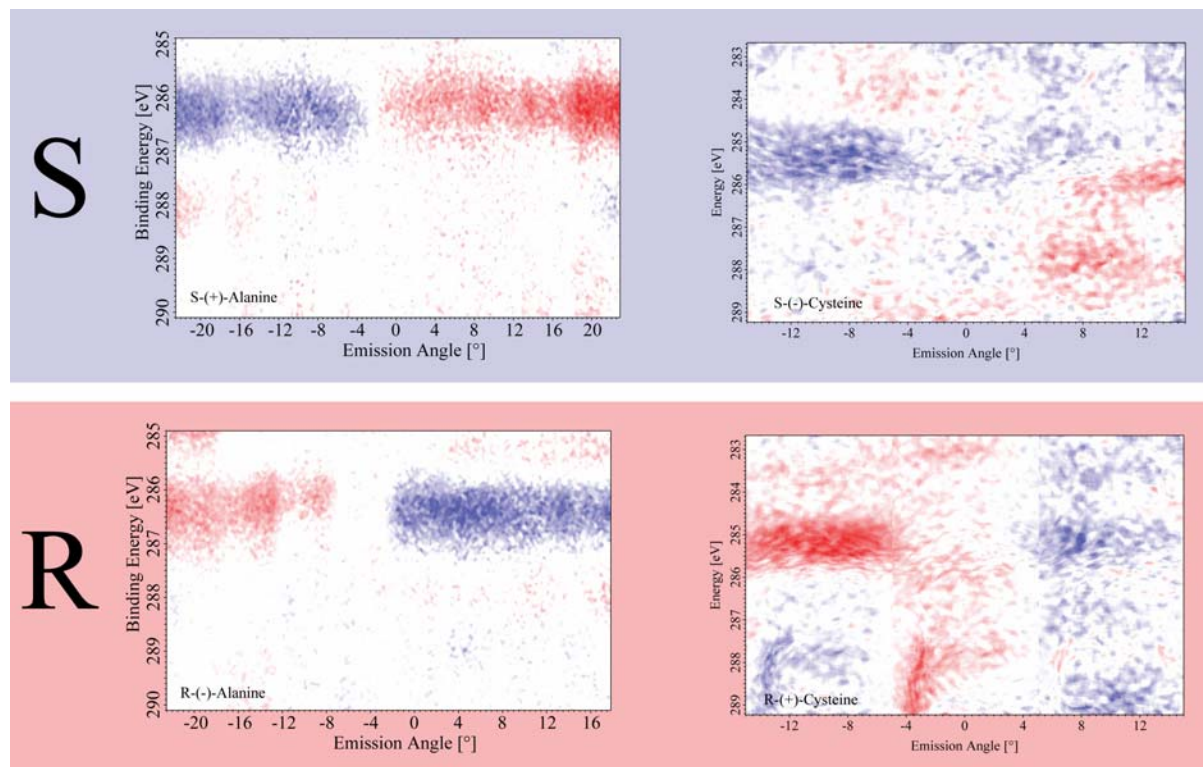


Figure 2: Angular distribution in the asymmetry of the different enantiomers of alanine and cysteine. The sample is rotated in the plane defined by the synchrotron light and the axis of hemispherical analyzer.

While circular dichroism as well as optical activity have been widely used in the visible and near UV region [3], the use of higher photon energies to analyze circular dichroism in valence and core level absorption or electron emission has been less actively pursued.

Here, we report on the characterization of adsorbed chiral molecules with respect to handedness and chemical composition using core-level photoemission spectroscopy with circular polarized light.

The molecules under investigation are alanine and cysteine, their chemical structure shown in Figure 1. These two amino acids show the same next-neighbour environment of the chiral center, where the amino-group, the carboxylic group, and the hydrogen are identical, but cysteine contains an methane-thiol-group instead of a simple methyl-endgroup for alanine, i.e. incorporating an additional sulphur atom. This subtle change in chemical structure leads to different adsorption behavior and opposite optical activity. While R- and S-alanine show negative and positive optical activity, respectively, R- and S-cysteine show positive and negative optical activity, respectively.

The enantiomers of both molecules have been evaporated on clean Cu(110) surfaces at 330 K. For R- and S-alanine the chiral adsorption geometries (2 2, -5 3) and (2 -2, 5 3), respectively, are obtained. R- and S-cysteine, on the other hand, adsorb in the chiral (4 -1, 1 5) and (4 1, -1 5) structures, respectively. According to their chemical structure both molecules possess three carbon atoms in different chemical environments and their contributions to the C1s core level emission can be readily detected (see Figure 1). However, only the contribution of the chiral

center shows a circular dichroism, that is, the intensity is different for excitation with left- or right-hand circular polarized light. Figure 2 shows the asymmetry plots for the alanine enantiomers. The asymmetry changes sign as a function of the emission angle. Changing the handedness of the molecule reverses the sign in the measured asymmetry. The asymmetry plots for cysteine shown in Figure 2 show the identical behaviour, that is, the right-handed enantiomer shows a negative asymmetry at negative emission angles. The above results show that the angular dependent asymmetry is an absolute representation of the molecular chirality and does not depend on the optical activity but only on the handedness of the molecule.

- [1] Agranat, I. ; Caner, H.; Caldwell, J. *Nat. Rev. Drug. Discov.* 2002, 1, 753–768.
- [2] Rikken, G. L. J. A.; Raupach, E. *Nature* 2000, 405, 932–935.
- [3] Berova, N.; Nakanishi, K.; Woody, R. W. *Circular Dichroism - Principles and Applications*, 2nd edition; Wiley-VCH: New York, 2000.

Electronic structure of trans- and cis-Stilbene

P. M. Schmidt, K. Horn, and T.U. Kampen

Fritz-Haber-Institut der Max-Planck-Gesellschaft, Abteilung Molekülphysik,
Faradayweg 4-6, 14195 Berlin, Germany

An intense search for digital optical data storage and novel electronic devices with increasing storage density has been pursued in the recent years. Promising results have been obtained by the use of molecular systems [1] with the advantage of easy fabrication, the possibility to shape organic compounds into desired structures by molecular engineering, and fine-tuning of many physical properties by small changes in molecular structure. Molecules with an extended π -electron-system are particularly promising candidates. Intermolecular interactions of the π -systems favor a stacking of molecules with their aromatic planes parallel to each other. In such highly ordered thin films or organic molecular crystals, overlap between π -orbitals takes place only in one direction leading to an anisotropy of optical and in physical properties. For large molecules with extended π -systems, the formation of bands has been observed [2] suggesting the occurrence of high carrier mobility due to band transport. A molecule with two different possible conformations incorporated into one-dimensional “molecular wires” would ideally serve as a “molecular switch”. The simplest model switch of this sort is the stilbene-molecule (1,2-Diphenylethylene) shown in Figure 1 for which the phenyl groups can be arranged on the same side or on opposite sides around the central C=C bridge, named as cis- or trans-stilbene, respectively.

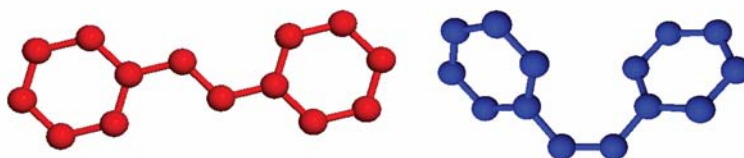


Figure 1: Molecular structure of trans(red)- and cis(blue)-stilbene.

The isomerisation of stilbene around its C=C-double bond can be triggered by UV irradiation, as already shown in the gas phase and in solution and described theoretically [3,4,5,6]. Two possible pathways for isomerisation are currently discussed. The “one-bond flip” corresponds to a rotation around the double bond excited by the UV photons and leads to a transition state conformation of the two phenyl rings perpendicular to each other. The “hula-twist” mechanism shown by Fuß and coworkers [6], being a low-energy pathway, is a simultaneous rotation around the central double-bond and one of the adjacent C-C-single bonds, keeping the phenyl groups parallel to each other at all times. The isomerization may be induced by UV-light in the wavelength range of 250-320nm, with isomerisation times in gasphase and solution of ~ 3 ps and ~ 100 ps for the cis-to-trans- and the trans-to-cis-isomerisation, respectively [4].

For molecular switching being a useful process in microelectronics, such a pathway has to work on surfaces, i.e. in a constrained situation. Bonding with the substrate surface, however, must not hinder the switching process. In this course we have already investigated the adsorption of both stilbene isomers on Si(100) [7]. Here, we present a study on the impact on isomerization on the electronic structure of the molecule.

The experiments were performed at the UE56/2 PGM1 Beamline. Photoelectrons were detected with a SPECS Phoibos 100 hemispherical analyzer equipped with a 2D CCD-detector. Cis- and trans-stilbene was used without further purification. Both isomers were evaporated from a glass tube, in the case of trans-stilbene heated to 90°C, through a leak-valve onto a Cu(110) surface cleaned by ion-bombardment and annealing. The difference in evaporation temperature correlates with the higher boiling point of trans-stilbene under standard conditions. All photoelectron spectra were taken with a fixed angle of 54.6° between photon source and electron analyzer.

In Figure 2 spectra of a several monolayer thick layer of cis- and trans-stilbene are shown. In addition, Figure 2 shows calculated valence band spectra. The binding energies for MOs are derived from DFT calculations of single molecules of the cis- and trans-isomer. The calculated spectra are obtained by convolution with a Gaussian function of 0.4 eV width to model broadening. Calculated binding energies have been aligned to the highest kinetic energy feature of the experimental spectra, which can be attributed to emission from the highest occupied molecular orbital (HOMO). Experimental and theoretical spectra show an excellent agreement, that is, all features in the experimental spectra can be attributed to emission from occupied molecular orbitals in the molecule. This is especially remarkable as the DFT calculations have been performed for single isolated molecules and binding interaction between the adsorbed molecules and the surface are thus neglected. Hence intensities in the calculated spectra may and do not resemble the intensities measured. Still the calculated binding energies for the MOs are in good agreement with measured values as shown before. This can be explained by the weak interaction of the molecules within this layers, which is lower than the molecule-substrate interaction as indicated by core level XPS (not shown here).

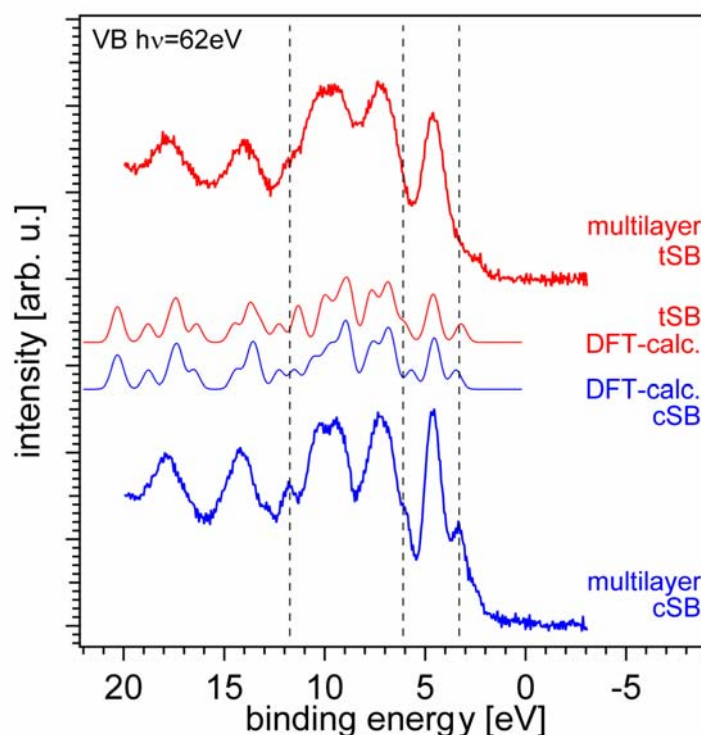


Figure 2: Experimental and theoretical valence state spectra of trans- and cis-stilbene multilayers deposited on clean Si(100) at low temperatures.

Measured as well as calculated spectra for the two isomers are similar to a large extent as can be expected. However, small differences are visible especially for the signals at about 3.5 eV, 6.0 eV, 10.9 eV and 11.9 eV binding energy. This differences in the spectra for the two

isomers are attributed to the differences in shape and thus in the binding energy of the respective MOs, a result of the different conformation of the molecules. These differences are large enough to permit a clear differentiation between the adsorbed isomers which is a prerequisite for the investigation of the stilbene isomerisation. Although other methods for the differentiation of both isomers are possible, e.g. through vibrational spectra [8], only the valence band spectra give direct access to the electronic structure of the molecule.

- [1] R.L. Carroll, C.B. Gorman, *Angewandte Chemie International Edition* **41** (2002), 4378 - 4400.
- [2] T. Kampen, *Applied Physics A: Materials Science & Processing* **82** (2005), 457-470.
- [3] V.D. Vachev, J.H. Frederick, B.A. Grishanin, V.N. Zadkov, N.I. Koroteev, *Chemical Physics Letters* **215** (1993), 306-314.
- [4] R.J. Sension, S.T. Repinec, A.Z. Szarka, R.M. Hochstrasser, *The Journal of Chemical Physics* **98** (1993), 6291-6315.
- [5] J.S. Baskin, L. Bacares, S. Pedersen, A.H. Zewail, *Journal of Physical Chemistry* **100** (1996), 11920-11933.
- [6] W. Fuß, C. Kosmidis, W.E. Schmid, S.A. Trushin, *Angewandte Chemie International Edition* **43** (2004), 4178-4182.
- [7] P.M. Schmidt, T. U. Kampen, J.H. Dil, K. Horn, *Surface Science (accepted)*
- [8] D.H. Waldeck, *Chemical Reviews* **91** (1991), 415-436.

Soft X-ray Ion Yield Spectroscopy of Free Cobalt Clusters

V. Zamudio-Bayer¹, M. Vogel¹, J. Rittmann¹, B. von Issendorff², T. Möller¹, and J.T. Lau¹

¹ Technische Universität Berlin, Institut für Optik und Atomare Physik, PN3-1, Hardenbergstraße 36, 10623 Berlin

² Albert-Ludwigs-Universität Freiburg, Fakultät für Physik/FMF, Stefan-Meier Straße 21, 79104 Freiburg

e-mail: tobias.lau@tu-berlin.de

Core level X-ray absorption spectroscopy (XAS) is a valuable tool to investigate the unoccupied local electronic density of states with element specificity [1, 2]. Because of the local nature of inner shell excitation, the chemical environment and bonding of individual chemical elements can be studied. In this respect, XAS is unique, offering the exciting prospect of studying the electronic properties of individual constituents in doped or binary clusters. In a first step towards this aim, mass resolved soft X-ray absorption of neutral, pure transition metal clusters was measured recently at BESSY, using ion yield spectroscopy at transition metal $L_{2,3}$ edges. Neutral transition metal clusters are produced with a magnetron source, ionized by soft X-ray radiation, and detected by time-of-flight mass spectroscopy. High mass resolution up to $m/\Delta m = 1500$ is used to record transition metal cluster mass spectra while scanning the photon energy across the $L_{2,3}$ absorption edges. This way, the first X-ray absorption spectra of free vanadium, chromium, cobalt, and nickel clusters could be recorded.

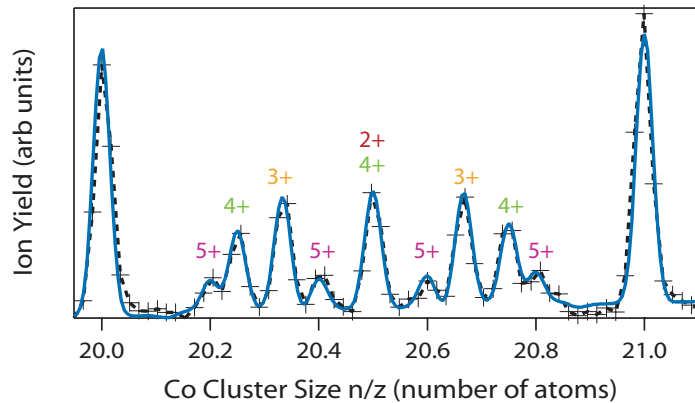


Figure 1: Detail of a soft X-ray ion yield spectrum of neutral cobalt clusters recorded at 780 eV photon energy. In the range of $n/z = 20$ – 21 , contributions of clusters with different z state are clearly discernible. Dashed line/markers: data; solid line: fit to the data. All charge states contribute to $n/z = 20$ and 21 .

Relaxation of the core excited state via Auger decay leads to multiply charged cluster ions, as shown in figure 1. Here, the individual contributions of Co_n^{z+} clusters with different n/z ratios to the mass spectrum can clearly be distinguished. The charge state distribution of cluster ions after soft X-ray absorption is analyzed as function of cluster size and excitation energy in the vicinity of the $L_{2,3}$ edges. Charge states extend from $z = 1+$ to $z = 5+$ with a maximum around triply and quadruply charged cluster ions, in line with experimental results on transition metal atoms [3].

The charge state of the Co_n^{z+} cluster ions detected after ionization with 780 eV photons varies smoothly as a function of cluster size. The results of a preliminary analysis indicate that even six- and sevenfold charged cluster ions contribute to the mass spectrum for larger clusters. A mass spectrum of neutral cobalt clusters with $\bar{n} = 250$ is shown in figure 2. The spectrum has again been decomposed into the individual charge state contributions as shown in figure 1. As for smaller clusters, the dominant contributions arise from quadruply and triply charged cobalt cluster ions. For larger clusters, a significant fraction of the cluster ions is five-, six-, and sevenfold charged. This might be due to several reasons. On the one hand, higher charge states may emerge because multiple ionization thresholds are reduced by screening effects in larger clusters, where valence electron delocalization due to metallic bonding is expected. In addition, outgoing Auger electrons

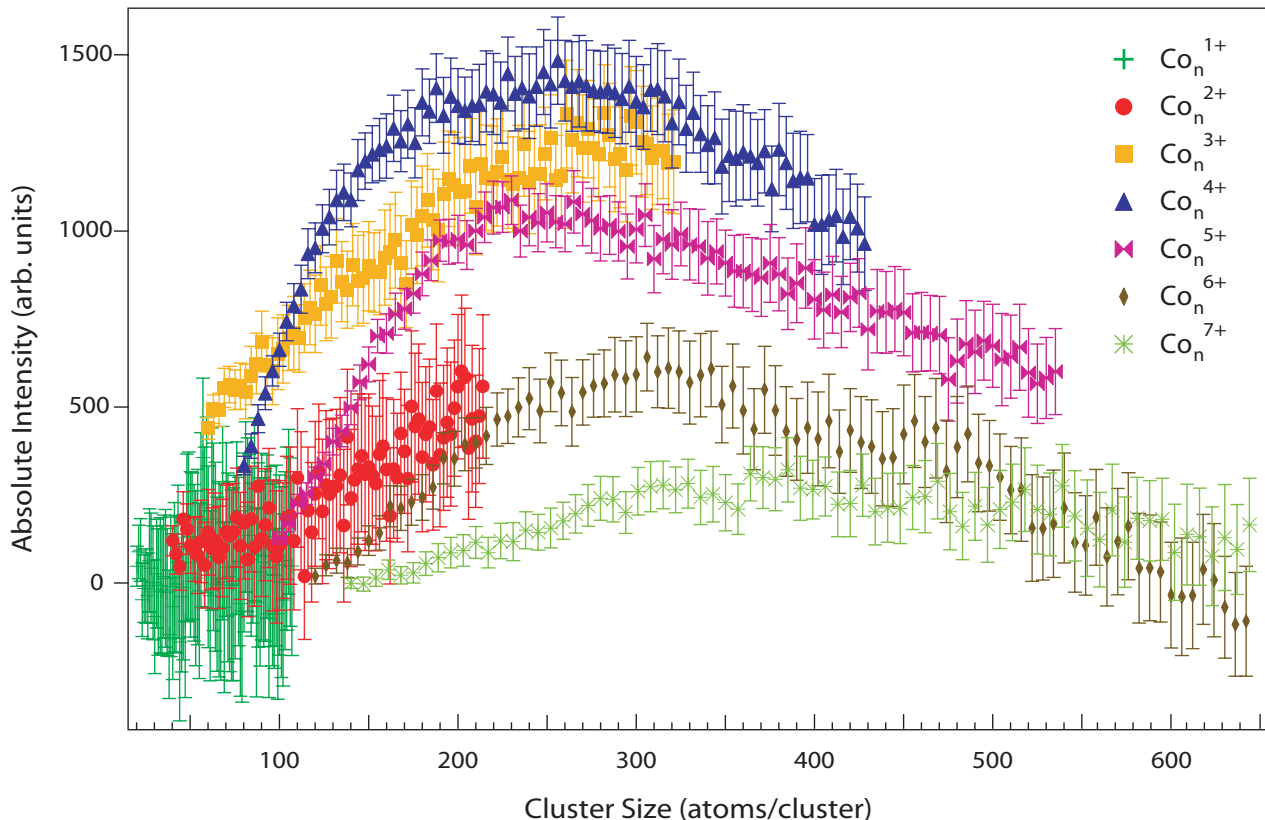


Figure 2: Neutral cobalt cluster mass spectrum obtained after ionization with soft X-rays at 780 eV. The spectrum has been decomposed into the individual contributions from different charge states. Cf. figure 1.

might induce electron impact ionization in larger clusters: For a given electron attenuation length, the secondary electron yield should increase with the cluster radius. On the other hand, the charge-resolved mass spectrum shown in figure 2 reflects the size-dependent stability of multiply charged cluster ions. For $n = 80$, the highest stable charge state is $z = 3+$. With increasing cluster size, higher charge states become more and more stable on the time scale of the experiment, indicating lifetimes of more than a few microseconds.

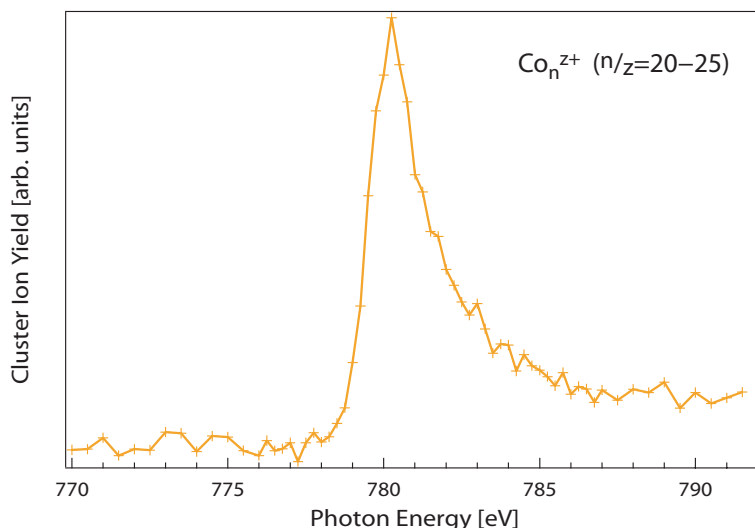


Figure 3: L_3 X-ray absorption of free cobalt clusters with $n/z=20-25$. Since dominant contributions are $z = 3$ and $z = 4$, this corresponds to the L_3 absorption of free $\text{Co}_{60}\text{-Co}_{100}$. The line shape is almost bulk like.

Fragmentation of the Co_n^{z+} cluster ions seems to be asymmetric. The only fragment ions observed below $n/z = 20$ for transition metal clusters after X-ray absorption are monomer and, to a much lesser extent, dimer ions. This is in contrast to soft X-ray ion yield experiments on silicon clusters (not shown here), where larger fragment ions were observed.

Soft X-ray absorption spectra can now be obtained by analyzing the cluster ion yield as a function of photon energy. In figure 3, the Co_n^{z+} ion yield for $n/z = 20\text{--}25$ is shown for $h\nu = 770\text{--}795$ eV. Since the main contributions are $z = 3+$ and $z = 4+$, this corresponds to the L_3 X-ray absorption of neutral $\text{Co}_{60}\text{--}\text{Co}_{100}$. As can be seen, the XAS line shape is almost bulk like for these clusters. This is, however, a preliminary result. A thorough analysis of the experimental data is currently in progress.

In summary, the first X-ray absorption spectra of neutral cobalt clusters were obtained. The cluster ion yield could be decomposed into contributions from different charge states. For clusters with $n = 60\text{--}100$, the line shape is almost bulk like. In the future, we will investigate smaller clusters in the size range $n \leq 50$.

The spectra shown here were obtained at BESSY beamline U49/2-PGM-1. Important preparatory work was performed at beamlines U49/2-PGM-1 and U125/2-SGM. Technical assistance was readily provided by BESSY staff members. We acknowledge funding by Technische Universität Berlin in the framework of research initiative project FIP 2/60.

References

- [1] O. Björneholm, F. Federmann, F. Fössing, and T. Möller, *Phys. Rev. Lett.* **74**, 3017 (1995).
- [2] P. Piseri, T. Mazza, G. Bongiorno, C. Lenardi, L. Ravagnan, F. D. Foglia, F. DiFonzo, M. Coreno, M. DeSimone, K. C. Prince, and P. Milani, *New J. Phys.* **8**, 136 (2006).
- [3] T. Richter and P. Zimmemann, private communication.

Soft X-ray Ion Yield Spectroscopy of Free Titanium and Vanadium Clusters: Proof of Principle and First Results

M. Vogel¹, J. Rittmann¹, V. Zamudio-Bayer¹, B. von Issendorff², T. Möller¹, and J.T. Lau¹

¹ Technische Universität Berlin, Institut für Optik und Atomare Physik, PN3-1, Hardenbergstraße 36, 10623 Berlin

² Albert-Ludwigs-Universität Freiburg, Fakultät für Physik/FMF, Stefan-Meier Straße 21, 79104 Freiburg

e-mail: tobias.lau@tu-berlin.de

Soft X-ray ion yield spectroscopy at the $L_{2,3}$ edges of titanium and vanadium clusters has been performed with high mass resolution at BESSY beamline U49/2-PGM-1 with the aim of following the evolution of atomic like to bulk like behaviour in transition metal clusters. Similar to the investigation of free cobalt clusters reported in this issue [1], neutral titanium and vanadium clusters were produced with a magnetron source and detected with a time-of-flight mass spectrometer after inner shell excitation at the titanium and vanadium $L_{2,3}$ edges. High mass resolution (up to $m/\Delta m = 1500$ in our case) is crucial to analyze the ion yield spectra.

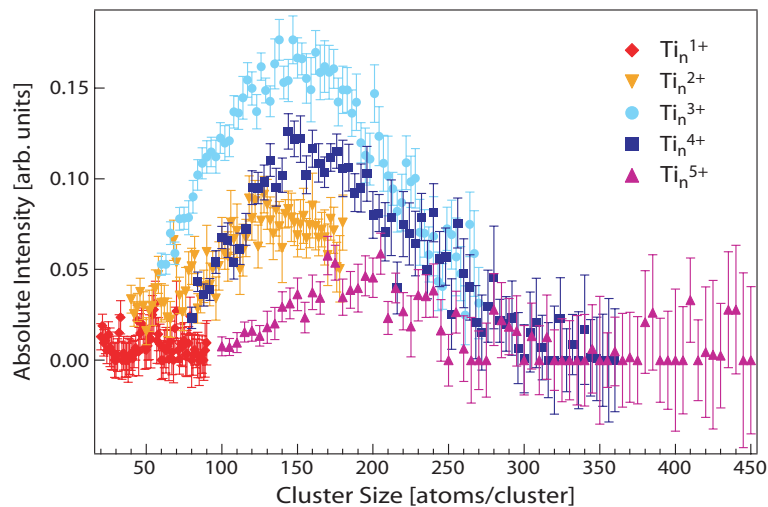


Figure 1: Neutral titanium cluster mass spectrum decomposed into contributions from different charge states. Evaluated for $n/z = 20-90$. Excited at the titanium L_3 edges.

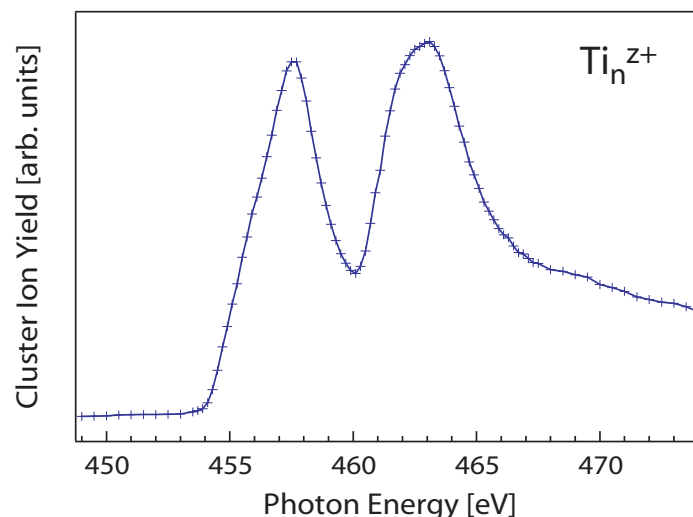


Figure 2: Soft X-ray ion yield spectrum of free titanium clusters with $\bar{n} = 150$.

A mass spectrum of neutral titanium clusters with $\bar{n} = 150$, photoionized at titanium L_3 edge, is

shown in figure 1. The Ti_n^{z+} spectrum has been decomposed into the individual charge state contributions, where the dominant contribution is $z = 3$ and $z = 4$. In the size range shown here, no contributions with $z > 5$ were observed.

According to our preliminary data analysis (see [1] for details), XAS line shapes and branching ratios are almost bulk like even for the smallest titanium clusters investigated. This surprising result is in contrast to a recent experiment reported for free titanium cluster XAS [2]. A thorough data analysis and further experiments on smaller clusters will help to clarify this issue. A typical X-ray absorption spectrum of free titanium clusters with $\bar{n} = 150$ is shown in figure 2. The full size range has been evaluated to improve statistics. It can clearly be seen that X-ray absorption spectra of free clusters can be obtained with excellent signal-to-noise ratio due to the high cluster flux density. Although titanium clusters are highly reactive, no oxygen contamination could be detected by XAS at the oxygen 1s edge.

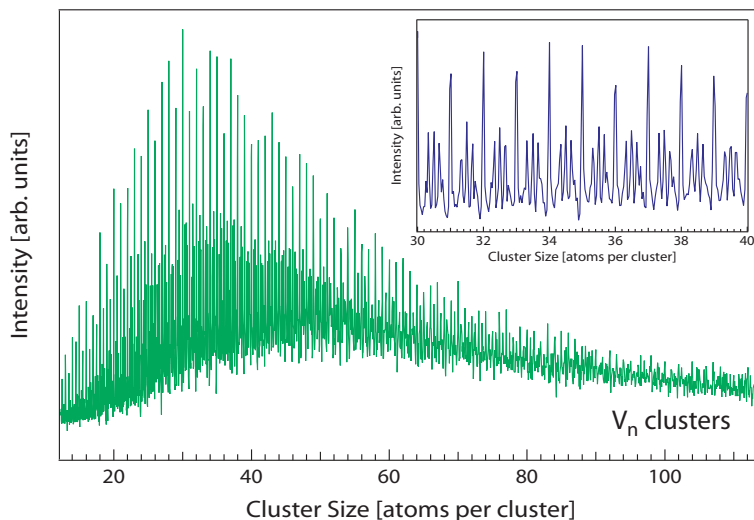


Figure 3: Neutral vanadium cluster mass spectrum, excited at the vanadium L_3 edge.

A mass spectrum of neutral vanadium clusters, excited at the vanadium L_3 edge, is shown in figure 3. The maximum is around $n/z = 30$. As can be seen in the inset, the distribution of charge states is similar to the case of titanium clusters. Again, even for the cluster size distribution investigated here, we obtain bulk like X-ray absorption spectra with good statistics. This is a clear indication that the transition to bulk like behaviour proceeds well below $n = 100$ for transition metal clusters. We therefore plan to investigate free clusters with $n=20-50$ in an upcoming beamtime.

In summary, we have demonstrated the ability to record soft X-ray ion yield spectra of neutral transition metal clusters after excitation at the $L_{2,3}$ edges with synchrotron radiation. This offers the exciting prospect of investigating the local electronic structure around dopant atoms in binary clusters. The experimental method will further be developed by our group.

The spectra shown here were obtained at BESSY beamline U49/2-PGM-1. Important preparatory work was performed at beamlines U49/2-PGM-1 and U125/2-SGM. We gratefully acknowledge technical assistance by BESSY staff members. This project was funded by Technische Universität Berlin as research initiative project FIP 2/60.

References

- [1] V. Zamudio-Bayer, M. Vogel, J. Rittmann, B. von Issendorff, T. Müller, and J. Lau, Soft X-ray Ion Yield Spectroscopy of Free Cobalt Clusters, BESSY annual report, 2006.
- [2] P. Piseri, T. Mazza, G. Bongiorno, C. Lenardi, L. Ravagnan, F. D. Foglia, F. DiFonzo, M. Coreno, M. DeSimone, K. C. Prince, and P. Milani, New J. Phys. **8**, 136 (2006).

Multiplet Splitting in L-edge X-ray Absorption Spectroscopy of Deposited Cobalt Clusters

V. Zamudio-Bayer¹, L. Glaser², M. Martins², W. Wurth², T. Möller¹, and J.T. Lau¹,

¹ Technische Universität Berlin, Institut für Optik und Atomare Physik, PN3-1, Hardenbergstraße 36, 10623 Berlin

² Universität Hamburg, Institut für Experimentalphysik, Luruper Chaussee 149, 22761 Hamburg

e-mail: tobias.lau@tu-berlin.de

In small metal clusters, the transition from atom like, localized, to bulk like, delocalized, electronic states takes place. The evolution of metal–metal bonding by inter-cluster hybridization of the 4s and 3d states can be followed by X-ray absorption spectroscopy (XAS) at the L_{2,3} edges of clusters deposited on weakly interacting substrates. Here, we report on a 2p–3d XAS study of small cobalt clusters on Cu(100).

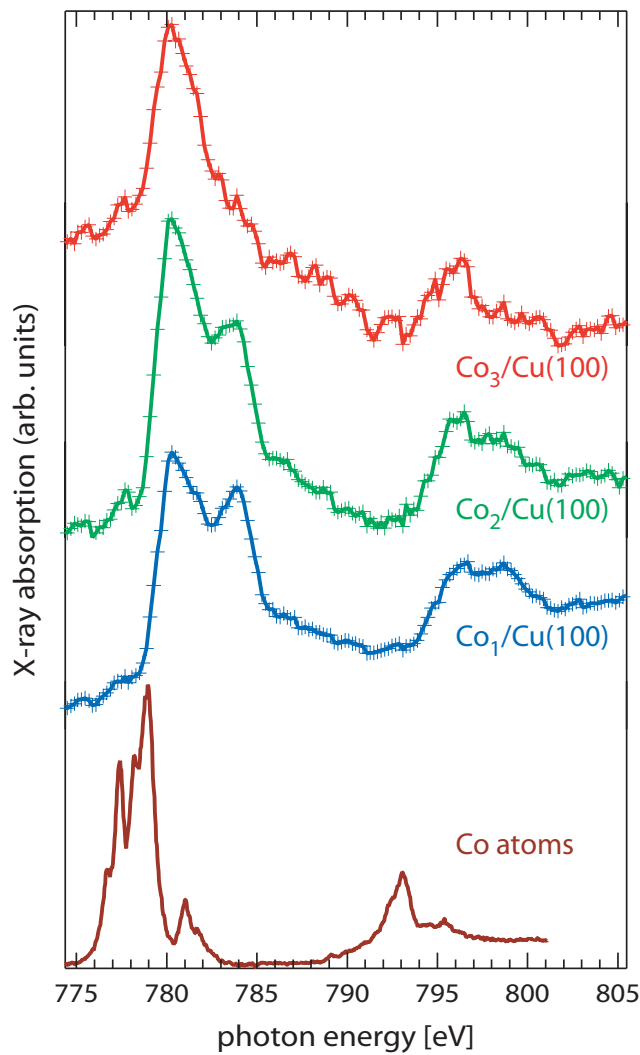


Figure 1: 2p–3d X-ray absorption of deposited cobalt clusters on Cu(100). The higher energy component at the cobalt clusters' L₃ edge decreases with increasing cluster size.

Mass-selected small chromium clusters ($n=1-3$) were produced by xenon sputtering [1] and soft-landed [2] in UHV onto a Cu(100) substrate. The evolution of the unoccupied electronic density of states was studied by XAS at the cobalt L_{2,3} edges at BESSY beamline UE52-SGM. The coverage has to be kept well below 0.01 monolayers in order to resolve the multiplet lines. In addition, residual gas adsorption even at 10^{-10} mbar leads to rapid degradation of the deposited cluster samples,

accompanied by changes in the spectral features. This makes XAS of small transition metal clusters a challenging task.

Two well resolved multiplet lines were observed at the 2p–3d absorption edge of small cobalt clusters on Cu(100). This clearly indicates that atom like XAS line shape can be obtained for small transition metal clusters on coinage metal substrates. As shown in figure 1, the L₃ absorption edge of small cobalt clusters is clearly split into two main components. By comparison to the corresponding spectrum of free cobalt atoms [3], also shown in figure 1, one could conclude that these two components are formed by the two separated sets of atomic multiplet lines at 776–779 eV and 781–782 eV, respectively. In deposited clusters, the lines are broadened and shifted to higher photon energy by interaction with the substrate.

Comparing the XAS spectra of Co₁, Co₂, and Co₃ on Cu(100), a general trend is apparent in the size-evolution of the spectral feature. Upon increasing the cluster size from deposited atoms via dimers to trimers, the L₃ component at higher photon energy decreases in intensity as compared to the low energy component. For cobalt trimers, the high-energy component has almost vanished. The same tendency is also visible at the L₂ edge of small cobalt clusters on Cu(100).

The onset of 2p–3d X-ray absorption is shifted to higher photon energy by approximately 4 eV for deposited clusters as compared to free cobalt atoms. In contrast, no significant shift of absorption energy is observed between the different cluster sizes. This indicates that the shift is induced by interaction with the underlying Cu(100) substrate. Most likely, delocalized copper valence electrons contribute to this effect by screening the Coulomb interaction of the cobalt 2p core hole with the cobalt 3d valence states. Since no size-dependence in 2p–3d X-ray absorption onset was observed, delocalization of cobalt cluster valence electrons, leading to a weakened 3d electron repulsion, does not seem to contribute a major effect in small cobalt clusters. A thorough analysis of the experimental data is currently in progress.

We gratefully acknowledge technical assistance by BESSY staff members.

References

- [1] J. T. Lau, A. Achleitner, H.-U. Ehrke, U. Langenbuch, M. Reif, and W. Wurth, *Rev. Sci. Instrum.* **76**, 063902 (2005).
- [2] J. T. Lau, W. Wurth, H.-U. Ehrke, and A. Achleitner, *Low Temp. Phys.* **29**, 223 (2003).
- [3] M. Martins, K. Godehusen, T. Richter, P. Wernet, and P. Zimmermann, *J. Phys. B: At. Mol. Opt. Phys.* **39**, R79 (2006).

Formation of 3D colloidal layers on structured substrates from colloidal dispersions

Th. Geue¹, P. Huber¹, W. Leitenberger² and M. Textor³

1 Laboratory for Neutron Scattering, ETH Zurich & PSI, CH-5232 Villigen PSI, Switzerland

2 Institute of Physics, University of Potsdam, D-14415 Potsdam, Germany

3 Materials Science Dept., ETH Zurich, CH-8093 Zurich, Switzerland.

Ordered colloidal assemblies are three-dimensional periodic structures formed from small polystyrene spheres suspended in solution. These assemblies attract considerable attention when used as optical filters, switches and materials with photonic band gaps.

Unluckily, a broad application of ordered colloidal assemblies is greatly restricted by numerous difficulties in the formation of large area ordered crystalline assemblies with uniform crystal orientation. We here present an approach using a holographically manufactured template (surface relief grating – SRG) made from a photopolymer which is pre-structured. The aim of these templates is to allow the growing of ordered colloidal assemblies by slow sedimentation to direct the crystallization of colloids towards bulky crystals and to allow a tailoring of the final lattice structure, orientation and size of the final colloidal assemblies. The understanding of the sedimentation process is hereby of great importance. Although there are optical [2,3] and confocal [4] microscopy well established as in-situ investigation techniques, both methods are limited.

To fully monitor the crystallization process in 3 dimensions, energy dispersive X-ray reflectometry was used to describe the phenomena taking place on the formation of colloidal layering. X-ray techniques are rarely used to investigate the formation of ordered colloidal assemblies so far [5, 6].

We used a monodisperse polystyrene latex with sphere diameter of 770 and 1030 nm delivered from *Microparticles*, Berlin at the EDR beamline. The experiment consists in the time dependent inspection of the colloidal deposition during the evaporation of the dispersant. For this purpose a droplet of colloidal dispersion in water was dropped onto the patterned substrate by a pipette. For homogeneity reasons a very small concentration of the colloids (about 0.01...0.06 %) was chosen. In order to guarantee stable conditions in temperature and humidity the sedimentation process was performed in a spatially limited, closed volume of 104 cm³. Because of the small cell volume the deposition process takes place close to the thermodynamic equilibrium between solid phase and colloidal droplet. The sedimentation velocity of spherical particles is estimated to be in the order of $v = 20\mu\text{m/h}$. Therefore several hours of stable experimental conditions are needed to follow the deposition process.

Fig. 1 shows the surface of the as prepared colloidal layers after finishing the experiment. The reflectometry sum signal during the evaporation of the dispersant as a function of time and humidity is displayed in Fig. 2. Short before the dry out of the dispersant a huge increase in the recorded diffusely scattered intensity was observed, while after the evaporation of the dispersant the intensity goes towards a reduced saturation value which indicates the final arrangement of the colloidal spheres on the template surface. The reason of this order-disorder behaviour is not yet finally understood. Preliminary calculations reveal an ordering process when the thickness of the remaining dispersant film is in the order of magnitude of the sphere diameter. If this film is then evaporated, a growth of defects may occur, which reduces the order of colloidal assembly due to spontaneous domain formation. It becomes urgently necessary to do these experiments again using a detector system which allows a better time resolution.

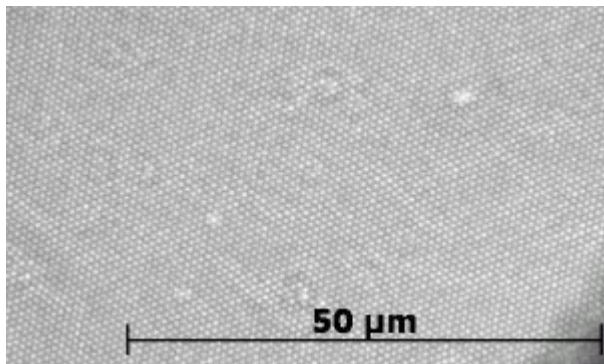


Figure 1: Colloidal assembly of 1030 nm spheres on a pre-patterned polymer template

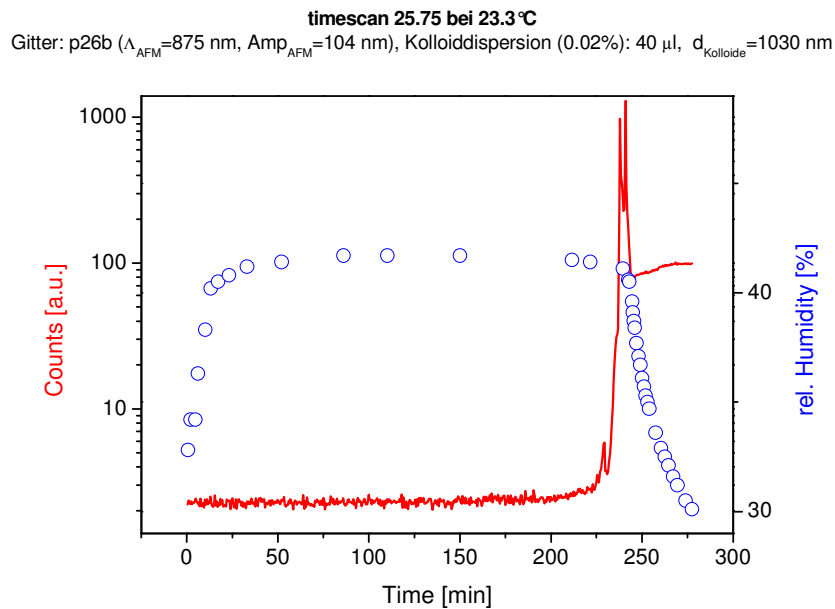


Figure 2: Time and humidity dependent ED-XRR of water evaporation from a 40 μ l colloidal suspension

References

- [1] Blaaderen, A. van, Ruel, R., Wiltzius, P. *Nature*, 385, 321 (1997)
- [2] Dushkin, C. D. et al. *Colloid Polym. Sci.*, 277, 914 (1999)
- [3] Yin, Y. et al. *J. Am. Chem. Soc.*, 123, 8718 (2001)
- [4] Hoogenboom, J. P., Vergeer, P., Blaaderen, A. van *J. Chem. Phys.*, 119, 3371 (2003)
- [5] Narayanan, S., Wang, J., Lin, X.-M. *Phys. Rev. Lett.*, 93, 135503 (2004)
- [6] Reinhold B., Geue T., Huber, P., Sant T., Pietsch U., Sztucki M. *J. Phys. Chem. B* 2007, to be submitted

Photoelectron Circular Dichroism in Core Level Photoemission from Randomly Oriented Chiral Molecules

BESSY-ID.06.1.078: Weeks 8/9 2006 UE56/2 PGM2

EU R II 3-CT-2004-506008

Chris Harding, Ivan Powis,

University of Nottingham, UK

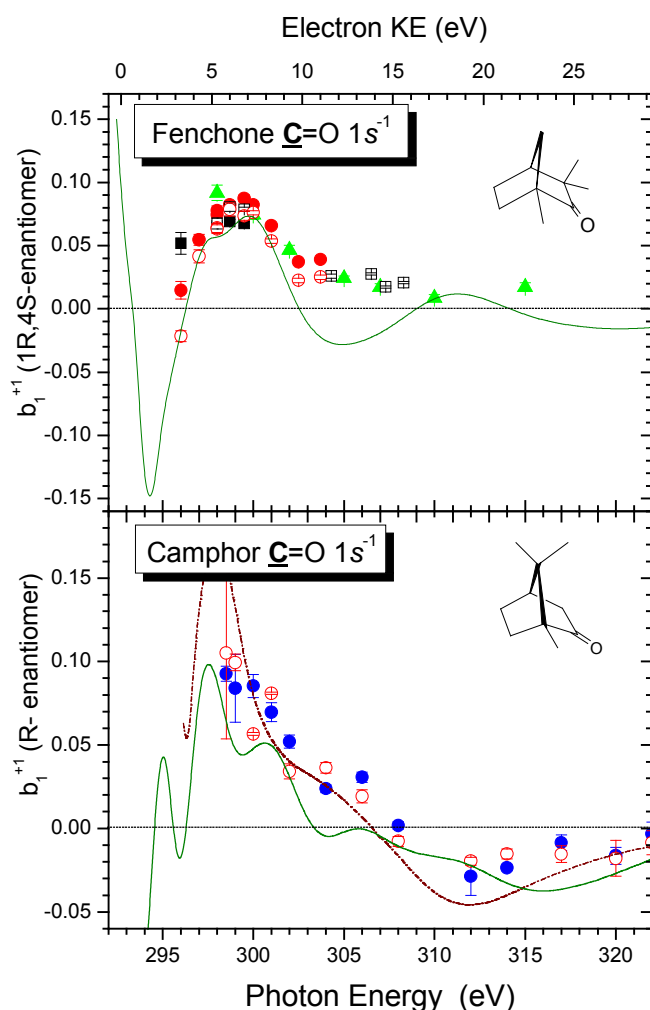
Volker Ulrich, Silko Barth, Sanjeev Joshi, Uwe Hergenhahn,

IPP, Euratom Association, Garching

Introduction

We have been investigating a new form of circular dichroism (CD) observable in the photoionization of chiral molecules that arises from an asymmetry in the photoelectron's angular distribution. Early predictions¹ of such asymmetry from an un-oriented sample of a chiral molecular enantiomer were made in the pure electric dipole approximation, leading to an expectation that any resulting dichroism (difference between behaviour observed with different polarizations of the light) might be very much greater than that traditionally associated with the absorption of circularly polarized light. More recent calculations confirmed asymmetry of the order of 10%, several orders of magnitude greater than traditional CD, might be realistically expected² and subsequently experimental measurements have started to confirm this.³⁻⁵

Photoelectron circular dichroism (PECD) arises from an angular distribution function of the form: $I_p(\theta) = 1 + b_1^p P_1(\cos\theta) + b_2^p P_2(\cos\theta)$



that has an 'additional' $\cos\theta$ term but only for a chiral molecule ionized with circularly polarized light (helicity, $p = \pm 1$). Consequently there can be a difference in the forward-backward photoemission yield (relative to the light propagation direction) for a given enantiomer and polarization, expressed by the chiral parameter $b_1^{\pm 1}$. This should reverse on changing either enantiomer or circular polarization.

Experiments at BESSY use the UE56/2 twin undulator beamline, providing rapid switching between left and right circularly polarized soft X-ray radiation to detect PECD. The photoemission yield is measured in a fixed detection direction, θ , and PECD then appears as a different current when switching polarization. By choosing $\theta = 57.4^\circ$, the magic angle where the second Legendry polynomial term disappears, we achieve an insensitivity to the $b_2^{\pm 1}$ (equivalent to the traditional β

asymmetry parameter) that simplifies analysis for the chiral b_1 terms.

It might be thought that observations of C 1s core emission make a poor choice for such work as the initial orbital is then achiral (spherical) and localized — so insensitive to the chirality of the molecular framework, but in fact the PECD effect is found to be of at least equal magnitude in core and valence ionization.^{3,5} Consequently, the observed dichroism and chiral asymmetry can be interpreted as a purely final state effect in C 1s photoemission. This however lends itself to theoretical modeling because of the essential simplicity of the initial state.

The figure shows new data obtained for the ionization of the carbonyl $\underline{\text{C}}=\text{O}$ 1s orbital in fenchone, a camphor related molecule. Measurements have been made over the course of two beamtimes, and both R- and S- enantiomers have been used. The PECD exhibited by the two enantiomers should be of the same magnitude, but of opposite sign according to the electric dipole approximation; higher order terms (electric quadrupole, magnetic dipole) might potentially cause a deviation from this expected mirroring of the PECD spectrum. In fact plotting the results obtained for the b_1^{+1} parameters, with those for the 1S,4R enantiomer negated, it can be seen that both then follow the same trend line, so that the dominant effect is in accord with the dipole approximation. This is further confirmed by a comparison with an electric dipole approximation calculated curves, included in the figure.

It is interesting to compare these results with those previously obtained for the related molecule, camphor^{5,6}. Whilst there are some similarities, there are also clear differences, even though the molecular structures are closely related. It has previously been noted that the dichroism especially, appears to be sensitive to molecular configuration and conformation⁷, and that even small changes in the scattering phase shifts can be expected to exert a significant influence upon the PECD measurement.

References

- ¹ B. Ritchie, *Physical Review A* **13**, 1411 (1976).
- ² I. Powis, *Journal of Chemical Physics* **112** (1), 301 (2000).
- ³ L. Nahon, G. A. Garcia, C. J. Harding, E. A. Mikajlo, and I. Powis, *Journal of Chemical Physics* **125**, 114309 (2006).
- ⁴ C. J. Harding, E. A. Mikajlo, I. Powis, S. Barth, S. Joshi, V. Ulrich, and U. Hergenbahn, *Journal of Chemical Physics* **123** (23), 234310 (2005); T. Lischke, N. Böwering, B. Schmidtke, N. Muller, T. Khalil, and U. Heinzmann, *Physical Review A* **70** (2), art. no.022507 (2004); S. Stranges, S. Turchini, M. Alagia, G. Alberti, G. Contini, P. Decleva, G. Fronzoni, M. Stener, N. Zema, and T. Prosperi, *Journal of Chemical Physics* **122** (24), 244303 (2005); A. Giardini, D. Catone, S. Stranges, M. Satta, M. Tacconi, S. Piccirillo, S. Turchini, N. Zema, G. Contini, T. Prosperi, P. Decleva, D. Di Tommaso, G. Fronzoni, M. Stener, A. Filippi, and M. Speranza, *Chemphyschem* **6** (6), 1164 (2005).
- ⁵ U. Hergenbahn, E. E. Rennie, O. Kugeler, S. Marburger, T. Lischke, I. Powis, and G. Garcia, *Journal of Chemical Physics* **120** (10), 4553 (2004).
- ⁶ M. Stener, D. D. Tommaso, G. Fronzoni, P. Decleva, and I. Powis, *Journal of Chemical Physics* **124** (2), 024326 (2006).
- ⁷ C. J. Harding and I. Powis, *Journal of Chemical Physics* **125**, 234306 (2006).

Actinic inspection of sub-40 nm extreme ultraviolet lithography mask blank defects using photoemission electron microscopy

Jingquan Lin¹, Nils Weber², Jochen Maul³, Stefan Hendel⁴, Karsten Rott⁴, Michael Merkel², Gerd Schoenhense³ and Ulf Kleineberg¹

¹Faculty of Physics, Ludwig Maximilians University, D-85748 Garching, Munich, Germany

²Focus GmbH, Neukirchner Str.2, D-65510 Huenstetten-Kesselbach, Germany

³Institute of Physics, Mainz University, Staudinger Weg7, D-55099 Mainz, Germany

⁴Faculty of Physics, Bielefeld University, Universitaetstr.25, D-33615 Bielefeld, Germany

A new actinic inspection technology to probe nanoscale defects buried underneath a Mo/Si multilayer on an extreme ultraviolet lithography mask blank has been implemented using EUV Photoemission Electron Microscopy (EUV-PEEM). EUV-PEEM images of programmed defect structures of various lateral and vertical sizes recorded at around 13.5 nm wavelength show that 35 nm wide and 4 nm high buried line defects are clearly detectable. The imaging technique proves to be sensitive to small phase jumps enhancing the edges visibility of the phase defects, which is explained in terms of a standing wave enhanced image contrast at resonant EUV illumination.

Extreme Ultraviolet Lithography (EUVL) is considered to be the next generation lithography at 32 nm node around 2009. Defect-free mask fabrication is a tremendous challenge to the successful implementation of EUVL, and has been listed among the top three critical issues remained unresolved in EUVL development [1]. According to the International Technology Roadmap for Semiconductor, defect size of less than 22 nm is required at the 32 nm node, and the defect density should be less than 5×10^{-3} defect/cm²[2]. This puts an extremely strict demand on mask blank manufacture including defect inspection. In this report we demonstrate that standing wave assisted EUV-PEEM is sensitive to buried line defects of 35 nm in width and 4 nm in height, and explain the contrast mechanism involved in the detection of mask blank defects with EUV-PEEM.

In our detection scheme, standing wave field illumination of a multilayer-coated mask blank is employed in the EUV-PEEM. When the inspection wavelength is chosen such that a node of standing wave appears at the multilayer surface (with minimal photoelectron yield as the number of photoelectrons emitted into vacuum is approximately proportional to the local electric field intensity at the multilayer surface, and this corresponds to dark in a PEEM image), defects usually appear bright because they lift the destructive interference condition present in the region of undisturbed multilayer [3].

The PEEM instrument (Focus GmbH, Germany) was used to detect the multilayer buried defect. Compared to a conventional PEEM with a shallow incidence angle (typically around 70° off sample normal), the novelty of the EUV-PEEM instrumentation is in that the mask blank sample is illuminated at an angle of 4° off normal of

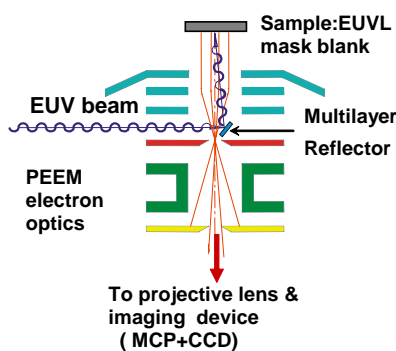


Fig.1 Scheme of the EUV-PEEM with the multilayer-coated microreflector inside the PEEM column, the EUV beam illuminates the mask blank sample at an angle of 4° off normal.

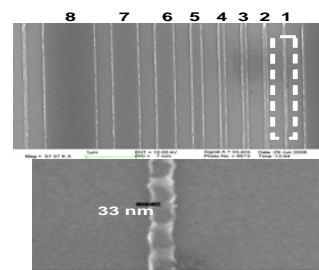


Fig.2 SEM image of an array of the programmed line defects after Ti lift-off but before Mo/Si multilayer coating (upper). Correspondingly labeled width for each line defect on the silicon substrate is as follows: line #1 (35nm), 2(70nm), 3(100nm), 4(125nm), 5(200nm), 6(300nm) 7(500nm) and line 8 (1000nm). The bottom image shows a typical measured result of the narrowest line in the pattern (the line marked by a dash-line box), which is about 33 nm in width.

the sample by the use of a 2 x 3 mm² broadband EUV multilayer coated micro-reflector placed close to the PEEM diffraction plane [4]. This modified EUV-PEEM instrument is sketched in Fig. 1. The Synchrotron Radiation facility BESSY II in Berlin, Germany, was used as light source to perform mask blank inspection in the EUV range. The mask inspection work was performed at beamline “UE112-PGM-1”, which is equipped with a plane grating monochromator and optimised for high spectral brightness in the EUV at around 100 eV. The available photon flux at 13.5 nm wavelength in first undulator harmonics is about 2×10^{13} photon/(s*100mA*0.1% bandwidth).

In order to study the contrast mechanism involved in the image formation and test the sensitivity of the EUV-PEEM, a mask blank sample including programmed nanosized “bump” defects on substrate was prepared. Several identical sets of line-space patterns, which have been fabricated in titanium by means of electron beam lithography and a lift-off technique, have repeatedly distributed on a silicon substrate. Each pattern, as shown in Fig. 2, includes a group of 8 line defects with different widths ranging from 35 to 1000 nm and all of equal length of 10 μm. For the convenience of addressing, each line of the pattern in Fig. 2 was numbered, namely from line “1” to “8”. Width parameters of the lines are given in the figure caption of Fig. 2. These titanium line defects were in the following overgrown with a 40 period Mo/Si multilayer (6.9 nm period thickness) by Ion Beam Deposition (IBD). Atomic Force Microscope (AFM) measurements show that the vertical height of the line defects is less than 4 nm at the surface after multilayer coating (Fig. 3).

Fig.4 displays a typical EUV-PEEM image obtained by focusing on one line pattern set on the mask blank sample, showing that all 8 buried line defects in the pattern set are clearly detectable. The smallest line defect with width of approximately 35 nm (labeled “1” in the Fig. 4) shows an intensity contrast of around 25% with respect to the undisturbed image background. The hexagonal shaped bright section appearing in the centre of PEEM image is an artifact of the contour of the iris aperture inside the electron column. Note that the true defect structure varies within about a factor of 28 in their lateral size (geometrical size ratio between the widest and narrowest line, as known from the SEM image in Fig. 1).

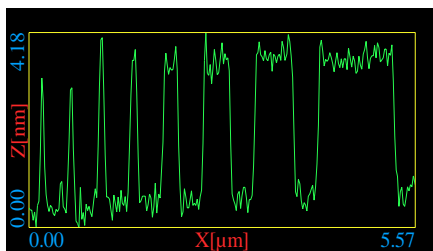


Fig.3 A linescan (perpendicular to the parallel line defects) in the AFM characterization of the multilayer-coated sample containing varied line width defects.

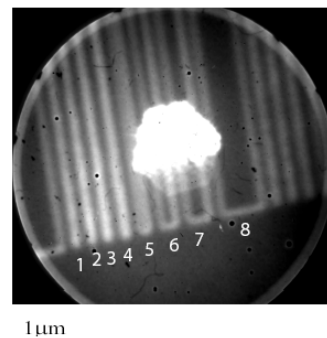


Fig.4 An EUV-PEEM image showing a pattern, which consists of a set of line defects of varying line width buried under a 40 bilayer Mo/Si multilayer, acquired at an inspection wavelength of 13.5 nm. The line marked with “1” corresponds to a 35 nm wide and 4 nm high defect. The lines are labeled according to Fig.2.

However, only a size variation of about a factor of 8 (FWHM) within the line array of an integrated pattern has been obtained from line scans of the defects displayed in the PEEM image of Fig.4. Moreover, the obtained size ratio of the defects from line scans of the PEEM image of Fig.4 is not in agreement with the size ratio of the structures measured at the multilayer surface arising from the buried defects either. AFM characterization of the multilayer coated sample (Fig. 3) shows that the size ratio of the bumps (FWHM) at the multilayer surface is only about 21 (due to a larger size expansion of the narrowest line compared to that of the widest line after the multilayer coating). This unusual defect size ratio obtained from the PEEM image as shown in fig.4 is not predominantly degraded by the lateral PEEM resolution (which is about 50-100 nm in this mode of operation) but is mainly due to the fact that the defect topographies are not imaged like in an optical microscope (because defects are buried and thus can not be in the focal plane of the PEEM); but the near-field wave front distortion caused by them is probed at the multilayer surface via imaging the EUV standing wave field induced photoelectrons. Standing wave enhanced PEEM employed in our detection scheme thus offers a combination of wave front phase sensitivity (like in interferometry) and lateral resolution at the surface (like in microscopy). The PEEM detects deviations from the interference pattern of the EUV standing wave field on the surface of the multilayer caused by internal defects, and this distortion is laterally extended because the wave fronts travels ~280 nm through the multilayer stack from the defect at the substrate to the multilayer surface. This result indicates that our EUV-PEEM can detect the internal reflectivity distribution inside multilayer stack and the near-field distribution at the multilayer surface.

Another feature of the PEEM image shown in Fig. 4 is that each line defect with a width of 200 nm or above (lines #5-8) appears as highlighted contour of the line structure against a dark multilayer surface at an inspection

wavelength of 13.5 nm. This observation result must be carefully analysed since it is away from one's expectation that whole surface of a line defect should appear white in EUV-PEEM image when the wave front of standing wave at undisturbed multilayer surface is in the node. In the case of depositing the EUV multilayer over a flat top "wide" step (wide line defect), the evolution of multilayer structure in the centre part of the flat step follows conformally the contour of the line step, and a deformation of multilayer structure occurs only around the edges of the step. This is the position where the EUV field shifts from the destructive interference condition present in the region of undisturbed multilayer. Since detection of the wave front phase of EUV standing wave field on the multilayer surface is employed in our scheme, only the contour part of the step is detected with an increased photoelectron yield from the undisturbed multilayer section [5, 6].

In summary, we have performed actinic defect metrology on programmed multilayer phase defects by standing wave enhanced EUV-PEEM. Due to the standing wave field illumination assisted contrast mechanism in the EUV-PEEM, the system is capable to detect buried defects with a width of less than 35 nm and a height of as low as 4 nm. By probing the defect-induced distortions of the near-field distribution of the standing wave field at the multilayer surface, further information about the printability of these defects can be expected by future simulations. The actual experimental detection limits of the EUV-PEEM are still not reached and need to be explored in future experiments.

This work was supported by the 6th Framework program of the European Union within the project 'Exploring new limits to Moore's law – More Moore' (subproject 3: "Innovative Technologies for 22 nm node and beyond", work package 4: "Low defect mask blanks").

We are indebted to BESSY II, Berlin, Germany and their staff for the excellent beamline support and for providing excellent working conditions.

References

- [1] Stephan Wurm, 2005 International Symposium on EUVL in San Diego, Nov.2005
- [2] International Technology Roadmap for Semiconductor, see www.itrs.org
- [3] G.Schoenhense, U.Kleineberg, German patent DE 100 32 979 A1 (Jan.17,2002)
- [4] Jingquan Lin, et al; J.Vac.Sci.Technol. B24, 2631 (2006)
- [5] Jingquan Lin, Ulrich Neuhaeusler, Jawad Slieh, Ulrich Heinzmann, Nils Weber, Matthias Escher, Michael Merkel, Andreas Oelsner, Dima Valdaitsev, Gerd Schoenhense, Etienne Quesnel and Ulf Kleineberg; Microelectronic Engineering. (in press April, 2007)
- [6] Jingquan Lin, Nils Weber, Jochen Maul, Stefan Hendel, Karsten Rott, Michael Merkel, Gerd Schoenhense and Ulf Kleineberg; Proceedings SPIE Vol. 6533 (in press 2007)

NEXAFS investigations of metalloporphyrin films

N. Schmidt¹⁾, G. Tzvetkov¹⁾, T. Strunskus²⁾, C. Wöll²⁾ and R. Fink¹⁾

¹⁾ Physikalische Chemie II, Universität Erlangen, Egerlandstr. 3, 91058 Erlangen

²⁾ Physikalische Chemie I, Ruhr-Universität Bochum, Universitätsstr. 150, 44780 Bochum

Due to their interesting optical and electronic properties metalloporphyrins are used in various organo-electronic devices like, e.g., in organic solar cells, OLEDs, OFETs, sensors or in photocatalysis. In order to tailor their properties in thin film applications, a detailed knowledge of film morphology and their electronic properties is required. Film morphology is influenced by intermolecular interactions like π -stacking or additional axial ligands. The frontier orbital energies (HOMO, SOMO, LUMO and adjacent) are mainly governed by the type and oxidation state of the complexed metal ion. In the case of transition metal ions, the interaction of metal d-orbitals with the nitrogen lone pairs in the porphyrin ligand plays a major role.

The present NEXAFS study includes a comparative investigation of various metalloporphyrins focusing on the interaction of the central metal ion with the surrounding porphyrin frame. The experiments were carried out at the BESSY HE-SGM and UE52-PGM beamlines. The samples were prepared by drop-coating chloroform solutions of the compounds onto Au-plated Si wafers. In addition, multilayer films of Sn(OH)₂TPP were prepared by organic molecular beam deposition (oven temperature: 680 K) onto a clean Ag(100) single crystal surface at room temperature.

Morphology of Sn(OH)₂TPP/Ag(100)

The C K-edge spectra of NEXAFS spectra of vacuum sublimated multilayer films of Sn(OH)₂-tetraphenylporphyrin ((Sn(OH)₂TPP) exhibit a strong polarization dependence (resonances at 284 eV) and around 287 eV in Fig. 1). These resonances are attributed to excitations into unoccupied orbitals located on the porphyrin ring system. The intensity of π^* -resonances the N K-edge spectra behave similarly. We may therefore conclude that the porphyrin rings are oriented coplanar to the substrate surface. The resonance at 285.5 eV is due to excitations in the phenyl rings of the TPP ligand. Almost no angular dependence is detected for this resonance which is in accordance with a tilt angle of about 50° of the phenyl rings with respect to the porphyrin frame as confirmed by single crystal x-ray analysis [1] or calculations [2].

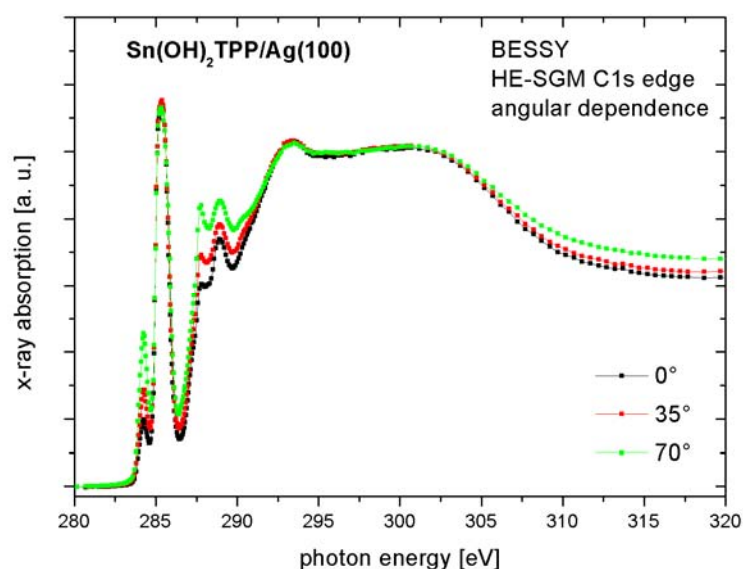


Fig. 1: Angle-dependent C K-edge NEXAFS spectra of Sn(OH)₂TPP multilayer films for different incidence angles.

Electronic structure of H₂TPP and MTPP (M=Mn³⁺, Fe³⁺, Co²⁺, Zn²⁺, Sn⁴⁺)

To gain insight into the electronic structure of various metallo-porphyrins, the analysis of N K-edge spectra is more sensitive, since the nitrogen atoms of the porphyrin system are directly bound to the center metal ions. The phenyl rings (or in the case of Sn(OH)₂TTBPP phenyl rings with additional substituents) do not affect the spectra since they are tilted with respect to the porphyrin plane and not conjugated to the porphyrin system. In the free base porphyrin (H₂TPP), there are two pyridinic and two pyrrolic (with attached proton) nitrogen atoms, leading to two different initial states separated by 3.4 eV [2]. The low-energy resonance at 397 eV therefore can be attributed to a pyridinic initial state. Since there are different allowed final states for both, the attribution of the other resonances is not straightforward.

In the metallo-porphyrins all four nitrogen atoms are identical, and thus only one initial state exists. Sn(OH)₂TTBPP and ZnTPP have a d¹⁰ configuration and behave very similar both for excitation into the LUMO (around 398.5 eV) and higher unoccupied π -type orbitals around 401.5 eV. CoTPP on the other hand, has a d⁷ configuration, which apparently leads to a higher intensity of the resonance at 400 eV. A slight shift of the whole spectrum to lower energies going from Co²⁺ to Zn²⁺ can be attributed to an orbital contraction by the higher core charge of Zn²⁺.

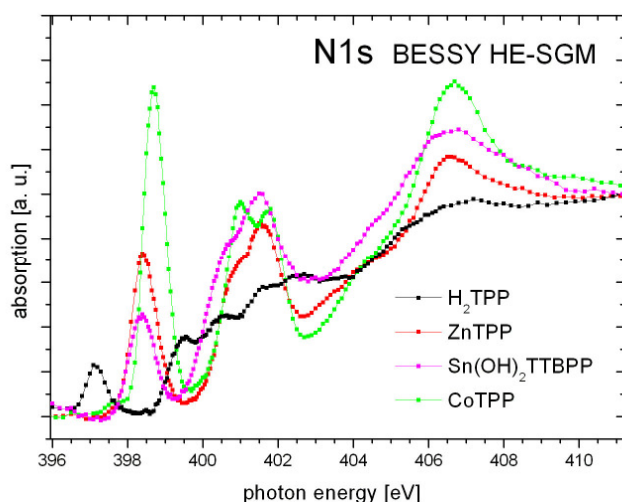


Fig. 2: N K-edge NEXAFS spectra of polycrystalline metallo-tetraphenyl porphyrin films with different metal ions in comparison with the free base H₂TPP.

A closer inspection of three different TPPs with first-row transition metal ions (Co²⁺, Mn³⁺, Fe³⁺, counter ion: Cl⁻) shows similarities between Co²⁺ and Fe³⁺. The metal ions of these substances have a d⁷ and d⁵ configuration, respectively, with singly occupied d_{z2} orbitals in both cases (according to calculations [1]). In Mn²⁺ (d⁴), the d_{z2} orbital is unoccupied. This is the main reason for the differences in the N 1s spectra. A more detailed attribution of resonances will be available from more detailed calculations which are currently under way.

Acknowledgements

We gratefully acknowledge experimental assistance of D. Batchelor (Univ Würzburg) and J.-F. Gnichwitz, A. Hirsch (Univ. Erlangen) for supplying the porphyrin substances. Financial support was given by the DFG (SFB 583) and the BMBF (contract 05 ES3XBA/5).

References

- [1] G. Smith, D. P. Arnold, C. H. L. Kennard, T. C. W. Mak, *Polyhedron* **1991**, *10*, 509-516.
- [2] M.-S. Liao, S. Scheiner, *J. Chem. Phys.* **2002**, *117*, 205-219.
- [3] S. Narioka, H. Ishii, Y. Ouchi, T. Yokoyama, T. Ohta, K. Seki, *J. Phys. Chem.* **1995**, *99*, 1332-1337

Investigations of lipid/protein membrane models by X-ray fluorescence methods

S.I.Zheludeva¹, N.N.Novikova^{1*}, V.V.Lider¹, N.D.Stepina¹, A.I.Erko²

¹*A.V.Shubnikov Institute of Crystallography RAS, Leninsky prosp. 59, 117333 Moscow, Russia.*

²*Berliner Electronenspeicherring-Gesselschaft fur Synchrotronstrahlung, Albert-Einstein-Strasse 15, 12489 Berlin, Germany.*

**e-mail: nn_novikova@ns.crys.ras.ru*

The use of ordered lipid/protein films on solid substrates, which are adequate models of biological membranes, gave rise to a new approach to studying the structural organization of cell membranes. These investigations make it possible to model various biophysical and biochemical processes in biological membranes. Such an approach is of great interest for the development of new drug compounds because in these model experiments the information about the differential data of the action of drug compound can be obtained in contrast to integral data provided by conventional studies on cells or living organism.

The great potential of spectroscopically selective X-ray techniques, such as X-ray standing wave (XRSW) measurements, for studying the structure and biological functions of membrane models has been demonstrated elsewhere. The XRSW technique is based on simultaneous measurements of angular dependence of X-ray reflection and fluorescence yield excited by the primary X-ray beam as the incident angle is scanned through the total external reflection (TER) region. In XRSW experiments energy spectra of characteristic fluorescence emitted from the sample are recorded at each point in the reflectivity curve, in contrast to the conventional X-ray fluorescence spectroscopy where the angle of incident X-ray beam is held constant. The integrated intensity under specific peak from selected element is plotted as a function of the incident angle. The key point of XRSW method is that the shape of these curves is strongly dependent on the mean position of the atoms in the direction normal to the surface and the thickness of the random distribution about this position. Thus XRSW method offers the opportunity to locate the atom position directly from the analysis of angular dependence of fluorescence yield.

Here, the possibilities the XRSW method for investigation of ordered lipid/protein films have been demonstrated. We studied the molecular mechanisms of the chelating effect of four drug compounds on membrane models, treated by lead ions. Molecular films of the metalloenzymes (alkaline phosphatase and catalase) deposited on silicon substrates have been used as model systems.

Experimental results and discussion. The samples under investigation were lipid/protein films of the membrane enzymes alkaline phosphatase and catalase deposited on silicon substrates.

Protein molecules were immobilized on a lipid monolayer, which had been preliminarily transferred onto a solid substrate by the Langmuir–Blodgett method. Thus the combination of the Langmuir–Blodgett method with molecular self-assembling has been used. In this report experimental results are presented for only 5 samples:

Sample 1. During solubilization of alkaline phosphatase we added to the solution of lead acetate, the mixture was incubated for an hour. The general scheme of deposition was as following: a monolayer of lipid mixture - dipalmitoylphosphatidylcholine and cholesterol (molar ratio 7:3), had been transferred onto a solid substrate by the Langmuir–Blodgett method. Adsorption immobilization of protein molecules on the transferred phospholipid monolayer was performed for 24 h. Finally the substrate with protein film was taken away through a newly formed langmuir monolayer of lipid mixture.

Samples 2-5. alkaline phosphatase treated by lead acetate was immobilized in the same way as for the sample 1. However, upon immobilization of protein molecules on the solid substrate, the sample was kept for 3 h in the solution chelating agents: sodium calcium EDTA (sample 2), succimerum (sample 3), xydiphone (K,Na-ETHIDRONATE) (sample 4) and mediphone (sample 5). Finally the substrate with protein film was taken away through a newly formed langmuir monolayer of lipid mixture.

XRSW measurements were performed at the station KMC2. The energy of X-ray beam was chosen to be 13 500 eV. The reflected X-ray beam was measured by a scintillation detector. The fluorescent signal was recorded by the Peltie cooled detector (ROENTEC). The synchrotron X-ray beam coming from bending-magnet was monochromatized by a double crystal monochromator (SiGe graded crystals), incident and reflected beams lay in the horizontal plane.

Typical X-ray fluorescence spectra for all 5 samples recorded at $\theta < \theta_c$ (θ_c is the critical angles of TER for silicon) are shown in fig. 1. In all these spectra the strong peaks of Ar K_α radiation (from argon of the surrounding atmosphere) and Si K_α radiation (from silicon substrate) can be seen. The most intensive fluorescence peak in fig. 1a (sample 1) is Pb L_α . In all other spectra (samples 2-5) Pb L_α fluorescence peak is hardly distinguished. This observation provides important information of the efficiency of studied drug compounds: the overwhelming majority of lead ions, bound to the protein molecules, have been removed by washing the lipid/protein films in the solution of chelating agents but no one of them ensured the elimination of all lead ions.

In Fig. 2 the integrated intensity of Pb L_α fluorescence from sample 1 is plotted as a function of angle. Quite remarkable is the shape of this curve – it can be formally described by $(1+R^2)$,

where R is the reflected amplitude. Perhaps the reason of such a behavior of Pb fluorescence curve is the features of lateral arrangement of lead ions inside the lipid/protein films - probably these ions formed discrete particles or islands.

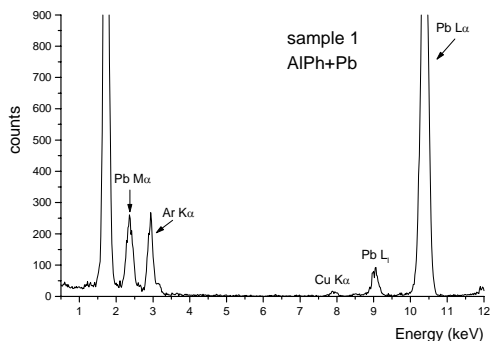


Fig. 1 (a).

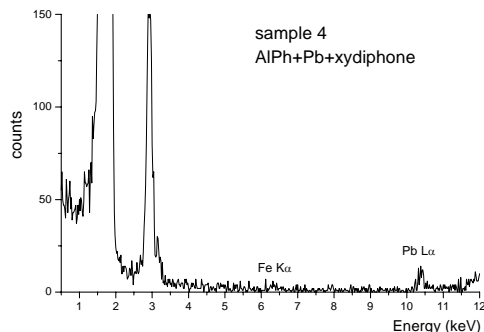


Fig. 1 (d).

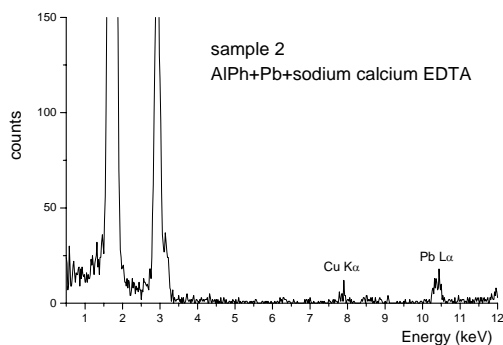


Fig. 1 (b).

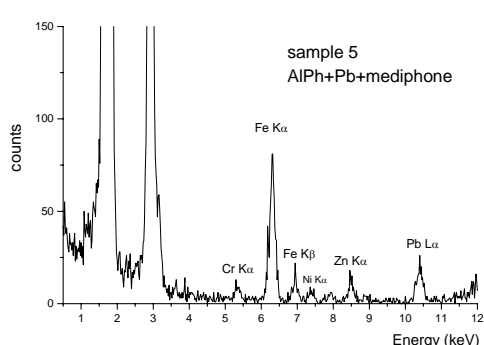


Fig. 1 (e).

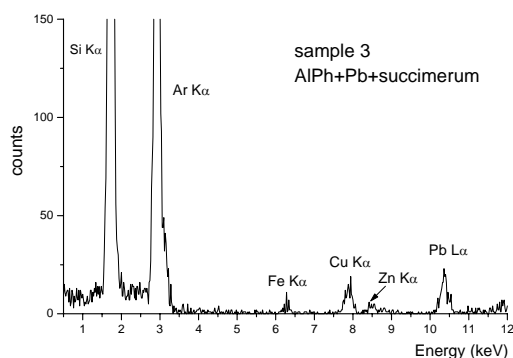


Fig. 1 (c).

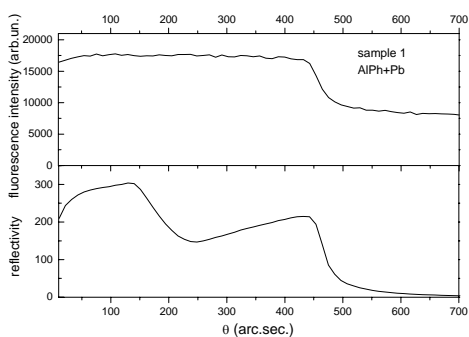


Fig. 2.

Figure 1. X-ray fluorescence spectra from the lipid/protein films.

Figure 2. Experimental angular dependencies of Pb L_{α} fluorescence from the lipid/protein films (sample 1). Bottom curve – X-ray reflectivity.

Layer-by-layer growth of thin epitaxial Fe₃Si films on GaAs(001)

*B. Jenichen, V. M. Kaganer, W. Braun, J. Herfort, R. Shayduk, C. Herrmann, K. H. Ploog
Paul-Drude-Institut für Festkörperelektronik, Hausvogteiplatz 5-7, 10117 Berlin*

Molecular-beam epitaxy (MBE) allows the controlled fabrication of epitaxial layer sequences with very sharp interfaces. The present work aims at the in-situ characterization of the Fe₃Si epitaxial growth process in the layer-by-layer growth mode by x-ray surface diffraction methods in order to achieve high-quality interfaces. The long-range ordering in the films is monitored by measuring different Fe₃Si superlattice reflections. The Fe₃Si films were grown on GaAs(001) templates by solid-source MBE in a chamber built into the six-circle diffractometer at the wiggler beamline U125/2 KMC (PHARAO) at the storage ring BESSY in Berlin.

The GaAs(001) templates were prepared in a separate III-V growth chamber using standard GaAs growth techniques. After capping the samples by As, the samples were transferred into the system at BESSY for the Fe₃Si deposition by means of an ultra-high-vacuum (UHV) shuttle. The Fe₃Si layers were grown on the clean As-rich GaAs surface at different substrate temperatures T_s near 200 °C, which is the optimum growth temperature for structural and interfacial perfection and a high degree of long-range atomic order. The Si and the Fe cell temperatures were tuned in order to achieve perfect lattice match of the Fe₃Si to the GaAs substrate and, at the same time, full stoichiometry of the films. During this process, the Si content of the film was determined from the position of the Fe₃Si layer peak.

We obtained optimum temperatures of 1239 and 1370 °C for the Fe and the Si cells, respectively, and achieved an almost perfect stoichiometry of the samples during and after growth. Annealing of the surface at 310 °C for about 1 h, while growing one monolayer (ML) of Fe₃Si, improved the surface quality considerably, as determined in situ by the increasing intensity of the x-ray surface reflections. The x-ray intensity oscillations shown in Fig. 1 were obtained after such an annealing procedure, demonstrating that Fe₃Si grows layer by layer. The intensity oscillations exhibit damping, indicating that several terrace levels contribute to the diffracted intensity. This is confirmed by subsequent atomic-force-microscope (AFM) measurements. One ML is grown in $t_p = 1220$ s. The time constant of the damping is $\tau = 1$ h. The growth rate was confirmed by comparison of rod scans with dynamic simulations

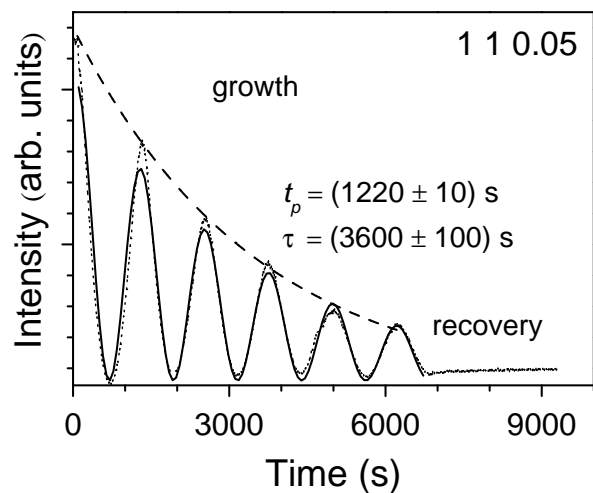


Fig. 1. X-ray oscillations (dotted line) with a period t_p observed by grazing-incidence diffractometry during the MBE growth of an Fe₃Si epitaxial layer on GaAs(001) at $T_s = 220$ °C. For the determination of the period t_p and the decay time τ , the measured curve is approximated by a function proportional to $\sin^2(\pi t/t_p) \exp(-t/\tau)$ (solid line).

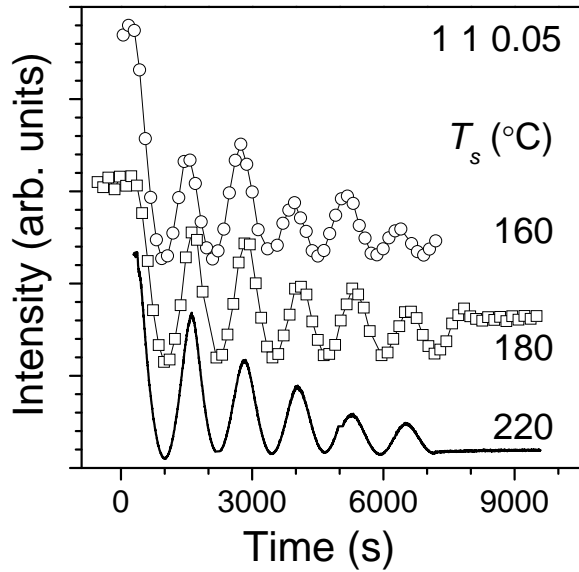


Fig. 2. Comparison of the x-ray oscillations measured during Fe_3Si growth at $T_s = 160, 180,$ and 220 °C. Each open symbol is derived from a measurement of a complete rocking curve. The data for 220 °C are a direct measurement of the time-dependent diffracted intensity.

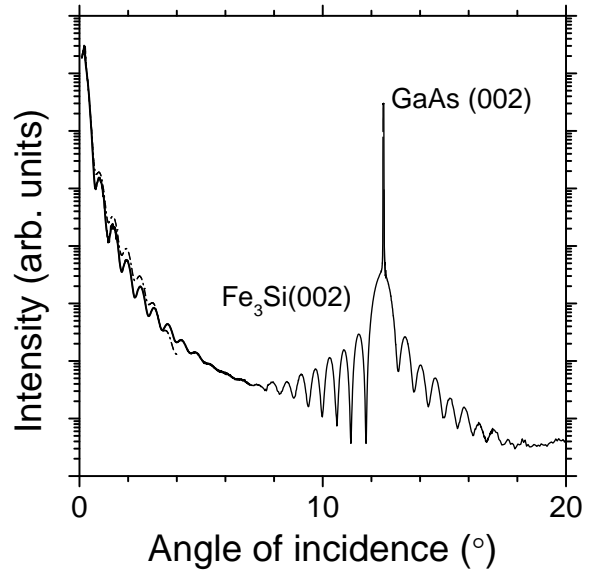


Fig. 3. Diffraction reflectivity curve along the (00) rod together with the 002 reflections of the GaAs substrate and the Fe_3Si film (solid line). The 20-monolayers-thick film is almost perfect with low surface and interface roughness as confirmed by reflectivity simulation (dash-dotted line).

using the layer thickness as a fitting parameter. The recovery of the diffracted intensity after the growth is very slow.

Figure 2 shows a comparison of the x-ray oscillations measured during Fe_3Si growth at $T_s = 160, 180,$ and 220 °C. Each open symbol was derived from a measurement of a complete rocking curve and represents its maximum. The data show a decay of the oscillations. At the lowest temperature, the maxima alternate between lower and higher values. Two length scales are found from fits by two Lorentz functions to each of these rocking curves. These findings are confirmed by a direct comparison with AFM measurements. On the reference sample, we observe pronounced terraces of about 50 nm width on the Fe_3Si surface. The step edges of the terraces are rough with many kinks so that we can attribute another length scale below 10 nm to the widths of the dendritic features of the edges and to some islands on the terraces.

Figure 3 shows an extended reflectivity curve including the 002 diffraction maximum (solid line), which is due to the epitaxial film and the substrate. The film is almost perfect with low surface and interface roughness as confirmed by reflectivity simulation (dash-dotted line). Only the epitaxial Fe_3Si film is present under UHV conditions, whereas an additional oxide layer is observed after the sample is exposed to air. The 002 reflection of GaAs is quasi-forbidden and thus very narrow. It can be distinguished from the 002 maximum of Fe_3Si , which is broad due to the small thickness of the film. The Fe_3Si 002 peak is a superlattice reflection which is sensitive to disorder. The relatively high intensity of the Fe_3Si maximum reveals a well ordered film.

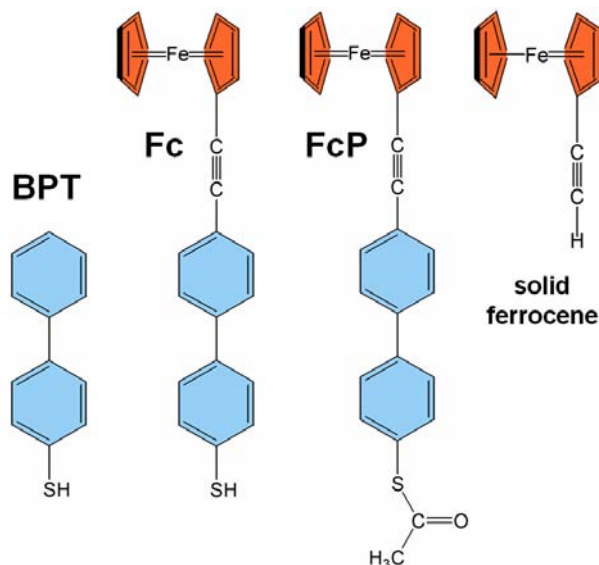
One-component and mixed self-assembled monolayers of ferrocene-substituted biphenyl ethynyl thiols on gold

A. Shaporenko¹, K. Rößler², H. Lang², and M. Zharnikov¹

¹*Angewandte Physikalische Chemie, Universität Heidelberg, Im Neuenheimer Feld 253, 69120 Heidelberg, Germany*

²*Lehrstuhl für Anorganische Chemie, Institut für Chemie, Technische Universität Chemnitz, Straße der Nationen 62, 09111 Chemnitz, Germany*

Recently, the well-established top-down technology for the fabrication of microelectronic devices and lithographic patterns was complemented by the bottom-up approach. This approach relies upon the ability of nanoscale structural elements to form a designed structure or pattern on their own, on the basis of mutual interactions, which are mostly governed by the exact composition, structure, and conformation of these elements. One of the respective systems are self-assembled monolayers (SAMs), which are 2D molecular films, spontaneously assembling on a suitable substrate. A SAM-constituent can be a simple rod-like molecule, a complex assembly, or even a molecular device, connected to the substrate over the spacer and headgroup. The presence of such an active element can, however, result in a poor quality of the SAM. A problem can also be an interaction of the densely packed active elements with each other, which can disturb their performance.



Scheme 1. Molecules of this study.

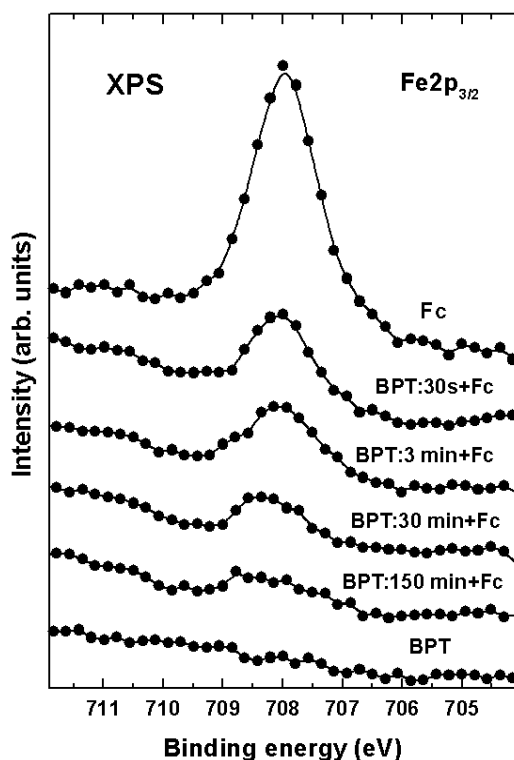


Fig. 1. Fe 2p_{3/2} XPS spectra of BPT, mixed BPT/Fc (prepared by the subsequent immersion procedure), Fc, and FcP SAMs on Au.

One of the respective systems are self-assembled monolayers (SAMs), which are 2D molecular films, spontaneously assembling on a suitable substrate. A SAM-constituent can be a simple rod-like molecule, a complex assembly, or even a molecular device, connected to the substrate over the spacer and headgroup. The presence of such an active element can, however, result in a poor quality of the SAM. A problem can also be an interaction of the densely packed active elements with each other, which can disturb their performance.

A suitable strategy to avoid these problems is to prepare a mixed SAM, in which the active elements are incorporated in a passive matrix. In this study, we are trying a new approach for the fabrication of such films by using subsequent immersion of the substrates into the solutions of the matrix and active species, going through the preparation of a poor quality matrix SAM at the first stage to the formation of a high-quality mixed SAM at the second stage. The latter process occurs via the incorporation of the active species into the poor-quality matrix film, which takes place preferably at the positions of defects stochastically distributed over the primary film.

The molecule of this study is a ferrocene-substituted biphenyl ethynyl thiol, $\text{Fc-C}\equiv\text{C-C}_6\text{H}_4\text{-C}_6\text{H}_4\text{-SH}$ (see Scheme

1), denoted as Fc. Ferrocenes are very robust compounds and excellent organometallic one-electron reservoirs. A homogeneous or mixed SAM comprising of ferrocene-substituted molecules can, thus, serve as an active electrochemical template, for which factors governing the rate of electron transfer across interfacial barriers can be precisely monitored and controlled. To promote an effective electron transfer between the ferrocene unit and the metal substrate, it should be connected to the headgroup by a molecular spacer with possibly high electric conductivity. This is the reason for the use of the biphenyl moiety as spacer in our study. At the same time, this spacer, together with the ethynyl unit, is long enough to guarantee that the ferrocene group and the metal substrate are decoupled.

As the matrix molecules we used a non-substituted biphenyl thiol, $C_6H_5-C_6H_4-SH$ (BPT, see Schema 1), which suits exactly to the molecular foot of the Fc molecule, promoting a proper self-assembly at a prolonged immersion of poor-quality matrix BPT film into a Fc solution.

Fe $2p_{3/2}$ XPS spectra of the films prepared by the subsequent immersion of the substrates into the BPT and Fc solutions (Figure 1) suggest that the mixed BPT/Fc were fabricated and that

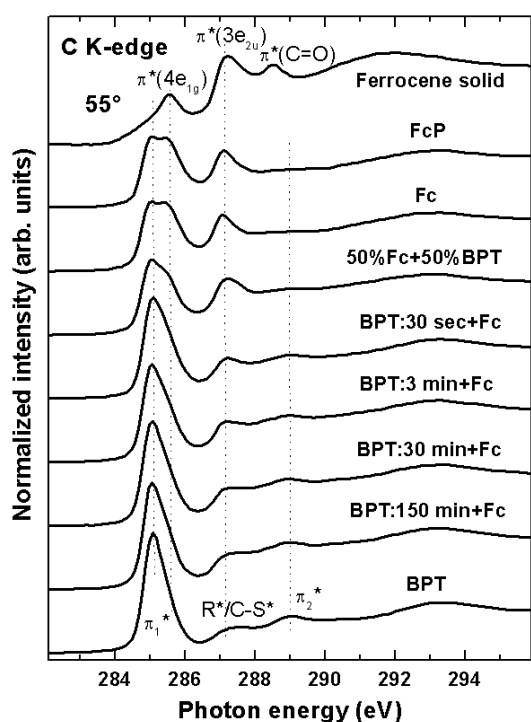


Fig. 2. C K-edge NEXAFS spectra of the BPT, Fc, FcP, and BPT-Fc films prepared by the subsequent adsorption and coadsorption. The spectrum of solid ferrocene is given for comparison.

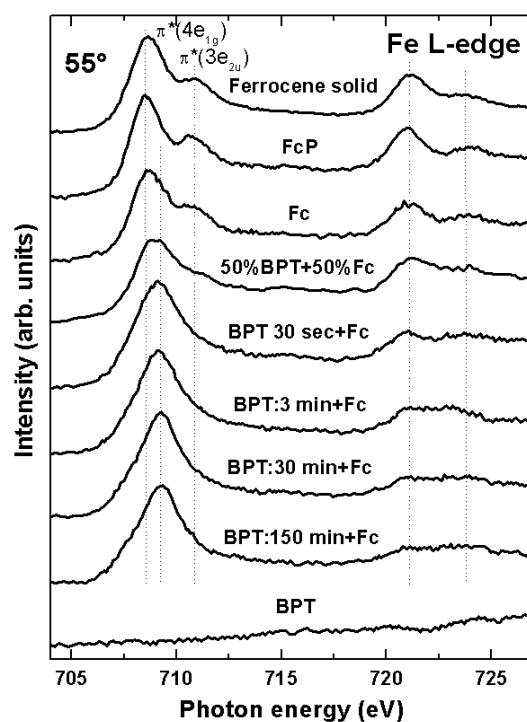


Fig. 3. Fe L-edge NEXAFS spectra of the BPT, Fc, FcP, and BPT-Fc films prepared by the subsequent adsorption and coadsorption. The spectrum of solid ferrocene is given for comparison.

the portion of the Fc molecules in these SAMs could be precisely controlled by the duration of the immersion into the BPT solution. This conclusion is supported by the C K-edge and Fe L-edge spectra of these films presented in Figs. 2 and 3 respectively – the spectra of the BPT/Fc films prepared by the subsequent immersion exhibit characteristic absorption resonances of both BPT and Fc. Comparison of these spectra with the spectra of the one-component Fc films and the mixed Fc/BPT films prepared by coadsorption from the mixed solution (50%Fc+50%BPT) suggests that the Fc molecules in the mixed films prepared by the subsequent immersion did not interact with each other. Thus, the initial goals to avoid a clustering of the individual SAM constituents and to obtain their stochastic intermixing have been achieved. Note that both BPT and Fc molecules in the mixed films have an upright orientation as follows from the angular-dependent NEXAFS spectra (not shown). Note also that the protection of the thiol headgroup by acetyl group (FcP molecules) do not hinder the formation of high-quality SAMs.

This work has been supported by DFG (ZH 63 9/2) and BMBF (05KS4VHA/4).

Electronic structure of thin ytterbium layers on W(110)

Yu. S. Dedkov, D. V. Vyalikh, M. Holder, M. Weser, S. L. Molodtsov, and C. Laubschat
Institut für Festkörperphysik, Technische Universität Dresden, 01062 Dresden, Germany

Yu. Kucherenko

Institute for Metal Physics, National Academy of Sciences of Ukraine, 03142 Kiev, Ukraine

M. Fonin

Fachbereich Physik, Universität Konstanz, 78457 Konstanz, Germany

A. Varykhalov and O. Rader

BESSY, Albert-Einstein-Strasse 15, D-12489 Berlin, Germany

Among the lanthanides, Yb and Ce are of fundamental interest, because of a strong interaction between $4f$ and valence-band (VB) states leading to mixed-valence and Kondo phenomena in a number of compounds [1,2]. This analogy between Yb and Ce systems has been explained on the basis of the electron-hole symmetry of the quasiautomatic $4f$ shell. While the correspondence has been established for a number of compounds, no evidence for such a symmetry has been reported up to now for the pure metals. Motivated by the recent work [3], in the present contribution we report on the results of the photoelectron studies of thin layers of Yb (1-3 ML-thick) on W(110) surface.

Photoemission (PE) experiments were performed at the U49/2-PGM-1 beamline (BESSY). The energy and angular resolution was set to 100 meV and 1° , respectively. A structurally ordered layers of Yb metal were grown on the W(110) substrate at room temperature. The samples prepared in this way exhibit a high crystalline quality as monitored by LEED. All PE spectra were taken at $h\nu = 110$ eV in order to increase the photoelectron emission from Yb $4f$ states considerably and to suppress that from W $5d$ states that are close to a Cooper minimum of the photoionization cross section at this photon energy. The base pressure in the experimental chamber was below 5×10^{-11} mbar rising to 1×10^{-10} mbar during metal evaporation. No presence of oxygen can be observed in PE spectra.

A series of PE spectra (taken at 5° off-normal emission in order to eliminate dispersions effects around the Γ point which are discussed later) of thin Yb layers on top of the W(110) surface is shown in Fig. 1. The initial spectrum of pure W(110) surface shows a valence band emission from $5d$ states between the Fermi level (E_F) and 2.5 eV of binding energy (BE) as well as from $6s$ states at about 7 eV. The deposition of Yb on the W(110) surface leads to the development of Yb $4f$ emission in the spectra: divalent component in the region between E_F and 3.5 eV of BE and trivalent component in the range of 4-12 eV of BE. We would like to note that the trivalent Yb $4f$ component is visible in the spectra only for thicknesses of Yb $\theta < 1$ ML due to possible emission of electrons from Yb atoms which are located at the steps of W(110) crystal or at the edges of Yb islands.

The spectral features of W(110) are quickly disappear upon Yb deposition and practically not visible already at the thickness of Yb layer of approximately 0.75 ML. At the thickness of Yb layer of exactly 1 ML, BE of the $4f$ spin-orbit doublet are 0.91 and 2.18 eV for $4f_{7/2}$ and $4f_{5/2}$ components, respectively. Continuous deposition of Yb leads to further modification of the spectra and respective $4f$ emission lines have BEs which are listed in Table 1 for 1, 2, and 3 ML thick Yb films on W(110) surface. The corresponding energy diagram (thick vertical lines) is shown as an inset of Fig. 1 together with the scheme showing the positions of Yb atom in the layer.

In order to interpret the measured BE of Yb $4f$ states for different positions of Yb atoms we have performed the calculations of the electronic structure of the Yb/W(110) system. The atomic structure was simulated by slabs consisting of three atomic layers of tungsten covered by one, two or three Yb layers. The atomic structure of Yb layers were chosen hexagonal, in agreement with LEED data and corresponding to the bulk Yb(111) plane.

The calculations were performed by LMTO method [4]. The full occupied Yb $4f$ states were treated as localized core levels, and their BEs were estimated by means of the Slater's transition state concept [5]. The theoretically calculated positions of $4f$ emission lines are also shown in the inset of Fig. 1 by thin lines. For better comparison with the experiment all presented data are shifted from originally calculated values by 0.6 eV to lower BE. This disagreement is caused by shortcomings of the theoretical model: In the calculations the excited electron was removed from each equivalent site of the respective Yb monolayer instead from only one site. In this case the screening charge of the final-state hole is strongly reduced.

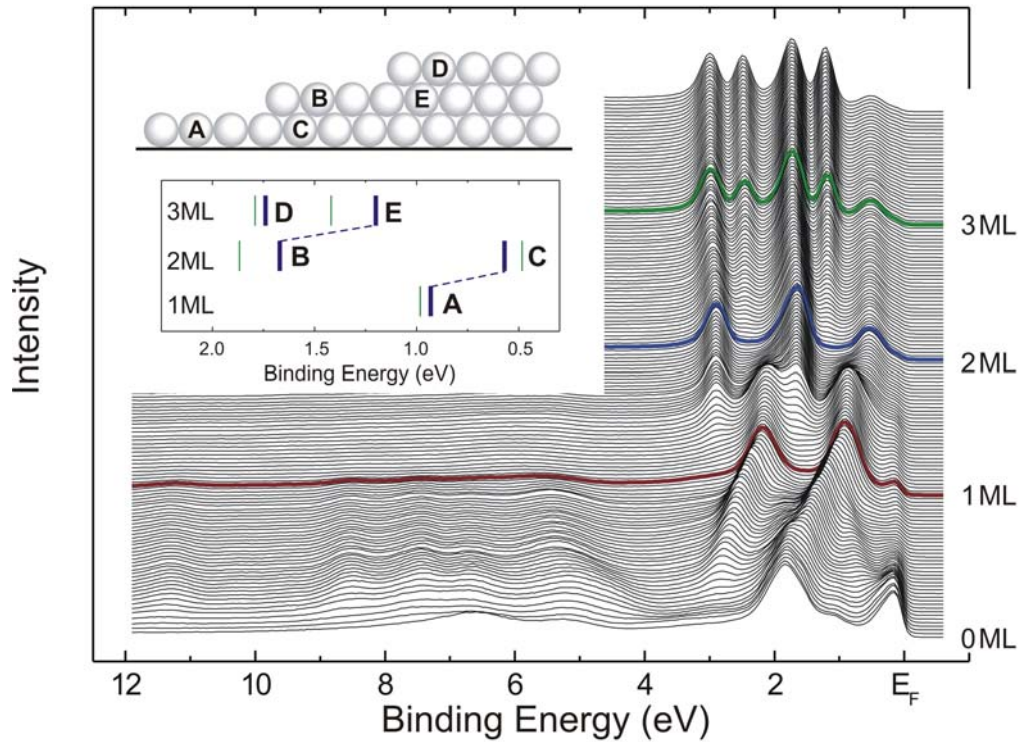


Fig. 1. PE spectra obtained during continuous Yb deposition on W(110) surface. Inset shows energy positions of Yb $4f_{7/2}$ line for 1, 2, and 3 ML thick film: thick lines - experimental data, thin lines - calculated data on the basis of the Slater's transition state concept.

In order to study the electronic structure of the Yb monolayer on the W(110) substrate the angle-resolved PE measurements were performed. Fig. 2 (left panel) shows the series of PE spectra of this system measured in the $\bar{\Gamma}-\bar{S}$ direction of the surface Brillouin zone (SBZ) of W(110) (see inset). Clear splitting of the Yb $4f_{7/2}$ state is visible in the PE spectra measured around $\bar{\Gamma}$ point. Additional spectral features which are visible in the spectra at approximately 1.3eV BE and in the vicinity of the Fermi level can be ascribed to the emission from the tungsten VB (see colour plot in the inset of Fig.2, right panel). It should be noted, that the energy bands measured by means of the angle-resolved PE for the pure W(110) surface agree well with the calculated energy bands for the $\bar{\Gamma}-\bar{S}$ direction (also shown in the inset of Fig. 2, right panel).

The measured PE spectra were analyzed by means of the simplified periodic Anderson model (PAM) that has been recently successfully applied for interpretation of angle-resolved PE data. However, in the case of Yb/W(110) system a determination of the valence states that could be hybridized with Yb $4f$ electrons is not straightforward. For Ce/W(110) system [3] the strong hybridization effects observed in PE spectra were caused by interaction of $4f$ states with Ce $5d$ electrons in the monolayer. This scenario, however, can not be realized for monolayer of divalent Yb atoms due to negligible contribution of the electron states with d symmetry in Yb-derived valence bands. The contribution of the W $5d$ electron states to the $4f$ -VB hybridization matrix elements can not be unambiguously estimated from the band-structure calculations due to incommensurate Yb and W surfaces. In this case, taking into account that escaping electrons are analyzed for the emission direction close to the surface normal (the

	1 ML		2 ML		3 ML	
	$4f_{7/2}$	$4f_{5/2}$	$4f_{7/2}$	$4f_{5/2}$	$4f_{7/2}$	$4f_{5/2}$
surface	A: 0.91	A: 2.18	B: 1.66	B: 2.89	D: 1.73	D: 2.98
bulk	-	-	-	-	E: 1.19	E: 2.45
interface	-	-	C: 0.54	C: 1.86	-	-

Table 1. Experimental binding energies (in eV) of Yb $4f$ emission lines for 1, 2, and 3 ML thick Yb film on W(110) surface.

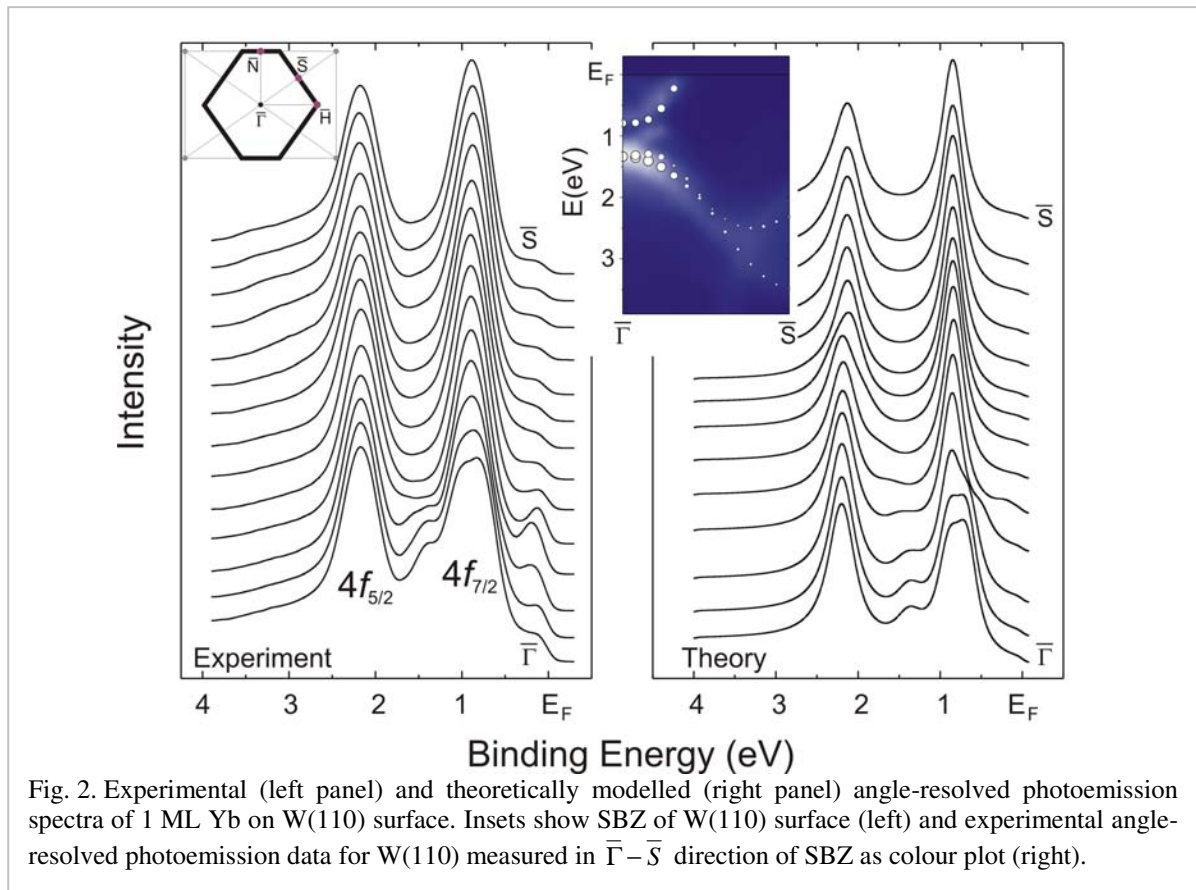


Fig. 2. Experimental (left panel) and theoretically modelled (right panel) angle-resolved photoemission spectra of 1 ML Yb on W(110) surface. Insets show SBZ of W(110) surface (left) and experimental angle-resolved photoemission data for W(110) measured in $\bar{\Gamma}-\bar{S}$ direction of SBZ as colour plot (right).

\bar{S} point is reached at the polar angle about 13°), we may expect that the PE intensities $I(E, \mathbf{k})$ measured for a pure W(110) surface are determined mainly by W 5d orbitals directed out-of-surface. Then, it could be assumed that namely these orbitals are responsible for 4f-VB hybridization, and the respective PE intensities could be chosen as a measure for the VB contribution to the hybridization matrix element: $V_k(E) = \Delta \sqrt{I(E, \mathbf{k})}$. We have taken the hybridization parameter $\Delta = 0.22 \text{ eV}$, the value used for other Yb compounds, whereas all $I(E, \mathbf{k})$ values were scaled in energy under the condition that the splitting of the Yb $4f_{7/2}$ component around $\bar{\Gamma}$ point is reproduced in the PAM calculations. The corresponding scaling factor can be considered as an adjustable parameter of the model (only one for the whole set of PE spectra). Other parameters were energies of 4f states $\varepsilon_{5/2} = 2.15 \text{ eV}$ and $\varepsilon_{7/2} = 0.85 \text{ eV}$. The initial values of these parameters were chosen to be equal to the energy positions of the Yb 4f PE peaks for emission angles where we may expect hybridization to be negligible.

The calculated results are presented in Fig. 2 (right panel). It can be seen that the form of measured spectra as well as the changes in the PE spectra with increasing polar angle are well described by the calculations. Because the calculated results show only Yb 4f PE intensities, we can conclude that the hybridization effects lead not only to the splitting of the Yb $4f_{7/2}$ component around $\bar{\Gamma}$ point, but also to the intensity variations between both spin-orbit split peaks and near Fermi energy up to the polar angle of 5° . These effects are caused by W 5d bands, one of them goes to the Fermi level and two others go to higher BE if the polar angle increases. In the experimental spectra these effects are enhanced due to direct VB emission from the W 5d bands. The W 5d bands cross also the position of the Yb $4f_{5/2}$ component, and in the calculated spectra a small dispersion of this component can be seen about 6° . The corresponding effect is not observed in the experimental spectra.

- [1] C. Laubschat et al., Phys. Rev. B **33**, 6675 (1986).
- [2] F. Patthey et al., Phys. Rev. B **42**, 8864 (1990).
- [3] D. V. Vyalikh et al., Phys. Rev. Lett. **96**, 026404 (2006).
- [4] O. K. Andersen, Phys. Rev. B **12**, 3060 (1975).
- [5] J. C. Slater, The self-consistent-field method for crystal, in *Computational methods in band theory*. Eds. P. M. Marcus, J. F. Janak, A. R. Williams (Plenum Press, New-York, 1971).

A photoelectron diffraction investigation of the structure of the clean $\text{TiO}_2(110)(1 \times 1)$ surface

E. A. Kröger¹, D. I. Sayago¹, F. Allegretti², M. J. Knight², M. Polcik¹, W. Unterberger¹, T. J. Lerotholi², K. A. Hogan³, C. L. A. Lamont³, D. P. Woodruff²

¹ Fritz-Haber-Institut der Max-Planck-Gesellschaft, Faradayweg 4-6, 14195 Berlin

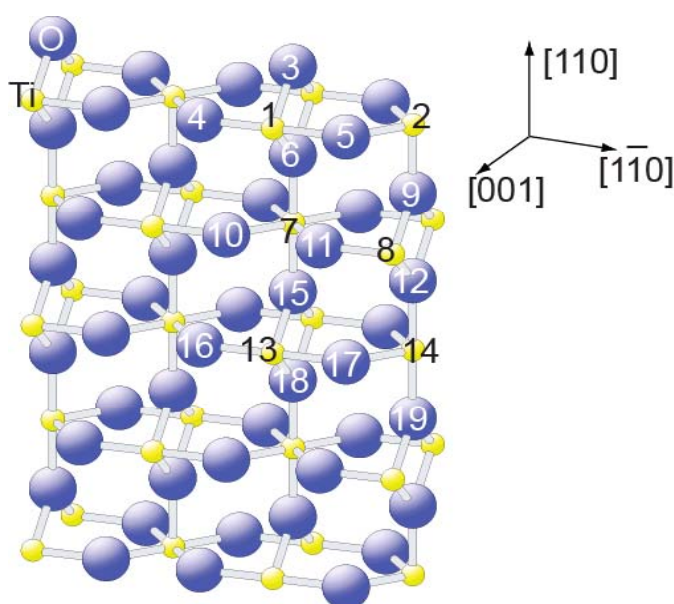
² Physics Department, University of Warwick, Coventry CV4 7AL, UK

³ Dept. of Chem. & Biol. Sciences, University of Huddersfield, Huddersfield, UK

The (110) face of rutile phase TiO_2 is perhaps the most studied of all oxide surfaces as a model system to investigate the range of catalytic applications of this material. Despite this, even the (1x1) clean surface structure has been the subject of significant controversy, with many different theoretical total energy calculations reporting large variations in both the amplitude and sign of the surface-induced relaxations of the atoms in the outermost few atomic layers [1]. For several years only one experimental structure determination existed, using surface X-ray diffraction (SXRD) [2], and a striking feature of this study was the finding of a large (0.27 Å) inward relaxation of the bridging oxygen atoms (labelled (3) in the diagram), relative to an ideally-terminated bulk structure. More recently, however, two new studies, one based on quantitative low energy electron diffraction (LEED) [3], the other on medium energy ion scattering (MEIS) [4] have both indicated that these bridging oxygen atoms relax outwards from the surface; other relaxations of the surface 6-fold and 5-fold coordinated Ti atoms (labelled (1) and (2) in the diagram) are more nearly consistent between the three studies. New theoretical work has sought to reproduce these new experimental results (e.g. [5]).

Schematic diagram of the $\text{TiO}_2(110)$ surface showing the labelling of the different near-surface atoms. The blue spheres represent O atoms, the smaller yellow spheres represent Ti atoms.

In order to cast further light on this problem we have conducted a scanned-energy mode photoelectron diffraction (PhD) study of this surface using both Ti 2p and O 1s photoemission signals. The PhD technique is really designed to investigate adsorbate structures on surfaces. The technique exploits the coherent interference of the directly-emitted photoelectron wavefield from a core level of an atom with other components of the same wavefield elastically scattered by the



neighbouring atoms. In the ~50-400 eV kinetic energy range used, backscattering is strong and the PhD spectra from an adsorbate atom provides quantitative information on the adsorbate-substrate registry. For a clean solid surface, however, identifying the core level binding energy does not generally distinguish emission from surface and sub-surface atoms, so the observed photoelectron diffraction comprises an incoherent sum of the PhD from atoms in several near-surface layers. In the present case of TiO₂(110) our multiple scattering calculations used to simulate the experimental PhD spectra included all emitters in the outermost 8 layers (one layer comprising two Ti atoms and 4 O atoms per surface unit mesh – e.g. atoms labelled 1 to 6 or 7 to 12 in the diagram), although latterly it was found that including emitters in only 4 such layers was sufficient.

The results, based on 6 Ti 2p PhD spectra, and 5 O 1s PhD spectra, recorded in different emission directions, proved to have significant sensitivity to the surface relaxations. The Table shows a comparison of the relaxations perpendicular to the surface (Δz defined as positive for outwards relaxation relative to an ideal bulk termination) of just the outermost Ti and O atoms, obtained in this study, with those of the other experimental investigations. The PhD results confirm, in particular, the *outward* relaxation of the bridging O atoms found in the other more recent experiments.

atom	Ti 6-fold $\Delta z(1)$ (Å)	Ti 5-fold $\Delta z(2)$ (Å)	O bridging $\Delta z(3)$ (Å)
SXRD [2]	0.12±0.05	-0.16±0.05	-0.27±0.08
LEED [3]	0.25±0.03	-0.19±0.03	0.10±0.05
MEIS [4]	0.19±0.07	-0.09±0.09	0.13±0.16
This study	0.19(-0.15/+0.10)	-0.26±0.08	0.17±0.15

This novel application of the PhD method to the determination of the surface relaxations of a clean oxide surface, and the consistency of the results with LEED and MEIS, is of particular importance in the context of an ongoing study by our group of the more complex and currently unstudied surface relaxations of the V₂O₃(0001) surface.

The authors acknowledge the financial support of the DFG through Sfb546, and of the EPSRC (UK), for this work.

References

- 1 U. Diebold, Surf. Sci. Rep. **48**, 53 (2003)
- 2 G. Charlton, P. B. Howes, C. L. Nicklin, P. Steadman, J. S. G. Taylor, C. A. Muryn, S. P. Harte, J. Mercer, R. McGrath, D. Norman, T. S. Turner, and G. Thornton, Phys. Rev. Lett. **78**, 495 (1997)
- 3 R. Lindsay, A. Wander, A. Ernst, B. Montanari, G. Thornton, and N..M. Harrison, Phys. Rev. Lett. **94**, 246102 (2005)
- 4 G. S. Parkinson, M. A. Muñoz-Márquez, P. D. Quinn, M. J. Gladys, R. E. Tanner, D. P. Woodruff, P. Bailey, T. C. Q. Noakes, Phys. Rev. B **73**, 245409 (2006)
- 5 S. J. Thompson and S. P. Lewis, Phys. Rev. B **73**, 073403 (2006)

Investigation of the system C60/ITO by X-ray absorption and resonant X-ray emission spectroscopy

K.H. Hallmeier¹, D. Wett¹, I. Lauermann², K. Fostiropoulos², B. Johnev²

¹Wilhelm-Ostwald-Institut, Universität Leipzig, Linnéstr.2, D-04103 Leipzig

²Hahn-Meitner-Institut Berlin GmbH, Dep. SE 2, Glienicke Str. 100, D-14109 Berlin

Motivation: The aim of the present work is the investigation of the system C60/ITO, which is currently used to develop organic solar cells. In order to characterize this system, X-ray absorption spectroscopy in the total electron yield mode (TEY) and resonant X-ray emission spectroscopy (XES) in dependence of the polarization of the incoming beam are used.

Experimental: The measurements were performed at beam-line U-41 PGM using the rotatable spectroscopic apparatus (ROSA) [1], equipped with a SCIENTA-GAMMADATA XES-300 grating spectrometer. Whereas the TEY measurement was done at an incoming angle of the synchrotron radiation of appr. 45° with respect to the surface normal, resonant XES measurements were performed at two different orientations of the XE spectrometer (+ 50° and -20° resp., relative to the synchrotron plane), using the energy of the prominent, highly resolved absorption lines for excitation: 283.7 eV, 285.5 eV, 287.5 eV, and finally 350 eV in the non-resonant case.

Sample choice and preparation: For the fabrication of organic photovoltaic devices metal-phthalocyanines and C60 are suitable candidates as donor and acceptor materials, respectively. Such devices consist of typically 30 nm thin layers of each molecular material. Precise knowledge of the electronic structure of these layers grown on ITO substrates is essential for the understanding of the device's functionality. In the present study we investigate layers of 50 nm C60 on ITO substrates. The material was deposited by vacuum thermal evaporation (below $<10^{-7}$ mbar) of commercially available powders from graphite crucibles. The evaporation temperatures were about 550°C. During deposition, the substrates were kept at room temperature and constantly rotated over the crucible to ensure uniform material coverage. Layer thicknesses were measured in situ, with calibrated quartz crystal deposition controllers. The evaporation rate was kept in the order of 1 Å/s.

Results and Discussion: Free carbon allotropes were extensively investigated by Guo and Nordgren [2]. Here we compare our results with those of the resonant XES of C60 and also HOPG. While all our resonant (and non-resonant) XES data (Fig. 1 and 2) are identical with the spectra for the free C60 powder [2] and with the first four absorption lines in the TEY spectrum, distinct differences appear in the high-energy (continuum) region (Fig. 3). The spectrum of Guo and Nordgren exhibits some well resolved absorption maxima of low intensity. In our spectrum, however, a high-intensity shape resonance with a fine structure of appr. three extrema (two shoulders and one maximum) appears in the energy region 290 – 295 eV.

We have two interpretations for this behaviour:

1. Electronic interaction: As known, the interaction between the substrate and the C60 layer is of van-der-Waals or dipole type. In the latter case we may assume that a dipole is formed between the uppermost ITO atoms (preferentially oxygen) and carbon atoms from a C60 molecule. As we found earlier, fourfold coordinated boron, carbon [3] or nitrogen atoms [4] with electronegative bonding partners lead to such high-energy

shape resonances. (In the XES the spectral information is generated by 1 – 2 coordination spheres. Therefore the small contribution from the atoms at the interface to the whole spectrum is not significant.) This interpretation is sound comparing the spectra of HOPG [2]. Also in this case strong absorption is found in the region 290 eV – 295 eV due to band structure effects.

2. Structural effects: Because the information depth in TEY spectra is relatively high (due to the contributions of the electrons with negligible kinetic energies) and also multiple scattering effects will contribute to the shape of the XA-spectrum, it is alternatively possible that we see a (multi-)backscattering effect of the electron excited from the carbon 1s level due to the uppermost atoms of the ITO-substrate.

The decision, which of the two interpretations dominates, is only possible when performing a calculation with the FEFF- [5] or the de-Groot-Codes [6]. In the moment, however, we see no possibility to construct a small enough representative cluster. The independence of the XE spectra from polarization angle reflects the spherical symmetry of the C60 molecules.

Conclusions: Investigating the system C60/ITO by XAS (C K TEY spectrum) and resonantly excited XES we found that all C K XE spectra behave like those of the free C60 molecule. In contrast to this we observed a structured shape resonance in the XA spectrum that does not appear in the spectrum of the free molecules (powder sample). Therefore, we conclude that the interface effects can only be found in the TEY-spectrum.

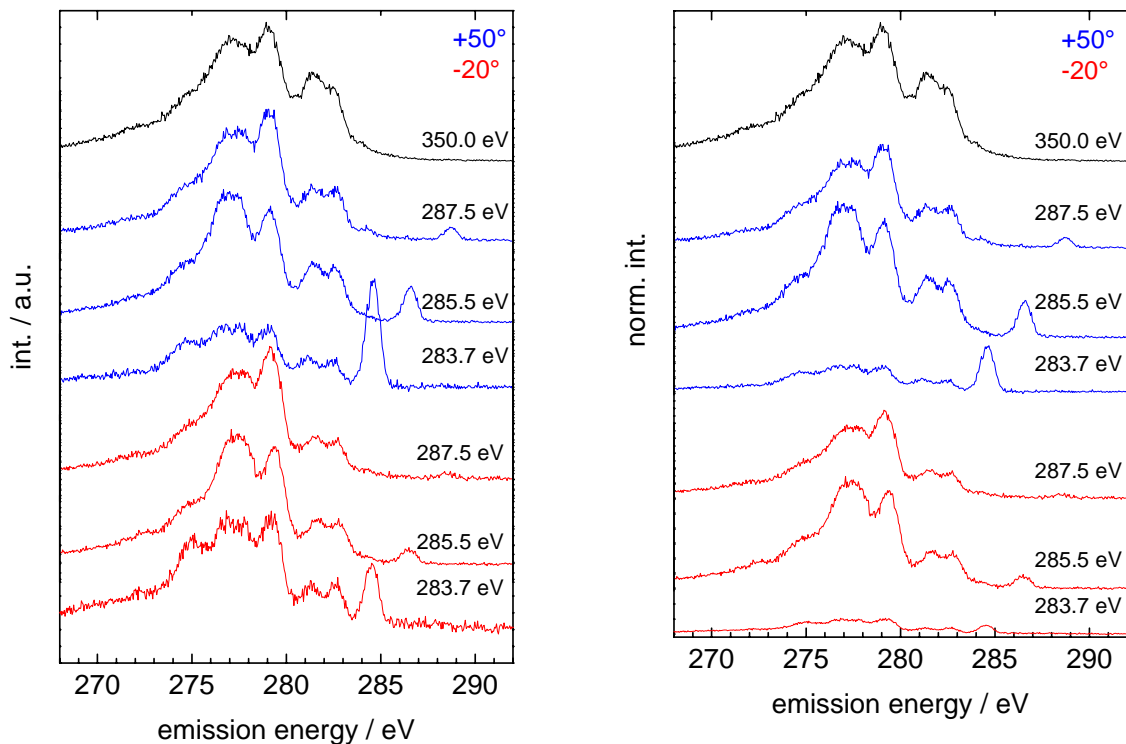


Fig. 1 (left) and 2 (right): Polarization dependent, resonant and non-resonant C K XE-spectra of the system C60/ITO with normalized intensity (left) and intensity normalized to beam current (right).

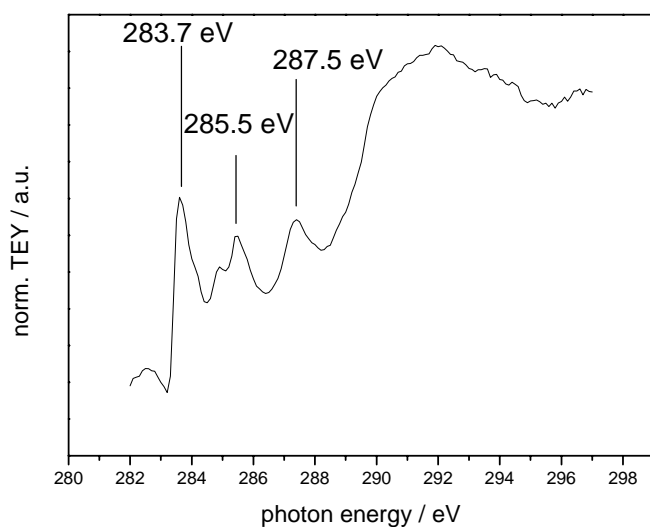


Fig. 3: C K TEY spectrum of the system C60/ITO

References:

- [1] R. Szargan, K.-H. Hallmeier, R. Hesse, A. Kopczynski, S. A. Krasnikov, L. Zhang; T. Chassé, O. Fuchs, C. Heske, E. Umbach, S. Molodtsov, F. Schiller, C. Laubschat, C. Jung, W. Braun, BESSY- Jahresbericht 2001, 309
- [2] J. Guo, J. Nordgren, J. Electron Spectrosc. Rel. Phen., 110-111 (2000) 105
- [3] W.H.E. Schwarz, L. Mensching, K.H. Hallmeier, R. Szargan, Chem. Phys. 82 (1983) 57
- [4] A.A. Pavlychev, K.H. Hallmeier, C. Hennig, L. Hennig, R. Szargan, Chem. Phys. 201 (1995) 547
- [5] J.J. Rehr, R.C. Albers, Rev. Mod. Phys. 72 (2000) 621
- [6] <http://www.anorg.chem.uu.nl/people/staff/FrankdeGroot/>

Acknowledgements

The authors are grateful to the BESSY staff, especially Dr. Ch. Jung and M. Mast. Financial support came from the DFG: FG 404-SZ58/15. The critical reading of the manuscript by Prof. Dr. R. Denecke is acknowledged.

Electron pair emission from surfaces excited with photons and electrons

F.O. Schumann, C. Winkler and J. Kirschner

Max-Planck Institut für Mikrostrukturphysik, Weinberg 2, 06120 Halle, Germany

Introduction

Electron pair emission from surfaces allows to study the electron correlation in momentum space.[1,2] Upon excitation with a primary electron one refers to the experiment as $(e,2e)$, whereas experiments with photons are called $(\gamma,2e)$ or double photoemission (DPE). Apart from the simultaneous ejection of two electrons upon photon absorption, another pathway of pair emission exists.[3] It is possible that the photon is absorbed by a single electron, which eventually scatters from another electron leading to pair emission. One may term this scenario an "internal" $(e,2e)$ process. The question arises to what extent the total coincidence intensity comes from a DPE process or the "internal $(e,2e)$ ". Until now there have been no studies which allow a direct comparison of $(\gamma,2e)$ and $(e,2e)$ experiments to unravel this issue. We performed $(e,2e)$ and $(\gamma,2e)$ experiments on the same sample, namely a Cu(111) surface by using the same experimental set-up.

Experiment

We employed a novel time-of-flight coincidence spectrometer, which consists of two channelplate detectors, see fig.1. Delay-line anodes allow the determination of the impact position. The photons and primary electrons hit the specimen along the surface normal.

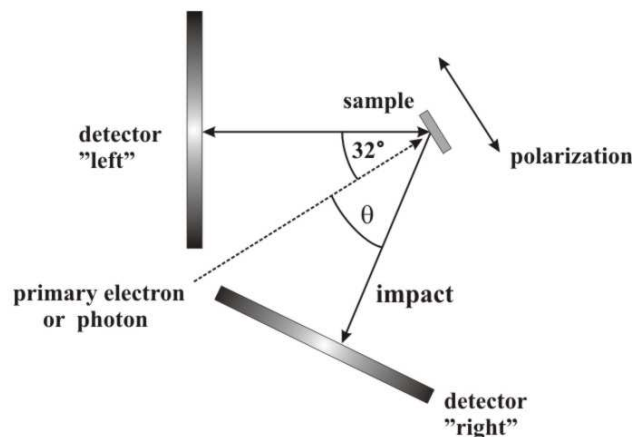


Fig.1 : Schematic view of the experiment. Primary electrons and photons hit the sample along the surface normal.

Photon energy and primary electron energy have been selected such that the maximum sum energy of the pair has the same value in both experiments. We used a photon energy of 50 eV and a primary electron energy of 45 eV. The $(\gamma,2e)$ experiments were performed at the beamline TGM 4 in the single bunch mode. We have recorded only those coincidence events,

where the electrons of the pair hit different detectors. Accordingly we label the electrons “left” and “right”, respectively.

Results

In fig.2 we show the 2D-Energy distribution for those coincidence events where the trajectories of the “left” and ”right” electrons have an angle of $\sim 45^\circ$ with the surface normal. We note that the contour lines are parallel to $E_{\text{left}}+E_{\text{right}}=\text{const.}$ lines. Further we can see that the coincidence intensity steadily rises if we move from the onset of pair emission (at $E_{\text{sum}}=40$ eV) to smaller sum energies. There are also no areas within the 2D-Energy region, where either enhanced or reduced intensity can be observed. This is in striking difference to the behavior of the $(\gamma,2e)$ experiment. Compared to the $(e,2e)$ data additional intensity at two symmetrically aligned pockets is visible. These are localized roughly at $20 \text{ eV} < E_{\text{left/right}} < 30 \text{ eV}$ and $E_{\text{right/left}} < 10 \text{ eV}$.

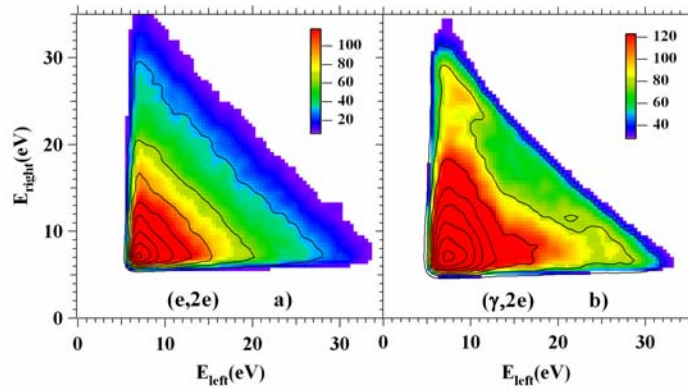


Fig.2: 2D-Energy distributions of coincidence pairs obtained from a Cu(111) surface. The trajectories of the “left” and “right” electron have an angle of 45° with the normal. Clearly there are distinct differences in the $(e,2e)$ and $(\gamma,2e)$ data. The primary energy and photon energy are 45eV and 50 eV, respectively.

Within the dipole approximation it was possible to show that the scalar product $\mathbf{e} \cdot (\mathbf{k}_{\text{left}} + \mathbf{k}_{\text{right}})$ enters in the formula of the transition probability.[4] This leads to a selection rule for the DPE intensity, which vanishes if $\mathbf{e} \cdot (\mathbf{k}_{\text{left}} + \mathbf{k}_{\text{right}}) = 0$. The vector \mathbf{e} describes the polarization plane of the linear polarized light. The momentum vectors of the electrons are labeled with \mathbf{k}_{left} and $\mathbf{k}_{\text{right}}$, respectively. Since in our geometry the polarization plane is in the surface plane (see fig.1) only the parallel components of $\mathbf{k}_{\text{left/right}}$ are of relevance. Therefore one expects no pair emission for electrons of same energy, which leave the sample in opposite emission directions, because $\mathbf{e} \cdot (\mathbf{k}_{\text{left}} + \mathbf{k}_{\text{right}}) = 0$. On the other hand, very unequal energies will lead to a finite value of $\mathbf{e} \cdot (\mathbf{k}_{\text{left}} + \mathbf{k}_{\text{right}})$. Such a behavior is qualitatively observed and explains the differences between the $(e,2e)$ and $(\gamma,2e)$ experiments. Fig.3 shows the 2D-Energy distribution

if the trajectories of the electrons have an angle of $\sim 12^\circ$ with the surface normal. Compared fig.2 the previously straight contour lines parallel to $E_{\text{sum}}=\text{const.}$ are now bent towards smaller E_{sum} values. Rephrased one can say that there is a tendency for one electron being "fast", while the other is "slow" rather than having the same energy. This behavior can be observed for both the (e,2e) and (γ ,2e) data. This can be understood if we recall our previous studies, where we found that the momentum distribution of the intensity displays reveals the exchange-correlation hole.[1,2] In other words electrons tend to stay away from each other if the angle between the trajectories is small. With our selection of the emission angle in fig.3 we have selected those electrons. If the electrons are forced to be close to each other they tend to have unequal energy sharing. The notation of the exchange-correlation hole is valid for (e,2e) and (γ ,2e) experiments, and the size of the hole is very similar in both instances. Therefore the 2D-Energy distributions of fig.3 are similar to each other.

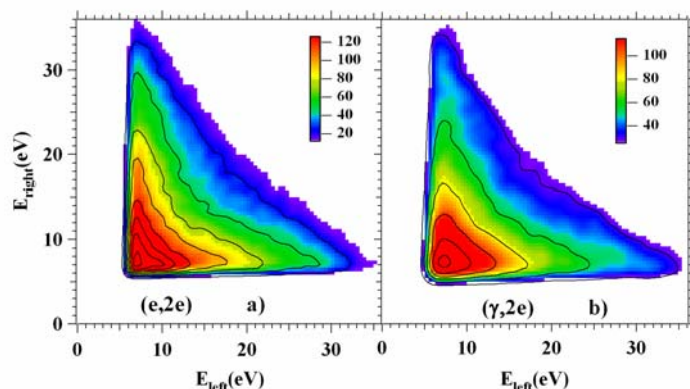


Fig.3: 2D-Energy distributions of coincidence pairs obtained from a Cu(111) surface. The trajectories of the “left” and “right” electron have an angle of $\sim 12^\circ$ with respect to the normal.

Conclusion

We have been able to demonstrate that a true intrinsic DPE process in contrast to an internal (e,2e) process exists. This follows from the different 2D-Energy distributions obtained in (γ ,2e) and (e,2e) experiments.

References

- [1] F.O. Schumann, J. Kirschner and J. Berakdar, Phys. Rev. Lett. **95**, 117601 (2005).
- [2] F.O. Schumann, C. Winkler, G. Kerherve and J. Kirschner, Phys. Rev. B **73**, 041404(R) (2006).
- [3] R. Herrmann, S. Samarin, H. Schwabe and J. Kirschner, Phys. Rev. Lett. **81**, 2148 (1998).
- [4] J. Berakdar, Phys. Rev. B **58**, 9808 (1998).

Grazing incidence x-ray diffraction study of Pr₂O₃/Si(001) heterostructures grown by molecular beam epitaxy using a high temperature effusion source

Tatsuro Watahiki, Brad P. Tinkham, Bernd Jenichen, Wolfgang Braun, and Klaus H. Ploog
Paul-Drude-Institut für Festkörperelektronik, Hausvogteiplatz 5-7, D-10117 Berlin, Germany

Introduction

The scaling of Si CMOS devices requires the reduction of the thickness of the gate dielectric, causing an exponential increase in leakage current. Since traditional SiO₂ with sub-nanometer thickness no longer exhibits reliable insulating properties, an alternative material with a high dielectric constant is required. Rare earth metal oxides, including La₂O₃, Gd₂O₃, and Pr₂O₃, are promising alternative high-k gate dielectrics for sub-0.1 micron CMOS technology. We have studied the growth of Pr₂O₃ using molecular beam epitaxy since it has a high dielectric constant (~30)[1] and close lattice match to Si[2]. However, an interfacial layer forms during the high temperature process since rare earth oxides are typically only metastable in contact with semiconductors. The effective dielectric constant of a typical Pr₂O₃/Si(001) stack can be lowered due to the interfacial layer. For the application of Pr₂O₃ as a gate material for CMOS devices, it is very important to investigate the formation and structure of the Pr₂O₃/Si interface. In this report, we present in situ grazing incidence x-ray diffraction (GIXRD) and x-ray reflectivity (XRR) data of Pr₂O₃/Si structure during the annealing at high temperature, and the effect of Si addition for the improvement of the interface.

Experimental

For the growth of Pr₂O₃, we have employed molecular beam epitaxy (MBE) on Si(001). Pr₆O₁₁ (99.996%) powder is used as a source material and loaded into a high-temperature effusion cell that can be operated up to 2500°C. Compared to e-beam evaporation, the effusion source shows a more stable control of temperature and reproducible flux. For the layer with Si addition, Si co-evaporation is performed from another effusion cell during the growth. The substrate temperature is 600-700°C. After the growth of the layer, the samples are transferred in UHV to a UHV chamber fixed on a diffractometer for the x-ray measurements. The measurements were performed with 10 keV x-rays at the PHARAO beamline[3] at BESSY using a 6-circle diffractometer. The beryllium windows on the measurement chamber allow access to a large range of reciprocal lattice space both in-plane and out-of-plane. In order to enhance the near-surface sensitivity, in-plane scans are made at a grazing incidence angle of 0.28°, which is slightly greater than the critical angle of Pr₂O₃ for 10 keV x-rays.

Results and discussion

First we investigate the structural changes of the Pr₂O₃/Si interface by annealing at high temperature. Figure 1 shows (a) an in-plane scan of the Pr₂O₃/Si(001) sample before and after annealing, and (b) a reflectivity measurement before and after annealing at 850°C and the density profile for the annealed sample. In figure 1(a), the peaks at H=K=1.34 and 2.66 originate from cubic Pr₂O₃, and the peaks at 0.90, 1.82 and 2.72 are due to from Pr-O-Si compounds at the interface. Before

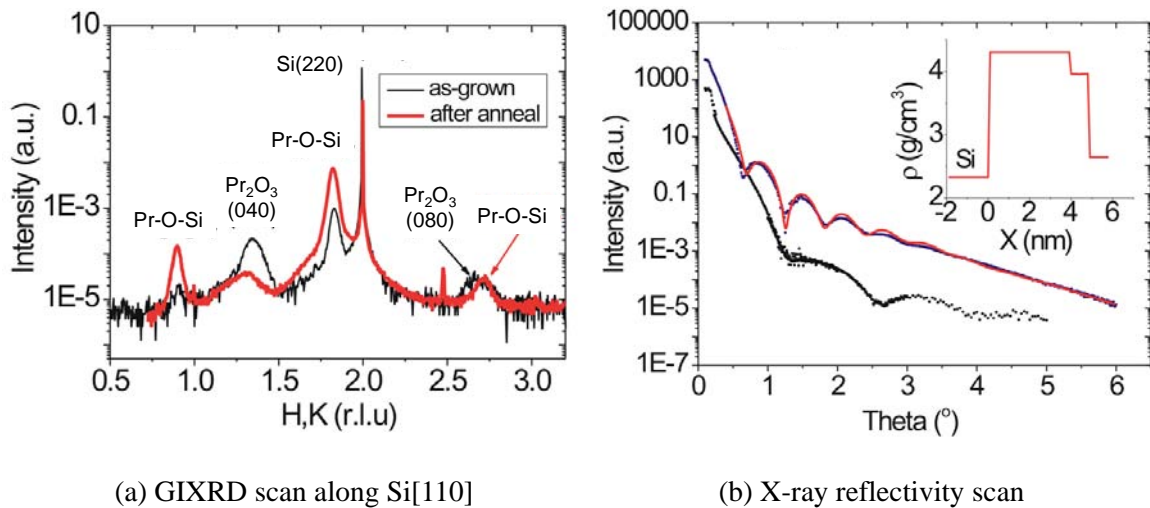


Figure 1. X-ray diffraction and reflectivity measurement for $\text{Pr}_2\text{O}_3/\text{Si}(001)$ for a sample as-grown and after annealing at 850°C .

annealing, the peaks of cubic Pr_2O_3 are clearly observed as well as the peak from Pr-O-Si interfacial reaction products due to the diffusion of Si atoms from the substrate into the Pr_2O_3 layer. After the annealing, the cubic oxide peaks become weaker and the silicate peaks become sharper and more intense. This indicates the expansion of interfacial compounds by thermal annealing, and the dominant structure of this annealed layer is of the Pr-O-Si (silicate or silicide) structure. The nominal thickness of the layer is deduced from the reflectivity result shown in figure 1(b) and it is 3 nm and 6.5 nm for as-grown and annealed sample, respectively. The density profile of the annealed layer (shown in the inset of figure 1(b)) shows the decrease in density by annealing. These results support the silicate formation via silicon diffusion hypothesis.

In order to obtain a thermally stable and uniform material with good interfacial structure, we investigate the alloying of Pr_2O_3 with Si because praseodymium silicate ($\text{Pr}_2\text{Si}_2\text{O}_7$) has a relatively high dielectric constant (15~19)[4] and better thermodynamic stability in contact with Si compared to Pr_2O_3 . Since the interfacial Pr-O-Si structure, which is formed unintentionally and causes a rough interface, has a lower dielectric constant than stoichiometric $\text{Pr}_2\text{Si}_2\text{O}_7$, it is important to control the formation of the Pr-O-Si interfacial layer. Figure 2(a) shows in-plane GIXRD patterns along Si[220] for the Pr_2O_3 layers (a) without Si and (b) with Si addition during growth. The peaks at $H=K=1.37$ and 1.94 correspond to the cubic Pr_2O_3 (040) and $(40\bar{4})$ reflections, respectively; the epitaxial Pr_2O_3 layer contains two orthogonal cubic domains on the Si surface[5]. Additional peaks at $H=K=0.90$ and 1.83 are clearly observed for sample (A). In this case, Pr-O-Si related material is dominant at the interface and the cubic Pr_2O_3 phase mainly exists above the interfacial layer. However, the peaks at $H=K=0.90$ and 1.83 do not appear for sample (B) with Si addition. Cubic Pr_2O_3 is the dominant structure for this layer.

Figure 2(b) shows the results of the x-ray reflectivity measurements on the same samples. Compared to the sample without Si, the interference fringes for the sample with Si addition are clearly observed even at higher angle, indicating a significant increase in the contrast of the density profiles of the layers due to the sharper interface and better morphology. From these results, we conclude that Si enhances the nucleation at the initial stage and/or restricts atomic intermixing probably by forming a

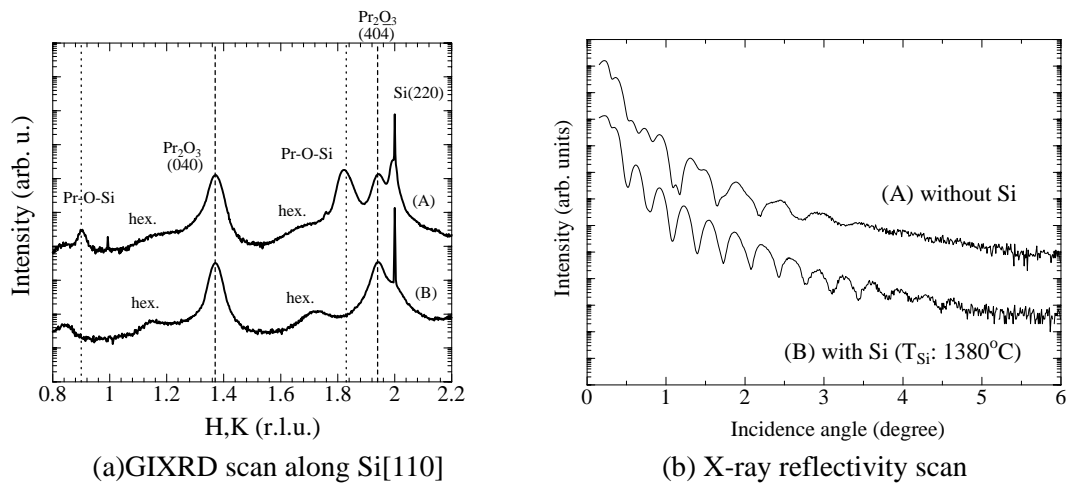


Figure 2. X-ray diffraction and reflectivity measurement for $\text{Pr}_2\text{O}_3/\text{Si}(001)$ with and without Si addition

stable silicate structure at the interface. However, from the x-ray and RHEED measurements, we could not find clear evidence of the formation of a stoichiometric crystalline $\text{Pr}_2\text{Si}_2\text{O}_7$ structure; instead, the dominant structure in the layer is cubic Pr_2O_3 . A small amount of the hexagonal phase of Pr_2O_3 is found as well by x-ray diffraction shown in Fig. 2(a). Further investigations of layers with Si addition are required to determine their structure and composition.

Summary

The epitaxial growth of praseodymium oxide (Pr_2O_3) together with the addition of silicon during growth with the aim to enhance the silicate formation was studied by in-plane grazing incidence x-ray diffraction and x-ray reflectivity. Annealing to 850°C activates significant bulk diffusion and the Pr-O-Si structure extends into the Pr_2O_3 layer. The addition of Si reduces the amount of Pr-O-Si near the interface. From the GIXRD measurements, we find that an adequate amount of Si results in a stable, mainly cubic Pr_2O_3 layer with some additional hexagonal Pr_2O_3 .

References

- [1] H. J. Osten, E. Bugiel, and A. Fissel, *Solid-State Electron.* **47**, 2161 (2003)
- [2] G. Adachi and N. Imanaka, *Chem. Rev.* **98**, 1479 (1998)
- [3] B. Jenichen, W. Braun, V. M. Kaganer, A. G. Shtukenberg, L. Daweritz, C. G. Schulz, K. H. Ploog, and A. Erko, *Rev. Sci. Instrum.* **74**, 1267 (2003)
- [4] A. Sakai, S. Sakashita, M. Sakashita, Y. Yasuda, S. Zaima and S. Miyazaki, *Appl. Phys. Lett.* **85**, 5322 (2004)
- [5] X. Guo, W. Braun, B. Jenichen, and K. H. Ploog, *J. Crystal Growth* **290**, 73 (2006)

Investigation of the Dielectric Function of Guanine and Cytosine Heterostructures

J. Sindu, S. Rudra, M. Friedrich, D. R. T. Zahn
Institut für Physik, TU Chemnitz, 09107 Chemnitz, Germany
S.D.Silaghi, C. Cobet, N. Esser
ISAS - Institute for Analytical Sciences, D-12489 Berlin
W. Braun
BESSY GmbH, 12489 Berlin, Germany

In recent year multilayered organic structures have attracted considerable attention¹. Compared to bulk materials multilayered heterostructures can have unusual optical and physical properties which open new possibilities for optoelectronic devices.

It is well known that the guanine and cytosine rich DNA molecule can show p-type semiconducting properties². In that case it is interesting to study the optical response of multilayer composed of very thin layers of guanine (C₅H₅N₅O) and cytosine (C₄H₅N₃O) molecules. Synchrotron radiation at BESSY II provides ideally suited means to investigate the optical properties of such DNA base heterostructures.

Bulk and thin multilayer films of guanine and cytosine on ZnO substrates were prepared by organic molecular beam deposition under ultra high vacuum (10⁻⁹ mbar) conditions and measured *in situ* by means of Vacuum Ultra Violet (VUV) Spectroscopic Ellipsometry at BESSY. This measurement technique is based on the determination of polarization of light before and after reflection on the sample surface. The *in situ* measurements were performed at an angle of incidence of 68° in the range between 4 to 9.5 eV. For thickness determination and anisotropy evaluation supplemental measurements were carried out in the transparent spectral range below 4 eV at different incidence angles.

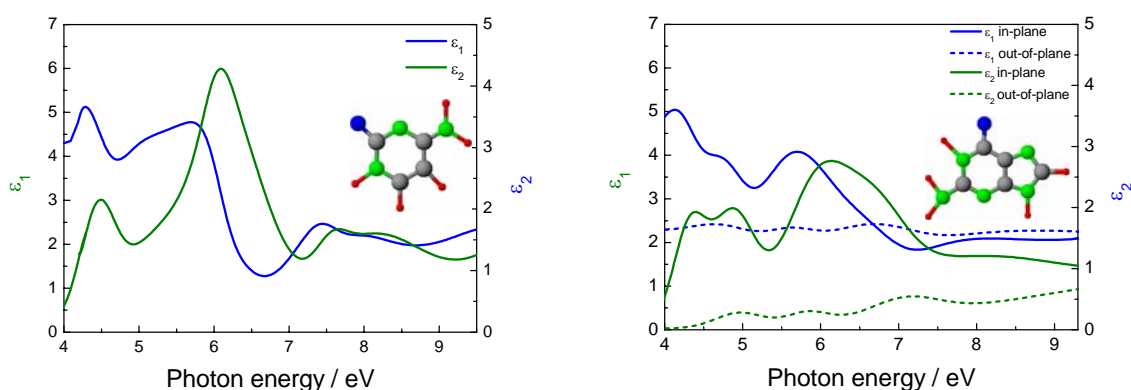


Figure 1: Dielectric functions and molecular structure of cytosine (left) and guanine (right).

Good agreement between the measured and simulated data was achieved using an isotropic model for cytosine and uniaxial anisotropic model for guanine. In Fig. 1 the resulting dielectric functions of thick bulk-like cytosine and guanine films are presented. These dielectric functions are used to simulate thin multilayer of these molecules.

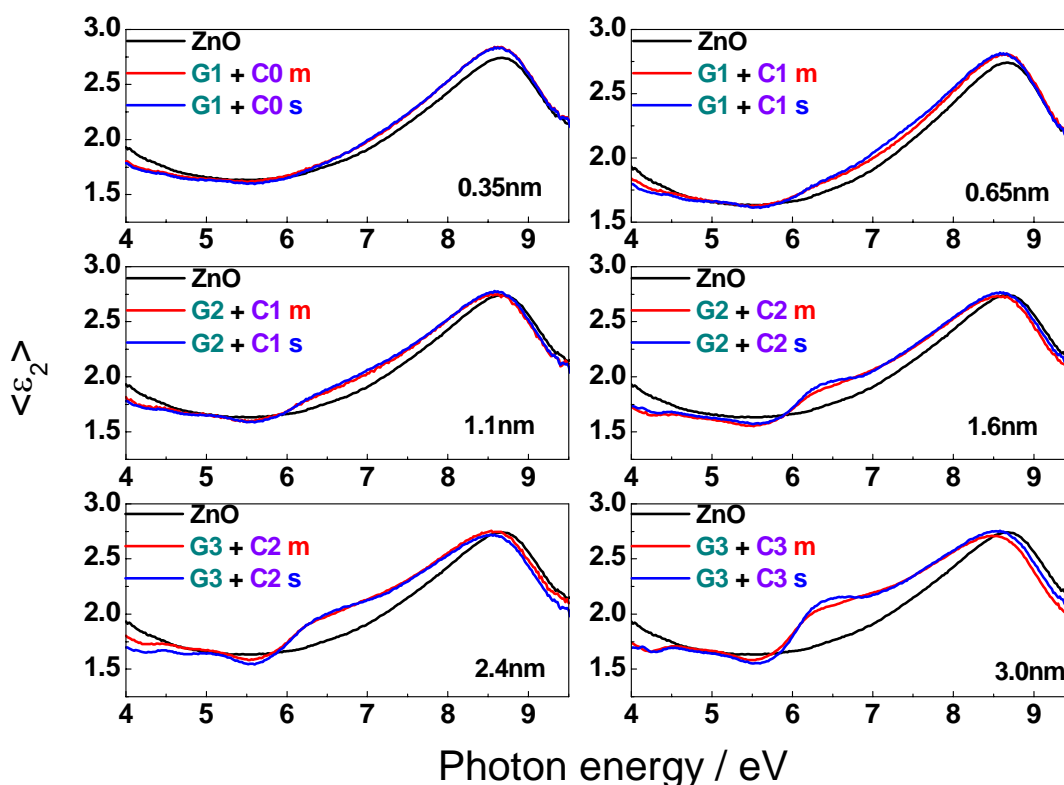


Figure 2: Measured (red) and simulated (blue) effective dielectric function for the multilayer structure and the clean substrate (black) for comparison. G2+C1 in the legend means that the effective dielectric function is measured after depositing the second guanine layer (G2) on the first guanine (G1) + cytosine (C1) layer stack.

Figure 2 shows the measured and simulated effective dielectric function of multilayer structures starting from guanine together with the effective dielectric function of the bare substrate. Three alternative layers of guanine and cytosine are grown on the ZnO substrate. From the determined thickness of the cytosine and guanine in the multilayer, we have a single layer of each to start with and have two layers after the first two depositions^{3,4}. As observed, even for the first thin layer there is considerable change in the effective dielectric function indicating the strong optical absorption of these DNA bases. The multilayer is modelled with sharp interfaces and the determined thickness is as expected suggesting a highly ordered multilayer structure. The slight deviation in the simulated spectra occurs because the cytosine layer is considered as isotropic as in the bulk films. However, in the ultra thin layers on silicon cytosine exhibits anisotropic behaviour³.

Layers	Peak position in the effective dielectric function / eV						
Cytosine	Bulk	-	4.44	5.10	6.05	7.50	8.10
	Thin Film	-	4.50	-	6.42	-	-
Guanine	Bulk	4.35	4.88	5.80	6.40	7.90	8.80
	Thin Film	4.46	5.06	-	6.92	-	-
Multilayer	4.52	5.05	-	6.32	-	-	

The peak positions present in the ultra thin multilayer are observed to be shifted to higher

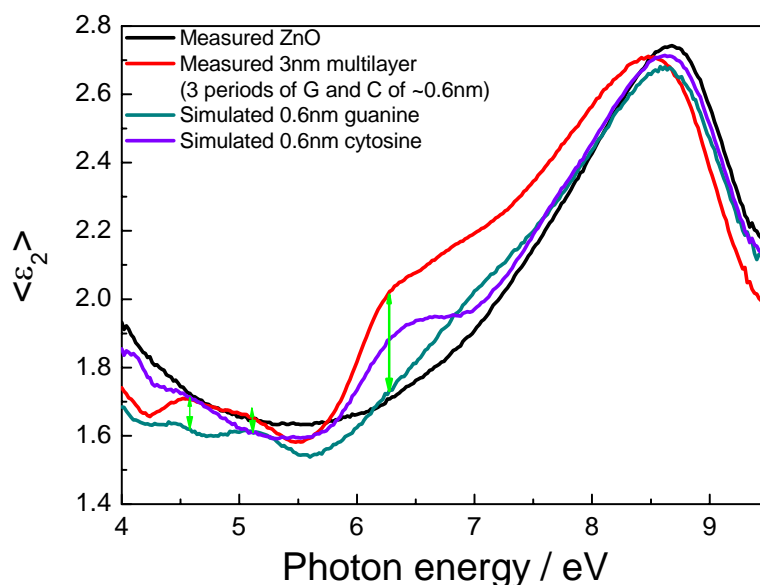


Figure 3: Compared $\langle \epsilon_2 \rangle$ of 3nm thick multilayer with simulated thin guanine and cytosine layer

energy. From figure 3 it is observed that the peak around 6.2 eV is strongly attributed by the cytosine layer while that between 4 eV to 5.4 eV stems more from the guanine layer.

The results presented are a good starting point for a more detailed understanding of the arrangement of molecules in the multilayers and their interaction. Further measurements are planned starting with a cytosine layer. The evaluation of first monolayer spectra will give insight in the interaction of molecules with the substrate.

Acknowledgement:

The author would like to acknowledge the BMBF projects 05 KS4KTB/3 and 05 ES3XBA/5, IRTG "Materials and Concepts for Advanced Interconnects" and the DFG Collaborative Research Center 379 "Arrays of Micromechanical Sensors and Actuators".

1. Y. Imanishi, S. Hattori, A. Kakuta and S. Numata, Phys. Rev. **71**, 2098 (1993).
2. Lee, H.Y., Tanaka, H., Otsuka, Y., Yoo, K.H., Lee, J.O. & Kawai, T. Control of electrical conduction in DNA using oxygen hole doping. *Appl. Phys. Lett.*, **80**, 1670–1672 (2002)
3. D. L. Barker, R. E. Marsh, Acta Cryst. **17**, 1581 (1964)
4. U. Thewalt, C. E. Bugg, R. E. Marsh, Acta Cryst. **B 27**, 2358 (1971)
5. Optical Characterisation of DNA Bases on Silicon Surfaces – PhD Dissertation by Simona Dorina Silaghi, TU Chemnitz (2005)

Structure of Organogel formed by Ionic Self Assembled 1, 3, 5-benzenetricarboxamide derivative and dihexadecylphosphate.

Elena Maltseva¹, Charl F. J. Faul², Franziska Emmerling¹ and Andreas Thünemann¹

¹ Federal Institute for Materials Research and Testing, Richard-Willstätter-Str. 11, 12489 Berlin, Germany

² Inorganic and Materials Chemistry Section, School of Chemistry, University of Bristol, Bristol BS8 1TS, UK

The generations of new ‘smart’ nanoscaled materials which are able to respond to external stimuli (i.e. magnetic or electrical field) in a defined way is one of the most important goals of supramolecular chemistry and nanotechnology. Recently a facile route for production of mesogenic materials by complexation of oligoelectrolytes with charged surfactant materials was introduced [1]. This process is called ionic self-assembly (ISA) and it uses the electrostatic interactions between the charged species to construct the mesogenic materials.

In a present work we focus our attention on ISA formed by dihexadecylphosphate and tris-(4-trimethyl-ammoniumphenyl)-1, 3, 5-benzenetricarboxamide (TRISDiC16) in benzene. The 1, 3, 5-benzenetricarboxamide derivatives are C₃ symmetrical molecules, which are able to associate into supramolecular stacks via hydrogen bonds [2].

The TRISDiC16 forms a gel in benzene at concentrations above 1 wt %. As shown in Figure 1, the SAXS pattern of the gel formed by 5 wt % TRISDiC16 in benzene has a set of relatively broad but pronounced peaks. These reflection peaks can be attributed to a hexagonal columnar phase (reflections at $1/d$, $\sqrt{3}/d$, $2/d$, $\sqrt{7}/d$, $3/d$, $\sqrt{12}/d$, $\sqrt{13}/d$, $4/d$, $5/d$ and $6/d$) with a repeating distance $d = 4.7$ nm and a lattice parameter $a = 5.4$ nm. The dimensions (~ 2.4 nm for the TRIS core and ~3 nm for phosphates) of the TRISDiC16 molecules enable the formation of the discs with 5.4 nm radius that can form hexagonal columnar phase.

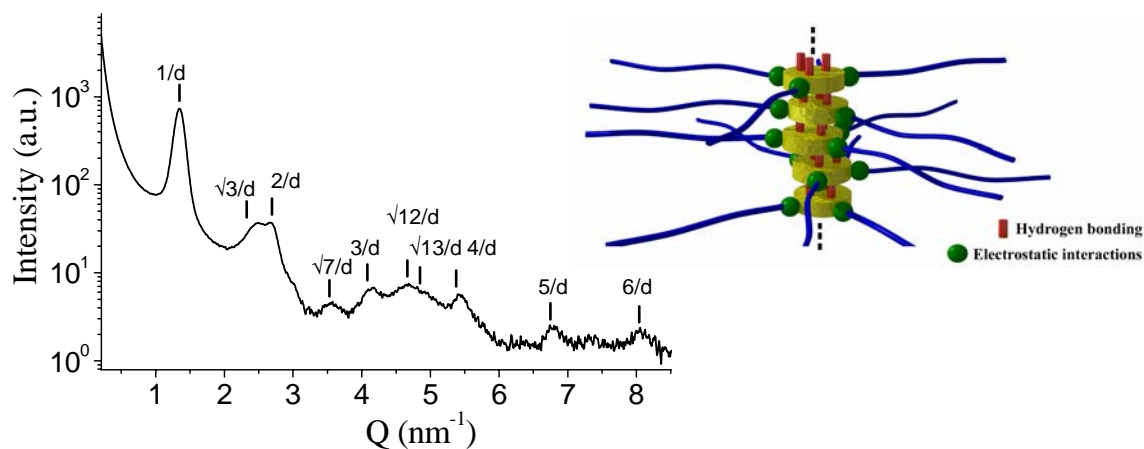


Figure 1. SAXS curve of 5 wt % benzene gel of TRISDiC16. The insert demonstrates possible arrangement of TRISDiC16 in a column.

Obviously, formation of the columnar phase by TRISDiC16 is promoted by hydrogen bonds between neighbouring 1, 3, 5-benzenetricarboxamide cores. Such structure allows withdrawing of the relatively hydrophilic groups inside the core of formed cylinders, while hydrophobic alkyl chains are located in the shell of the cylinders and exposed in the solvent (see insert into Figure 1). The hexagonal arrangement of the cylinders may be more attractive owing to the C₃ symmetry of the TRISDiC16 core.

This work was supported by the Adolf-Martins-Fellowship program of Federal Institute for Materials Research and Testing.

References:

[1] C.F.J. Faul and M. Antonietti, *Eur. J.*, 2002, **8(12)**, 2764

[2] J. J. van Gorp, J. A.J.M. Vekemans, and E. W. Meijer, *JACS.*, 2002, **124**, 14759

Shallow Concentration Depth Profiling with X-ray Photoelectron Spectroscopy

S. V. Merzlikin^a, N. N. Tolkachev^c, T. Strunskus^b, G. Witte^b, C. Wöll^b, W. Grünert^a

^aLaboratory of Industrial Chemistry, ^bLaboratory of Physical Chemistry I, Ruhr University Bochum, D-44780 Bochum, Germany, ^cN. D. Zelinsky Institute of Organic Chemistry, Russian Academy of Sciences, Moscow, Russia

It is well known that photoelectron spectroscopy, which is a popular tool for surface analysis, renders information averaged over a sampling depth which is related to the mean free path of the photoelectrons in the sample (λ). Concentration gradients normal to the surface may lead to strong differences between the properties of the topmost atomic layer usually targeted by XPS studies and the results obtained [1]. The problem is alleviated but not solved by diminishing the sampling depth, which may be achieved by decreasing the excitation energy $h\nu$ (synchrotron excitation) or by analysing the photoelectrons at grazing incidence (angle-resolved XPS (ARXPS)). Both approaches are in qualitative use, and ARXPS is widely employed to determine the thickness of segregated surface layers. The algorithms used there are, however, inadequate for nonsegregated mixtures as alloys or mixed oxides.

Photoelectron intensities analysed along the surface normal of an atomically flat surface are proportional to the integral over the concentration depth profile weighed by the photoelectron escape function, which may be approximated by

(σ – photoionisation cross section, $\rho_A(z)$ – concentration variation of element A over depth z , S –

$$I_A \propto \sigma_A(h\nu) S(E_{kin}) \int_0^{\infty} \rho_A(z) \exp\left(-\frac{z}{\lambda(E_{kin})}\right) dz$$

detector efficiency at kinetic energy E_{kin}). When lines of elements A and B (with similar binding energies, to cancel out $S(E_{kin})$) are measured at different excitation energies $h\nu$, the experimental intensity ratios I_A/I_B may be fitted to models of this type by varying the parameters of assumed depth profile functions $\rho_A(z)$ and $\rho_B(z)$, taking advantage of known energy correlations between σ_A , σ_B and $h\nu$, between λ and E_{kin} , and of stoichiometric relations if appropriate. The depth profiles $\rho_A(z)$, $\rho_B(z)$ which best reproduce the measured intensity ratios should be realistic estimates of the concentration

variations below the surface. In particular, they may be used to determine the composition of the outmost atomic layer by extrapolation. The method is somewhat complicated by the fact that λ is not a function of E_{kin} alone, but of material properties as well, which makes it depth dependent, too. The new concentration depth profiling version of XPS (“CDP-XPS”) takes this into account.

CDP-XPS has been validated with self-organized monolayers of n-octadecanethiol (“C₁₈-SAM”) on gold surfaces. Figure 1 shows experimental and modelled C 1s / Au 4d intensity ratios and, in the inset, the underlying depth distribution of (thiol) carbon measured with an atomically flat Au substrate ((111)-faceted Au on mica(111)). While independent measurements show the organic layer to be ca. 2.2 nm thick, a 2.24 nm thick surface layer with 101.2 % carbon has been found with CDP-XPS [2]. This result does not rely on previous knowledge of the layered structure because other function

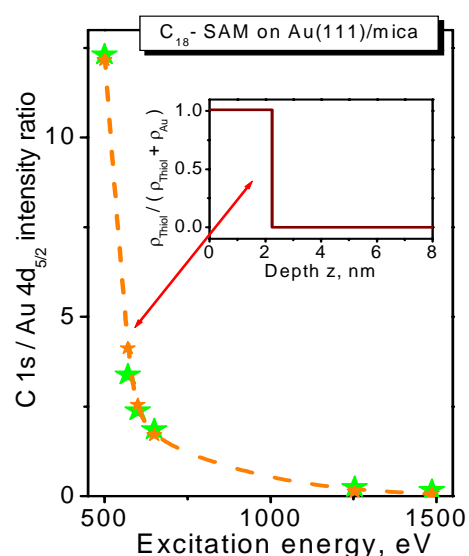


Figure 1. CDP-XPS analysis of a C₁₈-SAM on an atomically flat Au substrate

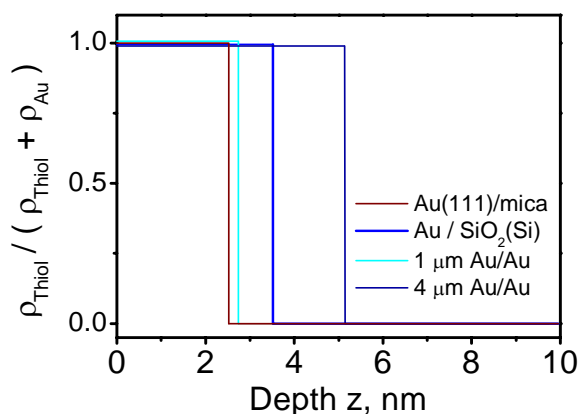


Figure 2. CDP-XPS with C_{18} -SAMs on rough Au substrates. Au/SiO₂(Si): Au on Si wafer, $n \mu\text{m}$ Au/Au: powders of grain size n sintered onto Au foil

types for $\rho_C(z)$ rendered inferior fits. An ARXPS measurement performed for comparison, allowed to determine the carbon layer thickness with similar accuracy. The influence of surface roughness on the results of CDP-XPS has been investigated by using gold substrates of different grain size, the morphology of which was studied by AFM and by confocal laser scanning microscopy [3]. Figure 2 compares the carbon depth distribution curves extracted from the data with that for the atomically flat Au surface. As expected, surface roughness tends to extend the depth coordinate in the CDP-XPS models, but the error remains in the order of 30-40 % except for extreme surface roughness (abundance of steep orientations) as has been found for the 4 μm Au/Au sample. In all cases, the concentration is correct at the external surface, i.e., surface roughness does not impair the analysis of the topmost surface layer by back-extrapolation of the concentration profile. In the comparative ARXPS study, surface roughness was seen to lead to an underestimation of the organic layer thickness. Remarkably, at extreme surface roughness (4 μm Au/Au), ARXPS failed completely, rendering no surface enrichment of carbon at all while CDP-XPS still detected the correct surface concentration of carbon though failing significantly with the extension of the depth coordinate. This suggests that the case of extreme surface roughness rendering excessive extension of the CDP-XPS depth coordinate may be identified by comparing CDP- and ARXPS results [3].

A first application of CDP-XPS deals with bulk mixed oxides (ZrV₂O₇, Fe₂(MoO₄)₃) where investigations by ion scattering spectroscopy (ISS) had identified a strong surface enrichment in vanadium (molybdenum) contrary to common expectations that the surface composition should be related to that of the bulk. The CDP-XPS analysis allows to confirm the ISS results and to determine the thickness of the surface vanadium (molybdenum) oxide layer. For ZrV₂O₇, a ≈ 0.6 nm surface vanadium oxide layer was found. Given the extension of the depth coordinate by 30-40 % due to surface roughness, the result indicates the presence of a monolayer of surface vanadium oxide species. For Fe₂(MoO₄)₃, where the experimental data were less accurate due to experimental reasons (charging, baseline problems), the almost exclusive exposure of surface molybdenum oxide species and a layer thickness in the order of a monolayer could be confirmed as well.

We acknowledge gratefully financial support by the German Science Foundation (Project Gr 1447/9) and support for travelling costs for the synchrotron measurements by the BMBF through grant 05 ES3XBA/5.

- [1] Heber, M., Grünert, W., J. Phys. Chem. B 104 (2000), 5288-5297.
- [2] Tolkachev, N.N., Merzlikin, S.V., Strunskus, T., Witte, G., Wöll, C., Grünert, W., Surf. Interface Anal., submitted.
- [3] Merzlikin, S.V., Tolkachev, N.N., Glogowski, T., Strunskus, T., Witte, G., Wöll, C., Grünert, W., Surf. Interface Anal., submitted.

Molecular ordering and thermally induced phase transitions in aromatic SAMs

*D. Käfer, G. Witte and Ch. Wöll,
Physikalische Chemie I, Ruhr-Universität Bochum, D-44780 Bochum*

Self-assembled monolayers (SAMs) have attracted considerable attention because of their versatile possibility of tailoring surface properties such as wetting behavior, adhesion, lubrication, and corrosion. More recently aromatic SAMs have become the focus of interest due to potential applications for charge transfer and electronic functionality. In particular, aromatic SAMs enable fundamental studies on issues directly related to molecular electronics i.e. molecular conductivity, molecular switching, or molecular transistors. So far the majority of related studies on aromatic SAMs have been carried out for oligo-phenylene-thiols. In this class of molecules the individual phenyl-units are separated, however, by single C-C bonds resulting in only partly aromatic molecular backbones with a rather large band gap (or HOMO-LUMO separation). Moreover, this single bonds enable a twisting of neighboring phenyl units and thus provide an additional conformational degree of freedom. To avoid this complications we have chosen anthracene-2-thiol (AnT, $C_{14}H_9SH$) which comprises a rigid, fully conjugated acene-backbone and have studied the formation and structural properties of SAMs with a particular emphasis on their thermal stability. In addition to a characterization based on STM, LEED, XPS, and TDS carried out at the Ruhr-University Bochum NEXAFS measurements were performed at the HE-SGM beamline of the synchrotron facility BESSY II in Berlin to characterize the orientational ordering within the SAMs as a function of the sample temperature.

For the saturated monolayer a $(2\sqrt{3} \times 4)$ rect-structure has been identified which can be rationalized by an attempt to fit the close packing arrangement adopted by anthracene molecules in their crystalline lattice with the surface lattice of the Au(111) substrate. Due to the misfit of the anthracene bulk lattice and the gold lattice the resulting SAM-structure shows an unidirectional compression as compared to the bulk structure which leads to the formation of characteristic stacking faults. An important results of the present study is the detailed quantitative analysis of the linear dichroism obtained in the C1s NEXAFS data. While an average tilt angle of the aromatic units can be easily derived from the dichroism of the π^* -resonance intensities measured for different angles of incidence (see Fig. 1a) a precise determination of the molecular orientation is frequently hampered because of an unknown twisting of the aromatic units (as mentioned above for case of oligo-phenylenes). Moreover, the quantitative analysis of the NEXAFS data is complicated by the presence of differently oriented molecules within the unit cell. In case of the typical face-on-edge herring bone packing motive adopted by the planar, rigid acene-units (see Fig. 1c) the twist angle can be related to the herringbone angle and thus allows a detailed analysis of the tilt angle for the individual molecules.

In the further course of the experiment the thermal stability and the molecular ordering of AnT as a function of the temperature have been investigated. Corresponding TD-spectra revealed the presence of two distinct desorption peaks at 505K and 550K. Based on additional XPS measurements the first peak has been assigned to a partial desorption of intact thiolate species while a fragmentation and dissociative desorption takes place at elevated temperature.

Corresponding NEXAFS measurements showed further that the partial desorption of intact molecules allows a reorientation of the remaining molecules which start to lie down (see Fig. 1d) until they form a (4×2) -structure (stripe phase). Attempts to also characterize this phase by means of STM under ambient conditions were not successful and are hampered by a partial oxidation of the sulfur head groups as evidenced by corresponding XPS measurements. The presently studied formation and stability of AnT-SAMs on gold substrates reveals a complex scenario which can be summarized by the schematic phase diagram shown in Fig. 2.

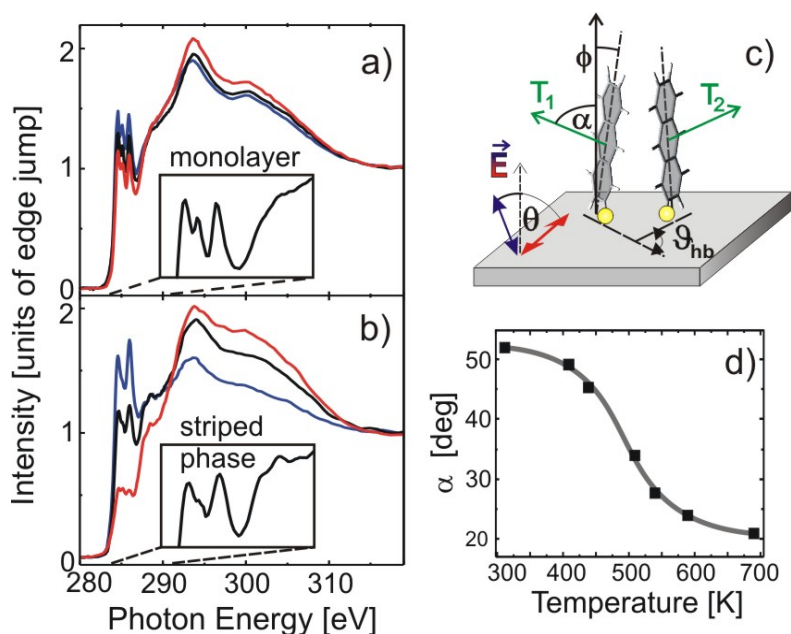


Fig. 1 Comparison of C1s NEXAFS of AnT recorded at different angles of incidence (blue curve: $\theta=30^\circ$, black: 55° , red: 90°) for a) the saturated monolayer and b) the diluted stripe phase (obtained after heating), together with the evolution of the molecular orientation as a function of the temperature (d). Panel c) shows the experimental geometry and the relative orientation of the transition dipole moments in the aromatic SAM.

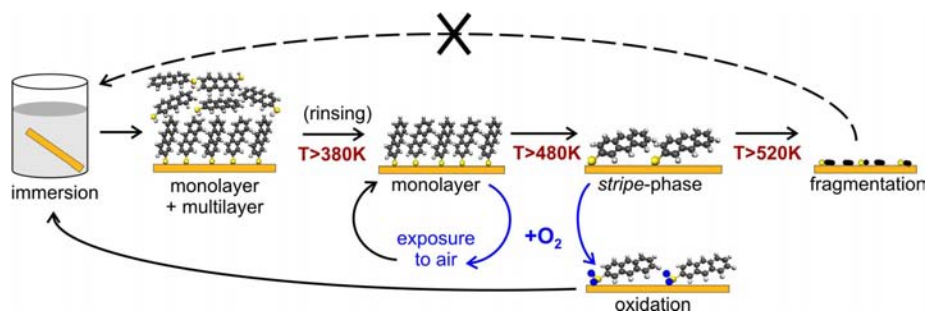


Fig. 2 Schematic phase diagram showing the various phases of anthracene-2-thiol on Au(111) as a function of coverage and temperature.

Reference

- [1] D. Käfer, G. Witte, P. Cyganik, A. Terfort, Ch. Wöll, J. Am. Chem. Soc. **128**, 1723 (2006).

Reductive UPD versus oxidative UPF processes on Cu(111): A combined electrochemical and SXPS study using the Solid-Liquid Analysis System (SoLiAS)

Sascha Hümann, Peter Broekmann and Klaus Wandelt
Department of Surfaces and Interfaces, Institute of Physical and Theoretical Chemistry,
University of Bonn

Ralf Hunger and Wolfram Jaegermann
Surface Science Division, Institute of Materials Science,
Darmstadt University of Technology

In this contribution we present combined electrochemical and SXPS measurements on the potential dependent reductive Cd under potential deposition (UPD) and the oxidative under potential formation (UPF) of a CuI film on Cu(111) electrode surfaces.

In general, the submonolayer or monolayer deposition of a metal onto an unlike metal substrate at potentials more positive than the corresponding reversible Nernst potential is known as under potential deposition (UPD). A similar phenomenon was recently discovered for binary compound formation processes in the course of an oxidative dissolution of the electrode material. E.g., CuI formation on Cu(111) starts with a 2D-CuI wetting layer at lower overpotentials than CuI_{bulk} formation at higher overpotentials. These phenomena are referred to under potential formation (UPF) and over potential formation (OPF) processes of binary compounds in analogy to metal UPD and OPD (over potential deposition) processes.

The electrochemical processing was performed in an Ar purged electrochemical cell allowing the transfer of the sample into the UHV without exposing it to air. Photoelectron spectroscopy measurements were performed using the SoLiAS experimental station [1] at the U49/2-PGM2 beamline at BESSY II. Photoelectron spectra were recorded with a Phoibos 150 MCD 9 analyzer after each preparation step, using photon energies of 125, 245, 720 and 1040 eV, respectively, thereby varying the information depth of the data. All spectra were recorded in normal emission and are referenced to the Fermi level of a clean, sputtered Cu foil.

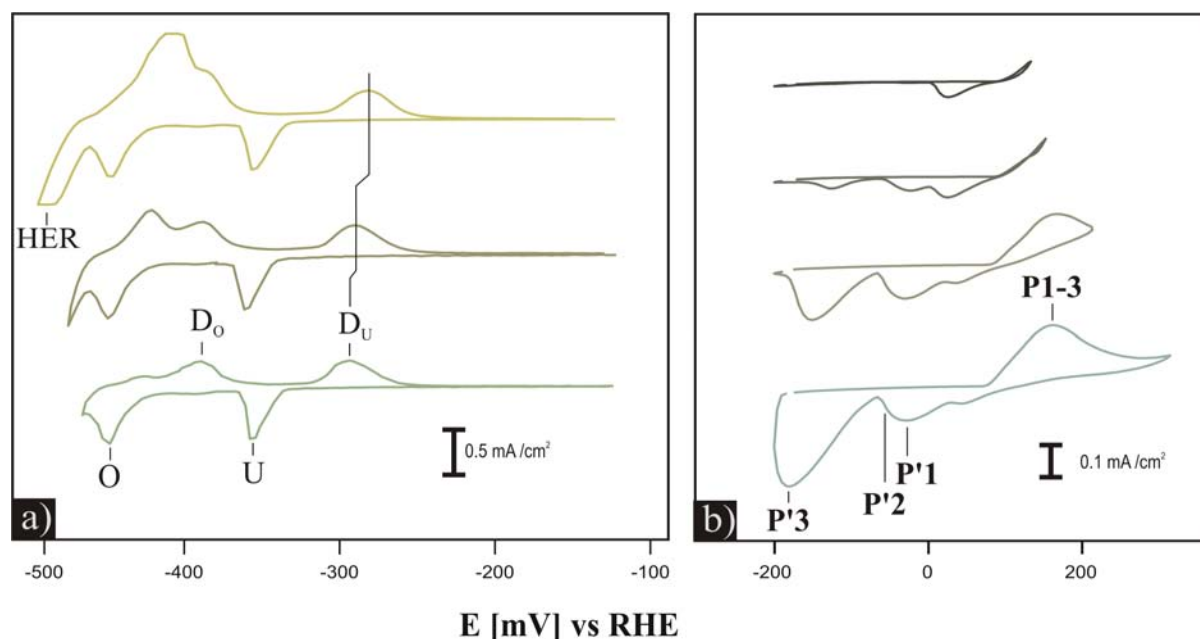


Figure 1: CVs showing (a) the Cd-UPD (U) and OPD (O) in a solution of 0.1mM CdI in 5mM H₂SO₄; (b) the anodic Cu dissolution at potentials above +80 mV.

Fig. 1 shows a series of representative CVs (Cyclic Voltammograms) of Cu(111) in 0.1 mM CdSO₄ and 10 mM KI in 5mM H₂SO₄ sulfuric acid with Fig. 1a being representative for the lower and fig. 1b being representative for the higher potential regime. Clearly visible in fig. 1a are the Cd UPD peak U and the Cd OPD peak O in the cathodic scan. The corresponding stripping peaks D_O and D_U appear in the anodic scan.

In the higher potential regime (Fig. 1b) peak system P1-3 in the anodic scan can be associated with copper oxidation from Cu⁰ to cuprous Cu⁺ species in the presence of iodide anions. According to previous STM measurements UPF of 2D-CuI is expected at the on-set of the anodic peak system. An exponential increase of an oxidation current at more positive potentials indicates the copper dissolution involving net mass transport of cupric Cu²⁺ species into solution. However, these are not stable in solution when iodide is also present. Iodide as reductive agent chemically reduces the Cu²⁺ to Cu⁺ species in solution leading to 3D-CuI cluster formation followed by cluster precipitation onto the electrode surface. CuI phases (2D-CuI film, 3D-CuI cluster) as reaction products of the copper oxidation are electro-reduced in the corresponding negative potential scan giving rise to the appearance of the complex cathodic peak system P'1-P'3.

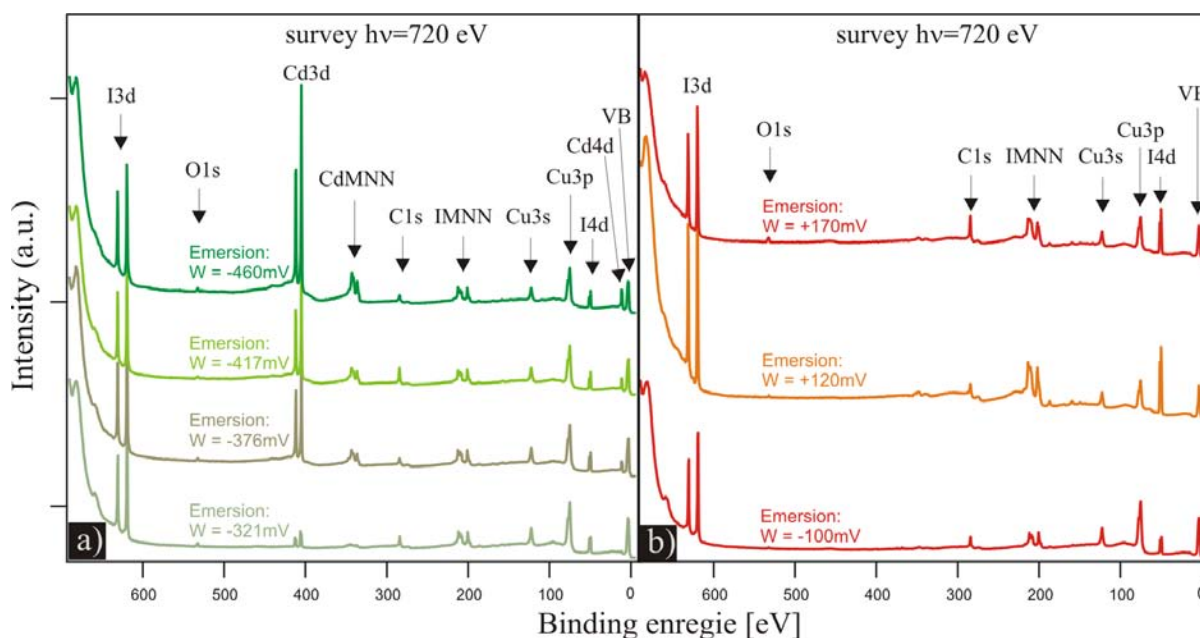


Figure 2: SXPS survey spectra (hv = 720 eV) of (a) CdI-UPD-film on Cu(111); (b) CuI on Cu(111).

Fig. 2 shows the photoelectron survey spectra of CdI (Fig. 2a) and CuI (Fig. 2b) obtained at hv = 720 eV comprising the following core levels and Auger emissions as indicated in the figure: I3d (~620 eV), O1s (~532 eV), Cd3d (~405 eV), Cd MNN (Auger, ~340 eV), C1s (~285 eV), I MNN (Auger, ~210 eV), Cu3s (~123 eV), Cu3p (75.1 eV), I4d (~50 eV) and Cd4d (~11 eV). The valence band emissions are observed at a binding energy of ~3 eV.

While the integrated intensities of Cd3d continuously increase upon Cd UPD and OPD the I3d and I MNN signatures remain constant pointing to a non-changing surface concentration of iodide species upon Cd deposition. Obviously iodide acts as a *surfactant* remaining adsorbed on the topmost atomic layer during Cd growth. From STM results it is known that iodide induces a layer-by-layer growth of Cd at least up to the fourth layer.

In contrast to the Cd deposition the integrated intensities of iodide photoelectron I3d, I4d and I MNN emissions increase (Fig. 2b) at positive potentials due to a 2-D- and 3-D-growth of CuI [2]. The 2D-growth of a well defined 2D-CuI(111) wetting layer has been explained in terms of a UPF process while the further growth of 3D-CuI clusters at higher potentials correspond to the OPF.

Here the role of iodide is different than in the case of the reductive Cd deposition.

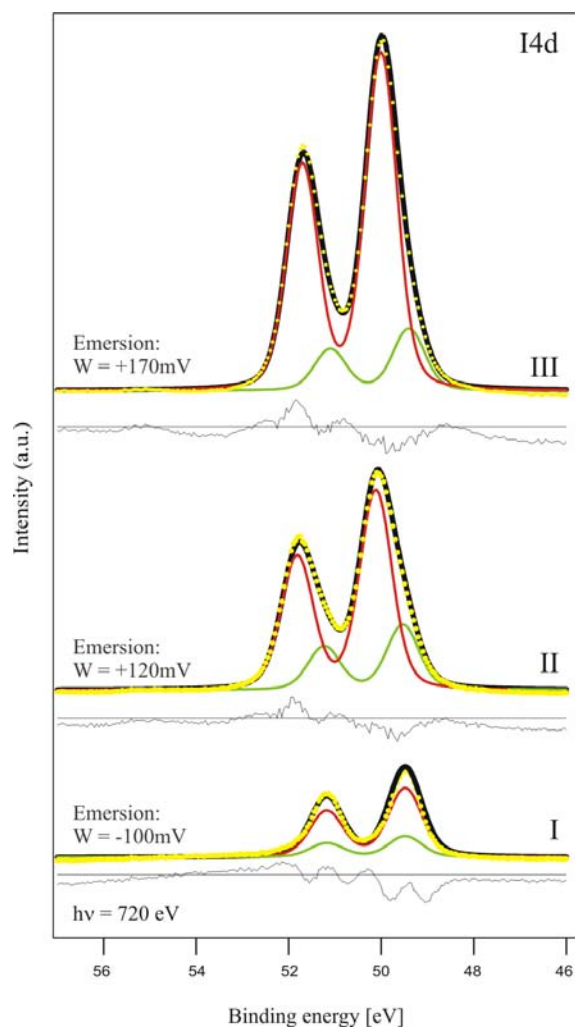


Figure 3: SXPS I4d spectra ($h\nu = 720$ eV) of CuI on Cu(111).

First, from the detailed analysis of the I4d-photoelectron emission of iodide at positive potential ranges (Fig. 3) one can conclude that the pre-existing iodide monolayer ($BE = 49.48$ eV) remains unchanged upon 2D- and 3D-CuI formation. Apparently, the 2D-CuI and the 3D-CuI cluster growth takes place on-top of an iodide modified Cu(111) electrode surface. Specifically adsorbed iodide on Cu(111) is not consumed upon CuI formation but it remains in contact with the metallic copper. Only iodide from the solution reacts with Cu^+ species that are formed upon copper oxidation. Iodide in the 2D- and 3D-CuI shows a chemical shift of 0.5 eV towards higher binding energies ($BE = 50.01$ eV) pointing to an almost covalent Cu-I bond. There is, however, no significant chemical shift between the iodide in the 2D and the 3D phase.

In conclusion, we have investigated the role of iodide anions in the reductive deposition of Cd on Cu(111) and the oxidative dissolution of the copper substrate. In both processes the anion plays a crucial role, either as a kind of surfactant (Cd UPD/OPD) or as reactant (CuI UPF OPF).

References:

- [1] T. Mayer, M. V. Lebedev, R. Hunger, and W. Jaegermann, *Applied Surface Science* **252** (2005) 31-42.
- [2] P. Broekmann, N.M.T. Hai, K. Wandelt, *J. Appl. Electrochem.* **36** (11) (2006) 1241
- [3] D. Briggs, M. P. Seah (Eds.), *Practical Surface Analysis by Auger and X-ray Photoelectron Spectroscopy*, Wiley, 1985.

List of Projects

Project leader	Institute	Project title
Adnane Achour	Karolinska Institutet	Structural Studies of TCR/MHC class I-dependent mechanisms for viral escape and virus-induced autoimmune diseases.
Adriana Miele	University of Rome La Sapienza	Structural biology for biotechnology a) Schistosome structural biology: identification of targets for drugs and vaccines b) How protozoa respond to host's nitrosative stress: the structure of Flavodiiron protein c) X-ray structure of N-Methyltryptophan oxidase
Adriana Miele	University of Rome La Sapienza	Structural genomics for biotechnology
Ajay Gupta	Inter-University Consortium for DAEF facilities	Study of swift heavy ion induced intermixing in metal/Si thin films
Alan Michette	King's College London	Measurement of the polarising properties of broadband multilayer soft x-ray and EUV mirrors
Alan Tennant	Hahn-Meitner-Institut Berlin GmbH	Test of the reflectometry option and alignment of the new 7 T high-field end station at UE46-PGM
Alexander Föhlisch	Universität Hamburg	Resonant inelastic X-ray scattering as a probe of excited states in matter
Alexander Okotrub	Russian Academy of Sciences	Electronic structure of carbon nanotubes with defects, generated by chemical and physical ways
Alexander Shikin	St. Petersburg State University	Effects of spin-orbit coupling on quantum-well and surface states in ultrathin Mg-films on W(110) and Mo(110).
Alexander Shikin	St. Petersburg State University	Role of features of electronic structure of substrate in development of QSW's in adsorbed films
Alexander Vinogradov	St. Petersburg State University	Electronic structure and features of chemical bonding for various nickel (II) porphyrinic complexes studied by X-ray absorption and photoemission
Alexander Vinogradov	St. Petersburg State University	The comparative study of titanium fluorides, TiF ₃ and TiF ₄ , with x-ray absorption and resonant photoemission at the Ti 2p and F 1s absorption edges
Alexei Erko	BESSY GmbH	Crystals of Langasite Family: New X-Ray Monochromators and Modulators
Alexei Nefedov	Ruhr-Universität Bochum	Coexistence of ferromagnetism and antiferromagnetism in Fe-doped TiO ₂ : XMCD and XCMS studies
Andreas Eichinger	Technische Universität München	Structure determination of Alpha-1-acid glycoprotein
Andreas Eichinger	Technische Universität München	Structure determination of the carbohydrate recognition domain of langerin
Andreas Heine	Philipps-Universität Marburg	De novo structure determination of Prephenate Dehydratase (PDT)
Andreas Heine	Philipps-Universität Marburg	Finding new lead structures for HIV-Protease
Andreas Heine	Philipps-Universität Marburg	Structural Characterization of Ectoine Hydroxylase (EctD) from Salibacillus Salixigenis
Andreas Heine	Philipps-Universität Marburg	Structure determination of aldose reductase inhibitor complexes
Andreas Heine	Philipps-Universität Marburg	Structure-based combinatorial library design for serine proteases
Andreas Klein	Technische Universität Darmstadt	Interfaces of Ceramics
Andreas Koitzsch	IFW Dresden	Low energy electronic structure of the heavy fermion superconductors Ce(M=Co,Rh,Ir)In ₅
Andrei Varykhalov	BESSY GmbH	Carbon-induced faceting of Ni(771): chemical state, geometry and electronic properties of graphite monolayers
Andrei Varykhalov	BESSY GmbH	Electronic structure of catalytically active Au bilayers
Andrei Varykhalov	BESSY GmbH	Photoelectron diffraction on metallic nanogratings
Andrei Varykhalov	BESSY GmbH	Self-organized nanostructures on stepped surface carbide
Andrei Varykhalov	BESSY GmbH	Valence transitions in nanostructures of rare-earth metals
Andrey Ionov	Russian Academy of Sciences	Investigation of electronic structure of clean and metal decorated vicinal Si surfaces.
Andrey Kaul	Moskow State University	Electronic Structure Investigation of Magnetic d-Metal-Doped ZnO Films by X-Ray Photoemission Spectroscopy and X-Ray Absorption Spectroscopy
Andrzej Wieckowski	University of Illinois at Urbana-Champaign	Studies of Novel Catalysts for New Generation Fuel Cells by Synchrotron High-Resolution XPS
Armin Hoell	Hahn-Meitner-Institut Berlin GmbH	ASAXS investigation of the nucleation of AgCl particles in photochromic sodium borate glass.
Armin Hoell	Hahn-Meitner-Institut Berlin GmbH	Component test of the new SAXS instrument installed at the 7T-Wiggler mags beamline
Armin Hoell	Hahn-Meitner-Institut Berlin GmbH	Element-sensitive study of the nano-structure of Ruthenium and Iron based catalysts by ASAXS
Armin Kleibert	Universität Rostock	X-ray magnetic linear dichroism in resonant absorption and reflection of soft X-rays
Arnaldo de Brito	Laboratorio Nacional de Luz Sincrotron	Laser cooling ion recoil momentum spectroscopy using synchrotron excitation
Arne Smalas	University of Tromsø Norwegian Structural Biology Centre	Structural genomics studies of Vibrio salmonicida. A grouped Beam Time application form The Norwegian Structural Biology Centre (NorStruct), University of Tromsø, Norway.
Arne Smalas	University of Tromsø Norwegian Structural Biology Centre	Structure studies of human receptor for activated C-kinase (RACK1) and human spectrin: Beam time application form The Norwegian Structural Biology Centre (NorStruct), University of Tromsø, Norway, in collaboration with Department of Molecular Biology, University of Bergen, Norway.
Arne Smalas	University of Tromsø Norwegian Structural Biology Centre	Structure-function studies of domains extending from the catalytic domain of peptidases, part of the structural genomics study of Vibrio salmonicida. Beam time application form The Norwegian Structural Biology Centre (NorStruct), University of Tromsø, Norway.
Arno Ehresmann	Universität Kassel	Spectroscopy of doubly excited states in Xe close to the 5s-electron ionization threshold
Astrid Haibel	Deutsches Elektronen-Synchrotron DESY	Quantitative Analysis of Thixotropic Aluminium and Magnesium Alloys by Holographic Synchrotron Tomography
Astrid Haibel	Deutsches Elektronen-Synchrotron DESY	Synchrotron Tomographic Investigations of Sintering Mechanisms
Axel Knop-Gericke	Fritz-Haber-Institut der Max-Planck-Gesellschaft	Oxidative Dehydrogenation of Alkanes using Vanadium and Chromium Based Catalysts
Axel Knop-Gericke	Fritz-Haber-Institut der Max-Planck-Gesellschaft	Preferential oxidation of CO over supported and alloy catalysts in H ₂ -rich gas for fuel cell applications

Axel Knop-Gericke	Fritz-Haber-Institut der Max-Planck-Gesellschaft	Propylene and propane oxidation to acrylic acid on Mo based model catalysts
Axel Knop-Gericke	Fritz-Haber-Institut der Max-Planck-Gesellschaft	Study of propylene epoxidation on chlorine modified Silver surfaces.
Ben Schuler Ben Schuler Bernd Hillemeier	Universität Zürich Universität Zürich Technische Universität Berlin	Elementary processes of protein folding and collapse using microfluidic mixing Microfluidic mixing devices for rapid protein folding kinetics with SRCD Eigenschaftsoptimierung von Porenbeton durch Kurzfaserverstärkung
Bernd Jenichen	Paul-Drude-Institut für Festkörperelektronik	Phase transition in small MnAs disks on GaAs(001)
Bernd Winter	Max-Born-Institut für Nichtlineare Optik und Kurzzeitspektroskopie	Photoelectron Spectroscopy at Liquid Aqueous Surfaces
Bernhard Lendl Berthold Borucki	Technische Universität Wien Freie Universität Berlin	Investigation of small water clusters in ionic liquids with Terahertz radiation Conformational changes in the formation of the activated state in bacterial photoreceptor proteins detected with UV Circular Dichroism
Berthold Borucki	Freie Universität Berlin	Structural Changes in the Photoreceptors Phytochrome and Photoactive Yellow Protein detected with UV Circular Dichroism
Birgit Kanngießer C. Laubschat	Technische Universität Berlin Technische Universität Dresden	3D Micro X-ray Fluorescence Spectroscopy at the μSpot beamline Spin-resolved photoemission experiments on Y/Co multilayers and YCo ₂ (111) thin films. Project Leader: Dr. Yu. S. Dedkov, Prof. Dr. C. Laubschat (TU Dresden).
Carla Vogt	Leibniz Universität Hannover	Characterization of organic structures in marine biomineralization products with spatially resolved Synchrotron-FTIR-spectroscopy
Carla Vogt	Leibniz Universität Hannover	High resolution analysis of organic structures in corrosion layers of implanted alloys with high resolution
Carla Vogt	Leibniz Universität Hannover	Spatially resolved analysis of organic and inorganic functionalities and compounds within micro scaled biological hard tissues of three different marine species with synchrotron-based IR-microspectroscopy
Carsten Winkler	Max-Planck-Institut für Mikrostrukturphysik	Two-Electron Photoemission (g _{2e}) from Solids
Carsten Winkler	Max-Planck-Institut für Mikrostrukturphysik	Two-electron photoemission from surfaces
Catherine Amiens Chhayabrita Biswas Chhayabrita Biswas Chhayabrita Biswas Chiara Renghini	LCC-CNRS BESSY GmbH BESSY GmbH BESSY GmbH Universit� Politecnica delle Marche	Magnetic properties of chemically synthesized ultrafine iron nanoparticles Antiferromagnetic band structure of an Fe monolayer Electronic structure and magnetic properties of Mn adlayers on Au(111) Evolution of pseudogap in Al-based Hume-Rothery alloys. Characterization of nano-hydroxyapatite coatings on titanium for tissue engineering applications.
Christian Freund	Forschungsinstitut f�r Molekulare Pharmakologie	SMY2-GYF domain in complex with ligand
Christian Pettenkofer Christian Pettenkofer Christian Pettenkofer Christian Sch��ler-Langeheine Christian Sch��ler-Langeheine Christian Sch��ler-Langeheine Christian Stamm	Hahn-Meitner-Institut Berlin GmbH Hahn-Meitner-Institut Berlin GmbH Hahn-Meitner-Institut Berlin GmbH Universit�t zu K�ln Universit�t zu K�ln Universit�t zu K�ln BESSY GmbH	Angular resolved photoemission on cleaved ZnO surfaces XPEEM at CuInS ₂ /ZnO interfaces XPEEM investigation of CIGSE absorber films Charge and orbital order in Fe ₃ O ₄ films Ni-K-edge resonant diffraction from stripes in La _{2-x} Sr _x NiO ₄ Probing orbital order in Fe ₃ O ₄ using resonant soft x-ray diffraction Dynamic investigation of antiferromagnetic-ferromagnetic transition in FeRh upon ultrafast laser heating
Christina Divne	AlbaNova University Center	Structural studies on glycosyl transferases and hydrolases involved in biosynthesis of plant cell walls in Populus.
Christine Boeglin Christine Knabe	Universit� Louis Pasteur Strasbourg Universit�tsklinikum Charit�	Exchange coupled oxide layers NiO / Cu-wedge/ Fe ₃ O ₄ (111). Synchrotron-tomography on regenerated bone tissue using rapidly resorbable bone substitute materials applying the Guided Bone Regeneration technique (Extension of proposal granted in 2005, i.e. for additional beam time in 2006)
Christof W�ll Christoph Bostedt Christoph Cobet	Ruhr-Universit� Bochum Technische Universit�t Berlin ISAS - Institutsteil Berlin	NEXAFS-characterisation of Metal-Organic Frameworks deposited on surfaces Photoelectron spectroscopy of size-selected and neutral diamond clusters Characterization of AlN/GaN crystals and layer structures by means of synchrotron ellipsometry
Christoph Genzel	Hahn-Meitner-Institut Berlin GmbH	Depth resolved X-ray residual stress analysis in CVD multi-layer hard coatings by angle-dispersive diffraction
Christoph Genzel	Hahn-Meitner-Institut Berlin GmbH	Depth resolved X-ray residual stress analysis in layered structures by means of the low incidence beam angle method (LIBAD)
Christoph Genzel Christoph Genzel	Hahn-Meitner-Institut Berlin GmbH Hahn-Meitner-Institut Berlin GmbH	Development of the stress scanning method Energy dispersive residual stress analysis in multilayer structures on the basis of the sin ² psi - technique
Christoph Genzel Christoph Genzel	Hahn-Meitner-Institut Berlin GmbH Hahn-Meitner-Institut Berlin GmbH	Layer thickness analysis by high resolution white beam diffraction Locally resolved residual stress analysis in hard coating multi-layer systems by means of energy dispersive diffraction
Christoph Genzel	Hahn-Meitner-Institut Berlin GmbH	Optimization of stress scanning experimental setup
Christoph Genzel	Hahn-Meitner-Institut Berlin GmbH	Residual stress gradient analysis by energy-dispersive diffraction - depth profiling by variation of the scattering angle 2theta
Christoph Hartnig	Zentrum f�r Sonnennenergie- und Wasserstoff-Forschung	Investigation of fuel cells components by means of synchrotron radiography and tomography
Christoph Hartnig	Zentrum f�r Sonnennenergie- und Wasserstoff-Forschung	Investigation of water evolution in operating fuel cells by means of in situ synchrotron radiography
Christophe Cartier Christophe Dejugnat	Universit� Pierre et Marie Curie Institut de Chimie S�parative de Marcoule	Magnetic moment on the ligand in molecular-based magnets. Direct quantitative characterization of polyelectrolyte microcapsules in water by soft X-ray microscopy
Claudia Felser	Johannes-Gutenberg-Universit�t Mainz	High energy photoemission and spin polarised photoemission from Heusler compounds
Claus Schneider	Forschungszentrum J�lich GmbH	MAGNETIC CHARACTERISTICS OF EPITAXIAL GE FILMS DOPED WITH MN AND FE (CRG-project of FZ-J�lich)
Claus Schneider	Forschungszentrum J�lich GmbH	Magnetodynamics of single-crystalline magnetic microstructures

Constanze Donner	Freie Universität Berlin	Underpotential deposition of different metal layers supported by adsorbed thymine on Au(111)
Danielle Dowek	Centre Universitaire Paris-Sud	Vector Correlation studies and nondipole effects, in K-shell photoionisation of small molecules in gas phase: molecular frame electron angular distributions (MFPADS) and circular dichroism.
Dante Gatteschi David Batchelor	Laboratory of Molecular Magnetism Universität Würzburg	XMCD of Self-Assembled Monolayers of Mn12 clusters on surfaces Commissioning the UFF-CRG beamline with new SCIENTA hemispherical electron analyser for parallel XANES and PES experiments
David Cobessi	Ecole Supérieure de Biotechnologie de Strasbourg UMR7100	Structural studies of FpvAl from Pseudomonas aeruginosa PAO1
David Ensling	Technische Universität Darmstadt	Electronic structure of ion conducting thin film materials $\text{Li}_x(\text{Ni}_y\text{Co}_{1-y})_1\text{-zMn}_2\text{O}_2$ in situ prepared by PE-MOCVD used as cathodes in Lithium ion batteries
David Ensling	Technische Universität Darmstadt	High resolution in situ XPS and XAS studies of the influence of repeated electrochemical Li intercalation/deintercalation on the chemical composition and on the electronic structure of $\text{LiNi}_x\text{Co}_{1-x}\text{O}_2$, $\text{Li}(\text{Fe},\text{CO};\text{Mn})\text{PO}_4$ cathode and C:SiCN anode materials (SFB 595, AK Ionenleiter)
David Ensling	Technische Universität Darmstadt	In situ UPS and ResPES characterization of the electronic structure of electrochemically modified sputtered oxide films
David Ensling	Technische Universität Darmstadt	SXPS and XAS on electrochemically modified $\text{Li}_2\text{Ni}_x\text{Co}_{1-x}\text{O}_2$ thin film surfaces deposited by PEMOCVD
Detlef Schmitz	Hahn-Meitner-Institut Berlin GmbH	Exchange bias and the role of uncompensated Fe spins in epitaxially grown fcc $\text{Fe}_x\text{Mn}_{1-x}$ at the interface to Co
Detlef Schmitz	Hahn-Meitner-Institut Berlin GmbH	Exchange bias and uncompensated spins of Co/FeMn bilayers: a comparison of epitaxially grown with sputtered samples
Dieter Scharnweber	Technische Universität Dresden	3-D analysis of bone structures to analyse the healing behaviour of bone in an osteoporotic animal model ζ influence of artificial extracellular matrices and hormone replacement therapy
Dieter Schmeißer	Brandenburgische Technische Universität Cottbus	Organische Ferroelektrika für nichtflüchtiger Speicher
Dieter Schmeißer	Brandenburgische Technische Universität Cottbus	Photoelektronenspektroskopie an Pr-O-N-Schichten: Dielektrika für 4H- und 3C- SiC Oberflächen
Dietrich Zahn	Technische Universität Chemnitz	Molecular Interactions in Organic Ultra Thin films Studied by VUV Spectroscopic Ellipsometry
Dietrich Zahn	Technische Universität Chemnitz	Multi-User-STage for ANGular resolved photoemission MUSTANG-Hochleistungsmessplatz bei BESSY
Dietrich Zahn	Technische Universität Chemnitz	Structural and Electronic Properties of Highly Ordered, Ultra-thin Organic Semiconductor Layers on Vicinal Silicon Surfaces
Dimitrios Argyriou Dirk Heinz	Hahn-Meitner-Institut Berlin GmbH Gesellschaft für Biotechnologische Forschung	Sodium ordering in Na_xCoO_2 and its relation to $\text{Co}^{3+}/\text{Co}^{4+}$ charge ordering InIB / Met complex
Ditlev Brodersen Dmitry Zemlyanov Eberhard Goering	Aarhus University University of Limerick Max-Planck-Institut für Metallforschung	Structure of the yeast nuclear exosome Reactivity of different palladium oxide phases towards CH_4 , C_2H_4 and CO Investigation of the interfacial coupling and magnetization in ferromagnet/antiferromagnet heterostructures by resonant magnetic reflectometry.
Eberhard Goering Eberhard Umbach Eberhard Umbach	Max-Planck-Institut für Metallforschung Universität Würzburg Universität Würzburg	XMCD in Co and Li doped ZnO Comissioning time- UE52-PGM Soft X-Ray Dispersive measurements: Pilot Setup High resolution electron spectroscopy with the aberration corrected SMART-spectromicroscope
Eberhard Umbach Eberhard Umbach Eberhard Umbach	Universität Würzburg Universität Würzburg Universität Würzburg	High-resolution NEXAFS experiments on large organic molecules in the gasphase Resonant Auger studies of Transition metal Phthalocyanines Spectroscopic investigation of organic thin films for the use in organic electronic devices
Eckart Rühl	Freie Universität Berlin	Elektronische Eigenschaften von freien, massenselektierten Nanopartikeln im Bereich der Innerschalenanregung
Eckart Rühl	Freie Universität Berlin	Investigation of the X-ray magnetic circular dichroism of dilute magnetic II-VI semiconductor nanoparticles
Eckart Rühl Eckart Rühl Eckart Rühl	Freie Universität Berlin Freie Universität Berlin Freie Universität Berlin	Multicoincidence Experiments on Core-Excited Covalent Clusters Structural and Electronic Properties of Free II-VI-Semiconductor Nanoparticles X-ray Excited Optical Luminescence of Structured II-VI-Semiconductor Nanoparticles
Eleni Paloura	Aristotle University of Thessaloniki	micro-XRF and micro-XAFS study of Zn- and Fe-contaminated vitrified industrial wastes.
Eleni Paloura Emad Aziz Bekhit	Aristotle University of Thessaloniki BESSY GmbH	Study of vitrified industrial wastes by i-XRF and i-XAFS Ion pair formation in Electrolytes and Transition Metal Complexes with Biomolecules
Emily Alice Kroeger	Fritz-Haber-Institut der Max-Planck- Gesellschaft	Photoelectron diffraction of adsorbed atoms, molecules and ultra-thin films
Enrique Ortega Enrique Ortega	NanoPhysics Lab San Sebastian NanoPhysics Lab San Sebastian	One-dimensional, supramolecular assemblies on vicinal surfaces Spectroscopic characterization of one-dimensional supramolecular assemblies on vicinal surfaces
Erhard Kemnitz	Humboldt-Universität zu Berlin	Optical constants in the UV wavelength range of chemically deposited thin fluoride films
Eric Beaurepaire	Université Louis Pasteur Strasbourg	Ultrafast precessional dynamics excited by femtosecond laser pulses in ferromagnetic nanoparticles
Ernst Pernicka Eugen Baitinger	Eberhard Karls Universität Tübingen Chelyabinsk State Pedagogical University	Analysis of metallic inclusions in archaeological gold from Romania using SR-XRF Study of features of shake up process in modified carbon nanotubes by X-ray photoelectron spectroscopy
Eugen Weschke Eugen Weschke Eugen Weschke Eugen Weschke Evelina Domashevskaya Fabrice Scheurer	Freie Universität Berlin Freie Universität Berlin Freie Universität Berlin Freie Universität Berlin Voronezh State University Université Louis Pasteur Strasbourg	Electronic structure of 3d transition metal monoxide thin films Electronic structure of MgO films Layer-resolved magnetization in EuTe films Magnetic correlations in $\text{HoNi}_2\text{B}_2\text{C}$ bulk and thin films XANES investigation of SnO_x nanostructures with metallic tin nanoparticles. Can Rhodium nanoclusters be magnetic ?

Florin Radu	BESSY GmbH	Reversal behavior of bulk AF spins and rotatable AF spins at the interface of exchange biased bilayers.
Francisco Garcia-Moreno	Technische Universität Berlin Fakultät III Prozesswissenschaften	Decomposition and oxidation behaviour of ZrH ₂ powder for metal foaming
Frank Schumann	Max-Planck-Institut für Mikrostrukturphysik	Energy correlation in two-electron photoemission from solids
Frank Schumann	Max-Planck-Institut für Mikrostrukturphysik	Energy correlation in Two-Electron Photoemission from Surfaces
Frank Wien Franz Bartl	Synchrotron Soleil Universitätsklinikum Charité	Investigations into structural stabilities of soluble proteins by SRCD FTIR spectroscopic investigations of the biological signal transduction in rhodopsin and of the dynamic of hydrogen bonds
Fredrik Ekström	Swedish Defense Research Agency, Division of NBC Defense	Crystallographic studies of the inhibition and reactivation of acetylcholinesterase inhibited by fenamifos and methamidfos
Friedmar Senf Georg Held	BESSY GmbH University of Reading	Blazed gratings for sub-nm wavelength Characterising chiral interfaces using synchrotron radiation: cysteine adsorption on Cu(531)
Georg Prümper	Tohoku University	Circular dichroism in the photo-fragmentation of core-excited methyloxirane studied by momentum resolved ion spectroscopy.
Georg Schulz Georg Schulz	Universität Freiburg Universität Freiburg	Apocarotenoid cleavage oxygenase ACO Complex of aminopeptidase from <i>Aeromonas proteolytica</i> with the inhibitor mycroginin FR1 from <i>Mycrocystis</i> sp.
Georg Schulz Georg Schulz Georg Schulz Georg Schulz Georg Schulz	Universität Freiburg Universität Freiburg Universität Freiburg Universität Freiburg Universität Freiburg	LanGT2 Legionella pneumophila UDP-glucosyltransferase LUGT Porin B Rhamnulose-1-phosphate (RhuA) mutants Structure determination of a complex consisting of PEX19 and the membrane protein PEX3, two human proteins involved in peroxisome biogenesis
Georg Schulz	Universität Freiburg	Structure determination of the N-Oxygenase AurF from <i>Streptomyces thioluteus</i> - molecular basis of N-Oxidation from Aminoarene to Nitroarene in natural products
Georg Schulz	Universität Freiburg	Structure solution of Early B-Cell Factor (EBF), a transcription factor that contains a novel type of DNA-binding domain
Georg Schulz	Universität Freiburg	Structure solution of PorB, a channel forming membrane protein from <i>Corynebacterium glutamicum</i>
Georg Schulz	Universität Freiburg	Structure solution of TAM, a new Tyrosine aminomutase from <i>Chondromyces crocatus</i>
Georg Schulz Georg Schulz George Sheldrick	Universität Freiburg Universität Freiburg Max-Planck-Institut für Biophysikalische Chemie	Tyrosine aminomutase (TAM) Urocanate hydratase (urocanase), engineered BioXhit test crystal project
Gerardo Garcés	CENIM, C.S.I.C.	ANISOTROPY OF THE RESIDUAL STRAIN IN Mg and Mg ALLOYS COMPOSITES
Gerd Reichardt Gerd Schneider Gerd Schneider Gerd Schneider Gerd Schneider	BESSY GmbH BESSY GmbH BESSY GmbH BESSY GmbH BESSY GmbH	Determination of higher order contamination at U125/2-NIM In-situ x-ray microscopy studies of electromigration in copper interconnects X-ray microscopy at the U41 X-ray microscopy with a PGM/condenser-system at the UE46-PGM beamline X-ray nano-tomography of higher order chromatin structure in a transcriptionally active domain
Gerd Schoenhense	Johannes-Gutenberg-Universität Mainz	Imaging of magnetic domains by means of MXCD-PEEM from new materials for spintronics
Gianina Gavrila	Technische Universität Chemnitz	Metal-organic semiconductor interfaces: impact of the chemical modification on the electronic properties, chemistry and carrier injection.
Gregers Andersen Hanna-Kirsti S. Leiros	Aarhus University University of Tromsø Norwegian Structural Biology Centre	Structure determination of complement factor 5 Therapeutic approaches to the correction of misfolding mutations in pterin-dependent enzymes. Crystallographic analysis of phenylalanine hydroxylases (PAH) from <i>Colwellia psycherythraea</i> and <i>Chloroflexus aurantiacus</i> , cold and warm adapted bacteria, respectively.
Hans Bartunik	Max-Planck-Arbeitsgruppen fuer Strukturelle Molekularbiologie	Catalytic reaction mechanisms of shikimate pathway enzymes from <i>M. tuberculosis</i>
Hans Bartunik	Max-Planck-Arbeitsgruppen fuer Strukturelle Molekularbiologie	Mycobacterial proteasome structure
Hans Bartunik	Max-Planck-Arbeitsgruppen fuer Strukturelle Molekularbiologie	Structural analysis of target proteins from <i>Mycobacterium tuberculosis</i>
Hans-Georg Gräber	RWTH Aachen	High Resolution Synchrotron-Tomography On Human Hard Tissue (Enamel) for De- and Remineralization Examinations.
Hans-Joachim Elmers Hans-Joachim Elmers	Johannes-Gutenberg-Universität Mainz Johannes-Gutenberg-Universität Mainz	Correlation of structural and magnetic properties of intermetallic Heusler alloys Magnetic circular dichroism (XMCD) of Heusler Co ₂ FeSi films and Co ₂ FeXMn _{1-x} Si compounds
Hans-Joachim Freund	Fritz-Haber-Institut der Max-Planck- Gesellschaft	Investigation of an aluminum silicate model catalyst
Hans-Peter Steinrück	Universität Erlangen-Nürnberg	In-situ investigation of surface reactions using high-resolution XPS in combination with a supersonic molecular beam
Hans-Peter Steinrück	Universität Erlangen-Nürnberg	Reaction and oxidation on stepped Pt surfaces studied by in-situ high-resolution XPS in combination with a supersonic molecular beam
Hans-Werner Schock Hans-Werner Schock Hartmut Zabel	Hahn-Meitner-Institut Berlin GmbH Hahn-Meitner-Institut Berlin GmbH Ruhr-Universität Bochum	Grazing incidence X-ray diffraction of Cu(In,Ga)Se ₂ thin films In situ growth studies of Cu(In,Ga)(S,Se) ₂ and Cu(Zn,Sn)S ₂ thin films Element-specific characterization of the interface magnetism in Co ₂ MnGe/Al ₂ O ₃ multilayers by x-ray resonant magnetic scattering
Hartmut Zabel	Ruhr-Universität Bochum	Time resolved XRMS studies from patterned magnetic films

Hartmut Zabel Hartmut Niemann Hauke Schollmeyer	Ruhr-Universität Bochum Universität Bielefeld Universität Göttingen	XMCD and XRMS studies of oxide-based diluted magnetic semiconductors Pasteurella multocida Toxin PMT Kinetics, intermediates, and mechanisms of the aggregation of amyloid protein systems
Heiko Peisert	Eberhard Karls Universität Tübingen	Interface properties and electronic structure of specially designed pi-conjugated molecules
Heiko Wende Heiko Wende Heinrich Riesemeier	Universität Duisburg-Essen Universität Duisburg-Essen Bundesanstalt f. Materialforschung und -prüfung	Local Spin-Correlations Close to the Curie Temperature Magnetic and electronic properties of switchable molecules on surfaces Materials research based on Sy- μ CT, Sy-Refracton-Topography, Sy-XRF
Heinrich Riesemeier	Bundesanstalt f. Materialforschung und -prüfung	SAXS/WAXS investigation of disperse systems
Heinz-Eberhard Mahnke	Hahn-Meitner-Institut Berlin GmbH	Small angle X-ray Scattering on ion-beam induced nanostructures in glasses and insulators
Heinz-Eberhard Mahnke Helmut Kühlenbeck	Hahn-Meitner-Institut Berlin GmbH Fritz-Haber-Institut der Max-Planck-Gesellschaft	Study of ion-beam induced nanostructures in glasses and insulators with SAXS Elektronischer Struktur molekularer Schichten auf reinen und modifizierten Oxid-, Karbid- und Nitridsubstraten
Henrik Freydank	Hahn-Meitner-Institut Berlin GmbH	Analysis of residual stress gradients within thin bent metal sheets in order to validate finite-element calculations of the bending process
Hermann Born	Staatliche Museen zu Berlin	Non-Destructive XRF Analysis of the gold and the patina of the so-called „Berlin Gold Hat“ (European Bronze Age ca. 1000 BC)
Hermann Dürr	BESSY GmbH	Excited charge carrier dynamics in doped semiconductor nanocrystallites probed by time resolved x-ray absorption spectroscopy
Hermann Dürr Hermann Dürr	BESSY GmbH BESSY GmbH	Is there a spin-dependent quasiparticle renormalization in 3d ferromagnets? Relationship of anisotropic conductivity and magnetic exchange interaction in dilute magnetic semiconductors
Hermann Dürr Hermann Rossner Holger Dau	BESSY GmbH Hahn-Meitner-Institut Berlin GmbH Freie Universität Berlin	Ultrafast Magnetization Dynamics studied by X-ray Circular Dichroism Investigation of EXAFS and MEXAFS at L-edges of 3d transition metals X-ray absorption spectroscopy on metalloproteins and biomimetic model complexes at KMC1
Holger Ott	Universität zu Köln	Resonant soft x-ray diffraction from defect order in transition-metal oxides
Holger Ott Ian McNulty Ian McNulty Ian McNulty Ignacio Jimenez	Universität zu Köln Advanced Photon Source Advanced Photon Source Advanced Photon Source Instituto de Ciencia de Materiales de Madrid	Resonant x-ray scattering study on the orbital order of Ca ₂ RuO ₄ Characterization of orbital angular momentum states by x-ray holography Feasibility study of hard x-ray coherent scattering Quantification of resolution and signal to noise in nano-scale x-ray holography XANES characterization of fullerene-based materials.
Igor Konovalov Igor Konovalov Ina Reiche	Universität Leipzig Universität Leipzig Centre de Recherche et de Restauration des Musées de France- UMR 171	Defect-induced resonant X-ray photoconductivity in compound semiconductors Ferroelectric semiconductive oxides with perovskite structure Spatially resolved XRF measurements of archaeological objects made of a silver and a gold alloy
Ingar Leiros	University of Tromsø Norwegian Structural Biology Centre	DNA repair in Archaeoglobus fulgidus. Beam Time application from The Norwegian Structural Biology Centre (NorStruct), University of Tromsø, Norway, in collaboration with the Faculty of Science and Technology, University of Stavanger, Norway.
Irene Paola De Padova	Consiglio Nazionale delle Ricerche	Electronic and magnetic properties in Mn _x Ge _{1-x} diluted magnetic semiconductors
Irina Sluchinskaya	Moscow State University	EXAFS studies of local atomic potential for Ge off-center atoms on PbTe and SnTe.
Ivan Powis	University of Nottingham	Photoelectron Circular Dichroism in Core Level Photoemission from Randomly Oriented Chiral Molecules
Ivo Zizak Jacek Biesiadka	BESSY GmbH Freie Universität Berlin	Texture Modification Using Swift Heavy Ions PX-CRG: Crystal structure of RelE and RelB Toxin-Antitoxin (TA) system from M. jannaschii and E. coli
Jacek Biesiadka Jacek Biesiadka Jacek Biesiadka	Freie Universität Berlin Freie Universität Berlin Freie Universität Berlin	PX-CRG: Crystallographic studies of cyanobacterial photosystem II PX-CRG: Crystallographic studies of human major histocompatibility complexes PX-CRG: Structural Studies of an arginine ATP-binding-cassette transporter of the thermophilic bacterium Geobacillus stearothermophilus
Jacek Biesiadka Jacek Biesiadka	Freie Universität Berlin Freie Universität Berlin	PX-CRG: Structure Analysis of the Novel Protease Milin PX-CRG: Structure and mechanism of human lysosomal SA-Proteins and lipid hydrolases
Jacek Biesiadka Jadwiga Bak-Misiuk	Freie Universität Berlin Institute of Physics	PX-CRG: The structure of a primase in complex with a DNA-template Study of non-uniform strain due to dislocations arrays at the GaAs/Si interface by GID.
Jan-Erik Rubensson	BESSY GmbH	Resonant Inelastic Photon Scattering at Double Excitations of Helium in External Fields.
Jan-Erik Rubensson Jan-Erik Rubensson Janina Kneipp	BESSY GmbH BESSY GmbH Bundesanstalt f. Materialforschung und -prüfung	Study of high-efficiency Soft X-ray detectors Two-Color Absorption to Study Double Excitations in Helium Molecular aspects of nanoparticle transfer into eukaryotic cells: In situ studies by synchrotron FTIR microspectroscopy
Janina Kneipp	Bundesanstalt f. Materialforschung und -prüfung	Ultrasensitive spectroscopic investigations of the interaction of nanoparticulate structures with eukaryotic cells
Jean-Louis Gallani Jean-Michel Mariot	Université Louis Pasteur Strasbourg Université Pierre et Marie Curie	2D assemblies of magnetic organic molecules Charge transfer in molecular solids studied by resonant x-ray emission at the C and N 1s edges
JeanPaul Kappler	Université Louis Pasteur Strasbourg	Onset of magnetic properties upon thermal stripping of organo-bimetallic molecules on surfaces
JeanPaul Kappler JeanPaul Kappler Jeroen Goedkoop	Université Louis Pasteur Strasbourg Université Louis Pasteur Strasbourg University of Amsterdam	Role of the 4f-band hybridization in Ce intermetallic systems studied by XMCD XMCD of a single molecule magnet (SMM) Measurement of critical dynamics of Ho thin films in the time domain with Resonant X-ray Intensity Fluctuation Spectroscopy
Joachim Schoenes Joachim Stöckigt	Technische Universität Braunschweig Johannes-Gutenberg-Universität Mainz	Optical Properties of Neodymium-hydride and Uranium-hydride Thin Films 3D-Analysis of perakine reductase

Joachim Tiedemann	Technische Universität Berlin	High ζ resolution tomography investigations of micro-cracks in hard rock
Jochen Geck	University of British Columbia	Coupled sodium, spin and charge order in Na _x CoO ₂ with x=0.5,0.75,0.9
Johan Weigelt	Karolinska Institutet	Structural Genomics on Human Proteins
Johannes Barth	Technische Universität München	Engineering Low-Dimensional Supramolecular Nanostructures at Metal Surfaces
Jongseok Lee	Seoul National University	Infrared microspectroscopy of the field-induced metal-insulator transition in the VO ₂ (2) film
Jongseok Lee	Seoul National University	Searching for the fingerprint of the quantum criticality in the layered Sr ₃ Ru ₂ O ₇ (7) by investigating the c-axis optical response
Jordi Fraxedas	CSIC	Characterization of charge ordering in TTF-derivatives by NEXAFS
José Crespo López-Urrutia	Max-Planck-Institut für Kernphysik	Resonant photon excitation and photoionisation of highly charged ions by synchrotron radiation.
Jozef Keckes	University of Leoben	Residual stress depth profiles in multilayered hard coatings ζ the influence of thermal fatigue.
Jozef Keckes	University of Leoben	Residual Stresses in Thermally Cycled Multilayered Coatings
Juergen Thieme	Universität Göttingen	Combining stereo imaging and elemental mapping to study the dynamics of a colloidal dispersion
Juergen Thieme	Universität Göttingen	X-ray microscopy of cement particles in aqueous dispersion and hydration products
Jürgen Kirschner	Max-Planck-Institut für Mikrostrukturphysik	Spectroscopic determination of the spin structure in bilayers composed metallic antiferromagnetic and ferromagnetic materials
Jürgen Lindner	Universität Duisburg-Essen	Size dependence of the magnetic moments of gas-phase prepared FePt nanoparticles
Kai Fauth	Max-Planck-Institut für Metallforschung	Magnetic properties of anisotropic nanoparticle arrays
Kai Fauth	Max-Planck-Institut für Metallforschung	Magnetism of magnetic wires on vicinal substrates
Kai Fauth	Max-Planck-Institut für Metallforschung	Magnetism of size selected Fe clusters on Pt(111)
Kai Fauth	Max-Planck-Institut für Metallforschung	X-ray fluorescence detection and X-ray emission spectroscopy of buried Co@SiO ₂ nanoparticles
Kai Rosnagel	University of Kiel	Magnetic dichroism in valence band photoemission of iron intercalated transition metal dichalcogenides TiS ₂ and TiTe ₂
Karen Pantleon	Technical University of Denmark	In-situ study of microstructure changes at room temperature and elevated temperatures in nanocrystalline electrodeposits
Karl-Michael Schindler	Martin-Luther-Universität Halle-Wittenberg	Magnetic and Geometric Structures of Transition Metal Oxide Ultrathin Film Systems
Karl-Peter Hopfner	Ludwig-Maximilians-Universität München	Structural studies on proteins in DNA double-strand break repair
Karsten Hinrichs	ISAS - Institutsteil Berlin	Analysis of the bonding geometry of a synthetic biosensor by IR synchrotron mapping ellipsometry
Karsten Hinrichs	ISAS - Institutsteil Berlin	IR micro ellipsometry for analysis of biodiagnostic arrays
Karsten Hinrichs	ISAS - Institutsteil Berlin	IR-Ellipsometry on stimuli-responsive 1D and 2D polymer brushes
Karsten Horn	Fritz-Haber-Institut der Max-Planck-Gesellschaft	Angle resolved photoemission study on a crystalline approximants of Al-Ni-Co
Kieran Hodnett	University of Limerick	A glancing incidence XRD study of the precipitation of Aluminium trihydroxide on steel.
Klaus Ploog	Paul-Drude-Institut für Festkörperelektronik	Analysis of the formation of the interface of praseodymium oxide on Si (001)
Klaus Ploog	Paul-Drude-Institut für Festkörperelektronik	Gd-induced magnetic moment in GaN
Klaus Ploog	Paul-Drude-Institut für Festkörperelektronik	modification of GaAs and AlGaAs growth by codeposition of Sb (surfactant growth)
Klaus Ploog	Paul-Drude-Institut für Festkörperelektronik	Surface, interface and layer structure of iron silicide and iron cobalt silicide during its heteroepitaxy on GaAs
Klaus Rademann	Humboldt-Universität zu Berlin	Formation of optically active nanoparticles in gold and silver doped silicate glasses: ASAXS studies of synchrotron activated growth
Klaus Rademann	Humboldt-Universität zu Berlin	X-ray activation and XANES spectroscopy of gold and silver doped glasses and glassy thin films
Kristina Djinovic Carugo	Universität Wien	X-ray diffraction experiments on repeats 19-21 from human gamma-filamin
Kyle Shen	University of British Columbia	Resonant Coherent X-Ray Spectroholographic Imaging of Colossal Magnetoresistive Manganites
Lada Yashina	Moscow State University	The influence of the non-stoichiometry on the MTe (M=Ge,Sn,Pb) surface reactivity and the atomic-scale mechanism of oxidation
Laurent Duda	Uppsala University	In-situ studies at liquid/solid- and gas/solid-interfaces using resonant soft x-ray emission spectroscopy
Leonard Müller	RWTH Aachen	X-ray photon correlation spectroscopy on premartensitic heterophase fluctuations in shape memory alloys
Leonid Pesin	Chelyabinsk State Pedagogical University	A STUDY OF EMPTY ELECTRONIC STATES IN HIGHLY ORIENTED POLY(VINYLLIDENE FLUORIDE) AND ITS CARBONIZED DERIVATIVES USING SYNCHROTRON RADIATION
Lothar Ley	Universität Erlangen-Nürnberg	Photoelectron spectroscopy on SiC surfaces
Lutz Werner	Universität Kassel	Interferenzeffekte zwischen benachbarten lebensdauererweiterten vibronischen Zuständen der NO (N1s ⁻¹)pi*-Resonanz.
Manfred Stamm	Institut für Polymerforschung Dresden e.V.	Fabrication and Characterization of Hard Magnetic Nanowires Prepared via Polymeric Nanotemplates
Manfred Stamm	Institut für Polymerforschung Dresden e.V.	Fabrication of nanotemplates of metals and conductive polymers
Marc Sacher	Universität Bielefeld	Low temperature surface sensitive X-ray magnetic circular dichroism measurements of Al ₂ O ₃ capped magnetite for the implementation in magnetic tunnel junctions
Marcel Miglierini	Slovak University of Technology	Formation of nanocrystallites in NANOPERM-type alloys
Marcin Klepka	Institute of Physics	Chemical state of minority elements in minerals used for white pigment production
Marcus Bär	University of Nevada Las Vegas	Tailoring buried interfaces in thin film solar cells by organic interlayers and wet-chemical substrate surface treatments - an X-ray emission, photoemission, and X-ray absorption study

Marina Gomoyonova	Russian Academy of Sciences	Reactive and oxide mediated epitaxy of iron silicides on silicon
Mario Birkholz	IHP-Microelectronics	Biomolecules on Semiconductors (Semi-Bio III)
Mario Birkholz	IHP-Microelectronics	Biomolecules on Semiconductors II (Semi-Bio II)
Mario Dähne	Technische Universität Berlin	Electronic structure of silicide nanostructures on high-index silicon surfaces
Mario Dähne	Technische Universität Berlin	Electronic structure of silicide nanowires on Si(001)
Mark Golden	University of Amsterdam	k-space microscopy of quantum electron matter: high Tc superconductors and colossal magnetoresistant maganites.
Mark Golden	University of Amsterdam	k-space microscopy of quantum electron matter: layered colossal magnetoresistant manganates.
Markus Gruyters	Humboldt-Universität zu Berlin	Spin-glass-like behaviour in CoO and the origin of exchange bias in layered CoO/ferromagnet structures
Markus Kühbacher	Hahn-Meitner-Institut Berlin GmbH	Spatial resolved elemental analysis of mutant mice brains serving as models for Parkinsons disease type of neurodegeneration
Markus Kühbacher	Hahn-Meitner-Institut Berlin GmbH	Spectroscopic characterisation of inflammatory bowel diseases with SRFTIR and SRXRF
Markus Rudolph	Universität Göttingen	Structural studies on helicases, isomerases, decarboxylases, and oxidoreductases
Marta Marmiroli	Università degli Studi di Parma	Micro-XANES speciation of Cs within leaves and roots of Arabidopsis thaliana mutants tolerant towards high Cs concentrations
Martha Lux-Steiner	Hahn-Meitner-Institut Berlin GmbH	In-situ monitoring of chemical reactions at interfaces between liquids and chalcopyrite surfaces by x-ray emission spectroscopy
Martin Schwell	Université Paris 12	VUV absorption spectroscopy of planetary molecules at low temperatures
Martin Schwell	Université Paris 12	VUV Photoion Mass Spectrometry of biogenic volatile organic compounds
Martin Götting	Universität Kassel	Analysis of local bending stress distributions for the highly textured Mg-base alloy AZ31 by means of energy dispersive diffraction
Martin Knupfer	IFW Dresden	Spectroscopic investigations on layered cobaltates and one dimensional lithium cuprates
Martin Weinelt	Max-Born-Institut für Nichtlineare Optik und Kurzzeitspektroskopie	Rumpfniveauspektroskopie an photochromen Schaltermolekülen -Azobenzolderivate in "self-assembling monolayers" auf Goldoberflächen (Fortsetzungsantrag)
Martin Weinelt	Max-Born-Institut für Nichtlineare Optik und Kurzzeitspektroskopie	Valenzbandphotoemission an selbstorganisierten Schichten - Azobenzol & Alkanthiole auf Goldoberflächen
Matthias Neeb	BESSY GmbH	Photoelectron spectroscopy on deposited size-selected metal clusters
Matthias Neeb	BESSY GmbH	Photoemission spectroscopy on deposited endohedral fullerene clusters
Max Wilke	Universität Potsdam	U-Th-Pb chemical dating of monazite by con-focal synchrotron-XRF
Michael Krumrey	Physikalisch-Technische Bundesanstalt	PTB Radiometry
Michael Ramsey	Karl-Franzens-Universität Graz	Growth of pentacene heterostructures on single crystalline films of sexiphenyl and sexithiophene
Michael Gajhede	Danish University of Pharmaceutical Sciences	Receptor and intracellular signaling
Michael Gensch	ISAS - Institutsteil Berlin	Chemical Reactions and Stimuli Response in mixed polyelectrolyte brush films
Michael Grunze	Universität Heidelberg	Digital in-line holography with synchrotron radiation: High resolution imaging and spectroscopical aspects
Michael Grunze	Universität Heidelberg	Intracellular Structures
Michael Grunze	Universität Heidelberg	Investigation of metal ions in melanosomes by XRF and XAFS.
Michael Haumann	Freie Universität Berlin	EXAFS on the Mn complex of oxygenic photosynthesis and on relevant model compounds at KMC-1
Michael Kolbe	Physikalisch-Technische Bundesanstalt	PX-CRG: Structural analysis of extracellular components of the TTSS
Michael Kolbe	Physikalisch-Technische Bundesanstalt	PX-CRG: Structural analysis of type three secretion systems
Michael Kolbe	Physikalisch-Technische Bundesanstalt	PX-CRG: Structural aspects of Toll-Reception
Michael Kolbe	Physikalisch-Technische Bundesanstalt	PX-CRG: Structural studies on effector protein complexes from Shigella flexneri
Michael Kolbe	Physikalisch-Technische Bundesanstalt	PX-CRG: Structure of bacterial ion channels
Michael Martins	Universität Hamburg	Magnetic properties of small, size-selected, deposited transition metal clusters
Michael Meyer	Centre Universitaire Paris-Sud	Correlation Effects in the Photoionization of Laser-excited Atoms and Molecules
Michael Meyer	Centre Universitaire Paris-Sud	Relaxation dynamics of inner-shell excited molecules
Michael Meyer	Centre Universitaire Paris-Sud	Symmetry and dissociation dynamics of inner-shell excited molecules
Michael Zharnikov	Universität Heidelberg	Röntgenspektroskopie an biologischen Systemen in nativer Umgebung
Michele Glass-Maujean	Université Pierre et Marie Curie	The hydrogen molecule: determination of the transition moments, dissociation and ionization yields of superexcited states
Michele Ortolani	BESSY GmbH	Conformational changes in Proteins monitored by Time-resolved Terahertz Spectroscopy with Synchrotron Radiation
Michele Ortolani	BESSY GmbH	Far-Infrared measurement of the superconducting gap of MgB2 films in the dirty-limit
Michele Ortolani	BESSY GmbH	Optically-active Terahertz modes in double-stranded DNA
Mihaela Gorgoi	BESSY GmbH	Set-up and test of Si(111) Channel-cut Postmonochromator for High Resolution Investigations at the 7T Wiggler DCM-beamline
Milton Stubbs	Martin-Luther-Universität Halle-Wittenberg	Structure determination of biphenyl synthase
Mitch Loan	University of Limerick	In situ time-resolved diffraction studies of crystallization and dissolution at 250oC and 50 bar pressure
Monika Koch-Mueller	GeoForschungsZentrum Potsdam	Location and quantification of OH in geologically relevant minerals
Monique Dubois	Max-Planck-Institut für Kolloid- und Grenzflächenforschung	COLLOID-NANOPARTICLE INTERACTION: QUANTIFICATION VIA ADSORPTION-DEPLETION EFFECTS DETECTED SOFT X- RAY TOMOGRAPHY
Mont Kumpugdee Vollrath	Technische Fachhochschule Berlin	Study of the structure of shed snake skins which are used as model membranes for medical applications
N. A. Voloshin	Rostov State University	Photoelectron and NEXAFS spectroscopies of spiroyrans
Nikolaus Schwentner	Freie Universität Berlin	High Resolution Study of Vibrational satellites in absorption spectra of Xe and Kr atoms with molecules near the atomic resonance lines.
Nikolaus Schwentner	Freie Universität Berlin	Spectroscopy and photochemical reactions of halogens and rare gases
Nikolay Kardjilov	Hahn-Meitner-Institut Berlin GmbH	Synchrotron-Radiography at Bragg-edges
Norbert Esser	ISAS - Institutsteil Berlin	Grenzflächenbildung organischer Moleküle mit Halbleiteroberflächen: Cyklopenten und Phthalocyanin auf InP(001)
Norbert Esser	ISAS - Institutsteil Berlin	VUV-XUV ellipsometry on polymers
Norbert Koch	Humboldt-Universität zu Berlin	Charge Transfer Type Interaction at Organic/Metal Interfaces
Norbert Krauß	Humboldt-Universität zu Berlin, Charité	PX-CRG Structure analysis of bacterial phytochromes

Norbert Krauß	Humboldt-Universität zu Berlin, Charité	Structure analysis of bacterial [NiFe] hydrogenases and hydrogenase maturation proteins
Olav Hellwig	Hitachi Global Storage Technologies	Imaging the reversal and switching mechanism in prototype patterned media via magnetic Spectro-Holography and resonant soft X-ray scattering
Olav Hellwig	Hitachi Global Storage Technologies	Scattering, SPECKLE and Spectro Holography Studies from Perpendicular Magnetic Multilayers on Nanospheres
Olav Hellwig	Hitachi Global Storage Technologies	Studying magnetic interactions in Ferromagnet/Insulator/Superconductor thin film structures
Olav Hellwig	Hitachi Global Storage Technologies	X-ray Resonant Magnetic Scattering and X-ray Magnetic Circular Dichroism from Perpendicular Hard/Soft Bilayer Systems
Oleg Vyvenko	St. Petersburg State University	X-ray excited deep level capacitance spectroscopy of localized electronic states in semiconductors and semiconductor structures - Capacitance XAFS
Oliver Ernst	Universitätsklinikum Charité	PX-CRG: The crystal structures of proteins involved in visual signal transduction and protein homologues
Oliver Hahn	Bundesanstalt f. Materialforschung und -prüfung	Investigation of Oxidation and Migration Processes of Inorganic Compounds in Ink Corroded Manuscripts
Oliver Henneberg	Universität Potsdam	Diffraction efficiency and long term stability of photosensitive polymer gratings in white x-ray beam
Oliver Rader	BESSY GmbH	Changes in the Fermi surface at the magnetic phase transition of Fe/Cu(100)
Oliver Rader	BESSY GmbH	Electronic states responsible for chain formation in Gd/W(110)
Oliver Rader	BESSY GmbH	Electronic structure of Ga _{1-x} Mn _x As studied by soft x-ray absorption and emission spectroscopy.
Oliver Rader	BESSY GmbH	Fermi surface and surface phonon dispersion of a new hydrogen-induced phase of W(110)
Oliver Rader	BESSY GmbH	Lateral electron quantization at stepped W(320) and related surfaces
Olle Björnehalm	Uppsala University	High resolution photoelectron spectroscopy of free clusters
Oskar Paris	Max-Planck-Institut für Kolloid- und Grenzflächenforschung	Scanning SAXS/WAXS/XRF of biological tissues
Pagona Papakonstantinou	University of Ulster	Local structure of potassium doped fullerene peapods studied by XAS
Paolo Calvani	University of Rome La Sapienza	Search for charge-order excitations in the very-far-infrared conductivity of manganites
Paolo Imperia	Universität Hamburg	Search for XMCD on the N K-edge in molecule-based magnetic materials
Paolo Imperia	Universität Hamburg	XMCD studies of Co/Pt core/shell and Co-Pt mixed clusters prepared by electron beam evaporation deposition
Paolo Imperia	Universität Hamburg	XMCD studies of triangles, rings and cup-like Co nanostructures prepared by nanosphere lithography
Pär Nordlund	Karolinska Institutet	Allosteric regulation and reaction mechanism in class II ribonucleotide reductase
Pär Nordlund	Karolinska Institutet	Crystal structure of RibD
Pär Nordlund	Karolinska Institutet	High throughput structural genomics of membrane proteins
Pär Nordlund	Karolinska Institutet	Human and mouse deoxyribonucleotidases
Pär Nordlund	Karolinska Institutet	Human B ζ /PR61 α subunit of PP2A phosphatase
Pär Nordlund	Karolinska Institutet	Human uridine cytidine kinase 1
Pär Nordlund	Karolinska Institutet	NAD kinase from Escherichia coli
Pär Nordlund	Karolinska Institutet	Structure determination of Hypothetical protein yhaK and tRNA isopentenyltransferase (IPP)
Pascal Lablanquie	Université Pierre et Marie Curie	Highly correlated excitation or multi-photoionisation processes studied by electron spectrometry with a magnetic bottle electron spectrometer Part II: Auger processes in selected atoms (alkali, Hg, ζ) and molecules (HBr, CH ₃ Br, ζ)
Patrick Cramer	Ludwig-Maximilians-Universität München	Structure of multiprotein transcription complexes
Patrick Hoffmann	Brandenburgische Technische Universität Cottbus	Commissioning of U49/2-PGM2
Patrick Hoffmann	Brandenburgische Technische Universität Cottbus	Organic ferroelectric material for non-volatile memories
Peggy Hofmann	Institut für Kristallzüchtung	Small angle x-ray scattering of colloid nutrient solutions for crystal growth.
Peter Baumgärtel	Universität Potsdam	CD spectra of carbohydrates in solution and films below 170 nm
Peter Baumgärtel	Universität Potsdam	Improvement of the UVIS Endstation by Dual Polarization Modulation
Peter Feulner	Technische Universität München	Electronic properties of physisorbed helium
Peter Fratzl	Max-Planck-Institut für Kolloid- und Grenzflächenforschung	Phase contrast enhanced tomography of human tooth dentin
Peter Guttmann	Universität Göttingen	Development of x-ray microscopy at the U41
Peter Klar	Justus-Liebig-Universität Giessen	Local N-environment in Ga(N,V) dilute nitrides (V = P, As, Sb)
Peter Zaumseil	IHP-Microelectronics	In-situ study of the effect of interface structure on the of the hexagonal -> cubic phase transition of Pr ₂ O ₃ films on Si(111) by XRR and GI-XRD
Peter Zimmermann	Technische Universität Berlin	Angular distribution of photoelectrons testing spin-orbit activated interchannel coupling
Peter Zimmermann	Technische Universität Berlin	Dichroism experiments of laserpolarized Mn atoms
Petra Hellwig	Universität Frankfurt	Low-far and far infrared spectroscopic studies on biological molecules using of conventional and synchrotron light sources
Petri Kursula	University of Oulu	Regulation of smooth muscle contraction
Petri Kursula	University of Oulu	Structural comparison of human profilin isoforms and Plasmodium profilin
Philippe Sainctavit	CNRS	Donor impurity band exchange in ferromagnetic oxides
Philippe Wernet	BESSY GmbH	Solute-Solvent Interactions and Hydrogen Bonds in Polar and Non-polar Media Studied by X-ray Absorption Spectroscopy
Philippe Wernet	BESSY GmbH	X-ray Absorption Spectroscopy of Liquids ζ Solute-Solvent Interactions, Hydrogen Bonds and Water
Poul Nissen	Aarhus University	Crystallographic studies of cation pumps
Rainer Fink	Universität Erlangen-Nürnberg	Elektronische Struktur von molekularen Nanomagneteten
Rainer Fink	Universität Erlangen-Nürnberg	NEXAFS investigations of interface-controlled organic thin films
Rainer Fink	Universität Erlangen-Nürnberg	X-Ray microscopy and microspectroscopy of biological objects and organic nanostructures

Rainer Grupp	Hahn-Meitner-Institut Berlin GmbH	In-situ analysis of particle rearrangements during sintering by synchrotron tomography
Rainer Kranold	Universität Rostock	Reversion of silica precipitates in phase separated soda-lime-silica glasses - an in situ high-temperature SAXS study
Rainer Schneider	Hahn-Meitner-Institut Berlin GmbH	In-situ Investigation of Residual Stress Gradients Through the Thickness of Thin Bent Steel Sheets
Ralf Feyerherm	Hahn-Meitner-Institut Berlin GmbH	Interplay of ferroelectricity and magnetism in REMnO ₃ , RE = Tb and Dy
Ralf Feyerherm	Hahn-Meitner-Institut Berlin GmbH	Sodium ordering in Na _x CoO ₂ and its relation to Co ³⁺ /Co ⁴⁺ charge ordering
Ralf Feyerherm	Hahn-Meitner-Institut Berlin GmbH	Study of magnetic ordering of RE in the orthorhombic manganites REMnO ₃ , RE= Tb, Dy by resonant magnetic scattering
Ralf Ficner	Institut für Mikrobiologie und Genetik GZMB	Human Histone Deacetylases
Ralf Ficner	Institut für Mikrobiologie und Genetik GZMB	Nuclear import factor Importin-7
Ralf Ficner	Institut für Mikrobiologie und Genetik GZMB	tRNA-modifying enzyme 2-Thiouridine Synthetase
Ralf Ficner	Institut für Mikrobiologie und Genetik GZMB	UsnRNA-specific m7G-cap Dimethyltransferase (TGS1)
Ralph Claessen	Universität Würzburg	Polarization-dependent x-ray absorption near edge spectroscopy (XANES) on oxyhalogenides
Ralph Puettnner	Freie Universität Berlin	Mechanism of sensor activity: the influence of the initial electromotive force of an electrochemical cell on the H ₂ S chemisorption
Ralph Puettnner	Freie Universität Berlin	Partial cross sections and angular distribution parameters of doubly excited helium
Recardo Manzke	Humboldt-Universität zu Berlin	1T-TiSe ₂ : Semimetal or Semiconductor?
Recardo Manzke	Humboldt-Universität zu Berlin	Energy dependence of one-dimensional electronic structure effects of single and double-layer cuprates Bi(Pb)-2201 and Bi(Pb)-2212
Recardo Manzke	Humboldt-Universität zu Berlin	Modification of the Phase transition of beta-Mo(1-x)W(x)Te(2-y)Se(y)
Recardo Manzke	Humboldt-Universität zu Berlin	Polarisation dependent x-ray absorption of the CuO ₂ -layer of Bi(Pb)-2201
Recardo Manzke	Humboldt-Universität zu Berlin	Röntgenabsorptionsspektroskopie an einkristallinen Lanthan- und Bleidotierten Hochtemperatursupraleitern Bi _{1-2y} Pb _y Sr _{1-2x} La _x CuO _{6+Δ} zur Bestimmung der Löcherkonzentration der CuO ₂ -Ebene
Reinhold Melcher	Universität Erlangen-Nürnberg	Irradiation-induced Changes in Short-Range Order in amorphous Zr-Ti-Cu-Ni-Alloy
Robert Locht	Université de Liège	Photoionization mass spectrometry and fluorescence spectroscopy of organic small molecules.
Robert Seckler	Universität Potsdam	Database, extended ultra-violet circular dichroism spectroscopy on proteins
Robert Seckler	Universität Potsdam	Upgrading of the SRCD Station for time resolved measurements using a microfluidic mixer
Roberta Sessoli	Laboratory of Molecular Magnetism	XMCD of a new Single Molecule Magnet with high spin and coercivity (Continuation)
Roland Stalder	Universität Göttingen	Hydrogen Diffusion and electrical conductivity in pyroxene
Rolf Jürgen Behm	Universität Ulm	In situ X-ray photoelectron spectroscopy of the CO oxidation on supported powder and model Au/TiO ₂ catalysts, influence of the material gap
Rolf Köhler	Humboldt-Universität zu Berlin	X-ray image magnification by asymmetric Bragg reflection
Roman Fedorov	Medizinische Hochschule Hannover	Structural studies of myosins complexed with nucleotide analogs and allosteric inhibitors.
Ronald Kühne	Forschungsinstitut für Molekulare Pharmakologie	ProlinRichMotif (PRM) recognizing domains (PRD) in complex with small molecules
Ru Lin Peng	Linköping University	Synchrotron study of fatigue damage mechanisms for dual-phase materials subjected to ultra-high cycle fatigue
Rüdiger Goldhahn	Technische Universität Ilmenau	Surface preparation of hexagonal InN films
Rüdiger Szargan	Universität Leipzig	Coordination dependence of the electronic structure in hexagonal and cubic ZnMg _{1-x} O films investigated by X-ray absorption, resonant and non-resonant angle dependent X-ray emission
Rudolf Winter	University of Wales Aberystwyth	In-situ ASAXS study of sintering and corrosion of refractory ceramics
Salia Cherifi	CNRS	Magnetic coupling and anisotropy in high T _c GeMn nano-columns
Sankaranarayanan Rajan	Centre for Cellular and Molecular Biology	Structural basis for enantioselectivity switching in an archaeal tRNA synthetase editing domain
Sergei Bozhko	Russian Academy of Sciences	Investigation of ordered low dimensional (1D, 2D) structures on the reconstructed Cu(410) and Cu(100) surfaces
Sergej Borisenko	IFW Dresden	Low energy electron dynamics in YBCO high-T _c superconductors
Sergey Fedoseenko	St. Petersburg State University	Comparative study of Metal Phthalocyanines (MPc, M=Cu,Ni) reactive (nonreactive) substrate interfaces formation studied by high-resolution PES and XAS: the molecular orientation in thin films, electronic structure of the interfaces and Energy Calibration in high-resolution NEXAFS spectroscopy
Sergey Troyanov	Humboldt-Universität zu Berlin	Structural Chemistry of Halogenated Derivatives of Fullerenes
Sergio Valencia Mollina	Freie Universität Berlin	Magneto-Optical Polarization spectroscopy on CMR thin film systems
Serguei Molodtsov	Technische Universität Dresden	Electron correlation effects in Yb and Eu compounds
Serguei Molodtsov	Technische Universität Dresden	Electronic structure of DNA oligonucleotides and fragments interacting with gold contact surfaces
Serguei Molodtsov	Technische Universität Dresden	Photoemission mapping of band structure and Fermi surface of Kondo insulator U ₂ Ru ₂ Sn
Serguei Molodtsov	Technische Universität Dresden	Resonant photoemission study of localization of electronic states in two-dimensional protein templates
Simona Silaghi	ISAS - Institutsteil Berlin	Vacuum Ultra-Violet Spectroscopic Ellipsometry of Spiro-linked Organic Derivatives
Søren Thirup	Aarhus University	Structural studies of the Vps10p domain of human Sortilin.
Spiros Zafeirotos	Fritz-Haber-Institut der Max-Planck-Gesellschaft	Alkenes epoxidation on Cu, Ag and Cu-Ag nanopowder catalysts: a comparative study of the oxidative surface chemistry
Stefan Cramm	Forschungszentrum Jülich GmbH	commissioning of additional Horizontal focusing
Stefan Cramm	Forschungszentrum Jülich GmbH	commissioning for improvements of the beamline: 1)on-the-fly mode 2)in line MXCD setup

Stefan Cramm	Forschungszentrum Jülich GmbH	CRG-Commissioning / improvements of the beamline: 1)improvement of refocussing 2)on-the-fly mode
Stefan Cramm	Forschungszentrum Jülich GmbH	MAGNETIC CHARACTERISTICS OF EPITAXIAL GE FILMS DOPED WITH MN AND FE (CRG-project of FZ-Jülich)
Stefan Cramm Stefan Eisebitt	Forschungszentrum Jülich GmbH BESSY GmbH	Temperature Dependence of the Magnetic Moments in NiMnSb Investigation of the Electronic Structure of Mo6SxI(9-x) Nanowires by Photon-in Photon-out Soft X-ray Spectroscopy.
Stefan Eisebitt Stefan Eisebitt	BESSY GmbH BESSY GmbH	Local Electronic Structure in Electrolyte Solutions Soft x-ray spectroscopy in liquid environments: towards an understanding of the electronic structure in biomolecules
Stefan Eisebitt Stefan Eisebitt Stefan Süllow	BESSY GmbH BESSY GmbH Technische Universität Braunschweig	Soft-X-Ray Photon Correlation Spectroscopy of Critical Fluctuations X-RAY HOLOGRAPHIC IMAGING OF LOW-CONTRAST OBJECTS Interplay between structural properties and electronic ground states in organic superconductors
Stefan Süllow Stephan König	Technische Universität Braunschweig Martin-Luther-Universität Halle-Wittenberg	Structural properties of the heavy fermion superconductor PrOs ₄ Sb ₁₂ Crystal structure of various thiamine diphosphate dependent enzymes in complex with specific ligands
Sudipta Roy Barman	UGC-DAE Consortium for scientific research	Photoemission studies on quasicrystalline adlayers
Svante Svensson	Uppsala University	High Kinetic Energy Core Photoelectron Studies of multilayers, polymer blended-, nanostructured- and related materials
Taisuke Ohta	Fritz-Haber-Institut der Max-Planck-Gesellschaft	Ultrahigh resolution angle resolved photoemission spectroscopy study of graphite
Tanja Gießel	Max-Born-Institut für Nichtlineare Optik und Kurzzeitspektroskopie	Laserinduzierte Bandstrukturänderungen an Halbleiteroberflächen
Thomas Brueckel	Forschungszentrum Jülich GmbH	Challenging the classic model of ionic charge ordering in mixed-valence 3d transition-metal oxides via soft X-ray resonant scattering
Thomas Carell Thomas Elsaesser	Ludwig-Maximilians-Universität München Max-Born-Institut für Nichtlineare Optik und Kurzzeitspektroskopie	Low fidelity DNA polymerases in ternary complexes with lesion containing DNA Ultrafast infrared-pump/x-ray probe spectroscopy of water
Thomas Geue	Paul Scherrer Institut	Formation of 3D colloidal layers on structured substrates from colloidal dispersions
Thomas Leisner	Universität Heidelberg	X-ray Absorption Spectroscopy of Trapped Semiconductor Nanoparticles
Thomas Mayer	Technische Universität Darmstadt	Elementary Processes in Contact Formation at Semiconductor/Electrolyte Interfaces
Thomas Mueller	Universität Würzburg - Biozentrum	Structure analysis of the complex of human Interleukin-5 and its receptor IL-5Ralpha
Thomas Mueller	Universität Würzburg - Biozentrum	Structure of the ternary complex of GDF-5 bound to its receptors BRIB and ActRIIB
Thomas Mueller Thomas Pichler	Universität Würzburg - Biozentrum IFW Dresden	Type I receptor recognition by GDF-5 Exploring the electronic structure of functionalized single-wall and double-wall carbon nanotubes
Thomas Seyller Thomas Seyller Thorsten Kampen	Universität Erlangen-Nürnberg Universität Erlangen-Nürnberg Fritz-Haber-Institut der Max-Planck-Gesellschaft	Graphite overlayers on SiC surfaces Metal overlayers on SiC Isomerization and Chirality
Thorsten Zandt Tobias Fey	Humboldt-Universität zu Berlin Universität Erlangen-Nürnberg	Fermi Surface Mapping an polymorphen MoTe2 Biomorphous SiC-ceramics derived from cellulose and 3D-indirect printed ceramics.
Tobias Lau	Technische Universität Berlin	Change of Valence d-Electron Occupation Numbers in Small Gasphase Copper, Silver, and Gold Clusters
Tobias Lau	Technische Universität Berlin	Electronic structure of free transition metal clusters: Comparison to free atoms, deposited clusters, and solids
Tobias Lau	Technische Universität Berlin	Electronic Structure of Free Transition Metal Clusters: Comparison to Free Atoms, Deposited Clusters, and Solids
Tobias Lau	Technische Universität Berlin	X-Ray Absorption Spectroscopy of Small, Size-selected Transition Metal Clusters on Alkali Metal Surfaces (Continuation of ongoing project BESSY.05.II.ID-140)
Tobias Panzner Tom Tiedje Tonica Valla Tushar Sant Udo Heinemann	Universität Potsdam University of British Columbia Brookhaven National Laboratory Universität Siegen Max-Delbrück-Centrum für Molekulare Medizin	Korrelationspektroskopie mit weißer Synchrotronstrahlung Resonant Coherent X-Ray Imaging of Red Blood Cells Electronic Excitations in Cuprates with Static Spin/Charge Order Energy Dispersive Small Angle X-ray Scattering PX-CRG Proposal: Protein-nucleic acid interaction
Udo Heinemann	Max-Delbrück-Centrum für Molekulare Medizin	PX-CRG: Human proteins of medical and pharmacological relevance
Udo Heinemann	Max-Delbrück-Centrum für Molekulare Medizin	PX-CRG: Proteins involved in vesicle transport & tethering
Udo Heinemann	Max-Delbrück-Centrum für Molekulare Medizin	PX-CRG: Structural analysis of the phytase of Klebsiella Sp. strain ASR1
Udo Heinemann	Max-Delbrück-Centrum für Molekulare Medizin	PX-CRG: Structural determinants of protein folding and stability
Udo Heinemann	Max-Delbrück-Centrum für Molekulare Medizin	Rational Drug Design of Shp-2 Tyrosine Phosphatase Inhibitors
Ulf Kleineberg Ulf Wiedwald	Universität Bielefeld Universität Ulm	Actinic defect inspection of EUVL multilayer mask blanks by EUV-PEEM Non-interacting hardmagnetic FePt Particles: Alignment of the Easy Axes of Magnetization
Ulf Wiedwald	Universität Ulm	Non-interacting L10-ordered FePt Particles: Temperature Dependence of the Magnetic Anisotropy (Ongoing Project)
Ulrich Hillebrecht Ulrich Hillebrecht Ulrich Hillebrecht	Forschungszentrum Jülich GmbH Forschungszentrum Jülich GmbH Forschungszentrum Jülich GmbH	Antiferromagnetic Oxide Micro- and Nanostructures Low Temperature Photoemission Microscopy Magnetization Dynamics in Exchange Coupled Heterostructures

Uwe Hergenbahn	Max-Planck-Institut für Plasmaphysik	Hochaufgelöste Photoelektron ζ Auger-Elektron Koinzidenzspektren von gasförmigen Molekülen
Uwe Hergenbahn Uwe Becker	Max-Planck-Institut für Plasmaphysik Fritz-Haber-Institut der Max-Planck-Gesellschaft	Photoionisation an einem freien Clusterstrahl Highly correlated excitation or multi-photoionisation processes studied by electron spectrometry with a magnetic bottle electron spectrometer Part I: Electron spectroscopy of Helium close to the double ionisation threshold
Uwe Becker	Fritz-Haber-Institut der Max-Planck-Gesellschaft	Photoionisation and -fragmentation of Fullerenes
Uwe Glatzel Vadim Efimov	Universität Bayreuth Joint Institute for Nuclear Research	Determination of crystal structure and transformation temperature of Pt3Al Oxygen K-edge XANES study of Co3+/Co4+ spin state configurations in the La1-xBaxCoO3 and La1-xSrxCo1-x/2Nbx/2O3
Vadim Galakhov	Russian Academy of Sciences - Ural Division	Electronic structure of doped protonic conductors SrCeO ₃ and BaCeO ₃
Vadim Galakhov	Russian Academy of Sciences - Ural Division	Spin and valence states of Co and Mn ions in complex manganese-cobalt oxides determined by means of X-ray absorption spectroscopy
Vadim Sikolenko Vadim Sikolenko Vadim Sikolenko	Hahn-Meitner-Institut Berlin GmbH Hahn-Meitner-Institut Berlin GmbH Hahn-Meitner-Institut Berlin GmbH	Magnetism in Ce2PdGe6 Spin-state and structural phase transitions in La1-xBaxCoO3 system XAFS and XRD studies of La1-xSrxCoO3 and La1-xSrxCo1-x/2Nbx/2O3 (x = 0.0; 0.15; 0.3; 0.5; 0.7 and 1.0) in the low and high temperature regions
Valeri Nazin	Russian Academy of Sciences	UPS study of initial stages of hafnium oxidation and a study Zr-Pd quasicrystal system
Valerii Bukhtiyarov	Boreskov Institute of Catalysis	Study of electronic properties of nano-sized gold clusters and planar and high-surface area aluminas
Valery Mikoushkin	Ioffe Physico-Technical Institute	Fabrication of a system of equal carbon nanoclusters as the first example of dry x-ray nanolithography
Valery Mikoushkin	Ioffe Physico-Technical Institute	X-ray induced Coulomb explosion of bio-molecule
Vera Adamchuk	St. Petersburg State University	Modification of electronic structure of gold and silver nanostructures by growth on clean and oxidized stepped Ni surfaces
Victor Aristov	Russian Academy of Sciences	The complementary study of electronic properties, chemistry and diffusion of metal-organic semiconductor interfaces: Al(Fe, Ti, Ag, Au and Cs) on copper phthalocyanine
Victor Aristov	Russian Academy of Sciences	The study of Fe (Co, Ni) contacts to CuPc single crystal for the potencial development of the OMTF based spin-transistor
Victor Sivkov	Sykytykar state university	Absolute oscillator strength measurements for electron transitions in 2p absorption spectra of Ca- and Sc- compounds.
Volker Ulrich	Max-Planck-Institut für Plasmaphysik	Hochaufgelöste Photoelektron ζ Auger-Elektron Koinzidenzspektren von gasförmigen Molekülen
Wilfried Wurth	Universität Hamburg	Interfaces of semiconductor systems studied by resonant inelastic X-ray scattering and NEXAFS: Interfaces of III-V semiconductor and Lanthanide-phosphate nanoclusters
Wolf-Dieter Schubert	Gesellschaft für Biotechnologische Forschung	Autolysin, a cell-wall modulating virulence factor from Listeria monocytogenes
Wolf-Dieter Schubert	Gesellschaft für Biotechnologische Forschung	Structure-based re-engineering of Internalin - the intestinal invasin of Listeria monocytogenes
Wolf-Dieter Schubert	Gesellschaft für Biotechnologische Forschung	Structure based analysis of SdsA1 mediated sulfate ester cleavage.
Wolfgang Höhne	Humboldt-Universität zu Berlin, Charité	PX-CRG Investigation of protein-ligand interactions in case of complexes of antibody Fab fragments and hydrolytic enzymes
Wolfgang Höhne Wolfgang Kuch	Humboldt-Universität zu Berlin, Charité Freie Universität Berlin	PX-CRG Structure analysis of cyanophycin synthetase II X-ray absorption spectroscopic and spectro-microscopic investigation of adsorbed switchable molecules
Wolfgang Kuch	Freie Universität Berlin	X-ray absorption spectroscopy of magnetic metal/antiferromagnetic oxide interfaces
Wolfgang Kuch	Freie Universität Berlin	Zeit- und lagenaufgelöste Magnetisierungsdynamik in magnetischen Mehrschichtsystemen
Wolfgang Unger	Bundesanstalt f. Materialforschung und -prüfung	NEXAFS of C-, N- and O K-edges of plasma polymerized nano-scaled organic films
Wolfgang Unger	Bundesanstalt f. Materialforschung und -prüfung	NEXAFS of CNO species in complex chemical environments
Wolfgang Unger	Bundesanstalt f. Materialforschung und -prüfung	NEXAFS study of nitrogen-rich plasma- and VUV-deposited polymer-like thin films for biomedical applications
Wolfram Jaegermann Wolfram Jaegermann	Technische Universität Darmstadt Technische Universität Darmstadt	Band gap states at wide band gap semiconductor surfaces and interfaces Studies of Electrochemically Processed Platinum/Ruthenium Catalysts by Synchrotron High-Resolution XPS
Wolfram Jaegermann	Technische Universität Darmstadt	Synchrotron photoelectron spectroscopy of interfaces for silicon/organic hybrid devices
Wolfram Leitenberger Yury Dedkov	Universität Potsdam Technische Universität Dresden	Determination of the spatial coherence properties of hard X-rays Spin-resolved photoelectron spectroscopy study of Ce/ferromagnet systems and intermetallic compounds on the basis of cerium (CeM2, M=Fe, Co, Ni)
Yury Dedkov	Technische Universität Dresden	Project Leader: Dr. Yu. S. Dedkov, Prof. Dr. C. Laubschat (TU Dresden) Spin-resolved photoelectron spectroscopy study of Fe and Co quantum wires on stepped Cu surfaces
Yves Bodenthin	Paul Scherrer Institut	Determination of coordination spheres of metal centres in metallo supramolecular assemblies
Yves Muller Yves Muller	Universität Erlangen-Nürnberg Universität Erlangen-Nürnberg	Allosteric mechanism of Tet-Repressor action Crystal structure determination of progesterone 5beta-reductase from Digitalis lanata.
Yves Muller Yves Muller Zoltan Erdelyi Zoltan Erdelyi	Universität Erlangen-Nürnberg Universität Erlangen-Nürnberg University of Debrecen University of Debrecen	Crystal structure of corticosteroid-binding globulin (CBG) Structure determination of Apolipoprotein M Beginning of the phase growth in Ni-Si system Interface motion during phase growth

List of Publications

- Abad, L., V. Laukhin, S. Valencia, M. Varela, L. Balcells and B. Martínez (2006). "Structural and magnetotransport properties of coherently La₂/3Ca₁/3MnO₃ epitaxial thin films." *Advance in science and technology* **52**.
- Abad, L., B. Martínez, S. Valencia, A. Gaupp, W. Gudat and L. Balcells (2006). "Surface resistance of La₂/3Ca₁/3MnO₃ epitaxial thin films grown on top of LaAlO₃." *Advance in science and technology* **52**.
- Abrahamyan, K., J. Bahr, J. P. Carneiro, K. Flottmann, J. H. Han, M. van Hartrott, M. Krasilnikov, D. Lipka, V. Miltchev, A. Oppelt, B. Petrossyan, D. Pose, D. Richter, S. Schreiber, L. Staykov and F. Stephan (2006). "Experimental characterization and numerical simulations of the electron source at PITZ." *Nuclear Instruments & Methods in Physics Research Section a-Accelerators Spectrometers Detectors and Associated Equipment* **558**(1): 249-252.
- Adamchuk, V. K., A. S. Vinogradov, G. G. Vladimirov, S. L. Molodtsov, G. V. Prudnikova, S. I. Fedoseenko and A. M. Shikin (2006). "Study of nanostructured materials by optical and photoelectron spectroscopy." *Crystallography Reports* **51**(5): 870-880.
- Allegretti, F., S. O'Brien, M. Polcik, D. I. Sayago and D. P. Woodruff (2006). "Quantitative determination of the local structure of H₂O on TiO₂(110) using scanned-energy mode photoelectron diffraction." *Surface Science* **600**(7): 1487-1496.
- Andriyevsky, B., N. Esser, A. Patryn, C. Cobet, W. Ciepluch-Trojanek and M. Romanyuk (2006). "Band structure and UV optical spectra of TGS crystals in the range of 4-10 eV." *Physica B: Physics of Condensed Matter* **373**(2): 328-333.
- Antoniak, C., J. Lindner, M. Spasova, D. Sudfeld, M. Acet, M. Farle, K. Fauth, U. Wiedwald, H. G. Boyen, P. Ziemann, F. Wilhelm, A. Rogalev and S. H. Sun (2006). "Enhanced orbital magnetism in Fe₅₀Pt₅₀ nanoparticles." *Physical Review Letters* **97**(11).
- Aristov, V. Y., O. V. Molodtsova, V. M. Zhilin, D. V. Vyalikh and M. Knupfer (2006). "Characterisation of metal-organic semiconductor interfaces: In and Sn on CuPc." *Journal De Physique Iv* **132**: 101-104.
- Aziz, E. F., J. E. Bugaj, G. Caglar, L. M. Dinkelborg and R. Lawaczeck (2006). "Novel approach in radionuclide tumor therapy: Dose enhancement by high Z-element contrast agents." *Cancer Biotherapy and Radiopharmaceuticals* **21**(3): 181-193.
- Aziz, E. F., M. Freiwald, S. Eisebitt and W. Eberhardt (2006). "Steric hindrance of ion-ion interaction in electrolytes." *Physical Review B* **73**(7).

- Aziz, E. F., A. Zimina, M. Freiwald, S. Eisebitt and W. Eberhardt (2006). "Molecular and electronic structure in NaCl electrolytes of varying concentration: Identification of spectral fingerprints." *Journal of Chemical Physics* **124**(11).
- Bagus, P. S., C. Woll and E. S. Ilton (2006). "A definitive analysis of the Rydberg and valence anti-bonding character of states in the OK-edge of H₂O." *Chemical Physics Letters* **428**(1-3): 207-212.
- Bansmann, J., M. Getzlaff, A. Kleibert, F. Bulut, R. K. Gebhardt and K. H. Meiwes-Broer (2006). "Mass-filtered cobalt clusters in contact with epitaxially ordered metal surfaces." *Applied Physics a-Materials Science & Processing* **82**(1): 73-79.
- Bär, M., A. Ennaoui, J. Klaer, T. Kropp, R. Sáez-Araoz, S. Lehmann, A. Grimm, I. Lauermann, C. Loreck, S. Sokoll, H.-W. Schock, C.-H. Fischer, M. C. Lux-Steiner and C. Jung (2006). "Intermixing at the heterointerface between ZnS/Zn(S,O) bilayer buffer and CuInS₂ thin film solar cell absorber." *Journal of Applied Physics* **100**(6).
- Bar, M., J. Reichardt, I. Sieber, A. Grimm, I. Kotschau, I. Lauermann, S. Sokoll, M. C. Lux-Steiner, C. H. Fischer and T. P. Niesen (2006). "ZnO layers deposited by the ion layer gas reaction on Cu(In,Ga)(S,Se)₂ thin film solar cell absorbers: Morphology, growth mechanism, and composition." *Journal of Applied Physics* **100**(2).
- Barra, M., M. Haumann, P. Loja, R. Krivanek, A. Grundmeier and H. Dau (2006). "Intermediates in assembly by photoactivation after thermally accelerated disassembly of the manganese complex of photosynthetic water oxidation." *Biochemistry* **45**(48): 14523-14532.
- Barth, S., S. Marburger, S. Joshi, V. Ulrich, O. Kugeler and U. Hergenbahn (2006). "Interface identification by non-local autoionization transitions." *Physical Chemistry Chemical Physics* **8**(27): 3218-3222.
- Barth, S., S. Marburger, O. Kugeler, V. Ulrich, S. Joshi, A. M. Bradshaw and U. Hergenbahn (2006). "The efficiency of Interatomic Coulombic Decay in Ne clusters." *Chemical Physics* **329**(1-3): 246-250.
- BenMoussa, A., J. F. Hochedez, U. Schuehle, W. Schmutz, K. Haenen, Y. Stockman, A. Soltani, F. Scholze, U. Kroth, V. Mortet, A. Theissen, C. Laubis, M. Richter, S. Koller, J. M. Defise and S. Koizumi (2006). "Diamond detectors for LYRA, the solar VUV radiometer on board PROBA2." *Diamond and Related Materials* **15**(4-8): 802-806.
- BenMoussa, A., U. Schuehle, F. Scholze, U. Kroth, K. Haenen, T. Saito, J. Campos, S. Koizumi, C. Laubis, M. Richter, V. Mortet, A. Theissen and J. F. Hochedez (2006). "Radiometric characteristics of new diamond PIN photodiodes." *Measurement Science & Technology* **17**(4): 913-917.

- BenMoussa, A., A. Theissen, F. Scholze, J. F. Hochedez, U. Schule, W. Schmutz, K. Hawnen, Y. Stockman, A. Soltani, D. McMullin, R. E. Vest, U. Kroth, C. Laubis, M. Richter, V. Mortet, S. Gissot, V. Delouille, M. Dominique, S. Koller, J. P. Halain, Z. Remes, R. Petersen, M. D'Olieslaeger and J. M. Defise (2006). "Performance of diamond detectors for VUV applications." *Nuclear Instruments & Methods in Physics Research Section a-Accelerators Spectrometers Detectors and Associated Equipment* **568**(1): 398-405.
- Berkebile, S., G. Koller, G. Hlawacek, C. Teichert, F. P. Netzer and M. G. Ramsey (2006). "Diffusion versus sticking anisotropy: Anisotropic growth of organic molecular films." *Surface Science* **600**(24): L313-L317.
- Bernhardt, R. (2006). Dreidimensionale Charakterisierung der Osseointegration von Titanimplantaten mittels Mikrocomputertomographie, TU Dresden.
- Bernhardt, R., D. Scharnweber, B. Müller, F. Beckmann, J. Goebbels, J. Jansen, H. Schliephake and H. Worch (2006). 3D analysis of bone formation around titanium implants using micro computed tomography (µCT). *Progress in Biomedical Optics and Imaging - Proceedings of SPIE*.
- Biswas, I., H. Peisert, L. Zhang, T. Chasse, M. Knupfer, M. Hanack, D. Dini, T. Schmidt and D. Batchelor (2006). "Orientation of differently substituted phthalocyanines: First layers and thin films." *Molecular Crystals and Liquid Crystals* **455**: 241-249.
- Blume, R., M. Havecker, S. Zafeirotos, D. Teschner, E. Kleimenov, A. Knop-Gericke, R. Schlogl, A. Barinov, P. Dudin and M. Kiskinova (2006). "Catalytically active states of Ru(0001) catalyst in CO oxidation reaction." *Journal of Catalysis* **239**(2): 354-361.
- Bodenthin, Y. (2006). Molekularer Magnetismus in Metallo-supramolekularen Funktionseinheiten, Universität Siegen.
- Borisenko, S. V., A. A. Kordyuk, A. Koitzsch, J. Fink, J. Geck, V. Zabolotnyy, M. Knupfer, B. Buchner, H. Berger, M. Falub, M. Shi, J. Krempasky and L. Patthey (2006). "Parity of the pairing bosons in a high-temperature Pb-Bi₂Sr₂CaCu₂O₈ bilayer superconductor by angle-resolved photoemission spectroscopy." *Physical Review Letters* **96**(6).
- Borisenko, S. V., A. A. Kordyuk, V. Zabolotnyy, J. Geck, D. Inosov, A. Koitzsch, J. Fink, M. Knupfer, B. Buchner, V. Hinkov, C. T. Lin, B. Keimer, T. Wolf, S. G. Chiuzbaian, L. Patthey and R. Follath (2006). "Kinks, nodal bilayer splitting, and interband scattering in YBa₂Cu₃O_{6+x}." *Physical Review Letters* **96**(11).
- Bovet, N., D. I. Sayago, F. Allegretti, E. A. Kroger, M. J. Knight, J. Barrett, D. P. Woodruff and R. G. Jones (2006). "The adsorption of CCl₄ on Ag(111): Carbene and C=C bond formation." *Surface Science* **600**(2): 241-248.
- Bradeanu, I. L., R. Flesch, N. Kosugi, A. A. Pavlychev and E. Ruhl (2006). "C 1s → π* excitation in variable size benzene clusters." *Physical Chemistry Chemical Physics* **8**(16): 1906-1913.

- Braun, W., G. Gavrilu, M. Gorgoi and D. R. T. Zahn (2006). "Influence of the molecular structure on the interface formation between magnesium and organic semiconductors." *Radiation Physics and Chemistry* **75**(11): 1869-1871.
- Buermann, L., B. Grosswendt, H. M. Kramer, H. J. Selbach, M. Gerlach, M. Hoffmann and M. Krumrey (2006). "Measurement of the x-ray mass energy-absorption coefficient of air using 3 keV to 10 keV synchrotron radiation." *Physics in Medicine and Biology* **51**(20): 5125-5150.
- Bukhtiyarov, V. I., A. I. Nizovskii, H. Bluhm, M. Havecker, E. Kleimenov, A. Knop-Gericke and R. Schlogl (2006). "Combined in situ XPS and PTRMS study of ethylene epoxidation over silver." *Journal of Catalysis* **238**(2): 260-269.
- Busch, I., J. Stumpel and M. Krumrey (2006). "Influence of growth interruption on the formation of solid-state interfaces." *Powder Diffraction* **21**(2): 122-124.
- Calvani, P., M. Ortolani, S. Lupi, U. Schade, A. Perla, M. Fujita and K. Yamada (2006). "Use of coherent synchrotron radiation in a study on cuprates exhibiting superconductivity and charge order." *Infrared Physics & Technology* **49**(1-2): 7-12.
- Camero, M. (2006). Nanostructured carbon and carbon nitride films. A study of the synthesis processes assisted by plasma (Capas de carbono y nitruro de carbono nanoestructuradas. Estudio de los procesos de sintesis asistidos por plasma), Universidad Autonoma de Madrid.
- Canas-Ventura, M. E., F. Klappenberger, S. Clair, S. Pons, K. Kern, H. Brune, T. Strunskus, C. Woll, R. Fasel and J. V. Barth (2006). "Coexistence of one- and two-dimensional supramolecular assemblies of terephthalic acid on Pd(111) due to self-limiting deprotonation." *Journal of Chemical Physics* **125**(18).
- Caretti, I. (2006). Synthesis and characterization of BCN coatings for tribological applications (Sintesis y caracterizacion de recubrimientos BCN para aplicaciones tribologicas), Universidad Autonoma de Madrid.
- Cavalleri, M., L. A. Naslund, D. C. Edwards, P. Wernet, H. Ogasawara, S. Myneni, L. Ojamae, M. Odelius, A. Nilsson and L. G. M. Pettersson (2006). "The local structure of protonated water from x-ray absorption and density functional theory." *Journal of Chemical Physics* **124**(19).
- Chandola, S., J. Jacob, K. Fleischer, P. Vogt, W. Richter and J. F. McGilp (2006). "Optical and electronic properties of Ag nanodots on Si(111)." *Journal of Physics-Condensed Matter* **18**(30): 6979-6986.
- Chebotaryov, S. (2006). "Radiative defluorination of poly (vinylidene fluoride) under soft X-ray radiation." *Radiation Physics and Chemistry* **75**(11): 2024-2028.

- Chen, W., N. Darowski, I. Zizak, G. Schumacher, H. Klingelhofer and W. Neumann (2006). "Lattice distortion in gamma' precipitates of single crystal superalloy SC16 under creep deformation." *Nuclear Instruments & Methods in Physics Research Section B-Beam Interactions with Materials and Atoms* **246**(1): 201-205.
- Cyganik, P., M. Buck, T. Strunskus, A. Shaporenko, J. Wilton-Ely, M. Zharnikov and C. Woll (2006). "Competition as a design concept: Polymorphism in self-assembled monolayers of biphenyl-based thiols." *Journal of the American Chemical Society* **128**(42): 13868-13878.
- Dau, H., W. Kuch and R. Püttner, Eds. (2006). *Freie Universität Berlin - Research with Synchrotron Radiation 2000-2005*. Aachen, Shaker Verlag.
- Dedyulin, S. N. (2006). *Ab initio and experimental study of doped PbTe*, Moscow State University.
- Dembski, S. (2006). *Synthese und Charakterisierung von II-VI-Halbleiter-Nanopartikeln in unterschiedlicher Umgebung*, Universität Würzburg.
- Deniozou, T., N. Esser, T. Schulmeyer and R. Hunger (2006). "A (4x2) surface reconstruction of CuInSe₂(001) studied by low-energy electron diffraction and soft x-ray photoemission spectroscopy." *Applied Physics Letters* **88**(5): 052102-3.
- Denks, I. A., M. Klaus and C. Genzel (2006). Determination of real space residual stress distributions $\sigma_{ij}(z)$ of surface treated materials with diffraction methods Part II: Energy dispersive approach. *Residual Stresses VII*. **524-525**: 37-42.
- Devred, A., B. Baudouy, D. E. Baynham, T. Boutboul, S. Canfer, M. Chorowski, P. Fabricatore, S. Farinon, H. Félice, P. Fessia, J. Fydrych, V. Granata, M. Greco, J. Greenhalgh, D. Leroy, P. Loverige, M. Matkowski, G. Michalski, F. Michel, L. R. Oberli, A. Den Ouden, D. Pedrini, S. Pietrowicz, J. Polinski, V. Previtali, L. Quettier, D. Richter, J. M. Rifflet, J. Rochford, F. Rondeaux, S. Sanz, C. Scheuerlein, N. Schwerg, S. Sgobba, M. Sorbi, F. Toral-Fernandez, R. Van Weelderen, P. Védrine and G. Volpini (2006). "Overview and status of the Next European Dipole Joint Research Activity." *Superconductor Science and Technology* **19**(3): S67-S83.
- Di Castro, D., M. Ortolani, E. Cappelluti, U. Schade, N. D. Zhigadlo and J. Karpinski (2006). "Infrared properties of Mg_{1-x}Al_x(B_{1-y}Cy)₂ single crystals in the normal and superconducting state." *Physical Review B* **73**(17).
- Dmitriev, A., H. Spillmann, S. Stepanow, T. Strunskus, C. Woll, A. P. Seitsonen, M. Lingenfelder, N. Lin, J. V. Barth and K. Kern (2006). "Asymmetry induction by cooperative intermolecular hydrogen bonds in surface-anchored layers of achiral molecules." *Chemphyschem* **7**(10): 2197-2204.

- Dmitrieva, O., M. Acet, G. Dumpich, J. Kastner, C. Antoniak, M. Farle and K. Fauth (2006). "Enhancement of L1(0) phase formation in FePt nanoparticles by nitrogenization." *Journal of Physics D-Applied Physics* **39**(22): 4741-4745.
- Drago, M., P. Vogt and W. Richter (2006). "MOVPE growth of InN with ammonia on sapphire." *Physica Status Solidi a-Applications and Materials Science* **203**(1): 116-126.
- Duati, M., C. Grave, N. Tcbeborateva, J. S. Wu, K. Mullen, A. Shaporenko, M. Zharnikov, J. K. Kriebel, G. M. Whitesides and M. A. Rampi (2006). "Electron transport across hexa-peri-hexabenzocoronene units in a metal-self-assembled monolayer-metal junction." *Advanced Materials* **18**(3): 329-+.
- Dudzik, E., R. Feyerherm, W. Diete, R. Signorato and C. Zilkens (2006). "The new HMI beamline MAGS: an instrument for hard X-ray diffraction at BESSY." *Journal of Synchrotron Radiation* **13**: 421-425.
- Ehresmann, A., L. Werner, S. Klumpp, P. V. Demekhin, M. P. Lemeshko, V. L. Sukhorukov, K. H. Schartner and H. Schmoranzer (2006). "Predissociation of the N-2(+) (C-2 Sigma(+)(u)) state observed via C-2 Sigma(+)(u) -> X (2)Sigma(+)(g) fluorescence after resonant 1s(-1)pi* excitation of N-2 molecule." *Journal of Physics B-Atomic Molecular and Optical Physics* **39**(6): L119-L126.
- Ehresmann, A., L. Werner, S. Klumpp, S. Lucht, H. Schmoranzer, S. Mickat, R. Schill, K. H. Schartner, P. V. Demekhin, M. P. Lemeshko and V. L. Sukhorukov (2006). "Studying the N-2(+) (C (2)Sigma(+)(u) -> X (2)Sigma(+)(g)) fluorescence excited via the 1s(-1)pi* resonance." *Journal of Physics B-Atomic Molecular and Optical Physics* **39**(2): 283-304.
- Eriksson, F., N. Ghafoor, F. Schäfers, E. M. Gullikson and J. Birch (2006). "Interface engineering of short-period Ni/V multilayer X-ray mirrors." *Thin Solid Films* **500**(1-2): 84-95.
- Ethirajan, A. (2007). "A Micellar Approach to Magnetic Ultrahigh-Density Data-Storage." *Advanced Materials* **19**(3): 406-410.
- Feyerherm, R., E. Dudzik, N. Aliouane and D. N. Argyriou (2006). "Commensurate Dy magnetic ordering associated with incommensurate lattice distortion in multiferroic DyMnO3." *Physical Review B* **73**(18).
- Fink, J., A. Koitzsch, J. Geck, V. Zabolotnyy, M. Knupfer, B. Buchner, A. Chubukov and H. Berger (2006). "Reevaluation of the coupling to a bosonic mode of the charge carriers in (Bi,Pb)(2)Sr2CaCu2O8+delta at the antinodal point." *Physical Review B* **74**(16).

- Fleischer, K., S. Chandola, T. Herrmann, N. Esser, W. Richter and J. F. McGilp (2006). "Free-electron response in reflectance anisotropy spectra." *Physical Review B* **74**(19).
- Fukumoto, K., W. Kuch, J. Vogel, F. Romanens, S. Pizzini, J. Camarero, M. Bonfim and J. Kirschner (2006). "Dynamics of magnetic domain wall motion after nucleation: Dependence on the wall energy." *Physical Review Letters* **96**(9).
- Gabasch, H., E. Kleimenov, D. Teschner, S. Zafeiratos, M. Havecker, A. Knop-Gericke, R. Schlogl, D. Zemlyanov, B. Aszalos-Kiss, K. Hayek and B. Klotzer (2006). "Carbon incorporation during ethene oxidation on Pd(111) studied by in situ X-ray photoelectron spectroscopy at 2×10^{-3} mbar." *Journal of Catalysis* **242**(2): 340-348.
- Gabasch, H., W. Unterberger, K. Hayek, B. Klotzer, E. Kleimenov, D. Teschner, S. Zafeiratos, M. Havecker, A. Knop-Gericke, R. Schlogl, J. Y. Han, F. H. Ribeiro, B. Aszalos-Kiss, T. Curtin and D. Zemlyanov (2006). "In situ XPS study of Pd(111) oxidation at elevated pressure, Part 2: Palladium oxidation in the 10(-1) mbar range." *Surface Science* **600**(15): 2980-2989.
- Galakhov, V. R., N. A. Ovechkina, A. S. Shkvarin, S. N. Shamin, E. Z. Kurmaev, K. Kuepper, A. F. Taka?cs, M. Raekers, S. Robin, M. Neumann, G.-N. Gavril, A. S. Semenova, D. G. Kellerman, T. Kaambre and J. Nordgren (2006). "Electronic structure and x-ray spectra of defective oxides $\text{Li}_{\{x\}}\text{CoO}_{\{2\}}$." *Physical Review B - Condensed Matter and Materials Physics* **74**(4).
- Gassenbauer, Y., R. Schafrank, A. Klein, S. Zafeiratos, M. Havecker, A. Knop-Gericke and R. Schlogl (2006). "Surface potential changes of semiconducting oxides monitored by high-pressure photoelectron spectroscopy: Importance of electron concentration at the surface." *Solid State Ionics* **177**(35-36): 3123-3127.
- Gavril, G., D. R. T. Zahn and W. Braun (2006). "High resolution photoemission spectroscopy: Evidence for strong chemical interaction between Mg and 3,4,9,10-perylene-tetracarboxylic dianhydride." *Applied Physics Letters* **89**(16).
- Gensch, M., E. H. Korte, N. Esser, U. Schade and K. Hinrichs (2006). "Microfocus-infrared synchrotron ellipsometer for mapping of ultra thin films." *Infrared Physics & Technology* **49**(1-2): 74-77.
- Gensch, M., E. H. Korte, N. Esser, U. Schade and K. Hinrichs (2006). *Infrared Physics +Acy- Technology* **49**(1-2): 74-77.
- Getzlaff, M., J. Bansmann, F. Bulut, R. K. Gebhardt, A. Kleibert and K. H. Meiwes-Broer (2006). "Structure, composition and magnetic properties of size-selected FeCo alloy clusters on surfaces." *Applied Physics a-Materials Science & Processing* **82**(1): 95-101.

- Ghafoor, N., P. O. A. Persson, J. Birch, F. Eriksson and F. Schafers (2006). "Interface engineered ultrashort period Cr-Ti multilayers as high reflectance mirrors and polarizers for soft x rays of $\lambda=2.74$ nm wavelength." *Applied Optics* **45**(1): 137-143.
- Glisoviv, A. (2007). "Transmission X-ray microscopy of spider dragline silk." *International Journal of Biological Macromolecules* **40**: 87-95.
- Gode, S. (2006). Optimization of a femtosecond VUV photon source based on high order harmonic generation, Ecole Nationale Supérieure de Physique de Strasbourg.
- Goldhahn, R., P. Schley, A. T. Winzer, G. Gobsch, V. Cimalla, O. Ambacher, M. Rakel, C. Cobet, N. Esser, H. Lu and W. J. Schaff (2006). "Detailed analysis of the dielectric function for wurtzite InN and In-rich InAlN alloys." *Physica Status Solidi a-Applications and Materials Science* **203**(1): 42-49.
- Goldhahn, R., P. Schley, A. T. Winzer, M. Rakel, C. Cobet, N. Esser, H. Lu and W. J. Schaff (2006). "Critical points of the band structure and valence band ordering at the Gamma point of wurtzite InN." *Journal of Crystal Growth* **288**(2): 273-277.
- Gomoyunova, M. V. (2006). "Interaction of iron atoms with the oxidized silicon surface." *Zhurnal Tekhnicheskoi Fiziki* **76**(9): 136-139.
- Gomoyunova, M. V. (2006). "Formation of ultrathin iron silicide layers on the single-crystal silicon surface." *Fizika Tverdogo Tela* **48**(10): 1898-1902.
- Gomoyunova, M. V. (2006). "Photoemission study of cobalt interaction with the oxidized Si(100)2x1 surface." *Surface Science* **600**(1-3): 2449-2456.
- Gordan, O. D., C. Himcinschi, D. R. T. Zahn, C. Cobet, N. Esser and W. Braun (2006). "Reduced intermolecular interaction in organic ultrathin films." *Applied Physics Letters* **88**(14).
- Gorner, W., M. Eichelbaum, R. Matschat, K. Rademann, M. Radtke, U. Reinholz and H. Riesemeier (2006). "Non-destructive investigation of composition, chemical properties and structure of materials by synchrotron radiation." *Insight* **48**(9): 540-544.
- Gottwald, A., U. Kroth, M. Krumrey, M. Richter, F. Scholze and G. Ulm (2006). "The PTB high-accuracy spectral responsivity scale in the VUV and x-ray range." *Metrologia* **43**(2): S125-S129.
- Graf, B. (2006). Elektronenspektroskopie von Mangan- und Eisenhaltigen supramolekularen Aggregaten, Univ. Erlangen-Nürnberg.
- Graf, C., S. Dembski, A. Hofmann and E. Ruhl (2006). "A general method for the controlled embedding of nanoparticles in silica colloids." *Langmuir* **22**(13): 5604-5610.

- Grimm, M., B. Langer, S. Schlemmer, T. Lischke, U. Becker, W. Widdra, D. Gerlich, R. Flesch and E. Ruhl (2006). "Charging mechanisms of trapped element-selectively excited nanoparticles exposed to soft X rays." *Physical Review Letters* **96**(6).
- Groh, U. (2006). *Spektromikroskopische Untersuchungen an organischen Nanostrukturen*, Universität Würzburg.
- Gunther, S., L. Zhou, M. Havecker, A. Knop-Gericke, E. Kleimenov, R. Schlogl and R. Imbihl (2006). "Adsorbate coverages and surface reactivity in methanol oxidation over Cu(110): An in situ photoelectron spectroscopy study." *Journal of Chemical Physics* **125**(11).
- Guo, X. X., W. Braun, B. Jenichen, V. M. Kaganer, B. P. Tinkham, A. Trampert and K. H. Ploog (2006). "Synchrotron x-ray scattering study of thin epitaxial Pr₂O₃ films on Si(001)." *Journal of Applied Physics* **100**(2).
- Gutierrez, A., C. Munuera, M. F. Lopez, J. A. Jimenez, C. Morant, T. Matzelle, N. Kruse and C. Ocal (2006). "Surface microstructure of the oxide protective layers grown on vanadium-free Ti alloys for use in biomedical applications." *Surface Science* **600**(18): 3780-3784.
- Han, L. (2006). *Improvement of array properties of micellar FePt and CoPt nanoparticle ensembles*, Universität Ulm.
- Harding, C. J. and I. Powis (2006). "Sensitivity of photoelectron circular dichroism to structure and electron dynamics in the photoionization of carvone and related chiral monocyclic terpenone enantiomers." *Journal of Chemical Physics* **125**(23).
- Hartmann, M. D. (2006). *Structural analysis of the catalytic mechanism of shikimate kinase from Mycobacterium tuberculosis*, Univ. Hamburg.
- Haumann, M., P. Liebisch, M. Barra, P. Loja, S. Löscher, O. Kirilenko, M. Mertin, F. Schäfers, A. Magnuson, M. Anderlund, S. Ott and H. Dau (2006). *Chemical mimics for small molecule catalysis by proteins investigated by X-ray absorption spectroscopy. Freie Universität Berlin - Research with Synchrotron Radiation 2000-2005*. Aachen, Shaker Verlag: 20-22.
- Hellwig, O., S. Eisebitt, W. Eberhardt, W. F. Schlotter, J. Luning and J. Stohr (2006). "Magnetic imaging with soft x-ray spectroholography." *Journal of Applied Physics* **99**(8).
- Heßler, M. (2006). *Spektroskopie an Übergangsmetallclustern*, Bayerische Julius-Maximilians-Universität Würzburg.
- Hloskovskyy, A. (2006). *Size-selective investigations of spectral and emission properties of small particles and nanotubes*, Johannes Gutenberg - Universität Mainz.

- Hoffmann, A., A. Kane, D. Nettels, D. E. Hertzog, P. Baumgartel, J. Lengefeld, G. Reichardt, D. A. Horsley, R. Seckler, O. Bakajin and B. Schuler (2007). "Mapping protein collapse with single-molecule fluorescence and kinetic synchrotron radiation circular dichroism spectroscopy." *Proceedings of the National Academy of Sciences of the United States of America* **104**(1): 105-110.
- Hofmann, A. (2006). *Synthese und Charakterisierung von magnetischen und magnetisch dotierten Nanopartikeln*, Universität Würzburg.
- Hofmann, T., U. Schade, K. C. Agarwal, B. Daniel, C. Klingshirn, M. Hetterich, C. M. Herzinger and M. Schubert (2006). "Conduction-band electron effective mass in Zn_{0.87}Mn_{0.13}Se measured by terahertz and far-infrared magneto-optic ellipsometry." *Applied Physics Letters* **88**(4).
- Hofmann, T., U. Schade, C. M. Herzinger, P. Esquinazi and M. Schubert (2006). "Terahertz magneto-optic generalized ellipsometry using synchrotron and blackbody radiation." *Review of Scientific Instruments* **77**(6).
- Hofmann, T., U. Schade, C. M. Herzinger, P. Esquinazi and M. Schubert (2006). "Terahertz generalized Mueller-matrix ellipsometry." *Proceedings of SPIE - The International Society for Optical Engineering*.
- Hoink, V., M. D. Sacher, J. Schmalhorst, G. Reiss, D. Engel, T. Weis and A. Ehresmann (2006). "Switchable resonant x-ray Bragg scattering on a magnetic grating patterned by ion bombardment." *Journal of Applied Physics* **100**(6).
- Holldack, K., S. Khan, R. Mitzner and T. Quast (2006). "THz pulses from Femtoslicing at BESSY." *Physical Review Letters* **96**(054601).
- Holldack, K., S. Khan, R. Mitzner and T. Quast (2006). "Femtosecond terahertz radiation from femtoslicing at BESSY." *Physical Review Letters* **96**(5).
- Holmström, E., W. Olovsson, I. A. Abrikosov, A. M. N. Niklasson, B. Johansson, M. Gorgoi, O. Karis, S. Svensson, F. Schäfers, W. Braun, G. Öhrwall, G. Andersson, M. Marcellini and W. Eberhardt (2006). "Sample Preserving Deep Interface Characterization Technique." *Physical Review Letters* **97**(266106).
- Hübers, H.-W., S. G. Pavlov, K. Holldack, U. Schade and G. Wüstefeld (2006). Long wavelength response of unstressed and stressed Ge:Ga detectors. *Proceedings of SPIE - The International Society for Optical Engineering*.
- Hunger, R., W. Jaegermann, A. Merson, Y. Shapira, C. Pettenkofer and J. Rappich (2006). "Electronic Structure of Methoxy-, Bromo-, and Nitrobenzene Grafted onto Si(111)." *Journal of Physical Chemistry B* **110**(31): 15432-15441.

- Janssen, D., H. Buettig, P. Evtushenko, U. Lehnert, P. Michel, K. Moeller, P. Murcek, C. Schneider, R. Schurig, F. Staufenbiel, J. Teichert, R. Xiang, J. Stephan, W. D. Lehmann, T. Kamps, D. Lipka, V. Volkov and I. Will (2006). "Technology challenges for SRF guns as ERL sources in view of Rossendorf work." Nuclear Instruments & Methods in Physics Research Section a-Accelerators Spectrometers Detectors and Associated Equipment **557**(1): 80-86.
- Jenichen, B., Y. Takagaki, K. H. Ploog, N. Darowski, R. Feyerherm and I. Zizak (2006). "Nucleation at the phase transition near 40 degrees C in MnAs nanodisks." Applied Physics Letters **89**(5).
- Joshi, S., S. Barth, S. Marburger, V. Ulrich and U. Hergenhahn (2006). "2p correlation satellites in neon clusters investigated by photoemission." Physical Review B **73**(23).
- Kafer, D., G. Witte, P. Cyganik, A. Terfort and C. Woll (2006). "A comprehensive study of self-assembled monolayers of anthracenethiol on gold: Solvent effects, structure, and stability." Journal of the American Chemical Society **128**(5): 1723-1732.
- Kallmayer, M., H. J. Elmers, B. Balke, S. Wurmehl, F. Emmerling, G. H. Fecher and C. Felser (2006). "Magnetic properties of Co₂Mn_{1-x}Fe_xSi Heusler alloys." Journal of Physics D-Applied Physics **39**(5): 786-792.
- Kallmayer, M., H. Schneider, G. Jakob, H. J. Elmers, K. Kroth, H. C. Kandpal, U. Stumm and S. Cramm (2006). "Reduction of surface magnetism of Co₂Cr_{0.6}Fe_{0.4}Al Heusler alloy films." Applied Physics Letters **88**(7).
- Kamakura, N., A. Kimura, T. Saitoh, O. Rader, K. S. An and A. Kakizaki (2006). "Magnetism of Fe films grown on Co(100) studied by spin-resolved Fe 3s photoemission." Physical Review B **73**(9).
- Kammer, S., K. H. Schartner, S. Mickat, R. Schill, A. Ehresmann, L. Werner, S. Klumpp, H. Schmoranzer, I. D. Petrov, P. V. Demekhin and V. L. Sukhorukov (2006). "Cross sections for photoabsorption and 3p(4)4s,3d satellite production at energies of the doubly excited Ar 3p(4)(P-3)4s P-2(3/2),(1/2) np resonances." Journal of Physics B-Atomic Molecular and Optical Physics **39**(12): 2757-2771.
- Kaun, N., S. Kulka, J. Frank, U. Schade, M. J. Vellekoop, M. Harasek and B. Lendl (2006). "Towards biochemical reaction monitoring using FT-IR synchrotron radiation." Analyst **131**(4): 489-494.
- Keckes, J., E. Eiper, K. J. Martinschitz, P. Boesecke, W. Gindl and G. Dehm (2006). "In-situ x-ray diffraction as a tool to probe mechanical phenomena down to the nano-scale." Advanced Engineering Materials **8**(11): 1084-1088.

- Kellerman, D. G., V. R. Galakhov, A. S. Semenova, Y. N. Blinovskov and O. N. Leonidova (2006). "Semiconductor-metal transition in defect lithium cobaltite." *Physics of the Solid State* **48**(3): 548-556.
- Kera, S., M. B. Casu, K. R. Bauchspiess, D. Batchelor, T. Schmidt and E. Umbach (2006). "Growth mode and molecular orientation of phthalocyanine molecules on metal single crystal substrates: A NEXAFS and XPS study." *Surface Science* **600**(5): 1077-1084.
- Kera, S., M. B. Casu, A. Scholl, T. Schmidt, D. Batchelor, E. Ruhl and E. Umbach (2006). "High-resolution inner-shell excitation spectroscopy of H-2-phthalocyanine." *Journal of Chemical Physics* **125**(1).
- Kern, B. (2006). Mizellare Herstellung und Charakterisierung von magnetischen Nanopartikeln, Universität Ulm.
- Khan, S., K. Holldack, T. Kachel, R. Mitzner and T. Quast (2006). "Femtosecond undulator radiation from sliced electron bunches." *Physical Review Letters* **97**(7).
- Kielich, W. (2006). Höchstaufauflösende Spektroskopie von Xe-Zweielektronenresonanzen mit hocheffizienter Fluoreszenzspektroskopie nach schmalbandiger Anregung mit Synchrotronstrahlung, TU Kaiserslautern.
- Klaas, M. (2006). Structural and Functional Studies on Bacterial Cold Shock Proteins: Nucleic-Acid Binding, the Architecture of a Domain Swap, and Mechanisms Contributing to their Stabilization, Freie Universität Berlin.
- Klaus, M., I. A. Denks and C. Genzel (2006). X-ray diffraction analysis of nonuniform residual stress fields $\sigma_{ii}(\tau)$ under difficult conditions. *Residual Stresses Vii*. **524-525**: 601-606.
- Kleibert, A. (2006). Massengefilterte Eisennanopartikel auf ultradünnen Kobaltfilmen - eine in situ Studie mit weicher Röntgenstrahlung, Rostock University.
- Klein, R., C. Laubis, R. Müller, F. Scholze and G. Ulm (2006). "The EUV metrology program of PTB." *Microelectronic Engineering* **83**(4-9): 707-709.
- Koch, N. and A. Vollmer (2006). "Electrode-molecular semiconductor contacts: Work-function-dependent hole injection barriers versus Fermi-level pinning." *Applied Physics Letters* **89**(16).
- Koch, N., A. Vollmer, I. Salzmänn, B. Nickel, H. Weiss and J. P. Rabe (2006). "Evidence for temperature-dependent electron band dispersion in pentacene." *Physical Review Letters* **96**(15).
- Koch-Müller, M., S. S. Matsyuk, D. Rhede, R. Wirth and N. Khisina (2006). "Hydroxyl in mantle olivine xenocrysts from the Udachnaya kimberlite pipe." *Physics and Chemistry of Minerals* **33**(4): 276-287.

- Koitzsch, A., S. V. Borisenko, J. Geck, V. B. Zabolotnyy, M. Knupfer, J. Fink, P. Ribeiro, B. Buchner and R. Follath (2006). "Current spinon-holon description of the one-dimensional charge-transfer insulator SrCuO₂: Angle-resolved photoemission measurements." *Physical Review B* **73**(20).
- Koller, G., S. Berkebile, J. R. Krenn, F. P. Netzer, M. Oehzelt, T. Haber, R. Resel and M. G. Ramsey (2006). "Heteroepitaxy of organic-organic nanostructures." *Nano Letters* **6**(6): 1207-1212.
- Konovalov, I. (2006). "X-ray photoconductivity due to trap-sensitive relaxation of hot carriers." *Applied Physics Letters* **88**(22).
- Konovalov, I. (2006). "Trap-sensitive relaxation of hot carriers in ZnO:Cu,Al." *Physica Status Solidi C* **3**(8): 2891-2894.
- Kordyuk, A. A., S. V. Borisenko, A. Koitzsch, J. Fink, M. Knupfer, B. Buchner and H. Berger (2006). "Life of the nodal quasiparticles in Bi-2212 as seen by ARPES." *Journal of Physics and Chemistry of Solids* **67**(1-3): 201-207.
- Kordyuk, A. A., S. V. Borisenko, V. B. Zabolotnyy, J. Geck, M. Knupfer, J. Fink, B. Buchner, C. T. Lin, B. Keimer, H. Berger, A. V. Pan, S. Komiyama and Y. Ando (2006). "Constituents of the quasiparticle spectrum along the nodal direction of High-T_c cuprates." *Physical Review Letters* **97**(1).
- Kotschau, I. M. and H. W. Schock (2006). "Compositional depth profiling of polycrystalline thin films by grazing-incidence X-ray diffraction." *Journal of Applied Crystallography* **39**: 683-696.
- Kouba, J., M. Bednarzik, R. Engelke, G. Ahrens, H. Miller and D. Haase (2006). "Optimizing SU-8 resist to fabricate micro-metallic structures." *Solid State Technology* **49**(4): 39-+.
- Kouba, J., W. Eberhardt and B. Loechel (2006). Wavelength filter for visible wavelengths based on photonic crystal. *Proceedings of SPIE - The International Society for Optical Engineering*.
- Kouba, J., M. Kubenz, A. Mai, G. Ropers, W. Eberhardt and B. Loechel (2006). "Fabrication of nanoimprint stamps for photonic crystals." *Journal of Physics: Conference Series* **34**(1): 897-903.
- Krasnikov, S. A., A. B. Preobrajenski, N. N. Sergeeva, M. M. Brzhezinskaya, M. A. Nesterov, A. A. Cafola, M. O. Senge and A. S. Vinogradov (2007). "Electronic structure of Ni(II) porphyrins and phthalocyanine studied by soft X-ray absorption spectroscopy." *Chemical Physics* **332**(2-3): 318-324.
- Kroll, T. (2006). Spectroscopic studies of Na_xCoO₂, Technische Universität Dresden.
- Kroll, T., M. Knupfer, J. Geck, C. Hess, T. Schwieger, G. Krabbes, C. Sekar, D. R. Batchelor, H. Berger and B. Buchner (2006). "X-ray absorption spectroscopy of Na_xCoO₂ layered cobaltates." *Physical Review B* **74**(11).

- Kronast, F., R. Ovsyannikov, A. Vollmer, H. A. Dürr, W. Eberhardt, P. Imperia, D. Schmitz, G. M. Schott, K. Brunner, M. Sawicki and L. W. Molenkamp (2006). "Surface magnetization deficit in (GaMn)As ferromagnetic semiconductors." *Physical Review B* **74**(225213).
- Kronast, F., R. Ovsyannikov, A. Vollmer, H. A. Durr, W. Eberhardt, P. Imperia, D. Schmitz, G. M. Schott, C. Ruester, C. Gould, G. Schmidt, K. Brunner, M. Sawicki and L. W. Molenkamp (2006). "Mn 3d electronic configurations in (Ga_{1-x}Mn_x)As ferromagnetic semiconductors and their influence on magnetic ordering." *Physical Review B* **74**(23).
- Kropp, J. M. (2006). Interface analysis of molecule terminated III-V semiconductors, TU Berlin.
- Krumrey, M., M. Gerlach, F. Scholze and G. Ulm (2006). "Calibration and characterization of semiconductor X-ray detectors with synchrotron radiation." *Nuclear Instruments & Methods in Physics Research Section a-Accelerators Spectrometers Detectors and Associated Equipment* **568**(1): 364-368.
- Krylov, A. V., H. Adamzig, A. D. Walter, B. Lochel, E. Kurth, O. Pulz, J. Szeponik, F. Wegerich and F. Lisdat (2006). "Parallel generation and detection of superoxide and hydrogen peroxide in a fluidic chip." *Sensors and Actuators B-Chemical* **119**(1): 118-126.
- Kuch, W., L. I. Chelaru, F. Offi, J. Wang, M. Kotsugi and J. Kirschner (2006). "Tuning the magnetic coupling across ultrathin antiferromagnetic films by controlling atomic-scale roughness." *Nature Materials* **5**(2): 128-133.
- Kuck, S., F. Brandt, H. A. Kremling, A. Gottwald, A. Hoehl and M. Richter (2006). "Absolute measurement of F-2-laser power at 157 nm." *Applied Optics* **45**(14): 3325-3330.
- Küller, A. (2006). Von der Chemischen Nanolithographie zur Dreidimensionalen Lithographie und freistehenden Nanofolien, Universität Heidelberg.
- Kurde, J. (2006). EXAFS- und MEXAFS-Untersuchungen an 3d- und 4f-Ferromagneten, Freie Universität Berlin.
- Lagutin, B. M., F. V. Demekhin, I. D. Petrov, V. L. Sukhorukov, A. Ehresmann, H. Schmoranzler and K. H. Schartner (2006). "Interference effects in alignment and orientation processes of atoms excited by polarized radiation." *Optics and Spectroscopy* **101**(6): 832-838.
- Lang, J., B. J. Kent, W. Paustian, C. M. Brown, C. Keyser, M. R. Anderson, G. C. R. Case, R. A. Chaudry, A. M. James, C. M. Korendyke, C. D. Pike, B. J. Probyn, D. J. Rippington, J. F. Seely, J. A. Tandy and M. C. R. Whillock (2006). "Laboratory calibration of the Extreme-Ultraviolet Imaging Spectrometer for the Solar-B satellite." *Applied Optics* **45**(34): 8689-8705.

- Lee, J. S., M. Ortolani, U. Schade, Y. J. Chang and T. W. Noh (2007). "Time-resolved visualization of the heat flow in VO₂/Al₂O₃ films." *Applied Physics Letters* **90**(1): 001-004.
- Lehmann, S., M. Bar, D. F. Marron, P. Pistor, S. Wiesner, M. Rusu, I. Kotschau, I. Lauer mann, A. Grimm, S. Sokoll, C. H. Fischer, T. Schedel-Niedrig, M. C. Lux-Steiner and C. Jung (2006). "CuGaSe₂-CuGa₃Se₅ phase transition in CCSVT-grown thin films." *Thin Solid Films* **511**: 623-627.
- Liepe, M. and J. Knobloch (2006). "Superconducting RF for energy-recovery linacs." *Nuclear Instruments & Methods in Physics Research Section a-Accelerators Spectrometers Detectors and Associated Equipment* **557**(1): 354-369.
- Locht, R., B. Leyh, D. Dehareng, K. Hottmann, H. W. Jochims and H. Baumgartel (2006). "About the photoionization of methyl bromide (CH₃Br). Photoelectron and photoionization mass spectrometric investigation." *Chemical Physics* **323**(2-3): 458-472.
- Loja, P., M. Barra, S. Löscher, O. Kririlenko, P. Liebisch, M. Mertin, F. Schäfers, M. Haumann and H. Dau (2006). X-ray spectroscopy to study catalytic metal centers: A new BioXAS experiment at the BESSY beamline KMC1. Freie Universität Berlin - Research with Synchrotron Radiation 2000-2005. H. Dau, W. Kuch and R. Püttner. Aachen, Shaker Verlag: 104-105.
- Loreck, C. (2006). Sputter-(Zn,Mg)O als Pufferschicht in cadmiumfreien Chalkopyrit-Dünnschichtsolarzellen: Präparation, elektronenspektroskopische Grenzflächenanalyse und Solarzelleneigenschaften, Technische Universität Berlin.
- Lud, S. Q., M. Steenackers, R. Jordan, P. Bruno, D. M. Gruen, P. Feulner, J. A. Garrido and M. Stutzmann (2006). "Chemical grafting of biphenyl self-assembled monolayers on ultrananocrystalline diamond." *Journal of the American Chemical Society* **128**(51): 16884-16891.
- Lundwall, M., A. Lindblad, H. Bergersen, T. Rander, G. Ohrwall, M. Tchapyguine, S. Peredkov, S. Svensson and O. Bjorneholm (2006). "Photon energy dependent intensity variations observed in Auger spectra of free argon clusters." *Journal of Physics B-Atomic Molecular and Optical Physics* **39**(16): 3321-3333.
- Makhova, L. (2006). "X-ray spectroscopic investigation of forbidden direct transitions in CuGaO₂ and CuInO₂." *Physica Status Solidi a-Applications and Materials Science* **203**(11): 2861-2866.
- Manns, T., J. Gibmeier and B. Scholtes (2006). Determination of real space residual stress distributions $\sigma_{ij}(z)$ of surface treated materials with diffraction methods Part 1: Angle-dispersive approach. Residual Stresses VII. **524-525**: 31-36.
- Marchetto, H. (2006). High-resolution spectro-microscopic investigation of organic thin film growth, Freie Universität Berlin.

- Marchetto, H., U. Groh, T. Schmidt, R. Fink, H. J. Freund and E. Umbach (2006). "Influence of substrate morphology on organic layer growth: PTCDA on Ag(111)." *Chemical Physics* **325**(1): 178-184.
- Martins, M., K. Godehusen, T. Richter, P. Wernet and P. Zimmermann (2006). "Open shells and multi-electron interactions: Core level photoionization of the 3d metal atoms." *Journal of Physics B: Atomic, Molecular and Optical Physics* **39**(5): R79-R125.
- Marutzky, M. (2006). *Elektronische Struktur von antiferromagnetischen UN und UPtGe Einkristallen aus optischer und magnetooptischer Spektroskopie*, TU Braunschweig.
- Marutzky, M., U. Barkow, S. Weber, J. Schoenes and R. Troc (2006). "- Optical and magneto-optical anisotropy of UPtGe single crystals." - **74**(- 20): - 7.
- Mavromati, A. (2006). *Study of biological samples using X-ray fluorescence spectroscopy*, Aristotle University of Thessaloniki.
- Mayer, T., M. V. Lebedev, R. Hunger and W. Jaegermann (2006). "Synchrotron Photoemission Analysis of Semiconductor/Electrolyte Interfaces by the Frozen-Electrolyte Approach: Interaction of HCl in 2-Propanol with GaAs(100)." *Journal of Physical Chemistry B* **110**(5): 2293-2301.
- McGuinness, C. L., A. Shaporenko, C. K. Mars, S. Uppili, M. Zharnikov and D. L. Allara (2006). "Molecular self-assembly at bare semiconductor surfaces: Preparation and characterization of highly organized octadecanethiolate monolayers on GaAs(001)." *Journal of the American Chemical Society* **128**(15): 5231-5243.
- McGuinness, C. (2006). *Molecular assembly at bare semiconductor surfaces*, The Pennsylvania State University.
- Menzel, A., Y. V. Tolmachev, K. C. Chang, V. Komanicky, Y. S. Chu, J. J. Rehr and H. You (2006). "Polarization-dependent resonant anomalous surface X-ray scattering of CO/Pt(111)." *Europhysics Letters* **74**(6): 1032-1038.
- Meyer, M., D. Cubaynes, F. J. Wuilleumier, E. Heineck, T. Richter, P. Zimmermann, S. I. Strakhova and A. N. Grum-Grzhimailo (2006). "Probing the KII 3p(5)4p fine structure by photoelectron spectroscopy of laser-excited potassium." *Journal of Physics B-Atomic Molecular and Optical Physics* **39**(7): L153-L158.
- Molodtsova, O. V., V. Y. Aristov, V. M. Zhilin, D. V. Vyalikh and M. Knupfer (2006). "Potassium doped CuPc: Electronic and atomic structure formation." *Journal De Physique Iv* **132**: 121-125.
- Moroz, L. V., M. Schmidt, U. Schade, T. Hiroi and M. A. Ivanova (2006). "Synchrotron-based infrared microspectroscopy as a useful tool to study hydration states of meteorite constituents." *Meteoritics & Planetary Science* **41**(8): 1219-1230.

- Muller, B. R. and M. P. Hentschel (2006). Computed Tomography - Application to Composites and Microstructures. Springer Handbook of Materials Measurement Methods, Springer Science+Business Media Inc.
- Muller, M., B. Beckhoff, G. Ulm and B. Kanngiesser (2006). "Absolute determination of cross sections for resonant Raman scattering on silicon." *Physical Review A* **74**(1).
- Müller, N., T. Khalil, M. Pohl, T. Uphues, M. Polcik, O. Rader, F. Heigl, K. Starke, S. Fritzsche, N. M. Kabachnik and U. Heinzmann (2006). "Interference of spin states in resonant photoemission induced by circularly polarized light from magnetized Gd." *Physical Review B - Condensed Matter and Materials Physics* **74**(16).
- Müller, R., A. Hoehl, R. Klein, G. Ulm, U. Schade, K. Holldack and G. Wüstefeld (2006). "Planned infrared beamlines at the Metrology Light Source of PTB." *Infrared Physics and Technology* **49**(1-2): 161-166.
- Munuera, C., T. R. Matzelle, N. Kruse, M. F. Lopez, A. Gutierrez, J. A. Jimenez and C. Ocal (2007). "Surface elastic properties of Ti alloys modified for medical implants: A force spectroscopy study." *Acta Biomaterialia* **3**(1): 113-119.
- Nefedov, A., N. Akdogan, H. Zabel, R. I. Khaibullin and L. R. Tagirov (2006). "Spin polarization of oxygen atoms in ferromagnetic Co-doped rutile TiO₂." *Applied Physics Letters* **89**(18).
- Neubauer, R. (2006). In situ - Untersuchungen zur Reaktivität ungesättigter, aromatischer und funktionalisierter Kohlenwasserstoffe auf einkristallinen Übergangsmetalloberflächen, Universität Erlangen-Nürnberg.
- Neuhausler, U. and G. Schneider (2006). "Non-destructive high-resolution X-ray imaging of ULSI micro-electronics using keV X-ray microscopy in Zernike phase contrast." *Microelectronic Engineering* **83**(4-9): 1043-1046.
- Oran, U., S. Swaraj, A. Lipitz and W. E. S. Unger (2006). "Surface analysis of plasma deposited polymer films, 7 - "In situ" characterization of plasma deposited allylamine films by ToF-SSIMS, XPS and NEXAFS spectroscopy." *Plasma Processes and Polymers* **3**(3): 288-298.
- Ortolani, M., P. Calvani, S. Lupi, U. Schade, A. Perla, M. Fujita and K. Yamada (2006). "Effects of superconductivity and charge order on the subterahertz reflectivity of La_{1.875}Ba_{0.125}-ySryCuO₄." *Physical Review B* **73**(18).
- Ortolani, M., S. Lupi, L. Baldassarre, U. Schade, P. Calvani, Y. Takano, M. Nagao, T. Takenouchi and H. Kawarada (2006). "Low-energy electrodynamics of superconducting diamond." *Physical Review Letters* **97**(9).
- Osan, J., S. Torok, B. Beckhoff, G. Ulm, H. Hwang, C. U. Ro, C. Abete and R. Fuoco (2006). "Nitrogen and sulfur compounds in coastal Antarctic fine aerosol particles - an insight using non-destructive X-ray microanalytical methods." *Atmospheric Environment* **40**(25): 4691-4702.

- Ott, H., C. Schussler-Langeheine, E. Schierle, A. Y. Grigoriev, V. Leiner, H. Zabel, G. Kaindl and E. Weschke (2006). "Magnetic x-ray scattering at the M-5 absorption edge of Ho." *Physical Review B* **74**(9).
- Ott, H., C. Schussler-Langeheine, E. Schierle, G. Kaindl and E. Weschke (2006). "Magnetic depth profiles from resonant soft x-ray scattering: Application to Dy thin films." *Applied Physics Letters* **88**(21).
- Otte, K. (2006). "Flexible Cu(In,Ga)Se-2 thin-film solar cells for space application." *Thin Solid Films* **511**: 613-622.
- Pagés-Camagna, S., I. Reiche, C. Brouder, D. Cabaret, S. Rossano, B. Kanngießler and A. Erko (2006). "New insights into the colour origin of archaeological Egyptian blue and green by XAFS at the Cu K-edge." *X-Ray Spectrometry* **35**(2): 141-145.
- Papp, C., T. Fuhrmann, B. Tränkenschuh, R. Denecke and H. P. Steinrück (2006). "Site selectivity of benzene adsorption on Ni(111) studied by high-resolution x-ray photoelectron spectroscopy." *Physical Review B* **73**(23).
- Pavlychev, A. A., X. O. Brykalova, R. Flesch and E. Ruhl (2006). "Shape resonances in molecular clusters: the 2t(2g) shape resonances in S 2p-excited sulfur hexafluoride clusters." *Physical Chemistry Chemical Physics* **8**(16): 1914-1921.
- Peisert, H., I. Biswas, L. Zhang, M. Knupfer, M. Hanack, D. Dini, D. Batchelor and T. Chasse (2006). "Molecular orientation of substituted phthalocyanines: Influence of the substrate roughness." *Surface Science* **600**(18): 4024-4029.
- Pinakidou, F. (2006). XAFS studies on stabilized industrial wastes, Aristotle University of Thessaloniki.
- Pinakidou, F., M. Katsikini, E. C. Paloura, P. Kavouras, O. Kalogirou, P. Komninou and T. Karakostas (2006). "Modification of the Fe-environment in Fe₂O₃ glass/glass ceramic systems containing Pb, Na and Si." *Nuclear Instruments and Methods in Physics Research, Section B: Beam Interactions with Materials and Atoms* **246**(1): 170-175.
- Pinakidou, F., M. Katsikini, E. C. Paloura, P. Kavouras, O. Kalogirou, P. Komninou, T. Karakostas and A. Erko (2006). "On the coordination environment of Fe- and Pb-rich solidified industrial waste: An X-ray absorption and Mo⁹⁹Tc^{99m} study." *Journal of Non-Crystalline Solids* **352**(28-29): 2933-2942.
- Pinakidou, F., M. Katsikini, E. C. Paloura, P. Kavouras, P. Komninou, T. Karakostas and A. Erko (2006). "Application of μ -XAFS for the determination of the crystallization ratio in a series of vitro-ceramic materials containing industrial waste." *Nuclear Instruments and Methods in Physics Research, Section B: Beam Interactions with Materials and Atoms* **246**(1): 238-243.

- Pinakidou, F., M. Katsikini, E. C. Paloura, P. Kavouras, P. Komninou, T. Karakostas and A. Erko (2006). "Application of mu-XAFS for the determination of the crystallization ratio in a series of vitro-ceramic materials containing industrial waste." *Nuclear Instruments & Methods in Physics Research Section B-Beam Interactions with Materials and Atoms* **246**(1): 238-243.
- Pozdnyakova, O., D. Teschner, A. Wootsch, J. Krohnert, B. Steinhauer, H. Sauer, L. Toth, F. C. Jentoft, A. Knop-Gericke, Z. Paal and R. Schlogl (2006). "Preferential CO oxidation in hydrogen (PROX) on ceria-supported catalysts, part I: Oxidation state and surface species on Pt/CeO₂ under reaction conditions." *Journal of Catalysis* **237**(1): 1-16.
- Pozdnyakova, O., D. Teschner, A. Wootsch, J. Krohnert, B. Steinhauer, H. Sauer, L. Toth, F. C. Jentoft, A. Knop-Gericke, Z. Paal and R. Schlogl (2006). "Preferential CO oxidation in hydrogen (PROX) on ceria-supported catalysts, part II: Oxidation states and surface species on Pd/CeO₂ under reaction conditions, suggested reaction mechanism." *Journal of Catalysis* **237**(1): 17-28.
- Radu, F., V. Leiner, M. Wolff, V. K. Ignatovich and H. Zabel (2006). "Quantum states of neutrons in magnetic thin films (vol 71, pg 214423, 2005)." *Physical Review B* **74**(6).
- Radu, F., A. Nefedov, J. Grabis, G. Nowak, A. Bergmann and H. Zabel (2006). "Soft X-ray resonant magnetic scattering studies on Fe/CoO exchange bias system." *Journal of Magnetism and Magnetic Materials* **300**(1): 206-210.
- Radu, F., A. Westphalen, K. Theis-Brohl and H. Zabel (2006). "Quantitative description of the azimuthal dependence of the exchange bias effect." *Journal of Physics-Condensed Matter* **18**(3): L29-L36.
- Rappich, J., A. Merson, K. Roodenko, T. Dittrich, M. Gensch, K. Hinrichs and Y. Shapira (2006). *Journal of Physical Chemistry B* **110**(3): 1332-1337.
- Rentenberger, S., A. Vollmer, E. Zojer, R. Schennach and N. Koch (2006). "UV/ozone treated Au for air-stable, low hole injection barrier electrodes in organic electronics." *Journal of Applied Physics* **100**(5).
- Rhie, H. S., H. A. Durr and W. Eberhardt (2006). "Femtosecond evolution of electronic interactions at the Ni(111) surface." *Applied Physics a-Materials Science & Processing* **82**(1): 9-14.
- Richter, M., A. Gottwald, F. Scholze, R. Thornagel and G. Ulm (2006). Calibration of space instrumentation with synchrotron radiation. *Thermospheric-Ionospheric-Geospheric (Tiger) Symposium*. **37**: 265-272.
- Romanens, F., J. Vogel, W. Kuch, K. Fukumoto, J. Camarero, S. Pizzini, M. Bonfim and F. Petroff (2006). "Influence of topography and Co domain walls on the magnetization reversal of the FeNi layer in FeNi/Al₂O₃/Co magnetic tunnel junctions." *Physical Review B* **74**(18).

- Roodenko, K., M. Gensch, H. M. Heise, U. Schade, N. Esser and K. Hinrichs (2006). "Influences of thick film inhomogeneities on the ellipsometric parameters." *Infrared Physics & Technology* **49**(1-2): 39-44.
- Rosenthal, D., I. Zizak, N. Darowski, T. T. Magkoev and K. Christmann (2006). "The growth and structure of titanium dioxide films on a Re(10-10) surface: Rutile(011)-(2 x 1)." *Surface Science* **600**(14): 2830-2840.
- Rößler, K. (2006). *Übergangsmetallkomplexe für die Molekulare Elektronik*, Technische Universität Chemnitz.
- Rosnagel, K. and N. V. Smith (2006). "Spin-orbit coupling in the band structure of reconstructed 1T-TaS₂." *Physical Review B* **73**(7).
- Rossner, H. H., D. Schmitz, P. Imperia, H. J. Krappe and J. J. Rehr (2006). "Bayes-Turchin analysis of x-ray absorption data above the Fe L-2,L-3-edges." *Physical Review B* **74**(13).
- Schade, U. (2006). "WIRMS 2005 - International Workshop on Infrared Microscopy and Spectroscopy with Accelerator-Based Sources - 26-30 June 2005, Rathen, Germany - Preface." *Infrared Physics & Technology* **49**(1-2): 1-2.
- Schade, U. (2006). "Editorial." *Infrared Physics and Technology* **49**(1-2): 1-2.
- Schade, U., O. Bock, S. Vornhusen, A. Jager, G. Busche, U. Lehmann and H. Kreipe (2006). "Bone marrow infiltration pattern in B-cell chronic lymphocytic leukemia is related to immunoglobulin heavy-chain variable region mutation status and expression of 70-kd zeta-associated protein (ZAP-70)." *Human Pathology* **37**(9): 1153-1161.
- Schadow, T. (2006). *Innerschalenspektroskopie an Kobalt- und Titanclustern*, Technische Universität Berlin.
- Schafranek, R. and A. Klein (2006). "In situ photoemission study of the contact formation of (Ba,Sr)TiO₃ with Cu and Au." *Solid State Ionics* **177**(19-25): 1659-1664.
- Schlappa, J. (2006). *Investigation of electronic order using resonant soft x-ray diffraction*, Universität zu Köln.
- Schley, P. (2006). *Optische Eigenschaften von InN und InGaN mit In- bzw. (In,Ga)- und N- Polarität*, Technische Universität Ilmenau.
- Schley, P., R. Goldhahn, A. T. Winzer, G. Gobsch, V. Cimalla, O. Ambacher, M. Rakel, C. Cobet, N. Esser, H. Lu and W. J. Schaff (2006). "Transition energies and Stokes shift analysis for In-rich InGaN alloys." *Physica Status Solidi B- Basic Solid State Physics* **243**(7): 1572-1576.
- Schlotter, W. F., R. Rick, K. Chen, A. Scherz, J. Stohr, J. Luning, S. Eisebitt, C. Gunther, W. Eberhardt, O. Hellwig and I. McNulty (2006). "Multiple reference Fourier transform holography with soft x rays." *Applied Physics Letters* **89**(16).

- Schmalhorst, J., M. D. Sacher, V. Hoink, G. Reiss, A. Hutten, D. Engel and A. Ehresmann (2006). "Magnetic and chemical properties of Co₂MnSi thin films compared to the Co₂MnSi/Al-O interface." *Journal of Applied Physics* **100**(11).
- Schmidt, M., N. Gierlinger, U. Schade, T. Rogge and M. Grunze (2006). "Polarized infrared microspectroscopy of single spruce fibers: Hydrogen bonding in wood polymers." *Biopolymers* **83**(5): 546-555.
- Schmidt, M., U. Schade and M. Grunze (2006). "Micro spectroscopic observation of vibrational linear dichroism using polarization-modulated infrared synchrotron radiation." *Infrared Physics & Technology* **49**(1-2): 69-73.
- Schmitz, S. (2006). Chemische Datierung mit konfokaler Synchrotron Mikro-RFA an Monaziten aus Saphirin-führender Granuliten des Gruf-Kplex (Zentralalpen, N-Italien), Universität Potsdam.
- Schneider, H., G. Jakob, M. Kallmayer, H. J. Elmers, M. Cinchetti, B. Balke, S. Wurmehl, C. Felser, M. Aeschlimann and H. Adrian (2006). "Epitaxial film growth and magnetic properties of Co₂FeSi." *Physical Review B* **74**(17).
- Scholze, F., B. Beckhoff, M. Kolbe, M. Krumrey, M. Muller and G. Ulm (2006). "Detector calibration and measurement of fundamental parameters for X-ray spectrometry." *Microchimica Acta* **155**(1-2): 275-278.
- Scholze, F., R. Klein and R. Muller (2006). "Characterization of detectors for extreme UV radiation." *Metrologia* **43**(2): S6-S10.
- Schwanitz, K., U. Weiler, R. Hunger, T. Mayer and W. Jaegermann (2007). "Synchrotron-Induced Photoelectron Spectroscopy of the Dye-Sensitized Nanocrystalline TiO₂/Electrolyte Interface: Band Gap States and Their Interaction with Dye and Solvent Molecules." *J. Phys. Chem. C* **111**(2): 849 - 854.
- Senkovskiy, B. V., A. Y. Varykhalov, A. M. Shikin, V. K. Adamchuk and O. Rader (2006). "Quantum-well states in a thin Ag film on a Ni(111) substrate." *Physics of the Solid State* **48**(10): 1974-1980.
- Sergeevich, C. S. (2006). Rentgenovskaya Spectroscopiya kvaziodnomernih produktov karbonizacii polivinilidenftorida" [X-ray spectroscopy of the poly(vinylidene fluoride) and its carbonized derivatives], Chelyabinsk State Pedagogical University.
- Seyller, T. (2006). Structural, Chemical and Electronic Properties of Hydrogen-saturated SiC Surfaces and their Interfaces with Oxides, Friedrich-Alexander-Universität Erlangen-Nürnberg.
- Seyller, T., K. V. Emtsev, K. Gao, F. Speck, L. Ley, A. Tadich, L. Broekman, J. D. Riley, R. C. G. Leckey, O. Rader, A. Varykhalov and A. M. Shikin (2006). "Structural and electronic properties of graphite layers grown on SiC(0001)." *Surface Science* **600**(18): 3906-3911.

- Shaporenko, A., M. Elbing, A. Baszczyk, C. von Hanisch, M. Mayor and M. Zharnikov (2006). "Self-assembled monolayers from biphenyldithiol derivatives: Optimization of the deprotection procedure and effect of the molecular conformation." *Journal of Physical Chemistry B* **110**(9): 4307-4317.
- Shaporenko, A., K. Rossler, H. Lang and M. Zharnikov (2006). "Self-assembled monolayers of ferrocene-substituted biphenyl ethynyl thiols on gold." *Journal of Physical Chemistry B* **110**(48): 24621-24628.
- Shaporenko, A., M. Zharnikov, P. Feulner and D. Menzel (2006). "Quantitative analysis of temperature effects in radiation damage of thiolate-based self-assembled monolayers." *Journal of Physics-Condensed Matter* **18**(30): S1677-S1689.
- Shikin, A. M., M. B. Visman, G. G. Vladimirov, V. K. Adamchuk and O. Rader (2006). "Quantum-well states in Ag/W(100) and their symmetric evolution in the atomic limit of thickness." *Surface Science* **600**(13): 2681-2687.
- Shu, J. N., K. R. Wilson, M. Ahmed, S. R. Leone, C. Graf and E. Ruhl (2006). "Elastic light scattering from nanoparticles by monochromatic vacuum-ultraviolet radiation." *Journal of Chemical Physics* **124**(3).
- Sivkov, V. N., A. S. Vinogradov, S. V. Nekipelov, D. V. Sivkov, D. V. Vyalykh and S. L. Molodtsov (2006). "Oscillator Strengths for the Shape Resonances in the N K Absorption Spectrum of NaNO₃ Measured with the Use of Synchrotron Radiation." *Optics and Spectroscopy* **101**: 724-730.
- Sorg, C., N. Ponpandian, M. Bernien, K. Baberschke, H. Wende and R. Q. Wu (2006). "Induced magnetism of oxygen in surfactant-grown Fe, Co, and Ni monolayers." *Physical Review B* **73**(6).
- Soriano, L., A. Gutierrez, I. Preda, S. Palacin, J. M. Sanz, M. Abbate, J. F. Trigo, A. Vollmer and P. R. Bressler (2006). "Splitting of Ni 3d states at the surface of NiO nanostructures." *Physical Review B* **74**(19).
- Sorokin, A. A., S. V. Bobashev, K. Tiedtke and M. Richter (2006). "Multi-photon ionization of molecular nitrogen by femtosecond soft x-ray FEL pulses." *Journal of Physics B-Atomic Molecular and Optical Physics* **39**(14): L299-L304.
- Sorokin, A. A., A. Gottwald, A. Hoehl, U. Kroth, H. Schoppe, G. Ulm, M. Richter, S. V. Bobashev, I. V. Domracheva, D. N. Smirnov, K. Tiedtke, S. Dusterer, J. Feldhaus, U. Hahn, U. Jastrow, M. Kuhlmann, T. Nunez, E. Plonjes and R. Treusch (2006). "Method based on atomic photoionization for spot-size measurement on focused soft x-ray free-electron laser beams." *Applied Physics Letters* **89**(22).
- Staats, G., L. Fernandez, K. Holldack, U. Schade and D. Schondelmaier (2006). "Coupling structures for terahertz near-field micro spectroscopy." *Infrared Physics & Technology* **49**(1-2): 122-127.

- Stacchiola, D., S. Kaya, J. Weissenrieder, H. Kühlenbeck, S. Shaikhutdinov, H. J. Freund, M. Sierka, T. K. Todorova and J. Sauer (2006). "Synthesis and structure of ultrathin aluminosilicate films." *Angewandte Chemie-International Edition* **45**(45): 7636-7639.
- Staufenbiel, F., H. Bttig, P. Evtushenko, D. Janssen, U. Lehnert, P. Michel, K. Moller, C. Schneider, R. Schurig, J. Teichert, R. Xiang, J. Stephan, W. D. Lehmann, T. Kamps, D. Lipka, I. Will and V. Volkov (2006). "Test of the photocathode cooling system of the 3 1/2 cell SRF gun." *Physica C-Superconductivity and Its Applications* **441**(1-2): 216-219.
- Stefan, N. (2006). *Self-Assembled Organic Layers on Solid Surfaces: Structure, Dynamics and Modification*, Technische Universität München.
- Steffes, H., A. Schleunitz, U. Gernert, R. Chabicovsky and E. Obermeier (2006). "A novel optical gas sensor based on sputtered $\text{In}_x\text{O}_y\text{N}_z$ films with gold-nanodots." *Microelectronic Engineering* **83**(4-9 SPEC. ISS.): 1197-1200.
- Steinrück, H. P., T. Fuhrmann, C. Papp, B. Tränkenschuh and R. Denecke (2006). "A detailed analysis of vibrational excitations in X-ray photoelectron spectra of adsorbed small hydrocarbons." *Journal of Chemical Physics* **125**(20).
- Stollberg, H. (2007). "Size selective colloidal-gold localization in transmission x-ray microscopy." *Journal of Microscopy* **225**(1): 80-87.
- Streber, R. (2006). *In-situ XPS-Untersuchungen des Einflusses von Silber auf die CO-Adsorption auf gestuften Platinoberflächen*, Universität Erlangen-Nürnberg.
- Teschner, D., E. Vass, M. Havecker, S. Zafeiratos, P. Schnorch, H. Sauer, A. Knop-Gericke, R. Schloegl, M. Chamam, A. Wootsch, A. S. Canning, J. J. Gamman, S. D. Jackson, J. McGregor and L. F. Gladden (2006). "Alkyne hydrogenation over Pd catalysts: A new paradigm." *Journal of Catalysis* **242**(1): 26-37.
- Teschner, D., A. Wootsch, O. Pozdnyakova, H. Sauer, A. Knop-Gericke and R. Schloegl (2006). "Surface and structural properties of Pt/CeO₂ catalyst under preferential CO oxidation in hydrogen (PROX)." *Reaction Kinetics and Catalysis Letters* **87**(2): 235-247.
- Tieg, C. (2006). *Growth, structure and magnetic properties of single-crystalline antiferromagnetic NiMn films and bilayers of NiMn and Co on Cu(001)*, Martin-Luther-Universität Halle-Wittenberg.
- Tinkham, B. P., M. Takahashi, B. Jenichen, T. Watahiki, W. Braun and K. H. Ploog (2006). "Structure and stability of $\text{Pr}_2\text{O}_3/\text{Si}(0\ 0\ 1)$ heterostructures grown by molecular beam epitaxy using a high temperature effusion source." *Semiconductor Science and Technology* **21**(12): 1552-1556.

- Tran, E., M. Duati, V. Ferri, K. Mullen, M. Zharnikov, G. M. Whitesides and M. A. Rampi (2006). "Experimental approaches for controlling current flowing through metal-molecules-metal junctions." *Advanced Materials* **18**(10): 1323-1328.
- Tränkenschuh, B. (2006). In-situ Untersuchungen zur chemischen Reaktivität von gezielt veränderten Metalloberflächen, Universität Erlangen-Nürnberg.
- Tränkenschuh, B., N. Fritsche, T. Fuhrmann, C. Papp, J. F. Zhu, R. Denecke and H. P. Steinrück (2006). "A site-selective in situ study of CO adsorption and desorption on Pt(355)." *Journal of Chemical Physics* **124**(7).
- Tränkenschuh, B., C. Papp, T. Fuhrmann, R. Denecke and H. P. Steinrück (2007). "The dissimilar twins - a comparative, site-selective in situ study of CO." *Surface Science* **601**(4): 1108-1117.
- Unger, W. E. S., S. Swaraj, U. Oran and A. Lippitz (2006). "Radio frequency (r.f.) plasma-deposited polymer films: influence of external plasma parameters as viewed by comprehensive in-situ surface chemical analysis by XAS, XPS and ToF-SIMS." *Surface and Interface Analysis* **38**(4): 522-525.
- Valencia, S., A. Gaupp, W. Gudat, L. Abad, L. Balcells, A. Cavallaro, B. Martinez and F. J. Palomares (2006). "Mn valence instability in La_{2/3}Ca_{1/3}MnO₃ thin films." *Physical Review B* **73**(10).
- Valencia, S., A. Gaupp, W. Gudat, L. Abad, L. Balcells, B. Martínez and V. Laukhin (2006). "Soft x-ray absorption spectroscopy of strained epitaxial manganite thin films." *Applied Physics Letters* **89**(17).
- Valencia, S., A. Gaupp, W. Gudat, H.-C. Mertins, P. M. Oppeneer, D. Abramsohn and C. M. Schneider (2006). "Faraday rotation spectra at shallow core levels: 3p edges of Fe, Co, and Ni." *New Journal of Physics* **8**: 1-11.
- Varykhalov, A., C. Biswas, W. Gudat and O. Rader (2006). "Fabrication of patterned Au films as supporting templates for one-dimensional magnetic nanostructures." *Physical Review B* **74**(19).
- Varykhalov, A., W. Gudat, V. K. Adamchuk and O. Rader (2006). "Magic numbers in two-dimensional self-organization of C-60 molecules." *Physical Review B* **73**(24).
- Vollmer, A., H. Weiss, S. Rentenberger, I. Salzmann, J. P. Rabe and N. Koch (2006). "The interaction of oxygen and ozone with pentacene." *Surface Science* **600**(18): 4004-4007.
- Vora, K. D., B. Lochel, E. C. Harvey, J. P. Hayes and A. G. Peele (2006). "AFM-measured surface roughness of SU-8 structures produced by deep x-ray lithography." *Journal of Micromechanics and Microengineering* **16**(10): 1975-1983.

- Voss, S. (2007). "Electronic structure of Mn₁₂ derivatives on the clean and functionalized Au surface." *Physical Review B* **75**: 045102.
- Wang, H. C., J. T. Zhu, Z. S. Wang, Z. Zhang, S. M. Zhang, W. J. Wu, L. Y. Chen, A. G. Michette, A. K. Powell, S. J. Pfauntsch, F. Schafers and A. Gaupp (2006). "Broadband Mo/Si multilayer analyzers for the 15-17 nm wavelength range." *Thin Solid Films* **515**(4): 2523-2526.
- Wang, Z. S., H. C. Wang, J. T. Zhu, F. L. Wang, Z. X. Gu, L. Y. Chen, A. G. Michette, A. K. Powell, S. J. Pfauntsch and F. Schafers (2006). "Broad angular multilayer analyzer for soft x-rays." *Optics Express* **14**(6): 2533-2538.
- Wang, Z. S., H. C. Wang, J. T. Zhu, F. L. Wang, Z. X. Gu, L. Y. Chen, A. G. Michette, A. K. Powell, S. J. Pfauntsch and F. Schäfers (2006). "Broadband multilayer polarizers for the extreme ultraviolet." *Journal of Applied Physics* **99**(5).
- Wang, Z. S., H. C. Wang, J. T. Zhu, Y. Xu, S. M. Zhang, C. X. Li, F. L. Wang, Z. Zhang, Y. R. Wu, X. B. Cheng, L. Y. Chen, A. G. Michette, S. J. Pfauntsch, A. K. Powell, F. Schafers, A. Gaupp and M. MacDonald (2006). "Extreme ultraviolet broadband Mo/Y multilayer analyzers." *Applied Physics Letters* **89**(24).
- Weidner, T. (2006). *Selbstorganisierte Monolagen starrer tripodaler Liganden auf Goldoberflächen*, Universität Kassel.
- Weidner, T., A. Kramer, C. Bruhn, M. Zharnikov, A. Shaporenko, U. Siemeling and F. Trager (2006). "Novel tripod ligands for prickly self-assembled monolayers." *Dalton Transactions*(23): 2767-2777.
- Weinhardt, L., O. Fuchs, A. Peter, E. Umbach, C. Heske, J. Reichardt, M. Bar, I. Lauermaun, I. Kotschau, A. Grimm, S. Sokoll, M. C. Lux-Steiner, T. P. Niesen, S. Visbeck and F. Karg (2006). "Spectroscopic investigation of the deeply buried Cu(In,Ga)(S,Se)(2)/Mo interface in thin-film solar cells." *Journal of Chemical Physics* **124**(7).
- Wende, H., C. Sorg, M. Bernien, A. Scherz, P. J. Jensen, N. Ponpandian and K. Baberschke (2006). "Spin fluctuations in coupled two-dimensional magnetic trilayers." *Physica Status Solidi B-Basic Solid State Physics* **243**(1): 165-168.
- Wernicke, G., J. Frank, H. Gruber, M. Dürr, A. Langner, S. Eisebitt, C. Günther, L. Bouamama, S. Krüger and A. Hermerschmidt (2006). Applications of the high-resolution optical reconstruction of digital holograms. *Proceedings of SPIE - The International Society for Optical Engineering*.
- Wiedwald, U. (2007). "Lowering of the L10 ordering temperature of FePt nanoparticles by He⁺ ion." *Applied Physics Letters* **90**(6): 062508-1-062508-3.
- Wilke, M., F. Farges, G. M. Partzsch, C. Schmidt and H. Behrens (2007). "Speciation of Fe in silicate glasses and melts by in-situ XANES spectroscopy." *American Mineralogist* **92**(1): 44-56.

- Wilke, M., C. Schmidt, F. Farges, V. Malavergne, L. Gautron, A. Simionovici, M. Hahn and P. E. Petit (2006). "Structural environment of iron in hydrous aluminosilicate glass and melt-evidence from X-ray absorption spectroscopy." *Chemical Geology* **229**(1-3): 144-161.
- Willneff, E. A., S. Braun, D. Rosenthal, H. Bluhm, M. Havecker, E. Kleimenov, A. Knop-Gericke, R. Schlogl and S. L. M. Schroeder (2006). "Dynamic electronic structure of a Au/TiO₂ catalyst under reaction conditions." *Journal of the American Chemical Society* **128**(37): 12052-12053.
- Winter, B., S. Berkebile, J. Ivanco, G. Koller, F. P. Netzer and M. G. Ramsey (2006). "Oxygen induced molecular reorientation on aluminum." *Applied Physics Letters* **88**(25).
- Winzer, A. T., G. Gobsch, R. Goldhahn, D. Fuhrmann, A. Hangleiter, A. Dadgar and A. Krost (2006). "Influence of excitons and electric fields on the dielectric function of GaN: Theory and experiment." *Physical Review B* **74**(12).
- Wurmehl, S. (2006). *Spin Polarised Heusler Compounds*, Johannes Gutenberg - Universität, Mainz.
- Wurmehl, S., G. H. Fecher, K. Kroth, F. Kronast, H. A. Dürr, Y. Takeda, Y. Saitoh, K. Kobayashi, H. J. Lin, G. Schönhense and C. Felser (2006). "Electronic structure and spectroscopy of the quaternary Heusler alloy Co₂Cr_{1-x}Fe_xAl." *Journal of Physics D-Applied Physics* **39**(5): 803-815.
- Zabolotnyy, V. B., S. V. Borisenko, A. A. Kordyuk, J. Fink, J. Geck, A. Koitzsch, M. Knupfer, B. Buchner, H. Berger, A. Erb, C. T. Lin, B. Keimer and R. Follath (2006). "Effect of Zn and Ni impurities on the quasiparticle renormalization of superconducting Bi-2212." *Physical Review Letters* **96**(3).
- Zarkadas, C., A. G. Karydas, M. Muller and B. Beckhoff (2006). "X-ray resonant Raman scattering on Ni employing polarized and unpolarized exciting radiation." *Spectrochimica Acta Part B-Atomic Spectroscopy* **61**(2): 189-195.
- Zemlyanov, D., B. Aszalos-Kiss, E. Kleimenov, D. Teschner, S. Zafeiratos, M. Havecker, A. Knop-Gericke, R. Schlogl, H. Gabasch, W. Unterberger, K. Hayek and B. Koltzer (2006). "In situ XPS study of Pd(111) oxidation. Part 1: 2D oxide formation in 10(-3) mbar O-2." *Surface Science* **600**(5): 983-994.
- Zickler, G. A. (2006). *Structure and mechanical properties of carbon- and silica-based nanomaterials*, University of Leoben (Austria).
- Zimina, A., S. Eisebitt, W. Eberhardt, J. Heitmann and M. Zacharias (2006). "Electronic structure and chemical environment of silicon nanoclusters embedded in a silicon dioxide matrix." *Applied Physics Letters* **88**(16).
- Zou, Y., L. Kilian, A. Scholl, T. Schmidt, R. Fink and E. Umbach (2006). "Chemical bonding of PTCDA on Ag surfaces and the formation of interface states." *Surface Science* **600**(6): 1240-1251.

Zubavichus, Y., A. Shaporenko, M. Grunze and M. Zharnikov (2006). "Solid-state near-edge X-ray absorption fine structure spectra of glycine in various charge states." *Journal of Physical Chemistry B* **110**(7): 3420-3427.

Zubavichus, Y., M. Zharnikov, Y. J. Yang, O. Fuchs, E. Umbach, C. Heske and M. Grunze (2006). "Oxygen K-edge X-ray absorption fine structure studies of vacuum-deposited ice films." *Langmuir* **22**(17): 7241-7247.

Authors Index

(click on page number to open selected page)

A abete, Carlo	39	Beerhues, L.	279
Abrudan, Radu	441, 489	Behlke, Joachim	272
Adamchuk, V. K.	568	Behm, R.J.	110
Adrian, H.	537	Benomar, M	555
Aeschlimann, M	543	Berger, H.	383
Akdogan, Numan	394, 463	Berger, Helmut	124
Alekseev, V.A.	66	Berkebile, Stephen	305
Alesandrovic, Vesna	179	Bernardi, Fabiano	549
Alings, Claudia	272	Bernhardt, Ricardo	260
Aliouane, Nadir	139	Bernien, Matthias	441, 489
Allegretti, Francesco	605	Beuerle, T.	279
Alpern, Peter	208	Biegger, Erwin	484
Alvarado, F.	254	Bienert, Ralf	269
Amiens, Catherine	80	Bigot, Jean-Yves	456
Anderlund, Magnus	282	Birke, Thomas	35
Andreazza, P.	385	Biswas, C	156
Andreazza-Vignolle, C.	385	Biswas, Indro	337
Andric, L.	367	Björneholm, Olle	362, 493
Andriyevsky, B.	150	Bodenthin, Y.	178
Arent, Susan	277	Boeglin, Christine	115, 179, 456
Argyriou, Dimitri	139	Bogdanoff, P.	321
Ariffin, Ahmad K.	523	Boltalina, O.V.	202
Arion, Tiberiu	571	Bondarenko, A	540
Aristov, V.Yu.	330	Borisenko, Sergey	124, 126, 495
Arnau, Andrés	308	Borninkhof, Jörg	35
Arveux, Emmanuel	314	Bostedt, Christoph	514
As, D.J.	529	Bourenkov, G.P.	258
Ash, Miriam-Rose	288	Bournel, F.	388
Awada, A.	526	Bousquet, Romain	187
Aziz, Emad F.	369	Bovensiepen, U.	534
B aberschke, K.	400	Boyen, Hans-Gerd	505
Badin, Mihaela	113	Braden, M	555
Bär, Marcus	193	Brand, Guido	5
Bagus, Paul S.	74	Brandt, Guido	35
Baitinger, Evgeniy Michailovich	136	Braun, W.	503, 508
Balbach, Jochen	269	Braun, Walter	319, 478, 616
Balkaya, B.	451	Braun, Wolfgang	598, 613
Balke, Benjamin	472, 549	Braune, M.	367
Balke, Benny	408	Bredow, T.	330
Ballentine, Greg	171	Bresch, Harald	117
Banhart, John	199, 352	Broekman, L.	565
Bansmann, J.	110	Broekmann, Peter	624
Barth, Joachim	472, 549	Brück, S.	537
Barth, Silko	362, 491, 493, 588	Brückel, Thomas	521
Bartunik, H.D.	258	Bruessing, Frank A.	414
Bashir, Asif	113	Bruhn, Thomas	478
Batchelor, David	130, 162, 337, 383, 403	Bruning, M.	258
Bauer, Eric	495	Brzhezinskaya, M.M.	391, 466, 560
Baumgärtel, H.	372, 375	Buchholz, Christian	14, 18, 20, 23
Bayer, D	543	Buck, J.	565
Bazlov, N	540	Büchner, B.	162, 383
Bazuev, Gennadii	324	Buechner, Bernd	124
Beaurepaire, Eric	456	Büchner, Bernd	126, 296, 495
Bechstedt, F.	529	Bürkman-Gehrlein, Klaus	35
Bechstein, K	97	Bukhtiyarov, V.I.	71
Becker, Uwe	117, 367	Burger, Sven	26
Beckhoff, Burkhard	32, 39, 41	Burgert, Michael	364
Bednarzik, Martin	60	Buschhorn, Stefan	414
		C afola, A.A.	391
		Calbucci, Vittorio	343
		Carlson, Robert M. K.	514
		Chang, C F	546
		Chang, Hong	458

Chang, Y. J.	552	Edlich, Frank	275
Chassé, Thomas	337	Edmonds, K. W.	443
Chatterji, Tapan	521	Ehresmann, A.	422, 424, 428, 430, 453
Chaudret, Bruno	80	Eichelbaum, Maik	327
Chebotaryov, Sergey	136	Eichhorn, Klaus-Jochen	355
Sergeevich		Eichhorn, Tobias	411
Chen, D.P.	383	Eiper, E.	144, 148
Chen, Lingyan	475	Eisebitt, S.	443
Chupakhina, Tatiana	324, 498	Eland, J.H.D.	367
Cibik, Levent	5, 11	Elmers, Hans-Joachim	408, 411
Ciepluch-Trojanek, W.	150	Emmerling, Franziska	103, 176, 619
Ciuculescu, Diana	80	Endrino, José Luis	133
Cobet, C.	150, 529	Epler, B.	279
Cobet, Christoph	319, 616	Eremin, Ilya	124
Cölfen, Helmut	214	Erko, A.	128, 246, 294
Cramm, Stefan	408, 411	Erko, A.I.	595
Croker, Denise	93	Erko, Alexei	205, 397, 438
Cubanes, Denis	532	Escher, Matthias	237
Cubaynes, Denis	426	Esser, N.	150, 529
		Esser, Norbert	319, 355, 478, 616
D ähne, Mario	168	Evsyukov, Sergey	136
Dahl, Jeremy	514	Evgenievich	
Damnik, Niklas	498		
Damnik, Nuklas	501	F aelber, Katja	288
Dargel, R	97	Farle, Michael	80
Dargel, Rainer	222	Faubel, Manfred	369
Darowski, N.	419	Faul, Charl F. J.	619
Darowski, Nora	291, 438	Fauth, Kai	80, 171, 505
Dau, Holger	282	Fecher, Gerhard	231, 472, 549
Daum, Reiner	35	Fedoseenko, S.I.	466
Dedkov, Yu. S.	602	Feikes, Jörg	35
Dedkov, Yurii	324	Felser, Claudia	231, 472, 549
Dedkov, Yuriy S.	364	Ferretti, N.	451
Dedkov, Yury S.	484	Feulner, Peter	173
Dedyulin, Sergey N.	100	Feyerherm, R.	461
Dembski, Sofia	119	Feyerherm, Ralf	139, 291, 296, 449, 555
Demchenko, Iraida N.	130	Fiechter, S.	321
Demekhin, Philipp	453	Findenegg, Gerald H.	181
Denecke, Reinhard	86	Fink, Joerg	124
Denks, I.A.	346	Fink, Jörg	126, 495
Denkwitz, Y.	110	Fink, R.	162
Dersch, Uwe	26	Fink, Rainer	357, 593
Diehl-Guilbaud, Segolène	532	Fischer, Andreas	14, 18, 20, 23
Dietrich, R.T. Zahn	516	Fischer, Christian-Herbert	193, 195
Dil, Hugo	573	Flesch, Roman	117, 487, 519, 571
Dittmar, G.	285	Fliegau, Rolf	35, 41
Dobrovolsky, Yuri A.	105	Follath, Rolf	124, 126, 162, 432, 495
Dorbandt, I.	321	Fonin, M.	602
Drechsler, Stefan-Ludwig	126	Fonin, Mikhail	364, 484
Dressler, Olaf	35	Fostiropolous, K.	607
Dudeck, Jan	260	Frank,	18, 20, 23
Dudy, Lenart	523	Fratzl, Peter	214, 260
Dudzik, E.	446, 449, 461, 555	Freund, Christian	288
Dudzik, Esther	139, 296	Freund, H.-J.	77
Dürr, Herrmann	231, 456, 543, 549	Friedrich, Christian	478
Dürr, Volker	35	Friedrich, Marion	616
Dunsch, L.	383	Fuchs, F.	529
Dunsch, Lothar	296	Fuchs, Martin	216
Dwelk, Helmut	523	Fuhrmann, Thomas	86
		Fuoco, Roger	39
E bbinghaus, Stefan G.	403		
Eberhardt, W.	451, 503, 508		
Eberhardt, Wolfgang	54, 231, 240, 380, 549		

G abasch, Harald	121	Haas, Sylvio	302, 311, 327
Gacic, M.	537	Haase, W.	178
Gago, Raul	349	Hävecker, M.	71, 94, 110
Gahl, C.	534	Hävecker, Michael	83, 89
Galakhov, Vadim	324, 498, 501	Hahn, Oliver	32, 205
Galaktionov, M.S.	202	Hallmeier, K.H.	607
Gallet, J.-J	388	Han, Luyang	505
Gamblin, G.	367	Hansen, Karsten	339
Garcia-Moreno, Francisco	352	Harding, Chris	588
Garrido, Jose	173	Harding, Clive	289
Gaudin, Jerome	240	Hartmann, M.D.	258
Gaudin, Jérôme	380	Hartnig, Christoph	199
Gaupp, Andreas	475	Harwardt, Michael	208
Gavrila, G.	478	Haug, Andrea	337
Geck, J.	383	Haumann, Michael	282
Geck, Jochen	124, 296, 495	Haverkort, M W	546
Geck, Jochen	126	Heim, Stefan	190, 234, 510
Gensch, M.	285	Heimbrodt, Wolfram	403
Gensch, Michael	355	Heinecke, Elke	426, 532
Genzel, C.	144	Heinemann, Udo	266, 269
Genzel, Ch.	346	Heitkamp, B	543
Gerlach, Martin	5, 8, 11	Helmbrecht, Tolga	288
Geue, Thomas	586	Helmuth, Berger	296
Gianina, Gavrila	516	Hendel, Stefan	590
Gibmeier, J.	346	Henriksen, Anette	277
Girard-Lauriault, P.-L.	248	Hentschel, Manfred P.	208
Glaser, Leif	179, 584	Herbort, C.	537
Glass, Holger	35	Herfort, Jens	598
Glass-Maujean, M.	422, 424, 428, 430	Hergenhahn, U.	362
Gleber, Gudrun	333, 335	Hergenhahn, Uwe	491, 493, 588
Gleber, Sophie-Charlotte	190, 234, 289	Herrmann, Claudia	598
Gloskovskii, Andrei	231, 472, 549	Hertel, Ingolf V.	369
Gode, Sophie	240	Heßler, Markus	171
Godehusen, Kai	240, 380	Hild, Kerstin	411
Goebbels, J.	165	Hinkov, Vladimir	126
Goebbels, Jürgen	260	Hinrichs, K.	285
Goering, E.	537	Hinrichs, Karsten	355
Goering, Eberhard	357	Hoberg, Hans Georg	35
Göritz, D.	165	Hoefl, Frank	216
Goldhahn, R.	529	Hoehl, Arne	29, 35
Goldt, I.V.	202	Hoell, A.	251, 299, 321
Gomoyunova, M.V.	417	Hoell, Armin	302, 311, 327
González, Nora	308	Hofmann, Andreas	115
Gordeev, Yu.S.	202, 254	Hogan, Kirsty	605
Gorgoi, M.	211, 446, 503, 508	Holder, M.	602
Gottwald, Alexander	14, 16	Holfeld, Christian	26
Gourdon, Andre	308	Hollack, Karsten	29, 216
Graf, Birgit	357	Horn, Karsten	308, 573, 576
Graf, Christina	115, 117, 119	Hu, Z	546
Grafe, H.J.	383	Huber, Patrick	586
Grimm, Alexander	193, 195	Hümann, Sascha	624
Groth, Ulrich	364	Hünlich, Klaus	458
Grünert, Wolfgang	620	Hunger, Ralf	74, 197, 359, 624
Grundmeier, Alexander	282	Hutchings, Graham	89
Gruyters, M.	558		
Gu, Zhongxiang	475	I mperia, P.	385
Güngerich, Martin	403	Inosov, Dmytro	124, 126, 495
Gupta, Ajay	438	Ioannides, D.	246
Gutiérrez, Alejandro	133	Ionov, Leonid	355
Guttman, P.	251		
Guttman, Peter	190, 234, 289, 510	J aegermann, Wolfram	74, 197, 359, 624
Gutzeit, Stefan	563	Jähnert, Susanne	181
		Jakob, G.	537
H aas, S.	321	Jakob, Gerhard	408, 411

Janke-Gilman, N.	565	Koitzsch, Andreas	124, 126, 495
Janowitz, Christof	225	Kolbe, Jörg	35
Janowitz, Christoph	523	Kolbe, Michael	32
Jansson, U.	503	Koller, Georg	305
Jaouen, N.	388	Konovalov, Igor	316, 469
Jenichen, Bernd	291, 598, 613	Kordyuk, Alexander	124, 126
Jentoft, Friederike	89	Korytar, D.	446
Jimenez, Catalina	352	Koteski, V.	481
Jiménez, Ignacio	349	Kotzsch, Alexander	243
Jochims, H.W.	372, 375	Kouba, Josef	54, 63
Johansson, E.M.J.	503, 508	Krakert, Simone	113
Johnev, B.	607	Kranold, Rainer	311
Joshi, S.	362	Krapf, Alica	523
Joshi, Sanjeev	491, 493, 588	Krasnikov, S.A.	391, 466, 560
Jung, C.	162	Krizikalla, Milusche	108
Jung, Christian	193, 195	Kröger, Emily	605
K äfer, Daniel	622	Kröhnert, Jutta	89
Kaganer, Vladimir	598	Kröning, S.	285
Kaindl, G	546	Kroll, T.	383
Kallmayer, Michael	408, 411	Kroll, Thomas	296
Kampe, Annett	14, 18, 20, 23	Kronast, Florian	231, 549
Kampen, Thorsten	308	Kropp, Timo	195
Kampen, Thorsten U.	573, 576	Kroth, Udo	14, 16
Kanngießer, Birgit	41, 187, 205, 219, 222	Krumrey, Michael	5, 8, 11
Karydas, Andreas	32	Kubalski, Markus	54
Germanos		Kubowic, Stefan	378
Katsikini, M.	128, 246, 294	Kuch, W	543
Kawwam, Mohammad	80	Kuch, Wolfgang	441, 489
Kaya, S.	77	Kucherenko, Yu.	602
Keckes, J.	144, 146, 148	Kudo, So	359
Keimer, Bernhard	126	Kümmel, Daniel	266
Kern, Birgit	505	Kuhlenbeck, H.	77
Khaibullin, Rustam	394, 463	Kumpugdee-Vollrath, M.	251, 299
Kielbassa, S.	110	Kurde, J.	400
Kielich, Witoslaw	453	Kurth, D. G.	178
Kim, Jeong Won	573	L ablanquie, P.	367
Kinza, Michael	171	Lamont, Christine	605
Kipp, L.	565	Lang, Heinrich	600
Kirschner, Jürgen	441, 458, 489, 610	Lang, M.	461
Klar, Peter J.	403	Lange, Axel	208
Klaus, M.	144, 346	Lange, Ralph	35
Kleibert, Armin	563	Langer, Burkhard	117, 119
Klein, Andreas	314	Laschewsky, André	378
Klein, Roman	5, 29, 35	Lau, J. Tobias	579, 582, 584
Kleineberg, Ulf	237, 590	Laubis, Christian	14, 18, 20, 23, 26
Klemradt, Uwe	153	Laubschat, C.	602
Klepka, Marcin	130	Lauermann, I.	607
Klimmer, Andreas	505	Lauermann, Iver	193, 195
Klötzer, Bernhard	121	Lawniczak-Jablonska, Krystyna	130
Klünder, Kathrin	514	Lázár, Károly	89
Klumpp, S.	422, 424, 428, 430	Le, Messurier Daniel	302
Klumpp, Stephan	453	Lee, J. S.	552
Knight, Matthew	605	Lehmann, Sebastian	193, 195
Knop-Gericke, A.	71, 94, 110	Lehnert, Werner	199
Knop-Gericke, Axel	83, 89, 121	Leisner, Thomas	117
Knupfer, M.	162, 330, 383	Leitenberger, W.	146
Knupfer, Martin	124, 126, 296, 337, 495	Leitenberger, Wolfram	153, 176, 333, 335, 406, 586
Koch-Müller, Monika	183	Leiterer, Jork	176
Könnecke, R.	443	Levchenko, Alexey V.	105
Kötschau, I.M.	346	Lewera, Adam	74
Kofler, Michael	288	Lewin, E.	503, 508

Lewinski, René	117, 119	Maul, Jochen	237, 590
Leyh, B.	372, 375	Mavromati, A.	294
Li, Chenghao	214	Mavromati, E.	246
Li, Haifeng	521	Max, Klaas EA	269
Lider, V.V.	595	Mayer, Gillian	484
Limberg, Christian	282	Mayer, Thomas	197
Lin, C.T.	383	Meiwes-Broer, Karl-Heinz	563
Lin, Jingquan	237	Melkozerova, Marina	324
Lin, Jinquan	590	Melnikov, A.	534
Lippitz, A.	159, 248	Meneghini, Carlo	438
Lischka, K.	529	Merkel, Michael	237, 590
Lischke, T.	362	Mertig, I.	330
Lischke, Toralf	491, 493	Mertin, M.	211, 446
Lisowski, M.	534	Mertoglu, Murat	378
Liu, S.	514	Mertsch, Olaf	57
Lobbenmeier, B.	526	Merzlikin, Sergej	620
Lochr, R.	375	Meuffels, Paul	521
Locht, R.	372	Meyer, Michael	426, 487, 519, 532
Loechel, Bernd	54, 57	Michael, G. Ramsey	305
Löchel, Bernd	60	Michette, Alan	475
Loechel, Bernd	63	Miguel, J	543
Löser, Karolin	168	Miguel, Jorge	441
Lommel, M.	178	Mikhaylova, Yulia	355
Lud, Simon Quartus	173	Mikoushkin, V.M.	202, 254
Lücke, Christian	275	Mitdank, Rüdiger	523
Lühl, Lars	219, 222	Mitrea, Genoveva	190, 234
Luo, J.	400	Mitschke, Stefan	263
Lux-Steiner, Martha	195	Möller, Andreas	187
Lux-Steiner, Martha Christina	193	Möller, Thomas	514, 579, 582, 584
		Mönig, Harry	193, 195
		Molodtsov, S.L.	202, 254, 417, 466, 602
M acdonald, Mike	475	Molodtsov, Serguei	324, 432, 498, 501, 435
Maestre-Martínez,	275		
Mitcheel		Molodtsova, O.V.	330
Maglione, Mario	314	Morgenstern, R.	254
Magnuson, Ann	282	Morris, D.J.P.	449
Mahnke, H.-E.	481	Mühlberger, Fabian	263
Mai, Alexander	48	Mülle,	35
Maier, Timm	272	Müller, Beate	523
Makhova, Liudmila	316, 469	Müller, Bernd R.	208
Malbrich, C.	383	Müller, Jan	69
Malbrich, Christine	296	Müller, Jürgen J.	266
Maltseva, Elena	103, 619	Müller, Leonard	153
Malygin, D. E.	417	Müller, Matthias	41
Malzer, Wolfgang	205, 219, 222	Müller, Peter	8, 11
Malzer, Wolfgang	187	Müller, Ralph	29, 35
Manescu, Adrian	343	Mueller, Thomas D.	243
Manier, Ch.-A.	159	Müller, Uwe	216
Manjubala, Inderchand	260	Munoz-Navia, Milton	458
Manke, Ericl	197	Murray, Joseph	92
Manke, Ingo	199		
Mantler, Michael	32		
Mantouvalou, Ioanna	222	N eeb, M.	451
Manzke, Recardo	225, 523	Nefedov, Alexei	394, 463, 521
Marburger, S.	362	Nekat, Bettina	205
Marczynski-Buehlow, M.	565	Nekipelov, Sergey	432, 435
Margeat, Olivier	80	Nesterov, M.A.	391
Mariot, J.-M.	388	Neudachina, Vera S.	100, 105
Martin, Zulima	349	Neumann, Manfred	324, 498, 501
Martins, Michael	179, 584	Neumann, P.	279
Martinschitz, K.J.	144, 148	Neumann, Piotr	275
Marutzky, M.	526	Nevedov, Alexei	414
Maslyuk, V.	330	Neville, John J.	571
Matsunaga, Mariko	359	Ngawhirunpat, T.	299

Nickel, Joachim	243	Pokapanich, W.	362
Niebling, Tobias	403	Pokapanich, Wandared	493
Niemann, Bastian	510	Polcik, Martin	605
Nikolaeva, E.V.	466	Polei, Stefan	563
Niwa, Daisuke	359	Pomplun, Jan	26
Noh, T. W.	552	Ponpandian, N.	400
Nolting, Dirk	369	Ponpandian, Nagamony	563
Noro, Massimo	289	Pontius, Niko J.	456
Novakova, Eva	190	Powell, A Keith	475
Novakovic, N.	481	Powis, Ivan	588
Novikov, A	540	Poygin, Maksim V.	100
Novikova, N.N.	595	Poygin, Maxim V.	105
O berschall, A.	258	Pozdnyakova-Tellingner, Olga	89
Öhrwall, G.	362	Prakash, R.	357
Öhrwall, Gunnar	493	Preobrajenski, A.B.	391, 466, 560
Oehzelt, Martin	305	Prima, H.	534
Oelsner, Andreas	237	Prinz, Manuel	324
Österreicher, Björn	117	Prokhnenko, Oleksandr	139
Opanasopit, P.	251	Pronin, I.I.	417
Ortega, Enrique	308	Pruskil, Gerd	168
Ortega, Luc	397	Puchegger, Stefan	142
Ortolani, M.	552	Pucher, Andreas	335
Osaka, Tetsuya	359	Püttner, R.	466
Osán, János	39	Püttner, Ralph	100, 105
Ossipyan, Yu.A.	330	Pütz, Michael	263
Ott, H	546	R ademann, Klaus	327
Ottosson, Niklas	369	Rader, O.	156, 443, 568, 602
Ovsyannikov, R	540	Raekers, Michael	324, 498, 501
Ovsyannikov, Ruslan	231, 498, 501, 549	Raeth, T.	279
P agels, Marcel	219	Rammelt, Stefan	260
Palacín, Sergio	133	Rehbein, Stefan	510
Palaudoux, J.	367	Reichardt, Gerd	228, 263
Paloura, E. C.	294	Reller, Armin	403
Paloura, E.C.	128, 246	Remmel, Natascha	272
Panne, Ulrich	176	Renghini, Chiara	343
Pantleon, Karen	339	Rennhofer, Harald	142
Panzner, Tobias	333, 335	Rensmo, H.	508
Papp, Christian	86	Repen, Boris	282
Paris, Oskar	142, 181, 214	Richter, Mathias	14, 16
Parthier, Christoph	275	Richter, Tobias	426, 514, 532
Paßmann, Regina	478	Richter, Wolfgang	478
Patel, Ram	458	Riesemeier, H.	165
Patryn, A.	150	Riesemeier, Heinrich	199
Paustian, Wolfgang	16	Riley, J.	565
Peisert, Heiko	337	Rittmann, Jochen	579, 582
Penent, F.	367	Rochet, F.	388
Penuelas, J.	385	Rodriguez, Alvarez H.	346
Persson, Jörg	521	Rößler, Karin	600
Pesin, Leonid Abramovich	136	Roodenko, Katy	355
Peterlik, Herwig	142	Roshchupkin, Dmitry	397
Peters, Sven	319	Roske, Yvette	266, 288
Pfauntsch, Slawka	475	Rossnagel, K.	565
Piantek, M	543	Rossner, H.H.	419
Piantek, Marten	441	Rossocha, Maksim	272
Pietsch, U.	178	Rosu, D.-M.	285
Pietsch, Ullrich	333, 335, 406	Rott, Karsten	590
Pinakidou, F.	128, 246, 294	Rudolph, Ivo	45, 48
Platzer-Björkman, C.	508	Rudra, Sukumar	616
Plenge, Jürgen	487, 519	Rüdiger, Ulrich	364, 484
Plöger, Sven	18, 20, 23	Rühl, Eckart	115, 117, 119, 487, 519, 571
Ploog, Klaus	291, 598	Ruiz-Osés, Miguel	308
Ploog, Klaus H.	613		

Rybkin, A. G.	568	Schütz, Gisela	80
Saalfrank, Rolf W.	357	Schulte-Ladbeck, Rasmus	263
Saenger, Wolfram	272	Schultz-Heienbrok, Robert	272
Salbeck, Josef	319	Schumacher, B.	110
Sanchez-Barriga, J	543	Schumacher, Gerhard	352
Sandell, A.	503, 508	Schumann, Frank O.	610
Sandhoff, Konrad	272	Schwanitz, Konrad	197
Sant, Tushar	333, 335	Schwarz, G.	178
Sarrao, John	495	Schwarzkopf, Olaf	240, 380
Sauer, Hermann	89	Schweitzer, D.	461
Sauer, J.	77	Schwentner, N.	66
Sayago, David	605	Sebald, Walter	243
Schade, U.	285, 552	Senge, M.O.	391
Schade, Ulrich	29, 355	Sergeeva, N.N.	391
Schadow, Theresa	579, 582	Shacham-Diamand, Yosi	359
Schäfers, F.	211, 446, 503, 508	Shaikhutdinov, S.	77
Schäfers, Franz	133, 216, 475	Shamin, Sergei	324
Schafranek, Robert	314	Shaporenko, Andrey	69, 600
Scharnweber, Dieter	260	Shatalova, Tatiana B.	105
Schartner, Karl-Heinz	453	Shayduk, Roman	598
Schattat, B.	481	Shekhah, Osama	108
Schaumann, Ina	222	Shikin, A. M.	568
Scheer, Michael	5	Shiozawa, Hide	495
Schefer, Senecio	187	Shkvarin, Alexei	324
Scheurer, Andreas	357	Shnitov, V.V.	202, 254
Schierle, E	546	Shtanov, Vladimir I.	100, 105
Schlappa, J	546	Siegbahn, H.	503, 508
Schlathölter, T.	254	Siegel, Stefan	214
Schlechter, Elke	186	Sierka, M.	77
Schleunitz, Arne	51, 63	Silaghi, S.-D.	285
Schley, P.	529	Silaghi, Simona	319, 616
Schlögl, R.	71, 94, 110	Silanes, Inaki	308
Schlögl, Robert	83, 89, 121	Sindu, John Louis	616
Schmidt, Frank	26	Sivkov, Danil	435
Schmidt, Norman	357, 593	Sivkov, Victor	432, 435
Schmidt, Philipp M.	573, 576	Sokaras, Dimosthenes	32
Schmidt, R.	534	Sokoll, Stefan	193, 195
Schmidt, Th.	162	Sorg, C.	400
Schmitz, D.	419, 558	Soriano, Leonardo	133
Schmitz, Sylvia	187	Spaltmann, D.	159
Schmoranzer, H.	422, 424, 428, 430	Spasova, Marina	80
Schmoranzer, Hans	453	Spehr, Till	319
Schneider, G. J.	165	Srivastava, P.	400
Schneider, Gerd	510	Stacchiola, D.	77
Schneider, Horst	408, 411	Stalder, Roland	186
Schnörch, P.	71, 94, 110	Stamm, Christian	456
Schnörch, Peter	83	Stamm, Manfred	355
Schnörch, Péter	89	Stefan, Seifert	516
Schock, H.W.	346	Steinrück, Hans-Peter	86
Schöll, A.	162	Stepina, N.D.	595
Schoenes, J.	526	Stolt, L.	508
Schönhense, Gerd	237, 549	Strack, Ch.	461
Schoenhense, Gerd	590	Streber, Regine	86
Schoeppe, Hendrik	14, 16	Streck, C.	346
Schörmann, J.	529	Strizhov, N.	258
Scholz,	18, 20, 23	Strunskus, Thomas	108, 113, 593, 620
Scholze, Frank	14, 18, 20, 23, 26	Stubbs, M.T.	279
Schondelmaier, Daniel	45, 48, 51, 57, 63	Stubbs, Milton T.	275
Schramm, Elisabeth	263	Stüber, M.	503
Schröter, H.	526	Stutzmann, Martin	173
Schubert-Bischoff, P.	481	Su, Yixi	521
Schüßler-Langeheine, C	546, 555	Süllow, S.	461
Schütz, G.	537	Süss, Björn	282
		Sukhorukov, Viktor	453

Svensson, S.	503, 508	Voronchihin, A.S.	417
T agirov, Lenar	394, 463	Voss, Sönke	364
Takagaki, Yuki	291	Vyalikh, D.V.	202, 254, 330, 417, 602
Tanaka, A	546	Vyalikh, Denis	432, 435
Tarasov, Andrey B.	105	Vyvenko, O	540
Tatchev, Dragomir	311, 327	W alter, A.	565
Taubitz, Christian	324, 498, 501	Walter, Antje D.	57
Tennant, D.A.	449, 558	Walter, Braun	516
Terfort, Andreas	69, 113	Wandelt, Klaus	624
Teschner, D.	71, 94	Wang, Fengli	475
Teschner, Detre	83, 89	Wang, Hongchang	475
Textor, Marcus	586	Wang, Hui	108
Thieme, Jürgen	190, 234, 289	Wang, Zhanshan	475
Thomas, Sylvia-Monique	183	Wanke, Martina	168
Thornagel, Reiner	16	Wassermann, Bernhard	117
Thünemann, Andreas	103, 378, 619	Watahiki, Tatsuro	613
Thünemann, Andreas F.	176	Weber, A.	346
Tieg, Carsten	441, 489	Weber, Nils	237, 590
Tietz, Thomas	282	Weber, R.	534
Tietze, T.	537	Weber, Ramona	126
Tilgner, Rainer	208	Weber, S.	526
Tinkham, Brad P.	613	Weidemann, G.	165
Tjeng, L H	546, 555	Weidemann, Gerd	260
Todorova, T.	77	Weidner, Tobias	69
Török, Szabina	39	Weinberg, G.	71
Tolkachev, N.	620	Weinelt, M.	534
Tomic, Stanko	403	Weiss, Roland	142
Tomkowicz, Z.	178	Weissenrieder, J.	77
Torres, Ricardo	349	Weller, Horst	179
Tränkenschuh, Barbara	86	Wende, H.	400
Tsurkan, Vladimir	501	Wendler, E.	128
Tzvetkov, George	593	Weniger, Christian	51
U lm, Gerhard	5, 11, 18, 20, 23, 29, 35, 39, 41	Werner, Christoph	319
Ulrich, V.	362	Werner, L.	422, 424, 428, 430
Ulrich, Volker	491, 493, 588	Werner, Lutz	453
Umbach, E.	162	Wernet, Philippe	51, 240, 380
Unger, W. E. S.	159	Wertheimer, M.R.	248
Unger, W.E.S.	248	Wesch, W.	128
Unterberger, Werner	605	Weschke, E	546
Usachev, D. U.	568	Weseloh, Gundolf	214, 219
V aldaitsev, Dima	237	Weser, M.	602
Valencia, S.	443	Wett, D.	607
van Buuren, Tony	514	Wieckowski, Andrzej	74
Varykhalov, A.	156, 568, 602	Wiedwald, Ulf	505
Vasiliev, Sergey Yu	100	Wilke, Max	187, 205
Vass, E.	71, 110	Willey, Trevor M.	514
Vass, E.M.	94	Winkler, Carsten	458, 610
Vass, Elaine	83, 89	Winnik, Françoise M.	103
Viefhaus, J.	367	Winter, Bernd	369
Vinogradov, A	540	Winter, Rudolf	302
Vinogradov, A.S.	391, 466, 560	Wirsing, Andreas	487, 519
Vinogradov, Alexander	435	Witte, F	97
Vogel, Marlene	579, 582	Witte, Gregor	620, 622
Vogt, C	97	Wöll, Christof	108, 113, 593, 620, 622
Vogt, Carla	222	Wolff, Timo	205
Vogt, Patrick	478	Wolter, A.U.B.	461
Volkmer, R. Esser N.	285	Woodruff, David	605
Vollmer, A.	451	Wootsch, Attila	89
Vollmer, Günter	260	Worch, Hartmut	260
von Issendorff, Bernd	579, 582	Woydt, M.	159
		Wüstefeld, Godehard	29

Wuilleumier, François	532
Wurth, Wilfried	179, 584
Y ashina, Lada V.	100, 105
Yurieva, E.A.	595
Z abel, Hartmut	394, 414, 463
Zabolotnyy, Volodymir	124
Zabolotnyy, Volodymyr	126, 495
Zafeiratos, S.	71, 94
Zafeiratos, Spiros	83, 89
Zahn, Dietrich R.T.	285, 478, 616
Zamudio-Bayer, Vicente	579, 582, 584
Zandt, Thorsten	225
Zarkadas, Charalambos	32
Zeeb, Markus	269
Zehl, G.	321
Zemlyanov, Dmitry	121
Zharnikov, Michael	69, 600
Zheludeva, S.I.	595
Zhilin, V.M.	330
Zhu, Jingtao	475
Zickler, Gerald A.	181
Ziemann, Paul	505
Zimina, A.	443
Zimmermann, Peter	426, 514, 532
Zimmermann, Ralf	263
Zittermann, Barbara	45
Zizak, I.	251, 299, 481
Zizak, Ivo	146, 291, 352, 438
Zverev, D.A.	466
Zyubin, Alexander S.	100

Keyword Index

(click on page number to open selected page)

(MoV)Ox	83	BPS	279
(MoVW)Ox	83	Br2	372
3-D XRF	219	broadband multilayers	475
3D micro-XRF	222	broadband polarizing elements	475
3d transition metal compounds	560	Ca F2	432
3s spectra	324	calcineurin	275
7T Wiggler	446	calcium	219, 275
A bsorption cross section	432	calcium hydroxide	93
activated adsorption	86	calibration	14, 41
adenine	254	calmodulin	275
adsorption	181	capacitance transient	540
aerosols	39	spectroscopy	
alanine	573	carbon coatings	349
alumina	302	carbon fibres	142
aluminium	228	carrier traps and	469
amino acids	369	recombination states	
anatase	93	catalysis	121, 568, 71
ancient chinese ceramic	32	catalyst	321, 74
Anderson model	602	catalytic intermediates	258
angle-resolved	193	CD characterization	26
angle-resolved photoemission	565	CD2BP2-GYF domain	288
anomalous scattering	302	cell adhesion	248
anomalous small angle X-ray	321	ceramics	302, 314
scattering		cerates	498
antarctica	39	CF4	491
antiferromagnetism	441	chalcopyrite	346
antiferromagnets	441	chalcopyrite solar cells	193
appearance energy	263	chalcopyrite surface corrosion	195
Ar	493	channelcut geometry	446
argon	367	charge order	546
ARPES	126	chemistry	80
artificial photosynthesis	282	chirality	573
ASAXS	302, 327	CIGS cells	508
at-wavelength	18	circular dichroism	573, 588
Au oxide	568	cluster	493, 568
auger	367	cluster deposition	584
auger spectra	491	cluster model	443
AZM	45	clusters	514, 519, 571
B ack-donation	391	CO	491
band bending	316	Co/FeMn/Cu(001)	558
band offset	316	Co2FeSi	408
band structure	168, 493, 529	cobalt	563, 579
BaTiO3	314	cobalt implantation	394
Bayes-Turchin	419	cobaltates	383
beam effect	173	cobaltites	324
beta-ketoacyl-ACP synthase	277	coherent X-ray	153, 406
beta-oxidation	277	coincidences	367
binding domain	275	computed tomography	165
biodegradation implant	97	confocal micro-XRF	222
biological materials	214	conversion	173
biology	282	CoO	441
biomolecular	285	copper	219
biophysics	190	copper cluster	451
biosensor	285	CoPt	179, 385
biphenyl synthase	279	core excitation	487, 519
BIS	279	core level excitation	119, 571
block copolymers	378	corrosion	302
blowing agent	352	covalent clusters	571
bone	260	critical slowing down	153
		cryogenic conditions	219
		cryogenic radiometer	11
		crystal optics	211, 446
		crystal structure	275

Cu(110)	573	FEM	26
cultural heritage	205	femtosecond	240
CuPc	330	femtosecond VUV pulses	380
CWA precursors	263	fenchone	588
cysteine	573	FePt	505, 80
Deep defect states	469	ferroelectric phase transition	150
defect spectroscopy	469	ferroelectricity	139
dense hydrous magnesium silicates	183	ferroelectrics	316
depth profile	620	FK506	275
depth profiling	438, 503	FKBP38	275
detector calibration	11, 8	fluorescence	130
detectors	14	fluorescence spectroscopy	487, 519
DFT calculations	330	fluorinated fullerenes	202
diamond	173, 514	foaming	352
dichroism	565	free clusters	362, 579, 582
dielectric function	529	fuel cell	199, 89
dielectric functions	150	fullerene	202, 349
dilute nitride semiconductors	403	fullerene derivatives	202
diluted ferromagnetic semiconductors	537	fundamental parameter	41
disorder	461	GaAs(001)	478
DNA bases	616	gadolinium	534
double crystal monochromator	446	GaMnAs	443
double photoemission	610	GaN	128
drug delivery	251	gas desorption	352
drug delivery system	299	Ge-analogue	183
duckweed	219	glass	327
dye molecule / solvent interaction	197	glasses	294, 311
dye sensitized solar cell	197, 508	goethite	92
Earth mantle	183	gold	327
EDXRD	346	growth	346
effective atomic number	246	growth process	327
elastic light scattering	117	GYF domains	288
electrochemical processing	74	H2O	493
electrodeposition	45	half-metallic ferromagnets	549
electron correlation	532	hard coatings	133
electron-electron coincidences	491	HAXPES	211, 472
electronic band structure	168	heavy fermions	495
electronic correlation	610	hematite	92
electronic relaxation	487	heteroepitaxy	305
electronic structure	156, 330, 391, 403, 466, 560, 579, 582	heterojunction	316
ellipsometry	526, 529	Heusler alloys	408, 411
emulsion	251	Heusler compounds	549
energy band dispersion	516	high energy photoemission	472
energy dispersive x-Ray reflectometry colloids template	586	high kinetic energy XPS	503
epitaxy	291, 598	high pressure analogue	183
ethene epoxidation	71	high pressure XPS	94
EUV	18, 20, 23, 26	high resolution	211, 446
EUV-PEEM	237	high-k dielectric	613
EUVL	237	high-order harmonic	240
EXAFS	128, 282, 419	high-order harmonic generation	380
exchange bias	441, 558	high-pressure XPS	121
explosives	263	high-resolution photoelectron spectroscopy	86
Fatty acid	277	HIKE	503, 508
fatty acid synthase	277	HIKE PES	211
Fe ₃ O ₄	546	hole states	498
		HOMO LUMO line up	197
		HTSC	126
		human nails	246
		hydrogen purification	89
		hydroxyapatite	343

fine structure		polymer micelles	251
NEXAFS	108, 113, 159, 173, 248, 305, 308, 330, 337, 39, 51, 560, 593, 71	polymeric materials	63
nickel	45	porphyrin	391
nickel phthalocyanine	466	Pr ₂ O ₃	613
nickelates	555	preferential CO oxidation	89
NiPc	540	proline-rich sequences	288
nitride semiconductor	529	prolyl cis/trans isomerase	275
nitrogen	435	propylene selective oxidation	83
non-volatile memory	316	protective coating	228
nucleobase	254	protonic conductors	498
		pulse plating	45
O ptical coating	228	Q uantification	222
optical constants	319	quantun well states	156
optoelectronics	469		
orbital order	546	R adiation damage	254
order-disorder transition	555	radiography	199
ordered thin films	516	radiometry	14, 16, 41
organic	305	radiometry wavelength shifter	5
organic films	319	rare earth magnanites	139
organic functionalisation	359	rare earth silicide	168
organic molecules	478	reference free	32
organic semiconductors	337, 516	reflection	563
organic superconductor	461	reflectometry	16, 18, 20, 228, 23
oscillator strength	432	refractories	302
oscillator strengths	435	relaxation dynamics	519
osteoporosis	260	residual stress	144, 148, 343
oxidation	121	resonant diffraction	555
oxide films	441	resonant inelastic X-ray	388
oxidic interfaces	441	scattering	
		resonant magnetic scattering	139
P -loop kinase	258	resonant photoemission	330, 443
p-reflectivity	228	resonant scattering	302
palladium	121	ringwoodite	183
particle trap	119	RIXS	443
Pb-Bi ₂ 201	523	room temperature	394, 463
PEEM	543	ferromagnetism	
pentacene	305	root	219
PEY	130	rotamase	275
phase separation	311	rotational structure	487
phenyl propanoid	279		
phosphoryl transfer	258	S AM	113, 173
photo ionization efficiency plot	263	SAXS	251, 299, 311, 327, 378
photoelectron correlation	458		
spectroscopy		SBA-15	181
photoelectron diffraction	359	scatterometry	26
photoelectron spectra	491	screening	316
photoelectron spectroscopy	254, 362, 369, 417, 532	secondary metabolism	279
photoemission	314, 324, 466, 484, 514, 602	selenium	571
photoemission spectroscopy	359, 472, 74	self absorption	130
photoionization	372, 588	self-assembled monolayers	308, 600, 69
photovoltaics	469	semiconductors	316
phthalocyanine	391	sexiphenyl	305
plasma cleaning	505	sexithiophene	305
plasma polymer	248	shape memory	411
plasma sprayng	343	shed snake skin	299
polarization	16, 20, 23	Si 2p	417, 540
polymer	355	Si bonded wafer	540
		Si(100)	576
		silicate	302
		silicide nanostructures	168
		silicides	417
		silicon	417

silicon stamp	63	thin film heterostructures	616
silver	71	thin film nanocomposites	503
single molecule magnets	364	thin film solar cells	508
skin	289	thin films	438, 602
small angle X-ray scattering	321, 481	thio acetate	113
small-angle scattering	302	thiol	113
smart surface	248	thymine	254
SMY2-GYF domain	288	TiH ₂	352
sodium cobaltate	449	time-resolved photoemission	534
soft X-ray diffraction	546	time-resolved spectroscopy	380
Soft X-Ray Dispersive electron	162	TiO ₂ gap state density	197
spectroscopy CFS CIS		titanium	582
resonant Auger Raman		titanium fluorides	560
NEXAFS		TM-doped ZnO	394, 463
soil science	190	TNCQ	388
solid liquid interface	197	tomography	510
solid-phase reaction	417	transistion probability	41
sorbus aucuparia	279	transition metal clusters	579, 582, 584
SPI TOF MS	263	transmission photodiode	8
spinel	501	transparent conductive coating	469
spintronics	291, 598	TRAPP	266
spiromolecules	319	tribo chemistry	159
spontaneous polarisation	316	TXRF	39
SrTiO ₃	314	U ltrafast dynamics	456
stepped surfaces	86	UNCD	173
stereo imaging	234	uncompensated spins	558
stilbene	576	V alence states	324, 501
stratified material	222	vanadia/alumina catalyst	94
stratum corneum	289	vanadium	582
stripes	555	vesicular transport	266
structural genomics	258	vibrational and Rydberg	435
structure analysis	355	transitions	
structure-building interactions	69	vicinal surface	156, 568
structuring	45	VUV ellipsometry	616
styrol butadien rubber	165	VUV photoabsorption	372
sum rules	537	VUV-spectroscopic	319
superconductivity	495	ellipsometry	
superlattice formation	449	W aste management	294
superparamagnetism	171	water	51
supramolecular chemistry	308	water management	199
surface acoustic wave	397	waveguide	438
surface electrochemistry	624	wavelength-dispersive	41
surface engineering	359	X -ray absorption	130, 294, 324, 383, 466, 484, 498, 501, 540
surface magnetism	408	X-ray absorption analysis	205
surface oxide	568	X-ray absorption spectroscopy	133, 391, 441, 579, 582
surface physics	458	X-ray crystallography	266
sustainability	205	X-ray diffraction	397, 449, 461
switchable mirror	526	X-ray emission spectroscopy	193, 195
synchrotron laue contrast	208	X-ray fluorescence analysis	205, 219, 32
radiograph		X-ray imaging	165
synchrotron radiation	202	X-ray magnetic circular	171, 456
synchrotron radiation	29	dichroism	
instrumentation		X-ray microscopy	234, 289, 510
Synchrotron Radiation	35	X-ray photoelectron	316
Instrumentation		spectroscopy	
T erahertz radiation	29	X-ray resonant magnetic	394, 463
ternary and multinary	469	scattering	
semiconductors			
tethering	266		
TGF-beta	243		
TGS crystals	150		
thin film	144, 146, 148, 285, 355		

X-ray spectromicroscopy	190
X-ray transmission	246
X-rays	211
XAFS	438
XANES	130, 205, 349, 432, 435, 451
XAS	282, 523, 537, 83
Xe/Cu(111)	458
xenon	362
XEOL	119
XES	41
XMCD	179, 385, 408, 411, 537, 543, 558, 80
XMCD-PEEM	549
XMLD	563
XPCS	153
XPS	173, 451, 620, 71
XRF	205, 32
XSW	438
Y BCO	126
ytterbium	602
Z irconia	302
ZnO	484, 537
ZrH2	352